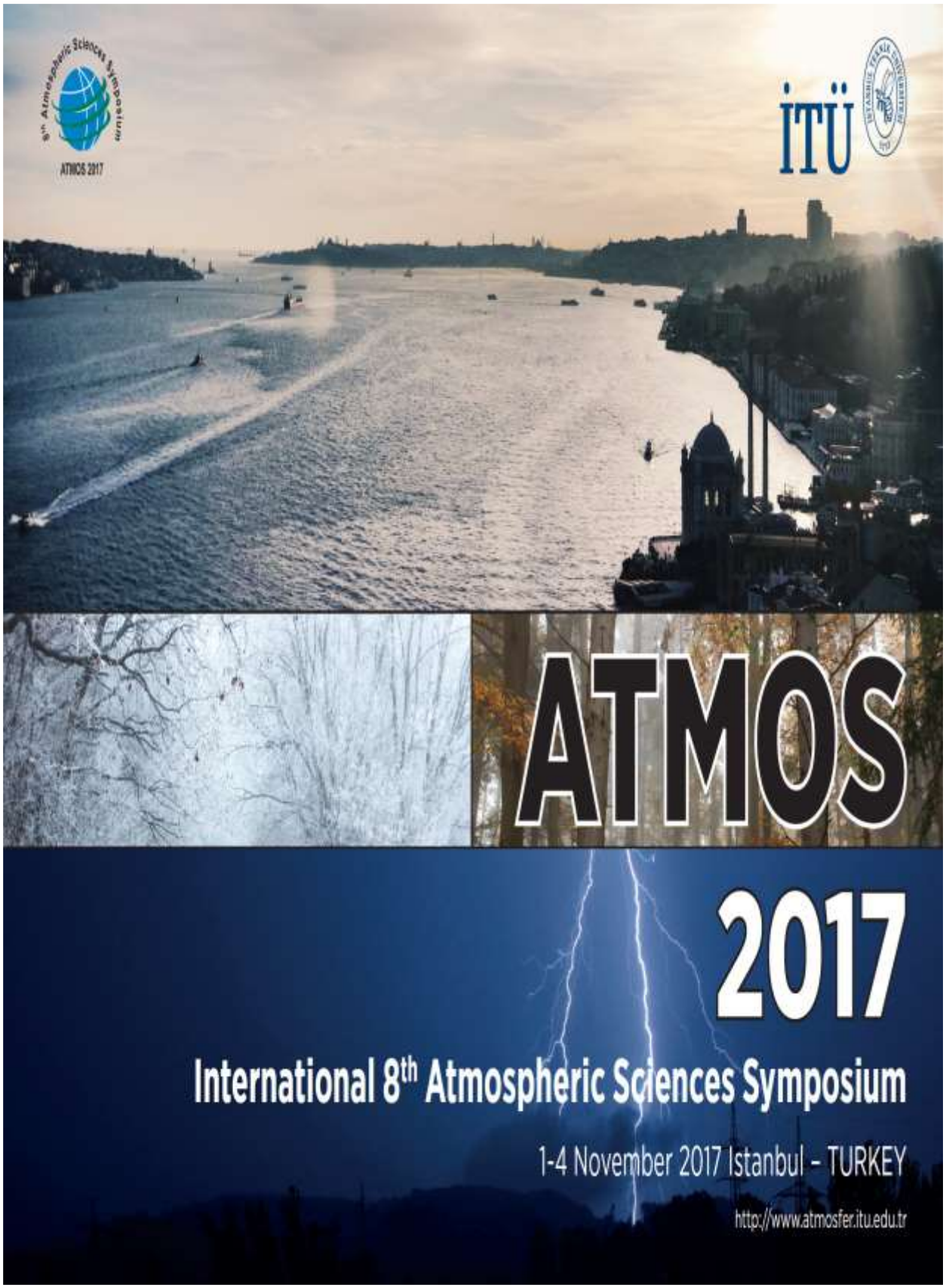
8th Atmospheric Sciences Symposium
ATMOS 2017
İTÜ
ATMOS
2017
International 8th Atmospheric Sciences Symposium
1-4 November 2017 Istanbul - TURKEY
http://www.atmosfer.itu.edu.tr

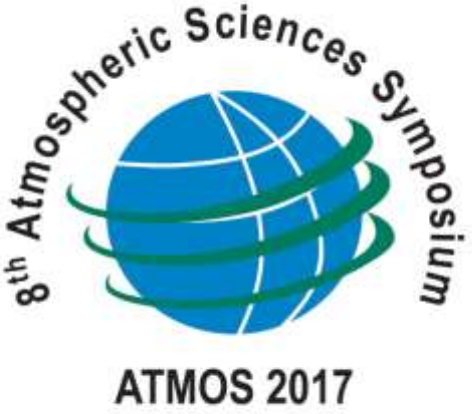
8th Atmospheric Sciences Symposium
ATMOS 2017

PREFACE

This 8th Atmospheric Sciences Symposium; ATMOS2017 built upon the series that began at Istanbul Technical University, Department of Meteorological Engineering in 1981. Subsequent meetings have been held in 1991; 2003; 2008; 2011; 2013 and 2015 in Istanbul, Turkey.

And it is not just enough to produce scientific data for people but it is also necessary to process the data and share the results of those data as a source for students and a starting point for all researchers, users and policy makers, it is a treasure for mankind.

We are very greatful and thankful to all the valuable researchers, session chairs and all participants who have contributed to ATMOS2017 from all around the world, whose valuable contributions made this event possible.

This e-Proceedings present a collection of 112 papers presented at the Symposium. The main themes covered in the Symposium include;

Agricultural and Forest Meteorology
Air Pollution and Modeling
Air Quality and Modeling
Air-Sea Interactions
Atmospheric Boundary Layer
Atmospheric Dynamics
Atmospheric Environment
Atmospheric Physics
Atmospheric Radiation
Aviation Meteorology
Biometeorology, Medical Meteorology
Causes of Climate Change
Chaos and Non-Linear Dynamics
Climate Change Impacts
Climate Change and Modeling
Climatology
Data Analysis
Extreme Weather Events (flood, storm, avalanche, drought …)
Hydrology and Hydrometeorology
Maritime Meteorology
Meteorological Disasters
Micrometeorology, Mesometeorology
Numerical Waether Prediction
Physics of Cloud and Precipitation
Remote Sensing in Atmospheric Sciences
Renewable Energy Sources
Solar and Wind Energy
Stratospheric Ozone
Solar and Climate System Interaction
Transportation Meteorology
Upper Atmosphere, Ionosphere Magnetospheric Physics
Urbanisation Meteorology
Water Resources and Management
Weather Analysis, Prediction and Modeling

We would like to thank Rectorate of Istanbul Technical University and the Deanship of Faculty of Aeronautics and Astronautics for supporting ATMOS2017. We would like to express our appreciation to Organizing Committee Members, Steering Committee Members and Scientific Committee Members for their precious support. Last but not least we would like to thank Turkish State Meteorological Service, Union of Chambers of Turkish Engineers and Architects; Chamber of Meteorological Engineers for their valuable support.

Editors

Dr. Orhan ŞEN - Dr. Ceyhan KAHYA
December 2017

ISBN: 978-975-561-490-8

Scientific Committee

Dr. Orhan ŞEN (Chair), Istanbul Technical University, Turkey
Dr. Abbasnia MOHSEN, University of Sistan and Baluchestan, Iran
Dr. Ahmet ARISOY, Istanbul Technical University, Turkey
Dr. Ahmet Duran ŞAHİN, Istanbul Technical University, Turkey
Dr. Ahmet ÖZTOPAL, Istanbul Technical University, Turkey
Dr. Alexander BAKLANOV, World Meteorological Organization, Switzerland
Dr. Alexander MAHURA, Danish Meteorological Institute, Denmark
Dr. Barış ÖNOL, Istanbul Technical University, Turkey
Dr. Barış ÇALDAĞ, Istanbul Technical University, Turkey
Dr. Ceyhan KAHYA, Istanbul Technical University, Turkey
Dr. Deniz DEMİRHAN BARI, Istanbul Technical University
Dr. Doğan KANTARCI, Istanbul University, Turkey
Dr. Doğanay TOLUNAY, Istanbul University, Turkey
Dr. Don COLLINS, Texas A&M University, USA
Dr. Elçin TAN, Istanbul Technical University, Turkey
Dr. Gürdal TUNCEL, Middle East Technical University, Turkey
Dr. Hasan TATLI, Çanakkale Onsekiz Mart University, Turkey
Dr. Hüseyin TOROS, Istanbul Technical University, Turkey
Dr. İsmail GÜLTEPE, Environment Canada, Canada
Dr. Josef EITZINGER, University of Natural Resources and Applied Life Sciences, Austria
Dr. Julia PALAMARCHUK ,FMI, Finland
Dr. Mehmet KARACA, Istanbul Technical University, Turkey
Dr. Mehmet Talad ODMAN, Georgia Institute of Technology, USA
Dr. Meral DEMİRTAŞ, Ondokuz Mayis University, Turkey
Dr. Mikdat KADIOĞLU, Istanbul Technical University, Turkey
Dr. Mykhaylo GRYGALASHVYLY, Leibniz-Institute of Atmospheric Physics, Germany
Dr. Ömer Lütfi ŞEN, Istanbul Technical University, Turkey
Dr. Robert BORNSTEIN, San Jose State University, USA
Dr. Roelof BRUINTJES, NCAR, USA
Dr. Sam Miller, Plymouth State University, USA
Dr. Sema TOPÇU, Istanbul Technical University, Turkey
Dr. Sergey IVANOV, Odessa State Environmental University, Ukraine
Dr. Sevinç SIRDAŞ, Istanbul Technical University, Turkey
Dr. Sibel MENTEŞ, Istanbul Technical University, Turkey
Dr. Tayfun KINDAP, Istanbul Technical University, Turkey
Dr. Yurdanur S. ÜNAL, Istanbul Technical University, Turkey
Dr. Zafer BOYBEYİ, George Mason University, USA
Dr. Zerefşan KAYMAZ, Istanbul Technical University, Turkey

Steering Committee

Dr. Orhan ŞEN (Chair), Istanbul Technical University
Dr. Ceyhan KAHYA, Istanbul Technical University
Dr. Hüseyin TOROS, Istanbul Technical University
Dr. Zafer ASLAN, Istanbul Aydın University
M.Sc. Deniz H. DİREN, Istanbul Technical University
M.Sc. Evren ÖZGÜR, Istanbul Technical University
Faruk ŞANLI, The Chamber of Meteorological Engineers
A. Alperen KARATAŞ, Istanbul Technical University
Gülsüm Ş. SOMUNCU, Istanbul Technical University
Zeki ÇELİKBAŞ, Istanbul Technical University

Organizing Committee

Dr. Orhan ŞEN (Chair), Istanbul Technical University
Dr. Ahmet Duran ŞAHİN, Istanbul Technical University
Dr. Zafer ASLAN, Istanbul Aydın University
İsmail GÜNEŞ, Turkish State Meteorological Service
Oğuz CAN, General Directorate of Renewable Energy
Ahmet KÖSE, The Chamber of Meteorological Engineers
Faruk ŞANLI, The Chamber of Meteorological Engineers
Dr. Hüseyin TOROS, Istanbul Technical University
Dr. Mikdat KADIOĞLU, Istanbul Technical University
Dr. Ceyhan KAHYA, Istanbul Technical University
Dr. Sema TOPÇU, Istanbul Technical University
Dr. Sevinç SIRDAŞ, Istanbul Technical University
Dr. Yurdanur S. ÜNAL, Istanbul Technical University
Dr. Barış ÖNOL, Istanbul Technical University
Dr. Sibel MENTEŞ, Istanbul Technical University
M.Sc. Evren ÖZGÜR, Istanbul Technical University

TABLE OF CONTENTS

CHANGE AND EREMOLOGY ASPECTS

Donald Gabriels
Dept. of Soil Management, UNESCO Chair on Eremology
Ghent University, Belgium, donaldgabriels@gmail.com

Climate change is a change in the mean of the climate system when considered over long periods of time; hence in general more than a few decades. The term "climate change" is often used to refer to *global warming. Global warming* refers to surface temperature increases while *climate change* includes global warming and also everything else that can affect the increase in *greenhouse gasses levels.*

Climate change is sometimes linked to a change in ***weather*** conditions. This involves rainfall (excess or lack), temperature (mainly rising) and also wind (hurricanes, typhoons, cyclones…) ***Eremology***, derived from the greek word '*eremos'*,which means 'desert', refers to the study of deserts and of the processes of desertification.

Desertification is land **degradation in drylands**, including the arid, semi-arid and dry subhumid areas. Those areas are defined according to the 'Aridity Index' (AI) which illustrates the relation between evapotranspiration and precipitation. When the ratio AI is between 5 and 65% the area is assumed to be part of the drylands.

Land degradation is the decline of productivity of land due to:

-**Soil degradation**: erosion by water, erosion by wind, chemical deterioration and physical deterioration
-**Vegetational degradation**: reduction of biodiversity

The UNESCO Chair on Eremology was inaugurated in 2008 at Ghent University, Belgium as a result of the already long cooperation between UNESCO and ICE, the International Centre for Eremology.

The research work was and still is focused on the study of the processes of desertification and ways to combat it, based on the three Rio 1992 UN Conventions: (1) Convention on Biodiversity, (2) Convention on **Climate Change**, and (3) Convention on **Combating Desertification.**

The UNESCO Chair on Eremology puts special emphasis on Combating Desertification, taking into account the 2006 Tunis Declaration: The UNESCO Research Priorities on Desertification. Specific attention is thereby given to sustainable soil and water management.

At the time of the establishment of the UNESCO Chair on Eremology, the UNESCO's Division of Ecological and Earth Sciences with its Man and the Biosphere (MAB) Programme in direct collaboration with the United Nations University - Institute for Water, Environment & Health (UNU-INWEH). The funding, provided by the Flemish Government of Belgium, implemented a 6 year's (2007-2013) project entitled **SUMAMAD** (Sustainable Management of Marginal Drylands), devoted to a better land and water management in arid and semi arid areas. Special attention is given to improve the livelihood of the populations living in these drylands.

Countries as Bolivia, Burkino Faso, Tunisia, Egypt, Jordan, Pakistan, India, Iran and China were involved in the SUMAMAD project. Dryland management was applied in sites mainly situated in UNESCO-MAB Reserves.

Two projects will be discussed in detail and lessons learned from succesfull and less successful results will be brought forward.

Tunisia: Institut des Régions Arides. Zeuss-Koutine Watershed and Bou Hedma Reserve, with its **Projects**: *Water harvesting and groundwater recharge*, and *Reforestation with Acacia trees*
Iran: Fars Research Center for Agriculture and Natural Resources. Gareh Bygone Plain, with the **project**: *Flood water spreading.*

THE INFLUENCE OF SPRING ARCTIC OSCILLATION ON THE SUBSEQUENT ENSO AND ITS INTERDECADAL CHANGES IN REANALYSIS DATA AND CMIP5 MODELS

When Chen[1], Shangfeng Chen[1], and Bin Yu[2]

[1]Center for Monsoon System Research, Institute of Atmospheric Physics, Chinese Academy of Sciences, Beijing, China

[2]Climate Research Division, Environment and Climate Change Canada, Toronto, ON, Canada

cw@post.iap.ac.cn

The influence of the spring Arctic Oscillation (AO) on El Niño-Southern Oscillation (ENSO) has been demonstrated in several recent studies. This talk firstly presents the physical process of the influence of AO on ENSO using the NCEP/NCAR reanalysis data. We focus on the formation of the westerly wind burst in the tropical western Pacific, and examine the evolution and formation of the atmospheric circulation, atmospheric heating, and sea surface temperature (SST) anomalies in association with the spring AO variability. The spring AO associated circulation anomalies are supported by the interaction between synoptic-scale eddies and the mean-flow and its associated vorticity transportation. Surface wind changes may affect surface heat fluxes and the oceanic heat transport, resulting in the SST change. The AO associated warming in the equatorial SSTs results primarily from the ocean heat transport in the face of net surface heat flux damping. The tropical SST warming is accompanied by anomalous atmospheric heating in the subtropical north and south Pacific, which sustains the anomalous westerly wind in the equatorial western Pacific through a Gill-like atmospheric response from spring to summer. The anomalous westerly excites an eastward propagating and downwelling equatorial Kelvin wave, leading to SST warming in the tropical central-eastern Pacific in summer-fall. The tropical SST, atmospheric heating, and atmospheric circulation anomalies sustain and develop through the Bjerknes feedback mechanism, which eventually result in an El Niño-like warming in the tropical eastern Pacific in winter.

We further reveal that the AO-ENSO relationship experienced a pronounced interdecadal shift using the HadISST, HadSLP2r, ERSSTv3b and NCEP-NCAR reanalysis data for the period 1948-2012. The spring AO influence on the subsequent ENSO is weak before 1970; while the influence becomes strong and statistically significant in the 1970s and 1980s. The spring AO associated circulation, SST and precipitation anomalies between the PRE (1949-1968) and POST (1970-1989) epochs are then compared to explore this interdecadal change of the AO-ENSO relationship. The spring AO-related anomalies of atmospheric circulation over the North Pacific mid-latitudes, cyclonic circulation over the subtropical western-central Pacific, and westerly winds in the tropical western-central Pacific are found to be stronger in the POST epoch than in the PRE epoch. The intensity of spring Pacific synoptic-scale eddy activity is seen to experience a significant interdecadal change around the early-1970s from a weak regime to a strong regime. Thus the strength of synoptic-scale eddy feedback to the low frequency flow becomes stronger after 1970. In the POST epoch, the strong synoptic-scale eddy feedback provides a favorable condition for the formulation of the spring AO-related cyclonic circulation and westerly wind anomalies over the western North Pacific. The tropical SST, precipitation and atmospheric circulation anomalies sustain and develop from spring to winter through the positive Bjerknes feedback, leading to an El Niño-like warming in the tropical central-eastern Pacific in the following winter.

Finally, the influence of boreal spring AO on the subsequent winter ENSO is examined using 15 climate model outputs from the Coupled Model Intercomparison Project Phase 5 (CMIP5). Results show that, out of the 15 CMIP5 models, CCSM4 and CNRM-CM5 can well reproduce

the significant AO-ENSO connection. These two models capture the observed spring AO related anomalous cyclone (anticyclone) over the subtropical western-central North Pacific, and westerly (easterly) winds over the tropical western-central Pacific. In contrast, the spring AO-related anomalous circulation over the subtropical North Pacific is insignificant in the other 13 models, and the simulations in these models cannot capture the significant influence of the spring AO on ENSO. Further analyses indicate that the performance of the CMIP5 simulations in reproducing the AO-ENSO connection is related to the ability in simulating the spring North Pacific synoptic eddy intensity and the spring AO's Pacific component. Strong synoptic-scale eddy intensity results in a strong synoptic eddy feedback on the mean flow, leading to strong cyclonic circulation anomalies over the subtropical North Pacific, which contributes to a significant AO-ENSO connection. In addition, a strong spring AO's Pacific component and associated easterly wind anomalies to its south may provide more favorable conditions for the development of spring AO-related cyclonic circulation anomalies over the subtropical North Pacific.

Keywords*: AO, ENSO, Interdecadal change, CMIP5, synoptic-scale eddy*

References

Chen, S., B. Yu, W. Chen, 2014a: An analysis on the physical process of the influence of AO on ENSO. *Clim. Dyn.*, 42, 973-989, DOI: 10.1007/s00382-012-1654-z.

Chen, S., W. Chen*, and B. Yu, 2014b: Asymmetric influence of boreal spring Arctic Oscillation on subsequent ENSO. *J. Geophys. Res. Atmos.*, 119, 11135-11150, doi: 10.1002/2014JD021831.

Chen, S., B. Yu, W. Chen*, 2015: An interdecadal change in the influence of the spring Arctic Oscillation on the subsequent ENSO around the early 1970s. *Clim. Dyn.*, 44, 1109-1126, Doi: 10.1007/s00382-014-2152-2.

Chen, S., W. Chen*, and B. Yu, 2017a: The influence of boreal spring Arctic Oscillation on the subsequent winter ENSO in CMIP5 models. *Clim. Dyn.*, 48, 2949-2965, doi:10.1007/s00382-016-3243-z.

CONTEMPORARY DEVELOPMENT IN APPLICATION OF WAVELET AND FRACTAL METHODS TO ATMOSPHERIC SCIENCE-I

A.H. Siddiqi
Sharda University, Greater Noida, UP, India
siddiqi.abulhasan@gmail.com

Abstract
Orthonormal wavelets and fractals have been used to study problems of atmospheric science, see for example work by Aslan, Manchanda, Siddiqi, Mousavi, Rehman, Yudytskiy, Velasquez valle etal cited in this paper. Our main goal is to discuss the possibility of extending these results to wavelet frames in general and particularly to tight frames and applications of these techniques to new class of data for example seismic data or meteorological data of countries like India, Turkey, Saudi Arabia and Oman.

Introduction
Aslan (Turkey) and her research collaborators, Siddiqi (India) and his research collaborators including Manchanda and Bhardwaj, Langston (US), Korvin (Mexico) and his collaborators etal have studied applications of wavelet and fractal methods to atmospheric science, see references [4,7,9,10,14,16-18, 20, 37, 38, 50, 51, 60, 62, 64,68, 69]. In 2016, Krivoshein Protasov and Skopina [30] have published an interesting monograph on "Multivariate Wavelet Frames". Wavelet frames, (framelets) are actively replacing orthonormal wavelets in signal processing including compression and transmission of information. This replacement is very effective in the image recovery from incomplete observed data, including the tasks of imprinting and image video enhancement. In the damaged and noisy samples, application of wavelet methods based on frames is more advanced due to the redundancy of frame systems.
Multivariate wavelet systems with matrix dilations have been increasingly used for digital processing of multidimensional signals such as images, videos, tomography and seismic and other signals. However multivariate wavelet frames over R^+ are yet to be studied. Application of multivariate wavelets to weather forecasting and prediction of earthquake are challenging problems to be solved.

In this talk we plan to discuss basic concepts of orthonormal wavelets, fractals application of wavelet fractal method to prediction of climate, wavelet frame and application of wavelet frame to prediction of climate and occurrence of earthquake.

Wavelet and Fractal Methods for Analysis of Meteorological data
Methods of Statistics and Fourier Analysis: were used to analyze time series before invention of wavelet and fractal methods till eighties. Study of wavelet and Fractal Methods for time series begin in mid nineties. A few standard references are:

R. H. Shumway & D. S. Stoffer, [54], A. Arneodo, [2], R. Gencay, F. Seluk [24], Paul S. Addison [1].
Wavelet Methods, specially orthoronormal wavelet systems have been used for:
Detecting discontinuity and breakdown points, Detecting long term evolution , Detecting self similarity, Identifying pure frequencies, Suppressing signals, De-Noising signals, and Compressing signals.

Wavelets – Categorization

1. Analytical or Numerical 2, Real or Complex, 3. Symmetric, antisymmetrical, asymmetric (e.g. db) 4. Compactly supported or not compact. 5. Causal, Non-causal wavelets 6. Do they have efficient computation algorithms such as FWT. 7. Wavelets with special features e.g. complex wavelet with real part (high freq) and complex part carry low frequency content. 8. Maximally flat wavelets (Flatness of spectrum, Rate of decay at ω=pi and origin). 9. Have Orthogonal, Biorthogonal analysis system.

Common Wavelets

Old Wavelets

Haar function, Gabor function and wavelet(1D,2D) , Morlet wavelets, Shannon function, 1st and 2nd Derivatives of Gaussian function (mexican hat), Truncated and lapped Sine or Cosine functions, Recent Wavelets, Db Wavelets (orthogonal, biorthogonal), Coiflets, Symlets, Biorthgonal wavelets, Mallat Wavelet (1D,2D), Bathlets, Curvelets, Ridgelets, Meyer wavelets, Banana Wavelets, Your Wavelets.

The Haar Wavelet

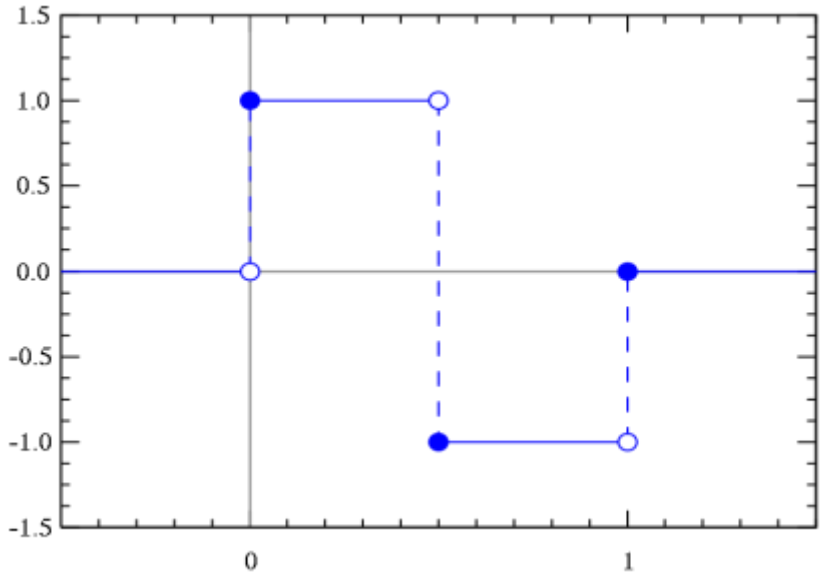

Daubechies Wavelets

The Daubechies wavelets, based on the work of Ingrid Daubechies, are a family of orthogonal wavelets defining a discrete wavelet transform and characterized by a maximal number of vanishing moments for some given support. With each wavelet type of this class, there is a scaling function (called the *father wavelet*) which generates an orthogonal multi resolution analysis. The Daubechies wavelets are not defined in terms of the resulting scaling and wavelet functions; in fact, they are not possible to write down in closed form.

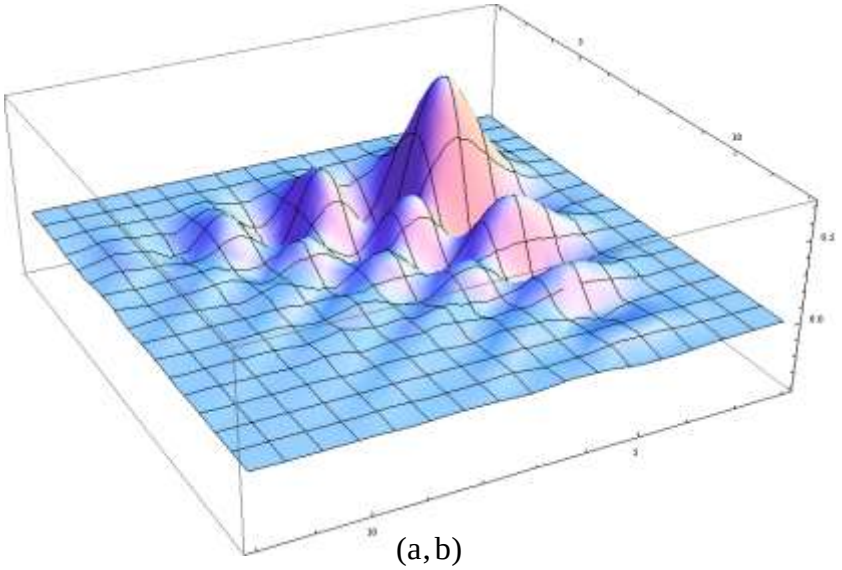

(a, b)

Remark 1.1:
Function may represent signals that vary with time, for example music, fluctuation of stock market or temperature variation of a particular place or heart beats. Variable ξ in $\hat{\psi}(\xi)$ is called frequency which is measured in hertz or cycles per second. Strictly speaking frequency is the inverse of time and in the case of functions (signals) depending on space, frequency is often termed as wave numbers, the inverse of space. It may be noted that a function and its Fourier Transform are two faces of the same information. The function displays the time information and hides the information about frequencies while the Fourier Transform displays information about frequencies and hides the time information. The energy of two signals represented by ψ and hat of ψ is the same, that is, it is clear that the wavelet transform.

Detection of Singularities
(rapid change of frequency)

coiflet wavelet order 5.

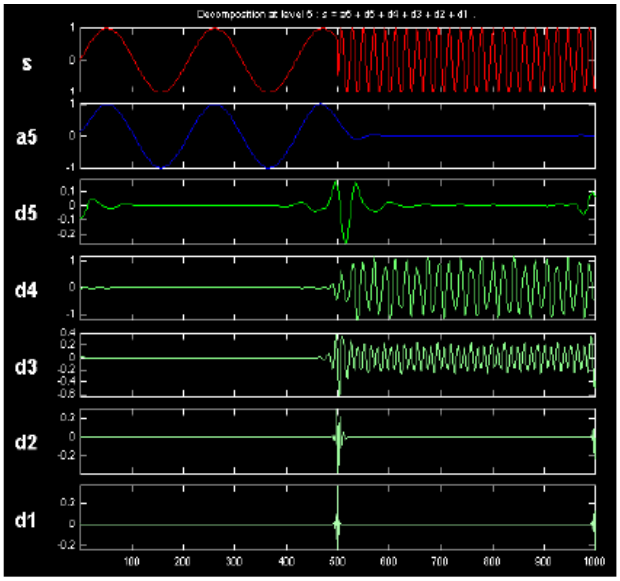

Detection of Singularities (singularity)

Two close discontinuities *Daubechies* order 2.

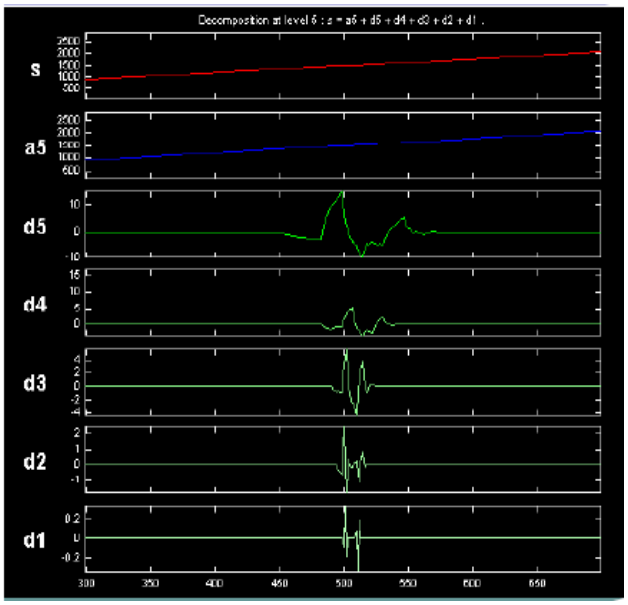

Scalogram

Scalogram is the graphical representation of the square of the wavelet coefficients verses wavelength. Scalogram shows more details and detects low frequency cyclicity of the signal.

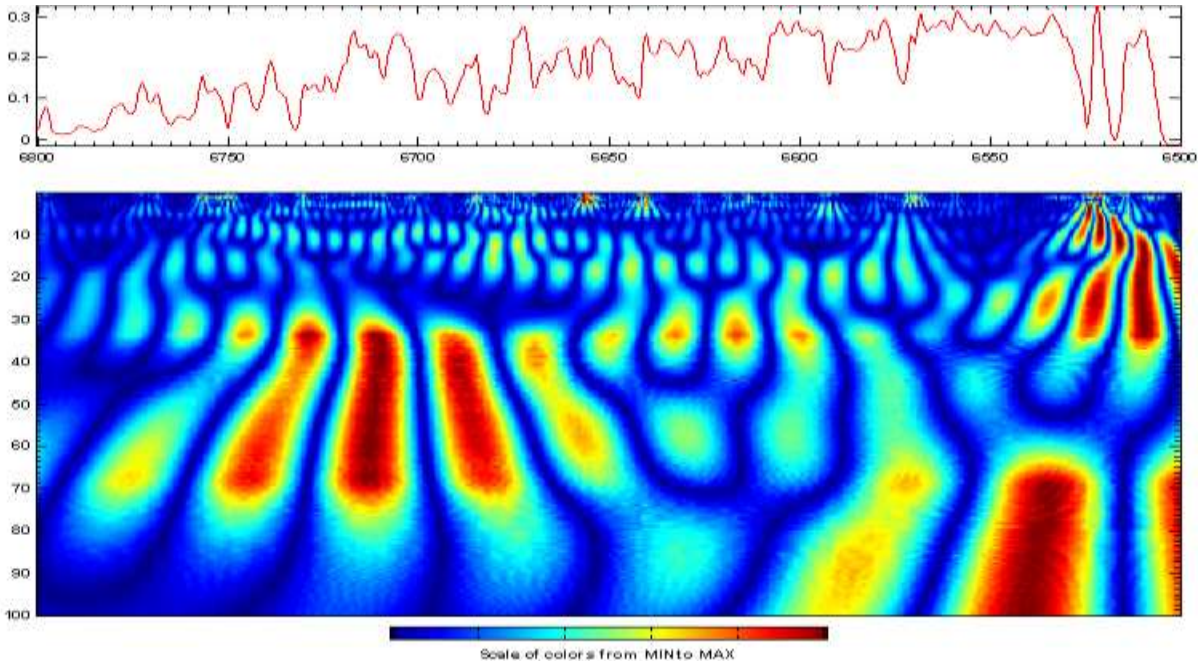

Scalogram of log- ARAMCO OIL FIELD

Wavelets and Fractals

Sharp signal Transitions create large amplitude wavelets coefficients.Singularities are detected by following across scales the local minimum of the wavelet transform. In images, high amplitude wavelet coefficients indicate the position of edges, which are sharp variations of the image intensity. Different scales provide the contours of image structures of varying sizes. Such multiscale edge detection is particularly effective for pattern recognition in computer vision. Introduction to Fractals and their Applications of Fractals comes from Latin word Fractus meaning broken, describe objects that are too irregular to fit into traditional geometrical settings. Fractals occur as graphs of functions. Indeed various phenomena display fractal features when plotted as functions of time. Examples include atmospheric pressure, labels of reservoir and prices of the stock market, usually when recorded over fairly long time spans.

Wavelet Transform is a Microscope /Prism

The zooming capability of the wavelet transform not only locates isolated singular events, but can also characterize more complex multi-fractal signals having non-isolated singularities. The Wavelet Transform takes advantage of multifractal self-similarities, in order to compute the distribution of their singularities. This singularity spectrum is used to analyze multifractal properties. Signals that are singular at almost every point called multi-fractals are also encountered in the maintenance of economic records, physiological data including heart records, electromagnetic fluctuations in galactic radiation noise, textures in images of natural terrain, variations of traffic flow, etc.

The daily average values of the following meteorological parameters were obtained from Presidency of Meteorology and Environment (PME)

- temperature
- pressure
- precipitation
- relative humidity
- wind speed

These five parameters determained climatic condition of a place. Fractal and wavelet methods are very useful for analyzing time series of these parameters, see reference 50, 51 and 64.

Fractal Dimension and predictability:

$$D = 2 - H$$

If the fractal dimension D for the time series is 1.5, there is no correlation between amplitude changes corresponding to two successive time intervals. Therefore, no trend in amplitude can be discerned from the time series and hence the process is unpredictable. However, as fractal dimension decreases, to 1, the process becomes more and more predictable as it exhibits "persistence".

Predictably indices (denoted by PI_T, PI_P and PI_R resp.) for temperature, pressure, and precipitation are defined as follows:

$$PI_{T=}2\left|D_T - 1.5\right|; PI_P = 2\left|D_P - 1.5\right|, PI_R = 2\left|D_R - 1.5\right|$$

Concepts of fractal and multifractal and their relevance to real world systems were introduced by Benoit B.Mandeldort, for updated references and interesting introduction of the theme we refer to Mandelbort and Richard L. Hudson [36]. In many real world systems, represented by time series, understanding of the pattern of singularities that is graph of points at which time series changes abruptly; is quite challenging task. The time series of rainfall data are usually fractal or multifractal.

Wavelet Frames

Riesz Bases and Frames.

In this section, we introduce and discuss an important notion for the wavelet theory, namely the notion of the Riesz basis for a Hilber space, which is a special case of the notion of frame and generalizes the notion of orthogonal basis preserving its most essential properties.

Let us denote by ℓ_2 the Hilbert space of sequences of complex numbers $c=\{c_n\}_{n=1}^{\infty}$ such that $\sum_{n=1}^{\infty}|c_n|^2<\infty$ with the scalar product $\langle c^1,c^2\rangle:=\sum_{n=1}^{\infty}c_c^1c_n^2$,where $c^1=\{c_n^1\}_{n=1}^{\infty},c^2=\{c_n^2\}_{n=1}^{\infty}$ and $c^1,c^2\in\ell_2$.

Definition 5.1 Let H be a Hilbert space. A system $\{f_n\}_{n=1}^{\infty}\subset$H is called *a Riesz system* with constant A, B > 0 if for any $c=\{c_n\}_{n=1}^{\infty}\in\ell_2$ the series $\sum_{n=1}^{\infty}c_n f_n$ converges in H and

$$A\|c\|_{\ell_2}^2\le\left\|\sum_{n=1}^{\infty}c_n f_n\right\|_H^2\le B\|c\|_{\ell_2}^2.$$

(5.1)

If a Riesz system is a basis then it is called a Riesz basis.

Theorem 5.1

Let H be a Hilbert space, and let $\{f_n\}_{n=1}^{\infty}$ *be a Riesz system in H with constatns A, B.Then,*

(*i*) $\{f_n\}_{n=1}^{\infty}$ *is a Riesz bais for the space*

$$v:=\left\{f=\sum_{n=1}^{\infty}c_n f_n,\ \sum_{n=1}^{\infty}|c_n|^2<\infty\right\};$$

(ii) v =span$\{f_n,n\in N\}$;

(iii) *For any element* $f\in v$, *the following inequality holds*:

$$A\|f\|_H^2\le\sum_{n=1}^{\infty}|\langle f,f_n\rangle|^2\le B\|f\|_H^2.$$

(5.2)

Definition 5.2. Let H be Hilbert space. A system $\{f_n\}_{n=1}^{\infty}\subset H$ is called *a frame,* if there exist constants $A,B>0$ such that the inequality

$$A\|f\|^2\le\sum_{n=1}^{\infty}|\langle f,\ f_n\rangle|^2\le B\|f\|^2$$

Hold for any $f\in H$.

The constants A and B are called the upper and lower frame bounds, respectively. If the frame bounds coincide. Then the frame is said to be *tight.* Tight frames with unit bounds $(A=B=1)$ are called Parseva's frames, and sometimes, they are also called orthogonal-like systems, which by the following statement.

Proposition *A.*

For a system $\{f_n\}_{n=1}^{\infty} \subset H$ *to be a Parseval's frame, it is necessary and sufficient that*

$$f = \sum_{n=1}^{\infty} \langle f, f_n \rangle f_n,$$

for any $f \in H$.

Corollary *If a Parseval's frame is a basis, then this basis is orthonormal.*

REFERENCES

Addison, P.S., The Illustrated Wavelet Transform Handbook: Introductory Theory and Application in Science, Engineering, Medicine and Finance, Institute of Physics Publication, Publishing Bristol and Philadelphia 2002.

Arneodo, A., Wavelet & Fractal Methods Oxford University, Press, 1996.

Arridge,S.R. , Optimization and Inverse Problems in Imaging ,Department of Computer Science, University College London, 2014,Preprint.

Aslan, Z.,Manchanda,P.and Siddiqi, A.H.,Temperature and precipitation variability over Euro-near East Asia, Journal of Food Agriculture & Environment 9(3&4);(2011) , 912-922.

Beck, A. and Teboulle,M. , A fast Iterative Shrinkage thresholding Algorithm for Linear inverse Problems, SIAM J. Imaging Sciences, 2(1) (2000) 183-202.

Bonesky,T.,Dahalke,S. ,Maass,P.,Raasch,T. , Adaptive Wavelet Methods and Sparsity Reconstruction for Inverse Heat Conduction Problems, Adv Comput Math 33 (2010) ,385-411.

Bottema, M.,Moran, B. and Sovorova , An Application of Wavelets in Tomography , Digital Signal Processing, 8(1998) 244-254.

Boukhguim, A.A , Modern Techniques in Seismic Tomography, In Iske & Randen [19] , 268-295

Can, Z. , Aslan, Z.,Qguz, O. and Siddiqi, A.H. Wavelets Transforms of meterology , Annals Geophysics, 23(2005), 650-663.

Colonna, F.,Easley ,G.,Guo,K. and Labate, D. ,Radon Transform Inversion using the Shearlet Representation , Appl.Comput.Harmon.Anal.29 (2010) 232-250.

Daubechies, I. Ten Lectures on Wavelets, SIAM Philadelphia, 1992.

Doicu , A. , Trautmann ,T and Schreier,F, Numerical Regularization for Atmospheric Inverse Problems, Springer, 2010.

Geoff Daugherty, Digital Image Processing for Medical Applications. Cambridge University Press. 2009.

Domingues , M.O. , Mendes Jr, O. , da Costa, A.M., on Wavelet techniques in atmospheric sciences, Advances in Space Research 35 (2005), 831-842.

Donoho, D., Non -linear Solution of Linear Inverse Problems by Wavelet.Vaguelette decomposition, Appl. Comput.Harmon. Anal 2(1995) 101-126.

Easley,G.R., Colonna,F. and Lahate, D., Improved Radon Based Imaging using the Shearlet Transform, in: Independent Component Analyses, Wavelets, Unsupervised Smart Sensors and Neural Networks II ,in: Proc. SPIE, vol.7343, 2009.

Ellebroek, B.L. and Vogel, C.R., Inverse Problems in Astronomical adaptive optics, Inverse Problems, 25 (2009), 1-37.

Enescu, K. I to, and Z.R. Struzik, Wavelet-based Multifractal Analysis of Real and Simulated Time Series of Earthquakes, Annuals of Disas, Prev. Res. Inst. Kyoto University, No. 47B, 2004.

Farkov, Yu. A., Manchanda, P., Siddiqi, A.H., construction of Wavelets through Walsh Functions, Industrial and Applied Mathematics Series, Springer, 2018.

Furati, K.M., Nashed, Z., Siddiqi, A.H., Mathematical Models and Methods for Real World Systems, Chapman & Hall/CRC, Taylor & Francis Group, 2006.

Hanke,M.,Iterative Regularization Techniques in Image Reconstruction, Surveys on Solution Methods for Inverse Problems [Colton, D. etal editors] Springer, Vienna, 35-52.

Helin, T. and Yuytskiy, Wavelet Methods in multi conjugate adaptic optics , Inverse Problems. 29 (8), 2013.

Huang,S., Xiang,J., Du,H. and Cao, X., Inverse Problems in Atmospheric Science and their Application ,Institute of Physics Publishing Journal of Physics: Conference Series, 12 (2005), 45-57.

Gencay, R., Seluk, F., An Introduction to Wavelets and other Filtering Methods in Finance and Economics, Academic Press, 2001.

Grohs,P.,Keiper,S.,Kutyniok,G. and Schfer, M., - Molecules: Curvelets,Shearlets, Ridgelets, and Beyond , Technical University, Berlin, 2014.

Isakov, V., Inverse Problems for Partial Differential Equations , Springer, 2005.

Iske, A. and Randen , T. , Mathematical Methods and Modelling in Hydrocarbon Exploration and production , Springer, Schlumberger, 2005.

Kirish, A. ,An Introduction to the mathematical theory Inverse Problems , Second Edition Springer, 2011.

Krivoshein,Skopina, M., Approximation by frame like Wavelet systems, Appl. Comput. Harmon.Anal.,2011.
Krivoshein, A., Protasov, V., Skopina, M., Multivariate Wavelet Frames, Industrial and Applied Mathematics Series, Springer, 2017.
Kuchment, P.,Generalized Transforms of Radon Type and their Applications, Proc.of Symp Appl.Math.63 AMS, 67-91,2006.
Kuchment ,P. The Radon Transform and Medical Imaging, SIAM, Philladalphia 2014 .
Kutyniok ,G., Mehrmann, V. and Peterson, Regularization and Numerical Solution of the Inverse Scattering Problem using Shearlet Frames, Technical University, Berlin, 2014.
Lee ,Y. and Lucier ,B.J. ,Wavelet Methods for Inverting the Radon Transform with Noisy Data, IEEE Transactions on Image Processing. 10(1) (2001),79-94.
Manchanda P., Prof. Lozi R., Siddiqi; A.H. (eds) Industrial Mathematics and Complex Systems, Springer, 2017.
Mandelbrot, B.B., Hudson, R.L., The (Mis) Behavior of Markets, Basic Books, New York (ISB No. 465-04355), 2004.
Mousavi, S.M., and Langston C.A., A Hybrid Denoising Using Higher Order Statistics and Improved Wavelet block thresh holding, Bulletin of the seismological Society of America, Vol. 100, August, 2016.
Mousavi, S.M., Langston, C.A., and Horton, S.P., Automatic Microcosmic Denoising and onset detection using the synchrosqeezed continuous Wavelet Transform Geophysics Vol. 81, July, August, 2016.
Nagma, I. & Siddiqi, A.H., Sine-Cosine Wavelets Approach in Numerical Evaluation of Hankel Transform for Seismology, Applied Mathematical Modeling, 40 (2016), 4900-4907, Elsevier.
Nagma, I., & Siddiqi A.H., A novel computational hybrid approach in solving Hankel Transform, Applied Mathematics and Computation 281 (2016), 121-129, Elsevier.
Nagma, I., & Siddiqi A.H., A wavelet Algorithm for Fourier-Bessel Transform Arising in Optics, International Journal of Engineering Mathematics, Vol. 2015, 1-9.
Nagma, I., & Siddiq, A.H., An Application of wavelet technique in numerical evaluation of Hankel transforms, int. J. Nonlinear Sci., Number. Simual 16 (6) (2005) 293299.
Narasimha, R. and Bhattacharyya, S. , A Wavelet Cross- Spectral analysis of solar- ENSO- rainfall connections in the Indian monsoons, Appl. Comp. Harmon. Anal. 28 (2010) ,285-295, Elsevier.
Natterer , F. The Mathematics of Computerize Tomography, SIAM , 2001 (Second Edition)
Natterer, F. and Wubbeling, Mathematical Methods in Image Reconstruction, Mongr. Math.Model Computation , SIAM , Philadallphia, PA , 2001.
Nolet [A Breviary of seismic tomography , Cambridge university Press, Cambridge, 2008].
Noor E Zahra, Analysis of Brain Signals and Images using Wavelet and its Variants Ph. D Thesis Sharda University, July 2016.
Noor E Zahra and Siddiqi, A.H., Vector Valued Radan Transform, IJIAM, Vol. 5, 1-17, 2016.
Prestini, E. , The Evolution of Applied Harmonic Analysis Models of the Real World Problems ,Birkhaeser, 2004.
Rehman, S. and Siddiqi ,A.H. , Wavelet based correlation coefficient of time series of Saudi Metrological Data , Chaos, Solutions and Fractals 39 (2009) , 1764-1789 .
Rehman, S. and Siddiqi ,A.H. , Wavelet based Hurst Exponent and Fractal Dimensional Analysis of Saudi Climate Dynamics , Chaos, Solitons and Fractals 40 (2009) ,1081-1090.
Ruchira, A., Application of Shearlet s to Medical Imaging, Ph.D. Thesis December, 2015, Sharda University.
Ruchira, A. and Siddiqi, A.H., Application of Shearlet to MRI denoising, Journal of Medical Imaging and Health Informatics, 2016, 2-16.
Shumway, R.S., & Stoffer, D.S., time Series Analysis and its Applications, Springer, 2000.
Siddiqi ,A.H. (Lead Editor) Arabian Journal for Science and Engineering , Part I 28 (IC) , Part II 29 (2C) (2003-2004) Thematic Issue on Wavelet and Fractal Methods in Science and Engineering .
Siddiqi ,A.H. ,Applied Functional Analysis, Marcel dekker , New York, 2005.
Siddiqi ,A.H. (Ed) Emerging Application of Wavelet Methods,Vol.1463, American Institute of Physics (AIP),USA,2012.
Siddiqi, A.H., Singh, R. C. ,Manchanda, P.(Eds) , Proceedings of Satellite Conference ICM 2010 on Mathematics in Science and Technology,World Scientific Publisher, Singapore,2011.
Siddiqi, A.H , Gupta, A.K ,Brokate, M. (Eds), Models of Engineering and Technological Problems, American Institute of Physics (AIP), USA, 2009.
Siddiqi, A. H. , Duff, I. , Christensen, O. (Eds.), Modern Mathematical Methods, Model and Algorithms, Anamaya/Anshan, New Delhi, London, 2007.
Siddiqi, A. H., Manchanda, P., Bhardwaj, R., Mathematical Models, Methods and Applications, Springer, 2016.
Siddiqi, A .H and Kocvara, M.(Eds), Trends in Industrial and Applied Mathematics, International Conference Proceedings-Kluwer Academic Publishers (Now Springer) Boston, 2002.
Van Den Berg, J.C. Van (ed.) Wavelets in Physics, Cambridge University Press, 1999.

Vela'squez Valle,M.A. ,Garcia, G.M., Cohen, I.S.,Oleschko, L.K., Corral,J. A.R. , and Korvin, G. Spatial Variability of the Hurst Exponent for the Daily scale Rainfall Series in the state of Zacatecas Mexico, American Meterological Society (2013), 2771-2780.
Vogel,C.R. , Computational Methods for Inverse Problems, SIAM , Philladalphia , 2002.
Yang , Q.,Vogel, C.R.,Ellebroek,B.L., Fourier domain preconditioned conjugate gradient algorithm for atmospheric tomography, Appl. Opt. , 45 (21), 528, 2006.
Yanusnkevich, S.N. et al, Biometric Inverse Problems, CRC Press, 2005. Yanushkevich, S.N.,Stonica,A., Shmerko, V.P. and Popel,D.V., Biometric Inverse Problems, CRC Press, Taylor and Francis 2005.
Yudytskiy, M., Helin, T. and Ramlau,R. , A frequency dependent preconditioned wavelet method for atmospheric tomography. Inprint, 2013.
Yudytskiy ,Y., Helin ,T.and Ramlau, R.,A finite wavelet hybrid algorithm for atmospheric tomography , RICAM-Report No. 2013-14.

Software

Benoit ™ Software, developed by B. Mandelbort
LastWave,http://www.cmap.polytechnique.fr/~bacry/
Lastwave, developed by E-Bacry et al.
WaveLab,http://www.stat.standford.edu/~wavelab/, developed by D.Donoh et al.
FracLab,http://fractals.inria.jr/index.php
page=fraclab,developed by J.Levy Vehel et al.

STRATEGY OF DEVELOPING RENEWABLE ENERGIES AND ENERGY EFFICIENCY IN MOROCCO: THE KEY ROLE OF THE UNIVERSITY

Abdelfettah Barhdadi
Semiconductors Physics and Solar Energy Research Team (PSES), Energy Research Centre
Ecole Normale Supérieure (ENS), Mohammed V University in Rabat (UM5R), Morocco
abdelbar@fsr.ac.ma

Morocco has increasing needs for electricity with regard to its economic growth and social development. With its huge renewable energy potential, and because it doesn't have any fossil energy resources, Morocco launched its National Strategy for the Development of Renewable Energies and Energy efficiency. The launching of this strategy was on May 2009 under the supervision of the highest authority in the country. This strategy has 2 main objectives. The first one is self-production of clean electricity from about 42% and 52% of the total Moroccan electricity production capacity by 2020 and 2030 respectively. The second main objective is the development and the integration of Moroccan competitive industry in renewable energies. To reach these two key objectives, Morocco is now working on 3 parallel and relevant ways: (a) Boosting the training for capacity building in the domain of renewable energies and energy efficiency by implementing various training programs covering all topics connected to this field, (b) Supporting specialized R&D&I projects aiming at innovative funding, (3) Pushing toward close connections between university skills and industrials to develop renewable energy technology.

This invited talk will be focused on the explanation of this strategy and the presentation of ways for its successful implementation. It will also clearly point out the key role of Moroccan university for reaching the main objectives of this strategy. The contribution of home Research Structure (PSES) will be given as example.

Keywords**:** *Renewable Energies, Moroccan National Strategy, Role of University, R&D obn Photovoltaics.*

INTRODUCTION AND CONTENT

According to the World Bank data for 2016, the GDP per capita in Morocco is about 3200 US $, and according to the recently published human development report, the HDI of Morocco is 0,647. These 2 important index show that Morocco is still considered as a developing country. Nevertheless, Morocco doesn't want to stay any more in this class of less developed countries. It is willing to progress and become an emerging country. Morocco is pushing more and more in this sense and several efforts and actions in terms of economic growth and social development are now under progress to reach this goal. This is somehow reflected in its energy needs which increase annually by about 6%. Unfortunately, to progress in this growing and development way, Morocco has to continue importing nearly all his energy needs because it doesn't have any fossil resources, This importation is very costly and impact considerably the budget of the country. Fortunately, Morocco has a huge potential of renewable energies from solar, from wind and from hydropower. The exploitation of this potential should allow the country to reduce considerably its fossil energy dependency.

From the side of solar energy, Morocco has an average DNI of about 5 $kWh.m^{-2}$ par day and about 3000 sun hours per year. From the side of wind energy, Morocco has the possibility to exploit up to 25 GW capacities from onshore only (without speaking about the additional high

offshore exploitation capacity, thanks to 3500 km coastal length). From the side of hydropower, Morocco has about 200 proper sites to implement small hydroelectricity power plants. With its huge renewable energy potential, and because morocco doesn't have any fossil energy resources, and because of its increasing needs for electricity with regard to its economic growth and social development, Morocco launched its national strategy for the development of renewable energies and energy efficiency. The launching of this strategy was on May 2009 under the hospice of his majesty kind Mohammed VI, the highest authority in the country. This strategy has 2 main objectives: the production of clean electricity. This production should cover 42% of the Moroccan electricity needs by 2020 and 52% by 2030. The second main objective of the strategy is the development and the integration of Moroccan competitive industry in renewable energies. To reach these main objectives of the strategy, Morocco is now following the methodology of 3 parallel approaches: (1) Boosting the training for capacity building in the domain of renewable energies by implementing various training programs covering all topics connected to this field. (2) Supporting specialised R&D seeking some innovative funding: R&D projects dealing with innovation are strongly supported and funded. (3) Pushing toward close connections between university skills and industry to develop the technology in the field.

In the talk, we will first give an overview on the strategy for developing renewable energies and energy efficiency in Morocco. We will explain the main topics of this strategy and how reaching its main objectives. This will allow us to outline and explain the key role of the Moroccan scientific and technical universities in the implementation of this strategy. We will then present, as example, the contribution of the research team on Physics of Semiconductors and Solar Energy (PSES) which is an officially accredited research structure actively working in the field of photovoltaic materials, technologies and systems. The new research approach of PSES is based on the development of innovative and advanced R&D projects on solar energy with international partners and industrial companies. Because of its scientific productivity and its relevant achievements, PSES becomes one of the most distinguished academic operators in PV. With its new orientation based on win-win partnership with industrial operators, combined with the perseverance and willing of its active members, PSES was able to get the material and logistical resources to implement the first public-university solar energy platform dedicated to training, research, innovation and clean electricity production in Morocco. In this unique platform in its kind, a new research dynamic on relevant topics in the field of solar energy has been developed and fruitfully under progress at one of the most important public universities in Morocco.

CARBON AND WATER VAPOR EXCHANGE PROCESSES IN THE SEMIARID TYPICAL STEPPE ECOSYSTEMS IN INNER MONGOLIA

Huizhi Liu, Lei Wang, and Qun Du

State Key Laboratory of Atmospheric Boundary Layer Physics and Atmospheric Chemistry, Institute of Atmospheric Physics, Chinese Academy of Science, Beijing, China

huizhil@mail.iap.ac.cn

Typical steppe ecosystems are mainly distributed in semiarid areas and degradation has been accelerated due to climate change and increasing grazing intensity. The effects of grazing intensity on water vapor and carbon exchange process were investigated using eddy covariance measurement data during the growing season (May to September) from 2005 to 2008 over typical steppes in Inner Mongolia, China. Four grazing intensities were examined (UG79, ungrazed since 1979; WG, winter grazed; CG, continuously grazed; HG, heavily grazed). The main results are: (1) Grazing decreased evapotranspiration (ET) on a seasonal scale. The most important climatic factor controlling ET on daily scale shifted from SWC to Net radiation (Rn) when grazing intensity increased. SWC, Rn and air temperature (or vapor pressure deficit) can explain 59%-71% of the variation in daily ET. The effect of grazing reducing leaf area index (LAI) on ET is not significant in this ecosystem. Soil evaporation compensates for most of the loss in transpiration due to reduced LAI. (2) Both the amounts and distribution of precipitation during the growing season affected the net ecosystem exchange (NEE). The effects of grazing on the CO2 flux increased with the grazing intensity. During the peak growth stage, heavy grazing and winter grazing decreased the saturated NEE (NEEsat) and gross primary production (GPP) due to leaf area removal. Both ecosystem respiration (RE) and Q10 were clearly reduced by heavy grazing. Heavy grazing changed the ecosystem from a CO2 sink into a CO2 source. The effects of grazing on the CO2 flux also varied with the vegetation growth stages and SWC. (3) Grazing effects on ET partitioning could vary with soil water conditions in this ecosystem. SWC significantly influenced daily T/ET by affecting T and E in different ways. On a monthly scale, T/ET at UG79 increased with vegetation growth. In the normal precipitation year (2006), WG and HG reduced T/ET because they significantly reduced T through the removal of leaf area. In the dry year (2005), this negative effect on T was depressed by summer droughts, while WG and HG decreased E primarily due to the decreased interception of rainfall by the canopy.

***Keywords**: eddy covariance, grazing intensity, carbon exchange, evapotranspiration, evapotranspiration*

CONTEMPORARY DEVELOPMENTS IN APPLICATION OF WAVELET AND FRACTAL METHODS TO ATMOSPHERIC SCIENCE-II

P. Manchanda
GNDU, Amritsar, India
pmanch2k1@yahoo.co.in

As discussed in the first part of the lecture Wavelet Theory is the outcome of a multidisciplinary endeavor that brought together researcher groups of different disciplines including atmosphere science. This theory has created a common interest between research group of Prof. Aslan in Turkey and our research group in India lead by Prof. A.H. Siddiqi and Prof. P. Manchanda. Feasibility of applying wavelet methods to earthquake studies will be explored in this lecture. It may be observed that till now, orthonormal wavelets have been used but now our group is exploring the possibility of applying new classes of wavelets namely; wavelets defined by Walsh Functions, Frame System & multivariate wavelet frames.

Introduction to Earthquake Studies:
Tomography is the study of the internal properties of a body by observing the behavior of rays passing through the body. Seismic tomography uses mathematical modeling of P and S wave travel times to map velocity perturbations in the interior of the Earth. The primary energy source used in global seismic tomography is seismic waves generated by earthquakes which pass through the Earth in all directions, and are recorded on seismograms around the world. Inversion of arrival time data is used to determine the speed of the waves at any given point in the Earth. Using seismic tomography to interpret the internal structure of the Earth is similar in technique to a CAT-scan.

Computer assisted tomography (CAT) uses X-rays transmitted through the body in many different directions. A mathematical method is then applied to explain the loss in intensity of the X-rays due to the varying absorptive capacity of different parts of the body. The comparison between CAT-scans and seismic tomography differs because X-rays travel in straight paths, whereas the ray paths of sound waves bend with changes in the velocity structure of the medium.

Seismic tomography has several applications in exploration and global geophysics. Crosshole transmission tomography is used to image subsurface features between boreholes with greater accuracy than conventional surface reflection methods. Seismic tomography can also be used to characterize fractured bedrock, map groundwater reservoirs, and locate ore bodies. Global seismic tomography is used to interpret the presence of ancient subducted slabs, locate the source of hotspots, and model convection patterns in the mantle.

Global seismic tomography is limited by the irregularity in time and space of the source, and by the incomplete coverage of recording stations. The primary source is earthquakes, which are impossible to predict and only occur at certain locations around the world. In addition, the global coverage of recording stations is limited due to economic and political reasons. Because of these limitations, seismologists must work with data that contains crucial gaps. Experimental data can not accurately replicate conditions deep in the Earth's interior, therefore making comparisons with real world data difficult. Another limitation in imaging deep structures is attenuation and absorption of energy due to the long distances waves travel through the Earth, which reduces the resolution which can be attained. Due to the problem of attenuation, the

minimum sizes of features in the mantle which can be resolved are blocks 100-200 km on each side.

In short, seismic tomography is a methodology for analyzing and computing earth properties. Seismologist treat seismic tomography as a part of seismic imaging, where they are mainly concerned with estimating properties such as propagating velocities of p-waves and s-waves. The seismic tomography may be thought as the derivation of three dimensional velocity structure of earth from seismic waves. Estimation of p-waves velocity is the simplest example of seismic tomography. Seismic tomography is formulated as an inverse problem. See references [24]: Mathematical Methods and modeling in Hydrocarbon Exploration and Production, Springer, New York-2006], Nolet [42] and Vogel [60].

Main Ideas

Several types of faults occur in the crust. The faults break due to accumulated stress along the fault. The sudden release of energy is called an earthquake. The energy is released as seismic waves that travel away from the earthquake location. Two major types of waves are produced: body waves and surface waves. The waves can be measured by an instrument named a seismometer. The timing and amplitude of the seismic waves can be used to determine the location and magnitude of the earthquake. Earthquakes commonly occur along plate boundaries. These waves also provide information on the structure of the earth. References: S. Mostafa Mausavi and Charles A. Langston [33], S. Mostafa Mausavi and Charles A. Langston and Stefan P. Horton [34], Enescu, Ito, Struzik [16] and Rehman Siddiqi [46, 47] provide clues for using wavelet and fractal method in prediction of earthquakes. This is a challenging problem but scientists are optimistic. Earthquake, a sudden and violent shaking of earth's surface is a natural disaster, the prediction of precise time of its occurrence is questionable. A vast majority of scientists are of the opinion that it cannot be predicted, on the other hand a sizable section believes prediction is possible. After going through the arguments of both sides, our group tend to agree with the second point of view. We like to quote a paragraph from an invited public lecture by Qinguen Zeng at Beijing in August 2015 printed in ICIAM 2015. Proceedings of the 8th International Congress on Industrial and Applied Mathematics, Higher Education Press, China, 2015. "Prospect of future advances in the monitoring and predictions of natural hazards-Besides meteorological hazards, application of mathematics and supercomputings related to study and management of other natural hazards are also very promising in my opinion. For example, in the present a lot of data obtained from the monitoring of geological stresses along some fault zones, in which earthquakes occur some times. And once an earthquake happens, its source location can be inverted by the propagation of waves resulted from earthquake. Probably, to make simulations by using geological dynamical model and by data assimilation method to introduce the observed stress data into the simulations, we can reveal some laws to formulate or correct the governing equations of dynamics and to determine some critical fracture parameters, hence to make earthquake and its related tsunami predictions possible in the future". This paragraph and many other observations during our research cited in references Rehman and Siddiqi, [46, 47] have motivated us to earthquake study using Fractal and Wavelet Methods. In part I P-wave, S-waves, Signal and Image Processing, Seismic waves, Seismic Tomography, Fractal and Wavelet Methods for analyzing Seismic Data have been introduced.
P-waves are a type of body waves, called seismic waves in seismology that travel through continuum and are the first waves from an earthquake to be recorded at a seismograph. The continuum is made up of gases (as sound waves), liquids or solids, including the earth. Secondary waves or S-waves are seismic waves produced by an earthquake. These are lateral waves that move side to side as sin waves perpendicular to the direction of the wave. They are the second seismic wave to be recorded during the earthquake. S-waves are more destructive

than P-waves. S-waves travel slower than P-waves. It may be recalled that an elastic wave in the earth produced by an earthquake or other means is called seismic waves (Seismic waves are the waves of energy caused by the sudden breaking of rock within earth or an exploration).
It may be also observed that X-rays travel in straight paths, where as the ray paths of sound waves (P-waves or seismic waves) bend with changes in the velocity structure of the medium. This leads to be difference in the study of Tomography (Radon Transform) and Seismic Tomography
There is a general discussion how to use wavelet and fractal method in prediction of earthquakes. This is a challenging problem but scientists are optimistic.

The following references [2, 5, 7, 15,17-19, 23, 27, 32-38, 46, 48-50, 56, 63, 64] may prove very useful for applying wavelet methods in analyzing, storing seismic data and subsequently for predicting next occurrence of earthquake. I would like to draw the attention to wavelet analysis of seismic data in [18, pp.245 – 272] which provides motivation for further study in this area. Our group is exploring the possibility of applying new classes of wavelets namely; wavelets defined by Walsh Functions, Frame System & multivariate wavelet frames.

REFERENCES

Arridge,S.R. , Optimization and Inverse Problems in Imaging ,Department of Computer Science, University College London, 2014,Preprint.

Aslan, Z.,Manchanda,P.and Siddiqi, A.H.,Temperature and precipitation variability over Euro-near East Asia, Journal of Food Agriculture & Environment 9(3&4);(2011) , 912-922.

Beck, A. and Teboulle,M. , A fast Iterative Shrinkage thresholding Algorithm for Linear inverse Problems, SIAM J. Imaging Sciences, 2(1) (2000) 183-202.

Bonesky,T.,Dahalke,S. ,Maass,P.,Raasch,T. , Adaptive Wavelet Methods and Sparsity Reconstruction for Inverse Heat Conduction Problems, Adv Comput Math 33 (2010) ,385-411.

Bottema, M.,Moran, B. and Sovorova , An Application of Wavelets in Tomography , Digital Signal Processing, 8(1998) 244-254.

Boukhguim, A.A , Modern Techniques in Seismic Tomography, In Iske & Randen [19] , 268-295

Can, Z. , Aslan, Z.,Qguz, O. and Siddiqi, A.H. Wavelets Transforms of meterology , Annals Geophysics, 23(2005), 650-663.

Colonna, F.,Easley ,G.,Guo,K. and Labate, D. ,Radon Transform Inversion using the Shearlet Representation , Appl.Comput.Harmon.Anal.29 (2010) 232-250.

Daubechies, I. Ten Lectures on Wavelets, SIAM Philadelphia, 1992.

Doicu , A. , Trautmann ,T and Schreier,F, Numerical Regularization for Atmospheric Inverse Problems, Springer, 2010.

Geoff Daugherty, Digital Image Processing for Medical Applications. Cambridge University Press. 2009.

Domingues , M.O. , Mendes Jr, O. , da Costa, A.M., on Wavelet techniques in atmospheric sciences, Advances in Space Research 35 (2005), 831-842.

Donoho, D., Non -linear Solution of Linear Inverse Problems by Wavelet.Vaguelette decomposition, Appl. Comput.Harmon. Anal 2(1995) 101-126.

Easley,G.R., Colonna,F. and Lahate, D., Improved Radon Based Imaging using the Shearlet Transform, in: Independent Component Analyses, Wavelets, Unsupervised Smart Sensors and Neural Networks II ,in: Proc. SPIE, vol.7343, 2009.

Ellebroek, B.L. and Vogel, C.R., Inverse Problems in Astronomical adaptive optics, Inverse Problems, 25 (2009), 1-37.

Enescu, K. I to, and Z.R. Struzik, Wavelet-based Multifractal Analysis of Real and Simulated Time Series of Earthquakes, Annuals of Disas, Prev. Res. Inst. Kyoto University, No. 47B, 2004.

Farkov, Yu. A., Manchanda, P., Siddiqi, A.H., construction of Wavelets through Walsh Functions, Industrial and Applied Mathematics Series, Springer, 2018.

Furati, K.M., Nashed, Z., Siddiqi, A.H., Mathematical Models and Methods for Real World Systems, Chapman & Hall/CRC, Taylor & Francis Group, 2006.

Hanke,M.,Iterative Regularization Techniques in Image Reconstruction, Surveys on Solution Methods for Inverse Problems [Colton, D. etal editors] Springer, Vienna, 35-52.

Helin, T. and Yuytskiy, Wavelet Methods in multi conjugate adaptic optics , Inverse Problems. 29 (8), 2013.

Huang,S., Xiang,J., Du,H. and Cao, X., Inverse Problems in Atmospheric Science and their Application ,Institute of Physics Publishing Journal of Physics: Conference Series, 12 (2005), 45-57.

Grohs,P.,Keiper,S.,Kutyniok,G. and Schfer, M., - Molecules: Curvelets,Shearlets, Ridgelets, and Beyond , Technical University, Berlin, 2014.
Isakov, V., Inverse Problems for Partial Differential Equations , Springer, 2005.
Iske, A. and Randen , T. , Mathematical Methods and Modelling in Hydrocarbon Exploration and production , Springer, Schlumberger, 2005.
Kirish, A. ,An Introduction to the mathematical theory Inverse Problems , Second Edition Springer, 2011.
Krivoshein,Skopina, M., Approximation by frame like Wavelet systems, Appl. Comput. Harmon.Anal.,2011.
Krivoshein, A., Protasov, V., Skopina, M., Multivariate Wavelet Frames, Industrial and Applied Mathematics Series, Springer, 2017.
Kuchment, P.,Generalized Transforms of Radon Type and their Applications, Proc.of Symp Appl.Math.63 AMS, 67-91,2006.
Kuchment ,P. The Radon Transform and Medical Imaging, SIAM, Philladalphia 2014 .
Kutyniok ,G., Mehrmann, V. and Peterson, Regularization and Numerical Solution of the Inverse Scattering Problem using Shearlet Frames, Technical University, Berlin, 2014.
Lee ,Y. and Lucier ,B.J. ,Wavelet Methods for Inverting the Radon Transform with Noisy Data, IEEE Transactions on Image Processing. 10(1) (2001),79-94.
Manchanda P., Prof. Lozi R., Siddiqi; A.H. (eds) Industrial Mathematics and Complex Systems, Springer, 2017.
Mousavi, S.M., and Langston C.A., A Hybrid Denoising Using Higher Order Statistics and Improved Wavelet block thresh holding, Bulletin of the seismological Society of America, Vol. 100, August, 2016.
Mousavi, S.M., Langston, C.A., and Horton, S.P., Automatic Microcosmic Denoising and onset detection using the synchrosqeezed continuous Wavelet Transform Geophysics Vol. 81, July, August, 2016.
Nagma, I. & Siddiqi, A.H., Sine-Cosine Wavelets Approach in Numerical Evaluation of Hankel Transform for Seismology, Applied Mathematical Modeling, 40 (2016), 4900-4907, Elsevier.
Nagma, I., & Siddiqi A.H., A novel computational hybrid approach in solving Hankel Transform, Applied Mathematics and Computation 281 (2016), 121-129, Elsevier.
Nagma, I., & Siddiqi A.H., A wavelet Algorithm for Fourier-Bessel Transform Arising in Optics, International Journal of Engineering Mathematics, Vol. 2015, 1-9.
Nagma, I., & Siddiq, A.H., An Application of wavelet technique in numerical evaluation of Hankel transforms, int. J. Nonlinear Sci., Number. Simual 16 (6) (2005) 293299.
Narasimha, R. and Bhattacharyya, S. , A Wavelet Cross- Spectral analysis of solar- ENSO- rainfall connections in the Indian monsoons, Appl. Comp. Harmon. Anal. 28 (2010) ,285-295, Elsevier.
Natterer , F. The Mathematics of Computerize Tomography, SIAM , 2001 (Second Edition)
Natterer, F. and Wubbeling, Mathematical Methods in Image Reconstruction, Mongr. Math.Model Computation , SIAM , Philadallphia, PA , 2001.
Nolet [A Breviary of seismic tomography , Cambridge university Press, Cambridge, 2008].
Noor E Zahra, Analysis of Brain Signals and Images using Wavelet and its Variants Ph. D Thesis Sharda University, July 2016.
Noor E Zahra and Siddiqi, A.H., Vector Valued Radan Transform, IJIAM, Vol. 5, 1-17, 2016.
Prestini, E. , The Evolution of Applied Harmonic Analysis Models of the Real World Problems ,Birkhaeser, 2004.
Rehman, S. and Siddiqi ,A.H. , Wavelet based correlation coefficient of time series of Saudi Metrological Data , Chaos, Solutions and Fractals 39 (2009) , 1764-1789 .
Rehman, S. and Siddiqi ,A.H. , Wavelet based Hurst Exponent and Fractal Dimensional Analysis of Saudi Climate Dynamics , Chaos, Solitons and Fractals 40 (2009) ,1081-1090.
Ruchira, A., Application of Shearlet s to Medical Imaging, Ph.D. Thesis December, 2015, Sharda University.
Ruchira, A. and Siddiqi, A.H., Application of Shearlet to MRI denoising, Journal of Medical Imaging and Health Informatics, 2016, 2-16.
Siddiqi ,A.H. (Lead Editor) Arabian Journal for Science and Engineering , Part I 28 (IC) , Part II 29 (2C) (2003-2004) Thematic Issue on Wavelet and Fractal Methods in Science and Engineering .
Siddiqi ,A.H. ,Applied Functional Analysis, Marcel dekker , New York, 2005.
Siddiqi ,A.H. (Ed) Emerging Application of Wavelet Methods,Vol.1463, American Institute of Physics (AIP),USA,2012.
Siddiqi, A.H., Singh, R. C. ,Manchanda, P.(Eds) , Proceedings of Satellite Conference ICM 2010 on Mathematics in Science and Technology,World Scientific Publisher, Singapore,2011.
Siddiqi, A.H , Gupta, A.K ,Brokate, M. (Eds), Models of Engineering and Technological Problems, American Institute of Physics (AIP), USA, 2009.
Siddiqi, A. H. , Duff, I. , Christensen, O. (Eds.), Modern Mathematical Methods, Model and Algorithms, Anamaya/Anshan, New Delhi, London, 2007.
Siddiqi, A. H., Manchanda, P., Bhardwaj, R., Mathematical Models, Methods and Applications, Springer, 2016.
Siddiqi, A .H and Kocvara, M.(Eds), Trends in Industrial and Applied Mathematics, International Conference Proceedings-Kluwer Academic Publishers (Now Springer) Boston, 2002.

Van Den Berg, J.C. Van (ed.) Wavelets in Physics, Cambridge University Press, 1999.
Vela'squez Valle,M.A. ,Garcia, G.M., Cohen, I.S.,Oleschko, L.K., Corral,J. A.R. , and Korvin, G. Spatial Variability of the Hurst Exponent for the Daily scale Rainfall Series in the state of Zacatecas Mexico, American Meterological Society (2013), 2771-2780.
Vogel,C.R. , Computational Methods for Inverse Problems, SIAM , Philladalphia , 2002.
Yang , Q.,Vogel, C.R.,Ellebroek,B.L., Fourier domain preconditioned conjugate gradient algorithm for atmospheric tomography, Appl. Opt. , 45 (21), 528, 2006.
Yanusnkevich, S.N. et al, Biometric Inverse Problems, CRC Press, 2005. Yanushkevich, S.N.,Stonica,A., Shmerko, V.P. and Popel,D.V., Biometric Inverse Problems, CRC Press, Taylor and Francis 2005.
Yudytskiy, M., Helin, T. and Ramlau,R. , A frequency dependent preconditioned wavelet method for atmospheric tomography. Inprint, 2013.
Yudytskiy ,Y., Helin ,T.and Ramlau, R.,A finite wavelet hybrid algorithm for atmospheric tomography , RICAM-Report No. 2013-14.
Jens Havskov and Lars Ottemöller, Processing Earthquake data, 2009.

THE SILK ROAD PATTERN AND THE EURASIAN SUMMER CLIMATE

Lin Wang[1], Peiqiang Xu[1,2], Wen Chen[1], and Yong Liu[1]

1 Center for Monsoon System Research, Institute of Atmospheric Physics, Chinese Academy of Sciences, Beijing, China

2 College of Earth Sciences, University of Chinese Academy of Sciences, Beijing, China

wanglin@mail.iap.ac.cn

Based on several reanalysis and observational datasets, this study suggests that the Silk Road pattern (SRP), a major teleconnection pattern stretching across Eurasia in the boreal summer, shows clear interdecadal variations that explain approximately 50% of its total variance. The interdecadal SRP features a strong barotropic wave train along the Asian subtropical jet, resembling its interannual counterpart. Additionally, it features a second weak wave train over the northern part of Eurasia, leading to larger meridional scale than its interannual counterpart. The interdecadal SRP contributes approximately 40% of the summer surface air temperature's variance with little uncertainty and 10~20% of the summer precipitation's variance with greater uncertainty over large domains of Eurasia. The interdecadal SRP shows two regime shifts in 1972 and 1997. The latter shift explains over 40% of the observed rainfall reduction over northeastern Asia and over 40% of the observed warming over Eastern Europe, West Asia, and northeastern Asia, highlighting its importance to the recent decadal climate variations over Eurasia. The Atlantic Multidecadal Oscillation (AMO) does not show a significant linear relationship with the interdecadal SRP. However, the Monte Carlo bootstrapping resampling analysis suggests that the positive (negative) phases of the spring and summer AMO significantly facilitate the occurrence of negative (positive) phases of the interdecadal SRP, implying plausible prediction potentials for the interdecadal variations of the SRP. The reported results are insensitive to the long-term trends in datasets and thereby have little relevance to externally forced climate change.

***Keywords**: Silk Road pattern, Atlantic Multidecadal Oscillation (AMO), precipitation, surface air temperature, interdecadal variation*

References

Wang, L., P. Xu, W. Chen, and Y. Liu, 2017: Interdecadal variations of the Silk Road pattern. *J. Climate*, doi: 10.1175/JCLI-D-17-0340.1, in press

USE OF HUMAN BIOCLIMATIC INFORMATION IN CITY PLANNING, IN THE SAMPLE OF SAMSUN CITY

Süleyman Toy[1], Gözde Güher Özcan[2]
[1]Atatürk University,
[2]City and Regional Planner
suleyman.toy@atauni.edu.tr, ggzde93@gmail.com

ABSTRACT
Relationship between humans and climate begins at birth since they are born in atmospheric environment. Even though human body is exposed to all atmospheric elements, it cannot differentiate the separate effect of each one, i.e. its thermoregulation system senses only combined effect, which is called thermal effect or thermal comfort. In this respect, atmospheric characteristics like temperature, (T_a), air humidity (vapour pressure VP or relative humidity RH), wind velocity (wv) and mean radiant temperature (T_{mrt}) are the most important factors regulate comfort of living organisms including humans. Bioclimatic comfort is the condition where people do not feel discomforted from the ambient air conditions.

Being in or providing bioclimatically comfortable conditions, people need less energy consumption for heating or cooling and pollute less; therefore, this topic is debated among architects, city planners / designers and landscape architects to create more liveable areas in consistently more and more populated and polluted urban areas causing negative impacts on both climatic elements and so human bioclimatic comfort conditions.

This study is related to the use of bioclimatic comfort information belonging to Samsun city centre in replanning one part of it considering Physiologically Equivalent Temperature (PET) index values, designing with bio-climate principles.

Keywords: *Bioclimatic comfort, urban planning, thermal index, PET, Samsun*

INTRODUCTION
As the size of urbanised areas and density of urbanisation increase in today's cities, quality of air blocks in which people have to live also reduces physically and physiologically, e.g. air pollution and heat stress. Humans can sense ambient thermal effects of air in their surroundings in the combination of some effective atmospheric elements (Ta, RH, Ws, etc.) and features or positons of their bodies (work, insulation by clothing etc.).

In order to measure human's affection rate by thermal environment, several calculation and estimation indices and models have been developed, results of which are concrete values being referred to numbers in generally well – known temperature degrees (Celsius etc.). Such concrete values obtained from the indices are mainly categorised according to some human thermal perception and stress levels predetermined in surveys by asking people their comfort levels outdoor.

Among such indices and models, Physiologically Equivalent Temperature (PET) and RayMan (Höppe 1999; Matzarakis et al. 1999; Matzarakis et al. 2010) are very well – known and useful tools being used all over the world.

The use of climatic and bioclimatic information in urban design and city planning is not a new concept. Since nearly the beginning of 19th century, practitioners or scientists have tried to design and plan cities by considering all extents of atmosphere e.g. air pollution and temperature

differences (Howard 1820; Landsberg 1956; Olgyay 1963; Oke 1982). In today's cities, as the results of a raising consciousness about climate change and the apparent effects of extreme weather conditions on life, people and especially responsible authorities have gradually realised that they are obliged to consider all climatic characteristics when establishing new housing areas and constructing new buildings. In this respect, city and regional planning occupational discipline remains in the centre of all hot debates about climate and urban developments.
This study is important since it is concerned with the attempt to use human thermal information in an urban design work in a Turkish city, Samsun by considering a widely used bioclimate index and model.

MATERIAL AND METHOD

The city of Samsun is located in the Middle Blacksea geographic and TR83 NUTS II regions (36.26E; 41.34N; Figure 1). It is on the main route connecting Central Anatolia to Blacksea coast and the city is known for its developing agricultural, industrial and service (logistic) sectors. Population of whole province is 1.295.927 and that of city centre is nearly 700.000. Structured surface area of the city has consistently been enlarging for nearly the last ten years as in other Turkish cities based on the national policies adopted targeting land profit/rant.

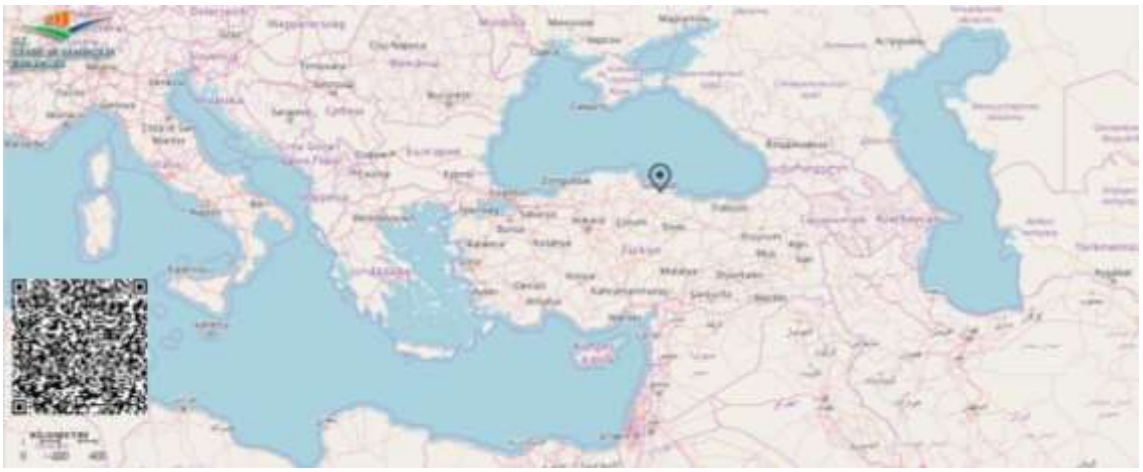

Figure 1. Location of Samsun city

In order to calculate thermal comfort values (bioclimatic conditions), Physiologically Equivalent Temperature (PET) index (Höppe 1993, 1999) and RayMan software (Matzarakis et al., 2007, 2010) were used considering hourly data – air temperature (Ta; in degrees Celsius), relative humidity (RH; %), cloudiness (CA; in octas), wind speed (WS; in meters per second) and estimated global radiation of the urban and rural characterized 15 meteorological stations of Samsun province from 2014 to 2016 (Table 1). The values obtained through the index and model are single temperature values in Celsius and represent standardised European man (gender), who is 1.75 m (height), 75 kg (weight), at 35 years old, in work suit (clothing 0.9 clo) and working in office (activity 80 w) and position standing (Höppe 1999; Mayer and Höppe 1987). PET values were categorised according to Table 2.

Table 1. Measurement points

Station No	Name	Longitude	Latitude	Altitude (m)
17623	Alaçam	36.6353	41,6307	7
18535	Asarcık	36,2228	410234	832
17622	Bafra	35,9247	41,5515	103
18133	Bafra/Top. Su.	35,9189	41,6017	15
18537	Canik /Kaşyayla	36,3186	41,2216	534
18538	Çarşamba	36,7347	41,2094	20
18539	Havza	35,7089	40,9908	675
18135	Ladik	35,9108	40,9102	900
18541	Ondokuzmayıs	36,1186	41,5139	5
17030	Samsun Regional Adm.	36,2564	41,3442	4
18507	Atakum / city centre	36,0375	41,3147	1309
18507	Terme Kozluk	37,1594	41,1389	8
18134	Vezirköpür	35,4544	41,1367	378
18545	Yakakent/Karaaba	35,4053	41,5511	660

Table 2.Thermal sensation and stress levels of PET (Matzarakis and Mayer 1996)

Thermal stress level	Human sensation	PET (°C)
Extreme cold stress	Very cold	<4
Strong cold stress	Cold	4.1-8.0
Moderate cold stress	Cool	8.1-13.0
Slight cold stress	Slightly cool	13.1 – 18.0
No thermal stress	Comfortable	18.1-23.0
Slight heat stress	Slightly warm	23.1-29.0
Moderate heat stress	Warm	29.1-35.0
Strong heat stress	Hot	35.1-41.0
Extreme heat stress	Very hot	>41.0

Temporal distribution of the calculated PET values was not considered since spatial distribution is important for urban design works. Therefore monthly PET distributions over the province was determined using ARCGIS 10.5 software.

RESULTS

Since in the study heat stress and thermally uncomfortable conditions based on hotness are investigated, the warmest months of the year were taken into consideration from May to September and PET distribution in this period is given in the Figure 2.

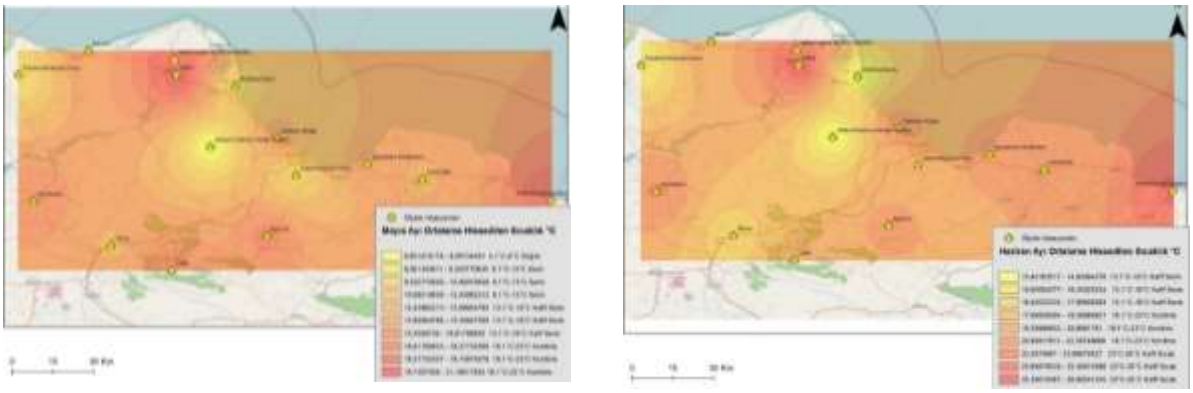

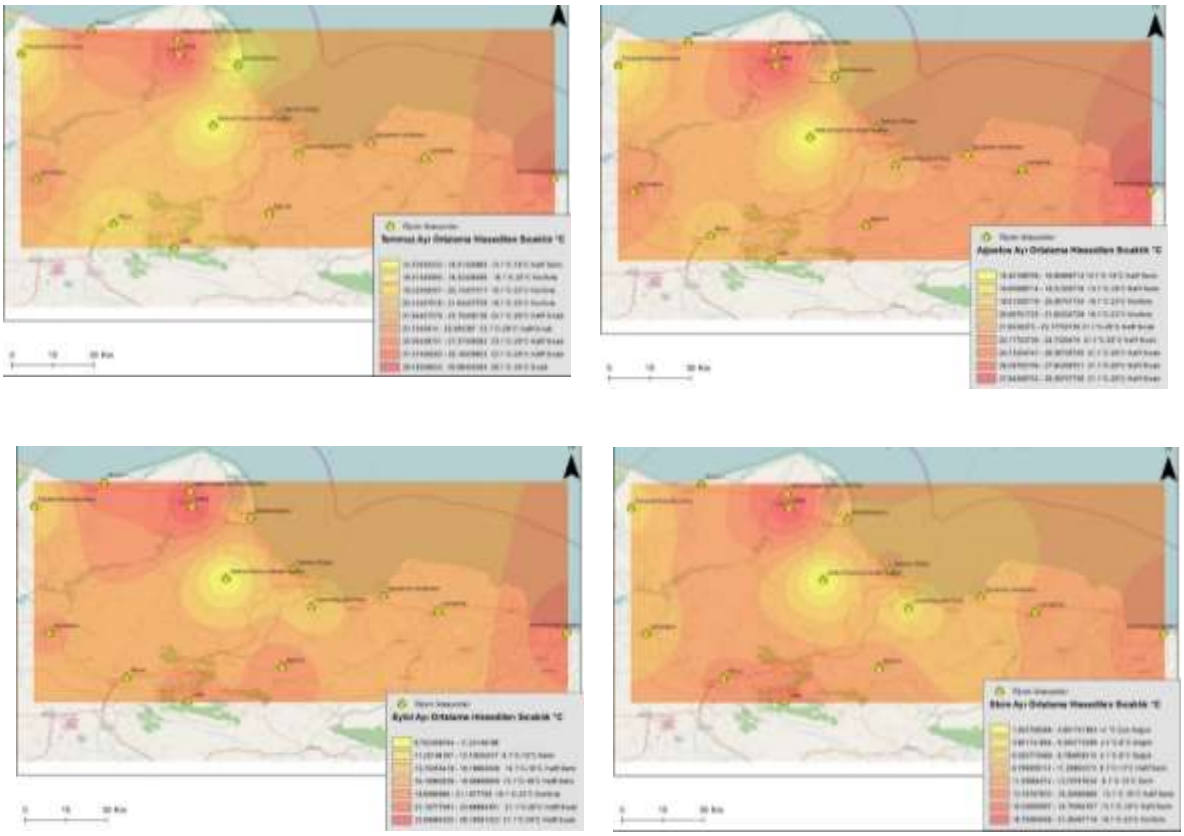

Figure 2. PET Distribution of the hottest months

APPLICATION OF BIOCLIMATIC INFORMATION TO URBAN DESIGN

In order to provide more comfortable ambient in the mentioned part of the city an urban design approach was adopted being sensitive to bioclimatic comfort conditions. The city centre exhibits urban characteristics with its densely built structure which block wind thus causing a stationary, humid and torrid air mass in urban area (Figure 3). It is expected in the city centre that humid air in hot summer months increases discomfort while wind gives coolness when combined with humidity effect. However, tall building blocks constructed in the prevalent wind direction prevent it from reaching inner parts of the city. It was determined by careful observation and modelling surveys that the main effective factor causing discomfort is the lack of wind therefore all the design works tried to be based on carrying wind to inner part of planning zone. Urban design problems thought to affect bioclimatic comfort conditions are given in Figure 3.

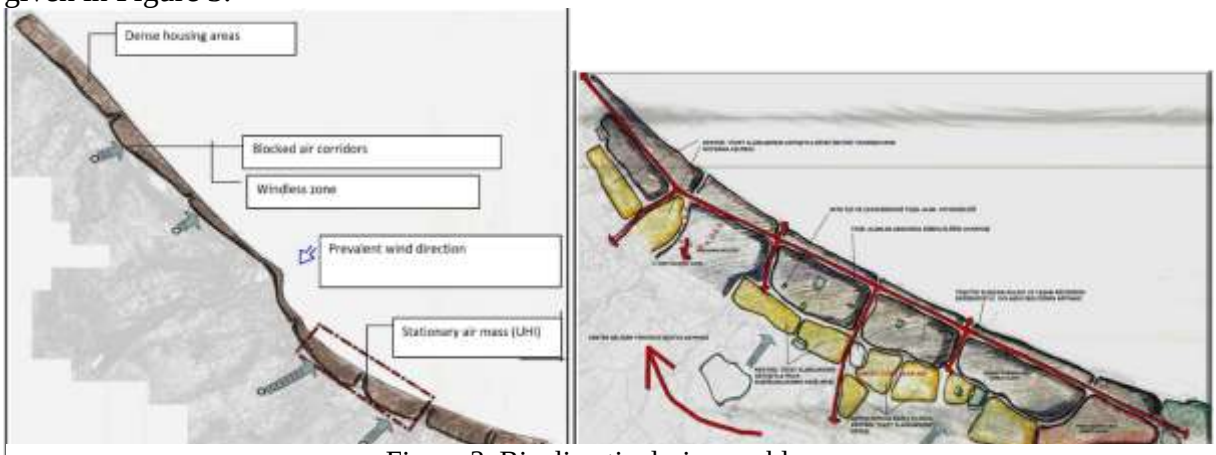

Figure 3. Bioclimatic design problems

SOLUTIONS TO THE BIOCLIMATIC URBAN DESIGN PROBLEMS

After the analysis of bioclimatic conditions taking into their spatial distribution over the hottest months of the year and onsite observations in the city parts to be designed, some design solutions were proposed in the area which may moderate the effects of heat stress mainly caused by urban heat island effect. Figure 4 represents two images of the proposed design solution to the planning zone.

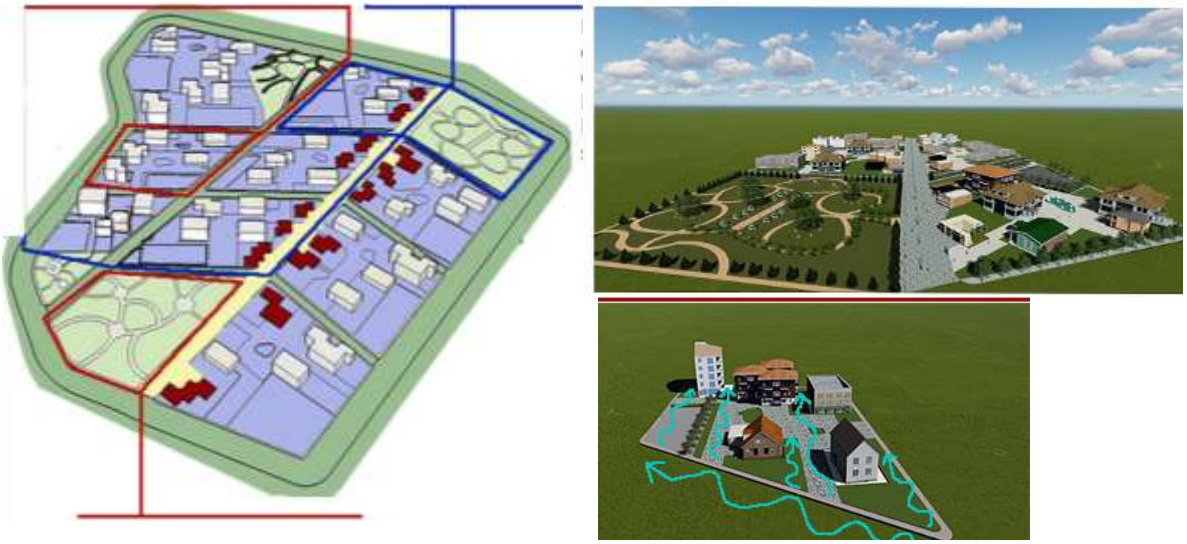

Figure 4. Urban design proposal to planning site

CONCLUSION

Living in a healthy environment is a right human guaranteed by the Constitutions all over the world and Turkey. In order to provide better living conditions to dwellers, city planners and landscape architects spend most of their time to find develop new concepts to struggle with the newly emerging problems such as lowering air quality in both physical and physiological ways. Among such problems air pollution, urban heat island effects and ultimately thermal comfort can affect people from both physical and physiological aspects.

This study is an example for those showing what an urban designer or landscape architect can do to make bioclimatically sensitive designs and what types of parameters he/she can consider. Such studies and design or planning practices are important not only to save energy but also to make people happy with their surroundings.

REFERENCES

Höppe P. 1993. Heat balance modelling. Experientia 49:741–746

Höppe P. 1999. The physiological equivalent temperature - a universal index for the biometeorological assessment of the thermal environment. Int J Biometeorol 43:71–75

Howard L. 1820. The Climate of London, Deduced from Meteorological Observations, Made at Different Places in the Neighbourhood of the Metropolis. 2. London 1818 –1820.

Landsberg H. 1956. The climate of towns . In W. L. Thomas (Ed.), Man's Role in Changing the Face of the Earth. Chicago, IL, USA : The University of Chicago Press .

Matzarakis, A., Mayer, H., and Iziomon, M.G. 1999. Applications of a universal thermal index: physiological equivalent temperature, Int. J. Biometeorol. 43: 76-84.

Matzarakis, A., Rutz, F., Mayer, H. 2007. Modelling Radiation fluxes in simple and complex environments – Application of the RayMan model. International Journal of Biometeorology 51, 323-334.

Matzarakis, A., Rutz, F., Mayer, H. 2010. Modelling Radiation fluxes in simple and complex environments – Basics of the RayMan model. International Journal of Biometeorology 54, 131-139.

Mayer H, Höppe P. 1987. Thermal comfort of man in different urban environments. Theor Appl Climatol 38, 43-49

Oke TR. 1982. The energetic basis of the urban heat island. Q J. R. Meteorol. Soc. 108: 1–24.

Olgyay V., Olgyay A. 1963. Design with Climate: Bioclimatic Approach to Architectural Regionalism, Princeton University Press, - 190p.

QUANTIFICATION OF BIOCLIMATE CONDITIONS FOR HUMANS FOR WINTER SPORT EVENTS – CANDIDATE CITY ERZURUM FOR WINTER OLYMPIC GAMES 2026

Süleyman Toy, Andreas Matzarakis
suleyman.toy@atauni.edu.tr, Andreas.Matzarakis@dwd.de

ABSTRACT
So far, the relationship between climatic / meteorological conditions or data and sportive branches has been very limited excepting for a few cases e.g. the data for instant atmospheric conditions for significant competitions like soccer finals or long-term data for sportive camping etc. Today, mega events like Olympics or those of world sportive federations (FIFA, UEFA, FIBA, FIS etc.) are not only prestigious, promotional and sometimes profitable for the host countries but also they obligatorily require successful organisational procedures which need taking into account all details including comfort conditions of spectacles. Among the mega events all over the world, Winter Olympic Games (WOG) is the most prestigious one for the countries sheltering efficient infrastructures like Turkey and the city of Erzurum, which hosted in 2011 an important winter sport organisation, UNIVERSIADE due to which significant amount of infrastructure was completed. The city is now trying to be a candidate for hosting 2026 WOG. Within the scope of present study, human thermal comfort conditions in the city were analysed to identify if these conditions are suitable for those coming or local to see the competitions outdoor under harsh winter conditions. One of the most widely used thermal indices; Physiologically Equivalent Temperature (PET) was used to estimate the conditions together with some meteorological parameters, temperature, humidity, wind velocity and cloudiness over a 40 – year period. The results show that for winter period, every daytime is not appropriate for individuals outdoor because of strong cold stress. However, there is no time - period to be evaluated to be suitable because this organisation must be held in the mentioned uncomfortable period. Main conclusion may be for the city that some cares should be taken to increase comfort conditions of people to see the competitions outdoor such as street heaters, extra clothes etc. by checking the examples form previous hosts. The method used here may be improved to show the exact situation of the individuals not playing games but seeing them since they produce nearly no metabolic heat.

Keywords: *Winter Olympic Games 2026, mega events, Physiologically Equivalent Temperature, cold stress, RayMan Pro*

INTRODUCTION
Mega sport events (e.g. Olympics both summer and winter, FIFA, UNIVERSIADE) are desired by many nations or governments to host since they can often provide several benefits to host countries/cities from promotion to the attraction of large-scale investments, improvement of sport branches to international interest (Gold and Gold 2011). During such events not only sportsmen but also visitors to come to accompany with their relatives or see competitions must be comfortable to any aspects including weather and ambient air conditions since they are accepted to be tourists who should be happy with the hosts (Matzarakis and Fröhlich, 2015).
Even though the largest international sport events have long been organised in summer months (e.g. FIFA), some of them must be performed in winter e.g. winter Olympics or UNIVERSIADE winter games etc. Visitors and players are not so much in trouble with ambient air characteristics when they are in venues however, outdoor thermal comfort conditions may sometimes be problematic for both groups in a short organisation time when all the competitions must be completed in a planned time schedule. Not game players but their spectators are

expected to be affected negatively by outdoor bioclimatic conditions since they are motionless to produce heat energy maybe only sitting.

Turkey is a country which is candidate for many mega sportive events such as big Olympic Games and hosting some of them like UNIVERSIADE summer and winter. Erzurum is the second most elevated and coldest city of Turkey and well – known for its winter sport and tourism activities and infrastructure which have been developing over the last twenty years. The city hosted UNIVERSIADE winter games in 2011 and gained strong sportive infrastructure invested by central government costing more than 400 million US dollars. This is a record investment in the city's history and it harbours now three venues for indoor winter sports, one jumping tower zone and several other pitches and organised runways.

Based on such large extended infrastructure, the city hosted European Youth Winter Olympic Festival (EYOF) in 2017. After such an important experience the city is now preparing to be candidate for 2026 Winter Olympic Games. However, because of either deficiencies in the organisation or cold stress on people during the games, neither of these organisations held in the city could not attract attentions from local or national scale and nearly all the games were played without spectators.

This study evaluates thermal comfort conditions of candidate visitors to a mega event (Winter Olympics) to be possibly held in the city of Erzurum and proposes some suggestions for spectators of outdoor competitions to watch the events in thermally comfortable ways.

AREA, METHOD AND DATA

The city of Erzurum is located in the eastern Anatolia geographical and TRA1 NUTS II statistical regions of Turkey (39º 55'N: 41º 16'E; Figure 1) and at an elevation 1 ranging from 850m to 2100m. The city harbours a worldwide – famous ski centre Palandöken Mountain. The city is a small - sized Turkish city with no heavy industry and people are employed mainly in public service sector. Population of the city centre is about 417.385 while that of the whole province is 762.021 according to Turkish State Statistics Institution in 2016.

Figure 5. Location of study area

The city is exposed to harsh continental climate (Köppen climate classification Dfd) where temperature extremes can reach up to 36.5ºC and down to -37.2ºC. Figure 3 and Table 1 represent mean and total of selected meteorological elements in 1950 to 2015 period (long term mean temperature is 5.6ºC, annual rainfall is 403.3mm and mean relative humidity is 66.3%).

In order to calculate human thermal comfort conditions in the study, among the most widely employed indices, Physiologically Equivalent Temperature (PET) index was used, which is based on the idea of balancing indoor and outdoor air temperature considering an energy balance of human body at the same core and skin temperatures (Höppe 1999; Mayer and Höppe 1987; Matzarakis et al. 1999) and the mean radiant temperature (Tmrt). Calculated temperatures are in Celsius unit. RayMan software (Matzarakis et al., 2007, 2010) was used to calculate PET values considering hourly data – air temperature (Ta; in degrees Celsius), relative humidity (RH; %), cloudiness (CA; in octas), wind speed (WS; in meters per second) measured at airport meteorological station from 1950 to 2016. Airport station (1758m; 39º.57'N-41º.10'E) runs for the aviation sector at a 7 – km distance from the city centre and the station is operated and maintained regularly by the Turkish State Meteorological Service (MGM).

PET values are obtained through the model as single temperature values in Celsius according to standardised European man (gender), who is 1.75 m (height), 75 kg (weight), at 35 years old, in work suit (clothing 0.9 clo) and working in office (activity 80 w) and position standing (Höppe 1999; Mayer and Höppe 1987) and categorised according to Table 2.

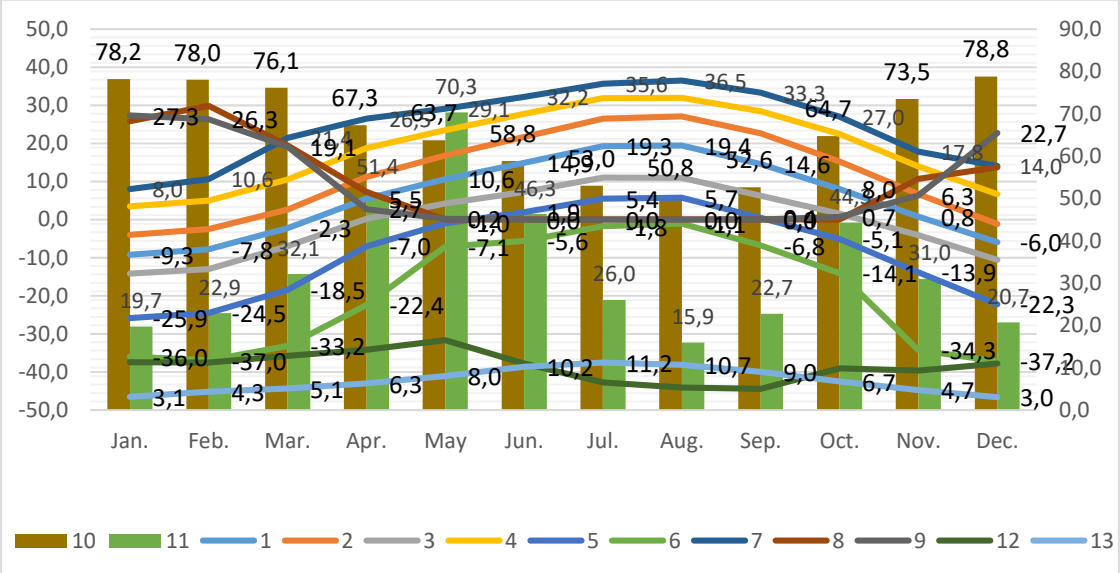

Figure 6. Long term situation of some meteorological parameters

Table 3. Long term yearly means and total of some meteorological parameters

Parameters		Mean	7	Record Maximum Temperature (ºC)	24.3
1	Mean Monthly Temperature (ºC)	5.6	8	Maximum Snow Cover (cm)	17.8
2	Mean Daily Maximum Temperature (ºC)	11.9	9	Number of Snow Covered Days (day)	13.2
3	Mean Daily Minimum Temperature (ºC)	-0.6	10	Relative Humidity (%)	66.3
4	Extreme Maximum Temperature (ºC)	18.7	11	Rainfall (mm/square meter)	403.3
5	Extreme Minimum Temperature (ºC)	-8.7	12	Mean Number of Wet Days (day)	10.3
6	Record Minimum Temperature (ºC)	-19.7	13	Mean Sunshine Duration (hour)	6.9

Table 4.Thermal sensation and stress levels of PET (Matzarakis and Mayer 1996)

Thermal stress level	Human sensation	PET (°C)
Extreme cold stress	Very cold	<4
Strong cold stress	Cold	4.1-8.0
Moderate cold stress	Cool	8.1-13.0
Slight cold stress	Slightly cool	13.1 – 18.0
No thermal stress	Comfortable	18.1-23.0
Slight heat stress	Slightly warm	23.1-29.0
Moderate heat stress	Warm	29.1-35.0
Strong heat stress	Hot	35.1-41.0
Extreme heat stress	Very hot	>41.0

RESULTS

Results of the study show that people in the city centre are under excessive cold stress in a long period from October to May when considered mean values given in Figures 3, 4, 5, 6 and 7 which represent the yearly distribution of (very) cold, comfortable and (very) hot PET and mPET intervals, climatic elements and PET and mPET.

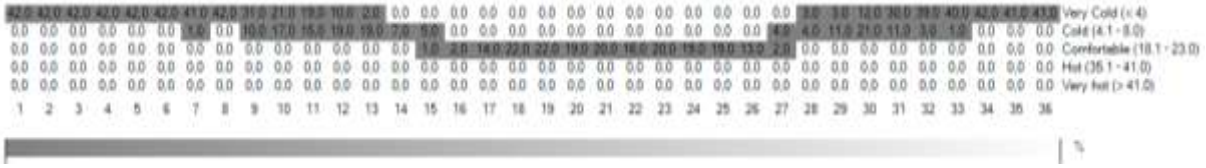

Figure 7. Distribution of some PET intervals

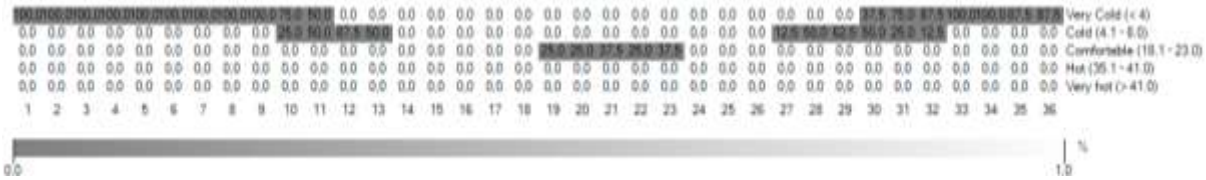

Figure 8. Whole year distribution of mPET

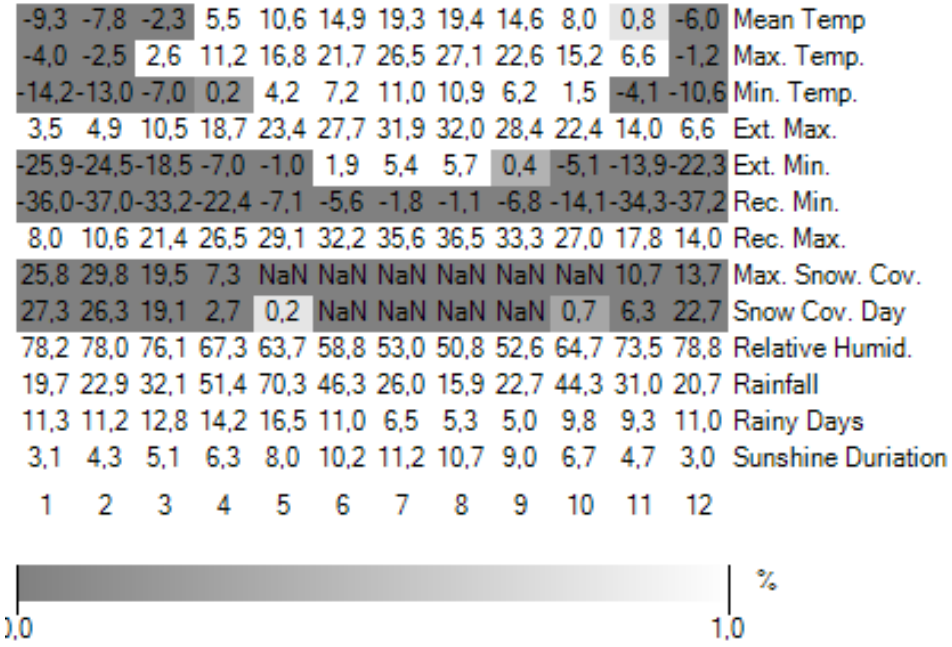

Figure 9. Distribution of some climatic elements

Figure 5 represents the suitability of the city for winter activities and its unfavourable characteristics for outdoor human thermal comfort in terms of extremely cold conditions.

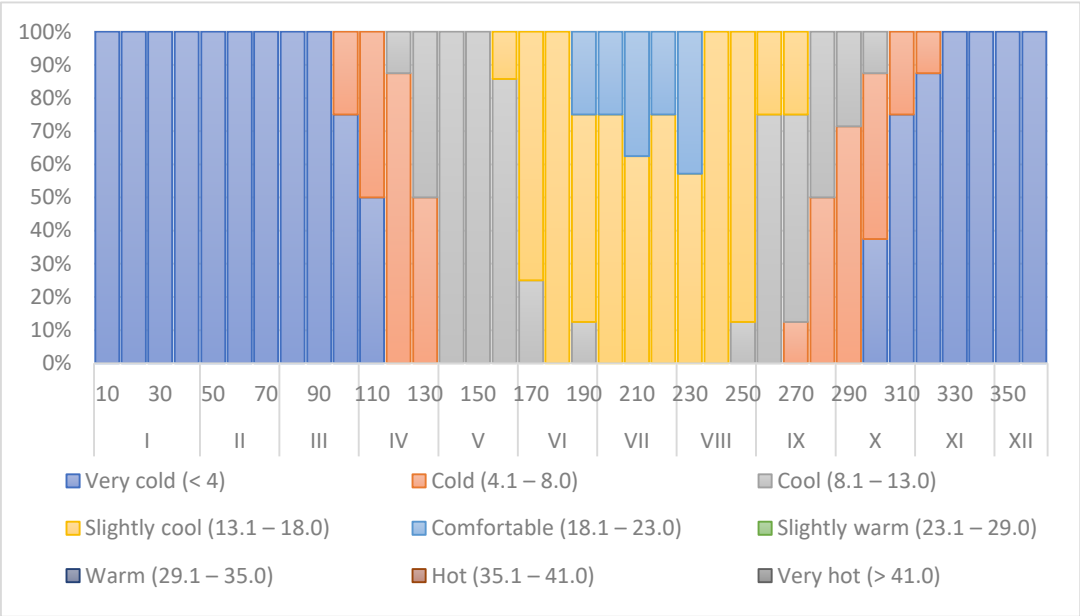

Figure 10. Distribution of some mPET intervals

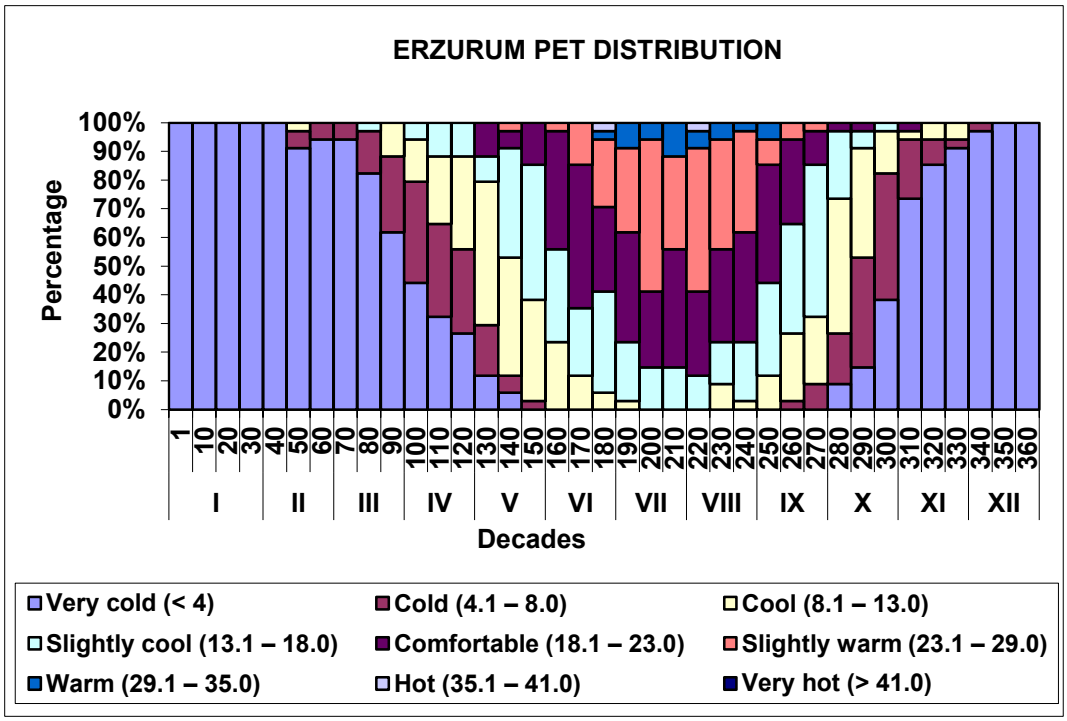

Figure 11. PET distribution of the area

DISCUSSION AND CONCLUSION

Quantification and assessment of human thermal comfort conditions in a given ambient air block are needed in many fields such as sportive training (Toy and Eymirli 2012) and urban design (Hwang et al 2011). Present study analyses climatic elements to determine how human thermal comfort conditions are effective under winter conditions when possible mega events

take place. In the analysis period (1950 to 2016), mean of extreme minimum temperatures between May and October is considerably below 0°C, which means people can always feel outdoor cold stress in the mentioned period as mentioned above from the PET evaluations.

Mega events provide huge amount of investments to a place in a very short time and generally since the length of the time to make preparation is so short that several aspects of organisation planning are missing such as outdoor thermal comfort conditions of visitors or locals wishing to see competitions. Today's technology can cope with the unfavourable characteristics of climate in any given places. Therefore, if the problems are known to organisers or investors they can easily be solved by considering all possible alternatives.

It is clearly stated in the study that in winter time when it is obliged to perform all competitions related to winter sports, no comfortable time interval is seen for outdoor spectators. Maybe, late spring or autumn when the ground is covered with snow in the mountain and daytime temperature can ease staying outdoor are preferred to be better time interval. Another interesting point is that due to reflection of solar radiation based on the albedo of snow cover the area is always expected to get warmer quickly and increase temperatures nearly 2 m aboveground. This situation may be seen as an advantage for the motionless spectators while watching competitions. In order to increase the advantage of solar radiation all outdoor events should be organised at noon hours.

REFERENCES

Gold, J.R. and Gold, M.M. (2011). Olympic Cities: Cities Agendas, Planning and The World`s Games, 1896-2016. Londres y Nueva York: Routledge.

Höppe PR (1999) The physiological equivalent temperature—a universal index for the bioclimatological assessment of the thermal environment. Int J Biometeorol 43:71–75

Matzarakis, A. and Fröhlich, D (2015) Sport events and climate for visitors – the case of FIFA World Cup in Qatar 2022. Int J Biometeorol 59:481–486 Hwang, R.L., Lin, T.P., Matzarakis, A., 2011, Seasonal effect of urban street shading on long-term outdoor thermal comfort, Building and Environment 46(4) 863-870 (SCI)

Matzarakis A, Mayer H (1996). Another kind of environmental stress: thermal stress. WHO Newslett 18:7–10

Matzarakis A, Mayer H, Iziomon MG (1999) Applications of a universal thermal index: physiological equivalent temperature. Int J Biometeorol 43:76–84

Matzarakis A, Rutz F, Mayer H (2007) Modelling radiation fluxes in simple and complex environments—application of the RayMan model. Int J Biometeorol 51:323–334

Matzarakis A, Rutz F, Mayer H (2010) Modelling Radiation fluxes in simple and complex environments: basics of the RayMan model. Int J Biometeorol 54:131–139

Mayer H, Höppe P (1987) Thermal comfort of man in different urban environments. Theor Appl Climatol 38:43–49

Toy S. and Eymirli EB. 2012. Potential of Erzurum city in terms of high altitude sportive camping. KUDAKA İnovasyona Dayalı Bölgesel Turizm Stratejisi Notları No: 8, Erzurum. 17 p.

CALCULATING THE TEMPERATURE-HUMIDITY INDEX FOR SELECTED STATIONS IN IRAQ

***Osama T. Al-Taai and **Salah M. Saleh**

**Department of Atmospheric Sciences, College of Science, University of Al-Mustansiriyah, Baghdad, Iraq.*
***Atmosphere and Space Science Center, Directorate of Space Technology and Communication, Ministry of Science and Technology, Baghdad-Iraq.*
Aus_tar77@yahoo.com

Abstract

The Temperature-Humidity Index (THI) is used to express a human comfort, depending on both humidity and temperature, In the case of high humidity, The person feels that the temperature is higher than recorded by the thermometer because decrease the process of evaporation of the body or stop it, which is responsible for reducing the temperature of the body. This research aim to clarify the relationship between the elements of the atmosphere (Temperature, Humidity) and the comfort of the human through the calculation of the Temperature-Humidity Index (THI), in terms of the use of data Temperature, Humidity for the period (2005-2015) of the Iraqi meteorological organization and seismology for different stations in Iraq (Mosul, Baghdad, Basrah) and use advanced statistics, The highest values for the index in the summer months and the highest value in the Basrah station 28.65^{o}C for the month of August, and the lowest values for the index in the winter months and the lowest value was in Mosul station 8.69^{o}C for the month of January, When calculating the seasonal of the (THI), it was found that the summer months and the months of April and May of the spring have high index values, in addition to the months of September and October of the fall also has high values due to the high relative humidity, as for the rest of the months of spring and autumn months considered as months close to human comfort as well as winter, It was also found by analyzing the annual average of the (THI) the highest value was in Basrah station 22.67^{o}C in 2010, the lowest value in Mosul station 17.84^{o}C in 2013, and found through the statistical processes between the temperature and the Temperature-Humidity Index (THI) is a strong positive relationship, The correlation coefficient (0.99) and the relation between the relative humidity and the index is a strong inverse relationship and the degree of correlation (-0.97).

Keywords: *Temperature, Relative humidity, Human comfort, Spearman Rho Test, Iraq.*

INTRODUCTION

Considered human attempts to see the impact of different climate in which elements directly as old as the human himself, and several attempts have emerged in the past trying to explain this effect, but it was limited to the limited availability of climate information elements, but the human himself and through his experiences he was able to note that influence simple, where the human recourse to the caves to prevent free direct sun or cold in the winter and heat in summer is an expression of doth human beings to the impact of climate elements on it, and the man went towards the leather put on his body naked and then different quality clothes different depending on changes the climate in that region, which turn them an expression in the same direction. The human feeling is comfortable in different climates, which is known as physiological climatology. In addition to the natural factors (heat, humidity, radiation, and winds), there are psychological factors that play a large role and there is an adaptation to the succession of generations in a given region. The natural side effect in rest only, it is not possible to deal with all the factors affecting human comfort in order to put a clear end to the human feeling comfortable, there are many cases of human sense of the elements of the climate on a certain aspect of his life, the concept of comfort varies between human and human group and another since there is a relationship between these elements, any element alone cannot be a

sufficient indicator of a sense of comfort and here came the complexity of the discovery of a law governing the human sense of comfort, and thus the emergence of the science of statistics and development has helped to bring the image to the human through the finding of the statistical relationship between phenomenon that is, the only method currently known to deal with some applied climate issues that can detect some aspects of the relationship between climatic elements and various matters of life. The study of climate and has become an important scientific field because of its great influence in living organisms on the earth, the most important of which are humans, Who lives in a climate environment that affects his activities, as well as affecting the body's organs and physiological functions (Musa, Ali Hassan, 2002).

Scientists have studied and determined the comfortable atmosphere of man despite the difficulty they found in the definition of a general concept of physiological comfort, because of human differences in interaction with environmental conditions, what is comfortable for someone may be annoying to another at the same time depends on the type of person and age and clothing and housing ... etc. In addition to the overlap of physiological and psychological factors, however, there have been attempts to develop a general concept of physiological comfort, has been known by some as that atmosphere that raises feelings of satisfaction and psychological warmth and meets perceptions of feelings in one way or another, and to create a sense of comfort must be met In the particular environment, consistent physical relationships or the concept established by the American Society of Refrigeration and Air Conditioning Engineers (ASRACE) 1973, (Holly et al., 1979). That rest is the state of mind in expressing its satisfaction with the environment 1989 (Omar, F. 1989).

Comfort physiological is a sense of stalking man and makes him feel psychological comfort fully in accordance with the specific climate and natural conditions, wants to sustain without an increase or decrease, a central nervous system condition that leads to human feeling good about the surrounding environment and be two types, physiological comfort and psychosomatic comfort, the former what however, expression of the state of thermal equilibrium between the body and the surrounding environment in light of maintaining the normal body temperature which is the body resulting from the chemical reactions that take place within the so-called process of metabolism, equal to the amount of heat outside through load, conduction, radiation and evaporation (Mahdi, A., F. 1990).

The interest in studying the climatic systems of any geographical region was an effective and successful means to highlight its impact on the human being within that region, Then these studies crystallized and became independent in the field of practical application known as science (Physiological Climate), a branch of biochemistry that takes into account the direct effects of climate on the human body and its rest and activity, The study examined the daily and annual changes of climate components, Such as solar radiation, air temperature, relative humidity, etc., and their various effects on human comfort, This led to the emergence of climatic studies based on the relationship between human and climate, Including climate classifications Tanjung and Maunder, (Tanjung W., 1966). which depend in their relationships on a number of variables that affect the human sense of the atmosphere and feel comfortable or narrow (Gouda, H. J., 1989), In addition to the development of some modern methods, such as the equivalent temperature of the cooling of the wind and heat and humidity and others, The impact of the local climate in determining the extent of human activity is important to many researchers because it affects the urban planning and the quality of the materials used in construction, as well as the parks and green spaces to find the physical comfort of the human and even the quality of clothing used in some areas (AL-Jabouri, M. H., 2007). The most prominent of these scientists Thom 1959,who invented the mathematical formula to calculate thermal comfort

using temperature and humidity, where he measured the temperature - Humidity Index or the Discomfort Index of the US climate (Thom E.C., 1959).

THE DATA AND STUDY AREAS

Were used the data for monthly averages of meteorological variables (temperature and relative humidity) from the Iraqi Meteorological organization and Seismology for a period for eleven years (2005-2015). Were calculated the Temperature-Humidity Index (THI) values of three different stations Mosul, Baghdad, and Basrah representing the northern, central and southern regions of Iraq, respectively. These areas differ in terms of climate change, terrain and altitude from sea surface level, see Figure (1) and Table (1) (IMOS, 2015).

Table (1). Latitude, Longitude, and Altitude from sea level for study stations.

Stations	Longitude (ºE)	Latitude (ºN)	Altitude above sea level
Mosul	43.15	36.32	223.5
Baghdad	44.23	33.23	31.7
Basrah	47.78	30.57	2.4

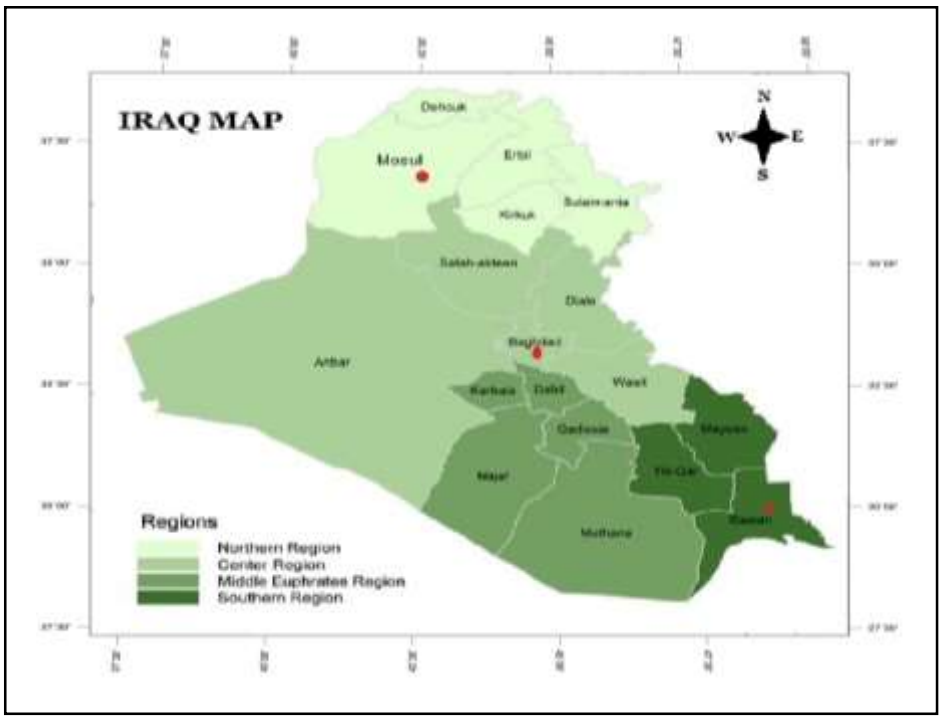

Figure (1). Study areas.

THE STATISTICAL USING

Simple Linear Regression (SLR)

Simple linear regression is the study of the relationship between two variables just to get to the linear relationship (i.e. a straight line equation) between these two variables, a parametric test, which assumes that the data are distributed normally distributed and to find out the gradient

value is calculated slope of the regression through the linear equation of the following (Yazdani M., 2011).

$$\bar{Y} = a + b\bar{X} \qquad (1)$$

$$b = \frac{\sum_{i=1}^{n}(X_i - \bar{X}) - (Y_i - \bar{Y})}{\sum_{i=1}^{n}(X_i - \bar{X})^2} \qquad (2)$$

Where a: Steady decline or part of the cross axis ($\overline{Y}$) to the equation of the straight line, equation (4) and b: The Slope of the regression.

Probability Value (P-Value)

Is purely a statistical term, a number is used to assess the statistical measures, which show that the value of the corresponding factor is actually an influential factor or not? If the (P-Value) less than 0.05, the corresponding factor is an influential factor in the variable that we are trying to study the change. Influential factor has even considered the value of (P-Value) is equal to 0.1, but that increased about 0.1, this factor should be excluded from the model is ineffective (Mohamed S. 2009).

Spearman Rho Test

Is a test of non-parametric range of observed data {X_i, i = 1,2, ..., n} based on nothingness any hypothesis that all (X_i) values are independent and have the same distribution and to calculate the Spearman rho coefficient statistical ranks (r_s) must be converted model original to the ranks mediated arranged in descending order in terms of amount is then calculate the amount of (d_i) through ($d_i = k_i$-i) where (i) value ranging from 1 to (n) and (r_s) is given by the following (Kendall's., 2011).

$$r_s = 1 - \frac{6\sum_{i=1}^{n} d_i^2}{n(n^2-1)} \qquad (3)$$

If the great value (n) can test the value of (r_s) importance by calculating the amount of (t_s) which is given by the equation:

$$t_s = r_s \sqrt{\frac{n-2}{1-{r_s}^2}} \qquad (4)$$

If the value of (t_s) false calculated within the trusted boundary for a two-tailed test of this we can deduce that there is no trend in the data series (MEI, 2007).

MATERIALS AND METHODS OF WORK

Some researchers have proposed special equations for calculating what is known as "effective temperature", the meaning is the temperature at which a person feels comfortable in a situation if the atmosphere is static and saturated with moisture, They replaced active temperature with other expressions such as the Discomfort Index (DI), or Temperature-Humidity Index (THI), The two expressions used by Thom in the United States in the years 1959 - 1960 respectively, They express one intent, This equation is widely used in the United States at present to assess summer heat intensity, The following mathematical formula was invented to calculate this indicator (Thom E.C., 1959).

$$THI = T - 0.55(1 - 0.01R.H.)(T - 14.5) \qquad (5)$$

Where T: Temperature, and RH: Relative Humidity.

The equations are interpreted on the basis that the output is the pointer, if the result is more than 25 most people in these circumstances feel uncomfortable, If the result is between (15-20) most people feel comfortable, in a study of a group of people of different ages, it was found by applying the results of these equations that most people feel comfortable when the results are between (15-20), and that 50% of people feel uncomfortable when the result 23, most people feel uncomfortable when the result of any of the equations is more than 25, Thom 1959 set a table showing values for THI versus levels of comfort, see Tables (2) and (3), (Giles, B.D., 1990).

Table (2). The Temperature-Humidity Index (THI) value and the equivalent of human comfortable feeling.

THI or Discomfort Index	Discomfort condition
DI<21	No discomfort
21≤DI<24	Less than 50% of the total population feels discomfort
24≤DI<27	More than 50% of the total population feels discomfort
27≤DI<29	Most of the population suffers discomfort
29≤DI<32	The discomfort is very strong and dangerous
DI≥32	State of medical emergency

Table (3). The Temperature-Humidity Index (THI) value by categories and symbols of human comfort.

Human Comfort	**Category**	**Symbol**	**Temperature-Humidity Index (THI)**
Discomfort cold	Severe cool	C^-	<11.9
	Too cool	C^*	14-12
	Cool	C	14.9-14.1
Perfect	Perfect	P	16-15
	Perfect	P^*	18-16.1
	Perfect	P^-	20-18.1
Discomfort heat	Warm	H	23-20.1
	Hot	H^*	25-23.1
	Very hot	H^-	25.1<

RESULTS AND DISCUSSION

In the practical aspect of research, equation (5) was used, which represents the equation of Temperature- Humidity Index (THI), by data of temperature and relative humidity recorded, the change in monthly temperature, Relative humidity and Temperature- Humidity Index (THI) For the period (2005-2015) and the stations (Mosul, Baghdad, and Basrah) through the Figure (2), can be observed change the behavior of temperature and by regions where the temperature is lower in the Mosul station and above in the Basrah station and the moderate in the Baghdad station, as for the relative humidity, it is convergent in the stations Basrah and Baghdad in some months, the end of April to the beginning of August, where the relative humidity in the Baghdad station is higher than Basrah station and the Mosul station it has the highest relative humidity of Basrah and Baghdad, as for the Temperature- Humidity Index (THI), Basrah station has the highest values 28.65ºC for August and the lowest values of the THI in Mosul station 8.69ºC for January, with noting that there are identical in the index values of stations Mosul and Baghdad in the summer months The three are June, July and August.

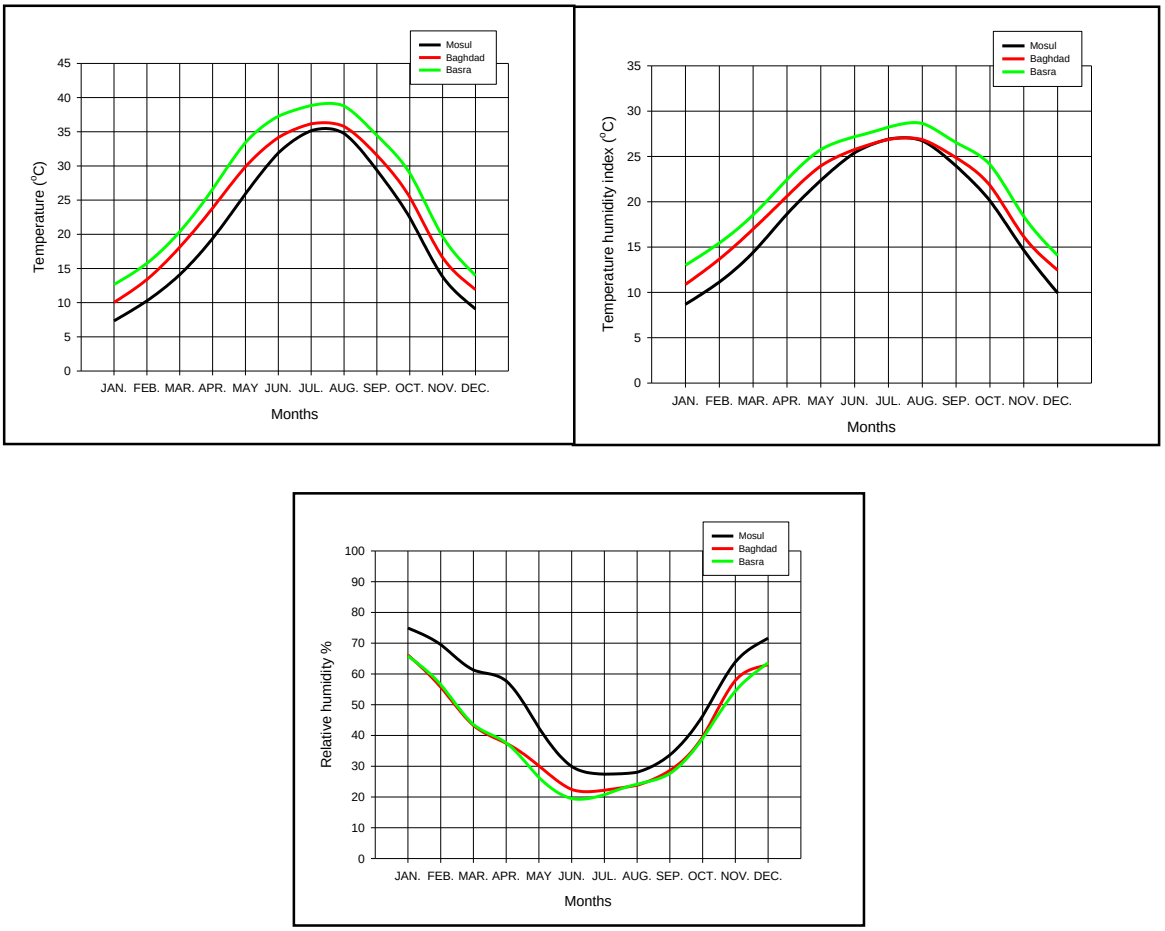

Figure (2). The change in the monthly average of temperature, relative humidity and Temperature- Humidity Index (THI) for the period (2005-2015) for stations (Mosul, Baghdad, and Basrah).

Through the Figure (3), that show the seasonal average change of the Temperature- Humidity Index (THI) for eleven years (2005-2015) for the stations (Mosul, Baghdad, Basrah) in winter can be observed the highest value of the index in Basrah 15.75ºC in 2010, The lowest value of the index was at Mosul station 8.32ºC in 2008, with a slight increase in the index values in each of the three stations from mid-2009 to 2010, and in the spring can be seen that the highest. The highest value in Basrah station 22.77ºC in 2010, the lowest value in the Mosul station 17.43ºC in 2007, in summer can be seen that the highest value in the Basrah station 28.74ºC in 2010, while the lowest value was in Mosul station 25.5ºC in 2013, note that the stations of Baghdad and Mosul have convergent values of the (THI) and this convergence extends from 2005 to the end of 2008, and in the autumn it can be noted that the highest value of the index was In Basrah station 23.85ºC in 2012, and the lowest value of the index was in Mosul station 18.03ºC in 2011, with noting that the Mosul station increases the values of the index to exceed the values of the Baghdad station in mid-2007 to mid-2008.

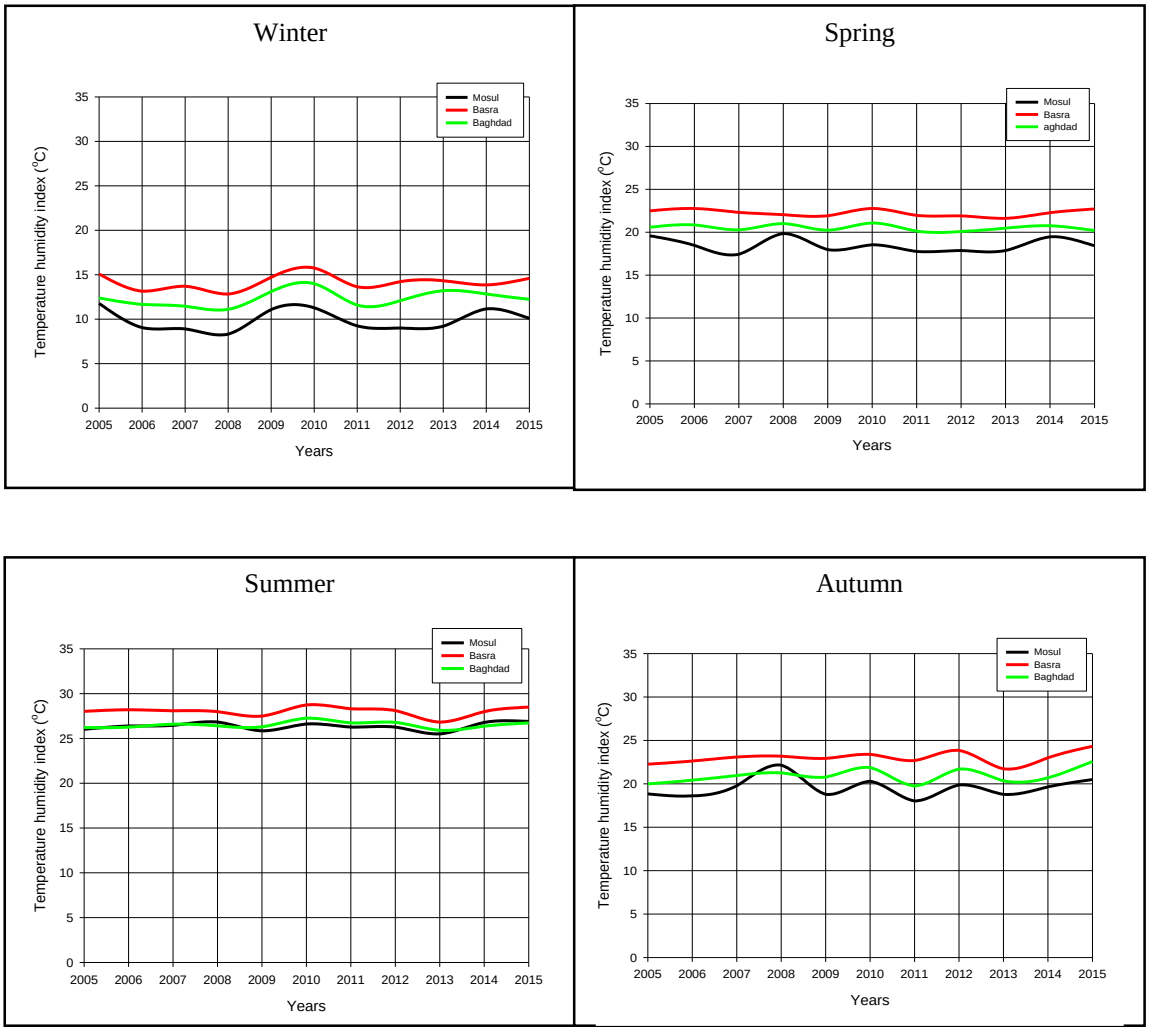

Figure (3). The change in the seasonal average of Temperature- Humidity Index (THI) for the period (2005-2015) for the stations (Mosul, Baghdad, and Basrah).

The Tables (4) and (5) showing values the seasonal change of the Temperature-Humidity Index (THI) at the Mosul station and the Baghdad station respectively for the period (2005-2015), it can be observed that the winter it is characterized by being very uncomfortable and severe cool and therefore will be not perfect for the comfort of the human only through the use of heating and wear heavy clothes, Note that the spring months at the Mosul station at the beginning of the season are uncomfortable cool and April is the only perfect month because the temperature starts to rise at the end of April until the season end is uncomfortable warm, as for the Baghdad station we notice that the spring months at the beginning of the season are perfect and the temperature increases during the rest of the spring months to become uncomfortable warm in April and uncomfortable hot at the end of spring, The summer months in Mosul and Baghdad are generally very uncomfortable and therefore are not perfect for the comfort of the human only through using air conditioning to high heat, Autumn season to Mosul and Baghdad begins with temperatures drop after hot summer until becomes at beginning of the season is uncomfortable hot and continues to decline until it becomes uncomfortably hot in the mid-season and uncomfortable cool at the end of the chapter and the Baghdad station at the end of the season become perfect,

Table (4). Values the seasonal change for the Temperature-Humidity Index (THI) by categories and symbols of human comfort in Mosul station for the period (2005-2015).

Seasons	Months	THI	Category	Symbol
Winter	DEC	9.94	Severe cool	C-
	JAN	8.69	Severe cool	C-
	FEB	11.9	Severe cool	C-
Spring	MAR	14.41	Cool	C
	APR	18.65	Perfect	P-
	MAY	22.36	Warm	H
Summer	JUN	25.41	Very hot	H-
	JUL	26.91	Very hot	H-
	AUG	26.74	Very hot	H-
Autumn	SEP	23.95	Hot	H*
	OCT	20.11	Warm	H
	NOV	14.66	Cool	C

Table (5). Values the seasonal change for the Temperature-Humidity Index (THI) by categories and symbols of human comfort in Baghdad station for the period (2005-2015).

Seasons	Months	THI	Category	Symbol
Winter	DEC	12.45	Too cool	C*
	JAN	10.88	Severe cool	C-
	FEB	13.67	Too cool	C*
Spring	MAR	16.99	Perfect	P*
	APR	20.61	Warm	H
	MAY	23.95	Hot	H*
Summer	JUN	25.77	Very hot	H-
	JUL	26.88	Very hot	H-
	AUG	26.86	Very hot	H-
Autumn	SEP	24.86	Hot	H*
	OCT	21.81	Warm	H
	NOV	16.15	Perfect	P*

The Table (6), shows values the seasonal change for the Temperature-Humidity Index (THI) in the Basrah station for the period (2005-2015), it can be observed that the winter it is characterized as uncomfortably cool and becomes uncomfortably too cool in the middle of winter. The only ideal month is the month of February therefore, the first two months of winter will be not perfect for the comfort of the human only through the use of heating and wear heavy clothes and the end of winter be perfect for living, we note that the spring months at the beginning of the season are perfect and the temperature increases during the rest of the spring months to become uncomfortable warm in April and uncomfortable very hot at the end of the spring, as for the summer season it is generally very uncomfortable and heat and therefore it is not perfect for the comfort of human except through the use of air conditioning to high heat, Autumn season temperatures start to drop slightly to become in the mid-autumn is uncomfortable hot and at the end of the season the heat goes down to become the perfect atmosphere.

Table (6). Values the seasonal change for the Temperature-Humidity Index (THI) by categories and symbols of human comfort in Basrah station for the period (2005-2015).

Seasons	Months	THI	Category	Symbol
Winter	DEC	14.07	Cool	C
	JAN	13.00	Too cool	C*
	FEB	15.45	Perfect	P
Spring	MAR	18.56	Perfect	P-
	APR	22.45	Warm	H
	MAY	25.75	Very hot	H-
Summer	JUN	27.19	Very hot	H-
	JUL	28.23	Very hot	H-
	AUG	28.65	Very hot	H-
Autumn	SEP	26.53	Very hot	H-
	OCT	24.11	Hot	H*
	NOV	18.38	Perfect	P-

Through the Figure (4), that show the annual average temperature change and the Temperature-Humidity Index (THI) for the study period (2005-2015) for the stations (Mosul, Baghdad, and Basrah), Mosul station and highest value were 19.28^{o}C in 2008, the lowest value was 17.82^{o}C in 2011, Baghdad station and note that the highest value of 21.05^{o}C in 2010, the lowest value of 19.55^{o}C in 2011, Basrah station the greatest value of the index was 22.67^{o}C in 2010, and the lowest value of the index of 21.12^{o}C in 2013. Also, from the observation of the shape, we find that the temperature values follow the same behavior as the Temperature-Humidity Index (THI) values, that is, they follow the same direction.

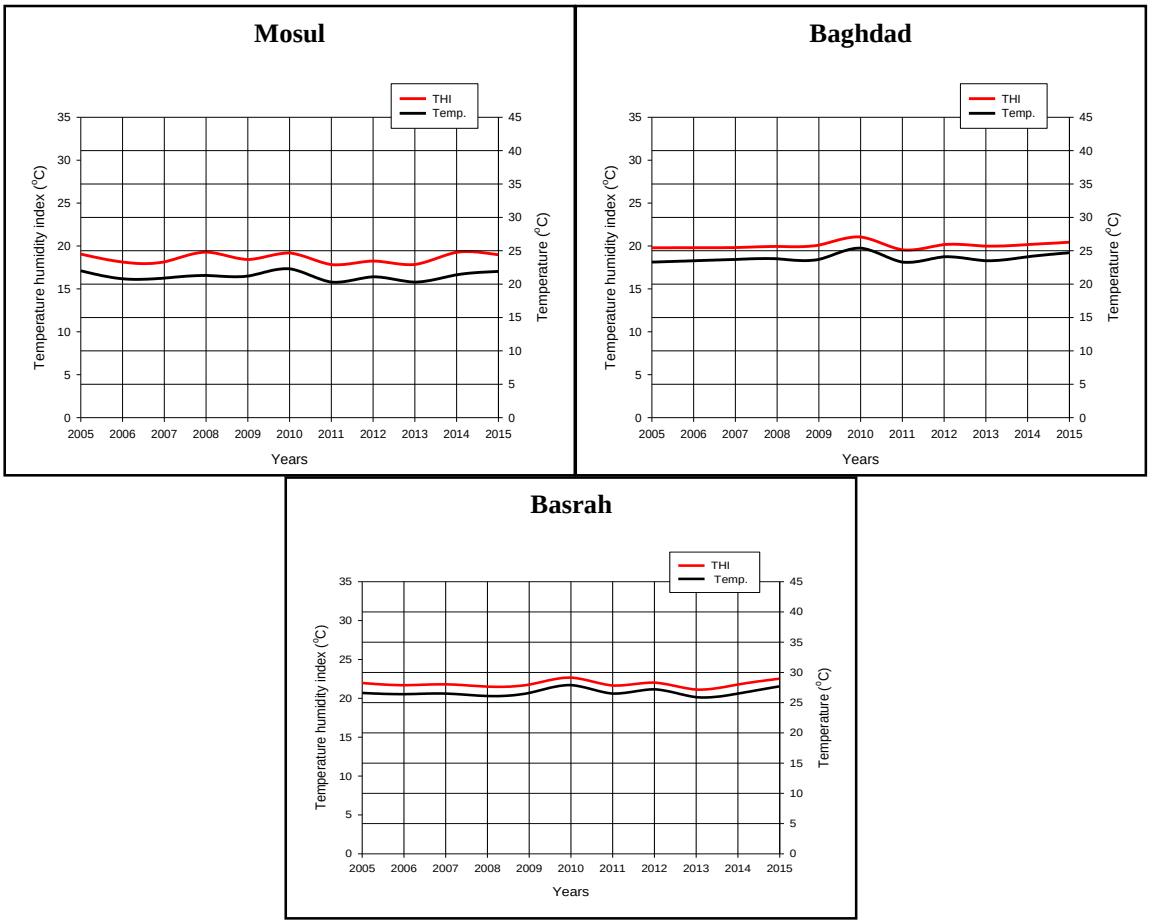

Figure (4). The annual change of Temperature (T) and the Temperature-Humidity Index (THI) for the period (2005-2015) for stations (Mosul, Baghdad, and Basrah).

The Figure (5), shows the annual relative humidity change and the Temperature-Humidity Index (THI) for the study period (2005-2015) and the stations (Mosul, Baghdad, and Basrah), Mosul station, where the index of Temperature-Humidity Index (THI) ranges between (15-20) and corresponding relative humidity between (42-52), Baghdad station and the value of the index between (18-22) and the corresponding relative humidity between (35-45), Basrah station the value of the index ranges between (19-22) and the corresponding relative humidity between (35-42), we also note that the behavior of relative humidity is contrary to the behavior of the (THI), The indicator is inversely proportional to the relative humidity, As the relative humidity increases, the indicator values decrease and vice versa, and Figure (6), which shows the values of the total annual change of the Temperature-Humidity Index (THI) for eleven years (2005-2015).

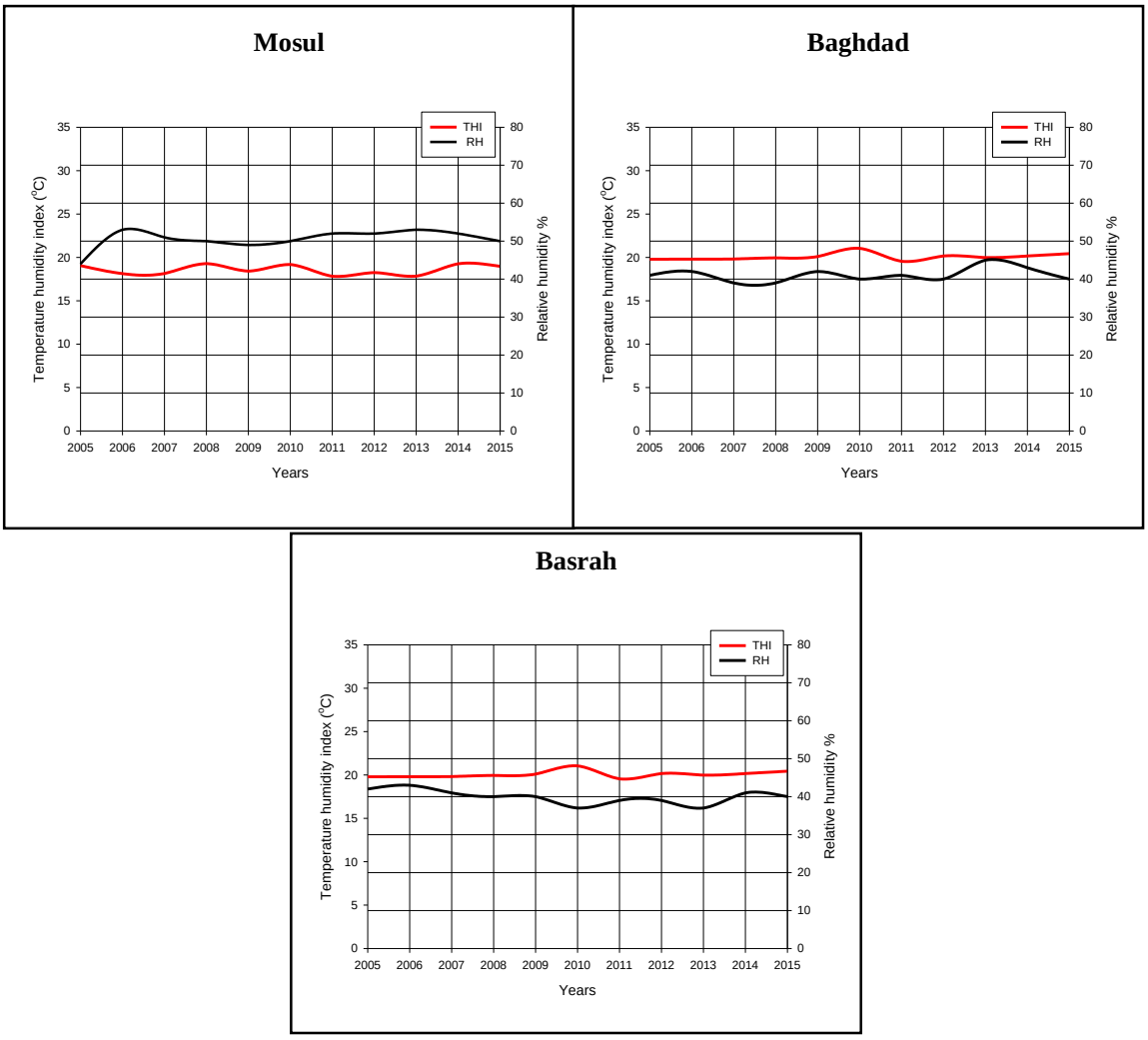

Figure (5). The annual change of relative humidity and the Temperature-Humidity Index (THI) for the period (2005-2015) for stations (Mosul, Baghdad, and Basrah).

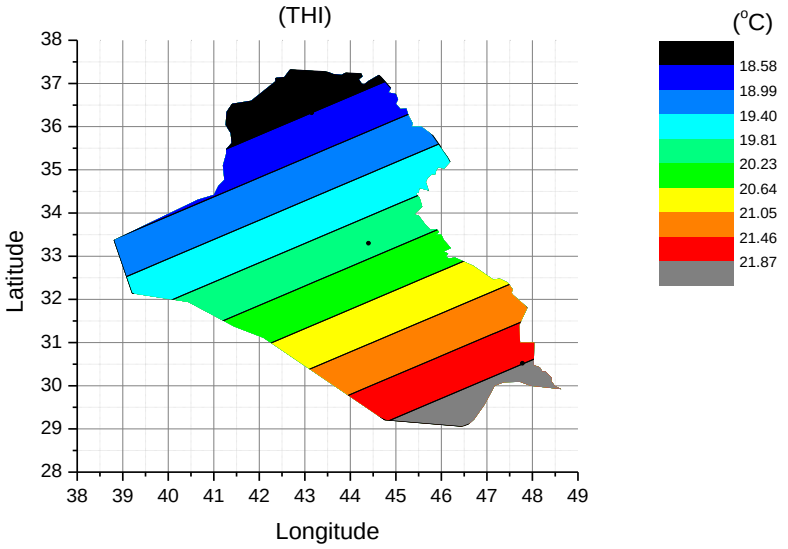

Figure (6). The total annual change of the Temperature-Humidity Index (THI) for the study period (2005-2015) and stations (Mosul, Baghdad, and Basrah).

The Figure (7) and Table (7), show that the relationship between temperature and Temperature-Humidity Index (THI), Is a strong positive relationship as the increase in temperature leads to an increase in the values of the (THI) for the three governorates (Mosul, Baghdad, Basrah). As for Simple Linear Regression (SLR) and low P-value, it is less than 0.001, so the relationship is linear.

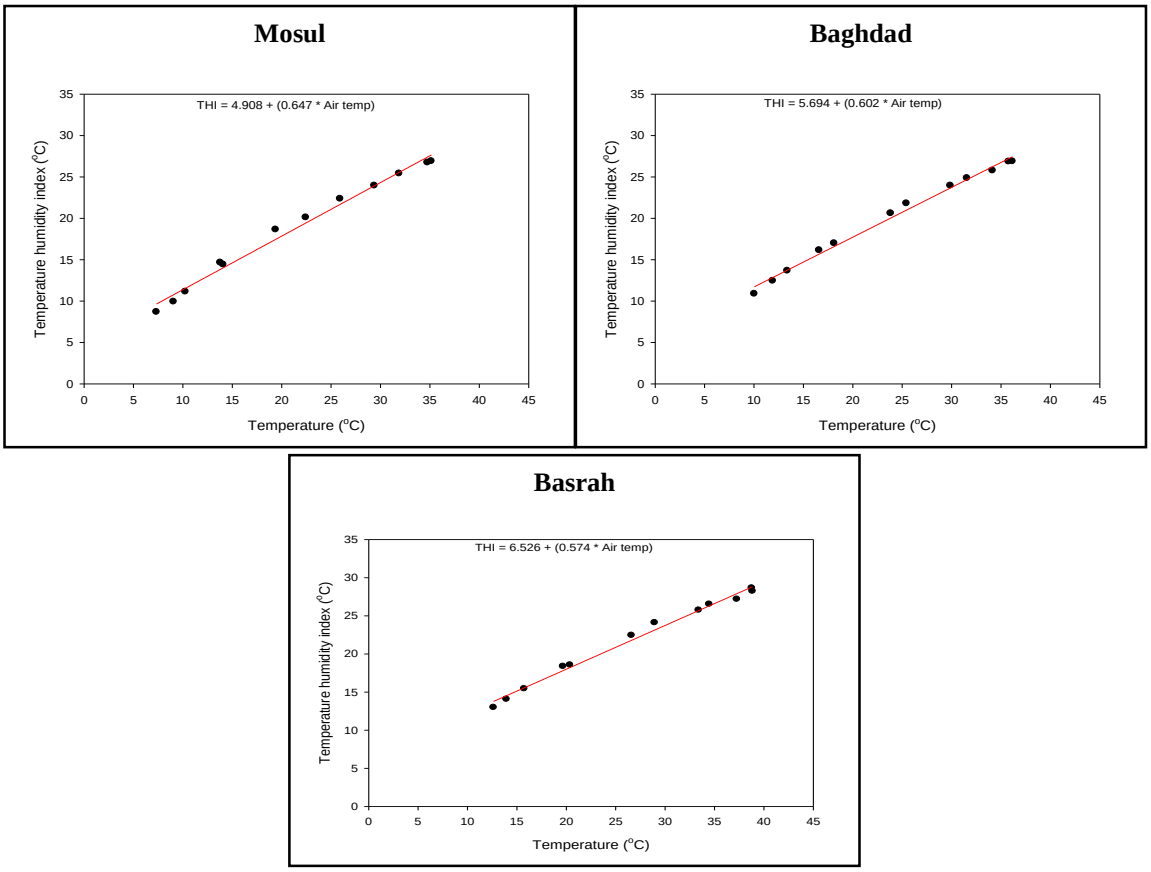

Figure (7). The relationship between Temperature and Temperature-Humidity Index (THI) for stations (Mosul, Baghdad, and Basrah) for the study period (2005-2015).

Table (7). The results of Simple Linear Regression and Spearman Rho Test and the strength of the relation between Temperature (T) and Temperature-Humidity Index (THI) for stations (Mosul, Baghdad, and Basrah), for the study period.

Stations	Simple Linear Regression		Spearman Rho Test	
	P-value	Interpretation	r_s	Correlation
Mosul	<0.001	Linear	0.993	Positive strong
Baghdad	<0.001	Linear	0.996	Positive strong
Basra	<0.001	Linear	0.993	Positive strong

The Figure (8) and Table (8), shows we find that the relationship between humidity and temperature and humidity index (THI) is a strong inverse relationship where increasing the relative humidity lead to decrease in values of heat and humidity index (THI), For the three stations (Mosul, Baghdad, Basrah), as for Simple Linear Regression (SLR) and low P-value, it is less than 0.001, so the relationship is linear.

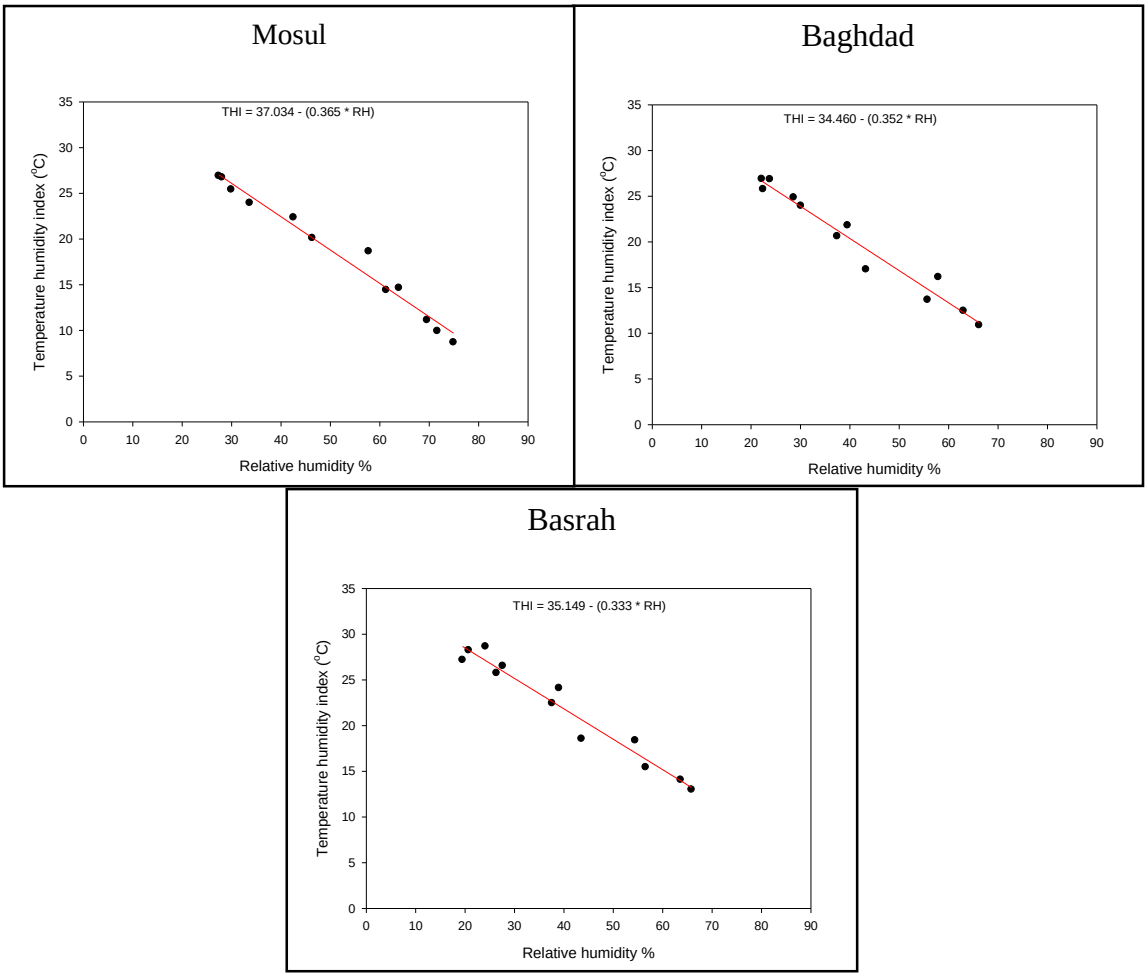

Figure (8). The relationship between relative humidity and Temperature-Humidity Index (THI) for stations (Mosul, Baghdad, and Basrah) for the study period (2005-2015).

Table (8). The results of Simple Linear Regression and Spearman Rho Test and the strength of the relation between relative humidity and Temperature-Humidity Index (THI) for stations (Mosul, Baghdad, and Basrah), for the study period.

Stations	Simple Linear Regression		Spearman Rho Test	
	P-value	Interpretation	r_s	Correlation
Mosul	<0.001	Linear	-0.993	Inverse High
Baghdad	<0.001	Linear	-0.979	Inverse High
Basra	<0.001	Linear	-0.958	Inverse High

CONCLUSIONS

The variation in weather conditions (temperature, relative humidity) during months and seasons of the year, It has led to the variation of human comfort from one season to another and from one city to another as the greatest comfort stations is the Mosul station and the least comfortable stations are Basrah and Baghdad are considered to be middle-class stations comfort. Uncomfortable weather during the summer months in all stations studied (June, July, August) due to high temperature, during the months of winter (December, January and February). It is also uncomfortable except for the month of February for the Basrah station is perfect due to the early heat rise of the spring. Spring is different between these stations in the Mosul station varies between the cool uncomfortable in March and perfect in April and the warm uncomfortable in the month of May, In Baghdad station, the feeling of comfort between the perfect in March and the warm uncomfortable in month April, and hot uncomfortable in month May, Basrah station is similar to the Baghdad station in of feeling comfortable for spring, but the month May is characterized as an extension of the summer is very uncomfortable heat. The autumn season for the Mosul station contrasts between the hot uncomfortable at the beginning of the season in month September and the month of October uncomfortable warm ,and uncomfortable cold in the month of November, Baghdad station is similar to the Mosul station for the first two months of the season, but it is perfect for rest in November, Basrah station. The beginning of the season is an extension of the hot summer where it is very hot uncomfortable in September and hot uncomfortable in October, and the only perfect month in the Basrah station for the autumn season is the month of November.

REFERENCES

AL-Jabouri, M. H., 2007: Assessing the Physiological Comfort of People in Iraq, Al-Mustansiriyah Science Journal, 18,

Giles, B.D., Balafoutis, C.H. and Maheras, P. (1990) too hot for comfort: the heat waves in Greece in 1987 and 1988. Ini. J. Biomet., 34, 98-104.

Gouda, H. J., 1989: Geographical and climatic geography, Alexandria Dar Al - Maarefah University.

Holly, et al. 1979. Human and the Environment, the Small Encyclopedia Magazine of the Ministry of Culture and Arts, 39 (Baghdad 1979).

Iraqi Meteorological Organization and Seismology (IMOS), 2015. Temperature and Wind Speed for the Period 2005-2015, Climate Section. (2015).

Kendall's Tau-b Correlation Coefficient, 2011.

DOI=http://www.support.sas.com/documentation/cdl/en/procstat/63104/HTML/default/viewer.htm#procstatcorrsect015.htm

Mahdi, A., F. 1990. Climate on the health and comfort of human impact in Iraq, Master Thesis, University of Baghdad, 15-110, (Baghdad 1990).

Mathematics in Education and Industry (MEI) , Spearman's rank correlation, (2007).

Mohamed S. 2009. Data analysis management and industrial engineering, (2009).

DOI=http://samehar.wordpress.com/2009/08/13/0120809/

Musa, Ali Hassan, 2002: physiological climate, Dar Nineveh, Damascus.

Omar, F. 1989. The Relationship between Climate and the Nature of Human Sense in Jordan, Master Thesis, University of Jordan, 62, (Jordan 1989).

Tanjung W., H. 1966. Physiology Climates of the Conterminous United states: A Bioclimatic Classification Based on Man, Annals of the Association of American Geographers, 56 (1966).

Thom E.C., 1959: "The discomfort index ", Weather wise, 12, 59-60.

Yazdani M., R., Khoshhal D., J., Mahdavi M., and Sharma A. 2011. Trend Detection of the Rainfall and Air Temperature Data in the Zayandehrud Basin, Journal of Applied Sciences, 11, 2125-2134 (2011).

AN EVALUATION OF TOURISM CLIMATE INDEX IN IRAQ

Alaa M. Al-Lami, Yaseen K. Altimimi, Hasanain K. A. AL-Shamarti
Atmospheric Sciences Department, College Of Science, Al-Mustansiriyah University, Baghdad, Iraq
alaamoter1975@gmail.com; yaseen.k.abbas@gmail.com; alshmirty@gmail.com

Abstract
Tourism represents one of the most important sectors of the global economy. It is very sensitive to the climate and weather conditions, and these conditions play a significant role for selecting the destination of tourists. Iraq has a high potential for attracting the tourists due to the variability of tourism sectors. The aim of this study is to evaluate the Tourism climate index (TCI),was developed by Mieczkowski for Iraq, using the actual daily measurements of five parameters (air temperature , relative humidity, wind speed, precipitation, , and sunshine duration) of 36 meteorological stations distributed over the whole study area and for a period of 33 years (1983-2016).Monthly and seasonal spatial distributions of TCI were analyzed using ArcGIS 10.3 tools for the study area. Results show a markable spatiotemporal variability of TCI values ranging from Marginal (40-49%) to Ideal (90-99%). During the months from (November to February), the central and southern parts of Iraq gave excellent and ideal rank due to moderate levels of rainfall and air temperature. The months March, April and October reveal favorite best times for tourism comfort for all Iraq regions with a peak values at the northwest part of Iraq. The results of hot months (May to September.) show that the southern area of Iraq namely (Basrah, Amara, and Nasiriyah) has low values of TCI with an acceptable score in comparison with the high TCI values in the northern parts, namely (Arbil,Duhook, Sulaymaniyah, Mosul, and Kirkuk).Seasonal maps of TCI indicated that spring and fall are the best seasons for tourism comfort for all parts of Iraq.

Key Words: *Tourism, Air temperature, Tourism climate index, Heat comfort, Iraq.*

INTRODUCTION
Tourism has a complex and highly variable relationship with climate.It is widely agreed that climate conditions have the ability for affecting many facets of the tourism sector (Becken and Hay 2012, Scott et al. 2012, Scott and Lemieux 2010, Gomez- Martin 2005). All tourism sectors and products are weather/climate sensitive to a degree and climate act both as a limiting constraint for tourist's activities and as a resource (Scott et al. 2012).

Many studies have been suggested to identify the impact of climate parameters on tourism comfort (Mieczkowski 1985; Becker 1998; Morgan et al. 2000; Maddison 2001; Lise and Tol 2002; Bigano et al. 2006). The impact of climate parameters such as air temperature, moisture, solar radiation, and precipitation is very critical for the tourism activities of a given area. The statistical results of the previous studies, confirm the role of climate factors on determination of the tourism requirements.

De Freitas (2003) defined three climate facets: thermal, physical and aesthetic components as comprising climate resources for tourist destinations. The thermal component represents the relationship with the thermal comfort of tourists; The physical component is related to the precipitation and wind speed, which may be considered as a limiting factor for some tourist activities, but is necessary for others. The aesthetic component includes cloud cover, sunshine, sky color, and fog. Climate is not always a beneficial resource for destinations, it may also act as a constraint, as the distribution of climate resources varies seasonally and is not homogeneous across earth surface (Gomez-Martin 2005 and Andriotis 2005).

Mieczkowski (1985) suggested the first formula for evaluating the effect of climate on tourism activities which is called the Tourism climate index(TCI). This index gives a detailed and conceptive measure for evaluation purposes of the general activities of tourism by employing all climatic parameters relevant to the tourism comfort. Mieczkowski index consists of seven climate parameter and used to compute five sub-indices of TCI formula: CDI (daytime comfort index, combination of minimum daily relative humidity and maximum daily temperature), CIA (mean daily relative humidity and mean daily temperature), sunshine duration (hrs), wind velocity (km/h) and precipitation (mm).TCI used to assess projected climate changes and the suitability of the climate for different destination and also for global world(Scott et al. 2016**)**. Mieczkowski has calculated tourism climate index of 453 meteorological stations and organized the output during 12 months of the year for the global world.

The formula of Mieczkowski it is widely used in many research studies for different locations in the world to choose the best time and place for tourism comfort by employing the synoptic measurement for a long period (Matzarakis 2006, Farajzadeh.&Ahmadabadi 2014, Fang and Jie Yin, 2015, Scott et al. 2016).

Frome this point of the view the aim of this study is to evaluate the tourism climate index TCI of Iraq using the real measurement of five parameters in 36 meteorological stations and for a period of 33 years in addition to study the monthly and seasonal spatial distribution of TCI for the area of study.

MATERIAL AND METHODS

Area of Study and Data Acquisition

The overall area of Iraq is 438 320 km2, bordered by Kuwait and Saudi Arabia in the south, Turkey from the north, from east the Islamic Republic of Iran, the Arabian Gulf to the southeast, and the Syrian and Jordan to the west. Topographically, the shape of Iraq is like a basin, consisting of the Great Mesopotamian alluvial plain of the Tigris and the Euphrates rivers (Figure 1). The mountains surrounding This plain in the north and the east, and reach altitudes of 3550 m above sea level. 40% of the land area covered by desert area in the east and south of Iraq. Iraq climate is continental and subtropical semi-arid type, the northern parts of Iraq having a Mediterranean climate type. Rainfall occurs mostly during the winter months (December.-February.), and the rainfall rate has seasonal variations. In the northern parts of Iraq, the rainy period is from (Nov.-Apr.). The mean annual of precipitation is about 216 mm, and ranging from less than 100 mm in the south and 1200 mm in the northern parts of the country. The summer is extremely hot; maximum averages happened in July and August 42 °C. Winter, in general, are cool to cold, the temperature during daytime it is about 16 °C and decreasing to 2 °C at night (AL-Lami et al. 2014 and AL-Salihi et al. 2014).

Daily routinely measurements of 36 meteorological stations for 33 years span (1983-2016) were used in this study. The elements which include five parameters (air temperature, wind speed, relative humidity, and precipitation) were used to compute the five sub-indices of TCI (Daytime Comfort Index CDI, Daily Comfort Index CIA, Precipitation (in mm), wind speed (in km/h) and sunshine duration (in hours)). The meteorological stations are distributed above all the study area and run by the Iraqi Meteorological Organization and Seismology (IMOS). Table 1 lists the names and geographical coordinates of the selected stations. A quality control process of the measurements of these stations was achieved using ClimPACT2 computer application. The procedure includes extreme, threshold and completeness checking which proved that all data satisfied the requirements of TCI. A MATLAB program was build to obtain all the data required by the index and the output data stored in EXCEL worksheets.

Figure 1. The distribution of weather stations throughout the whole area of Iraq

Table 1. The names and geographical locations of the selected stations in Iraq

	Station	*Lon.*	*Lat.*	Elev.		*Station*	*Lon.*	*Lat.*	*Elev.*
1	*Taleafer*	*42.48*	*36.37*	*373*	19	*Emadiyah*	*43.3*	*37.05*	*1236*
2	*Samawa*	*45.27*	*31.27*	*11*	20	*Fao*	*48.5*	*29.98*	*01*
3	*Duhook*	*43*	*36.78*	*554*	21	*Heet*	*42.75*	*33.63*	*58*
4	*Kirkuk*	*44.35*	*35.74*	*331*	22	*Hella*	*44.45*	*32.45*	*27*
5	*Kerblaa*	*44.05*	*32.57*	*29*	23	*Kut*	*45.75*	*32.49*	*21*
6	*Samara*	*43.88*	*34.18*	*75*	24	*Najaf*	*44.32*	*31.95*	*53*
7	*Haditha*	*42.35*	*34.13*	*108*	25	*Nukheb*	*42.28*	*32.03*	*305*
8	*Biji*	*43.53*	*34.9*	*116*	26	*Qaim*	*41.02*	*34.38*	*178*
9	*Nasiryah*	*46.23*	*31.02*	*05*	27	*Rabiah*	*42.1*	*36.8*	*382*
10	*Mousl*	*43.15*	*36.31*	*223*	28	*Ramadi*	*43.32*	*33.45*	*48*
11	*Rutba*	*40.28*	*33.03*	*222*	29	*Salahaddin*	*44.2*	*36.38*	*1075*
12	*Diwaniya*	*44.95*	*31.95*	*20*	30	*Sinjar*	*41.83*	*36.32*	*583*
13	*Hai*	*46.03*	*32.13*	*17*	31	*Sulaymaniyah*	*45.45*	*35.53*	*843*
14	*Basara*	*47.78*	*30.52*	*02*	32	*Sumeel*	*42.75*	*36.87*	*250*
15	*Amara*	*47.17*	*31.83*	*09*	33	*Tikrit*	*43.7*	*34.57*	*107*
16	*Anah*	*41.95*	*34.37*	*175*	34	*Tuz*	*44.65*	*34.88*	*220*
17	*Arbil*	*44*	*36.15*	*420*	35	*Zakho*	*42.72*	*37.13*	*433*
18	*Dukcan*	*44.95*	*35.95*	*276*	36	*Baghdad*	*44.4*	*33.3*	*32*

Methodology

The TCI was designed by Mieczkowski (1985) as a quantitative method to evaluate a specific location's climate suitability for general tourism activities. The TCI assesses the climate suitability in a specific destination for tourism by employing seven climatic parameters in relation to tourism. These parameters which include: mean air temperature, maximum air temperature, mean relative humidity, minimum relative humidity, the amount of precipitation, hours of sunshine and average wind speed were grouped into five sub-indices (see Table 2). It is worth to notice, that in Mieczkowski's original design, mean monthly climate data is required for index input. In this study, daily climatic data was used as a TCI input.

The Mieczkowski index adopted the following formula:

$$TCI = 2 * (4CID + CIA + 2R + 2S + 2W) \qquad (1)$$

CID has the high weight (40%) because the activity of the tourists reaches the maximum at the daytime. 20% is given for both of sunshine and precipitation variables. Less weight (10%) is given to the wind speed and the daily comfort index (CIA).

Table 2: Components of Tourism Climate Index (TCI) (Mieczkowski 1985)

Subindex	*Monthly climate variable*	*scores*
Daytime comfort (CID)	*Mean of maximum of temperature* *Mean of minimum of relative humidity*	*40%*
Daily comfort (CIA)	*Mean daily of temperature* *Mean daily of relative humidity*	*10%*
Precipitation (R)	*Precipitation*	*20%*
Sunshine (S)	*Total hours of sunshine per day*	*20%*
Wind speed (W)	*Average wind speed*	*10%*

Each sub-index takes an optimal rating of 5, by employing a standardized rating system. A classification scheme for the TCI scores was suggested by Mieczkowski. Also, he presents a simplified rating system combined with the TCI classification scheme as shown in Table 3. In the present study, a 70% or higher values of TCI was considered attractive to the "typical" tourist engaged in relatively light activities such as sightseeing and shopping. We have to clarify the fact that the TCI is inappropriate for making predictions for a number of tourist visits. The index was designed solely to indicate levels of climatic comfort for tourism activity and did not consider the existence and quality of vital tourism infrastructures such as transportation and attractions. Thus, the region with a high TCI may experience low levels of tourist visitors and vice versa, because a multitude of factors other than climatic conditions influences tourism activity.

Table 3. A classification scheme for mapping TCI (Mieczkowski 1985)

Numerical value of indices	*Descriptive category*
90-99	*Ideal*
80-89	*Excellent*
70-79	*Very Good*
60-69	*Good*
50-59	*Acceptable*
40-49	*marginal*
30-39	*unfavorable*
20-29	*Very unfavorable*
10-19	*Extremely unfavorable*
Below 10	*Impossible*

The calculation of CID and CIA values was done by using the psychrometric chart, modified from ASHRAE (1972) standards of effective temperature (Figure 2).

The values of R, S, and W were calculated using the rating scales developed by Mieczkowski for sunshine, precipitation and wind speed, a tabulated values for rating scales of the three sub-indices were given detail in the original paper of Mieczkowski (1985).

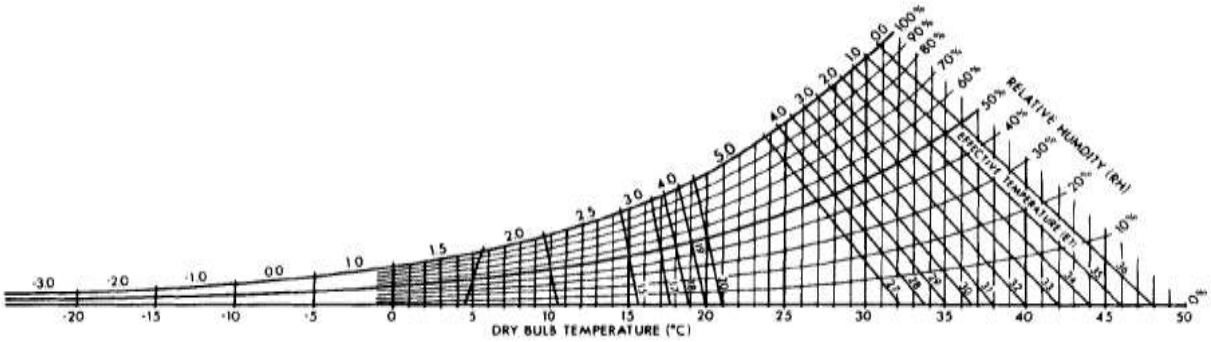

Figure (2): Psychrometric chart, modified from ASHRAE 1972 (Mieczkowski 1985)

RESULTS AND DISCUSSION

The monthly and seasonal results of TCI scores for all stations were converted into ArcGIS 10.3 system to make mapping of the spatial distribution of this index for the whole Iraq area. A technique of Inverse Distance Weighting (IDW) model was used for interpolation of the values of TCI. The monthly values of TCI for 36 meteorological stations in the area of study were presented in figure 3. Overall, the rank of values is ranging between acceptable and ideal, there is a significant spatial variation of TCI due to climate variety of different sites of Iraq. During the cold months (November-February) it was seen that the southern and central regions of Iraq (below latitude. 34) would be the best places for tourism comfort due to moderate values of air temperature and relative humidity.The highest values of TCI appeared in Basra, Nasiriyah, and Amara in this period of year (between 75% and 95%), conversely, the north and northeast part of Iraq was almost acceptable to good during this time, because of the low level of air temperature (less than 5 °C) and heavy precipitation. The lowest values were in Sinjar station especially during the January and February (around 40%). The mapping of the average TCI during the months of spring and autumn equinoxes (March, April, September, and October) shows excellent to ideal scores for most Iraq area especially in the northern part in September and October and southern part in March and April. According to the results of TCI mapping, April and October months could be considered as the best time for tourism in Iraq, This finding can be justified by the score of TCI was ideal for 75% of all Iraq and 25% from good to excellent, this ideal results it is due to the typical values of most climate parameter especially air temperature, relative humidity, and precipitation. This typical condition lead to lower energy consumption during these months for cooling and heating. The results of hot months (May-August) shows that the southern part of Iraq it not suitable for tourism activities especially in Basrah, Nasiriyah, Amara, Samaua, and Diwanyia during July and August because the extremely high temperature and low level of moisture, the TCI scores of latter stations were Marginal for most times of dry season. In the last years, these stations recorded among the hottest places in the world where the maximum air temperature reach to 50 °C for some days in July and August in addition to the effects of thermal syclone from red sea and persistent dust storms. In the central cities of Iraq, the score was acceptable to good for all hot months, while the best result appeared in the northern part with a score between good and very good especially in the northwest of Iraq. Figure 4 depicts the results of TCI mapping across Iraq of the different seasons. Most of Iraq cities are suitable for tourism activities during all seasons and have very good score, especially the area between the latitude of 34 and 36°. According to the results, spring season is the best period for tourism comfort so that about 80% of Iraq is having scores between excellent and ideal especially in the area between the latitudes 29 and 35° from west to east. The score is very good for the north of 35° latitude, except Emadiyah and Sinjar stations (good scores).The northern parts are suggested for tourism during summer season while the

central and southern regions are good and recommended during winter season. Table (4) shows the monthly and seasonal values of TCI scores of all selected stations.

Table 4. The monthly and seasonal values of TCI scores for 36 stations in Iraq.

1	*Station*	*Jan*	*Feb*	*Mar*	*Apr*	*May*	*Jun*	*Jul.*	*Aug*	*Sep*	*Oct*	*Nov*	*Dec*	*Spr*	*Fal*	*Win*	*Sum*
2	*Taleafer*	*58*	*58*	*60*	*88*	*94*	*86*	*74*	*76*	*86*	*94*	*70*	*59*	*81*	*90*	*61*	*79*
3	*Samawa*	*76*	*84*	*95*	*92*	*78*	*64*	*57*	*57*	*68*	*87*	*97*	*84*	*88*	*78*	*85*	*59*
4	*Duhook*	*54*	*56*	*60*	*79*	*96*	*90*	*80*	*80*	*98*	*94*	*66*	*54*	*78*	*96*	*58*	*83*
5	*Kirkuk*	*61*	*61*	*67*	*92*	*98*	*86*	*79*	*80*	*90*	*98*	*74*	*61*	*86*	*94*	*64*	*82*
6	*Kerblaa*	*71*	*82*	*92*	*98*	*81*	*71*	*61*	*61*	*72*	*91*	*97*	*76*	*90*	*82*	*81*	*64*
7	*Samara*	*71*	*71*	*82*	*97*	*91*	*76*	*65*	*65*	*81*	*99*	*93*	*69*	*90*	*90*	*76*	*69*
8	*Haditha*	*71*	*71*	*84*	*97*	*91*	*80*	*72*	*71*	*81*	*95*	*95*	*69*	*91*	*88*	*77*	*74*
9	*Biji*	*69*	*69*	*82*	*97*	*87*	*76*	*66*	*66*	*76*	*95*	*93*	*67*	*89*	*86*	*75*	*69*
10	*Nasiryah*	*76*	*84*	*94*	*90*	*76*	*66*	*56*	*57*	*70*	*83*	*97*	*80*	*87*	*77*	*84*	*60*
11	*Mousl*	*60*	*50*	*54*	*72*	*82*	*80*	*74*	*75*	*88*	*87*	*60*	*52*	*69*	*88*	*55*	*76*
12	*Rutba*	*76*	*80*	*94*	*98*	*77*	*65*	*61*	*61*	*68*	*87*	*97*	*76*	*90*	*78*	*82*	*62*
13	*Diwaniya*	*76*	*80*	*94*	*98*	*77*	*65*	*61*	*61*	*68*	*87*	*97*	*76*	*90*	*78*	*82*	*62*
14	*Hai*	*69*	*76*	*93*	*96*	*85*	*70*	*61*	*65*	*73*	*91*	*94*	*76*	*91*	*82*	*79*	*65*
15	*Basara*	*78*	*84*	*95*	*91*	*89*	*52*	*52*	*54*	*68*	*83*	*97*	*84*	*92*	*76*	*86*	*53*
16	*Amara*	*74*	*84*	*93*	*97*	*80*	*62*	*61*	*57*	*71*	*82*	*95*	*82*	*90*	*77*	*84*	*60*
17	*Anah*	*67*	*67*	*76*	*91*	*91*	*80*	*67*	*68*	*83*	*95*	*90*	*65*	*86*	*89*	*72*	*72*
18	*Arbil*	*54*	*58*	*64*	*71*	*94*	*98*	*85*	*90*	*98*	*93*	*67*	*54*	*76*	*96*	*58*	*91*
19	*Dukcan*	*52*	*53*	*59*	*85*	*96*	*86*	*75*	*76*	*90*	*95*	*66*	*51*	*80*	*93*	*56*	*79*
20	*Emadiyah*	*51*	*51*	*53*	*63*	*83*	*99*	*98*	*98*	*97*	*72*	*54*	*49*	*66*	*85*	*51*	*98*
21	*Fao*	*78*	*85*	*96*	*99*	*77*	*67*	*61*	*61*	*67*	*83*	*99*	*85*	*91*	*75*	*87*	*63*
22	*Heet*	*71*	*75*	*88*	*97*	*91*	*78*	*67*	*68*	*78*	*99*	*95*	*70*	*92*	*89*	*78*	*71*
23	*Hella*	*71*	*82*	*92*	*98*	*82*	*71*	*61*	*61*	*73*	*91*	*94*	*76*	*91*	*82*	*81*	*64*
24	*Kut*	*70*	*76*	*92*	*96*	*82*	*71*	*61*	*61*	*72*	*91*	*94*	*76*	*90*	*82*	*79*	*64*
25	*Najaf*	*76*	*82*	*94*	*98*	*78*	*67*	*61*	*61*	*69*	*91*	*96*	*78*	*90*	*80*	*83*	*63*
26	*Nukheb*	*71*	*77*	*92*	*99*	*91*	*77*	*67*	*67*	*79*	*99*	*95*	*72*	*94*	*89*	*79*	*70*
27	*Qaim*	*71*	*71*	*80*	*95*	*95*	*82*	*71*	*72*	*87*	*99*	*91*	*69*	*90*	*93*	*76*	*75*
28	*Rabiah*	*58*	*60*	*65*	*91*	*96*	*90*	*80*	*77*	*90*	*99*	*74*	*61*	*84*	*95*	*63*	*82*
29	*Ramadi*	*71*	*76*	*95*	*99*	*87*	*72*	*66*	*66*	*78*	*95*	*94*	*74*	*94*	*87*	*79*	*68*
30	*Salahaddin*	*50*	*52*	*56*	*67*	*94*	*98*	*86*	*90*	*98*	*94*	*63*	*50*	*72*	*96*	*54*	*91*
31	*Sinjar*	*41*	*41*	*49*	*59*	*67*	*81*	*95*	*77*	*73*	*64*	*53*	*39*	*58*	*69*	*44*	*84*
32	*Sulaymaniya*	*54*	*54*	*56*	*73*	*92*	*94*	*82*	*86*	*98*	*94*	*63*	*52*	*74*	*96*	*56*	*87*
33	*Sumeel*	*56*	*59*	*63*	*90*	*96*	*90*	*76*	*77*	*94*	*97*	*70*	*57*	*83*	*96*	*61*	*81*
34	*Tikrit*	*71*	*71*	*86*	*97*	*91*	*76*	*66*	*66*	*78*	*99*	*93*	*70*	*91*	*89*	*76*	*69*
35	*Tuz*	*67*	*67*	*82*	*95*	*94*	*76*	*66*	*71*	*86*	*99*	*91*	*69*	*90*	*93*	*74*	*71*
36	*Zakho*	*49*	*51*	*52*	*72*	*94*	*99*	*94*	*94*	*99*	*89*	*65*	*50*	*73*	*94*	*54*	*96*
37	*Baghdad*	*72*	*76*	*92*	*97*	*81*	*70*	*64*	*66*	*77*	*95*	*94*	*76*	*90*	*86*	*79*	*67*

Table 5 presents the monthly and seasonal ratio of TCI descriptive category for Iraq. The best ratio appeared in spring and fall months especially in April and October where more than 90% of Iraq was very excellent to ideal for tourism Comfort. The lowest ratio occurred in July and August months

Table 5. Monthly and seasonal ration of TCI descriptive category of Iraq

	TCI Category	Jan	Feb	Mar	Apr	May	Jun	Jul	Aug
1	*Ideal*	-	-	*56.32*	*80.48*	*30.83*	7.69	1.81	0.97
2	*Excellent*	-	*33.6*	*19.5*	*10.13*	*61.5*	18.38	9.15	9.14
3	*Very good*	*71.98*	*39.68*	*6.54*	*8.46*	*7.67*	43.71	15.16	18.02
4	*Good*	*12.49*	*11.32*	*11.01*	*0.93*	-	28.52	59.69	57.57
5	*Acceptable*	*14.76*	*14.67*	*6.63*	-	-	1.7	14.28	14.29
6	*Marginal*	*0.77*	*0.73*	-	-	-	-	-	-
7	*Other*	-	-	-	-	-	-	-	-
	TCI Category	Sep	*Oct*	*Nov*	*Dec*	*Spr*	Fal	Win	Sum
	Ideal	12.78	*71.29*	*75.27*	-	*63.57*	19.67	-	1.81
	Excellent	21.29	*27.57*	*6.35*	*19.16*	*23.43*	60.12	48.21	14.59
	Very good	62.44	*0.98*	*5.75*	*49.56*	*12.03*	20.21	31.36	26.11
	Good	3.48	*0.16*	*12.63*	*14.96*	*0.97*	-	8.54	54.64
	Acceptable	-	-	-	*15.37*	-	-	11.52	2.84
	Marginal	-	-	-	*0.95*	-	-	0.37	-
	Other	-	-	-	-	-	-	-	-

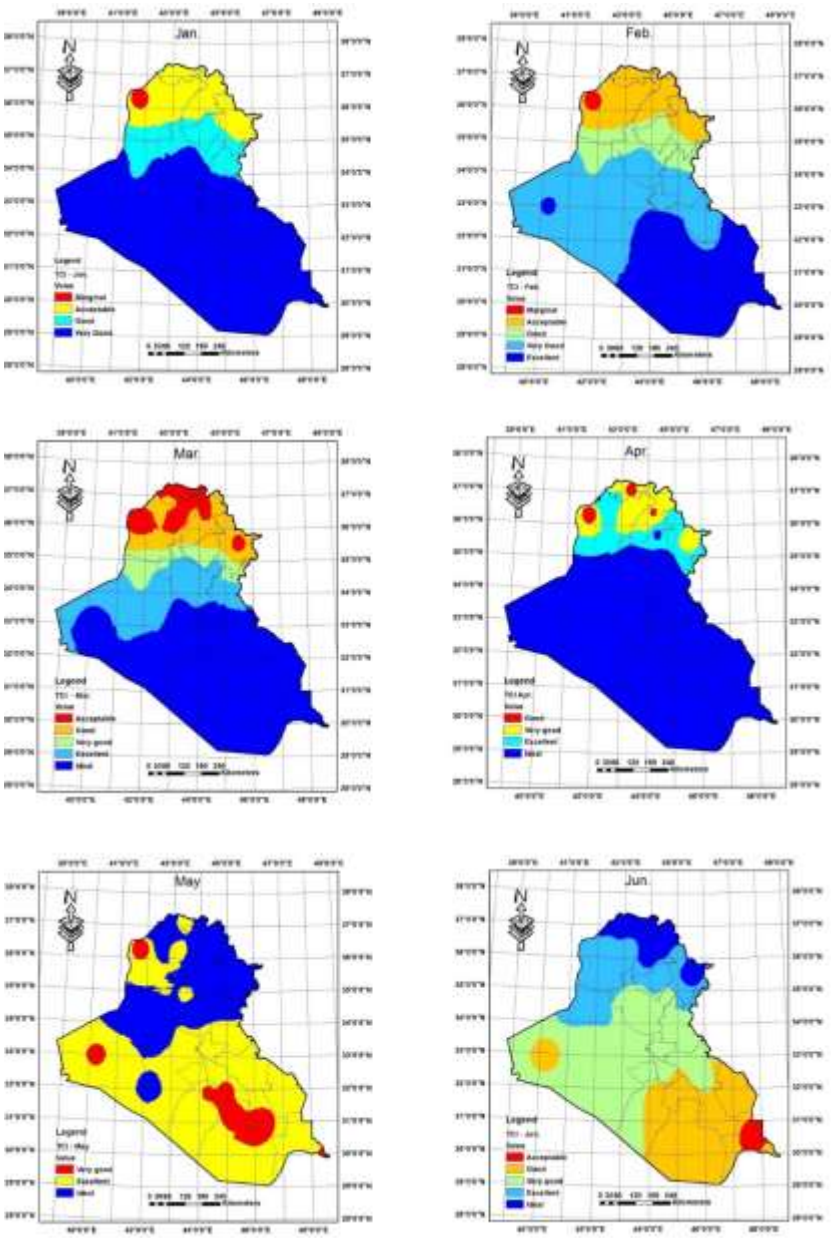

Figure 3. The Monthly spatial distribution of TCI values of Iraq

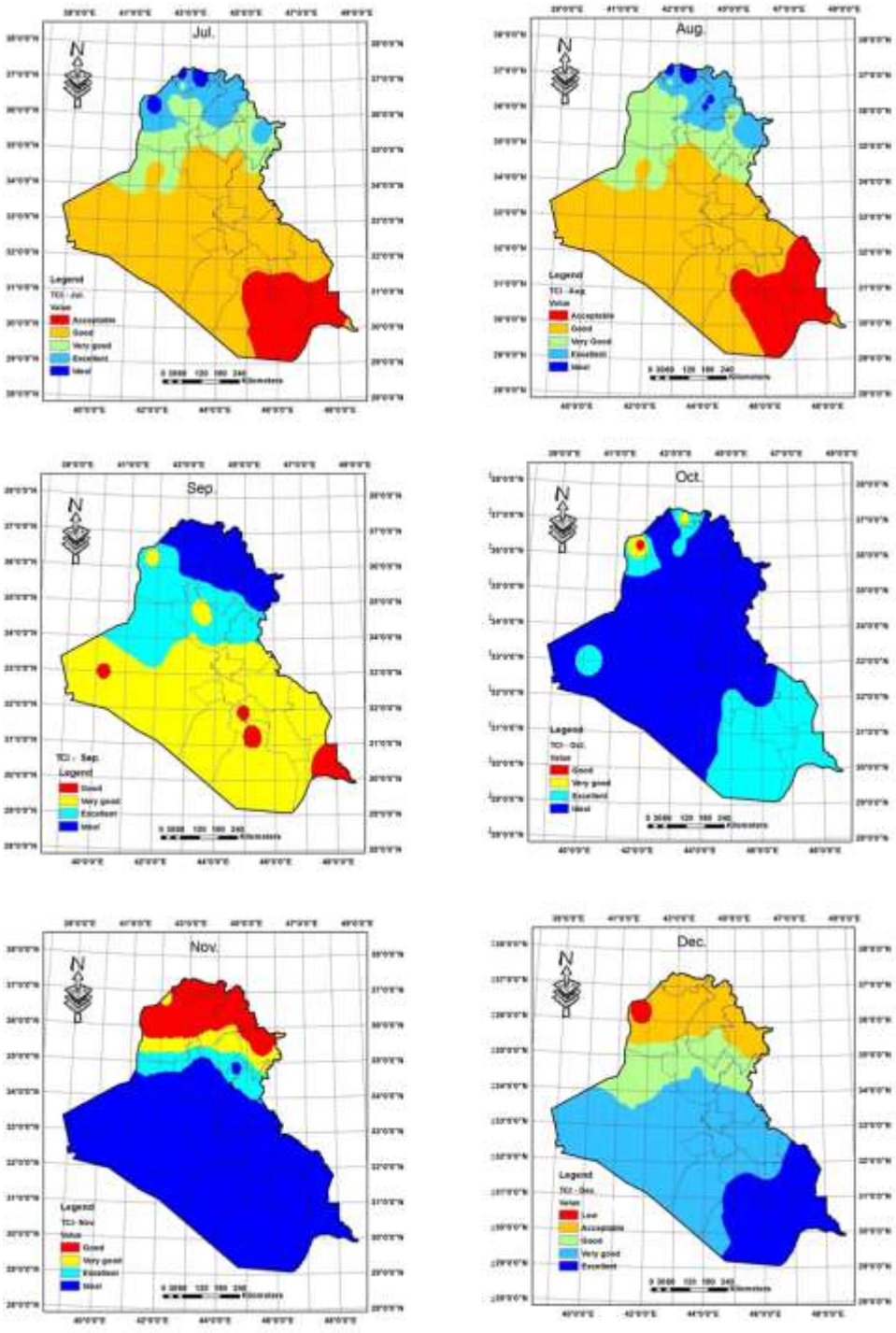

Figure (3): continued

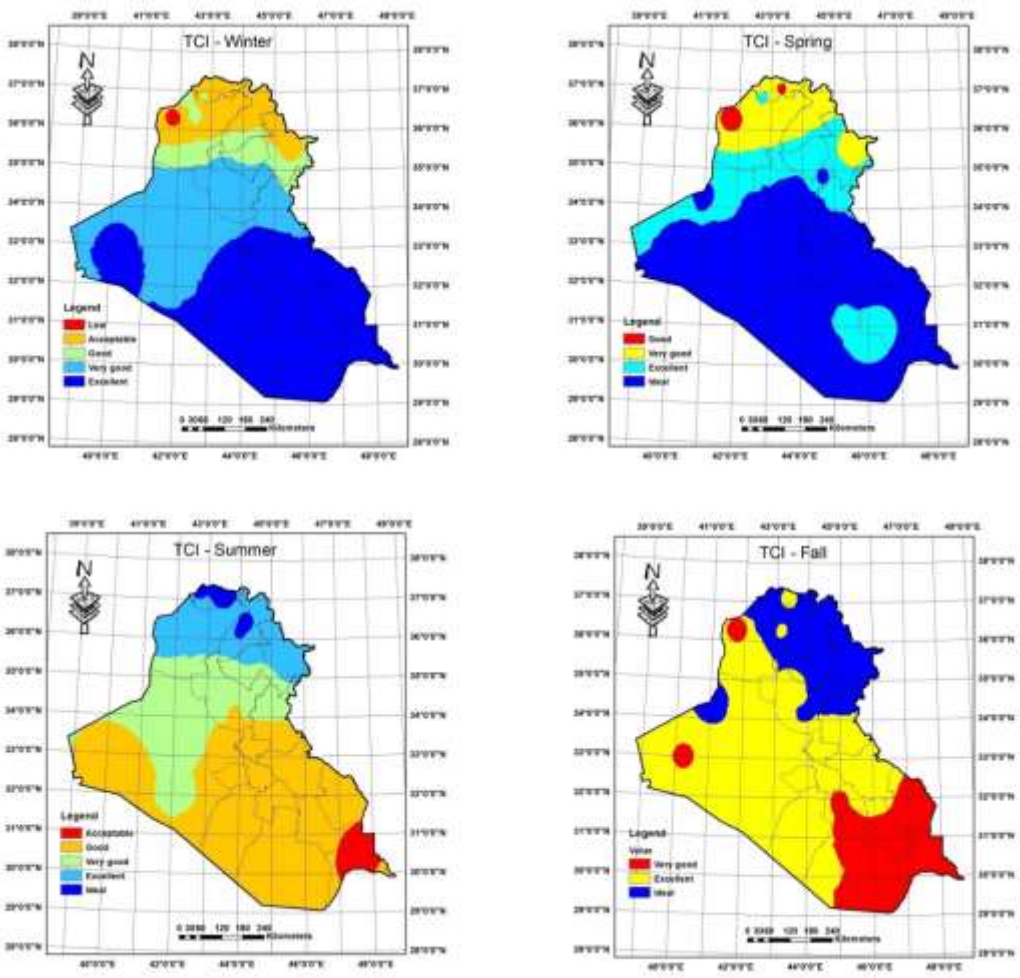

Figure 4. The seasonal spatial distribution of TCI values of Iraq

Four stations (Mosul, Baghdad, Rutba, and Basra) were selected from different locations in Iraq with different climate patterns to evaluate the monthly changes for the contribution of sub-indices of TCI, The results of this evaluation presented in figure 5. The contribution of mean daily sunshine hours was 20% (full score) for all four stations and for all 12 months. This can be attributed to the rather high average of daily sunshine which is more than 10 hours most of the year.The maximum values of CID and CIA occurred in spring and fall months (March, April, September, and October), for all stations and reached to the full score (40% and 10%). The score of CID was low in summer months (less than 25%) due to the effects of high heat index.The scores were near zero in Basra station (south of Iraq) in July and August while the best score appeared in Mosul station (north of Iraq).The effect of height level of precipitation in winter months was remarkable on the decreasing scores of R especially in Mosul and Rutba. Conversely, the best score was in spring and fall months due to the moderate average of precipitation. The change in W scores values was meager due to the few variations in wind speed values during the year, Most values were close to 10% of all stations, and lowest values occurred during the summer months, July and June. A comparison between the values of TCI for the four stations was presented in Figure 6. All stations had a peak TCI distribution in spring and fall months (more than 80%), and the lowest distribution appeared in July and August for Basra station, less than half. The TCI category was very good during the winter month in Basra, Baghdad, and Rutba.

Figure 5. The monthly contribution of TCI sub-indices for four stations in Iraq

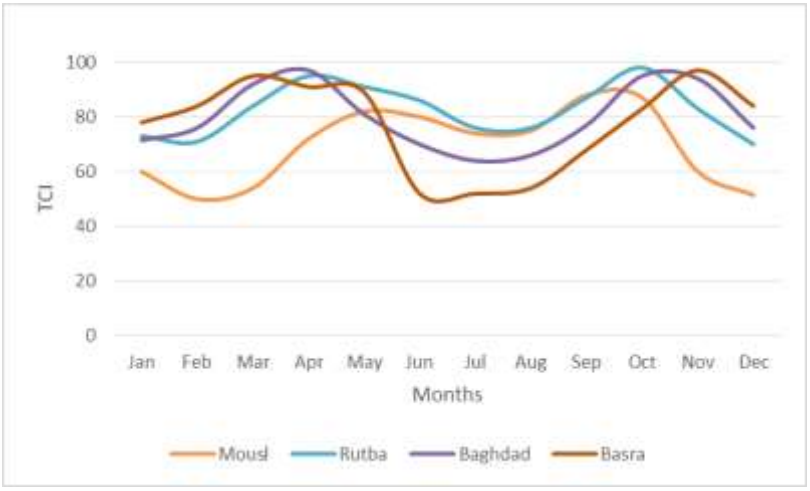

Figure 6. the monthly variation of TCI values in four stations for Iraq.

CONCLUSIONS

The present paper presents an evaluation study of the effect of climate conditions on the tourism activities in Iraq using the recorded measurements for related climate variables of 36 meteorological stations in Iraq from 1983-2016. The tourism climate index which developed by Mieczkowski was employed in this work. The results indicate that all regions of Iraq are suitable for tourism and the scores of TCI ranging between Marginal and Ideal. March, April, September, October are the optimum months for tourism comfort in Iraq. The northern parts are very good to ideal for tourism during eight months of the year and acceptable to good during the winter months. The southern regions namely, Basra, Nasiriyah, Amara, and Samawa are not recommended in hot season and have a good to ideal scores during spring, fall, and winter season. The condition of central cities are good to ideal for all year, and the best period was in spring and fall months. The contribution of CID and CIA was meager in summer months and

reach to maximum values during the spring and fall months, the values of S and W was nearly constant during all the year and reach the highest score of almost months.The poor contribution of precipitation was during winter months, particularly in the northern regions. This work is very beneficial for the local governments to improve new destinations of tourism in Iraq and to improve the promised and existing destinations by adopting a new project of tourism. The variety of climate conditions in Iraq will be beneficial to enhance the strategy of tourism development in country.

REFERENCES

AL-Lami, Alaa M., AL-Timimi, Yaseen K., and AL-Salihi.M, Ali (2014): The Homogeneity Analysis of Rainfall Time Series for Selected Meteorological Stations in Iraq. Diyala journal for pure science, Vol: 10 No:2: 53-63

AL-Salihi.M,Ali, AL-Lami,Alaa M. and AL-Timimi, Yaseen K. (2014). Spatiotemporal Analysis of Annual and Seasonal Rainfall Trends for Iraq. Al- Mustansiriyah J. Sci., 25, No 1:153-168

Andriotis, K. (2005). Seasonality in Crete. Problem or a Way of Life? Tourism Economics, 11(2), 207-227.

Bakhtiari ,B.and Bakhtiari A. (2013). Determination of tourism climate index in Kerman province. *DESERT Journal*, 18:113-126.

Becken, S., Wilson, J. & Reisinger, A. (2010). Weather, Climate, and Tourism: A New Zealand Perspective. Land Environment and People – Technical Report 20. Lincoln University, Lincoln, NZ.

Becker, S. (1998). Beach comfort index: a new approach to evaluate the thermal conditions of beach holiday resort using a South Africa example. Geo. J., 44(4): 297-307.

Bigano, A., J.M. Hamilton and R.S.J. Tol, 2006. The impact of climate on holiday destination choice. Clim. Chang., 76(3-4): 389-406.

De Freitas, C.R. (2003). Tourism Climatology: Evaluating Environmental Information for Decision Making and Business Planning in the Recreation and Tourism Sector. International Journal of Biometeorology, 48, 45-54.

Fang , Yan and Jie Yin, (2015). National Assessment of Climate Resources for Tourism Seasonality in China Using the Tourism Climate Index. Atmosphere Journal, 6, 183-194.

Farajzadeh M.&Ahmadabadi, A**.(**2010), Evaluation and zoning of Iran tourism climate using TCI. The Journal of Natural Geographic Researches.,5, 71- 88.

Gomez-Martin, B. (2005). Weather, Climate, and Tourism. A Geographical Perspective. Annals of Tourism Research, 32(3), 571-591.

Lise, W. and R.S.J. Tol, 2002. Impact of climate on tourist demand. Clim. Chang., 55 (4):429-49.

Maddison, D. 2001. In search of warmer climates? The impact of climate change on flows of British tourists. Clim. Chang., 49:193–208.

Matzarakis, A., (2006). Weather- and Climate-Related Information for Tourism. Tourism and Hospitality Planning & Development, 3, No. 2: 99–115.

Mieczkowski, Z. (1985). The Tourism Climatic Index: A Method of Evaluating World Climates for Tourism. Anadian Geographer, 29(3), 220-233.

Morgan, R., E. Gatell, R. Junyent, A. Micallef, E. Özhan and A. Williams, 2000. An improved user-based beach climate index. J. Coast. Conserv., 6:41-50.

Scott, D. & Lemieux, C. (2010). Weather and Climate Information for Tourism. Procedia Environmental Sciences. 1, 146-183.

Scott, D., Rutty M., Amelung B. and Tang, M. (2016). An Inter-Comparison of the Holiday Climate Index (HCI) and the Tourism Climate Index (TCI) in Europe. Atmosphere J, 7, 80: 1-17

Scott, D., Hall, C.M. & Gossling, S. (2012). Tourism and Climate Change: Impacts, Adaptation and Mitigation. Oxon, UK: Routledge.

Scott, D., Hall, C.M., Gossling, S. (2016). A review of the IPCC 5th assessment and implication for tourism sector climate resilience and decarbonization. Journal of Sustainable Tourism,24(1), 52-72.

THE ANALYSIS OF THE HEAT INDEX AND WIND CHILL IN MARMARA REGION

Canan Bursalı and Orhan Şen
İstanbul Technical University, Faculty of Aeronautics and Astronautics, Deparartment of Meteorological Engineering, Maslak, Istanbul, Turkey. seno@itu.edu.tr.

Abstract
Meteorological parameters affect the temperature of human body and the heat exchange with its surroundings directly. These parameters basically include wind, temperature, relative humidity etc. As a result of these parameters varying with time and place, the actual temperature and sensible heat felt by human are different from each other. The main reason for this is that the human body is constantly exchanging energy with its surroundings to ensure the temperature balance. At this point, the heat index and wind chill arise and affect the thermal comfort of people.Thermal comfort while performing the person's physical and mental activities the current temperature, humidity and wind conditions is the degree of comfort or discomfort felt by the body. The person is able to continue to their daily life so easily in terms of thermal comfort. Sensible heat values are higher than actual temperature values because of humidity and high temperature values in May to September compared to the other months. Indices describing this condition are expressed as heat index, level of oppressiveness and thermal comfort level of human being is affected. In winter, there is an opposite situation; Thus, the sensible heat values are lower than the actual temperature values related to the wind speed and it is called the wind chill. The cooling effect of the wind and the current air temperature on the human body. The purpose of this study is that distribution of heat index and wind chill in Marmara Region according to months. And it makes possible to identify habitable zones in terms of human health and feeling comfortable in certain conditions.

Key Words: *Heat Index, wind chill*

INTRODUCTION
Many human activities and adaptation of daily life are based on counted meteorological parameters in a large scale. In addition to whole meteorological factors, heat index and wind chill vary from environmental aspects, age, medical condition, clothing etc. Therefore, the calculation criteria are considered according to the average values, not the extreme values.

So, Marmara Region which has the highest population density in Turkey is examined. Relative humidity, wind speed and temperature data taken from 14 weather observation stations in Marmara Region are utilized with the aim of calculation of monthly heat index and wind chill for period of 2007 and 2016. The average humidity and average maximum temperature are used in the heat index calculations. Wind chill index calculations use maximum wind speed and average minimum temperature data for finding Equivalent temperature (Te).

The Earth’s atmosphere is one of the most significant elements of the ecosystem that human beings are living inside. Therefore, weather conditions and their effects play a dramatic role about human life. They enable people to rise their life standards and quality of their activities during the day.

Meteorological parameters such as temperature, humidity and wind speed have directly effects on human thermal comfort. Generally, human metabolic functioning works to heat and cool their bodies. So, there is energy flow between environment and human body, because human

body radiates energy according to environmental temperature for the purpose of keeping the body temperature constant. In fact, extreme warm and cold air temperature increase morbidity rates in the world lack of temperature balance in a body. Latent heat is discharged via perspiration on the body and energy flow from the body to air is negative in cold air, positive is in warm air. Additionally, medical conditions, age, clothing, physiological being can affect sensible heat. In other words, sensible heat change person to person. Counted meteorological parameters and individuals lead to difference between actual air temperature and sensible temperature felt by human beings, and this difference fluctuates according to seasons. The heat index and wind chill concepts come up with this difference.

Heat index is that how sensible heat felt by human being changes with relative humidity and actual air temperature. Temperature that measured by thermometer, wind speed, relative humidity and radiation are the four major meteorological factors that affect heat index. Radiation is slightly different from the other three factors because if actual air temperature and the temperature that the person in is 20 ^{o}C, person does not feel cold. However, if it is lower than 20 ^{o}C person feels cold (TSMS, 2017). The more humidity in the air, the less the body is cooling through perspiration. So, especially in summer, sensible temperature is higher than rest of the year because of high humidity values. This situation leads to appear the sultry. To be brief air temperature and humidity are directly proportional with the heat index. Besides that, age, sex, psychological state etc. which are personal characteristics should take in to consideration. For that matter heat index is subjective and depends on the person so calculations done by average and approximate data.

Wind chill is the common cooling effects of air temperature and wind speed on human body. As H.Toros et al. (Toros, et al. 2003) explained, "Wind Chill is based on the heat transfer by wind from the human body (IMO, 2017). The warm air around a body is replaced with colder air; therefore, it causes the body to cool faster." Especially in winter, sensible temperature is lower than actual temperature because of high wind speed and low air temperature.

Considering the warm weather conditions, deciding meteorological factor is humidity; however, its wind in the cold weather conditions and it directly affects thermal comfort. To sum up heat index is humidity's and wind chill is the wind's effect on the sensible temperature.
In this study, the Marmara Region which Turkey's the most populated and the most active region in terms of economic activities; is located in the tropic and sub-tropic region. Humidity, wind and temperature data between 2007 and 2016 from 14 meteorological observation stations in the region are used in the analysis of the monthly distribution of heat index and wind chill.

METEOROLOGICAL DATABASE AND METHODS

In this study, heat index and wind chill values are calculated for stations in Figure 1.

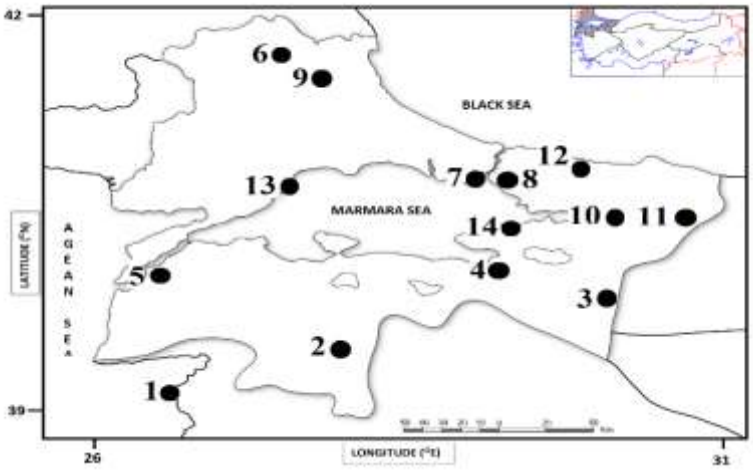

Figure 1: Study region and location of the stations.

Steadman (1979) states that in warm weather conditions which are generally greater than 21 ºC, heat index related with the amount of humidity in air is calculated as shown below (Steadman, 1979, 1984).

$$HI = -42.379 + 2.04901523 * T + 10.1433127 * RH - 0.22475541 * T * RH - 6.83783 * 10^{-3} * T^2 - 5.481717 * 10^{-2} * RH^2 + 1.22874 * 10^{-3} * T^2 * RH + 8.5282 * 10^{-4} * T * RH^2 - 1.99 * 10^{-6} * T^2 * RH^2 \quad \textbf{(1)}$$

In this equation;

HI : Heat Index (ºC)
RH : Relative Humidity (%)
T : Temperature (ºC)

Monthly average maximum temperature values and monthly average humidity values are substituted in the above formula and the heat index values are found as in Table 1.

If the calculated heat index is;

equal to 21ºC, theoretically human beings live under comfortable circumstance,

equal to 24ºC, theoretically human beings live under semi-comfortable circumstance,

equal to 27ºC, theoretically most of the human beings live under uncomfortable circumstance,

greater than 27ºC, theoretically all of the human beings live under uncomfortable circumstance.

Table 1: Heat Index values in terms of Relative Humidity and Air Temperature (TSMO, 2017).

Air Temperature (°C) \ Relative Humidity (%)	5	10	15	20	25	30	35	40	45	50	55	60	65	70	75	80	85	90	95
50	45	48	53	58	66	69	76	83	91	99									
49	44	47	51	55	61	66	72	79	86	94									
48	43	46	49	53	58	63	68	75	81	88	96								
47	42	45	48	51	55	60	65	70	76	83	90	98							
46	41	43	46	49	53	57	62	67	72	78	85	91	99						
45	41	43	45	48	52	56	62	65	70	76	82	88	96						
44	40	42	44	46	49	52	57	61	66	71	77	83	89	96					
43	39	40	42	44	47	50	54	58	62	67	72	77	83	90	97				
42	38	39	41	43	45	48	51	54	58	62	67	72	78	83	90	96			
41	37	38	39	41	43	45	48	51	55	59	63	67	72	78	83	89	96		
40	36	37	38	39	41	43	46	48	51	55	59	63	67	72	77	83	88	95	
39	35	36	37	38	39	41	43	46	48	51	55	58	62	67	71	76	81	87	93
38	35	35	36	37	38	40	42	44	47	50	53	56	60	64	68	73	78	83	89
37	34	34	35	36	37	38	40	42	44	46	49	52	56	59	63	67	72	76	81
36	33	33	34	34	35	36	38	39	41	43	46	48	51	55	58	62	66	70	74
35	32	32	33	33	34	35	36	37	39	41	43	45	48	50	53	57	60	64	68
34	31	31	32	32	32	33	34	35	37	38	40	42	44	46	49	52	55	58	61
33	31	31	31	31	32	32	33	34	36	37	39	40	42	45	47	49	52	55	58
32	30	30	30	30	31	31	32	33	34	35	36	38	39	41	43	45	47	50	53
31	29	29	29	29	29	30	30	31	32	33	34	35	36	38	40	41	43	45	47
30	28	28	28	28	28	29	29	30	30	31	32	33	34	35	36	38	39	41	42
29	27	27	27	27	28	28	28	28	29	30	30	31	32	32	33	34	36	37	38
28	26	26	26	27	27	27	27	27	28	28	29	29	30	30	31	32	32	33	34
27	26	26	26	26	26	27	27	27	27	28	28	28	29	29	30	30	31	31	32
26	25	25	25	26	26	26	26	26	26	27	27	27	27	27	28	28	28	28	29

(-1)-26	Cold/Cool Condition	No Danger or Caution	No discomfort
27 - 32	Warm Condition	Caution	Slight discomfort sensation
33 - 41	Severe Warm Condition	Extreme Caution	Strong discomfort, Limit the heaviest physical activities
42 - 54	Extreme Warm Condition	Danger	Serious danger, Stop all physical activities
>54	Extreme Warm Condition	Extreme Danger	Death danger, Imminenet heatstroke

The Wind Chill Index formula deals with actual air temperature and wind speed. The basic principle of the formula is that the calculated values give the cooling effect of the wind on the skin. The first works on this subject were made by Paul Siple and Charles F. Passel. They estimated the heat flux rate by measuring how much water was frozen over time under actual atmospheric and wind speeds. As a result, they have obtained a formula. In the course of time, several workshops and researches were conducted in Canada to make minor changes to the meeting held on the internet and received the following final status.

$$Te = 33 - \frac{18.97\sqrt{V} - V + 37.62)}{(18.97\sqrt{WV} - WV + 37.62)} (33 - T) \qquad \textbf{(2)}$$

In this equation;
Te : Equivalent Temperature (ºC)
WV: Walking velocity (km/h), (average walking velocity that equal to 6 km/h)
V : Wind speed (km/h)
T : Air temperature (ºC)

Average minimum temperature and maximum wind speed values are used while wind chill values are calculated in according to Formula 2. Calculations are shown in the Table 2. The results obtained were evaluated according to the following Table 2.

Table 2: Wind chill index related to air temperature and wind speed (IMO, 2017).

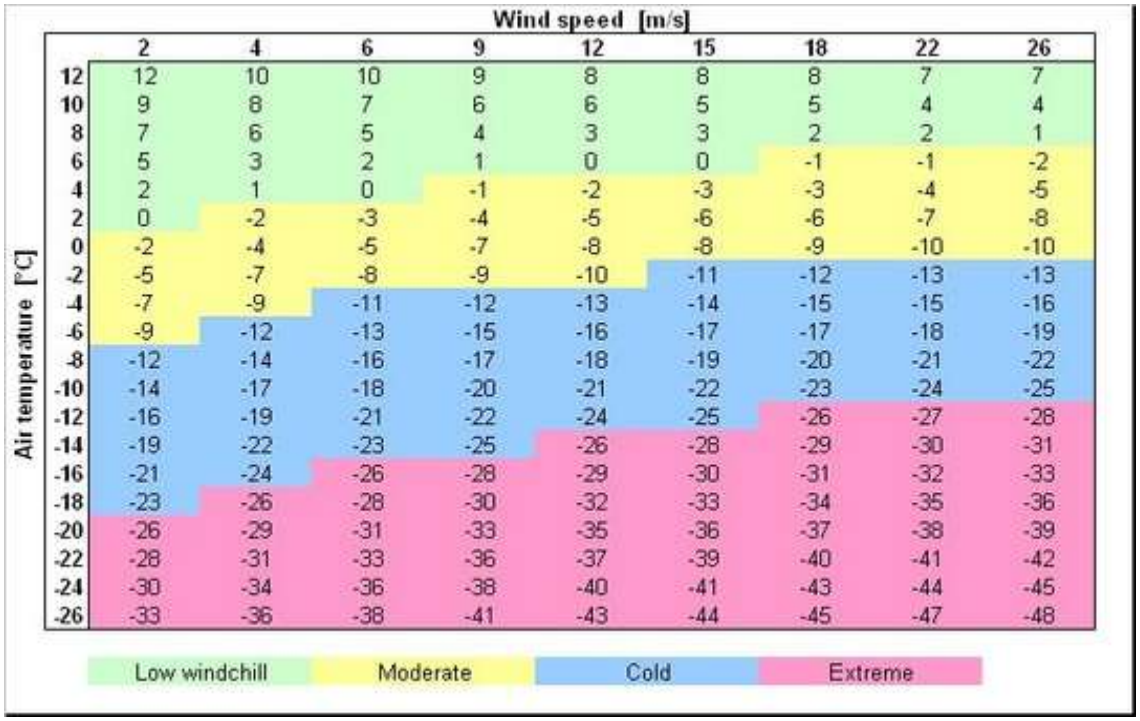

Air temperature [°C] \ Wind speed [m/s]	2	4	6	9	12	15	18	22	26
12	12	10	10	9	8	8	8	7	7
10	9	8	7	6	6	5	5	4	4
8	7	6	5	4	3	3	2	2	1
6	5	3	2	1	0	0	-1	-1	-2
4	2	1	0	-1	-2	-3	-3	-4	-5
2	0	-2	-3	-4	-5	-6	-6	-7	-8
0	-2	-4	-5	-7	-8	-8	-9	-10	-10
-2	-5	-7	-8	-9	-10	-11	-12	-13	-13
-4	-7	-9	-11	-12	-13	-14	-15	-15	-16
-6	-9	-12	-13	-15	-16	-17	-17	-18	-19
-8	-12	-14	-16	-17	-18	-19	-20	-21	-22
-10	-14	-17	-18	-20	-21	-22	-23	-24	-25
-12	-16	-19	-21	-22	-24	-25	-26	-27	-28
-14	-19	-22	-23	-25	-26	-28	-29	-30	-31
-16	-21	-24	-26	-28	-29	-30	-31	-32	-33
-18	-23	-26	-28	-30	-32	-33	-34	-35	-36
-20	-26	-29	-31	-33	-35	-36	-37	-38	-39
-22	-28	-31	-33	-36	-37	-39	-40	-41	-42
-24	-30	-34	-36	-38	-40	-41	-43	-44	-45
-26	-33	-36	-38	-41	-43	-44	-45	-47	-48

RESULTS AND RECOMMENDATIONS

Since the maximum temperature values used in the heat index do not exceed 27 ºC, the May heat index values for 14 stations could not be calculated. In June, July and August, heat index values increased to 30ºC and 40ºC depending on high temperature and humidity values. Especially in Edirne, Balikesir ,Sakarya and Kocaeli, the temperature is 34ºC and the humidity values are higher than 60%. Not suitable for thermal comfort. On Istanbul, the temperature has exceeded 30ºC and the humidity values range between 65-75%. The wind usually varies between 2km / h and 3km / h, and the determining factor here is mostly air temperature. In wind chill calculations, the Te values for Istanbul decreased from 17ºC to 9ºC on the October-April scale.

In this study heat index and wind chill values were calculated and analyzed for Marmara Region over twelve months. For the heat index calculations, average humidity and average maximum temperature values are used. In the wind chill calculations, new wind speed and average minimum temperature values are applied to the formulas known as WCI and Siple-Passel formulas (Siple and Passel, 1945) . In both the heat index and wind chill calculations, it has been understood that there is constant heat exchange with the environment in order to provide temperature balance to the environment of the human body, depending on temperature, humidity and wind speed.

In heat index calculations, it was found that the temperature experienced during the summer months with high humidity values is higher than the other months (Table 1). Since the heat averages are below the critical value of 27 °C in the heat index calculations, the heat index values in May are not taken into account. So in May, sensible heat did not reach dangerous values. In June, July and August, it has exceeded the critical value and theoretically all the human beings live under uncomfortable circumstance.

Since the maximum temperature values used in the heat index do not exceed 27 °C, the May heat index values for 14 stations could not be calculated. In June, July and August, heat index values increased to 30°C and 40°C depending on high temperature and humidity values. Especially in Edirne, Balikesir and Sakarya-Kocaeli, the temperature is 34°C and the humidity values are higher than 60%. Not suitable for thermal comfort. On Istanbul, the temperature has exceeded 30°C and the humidity values range between 65-75%. This causes the temperature to be felt too much.

The heat index value was highest in August with a maximum of 35%. In September, the heat index values dropped to below 30 °C, depending on the decrease in air temperatures and humidity. In Canakkale, Tekirdağ, Florya, Bilecik and Şile, the heat index calculation was not performed because the critical value did not exceed 27°C. This also indicates that sensible heat is decreasing and providing us with favourable conditions in terms of thermal comfort. On the other hand, temperature and humidity values of the Şile are decreasing due to the cold wind coming from the Black Sea and become suitable for human thermal comfort. In short, the difference between the temperature felt in May-September and the actual air temperature started to open. Heat index is higher. Among the places that can be experienced are Şile, Çanakkale, Tekirdağ and Yalova. Istanbul is on the 33-41 scale according to Table 1, so it is affected by a severe warm condition and requires taking precautions.In May, June and September in Marmara region, humidity was high compared to other months (>56). Especially in June, July and August months, it seems to be dangerous in terms of human health. In May and September, the heat index values are below 27°C, the overwhelming critical value. In Edirne and Kırklareli where the effect of terrestrial climate is seen, heat index values above 30°C are seen. Especially when we look at Şile, the most important reason why we have values below the value of overwhelming value is that the cool air of the Black Sea is moved by the wind.

In the winter months, the heat index results are not subject to any evaluation because the temperature and humidity values do not give the results to be evaluated according to Table 1. Therefore, only the values between May and June are plotted in Figure B3. Due to high humidity, the sensible heat is higher in the Marmara Region than in the Thrace region compared to the actual air temperature.

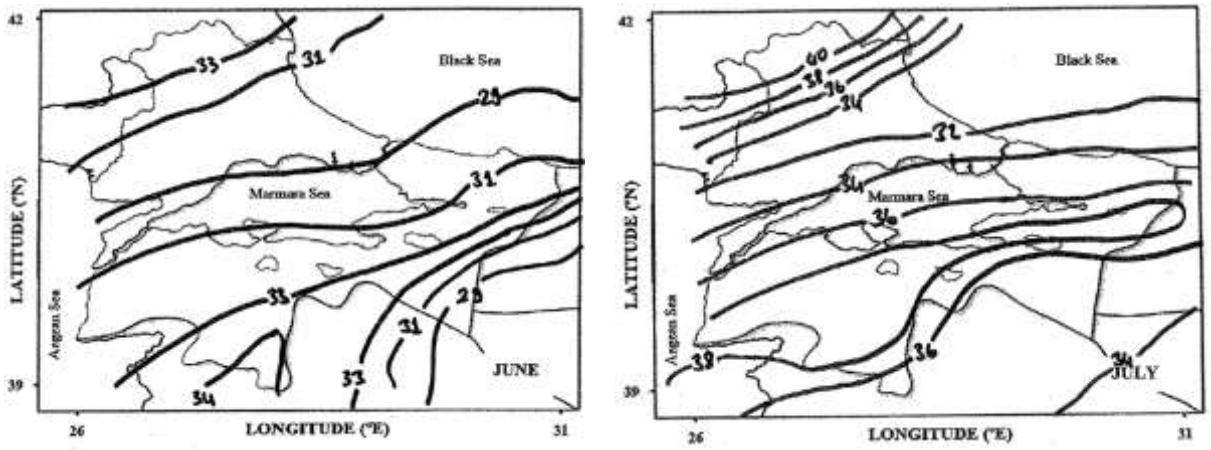

Figure B.3: Contour maps of monthly distribution of heat index (°C).

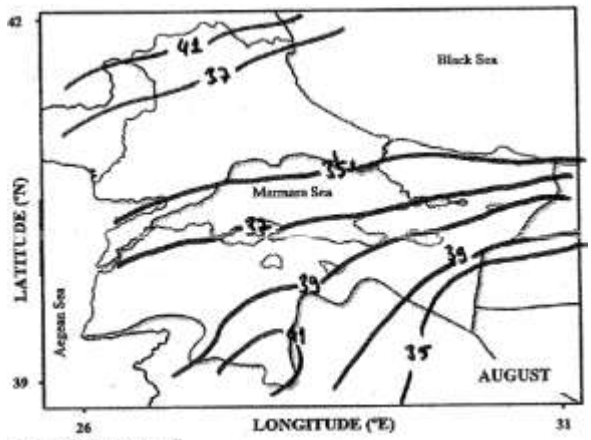

Figure B.3 *(continued)*

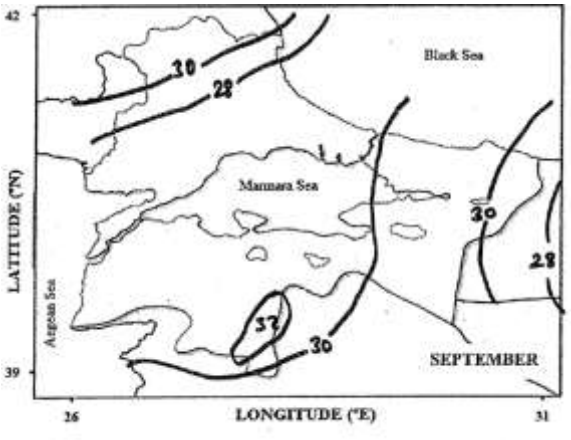

Figure B.3 *(continued)*

Wind chill calculations were made by setting maximum wind speed and average minimum values. Considering the winter months, especially when the low wind speed of the heat is high, the cooling is more than that, so the values between November and March are reflected in Figure C3, in forms of Formula 2. Chill temperatures,

Çanakkale, Florya and Tekirdağ are the places where temperatures are generally felt the most. In January, February and December temperatures in Chile, Canakkale, Florya and Tekirdağ are about 5 ° C and above. At these stations there is a sea effect. However, the temperatures at the stations of Balıkesir, Edirne, Kocaeli, Sakarya and Yalova are below 1 ° C. The wind usually varies between 2 km/h and 3 km/h, and the determining factor here is mostly air temperature.

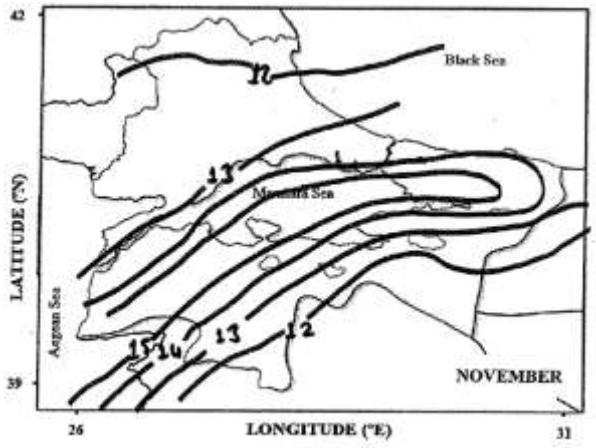

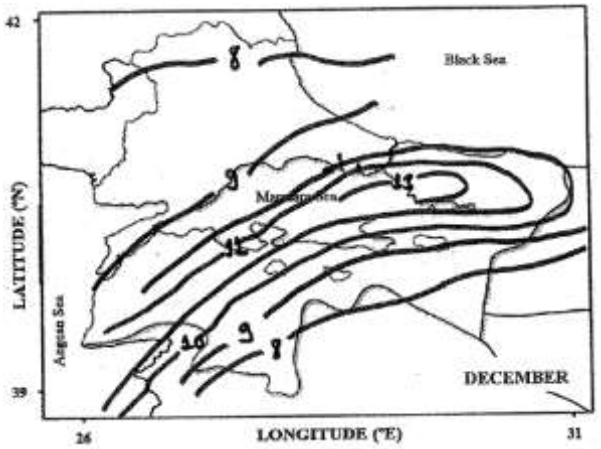

Figure C.3: Contour maps of monthly distribution of equivalent temperature (°C).

In wind chill calculations, the Te values for Istanbul decreased from 14°C to 11°C on the November-March scale.

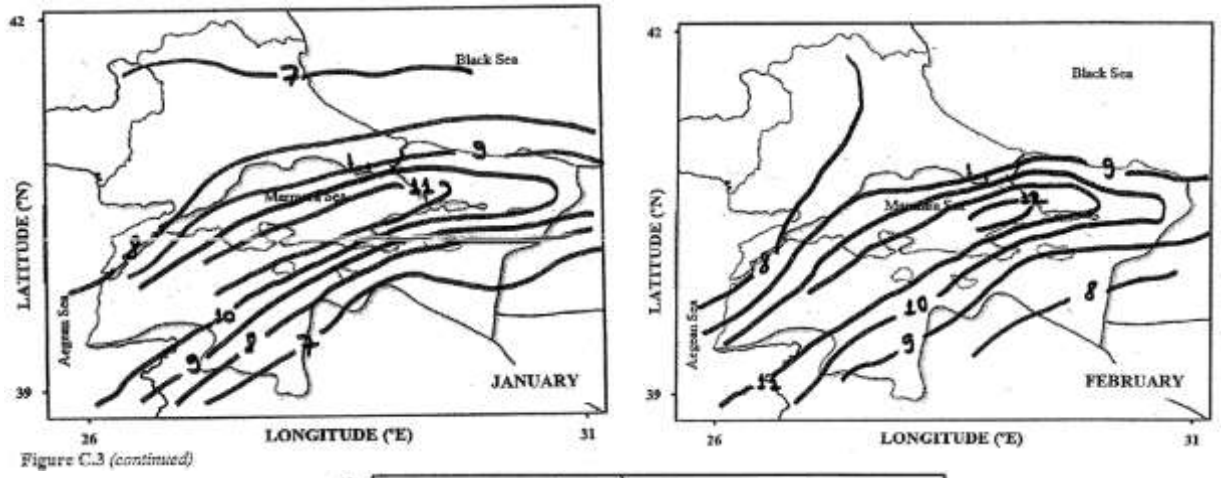

Figure C.3 *(continued)*

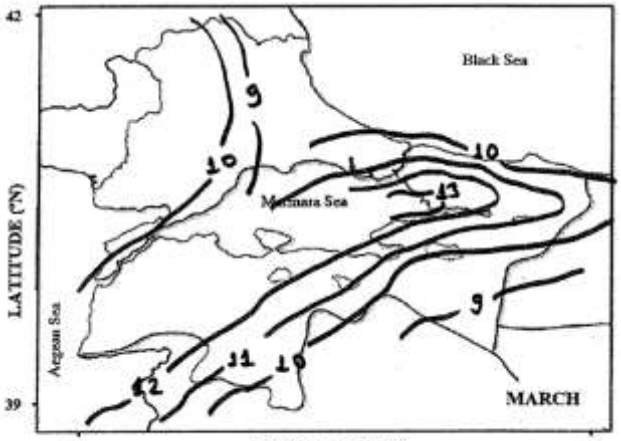

Figure C.3 *(continued)*

The heat index and wind chill values were analyzed in the Marmara Region in the calculations in the direction of the maps in Figure B.3 and Figure C.3. In this respect, it has been revealed that people can live in places, thermal comfort, and in what season and months, measures can be taken to stimulate.

REFERENCES

H. Toros, Deniz, A., L. Şaylan, O. Şen and M. Baloğlu (2003). The WindChill Distribution in Marmara Region III. Atmospherical Sciences Symposiums, 19-21 March 2003, İstanbul, 69-77.

Deniz, A., H. Toros, L. Şaylan, O. Şen and M. Baloğlu (2003). Analysis of Sweltering Temparature in Marmara Region, III. Atmospherical Sciences Symposiums, 19-21 March 2003, İstanbul, 78-83.

Steadman RG (1971). Indices of wind chill of clothed persons. J Appl Meteor 10: 674–683.

Siple PA, Passel CF. (1945). Measurements of dry atmospheric cooling in subfreezing temperatures. Proc Amer Phil Soc 89: 177–199.

Steadman RG (1984). A universal scale of apparent temperature. J Clim Appl Meteorol 23: 1674–1687.

Icelandic Met Office (2017) : <http://en.vedur.is/weather/articles/nr/1827> date retrived

Turkish State Meteorological Office (2017): https://www.mgm.gov.tr/genel/sss.aspx?s=hissedilensicaklik> date retrived

PERFORMANCE EVALUATION OF CORDEX PRECIPITATION SERIES ON A BASIN SCALE

Saeed Vazifehkhah, Ercan Kahya
Istanbul Technical University, Faculty of Civil Engineering, vazifehkhah@itu.edu.tr
Istanbul Technical University, Faculty of Civil Engineering, kahyae@itu.edu.tr

Abstract
Climate change is expected to have substantial impacts on natural resources along hydrological cycle. Choosing proper climate change scenarios for assessing future deviations on various climatic variables is crucial for hydrologists and climatologists. Although several Global Climate Models (GCMs) and Regional Climate Models (RCMs) have been developed and are utilized for predicting future changes on different climatic variables, there are still many obstacles to be solved regarding reliability, uncertainty and computing times. This paper presents our work analyzing the performance of 18 GCMs from Climate Model Intercomparison Project Phase 5 (CMIP5) forced by different RCMs of Coordinated Regional Climate Downscaling Experiment (CORDEX) precipitation data over the Konya Closed Basin (KCB) in central Turkey. Monthly observed precipitation data for the period 1970-2005 for nine stations fully distributed over the KCB has been assessed with spatially averaged historical datasets of CORDEX using mean, median, standard deviation, coefficient of variation, relative change and linear correlation. Our results indicate that even though five out of the 18 CORDEX models are approved to be used over KCB some of them failed to be paired by the specific factors such as median. Moreover, different driving models with the same RCMs and vice versa explains a huge deviation in results that should be noticed in future research. Furthermore, all available datasets should be assessed by various statistical techniques for better results in predicting projected changes for climate change analysis.

Keywords: *GCM, CMIP5, RCM, CORDEX, Precipitation*

Introduction
According to the fifth Assessment Report (AR5) by the Intergovernmental Panel on Climate Change (IPCC), there is no doubt that the temperature has considerably increased during the past century; from 1880 to 2012, the global surface air temperature has increased by 0.85℃. Global warming will have a significant impact on local climatic and hydrologic processes, resulting in a series of problems such as mutated water cycles, inhomogeneous spatial distribution of precipitation, and probably more frequent extreme climatic events, which in turn will affect the social, ecological and economic systems of human societies. According to the AR5 of the IPCC, the frequency of heat waves increased and the number of extreme rainfall events augmented in most parts of Europe and Asia (IPCC, 2013). Agricultural productions has already tended to decline and water resources are also at risk under climate change (Perelet, 2007). Therefore, it is essential to perform quantitative and qualitative predictions of future climate change scenarios from a regional perspective as well.

In the time line of the AR5 of the IPCC, the simulations from a new generation of Global Climate Models (GCMs) are becoming available for analysis within the Coupled Model Intercomparison Project Phase 5 (CMIP5) (Taylor et al., 2012). In comparison with the previous model generation (CMIP3) (Meehl et al., 2007) CMIP5 includes more comprehensive global climate models (i.e., Earth system models) with generally higher spatial resolution enabling the research community to address a wider variety of scientific questions (Silman et al., 2013). Temperature and precipitation are important climatic elements and key factors of hydrological

process. Precipitation, as well as other hydrometeorological variables (e.g. temperature and humidity) are primarily provided by the CMIP5 models for climate studies. However, there are numerous models developed by different institutes and it is difficult to decide which model is more adequate for hydroclimate applications on a specific region.

It is known that many sources of uncertainty, including GCMs (Maurer and Duffy, 2005; Vano et al., 2014) can affect climate change predictions, in particular to the precipitation prediction. Several studies reported GCM model structure as the major contributor to projection uncertainties (Zhu et al. 2017). Based on the (IPCC 2013) report, central Turkey will experience increase in temperature and decrease in precipitation in the 21st century. Hence, studying the climatology of different hydroclimate variables on the basis of different Representative Concentration Pathways (RCPs) projected by various GCMs for Regional Climate Models (RCMs) is increasingly important.

Recently, the Konya Closed Basin (KCB) located in the central Turkey with an approximate area of 55000 $_{km}^2$ has been experiencing decrease in precipitation and needs urgent attention in planning a long-term water resources conservation strategy. In this study, we attempt to evaluate the quality of projected RCMs forced by several institutes of different GCMs from Coordinated Regional Climate Downscaling Experiment (CORDEX) project with observed historical data over the region. A wide range of univariate statistical methods such as mean, median, standard deviation, coefficient of variation, relative change and linear correlation have been applied on the raw simulations from historical CORDEX precipitation and averaged observational data over the KCB to evaluate their efficiency based on the properties captured by the particular statistical method in the period 1970–2005.

Study Area, Data and Methods

Study area

A smooth plane at 900–1,050 m of altitude formed the main part of the Central Anatolia Plateau in KCB, Turkey's largest closed basin in which more than three million people live, 45 % in rural areas and 55 % in urban areas. The shallow lake and reed beds at the center of the basin are fed by many rivers flowing to the region. The southern border of the basin is surrounded by central Taurus Mountains which partly reaches 2,500 to 3,000 m of altitude. The central Taurus Mountains prevent rainfall passing from Mediterranean Sea to the basin. The climate characteristics of the basin present the Mediterranean climate (mild and rainy winters, hot and dry summers) at the south, the terrestrial climate (cold winters, hot and dry summers) at the center and north of the basin, and the desert climate in Karapinar and its vicinity. The rainfalls were mostly observed in winter and spring seasons. Annual mean precipitation is 374 mm, however records range between 275 mm in the eastern part of the basin and 755 mm in the western part of the basin (Turkish State Meteorological Service). The natural richness and the lakes of the basin provide significant living places for the migratory birds.

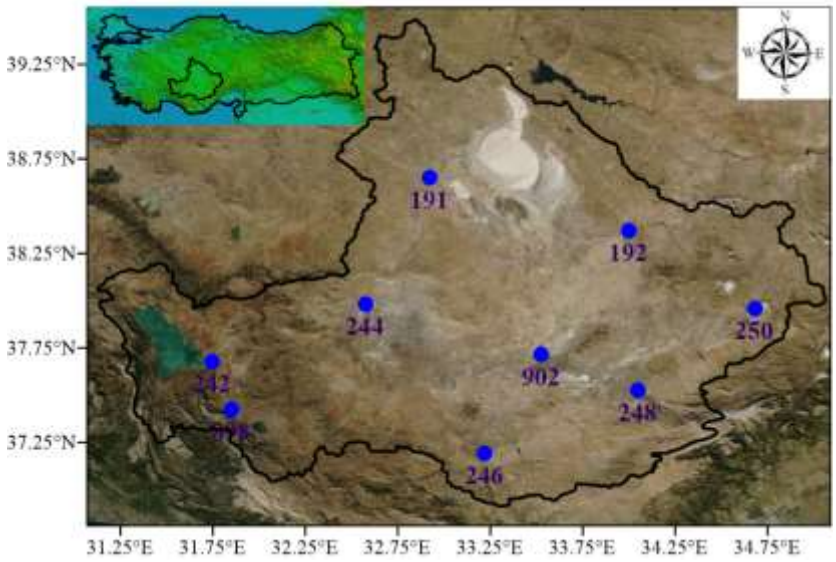

Figure 1. Geographic position of observed precipitation stations. The background map of KCB has been downloaded online from https://earthexplorer.usgs.gov/.

Data

In this study, the observed daily precipitation data for the period 1970–2005 from 9 rainfall stations fully distributed throughout the basin were selected and obtained from the Turkish State Meteorological Service (TSMS, http://www.mgm.gov.tr/) and converted to monthly series. The detailed geographic and statistic information regarding used precipitation stations are shown in Table 1.

For the sake of brevity and having analyzed the precipitation series on a basin scale, also to minimize the uncertainties, we decided to utilize spatially averaged series over nine stations in the KCB and extract a unique dataset to evaluate with the projected historical series. Figure 2 shows the average of monthly precipitation series over the KCB during the study period (1970-2005).

Table 1. Summary of geographic and descriptive statistics of used precipitation stations.

Station Name - Code	Used code	Long. (˚E)	Lat. (˚N)	Alt. (m)	Mean (mm)	Standard. Deviation	Coefficient of Variation	Skewness	Kurtosis
Cihanbeyli 17191	191	32.9226	38.6503	969	27.65	24.06	0.87	1.31	2.54
Aksaray 17192	192	33.9987	38.3705	970	28.96	24.20	0.83	0.80	0.14
Beyşehir 17242	242	31.7463	37.6777	1141	41.71	39.01	0.93	1.54	3.19
Konya Havaalanı 17244	244	32.5740	37.9837	1031	27.55	24.08	0.87	1.11	1.21
Karaman 17246	246	33.2202	37.1932	1018	27.57	24.03	0.87	0.93	0.61
Ereğli 17248	248	34.0485	37.5255	1046	25.47	22.07	0.86	1.00	0.87
Niğde 17250	250	34.6795	37.9587	1211	28.73	23.42	0.81	0.80	0.20
Seydişehir 17898	898	31.8490	37.4267	1129	64.29	65.97	1.02	2.04	6.78
Karapınar 17902	902	33.5267	37.7143	996	24.19	21.39	0.88	1.03	0.92

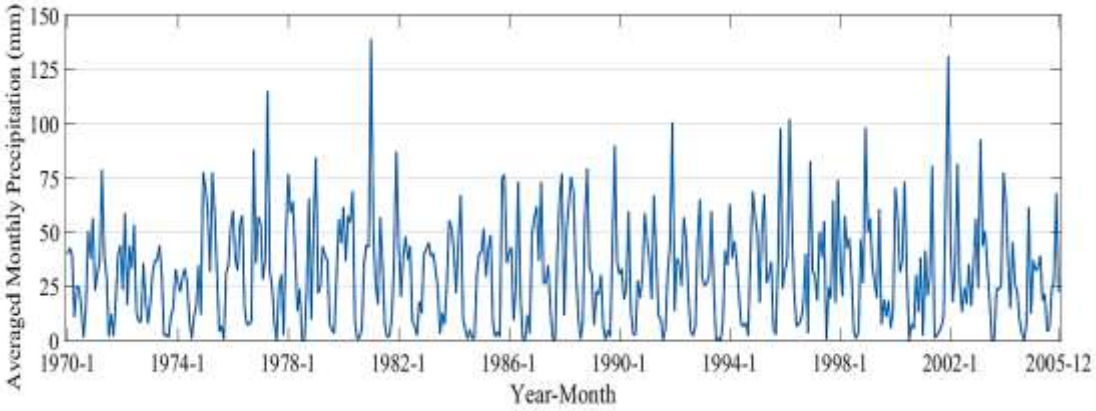

Figure 2. Spatially averaged monthly precipitation series over KCB during the study period.

The Coupled Model Intercomparison Project Phase 5 (CMIP5), a globally coordinated set of GCMs simulations of different modeling groups provides historical and future climate simulations (Taylor et al., 2012). Recently, the Coordinated Regional Climate Downscaling Experiment (CORDEX) was established as a global framework for improving coordination of international efforts to produce high-resolution regional climate change scenarios downscaled from the CMIP5, using multiple Regional Climate Models (RCMs) ensembles for uncertainty reduction (Christensen et al., 2007; Giorgi et al., 2009; Jin et al., 2016).

The selection of driving models were depended on the availability of GCMs on the study area with finest resolution for Representative Concentration Pathways (RCPs) RCP4.5 (medium greenhouse gas emission scenario) and RCP8.5 (high greenhouse gas emission scenario) of IPCC fifth assessment report (AR5) along with related historical data. As the KCB is located between 31˚36'E- 34˚52'E and 36˚51'N- 39˚29'N, the Europe (EUR) and Middle-east and North Africa (MNA) CORDEX domains could be utilized to extract desired precipitation series. Hence, we excavated for all available CORDEX historical precipitation datasets from different institutions forced by several driving models. The 18 CORDEX precipitation models forced by different GCMs for CMIP5 were used in this study was collected from Centre for Environmental Data Analysis (CEDA) website; https://esgf-index1.ceda.ac.uk.

Table 2. Models used in this study and their characteristics

Used No.	Institution	Driving Model	Ensemble	RCM Model	Domain-Resolution
*1	*SMHI	CNRM-CERFACS-CNRM-CM5	r1i1p1	RCA4	EUR-11i
2	CLMcom	CNRM-CERFACS-CNRM-CM5	r1i1p1	CCLM4-8-17	EUR-11
3	SMHI	CNRM-CERFACS-CNRM-CM5	r1i1p1	RCA4	EUR-11
4	SMHI	ICHEC-EC-EARTH	r12i1p1	RCA4	EUR-11i
5	DMI	ICHEC-EC-EARTH	r3i1p1	HIRHAM5	EUR-11
6	CLMcom	ICHEC-EC-EARTH	r12i1p1	CCLM4-8-17	EUR-11
7	KNMI	ICHEC-EC-EARTH	r1i1p1	RACMO22E	EUR-11
8	SMHI	ICHEC-EC-EARTH	r12i1p1	RCA4	EUR-11
9	SMHI	ICHEC-EC-EARTH	r12i1p1	RCA4	MNA-44i
10	SMHI	IPSL-IPSL-CM5A-MR	r1i1p1	RCA4	EUR-11i
11	CLMcom	MOHC-HadGEM2-ES	r1i1p1	CCLM4-8-17	EUR-11
12	SMHI	MOHC-HadGEM2-ES	r1i1p1	RCA4	EUR-11i
13	KNMI	MOHC-HadGEM2-ES	r1i1p1	RACMO22E	EUR-11
14	SMHI	MPI-M-MPI-ESM-LR	r1i1p1	RCA4	EUR-11i
15	CLMcom	MPI-M-MPI-ESM-LR	r1i1p1	CCLM4-8-17	EUR-11
16	MPI-CSC	MPI-M-MPI-ESM-LR	r1i1p1	REMO2009	EUR-11
17	DMI	NCC-NorESM1-M	r1i1p1	HIRHAM5	EUR-11
18	SMHI	NOAA-GFDL-GFDL-ESM2M	r1i1p1	RCA4	MNA-44i

SMHI: Swedish Meteorological and Hydrological Institute, CLMcom: Climate Limited-area Modelling Community, DMI: Danish Meteorological Institute, KNMI: Royal Netherlands Meteorological Institute, MPI-CSC: Max Planck Institute for Meteorology. *The used numbers will be used for utilized CORDEX models.

The detailed information regarding utilized RCMs as RCA4, CCLM4-8-17, HIRHAM5, RACMO22E and REMO2009 could be reached comprehensively at https://esgf-index1.ceda.ac.uk. It is worth noting that, on our knowledge the selected models are in their finest resolution available presented by different institutes.

Method

Although, there are various methods found in the literature regarding the evaluation of model/observational experiments (Hawkins and Sutton 2011; Deser et al. 2014; Danandehmehr and Kahya 2017), we decided to analyze the evaluation on a number of different univariate metrics on monthly time scale. In this study, the values of mean, median, standard deviation, coefficient of variation, relative change for the observed and extracted models along with the linear correlation between the monthly observational and models has been calculated. Each method/statistic has been defined as a metrics in many previous studies. Furthermore, it is possible to compare the ability of different methods as they address various statistical properties (Ahmadalipour et al. 2017).

Mean of dataset refers to the central tendency either of a probability distribution or of the random variable characterized by that distribution, and standard deviation calculates the variation amount or dispersion of data from mean. Computing them will reveal how data is distributed and the range that most of the average values occur. The coefficient of variation is determined as the ratio of the standard deviation σ to the mean μ, i.e., normalized measure of dispersion of a probability/frequency distribution. It removes the dependency of standard deviation on the mean and investigates the variability in relation to mean of population. Relative change (RC), in quantitative science, evaluates the relative difference or variability of datasets while taking into account sizes of things being compared. Moreover, the Taylor diagram (Taylor, 2001) has been assessed for different models. The top 10 models in any of the above-mentioned criteria will be listed and the best model chosen upon the abundance of the model(s) superiority on all methods.

Results and Discussion

Results of mean, median, standard deviation, coefficient of variation, and linear correlation for each historical CORDEX precipitation models and observational data are presented in Table 3. Comparing the mean value of observational data with the models explain the overestimations (underestimations) for higher (lower) results along with near normal prediction but those who obtained mean values with a few difference (less than 10%).

Table 3. Mean, Median, Standard Deviation (S.D), Coefficient of Variation (C.V) and Linear correlation of observed and CORDEX RCMs historical models.

Model No.	Mean	Median	S.D	C.V	Linear Corr.	Model No.	Mean	Median	S.D	C.V	Linear Corr.
Obs.	31.6	29.7	24.2	0.77	N/A	10	21.3	17.3	18.5	0.87	0.39
1	30.0	26.7	21.3	0.71	0.36	11	37.5	34.5	30.9	0.82	0.48
2	50.3	47.8	30.7	0.61	0.33	12	29.5	26.4	24.1	0.82	0.45
3	27.1	23.6	20.7	0.77	0.38	13	31.3	28.1	24.9	0.80	0.47
4	25.5	22.9	21.2	0.83	0.48	14	28.8	24.5	24.4	0.85	0.45
5	21.1	17.8	18.0	0.85	0.46	15	36.9	31.6	32.0	0.87	0.48
6	34.2	28.3	29.2	0.85	0.43	16	26.8	24.0	21.0	0.78	0.44
7	24.9	22.0	19.2	0.77	0.37	17	20.2	18.7	17.8	0.88	0.41
8	23.7	20.3	20.6	0.87	0.48	18	42.0	35.3	29.6	0.71	0.38
9	40.0	33.7	34.9	0.87	0.45						

The models # 2, 9, 11, 15 and 18 are assumed to be overestimated while the models # 3, 4, 5, 7, 8, 10 and 17 showed underestimation and the rest (#1, 6, 12, 13, 14 and 16) are characterized as to be near normal. By applying the same criteria to median values one can say that, the models # 2, 11 and 18 got higher results, # 1, 3, 4, 5, 7, 8, 10, 12, 14, 16 and 17 obtained lower values and the rest (# 6, 9, 13 and 15) are assumed to be near normal. The boxplots representing the distribution of monthly precipitation for observed and models is depicted in Figure 3.

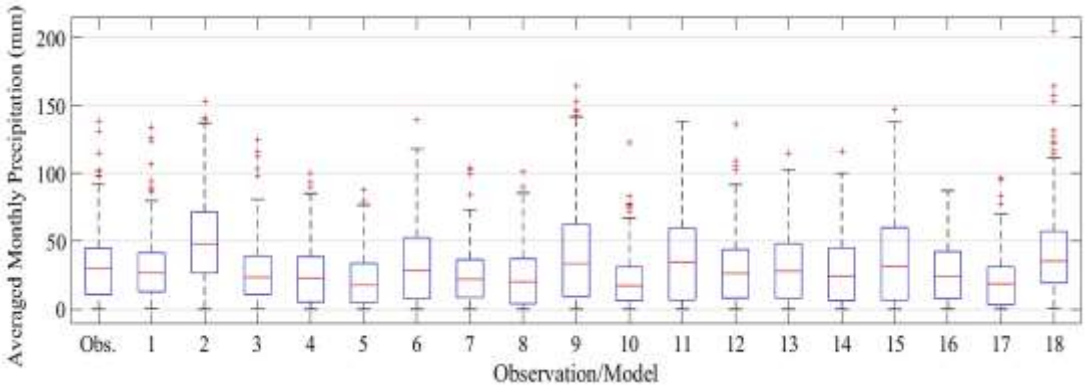

Figure 3. Boxplots depicting the distribution of monthly precipitation in models and observation.

The outcomes for standard deviation values depict a range of 159 to 314 where it is 217 for observation data. The overestimated models (# 2, 6, 9, 11, 15 and 18) got the highest values which shows a higher dispersion on the outputs. The closest values for coefficient of variations obtained for models to the observation data are for models #3 and 7 which means the variability against the mean of models are close to those obtained by observational data. The maximum linear correlation between observational data and models are for the models # 4, 8, 11 and 15 with 0.48 followed by #13 with 0.47. The least results are calculated for the models #2 and 1 with 0.33 and 0.36 respectively.

By taking into consideration the average annual cycle of precipitation for observed and utilized CORDEX historical precipitation data it is apparent that except models # 2 and 18, almost all of the models could capture similar simulations on dry months (Jul-Sep) while, the differences got greater amounts in wet months (Oct-Jun). Although some of the models has modeled the

historical precipitation with a lower values (underestimated), most of the models seemed to exhibit a greater simulations (Figure. 4).

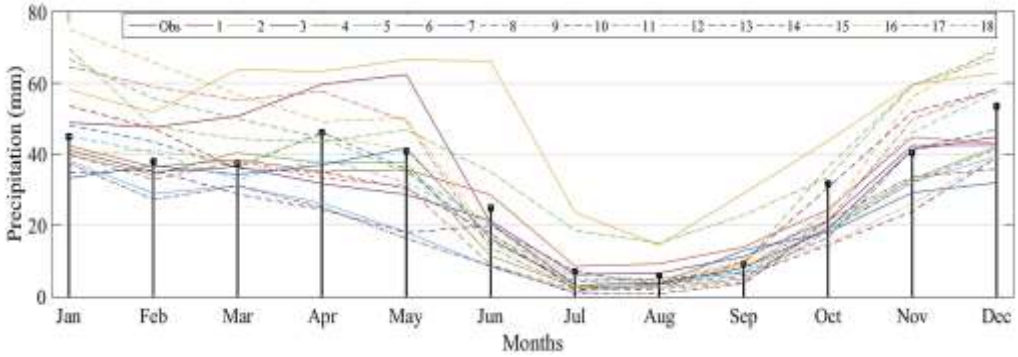

Figure 4. Average annual cycle of precipitation for observed and utilized CORDEX historical precipitation data.

Analyzing the Relative Change (RC) of precipitation for observational and CORDEX historical data on monthly scale depicted a coarse outcomes on whole models, hence we decided to capture on annual scale as well (Figure. 5). The results indicates a higher values of RC regarding to observed data for models # 2, 6, 9, 11, 15 and 18 and lowers for 4, 5, 8, 10, 16 and 17. The rest of the models (# 1, 3, 7, 12, 13 and 14) appeared to have a similar RC with observational data on the study period on KCB.

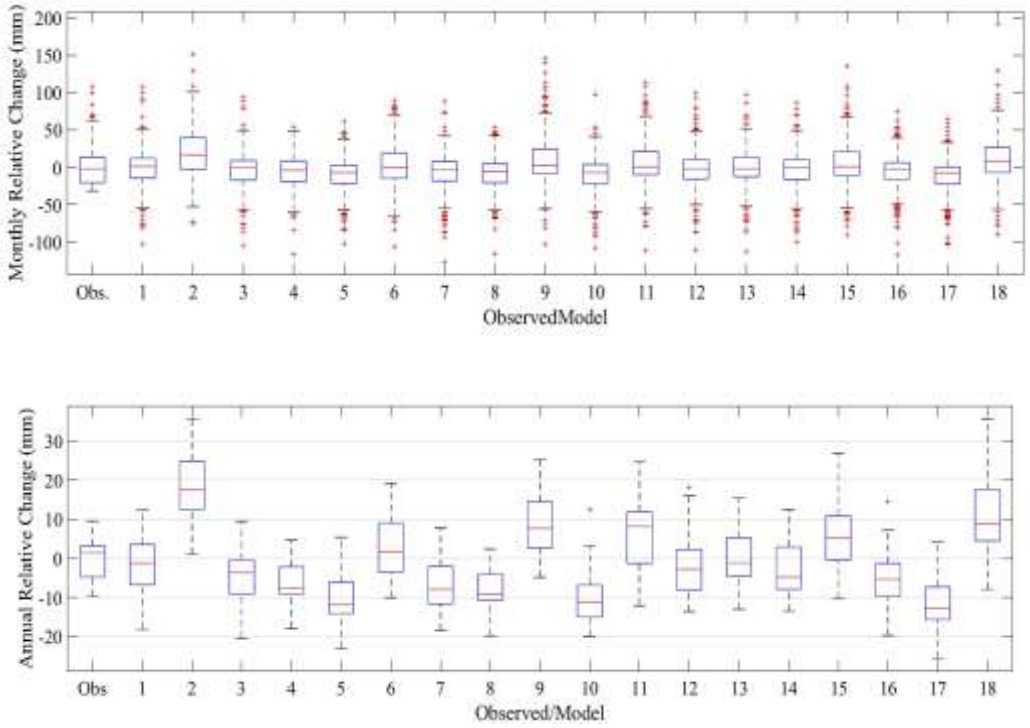

Figure 5. Boxplot of Relative Change (RC) for precipitation on monthly scale (Top) and annual for all 36 years of data analysis (Bottom).

A diagram has been devised by Taylor (2001) that provide a concise statistical summary of how well patterns match each other in terms of their correlation, their root-mean-square difference,

and the ratio of their variances. Although the form of this diagram is general, it is especially useful in evaluating complex models, such as those used to study geophysical phenomena. The Taylor diagram for various models has been depicted in Figure 6. It is apprehensible from figure 6 that except models # 2, 9 and 18 which got a higher values of standardized deviations, the other models appear to obtain standardized deviation in a limited range.

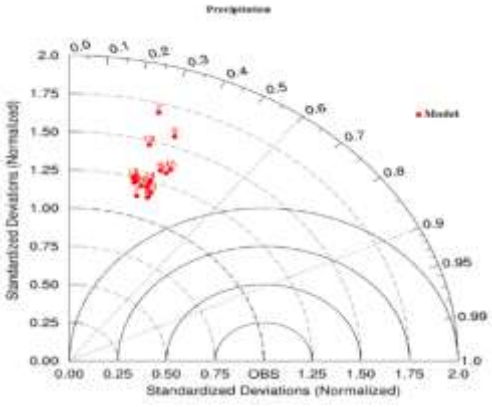

Figure 6. Taylor diagram of utilized CORDEX historical precipitation data.

Additionally, the top 10 models in each criteria regarding closest univariate statistic values as mean, median standard deviation, coefficient of variation, linear correlation and average of annual relative change on the observational data and extracted models are listed in table 4.

Table 4. Model ranking based on various statistical approaches.

Criteria	Mean	Median	S.D	C.V	Linear Corr.	R. C
Model No.*	13	6	12	3	11	16
	1	3	14	7	15	1
	12	15	13	16	8	4
	14	1	1	13	4	14
	6	12	4	12	13	5
	3	9	16	11	5	10
	16	11	3	4	14	18
	15	14	8	1	9	17
	4	18	7	18	12	15
	11	16	10	14-6-5	16	2

*In order of decreasing ranks from top to bottom.

Having discussed the model rankings, models # 1, 12, 14, 16 and 4 with five time being ranked between the models shows the superiority among others followed by models # 13, 3, 15, and 11 emerging four times between the top models on different criteria. It is worth noting that, the above-mentioned models that ranked on top positions are not necessarily obtained from the same driving model or RCMs. For instant, the models # 1 and 2 which exhibited an opposite results, are forced by the same driving model (CNRM-CERFACS-CNRM-CM5) with different RCMs from different institutes. This is a substantial consequence for researchers and decision makers not to rely only on one model of any available driving model but to analyze every published models from different sources to reach the final desired model.

Conclusion

In this study, we attempted to assess the performance of 18 different CORDEX historical precipitation models over Konya Closed Basin in Turkey on a monthly scale. Although some

models are extracted from the same Global Climate Models (GCMs), different institutes evaluated various Regional Climate Models (RCMs) resulting in different model outputs. Although the GCMs along with related RCMs have been processed with different coordinates, the analysis on spatially averaged over the study area managed to fix these inconsistency. The finest resolution has been utilized to overcome the uncertainty resulting from coarse simulations of GCMs and RCMs. Even we could analyze the evaluation process of a model's grid to observational stations for precipitation data, we chose the spatially averaged approach to extract the unite outputs in each calculation procedure to minimize the probable uncertainties. The assessment of seven different driving models from six institutes forced by six different RCMs on two CORDEX domain covering the study area concluded a comprehensive evaluation process on historical precipitation data. The outcomes of model ranking based on various statistical approaches explain the superiority of models # 1, 12, 14, 16 and 4 followed by # 13, 3, 15 and 11 over the available historical precipitation CORDEX models on the study are. By choosing the appropriate model(s), one can reduce future predictions uncertainties which is crucial for future precipitation projections of different available projected datasets.

References

Ahmadalipour, A., Rana, A., Moradkhani, H. et al. Theor Appl Climatol., 2017. 128: 71. https://doi.org/10.1007/s00704-015-1695-4.

Centre for Environmental Data Analysis. https://esgf-index1.ceda.ac.uk.

Christensen, J.H., Carter, T.R., Rummukainen, M., Amanatidis, G., 2007. Evaluating the performance and utility of regional climate models: the PRUDENCE project. Clim. Change 81, 1–6.

CMIP Coupled Model Intercomparison Project, 2013. http://cmip-pcmdi.llnl.gov/index.html.

Coordinated Regional Climate Downscaling Experiment, http://www.cordex.org.

Deser C, Phillips AS, Alexander MA, Smoliak BV. 2014 Projecting north american climate over the next 50 years: uncertainty due to internal variability. J Clim 27:2271–2296. doi:10.1175/JCLI-D-13-00451.1

Giorgi, F., Jones, C., Asrar, G.R., 2009. Addressing climate information needs at the regional level: the CORDEX framework. World Meteorological Organization (WMO) Bulletin 58 (3), 175.

Hawkins E, Sutton R. 2011. The potential to narrow uncertainty in projections of regional precipitation change. Clim Dyn 37:407–418. doi:10.1007/s00382-010-0810-6.

Intergovernmental Panel on Climate Change (IPCC). Climate Change 2013: The Physical Science Basis; Contribution of Working Group I to the Fifth Assessment Report of the Intergovern-Mental Panel on Climate Change; Cambridge University Press: Cambridge, UK; New York, NY, USA, 2013.

Jin, C.-S., Cha, D.-H., Lee, D.-K., Suh, M.-S., Hong, S.-Y., Kang, H.-S., Ho, C.-H., 2016. Evaluation of climatological tropical cyclone activity over the western North Pacific in the CORDEX-East Asia multi-RCM simulations. Clim. Dyn. 47 (3–4).

MATLAB and Statistics Toolbox Release 2016b, the Math Works, Inc., Natick, Massachusetts, United States.

Mehr, A.D. and Kahya, E., 2017. Grid-based performance evaluation of GCM-RCM combinations for rainfall reproduction. Theoretical and Applied Climatology, 129(1-2), pp.47-57.

Maurer EP, Duffy PB. 2005. Uncertainty in projections of streamflow changes due to climate change in California. Geophys. Res. Lett. 32. 765–778.

Perelet, R., 2007. Central Asia: background paper on climate change, human development report 2007/2008 fighting climate change: human solidarity in a divided world. Human Development Report Office Occasional Paper.

Sillmann, J., Kharin, V.V., Zhang, X., Zwiers, F.W. and Bronaugh, D., 2013. Climate extremes indices in the CMIP5 multimodel ensemble: Part 1. Model evaluation in the present climate. Journal of Geophysical Research: Atmospheres, 118(4), pp.1716-1733.

Taylor, K. E. 2001. Summarizing multiple aspects of model performance in a single diagram, J. Geophys. Res., 106(D7), 7183–7192, doi: 10.1029/2000JD900719.

Taylor, K.E., Stouffer, R.J., Meehl, G.A., 2012. An overview of CMIP5 and the experiment design. Bull. Am. Meteorol. Soc. 93, 485–498.

Turkish State Meteorological Service (TSMS) http://www.mgm.gov.tr.

Vano JA, Udall B, Cayan DR, Overpeck JT, Brekke LD, Das T, Hartmann HC, Hidalgo HG, Hoerling M, McCabe GJ, Morino K. 2014. Understanding uncertainties in future Colorado River streamflow. Bull. Am. Meteorol. Soc. 95: 59–78.

Zhu, Q., Hsu, K.L., Xu, Y.P. and Yang, T., 2017. Evaluation of a new satellite-based precipitation data set for climate studies in the Xiang River basin, southern China. International Journal of Climatology.

GRIDDED PRECIPITATION DATASETS: HOW CONSISTENT ARE THEY FOR TURKEY, A COUNTRY WITH COMPLEX TOPOGRAPHY?

Gizem Girgin, Ömer Lütfi Şen
Istanbul Technical University, Eurasia Institute of Earth Sciences, Istanbul (Turkey)
Email: gizem.girgin@hotmail.com

ABSTRACT
Precipitation, a crucial climate parameter, is in high demand for the research and operational activities in many different sectors as well as disciplines. However, precipitation is highly variable in space, and this attribution makes its accurate spatial estimation very difficult. Various gridded global and regional precipitation datasets are available, but they have discrepancies resulting primarily from the differences in the number of stations and interpolation techniques used to create them. The primary objective of this research is to gain insight into how consistently these datasets represent the spatial distribution of precipitation in Turkey whose topography is quite complex. The gridded datasets include those obtained from station and satellite measurements and those produced by reanalysis and climate models. The results indicate that there are substantial differences between all datasets. The major differences between the observation-based datasets arises primarily from the differences in the station network used in the distribution models. The main differences between the model and observation-based datasets occur in the mountainous areas lacking an adequately dense station network.

Key Words: *Precipitation datasets, Taylor diagram, Turkey*

INTRODUCTION

Spatial and temporal distribution of both observed and modeled precipitation datasets are compared and analyzed in numerous study before. The main common result of these studies is that the discrepancy between the precipitation datasets is higher in the mountainous areas with less dense station network. (Chen et al, 2016; Yin et al., 2014; Andermannet al, 2011; Tanarhteet al, 2012; Contractor et al, 2015; Prein ve Gobiet, 2016; Sylla et al, 2012). Tanrthte et al. (2012) compared the gridded temperature and precipitation datasets, based on observations in the Mediterranean and the Middle East including Turkey. According to their study E-OBS precipitation dataset shows very dry conditions in the eastern parts of Turkey, and CPC dataset shows wetter condition over Turkey. All datasets used indicate negative trend only in winter over Turkey (Tanarhthe et al, 2012). Sahin and Cigizoglu (2010) performed the missing value interpolation and homogeneity analysis on the meteorological data of Turkey. Using non-parametric methods Partal and Kahya (2006) determined the trends in the long-term annual mean and monthly total precipitation series.

Andermann et al. (2011) reported huge variations between the precipitation datasets in mountainous areas in their study of Himalayas which is a large orogenic belt. Mostly APHRODITE (Chen et al., 2016; Yin et al., 2014; Andermann et al., 2011; Tanarhte et al., 2012), E-OBS (Tanarhte et al., 2012; Prein ve Gobiet, 2016; Contractor et al., 2015; Yin et al., 2014), GHCN (Yin et al., 2014; Contractor et al., 2015; Prein ve Gobiet, 2016; Tanarthe et al., 2012) as observation datasets, TRMM (Contractor et al., 2015; Chen et al., 2016; Andermann et al., 2011; Sylla et al., 2012) as satellite dataset and GPCP (Prein ve Gobiet, 2016; Sylla et al., 2012; Contractor et al., 2015) as hybrid datasets are used in the studies. Turkey is a country that has a complex topography and there is no study specifically done to quantify the

inconsistencies between the observed and modeled precipitation datasets. This research, therefore, aims to gain insight into how consistently various datasets represent the spatial distribution of precipitation in Turkey.

DATA

The datasets included in this study and their spatial and temporal characteristics are given in Table 1. Several datasets of observations, satellite, model, hybrid and reanalysis are collected from different sources. These datasets have different spatial resolutions and temporal coverage. In order to compare, all datasets are brought to the high resolution of 3km grid system, proper for GIS shape file processing. For comparison, two common periods are selected as 1961-1990,1998-2007 considering the overlapping coverage periods of datasets. Despite the fact that the WorldClim dataset covers 1961-1990 period, it is considered in the 1960-1990 period. We used all available station data to create a reference precipitation dataset called TR_STA_GRIDDED. Another reference dataset (called ENSEMBLE) is created by averaging all available gridded observational datasets.

Table 1. Datasets and information about their characteristics.

Datasets	Domain	Period	Time step	Resolution	Type
TR_STA_GRIDDED	Turkey	1961-1990/1998-2007	Monthly	0.25°x0.25°	Observation
CRU /TS3.21	Global	1901-2012	Monthly	0.5°x0.5°	Observation
GPCC /V6	Global	1901-2010	Monthly	0.5°x0.5°	Observation
E-OBS/V12.0	Europe	1950-2015	Daily	0.25°x0.25°	Observation
APHRODITE/V1101	Asia	1951-2007	Daily	0.25°x0.25°	Observation
UDEL/V3.01	Global	1900-2010	Monthly	0.5°x0.5°	Observation
PREC/L	Global	1948-2017	Monthly	0.5°x0.5°	Observation
WorldClim/V1	Global	1960-1990	Monthly	10 minutes	Observation
GPCP/V2.2	Global	1979-2015	Monthly	2.5°x2.5°	Satellite-observation
TRMM/V7	Global	1998-2014	Monthly	0.25°x0.25°	Satellite
RegCM3/NCEPNCAR	Turkey	1991-2010	Monthly	12 km	Model
RegCM4/NCEPNCAR	Turkey	1961-1990	Monthly	27 km	Model
RegCM3/HADCM3	Turkey	1960-1990	Monthly	27 km	Model
ENSEMBLE MODEL DATASET	Global	1961-2000	Monthly	0.25°x0.25°	Model
CORDEX	Global	1951-2099	Monthly	0.5°x0.5°	Model
NCEP-NCAR	Global	1948-2016	Monthly	2.5°x2.5°	Reanalysis
ERA-INTERIM	Global	1979-2016	Daily	0.75° x 0.75°	Reanalysis

RESULTS

The precipitation datasets demonstrate broad agreement in their countrywide distributions (Figure 1). They accurately show the high precipitation areas of northeast Turkey and low precipitation areas of central Anatolia. However, a close examination reveals that there are important spatial differences between these datasets. The major spatial differences are observed over the mountainous areas of the Black Sea and eastern Anatolia regions. Some datasets (e.g., CRU) do not show the high precipitation of the eastern Black Sea coastal areas, most likely due to the lack of the coastal stations in their spatial estimations. In general, the model and re-analysis datasets estimate higher precipitation than the observational datasets. The highest annual precipitation amounts for Turkey in the periods of 1961-1990 and 1998-2007 belong to the CORDEX model dataset, and the lowest amounts belong to the APHRODITE dataset. Although we do not include the seasonal analysis, it is important to note that the discrepancy between the datasets is usually larger in winter and spring seasons.

Taylor Diagram shows discrepancies amongst the datasets in terms of three statistical measures: spatial correlation, standardized deviations and root mean squared errors (Figure 2.). While model datasets show weaker match, observational datasets show better match with the reference dataset (ENSEMBLE). The dataset with the highest correlation with the reference dataset amongst the observation datasets is the TR_STA_GRIDDED dataset, and the lowest correlation is the CRU dataset (Figure 2).

In conclusion, it could be said that the results of this study indicate that there are substantial differences between all datasets, whether they are completely observation based or not. The major differences between the observation-based datasets arises primarily from the differences in the station network used in the distribution models. The main differences between the model and observation-based datasets occur in the mountainous areas lacking an adequately dense station network. This could be due to the inadequate measurement of such areas as well as the inadequacies in the model estimations.

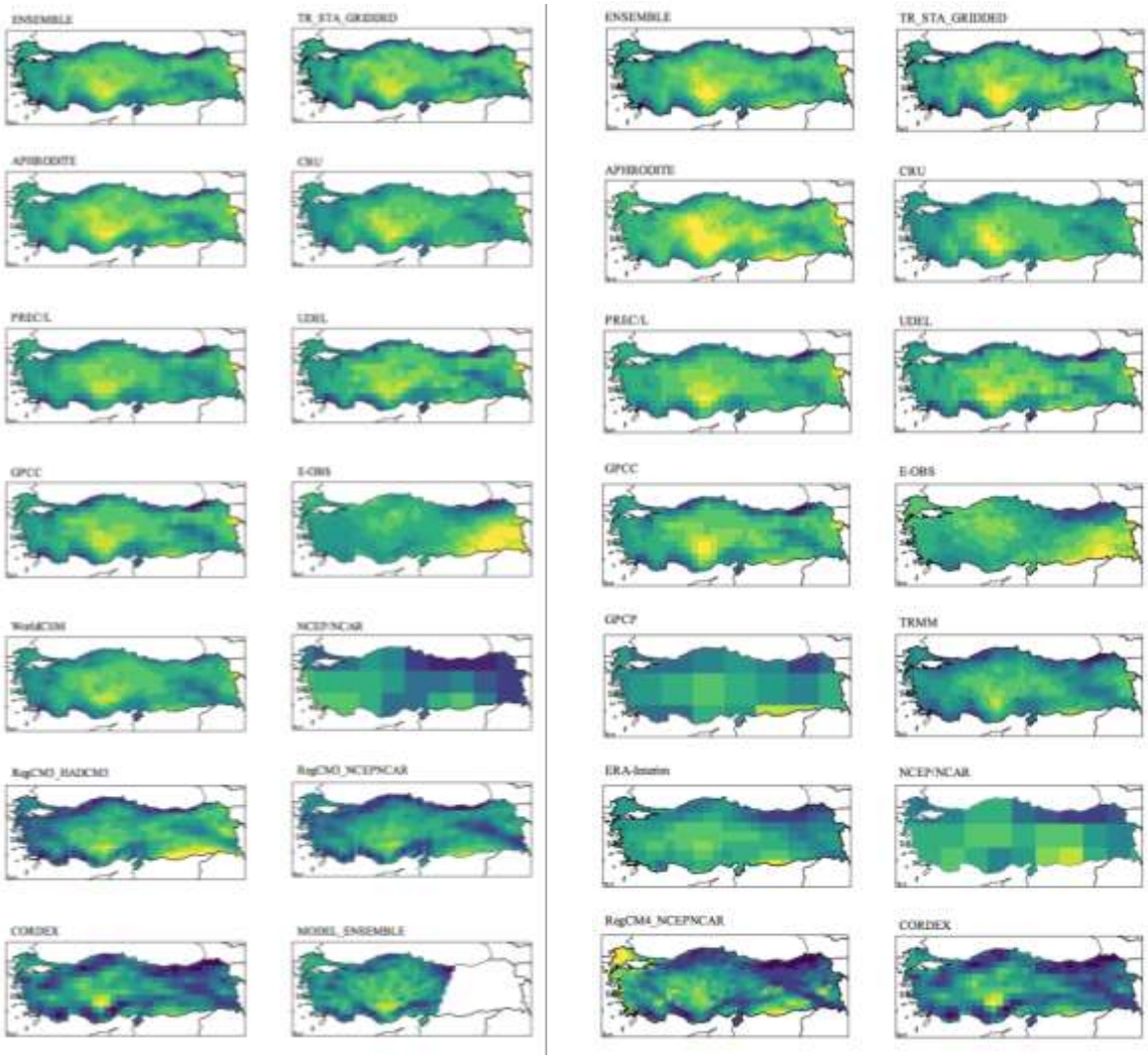

Figure 1. Annual precipitation distribution maps for 1961-1990 (left) and 1998-2007 (right) periods

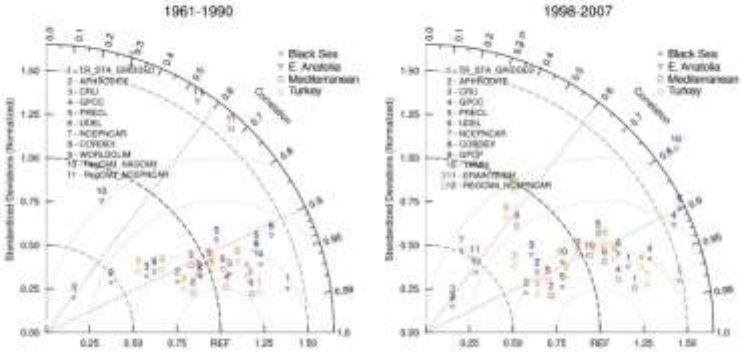

Figure 2. Taylor diagram showing the consistencies of different datasets with respect to a reference (REF) dataset, which is taken as the average of observational datasets used in this study.

Acknowledgment

This study was supported by TUBITAK under project number 114Y114.

REFERENCES

Adler, R.F., Huffman, G.J, Chang, A., Ferraro, R., Xie, P.P, Janowiak, J., Rudolf, B., Schneider, U., Curts, S., Bolvin, D., Gruber, A., Susskind, J., Arkin, P. & Nelkin, E. (2003). The Version-2 Global Precipitation Climatology Project (GPCP) Monthly Precipitation Analysis (1979–Present), *Journal of Hydrometeorology* (Vol. 4, pp.1147-1167).

Andermann, C., Bonnet, S. & Gloaguen, R. (2011), Evaluation of precipitation datasets along the Himalayan front, *Geochemistry Geophysics Geosystems* (Vol. 12, pp.1-16).

Becker, A., Finger, P., Meyer-Christoffer, A., Rudolf B., Schamm K., Schneider, U. & Ziese M. (2013), A description of the global land-surface precipitation data products of the Global Precipitation Climatology Centre with sample applications including centennial (trend) analysis from 1901–present, *Earth System Science Data* (Vol.5, pp.71-99).

Chen, C.J., Senarath, S.U.S., Dima, West, I.M & Marcella M.P. (2017), Evaluation and restructuring of gridded precipitation data over the Greater Mekong Subregion, *International Journal of Climatology* (Vol.37, pp.180-196).

Harris, I., Jones, P.D., Obsorn, T.J & Lister, D.H. (2014), Updated high-resolution grids of monthly climatic observations – the CRU TS3.10 Dataset, *International Journal of Climatology* (Vol. 34, pp.623-642).

Hofstra, N., Haylock, M., New, M., Jones P.D. (2009), Testing E-OBS European high-resolution gridded data set of daily precipitation and surface temperature, *Journal of Geophscical Research* (Vol. 114, pp.1-16).

Partal, T., Kahya, E., (2006), Trend analysis in Turkish precipitation data, *Hydrological Processes* (Vol.20, pp.2011-2026).

Prein, A.F. & Gobeit, A. (2017), Impacts of uncertainties in European gridded precipitation observations on regional climate analysis, *International Journal of Climatology* (Vol. 20, pp.2011-2026).

Sahin, S. & Cigizoglu K., (2010), Homogeneity analysis of Turkish meteorological dataset, *Hydrological Processes* (Vol. 24, pp.981-992).

Sylla, M.B., Giorgi, F., Coppola, E. & Mariotti, L. (2012), Uncertainties in daily rainfall over Africa: assessment of gridded observation products and evaluation of a regional climate model simulation, *International Journal of Climatology* (Vol. 33, pp.1805-1817).

Tanarthe M., Hadjinicolaou P. & Lelieveld, J. (2012), Intercomparison of temperature and precipitation datasets based on observations in the Mediterranean and the Middle East, *Journal of Geophscical Research* (Vol. 117, pp.1-24).

***Yatagai, A., Xie P., Alpert, P.** (2008). Development of a daily gridded precipitation data set for the Middle East, Advances in Geosciences (Vol. 12, pp.165-170).*

Url-1 *< https://www.mgm.gov.tr >*

Url-2 *< https://climatedataguide.ucar.edu/climate-data/precipitation-data-sets-overview-comparison-table>*

Url-3 *< http://www.worldclim.org/current >*

Url-4 *< https://climexp.knmi.nl/ >*

Url-5 *< http://www.euro-cordex.net>*

ASSESSING DROUGHT BY STANDARDIZED PRECIPITATION INDEX WITH OBSERVATION AND RCM DATA IN TURKEY'S MEDITERRANEAN REGION

Anıl Yıldırım Poyraz[1], İsmail Yücel[2]
[1]*Middle East Technical University, Ankara*
anil.poyraz@metu.edu.tr
[2] *Middle East Technical University, Ankara*
iyucel@metu.edu.tr

Abstract
This study aims to assess the trends in drought by using the Standardized Precipitation Index(SPI) for 14 stations from Mediterranean climate region of Turkey. The SPI values for different timescales - from 1month to 1 year - are estimated for past and future by using the observed, uncorrected and bias corrected model data. The model data that correspond the grids which consist these 14 stations was obtained from 12 different climate models on CORDEX project. Bias correction method was applied using equivalent quantile method(EQM) for both historical (1971-2005) and future (2006-2050) model data. Then, observed and model precipitation data and SPI values were compared in order to select the most reliable models for the region. The root mean square error of SPI and precipitation values was the first statistic to measure the closeness of the models to the observed data. Finally, modified Mann-Kendall trend analysis test was applied on the SPI and precipitation values for the whole period (1971-2050) for the most reliable models.

Keywords: *Drought, Standardized Precipitation Index, Trend analysis*

INTRODUCTION
We have witnessed a number of weather events cause significant losses of lives and property in recent years. The studies on changes in climate variability and extreme climatic events like drought have received increased attention in addition to the many ongoing studies that are devoted to mean climate changes due to increasing greenhouse gases concentration.

Considering the droughts, The Mediterranean region is one of the hotspots of the world. Summer dryness signals that were shown by different model projections makes the region on of the most responsive regions to climate change. (Giorgi, 2006)

SPI is a commonly used drought index method owing to its some superiorities to the other meteorological drought indices (Keyantash and Dracup, 2002). In this study, 12 different CORDEX climate models were evaluated on their past precipitation data and the selected model predictions were used to estimate trend in precipitation and SPI.

DATA AND METHODS
Observed precipitation data has been obtained from MGM (Turkish State Meteorological Service) while model precipitation data have been obtained from the CORDEX project. All models have been selected from Eur11 domain. Table.1 shows the 12 RCM-GCM couplings that have been studied for past precipitation and SPI values.

Table 5: The 12 models from given GCM-RCM coupling and Institute database

Model No	GCM	Institute	RCM
1-1	ICHEC-EC-EARTH	DMI	HIRHAM5
1-2		CLMcom	CCLM4-8-17
1-3		SMHI	RACMO22E
1-4		KNMI	RCA4
2-1	CNRM-CERFACS-CNRM-CM5	CNRM	ALADIN53
2-2		SMHI	CCLM4-8-17
2-3		CLMcom	RCA4
3-1	MOHC-HadGEM2-ES	CLMcom	CCLM4-8-17
3-2		KNMI	RACMO22E
3-3		SMHI	RCA4
4-1	IPSL-IPSL-CM5A-MR	IPSL-INERIS	RCA4
4-2		SMHI	WRF331F

As the closeness of the models to reality was analyzed, the future precipitation data was obtained for the most reliable models. The worst emission scenario(rcp85) was considered for future.

Standardized Precipitation Index

The Standardized Precipitation Index is a meteorological drought index that was developed by McKee et al. (1993) It interprets observed rainfall as a standardized departure with respect to a rainfall distribution function. The calculation of SPI value for desired period is based on the long-term precipitation record. This long-term record is assumed to follow an incomplete gamma distribution, which is then transformed into a normal distribution so that the mean SPI for the location and desired period is zero (Edwards and McKee, 1997). McKee and others used a classification system based on SPI values to define drought intensities. It extends from extremely wet to extremely dry.

The SPI can be computed for any chosen timescales -1 month to 48 months. This flexibility is a powerful feature of the SPI that can provide a plenty of information unless we have a clear idea of the desired intervals. In this study SPI was calculated for three intervals -1,3,6,9 and 12 months- for given periods.

Bias Correction

Considering the highly biased data that has appeared from the comparisons in this study and other analyses (Teng, et al. 2015; Osuch et al.,2016), the data for 1971-2100 period was corrected by an empirical distribution-based quantile mapping method while the reference period was 1971-2005. Bias correction methods aim to correct the mean, variance or distribution of the modelled precipitation by using a function h:

$$\hat{p}_{obs} = h(p_{mod})$$

so that the corrected precipitation values match the observed values more closely than the raw values. The relation in this equation can also be modelled by cumulative distribution function:

$$\hat{p}_{obs} = F^{-1}_{obs}(F_{mod}(p_{mod}))$$

These CDFs can either be theoretical or empirical. In this study, the empirical distribution was used. Therefore, the distribution was estimated by sorting the data.

Modified Mann-Kendall Test

Mann Kendall test is one of the widely used non-parametric tests for detecting trends in time series (Mann, 1945; Kendall, 1955). The Mann-Kendall trend test is derived from a rank correlation test for two groups of observations proposed by Kendall (1955). The correlation between the rank order of the observed values and their order in time is the key part of Mann-Kendall trend test. However, a modified Mann– Kendall test has been developed in order to

avoid problems with autocorrelation (Hamed and Rao, 1998). Since we are detecting the trend in SPI values, it is important to use such a modified trend test that considers serial correlation.

APPLICATION AND RESULTS

In the first step of analysis, the observed and uncorrected simulation precipitation data was compared for monthly totals of the period 1971-2005. The precipitation values for all stations were combined and distribution graph (Figure 1) was plotted. Secondly, another distribution graph was derived from the root mean square error values of the simulated precipitation data.

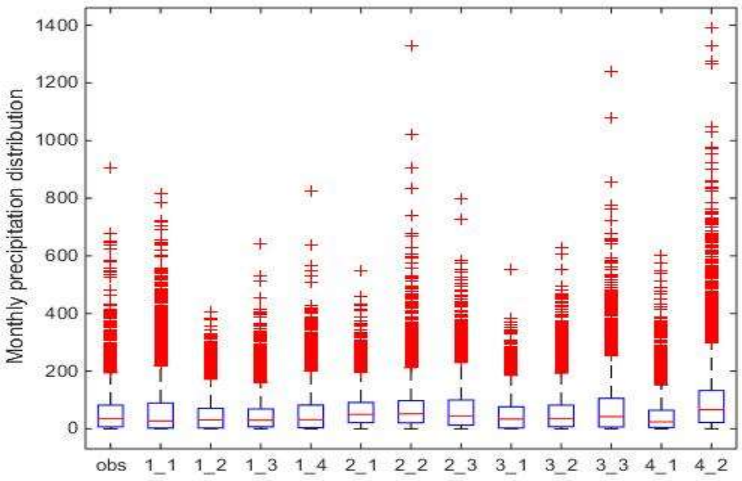

Figure 12: Boxplot for monthly total precipitation values for all stations

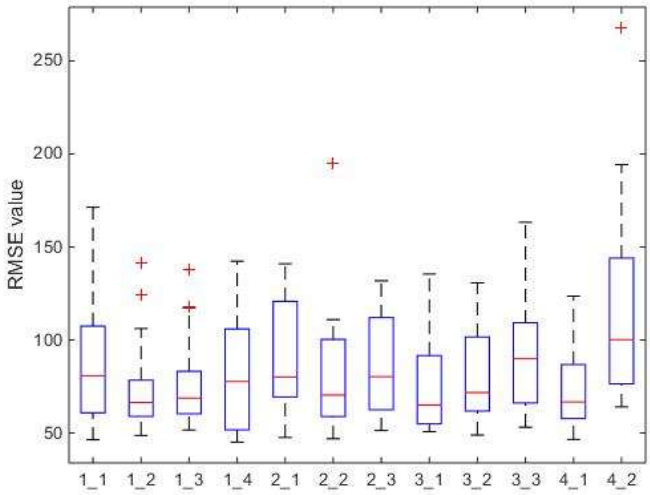

Figure 13: Root mean square error values of uncorrected simulation data

Based on these two plots, some simulations can be distinguished by their closeness to the real amounts. Following the selection of the most reliable models, bias correction was applied for the period 1971-2050. Finally, modified Mann-Kendall test was applied to the SPI(for five timescales-1,3,6,9,12) and annual precipitation.

Table 6. The Modified Mann-Kendall test results for ICHEC-EC-EARTH CCLM4-8-17 GCM-RCM coupling with CLMcom Institute data

	MUĞLA	ANTALYA	MERSİN	ADANA	AYDIN	İZMİR	DENİZLİ	BURDUR	ISPARTA	ANTAKYA	K.MARAŞ	KİLİS	Ç.KALE	MANİSA
SPI1	↗	↗	↔	↔	↔	↔	↔	↔	↔	↔	↔	↔	↔	↔
SPI3	↗	↗	↗	↗	↔	↗	↔	↔	↔	↗	↔	↔	↔	↗
SPI6	↗	↗	↗	↗	↔	↗	↔	↔	↔	↗	↗	↔	↔	↗
SPI9	↗	↗	↗	↗	↔	↗	↔	↔	↔	↗	↗	↔	↔	↗
SPI12	↗	↗	↗	↗	↔	↗	↔	↔	↔	↗	↗	↔	↔	↗
Annual rainfall	↘	↘	↘	↘	↗	↔	↔	↗	↔	↔	↔	↔	↘	↘

Table 2 demonstrates the trends in drought based on the corrected data of one of the selected models (ICHEC-EC-EARTH CCLM4-8-17). An increase in SPI means a significant increasing trend in drought frequency for that timescale. Muğla, Antalya, Mersin, Adana and Manisa are the provinces that most sensitive to drought in future. The simulation points increase in drought frequency while there is a significant decreasing trend at annual total precipitation.

CONCLUSIONS AND RECOMMENDATIONS

Muğla, Antalya, Mersin, Adana and Manisa are the provinces that are the most sensitive to drought in future. The simulation points increase in drought frequency while there is a significant decreasing trend at yearly total precipitation. It can be interpreted that the increase in drought frequency may have a relation with decrease in annual precipitation for the region. This possible relation should be considered separately.

REFERENCES

Edwards, D. C., and T. B. McKee, 1997: Characteristics of 20th century drought in the United States at multiple time scales. Climatology Report No. 97-2, Colorado State Univ., Ft. Collins, CO.

Giorgi, Climate change hotspots. Geophysical Research Letters 33, 8, 2006

Hamed, K. H. and Rao, A. R.: A modified Mann–Kendall trend test for autocorrelated data, J. Hydrol., 204, 182–196, 1998.

Kendall, M.G. (1955) Rank Correlation Methods. Charles Griffin & Co. Ltd., London.

Keyantash, J. and Dracup, J.A., The Quantification of Drought: An Evaluation of Drought Indices, Bulletin of the American Meteorology Society, August 2002, 1172, 2002

Mann, H. B.: Non-parametric tests against trend, Econometrica, 13, 163–171, 194

Marzena Osuch, Renata J. Romanowicz, Deborah Lawrence, and Wai K. Wong, Trends in projections of standardized precipitation indices in a future climate in Poland, Hydrol. Earth Syst. Sci., 20, 1947–1969, 2016

McKee, T. B., Doeskin, N. J., and Kleist, J.: The relationship of drought frequency and duration to time scales, in: Proceedings of the 8th Conference on Applied Climatology, 17–22 January 1993, Anaheim, CA, 179–184, 1993.

Teng, J., Potter, N. J., Chiew, F. H. S. , Zhang, L., Wang, B., Vaze, J., and Evans, J. P., How does bias correction of regional climate model precipitation affect modelled runoff?, Hydrol. Earth Syst. Sci., 19, 711–728, 2015

DATA ANALYSIS OF TURKEY'S SHALE GAS POTENTIAL: ANATOLIAN REGION

Javier A. Bravo[1], Onder Ozgener[2]
[1] Graduate School of Natural and Applied Sciences, Solar Energy Science Branch, Ege University, Bornova, Izmir, Turkey, jbra_13@hotmail.com
[2] Solar Energy Institute, Ege University, Bornova, Izmir, Turkey
onder.ozgener@ege.edu.tr

Abstract
In the past few decades, the development of unconventional hydrocarbon resources has played an important role in the energy revolution, significantly changing the world's energy outlook. A decrease in the usage of conventional resources has forced countries to search deeper for alternative sources of supply in order to fulfill increasing energy demand. In this study, the advancements and potential of Turkey's shale gas scenario are analyzed. Turkey, a country that has been dependent on imported fossil fuels and with a high energy demand envisages the possibility to counterbalance some of the weaknesses in the energy sector by developing a major shale industry that could reduce significantly the dependency on imported gas as well as create a more self-sufficient energy structure. Although the country finds itself in an early shale developmental stage due to the lack of geological information and industrial infrastructure, the drilling of exploration wells has been done, which will help to determine the necessary parameters of Turkey's shale gas capacity. Recent evaluations performed by foreign sources estimate the presence of shale gas potential in multiple basins across the country. Although estimates suggest that the Thrace and Southeastern Anatolian Basins are the most promising, this paper will focus its study on the shale gas data available for the Anatolian region of Turkey.

Keywords: *Shale gas, energy, Turkey, unconventional gas, fracking*

Abbreviations

Bcf	Billion cubic feet
BOTAŞ	Petroleum Pipeline Corporation
EIA	U.S. Energy Information Administration
EPA	U.S. Environmental Protection Agency
IEA	International Energy Agency
MENR	Ministry of Energy and Natural Resources
Tcf	Trillion cubic feet

INTRODUCTION
The total world energy demand increases day by day creating a need for new and alternative sources of energy that can fulfil this necessity. Nowadays, diverse forms of energy that expand from renewables such as wind, solar, hydro and geothermal to primary forms like oil, natural gas and coal are available to mankind. Each one of these sources with its own unique characteristics, pros and cons play an essential role in the world's energy development. Within these primary forms of energy, shale gas stands out. This unconventional resource of natural

gas has changed and transformed some of the world's energy markets; with an aim to expand the emerging natural gas supply.

Traditionally, Turkey is a country that has been dependent on imported fossil fuels; more than 90% of consumed oil and 99% of natural gas is brought from outside the country (EPA, 2010). For this reason, Turkey is now analyzing possibilities to overcome this dependency, reduce import costs and create a self-sufficient energy structure. Based on previous investigations, Turkey has significant quantities of shale gas reserves and an exploration phase is being carried out. Although the country finds itself in an early shale developmental stage due to the lack of geological information and industrial infrastructure, the drilling of exploration wells has been done in South Eastern Anatolian, which will help to determine necessary parameters of Turkey's "frack gas" potential.

Despite the fact that precise volumes and reservoir characteristic information are lacking, recent evaluations estimate the presence of shale gas potential in multiple basins across the country. The regions with shale gas potential are the Thrace Basin, the South Eastern Anatolian Basin, the Salt Lake Basin, the Sivas Basin and the Gurun Basin; estimates suggest that the South Eastern Anatolian Basin is one of the most promising. As a matter of fact, the Dadaş shale located in Southern Anatolia contains 130 Tcf of risked gas in place of which 17 Tcf is estimated to be technically recoverable, containing the highest shale gas presence in the country (EIA, 2015).

The purpose of this study is to analyze the potential and current development of shale gas in the Anatolian region of Turkey. Also, a brief overview of the country's current energy scenario along with statistical data that is utilized for analytical ends.

ANALYSIS

Turkey's Energy Overview

The energy sector in Turkey is one of the fastest emerging markets in the world due to its rapidly growing economy. It is considered a vital point in the global energy sector due to its strategic location as it is in the middle of the Europe, Caspian Region, and the Middle East. Turkey has experienced an accelerated progress in all of its energy divisions and it is estimated that the energy demands will keep increasing in the future (MENR, 2016). Most of the energy demand is mainly covered by foreign sources creating a big dependence, primarily of oil and gas. As reported by the Turkish Ministry of Energy and Natural Resources, during the last 12 years, the energy demand has grown by 5,7% annually and is projected to keep growing by 7,5% per year until 2023. Currently, about 25% of the total energy demand comes from domestic resources while the rest of it is covered by external sources (MENR, 2016).

In order to supply the growing demand, Turkey must boost its investments in electricity, natural gas and renewable energies. At the end of 2016, the installed power generation capacity of Turkey was approximately 78 GWh with a projected capacity of 100 GWh by 2023. Out of the total, 33,7% consisted of hydropower, followed by natural gas at 29%, coal at 22,1%, wind at 6,7%, multi-fueled at 5,9%, geothermal at 0,9% and other sources at 6,8% (MENR, 2016). Turkey's electricity generation is obtained from different sources. In December 2016, the total power generation reached 261 TWh (IEA, 2016). That same year, the highest share was accredited to coal with 32,44% of the total electricity generation. Additional energy sources used for electricity generation in 2016 were natural gas at 32,40%, hydro at 26,20%, wind at 5,56% geothermal, solar, biogas and others at 3,40% (MENR, 2016).

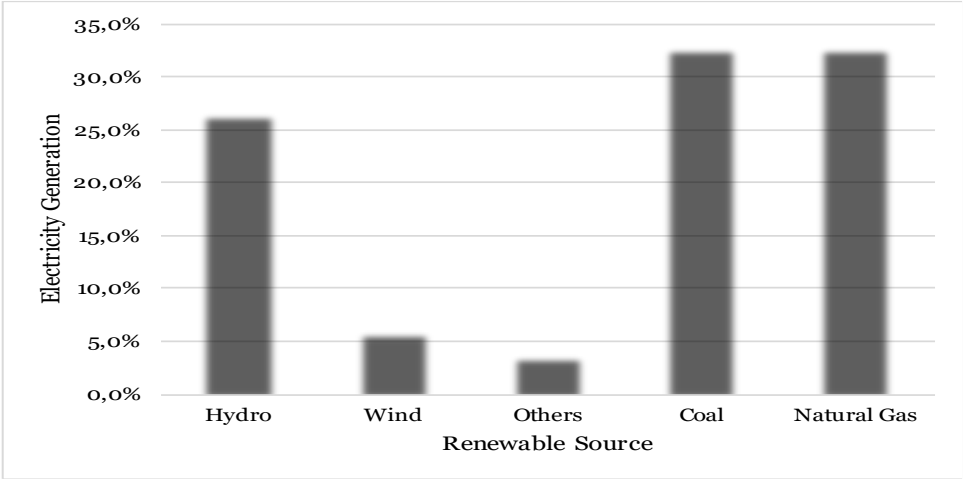

Figure 1. Turkey's electricity generation by resource at the end of September of 2016 (MENRı, 2016)

Turkey, as a major natural gas user imports almost 90% of the natural gas it consumes. According to MENR, in 2015 Turkey imported 48,4 bcm of natural gas from five countries: Russia 55,1%, Iran 16,2%, Azerbaijan 12,3%, Algeria 81% and Nigeria 2,6%. Furthermore, its total electricity demand has been increasing rapidly and by the end of September 2016, it reached 207 TWh. Based on the predictions carried out by MENR, Turkey will reach a final electricity demand of 480 TWh in 2023 (MENR, 2016). In order to counterbalance these energy demands the country needs to execute considerable investments in the energy sector, specifically in infrastructure, electricity and natural gas. Turkey's demand growth and energy manufacturing industry will require competitive energy supplies.

Natural Gas

Turkey is considered one of the highest consumers of natural gas among European countries and continuously exhibits a strong growth within the sector. This consumption has forced the development of new pipelines to introduce natural gas into the country. Natural gas plays a vital role in the country's economy, contributing substantially to its development. The natural gas sector in Turkey is primarily controlled by the Petroleum Pipeline Corporation (BOTAŞ), which is a state-owned company. BOTAŞ is responsible for most of the natural gas imports (approximately 80%), the construction and operation of pipelines and market wholesalers (BOTAŞ, 2016).

Natural gas consumption in the country has been increasing rapidly since the last decade. The consumption in 2016 was 46,5 million m^3. In 2014, approximately half of the total consumption of natural gas was used mainly in electricity generation. The rest was divided between the construction (residential and commercial) and industrial sectors. (IEA, 2016). Consumption is expected to continue due to the expansion of the industrial sector and high electricity demand. In 2015, Turkey imported 55% of natural gas from Russia, representing the second largest natural gas market for Russia after Germany (TPAO, 2016). Conversely, BOTAŞ exported 22 Bcf of natural gas in 2015 (BOTAŞ, 2016).

Shale Gas Potential

Turkey has at least five basins in which the potential of fossil fuels is assessed to be exceptional; the Southeastern Anatolia Basin, the Thrace Basin, the Eastern Anatolia Basin, the Black Sea Basin and the Central Anatolian Basin. A general analysis will be carried out, however, we will

focus specifically in the two highest potential basins, the Southeastern Anatolia and the Thrace basins (Altun et al., 2006; Aydemir, 2010).

Turkey's largest and most promising shale basins are situated in the Southeastern Anatolia and Thrace regions. The Southeastern Anatolia Basin often referred to as the super source rock is by far the most promising of the two, containing almost all of the resources. As of yet, there is no official or exact reservoir data for all of Turkey's resources until the exploration reaches more advanced stages. These explorations are being performed by the Turkish Petroleum Company (TPAO) and several international companies, such as Valeura Energy Inc., Transatlantic Petroleum, Anatolia Energy Corp. and Royal Dutch Shell. There are also high possibilities that shale gas resources might be available in the Sivas and Salt Lake basins, unfortunately, the reservoir is not sufficient to evaluate deeply these two lightly explored basins (EIA, 2015). According to the assessment performed by ARI, it is expected that the Dadaş Shale in Southeast Anatolia and the Hamitabat Shale in Thrace, collectively contain approximately 163 Tcf of technically recoverable shale gas.

Southeastern Anatolian Basin

Within the Turkish border, the Southeastern Anatolian Basin covers an area of 32.100 square miles of the Arabian plate. This basin contains the Silurian Dadaş Shale, which is located in a central lot of the basin. On the north, is surrounded by the Zagros suture zone and in the south and east by Syria and Iraq. According to the research performed by ARI under the initiative of the EIA, the Southeastern Anatolian Basin is basically an active oil-prone basin with almost 100 oil fields discovered (EIA, 2015).

Test wells have been drilled in this basin by several companies in order to obtain the necessary parameters to determine gas potential. The industry activity is composed by TPAO and Shell in a joint venture performing in the Dadaş and Saribugday-1 wells, Transatlantic Petroleum is performing in the Göksu 1 and 2, Bahar 1, Molla, Selmo and Arpatepe wells and Anatolia Energy is performing in the Çalıktepe 1&2 wells.

The Southeastern basin shares a similar geology with those of the middle east oil producing regions. The most promising source rock in the basin is the Silurian-Devonian Dadaş Shale. Based on the reservoir data and mapping performed by ARI, the Dadaş shale is prospective for shale gas development in an area of 4040 square miles. According to TPAO, the area is feasible for shale gas and shale oil developments. Thermal maturity data of the formation is being carried out (TPAO, 2016).

The shale formation within the prospective basin is estimated to have 130 Tcf of risked gas in place of which 17 Tcf is estimated to be technically recoverable. Even though the area shows heavy faulting that could alter the process, it demonstrates favorable properties for shale gas development. Once the exploration stage is concluded and additional data is obtained, major advances will be made throughout the Dadaş Shale (EIA, 2015).

As mentioned before, the Southeast basin has been largely leased for oil and gas exploration with TPAO holding the majority of the leases, along several foreign firms. Major advances are going to be shown as these limitations are being overcome.

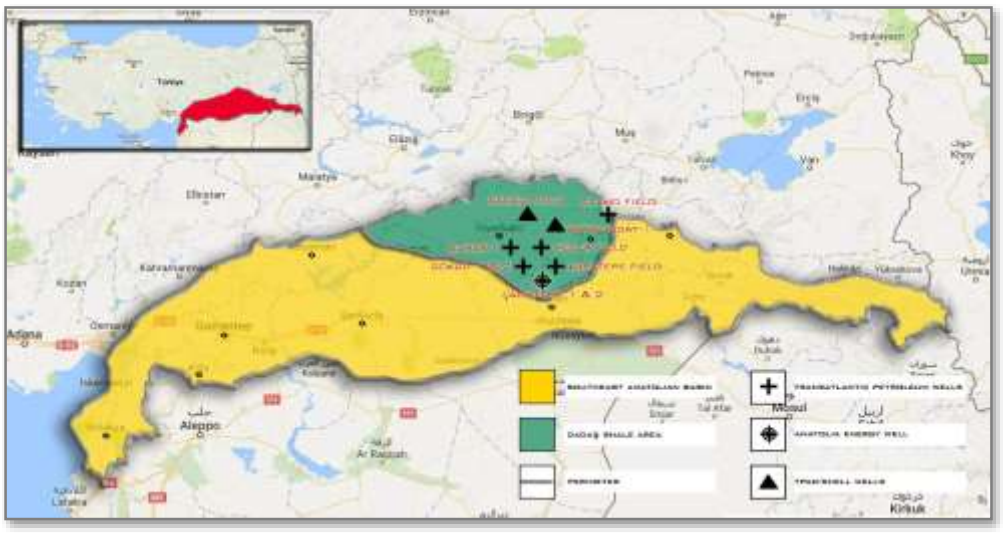

Figure 2. Outline, depositional limit and prospective areas of the Dadaş Shale in the Southeastern Anatolian Basin.

Table 1. Shale gas reservoir properties of Turkey: Dadas Shale (EIA, 2015)

	Basin/Gross Area	*SE Anatolian (32100 mi²)*	
	Shale Formation	*Dadas*	
Basic Data	*Geologic Age*	*Silurian-Devonian*	
Physical extent	Prospective Area (mi²)	3540	500
	Thickness (ft)		
	Organically rich	394	377
	Net	216	207
	Depth (ft)		
	Interval	6000-11500	5500-13000
	Average	9000	9500
Reservoir properties	Reservoir pressure	Mod. Overpress.	Mod. Overpress
	Average TOC (wt%)	3.6%	3.6%
	Thermal maturity (%Ro)	0.85%	1.15%
	Clay content	Med./High	Med./High
Resource	Gas phase	Assoc. Gas	Wet Gas
	GIP concentration (Bcf/mi²)	48.2	91.4
	Risked GIP (Tcf)	102.4	27.4
	Risked recoverable (Tcf)	10.2	6.9

Central Anatolian Basins

The interior basins in Central Anatolia comprise under-explored deep basins. These basins are the Salt Lake Basins, Sivas Basin and Gurun Basin. Due to the light exploration thus far in these basins, the information available regarding shell well data is very limited. However, in accordance with Transatlantic Petroleum, surface geology, magnetic data and regional well data indicate possibilities of significant resources (Valeura Energy, 2015).

Salt Lake Basin

The Salt Lake Basin involves both the north and south basins. The North basin has an area of 763 square miles and the South Basin 1146 square miles making a total of 1909 square miles. Based on gravity and magnetic data provided by Transatlantic Petroleum, sedimentary basins up to 10 km deep are reachable in the area (Valeura Energy, 2015). Oil and gas exploration

companies have launched an extensive program to confirm hydrocarbon potential in these basins as well as the drilling of several exploration wells.

Figure 3. Map of the North and South Salt Lake Basin, Central Anatolia.

Sivas Basin

The Sivas Basin contains an area of 3320 square miles. Gravity and magnetic data obtained shows a presence of thick low-density sedimentary sequence. Alternative studies based on surface outcrops demonstrate the presence of working gas and petroleum systems. Since this basin is located in an area where gas pipelines and infrastructure already exist, it would make it accessible for exploration and distribution of gas, if discovered (EIA, 2017).

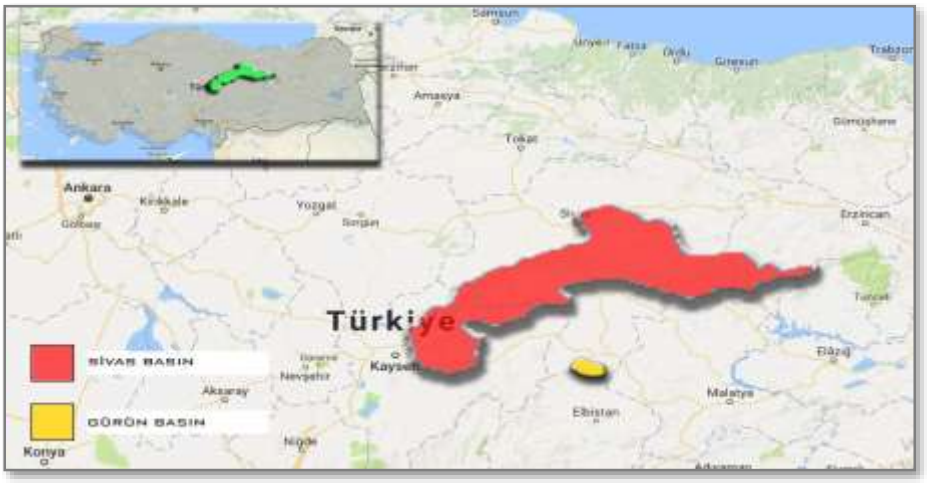

Figure 4. Map of the Sivas Basin and Gurun Basins.

CONCLUSIONS

The estimated shale gas quantities available in the Anatolian region are exceptional, however not enough to supply the country's total demand of natural gas. Although the Southeastern Anatolian basin is the most promising of all the basins, containing most of the shale gas reserves, its mainly an oil prone region. More exploration and analysis is required in the other unexplored basins such as Sivas, Gurun and Salt Lake in order to determine more precise volumes. Gas pricing and available technologies are two aspects that will play an important role in Turkey's shale gas exploration, development, and production projects. Modifications of these

aspects can affect considerably the feasibility, both economically and operationally of the projects. Furthermore, modern technologies such as hydraulic fracturing and horizontal drilling will have a considerable impact on the success of shale gas development.

It can be stated that it will take some time before Turkey fully develops a shale gas industry in significant quantities; an industry capable of covering the complete national demand. The initial investment will be high, thus, a more detailed feasibility study should be carried out. Nevertheless, the government is encouraging private companies to keep investing in shale gas exploration by granting them advantageous conditions within the commercial and legal frameworks. This policy, and Turkey's crucial location as an international gas supplier will keep attracting investment that might lead to a long-term success of shale gas exploration and production. For the time being, Turkey can focus on alternative options such as the domestic production of renewable energies and cheaper gas imports to meet the energy demand. However, if a shale gas industry develops in Turkey, it will make the country self-sufficient in terms of energy needs and hence, help generate an increase in the economy.

REFERENCES

Altun, N. E., Hiçyılmaz, C., Hwang, J. Y., Bağcı, A. S., & Kök, M. V., 2006, "Oil shales in the world and Turkey; reserves, current situation and future prospects: A review", pp. 211-227, Estonian Academy Publishers.

Aydemir, A., 2010, Potential unconventional reservoirs in different basins of Turkey, AAPG European Region Annual Conference, Kiev.

Bravo, Javier A., Ozgener, Onder, 2017, "Shale Gas in Turkey: An Overview", *2017 International Energy Raw Materials and Energy Summit INERMA*, Istanbul, Turkey.

BOTAŞ, "Natural Gas Export", http://www.botas.gov.tr (Accessed date: 21.4.2017)

EIA, 2017, Country Analysis Brief: Turkey.

EIA, 2015, Technically Recoverable Shale Oil and Shale Gas Resources: Turkey, Washington, USA.

EIA, 2015, "Turkey Report", https://www.eia.gov/beta/international/analysis.cfm?iso=TUR (Accessed date: 5.3.2017)

EPA, 2010, "Hydraulic fracturing research study", EPA/600/F-10/002, Accessed October 2016.

IEA, 2016, Turkey 2016 Overview, Energy policies of IEA countries: Turkey 2016 Overview, Paris, France.

Ministry of Energy and Natural Resources (MENR), 2016, World and national energy and natural resources outlook, Ed.14, Turkey

TPAO, 2016, Crude Oil and Natural Gas Sector Report.

TPAO, Unconventional Exploration, http://www.tpao.gov.tr/eng/?tp=m&id=45 (Accessed date: 19.4.2017)

Transatlantic Petroleum Ltd., 2011, Turkey Exploration Portfolio.

Valeura Energy, 2015, "Unlocking Turkey's Unconventional Gas Potential", http://www.valeuraenergy.com/upload/news_release/133/01/valeura-november-2015-corporate-presentation-v1-november-12-2015-final.pdf (Accessed date: 6.1.2017)

Valeura Energy, 2014, "Turkey Overview 2014",http://www.valeuraenergy.com/operations/turkey/overview.html (Accessed date: 14.2.2017)

INVESTIGATION OF CHANGES IN THE PERSISTENCE OF PREVAILING WIND IN WESTERN PART OF TURKEY USING DIRECTIONAL STATISTICAL METHOD

Evren Özgür
Istanbul Technical University, Faculty of Aeronautics and Astronautics, Department of Meteorological Engineering, Maslak, Istanbul, Turkey
ozgurev@itu.edu.tr

ABSTRACT
Prevailing wind directions in western part of Turkey are north and northeast. Second prevailing winds are south and southwest. In the study, seasonalities of northern and southern winds were examined by using directional statistical method. Daily maximum wind velocity and direction data of Manisa, Akhisar and Çeşme stations were used in order to apply the method. The observation period was taken to be 1965-2014 for Manisa and Akhisar. On the other hand, observation period was selected as 1967-2006 for Çeşme station. In directional statistical method, individual dates of northern and southern winds are defined as directional variables and directional mean and variance are calculated. Wind dates are being converted to angular values and these days are being considered as a unit vector which has direction Θ. In polar coordinate, the measures of directional mean and variance have been expressed as a vector that has direction $\bar{\theta}$ and magnitude r. While applying calculations, total time period was divided into subperiods and changes of persistence in prevailing wind directions as far as subperiods were presented. Persistence is a very substantial concept especially in climate studies. For instance, persistence can be used in different kinds of study areas such as control of forest fires, dispersion of pollutants, calculation of wind energy potential. The r value explained above can be considered as a measure of persistence, as well. In the study, persistence values for each period was calculated and investigated seperately.

Key Words: *wind, persistence, directional statistics, seasonality.*

INTRODUCTION
The term "persistence" is the measure of continuity for any variable with time in any point or region (Korkmaz, 2012). Persistence of wind direction is usually ignored in many studies. However, this term is one of the most important parameter in short term transportation of pollutants (Shirvaikar, 1967). While considering wind direction information together with wind speed data, they can use in many different purposes such as forest fires, dispersion of air pollutants and ventilation of the buildings (Koçak, 2008).

Directional statistical method is used in many areas such as astronomy, earth sciences, meteorology and biology. The method has been applied different kinds of meteorologic and hydrologic variables in last years. For example, in a study conducted in 2007, the seasonality of the Yeşilırmak basin floods was examined. In the study of 13 current monitoring station data, the data period was divided into two parts in order to show the changes that occurred in seasonality. The data from 1938-2003 were compared with the last 12 years and the two periods were compared and it was attempted to determine whether there was any shift at average flood time. A forward shift was detected in 11 stations according to their average flood time. The station that had the highest shift was station number 1413 with a shift of nearly two months (Pala, 2008).

In another study, the method was applied to extreme rainfall data of Göztepe, Florya and Kirecburnu stations. Threshold values between 20 mm and 60 mm were increased by 10 mm and the periods of precipitation data were recorded in two equal periods. As a result of the study, a backward shift (27 days) was observed for Göztepe stations with the 40 mm and above threshold values. It can be said that three weeks backward shift was observed for Florya station (Tanrıkulu, 2008).

In the other study, the method was applied to the temperature data of Kireçburnu, Göztepe and Florya stations. In the study, 3 threshold values were determined for the temperature data. These threshold values are 19 °C, 24 °C and 29 °C, respectively. According to the results of the analysis, there was a backward shift in seasonality of extreme temperatures for all stations in every threshold values (Afif, 2009).

In this study, directional statistical method was applied to maximum wind data for Akhisar, Çeşme and Manisa stations. The threshold value was selected as is 17,2 m/s which is the storm limit value in bofort scale. In all stations, the changes in the seasonality and the differences in persistence values have been examined.

DATA AND METHODOLOGY

Data

In the study, daily maximum wind speed and directions data were used for all stations. The data period was 1965-2014 for Akhisar and Manisa stations. On the other hand, the observation period was selected as 1967-2006 for Çeşme station. The total period was separated into decades in order to detect the changes in persistence. Figure 1 shows the locations of the stations used in the study.

Figure 1. Locations of the stations used in the study.

Methodology

The method used in the study is called “directional statistical method”. Firstly, the days with extreme values are calculated as radian angular type. The angular values of extremes were calculated by using the formula below:

$$\theta_i = (TakvimGünü)_i \left(\frac{2\pi}{365}\right) \quad (1)$$

where "TakvimGünü" is the day of the year (Pala, 2007). This θ values are transformed to x and y values in order to place on unit circle.

$$x = \cos(\theta_i) \quad (2)$$

$$y = \sin(\theta_i) \quad (3)$$

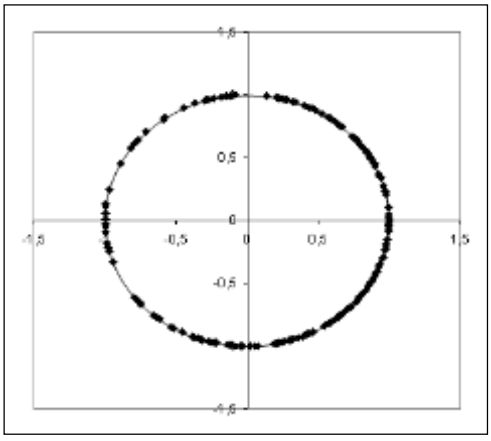

Figure 2. Distribution of x and y values on unit circle.

The arithmetic means of all x and y values are the coordinates of average date for extreme values.

$$\bar{x} = \frac{1}{n}\sum_{i=1}^{n} \cos(\theta_i) \quad (4)$$

$$\bar{y} = \frac{1}{n}\sum_{i=1}^{n} \sin(\theta_i) \quad (5)$$

Angular value of average date is calculated by using Eq.6 while $\left(\frac{\bar{y}}{\bar{x}}\right)$ is positive. On the other hand, Eq.7 is used while $\left(\frac{\bar{y}}{\bar{x}}\right)$ is negative. This angular value shows the directional location of most this average date (Pala, 2007).

$$\bar{\theta} = \tan^{-1}\left(\frac{\bar{y}}{\bar{x}}\right) \quad (6)$$

$$\bar{\theta} = \tan^{-1}\left(\frac{\bar{y}}{\bar{x}}\right) + \pi \quad (7)$$

While MD is the average day of maximum winds on unit circle, Julian day of the year can be calculated by using the formula below:

$$MD = \bar{\theta}\left(\frac{365}{2\pi}\right) + 180 \quad (8)$$

The frequency of these maximum winds around the average day was defined as "*r*". This r value changes between "0" and "1". It is clearly said that the higher r value means the higher persistence around the average julian day. On the other hand, the smallest r value implies that a very large fluctuation for extreme values around the whole year. A dimensionless r value that express the persistence of extreme values can be calculated the formula given below:

$$r = \sqrt{(\bar{x})^2 + (\bar{y})^2} \quad (9)$$

APPLICATION AND RESULTS

Northern Winds

Figure 3 shows the extreme winds of Akhisar stations for 1., 3. and 5. period. While looking at the figure, it is easily said that extreme winds were distributed nearly whole year in first period. On the other hand, extreme winds were observed in March and earlier September in last decades. The average extreme day was 11 for first ten years while this was 81 for last period.

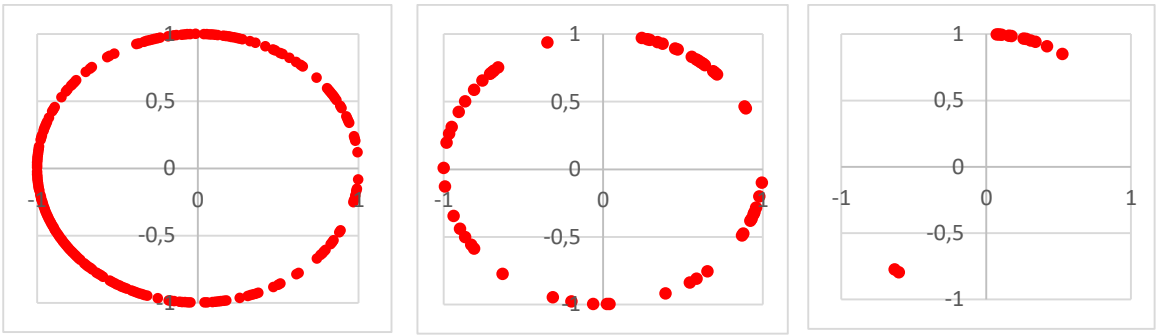

Figure 3. Extreme winds of Akhisar for 1., 3. and 5. Period

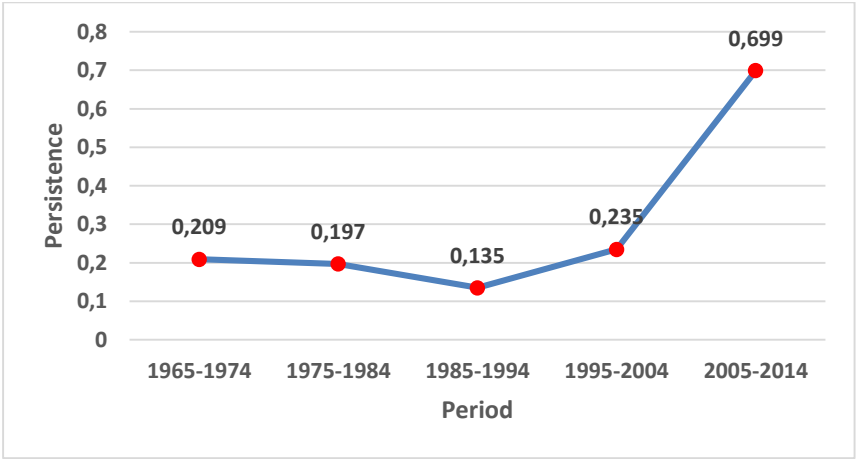

Figure 4. Persistence values of Akhisar station for Northern winds

Figure 4 shows the changes in persistence values for five different periods. It is clear that there was an obvious increase in persistence especially in last decade. The persistence value was 0,209 in first period. On the contrary, nearly 0,7 persistence value was observed for last ten years.

Figure 5 shows the extreme winds of Çeşme stations for 1, 3. and 4. period, respectively. It was observed that number of extreme values were decreased. Extreme values were observed in the winter and earlier spring season in last decade.

Figure 6 shows the changes in persistence values for four different periods. It is clear that there was an obvious increase in persistence similar with Akhisar station. The persistence value was 0,285 in first period. On the contrary, more than 0,72 persistence value was observed for last ten years.

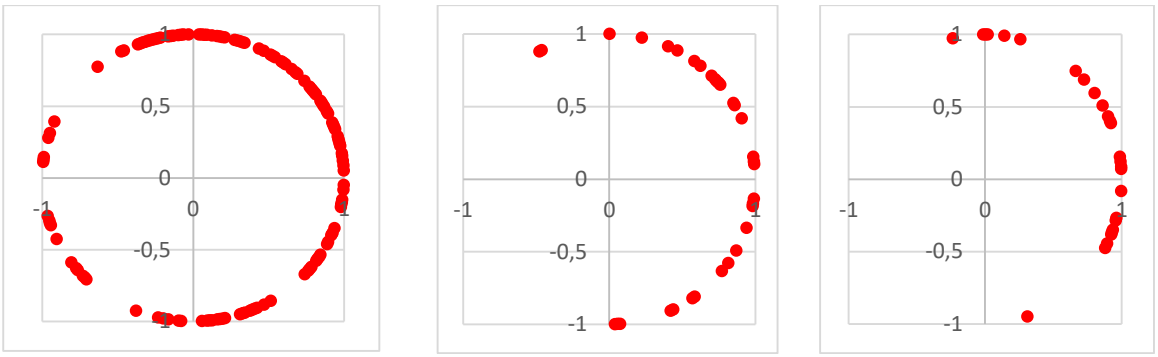

Figure 5. Extreme winds of Çeşme for 1., 3. and 4. Period

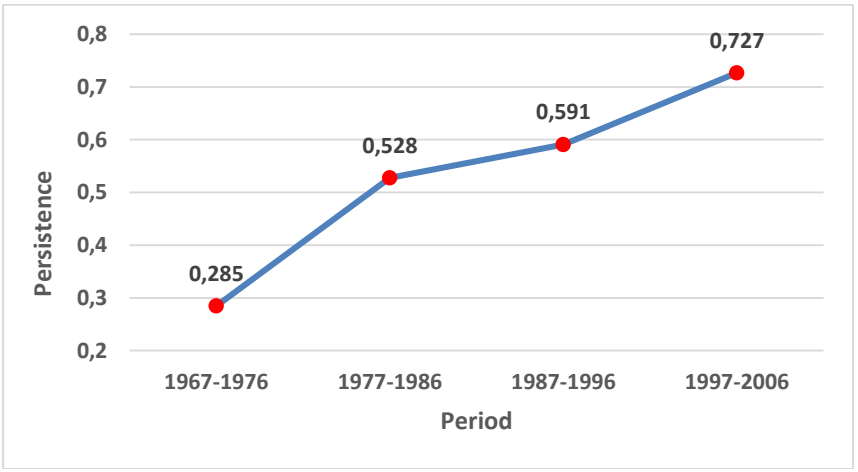

Figure 6. Persistence values of Çeşme station for Northern winds

Figure 7 shows the extreme winds of Manisa stations for 1, 2. and 3. period, respectively. It was observed that number of extreme values were decreased. Only three extreme values were observed in the last decade. Figure 8 shows the changes in persistence values for three different periods. It is clear that there was an obvious increase in persistence similar with the other stations. Especially in last period, persistence value was 0,99 which means extreme values were spread around one specific date.

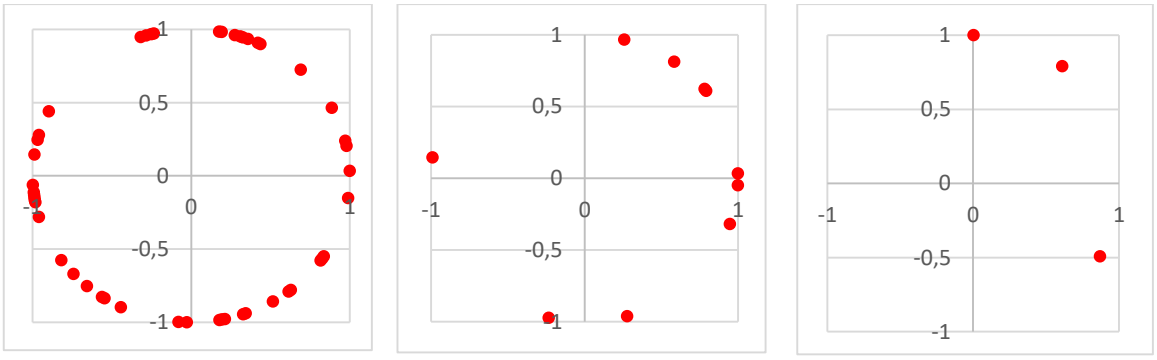

Figure 7. Extreme winds of Manisa for 1., 2. and 3. Period

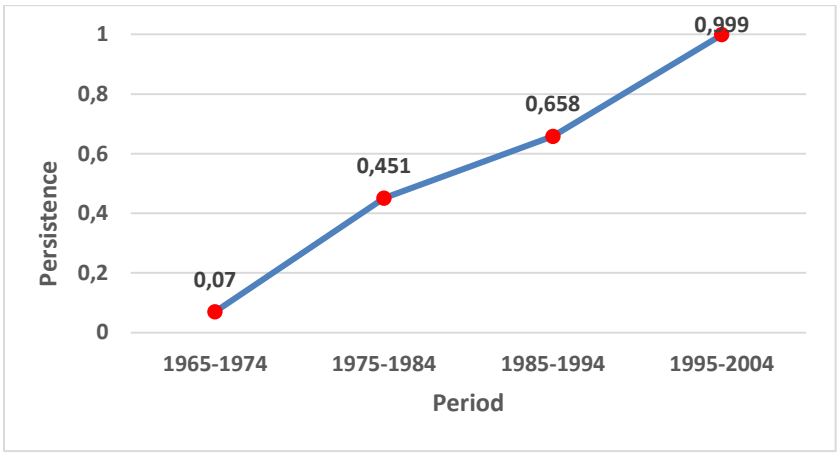

Figure 8. Persistence values of Manisa station for Northern winds

Southern Winds

Figure 9 shows the extreme winds of Akhisar stations for 2., 4. and 5. period. While looking at the figure, it is easily said that extreme winds were distributed into whole year except summer and half of autumn season for first period. Number of extreme days were decreased especially in last 20 years period. Figure 10 shows that no statistically change was observed in persistence values of Akhisar station for southern winds.

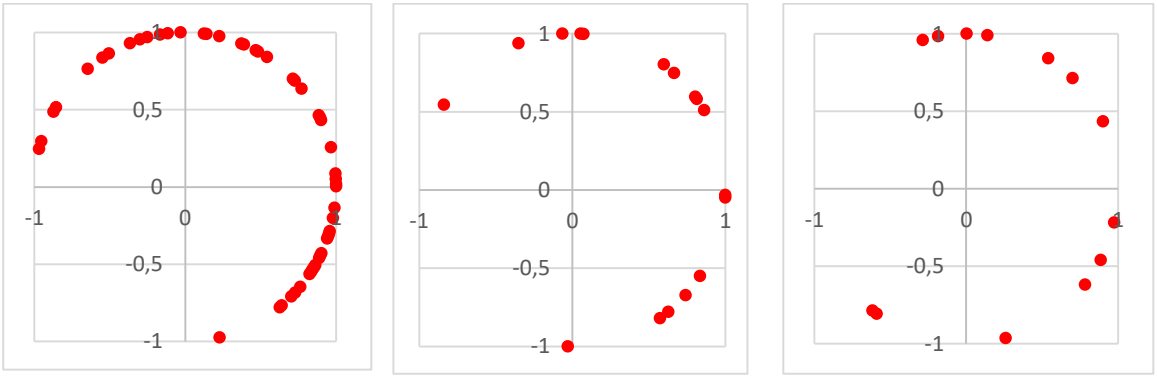

Figure 9. Extreme winds of Akhisar for 2., 4. and 5. Period

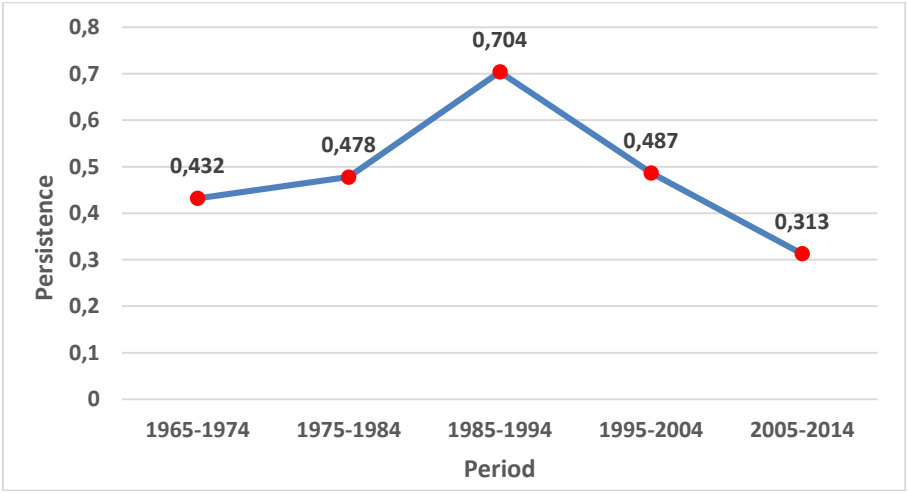

Figure 10. Persistence values of Akhisar station for Southern winds

Figure 11 and 12 shows the extreme winds and persistence values of Çeşme station, respectively. While looking at the Figure 11, no significant changes were observed with the

dates of extreme wind speed values, especially in last 20 years. Figure 12 shows the increases in persistence values with time.

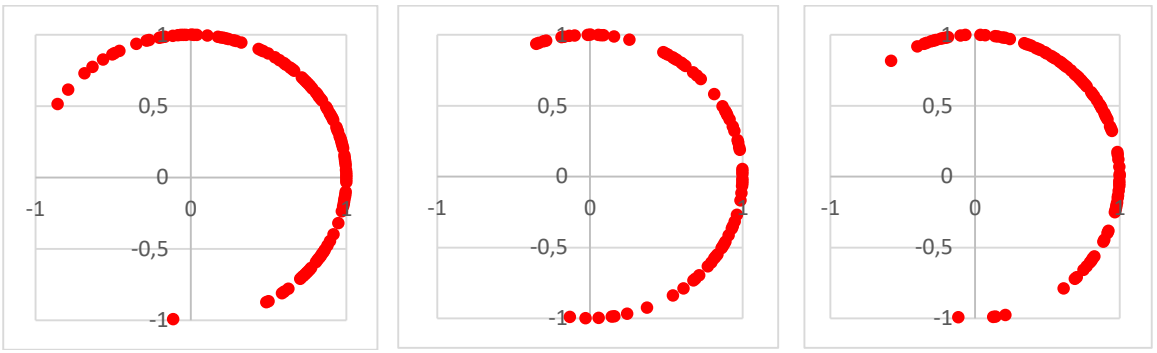

Figure 11. Extreme winds of Çeşme for 2., 3. and 4. Period

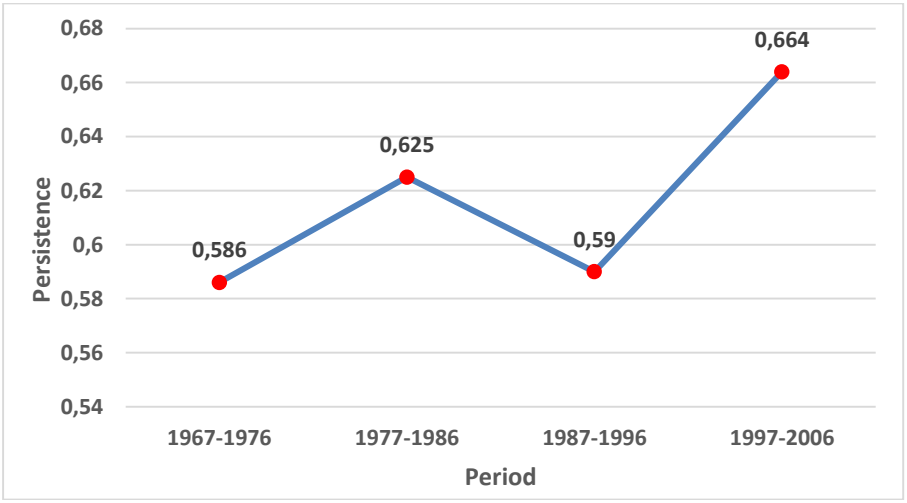

Figure 12. Persistence values of Çeşme station for Southern winds

Figure 13 shows the extreme winds in Manisa station for 1., 3. and 5. period. In last decade, number of extreme days were decreased one third of the values in the first period. In addition, Figure 14 revealed that persistence value of extreme winds in last period was two times higher than the value in the first period. It means the extreme days were distributed steadily around the average day. Finally, calculations showed that average extreme days for Manisa station shifted two weeks foreward in 40 years.

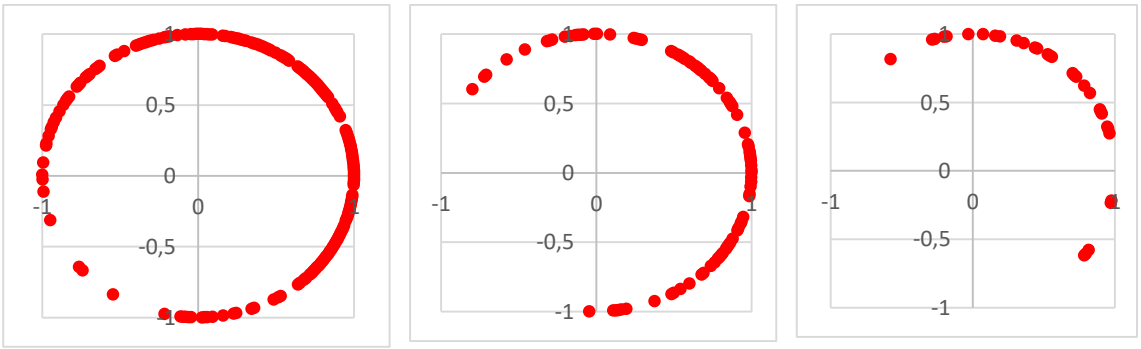

Figure 13. Extreme winds of Manisa for 1., 3. and 5. Period

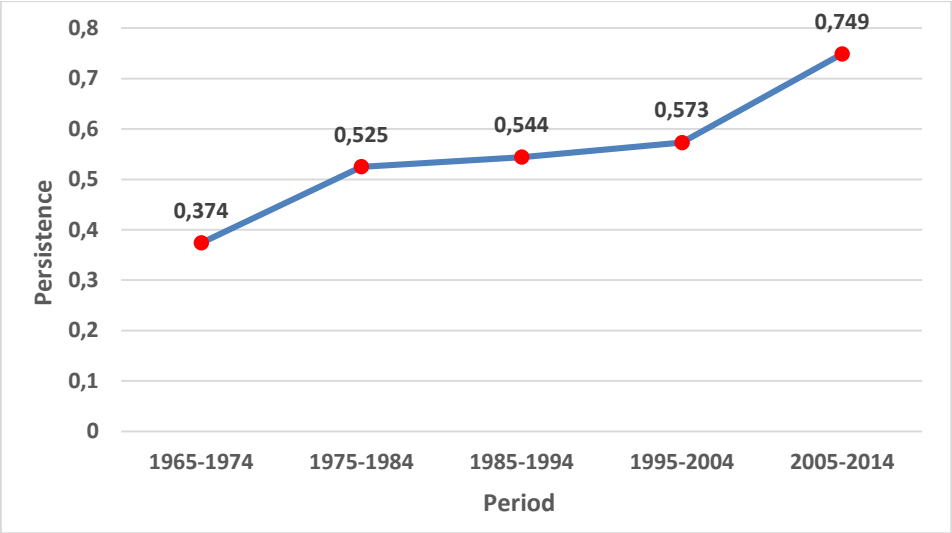

Figure 14. Persistence values of Manisa station for Southern winds

REFERENCES

Afif, M. (2009). Investigation of Seasonality for Temperature Data, Undergraduate Thesis, ITU (in Turkish).

Koçak, K. (2008). *Practical Ways of Evaluating Wind Speed Persistence*, Energy, 33: 65-70.

Korkmaz, F. M. (2012). Comparatıve Investıgation of Wind Persistence Over Turkey Using Different Methods, Graduate Thesis, ITU (in Turkish)

Pala, M. (2008). Investigation of Seasonality of Floods for Yeşilırmak Basin, Graduate Thesis, ITU (in Turkish)

Shirvaikar, V. V. (1967). Persistence of Wind Direction, Atmospheric Environment, 6(12): 889-898.

Tanrıkulu, G. (2008). Investigation of Seasonality for Precipitation Data, Undergraduate Thesis, ITU (in Turkish).

COMPARISON OF GRIDDED OBSERVATION DATA SETS ON TURKEY

Ceyhun Özcan and Barış Önol
Department of Meteorological Engineering, Faculty of Aeronautics and Astronautics, Istanbul Technical University
ozcan.ceyhunn@gmail.com ; onolba@itu.edu.tr

Abstract
The purpose of this study is to analyze all observed gridded data sets available over Turkey and to reveal differences among them. We used 9 different global and regional gridded data sets for temperature and precipitation parameters to define temporal and spatial differences. Seasonal mean analysis, bias analysis, distribution function and Q-Q analysis have been applied to find out the most suitable data set over Turkey. The analysis indicate that the correlations between data sets are generally high, however there are many differences in terms of spatial distribution and seasonal change. When the data sets are compared with station data, annual mean biases for all data sets tend to lower than station values for temperature. For precipitation data sets, annual mean biases also show different temporal and spatial pattern. Generally, GHCN/CAMS and GPCC have better representation over Turkey for temperature and precipitation, respectively.

Keywords: *Global data sets, observation, Turkey, data analysis*

INTRODUCTION
Main goal of this paper is to compare gridded temperature and precipitation observation data sets over Turkey. There are many data sets which could be used in climate studies but how well they resemble each other and how well they represent station observations should be analyzed. There have many researches on such studies. Recently, Tanarthe et al. (2012) compared the data sets based on observation over the Mediterranean region and the Middle East and we extend their study to focus on details over Turkey. We compare to data sets with long term monthly means for the period of 1981-2008 (temperature) and for the period of 1981-2007 (precipitation). We have also calculated biases for all the data sets by using the 187 meteorological station over Turkey for period of 1971-2000. The main results indicate that most of the data sets represent the climatology of Turkey generally well. However, there are some distinctions among the data sets, which generally appears over the coastal and the mountainous regions. The main causes of these differences can be produced by the temporal and spatial differences for station observations used by the data sets, the process of quality check for the raw data and the interpolation techniques applied by the griddes data sets.

DATA AND METHODS
In this study, Climate Research Unit (CRU) (Harris et al., 2014), University of Delaware (UDEL) (Matsuura and Willmott, 2009), ENSEMBLES gridded data (E-OBS) (Haylock et al., 2008) and Global Historical Climatology Network/Climate Anomaly Monitoring System (GHCN/CAMS) (Fan and Van den Dool, 2008) data sets are used for temperature analysis. In addition, CRU, UDEL (Matsuura and Willmott, 2009), E-OBS, Global Precipitation Climatology Center (GPCC) (Schneider et al., 2014) and Asian Precipitation – Highly Resolved Observational Data Integration Toward Evaluation of Water Resources (APHRODITE) (Yatagai et al., 2012) data sets are used for precipitation analysis. We compared these data sets in two ways. In the first step, 30-years (1981-2010) monthly averages for each month have been analyzed. As a next step, we used daily temperature and precipitation data from 187 stations to compare with the data sets. In addition, the nearest grid points correspond to the meteorological

stations were found for each gridded data sets. The correlation between the data sets and the stations was examined by statistical methods such as bias analysis, scatter diagram and Q-Q analysis.

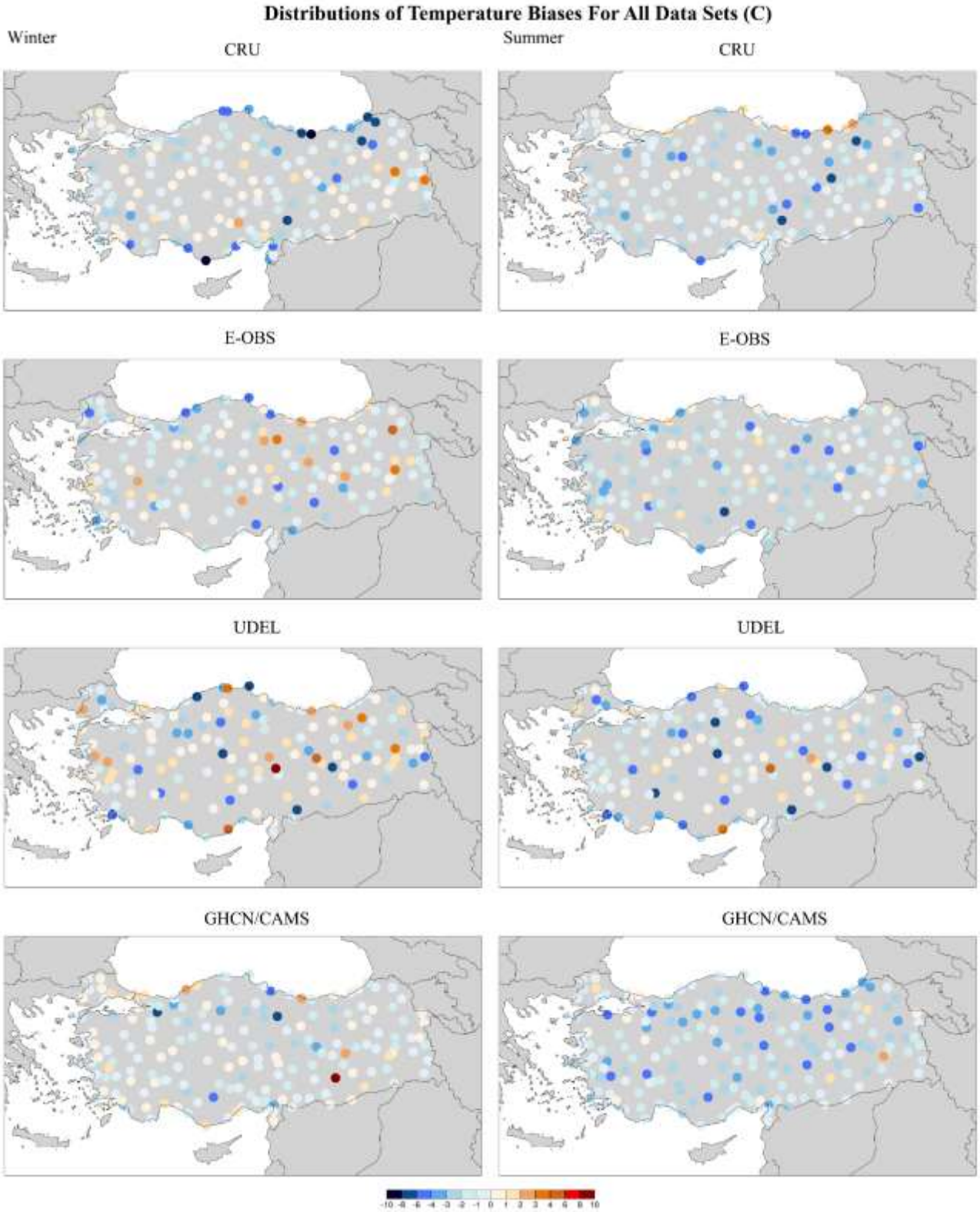

Figure 1. Comparison between stations means and nearest grid means of data sets for temperature

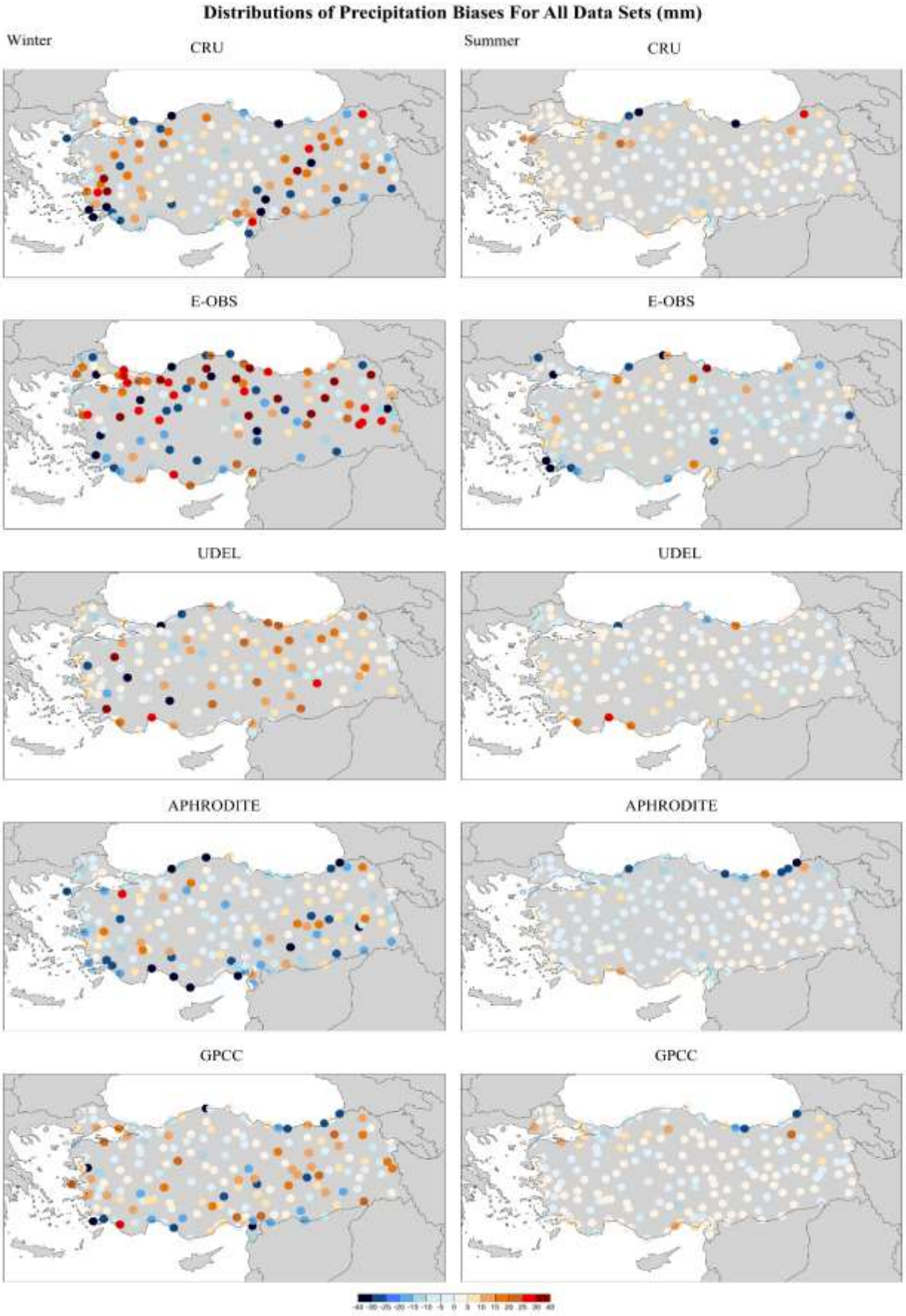

Figure 2. Comparison between stations means and nearest grid means of data sets for precipitation

APPLICATION AND RESULTS

By examining the results, the discrepancies among the data sets are mostly prominent over the coastal and mountainous regions. CRU, GHCN/CAMS, GPCC and APHRODITE represent climatology much better over the coastal regions than E-OBS and UDEL. E-OBS tends to colder and GHCN/CAMS tends to warmer than the other data sets in coastal regions. There are also many differences among the data sets for precipitation. While GPCC indicates more precipitation than the other data sets in coastal regions, UDEL represents positive bias over the Southeast Anatolia region. E-OBS is very dry in eastern parts of Turkey which is most probably associated with the low number of stations used. The biases of the annual temperature averages of CRU, GHCN/CAMS, E-OBS and UDEL data sets are -0.94, -1.12, -1.36 and -1.39 ^{o}C, respectively. All the data sets have cold bias based on station observations. In terms of precipitation biases, GPCC, UDEL, CRU, APHRODITE and E-OBS data sets have +0.27, -2.27, -2.67, -3.7 and -8.24 mm values, respectively. However, the ranking of these data sets changes seasonally. The bias analysis (Figure 1), scatter and Q-Q plots (not shown) for temperature show that CRU, E-OBS and GHCN/CAMS represent the station values reasonably well. We have also calculated the correlation coefficients from the scatter diagrams. For temperature, the correlation coefficients of GHCN/CAMS, E-OBS, CRU and UDEL are in the range of 93-96%, 88-93%, 89-92% and 78-84%, respectively. The precipitation analysis (Figure 2) indicate that GPCC, APHRODITE and UDEL data sets have better representations. The correlation coefficients of GPCC, APHRODITE, UDEL, CRU and E-OBS are in the range of 90-96%, 93-98%, 90-93%, 63-85% and 10-77%, respectively.

CONCLUSION AND RECOMMENDATIONS

In this study, temperature and precipitation data sets based on the observations produced by the different organizations have been compared for Turkey. The climatological analysis reveal that there are many diffences among these data sets. The geographical structures of the region, the interpolation technique used and the number of stations applied for these data products are the major reasons of these diversities. Generally the temperature and precipitation data sets have lower values than the station data. In terms of spatial and temporal variability, all data sets generally reproduced the mean climatology substantially well. It is noteworthy that GHCN/CAMS and GPCC, both data sets are based on satellite data in addition to stations, have better data coverage over Turkey for temperature and precipitation, respectively.

REFERENCES

Fan, Y., & Van den Dool, H. (2008). A global monthly land surface air temperature analysis for 1948–present. *Journal of Geophysical Research: Atmospheres*, *113*(D1).

Harris, I. P. D. J., Jones, P. D., Osborn, T. J., & Lister, D. H. (2014). Updated high-resolution grids of monthly climatic observations–the CRU TS3. 10 Dataset. *International Journal of Climatology*, *34*(3), 623-642.

Haylock, M. R., Hofstra, N., Klein Tank, A. M. G., Klok, E. J., Jones, P. D., & New, M. (2008). A European daily high-resolution gridded data set of surface temperature and precipitation for 1950–2006. *Journal of Geophysical Research: Atmospheres*, *113*(D20).

Matsuura, K., & Willmott, C. J. (2009). Terrestrial air temperature: 1900–2008 gridded monthly time series (version 2.01). *Center for Climatic Research DoG, University of Delaware, editor. Newark, DE, USA*.

Matsuura, K., & Willmott, C. J. (2009). Terrestrial precipitation: 1900–2008 gridded monthly time series. *Center for Climatic Research Department of Geography Center for Climatic Research, University of Delaware*.

Schneider, U., Becker, A., Finger, P., Meyer-Christoffer, A., Ziese, M., & Rudolf, B. (2014). GPCC's new land surface precipitation climatology based on quality-controlled in situ data and its role in quantifying the global water cycle. Theoretical and Applied Climatology, 115(1-2), 15-40.

Tanarhte, M., Hadjinicolaou, P., & Lelieveld, J. (2012). Intercomparison of temperature and precipitation data sets based on observations in the Mediterranean and the Middle East. *Journal of Geophysical Research: Atmospheres*, *117*(D12).

Yatagai, A., Kamiguchi, K., Arakawa, O., Hamada, A., Yasutomi, N., & Kitoh, A. (2012). APHRODITE: Constructing a long-term daily gridded precipitation dataset for Asia based on a dense network of rain gauges. *Bulletin of the American Meteorological Society*, *93*(9), 1401-1415.

PRECIPITABLE WATER VAPOR ESTIMATIONS OF ERZURUM PROVINCE BASED ON GPS DATA

Sacit Özdemir[1], Recep Balbay[2], Bahadır Aktuğ[3], Cahit Yeşilyaprak[4],[5], Derya Öztürk[1], Deniz Çoker[1], Yavuz Güney[6], Funda Yüzlükoğlu[5], Mohammad Shameoni-Niaei[5], Emre Doğan[5]

[1]Ankara University, Faculty of Science, Department of Astronomyand Space Sciences, 06560 Yenimahalle, Ankara, Turkey
Sacit.Ozdemir@ankara.edu.tr
[2]Erciyes University, Faculty of Science, Department of Astronomy and Space Sciences, 38039, Melikgazi, Kayseri, Turkey
rbalbay@gmail.com
[3]Ankara University, Faculty of Engineering, Department of Geophysics, 50. Yıl Campus, 06830 Gölbaşı, Ankara, Turkey
aktug@ankara.edu.tr
[4]Atatürk University, Faculty of Science, Department of Astronomy and Astrophysics, 25030 Yakutiye, Erzurum, Turkey
cahity@atauni.edu.tr
[5]Atatürk University, Astrophysics Research and Application Center, 25240, Yakutiye, Erzurum, Turkey
cahity@atauni.edu.tr
[6]Atatürk University, Faculty of Science, Department of Physics, 25030 Yakutiye, Erzurum, Turkey
yguney@atauni.edu.tr

Abstract

A new 4-meter class of optical and near infrared astronomical observatory is under construction in the Erzurum province of Turkey. The Eastern Anatolia Observatory (DAG) is expected to become operational at the end of 2020. For this kind of astronomical observatory, atmospheric conditions such as percentage of yearly cloud coverage, amount of atmospheric precipitable water vapor (PWV), wind speed and direction, etc., are vital factors in determining the astronomical quality of the site. We present the first results of atmospheric PWV variations in Erzurum through the 2016 – 2017 seasons estimated by GNSS (Global Navigation Satellite System) communication. PWV measurements showed that the site of the observatory, at an elevation of 3170 meters above sea level, has a rather dry atmosphere and is a favorable place for near infrared observations. Comparison of these preliminary PWV estimations with a few other major observatories in the world shows the relative advantages of the site. Furthermore, we expect that the results of atmospheric PWV gathered from such an high location will be helpful for meteorological studies.

Keywords: *Atmospheric precipitable water vapor, astronomical observatory, GNSS*

INTRODUCTION

Studying signal delay in communication of Global Positioning Systems (GPS) is a useful tool to estimate the amount of precipitable water vapor (PWV) in the troposphere. Although the total delay occurs in both ionospheric and neutral layers (troposphere, the stratosphere, and partly mesosphere), ionospheric delay, due to its dispersive nature, can be easily removed by means of processing dual frequency broadcast of GPS satellites. Total signal delay in the neutral and nondispersive atmospheric layers is composed of two components, hydrostatic delay (HD) and wet delay (WD) (Saastamoinen, 1972). Meanwhile, the hydrostatic delay is caused by the dry gases in the atmosphere, i.e., N2, O2, Ar, CO2, CO, CH4, etc., the wet delay is just caused by highly varying water vapor (H2O) in the atmosphere. The hydrostatic delay is responsible for about 90% of the total tropospheric delay and entirely dependent on the atmospheric weather conditions in the troposphere. On the other hand, wet delay (WD) component of radio signals emitted by GPS satellites that takes places in the troposphere layer contains some information about the PWV content of the atmosphere. Since the hydrostatic delay has a nature of smooth and slowly time-varying behavior due to its strong dependence on surface pressure, it can be modeled and made accurate range determinations to obtain precise positions by using surface meteorological conditions such as temperature and pressure. However, the wet delay strongly depends on water vapor content in the troposphere and is highly variable in nature with spatial

position and time. Therefore, it cannot be modeled precisely by surface measurements but is able to be estimated by combining geodetic-quality data from GPS communication and accurate barometric measurements (Bevis et al., 1992, 1994; Rocken et al. 1995). By measuring the total delay, and estimating the hydrostatic delay from theoretical models using surface measurements and then, subtracting it from total signal delay, the remaining wet delay and the total amount of precipitable water vapor (PWV) in the troposphere, can be recovered. This technique is widely used for PWV estimations by, e.g., Moon et al. (1999), Fujita et al. (2008), García-Lorenzo et al. (2009), Okamura and Kimura (2013), Castro-Almazán et al. (2016). Furthermore, an online network of PWV estimations based on GPS data in North America are maintained by the University Corporation for Atmospheric Research (UCAR), at SuomiNet (*http://www.suominet.ucar.edu*).

In this study, on the basis of measuring signal delays in GNSS communication, we present PWV content and its variation in time over Erzurum province. We unveil that the site is rather convenient for near-infrared (NIR) observations when PWV content is compared to other major observatories in the World. Furthermore, we expect that the results of PWV measurements will assist for short term weather forecasting studies.

DATA AND METHODS

The neutral atmosphere, mainly consisted of the troposphere, tropopause and the stratosphere, has a delay effect on GPS signals. This delay including both HD and WD components is mainly caused by the troposphere. Askne and Nordius (1987) first reported the relation between zenith wet delay (ZWD) and precipitable water vapor (PWV), which makes it possible to use GPS communications to estimate the amount of tropospheric PWV. Later, Bevis et al. (1994) introduced a relation between PWV and ZWD:

$$\mathrm{PWV} = \prod \cdot \mathrm{ZWD} \qquad (1)$$

where PWV and ZWD are given in units of length, and $\prod$ is the dimensionless proportionality constant that is given by Bevis et al. (1994):

$$\prod = \frac{10^6}{\rho R_v [\frac{k_3}{T_m} + k_2']} \qquad (2)$$

where ρ is the density of liquid water, Rv is the specific gas constant of water vapor, Tm is the weighted mean temperature of the atmosphere. k_2' and k_3 are the atmospheric refractivity constants given by Bevis et al. (1994). It is shown that the PWV content in the atmosphere strongly correlates with mean temperature, T_m, which is expressed in terms of pressure and temperature by integrating through the altitude as given by Lan et al. (2016).

There are some models for wet delay estimations developed by, e.g., Saastamoinen (1973), Hopfield (1969). After obtaining wet delay component in GNSS communication recorded by the GPS station, we apply a mapping function to perform a conversion between slant wet delay and zenit wet delay (ZWD). Such mapping functions are reported by various authors, Hopfield (1969), Black (1978), Neill (1996). There is another component in the atmosphere, the ionosphere, that also contributes signal delay in GPS broadcasting. However, the ionosphere has a dispersive nature, i.e., the delay depends on the frequency of the signal. Therefore, this delay can be reduced in a millimeter scale or less accuracy by processing signals emitted at two separate *frequencies by the satellites.*

The data analyzed in this study are collected from Erzurum province by means of a GNSS receiver in 2016 and 2017 years. The model of the station that we used is a STONEX S8-plus equipped with a choke ring antenna to avoid multipath effects. The receiver was positioned in two distinct places in the area, Atatürk University Campus with an altitude of 1860 m in between 8 March - 5 October 2016 and, Karakaya Hills with an altitude of 3170 m after 6 October 2016, to gather the data. The data were analyzed by means of GAMIT ver. 9.9 software, a comprehensive GPS analysis package developed at MIT. The software enables to estimate three-dimensional relative positions of ground stations and satellite orbits. During analysis, coordinates of two more IGS stations, Istanbul (ISTA), Kars (KRS1), Nicosia (NICO), Ankara (ANKR), Gebze (TUBI), Zelenchukskaya (ZECK), Sofia (SOFI), Graz (GRAZ) and Erivan (ARUC), were used to better estimate the position of our station. Furthermore, ground meteorological data were taken from convenient ground stations situated near involved places. In addition to GNSS data, ravinsonde observations carried out in Erzurum province two times in a day, at noon and midnight, were gathered from the radio-sounding database of the University of Wyoming to compare our PWV results.

APPLICATION AND RESULTS

The GPS receiver, STONEX S8-plus model, was first assembled in an easily accessible place to perform test observations inside the Atatürk University's Campus, next to ATA50 observatory. In this location, data acquisition was maintained from 8 March 2016 to 5 October 2016, the date on which the system was transported to the summit. The first location (LOC1) has the geographic coordinates of 39^0 54' 16".57 N, 41^0 14' 40".89 E, and an elevation of h=1858 m from sea level. After 5 October 2016, the station was positioned on the summit of Karakaya Hills (LOC2) with an altitude of 3170 m where the observatory is being constructed.

Preliminary results of recorded data were previously presented by Atalay et al. (2016). These data, sampled about 30 minutes of time interval, cover between 1 July and 1 October 2016. PWV values in this interval produced by the GAMIT release 10.61 software are graphically presented in Figure 1. Furthermore, corresponding radiosonde measurements taken in the same interval are also included in the graph to compare PWV results obtained by two different methods. It is shown that PWV values fluctuate between 30 mm and 5 mm and well correlate with ravinsonde data.

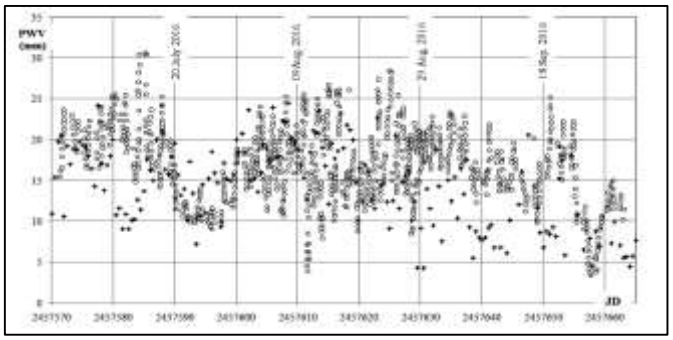

Figure 1. Precipitable water vapour (PWV) estimations in between 1 July and 1 October 2016 obtained from GPS measurements (open circles) (Atalay et al., 2016) and radiosonde integrations (plus signs) are plotted against Julian Day[1].

[1] The Julian Day (JD) is a continuous count of days from 1 January 4713 BC (= -4712 January 1), Greenwich mean noon (= 12h UT)

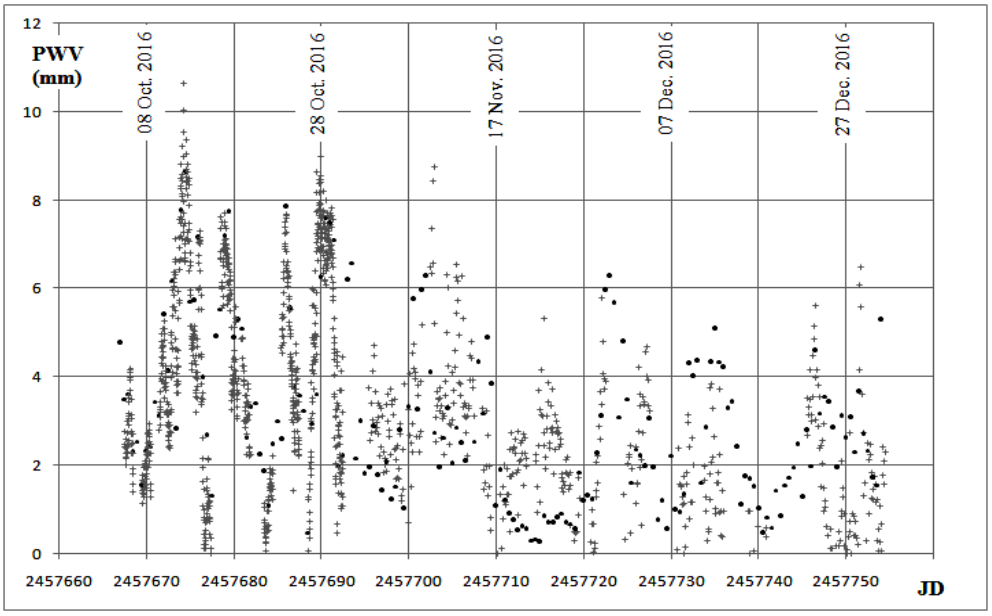

Figure 2. GPS originated PWV values (plus signs) registered in the site of Eastern Anatolia Observatory (LOC2), where the largest astronomical telescope of Turkey will be operated. PWV values from radiosonde measurements (filled circles), shown for comparison, were integrated from the altitude of LOC2 (h= 3170 m) by following expressions given by Boccolari et al[2].

After October 5th, the GPS receiver was moved to the summit of Karakaya Hills and fixed on an observing tower of 7 m tall. The second location (LOC2) with its 3170 m altitude is one of the highest sites on which no GPS receiver is standing around the World. GPS data recorded in LOC2 were also similarly processed by GAMIT software. PWV estimations of the first 19 days in the summit are presented in graphical form in Figure 2 together with measurements of radio-sounding flights launched from Erzurum city center.

CONCLUSIONS AND RECOMMENDATIONS

For astronomical observatories, atmospheric properties such as the yearly percentage of cloud coverage, altitude from sea level, atmospheric seeing, amount of aerosols, tropospheric PWV content, are decisive criteria to choose a site. The Eastern Anatolia Observatory (shortly DAG), which has been fully supported by the Ministry of Development of Turkey, is just rising above its foundations. The observatory will serve in optical and near infrared (NIR) spectral regions by its 4 m class, Turkey's largest telescope. Due to being main absorber component of the atmosphere in NIR regions and fast changing nature, we study the amount of atmospheric PWV content and its seasonal variation over Erzurum province on the basis of GPS communication technique.

Average value of PWV values deduced from GPS data during 2016 summer season covering 1 July - 1 October interval is 17.2±4.6 mm (Atalay et al. 2016). Meanwhile, for the same interval, PWV results based on radiosonde records produces an average value of 14.2±4.9 mm. It is seen that, towards the beginning of autumn, tropospheric PWV content starts to decrease as the result of decreasing average temperature (Tm) (see Figure 1). This decreasing trend continues in a similar way after carrying the receiver to the summit (LOC2) (see Figure 2). PWV results from GPS obtained at LOC2 in October 2016 produce an average value of 4.2±2.3 mm whereas

[1] The Julian Day (JD) is a continuous count of days from 1 January 4713 BC (= -4712 January 1), Greenwich mean noon (= 12h UT)

[2] http://www.map.meteoswiss.ch/map-doc/NL15/boccolari_II.pdf

radiosonde PWV's records integrated from the altitude of the city (h= 1860 m) generate 8.1±2.9 mm for the same time interval. We suppose that this difference comes from higher elevation of LOC2. The results are summarized in Table 1.

Table 1. Comparison of tropospheric PWV measurements obtained from two different techniques in Erzurum province.

Date interval	01.07 - 01.10.2016		06.10 - 31.10.2016	
Location and coordinate	GPS receiver* LOC1 $39^0$54'16".57N, $41^0$14'40".89E, h= 1858 m	Radiosonde measurement** $39^0$54'21".00N, $41^0$15'18".32E, h= 1870 m	**GPS receiver* LOC2 $39^0$46'48".9N, $41^0$13'37".21E h= 3170 m**	Radiosonde measurement** $39^0$54'21".00N, $41^0$15'18".32E, h= 1870 m
<PWV> (mm)	17.2±4.6	14.2±4.9	**4.2±2.3**	8.1±2.9
Max. value (mm)	30.6	24.5	**10.6**	13.3
Min. value (mm)	3.9	4.3	**0.0**	3.0

** STONEX S8-plus model equipped with a choke ring antenna (IGS code: HX-CG77601A)*
*** PWV integration were started to integrate from the altitude of Erzurum city, i.e., h= 1860 m.*

Chacon et al. (2011) reports PWV measurements depending on radiosonde observations performed in four distinct campains at the La Silla, APEX (Atacama Pathfinder Experiment) and Paranal observatory sites in Chile. In another study, Pozo et al. (2011) presents PWV measurements of ALMA observatory, which is the highest ground based observatory located in the Chajnantor plateau at 5104 m above sea level. They used a radiometer located in the APEX site to obtain PWV estimations during April – December 2007 interval. In both study, the PWV measurements were compared with theoretical PWV estimations performed by means of the WRF (Weather Research and Forecasting) atmospheric model. They report that WRF results overestimates PWV values than those of observations. Our PWV measurements performed in Erzurum based on GPS and radisonde techniques are given in Table.2 for comparison.

Table 2. A comparison of mean PWV values for the DAG observatory site (h= 3170 m) with those of other observatories in the world. Corresponding time intervals of averaged PWVs are given in 3rd column. Notice that all PWV calculations based on radiosonde flights were integrated from the altitude of the DAG observatory site, i.e., ~3170 m.

Observatory Site	<PWV> (mm)	Time interval of measurements	Reference
La Silla (2400 m)	8.8	5 – 15 May 2009	Chacon et al. (2011)
DAG – Radiosonde	4.4	5 – 15 May 2009	This work
DAG – GPS	4.8	30 Apr – 30 May 2017	This work
APEX (5100 m)	2.0	7 – 16 July 2009	Chacon et al. (2011)
DAG – Radiosonde	6.3	7 – 16 July 2009	This work
APEX (5100 m)	1.3	5 Apr. – 31 Dec. 2007	Pozo et al. (2011)
DAG – Radiosonde	5.3	5 Apr. – 31 Dec. 2016	This work
Paranal (2635 m)	4.2	9 – 19 Nov. 2009	Chacon et al. (2011)
DAG – Radiosonde	4.3	9 – 19 Nov. 2009	This work
DAG – GPS	4.7	9 – 19 Nov. 2016	This work
Paranal (2635 m)	3.3	29 July – 10 Aug. 2009	Chacon et al. (2011)
DAG – Radiosonde	7.2	29 July – 10 Aug. 2009	This work
DAG – GPS	2.8	25 Oct. 2016 – 01 Jan. 2017	This work

It should be also noticed that the time resolution of radiosonde observations is 12 hours a day meanwhile GPS based PWV observations have 30 minutes or 2 hours of sampling intervals. Additionally, we expect that PWV values obtained from an elevation of 3170 m may lead to help to predict short term weather forecasts for meteorological sciences.

Acknowledgements: This study was supported by TUBITAK, The Scientific and Technological Council of Turkey, under the contract number of 115F032. The Eastern Anatolia Observatory, DAG, is fully funded by the Ministry of Development of Turkey (Project ID : 2011K120230).

REFERENCES

Askne, J., and Nordius, H., 1987, Radio Sci. 22(3), 379
Atalay, B., Aktuğ, B., Gürbüz, G., Öztürk, D., Yeşilyaprak, C., Çoker, D., Özdemir, S., Yüzlükoğlu, F., 2016, Proceedings of 20th National Astronomy Meeting, 5-9 September 2016, Atatürk University, Erzurum, Turkey
Bevis, M., Businger, S., Herring, T.A., Rocken, C., Anthes, R.A., and Ware, R.H., 1992, Journal of Geophysical Research, 97, No. D14, 15787
Bevis, M., Businger, S., Chiswell, S, Herring, T.A., Anthes, R.A., Rocken, C., et al., 1994, Journal of Appl. Meteorol. 33 (3), 379
Black, H.D., 1978, Journal of Geophysical Research 83 (B4), 1825
Castro-Almazán, J.A., Muñoz-Tuñón, C., García-Lorenzo, B., et al., 2016, Proceedings of the SPIE 99100P
Chacon, A., Cuevas, O., Pozo, D., Marin, J., et al., 2011, Rev. Mex. A. A. (Serie de Conferencias), 41, 20
Fujita, M., Kimura, F., Yoneyama, K., Yoshizaki, M., 2008, Geophysical Research Letters 35 (13), CiteID L13803
García-Lorenzo, B., Castro-Almazán, J. A., Eff-Darwich, A., et al., 2009, Proceedings of the SPIE 74751H
Hopfield, H.S., 1969, Journal of Geophysical Research 74 (18), 4487
Lan, Z., Zhang, B., Geng, Y., 2016, Geodesy and Geodynamics 7 (2), 101
Moon, Y.-J., Choi, K.-H., Park, P.-H., 1999, Journal of Astronomy and Space Sciences 16 (1), 61
Neill, A.E., 1996, Journal of Geophysical Research 111 (B2), 3227
Okamura, O., and Kimura, F., 2003, Geophysical Research Letters 30 (14), ASC 5-1
Pozo, D., Illanes, L., Caneo, M., and M. Cure, M., Rev. Mex. A.A. (Serie de Conferencias), 41, 55
Rocken, C., Hove, T. V., Johnson, J., Solheim, F., Ware, R., Bevis, M., Chiswell, S., and Businger, S. 1995, Journal of Atmos. Ocean. Technol. 12, 468
Saastamoinen, J., 1972, Geophysical monograph, 15, American Geophysical Union, Washington, D.C., 247
Saastamoinen, J., 1973, Bulletin of Geodesique 105, 279.

DROUGHT FORECASTING USING GENETIC PROGRAMMING IN ASSOCIATION WITH SOUTHERN OSCILLATION INDICES

Buğrayhan BİÇKİCİ ARIKAN[1], Ercan KAHYA[2]
[1]Istanbul Technical University, Hydraulics and Water Resources Department,
Istanbul Medeniyet University, Department of Civil Engineering, Istanbul/TURKEY
bugrayhan.bickici@medeniyet.edu.tr
[2]Istanbul Technical University, Department of Civil Engineering, Istanbul/TURKEY
kahyae@itu.edu.tr

Abstract
Drought ranks top in the list concerning the characteristics and impact ratings of natural disasters that are effective in the world. Reducing the adverse effects of drought is possible through (i) prediction of drought, (ii) mitigating measures prior to drought event, and (iii) rationale actions when droughts are experienced. In this study, we used genetic programming model to forecast drought conditions during the period 1970 to 2014 in the Nigde station in eastern Konya closed basin at 3-and 6-month lead times. The Southern Oscillation indices and historical Palmer Drought Severity Index (PDSI) series were selected as predictors in order to predict future PDSI. Our results obtained from Linear Genetic Programming revealed reasonable estimates for the 3- and 6-month lead-time drought series for Southern atmospheric oscillation.

Keywords: *PDSI, Nigde, drought forecasting, southern oscillation, genetic programming*

INTRODUCTION
Drought is defined as a natural event that causes the land and water resources to be adversely affected and the hydrological balance to deteriorate due to the fact that the recorded normal levels of precipitation fall significantly below. Drought is at the top of the evaluation according to the characteristic features and impact ratings of natural disasters that are effective in the world. For this reason, drought forecasting is of great importance in terms of drought risk management. Due to water scarcity which has frequently occurred in the world in recent years, the prospect of predicting drought is increasing. Drought forecasting in engineering applications is an important knowledge, which is needed to be prepared against the drought and to minimize the negative effects of drought. In recent years, many drought forecasting models have been developed and extensive reviews have been made on different drought forecasting approaches (e.g., Rao and Padmanabhan, 1984; Bogradi et al., 1994; Lohani and Loganathan, 1997; Cancelliere et al., 2007; Modarres, 2007; Fernandez et al., 2009; Danandeh Mehr et al., 2014a; Uyumaz et al., 2014). In addition Mishra and Desai (2005), Mishra and Singh (2011), Kim and Valdes (2003) and Morid et al. (2007) have provided an excellent overview of research on drought forecasting.

It has been increasing interest to study the relation between North Atlantic Oscillation (NAO) and drought in mid-latitude regions; among others, Kahya (2011) and Şarlak et al. (2009) documented such relations for the Eastern Mediterranean and southern part of Turkey. Kalaycı et al (2004) were examined the influences of somewhat quasi– periodic El Nino occurrences on streamflow and precipitation patterns in Turkey using the spectral analysis. Karabörk and Kahya (2009) documented the linkage between hydrologic and climate variables in Turkey and Southern Oscillation (SO). Following this trend, we intended to analyze the influences of Southern Oscillation (SO) on the estimation of drought is analyzed in this study. We have thus considered 3- and 6-month lead times performing drought forecasting model in Nigde Station in Konya Closed Basin using the linear genetic programming (LGP) technique.

DATA AND METHODS

Drought events are sometimes connected to atmospheric oscillations. In this study SO index (SOI) was examined for its contributions to drought forecasting. SOI is a standardized index based on the observed sea level pressure differences between Tahiti and Darwin, Australia. The SOI is one measure of the large-scale fluctuations in air pressure occurring between the western and eastern tropical Pacific (i.e., the state of the Southern Oscillation) during El Niño and La Niña episodes.

Over a region or an area, many drought indices have been developed for monitoring and examining of meteorological drought. From these indices, the Palmer Drought Severity Index (PDSI) is widely used. PDSI is a meteorological drought index, which provides a standardized measurement of moisture conditions to compare between locations and over time (Palmer, 1965). For these reasons, PDSI was used as a drought indicator in this study. Table 1 provides a drought classification based on PDSI.

Table 1. The values for Palmer Classifications (Palmer, 1965)

Palmer Classifications	
Palmer Values	**Possibilities**
4.0 or more	Extremely wet
3.0 to 3.99	Very wet
2.0 to 2.99	Moderately wet
1.0 to 1.99	Slightly wet
0.5 to 0.99	Incipient wet spell
0.49 to -0.49	Near normal
-0.5 to -0.99	Incipient dry spell
-1.0 to -1.99	Mild drought
-2.0 to -2.99	Moderate drought
-3.0 to -3.99	Severe drought
-4.0 or less	Extreme drought

Generally, if PDSI values are positive, wet periods will be indicated and if they are negative, they will illustrate dry periods. Monthly PDSI data for Nigde station in Konya Closed Basin from 1970 to 2016 used in this study was obtained from the Turkish State Meteorological Service. Coordinate informations of Nigde Station showed Table 2.

Table 2. Coordinate Informations of Nigde Station

Station Number	**Station**	**Coordinates**		**Elevation(m)**
		Latitude	**Longitude**	
17250	Niğde	37,58	34,41	1211

The PDSI time series employed in current study is values of Nigde Station in Central Anatolia Region, Turkey (namely station 17250).The monthly time series of SOI (1970-2016) and persistence in PDSI values (1970-2016) were used as original drought predictor variables in this study. Future PDSI values were considered as target variable (predictand) of the model.

Linear Genetic Programming (LGP)

The nature inspired soft computing technique of Genetic Programming (GP) evolves the best individual (program) through combination of cross-over, mutation and reproduction processes.

It works on the Darwinian principle of 'survival of the fittest' (Koza 1992). The steps generally followed in GP are:

1. Creation of an Initial Population of Individuals (i.e. programs or equations).
2. Evaluation of Fitness of Individuals.
3. Selection of the fittest Individuals as Parents.
4. Creation of new Individuals (also called the Children or Off-spring) through the genetic operations of cross over, mutation and reproduction (copy)
5. Replacing the weaker parents in the population by the stronger ones.
6. Repetition of steps 2 through 5 until the user defined termination criterion is satisfied.

The termination criterion can be completion of a specified number of generations or fitness criterion such as minimum error reached.

GP simultaneously works on a group of possible solutions instead of a single solution. This group of candidate solution is called a "population". The GP tries to find the best solution. Since the original function is unknown, GP searches for an approximate hence, an "acceptable" solution. GP is an extension to genetic algorithms where individuals are programs or functions (Karabulut et al. 2008).

In this study, different mathematical functions including basic arithmetic (+,-,x,/), absolute value, square root, trigonometric (sine, cosine) functions were utilized in modeling function sets. SO indices and PDSI values are also defined as our terminal set. The mean square error (MSE) fitness function is used to rank the randomly generated initial programs and then new programs are evolved by using both by using both mutation and crossover operators. As it given Table 3, in order to avoidance overfitting problem, the maximum size of the program and maximum number of generations was limited to 512 byte and 1000 generations, respectively (Danandeh Mehr, et al. 2014b). Further information concerning these parameters can be found at Francone (2010). We applied Discipulus, the LGP software package developed by Francone (2010), to establish our LGP models.

Table 3. Parameter settings for the LGP system

Parameter	**Value**
Initial populations (programs)	500
Mutation frequency	95%
Crossover frequency	50%
Initial program size	80 (Byte)
Maximum program size	512 (Byte)
Generation without improvement	300
Generation since start	1000

APPLICATION AND RESULTS

The monthly PDSI data from Nigde station in the Konya Closed Basin was obtained from Turkish State Meteorological Service. The monthly time series of SOI (1970-2016) and persistence in PDSI values (1970-2016) were used as original drought predictor variables in this study. Future PDSI values were considered as target variable (predictand) of the model. In this study, we have considered 3- and 6-month lead times performing drought forecasting model. Some possible structures for short LT drought forecasting in Nigde Station as follows:

3-Month LT: $PDSI_{t+3} = f(\mathbf{SOI}_t, PDSI_t, PDSI_{t-1}, PDSI_{t-12})$
6-Month LT: $PDSI_{t+6} = f(\mathbf{SOI}_t, PDSI_t, PDSI_{t-1}, PDSI_{t-2}, PDSI_{t-12})$

For each of these structures, we applied the LGP modelling. Monthly observation data (the PDSI and SOI series during the period 1970-2016) was divided into two parts. 70% of the entire data set was employed for the training period and the remaining part was used to test the validity of the model.

The PDSI time series employed in current study is values of Nigde Station in the Konya Closed Basin, Turkey (namely station 17250). Fig.1 shows the observed and forecasted PDSI series for 3- and 6- months LT in Nigde Station (for using southern oscillation index values scenarios). The figures illustrates that LGP reasonably forecasts the general behavior of the observed data.

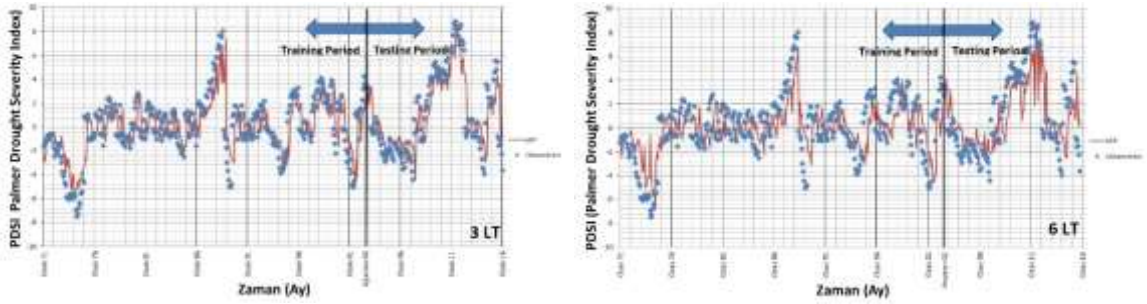

Figure 1. Results of 3- and 6- months LT LGP drought forecasting model in Nigde Station

The coefficient of determination (R^2) and the mean square error (MSE) measures, which widely used in the hydrological forecasting studies, were applied to measure the efficiency, goodness of fit, of the proposed forecasting model in this study. Obviously, a high value for R^2 (up to 1) and small values for MSE indicate high efficiency of the model. The obtained efficiency results of the LGP model for drought forecasting in the Nigde station with 3- and 6- month LT are summarized in Table 4.

Table 4. Skill scores of 3- and 6- months LT scenarios employed for LGP model in Nigde Station

Prediction Scenario	**Mean Squared Error (MSE)**		**R-Squared (R^2)**	
	Train	**Test**	**Train**	**Test**
3-month LT	2,993	3,4112	0,5594	0,7086
6-month LT	4,1123	5,8468	0,399	0,5026

Table 4 indicates that the LGP produce sufficient accuracy for drought forecasting in 3- and 6-months scenarios.

CONCLUSIONS AND RECOMMENDATIONS

Drought monitoring and forecasting are essential tools for implementing appropriate mitigation measures in order to reduce negative impacts of drought. Drought forecasting remains a difficult but vitally important task for hydro-meteorologists and water resources managers. In current study, the LGP model for short term and mid term LT drought forecasting using PDSI and southern oscillation indices (SOI) values as predictors and forthcoming PDSI index as a predictand. This study investigated the ability of data driven models to forecast drought. This study also proposed and evaluated, the use of the genetic programming for short and mid-term drought forecasting.

ACKNOWLEDGEMENTS

This research was supported by TUBITAK-2211C (Scientific and Technological Research Council of Turkey). We would like to thank TÜBİTAK for its support. The authors also acknowledge MGM (Turkish State Meteorological Service) authorities for providing data.

REFERENCES

Bogradi, I., Matyasovsky, I., Bardossy, A., Duckstein, L. (1994). A hydroclimotological model of arial drought. *J. Hydrol.* 153, 245–264.

Cancelliere, A., Mauro, G.D., Bonaccorso, B., Rossi, G. (2007). Drought forecasting using the standardized precipitation index. *Water Resour. Manage.* 21, 801–819.

Danandehmehr A., E. Kahya and M. Özger, (2014a). A gene-wavelet model for long lead-time drought forecasting. *Journal of Hydrology,* Vol. 517, 691–699, DOI: 10.1016/j.jhydrol.2014.06.012.

Danandehmehr, A., E. Kahya and C. Yerdelen, (2014b). Linear genetic programming application for monthly streamflow prediction. *Computers & Geosciences,* Vol. 70, 63–72, DOI: 10.1016/j.cageo.2014.04.015.

Fernandez, C., Vega, J.A., Fonturbel, T., Jimenez, E. (2009). Streamflow drought time series forecasting: a case study in a small watershed in North West Spain. *Stoch. Environ. Res. Risk Assess*. 23, 1063–1070.

Francone, F.D. (2010). DiscipulusTM with Notitia and solution analytics owner's manual. *Register Machine Learning Technologies Inc*., Littleton, CO, USA.

Kahya, E. (2011). The Impacts of NAO on the Hydrology of the Eastern Mediterranean. *In Hydrological, Socioeconomic and Ecological Impacts of the North Atlantic Oscillation in the Mediterranean Region* (pp. 57-71). Springer Netherlands.

Kalaycı, S., M.Ç. Karabörk and E. Kahya, 2004: Analysis of El Nino Signals on Turkish Streamflow and Precipitation Patterns Using Spectral Analysis. *Fresenius Environmental Bulletin*, Vol. 13, No 8, 719-725.

Karabörk, M. Ç. and E. Kahya, (2009) The Links between the Categorized Southern Oscillation Indicators and Climate and Hydrologic Variables in Turkey. *Hydrological Processes,* Vol. 23, No 13, 1927-1936, DOI: 10.1002/hyp.7331.

Karabulut K., Alkan A., Yılmaz A.S. (2008). Long term energy consumption forecasting using genetic programming. Mathematical and Computational Applications, Vol. 13. No:2. 71-80.

Kim, T.W., Valdes, J.B. (2003). Nonlinear model for drought forecasting based on a conjunction of wavelet transforms and neural networks. *J. Hydrol. Eng.* 8 (6), 319–328.

Koza, J.R. (1992). Genetic programming: on the programming of computers by means of natural selection. *MIT Press*, Cambridge, MA, USA.

Lohani, V.K., Loganathan, G.V. (1997). An early warning system for drought management using the Palmer drought index. *J. Am. Water Res. Assoc*. 33 (6), 1375–1386.

Mishra, A.K., Desai, V.R. (2005). Drought forecasting using stochastic models. *J. Stoch. Environ. Res. Risk Assess.* 19, 326–339.

Mishra, A.K., Singh, V.P. (2011). Drought modelling – a review. *J. Hydrol*. 403, 157–175.

Modarres, R. (2007). Streamflow drought time series forecasting. *Stoch. Environ. Res. Risk Assess*. 15 (21), 223–233.

Morid, S., Smakhtin, V., Bagherzadeh, K. (2007). Drought forecasting using artificial neural networks and time series of drought indices. *Int. J. Climatol*. 27 (15), 2103–2111.

Palmer, W. C. (1965). Meteorological drought, Weather Bureau Research Paper No.45, US Department of Commerce. Washington, DC. (Vol. 30).

Rao, A.R., Padmanabhan, G. (1984). Analysis and modeling of palmer's drought index series. *J. Hydrol*. 68, 211–229.

Şarlak, N., E. Kahya and A.O. Bég, (2009): Critical Drought Analysis: A Case Study of Göksu River (Turkey) and North Atlantic Oscillation Influences. Journal of Hydrologic Engineering, Vol. 14, No 8, 795-802, DOI:10.1061/(ASCE)HE.1943-5584.0000052.

Uyumaz, A., A. Danandehmehr, E. Kahya and H. Erdem, (2014). Rectangular side weirs discharge coefficient estimation in circular channels using linear genetic programming approach. Vol. 16, No. 6, 1318-1330, *Journal of Hydroinformatics,* doi:10.2166/hydro.2014.112.

ASSESSING BIAS SOURCES IN WEATHER RADAR RAINFALL ESTIMATES DURING MESOSCALE CONVECTIVE EVENTS

Kurtuluş Öztürk[(1)] and Alper Çubuk [(2)]
[1] *Turkish State Meteorological Service*
kozturk@mgm.gov.tr
[2] *Turkish State Meteorological Service*
acubuk@mgm.gov.tr

Abstract
Weather radars are known as the best instruments to estimate quantitative rainfall, but they are not perfect. They suffer from many kind of bias sources and small scale variabiliy of rainfall especially during concevtive events. This causes remarkable difference between ground observations and radar rainfall estimates. In this study, Marshall-Palmer relationship (MP) and polarimetric estimator R(K_{DP}) are compared with reliable ground observations during three different mesoscale convective storms occured in September 2015 and 2016 within the İzmir radar area. In order to have reliable ground observations, Turkish State Meteorological Service (TSMS) has installed triple rain gauges at 50 different sites. Assessment Factors (AF) which is the ratio of total radar rainfall to gauge rainfall are compared for three events. While weather radars mostly underestimate rain, positive bias is obtained at some sites. This study investigates the possible reasons for posivitive and negative biases and suggests that it is very difficult to apply a real-time statistical rainfall improvement technique during such mesoscale convective events due to the small scale of variability of rainfall and other bias sources such as bright band and beam shielding.

Keywords**:** *Weather Radar, Rain Gauge, Z-R Relationship, Assessment Factor, Bright Band, Beam Shielding*

INTRODUCTION

Weather radars estimate rainfall rate employing empirical reflectivity-rainfall rate (Z-R) relationships or polarimetric relationships/algorithms. However, due to some bias sources such as hardware and software related problems, beam geometry and shielding, environment or atmospheric conditions and small scale variability of rainfall, rainfall estimates may vary from ground observations. On the other hand, reliable ground observation is still one of the most challenging questions for radar QPE studies. In this study, the radar rainfall rate calculated by Marshall-Palmer relationship (MP) and polarimetric estimator R(K_{DP}) are compared with reliable ground observations during three different mesoscale convective storms occurred in September 2015 and 2016 in the İzmir radar coverage area. Dense rain gauge networks that are operated in field campaigns help to determine the variability of rainfall within the scale of a radar pixel and satellite footprint (Tokay and Ozturk 2012). In order to have reliable ground observations, Turkish State Meteorological Service (TSMS) has been collecting rainfall observations from 50 sites containing triple collocated rain gauges since 2014. As the 5-minute rain total is considered to be shortest reliable gauge rainfall (Habib and Krajewski 2002), total rainfall ranging from 5-minute to 1-day is calculated even if only one gauge reported rainfall.

DATA AND METHODS

There are 11 among 50 sites having triple collocated gauges employed in the area, the radius of which is 120 km with the İzmir radar location as being the center (See Figure 1). During three-year observational period, the number of rainy samples between 22876 and 31228 were received at 1-minute integration. Nine different statistics are computed for the rain gauge pairs of three collocated gauges and the comparison of correlation for different rain accumulations is

given in Figure 1. The scatter diagrams of gauge pairs (1-2, 1-3, 2-3) are also given for all sites and some selected diagrams are given in Figure 2. Assessment Factor (AF), which is the ratio of 24-hour total radar rainfall to gauge rainfall, is needed as stable as possible for successful improvement of the accuracy of radar rainfall estimates by means of statistical gauge adjustment techniques. The graphs of AF-C (the radar pixel where a rain gauge station located), AF-M (mean value of 25 pixels -center pixel and neighboring 24 pixels-) and AF-N (the nearest value to gauge observation among 25 pixels) are given in Figure 3 for 3 convective storm cases to investigate the stability of AF for different cases. PBB (Partial Beam Blockage) diagrams and beam blockage fractions are derived for all rain gauge sites by using 30m resolution digital elevation database and the diagram of Yenipazar is given in Figure 4a as an example. Figure 4b is the Vaisala Hydroclass product showing bright band over some sites.

APPLICATION AND RESULTS

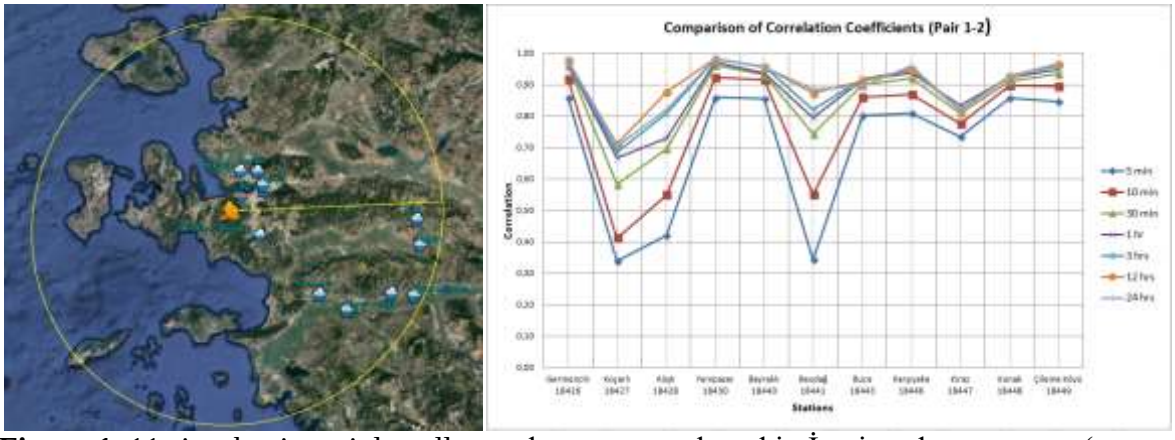

Figure 1. 11 sites having triple collocated gauges employed in İzmir radar coverage (range: 120 km) and the comparison of correlation coefficient for different rain accumulations (Pair: 1-2)

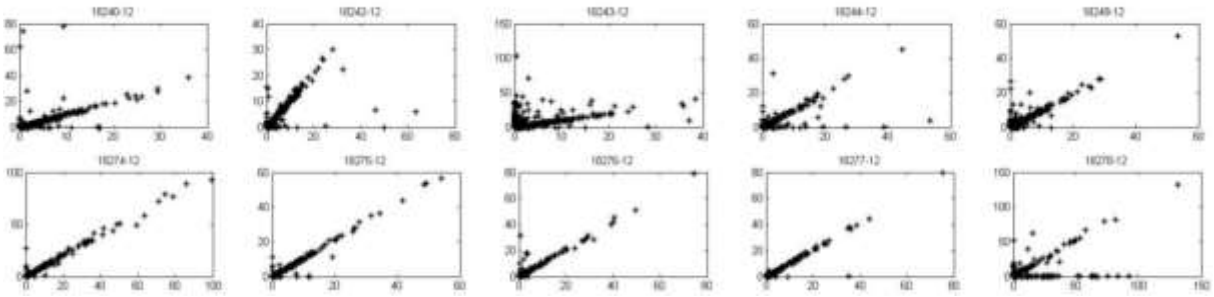

Figure 2. Scattering diagrams of some collocated gage pairs (1-2)

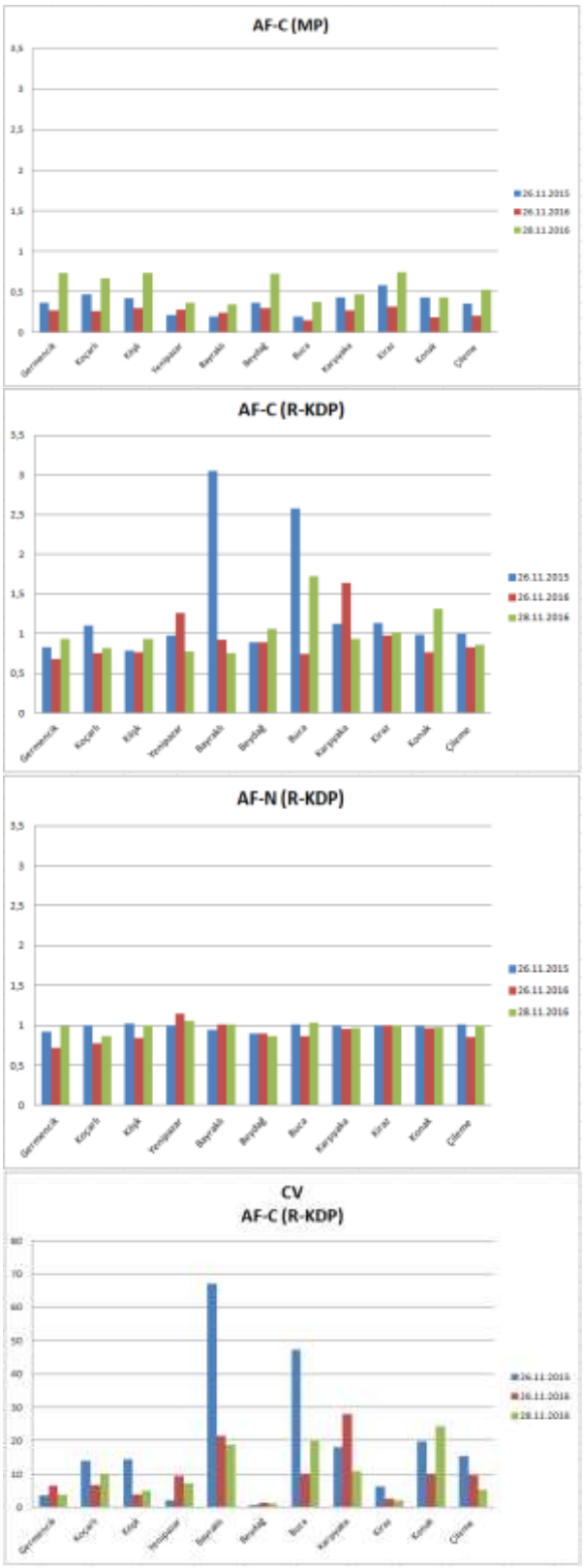

Figure 3. The comparison of Assessment Factors of 3 convective events and coefficient of variation

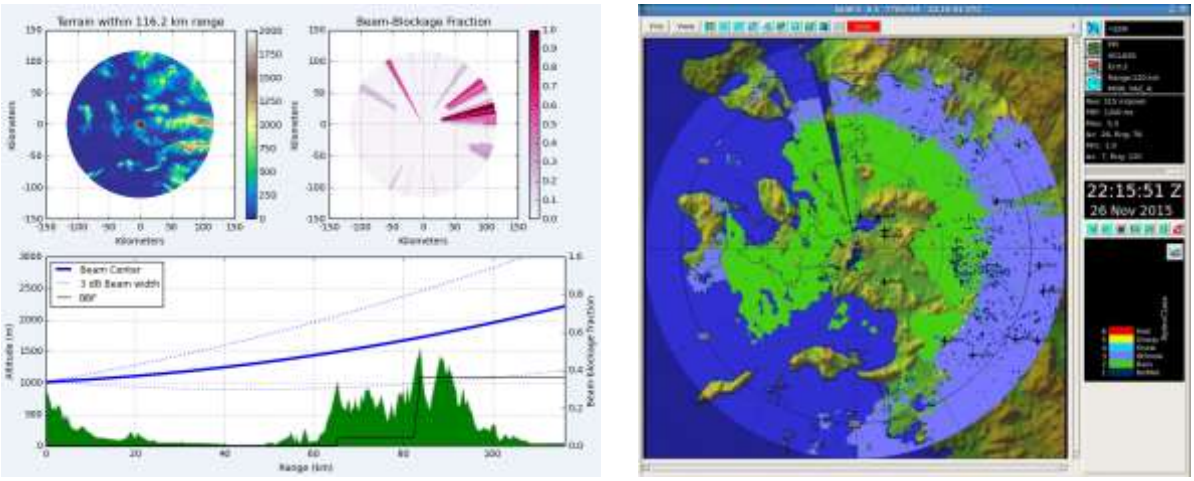

(a) (b)

Figure 4. a) Partial beam blockage diagram and information for Yenipazar , b) Vaisala Hydroclass product

CONCLUSIONS AND RECOMMENDATIONS

The correlation coefficient between gauge pairs (1-2, 1-3, 2-3) varies from 0.34 to 0.63 for 5-minute accumulation and from 0.75 to 0.81 for 1-hour accumulation of Beydağ site, for instance. By the help of the statistics, inaccurate observations are easily removed from data set and reliable gap-free data set is obtained. The best AF is calculated from $R(K_{DP})$ while MP significantly underestimates rain at all sites during all 3 cases. Despite the fact that $R(K_{DP})$ gives mostly negative biases, there are significant positive biases at 4 sites (Bayraklı, Buca, Karşıyaka, Konak). High standard deviation (SD) and high coefficient of variation (CV) of 25 radar pixels (radar pixel where a rain gauge station located and its 24 neighboring pixels) indicate that the positive bias is due to the small scale variability of rainfall during convective storms (25 pixels represent approximately 2.77 km^2). On the other hand, 30% of first radar beam between İzmir radar and Yenipazar site is blocked by the hilly areas (first elevation angle of radar scan: 0.2 degree), however, $R(K_{DP})$ estimator still results positive bias. It clearly explains that $R(K_{DP})$ is immune to PBB. On the contrary, MP significiantly underestimates rain at Yenipazar since MP is affected by PBB. MP estimates are corrected by bright band correction algorithm of Vaisala IRIS software by means of sounding observations to mitigate the effect of bright band. However, $R(K_{DP})$ is affected by bright band. Sounding observations, radar dual polarization products and Vaisala Hydroclass algorithm shows that the bright band over the region including Yenipazar, Koçarlı, Beydağ and Kiraz is possibly the reason for some slight overestimations. While AF-N is quite stable and close to 1 for all three cases, AF-C and AF-M fluctuate. This study depicts that it is very difficult to apply a real-time statistical rainfall improvement technique during such mesoscale convective events due to the small scale of variability of rainfall and other bias sources such as bright band and partial beam blockage. Despite all the bias sources, $R(K_{DP})$ estimator works quite well in 2.77 km^2 (~1.66 x 1.67 km) which is a quite good resolution compared to other QPEs.

REFERENCES

Habib, E., and Krajewski, W. F., 2002: Uncertainty analysis of the TRMM ground-validation radar-rainfall products: Application to the TEFLUN-B field campaign.J.Appl.Meteor.,41, 558–572.

Tokay, A., and Ozturk, K., 2012: An experimental study of the small-scale variability of rainfall. J. Hydrometeor., 13, 351–365.

THE COLD SPELLS OF 2016/2017 OVER TURKEY – IN ASSOCIATION WITH ATMOSPHERIC BLOCKING

Meral Demirtaş[1]
[1]*University of Ondokuz Mayıs, Department of Meteorological Eng.*
mdemirtas@omu.edu.tr

Abstract
During the December-January-February (DJF) 2016/2017, Turkey experienced contiguous cold temperatures. This study investigated the connection between the cold temperatures and atmospheric blocking, using a recently developed cold wave detection method and a two-dimensional atmospheric blocking detection method. The cold wave detection method provided an objective analysis of the cold waves of DJF-2016/2017 throughout different regions of Turkey which otherwise would have required the use of spatially varying temperature threshold due to the variation in topography and micro-climatic features across the country. The atmospheric blocking detection method has emerged as a valuable tool for representing the phenomenon. The spatial distribution of the composite anomalies of surface temperature showed that temperature anomalies (up to −8 degC) were pronounced over north-west part of Turkey. The spatial distribution of the composite anomalies of 500 hPa geopotential height field implied that the Azores anticyclone was displaced northwards. An analysis of the total number of cold wave days showed that the north west of Turkey was under wintry conditions for about 16-27 days, and the eastern part of Turkey was under such conditions for about 20-35 days. 3-5 cold wave events took place over the western part of Turkey and there were 5-6 cold waves over the eastern Turkey. Atmospheric blocking conditions persisted over the eastern Atlantic for about three weeks. The link between cold waves and atmospheric blocking is important both for weather and the investigation of temperature extremes in the frame work of climate. Results from this analysis indicate that the atmospheric blocking was likely to be responsible for maintaining the cold wintry conditions. The results may also contribute to a better understanding of cold waves in context of climate variability.

***Keywords*:** *Cold waves, atmospheric blocking, high impact weather, climate variability, Turkey*

INTRODUCTION
Addressing cold temperatures of the south Eastern European winter 2016/2017 may sound strange in the context of global warming. But, as the European winter of 2009/2010 (Cattiaux *et al.,* 2010) has shown, global warming does not eliminate the occurrence of cold waves and snowstorms in the Northern mid-latitudes. Several cold spells have happened during the 20th century such as; February 1929 and 1956, January-February 1963, the mid-1980s, the December-January of 2009/2010, and the January-February 2012 (WMO, 2013; Cattiaux *et al.,* 2010; Demirtaş, 2017). Cold extremes may lead to high impact weather and they may pose a big challenge to societies and ecosystems, as they are rather difficult to deal with than changes in the temperature of a place.

Climate change may lead to intense responses in regional temperature variability, particularly in extreme weather and climate events (*e.g.,* heat-waves and cold waves). These types of events may pave a way for the high impacts on societies and ecosystems. Thus, it is essential to examine their triggering mechanisms and evolution under a warmer climate as foreseen by the climate projection scenarios for the twenty first century, including the associated underlying uncertainties (Cattiaux *et al.,* 2013).

The period of DJF 2016/2017 was notable for a series of cold spells and snow accumulation in various parts of Europe. The north-eastern central and south-eastern part of Europe was hit by a cold spell resulting in temperatures below 40°C in Sweden and Finland, and temperatures below 30°C on the various parts of Europe. Cold air together with a strong moisture flux from the Black Sea led to heavy snowfall over parts of south-eastern Europe (*e.g.* Italy, Poland, Romania, Bulgaria, Bosnia, Greece and Turkey). Snow on the Balkans was widespread and abundant; snow covers of 50-100 cm were reported in many places and above 100 cm in mountain regions.

Previous studies have shown that European temperature extremes occur in connection with specific atmospheric circulation patterns (Bieli *et al.*, 2014; Pfahl, 2014; Cattiaux *et al.*, 2010; Pfahl and Wernli, 2012; Demirtaş, 2017). It has shown that cold wintry conditions in Europe are closely associated with atmospheric blocking in the eastern North Atlantic (Sillmann *et al.*, 2011; Pfahl, 2014; Demirtaş, 2017). Understanding and improving the predictability of cold spells prior to high impact events is a key societal issue, since their frequency and intensity affect sectors of energy, transport and social emergency systems.

Cold waves may be investigated from a climatological perspective, but in fact they are meteorological events which are governed by the temporal and spatial scales they occur on. Inter-annual to intra-seasonal variations in the regional weather are usually driven by chaotic nature of the atmospheric dynamics which are due to baroclinic instabilities underlying meridional temperature gradient. The dynamical and physical factors works in concert have been studied extensively. There is one common atmospheric dynamical ingredient in cold wave composition which is persistent anticyclones. It is also referred as atmospheric blocking or persistent highs which is a stationary system that remains in the same place for several days and remotely contributes to maintaining cold wave.

Atmospheric blocking may exert strong impact on the upstream, *in situ*, and the downstream weather conditions (Schwierz *et al*., 2004; Pfahl and Wernli, 2012; Demirtaş, 2017). The spatial coverage of a block is a conspicuous synoptic event with a life time stretching from day-to-day weather to weeks-to-months climate variations (Croci-Maspoli *et al.*, 2007). The collocated and remote influence of atmospheric blocking in the winter and the summer seasons are described in a previous study (Demirtaş, 2017).

This study investigates the salient features of the DJF 2016/17 cold wave and the influence of large-scale atmospheric patterns. For this purpose: (i) a cold wave detection method which is based on spatially and temporally varying minimum temperature threshold is employed; (ii) a 500 hPa geopotential height based bi-dimensional atmospheric blocking detection method is implemented; (iii) in order to analyze the DJF 2016/2017 from a dynamical point of view, the episode mean and composite anomalies of the 500 hPa geopotential height and surface temperature at 2 m height are computed.

DATA AND METHODS

The ERA-Interim (EI) reanalysis data of European Centre for Medium-Range Weather Forecast (Dee *et al*., 2011) are employed with a 1°x1° longitude-latitude grid horizontal resolution. The mean of the 500 hPa geopotential height and temperature at 2 m height, *i.e.* 01 December 2016 - 28 February 2017 were computed. Composite anomalies (with respect to 1979-2009) of geopotential height at 500 hPa and temperature anomalies at 2 m height are computed by removing the December-January-February 1979–2009 climatological mean.

Cold Wave Detection Method

An easy and simple approach to identify cold wave is based on a daily minimum temperature being below a fixed absolute threshold. A detection based on being below an absolute temperature threshold cannot be applied to all regions, because each region is often characterized by different micro-climatic conditions. For example, in relatively warmer regions absolute thresholds may not be achieved, and temperatures may have to be even colder over cold regions.

In order to reduce the degree of arbitrariness involved in the selection of a threshold temperature and to provide a dynamic definition, which may also be easily transferable to other places, percentiles turns out to be more appropriate. This study deals with spatial distributions and utilizes a nonparametric method to determine a spatially and temporally varying minimum temperature threshold, which is based on a 10^{th} percentile from a 7-day time window (Demirtaş, 2017). The 10^{th} percentile minimum temperature is computed on a grid point basis as outlined below.

i. Spatially and daily varying minimum temperature threshold: For a given grid point, a temperature value with respect to the climatology (1979–2009) is considered to be extreme when its value falls below the 10^{th} percentile. The threshold minimum temperature is computed for a respective calendar day (RCD) using the temperature data of the 1979–2009 period between *d-3* and *d+3* days. For each January day, a 10^{th} percentile is computed from a sample of seven days (three days on each side of the RCD). For example, on 6 January, the temperature values between 3 January and 9 January of the years 1979-2009 are used.

$$T_{(i,j,y,d)threshold,10^{th}} = \bigcup_{y=1979}^{2009} \bigcup_{t=d-3}^{d+3} T_{(i,j,y,d)}$$

where ∪ denotes the union of sets and $T_{i,j,y,d}$ is the daily minimum temperature at 2 m height belonging to the RCD in the year (*y*). The indices *i,j,y,d* represent latitude, longitude, year and day, respectively.

ii. **Temporal threshold*:*** The above described temperature threshold is to be satisfied on three consecutive days**.**

iii. **Cold wave detection:** A cold spell that satisfies (i) and (ii) is identified as cold wave.

iv. **Cold wave intensity:** It is computed by summing up the absolute differences between the temperature values and the percentile threshold for the duration of the event, and then the sum is divided by the duration of cold wave (Spinoni *et al.,* 2015; Shevchenko *et al.,* 2014; Demirtaş, 2017).

Atmospheric Blocking Detection Method

Proper detection of blocking is essential for weather forecasting, since it emposes a strong influence on the upstream, *in-situ*, and downstream weather. A bi-dimensional index based on the reversal of the meridional gradient of geopotential height at 500 hPa is applied (Tibaldi and Molteni, 1990; Scherrer *et al.*, 2006; Davini *et al.*, 2012; Demirtaş, 2017). For each grid point, the following metric is defined:

$$GHGS(\lambda_0, \Phi_0) = \frac{Z500(\lambda_0, \Phi_0) - Z500(\lambda_0, \Phi_S)}{\Phi_0 - \Phi_S} \quad (1)$$

$$GHGN(\lambda_0,\Phi_0)=\frac{Z500(\lambda_0,\Phi_N)-Z500(\lambda_0,\Phi_0)}{\Phi_N-\Phi_0} \quad (2)$$

$$\Phi_s=\Phi_0-15° \quad (3)$$

$$\Phi_N=\Phi_0+15° \quad (4)$$

where $Z500(\lambda_0,\Phi_0)$ represents the grid point 500 hPa geopotential height at longitude (λ_0) which ranges from 0° to 360° and latitude (Φ_0) which ranges from 30° to 70°N. An instantaneous local blocking (LIB) is assigned for a grid point, if both of the following conditions are satisfied:

$$GHGS(\lambda_0,\phi_0)\succ 0 \quad (5)$$

$$GHGN(\lambda_0,\phi_0)\prec -10\,\text{m/°latitude} \quad (6)$$

A grid point is assigned for instant blocking if conditions given in Equations (5-6) are satisfied. A sector is defined as large-scale blocking, if the above criteria are satisfied for at least 15 continuous longitudes. A time-scale of 4 days is used to define a blocking episode. A blocking event is considered as large scale episode of blocking if afore mentioned both spatial and temporal conditions are satisfied.

ANALYSIS OF THE COLD SPELLS OF DJF 2016/2017

Overview of Circulation Mean and Anomalies

The nature and origins of cold waves are closely tied to the prevailing atmospheric circulation dynamics. Figure 1(a) illustrates the mean 500 hPa geopotential height of the study period of 01 December 2016 - 28 February 2017 (hereafter, DJF 2016/2017), which highlights the panoply of large-scale weather systems. The prevalence of an upstream northeast–southwest tilted ridge over the eastern Atlantic orchestrates the atmospheric circulation. To its east, the north westerly winds associated with the northeast–southwest tilted trough advect maritime air from high northern latitudes to southeast Europe and warm-moist Mediterranean air towards northerly latitudes.

Inspection of the spatial distribution of the composite DJF 2016/2017 anomalies (with respect to the 1979–2009 climatological mean) of the 500 hPa geopotential height field suggests that the Azores anticyclone is displaced towards the north. The positive anomaly over the mid-Atlantic exceeds 80 gpm, while the negative anomaly over northeast exceeds −80 gpm (Figure 1(b)). The nature of these anomalies indicates that they may be due to the steady residence of the same prevailing atmospheric circulation. Supporting evidence for this assertion may be inferred from the duration of atmospheric blocking over the region.

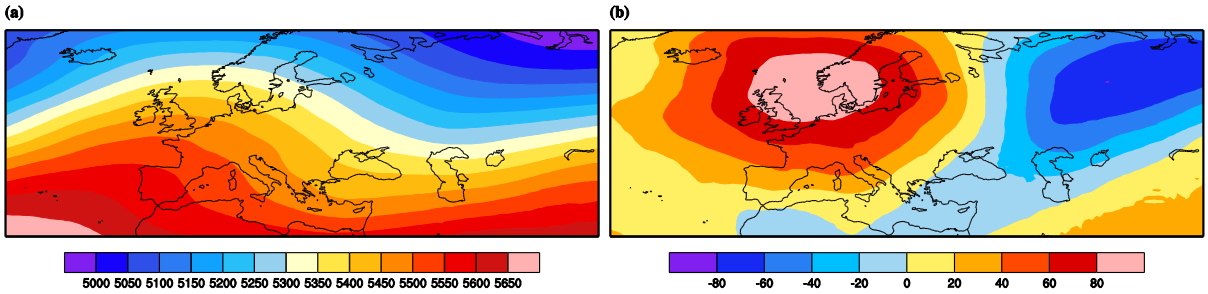

Figure 1. For the 01 December 2016 - 28 February 2017 period: (a) Time-mean 500hPa geopotential height (in gpm), (b) The composite 500hPa geopotential height anomaly.

The spatial distribution of the DJF 2016/2017 surface air temperature at 2 m height indicates that the coldest regions, with low temperatures ranging from −8 to −2°C, were around coastal regions (Figure 2(a)). It should be noted that temperatures shown here are grid-point values at 1° × 1° resolution, and they represent the time-mean of the DJF 2016/17 period. (Station-based daily minimum temperatures show much lower values, as outlined in the introduction to this article.)

Examination of the spatial distribution of the composite anomalies (with respect to the 1979–2009 climatological mean) of the DJF 2016/2017 surface temperature at 2 m implies that temperature anomalies are pronounced over north-west part of Turkey (up to −8 degC; Figure 2(b)). The DJF 2016/2017 surface air temperature anomalies correspond to roughly −1σ (with respect to the 1979–2009 ECMWF-EI) in some places (not shown). Analysis of the cold winter of 2012 indicated that the largest anomaly – which covers 16 January – 19 February 2017 period, was a departure of −3σ from the 1979–2009 climatological mean (Demirtaş, 2017).

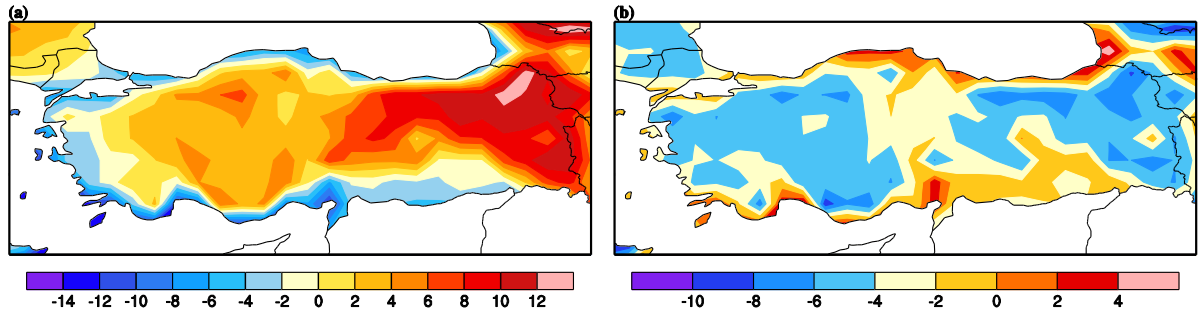

Figure 2. For the 01 December 2016 - 28 February 2017 period: (a) Time-mean temperature at 2 m (°C), (b) The composite temperature at 2 m anomaly (degC).

Cold Wave Analysis

The cold wave detection technique outlined in Section 2.1 is applied to 1 December 2016 - 28 February 2017 period. It should be kept in mind that minimum reference temperature changes spatially and temporally, therefore impact of wintry conditions on surface air temperature differs throughout the country. An analysis of the total number of contiguous cold wave days shows that the north west of Turkey is under cold wintry conditions for about 16-27 days, and the eastern part of Turkey is under such conditions for about 20-35 days (Figure 3a), these results can be expected since 2 m temperature anomalies are also located over the same area (Figure 2(b)). As it can be inferred from Figure 3(b), there are 3-5 cold wave events over the western part of Turkey and there are 5-6 cold waves over the eastern Turkey, these regions are in line with the 2 m surface air temperature anomalies depicted in Figure 2(b). On the other hand, the intensity of the cold waves is higher over the eastern Turkey and over mid-part of

Mediterranean region (Figure 3c) which is again coincides well with the composite 2 m temperature anomal of the region (Figure 2(b)).

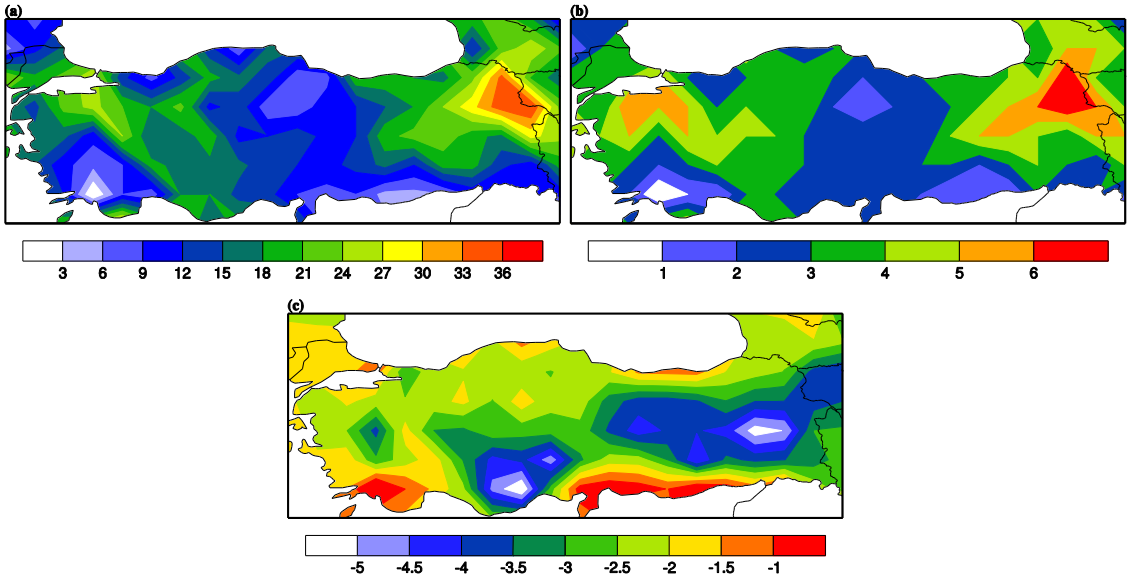

Figure 3. For the 1 December 2016- 28 February 2017: a) Total number of cold wave days, b) Total number of cold waves, c) Cold wave intensity (°C).

Atmospheric Blocking Analysis

The atmospheric detection technique outlined in Section 2.2 is applied to 1 December 2016 - 28 February 2017 period. Analysis of atmospheric blocking of the DJF 2016/2017 period indicates that the blocking area extends from west of Spain to over northern latitudes (Figure 4a-b). Instant atmospheric blocking frequency is over 35% to the west of Spain, and it is 30-35 % over Scandinavia (Figure 4a). These instantaneous atmospheric blocking frequencies are above the climatological means (Davini *et al.,* 2012). Wintertime cold spells in Europe can be followed by upstream blocking events, for example, the 2009/2010 winter was reported to have 33% blocking frequency (Cattiaux *et al.*, 2010) and instantaneous atmospheric frequency of the winter 2012 was over 50% in western Europe, and 75% over Siberia (Demirtaş, 2017). The duration of atmospheric blocking is very crucial in maintaining collocated and remote impacts of atmospheric blocking. The total duration of atmospheric blocking -which considers at least 4-days of uninterrupted blocking- shows that anticyclonic conditions persisted over the eastern Atlantic for about three weeks (Figure 4b). These durations are well above the climatological studies of average blocking duration of these locations (Davini *et al.*, 2012).

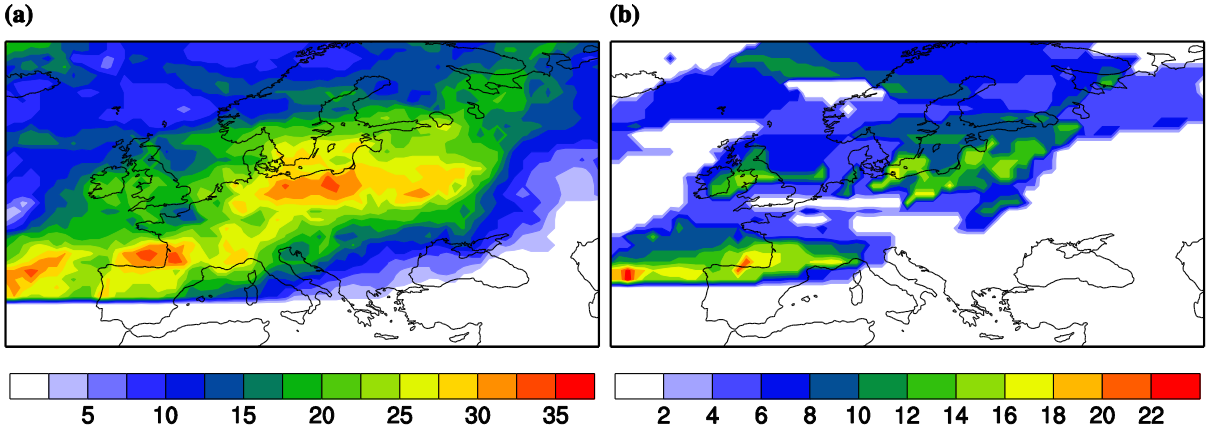

Figure 4. For the 1 December 2016- 28 February 2017: a) Frequency of instant atmospheric blocking in (%), b) Total episode of blocking days.

ANALYSIS OF JANUARY 2017 PERIOD

This section is devoted for the January 2017 period, since a detailed analysis highlighted that this period exhibited highest anomalies compared to other months of DJF 2016/2017 period. Figure 5(a) depicts the mean 500 hPa geopotential height of the study period of 01-31 January 2017 (hereafter, January 2017), which highlights the conspicuous large scale underlying mid-Atlantic ridge and the northeast–southwest tilted trough over Eastern Europe. On its downstream, the north westerly winds associated with the northeast–southwest tilted trough advect maritime air from high northern latitudes to southeast Europe and south-westerly winds brings moist and relatively warm air from the Eastern Mediterranean (Figure 5(a)). The overall circulation pattern is very similar to that of Figure 1(a), but tilting and deepening is more pronounced in January 2017.

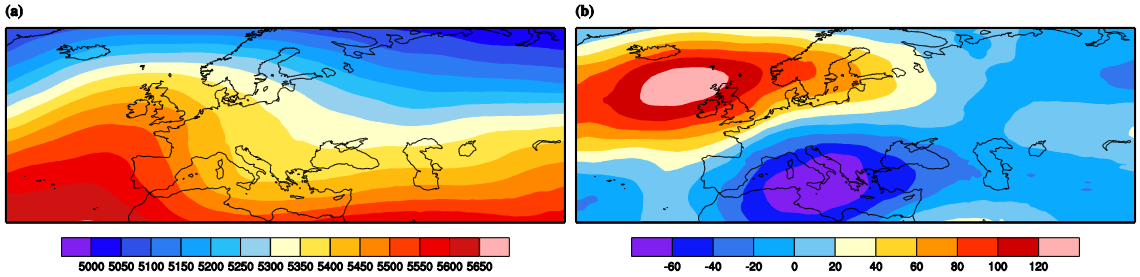

Figure 5. For the 1-31 January 2017 period: (a) Time-mean 500hPa geopotential height (in gpm), (b) The composite 500hPa geopotential height anomaly.

Examination of the spatial distribution of the composite January 2017 anomalies (with respect to the 1979–2009 climatological mean) of the 500 hPa geopotential height field highlights that the positive anomaly is over 120 gpm, and it is located to the north west of the UK. The negative anomaly which is centred between Italy and Greece extends towards western part of Turkey exceeds −60 gpm (Figure 5(b)). Comparing Figure 5 (b) with that of Figure 1 (b) shows that the negative anomaly in particular is located further south, and that this might have posed strong wintry conditions over the area. This can be inferred from the examination of the spatial distribution of the composite anomalies (with respect to the 1979–2009 climatological mean) of the January 2017 surface temperature and related anomalies (Figure 6 (a-b)). Temperatures lower than climatological averages (ranging from -8°C to -2°C) are evident in most parts of the country (Figure 6 (a)).

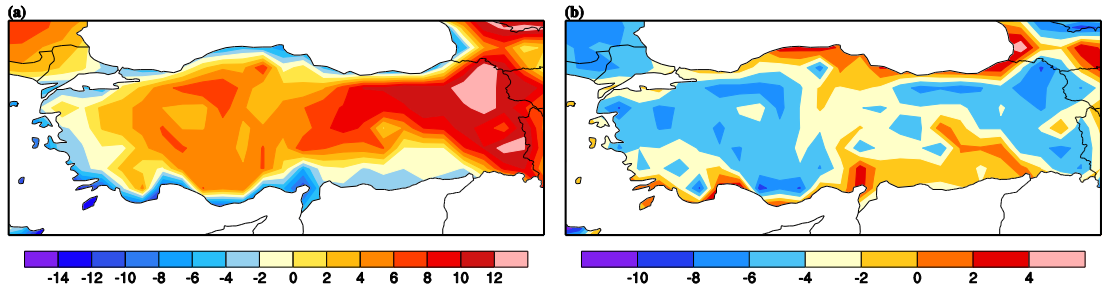

Figure 6. For the 01-31 January 2017 period: (a) Time-mean temperature at 2 m (°C), (b) The composite temperature at 2 m anomaly (degC).

An analysis of the total number of cold wave day analysis highlights that the north west of Turkey has about 7-10 cold wave days, and the eastern part of Turkey has about 10-12 cold wave days (Figure 7(a)). As it can be inferred from Figure 7(b), there are 2 cold wave episodes over the western and eastern parts of Turkey. Inspection of the intensity of the cold waves shows

that north-west part of Turkey had much colder conditions compared to the rest of the country (Figure 7(c)).

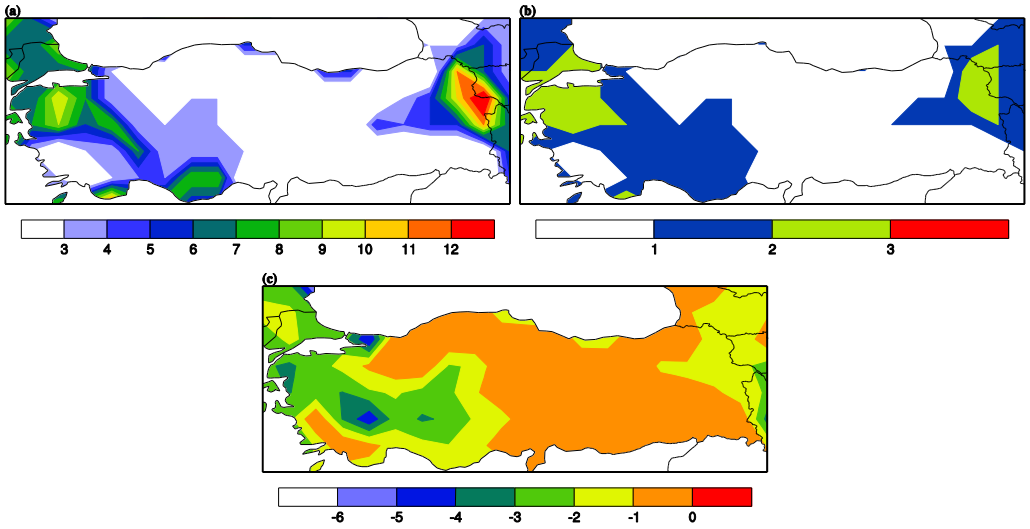

Figure 7. For the 1-31 January 2017: a) Total number of cold wave days, b) Total number of cold waves, c) Cold wave intensity (°C).

Analysis of atmospheric blocking of the January 2017 period implies that the blocking area extends from west of Spain to over northern latitudes (Figure 8(a-b)). Instantaneous atmospheric blocking frequency is above 40-50% over northern Europe (Figure 8(b)). The duration of atmospheric blocking plays a pivotal role in sustaining regional and remote impacts of atmospheric blocking. The total episode of atmospheric blocking is 12-16 days over northern Europe which satisfies the condition for total number of consecutive blocking days for an episode of blocking (Figure 8(c)). Over the same region, episode of large scale blocking is 12-14 days (Figure 8(d)). Note that Figure 8 (c) and (d) are similar, but spatial extent is smaller in Figure 8(d), this is related to the large scale condition applied in the computation of large scale episode of blocking.

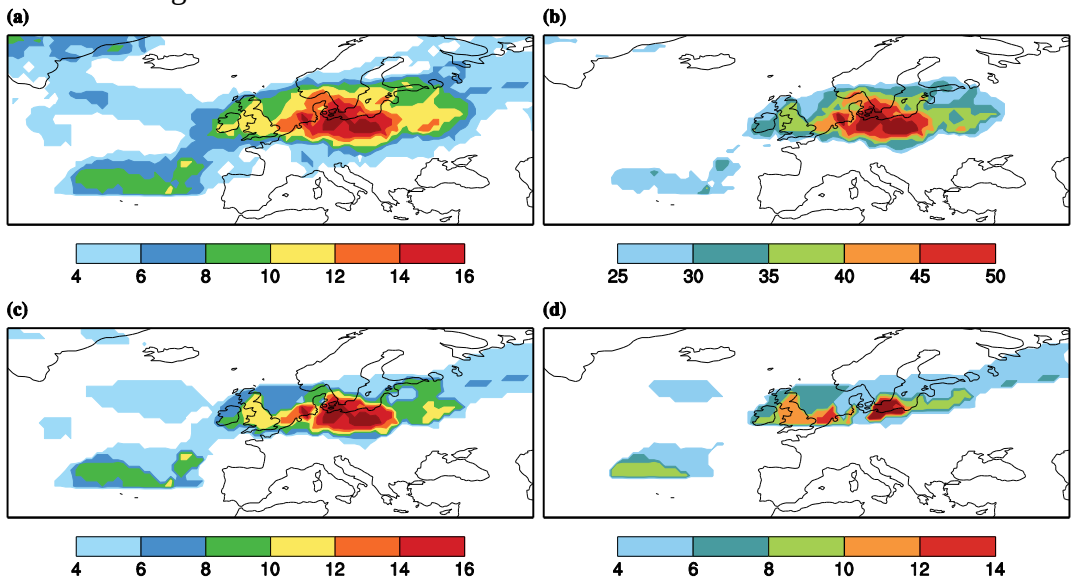

Figure 8. For the 1-31 January 2017 period: (a) Total number of instantaneous atmospheric blocking days (# days), (b) Frequency of instantaneous atmospheric blocking days (%), (c) Total number of episode of atmospheric blocking days (# days), (d) Total number of episode of large scale atmospheric blocking days (# days).

CONCLUDING REMARKS

This study investigated the connection between the cold temperatures of DJF-2016/2017 and atmospheric blocking, using a cold wave detection method and an atmospheric blocking detection method. Results indicated that the cold snaps of DJF-2016/2017 were not exceptional in terms of temperature anomalies but remarkable event for its duration and spatial extent. Examination of the spatial distribution of the composite anomalies of the DJF 2016/2017 surface temperature at 2 m showed that temperature anomalies (up to −8 degC) were pronounced over north-west part of Turkey, the associated anomalies correspond to roughly −1σ in some places. Inspection of the spatial distribution of the composite DJF 2016/2017 anomalies of the 500 hPa geopotential height field implied that the Azores anticyclone was displaced towards the north. The positive anomaly over the mid-Atlantic exceeded 80 gpm, while the negative anomaly over north east exceeded −80 gpm. An analysis of the total number of contiguous cold wave days showed that the north west of Turkey was under wintry conditions for about 16-27 days, and the eastern part of Turkey was under such conditions for about 20-35 days. 3-5 cold wave events took place over the western part of Turkey and there were 5-6 cold waves over the eastern Turkey. The intensity of the cold waves was noted to be higher over the eastern Turkey and over mid-part of Mediterranean region.

Instant atmospheric blocking frequency was over 35% to the west of Spain, and it was 30-35% over Scandinavia. These instantaneous atmospheric blocking frequencies are above the climatological means (Davini *et al.,* 2012). Wintertime cold spells in Europe can be followed by upstream blocking events, for example, the 2009/2010 winter was reported to have 33% blocking frequency (Cattiaux *et al.,* 2010) and instantaneous atmospheric frequency of the winter 2012 was over 50% in western Europe, and 75% over Siberia (Demirtaş, 2017). The duration of atmospheric blocking is very crucial in maintaining collocated and remote impacts of atmospheric blocking. The analysis of the total duration of atmospheric blocking showed that anticyclonic conditions persisted over the eastern Atlantic for about three weeks. These durations are above the climatological studies of average blocking duration of these locations (Davini *et al.,* 2012).

The close inspection of January 2017 period showed that the composite 500 hPa geopotential height anomaly centre was located over southern Europe and extended over western part of Turkey. The atmospheric blocking was pronounced over north east Europe. During this period, the western part of Turkey had intensive cold wave episodes. Examination of the spatial distribution of the composite January 2017 anomalies of the 500 hPa geopotential height field highlighted that the positive anomaly is over 120 gpm, and it was located to the north west of the UK. The negative anomaly which was centred between Italy and Greece extended towards western part of Turkey exceeded −60 gpm. The analysis of the surface temperatures and related anomalies showed that below zero temperatures (ranging from -8°C to -2°C) are apparent over the coastal regions.

The cold wave detection method provided an objective analysis of the cold wave episodes of DJF 2016/2017 throughout different regions of Turkey which otherwise would have required the use of spatially varying temperature threshold due to the variation in topography and micro-climatic features across the country. This detection method can be useful for investigating salient features of cold waves; their spatial distribution, duration, number and intensity. The objective atmospheric blocking detection method has emerged as a valuable tool for representing the phenomenon. This method can be useful for investigating the spatial coverage and time persistence of blocking events important for the occurrence of temperature extremes. The link between high impact cold waves and persistent atmospheric blocking anticyclones is

important both for weather and the investigation of temperature extremes in the frame work of climate variability. Results from this analysis indicate that the atmospheric blocking was likely to be responsible for maintaining the cold wintry conditions.

There have been cold spells with deep and extensive snow cover in recent winters such as the European winter of 2009/2010 (Cattiaux *et al.*, 2010) and the winter of 2012 (Demirtaş, 2017). The DJF 2016/2017 can be thought of as an example of a high impact cold wave superimposed on a warming climate. Since climate projection studies suggest that the European warming may continue in the twenty first century, a further decrease in the frequency of cold waves can be expected. The association between cold waves and atmospheric blocking is important both for weather prediction and for the investigation of temperature extremes in the frame work of climate variability. The results indicate that winter climate might experience year-to-year variability. Increase in variability might be able to explain the high impact cold waves, and would strongly affect their incidence in the future. Society is faced not only with addressing current climate variability, but also with finding ways to adapt to future changes relating to cold waves, such as the one described here, and their societal and environmental impacts.

Acknowledgements. Meteorological data were obtained from the Turkish State Meteorological Service and the European Centre for Medium-Range Weather Forecasts. Plots were created using the NCAR Command Language (NCL, 2016). The author is very grateful to these organizations.

REFERENCES

Bieli M, Pfahl S, Wernli H. 2014. A Lagrangian investigation of hot and cold temperature extremes in Europe. *Q. J. R. Meteorol. Soc.*, doi:10.1002/qj.2339

Cattiaux J, Vautard R, Cassou C, Yiou P, Masson-Delmotte V, Codron F. 2010. Winter 2010 in Europe: a cold extreme in a warming climate. *Geophys. Res. Lett.*, 37:L20704. doi:10.1029/2010GL044613

Cattiaux J, Douville H, Ribes A, Chauvin F, Plante C. (2013): Towards a better understanding of changes in winter time cold extremes over Europe: a pilot study with CNRM and IPSL atmospheric models. *Clim Dyn*, 40:2433–2445, DOI 10.1007/s00382-012-1436-7

Croci-Maspoli M, Schwierz C, Davies H. 2007. Atmospheric blocking: space-time links to the NAO and PNA. *Clim. Dyn.* 29:713–725

Davini P, Cagnazzo C, Neale R, Tribbia J. 2012. Coupling between Greenland blocking and the North Atlantic Oscillation pattern. *Geophys. Res. Lett.*, 39:L14701, doi:10.1029/2012GL052315.

Dee DP, et al. (2011): The ERA-Interim reanalysis: Configuration and performance of the data assimilation system. *Q. J. R. Meteorol. Soc*. 137: 553–597, doi:10.1002/qj.828.

Demirtaş, M. (2017): The large scale environment of the European 2012 high-impact cold wave: prolonged upstream and downstream atmospheric blocking. *Weather*, doi:10.1002/wea.3020.

Pfahl S, Wernli H. 2012. Quantifying the relevance of atmospheric blocking 1 for co-located temperature extremes in the Northern Hemisphere on (sub-)daily time scales. *Geophys. Res. Lett.*, 39: L12807, doi:10.1029/2012GL052261

Pfahl S. 2014. Characterising the relationship between weather extremes in Europe and synoptic circulation features. *Nat. Hazards Earth Syst. Sci.*, 14: 1461-1475, doi:10.5194/nhess-14-1461-2014

Scherrer S, Croci-Maspoli M, Schwierz C, Appenzeller C. 2006. Two-dimensional indices of atmospheric blocking and their statistical relationship with winter climate patterns in the Euro-Atlantic region. *Int. J. Climatol.*, 26: 233–249.

Schwierz C, Croci-Maspoli M, Davies HC. 2004. Perspicacious indicators of atmospheric blocking. *Geophys. Res. Lett.*, 31: L06125, doi:10.1029/2003GL019341

Shevchenko O, Lee H, Snizhko S, Mayer H. 2014. Long-term analysis of heat waves in Ukraine. *Int. J. Climatol*. 34(5): 1642–1650.

Sillmann J, Croci-Maspoli M, Kallache M, Katz R. 2011. Extreme cold winter temperatures in Europe under the influence of North Atlantic atmospheric blocking. *J. Clim.*, 24: 5899-5913, doi: 10.1175/2011JCLI4075.1

Spinoni J, Lakatos M, Szentimrey T, Bihari Z, Szalai S, Vogta J, Antofiea T. 2015. Heat and cold waves trends in the Carpathian Region from 1961 to 2010. *Int. J. Climatol.*, 35: 4197– 4209, DOI: 10.1002/joc.4279

Tibaldi, S. and Molteni F. (1990): On the operational predictability of blocking. *Tellus*, Ser. A, 42:343-365.

The NCAR Command Language (Version 6.3.0) [Software]. (2016): Boulder, Colorado: UCAR/NCAR/CISL/TDD. doi:10.5065/D6WD3XH5

World Meteorological Organization (WMO). 2013. Assessment of the observed extreme conditions during late boreal winter 2011/2012. WCDMP No.80, 16pp.

A REVIEW OF THE TURKEY FEBRUARY HEAT WAVE OF 2016

Mesut DEMİRCAN, Hüseyin ARABACI, Alper AKÇAKAYA, Serhat SENSOY, Erdoğan BÖLÜK, Ali Ümran KÖMÜŞCÜ, Mustafa COŞKUN

[1]Turkish State Meteorological Service, Ankara, Turkey

mdemircan@mgm.gov.tr, harabaci@mgm.gov.tr, aakcakaya@mgm.gov.tr, ssensoy@mgm.gov.tr, , aukomuscu@mgm.gov.tr, eboluk@mgm.gov.tr, mustafacoskun@mgm.gov.tr

Abstract

Climate change, in other word global warming, is one of the most serious environmental, economic, and social threats that this world faces. A change in the Earth's surface temperature also leads to increase in extreme events as well as extreme temperatures. Increasing in magnitude, severity and duration of extreme temperature events are harmful to both as the ecosystem and on human health. Human influence has also led to significant regional temperature increases at the continental and subcontinental levels. Humans cannot realise heatwaves impact which occurs in spring and autumn as much as ecosystems and habitats. Warming continued in 2016, setting a new temperature record of approximately 1.1 °C above the pre-industrial period. Heat wave is a period of abnormally hot weather. Heat wave is daily maximum temperature on more than five consecutive days exceeding the average maximum temperature by 5°C. Heat waves effected most of the Turkey in February 2016 and they were very intense between 15 and 19 February in 2016. In this study we investigate these extreme events and used mean maximum, maximum and mean temperature values of Turkish State Meteorological Service's 130 stations. During the period, extreme maximum temperatures were exceed their long term February's extreme maximum temperature records in 65 stations. Heat waves were seen in 123 stations and repeated in 36 of these stations again and continued until mid of March in some stations.

Keywords: E*xtreme events, heat wave, climate change, climate impact*

INTRODUCTION

Climate change, in other word global warming, is one of the most serious environmental, economic, and social threats that this world faces. There are many assessments to monitor climate and to estimate climate variability over many regions and also globally by national and international institutions. A change in the Earth's surface temperature also leads to increase in extreme events as well as extreme temperatures. Increasing in magnitude, severity and duration of extreme temperature events are harmful to both as the ecosystem and on human health.Human influence has also led to significant regional temperature increases at the continental and subcontinental levels. Warming continued in 2016, setting a new temperature record of approximately 1.1 °C above the pre-industrial period (WMO, 2016)

According to WMO's Meteoterm vocabulary, a heat wave is an extreme weather event with marked warming of the air, or the invasion of very warm air, over a large area; it usually lasts from a few days to a few weeks (TT-DEWCE, 2015). Heat wave (also referred to as extreme heat event) is a period of abnormally hot weather. Heat waves and warm spells have various and in some cases overlapping definitions (IPCC, 2012). Changes in many extreme weather and climate events have been observed since about 1950. It is very likely that the number of cold days and nights has decreased and the number of warm days and nights has increased on the global scale. It is likely that the frequency of heat waves has increased in large parts of Europe, Asia and Australia (IPCC, 2013).

Heat or hot weather that lasts for several days, often referred to as a "heatwave", is a pervasive natural hazard that can exact a heavy toll on human systems, affecting health, livelihoods and infrastructure. Natural systems can also be severely affected by the impacts sustained beyond the duration of a heatwave. Although there is no universally acceptable definition of heatwaves (Perkins and Alexander, 2013; Robinson, 2001), they are understood to be periods of unusually hot and dry or hot and humid weather that have a subtle onset and cessation, a duration of at least two to three days and a discernible impact on human activities (WMO-No:1142, 2015).

TT-DEWCE recommended 4 metrics for standard characterization of a heat wave to quantitatively reflect a heat wave event. The definition of heat wave should be complemented by characterization with magnitude, duration, severity and extend (TT-DEWCE, 2015). Magnitude should be computed based on an index or a set of indices of thermal condition(s) exceeding certain threshold(s). Duration will lead to the computation of the persistence of a heat wave and should be based on recording the starting time and the ending time of the event. Severity is a measure which integrates two aspects of the event, its magnitude, and its persistence. Extent is computed to inform on the geographical area affected and the widespread aspect of the heat wave.

Heat wave is daily maximum temperature on more than five consecutive days exceeding the average maximum temperature by 5°C. Cold wave is daily minimum temperature on more than five consecutive days below the average minimum temperature by 5°C (Frich et al., 2002; Coskun et al., 2017).

200 stations had heat waves in 2016. Total number of heat wave is 561 (some of the stations had more than once) (based on 1971-2000 normals). There was no cold wave in 2016. Highest number of heat wave occurred in 2010 which was the warmest year in Turkey. Highest number of cold wave occurred in 1992 which was the coldest year in Turkey after Pinatubo Volcano eruption (Coskun et al., 2017) (Fig. 1).

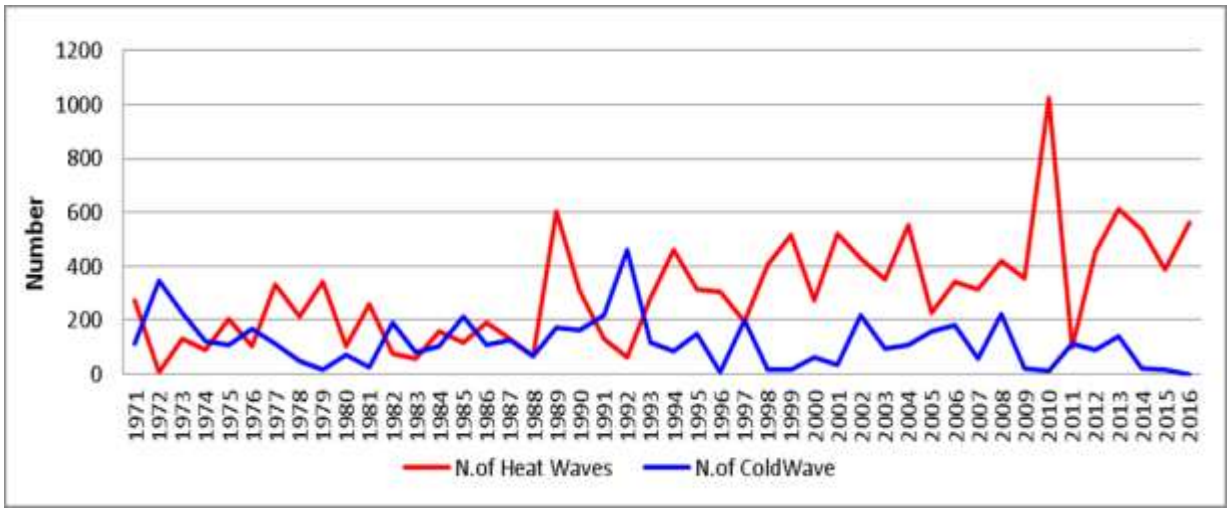

Figure 1. Annual Number of Heat & Cold Waves in Turkey (Coskun et al., 2017).

Unal et al. (2013) had a results confirm that the number of excessive hot days, heat waves, and their durations have increased through the 2000s, especially on the southern part of the western Turkey.

DATA AND METHODS

Heat waves effected most of the Turkey in February 2016 and they were very intense between 15 and 19 February in 2016. In this study we investigate these extreme events and use mean maximum, maximum and mean temperature values of Turkish State Meteorological Service's 130 stations.

In line with the definition of Frich et al., (2002); we used daily maximum temperature which were exceeding their average maximum temperature by 5°C and continue at least 5 days to calculate heat wave events for every stations.

Mean temperatures were higher than normal (1981-2010) between the January and the May in 2016. The average temperature of Turkey in February 2016 was 8.2 ° C and it was 4.7°C above 1981-2010 normal (3.5° C). With this figure, it was the hottest February since 1971 (Figure 1). In February 2016, extreme maximum temperatures were exceed their long term February's extreme maximum temperature records in 65 stations (Figure 2). Heat waves were seen in 123 stations and repeated in 36 of these stations again and continued until mid of March in some stations.

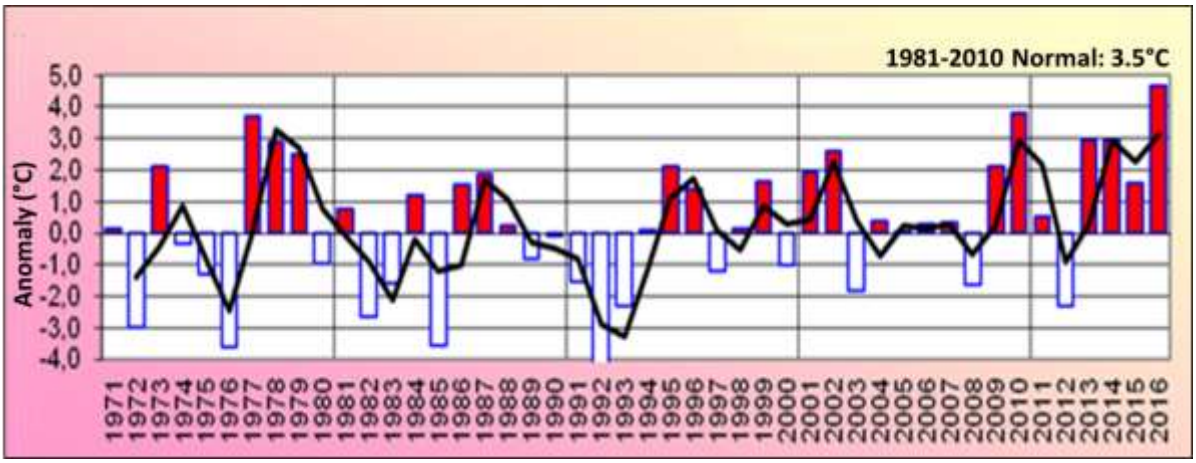

Figure 1. February mean temperature anomalies (TSMS, 2016-a)

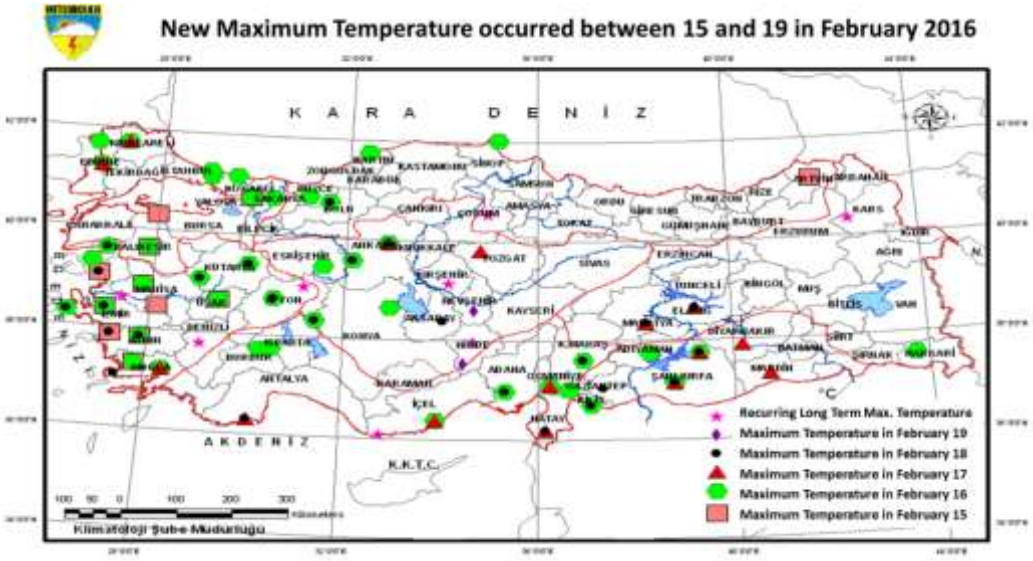

Figure 2. New maximum temperature occurred between 15 and 19 February in 2016 (TSMS, 2016-b)

In the Marmara Region: Maximum temperatures set a new record at 10 meteorological stations, including Balikesir, Bandırma, Edirne, Sarıyer, Kırklareli, Kocaeli, Kumköy, Sakarya, Şile and Uzunköprü in February (Fig. 3; 4).

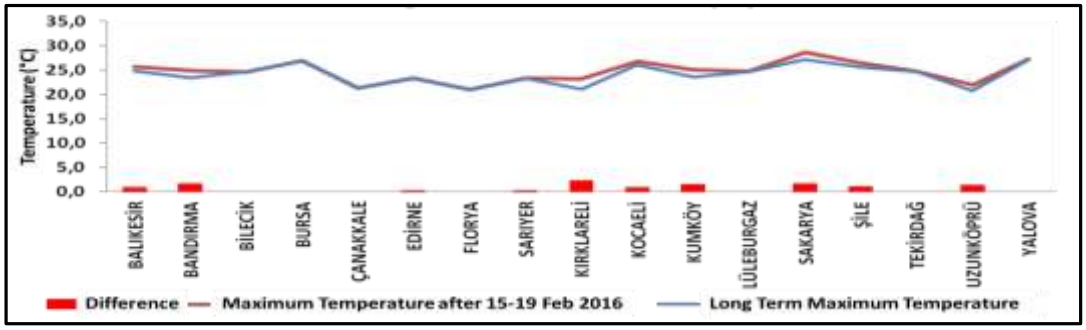

Figure 3. Long term maximum temperature, new maximum temperature occurred between 15 and 19 February in 2016 and their differences in the Marmara Region (TSMS, 2016-b).

		February Long Term Maximum Temperature	15 Feb 2016 Maximum Temperature	16 Feb 2016 Maximum Temperature	17 Feb 2016 Maximum Temperature	18 Feb 2016 Maximum Temperature	19 Feb 2016 Maximum Temperature	February Maximum Temperature after 15-19 Feb 2016
MARMARA REGION	BALIKESİR	24,8	25,0	25,6				25,6
	BANDIRMA	23,4	24,9					24,9
	BİLECİK	24,6						24,6
	BURSA	26,9						26,9
	ÇANAKKALE	21,3						21,3
	EDİRNE	23,2		23,3				23,3
	FLORYA	21,0						21,0
	SARIYER	23,2		23,3				23,3
	KIRKLARELİ	21,0		22,0	23,1			23,1
	KOCAELİ	26,0	26,1	26,7				26,7
	KUMKÖY	23,6	25,6	25,0				25,0
	LÜLEBURGAZ	24,7						24,7
	SAKARYA	27,1		28,7				28,7
	ŞİLE	25,6		26,5				26,5
	TEKİRDAĞ	24,7						24,7
	UZUNKÖPRÜ	20,8		21,5	22,0			22,0
	YALOVA	27,2						27,2

Figure 4. Long term maximum temperature, new maximum temperature occurred between 15 and 19 February in 2016 and their values by stations in the Marmara Region (TSMS, 2016-b).

In the Aegean Region: Maximum temperatures set a new record at 16 meteorological stations, including Afyonkarahisar, Akhisar, Aydın, Ayvalık, Bodrum, Çeşme, Dikili, Edremit, Izmir, Kuşadası, Kütahya, Milas, Muğla, Salihli, Simav and Uşak in February. Denizli, Emirdag and Manisa stations repeated their long term values. (Fig. 5; 6).

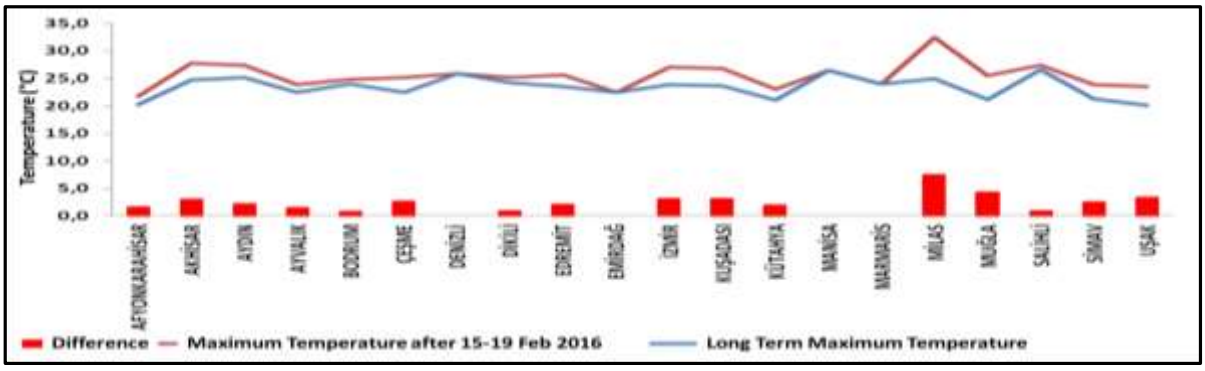

Figure 5. Long term maximum temperature, new maximum temperature occurred between 15 and 19 February in 2016 and their differences in the Aegean Region (TSMS, 2016-b).

		February Long Term Maximum Temperature	15 Feb 2016 Maximum Temperature	16 Feb 2016 Maximum Temperature	17 Feb 2016 Maximum Temperature	18 Feb 2016 Maximum Temperature	19 Feb 2016 Maximum Temperature	February Maximum Temperature after 15-19 Feb 2016
AEGEAN REGION	AFYONKARAHİSAR	20,2		21,6				
	AKHİSAR	24,7	26,6	27,7				27,7
	AYDIN	25,2	25,9	26,9				
	AYVALIK	22,4		23,9				23,9
	BODRUM	24,0						
	ÇEŞME	22,4		24,9				
	DENİZLİ	25,9						
	DİKİLİ	24,2	24,6					
	EDREMİT	23,5		25,2				
	EMİRDAĞ	22,5						
	İZMİR	23,9	24,7	26,9				
	KUŞADASI	23,6	25,9					
	KÜTAHYA	21,0		22,0				
	MANİSA	26,4						
	MARMARİS	24,0						24,0
	MİLAS	24,9	26,0	32,4				32,4
	MUĞLA	21,2		25,0	25,5			
	SALİHLİ	26,5	27,4					27,4
	SİMAV	21,3		22,8				
	UŞAK	20,1	20,4	23,5				23,5

Figure 6. Long term maximum temperature, new maximum temperature occurred between 15 and 19 February in 2016 and their values by stations in the Aegean Region (TSMS, 2016-b).

In the Mediterranean Region: Maximum temperatures set a new record at 9 meteorological stations, including Adana, Antakya, Burdur, Finike, Isparta, Islahiye, Kahramanmaraş, Osmaniye and Silifke in February. Anamur station repeated their long term value (Fig. 7; 8).

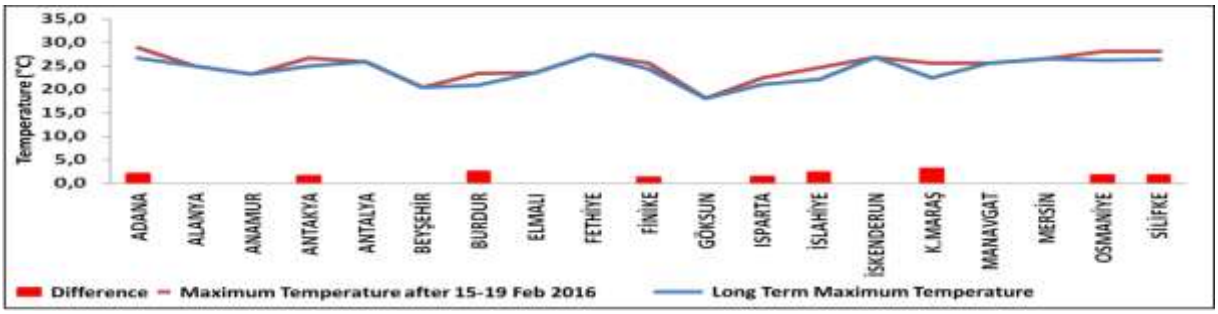

Figure 7. Long term maximum temperature, new maximum temperature occurred between 15 and 19 February in 2016 and their differences in the Mediterranean Region (TSMS, 2016-b).

		February Long Term Maximum Temperature	15 Feb 2016 Maximum Temperature	16 Feb 2016 Maximum Temperature	17 Feb 2016 Maximum Temperature	18 Feb 2016 Maximum Temperature	19 Feb 2016 Maximum Temperature	February Maximum Temperature after 15-19 Feb 2016
MEDITERRANEAN REGION	ADANA	26,7		28,2				
	ALANYA	25,0						25,0
	ANAMUR	23,2						
	ANTAKYA	25,0			25,9			
	ANTALYA	25,9						25,9
	BEYŞEHİR	20,4						20,4
	BURDUR	20,9		23,4				23,4
	ELMALI	23,5						23,5
	FETHİYE	27,4						27,4
	FİNİKE	24,3			24,9			
	GÖKSUN	18,1						18,1
	ISPARTA	21,0		22,5				22,5
	İSLAHİYE	22,2		24,6		24,6		24,6
	İSKENDERUN	26,8						26,8
	K.MARAŞ	22,4		24,6				
	MANAVGAT	25,6						25,6
	MERSİN	26,5						26,5
	OSMANİYE	26,2		26,5	28,0			28,0
	SİLİFKE	26,3		27,8	28,1			28,1

Figure 8. Long term maximum temperature, new maximum temperature occurred between 15 and 19 February in 2016 and their values by stations in the Mediterranean Region (TSMS, 2016-b).

In the Central Anatolian Region: Maximum temperatures set a new record at 9 meteorological stations, including Aksaray, Aksehir, Ankara, Cihanbeyli Nevsehir, Polatlı, Sivrihisar, Ulukısla and Yozgat in February. Kırsehir and Nigde stations repeated their long term values. (Fig. 9; 10).

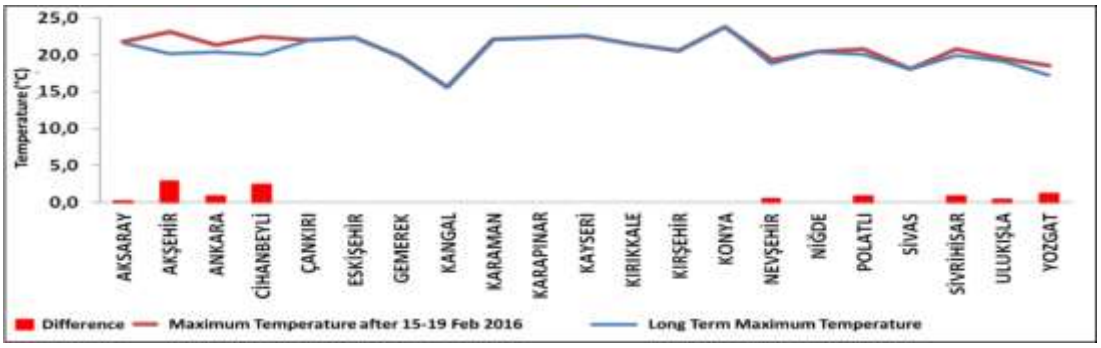

Figure 9. Long term maximum temperature, new maximum temperature occurred between 15 and 19 February in 2016 and their differences in the Central Anatolian Region (TSMS, 2016-b).

		February Long Term Maximum Temperature	15 Feb 2016 Maximum Temperature	16 Feb 2016 Maximum Temperature	17 Feb 2016 Maximum Temperature	18 Feb 2016 Maximum Temperature	19 Feb 2016 Maximum Temperature	February Maximum Temperature after 15-19 Feb 2016
CENTRAL ANATOLIAN REGION	AKSARAY	21,6						
	AKŞEHİR	20,2		22,3				
	ANKARA	20,4		20,5	20,6			
	CİHANBEYLİ	20,0		22,4				22,4
	ÇANKIRI	22,0						22,0
	ESKİŞEHİR	22,3						22,3
	GEMEREK	19,8						19,8
	KANGAL	15,6						15,6
	KARAMAN	22,1						22,1
	KARAPINAR	22,3						22,3
	KAYSERİ	22,6						22,6
	KIRIKKALE	21,4						21,4
	KIRŞEHİR	20,6			20,6			
	KONYA	23,8						23,8
	NEVŞEHİR	18,8					19,3	
	NİĞDE	20,4						
	POLATLI	20,0		20,2				
	SİVAS	18,1						18,1
	SİVRİHİSAR	19,9		20,8				20,8
	ULUKIŞLA	19,2						
	YOZGAT	17,3			18,5			18,5

Figure 10. Long term maximum temperature, new maximum temperature occurred between 15 and 19 February in 2016 and their values by stations in the Central Anatolian Region (TSMS, 2016-b).

In the Blacksea Region: Maximum temperatures set a new record at 5 meteorological stations, including Amasra, Artvin, Bolu, Duzce and Sinop in February. Corum station repeated their long term value. (Fig. 11; 12).

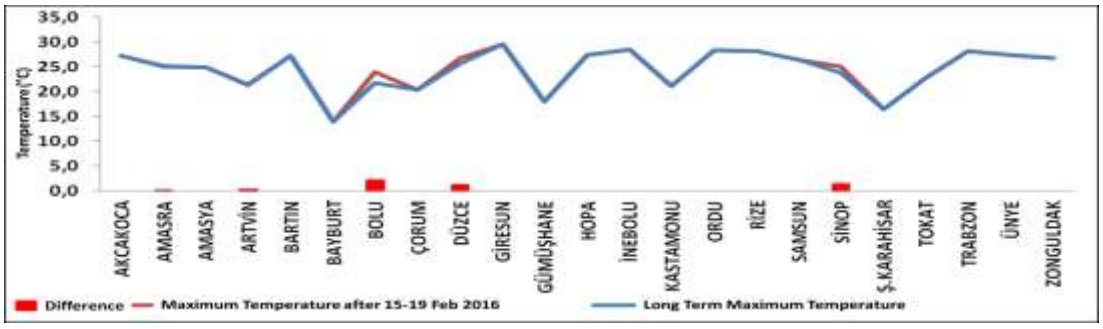

Figure 11. Long term maximum temperature, new maximum temperature occurred between 15 and 19 February in 2016 and their differences in the Blacksea Region (TSMS, 2016-b).

		February Long Term Maximum Temperature	15 Feb 2016 Maximum Temperature	16 Feb 2016 Maximum Temperature	17 Feb 2016 Maximum Temperature	18 Feb 2016 Maximum Temperature	19 Feb 2016 Maximum Temperature	February Maximum Temperature after 15-19 Feb 2016
BLACKSEA REGION	AKCAKOCA	27,2						27,2
	AMASRA	25,0		25,1				25,1
	AMASYA	24,8						24,8
	ARTVİN	21,2	21,5					21,5
	BARTIN	27,2						27,2
	BAYBURT	13,9						13,9
	BOLU	21,8		23,9		24,0		24,0
	ÇORUM	20,4				20,4		20,4
	DÜZCE	25,6		26,8				26,8
	GİRESUN	29,5						29,5
	GÜMÜŞHANE	18,0						18,0
	HOPA	27,3						27,3
	İNEBOLU	28,4						28,4
	KASTAMONU	21,1						21,1
	ORDU	28,3						28,3
	RİZE	28,1						28,1
	SAMSUN	26,5						26,5
	SİNOP	23,7		25,0				25,0
	Ş.KARAHİSAR	16,4						16,4
	TOKAT	22,8						22,8
	TRABZON	28,2						28,2
	ÜNYE	27,3						27,3
	ZONGULDAK	26,7						26,7

Figure 12. Long term maximum temperature, new maximum temperature occurred between 15 and 19 February in 2016 and their values by stations in the Blacksea Region (TSMS, 2016-b).

In the Eastern Anatolia Region: Maximum temperatures set a new record at 3 meteorological stations, including Elazıg, Hakkari and Malatya in February. Sarıkamıs station repeated their long term value (Fig. 13; 14).

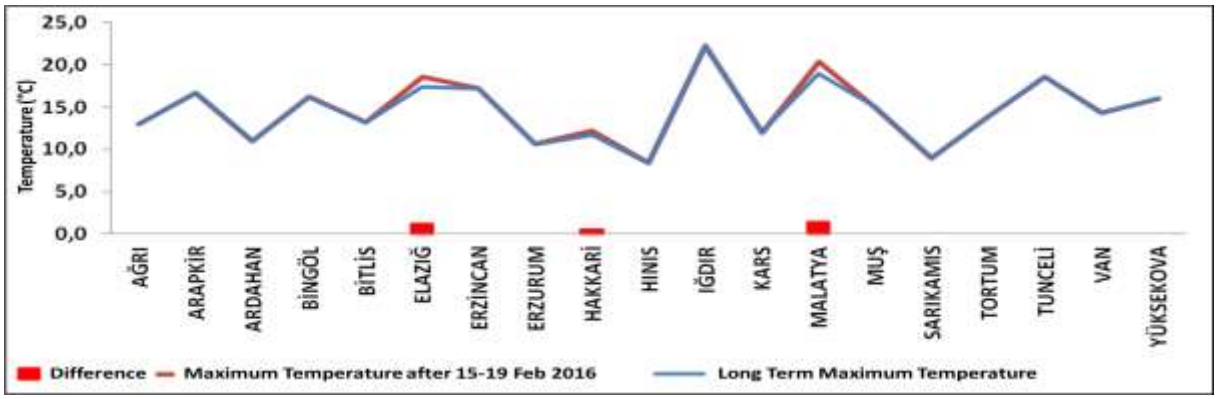

Figure 13. Long term maximum temperature, new maximum temperature occurred between 15 and 19 February in 2016 and their differences in the Eastern Anatolia Region (TSMS, 2016-b).

		February Long Term Maximum Temperature	15 Feb 2016 Maximum Temperature	16 Feb 2016 Maximum Temperature	17 Feb 2016 Maximum Temperature	18 Feb 2016 Maximum Temperature	19 Feb 2016 Maximum Temperature	February Maximum Temperature after 15-19 Feb 2016
EASTERN ANATOLIAN REGION	AĞRI	13,0						13,0
	ARAPKİR	16,7						16,7
	ARDAHAN	11,0						11,0
	BİNGÖL	16,2						16,2
	BİTLİS	13,2						13,2
	ELAZIĞ	17,4			18,2	18,6		18,6
	ERZİNCAN	17,2						17,2
	ERZURUM	10,6						10,6
	HAKKARİ	11,7		12,2				12,2
	HINIS	8,4						8,4
	IĞDIR	22,2						22,2
	KARS	12,0						12,0
	MALATYA	18,9			19,0	20,3		20,3
	MUŞ	15,0						15,0
	SARIKAMIS	9,0			9,0			9,0
	TORTUM	13,9						13,9
	TUNCELİ	18,6						18,6
	VAN	14,3						14,3
	YUKSEKOVA	16,0						16,0

Figure 14. Long term maximum temperature, new maximum temperature occurred between 15 and 19 February in 2016 and their values by stations in the Eastern Anatolia Region (TSMS, 2016-b).

In the Southeast Anatolia Region: Maximum temperatures set a new record at 7 meteorological stations, including Adiyaman, Diyarbakir, Gaziantep, Kilis, Mardin, Siverek and Sanlıurfa in February (Fig. 15; 16).

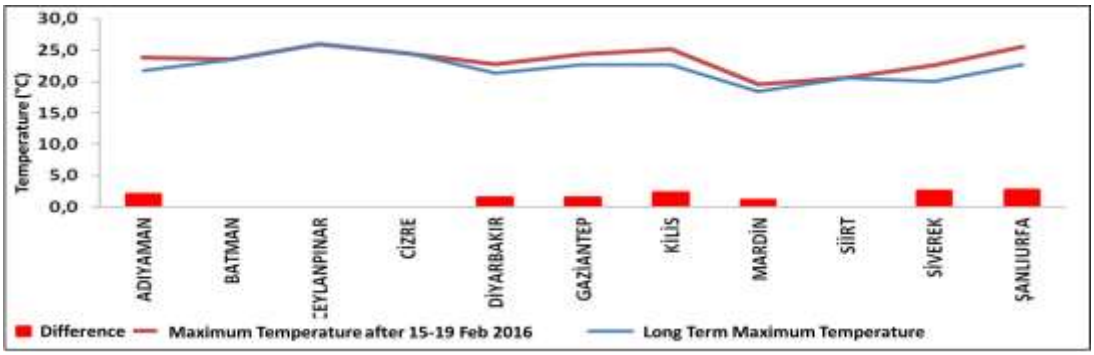

Figure 15. Long term maximum temperature, new maximum temperature occurred between 15 and 19 February in 2016 and their differences in the Southeast Anatolia Region (TSMS, 2016-b).

		February Long Term Maximum Temperature	15 Feb 2016 Maximum Temperature	16 Feb 2016 Maximum Temperature	17 Feb 2016 Maximum Temperature	18 Feb 2016 Maximum Temperature	19 Feb 2016 Maximum Temperature	February Maximum Temperature after 15-19 Feb 2016
SOUTHEAST ANATOLIAN REGION	ADIYAMAN	21,7		23,8		23,8		23,8
	BATMAN	23,5						23,5
	CEYLANPINAR	26,0						26,0
	CİZRE	24,5						24,5
	DİYARBAKIR	21,3			22,8			22,8
	GAZİANTEP	22,7				24,1		24,1
	KİLİS	22,7		25,0		25,1		25,1
	MARDİN	18,4			19,5			19,5
	SİİRT	20,6						20,6
	SİVEREK	20,0		20,2	21,2	22,6		22,6
	ŞANLIURFA	22,7		23,3	24	25,5		25,5

Figure 16. Long term maximum temperature, new maximum temperature occurred between 15 and 19 February in 2016 and their values by stations in the Southeast Anatolia Region (TSMS, 2016-b).

CONCLUSIONS AND RECOMMENDATIONS

In a line with climate change, global mean temperature continue to rise. Almost every year and every month has signed a new record especially for two decades. A change in the Earth's surface temperature also leads to increase in extreme events as well as extreme temperatures. Increasing in magnitude, severity and duration of extreme temperature events are harmful to both as the ecosystem and on human health. Human influence has also led to significant regional temperature increases at the continental and subcontinental levels. Humans cannot realise heatwaves impact which occurs in winter, spring and autumn as much as ecosystems and habitats. Due to heatwaves are occurred and continued end of winter or early spring; the nature waking up earlier, trees are blooming earlier then their blooming time and so on. Then short term cold weather or winter are appearing and harmful to trees. Other issue is snow layers on mountain are starting to melt earlier with heatwaves.

Turkoglu et al. (2016) conclude that in Turkey, positive temperature anomalies have been observed since 1994 until present days. Negative relationships were found between phenological periods of apple, cherry and wheat and the average temperatures of February-May period when the plants grow faster. This situation shows that the plants shift their phenological periods to the earlier times in response to the increasing temperatures.

Demircan et al. (2017) concluded that probability of occurring maximum temperature in certain time interval in a month may show a pattern in month and also the pattern is inclined to change with increasing temperature trend due to climate change. Daily maximum temperatures were increasing about 12 to 17 days in February since 1981. They offered third week of February is possible heatwave occurring time according to the long terms patterns and heatwave occurred in February 2016 was appropriated with this pattern.

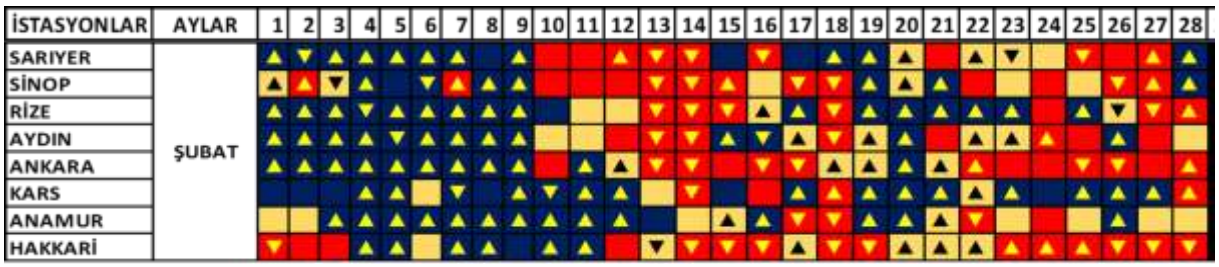

Figure 3. Monthly pattern of daily extreme maximum temperatures. (According to 1971-2000 term; Red= Warm, Blue= Cold, Yellow= normal; according to 1981-2015 term; increasing=▲, decreasing=▼) (Demircan et al., 2017)

REFERENCES

WMO-No. 1189, WMO Statement on the State of the Global Climate in 2016, World Meteorological Organization, 2017

TT-DEWCE WMO, Guidelines on the Definition and Monitoring of Extreme Weather and Climate Events, draft version – first review by TT-DEWCE, December 2015

IPCC, Glossary of terms. In: Managing the Risks of Extreme Events and Disasters to Advance Climate Change Adaptation [Field, C.B., V. Barros, T.F. Stocker, D. Qin, D.J. Dokken, K.L. Ebi, M.D. Mastrandrea, K.J. Mach, G.-K. Plattner, S.K. Allen, M. Tignor, and P.M. Midgley (eds.)]. A Special Report of Working Groups I and II of the Intergovernmental Panel on Climate Change (IPCC). Cambridge University Press, Cambridge, UK, and New York, NY, USA, pp. 555-564, 2012.

Intergovernmental Panel on Climate Change (IPCC): Summary for policymakers. In: Climate change 2013: The physical science basis. Contribution of working group I to the fifth assessment report of the intergovernmental panel on climate change. Cambridge and New York: Cambridge University Press, 2013.

Perkins, S.E., L.V. Alexander and J.R. Nairn, Increasing frequency, intensity and duration of observed heatwaves and warm spells. Geophys. Res. Lett., 39, L20714. doi: 10.1029/2012GL053361, 2012.

WMO-No. 1142, Heatwaves and Health: Guidance on Warning-System Development, World Meteorological Organization and World Health Organization, 2015
Frich, A.; L.V. Alexander, P. Della-Marta, B. Gleason, M. Haylock, A.M.G. Klein Tank, and T. Peterson (January 2002). "Observed coherent changes in climatic extremes during the second half of the twentieth century" (PDF). Climate Research 19: 193–212. doi:10.3354/cr019193
Coşkun, M., Sümer, U.M., Ulupınar, Y., Şensoy, S., Demircan, M., Bölük, E., Arabacı, H., Eskioğlu, O., Kervankıran, S., State of the Climate in Turkey in 2016, Turkish State Meteorological Service, 2017
Unal, Y.S., E. Tan, and S.S. Mentes, Summer heat waves over western Turkey between 1965 and 2006, Theor. Appl. Climatol. 112, 1-2, 339-350, DOI: 10.1007/s00704-012-0704-0, 2013.
Turkish State Meteorological Service, Temperature Analysis of February 2016, https://www.mgm.gov.tr/FILES/Haberler/2016/subat2016.pdf, 2016 (a)
Turkish State Meteorological Service, Extreme Temperature between 15 and 19 February in 2016, https://www.mgm.gov.tr/FILES/iklim/subat-rekor.pdf, 2016 (b)
Türkoğlu, N., Şensoy, S. and Aydın, O.; Effects of climate changes on phenological periods of apple, cherry and wheat in Turkey, Journal of Human Sciences, Vol 13, No 1, DOI: https://doi.org/10.14687/ijhs.v13i1.3464, 2016
Demircan, M., Arabaci, H., Coskun, M., Turkoglu, N., Cicek, I., Climate Change and Public Calendar: Maximum Temperature Patterns and It's Change, Turkey Climate Change Congress - TCLCC'2017 5-7 July 2017, Istanbul, Turkey

DIURNAL VARIATION OF VOLATILE ORGANIC COMPOUND CONCENTRATIONS IN SUBURBAN ANKARA ATMOSPHERE

Elif Sena Uzunpınar[1], Ezgi Sert[1], Seda Aslan Kılavuz[2], İpek İmamoğlu[1], Gürdal Tuncel[1]
[1]Middle East Technical University, Department of Environmental Engineering
sena@metu.edu.tr
[2]Kocaeli University, Department of Environmental Engineering
sedaaslan@kocaeli.edu.tr

Abstract
Volatile Organic Compounds (VOCs) are released from both natural and anthropogenic sources into the atmosphere. They are a very important group of organic compounds, as they have adverse impacts on photochemical ozone formation, on human health and on ecology. Due to these effects, knowing their concentrations under different atmospheric conditions is essential. In this study, concentrations of 55 U.S.EPA – Photochemical Assessment Monitoring Stations (PAMS) VOCs were measured in suburban METU campus, with one-hour intervals, to determine their levels and sources contributing to their measured concentrations in Ankara atmosphere. High resolution data is provides an advantage in source apportionment studies. The VOC concentrations were measured using an online GC-FID system during summer and winter seasons. In summer, hourly measurements were conducted in August, 2014 and in winter, measurements were conducted in October, and November, 2013. Four different patterns of diurnal variations were observed in VOC concentrations. The first group included VOCs those have peak concentration during traffic rush hours. The second group includes solvent-based VOCs, which does not show a diurnal variation. The third group of VOCs have maximum concentrations during morning rush hour, but do show a similar maxima in afternoon rush hour. Finally the fourth group included VOCs that high concentrations during day-time, which decreases significantly at night. These four patterns suggest that traffic related sources, solvent usage and gasoline evaporation are dominant VOC contributors and meteorological parameters have a significant role in the measured concentrations.

Keywords: *VOC, METU, Ankara, Suburban, Diurnal variation*

INTRODUCTION
Different definitions of volatile organic compounds (VOCs) in the literature suggest that these organic compounds includes a very wide range of organic chemical compounds. Therefore, VOCs can include low boiling point compounds with different functional groups, such as aldehydes, ketones, carbonyls, halocarbons and non-methane hydrocarbons (NMHCs). The U.S. Environmental Protection Agency has also decided to measure fifty-five $C_2 – C_{12}$ NMHCs that are ozone precursors at Photochemical Assessment Monitoring Stations (U.S.EPA – PAMS).

Volatile Organic Compounds are emitted from both anthropogenic (motor vehicle exhaust, industrial processes, combustion, evaporation etc.) and natural (plants, oceans, soil and sediments, organic matter decomposition etc.) sources. Although global emissions of biogenic VOCs are much higher compared to anthropogenic ones [1] the rate of anthropogenic emissions continues to increase. Moreover, impact of these compounds on human health (cancer, respiratory diseases and stroke etc.), on vegetation (growth inhibition, cutting of the leaves and discoloration etc.) and on atmospheric composition (secondary organic aerosol and tropospheric ozone formation, and for some VOCs ozone layer degradation) makes the control of these sources a priority.

In this study, hourly concentrations of 55 U.S.EPA – Photochemical Assessment Monitoring Stations (PAMS) VOCs were measured in suburban METU campus to; (1) determine concentrations of these compounds in suburban area and (2) determine sources that are contributing to their measured concentrations. Air samples were collected and analyzed by a GC-FID system operated in online mode during summer and winter seasons. During summer, measurements were conducted in August, 2014 and in winter, measurements were conducted for two months in October and November, 2013.

DATA AND METHODS

Air samples were collected in Middle East Technical University Environmental Engineering Department (39°53'13.04"N, 32°46'59.19"E), which is located at a sub-urban area approximately 8 km from the Ankara city center. Ankara, which is the capital of Turkey, is the second most populated city in the country, with a population of approximately 5 million. Air samples were collected by GC-FID system (Agilent, model XX) operated in online mode during summer and winter seasons. In this system VOCs in the air is collected on a trap for 45 min by passing air through the trap at a flow rate of 10 mL min^{-1}. At the end of 45-min sampling period, the trap is heated and VOCs collected on the trap is fed to the GC column. While the chromatogram is generated in the GC, a new cycle of sample collection was started at the trap. In this way, hourly measurement continued without interruption. Fifty-five VOCs were measured in each hourly cycle.

Summer measurements was performed in August, 2014 and winter measurements were carried out in October, and November, 2013. Approximately 1000 hourly samples were collected and analyzed for summer and winter seasons in total.

RESULTS AND DISCUSSIONS

In order to observe the hourly concentration variations, average concentrations for each compound were calculated and plotted against the hours of day. Diurnal variations of VOC concentrations resulting from changes of emissions and meteorological parameters such as wind speed and mixing height show four different patterns. The first pattern is represented by benzene in Figure 1. Benzene is a vehicle exhaust marker [2], [3], [4]. It shows a very significant peak during morning hours and starts to decrease from 11:00 A.M. up to 05:00 P.M. After 05:00 PM it increases again but not as much as in the morning. Even though this pattern shows very similar trend with traffic pattern, explaining this increase and decrease with traffic before and after work hours would not be enough. If it was the only explanation, two peaks should have shown the similar heights. Nevertheless, as it can be seen from the benzene concentrations, second peak is rather broad and not like a peak. Lower concentrations of Benzene and other traffic markers during afternoon rush hour is due to higher mixing height during afternoon rush hour, compared to morning rush hour. Therefore, it would be logical to explain the diurnal concentration variations because of both changes in emissions and the changes in mixing height and ventilation coefficients.

Although traffic emissions decrease to very low levels during night hours, concentrations of benzene and other traffic markers do not drop to expected very low levels at night. This diurnal pattern is probably a result of accumulation of traffic-related VOCs from previous day and low mixing height and ventilation coefficient during night-time.

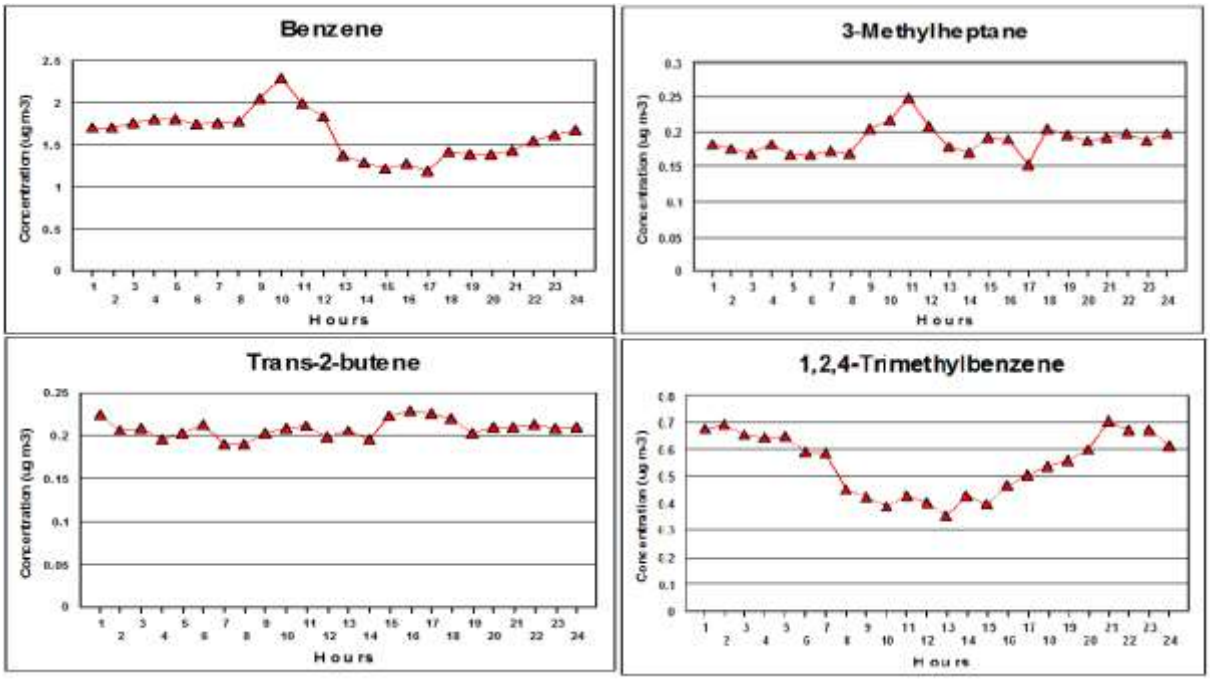

Figure 14: Diurnal variations of Benzene (pattern 1), Trans-2-butene (pattern 2), 3-Methylheptane (pattern 3) and 1,2,4-Trimethylbenzene (pattern 4).

The second pattern is represented with trans-2-butene in Figure 1. Trans-2-butene is associated with vehicle exhaust [4] and gasoline evaporation [5], [6]. Even though, the compounds in these patterns are mostly related with traffic-based sources, the pattern in this study does not shoes parallel trend with diurnal traffic variation. This indicates that the majority of the emissions of these compounds are due to non-traffic sources.

The third pattern is represented in the Figure 1 as 3-methylheptane. 3-methylheptane is released from petroleum product emissions [7], [8] in this pattern (3-methylheptane and 2 methylhexane) are mostly released from incomplete combustion, gasoline evaporation and refineries. They also show good correlation with each other and BTEX compounds [9].

The final pattern is represented by 1,2,4-trimethylbenzene (Figure1). This compound is associated with vehicle exhausts [7], [8], [10], [11] and it is very different from the rest. Concentrations are increasing between 12:00 A.M. – 12:00 P.M. and starting to decrease gradually. These different patterns for mostly traffic related compounds can be resulting from meteorological effects, photochemistry and non-traffic sources [6]. However, factor analysis should be performed to determine the sources of these compounds.

CONCLUSIONS

Measurement of hourly VOC concentrations during summer and winter seasons revealed four different patterns. Although METU campus is considered as sub-urban area, the dominant pattern is found to be following traffic emissions. While majority of the compounds follow this pattern, for others the contribution of sources other than traffic was also observed. Moreover, the impact of the meteorological conditions and the photochemistry on the measured concentrations and observed patterns was obvious. Therefore, identification of the emission sources should be backed up by factor analysis and meteorological conditions should not be disregarded during source identification.

REFERENCES

[1] Atkinson, R.; Arey, J. Gas-Phase Tropospheric Chemistry of Biogenic Volatile Organic Compounds: A Review. *Atmos. Environ.* 2003, *37* (2), 197–219.

[2] Watson, J. G.; Chow, J. C.; Fujita, E. M. Review of Volatile Organic Compound Source Apportionment by Chemical Mass Balance. *Atmos. Environ.* 2001, *35* (9), 1567–1584.

[3] Parra, M. a; González, L.; Elustondo, D.; Garrigó, J.; Bermejo, R.; Santamaría, J. M. Spatial and Temporal Trends of Volatile Organic Compounds (VOC) in a Rural Area of Northern Spain. *Sci. Total Environ.* 2006, *370* (1), 157–167.

[4] Cai, C.; Geng, F.; Tie, X.; Yu, Q.; An, J. Characteristics and Source Apportionment of VOCs Measured in Shanghai, China. *Atmos. Environ.* 2010, *44* (38), 5005–5014.

[5] Schauer, J. J.; Rogge, W. F.; Hildemann, L. M.; Mazurek, M. A.; Cass, G. R.; Simoneit, B. R. T. Source Apportionment of Airborne Particulate Matter Using Organic Compounds as Tracers. *Atmos. Environ.* 1996, *30* (22), 3837–3855.

[6] Yurdakul, S. Temporal Variation of Volatile Organic Compound Concentrations in Bursa Atmosphere, Middle East Technical University, 2014.

[7] Badol, C.; Locoge, N.; Léonardis, T.; Galloo, J.-C. Using a Source-Receptor Approach to Characterise VOC Behaviour in a French Urban Area Influenced by Industrial Emissions. Part I: Study Area Description, Data Set Acquisition and Qualitative Data Analysis of the Data Set. *Sci. Total Environ.* 2008a, *389* (2-3), 441–452.

[8] Liu, Y.; Shao, M.; Fu, L.; Lu, S.; Zeng, L.; Tang, D. Source Profiles of Volatile Organic Compounds (VOCs) Measured in China: Part I. *Atmos. Environ.* 2008, *42* (25), 6247–6260.

[9] Chang, C.-C.; Wang, J.-L.; Liu, S.-C.; Candice Lung, S.-C. Assessment of Vehicular and Non-Vehicular Contributions to Hydrocarbons Using Exclusive Vehicular Indicators. *Atmos. Environ.* 2006, *40* (33), 6349–6361.

[10] Civan, M. Y.; Kuntasal, Ö. O.; Tuncel, G. Source Apportionment of Ambient Volatile Organic Compounds in Bursa, a Heavily Industrialized City in Turkey. *Environ. Forensics* 2011, *12* (4), 357–370.

[11] Dumanoglu, Y.; Kara, M.; Altiok, H.; Odabasi, M.; Elbir, T.; Bayram, A. Spatial and Seasonal Variation and Source Apportionment of Volatile Organic Compounds (VOCs) in a Heavily Industrialized Region. *Atmos. Environ.* 2014, *98*, 168–178.

ATMOSPHERIC DISPERSION AND DOSE/RISK ESTIMATION OF 137CS RELEASED FROM A POTENTIAL ACCIDENT IN AKKUYU NUCLEAR POWER PLANT, TURKE

Efem Bilgic[1], Orhan Gunduz[2]
[1]Dokuz Eylul University Graduate School of Natural and Applied Sciences, Izmir, TURKEY
efem.bilgic@deu.edu.tr
[2]Dokuz Eylul University Department of Environmental Engineering Izmir, TURKEY
orhan.gunduz@deu.edu.tr

Abstract
Turkey plans to build the 4800 MW (4x 1200) installed capacity Akkuyu Nuclear Power Plant (NPP) in the Province of Mersin along its Mediterranean coastline. Prior to its commissioning, a modeling study was conducted to simulate the atmospheric dispersion and deposition of Cs-137 to be released from a possible nuclear power plant accident in the proposed plant. In addition to atmospheric modeling, ground level dose/risk calculations were made for Cs-137 to assess the extent of contamination along the areas that will be potentially exposed to radioactive nucleoids. Atmospheric dispersion and deposition simulations were conducted with a Lagrangian Particle transport and dispersion model (FLEXPART) with 6 hourly 0.5°x0.5° meteorological input data obtained from NCEP/NCAR Reanalysis data set. A total of six scenarios were specified for 3 different source terms and 2 distinct time periods representing extreme meteorological conditions. The results obtained from the simulations were then processed with MATLAB to obtain dose and risk values associated with each scenarios and spatial distribution maps were created. The risk outcomes were later compared with those of other NPP accidents.

Keywords: *Atmospheric dispersion, radionuclides, dose, risk, akkuyu nuclear power plant.*

INTRODUCTION
The 4800 MW installed capacity Akkuyu Nuclear Power Plant (NPP) is planned to be constructed in the Province of Mersin along the Mediterranean coastline of Turkey. It is announced that the first unit of Akkuyu NPP will start to operate in 2021 (MENR, 2017). Although there is a widespread belief that generation of electricity from nuclear energy is economical, there is also a significant social opposition against nuclear power plants, especially on the grounds that the environmental impacts are very high. It would not be wrong to predict that these discussions will continue for a long time considering the catastrophic impacts that may be caused by possible accidents as well as the environmental impacts that may be caused by operational practices. Chernobyl accident happened due to personal operational mistakes and its effect was devastating because of the old technology used in the plant. Nevertheless, the accident that occurred in the Fukushima Daichi Nuclear Power Plant, which had an advanced technology compared to Chernobyl, was due to the consequences of a natural disaster. These cases demonstrate that nuclear power plants will always carry significant accident risks despite the development of cutting-edge security technologies. Based on these fundamentals, this study aims to identify and assess the atmospheric dispersion, deposition and effects of radionuclides to be released from Akkuyu NPP project in case of potential accidents under various scenario conditions.

MODELING METHODOLOGY, DATA AND APPLICATION
Atmospheric dispersion and deposition simulations were conducted with a Lagrangian Particle transport and dispersion model (FLEXPART) with 6 hourly 0.5°x0.5° meteorological input

data obtained from NCEP/NCAR Reanalysis data set. FLEXPART can simulate the long-range and mesoscale transport, diffusion, dry and wet deposition, and radioactive decay of tracers released from point, line, area or volume sources (Stohl et al., 2005). The model results were then processed with MATLAB software to obtain dose and risk values associated with each scenario. International Atomic Energy Agency equations were used for dose and risk estimations (IAEA, 2000). The risk outcomes were compared with those of Chernobyl and Fukushima NPP accidents to have an overall understanding of the extent of an accident and the damage it could create. Finally, spatial distribution maps were generated by ArcGIS software.

RESULTS AND DISCUSSIONS

A total of six scenarios were specified for 3 different source terms. The source terms used in this study were taken as the source term of a similar VVER-1200 reactor (Nalbandyan et al., 2012) and the source terms of Chernobyl and Fukushima NPP accidents. The study covered 2 distinct time periods representing extreme meteorological conditions of December 2009 and August 2010. All scenarios were simulated for two different time periods which represented distinct meteorological conditions and seasonal patterns. The atmospheric motion in Akkuyu region was found to be mainly towards south in August 2010 (Figure 1), which clearly represented summer conditions with the hottest and driest period of the year. Thus, the total ground level depositions of ^{137}Cs were found to be higher in the south territories of the study area when compared to the northern regions, thus verifying the characteristic southerly movement pattern of the atmospheric motion. On the other hand, atmospheric motion was found to be mostly towards north and northeast direction in December 2009, which represented winter conditions with the highest precipitation values and relatively stormy period of the year. Consequently, the total ground depositions of ^{137}Cs were simulated to be higher in the northern territories of the study area compared to the south in parallel to the direction of the atmospheric motion.

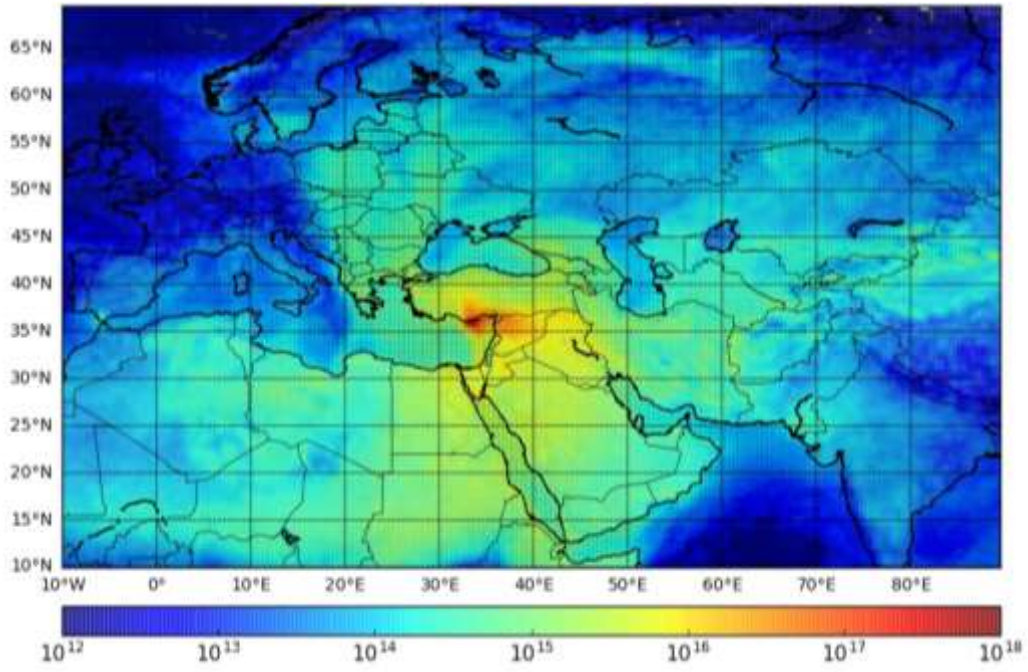

Figure 1. Total ground deposition of ^{137}Cs released from Akkuyu NPP in August 2010 for Chernobyl source term (pBq/m^2)

The results also revealed that as ^{137}Cs input (source term) were increased, ^{137}Cs concentrations in the air as well as the ground depositions were also increased. While the maximum ^{137}Cs

concentrations in the air were in the order of 10^2 Bq/m^3 for first source term (Nalbandyan et al., 2012), the maximum ^{137}Cs concentrations were in the order of 10^3 - 10^4 Bq/m^3 for the second and third source terms (Chernobyl and Fukushima accidents). Maximum ground deposition values of ^{137}Cs occurred around the Akkuyu NPP was in the order of 10^5 Bq/m^2 for the first source term. For other source terms, maximum ground deposition values were found to be even higher with values reaching to the order of 10^6 Bq/m^2. Based on these values, dose values for a month around the Akkuyu NPP reached 572 mSv for Chernobyl source term (Figure 2).

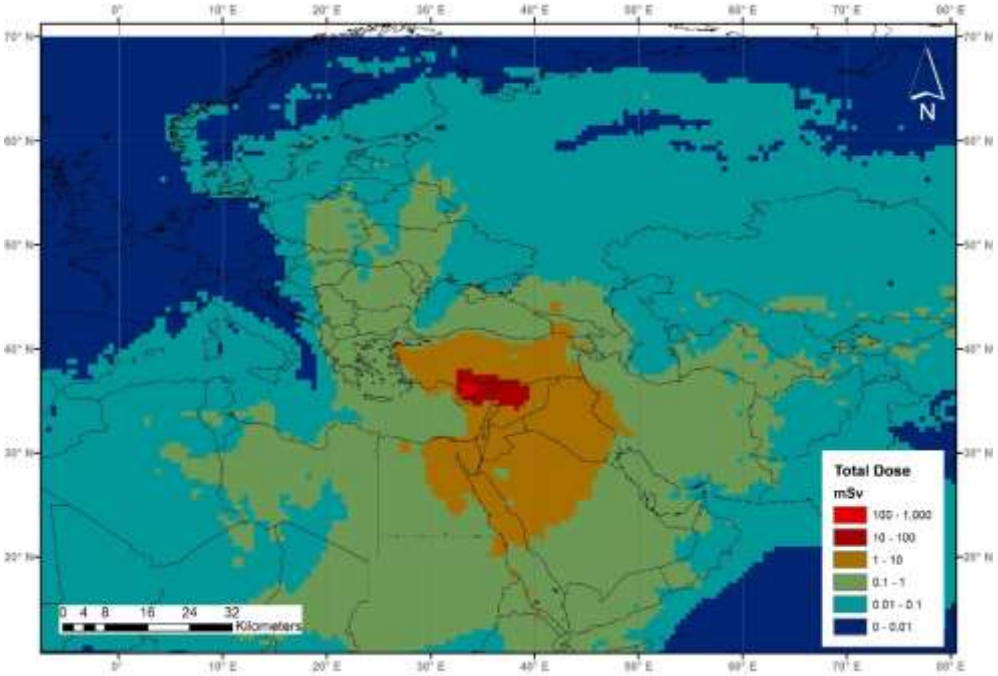

Figure 2. Total dose value of ^{137}Cs originating from potential Akkuyu NPP accident in August 2010 for Chernobyl source term (31 August 2010)

CONCLUSIONS AND RECOMMENDATIONS

The simulation of a potential accident in Akkuyu NPP site revealed the fact the expected impacts will be a strong function of instantaneous meteorology of the site and its immediate vicinity. Thus, the seasonal time of occurrence of the accident will influence the area and the population to be impacted from the catastrophe. Being located in the southernmost parts of the Anatolian peninsula, a potential accident in Akkuyu NPP during summer will likely influence the island of Cyprus, the northern parts of Africa and the Middle East whereas an accident in winter will most likely impact the Anatolian peninsula, Black Sea and southeastern parts of Europe. Further research is necessary to develop novel tools for assessing the risk likelihoods of areas to be influenced under distinct extreme conditions as well as stable long term patterns of regional meteorology. The study also revealed that the source term used in the model strongly influences the simulation results. Thus, an official source term value of the reactors of Akkuyu NPP should be accurately documented and released for scientific studies such as the one presented herein. Finally, the results of this study clearly demonstrated the fact that nuclear power plant accidents influence not only its country of origin but also its neighbouring countries and regions. Therefore, nuclear energy politics of countries should be clear for the international community and an ultimate international consensus should always be searched for due to cross border effects of potential detrimental catastrophes.

REFERENCES

IAEA (International Atomic Energy Agency), 2000. Generic procedures for assessment and response during a radiological emergency, *International Atomic Energy Agency*. Retrieved June 6, 2017, from http://www-pub.iaea.org/MTCD/Publications/PDF/te_1162_prn.pdf.

MENR (Republic of Turkey Ministry of Energy and Natural Resources), 2017. Akkuyu Nuclear Power Plant, *Republic of Turkey Ministry of Energy and Natural Resources.* Retrieved June 6, 2017, from http://nepud.enerji.gov.tr/tr-TR/Sayfalar/Akkuyu-Nukleer-Guc-Santrali-----.

Nalbandyan, A., Ytre-Eide, M., Thørring, H., Liland, A., Bartnicki, J., Balonov, M., 2012. *Potential consequences in Norway after a hypothetical accident at Leningrad nuclear power plant. Potential release, fallout and predicted impacts on the environment.* Statens Straalevern. Retrieved July 15, 2016, from http://www.nrpa.no/dav/5a90fe6c50.pdf.

Stohl, A., Forster, C., Frank, A., Seibert, P., Wotawa, G., 2005. Technical note: The Lagrangian particle dispersion model FLEXPART version 6.2., *Atmospheric Chemistry and Physics*, 5, 2461-2474.

EVALUATION OF A THERMAL DESORPTION METHOD FOR COMPLETE CHARACTERIZATION OF ORGANIC AEROSOLS

A.E. Gok[1], R.M. Flores[1], H. Ozdemir[2], B. Akkoyunlu[1], G. Demir[3], A. Unal[4], M. Tayanc[1]

[1] *Environmental Engineering Department, Marmara University Göztepe Campus, 34722, Istanbul, TURKEY.*
rflores@marmara.edu.tr, akingok@marun.edu.tr, bulentoktay@marmara.edu.tr, mtayanc@marmara.edu.tr

[2] *Istanbul Technical University, Maslak, 34469, Istanbul, TURKEY*
ozdemirhuseyin@itu.edu.tr

[3] *Department of Urban and Regional Planning, Kirklareli University, TURKEY*
goksel.demir@klu.edu.tr

[4] *Climate and Sea Sciences Department, Eurasia Institute of Earth Sciences, Istanbul Technical University, Maslak 34469, Istanbul, TURKEY*
alper.unal@itu.edu.tr

Abstract

Organic aerosols (OA) have an important role in human health, ecosystems, and climate change. Black carbon and organic aerosol affect Earth's radiation balance by absorbing and scattering light. In addition, organic aerosol affects cloud formation and lifetime by acting as cloud condensation nuclei, thereby altering the water cycle. Uncertainties of their impacts are large due to gaps in knowledge regarding emission sources, change in composition with respect to time, and participation in chemical reactions. Studies of organic aerosol composition are generally performed every 24 h. These studies lack the necessary temporal resolution to understand sources, kinetics, transport and transformation, and effects on human health. In Turkey, chemical speciation of organic aerosol has been scarcely studied. Collection of high-time resolved samples is necessary due to high reactivity of the organic compounds. In this work, we developed an on-line thermal desorption-gas chromatography-mass spectrometer (TD-GC-MS) method that allows complete identification and quantification of semi-volatile organic compounds in high-time resolved ambient air samples. The method is tested with 24 $PM_{2.5}$ (particulate matter smaller than 2.5 μm) samples collected every two hours from 700h to 1900h. The sampling site is located in Beşiktaş, Istanbul, in a traffic-influenced area. Preliminary results show the identification of 16 PAH and 28 n-alkanes. It was also observed that the receptor site is strongly dependent on traffic density variations during weekend/weekdays and during the day. Qualitative and quantitative analysis of OA composition is presented during the weekend and weekdays and with meteorological conditions such as temperature, solar radiation, and air mass trajectories.

Keywords: *Organic aerosol, thermal desorption, SVOCs, GC-MS, Istanbul*

INTRODUCTION

Air pollution is one of the biggest problems nowadays due to rising population and industry. Especially in Megacities, air pollution is a bigger problem due to a larger population. Megacities are defined as cities that have a population larger than 10 million. Istanbul (Turkey) is suitable for this definition with its more than 14 million population (UN 2015). Effects like unplanned urbanization, industrialization, atmospheric conditions, meteorological parameters, building, and population density are the reasons for the rise of air pollution. Istanbul is the most important city in Turkey and one of the most important cities of the world due to its geological transcontinental location, population, and industry. The main reasons for air pollution in Istanbul are (1) the excessive use of low quality fossil fuels for residential heating and transportation, (2) continuous expansion on industrial areas, (3) rising vehicle number and traffic, (4) insufficient green areas, and (5) unplanned urbanization (Tayanç 2000). Particulate Matter (PM) term defines the solid or liquid matter in microscopic sizes suspended in the air. Particulate matter can be generated both, through human activities and naturally; however, fine

particles emitted by human activities have more important effects on human health and climate change. The $PM_{2.5}$ term defines particles with diameter smaller than 2.5 μm and the increased concentrations are of special concern because these particles move through the respiratory system and accumulate there (Weschler and Nazaroff 2008). $PM_{2.5}$ particles contain organic and elemental carbon, trace metals, sulfates, nitrates, minerals and oxidized forms of these minerals (Ding, Chan et al. 2014). The composition and relative abundance of PM vary according to its origin. Thus, organic compounds comprise a large fraction of the atmospheric aerosol mass in the range 20-90%. These organic compounds can contain numerous complex forms such as aromatics, alcohols, alkanes, and carboxylic acids; most of them toxic for life forms (Wendy Hsiao, Mo et al. 2000). Some of these compounds are named as semi volatile organic compounds (SVOC) and are generally identified as organic molecules that can be abundant in both the gas phase and condensed phase, represented by vapor pressures between 10^{-14} and 10^{-4} atm. SVOC origins are mainly due to human products such as cleaning agents, food packaging, clothing, furniture, electronics, and pesticides. Some SVOCs cause biological disorders and some kinds of cancer because of their ability to affect hormones in humans and wildlife. In addition, SVOCs can cause neurodevelopmental and behavioral problems and diseases like autism, reproductive abnormalities and metabolic disorders (Weschler and Nazaroff 2008).

Aerosols also have an important role in radiation balance and in the lifetime and properties of clouds by absorbing and scattering solar radiation (i.e., direct effect) and acting as cloud condensation nuclei, CCN, (i.e., indirect effect), respectively. The physicochemical properties of atmospheric aerosols determine their role at absorbing and scattering radiation. Atmospheric aerosols are in the size range close to the wavelength of the visible radiation (i.e., 0.39-0.7 μm). Thus, due to their longer lifetime in the atmosphere, fine aerosols are expected to have greater impact on climate change due to their interaction with solar radiation and water vapor. Black carbon (BC) absorbs radiation, therefore contributes to the warming of the atmosphere. On the other hand, most organic PM components are considered to cool the atmosphere (Kanakidou, Seinfeld et al. 2005). The indirect effect of aerosols is defined as the influence of aerosols on cloud albedo and cloud lifetime. Various physicochemical properties of aerosols determine the magnitude of the aerosol indirect effect. Some of these physicochemical properties include aerosol mass, concentration of organic compounds acting as CCN, concentration of organic compounds acting as ice nucleation (IN), ability of the organic compounds to partition into the water phase, cloud optical depth, among others (Penner, Andreae et al. 2001).

Semi-volatile organic compounds are highly reactive and contribute to the formation of secondary organic aerosol, SOA, (Derwent, Jenkin et al. 2010). Despite their active role on climate change and effects on ecosystems and human health, their sources, reaction mechanisms, removal processes, and climate and health effects are highly uncertain (Jimenez, Canagaratna et al. 2009). This lack of understanding is partly due to deficiency of suitable methodologies to quantitatively measure and identify the thousands of compounds with very different physicochemical properties that comprise the OA (Alves 2008).

In Turkey, continuous measurement of PM_{10} and $PM_{2.5}$ concentrations are available through the Ministry of Environment and Urbanization (http://mthm.havaizleme.gov.tr/secure/index2.htm). In Istanbul, PM_{10} concentrations are available in 28 stations. In contrast, only 4 stations are currently measuring $PM_{2.5}$ concentrations continuously (i.e., Çatladikapi, Kagithane, Silivri, and Umraniye). Currently, the average annual PM_{10} and $PM_{2.5}$ air quality standards are 50 and 12 $\mu g/m^3$, respectively. The air quality in Istanbul considerably improved in 1996 due to the establishment of natural gas

pipelines across the country and a regulation to use coal with less than 1.5% sulfur content (Tayanç 2000). However, it has been reported multiple times that average concentrations of PM_{10} continuously exceed the established limits (Karaca, Alagha et al. 2005, Unal, Toros et al. 2011, Erdun, Öztürk et al. 2015). In addition to PM_{10} and $PM_{2.5}$ concentrations, criteria pollutants in the gas phase (i.e., NO, NO_2, SO_2, CO, and O_3) are continuously monitored by the Ministry of Environment and Urbanization. However, detailed chemical speciation studies are limited (Karaca, Alagha et al. 2008). Specially, studies performed at high-time resolved intervals are not available.

Studies about SVOCs are generally performed every 24 h and many compounds are not included. Short sampling times are important because SVOCs are highly reactive. In Turkey, chemical speciation of organic aerosol has been scarcely studied (Karaca, Alagha et al. 2008, Ozdemir, Pozzoli et al. 2014). OC and EC concentrations in daily PM_{10} were studied for approximately 10 days in July 2008- June 2009 (Theodosi, Im et al. 2010). Concentrations of black carbon (BC) have been also investigated in Istanbul in the spring seasons of 2009 and 2010 (Ozdemir, Pozzoli et al. 2014). (Hanedar, Alp et al. 2014) studied the seasonal variation and sources of 16 PAHs in total suspended particles (TSP). (Kuzu, Saral et al. 2014) studied the concentration of 84 PCB during the summer and fall in the gas and particle phases.

Routine measurements of organic chemical composition require an initial method validation that provides quantitative, reliable, and accurate data. Results of method validation are also useful to continuously evaluate GC-MS results in a reliable and consistent manner. Method validation is also a requirement by governmental organizations that any analytical laboratory needs to follow (Huber 2010). Standard methods related to this project that will be followed are Environmental Protection Agency (EPA) SW-846 CH1 (Project Quality Assurance and Quality Control) and CH 4 (organic analytes), Method 8270D (SVOC analysis by GC-MS), TO-4A (determination of pesticides and PCBs using hi-volume sampler), TO-9A (determination of toxic organic compounds in ambient air), and TO-13A (determination of PAHs in ambient air using GC-MS).

DATA AND METHODS

Materials:

Semi-volatile organic compounds were obtained in the highest purity available as follows: (1) light aromatic compounds benzene, ethylbenzene, xylenes, naphthtalene, toluene, (2) PAH Acenaphthene, Acenaphthylene, Anthracene, Benz[a]anthracene, Benzo[a]pyrene, Benzo[b]fluoranthene, Benzo[ghi]perylene, Benzo[k]fluoranthene, Chrysene, Dibenz[a,h]anthracene, Fluoranthene, Fluorene, Indeno[1,2,3-cd]pyrene, Naphthalene, Phenanthrene, Pyrene, and (3) C_8-C_{40} n-alkanes.

$PM_{2.5}$ concentrations, Meteorological Data, and Traffic Data:

Meteorological data and air mass backward trajectories were obtained from weather underground and NOAA-HYSPLIT, respectively. The data reported here includes hourly temperature, wind speed, and solar radiation that were averaged for 2h to obtain conditions for each sample. Air mass backward trajectories were also obtained for two hours with the sampling location coordinates as the starting point at three heights 500, 1000, and 1500 m. Hourly $PM_{2.5}$ concentrations were provided by the Ministry of Environment and Urbanization of Turkey for Kagithane, Silivri, and Umraniye for 28-31 January 2017. Hourly $PM_{2.5}$ concentrations were used to calculate daily averages. Traffic density collected every minute was provided by the department of transportation in Istanbul (İBB trafik müdürlüğü) for sensor no. 263 which is

located approximately 460 m from our sampling location on Barbaros Bulvari. Total vehicle counts were calculated for each sample with time resolution of 2h.

TD-GC-MS:

The Markes Unity-xr thermal desorption unit (TDU) is connected to an Agilent 7890B gas chromatograph and an Agilent 5877E mass spectrometer (TD-GC-MS, Fig. 1) through a deactivated silica column. The GC-MS contains an Agilent DB5ms column with the following dimensions: 30m×0.25µm×0.25mm. The sample is inserted into a glass tube that is inserted in the tube oven section of the TDU. The TD-GC-MS process is as follows: (1) the tube oven heats at chosen temperature and time, (2) the volatile compounds are collected into a carbon trap at a chosen temperature, and (3) the compounds of interest are desorbed from the carbon trap at given temperature and time and transported to the GC-MS for speciation and quantification.

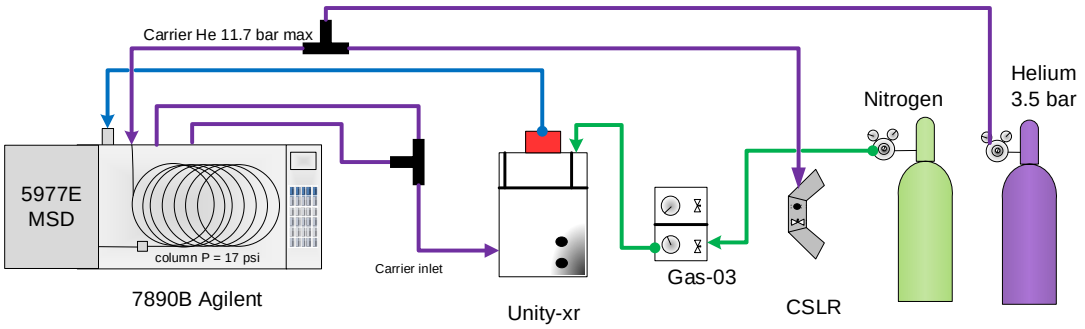

Figure 1. TD-GC-MS system

Method development:

In order to determine the best method conditions that provide the maximum recoveries of SVOCs, various parameters in the TDU and GC-MS were varied as follows: (1) trap desorption flowrate at 20, 30, 50, and 70 ml/min; (2) trap desorption temperature at 310, 320, and 360°C; (3) trap desorption time at 5, 7, and 10 min; (4) GC column pressure at 17 psi, 23 psi, and constant flow at 1.2 ml/min; and (5) trap sorption temperature at -15, 0, and 20°C.

Collection of high-time resolved samples:

In order to evaluate the effectivity of the TD-GC-MS method, $PM_{2.5}$ samples were collected every 2h between 7am and 7pm for four days from Saturday 28 January 2017 to Tuesday 31 January 2017. The sampling collection area is located in Beşiktaş as shown in Fig. 2.

Figure 2. Location of sampling and meteorological stations in Beşiktaş

RESULTS

Method development

Effect of trap desorption flowrate

Figure 3 shows the instrument response of 20 ng light aromatics, 10 ng n-alkanes, and 10 ng PAH at general conditions of 17 psi and desorption temperature 310°C for 5 min with different sample desorption flow rates of (a) 50, 70, 30, and 20 ml/min. Sample desorption flowrates are the same flowrates going through the trap (i.e., trap sorption flowrate). Overall, it can be observed very large aromatics peaks because the amount of aromatics spiked is 2× the n-alkanes and PAH. The best recoveries of lighter SVOCs was obtained at average flowrates of 30 and 50 ml/min. Middle volatility SVOCs did not show considerable improvements in recoveries. Better recoveries were observed for C32-C36 n-alkanes at 50 ml/min, however, C37-C40 n-alkanes and heavy PAH were poorly recovered. For our application, we chose 50 ml/min.

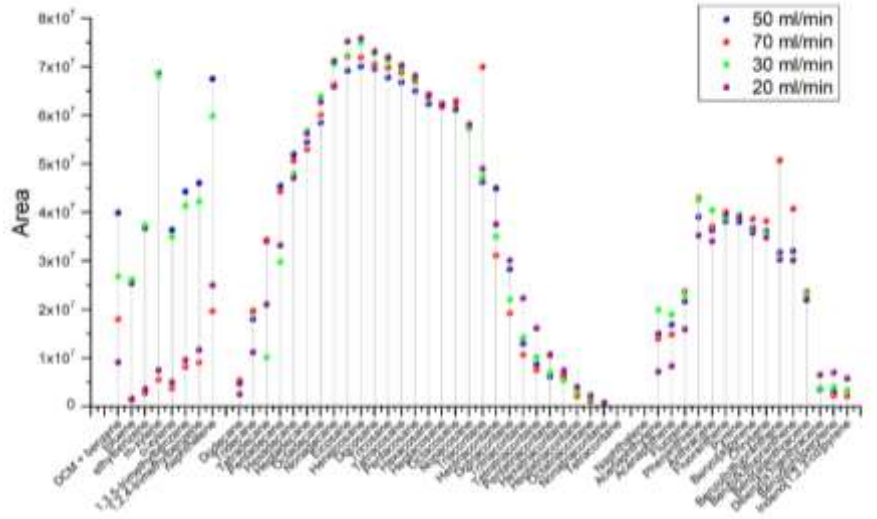

Figure 3. Effect of trap desorption flowrate

Effect of trap desorption temperature

Figure 4 shows the instrument response of 10 ng light aromatics, 10 ng n-alkanes, and 10 ng PAH at general conditions of 17 psi and desorption temperatures of (a) 310, (b) 320, and (c) 360°C for 5 min at sample desorption flow rates of 50 ml/min. Higher responses are obtained for aromatic compounds as desorption temperature decreases, this may be due to thermal degradation since normal desorption temperatures are 275°C. Average recoveries of n-alkanes and PAH did not considerably differ at 310 and 320°C. On the other hand, average recoveries of SVOCs improved 30-40% and 3-6× for n-alkanes and PAH larger than C30 at high temperatures of 360°C for 5 min. However, in order to preserve lifetime of the carbon trap, we chose 310°C.

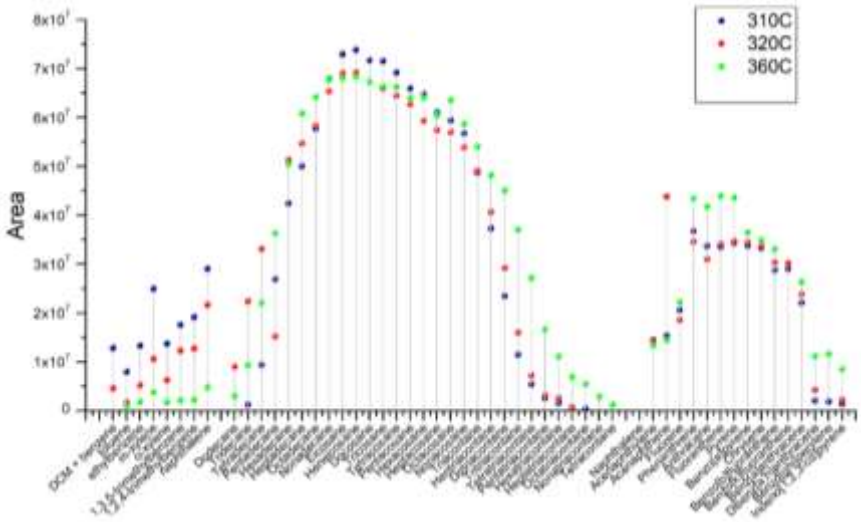

Figure 4. Effect of trap desorption temperature

Effect of trap desorption time

Figure 5 shows the instrument response of 10 ng light aromatics, 10 ng n-alkanes, and 10 ng PAH at general conditions of 17 psi and desorption temperature 310°C for (a) 5 min, (b) 10 min, and (c) 10 min at sample desorption flow rates of 50 ml/min. Desorption time is one of the parameters that shows the highest selectivity of SVOCs. Desorption time of 5 minutes provides the highest recovery of lighter SVOCs such as light aromatics and n-alkanes below C17. On the other hand, 10 minutes provides the highest recovery of heavy SVOCs heavier than C18 n-alkane. N-alkanes lighter than C14 are not typically present in the aerosol phase, therefore, for our application, we chose desorption time of 10 min.

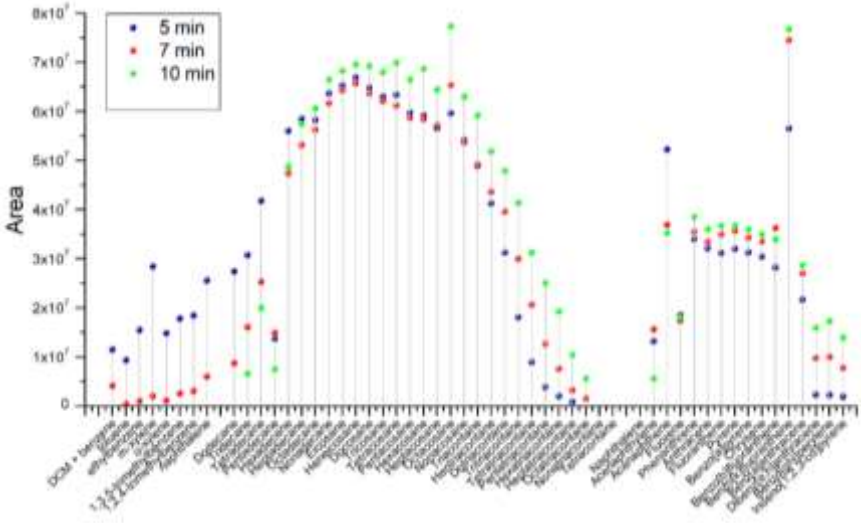

Figure 5. Effect of trap desorption time

Effect of GC column pressure

Figure 6 shows the effect of GC column pressure on recovery of SVOCs. All experiments were performed at trap desorption 310°C for 10 min and 17 psi, 23 psi, or (c) constant flow at 1.2 ml/min. The TD-GC-MS system pressure and flow through the TD-GC transfer line are determined by the GC column pressure and column flow, respectively. In Fig. 5, breakthrough of aromatics possibly happened at desorption times higher than 5 min. In this experiment, aromatics were recovered when the system was operated at 1.2 ml/min for 10 min (Fig. 6).

GC column flows are 2.92-2.56 ml/min and 2.77-2.17 ml/min at 23 and 17 psi, respectively. Therefore, better recoveries for SVOCs heavier than C27 n-alkane are expected at 23 psi compared to 17 psi. Average recoveries of C14-C24 n-alkanes and PAH of 85% and 91 %, respectively, are obtained when a GC column pressure of 23 psi is used compared to 17 psi. On the other hand, average recoveries of heavy PAH were 2× with a GC column pressure of 23 psi. Due to the nature of the compounds typically present in the aerosol phase, we choose 23 psi.

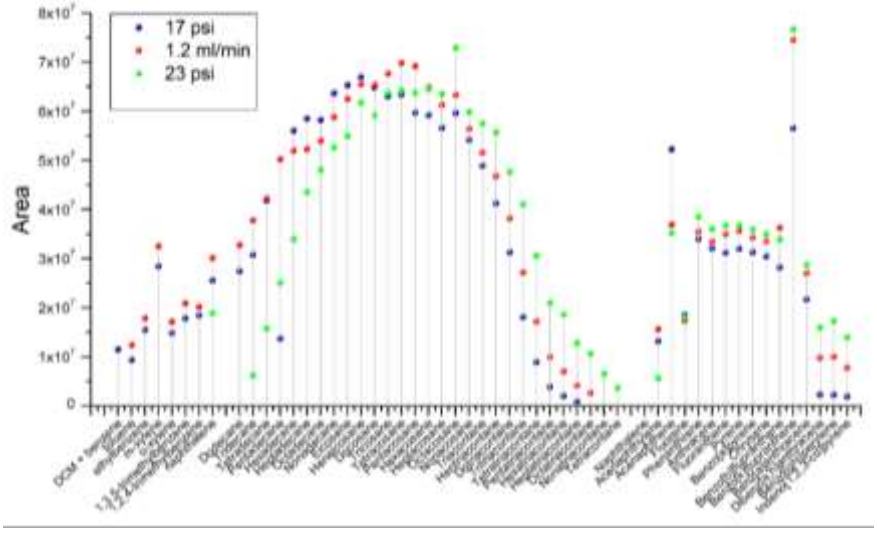

Figure 6. Effect of GC column pressure

Effect of trap sorption temperature

Figure 7 shows instrumental responses and the effect of trap sorption temperature at 0 °C, -15 °C, and 20 °C. All experiments were performed at trap desorption temperature of 310°C for 10 min and GC column pressure 23 psi. Overall, it can be observed that the studied temperatures do not considerably influence the sorption recoveries. In this experiment, better recoveries of light aromatics and C14 and C15 n-alkanes were obtained at a temperature of -15°C. Similar results were obtained at a trapping temperature of 0°C with average recoveries of 106% and 100% for n-alkanes and PAH, respectively. Therefore, a trapping temperature of 0°C was chosen.

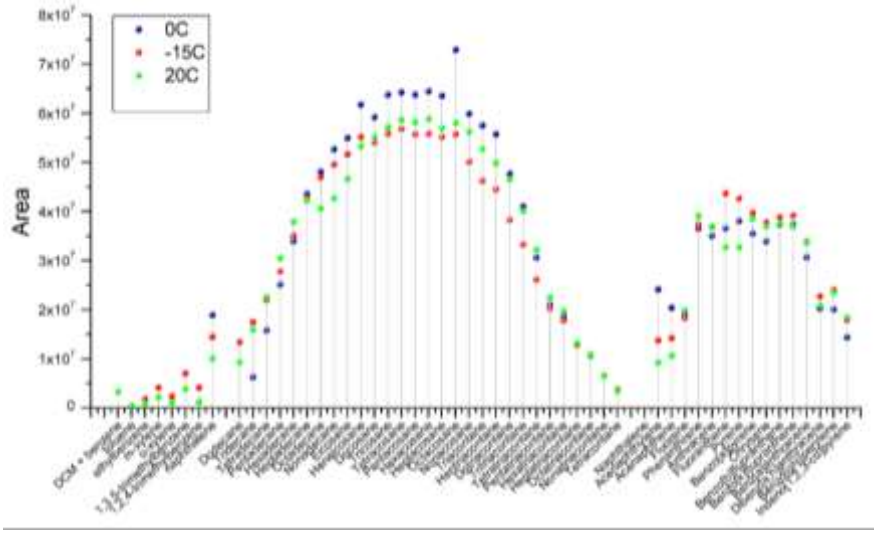

Figure 7. Effect of trap sorption temperature

Meteorology

Figures 8 and 9 show temperature, wind speed, solar radiation, and air mass trajectories observed during each 2-hour sample on January 28-31, 2017, respectively. Meteorological data and air mass backward trajectories were obtained from weather underground and NOAA-HYSPLIT, respectively. During these sampling days, typical winter weather conditions of low temperatures, wind speed, and solar radiation were observed. The lowest temperatures below zero were observed on 28-Jan and 31-Jan at 700 h. Normal temperature patterns were observed on 29-31 Jan with highest temperatures of 2.5-4 ℃ at 1300 h or 1500 h. On 28-Jan a different trend with increasing temperature thorough the day was observed. Due to low temperatures, low wind speeds were observed during these sampling dates. Average wind speeds ranged 2.0-4.99 ms^{-1} corresponding to light air or light and gentle breeze according to Beaufort wind scale. Very low solar radiation was observed on 28-30 Jan with highest levels of 89-298 Wm^{-2} observed between 1100h and 1300h. In comparison, radiation during the summer may be 600-800 W m^{-2}. On 31-Jan maximum radiation was 467-524 W m^{-2} between 1100-1500 h (Fig. 8). Wind direction varied from NNW to NE on 28-29 Jan and remained from NE on 30-31 Jan (Fig. 9). Stable conditions in the atmosphere were observed on 28-Jan due to very low radiation and low temperatures. This is shown in Fig. 9a due to the lack of vertical motion in air mass trajectories. Similar behavior is observed on 30-Jan (Fig. 9c) with air mass trajectories arriving from maximum a couple hundred meters above ground level (m.a.g.l). Greater vertical motion, and possible dispersion of pollutants, can be observed on 29 and 31 of January with air masses arriving from approximately 500-1000 m.a.g.l (Fig. 9b and 9d).

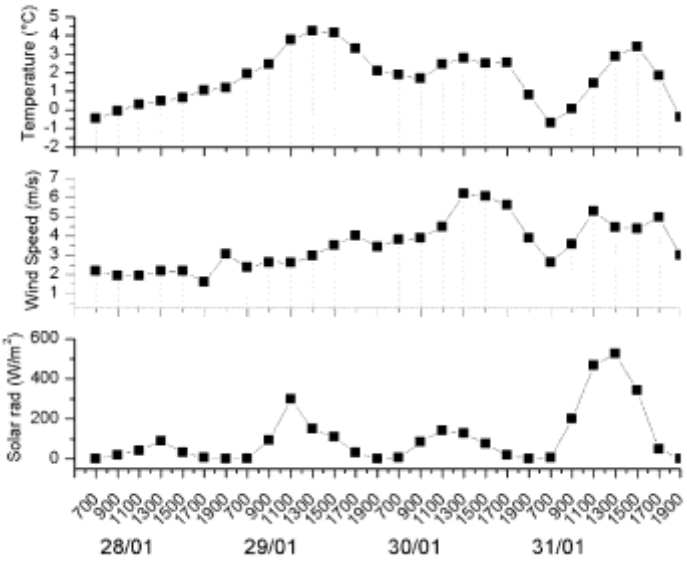

Figure 8. Average meteorological conditions per 2 h sample

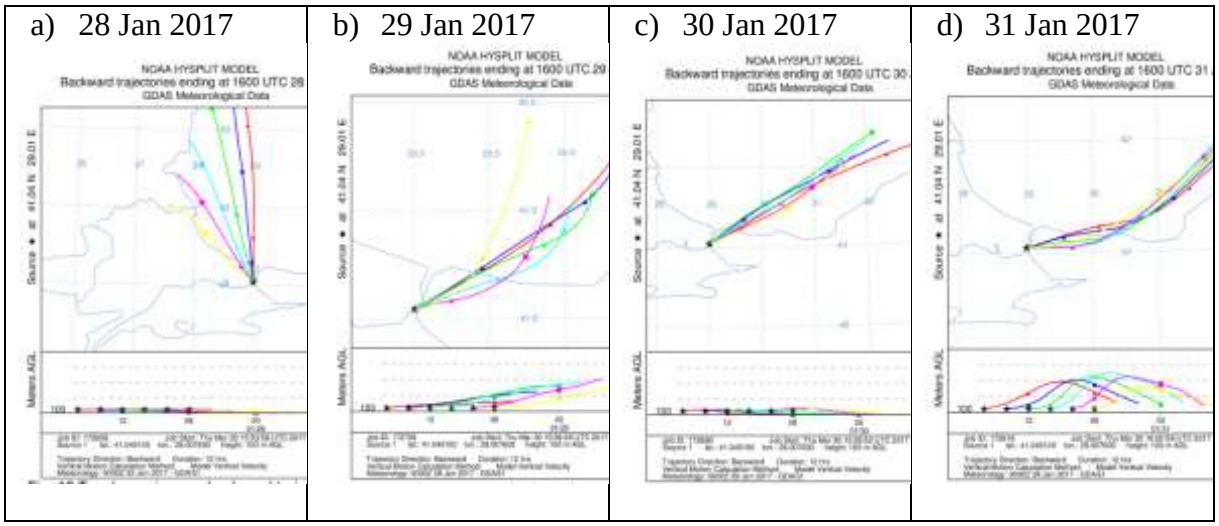

Figure 9. HYSPLIT simulations of air mass backward trajectories for each 2h sample

Traffic density

Traffic density collected every minute was provided by the department of transportation in Istanbul. Total vehicle counts were calculated for all six lanes of Barbaros Bulvari for every 2-h sample. This data is organized according to sampling time (Fig. 10a) and consecutively from 28-31 Jan (Fig. 10b). Barbaros Bulvari is a very busy road due to its location in a touristic/business area and connection to the first bridge that joins the European to the Asian side. As can be observed on Fig. 10, traffic counts follow an interesting behavior according to people activities for specific time and day of the week. The samples reported here were collected on Saturday-Tuesday in order to evaluate the effect of traffic during weekend/weekdays on air pollutant levels. Overall, lower vehicle counts can be observed on Saturday and Sunday from 0700 h to 1500 h. Vehicle density increases after 1500 h and reaches similar levels to Monday and Tuesday after 1500 h. On weekdays (i.e., Monday and Tuesday), traffic density is higher than on weekends and shows a slowly increasing trend from 0700h-1300h that slowly decreases after 1500h (Fig. 10a). The total vehicle count observed over the range of 2h ranged 2353-9496 on Sunday 0700-900h and Monday 1500-1700h, respectively. Over the sampling period, vehicle density shows an increasing trend from 0700h and reaches a maximum at 1300h or 1500 h. The total vehicle counts registered at this point were 38,043-33,941 on Saturday-Sunday, respectively, and 45,339-46,800 on Monday-Tuesday, respectively.

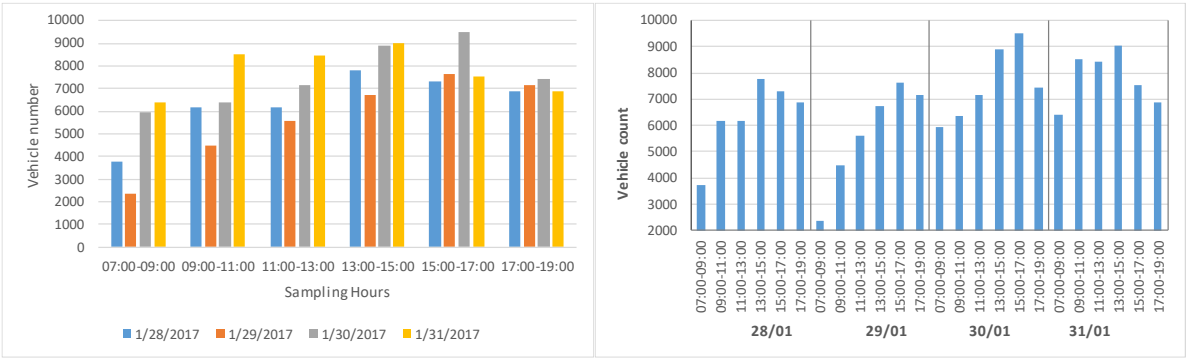

Figure 10. Traffic density per sample (a) daily comparison and (b) consecutive for this sampling campaign

$PM_{2.5}$ concentrations

Hourly $PM_{2.5}$ concentrations were provided by the Ministry of Environment and Urbanization of Turkey for Kagithane, Silivri, and Umraniye. Data for Catladikapi was not available on 28-31 January. Umraniye station also missed some of the data, however, it appears to follow similar concentrations and behavior as Kagithane. Both Kagithane and Umraniye have a population of approximately 400,000 and 700,000, respectively. Lower population of 150,000 live in Silivri, thus lower concentrations of $PM_{2.5}$ are expected during the winter. The 24-h air quality standards established by World Health Organization (WHO) and United States Environmental Protection agency (US-EPA) are 25 and 35 μg m^{-3}, respectively. Daily averages have not been established in the European Union and Turkey. Yearly averages are 10, 12, and 25 μg m^{-3} according to WHO, EPA, and EU, respectively. The 24-h WHO air quality standard of 25 μg m^{-3} was exceeded five times during the study period, mainly in Kagithane and Umraniye (Table 1). On the other hand, the 24-h US-EPA air quality standard of 35 μg m^{-3} was exceeded on 28-Jan on all three sampling stations, possibly due to the absence of vertical atmospheric motion (Fig. 9a). During the study period, hourly $PM_{2.5}$ concentrations were below 30 μg m^{-3}, except a few spikes of maximum concentrations of approximately 50-65 μg m^{-3} observed at noon. The diurnal pattern of $PM_{2.5}$ concentrations is variable in Kagithane and Silivri. Overall, both of the stations show a decreasing trend from Saturday to Monday that increases on Tuesday afternoon. However, the maximum concentrations occur at different times during the day. This may be due to a combination of traffic/industrial emissions in Kagithane and residential heating emissions in both sampling stations.

Table 1. Daily average $PM_{2.5}$ concentrations (μg/m^3)

Date	Kağıthane	Silivri	Ümraniye
28/01/2017	47.29	38.25	65.00
29/01/2017	21.00	18.71	21.14
30/01/2017	20.29	12.78	26.29
31/01/2017	27.13	17.00	19.09

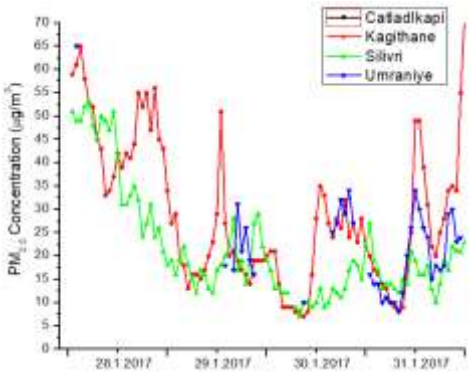

Figure 11. Hourly $PM_{2.5}$ concentration (μg/m^3)

Preliminary identification and quantification of SVOCs in $PM_{2.5}$

In order to evaluate the developed TD-GC-MS method, $PM_{2.5}$ samples were collected every two hours from 0700 h to 1900 h during four days in the winter season. A total of 15 PAH and 28 *n*-alkanes (C_{13}-C_{40}) were identified and quantified in 24 samples. Fluorene was not found in any sample and acenaphthene was only found in one sample. Acenapthylene and anthracene were found in half of the analyzed samples. All n-alkanes of interest were identified and quantified in the samples, except tetracontane which was only quantified in half of the samples. The descriptive statistics are shown in Table 2 and graphically in Fig. 12. Overall, all PAH ranged from below detection to 13.64 ng m^{-3}. *n*-alkanes ranged from 0.01-50.54 ng m^{-3}. The average sum of PAH and n-alkanes found in 0700-1900 h is 43.69 and 223.02 ng m^{-3}, respectively. The total levels of PAH found in Beşiktaş are comparable to other studies in the megacity of Guangzhou, which is the third largest city in China (Wang, Huang et al. 2015, Wang, Ho et al. 2016). The total levels of *n*-alkanes in Beşiktaş during this study period are 2× the levels found by Ho et al. (2016) and comparable to the levels reported by (Wang, Huang et al. 2015). This finding shows the impact of a traffic area in air pollution levels during the winter

season, which is when low dispersion and accumulation of pollutants are found in the atmosphere. Overall, PAH concentrations represent approximately 5-30% of the total concentration of *n*-alkanes and PAH found in the samples over the study period (Fig. 12).

Table 2. Concentration of SVOCs (ng m^{-3}) in $PM_{2.5}$

Compound	***N***	***Mean***	***Std dev***	***Min***	***Max***
naphthalene	24	6.40	1.60	3.99	9.65
acenapthylene	13	0.90	0.75	0.07	2.32
Acenaphthene	1	7.59	--	7.59	7.59
Fluorene	0	--	--	--	--
Phenanthrene	24	2.79	2.00	0.23	7.71
Anthracene	13	0.50	0.47	0.02	1.37
Fluoranthene	24	5.97	3.30	1.57	13.64
Pyrene	24	5.26	2.89	0.09	12.31
chrysene	24	2.29	2.18	0.00	7.78
Benzaanthracene	24	2.88	2.59	0.16	9.98
Benzobfluoranth	24	3.13	2.68	0.37	9.80
Benzokfluoranth	24	1.57	2.94	--	9.80
Benzoapyrene	24	1.61	1.39	0.06	5.07
Benzoghiperylen	24	1.16	0.59	0.53	2.49
Dibenzahanthra	24	0.44	0.15	0.29	0.79
Indeno123cdp	24	1.17	0.42	0.61	2.18
Tridecane	24	2.14	0.99	0.53	4.24
Tetradecane	24	3.01	2.26	0.57	9.88
Pentadecane	24	6.19	3.79	2.81	20.94
Hexadecane	24	9.76	6.34	3.86	31.52
Heptadecane	24	20.50	9.69	10.10	46.56
octadecane	24	28.96	9.09	14.58	50.54
nonadecane	24	26.67	7.49	14.18	43.50
eicosane	24	21.63	6.38	11.01	33.84
Heneicosane	24	18.35	4.89	9.06	27.43
Docosane	24	14.58	3.86	6.57	20.87
Tricosane	24	11.25	2.51	5.88	16.40
Tetracosane	24	8.67	2.03	5.06	13.30
Pentacosane	24	8.21	2.86	4.33	15.60
Hexacosane	24	6.64	3.58	2.97	16.83
Heptacosane	24	6.92	2.88	3.63	14.36
Octacosane	24	4.34	2.33	1.98	10.60
Nonacosane	24	4.45	2.78	1.51	10.42
Triacontane	24	3.97	2.42	1.59	9.95
Hentriacontane	24	5.23	2.56	2.45	10.81
Dotriacontane	24	2.54	1.62	1.05	6.25
Tritriacontane	24	2.29	1.52	1.14	5.70
Tetratriacontane	24	1.28	0.80	0.52	3.10
Pentatriacontane	24	1.12	0.55	0.61	2.32
Hexatriacontane	24	1.03	0.36	0.61	1.79
Heptatriacontane	24	1.13	0.31	0.76	1.98

Compound	*N*	*Mean*	*Std dev*	*Min*	*Max*
Octatriacontane	24	0.92	0.31	0.34	1.62
Nonatriacontane	24	0.71	0.29	0.34	1.47
Tetracontane	11	0.55	0.36	0.01	1.08

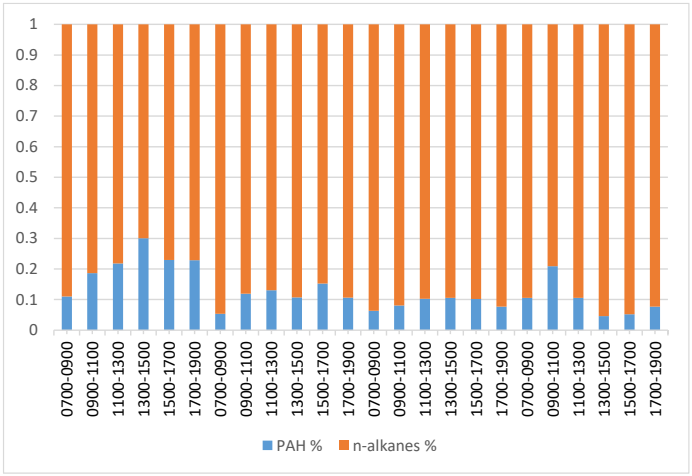

Figure 12. Fractional distribution of n-alkane and PAH species in 2-h $PM_{2.5}$ samples

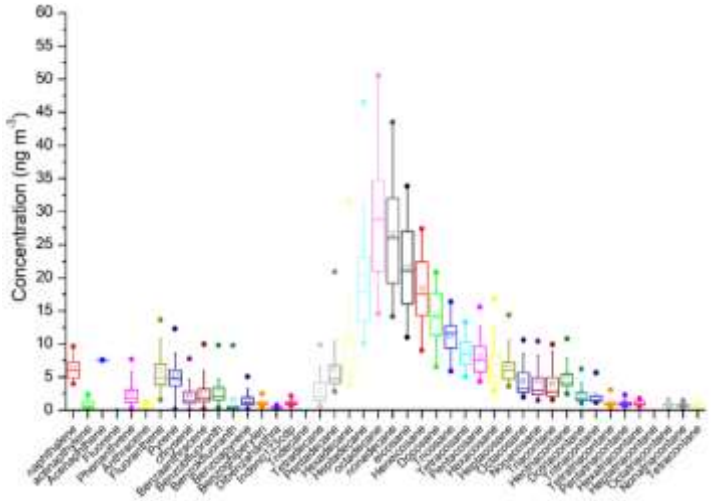

Figure 13. Box plot of SVOC species identified and quantified in this study

Figure 14 shows the diurnal variation and distribution of PAH and n-alkanes in 2-h samples collected in the traffic-influenced area of Beşiktaş during the winter. The study of organic compounds in high-time resolved samples presented here is reported for the first time in Turkey and has been scarcely reported in the world see e.g., (Williams, Goldstein et al. 2006, Zhao, Kreisberg et al. 2013, Isaacman, Kreisberg et al. 2014). Concentrations of organic compounds in the atmosphere depend on physicochemical properties that determine reactivity and volatility, sources, and transport or dispersion through the atmosphere. Therefore, traffic density and meteorological conditions such as temperature, solar radiation, wind speed, wind direction, and stability of the atmosphere play a very big role on their diurnal variations. The main sources of organic compounds in the atmosphere have been identified as coal combustion mostly for residential heating (20-29%), vehicle emissions (13-15%), and secondary organic carbon (15-17%). The distribution of these sources varies during the winter and summer and includes additional contributions from cooking (11-13%) and biomass burning (3-8%) (Wang,

Ho et al. 2016). In our work we found a strong correlation between total concentration of SVOCs and traffic (R^2 = 0.5) that can be observed in Fig. 14 and Fig. 10b. An inverse correlation was found with temperature (R^2 = -0.35), relative humidity (R^2 = -0.24), and solar radiation (R^2 = -0.19). These small correlations will require the use of multivariate factor analysis to better understand the complex relationship among various factors.

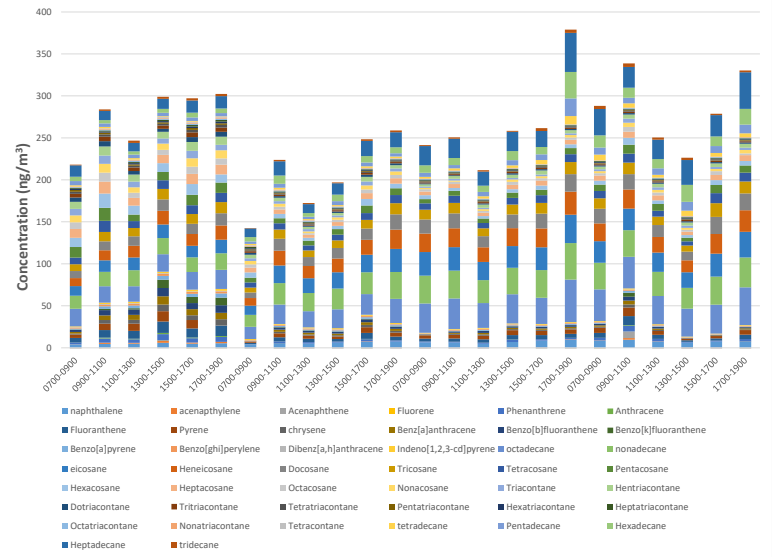

Figure 14. Diurnal variation of SVOCs in $PM_{2.5}$

CONCLUSIONS

A thermal desorption method was developed and applied to identify and quantify 15 PAH and 28 *n*-alkanes in 2-h $PM_{2.5}$ samples with gas chromatography – mass spectrometry (TD-GC-MS). The samples were collected in a traffic-influenced area for four days to compare the impact of traffic over the weekend and weekdays. A high correlation between concentration of SVOCs and traffic was found (R^2 = 0.5). However, stability of the atmosphere also influenced the concentration of SVOCs in the particle phase, particularly on Saturday, when no vertical motion was observed. The use of the developed thermal desorption method will allow the analysis of highly-time resolved samples for better apportionment of sources and understanding of transport and transformation of organic compounds in the atmosphere.

Acknowledgements

The authors thank TUBITAK and BAP for their financial support [Project number: TUBITAK-115Y625, FEN-C-YLP-090217-0060], Bahçeşehir University, and IETT (Beşiktaş) for use of their facilities. The authors appreciate the data provided by the Ministry of Environment and Urbanization, Department of Transportation, and Turkish State Meteorological Center. Meteorological data was also obtained from Weather Underground. Backward air mass trajectories were provided by the Air Resources Laboratory at NOAA with the web version of HYSPLIT model.

REFERENCES

Alves, C. A. (2008). "Characterisation of solvent extractable organic constituents in atmospheric particulate matter: an overview." Anais da Academia Brasileira de Ciências 80: 21-82.

Derwent, R. G., et al. (2010). "Secondary organic aerosol formation from a large number of reactive man-made organic compounds." Science of the Total Environment 408(16): 3374-3381.

Ding, L., et al. (2014). "Characterization of chemical composition and concentration of fine particulate matter during a transit strike in Ottawa, Canada." Atmospheric Environment 89: 433-442.

Erdun, H., et al. (2015). "Spatial Variation of PM10 in Turkey." VII Atmospheric Sciences Symposium ITU and IAU: 311-323.
Hanedar, A., et al. (2014). "Toxicity evaluation and source apportionment of Polycyclic Aromatic Hydrocarbons (PAHs) at three stations in Istanbul, Turkey." Science of the Total Environment 488–489: 437-446.
Huber, L. (2010). Validation of Analytical Methods. A. Technologies. Germany.
Isaacman, G., et al. (2014). "Online derivatization for hourly measurements of gas- and particle-phase semi-volatile oxygenated organic compounds by thermal desorption aerosol gas chromatography (SV-TAG)." Atmos. Meas. Tech. 7(12): 4417-4429.
Jimenez, J. L., et al. (2009). "Evolution of Organic Aerosols in the Atmosphere." Science 326(5959): 1525-1529.
Kanakidou, M., et al. (2005). "Organic aerosol and global climate modelling: a review." Atmospheric Chemistry and Physics 5(4): 1053-1123.
Karaca, F., et al. (2005). "Statistical characterization of atmospheric PM10 and PM2.5 concentrations at a non-impacted suburban site of Istanbul, Turkey." Chemosphere 59(8): 1183-1190.
Karaca, F., et al. (2008). "Seasonal Variation of Source Contributions to Atmospheric Fine and Coarse Particles at Suburban Area in Istanbul, Turkey." Environmental Engineering Science 25(5): 767-782.
Kuzu, S. L., et al. (2014). "Ambient polychlorinated biphenyl levels and their evaluation in a metropolitan city." Science of the Total Environment 472: 13-19.
Ozdemir, H., et al. (2014). "Spatial and temporal analysis of black carbon aerosols in Istanbul megacity." Science of the Total Environment 473–474: 451-458.
Penner, J. E., et al. (2001). Aerosols, their direct and indirect effects. Climate Change 2001: The Scientific Basis. Contribution of Working Group I to the Third Assessment Report of the Intergovernmental Panel on Climate Change, Cambridge University Press: 289-348.
Tayanç, M. (2000). "An assessment of spatial and temporal variation of sulfur dioxide levels over Istanbul, Turkey." Environmental Pollution 107(1): 61-69.
Theodosi, C., et al. (2010). "Aerosol chemical composition over Istanbul." Science of the Total Environment 408(12): 2482-2491.
UN, U. N. (2015). World Urbanization Prospects: The 2014 Revision, New York: United Nations Department of Economics and Social Affairs, Population Division.
Unal, Y. S., et al. (2011). "Influence of meteorological factors and emission sources on spatial and temporal variations of PM10 concentrations in Istanbul metropolitan area." Atmospheric Environment 45(31): 5504-5513.
Wang, J., et al. (2016). "Characterization of PM2.5 in Guangzhou, China: uses of organic markers for supporting source apportionment." Science of the Total Environment 550(Supplement C): 961-971.
Wang, Q. Q., et al. (2015). "Organic tracer-based source analysis of PM2.5 organic and elemental carbon: A case study at Dongguan in the Pearl River Delta, China." Atmospheric Environment 118: 164-175.
Wendy Hsiao, W. L., et al. (2000). "Cytotoxicity of PM2.5 and PM2.5–10 ambient air pollutants assessed by the MTT and the Comet assays." Mutation Research/Genetic Toxicology and Environmental Mutagenesis 471(1–2): 45-55.
Weschler, C. J. and W. W. Nazaroff (2008). "Semivolatile organic compounds in indoor environments." Atmospheric Environment 42(40): 9018-9040.
Williams, B. J., et al. (2006). "An In-Situ Instrument for Speciated Organic Composition of Atmospheric Aerosols: Thermal Desorption Aerosol GC/MS-FID (TAG)." Aerosol Science and Technology 40(8): 627-638.
Zhao, Y., et al. (2013). "Development of an In Situ Thermal Desorption Gas Chromatography Instrument for Quantifying Atmospheric Semi-Volatile Organic Compounds." Aerosol Science and Technology 47(3): 258-266.

IDENTIFICATION OF AEROSOL ORIGIN IN YILDIZ TECHNICAL UNIVERSITY DAVUTPASA CAMPUS

S. Levent KUZU[1], Arslan SARAL[1]
[1]Yildiz Technical University
skuzu@yildiz.edu.tr, saral@yildiz.edu.tr

Abstract
In this study, ambient air sampling was performed where is crowded with student population. Collected particle samples were comprised of diameters less than 2.5 μm and between 2.5-10 μm. In order to make a deeper research, collected samples were subjected to metal and ion analyses. PM_{10} concentration was observed to be 42 $\mu g.m^{-3}$, whereas $PM_{2.5}$ was found to be 20 $\mu g.m^{-3}$. Although most of the particles are found in the coarse fraction, fine particles comprise nearly the half of the whole particle mass. Calcium and sulfate seem to be important constituents of the particles. Source apportionment was applied by PMF. 5 different source categories were detected. These categories are; glass industry, soil, marine aerosol, traffic and small scale metallurgy industry.

Keywords: *$PM_{2.5}$, PM_{10}, PMF, metallic and ionic composition*

INTRODUCTION
Many studies have examined the relationship between air pollution and human health. Detailed exploration of the chemical characterization of atmospheric PM is also important for explaining both the role of particulate toxicity and its role in climate change. One of the most important events of air pollution caused by particulate matter is the so-called Asian Dust (AD) or Yellow Sand, which many Asian people are subjected to in the spring each year. The most intense season is spring. Recently there has been a significant increase in the number of days of AD and the concentration of PM formed during the AD event. The rapid increase in soil losses and loss of green space due to rapid industrialization, forest fires, and the destruction of forests in China and Mongolia have contributed significantly to the recent increases (Singer, 1988, Gomes and Gillette, 1993, Rost, 2001). However, the expansion of arid regions, regional meteorological changes, or changes that cause global warming have increased the severity of AD (Zhang et al., 1999, Heslop et al., 2001; Zhang et al., 2002). At the same time long-distance transport of the AD event can cause significant effects on particulate matter and soil in California (USA) and Hawaiian Islands (Braaten and Cahill, 1967; Husar, et al., 2001; Kurtz, et al., 2001; Lin, et al., 2001; Pettke, et al., 2001; Uno, et al., 2001; Jaffe et al., 2003). AD causes damage to animals and plants as well as to respiratory diseases and eye problems in humans (Takayama and Takashima, 1986). However, this is the natural mechanism generating ambient particle problem.

Especially, in the late 19th century there was a significant increase in the air pollution caused by the industrial revolution along with the combustion. One of the most important of these pollutants in the atmosphere is particulate matter (PM). The PM has the negative effects of diminishing the visibility of the light, such as having harmful effects on the lungs by entering the body through the alveoli during respiration. The most important parameter in the amount of these effects is PM size. So small particles smaller than 10 microns (PM_{10}) are the peentrable particles that can enter the respiratory system and are more susceptible to human health. Again, the small particles less than 2.5 micrometres ($PM_{2.5}$) contained within the PM_{10} are a fraction of particles that can reach the lungs and cause serious respiratory tract diseases. For this reason, it is necessary to know the distribution of PM in the air in the air where the air pollution is intense, in order to evaluate the health of these particles. As a matter of fact, the concentration

of thoracic particle (PM_{10}), which is much more important for health than the total particle is regarded as PM indicator for air quality standards.

Composition of the particulate matter contains important information about the source activities. Many studies have been conducted so far to understand the sources of particles (Argyropoulos et al, 2017; Kalaiarasan et al, 2016; Uwayemi et al, 2015; Theodosi et al, 2010; Yatkin and Bayram, 2007). The technique so-called receptor modeling is used to identify the sources of particles. For that purpose, one has to have a series of sampling data for some pollutant species. These species are extracted from the particles and then they are subject to quantification. Later, mathematical or statistical procedures are applied in order to identify and quantify the sources of air pollutants at a receptor location.
The objective of the research on particulate matter and air pollution is to identify the source of PM. In this study, atmospheric particulate matter sampler was used to determine $PM_{2.5}$ and PM_{10} concentrations at the Yildiz Technical University Davutpasa campus and positive matrix factorization was applied to identify the pollutant sources in the sampling area.

MATERIALS AND METHODS

Experimenta

Davutpasa Campus is close to Bayrampaşa and Topkapi districts, where numerous industrial facilities are located. The samples were taken from the roof of the faculty building so that the effects of the pollution that may surround it can be reached without hindrance. The sampling point was 10 m above ground level. Global position of the sampling point is 41° 01′ 26″ N latitude and 28° 53′ 16″ E longitude. A TCR Tecora brand Echo PM model sampler was used to collect the particulate matter. Two different types of particulate matter fractions were collected using the $PM_{2.5}$ and PM_{10} separators. In the sampling, the flow rate was fixed to 38 L/min. The instrument was calibrated using an external calibrator. Before sampling, the filters were heated to 103 ° C for 2 hours to remove moisture. The filters were then placed in petri dishes and kept in desiccator at 20 ° C in open-lid position for 2 days and weighed on the micro scale. After sampling, the same procedure was applied to the filters excluding the heating section.

After the weighing process, filters were divided into two parts. For this purpose, digestion was carried out with a Berghof brand MWS-3 model microwave device in order to pass the particles-bound pollutants present on the filters to the liquid medium. 4.4 mL HNO_3, 1.1 mL H_2O_2 and 0.6 mL HF was consumed for each filter. The device was operated at 5 steps. Samples were heated to 120 ° C in 2 minutes under 15 bar pressure and waited for 10 minutes; heated to 140 ° C in 2 minutes at 15 bar pressure and waited for 10 minutes; the temperature was raised to 180 ° C in 2 minutes at 20 bar pressure and waited for 10 minutes; and then decreased to 135 ° C at 5 minutes and then to 100 ° C at 2 minutes. After the completion of the digestion process, sample was filtered through 0.45 μm pore sized filter. The acquired volume was diluted with distilled water to 50 ml. After completing the sample preparation step, the samples were subjected to elemental analysis by the ICP-OES instrument. Among these elements are Na, K, Ca, Mg, V, Co, Ni, Zn, Al, Cd, Cr, Pb and Fe. Na, K, Ca, Mg, Al, and Fe were the most frequently found metals in the soil, and they were higher than other elements during analysis. V, Ni, Zn, Cd, Cr, Pb, Fe, Mn and Cu are among the metals that may be from traffic sources.

Following gravimetric analysis, ion analysis was performed on the remaining half of the filters. In order to make the particulate matter-bound ions soluble in the water medium, the filters were treated in a shaker unit. Each filter was placed in a flask including 50 ml of deionized water. Afterwards, the mouths of these flasks were covered by parafilm and placed in a shaker and

operated for 24 hours. At the end of this process, acquired liquid was filtered through 0.45 μm pore sized filter. Then, 10 ml of the sample was placed in the ion chromatograph vials. More details about metal and ion analysis and sample preparation is present elsewhere (Kuzu et al, 2013).

Methods

Source identification for particulate matter in the urban atmosphere is complicated by many reasons because there are several emission sources in the urban atmosphere that leads to a large number of primary and secondary aerosol formations. Depending on the geographical characteristics of the region, particle emissions, particle size, pollutant lifetime and atmospheric chemistry may vary. In the source identification models, the chemical composition of the particulate material, formed in the region, is utilized to determine the principal sources of PM in a particular region. The most preferred models used in source identification are principal component analysis, chemical mass balance, and positive matrix factorization. In this study, Positive Matrix Factorization (PMF) was used to estimate source profiles.

The basic principle of source / receptor relationships can be considered as conservation of mass. The mass balance analysis can be used to share and identify particulate matter air resources in the atmosphere. This method is generally described by the community of air pollution as receptor modeling (Hopke, 1991). The database acquisition approach for receptor modeling is intended to detect a large number of chemical entities, such as in a range of elemental concentrations. Alternatively, automated electron microscopy is used to characterize the composition and shape of a series of particle samples. The general definition of a receptor model considering mass balance for all m chemical species in the n samples as contributions from p independent sourcesis given in Eq 1.

$$x_{ij} = \sum_{k=1}^{p} f_{ik} \times g_{kj} \quad (1)$$

Where, I=1, …, n samples, j=1, …, m species, and p=1, …., m sources. The object function Q for positive matrix factorization is given in Eq 2.

$$Q = \sum_{i=1}^{n} \sum_{j=1}^{m} \left[\frac{x_{ij} - \sum_{k=1}^{p} g_{ik} \times f_{kj}}{s_{ij}} \right]^2 \quad (2)$$

RESULTS AND DISCUSSION

$PM_{2.5}$ and PM_{10} samples were collected between 15.09.2010 and 15.09.2012 during the study of two years. With the results, mass ratios and concentrations of particles in coarse and fine size are measured in general terms. However, metal and ion determinations were made at different times in the particles. With these analyzes, the fingerprints of the industries in the region were investigated and the possible contributions were tried to be revealed through receptor modeling.

Particulate matter concentrations and distribution

The obtained measurement results were evaluated statistically and the results are presented in Fig 1.

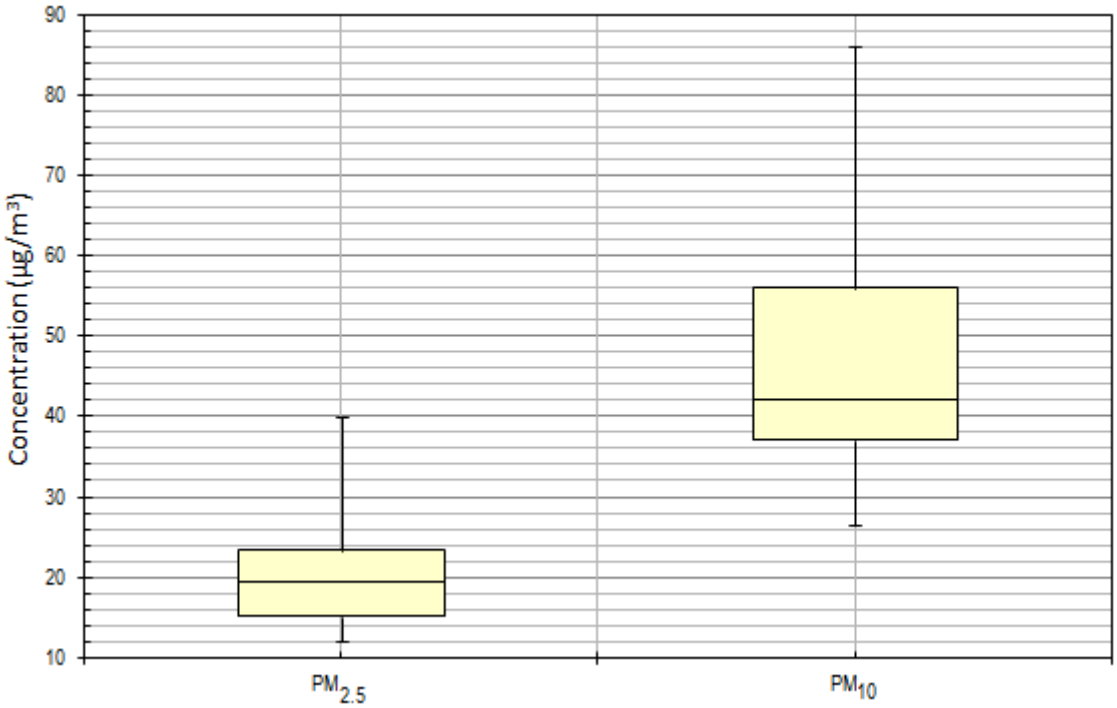

Figure 1. PM concentrations within the sampling period

Accordingly, in the box-bar graphs, the middle line shows the median value. Approximately 40% of the particles are $PM_{2.5}$. Pateraki et al (2012) stated that $PM_{2.5}/PM_{10}$ ratio ranges between 0.4 and 0.8. This is in line with the previously expressed $PM_{2.5}/PM_{10}$ ratio in urban atmosphere. However, Kuzu and Saral (article in press) reported higher $PM_{2.5}/PM_{10}$ ratio for the same location. $PM_{2.5}$ fraction of the particles provides us with more information for anthropogenic sources. The upper and lower sides of the boxes give upper and lower quartile, respectively. Lines extending out of the box correspond to 5% and 95%. In general, it is observed that the particulate matter is observed below air quality standard level, but it exceeds the threshold value at more than 10% of the year.

Particulate matter composition

The combination of PM gives us the opportunity to take a first step in making resource estimation with the model. Anion, cation and metal contents of $PM_{2.5}$ are presented in Figures 2, Figure 3 and Figure 4, respectively.

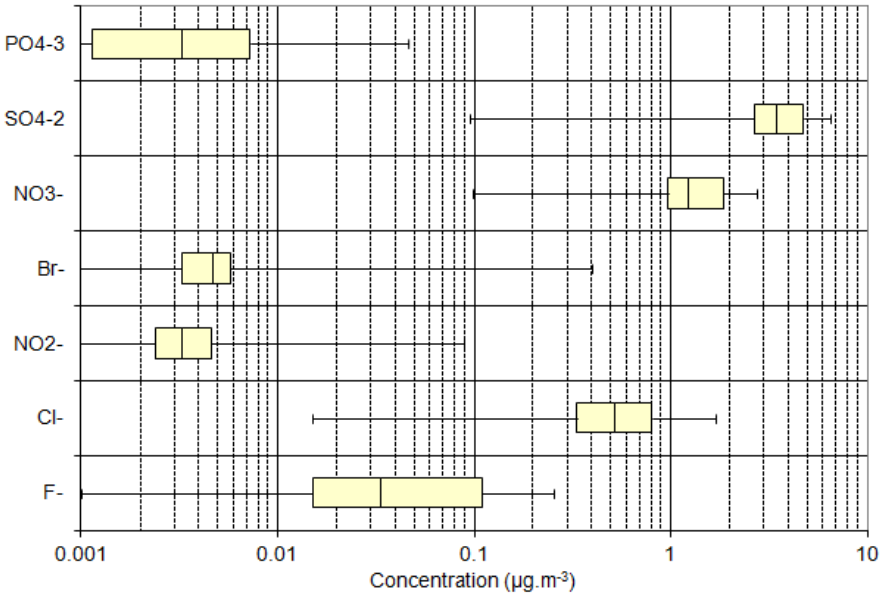

Figure 2. Anion concentrations

The highest anion concentrations were sulfate, nitrate, and chloride respectively. Especially, sulfate and nitrate constituents are important from atmospheric chemistry viewpoint. Observed concentrations of these three anions are an order of degree higher than another point in Istanbul (Kuzu et al, 2013). Sulfate concentration is higher than nitrate concentration in this study. The relation was transverse in the previous study (Kuzu et al, 2013).

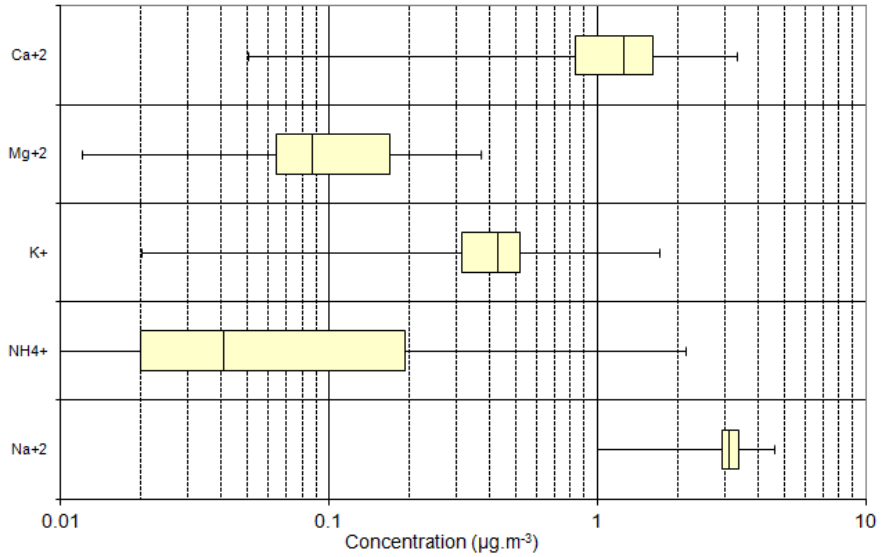

Figure 3. Cation concentrations

Magnesium cation is in the same order that was measured in Yildiz, Istanbul (Kuzu et al, 2013). Calcium and potassium concentrations are somewhat higher in this study. Sodium is an order of magnitude higher than the previous study. Ammonium is also 10 times higher in this study. Ammonium has potential to develop secondary aerosols with sulfate and nitrate compounds.

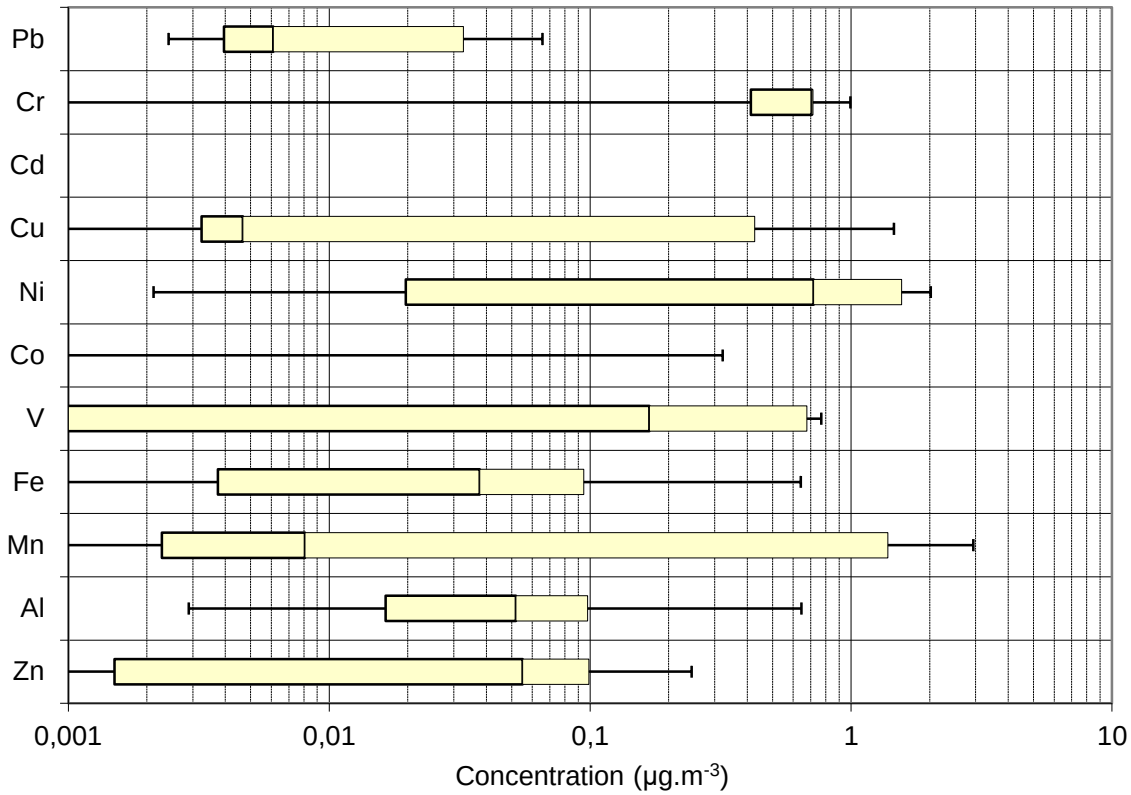

Figure 4. Metal concentrations

Mean lead concentration was below the air quality standards. Its concentration was comparable with the observed level in Beşiktaş, Istanbul. Threshold values were also present for cadmium and Nickel. The limit values are 5 and 20 ng/m^3 for Cd and Ni, respectively. Cadmium was not detected in most of the samples. However, excessive Ni concentration was observed during the sampling. Co was absent in most of the samples. Chromium had elevated concentration in the samples, possible suggesting industrial sources.

PM source identification by PMF

PMF results yielded 5 different factors for $PM_{2.5}$. Eighteen measured constituents were investigated in the study. These factors are as follows:

Factor 1: Glass manufacturing industry
Factor 2: Soil
Factor 3: Marine aerosol
Factor 4: Traffic
Factor 5: Small metalworking workshops

The distributions of the source profiles of the eighteen components are given in different colors in the pie charts. Orange color represents glass manufacturing industry, green color represents soil, yellow color represents marine aerosol, pink color represents traffic, blue color represents metalworking activities.

According to the Figure 5(a), 9.6% of aluminum was from glass industry, 61.9% is from soil and 28.5% is from metalworking workshops. 5.6% of the calcium stemmed from the sea, 75.9% from the soil and 18.5% from the metalworking workshops Figure 5(b). 37.3% of cadmium originated from glass industry, 30.9% is from soil and 31.8% is from sea Figure 5(c). 72.7% of

cobalt was from traffic and 27.3% is from soil Figure 5(d). 17.2% of chromium is emitted from the glass industry, 44.7% from earth, 22.5% from soil, and 15.6% from metal processing workshops Figure 5(e). 8.2% of copper was from traffic, 38% from soil and 53.8% from sea Figure 5 (f). 26.2% of the iron stemmed from soil and 73.8% is from metalworking workshops Figure 5(g). 10.7% of potassium is originated from glass industry, 35% from soil, 52% from sea and 2.3% from traffic Figure 5(h). 24.1% of the lithium emitted from the glass industry, 16.7% from the earth, 47.3% from the sea, 4.9% from the traffic and 7% from the metalworking workshops Figure 5(i). Lithium originated from each of the sources.

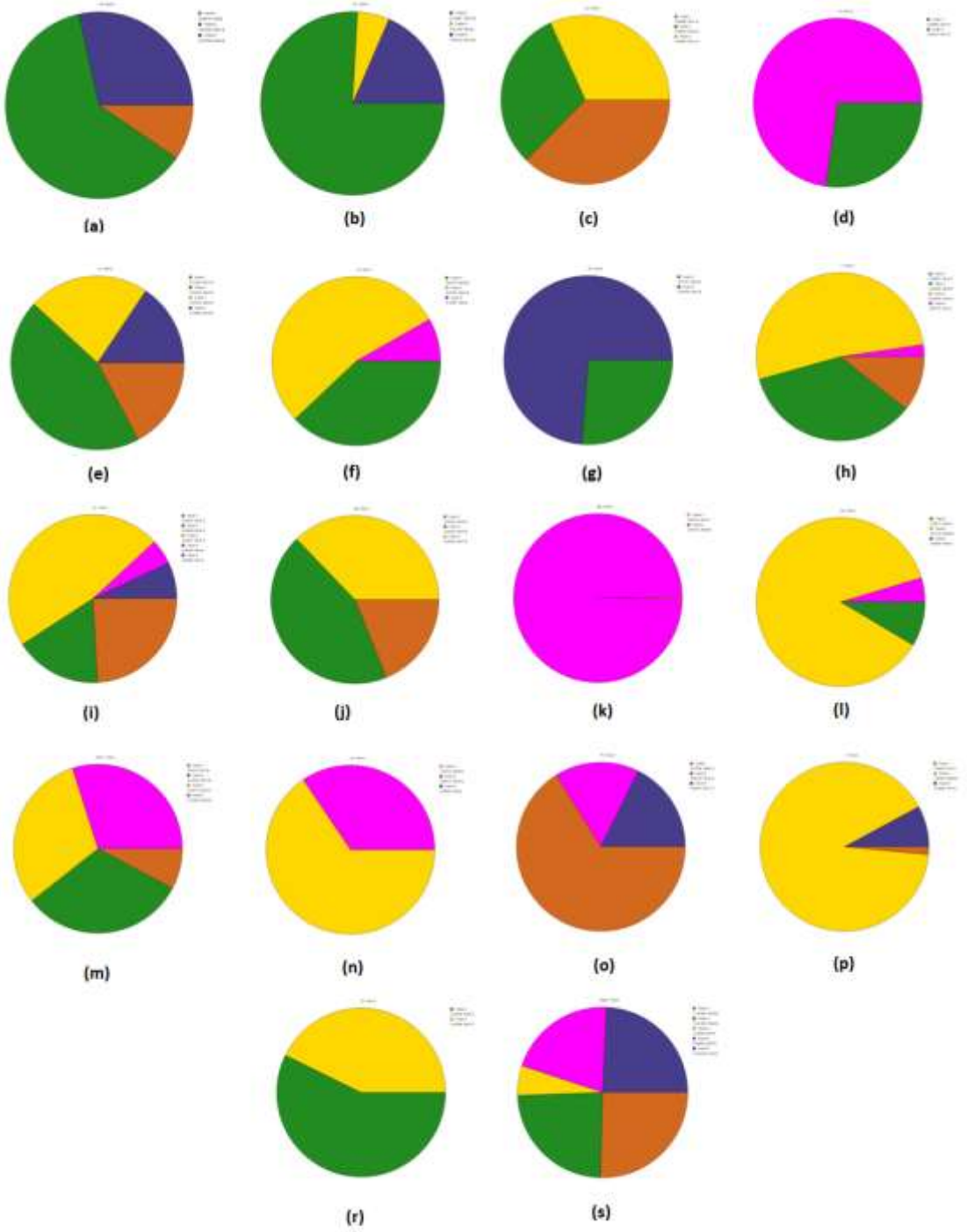

Figure 5. Factor distribution for (a) aluminum (b) calcium (c) cadmium (d) cobalt (e) chromium (f) copper (g) iron (h) potassium (i) lithium (j) magnesium (k) manganese (l) sodium (m) ammonium (n) nickel (o) lead (p) vanadium (r) zinc (s) $PM_{2.5}$

18.9% of magnesium was from glass industry, 43.9% from soil and 37.2% from sea Figure 5(j). Although 0.2% of manganese originated from the sea and 99.8% from the traffic Figure 5(k). It can be said that manganese was entirely from traffic source. 88.8% of sodium comes from the sea, 8.6% from the soil and 4.6% from the traffic Figure 5(l). Major contributor for sodium was sea. 7.8% of the ammonium emitted from the glass industry, 31.6% from soil, 30.7% from the sea and 29.9% from the traffic Figure 5(m). 65.6% of nickel originated from the sea and 34.4% from the traffic Figure 5(n). 66.2% of lead originated from the glass industry, 16.2% from traffic and 17.7% from metalworking workshops Figure 5(o). 1.5% of vanadium is emitted from the glass industry, 90.6% from the sea and 7.9% from metalworking workshops Figure 5(p). 57.3% of the zinc was originated from soil and 42.7% is from the sea Figure 5(r). Particulate matter concentration was included as a pollutant component. 25.4% of $PM_{2.5}$ emitted from glass industry, 24% from soil, 5.6% from sea, 20.7% from traffic and 24.3% from metal processing workshops. The least contribution was from marine aerosol. The other sources had similar shares.

CONCLUSIONS AND RECOMMENDATIONS

Davutpaşa campus is located close to Bayrampaşa and Topkapi where there are numerous of facilities. These industries and small-scale workshops are thought to contribute to air pollution as particulate matter. In order to determine the chemical composition of the particulate matter, ion and elemental analysis were performed. Determination of the source profile was carried out by using the receptor model. PMF was executed for Fe, Ca, Li^+, Mg, Al, K, Mn, Cu, Ni, Cr, Zn, Pb, Na, Cr, V, Cd, Co and NH_4^+ components. PMF results suggested that 5 principal source profiles were present. These sources were glass industry, soil, marine aerosol, traffic, and small-scale metal processing workshops.

At the end of the measurement period, the glass manufacturing factory located to the west of the campus area has been shut down and, in the present case, the effect of this can be considered to be exhausted from the ambient air. Hence, the influence of other sources would become more dominant. Along with the change of the socio-economic environment of the region, the amount, concentration and content of airborne particles will change. As industrial activities are being stopped in this region, traffic source is expected to become the major source in the area. This statement should be supported by future scientific research studies.

ACKNOWLEDGEMENTS

This research has been supported by the Yildiz Technical University Scientific Research Projects Coordination Department (Project no. 2010-05-02-ODAP02).

REFERENCES

Argyropoulos G, Samara C, Diapouli E, Eleftheriadis K, Papaoikonomou A, (2017) Source apportionment of PM_{10} and $PM_{2.5}$ in major urban Greek agglomerations using a hybrid source-receptor modeling process, Science of the Total Environment, 601-602, 906-917.

Braaten DA, Cahill TA, (1967) Size and composition of Asian dust transported to Hawaii, Atmospheric Environment, 20, 6, 1105-1109.

Gomes L, Gillette DA, (1993) A comparison of characteristics of aerosol from dust storms in central Asia with soil-derived dust from other regions, Atmospheric Environment, 27, 16, 2539-2544.

Heslop D, Shaw J, Bloemendal J, Chen F, Wang J, Parker E, (2001) Sub-millennial scale variations in east asian monsoon systems recorded by dust deposits from the North-western Chinese Loess Plateau, Physics and chemistry of the earth, 24, 9, 785-792.

Hopke PK, (1991) Receptor Modeling for Air Quality Management, Elsevier Science, Amsterdam.

Husar RB, Tratt DM, Schichtel BA, Falke SR, Li F, Jaffe D, Gasso S, Gill T, Laulainen NS, Lu F, Reheis MC, Chun Y, Westphal D, Holben BN, Guymard C, Mckendry I, Kuring N, Feldman GC, McClain C, Frauin RJ, Merrill J, Dubois D, Vignola F, Murayama T, Nickovic S, Wilson WE, Sassen K, Sugimoto N, Malm WC, (2001) Asian dust events of 1998, Journal of Geological Research, 106, 16, 18317-18330.

Jaffe D, McKendry I, Anderson T, Price H, (2003) Six 'new' episodes of trans-pascific taransport of air pollutants, Atmospheric Environment, 37,3, 391-404.
Kalaiarasan G, Balakrishnan RM, Khaperde VV, (2016) Receptor model based source apportionment of PM10 in the metropolitan and industrialized areas of Mangalore, Environmental Technology & Innovation, 6, 195-203.
Kurtz AC, Derry LA, Chadwick OL, (2001) Accretion of asian dust to Hawaiian soils: isotopic, elemental and mineral mass balance", Geochimica et Consmochimica Acta, 65, 12, 1971-1983.
Kuzu SL, Saral A, Demir S, Summak G, Demir G (2013) A detailed investigation of ambient aerosol composition and size distribution in an urban atmosphere, Environmental Science and Pollution Research, 20, 2556-2568.
Kuzu SL, Saral A (article in press) The effect of meteorological conditions on aerosol size distribution in Istanbul, Air Quality, Atmosphere & Health, doi: 10.1007/s11869-017-0491-y
Lin TS, (2001) Long-range transport of yellow sand to Taiwan spring 2000: observed evidence and simulation, Atmospheric Environment, 35, 5873-5882.
Pateraki S, Asimakopoulos DN, Flocas HA, Maggos T, Vasilakos C (2012) The role of meteorology on different sized aerosol fractions (PM10, PM2.5, PM2.5-10) Science of the Total Environment, 419, 124-135
Pettke T, Halliday AN, Hall CM, Rea DK, (2000) Dust production and deposition in Asia and the North Pacific Ocean over the past 12 Myr, Earth and Planetary Science Letters, 178, 3-4, 397-413.
Rost KT, (2001) Late Holocene Losses deposits and dust accumulation in the alpine meadow belt of the Wutai Shan, Quaternary International, 76-77, 85-92.
Singer A, (1988) Illitein aridic soils, desert dusts and desrt loses, Sedimentary, Geology, 59, 251, 251-259.
Theodosi C, Im U, Bougiatioti A., Zarmpas P, Yenigun O, Mihalopoulos N, (2010) Aerosol chemical compositon over Istanbul, Science of the Total Environment, 408, 12, 2482-2491.
Uno I, Amano H, Emori S, Kinoshita S, Matsui I, Sugimoto N, (2001) Trans-pacific yellow sand transport observed in april 1988, Journal of Geophysical Research, 106, 16, 18331-18344.
Uwayemi MS, Su Y, Dabek-Zlotorzynska E, Rastogi AK, Brook J, Hopke PK, (2015) Sources and temporal variations of constrained PMF factors obtained from multiple-year receptor modeling of ambient $PM_{2.5}$ data from five speciation sites in Ontario, Canada, Atmospheric Environment, 108, 140-150.
Yatkin S, Bayram A, (2007) Elemental composition and sources of particulate matter in the ambient air of a metropolitan city, Atmospheric Research 85, 126-139.
Zhang XY, Arimoto R, An ZS, (1999) Glacial and interglacial patterns for asian dust transport. Asian dust linked to global change, Quaternary Science Review, 18, 811-819.
Zhang XY, Lus HY, Arimoto R, Gong SL, (2002) Atmospheric dust loadings and their relationship to rapid oscillations of Asian winter moonsoon climate: two 250-kyr loses records, Earth and planetary science Letters, 202, 637-643.

AN EXPERIMENTAL AND ANALYTICAL INVESTIGATION ON THE EXHAUST EMISSIONS OF A FERRY

Murat Durmaz, Selma Ergin*
Istanbul Technical University, Faculty of Naval Architecture and Ocean Engineering,
Maslak 34469 Istanbul, Turkey.
**ergin@itu.edu.tr*

ABSTRACT
Ship exhaust emissions contribute to local and global air quality degradation and have adverse effects to the environment and human health. In this study, exhaust emissions of a ferry running with ultra-low sulphur diesel fuel (ULSD) were investigated experimentally and analytically. NOx, SOx, CO, CO_2, HC and PM emission concentrations as well as shaft power were measured on board ferry at various engine loads. Emission factors for different engine loads and weighted emission factors were determined. The weighted emission factors of NOx, SOx, CO, CO2, HC and PM emissions are obtained as 11.91 g/kWh, 0.10 g/kWh, 0.67 g/kWh, 611.14 g/kWh, 0.62 g/kWh and 0.079 g/kWh, respectively. Furthermore, emission factor, engine load factor and voyage time were determined for different voyage stages of ferry, in order to calculate amount of emissions emitted from the ferry, annually. These emission calculations were performed using data in the literature and compared with the measurements. It is seen that the emission factors are the major parameter in emission calculations and should be selected carefully, especially for the local emission inventory studies.

Keywords: *ship emissions; air pollution, marine diesel engine; ultra-low sulphur diesel fuel .*

INTRODUCTION
Shipping based emissions have substantial contribution to the amount of global emissions, which are produced by human activity (Corbett J.J. et al., 1999). Ship emissions have adverse effects to the environment as well as human health. Diesel engines are used mostly to provide propulsion power and electricity needs of ships. Diesel engines are durable, reliable and most efficient internal combustion engines, however, they emitted gaseous and particulate emissions as a result of combustion process. Main exhaust emissions of diesel engines are carbon dioxide (CO_2), nitrogen oxides (NOx), sulphur oxides (SOx), carbon monoxide (CO), hydrocarbons (HC) and particulate matters (PM). HC, CO, NOx and PM originate from engine technology whereas CO_2, SOx, heavy metals and further PM become from fuel property (ENTEC, 2002).
Due to the substantial contribution of shipping based emission to global air pollution and increasing environmental concerns, shipping based emissions have become a great concern in many studies recently. For example, Corbett et al. (1999), Van Aardenne et al. (2013) and Smith et al. (2014) were carried out detailed emission inventory studies. Besides of the global emission inventory studies, effects of emissions on special regions such as harbors, ports and coastal areas, were investigated in many studies (see, for example, Fu et al. (2013), Goldsworthy et al. (2015), Tzannatos (2010) and Ergin (2011)). Ergin (2011) calculated exhaust emissions from ships sailing through Turkish Straits and Marmara Sea using 2010 AIS data and national statistics. Emissions from these vessels were calculated as, 56.49 ktons/year of NOx emissions, 18.57 ktons/year of SO2 emissions, 2518.2 ktons/year of CO2 emissions, and 18.57 ktons/year of PM emissions. Other emission inventory studies about emissions from ships sailing Marmara Sea were presented in the studies of Kesgin et al. (2001) and Deniz et al. (2008). Also, Ergin (2011) and Viana et al. (2014) showed that the implementation of ECA emission limits for ships in Bosphorous Strait would reduce shipping based emissions and substantial air quality improvement can be achieved.

In addition to emission inventory studies there are also experimental studies about shipping emissions. However they are limited in number. Cooper et al. (2003), Agrawal et al. (2009), Melo et al. (2013), Fu et al. (2013) and Peng et al. (2016) present measured emission factors for different engine loads and weighted emissions for different pollutant species. It is highlighted that there was substantial differences on the emission factors for some types of ships. Especially, ships that have different design characteristics and have different operational parameters. Due to these reasons, on board exhaust emission measurements provide important knowledge and data for emission inventory calculations. Furthermore, experimental measurements are also useful to show the condition of the engine.

This study extends the works of authors (Ergin, Kalender and Durmaz (2016), Ergin et al.(2016), Kalender et al. (2016), Durmaz et al. (2016), Kalender and Ergin (2017) and Durmaz et al. (2017)) further and presents new original data on ship emissons.

The main aim of this study is to investigate the effects of ultra-low sulfur diesel fuel on the gaseous and particulate emissions of a ferry sailing at Marmara sea, experimentally and analytically. In this study NOx, SOx, CO, CO_2, HC and PM emissions of the main engine were measured on board, at various engine loads. In order to obtain the emission factors and weighted emissions, the shaft power, the temperature and differential pressure of the exhaust gases and the temperature, pressure and humidity of the intake air were measured. The emission factors for different engine loads, the weighted emission factors, load factors, monthly emissions and annual emissions are presented and discussed. Also, the annual emissions were calculated using the emission factors and load factors in the literature and compared with the results of this study.

EXPERIMENTAL METHODOLOGY

The gaseous and particulate emissions, namely, NOx, SO_2, CO, CO_2, HC and PM emissions were measured on board of a ferry sailing at Marmara Sea. The main properties of the ferry and specifications of the main engine are presented in Table 1. In addition to the information given in Table 1, the ferry has three four-stroke medium speed auxiliary engines which are 175 kW at rated speed of 1500 rpm. Since the ferry was built in 2000, the ferry must meet the IMO Tier I NOx emission limits.

In Table 2, properties of the fuel used during the experimental study were presented. Both main and auxiliary engines are running with ultra-low sulfur diesel fuel (ULSD).

Table 1. Properties of The Ferry.

Parameter	Value
Ship length (m)	80.71
Gross tonnage (m^3)	1595.72
Engine speed (rpm)	750
Engine power (kW)	2x883
SFOC of main engine (g/kWh)	198

Table 2. Properties of the ultra-low sulfur diesel fuel.

Parameter	Value
Density, kg/m3	831.1
Water content, mg/kg	48
Sulfur, mg/kg	4.4
Cetan Index	58.6

The emissions were measured in the exhaust stack of the main engine in the engine room at different engine loads. Measurements were carried out according to the IMO MARPOL Annex VI (2008). During measurements E2 internal combustion engine test cycle were employed for the main engine of the ferry. Also, the measurements complies with ISO 8178 standards (2008).

Experimental set-up can be seen in Figure 1. As described in the measurement standards, the sampling port location were determined regarding whether there is convenient distant between sampling port and any flow disturbing elements. Also, the sampling port location were after turbocharger. During measurements, for each engine load the shaft power, the exhaust temperature and the exhaust differential pressure were measured. Furthermore, the humidity, temperature and pressure of the intake air were measured.

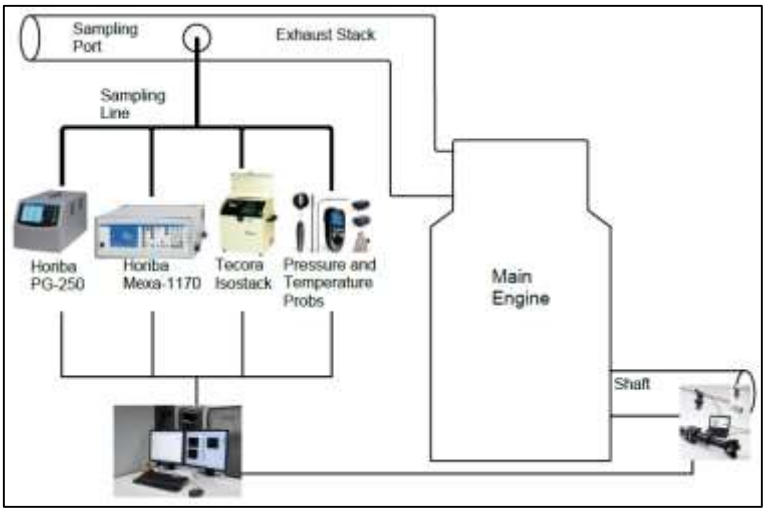

Figure 1. Experimental Set-Up.

The engine brake power at different engine loads were measured using strain gauges located on shaft. The reduction gear losses were added to shaft power and it is considered to be 5%. The engine brake power during a voyage for different stages of trip can be seen in Figure 2.

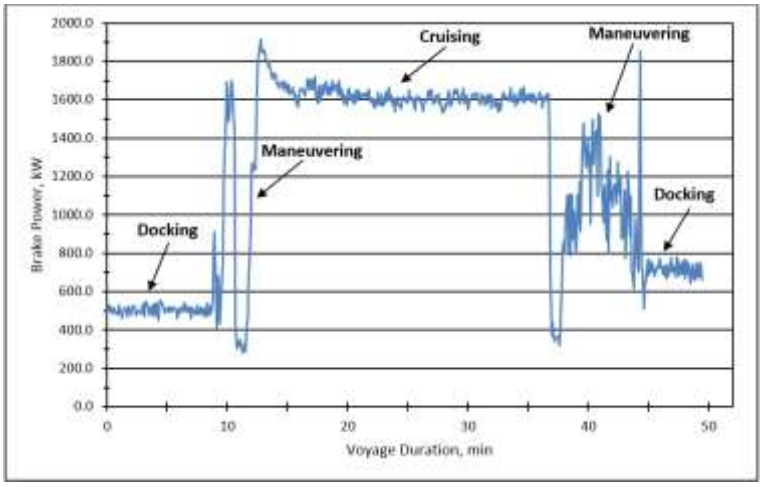

Figure 2. The voyage durations for different phases of a trip.

The gaseous emissions, NOx, SO_2, CO, CO_2 and O_2 were measured in raw exhaust gas using Horiba PG-250 gas analyzer. According to the E2 internal combustion engine test cycle, the measurements were carried out at 25%, 50% 75%, and 100% engine loads. The unburned

hydrocarbons (HCs) were measured using with Horiba Mexa 1170. Particulate matter (PM) emissions were measured with Tecora Isostack Basic. PM emissions were collected on glass micro fiber filters and analyzed gravimetrically. Filters were weighted on a micro balance before and after sampling. The PM emission measurements were carried out in accordance with the ISO 9096 standard under isokinetic sampling conditions.

ESTIMATION OF THE EMISSONS

The emission factors for gaseous pollutants and particulate matter were calculated for different engine loads. The weighted emission factors were also calculated. The calculation methodology given in IMO MARPOL Annex VI (2008) is used to obtain the results.

Annual emissions dissipated from ferry were calculated by using bottom-up methodology and details of the method given in Trozzi (2010) and Van Aardenne et al. (2013). According to this methodology, the emissions dissipated from ferry at different phases of voyage can be calculated using Equation 1. As can be seen from Figure 2, one trip of ferry consists of two docking, two maneuvering and the cruising phases. Also, the duration of each phases of the trip and total voyage duration are presented in Figure 2. Furthermore, the main engine brake power of the ferry for different voyage stages are presented in Figure 2. The symbols T, P, LF and EF in Equation 1 means the voyage duration, engine power, load factor and emission factor, respectively.

$$E_{trip,i,j,m} = \sum_{p}\left[T_p \times \sum_{e}\left(P_e \times LF_e \times EF_{e,i,j,m,p} \right) \right] \quad \textbf{(1)}$$

The emissions were calculated using the load factors from the literature and this study. The load factors (LF) for different stages of the trip are presented in Table 3.

Table 3. Engine load factors.

Voyage Stage	LF (Ritchie et al. (2005))	LF (this study)
Port	0.20	0.25-0.3
Maneuvering	0.20	0.5-0.6
Cruising	0.80	0.75-0.8

Table 4 shows the emission factors (EF) from the literature and this study. The EF values from literature were taken from Ritchie et al. (2005) and Smith et al. (2014).

Table 4. The voyage numbers.

Emission Species	Voyage Stage	EF in Literature (g/kWh)	EF in this study (g/kWh)
NO_X	Cruising	13.2	11.8
NO_X	Maneuvering	10.6	11.3
NO_X	Port	10.6	15.3
SO_2	Cruising	1	0.49
SO_2	Maneuvering	1	0.89
SO_2	Port	1	2.03
CO	Cruising	0.54	0.07
CO	Maneuvering	0.54	0.11
CO	Port	0.54	0.16
CO_2	Cruising	697	536.58
CO_2	Maneuvering	747	522.66
CO_2	Port	725	737.80

HC	Cruising	0.46	0.57
HC	Maneuvering	0.97	0.74
HC	Port	0.5	1.36
PM	Cruising	0.73	0.07
PM	Maneuvering	1.57	0.07
PM	Port	0.9	0.13

The amount of emissions for docking, maneuvering and cruising phases of a trip were calculated using Equation 1 and then they were summed to find the total emissions from one trip of the ferry.

The total voyage numbers and daily average voyage numbers per month in 2015 are presented in Figure 3. Using this statistical values, the amount of gaseous and particulate emissions were calculated monthly and annually.

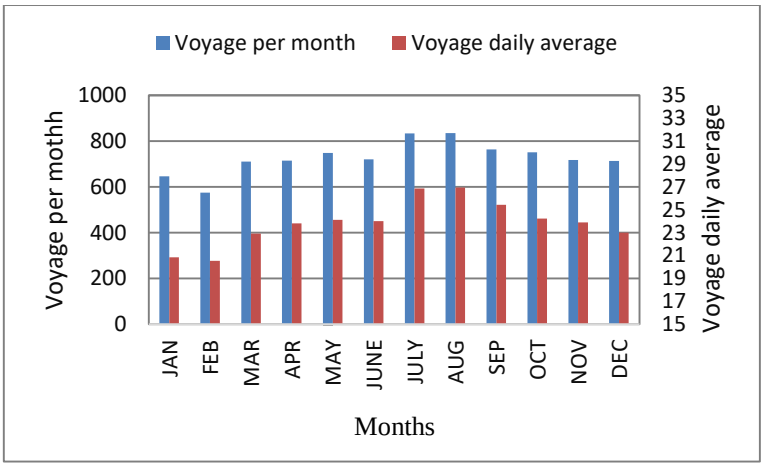

Figure 3. The voyage numbers.

RESULTS AND DISCUSSIONS

The nitrogen oxides (NO_X), sulfur dioxide (SO_2), carbon dioxide (CO_2), carbon monoxide (CO), hydrocarbons (HC) and particulate matter (PM) emissions are presented in Figures 4-9 for different engine loads of the main engine. The gaseous emissions are presented both in ppm and g/kWh. Figure 10 shows the weighted emission factor.

As can be seen from Figure 4, the amount of NO_X emissions in ppm, increases when engine load increases. It is fact that, when engine load increases, pressure and temperature in combustion chamber increases. As a result of higher temperatures, NOx emissions increase. On the other hand, the highest NOx emission (gr/kWh) is observed at 25% engine load. These mean that more NOx emissions dissipated at lower loads. This is due to the lean mixture of fuel/air operation conditions (EPA (1999)).

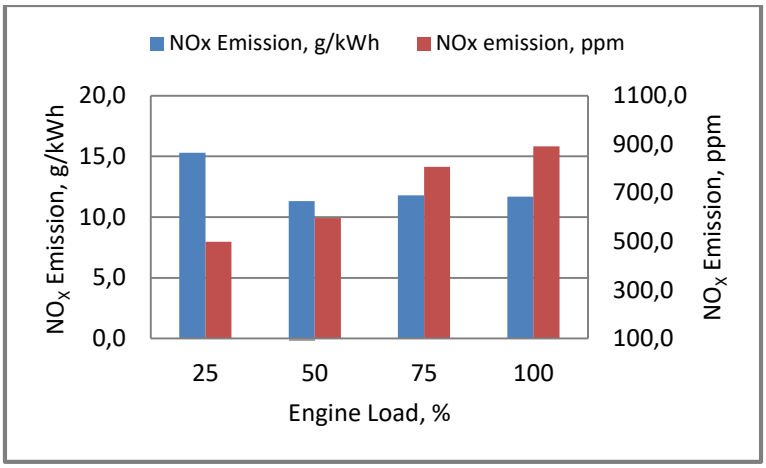

Figure 4. NO_X emissions for the main engine.

The CO emission is an incomplete combustion product and occur in exhaust gases as a result of low temperature combustion and lack of the oxygen. As can be seen from Figure 5, the CO emission gets its lowest value at nearly 75% engine load. It increases when engine load increases to 100% as a result of lower air to fuel ratio. However, the highest value of the CO emission is observed at 25% engine load. This can be as a result of the low temperatures in the combustion chamber. Also, degradation of the the fuel atomization may result higher CO emissions (EPA (2010)).

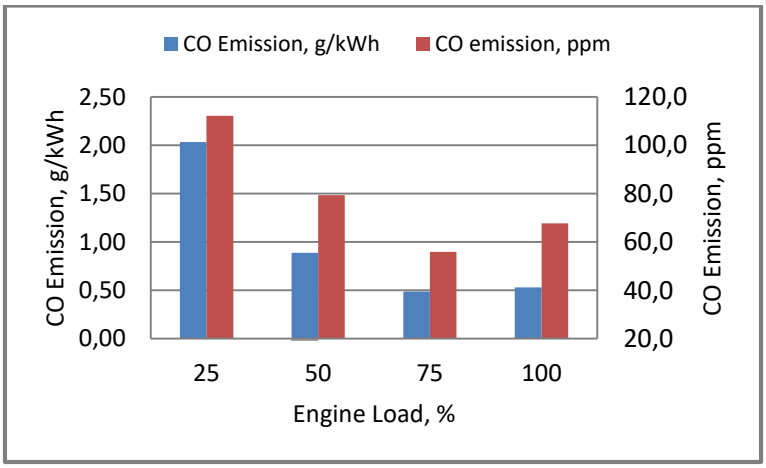

Figure 5. CO emissions for the main engine.

The CO_2 emission is a product of the combustion phenomena, formed as a result of oxidation of the carbon in the fuel. It is considered as a greenhouse gas, therefore IMO limits the CO_2 emission for ships built after 1 January 2013. As can be seen from Figure 6, the CO_2 emission gets its highest value at 25% engine load, where the engine operating with low thermal efficiency.

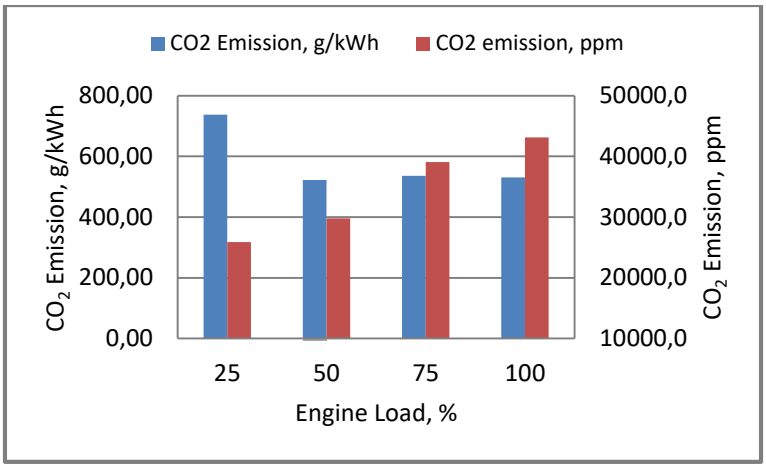

Figure 6. CO_2 emissions for the main engine.

The SO_2 emissions related with fuel properties. In this study, due to low sulphur content of ULSD, the SO_2 emissions are quite low as seen from Figure 7.

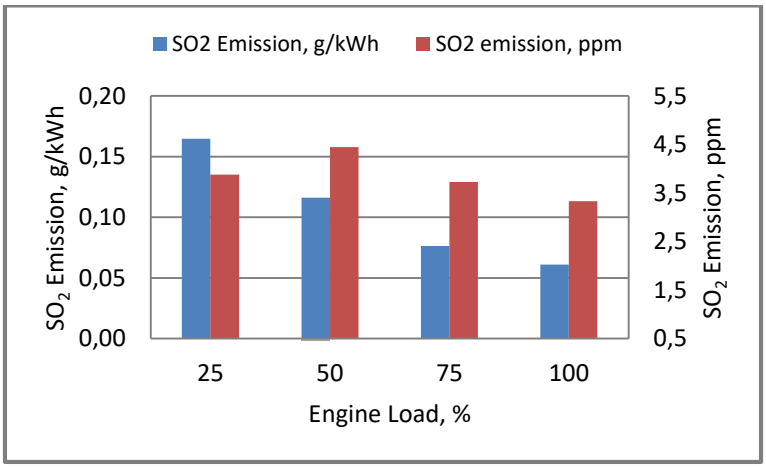

Figure 7. SO_2 emissions for the main engine.

Analogously with the CO emissions, the HC emissions occur as a result of incomplete combustion. As can be seen from Figure 8, the HC emissions have higher values at low engine loads. This is due to the low combustion temperatures at low engine loads.

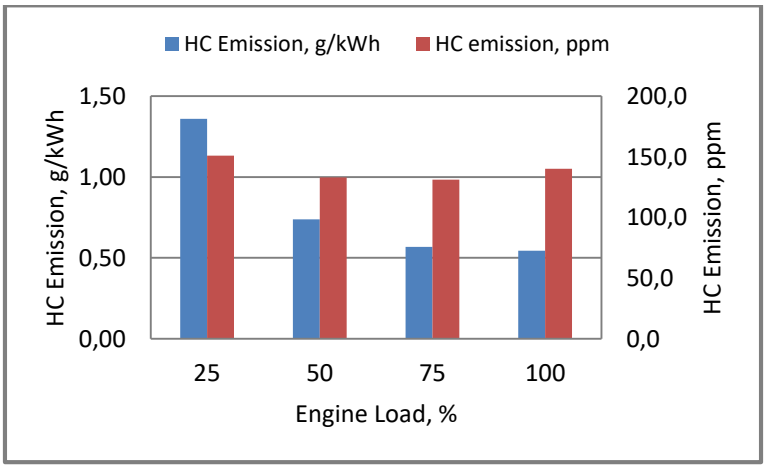

Figure 8. HC emissions for the main engine.

In Figure 9, the particulate emissions are presented. The PM emissions mostly depend on the amount of sulphur in the fuel. Due to this reason, PM emissions are obtained quite low. On the other hand, it can be seen from Figure 9, the highest PM emission occur at 25% engine load. The low combustion efficiency, low combustion temperature also inadequate fuel atomization may cause this peak PM value.

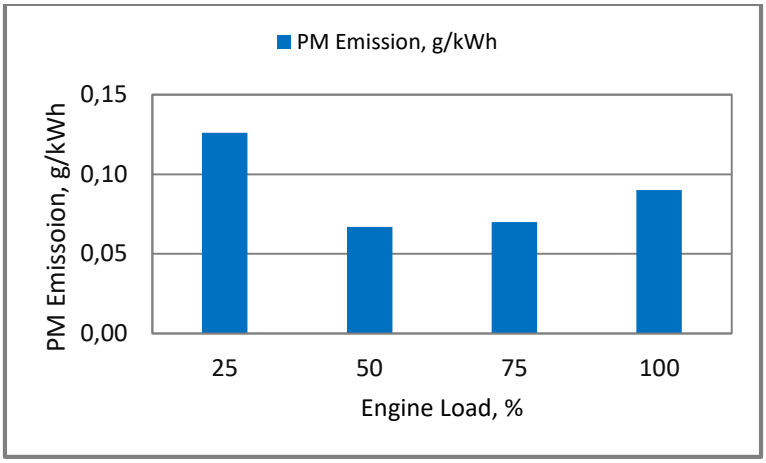

Figure 9. PM emissions for the main engine.

In Figures 4-9, the values of different emission species at different engine loads are presented. In Figure 10, weighted emission factors for each species are presented. The weighted emission factors were calculated according to E2 test cycle given in IMO MARPOL Annex VI. It can be seen from Figure 10, this ferry complies with IMO MARPOL Annex VI Tier I NOx limits.

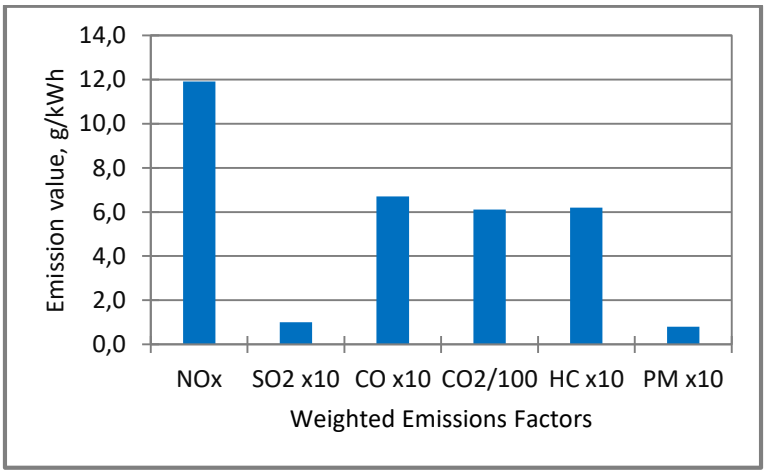

Figure 10. Weighted emissions for the main engine.

The gaseous and particulate emissions dissipated from the ferry were calculated for 2015 year, monthly and annually. Figure 11 presents the amounts of the pollutants from ferry, monthly. The figure shows that the emission values are higher in the summer season than in the winter, autmun and spring seasons.

The amount of emissions dissipated from ferry, annually are presented in Figure 12. The amount of emissions calculated using the emissions factors and engine load factors of this study and literature are compared in Figure 12. The annual emissions of the ferry are 97 tons of NOx, 0.8 tons of SO_2, 4467 tons of CO2, 6.2 tons of CO, 5.6 tons of HC and 0.6 tons of PM. The comparisons between the annual emissions of this study and the emissions obtained using EF

and LF data from the literature show that there are high differences especially for SO2, CO, HC and PM emissions.

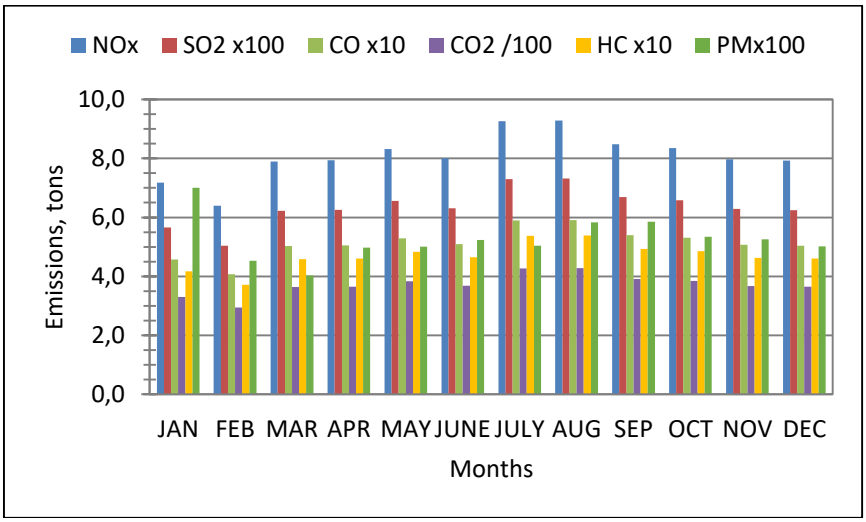

Figure 11. The monthly emissions of the ferry.

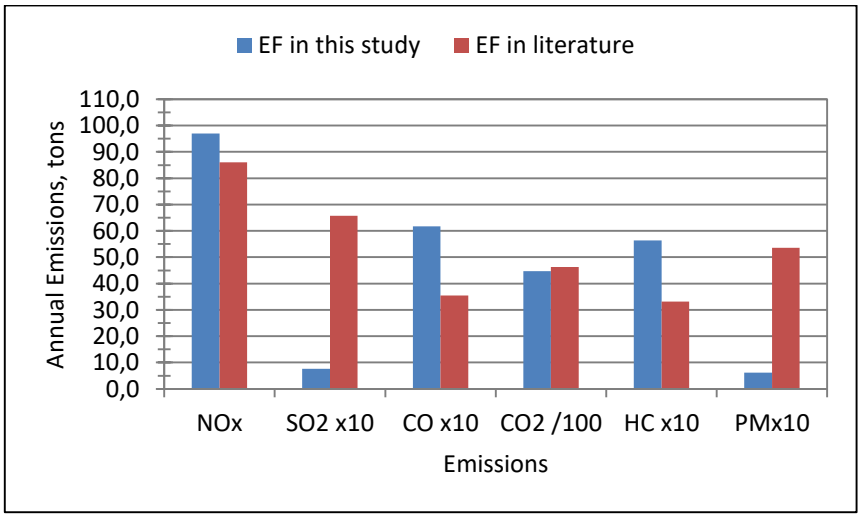

Figure 12. The comparison of the annual emissions of the ferry.

CONCLUSIONS

The effects of the ultra-low sulfur diesel fuel (ULSD) on the emissions of a ferry are investigated, experimentally and analytically. The gaseous and particulate emissions from the main engine of the ferry were measured on board at various engine loads. The emission factors for different engine loads and weighted emission factors are determined. The weighted emission factors of NOx, SOx, CO, CO_2, HC and PM emissions are obtained as 11.91 g/kWh, 0.10 g/kWh, 0.67 g/kWh, 611.14 g/kWh, 0.62 g/kWh and 0.079 g/kWh, respectively. The weighted NOx emission value show that the ferry meets the Tier 1 NOx emissions limits. The SO_2 and PM emission values are obtained quite low. This is due to using the ultra-low sulfur diesel fuel (ULSD) in the main engine. It is found that the HC and CO emissions are higher at low engine loads. This can be attributed to the poor combustion performance of the engine at low loads. The NOx, SOx, CO, CO_2, HC and PM emissions are presented, monthly and annually. The monthly results show that the emissions at summer season are higher than the emissions at other seasons. The annual emissions of the ferry are obtained as 97 tons of NOx, 0.8 tons of SO_2, 4467 tons of CO_2, 6.2 tons of CO, 5.6 tons of HC and 0.6 tons PM. Also, the comparisons between the annual emissions obtained using the emission factors and load factors of this study

and literature show that there are quite high differences in the SO2, CO, HC and PM emissions of the ferry. Therefore, the emission factors and load factors for the emission inventory studies should be chosen carefully. The shipping activity in the Marmara sea increases, therefore, the emissions from shipping becoming a dominant source of the air pollution. Therefore, the studies on the ship emissions are beneficial to foresee and reduce the impacts of ship emissions.

ACKNOWLEDGEMENTS

The authors thank the ship owner company, IDO for their support on the experimental study. Also, masters, chief engineers and crew are thanked for their help during on-board measurements.

The study was partially supported by the Research Projects Coordination Unit (BAP), Istanbul Technical University, Turkey. The authors also thank them for the financial support.

REFERENCES

Agrawal, H. (2009). *Analyses and Impacts of Emissions From Marine Engines* (Doctoral dissertation, University of California, Riverside) Retrieved from http://search.proquest.com/docview/304851201

Cooper, D. (2003). Exhaust emissions from ships at berth. *Atmospheric Environment, 37*(27), 3817-3830. doi: 10.1016/s1352-2310(03)00446-1

Corbett, J. J., Fischbeck, P. S., & Pandis, S. N. (1999). Global nitrogen and sulfur inventories for oceangoing ships. *Journal of Geophysical Research: Atmospheres (1984–2012), 104*(D3), 3457-3470.

Deniz, C. and Durmuşoğlu, Y. (2008). Estimating shipping emissions in the region of the Sea of Marmara, Turkey. *Science of the total environment, 390*(1), 255-261.

Durmaz, M., Kalender, S.S. & Ergin, S. (2017) Experimental Study on The Effects of Ultra-Low Sulfur Diesel Fuel to The Exhaust Emissions of A Ferry. *Fresenius Environmental Bulletin*, 26(10), 5833-5840.

Durmaz, M., Kalender, S.S. & Ergin, S. (2016). Measurements Of Particulate Emissions From A Ferry, *Proc. of the The Second Global Conference On Innovation In Marine Technology And The Future Of Maritime Transportation, GMC 2016*, 24-25.10.2016, Muğla, Turkey, 377-386, ISBN: 978-605-01-0930-6

Entec (2002). Quantification of emissions from ships associated with ship movements between ports in the European Community. *Report for the European Commission. Entec UK Limited, Northwich, Great Britain*.

EPA (1999). Technical Bulletin, Nitrogen Oxides (NOx), Why and How They Are Controlled. *US Environmental Protection Agency Washington, DC*.

EPA (2010). AP 42, Chapter 1: External Combustion Sources. *US Environmental Protection Agency Washington, DC, Fifth Edition, I*.

Ergin, S. (2011). Gemi Kaynaklı Hava Kirliliğinin Kontrolü Projesi Sonuç Raporu.

Ergin, S., Kalender, S.S. & Durmaz, M. (2016). On Board Measurements Of Exhaust Emissions From A Ferry Sailing At Marmara Sea, *Proc. Of the 1st International Congress On Ship And Marine Technology, GMO SHIPMAR 2016*, 08-09.12.2016, Istanbul, Turkey

Ergin, S., Durmaz, M. & Kalender, S.S. (2016). An Experimental Investigation of Exhaust Emissions From A Ferry, *Proc. Of the 30th Asian-Pacific Technical Exchange and Advisory Meeting on Marine Structures, TEAM 2016*, 10-13.10.2016, Mokpo, Republic of Korea, 406-412,

Fu, M., Ding, Y., Ge, Y., Yu, L., Yin, H., Ye, W., & Liang, B. (2013). Real-world emissions of inland ships on the Grand Canal, China. *Atmospheric Environment, 81*, 222-229.

Goldsworthy, L., & Goldsworthy, B. (2015). Modelling of ship engine exhaust emissions in ports and extensive coastal waters based on terrestrial AIS data–An Australian case study. *Environmental Modelling & Software, 63*, 45-60.

IMO. (2008). Revised MARPOL Annex VI: Regulations for the Prevention of Air Pollution from Ships and NOx Technical Code 2008.

ISO 8178. (2008). Reciprocating Internal Combustion Engines-Exhaust Emission Measurement: Moteurs Alternatifs À Combustion Interne-Mesurage Des Émissions de Gaz D'échappement. Steady-state Test Cycles for Different Engine Applications. Cycles D'essai en Régime Permanent Pour Différentes Applications Des Moteurs: ISO.

Kalender, S.S., Durmaz, M. & Ergin, S. (2016). On-board measurements of emissions from a ferry, *Proc. of the 3rd Int. Conf.on Maritime Technology and Engineering, MARTECH 2016*, 4-6 July 2016, Lisbon, Portugal *745-749 Volume 2, ISBN 978-1-138-03000-8*.

Kalender, S.S. & Ergin, S. (2017). An Experimental Investigation Into The Particulate Emissions of A Ferry Fuelled With Ultra-Low Sulfur Diesel. *Journal of Marine Science and Technology*, 25(5), doi: 10.6119/JMST-017-0418-2.
Kesgin, U. and Vardar, N. (2001). A study on exhaust gas emissions from ships in Turkish Straits. *Atmospheric Environment, 35*(10), 1863-1870.
Melo Rodríguez, G. d., & Murcia Cuenca, J. M. (2013). Analysis and measurement of NOx emissions in port auxiliary vessels. *The International Journal on Marine Navigation and Safety of Sea Transportation*, 7(3), doi: 10.12716/1001.07.03.15
Peng, Z., Ge, Y., Tan, J., Fu, M., Wang, X., Chen, M., ... & Ji, Z. (2016). Emissions from several in-use ships tested by portable emission measurement system. *Ocean Engineering*, *116*, 260-267.
Ritchie, A., De, J. E., Hugi, C., & Copper, D. (2005). Service Contract on Ship Emissions: Assignment, Abatement and Market-Based Instruments. Task 2c–SO2 Abatement. Final report prepared for the European *Commission DG Environment by ENTEC UK*.
Smith, T.W.P., Jalkanen, J.P., Anderson, B.A., Corbett, J.J., Faber, J., Hanayama, S., O'Keefe, E., Parker,S., Johansson, L., Aldous, L., Raucchi, C., Traut, M., Ettinger, S., Nelissen, D., Lee, D.S., Ng, S., Agrawal A., Winebrake, J.J. Hoen, M., Chesworth, S. & Pandey, A. (2014). Third IMO GHG Study 2014. IMO, London.
Tzannatos, E. (2010). Ship emissions and their externalities for the port of Piraeus – Greece. *Atmospheric Environment, 44*(3), 400-407. doi: 10.1016/j.atmosenv.2009.10.024
Trozzi, C. (2010). Emission estimate methodology for maritime navigation. *Techne Consulting, Rome*.
Van Aardenne, J., Colette, A., Degraeuwe, B., Hammingh, P., & De Vlieger, I. (2013). *The impact of int. shipping on European air quality and climate forcing* (Vol. 4).
Viana, M., Hammingh, P., Colette, A., Querol, X., Degraeuwe, B., Vlieger, I. d., & van Aardenne, J. (2014). Impact of maritime transport emissions on coastal air quality in Europe. *Atmospheric Environment, 90*, 96-105. doi: 10.1016/j.atmosenv.2014.03.046
Winnes, H., Moldanova, J., Anderson, M., & Fridell, E. (2014). On-board measurements of particle emissions from marine engines using fuels with different sulphur content. *Proceedings of the Institution of Mechanical Engineers, Part M: Journal of Engineering for the Maritime Environment*.

AN EVALUATION ON EFFECT ON CITY AIR QUALITY AND CREATION OF HEAT ISLAND BY ATATÜRK AIRPORT AND ISTANBUL 3rd AIRPORT

Orhan Sen[1], Doğan Kantarcı[2]
[1]Istanbul Technical University, Department of Meteorological Engineering
seno@itu.edu.tr
[2]Istanbul University, Faculty of Forestry
mdkant@istanbul.edu.tr

It is understood that in addition to the two existing airports in Istanbul, an attempt to build a third air port in the north will adversely affect the quality of the city's air and create a "heat island" on the city. The calculations made at Ataturk Airport on the number of flights and LTO rates in the first 10 months of 2016 show that significant amounts of CO, HC, NOx, SO_2 gases are released (Şen, 2016 and Sen and Dursun, 2017). In this study, CO_2 gas emission was also calculated and evaluated. The findings were also compared with the data on long-term (2016) and air pollution data of "Istanbul 3rd Airport" calculated by Tuna et al, (2016). In Atatürk Airport, the amount of carbon dioxide (CO_2) absorbed according to the LTO values of the landing / take-off and runway / departure movements of the different models in the first 10 months of 2016 is given as 662 798,64 tons. The emissions of CO_2 are 4845,02 – 4360,52 ppm/months (88,373 – 79,586 ppm/year) at the Ataturk Airport's airplane movement area (9-10 km³ volume) and In the vicinity of the airport 218,03 ppm/year (20x0 km x1 km), 72,68 ppm/ year in the vicinity of the airport (30x20 km x 1 km) and 29 ppm/month, 348,8 ppm/year in the vicinity of the airport (50<30x 1 km). When these CO2 values are added to the air present at 400 ppm CO_2, An important "Heat Island formation" emerges in Atatürk Airport. The "Heat Island" is spread by the northern winds over the Marmara Sea and absorbed by evaporation on the surface of the sea. However, if the same (or similar) values occur on the Istanbul 3. Airport, "Heat Island" will be spread over the city of Istanbul. CO_2, which precipitates in the valleys and lowlands, will be added to the "heat island" formed by the concrete of the city and will further increase the warming and all the related climate changes. Naturally, the "negative ecological" effects of climate change will also increase.Airplane movements at Ataturk Airport cause significant amounts of air pollutant exhaust gases to be released. At the Airport 10 km³ (10 km²x1 km) in volume; (Carbon monoxide) 195 180 µg /m³/year, HC (hydrocarbons) 22 464 µg/m³/ year, NOx (nitrogen oxides) 391 668 µg /m³/ year, SO_2 (sulfur dioxide) 25 200 µg / m3/ year was calculated. When these air pollutant gases are spread over a 600 km² (30x20 km) area, with a height of 1000 m (600 km³); It is calculated that CO is 3253 µg / m³ / year, HC is 374,4 µg / m³ / year, NOx is 6527,8 µg / m³ / year and SO_2 is 420 µg / m³ / year. These gases are drifting on the Marmara Sea with the northern winds and are diluting there. However, it is understood that if the same amount of gas is caused by the 3rd airport in Istanbul, it will create an air pollution that will spread over the city and not be underestimated.

According to an account made for the flight number 6, which is planned to open at 4th stage in İstanbul 3. Airport Annual and hourly emissions were calculated as 5314 ton / year and 9180 µg / m³ / hour for CO, 10006 ton / year and 17286 µg / m³ / hour for NOx, 557 ton / year and 960 µg / (Uzun, 2016). The findings of this study, which are made according to the number of flights, aircraft types and other assumptions, are lower than those of Atatürk Airport. Despite the differences, findings from both studies show that Istanbul 3rd Airport will cause climate change and air pollution in the city.

***Keywords*:** Airport, CO_2, LTO, Heat Island

AN ECOLOGICAL ANALYSISON CLIMATE CHANGE WITH THE SEA AND ATMOSPHERE HEATING THE POWER PLANT IN THE İSKENDERUN GULF

Doğan KANTARCI, Orhan ŞEN[2]
[1] Istanbul University, Faculty of Forestry, Turkey
[2]Istanbul Technical University, Department of Meteorological Engineering, Turkey
mdkant@istanbul.edu.tr, seno@itu.edu.tr

In addition to the existing thermal power plants near Iskenderun Bay, new thermal power plants with imported coal and natural gas are operated, corresponding approvals and licenses are on the agenda.Of course there are legal cases against these thermal power plants to ensure the continuity of the viability of the zone. Many studies and publications on the topic were also made. In this study the cumulative effect of thermal power plants in the region;
(1) Heating by the effect of the greenhouse effect on carbon dioxide (CO_2) and climate change,
(2) On the increase of the sea temperature with the hot water of thermal power plants, were examined and evaluated with regard to climate change.

A total of 33 thermal power plants were built or planned in İskenderun Bay. One of them is founded in the mountain region (Tufanbeyli) in the north.Of the 32 thermal power plants, 25 will be used with imported coal, 6 natural gas and 1 petroleum. Of the 26 thermal power plants are the air pollutants CO, NOx, SO_2 and other gases such as CO_2 and particles (PM ≤ 10 μm), and 45-46 heavy metals (PM ≤ 2.5 μm) added from the coal through the electrostatic filters on the atmosphere with the flue gas.

CO_2 is an important greenhouse gas. Carbon dioxide is concentrated in the narrow coastal region between Yumurtalık and Aşağı Burnaz (Erzin) and Payas, where the thermal power plants are arranged side by side. The warm exhaust gases will rise to a height of 1000 m and the density of CO_2 will reach 17736.2 ppm in a 10x30 km area. The CO_2 will spread with the exhaust gases About Çukurova about 100x50 km of land and dilute the density of CO_2 to 10.6 ppm

Air masses that blow north or rise in the mountains and lean against the mountain slope will cool down at night and flow into the low country (Çukurova) as a "mountain breeze" and "country breeze". At night CO_2 and the exhaust gases will not rise too high, they are also added in the lowland deposited CO_2.In addition, the smoke gases and CO_2 from the Tufanbeyli power station sink into the lowland and Çukurova with mountain breezes.

All these CO_2 deposition densities in Çukurova are estimated to be 63-65 ppm (even more in winter). The addition of up to 63-65 ppm CO_2, which will precipitate in Çukurova and its surroundings, results in a significant warming (≈1 °C) and climate change to achieve a CO_2 concentration of 400 ppm in the Earth's atmosphere.

The cooling water of the power stations is taken from the sea (except Tufanbeyli). The sea water is already warm (≈28 °C). For cooling, more water is needed.Only 20 power plants between Yumurtalık and Aşağı Burnaz have an annual cooling water volume of 28.7 billion m^3/year.It is calculated that the water in the sea volume is taken up to a depth of 100 m and the distance of 10 km from the coast as cooling water in one year and is reproduced. The seawater is to be taken and returned in 2 years to the sea water volume up to 20 km from the coast.The width of the İskenderun Gulf between Yumurtalık-Payas is 30 km Considering Payas and its southern

power plants and other industrial facilities, on this part of the Gulf. This means all sea water can be transferred as cooling water up to 100 m depth in 2 years.It is assumed that the cooling water is let up to a depth of 60 m in the sea and produces a temperature difference of ≈ 1 °C on the surface. However, 10-12 or 20 °C warm water is given to the 60 m depth of the sea. There will be a substantial massive heating. The effect of warmer sea water on warming the atmosphere should also be viewed as a major climate change. On the other hand, the effect of cleaning chemicals in water system on the marine ecosystem is deathly.

INTRODUCTION

Natural ecosystems consist of two parts; "Living Societies" and "Site / Environment" where they are born, grown and live. The ecosystem itself has a "balance between the circulation and transformation of energy with matter". This balance is somewhat contrary to the negative effects of the outside. That is, the ecosystem can compensate or damage to some degree compensate. However, if the damage across the site is very strong, changing the characteristics of the location, it will cause living things to disappear in the ecosystem.

If you open a stone quarry in the forest area, you destroy the forest. The forest does not grow there again. If you operate an open coal stove in agricultural areas, you will destroy the land. There is no more farming there.

ISKENDERUN AND MERSIN GULF IN EASTERN MEDITERRANEAN

In the Mediterranean Basin; Under the influence of the Azor high pressure area in the Atlantic Ocean, the winds are from the West Mediterranean to the Eastern Mediterranean (GB Lodos winds). The air masses, between Cyprus Island in the south and the Bolkar Mountains Massive in the north and the massifs of the Amanos Mountains in the east, move through the Gulf of Iskenderun towards Çukurova to the northeast (Map 1). Warm air masses coming from the western Mediterranean are warmer in this area and to cause the seawater to warm up and high evaporation. Therefore, the sea water in this region is hot (≥ 30 ° C) in the summer months and very salty (it is salted to the Red Sea 2nd).

The Iskenderun Gulf is 56-60 km in length, 30-32 km in width, and 152 km in circumference. The thermal power plants (including the Akkuyu nuclear power plant), which will use seawater as cooling water in the region, will extract water from the sea and deliver the foul water back to the sea(Table 1, 2, 4.).

Table 1. The estimated amount of CO_2 as waste gases from coal-power plants to their installed capacity around İskenderun bay.

PLACE OF THERMAL POWER PLANT	CAPACITY of TPP (MW)	ESTİMATED AMOUNT OF CO_2	Mean values of CO_2 waste Ton/MW/yıl	FUEL
ADANA-CEYHAN	1200	7 200 000	6000,00	Imported coal
ADANA-TUFANBEYLİ	453	375 000	827,81	Lignite
ADANA-YUMURTALIK	800	5 000 000	6250,00	Imported coal
ADANA-YUMURTALIK	600	3 600 000	6000,00	Imported coal (+fuel-oil)
ADANA-YUMURTALIK	120	720 000	6000,00	Imported coal
ADANA-YUMURTALIK	110	665 000	6045,45	Imported coal
ADANA-YUMURTALIK	600	3 600 000	6000,00	Imported coal
HATAY-DÖRTYOL-YENİYURT	300	1 800 000	6000,00	Imported coal
HATAY-ERZİN-AŞAĞI BURNAZ	1200	7 200 000	6000,00	Imported coal
HATAY-ERZİN-AŞAĞI BURNAZ	900	7 200 000	8000,00	Imported coal
HATAY-İSKENDERUN	600	4 260 000	7100,00	Imported coal
HATAY-İSKENDERUN	600	3 600 000	6000,00	Imported coal
TOTAL	7483	45 220 000	6043,03	

Koment:
1. The CO_2 emissions are based on the capacity of coal-powerplants (6043.03 ton/MW/year).
2. The CO_2 emissions of the power plants surrounding İskenderun Golf are calculated according to their planned capacity and the value 6043.03 ton/MW/year.
3. The quantity of CO_2 is calculated as the weight (ton/year). This CO_2 weight is converted with the value 1520 g / Nm^3 to the volume (m^3).
4. During the day the exhaust gases with the wind are spread over the Mediterranean after the Çukurova and increase to the mountain slopes. The calculations are made for 30 km, 50 km and 100 km distance.
5. At night the air in the mountains will cool down. This will condense water vapor. The air becomes heavier and flows to the lowlands as a mountain breeze. So the CO_2 and other exhaust gases will also flow over Çukurova and accumulate there (Greenhouse effect).

M. DOĞAN KANTARCI

ESTABLISHED AND ESTABLISHED IN THE ISKENDERUN AND MERSIN GULF FORECASTED POWER PLANTS AND INSTALLED POWER

According to the information and documents available; A total of 32 thermal power plants, including 22 in Iskenderun Bay, 4 in Mersin Bay, 2 in Ceyhan, 3 in Payas-Iskenderun and 1 in Adana, as well as the Akkuyu Nuclear Power Plant were added and 33 power plants were built and operated (Except Tufanbeyli). Tufanbeyli thermal power plant which will use domestic coal is excluded from this account (Total 33 + Akkuyu NGS=34) (Map 1, tables 1 and 2, table 4.1.).

AMOUNT OF CARBON DİOXİDE RELEASE FROM COAL POWER PLANTS

Above all, CO_2 that is released into the air is an important greenhouse gas. Carbon dioxide will be concentrated in the narrow coastal zone between Yumurtalık and AşağıBurnaz (Erzin) and Payas, where the thermal power plants are arranged side by side and will reach 1000 m in height with warming air and the density will reach 5407,26 ppm/year in r = 30 km area, spreading on the wind withÇukurova r = 100 km (92,21 ppm/year) was calculated (Table 3, 4 and Map 1).

EFFECTS OF CO_2 EMISSION ON THERMAL POWER PLANTS ON HEATING THE ATMOSPHERE

The air masses, that are blown to the north or rise into the surrounding mountainside and lean on the slopes, will cool off at night and flow to the low area (Çukurova) as "mountain breezes" and "continental breezes" and settle down. Night CO_2 released from the chimney can not rise high enough in the atmosphere and the precipitate CO_2 is added. In addition, the exhaust gases of the Tufanbeyli thermal power plant sink into the lowlands and Çukurova through the mountain breeze. It is estimated that all these CO_2 precipitation will reach 170-220 ppm / year (even more in winter). The addition of the CO_2 intensity in the Earth's atmosphere from 400 ppm of CO_2 to 170-220 ppm / year, which precipitates in Cukurova and the surrounding area, will cause significant warming (≈ 1 ° C) and climate change.

EFFECTS OF COOLING WATERS ON SEA WATER AND SEA ECOSYSTEM

The cooling water of the thermal power plants will be taken from the sea (except Tufanbeyli).The sea water is already warm (≈ 28 ° C). More water is required for cooling. The annual output of 20 thermal power plants between Yumurtalık and AşağıBurnaz only amounts to 28.7 billion m3 / year. It is calculated that the water in the sea volume up to a depth of 100 m and the distance of 10 km from the coast will be taken as cooling water in 1 year and the sea water volume up to 20 km from the coast will be given to the sea in 2 years. The width of Iskenderun Gulf between Yumurtalık-Payas is 30 km. Considering Payas and its southern thermal power plants and other facilities, it is concluded that in this part of the Gulf, all seawater can be transferred as cooling water for 2 years up to 100 m depth. It is assumed in the projects that the cooling water will be discharged to a depth of about 60 m at sea and will create a temperature difference of ≈1 ° C on the surface. However, water that is 10-12 °C warmer than sea water will cause significant massive heating. The warming of sea water will affect the marine ecosystem on the one hand. On the other hand, contribution to warming the atmosphere of the warming of the sea should be considered as an important factor of climate change.

Table 2. The calculation of CO_2 exhaust gases according to the installed capacity as MW of the 26 coal-power plants stations around the İskenderun bay.

YER	CAPACITY of TPP MW	FUEL	TOTAL CAPACITY MW	CO_2 WASTE (Mean) Ton/MW	Total CO_2 WASTE Ton/Capacity	Total CO_2 WASTE kg/Capacity	Total CO_2 WASTE mg/Capacity	Total CO_2 WASTE µg/Capacity
İSKENDERUN	1200	COAL						
İSKENDERUN	1236	COAL						
İSKENDERUN	680	COAL						
Total (3)	3116		3116	6043,03	18830084,191	18830084191	1,88301E+16	1,88301E+19
CEYHAN	100	COAL						
CEYHAN	110	COAL						
Total (2)	210		210	6043,03	1269036,483	1269036482,694	1,26904E+15	1,26904E+18
YUMURTALIK	1210	COAL		6043,03	7312067,353			
YUMURTALIK	1200	COAL						
YUMURTALIK	600	COAL						
YUMURTALIK	600	COAL						
YUMURTALIK	600	COAL						
YUMURTALIK	600	COAL						
YUMURTALIK	600	COAL						
YUMURTALIK	1600	COAL						
YUMURTALIK	1220	COAL						
YUMURTALIK	1200	COAL						
YUMURTALIK	600	COAL						
YUMURTALIK	815	COAL						
YUMURTALIK	800	COAL						
YUMURTALIK	600	COAL						
YUMURTALIK	1320	COAL						
YUMURTALIK	1320	COAL						
YUMURTALIK	200	COAL						
YUMURTALIK	1320	COAL						
ERZİN	900	COAL			104,6 MİLYON TON			
Total (19)	17305	COAL	17 305	6 043,0	104 574 649,21	104 574 649 204,9	1,04575E+17	1,04575E+20
MERSİN	260	KÖMÜR	260	6 043,03	1571188,026	1 571 188 026,193	1,57119E+15	1,57119E+18
Total	17565		17 565	6 043,03	106145837,231	106 145 837 231,057	1,06146E+17	1,06146E+20
TUFANBEYLİ	450	KÖMÜR	450	6 043,03	2719363,891	2719363891,487	2,71936E+15	2,71936E+18
Total (26)	21341		21 341	6 043,0	108 865 201,12	10 886 5201 122,5	1,08865E+17	1,08865E+20

Comment: A total of 26 coal-fired power plants with 21341 MW capacity will blow 108.87 million tonnes of CO_2 into the air.

M. DOĞAN KANTARCI

Table 3. The calculation of CO_2 exhaust gases as a volume and ppm of coal-power plants and their spread across the country environment İskenderun bay

COAL-POWER PLANTS	TOTAL CO_2 WASTE g/Capacity MW	1 ppm CO_2 g/m³	TOTAL CO_2 WASTE m³/Year
TOTAL 24 PP	1,04575E+14	0,00152	6,87991E+16
MERSİN 1 PP	1,57119E+12	0,00152	1,03368E+15
TOTAL 25 PP	1,06146E+14	0,00152	6,98328E+16
TUFANBEYLİ 1 PP	2,71936E+12	0,00152	1,78906E+15
TOTAL 26PP	1,08865E+14	0,00152	7,16218E+16

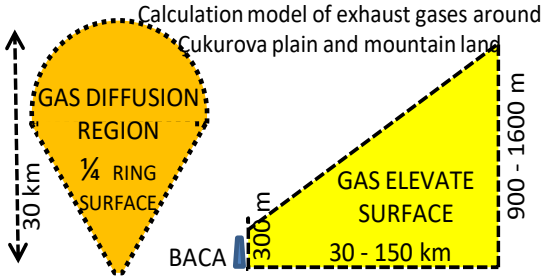

R= 30 km Stack gas diffusion region 706,86 km²
Flue gas elevate height 300+900=1200/2=600 m
and surface 0,6 km x 30 km = 18 km²
Flue gas diffusion volume: 706,86 x 18 = 12723,48 km³

R= 30 km Stack gas diffusion region 706,86 km²
Flue gas elevate height 300+500=800/2=400 m
and surface 0,4 km x 30 km = 12 km²
Flue gas diffusion volume: 706,86 x 12 = 8482,32 km³

COAL-POWER PLANTS	TOTAL CO_2 m³/year	Gas diffusion volume m³	TOTAL CO_2 ppm/year	TOTAL CO_2 ppm/month	Gas diffusion volume m³	TOTAL CO_2 ppm/year	TOTAL CO_2 ppm/month
	DAYS(10 HOUR) GAS EMMISION VOLUME				NIGTS (14 HOUR) GAS EMMISION VOLUME		
TOTAL 24 TS	6,87991E+16	1,27235E+13	5407,26	450,60	8,48232E+12	8110,88	675,91
MERSİN 1 TS	1,03368E+15	1,27235E+13	81,24	6,77	8,48232E+12	121,86	10,16
TOTAL 25 TS	6,98328E+16	1,27235E+13	5488,50	457,37	8,48232E+12	8232,75	686,06
TUFANBEYLİ1 TS	1,78906E+15	1,27235E+13	140,61	11,72	8,48232E+12	210,92	17,58
TOTAL 26 TS	7,16218E+16	1,27235E+13	5629,11	469,09	8,48232E+12	8443,66	703,64

R= 50 km km Stack gas diffusion region 1963,5 km²
Flue gas elevate height 300+1200=1500/2=750 m
and surface 0,75 km x 50 km = 37,5 km²
Flue gas diffusion volume : 1963,5 x 37,5 = 73631,25 km³

R= 50 km Stack gas diffusion region 1963,5 km²
Flue gas elevate height : 300+1000=1300/2 = 650 m
and surface 0,75 km x 50 km = 32,5 km²
Flue gas diffusion volume : 1963,5 x 32,5 = 63813,75 km³

COAL-POWER PLANTS	TOTAL CO_2 m³/yıl	Gas diffusion volume m³	TOTAL CO_2 ppm/year	TOTAL CO_2 ppm/month	Gas diffusion volume m³	TOTAL CO_2 ppm/year	TOTAL CO_2 ppm/month
TOTAL 24 TS	6,87991E+16	7,36313E+13	934,37	77,86	6,38138E+13	1078,12	89,84
MERSİN 1 TS	1,03368E+15	7,36313E+13	14,04	1,17	6,38138E+13	16,20	1,35
TOTAL 25 TS	6,98328E+16	7,36313E+13	948,41	79,03	6,38138E+13	1094,32	91,19
TUFANBEYLİ 1 TS	1,78906E+15	7,36313E+13	24,30	2,02	6,38138E+13	28,04	2,34
TOTAL 26 TS	7,16218E+16	7,36313E+13	972,71	81,06	6,38138E+13	1122,36	93,53

R= 100 km Stack gas diffusion region 7854 km²
Flue gas elevate height 300+1600=1900/2 = 950 m
and surface 0,95 km x 100 km = 95 km²
Baca gazı yayılma hacmi : 7854 x 95 = 746130 km³

R= 100 km Stack gas diffusion region 7854 km²
Flue gas elevate height: 300+1000=1300/2 = 650 m
and surface 0,65 km x 100 km = 65 km²
Baca gazı yayılma hacmi : 7854 x 65 = 510510 km³

COAL-POWER PLANTS	TOTAL CO_2 m³/yıl	Gas diffusion volume m³	TOTAL CO_2 ppm/year	TOTAL CO_2 ppm/month	Gas diffusion volume m³	TOTAL CO_2 ppm/year	TOTAL CO_2 ppm/month
TOTAL 24 TS	6,87991E+16	7,4613E+14	92,21	7,68	5,1051E+14	134,77	11,23
MERSİN 1 TS	1,03368E+15	7,4613E+14	1,39	0,12	5,1051E+14	2,02	0,17
TOTAL 25 TS	6,98328E+16	7,4613E+14	93,59	7,80	5,1051E+14	136,79	11,40
TUFANBEYLİ 1 TS	1,78906E+15	7,4613E+14	2,40	0,20	5,1051E+14	3,50	0,29
TOTAL 26 TS	7,16218E+16	7,4613E+14	95,99	8,00	5,1051E+14	140,29	11,69

R= 150 km Stack gas diffusion region 17671,5 km²
Flue gas elevate height: 300+1600=1900/2 = 950 m
and surface 0,95 km x 100 km = 95 km²
Flue gas diffusion volume: 17671,5 x 95 = 1678792,5 km³

R= 150 km Stack gas diffusion region 17671,5 km²
Flue gas elevate height: 300+1000=1300/2 = 650 m
and surface 0,65 km x 100 km = 65 km²
Flue gas diffusion volume : 17671,5 x 65 = 1148647,5 km³

COAL-POWER PLANTS	TOTAL CO_2 m³/year	Gas diffusion volume m³	TOTAL CO_2 ppm/year	TOTAL CO_2 ppm/month	Gas diffusion volume m³	TOTAL CO_2 ppm/year	TOTAL CO_2 ppm/month
TOTAL 24 TS	6,87991E+16	1,67879E+15	40,98	3,42	1,14865E+15	59,90	4,99
MERSİN 1 TS	1,03368E+15	1,67879E+15	0,62	0,05	1,14865E+15	0,90	0,07
TOTAL 25 TS	6,98328E+16	1,67879E+15	41,60	3,47	1,14865E+15	60,80	5,07
TUFANBEYLİ 1 TS	1,78906E+15	1,67879E+15	1,07	0,09	1,14865E+15	1,56	0,13
TOTAL 26 TS	7,16218E+16	1,67879E+15	42,66	3,56	1,14865E+15	62,35	5,20

M. DOĞAN KANTARCI

Map 1. The distribution area of the CO_2 exhaust gases from 26 coal-power plants of İskenderun bay.

Table 4.Different deposition intensity of the CO_2 exhaust gases in atmospheres over Çukurova and surrounding mountain.

Stack Gase diffusion region	DAYS CO_2 ppm/m³/10 hour	NIGTH CO_2 ppm/m³/14hour	DAYS CO_2 ppm/m³/24 hour	MONTHLY CO_2 ppm/m³	YEARLY CO_2 ppm/m³/YIL
r=30 km	6,17	12,96	19,14	582,03	6984,37
r= 50 km	1,07	1,72	2,79	84,85	1018,23
r= 100 km	0,11	0,22	0,32	9,75	117,03
r= 150 km	0,05	0,10	0,14	4,33	52,01

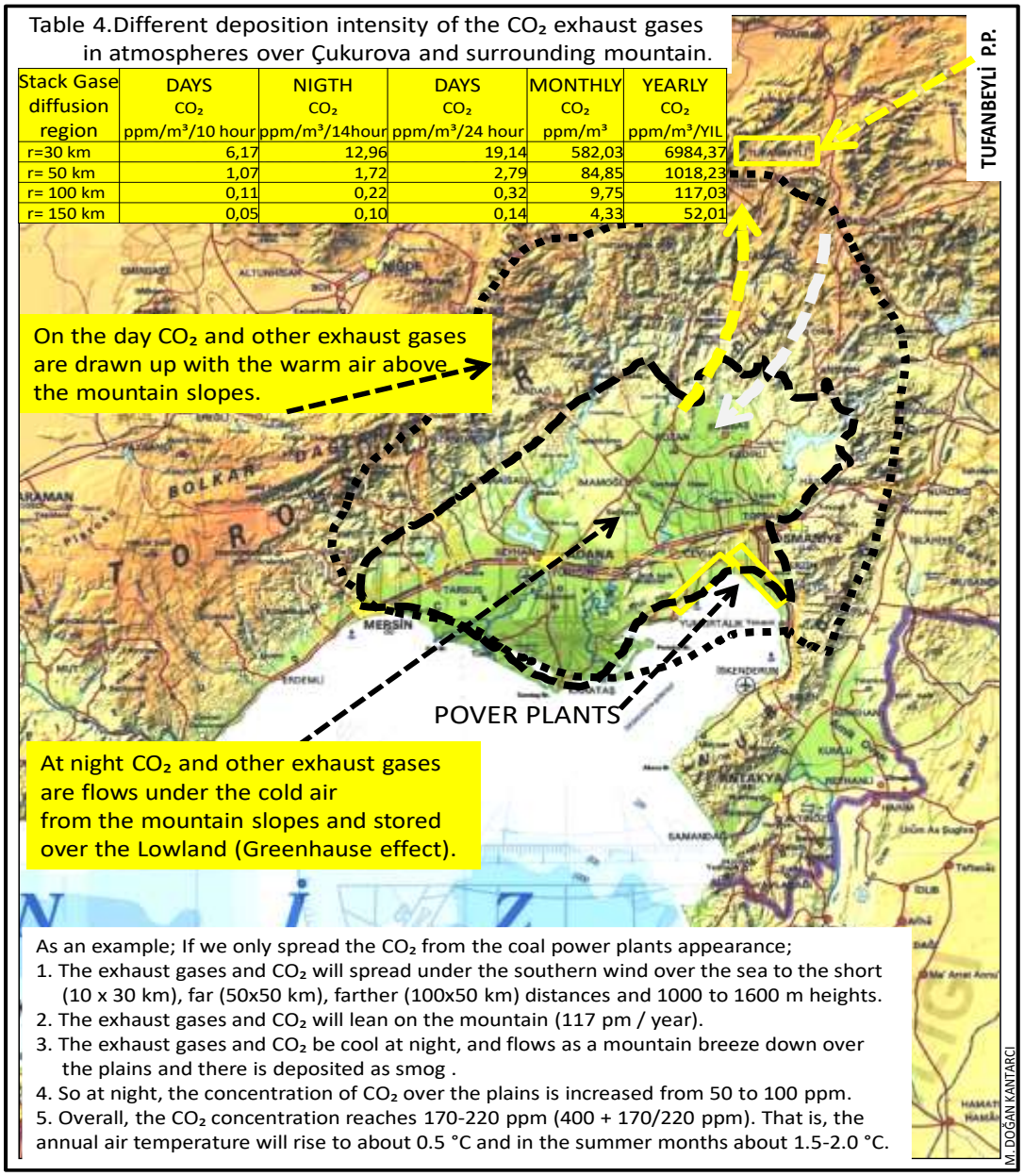

CONCLUSION

You build a thermal power plant that works with lignite coal to a region. By burning coal in a fluidized bed, you keep 80% to 85% sulfur dioxide (SO2) gases coming out of the flue. If you install a second thermal power plant in the same region, the SO2 given to the atmosphere increases to 30-40%. It starts to damage the agriculture and forest areas in the environment. If you establish a third thermal power plant, the SO2 content in the atmosphere increases to 45-60%. A significant proportion of people may be suffering from respiratory diseases and lung cancer. On the other hand, the effect of cooling water temperature, oxygen deficiency and chemicals used to clean water pipes on marine ecosystem is death. What happens if you install 22 thermal power plants in a 28 km coastal zone in the same area? The EIA report of each thermal power plant should be evaluated collectively as "together / total effect", not separately.The climate change and the damages that they will cause in of Çukurova and Iskenderun Gulf of the thermal power plants will be more costly than the money they will get the ecological cost.

Map 2. The cooling water of the power plants will come from the sea and hot water will Return to the sea. The 20 power plants are 28 km along the coast. You need the whole sea water volume of 1 year (up to 10 km from the coast) and in 2 years (up to 20 km from the coast) to 100 m depth.

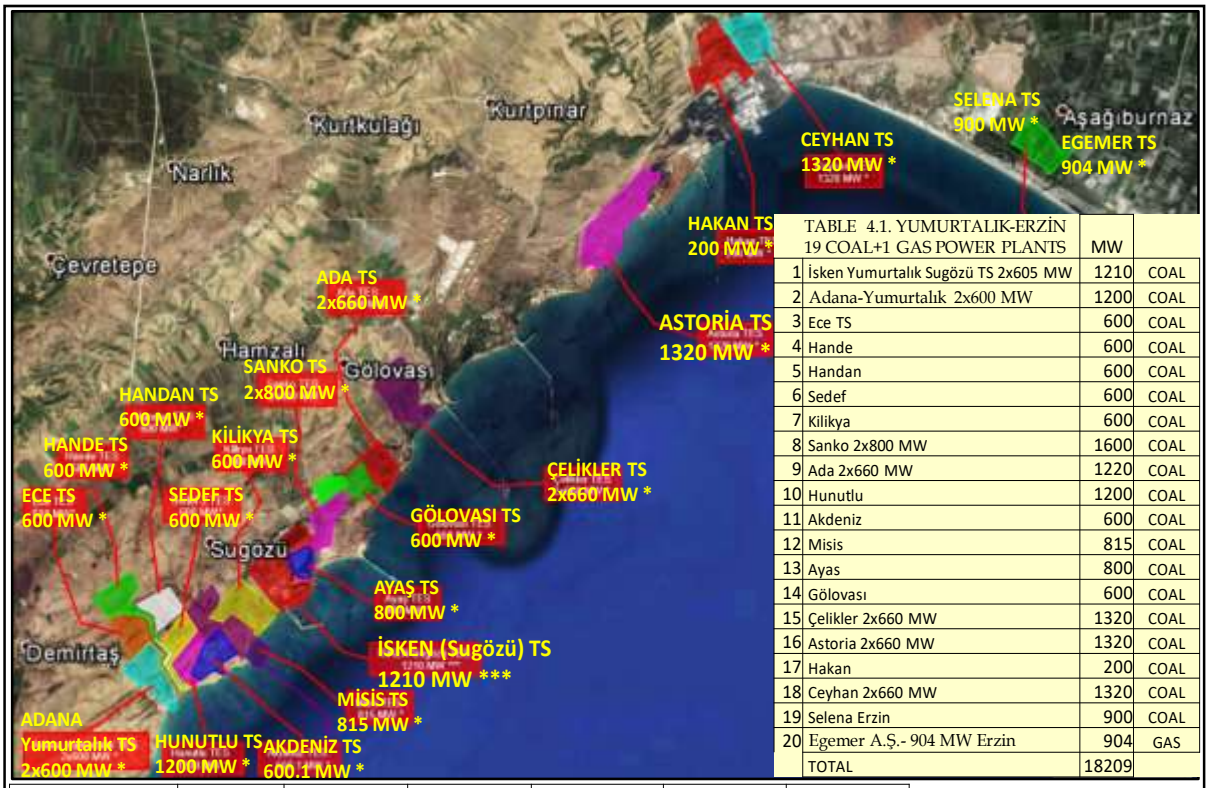

TABLE 4.1. YUMURTALIK-ERZİN 19 COAL+1 GAS POWER PLANTS		MW	
1	İsken Yumurtalık Sugözü TS 2x605 MW	1210	COAL
2	Adana-Yumurtalık 2x600 MW	1200	COAL
3	Ece TS	600	COAL
4	Hande	600	COAL
5	Handan	600	COAL
6	Sedef	600	COAL
7	Kilikya	600	COAL
8	Sanko 2x800 MW	1600	COAL
9	Ada 2x660 MW	1220	COAL
10	Hunutlu	1200	COAL
11	Akdeniz	600	COAL
12	Misis	815	COAL
13	Ayas	800	COAL
14	Gölovası	600	COAL
15	Çelikler 2x660 MW	1320	COAL
16	Astoria 2x660 MW	1320	COAL
17	Hakan	200	COAL
18	Ceyhan 2x660 MW	1320	COAL
19	Selena Erzin	900	COAL
20	Egemer A.Ş.- 904 MW Erzin	904	GAS
	TOTAL	18209	

TABLE 4. 2.	For 200 MW	18209 MW m³/sk	m³/hour	m³/day	m³/year	DURATION OF
COOLING WATER	10,00	910,45	3 277 620	78 662 880	28 711 951 200	USE OF WATER
FROM THE COAST	(18209/200=)	(x 91,045)	AREA 28x10 km	DEPTH100 m	VOLUME m³	IN YEAR
ABSTAND 10 km		VOLUME	280 000 000	100	28 000 000 000	0,975
ABSTAND20 km		VOLUME	560 000 000	100	56 000 000 000	1,95

Coment: 20 power plant in 28 km of coasts Along the coast will take 28 km³ into a year, 56 km³ into two years as cooling water and return as hot water.

M. DOĞAN KANTARCI

REFERENCES

AKKUYU NGS Elektrik Üretim Anonim Şirketi 2011;*Akkuyu nükleer güç santralı projesi çevresel etki değerlendirmesi başvuru dosyası.* Ankara

DOKAY-ÇED Çevre Mühendisliği Ltd. Şti.2015; SankoYumurtalıktermiksantralı kapasite artışı, beton santralı,kırma-elemetesisivederindenizdeşarjı(2x800 MWe/ 2x810 MWm/2x2187 MWt) çevresel etki değerlendirmesi başvuru dosyası-Ankara 2015.

Çınar Mühendislik Müşavirlik A.Ş. 2013; Adana-Yumurtalık İthal KömürTermik Santralı entegreprojesi(1.218,26 MWm/1.200 MWe/2.717 MWt)(Endüstriyel atık (kül) depolama alanı,iskele yapısı ve dolgu alanı projesi dahil) Çevresel Etki Değerlendirmesi (ÇED)başvuru dosyası Adana İli, Yumurtalık İlçesi-Ankara 2013.

Çınar Mühendislik Müşavirlik A.Ş. 2013; Tosyalı İskenderun Termik SantralıEntegre Projesi (Endüstriyel atık depolama alanı dâhil-santralın kurulu gücü 1200 MWe/3012 MWt) Çevresel Etki Değerlendirmesi (ÇED)Raporu. Hatay İli, İskenderun ilçesi cilt-1 ÇED raporu, nihai ÇED raporu Ankara-Tosyalı Elektrik Enerjisi Üretim Sanayi ve Ticaret A.Ş.

Enerji Atlası; Kömür ve linyit yakıtlı termik santralla

Enerji Enstitüsü 2003; Türkiye'nin ithal kömür santralları

Devlet Meteoroloji Gnl. Md'lüğü 1975-2005 İskenderun Meteoroloji İstasyonu verileri.

Kocabaş, A. 2016;*İskenderun Prof. Dr. Kocabaş Termik Santraller Yüzünden Bölgede Ölümler Artar.* Haberler com. 14 Şubat 2016 Pazar 18:26

TMMOB Çevre Müh. Odası İstanbul Şb.2014; *Akkuyu Nükleer Güç Santralı teknik değerlendirme raporu*; İstanbul (29 sh).

BLACK CARBON AND PARTICULATE MATTER CONCENTRATION AT URBAN TRAFFIC SITE IN ISTANBUL

Burcu Onat[1], Ülkü Alver Şahin[1], Nizamettin Mangır[2], Muhammet Doğan[2]
[1]Istanbul University, Engineering Faculty, Environmental Engineering Department
bonat@istanbul.edu.tr, ulkualver@istanbul.edu.tr
[2]Istanbul Metropolitan Municipality
nizamettin.mangir@ibb.gov.tr, muhammet.dogan@ibb.gov.tr

Abstract
We monitored black carbon concentrations in the period of May 2016 - March 2017 to observe the temporal trend of BC particles in a traffic site. We used a multi-angle absorption photometer (MAAP) to continuously monitor the BC concentration. PM_{10} and $PM_{2.5}$ concentrations were monitored simultaneously using by Beta Gauge particulate monitor. The monthly average BC concentrations were observed between 5.55 ± 1.59 μg/m^3 and 7.34 ± 2.69 μg/m^3. In the non-heating period, the mean concentration of BC was 6.06 ± 1.91 μg/m^3 and in the heating period the mean concentration of BC was 6.96 ± 2.21μg/m^3. PM_{10} and $PM_{2.5}$ concentrations were observed higher statistically at nighttime (22 pm to 07 am) than at daytime (8 am to 21 pm). On the contrary, the average daily value of BC was 6.7 μg/m^3 and the mean value of night was 6.3 μg/m^3. In addition, the average of the measured values at the peak hours of the BC was measured as 6.8 μg/m^3 and the average at the non-peak hours was 6.0 μg/m^3.

Keywords: *Black carbon, particulate matter, traffic.*

INTRODUCTION

Traffic sourced emissions have become one of the most important environmental problems because of the rising with the increasing of number of vehicle, traffic load and the commuting time. Traffic sourced emissions has got harmful effects on the city air quality, also it has potential harmful effects on the population who live nearby the main road and commute every day.

Particulate matter (PM) is a complex mixture of solid fragments and liquid droplets, exerts a large influence on public opinion and with policy makers because of its known adverse effects on human health (Heal et al., 2012 Pope et al. 2009; WHO, 2013). Black carbon (BC) is one of the important light absorbing component of airborne PM. Measuring black carbon is critical to understand the impact of combustion aerosols on air quality and climate change (Ji et al., 2017). Airborne black carbon from urban traffic is a climate forcing agent and has been associated with health risks to near-road populations (Liang et al., 2013). BC is directly emitted from incomplete combustion of fossil fuel, biomass and agricultural waste and forest fire. In developing countries, the estimated emission of BC is the highest due to the fossil fuel (Novakov et al., 2003). The main source of BC in the cities is traffic. BC is an important traffic sourced pollutant and accepted as a new indicator for determining the relation between adverse health effects and traffic. The total BC emission is caused by 67% diesel exhaust and 20% gasoline exhaust in the cities. Additionally, BC contributes to the global warming because it can absorb the solar radiation. BC may not be a major toxic component of $PM_{2.5}$ but it may act as a carrier of toxic components to the body (IARC, 2012). The measurement of BC at air quality monitoring sites alongside measurements of PM mass reflects the impact of vehicle exhaust emissions on ambient quality (Milford et al, 2016).

The important rate of fine PM and BC emissions in cities is sourced from traffic, but it has some misunderstandings about time trend, traffic density and the relation to the other pollutants such

as PM, because the studies about this subject are so few. Additionally, fine PM and BC emissions emitting from vehicle exhaust cause the high level of air pollutants inside the vehicle and outdoor. In this study, the real time measurements of BC and PM concentrations were determined and the relation between the parameters and traffic load were investigated.

METHODOLOGY

Istanbul is the most crowded metropolitan city with 16 million population and 4 million registered vehicle in Turkey. There are 17 Air Quality Monitoring Station (AQMS) which belongs to the Istanbul Metropolitan Municipality (IMM) in Istanbul city. Aksaray AQMS represents the traffic emissions and locates near Atatürk Boulevard road. The average daily traffic volume is about 50000 vehicle on Atatürk Boulevard road. The monitoring campaign was carried on between May 2016 - March 2017 in Aksaray AQMS for observing the road-site BC and PM mass concentrations. BC less than 2.5 μm were monitored by placing a $PM_{2.5}$ impactor into the inlet of a multi-angle absorption photometer-MAAP (Thermo^{TM} 5052). PM_{10} and $PM_{2.5}$ measurements were monitored simultaneously by Beta Gauge particulate monitors who belong to the IMM. The diurnal trend of BC and PM was investigated with considering the temperature and traffic load.

RESULTS AND DISCUSSION

Monthly average BC concentrations were given in Table 1. Because of the technical problems, there was no data recorded in November and December. The monthly mean and standard deviation values of BC were changed between 5.55±1.59 μg/m^3 and 7.34±2.69 μg/m^3. The minimum and maximum BC concentrations observed in August and February, respectively. The average BC concentrations in winter is higher than in summer. The mean concentration of BC was 6.06 ± 1.91 μg/m^3 in the period without heating (May-October) and the mean concentration of BC was 6.96 ± 2.21 μg/m^3 in the period of heating (January-March). Previous studies showed that BC values vary according to the region and the BC concentrations are measured higher in the city during the winter period. In Beijing, the mean concentrations of BC near roadside were found to be 12.9 μg/m^3 in summer and 17.9 μg / m^3 in winter (Song et al. 2013). Bibi et al (2017) measured BC concentrations at an urban site in Karachi, they found the monthly averaged concentrations of BC between 2.2 and 12.5 μg/m^3. Cheng et al. (2016) conducted a study in Taipei / Taiwan in the traffic area; it was found that the mean BC concentration was changed between 2.5-4.5 μg / m^3. In the airport of Venice/Italy, the highest average BC concentrations was determined as 1.2 μg / m^3. BC concentrations determined in this study are similar to the studies in the literature.

The temporal trend of BC, PM_{10}, $PM_{2.5}$ and PM_1 was shown in Figure 1. ANOVA and t-test were applied for this data and mean differences between weekday and weekday were analyzed. There was no statistically significant difference between PM_{10} and $PM_{2.5}$ on weekdays (49.6 μg/m^3 and 22.4 μg/m^3) and the weekend (48.7 μg/m^3 and 22.7 μg / m^3)(p=0,4). PM_1 weekend mean (8.5 μg/m^3) was statistically higher than weekdays average (7.3 μg/m^3) ($p < 0.01$). This difference is a significant difference with 95% confidence.

Table 1. The monthly average BC concentrations at Aksaray traffic area

Months	BC concentration (mean ± standard deviation) ($\mu g/m^3$)
May 2016	6,03 ± 1,67
June 2016	6,65 ± 1,99
July 2016	5,79 ± 2,03
August 2016	5,55 ± 1,59
September 2016	6,16 ± 2,08
December 2016	6,48 ± 2,10
November 2016	ND
December 2016	ND
January 2017	6,25 ± 1,86
February 2017	7,34 ± 2,69
March 2017	7,30 ± 2,10

ND: no data recorded

PM_{10} and $PM_{2.5}$ were higher statistically at nighttime (22 pm to 07 am) concentrations than at daytime (8 am to 21 pm) concentrations. For BC, the opposite situation was observed. The average daily value of BC was 6.7 $\mu g/m^3$ and the mean value of night was 6.3 $\mu g/m^3$. The diurnal cycle of BC exhibit highest concentrations in the morning and in the evening. These patterns are mainly driven by interaction of emissions, dispersion and atmospheric chemical processes (Masiol et al, 2017). In addition, the average of the measured values at the peak hours of the BC was 6.8 $\mu g/m^3$ and the average at the non-peak hours was 6.0 $\mu g/m^3$

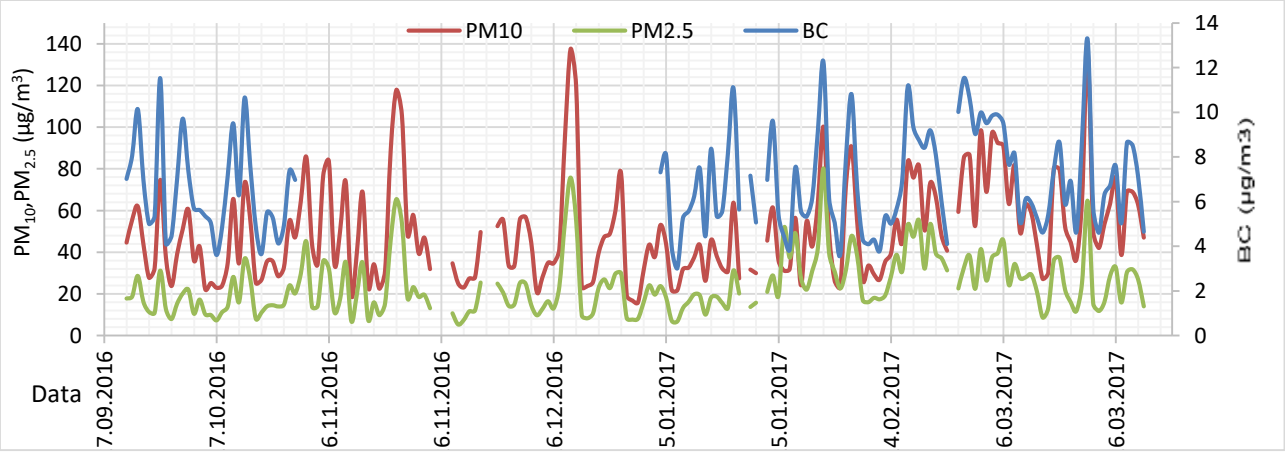

Figure 1. The temporal trend of BC, PM_{10} and $PM_{2.5}$ concentrations

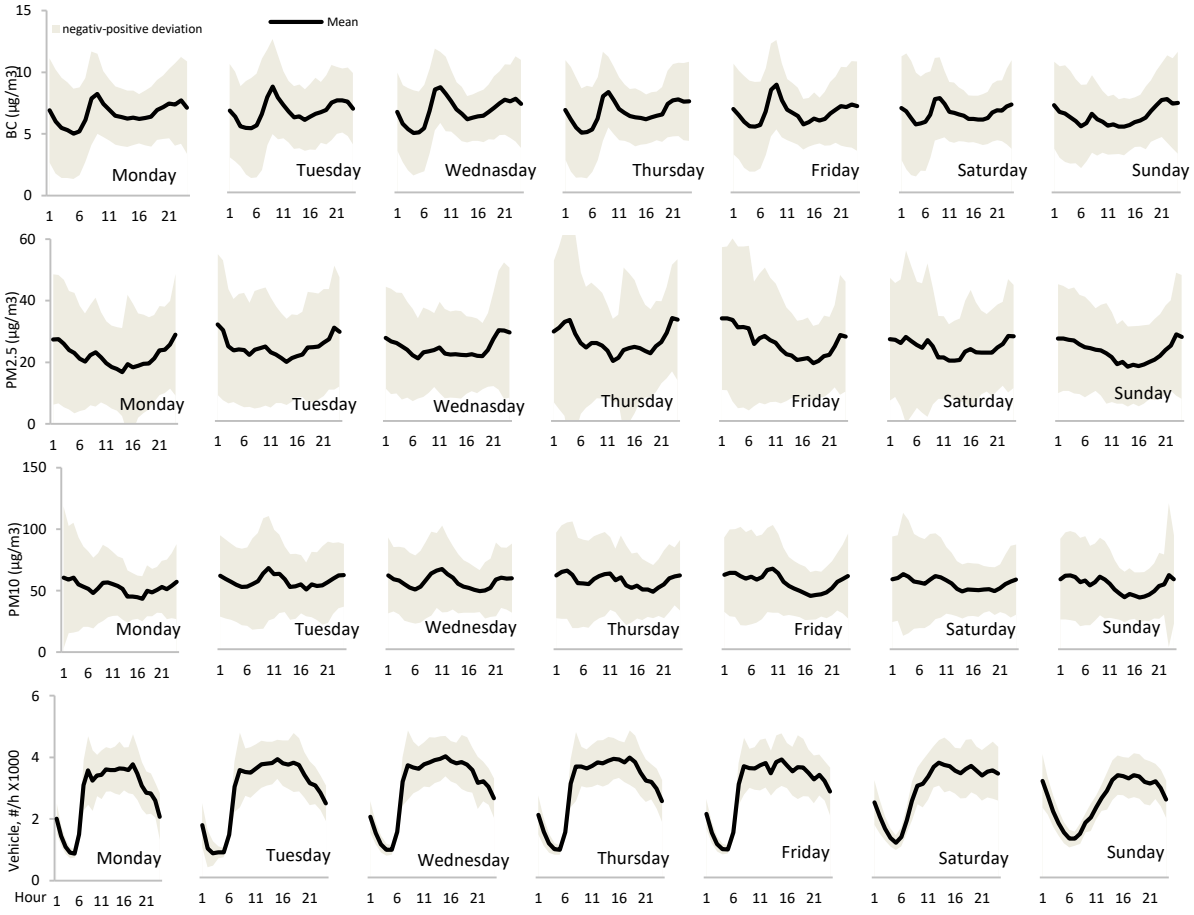

Figure 2: Mean and negative-positive deviation of BC, PM_{10} and $PM_{2.5}$ concentrations and vehicle number for weekdays at Aksaray traffic area.

The mean and standart deviations of BC, PM_{10}, $PM_{2.5}$ concentrations and vehicle number of weekdays were given in Figure 2. The diurnal variation of working days shows similarity. The highest BC concentrations were observed during the heavy traffic hours; between 07:00-9:00 in the mornings and between 18:00-21:00 in the evenings. $PM_{2.5}$ and PM_{10} concentrations have small peaks in rush hours. PMs exhibit highest concentrations in the early morning and in the evening. It can be interpreted as nighttime pollution, i.e. spectra affects by the rise of atmospheric pollutants due to the reduced height of the mixing layer and probably, by the formation of nighttime nitrate due to the chemistry driving the reactions of N_2O_5 and NO_3 on aerosol surfaces (Masiol et al., 2016). At the weekend, especially on Sundays morning hours, BC concentrations were observed lower than on Saturdays and in working days.

CONCLUSIONS AND RECOMMENDATIONS

The diurnal variation of BC in the fixed monitoring station near roadside showed that the high concentrations were observed in daily time and the highest BC concentrations were observed in traffic peak hours. It can be said that the BC levels will be tendency of rise depending on the increase of the number of diesel vehicles in traffic. PM concentrations were effected by other combustion sources and mainly driven by interaction of emissions, dispersion and atmospheric chemical processes in the monitoring area. To understand clearly that the behaviour of BC in urban area, the relation between BC and some parameters such as meteorology, long transport and other pollutants should be evaluated in future studies.

ACKNOWLEGMENT

We gratefully acknowledge the Scientific and Technical Research Council of Turkey (TUBITAK) with project no 115Y263 for financially supporting this study.

REFERENCES

Bibi S, Alam K, Chishtie F, Bibi H, Rahman S. (2017) Temporal variation of black carbon concentration using Aethalometer observations and its relationships with meteorological variables in Karachi, Pakistan. Journal of Atmospheric and Solar-Terrestrial Physics 157-158, 67-77.

Cheng Y.H., Liao C.W., Liu Z.S., Tsai C.J. (2014) A size-segregation method for monitoring the diurnal characteristics of atmospheric black carbon size distribution at urban traffic sites. Atmosphetic Environment 90, 78-86.

IARCH, 2012. Diesel Engine Exhaust Carcinogenic. International Agency for Research on Cancer. World Health Organisation. Press Release No.213, June 12, 2012.

Ji D, Li L, Pang B, Xue P, Wang L, Wu Y, Zhang H, Wang Y (2017) Characterization of black carbon in an urban-rural fringe area of Beijing. Environmental Pollution 223, 524-534.

Liang M, Keener T, Birch ME, Baldauf, R, Neal J, Yang YJ (2013) Low-wind and other microclimatic factors in near-road black carbon variability: A case study and assessment implications. Atmospheric Environment 80, 204-215.

Masiol M, Vu VT, Beddows DCS, Harrison RM (2017) Source apportionment of wide range particle size spectra and black carbon collected at the airport of Venice (Italy) Atmospheric Environment, 139 56-74.

Milford, C., Fernandez-Camacho, r. Et al. 2016. Balack carbon aerosol measurements and simulation in two cities in south-west Spain Atmos. Environ. 126, 55-65.

Novakov T, Ramanathan V, Hansen J, Kircstetter T, Sato M, Sinton J, Sathaye J. (2003) Large historical changes of fossil-fuel black carbon aerosols. Geophys. Res. Lett. 30. 1324, doi:10.1029/2002GL016345, 6.

Pope, C.A., Ezzati, M., Dockery, D.W. 2009. Fine-particulate air pollution and life expectancy in the United States. N.Engl. J. Med.

Song S., Wu Y., Xu J., Ohara T., Hasegawa S., Li J., Yang L., Hao J. (2013) Black carbon at a roadside in Beijing: Temporal variations and relationships with carbon monoxide and particle number size distribution. Atmosphetic Environment 77, 213-221.

WHO, 2013. Review of evidence on health aspects of air pollution-REVIHAAP Project. World Health Organization, Regional Office for Europe, Copenhagen, p.302.

DETERMINATION OF AMBIENT ELEMENTEL AND ORGANIC CARBON CONCENTRATIONS IN URBAN AND SUBURBAN ATMOSPHERES IN ANKARA: ESTIMATION OF SECONDARY ORGANIC AEROSOL

Ebru Koçak[1], Fatma Öztürk[2], Seda Aslan Kılavuz[3], İpek İmamoğlu[4], Gürdal Tuncel[5]

[1]Environmental Engineering Department, Middle East Technical University, Ankara, Turkey
ebsarika@metu.edu.tr
[2]Environmental Engineering Department, Abant İzzet Baysal University, Bolu, Turkey
ozturk_fatma@ibu.edu.tr
[3]Environmental Engineering Department, Kocaeli University, Kocaeli, Turkey
sedaaslan@kocaeli.edu.tr
[4]Environmental Engineering Department, Middle East Technical University, Ankara, Turkey
ipeki@metu.edu.tr
[5]Environmental Engineering Department, Middle East Technical University, Ankara, Turkey
tuncel@metu.edu.tr

Abstract

The concentrations of organic carbon (OC), elementel carbon (EC) and secondary organic aerosol (SOA) in atmospheric particles were investigated at two sites in Ankara, Turkey. The results show that, mean values of EC, OC, SOA for urban station are 2.30, 10.44 and 13.59 μg/m^3 respectively; the mean values of EC, OC, SOA for the suburban station were recorded as 0.85, 5.40 and 7.49 μg/m^3 respectively. The summer and winter values of the EC concentration in the urban station were found to be 2.17, 2.48 μg/m^3, and 0.72, 1.04 μg/m^3 in suburban station. Looking at the monthly changes, the EC values for October, November, December and October, November, December and January for urban station are higher than the EC values obtained for the other months. OC concentrations were also found to be higher in winter than in EC concentrations. When the weekend and weekday EC-OC distributions were examined, it was observed that the concentrations measured during the weekday were higher in both stations. According to the results obtained using the EC tracer approach, approximately 21% of the $PM_{2.5}$ concentrations measured at the urban station can be defined as secondary organic aerosol. It is also seen that the secondary value of OC is about 12% of the total $PM_{2.5}$. In suburban station, approximately 17% of the measured $PM_{2.5}$ concentrations can be identified as secondary organic aerosol and secondary OC concentration is found to account for approximately 8% of the total $PM_{2.5}$.

Keywords: *$PM_{2.5}$, organic carbon (OC), elementel carbon (EC), secondary organic aerosol (SOA), EC tracer method*

INTRODUCTION

Identification of sources contributing to pollutant levels in a settlement area is important for ensuring that measures are taken to improve air quality in that city in a healthy way. For this reason, efforts to determine what sources are and how much of their contribution is, and developments in these studies have been frequently found in the literature in recent years. Particles (PM) in the atmosphere are the main element of the source determination studies. Particulate matter has a complex structure with organic and inorganic components released from many different sources. When we look at the sources of particles, we see two basic classes that are defined as primary and secondary particles. Primary particles are particles that are released directly from natural and anthropogenic sources. Secondary particles are not released into the atmosphere from any source, resulting in the reactions of gases in the atmosphere. Some

of the particles in the atmosphere are inorganic and some are organic. The levels and chemical compositions of inorganic particles found in the urban atmosphere have been investigated for many years. Inorganic compounds of particulates have been used since 1980s by way of receptor modeling. However, due to the recent development of analytical techniques, it has only been possible in recent years to investigate the composition of organic particles.

Atmospheric carbons are an important component for particles whose aerodynamic radius is less than 2.5μm (Zhang et al., 2011). The carbon in atmospheric particles can be classified into two main categories: elemental carbon (EC) and organic carbon (OC) (Pandis et al., 1992). Determination of elemental carbon (EC) and organic carbon (OC) concentrations is one of the important methods in determining aerosol source and species (Seinfeld and Pandis, 1998). EC is also known as black carbon and is exhausted into the atmosphere as a combustion boost. Its structure is graphite with black color. The carbon in the EC is generated from combustion reactions that occur at high temperatures and the isotopic structure does not change much due to its inert nature. For this reason, almost all of the particulate phase EC can be assumed to have reached to atmosphere from primary combustion sources (Pandis et al., 1992). OC part could exhaust from primary sources, on the other hand, the OC part can undergo many modifications due to photochemical reactions in the atmosphere, and it is formed from hundreds of organic compounds (Rogge et al., 1993). Particulate OC contains basically hydrocarbons and other organic compounds of various oxidation products (Lim and Turpin, 2002, Castro et al., 1999). If the ratio of organic carbon (OC) to elemental carbon (EC) is calculated, SOA can be simply calculated with a relatively simple empirical method (Dusek, 2000). The atmospheric aerosol has different sources, such as fossil fuel burning, biomass burning, as well as burning reactions at high temperatures, and plant reactions and photochemical reactions at low temperatures. Thus, elemental carbon (EC) appears to be a tracer of primary human resources and has an inert character in atmospheric reactions (Klouda et al., 1990; Currie et al., 2002). Organic carbon (OC), on the other hand, contains numerous compounds of both primary and secondary origin (Slater et al., 2002).

The EC tracer method is the most commonly used method for calculating the primary and secondary parts of the OC in the measured fine particles (Castro et al., 1999, Yu et al., 1999, Cao et al., 2004). Considering that all of the primary OC and EC are left to the atmosphere from the same sources, it can be assumed that the EC component can be regarded as a good tracer for the part released from the primary combustion sources of the OC. In this direction, secondary aerosol formation directly increases the outdoor concentration of the OC and the numerical value of the OC/EC ratio. As a result, it can be said that the formation of secondary organic particles occurs in situations that exceed the expected OC/EC ratio for emissions of primary resources in the sampling area (Cabada et al., 2004). For the situations at which OC released from combustion sources as well as non-combustion sources;

$$OC_{masured} = OC_{primary} + OC_{secondary} \quad (1)$$

and

$$OC_{primary} = OC_{combustion} + OC_{non\text{-}combustion} \quad (2)$$

By assuming that the primary rate of EC concentrations (OC / EC) measured in the calculation of OCcombustion is constant;

$$OC_{combustion} = (OC / EC)_{primary} \text{ x } EC \quad (3)$$

$$OCs_{econdary} = OC_{measured} - [OC_{non\text{-}combustion} + (OC/EC)_{primary} \text{ x } EC] \quad (4)$$

The concentrations of atmospheric secondary organic aerosols are;

$$SOA = 1.6 \text{ x } [OC - (EC^* (OC / EC)_{primary})] \quad (5)$$

(Saylor et al., 2006).

In the previous study of our team, $PM_{2.5}$ samples were collected urban and suburban sites in Ankara daliy (24hr), and concentrations of 46 organic compounds were measured using GC-MS technique. Sampling began in July 2014 and ended at the end of September 2015. The composition of the organic compounds was used to enrich the receptor modelling as tracers of specific sources. The lack of EC and OC measurements in this study has emerged as an important shortcoming. With this study, this deficiency was tried to be solved. Moreover, for the first time in Turkey, such a large EC/OC data set has been established.

METHODOLOGY

$PM_{2.5}$ SAMPLING

The samples were collected from two different stations in Ankara. The first one is located in the back garden of the METU Environmental Engineering Department (39 ° 53'12.9 "N 32 ° 46'58.8" E). This station has been selected because it is classified as semi-urban, but is within campus boundaries, away from main roads and point sources. There are two main roads outside the campus. One is Dumlupınar Boulevard and the other one is 1071 Malazgirt Boulevard. The second station is located at Ankara University Faculty of Agriculture (39 ° 57'47.4 "N 32 ° 51'42.6" E) in Dışkapı. Compared to the first station, there are many schools, houses and hospitals around it, with this being classified as urban. This station is in the middle of two very busy highways. These are Turgut Özal Boulevard and İrfan Başbuğ Street.

Thermo Scientific, HVAIR100 high-volume sampler was used for sampling. The sampler title has a special geometric structure to collect $PM_{2.5}$ specimens. According to the changing flow, the sampling air flow is in the range of 1,01-1,18 m^3/min and the change was very small. The average flow value was used for calculations. The mean flow values were calculated by taking the average of the flow values received from the flow diagrams on the device are changed daily. The quartz fiber filters (Pallflex, Tissuquartz 2500QAT-UP, 8 × 10 $inch^2$) to be used before the sampling were conditioned for 5 hours at 500°C.

The filters preparing for Ankara University were sent under suitable conditions (in aluminum foil) and the filters were collected twice a week from station. The filters were then brought to METU Environmental Engineering at appropriate conditions and kept in the conditioning cabinet one day after the weighing. The filter exchange in the METU station was also carried out daily and the sampled filters were stored on the same day in the conditioning cabinet and then stored in aluminum foil and airtight plastic bags at -20°C until the day of analysis. A laboratory and a field blank sample were taken for each six-day.

Sampling started in July 2014. It was completed at the end of September 2015 and a total of 336 days of samples were collected from the METU station at 275 and the Ankara University station. In addition, 30 sites and 30 laboratories were analyzed using blind samples.

CARBON ANALYSIS

In this study, EC/OC analyzes of $PM_{2.5}$ samples collected on quartz fiber filters were completed with thermo-optical carbon aerosol analyzer provided from Sunset Lab., Oregon, USA. In the collected samples, 1.5 cm^2 pieces were cut from the filter for OC and EC analysis, and then they were placed in the glass sample paddle of the device and then analyze was started. In this method, PM loaded quartz filters cut in standard size (1.5 cm^2) are placed in the quartz furnace. Temperature of the helium gas sent to the furnace raises to 870°C and the organic compounds which are desorbed from the sample with increasing temperature are converted into pyrolysis products and move to manganese dioxide (MnO_2) oxidizing furnace. Carbon fragments moving

in the MnO_2 furnace are transformed into CO_2 gas here. The CO_2 swept by the helium gas from the oxidizing medium mixes with the hydrogen gas. This mixture is then converted to CH_4 gas by heated nickel catalysis and the carbon found in the sample is determined by the flame ionization detector (FID). After the first step in the quartz sampling furnace is completed, the temperature in the furnace is reduced to 550°C and the helium / oxygen carrier gas mixture flows through the furnace. With this oxidizing gas mixture, the elemental carbons in the specimen with a second temperature spike act as MnO_2 fume as the oxides of the filtrate. Then elemental carbon is determined by FID detector like organic carbon.

RESULTS AND DISCUSSION

THE CONCENTRATIONS OF OC AND EC AND THEIR SPATIAL AND SEASONAL CHARACTERIZATIONS

Summer and winter $PM_{2.5}$ values of urban station were calculated as 76 and 51 μg/m^3 and 54 and 36 μg/m^3 for suburban station, respectively. Average $PM_{2.5}$ summer values were calculated higher in both stations. With a high-volume sampler, an average of 1600 m^3 of air is drawn daily. Because the air is dry and stagnant in the summer months, more $PM_{2.5}$ is collected in the filter and in the winter months there is more precipitation and windy air leads less $PM_{2.5}$ in the filter. The summer and winter values of the particulate phase EC concentrations were 2.17, 2.48 μg/m^3 for urban station, and 0.72 and 1.04 μg/m^3 for suburban station. It is expected that the winter values will be higher when the carbon in $PM_{2.5}$ is thought to come from anthropogenic sources to a large extent. Elemental carbon (EC), also known as black carbon, is thrown into the atmosphere as a combustion gas. Since combustion reactions take place at high temperatures, elemental carbons with inert character are not expected to change too much. On the other hand, the situation is different for OC. This is because the OC portion can also be influenced by other factors, such as photochemical reactions in the atmosphere, as well as primary sources. Under the light of this information, EC values for October, November, December for urban station and October, November, December and January for suburban station are higher than the EC values obtained for the other months. OC concentrations also show higher concentrations in the winter months, as in EC concentrations. The summer and winter values of the OC concentrations were calculated as 7.91, 14.25 μg/m^3 for urban station, and 5.07 and 5.89 μg/m^3 for suburban station. Monthly averages of $PM_{2.5}$, EC and OC values are given in Figure 1-2.

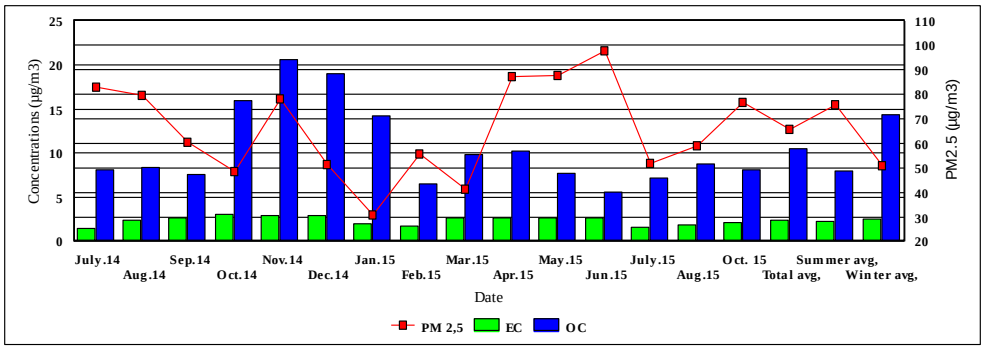

Figure 1. Urban Station- monthly $PM_{2.5}$, EC and OC concentrations

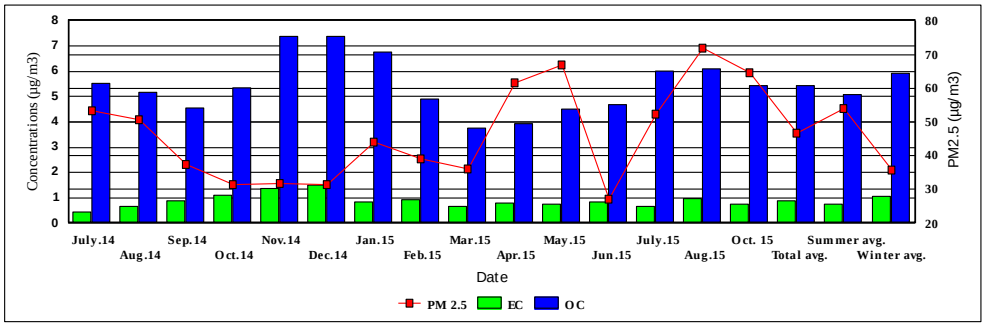

Figure 2. Suburban Station- monthly $PM_{2.5}$, EC and OC concentrations

THE RELATIONSHIP BETWEEN OC AND EC

Elementel carbon is emitted from anthropogenic combustion sources and is not formed by photochemical reactions in the atmosphere. on the other hand, organic carbon could be both emitted from primary sources and formed as secondary organics in the atmosphere from the atmospheric chemical reactions. The regression between OC and EC concentrations is shown in Figure 3 and 4. R-square values were determined as 0.32 for urban station and 0.51 for sub-urban station. At sub-urban site, relatively stronger OC-EC correlations were observed. Still the regression coefficients are lower than 0.6 for both sites and this implies non-similar emission sources contributing to atmospheric carbonaceous particle concentrations.

The ratio of OC to EC differentiate according to the dataset and the sampling period used. A steady set of concentrations of OC and EC has to be used to estimate the secondary organic aerosol concentration. Particulate OC to EC ratios exceeding 2.0 have been used to determine origin of secondary organic aerosol formation (Chow et al., 1993, 1996). Average OC/EC ratios were determined as 3.1 and 5.6 for summer and winter respectively at urban station; 8.2 and 6.3 for summer and winter respectively at sub-urban station. These value are higher than 2.0 and thus there is an evidence of a dense SOA formations (Cao et al., 2005).

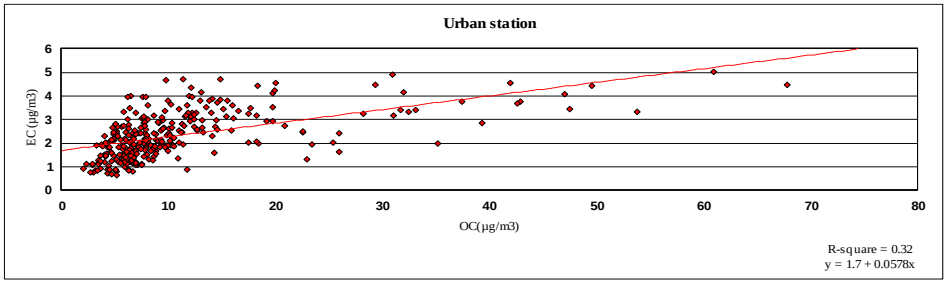

Figure 3. Urban Station- relationship between EC-OC concentration in $PM_{2.5}$ samples

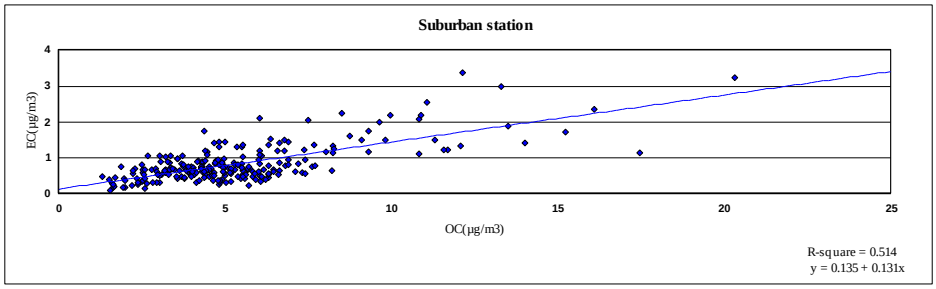

Figure 4. Sub-urban Station- relationship between EC-OC concentration in $PM_{2.5}$ samples

ESTIMATION FOR THE SECONDARY ORGANIC CARBON CONCENTRATION

The Quantification of the secondary organic aerosol have been difficult to achieve. Since there is no simple and single formulation is available. The EC tracer method is the most commonly used method for calculating the primary and secondary parts of the OC in the measured fine particles (Castro et al., 1999, Yu et al., 1999, Cao et al., 2004). $(OC/EC)_{primary}$ for this study was accepted as 0.85, as $(OC/EC)_{primary}$ values measured in studies performed in different regions in the literature ranged from 0.7 to 1.0. Another parameter has to be decided was $OC_{non\text{-}combustion}$. Since the data was approxomi taley one-and-a-half-year period, its estimation was made according to the methods given in the literature. EC vs OC charts obtained by using annual data show different y-axis cut-off points. For the sampling period, the numerically smallest value of OC was measured as 2.1 for urban and 1.3 μg/m^3 for suburban station. Based on this data, $OC_{non\text{-}combustion}$ was chosen as 2.5 for urban and 1.5 for suburban station and they were not to be too far away from the y-axis cut-off points obtained from the $OC_{non\text{-}combustion}$ summer charts. As can be seen from the Figure 5 and 6, approximately 21% of the $PM_{2.5}$ concentrations measured at the urban station can be defined as secondary organic aerosols according to the results obtained using the EC tracer approach. It is also seen that the $OC_{secondary}$ value is about 12% of the total $PM_{2.5}$. At the suburban station, approximately 17% of the measured $PM_{2.5}$ concentrations can be defined as secondary organic aerosols. It is also seen that the $OC_{secondary}$ value is about 8% of the total $PM_{2.5}$.

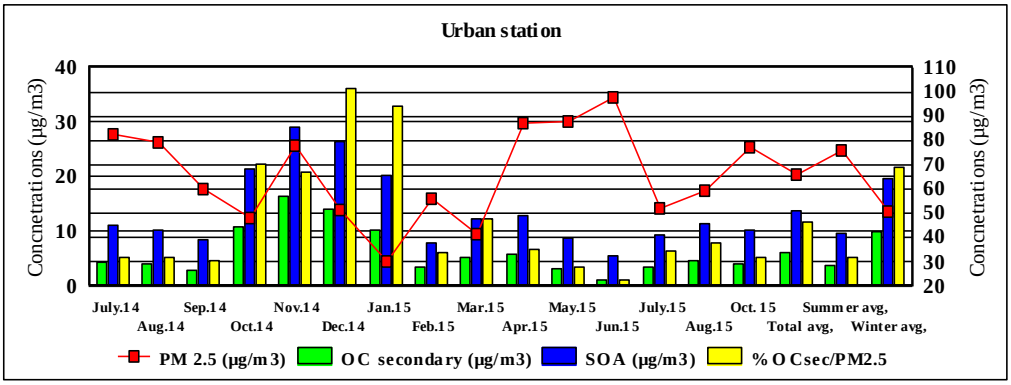

Figure 5. Urban station- relationship between $PM_{2.5}$, $OC_{secondary}$, SOA and $\%OC_{sec}/PM_{2.5}$

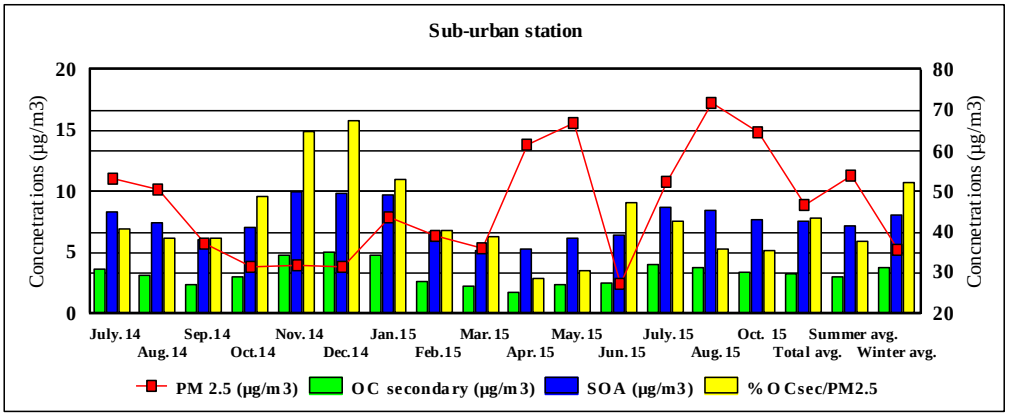

Figure 6. Sub-urban station- relationship between $PM_{2.5}$, $OC_{secondary}$, SOA and $\%OC_{sec}/PM_{2.5}$

CONCLUSION

Ambient air $PM_{2.5}$ samples were collected from urban and suburban sites of Ankara in between July 2014 and September 2015. It was found that summer and winter values of EC concentrations were 2.17, 2.48 μg/m^3 for urban station, and 0.72 and 1.04 μg/m^3 for suburban

station; summer and winter values of the OC concentrations were calculated as 7.91, 14.25 $\mu g/m^3$ for urban station, and 5.07 and 5.89 $\mu g/m^3$ for suburban station; 21% of the $PM_{2.5}$ concentrations measured at the urban station can be defined as SOA according to the results obtained using the EC tracer approach and $OC_{secondary}$ value is about 12% of the total $PM_{2.5}$; at the suburban station, 17% of the measured $PM_{2.5}$ concentrations can be defined as SOA and $OC_{secondary}$ value is about 8% of the total $PM_{2.5}$. The determination of SOA (secondary organic aerosols) concentrations is of great importance in terms of determining the measures to be taken in the reduction of particulate matter concentrations. Urban and suburban background particulate matter concentrations and the level of SOA formation can be at levels that may lead to failure of measures taken in some areas. These also show that the addition of SOA concentrations to future air pollution measurement studies is important. However, it is also important that the chemical characterization of the particulate matter should be explained in as much detail as possible in order to determine the possible health effects of the atmospheric particles.

ACKNOWLEDGEMENT

This research is supported by Scientific and Technological Research Council of Turkey project (1002), Project No: 115Y484.

REFERENCES

Cabada, J. C., Pandis, S.N., Subramanian, R., Robinson, A.L., Polidori, A., 2004. "Estimating the secondary organic aerosol contribution to PM2.5 using the EC tracer method", Aerosol Science and Technology, 38, 140-155.

Cao J. J., Lee S. C., Ho K. F., Zou S. C., Fung K., Li Y., Watson J. G., Chow J. C. 2004. "Spatial and seasonal variations of atmospheric organic carbon and elemental carbon in Pearl River Delta Region, China", Atmospheric Environment, 38, 4447–4456.

Cao, J.J., Wu, F., Chow, J.C., Lee, S.C., Li, Y., Chen, S.W., An, Z.S., Fung, K.K., Watson, G., Zhu, C.S. and Liu, S.X. 2005. "Characterization and Source Apportionment of Atmospheric Organic and Elemental Carbon during Fall and Winter of 2003 in Xi'an, China", Atmos. Chem. Phys. 5: 3127–3137.

Castro LM, Pio CA, Harrison RM, Smith DJT. 1999. "Carbonaceous aerosol in urban and rural European atmospheres: estimation of secondary organic carbon concentrations", Atmos Environ, 33:2771– 2781.

Chow, J.C., Watson, J.G., Lowenthal, D.H., Solomon, P.A., Magliano, K.L., Ziman, S.D., Richards, L.W., 1993. "PM10 and PM2.5 compositions in California's San Joaquin Valley", Aerosol Science and Technology 18, 105–128.

Chow, J.C., Watson, J.G., Lu, Z., Lowenthal, D.H., Frazier, C.A., Solomon, P.A., Thuillier, R.H., Magliano, K.L.1996. "Descriptive analysis of PM2.5 and PM10 at regionally representative locations during SJVAQS/AUSPEX". Atmospheric Environment 30 (12), 2079–2112.

Currie, L. A., 2002. "A critical evaluation of interlaboratory data on total, elemental, and isotopic carbon in the carbonaceous particle reference material, NIST SRM 1694a", J. Res. Natl. Inst. Stand. Technol., 107, 279–298.

Dusek, U., 2000. "Secondary Organic Aerosols – Formation Mechanisms and Source Contributions in Europe, (Interim Report), IR-00-066. International Institute for Applied Systems Analysis", Laxenburg, Austria.

Klouda, G. A., L. A. Currie, A. E. Sheffield, B. I. Diamondstone, B. A. Benner, S. A. Wise, R. K. Stevens, and R. G. Merrill. 1990. "14C source apportionment technique applied to wintertime urban aerosols and gases for the EPA Integrated Air Cancer Project, in Emissions from Combustion Processes: Origin, Measurement, Control", edited by R. Clement, and R. Kagel, pp. 153–157, Lewis, Chelsea, Mich.

Slater, J. F., L. A. Currie, J. E. Dibb, B. A. Benner Jr. 2002. "Distinguishing the relative contribution of fossil fuel and biomass combustion aerosols deposited at Summit, Greenland through isotopic and molecular characterization of insoluble carbon", Atmos. Environ., 36, 4463–4477.

Lim H, Turpin B. 2002. "Origins of primary and secondary organic aerosol in Atlanta: results of time-resolved measurements during the Atlanta supersite experiment", Environ Sci Tech 36:4489–4496.

Pandis S. N., Harley R. A., Cass G. R., Seinfeld J. H., 1992. "Secondary organic aerosol formation and transport", Atmospheric Environment, 26(13): 2269–2282.

Saylor, R.D., Edgerton, E.S., Hartsell, B.E. 2006. "Linear regression techniques for use in the EC tracer method of secondary organic aerosol estimation", Atmospheric Environment, 40, 7546-7556.

Rogge W F, Hildemann L M, Mazurek M A, Cass G R, Simoneit B R T, 1993. "Sources of fine organic aerosol. 3. road dust, tire debris, and organometallic brake lining dust-roads as sources and sinks". Environmental Science and Technology, 27(9): 1892–1904.Seinfeld J H, Pandis S N, 1998. "Atmospheric Chemistry and Physics: from Air Pollution to Climate Change". John Wiley & Sons, New York.

Zhang F., Zhao J., Chen J., Xu Y., Xu L., 2011. "Pollution characteristics of organic and elemental carbon in PM2.5 in Xiamen", China. Journal of Environmental Sciences, 23(8) 1342–1349.

THE USE OF BACK TRAJECTORY CLUSTER ANALYSIS WITH $PM_{2.5}$ COMPOSITION AT THE EASTERN BLACK SEA OF TURKEY

İlker Balcılar[1], Abdullah Zararsız[2], Güray Doğan[3], Gürdal Tuncel[4]

[1]*Environmental Engineering Department, Middle East Technical University, Ankara, Turkey*
balcilar@metu.edu.tr

[2]*Turkish Atomic Energy Authority, Ankara Nuclear Research and Training Center, Ankara, Turkey*
abdullah.zararsiz@taek.gov.tr

[3]*Environmental Engineering Department, Akdeniz University, Antalya, Turkey*
gdogan@akdeniz.edu.tr

[4]*Environmental Engineering Department, Middle East Technical University, Ankara, Turkey*
tuncel@metu.edu.tr

Abstract

In this study, the influence of synoptic-scale atmospheric transport patterns on observed levels of trace elements at Eastern Black Sea region of Turkey was examined. Daily $PM_{2.5}$ samples were collected at station (40°32'34"N, 39°16'57"E) on the Eastern Black Sea region of Turkey and collected samples were analyzed with ICP-MS for trace element composition. Five-day long back trajectories for March 2011 to December 2013 were calculated for 3 different arrival heights, 100m, 500m and 1500m, and combination of these 3 arrival heights. Back trajectories of air masses arriving in Eastern Black Sea of Turkey were classified into distinct transport patterns by cluster analysis. Cluster Analysis grouped back trajectories into 10 clusters depending on their direction and speed. Measured concentrations of trace elements were assigned to clusters to examine their cluster to cluster variations. Kruskal Wallis test was used to test for significant differences in mean elemental concentration across clusters. Significant cluster to cluster differences were observed in levels of crustal, anthropogenic and mixed origin source elements.

Keywords: *Black Sea, Cluster Analysis, ICP-MS, Trace Elements*

INTRODUCTION

Identifying the sources of airborne pollutants is of great importance to the study of fine particulate matter ($PM_{2.5}$), which has been linked to adverse health effects (Owege et al., 2006). Trajectories are defined as the paths of infinitesimally small particles of air (Abdalmogith and Harrison, 2005). The examination of transport patterns of air masses through the use of back trajectories is commonly performed for source identification.

Flow climatology provides an improved understanding of typical air-flow patterns and when combined with the ambient monitoring of atmospheric pollutants, it provides information about the variability in measured concentrations of elements. Trajectory models are used extensively to calculate flow climatology for different receptor sites (for example Sancho et al., 1992; Katsoulis et al., 1993).

Cluster Analysis (CA) is a multivariate statistical technique that "combines the flow climatology and pollutant transport pathways with particle or gas measurements at a sampling station" (Wang et al., 2009). CA is used to determine the atmospheric transport pattern and to examine the influence of different atmospheric transport pattern on observed chemical composition at the receptor. Many researchers have used CA to examine the relation between synoptic scale transport patterns and atmospheric pollution (Cape et al., 2000, Borge et al., 2007). The application of cluster analysis to trajectories for interpreting atmospheric chemical

measurements goes back at least as far as Moody and Galloway (1988), who used cluster analysis to group 3-day isobaric trajectories at two pressures in a study of precipitation composition on Bermuda.

In this study all back trajectories were allocated to clusters based on their transport speed and direction. Trace element composition of collected $PM_{2.5}$ samples collected on the Eastern Black Sea region of Turkey were assigned to clusters to examine the effect of synoptic scale atmospheric patterns on observed chemical composition and to establish source-receptor relationship.

METHODS

SAMPLING AND ANALYTICAL

The sampling station was located at a log storage area of the Ministry of Forestry, which was located at approximately 5 km to southwest of the Torul town on the Eastern Black Sea region of Turkey (40°32'34"N, 39°16'57"E). Altitude of the station was 1115 m above sea level. The station was approximately 70 km from the coastline. The station was established at a relatively pristine site, where there was no significant local sources, to investigate the influence of synoptic-scale atmospheric transport patterns. Daily $PM_{2.5}$ samples were collected on polycarbonate (Nuclepore) filters using Gent Stacked Filter Unit (SFU) (Hopke et al., 1997). The SFU was operated at a fixed flow rate of 16.7 L min^{-1}.Sampling was performed between March 2011 and December 2013. During this time 357 daily samples were collected.

Before and after sampling, filters were desiccated in a constant humidity (26 ± 4) % and temperature (25 ± 5) ^{o}C chamber for 24 h to reach a constant humidity and weighed using microbalance (Sartorius, Model MC-5). Mass concentrations particles were determined gravimetrically from the difference in filter weights before and after sampling. Collected $PM_{2.5}$ samples for trace element analysis were first digested using a microwave digestion procedure. Then digested samples were analyzed using a Perkin Elmer DRC II Model ICP-MS for SO_4^{2-} and approximately 50 trace elements, including Li, Be, Na, Mg, Al, P, K, Ca, Ti, V, Cr, Mn, Fe, Ni, Cu, Zn, Ge, As, Se, Rb, Sr, Y, Mo, Cd, Sn, Sb, Cs, La, Ce, Pr, Nd, Eu, Sm, Gd, Tb, Dy, Ho, Er, Tm, Yb, Lu, Hf, W, Pt, Au, Tl, Pb, Bi, Th and U.

TRAJECTORY CALCULATION AND CLUSTERING

For trajectory calculations, TrajStat (Wang, 2009) software was used. Trajstat employs the Hybrid Single Particle Langragian Integrated Trajectories (HYSPLIT) model for trajectory calculations. The model is developed by the Air Resources Laboratory, U.S. National Oceanic and Atmospheric Administration (ARL, NOAA). Reanalysis meteorological data archive of the NOAA was used as input data for trajectory calculations. Isentropic vertical motion method type was selected in the model calculation. Five-day back trajectories starting at the sampling point at altitudes of 100 m, 500 m and 1500 m were calculated for time period between March 2011 and December 2013. Assuming all trajectories ending within and below the boundary layer may influence the air quality, a new trajectory group was defined. This trajectory group is called as combined back trajectory and defined as the sum of 100, 500 and 1500 m trajectories. Number of back trajectories calculated for 100, 500 and 1500 m arrival height and combined back trajectories were 357, 357, 357 and 1071, respectively.

The criterion used in CA is to split a large trajectory data set into a number of groups based on trajectory transport speed and direction, simultaneously (Abdalmogith and Harrison, 2005, Brankov et al., 1998). The produced groups in CA are called clusters. Members of each cluster have similar trajectory length and curvature, while distinct clusters represent different synoptic

regimes. In this study, TrajStat software (Wang et al., 2009) was used for CA. Ward's hierarchical method (Ward, 1963) and 2D Euclidean distance were used in TrajStat. Two dimensional Euclidean distance using longitude and latitude coordinates between trajectories were calculated, and then nearest trajectories were combined to form clusters.

RESULTS AND DISCUSSIONS

Different number of clusters (maximum 20) were calculated and inspected. A procedure developed by Dorling et al. (1992) was adopted to determine optimal number of clusters. According to this procedure percent change in total root-mean-square-deviation (TRMSD) between clusters was used. A threshold value of 5% change in TRMSD was assumed to be significantly large and constituted the criterion for merging of different clusters (Dorling et al., 1992). Total root-mean-square-deviation for different number of clusters was calculated using SPSS software. Clusters formed at 100 m and 500 m starting altitudes were identical, therefore runs were performed with 500 and 1500 m starting altitudes and combined trajectories. The plot of percent change in TRMSD against number of clusters is depicted in Figure 1. This figure shows that when decreasing cluster number from 10 to 9, percent change in TRMSD exceeds 5% threshold value (purple line) for all arrival heights trajectory data set. Therefore, 10 clusters were used to explain transport-related variations in data set.

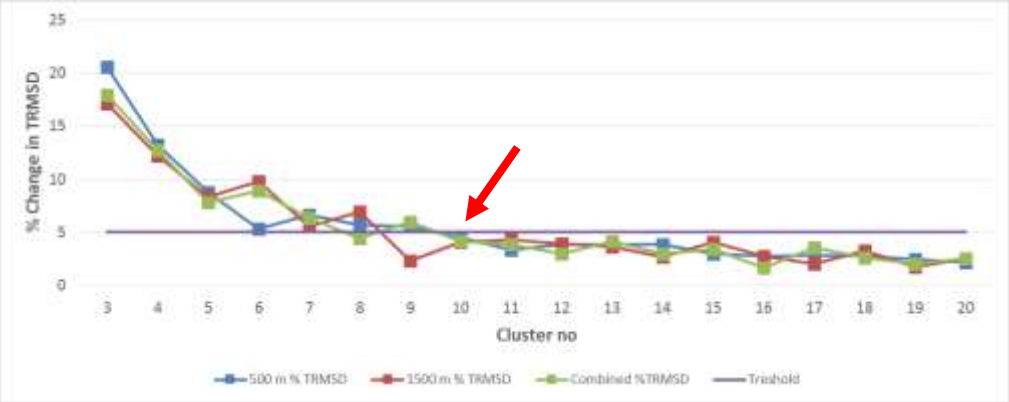

Figure 1. Selection of optimum number of clusters for 500, 1500 m and combined arrival height trajectories

Cluster centroids generated for 500 m and 1500 m arrival height back trajectories are given in Figure 2 (a) and (b), respectively. As can be seen from the figures, calculated cluster centroids for different starting altitudes were generally similar in direction and curvature. Therefore, combined trajectories (sum of 100, 500 and 1500 m trajectories) could be more representative for this study. For this reason, combined trajectories were used and 10 clusters were calculated for them in interpretation of transport of elements to the region. CA was applied for combined trajectory data set and 10 clusters are generated (Figure 2 (c)). The percentage of trajectories assigned to each cluster is given Table 1.

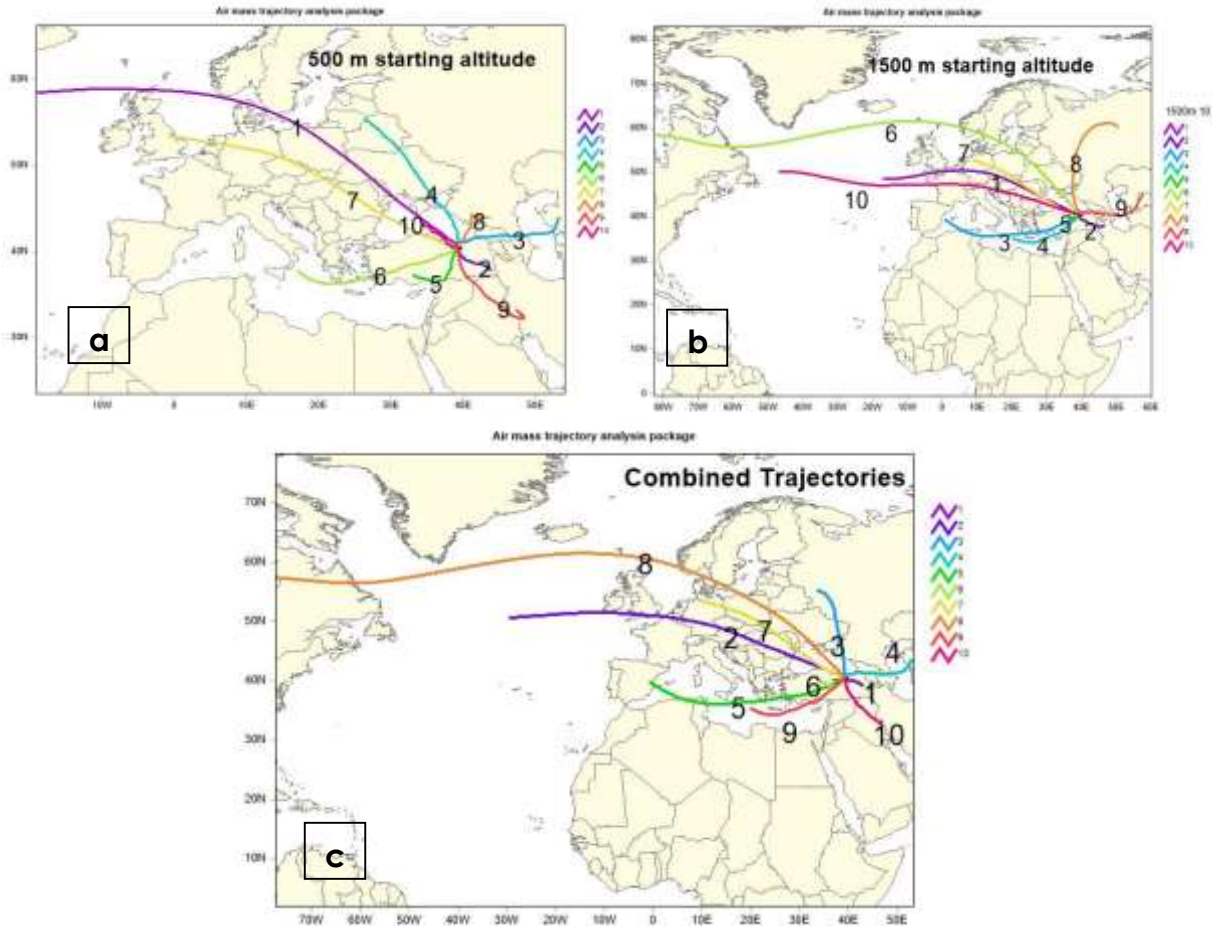

Figure 2. Cluster centroids calculated for trajectories with 500 m (a) and 1500 m (b) starting altitudes and for combined trajectories (c)

Table 7. Percentage of trajectories allocated in each cluster

Cluster	500 m Ratio	1500 m Ratio	Combined Ratio
1	2.20%	5.00%	18.90%
2	16.00%	18.50%	4.10%
3	18.20%	8.70%	6.90%
4	7.80%	17.40%	16.40%
5	14.80%	22.10%	4.30%
6	9.00%	1.40%	24.20%
7	8.70%	11.80%	9.70%
8	7.00%	3.90%	1.40%
9	4.20%	6.70%	8.40%
10	12.00%	4.50%	5.70%

Back trajectories corresponding to cluster centroids for the combined data set is given in Figure 3. The colored line in each trajectory cluster shows the final cluster center obtained from the last iteration of cluster analysis. Characteristics of each cluster can be defined as follows:
Cluster 1: Accounted for 18.9 % of all trajectories. Cluster 1 covers the Eastern Black Sea, Georgia and eastern Turkey. Consequently, this group trajectories represent slow moving air

masses and is important as the samples corresponding to these trajectories represent contribution of relatively local sources on measured concentrations of pollutants.
Cluster 2: Accounted for 4.10 % of all trajectories. Cluster 2 covers European countries and include long fetch of air masses. Some of the back trajectories in this group extends all the way to Atlantic Ocean which then passes through north-western Europe and then Balkans.
Cluster 3: Accounted for 6.90 % of all trajectories. Cluster 3 covers Black Sea, Georgia, Ukraine and some part of Russia, include medium fetch of air masses.
Cluster 4: Accounted for 16.40 % of all trajectories. Cluster 4 covers the countries all the way to Caspian Sea region include medium fetch of air masses.
Cluster 5: Accounted for 4.30 % of all trajectories. Cluster 5 covers Western Mediterranean Sea and countries surrounding it, include long fetch of air masses and hence, fast moving air masses.
Cluster 6: Accounted for 24.20 % of all trajectories. Cluster 6 covers western part of Turkey, Black Sea, and some part of Middle East including Syria, Israel, Jordan and Iraq. It has the highest percentage and shows the shortest length like Cluster 1 among the other clusters. These short trajectories are indicating very slow movement of air masses. Like Cluster 1, trajectories represent contribution of relatively local sources on measured concentrations of pollutants.
Cluster 7: Accounted for 9.70 % of all trajectories. Trajectories that are associated with Cluster 7 comes nearly from the same direction (same travel path) Cluster 2 but having a lower speed, and hence Cluster 7 has a shorter length compared to Cluster 2.
Cluster 8: This cluster includes the fastest moving air masses. Back trajectories in this cluster cover most of the Europe, and also crosses Atlantic Ocean and extends to North America. This interesting cluster accounts for only 1.40 % of trajectories.
Cluster 9: Accounted for 8.40 % of all trajectories. Cluster 5 covers Eastern Mediterranean Sea and countries surrounding it, include medium fetch of air masses and hence, moderate moving air masses.
Cluster 10: Accounted for 5.70 % of all trajectories. Cluster 10 covers all the way to Gulf countries, region include medium fetch of air masses.

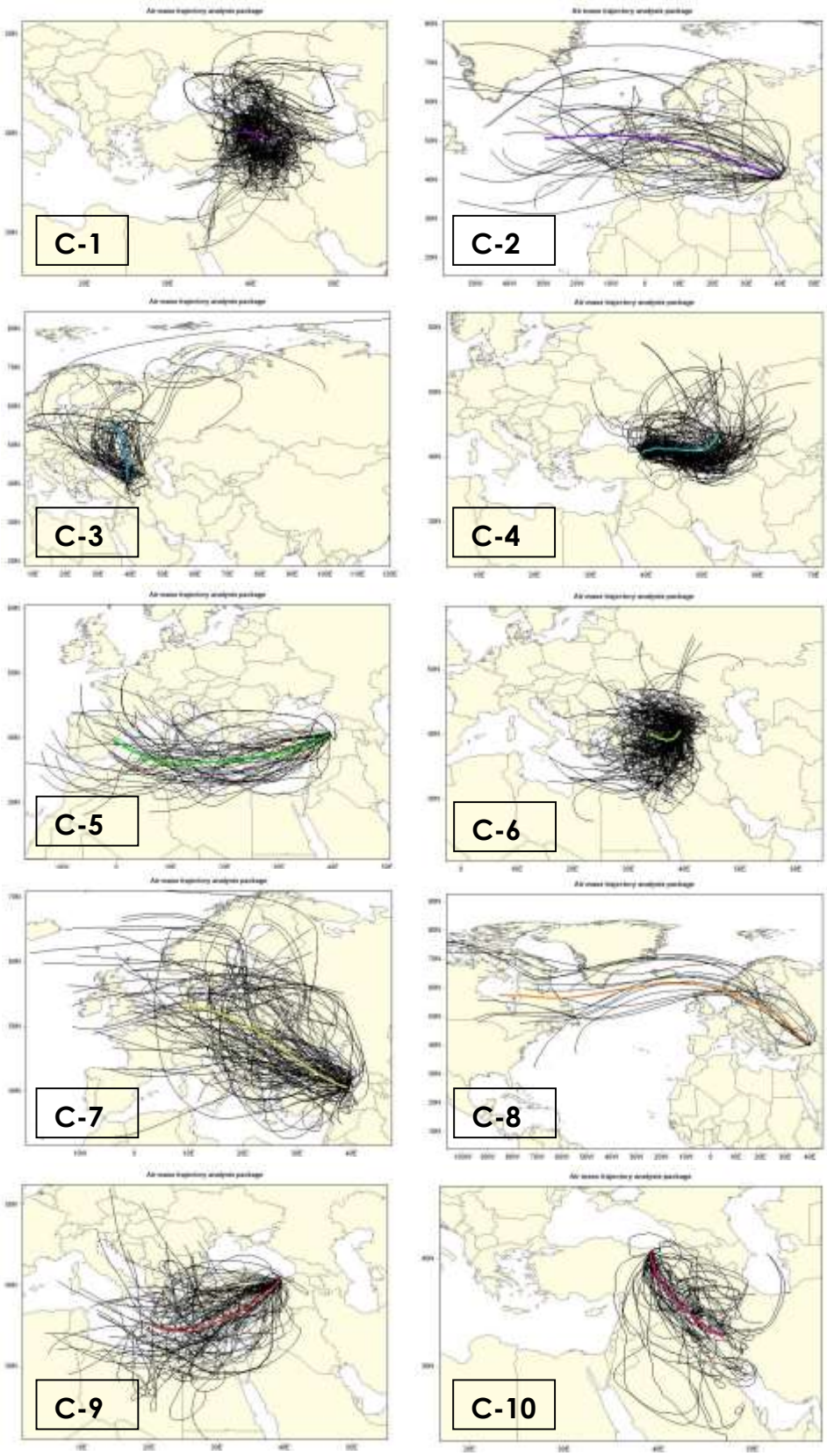

Figure 3. Trajectories allocated to different clusters.

Measured concentrations of trace elements on Eastern Black Sea region of Turkey were assigned to clusters calculated in the CA. Cluster to cluster variations of median concentrations

of selected elements with crustal, anthropogenic and mixed sources were examined at this part of the study. Kruskal Wallis (K-W) test at 95% confidence level was used to examine if median concentrations of elements were different between different cluster pairs. All of the parameters were statistically different at least in one of the sectors with the exception of K, Sm, Ba, As, Ge, Na, Mg, Ga, Eu, Be, Cu, Fe, Hf, Pb. These elements seem not to vary from one to another at 95 % confidence interval. Cluster-to-cluster variations of median concentrations of selected elements with crustal, anthropogenic and mixed sources are plotted in Figure 4.

Crustal elements Al and Ca followed the similar trends in terms of their concentrations in clusters. The highest concentrations were observed in Cluster 2. Corresponding back trajectories in Cluster 2 could be linked to the transport from arid regions in the Mediterranean basin, such as Spain and Northern parts of Italy. Also Al and Ca also had high concentrations in Cluster 5 with the rare crustal elements like, La, Y, Nd, Tm, Tb, Yb. Cluster 5 covers Western Mediterranean Sea and countries surrounding it. Trajectories originating from arid regions at northern Africa may be responsible for observed crustal concentrations at our station. Concentration patterns of elements with mixed sources Cr, Ni and Ti, with higher median concentrations in Cluster 5, is generally similar to those with crustal origin. Cr and Ni also have high concentrations in Cluster 10. Cluster 10 covers the arid regions all the way to Gulf countries. Also, most of the crustal elements have high concentrations in Cluster 10. Variation in median concentrations of pollution-derived elements from one cluster to another was also examined. Cluster 3 and Cluster 4 are the important clusters as they covers the pollution sources around the Black Sea basin. Cluster 3 covers Georgia, Ukraine and some part of Russia. Cluster 4 covers countries all the way to Caspian Sea. As expected anthropogenic species, SO_4^{2-}, P, Cd have higher concentrations in Cluster 3 and Cluster 4. Zn has high concentration in Cluster 8 rather than Cluster 3 or 4. Cluster 8 represents the fastest air movements from northwest and extend all way up to North America.

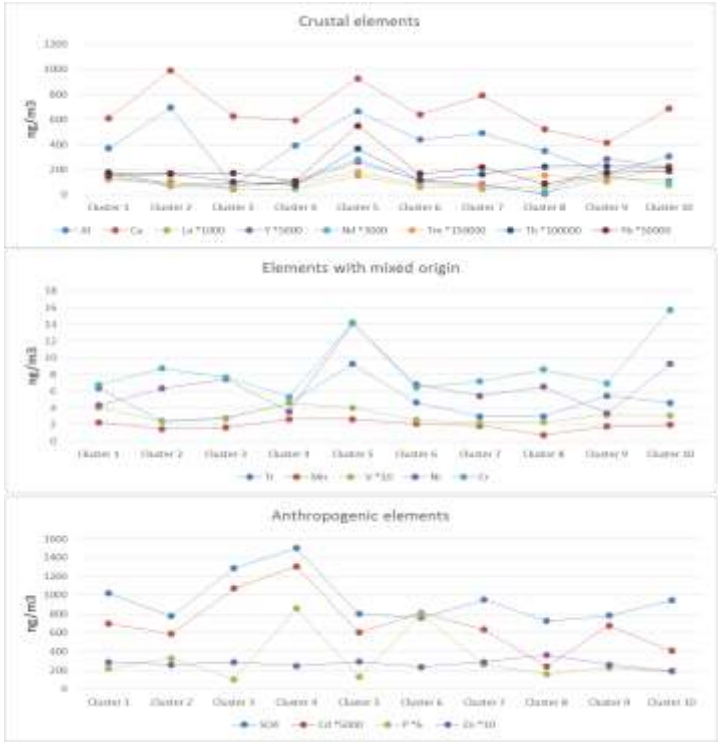

Figure 4. Median concentrations of elements with crustal, anthropogenic and mixed sources in clusters

CONCLUSIONS

Cluster Analysis provides an improved understanding of typical air-flow patterns and when combined with the ambient monitoring of atmospheric pollutants, it provides information about the variability in measured concentrations of elements. In this study, measured elemental concentrations at the Eastern Black Sea region of Turkey were combined with clusters. 10 clusters were selected as the optimum cluster number for all arriving heights and combined trajectories. The findings of CA showed that trajectories originating from arid regions at the European countries and Western Mediterranean Sea basin were source regions for crustal elements. For mixed origin elements, observed levels were higher at the trajectories originating from Western Mediterranean Sea basin and Gulf region countries. And for pollution-derived elements, trajectories originating from Georgia, Ukraine, some part of Russia and Caspian Sea basin carried higher levels of these elements to the Eastern Black Sea atmosphere.

REFERENCES

Abdalmogith, S. S. & Harrison, R. M. 2005. The use of trajectory cluster analysis to examine the long-range transport of secondary inorganic aerosol in the UK. Atmospheric Environment, 39, 6686-6695.

Brankov, E., Rao, S. T. & Porter, P. S. 1998. A trajectory-clustering-correlation methodology for examining the long-range transport of air pollutants. Atmospheric Environment, 32, 1525-1534.

Borge, R., Lumbreras, J., Vardoulakis, S., Kassomenos, P. & Rodriguez, E. 2007. Analysis of long-range transport influences on urban PM10 using two-stage atmospheric trajectory clusters. Atmospheric Environment, 41, 4434-4450.

Cape, J. N., Methven, J. & Hudson, L. E. 2000. The use of trajectory cluster analysis to interpret trace gas measurements at Mace Head, Ireland. Atmospheric Environment, 34, 3651-3663.

Dorling, S. R., Davies, T. D. & Pierce, C. E. 1992. Cluster- Analysis- A Technique for Estimating The Synoptic Meteorological Controls on Air and Precipitation Chemistry - Method and Applications. Atmospheric Environment Part a-General Topics, 26, 2575-2581.

Hopke, P.K., Xie, Y., Raunema, T., Biegalski, S., Landsberger, S., Maenhaut, W., Artaxo, P. & Cohen, D. 1997. Characterization of the Gent Stacked Filter Unit PM10 Sampler. Aerosol Science and Technology, 27, 726-735.

Katsoulis, B.D. & Whelpdale, D.M. 1993. "A Climatological Analysis of Four-Day back Trajectories from Aliartos, Greece". Theoretical Applied Climatology 47, 93-103.

Moody, J.L. & Galloway, J.N. 1988. Quantifying the relationship between atmospheric transport and the chemical composition of precipitation on Bermuda. Tellus 40B, 463}479.

Owega, S., Evans, G. J., Jervis, R. E. & Fila, M. (2006). Identification of long-range aerosol transport patterns to Toronto via classification of back trajectories by cluster analysis and neural network techniques. Chemometrics and Intelligent Laboratory Systems, 83(1), 26-33.

Sancho, P., De La Cruz, J., Diaz, A., Martin, F., Hernandez, E., Valero, F. & Albarran, B. 1992. A five year climatology of back trajectories from Izana baseline station, Tenerife, Canary Islands. Atmospheric Environment 26A, 1081-1096.

Wang, Y. Q., Zhang, X. Y. & Draxler, R. R. 2009. TrajStat: GIS-based software that uses various trajectory statistical analysis methods to identify potential sources from long-term air pollution measurement data. Environmental Modelling & Software, 24, 938-939.

Ward, J. H. 1963. Hierarchical Grouping to Optimize an Objective Function. Journal of the American Statistical Association, 58, 236.

DETERMINATION OF ATMOSPHERIC PCB CONCENTRATIONS IN A SEMI-RURAL AREA OF BURSA

Burak ÇALIŞKAN[1], Yücel TAŞDEMİR[2], Nihan ŞUMNULU[3]
Department of Environmental Engineering, Faculty of Engineering, Uludag University, Bursa, Turkey
[1]burakcaliskan@uludag.edu.tr
[2]tasdemir@uludag.edu.tr
[3]nihan_durak@hotmail.com

ABSTRACT
In this study, samples were collected with the passive air samplers (PASs) containing PUF discs to determine the atmospheric levels of polychlorinated biphenyls (PCBs) at the Uludag University Görükle Campus (UUC). Each sampling duration was about one month. 82 PCBs were targeted in the collected samples. The total average PCB concentration in the UUC atmosphere was determined as 87.91±22.07 pg/m^3, the concentration of indicator species was 29.88±7.35 pg / m^3 and the concentration of dioxin-like PCBs (dl-PCBs) was 8.70±3.30 pg / m^3. Checking our result with the previous studies at the UUC, it was determined that there was a decrease in the PCB concentration in the region. The most dominant PCB homolog type in the region atmosphere was the 5-CBs, followed by 4-CBs and 3-CBs. It could also be detected in 9-CB heavy species in the regional atmosphere. The highest PCB concentration was found during the spring season.

***Key Words**: PUF discs, Passive air sampling*

INTRODUCTION

Persistent organic pollutants (POPs) are a group of chemical substances that are usually halogenated (chlorinated or brominated), persistent, and bio-accumulating pollutants (Jones and de Voogt 1999). POPs can pose a risk to humans and nature. These pollutants are carried along long distances and accumulate in water and terrestrial ecosystems where there are no sources.

Polychlorinated biphenyls (PCBs), an important member of the POPs, are a group of pollutants that persist in nature and in the living organism. The disintegration of these chemicals, which are completely human production, is also very difficult. It can be transferred from the landfills to the atmospheres, or by combustion of PCB or chlorine-containing materials (Taşdemir et al., 2005). PCBs were synthesized in the laboratory environment for the first time in 1881 and began to be used from 1930. Their production has been limited due to the effects of the environment and the people since 1979 (Wan and Mackay, 1986, Jones et al., 1992, Ross, 2004).

POPs are sampled by passive or active sampling methods (Birgül et al., 2017, Odabasi et al., 2015, Persoon and Hornbuckle, 2009). Active samples are costly due to the use of electricity. For this reason, passive sampling has been a frequent example in recent years as it is both easier to operate and less costly than active (Estellano et al., 2012, Yoonki et al., 2014). PUF passive samplers are widely used in recent years for the measurement of semi-volatile organic pollutants because of their ease of control, long-term use and low cost, and atmospheric POPs concentrations can easily be determined (Li et al., 2012).

In this study, a sampling campaign was carried out at the Bursa Uludag University Görükle Campus (UUC) using PUF discs between January 2016 and June 2016 period. It was aimed to determine atmospheric PCB concentrations and their seasonal trends.

MATERIAL METHOD

Sampling Site

The study was carried out at the Uludag University Görükle Campus (UUC) at 40°15'3.49"N 28°51'20.83"E coordinates (Fig. 1). The UUC sampling point was approximately 1 km from Bursa highway and 2 km from Görükle. The distance to Nilüfer organized industrial site was 5.5 km. There was also a small lake 500 meters away from the sampling point.

The PUF discs were used to collect the PCBs in the air. PUF disc samplers were placed at a height of 1.5 m. Dominant wind direction was north in the sampling site.

Figure 1. Sampling point

Extraction and Analysis

Collected PUF samples from the PASs were extracted with a 200 mL ACE: HEX (1:1, volume) mixture by a Soxhlet extraction method. During extraction, the PUF discs were carefully folded and placed to ensure that the discs were below the siphon level. Extraction was carried out for 24 hours. After the extraction step, the volume of the extracts was reduced by a rotary evaporator (Heidolph Rotary Evaporators Laborota 4001). The rotary evaporator was operated at 30 rpm and 23-35 °C. The sample volume was first reduced to 5 mL and then 10 mL HEX was added. Afterwards, the sample volume was reduced to 2 mL (Cindoruk and Taşdemir 2010b). Until the next stage, samples were stored in a deep freeze.

A column including silicic acid, alumina and sodium sulfate was used to clean and fractionate the samples (Taşdemir et al., 2004, Taşdemir and Holsen 2006, Yolsal et al., 2014). Activation and deactivation of silicic acid and aluminum oxide were performed prior to fractionation. For this reason, silicic acid (H_4SiO_4; Sigma Aldrich; ≤ 100 mesh) was activated for 24 hours at 105 ° C. After cooling in the desiccator, 3 grams were weighed and 100 µL of purified water was added (Taşdemir et al., 2004). After it was shaken well for homogeneous distribution, the deactivation process was completed. Aluminum oxide (Al_2O_3; Merck) was activated at a 450 °C ash furnace. Glass wool and sodium sulfate (Na_2SO_4) were also used in the column. Aluminum oxide was cooled in a desiccator and 2 grams were weighed and then 120 µL of pure water was added and shaken well for homogenous distribution (Taşdemir and Holsen 2006). Both silicic acid and aluminum oxide were waited for 1 hour before being used in the fraction.

The prepared chemicals were added in the order of silicic acid, aluminum oxide and sodium sulfate, with an internal diameter of 1.5 cm and glass wool placed at the end. The column was first washed with 20 mL of DCM and then with 20 mL of petroleum ether (PE) for possible contamination. Then a 2 mL condensed sample was poured into the column. After completely passing through the sample from the column, 25 mL of PE was added and the PCBs were collected at this stage. The sample was reduced to volume of 2 mL after HEX exchange (Günindi and Taşdemir, 2011).

The acid washing step was applied to the samples to remove organic contaminants (Sakın et al., 2017). In this step, sulfuric acid (H_2SO_4) was added into the samples and placed into centrifuge tubes. After that the covers of the tubes were tightly closed, they were shaken by hand for a while and then centrifuged (Hermle Z 306). The device has run for 2 minutes at 2000 cycles. The samples from the centrifuge were examined for color transparency and they were washed again with acid until reaching a transparent sample. Samples from the acid washing step were reduced to 1 mL under nitrogen gas. All samples ready to be read on GC-ECD were stored in deep freezing at -20 ºC.

Quality Assurance / Quality Control (QA/QC)

Throughout the study, equipment and glassware were cleaned with tap water, pure water, acetone (ACE), dichloromethane (DCM) respectively. In order to prevent any organic contamination in all stages during the sampling, extraction, and analysis, Teflon, glass, and stainless-steel materials were used in all steps. Surrogate standards containing PCB#14, PCB#65, and PCB#166 were employed to determine the efficiencies of the experiments. All of the data were reported after recovery and volume correction. Blank samples were also collected in order to determine contamination at sampling and experiment stages. In addition, LOD (limit of detection) correction was made for all species in the study. LOD was calculated for each PCB congener based on the results obtained from blanks (Sakın and Taşdemir, 2016).

RESULTS AND DISCUSSION

Sampling was achieved with PUF discs to determine the atmospheric PCB concentration at the Uludag University Görükle Campus (UUC). Sampling took place between January 2016 and June 2016. The atmospheric PCB concentrations in the UUC region varied between 47.15 and 116.10 pg/m^3 and the mean concentration in the region was determined as 87.91±22.07 pg/m^3 (Fig. 5). Figure 2 illustrates the average PCB congener distribution over the sampling period.

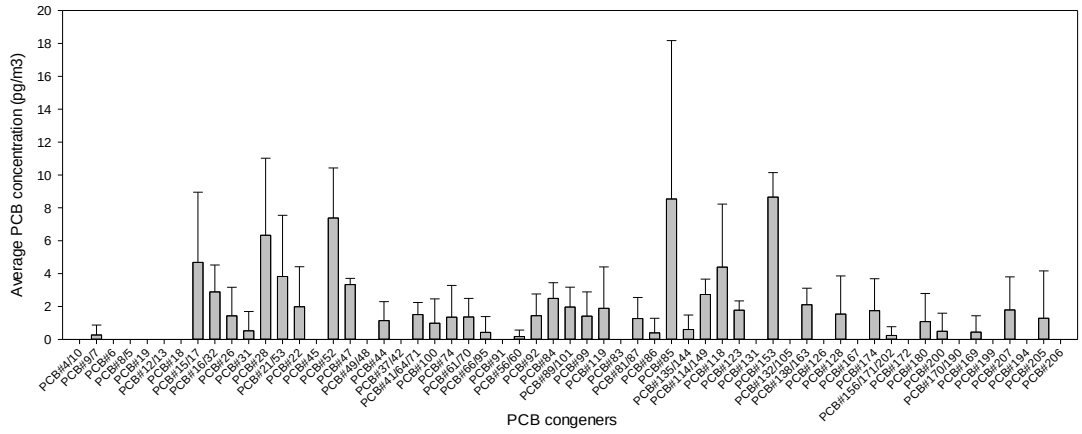

Figure 2. Average PCB congener concentrations

Astivize et al. have looked at 42 species in rural and suburban regions in Argentina (Astoviza et al., 2016). The average concentrations obtained in rural and suburban areas were 23 pg / m^3 and 37 pg / m^3, respectively. In this study, the PCB concentration was determined to be 40.84 pg / m^3 when considering the species of Astovize et al. This concentration value is higher than the concentration in the rural area, it is closer to the concentration in the suburban area. This is probably due to the prevailing wind transport effect. In addition, Astivize et al. (2016) also reported the concentrations of PCBs in urban areas. In their study conducted in three different urban areas, they found average PCB concentrations of 63 pg / m^3, 190 pg / m^3 and 287 pg / m^3. They classified these regions as low (10,000-100,000), medium (100,000-1,000,000) and high (> 1,000,000) populations and found concentrations of 63 pg / m^3, 190 pg / m^3 and 287 pg / m^3 respectively. It is seen that the value obtained in this study gives closer results to the less populated region. As a result, we find that our average value is much lower than the concentrations in the industrial areas but higher in the rural areas as compared to other PCB concentrations in the literature (Taşdemir, 1997, Colombo et al 2013, Tombesi et al 2014, Birgül et al 2017).

5-CBs in the UUC had the highest homolog group with 30.7%, while the order of the other groups was 4-CB (21.6%)> 3-CB (19.8%)> 6-CB (17.5%)> 7-CB (3.3%)> 2-CB (2.1%)> 8-CB (2.1%)> 9-CB (2.0%) (Figure 3). Similarly, a study conducted by Sakın and Taşdemir in 2013, 4-CBs > 3-CBs>5-CBs were also found to be the first 3 dominant homolog groups in the UUC. Cindoruk and Taşdemir (2010 a) and Birgül et al. (2017) also reported the highest concentration levels for 4-CBs and 3-CBs homologs. Heavy PCB homologs were not generally observed in the gas phase PCBs yet in our study, heavy PCB homologs were also detected. This was probably due to the dumping of some electronic garbage near to our sampling site.

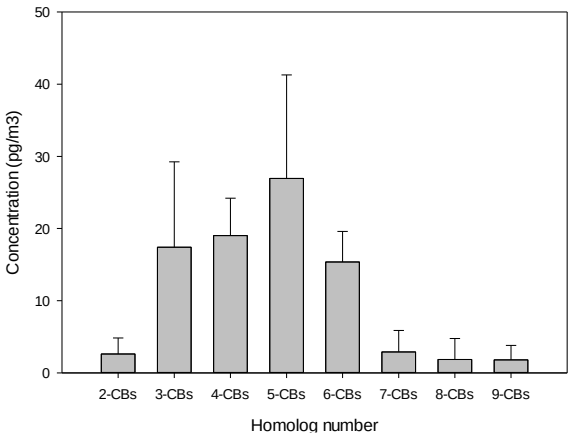

Figure 3. PCB homolog distribution

The concentration of indicator PCB congeners, which are PCB#28, PCB#52, PCB#101, PCB#118, PCB#138, PCB#153 and PCB#180, in the region ranged from 21.62 to 43.52 pg / m^3 and the average was calculated to be 29.88±7.45 pg / m^3. Indicator PCBs constituted 34% of the total PCB concentration in the region. The highest levels in this area belonged to PCB # 153 (8.65 pg / m^3), PCB # 52 (7.38 pg / m^3) and PCB # 28 (6.33 pg / m^3). Furthermore, the average dioxin-like PCBs (dl-PCBs which we look at PCB#81, 105, 114, 118, 123, 126, 156, 167, 169) were calculated to be 8.70±3.52 pg / m^3 and these species were found to constitute 9.90% of the total atmospheric concentration. The dl-PCBs with the highest concentration in the area was identified as PCB # 118 (4.40 pg / m^3). A graphical representation of the indicators and dl-PCBs observed at the UUC is given in Figure 3.

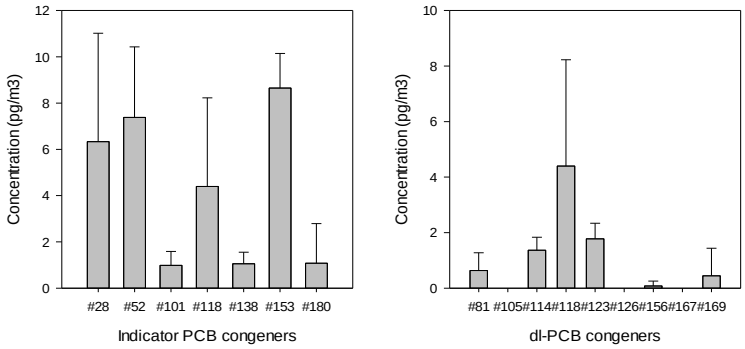

Figure 4. Atmospheric indicator PCB and dl-PCB congener levels

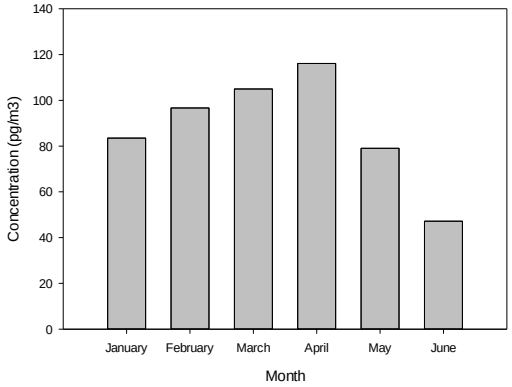

Figure 5. Monthly total PCB concentrations

The UUC has been used as a sampling point in some other studies. In a study conducted in the campus area during 2008-2009, the total average concentration of 83 congeners was calculated as 412 pg / m^3 (Cindoruk and Taşdemir 2010a). The average concentration of the indicator species was 67.8 pg / m^3 on the campus. Another study carried out in the UUC in 2013 was targeted 87 PCBs and found an average total concentration of 345 pg / m^3 (Sakın and Taşdemir 2016). In the same study, indicator species were also examined and their total average concentration was calculated as 43.4 pg / m^3. In our study, the concentration of the UUC area was calculated as 87.91±22.07 pg / m^3 and this value was found to be quite low when compared to the work done by Cindoruk and Taşdemir (2010a) and Sakin and Taşdemir (2016). However, these both studies have been performed with high-volume air samplers (HVASs). The sampler had an effect on the concentration discrepancies. Another possible reason for the differences between our results and previous reported results would be the decreasing tendency of PCBs in the atmosphere. This is probably due to law enforcement on the limitations of PCBs.

In another study conducted by Birgül et al. at the UUC, 43 PCBs were examined and the mean total PCB concentration was 43.8±24.4 pg / m^3 (Birgül et al., 2017). Our average PCB concentration level was higher than 43.8 pg / m^3. On the other hand, when we considered the same targeted PCB congeners, our average concentration became 49.57±8.79 pg / m^3 which was not statistically different from a recent work published Birgül et al (2017). The difference between the averages obtained from both studies were mainly sampling duration and used sampling coefficients. For example, the sampling period varied between 44 and 71 days for the study of Birgül et al. (2017) yet our sampling period was constant and it was about 30 days.

Moreover, the sampling coefficients ranged from 5.03 to 7.64 m^3/day in the study done by Birgül et al. (2017); however, the sampling coefficient was accepted as 3.5 m^3/day in our study.

Moreover seasonal changes were also discussed in our text. In general, atmospheric PCB concentrations in summer were found to be higher than those obtained in winter due to evaporation of PCBs from soil, water and other places (Taşdemir 1997). This was true for places far from the PCB sources. In our study, we generally observed this pattern except last two months. This result may indicate the effect of transportation of PCBs and possible PCB sources near our sampling site. Figure 4 shows the seasonal changes of PCBs in our sampling site.

People are exposed to PCBs with food, air and drinking water. An equation was developed by USEPA for respiration, one of these exposures (Equation 1).

$$CDI = \frac{C*IR*ED*EF}{BW*AT} \quad (1)$$

In this equation CDI is the inhalation chronic daily intake (pg/kg/day), C is concentration. (pg/m^3), IR is inhalation rate (m^3/ day), ED is exposure duration (yr), EF is exposure frequency (days/yr), BW is body weight (kg), AT is averaging time which is assumed as lifetime and calculated as ED*365 day/yr. In this study we have taken IR as 20 m3 / day BW as 65 kg (Yılmaz Civan 2010). The EF value is taken as the sampling period (30 days). In order to determine the risk of cancer, equation 2 is used. In this equation, SF values for non-dl PCBs are taken as $2x10^{-9}$ (pg/kg/day)$^{-1}$, and for dl-PCBs as $1{,}5x10^{-4}$ (pg/kg/day)$^{-1}$ (USEPA 2007).

$$R = CDI\ x\ SF \quad (2)$$

The risk of cancer was calculated separately for dl-PCBs and non-dl PCBs and total cancer risk values were determined via equation 3. The cancer risk profile of the region is shown in Table 1.

$$R(Total) = R(\sum_9 dl - PCBs) + R(\sum_{73} non - dl\ PCBs) \quad (3)$$

Table 1. The calculated inhalation exposure (CDI, pg/kg/day) and risk (R) for dl-PCBs, non-dl PCBs and total

Month	**CDI (dl-PCBs)**	***R* (dl-PCBs)**	**CDI (non-dl PCBs)**	***R* (non-dl PCBs)**	***R (Total)***
January	0,214361	$3{,}22x10^{-5}$	1,897938	$3{,}80x10^{-9}$	$3{,}22x10^{-5}$
February	0,177028	$2{,}66x10^{-5}$	2,267650	$4{,}54x10^{-9}$	$2{,}66x10^{-5}$
March	0,407045	$6{,}11x10^{-5}$	2,247177	$4{,}49x10^{-9}$	$6{,}11x10^{-5}$
April	0,216770	$3{,}25x10^{-5}$	2,719253	$5{,}44x10^{-9}$	$3{,}25x10^{-5}$
May	0,180641	$2{,}71x10^{-5}$	1,818456	$3{,}64x10^{-9}$	$2{,}71x10^{-5}$
June	0,124040	$1{,}86x10^{-5}$	1,068192	$2{,}14x10^{-9}$	$1{,}86x10^{-5}$

The risk of cancer that can be accepted by the USEPA is set at one in a million. In this study, results of R values were above the accepted risk level. Total cancer risk varied between $6.11x10^{-5}$ (March) and $1.86x10^{-5}$ (June). These results may have been obtained due to the presence of the electronic waste storage area near the zone and the location of the sampling point near the Bursa highway.

ACKNOWLEDGEMENT

This work was supported by TUBITAK (The Scientific and Technological Research Council of Turkey) (Project No: 114Y577). We would like to thank A. Egemen Sakın who helped us in our experimental work.

REFERENCES

Astoviza, M.J., Cappelletti, N., Bilos, C., Migoya, M.C., Colombo, J.C. 2016. Airborne PCB patterns and urban scale in the Southern Rio de la Plata Basin, Argentina. *Sci Total Environ,* 572 16-22.

Birgül, A., Taşdemir, Y. 2012. Determination of the Sampler Type and Rainfall Effect on the Deposition Fluxes of the Polychlorinated Biphenyls. *Sci World J*.

Cindoruk, S.S., Taşdemir, Y. 2010a. Ambient Air Levels and Trends of Polychlorinated Biphenyls at Four Different Sites. *Arch Environ Con Tox,* 59 (4): 542-554.

Cindoruk, S.S., Taşdemir, Y. 2010b. Dynamics of atmospheric polychlorinated biphenyls (PCBs): concentrations, patterns, partitioning, and dry deposition level estimations in a residential site of Turkey. *Environmental monitoring and assessment,* 162 (1-4): 67-80.

Colombo, A., Benfenati, E., Bugatti, S.G., Lodi, M., Mariani, A., Musmeci, L., Rotella, G., Senese, V., Ziemacki, G., Fanelli, R. 2013. PCDD/Fs and PCBs in ambient air in a highly industrialized city in Northern Italy. *Chemosphere,* 90 (9): 2352-2357.

Estellano, V.H., Pozo, K., Harner, T., Corsolini, S., Focardi, S. 2012. Using PUF disk passive samplers to simultaneously measure air concentrations of persistent organic pollutants (POPs) across the Tuscany Region, Italy. *Atmos Pollut Res,* 3 (1): 88-94.

Gunindi, M., Tasdemir, Y. 2011. Wet and Dry Deposition Fluxes of Polychlorinated Biphenyls (PCBs) in an Urban Area of Turkey. *Water Air Soil Poll,* 215 (1-4): 427-439.

Jones, K.C., de Voogt, P. 1999. Persistent organic pollutants (POPs): state of the science. *Environ Pollut,* 100 (1-3): 209-221.

Jones, K.C., Sanders, G., Wild, S.R., Burnett, V., Johnston, A.E. 1992. Evidence for a Decline of Pcbs and Pahs in Rural Vegetation and Air in the United-Kingdom. *Nature,* 356 (6365): 137-140.

Li, Y.M., Geng, D.W., Liu, F.B., Wang, T., Wang, P., Zhang, Q.H., Jiang, G.B. 2012. Study of PCBs and PBDEs in King George Island, Antarctica, using PUF passive air sampling. *Atmospheric Environment,* 51 140-145.

Odabasi, M., Falay, E.O., Tuna, G., Altiok, H., Kara, M., Dumanoglu, Y., Bayram, A., Tolunay, D., Elbir, T. 2015. Biomonitoring the Spatial and Historical Variations of Persistent Organic Pollutants (POPs) in an Industrial Region. *Environ Sci Technol,* 49 (4): 2105-2114.

Persoon, C., Hornbuckle, K.C. 2009. Calculation of passive sampling rates from both native PCBs and depuration compounds in indoor and outdoor environments. *Chemosphere,* 74 (7): 917-923.

Ross, G. 2004. The public health implications of polychlorinated biphenyls (PCBs) in the environment. *Ecotox Environ Safe,* 59 (3): 275-291.

Sakın, A.E., Taşdemir, Y. 2016. Determination of Atmospheric PCB Level Variations in Continuously Collected Samples. *Arch Environ Con Tox,* 71 (2): 235-245.

Sakin, A.E., Esen, F., Tasdemir, Y. 2017. Effects of sampling interval on the passive air sampling of atmospheric PCBs levels. *J Environ Sci Heal A,* 52 (7): 673-679.

Taşdemir, Y., 1997. Modification and Evaluation of Water Surface Sampler to Investigate the Dry Deposition and Air-Water Exchange of Polychlorinated Biphenyls (PCBs). *PHD Thesis*, Illinois Institute of Technology, Chicago, IL, ABD.

Taşdemir, Y., Holsen, T.M. 2006. Gas-phase deposition of polychlorinated biphenyls (PCBs) to a water surface sampler. *J Environ Sci Heal A,* 41 (10): 2071-2087.

Taşdemir, Y., Odabasi, M., Holsen, T.M. 2005. Measurement of the vapor phase deposition of polychlorinated bipheyls (PCBs) using a water surface sampler. *Atmospheric Environment,* 39 (5): 885-897.

Taşdemir, Y., Vardar, N., Odabasi, M., Holsen, T.M. 2004. Concentrations and gas/particle partitioning of PCBs in Chicago. *Environ Pollut,* 131 (1): 35-44.

Tombesi, N., Pozo, K., Harner, T. 2014. Persistent Organic Pollutants (POPs) in the atmosphere of agricultural and urban areas in the Province of Buenos Aires in Argentina using PUF disk passive air samplers. *Atmos Pollut Res,* 5 (2): 170-178.

USEPA, 1997. Exposure Factors Handbook, EPA/600/P-95/002Fa. US Environmental Protection Agency, Office of Research and Development National Center for Environmental Assessment, Washington, DC.

Wan, Y.S., Mackay, D. 1986. A Critical-Review of Aqueous Solubilities, Vapor-Pressures, Henry Law Constants, and Octanol-Water Partition-Coefficients of the Polychlorinated-Biphenyls. *J Phys Chem Ref Data,* 15 (2): 911-929.

Yılmaz Civan, M., 2010. Spatial Distribution of Organic Pollutants in Bursa Atmosphere: Seasonality and Health Effects. Environmental Engineering Department, Middle East Technical University (Thesis)

Yolsal, D., Salihoglu, G., Tasdemir, Y. 2014. Air-soil exchange of PCBs: levels and temporal variations at two sites in Turkey. *Environ Sci Pollut R,* 21 (5): 3920-3935.

Yoonki, M., Jongwon, H., Meehye, L. 2014. Determination of toxic congeners of 17 PCDDs/PCDFs and 12 dl-PCBs using polyurethane foam passive air samplers in ten cities around Seoul. *Sci Total Environ,* 491 17-27.

PARTICLE SIZE DISTRIBUTION OF PCDD/FS AND PCBS IN ISTANBUL ATMOSPHERE

Gulten GUNES[1], S. Levent KUZU[2], Arslan SARAL[2]

[1]Bartin University, Engineering Faculty, Department of Environmental Engineering, Kutlubey-Yazicilar 74110, Bartin, Turkey, ggunes@bartin.edu.tr,

[2]Yildiz Technical University, Department of Environmental Engineering, Esenler 34220, Istanbul, Turkey, skuzu@yildiz.edu.tr, saral@yildiz.edu.tr

Abstract

In this study, gas/particle concentration and particle size distribution of polychlorinated dioxin/furans (PCDD/F) and dioxin-like PCB compounds were investigated. A five-stage high volume cascade impactor was operated along with a high volume air sampler to collect ambient particle samples. Total suspended particle matter (TSP) concentration was determined to be 101 μg/m^3. Particles exhibited tri-modal size distribution (3-7.2 μm, 0.95-1.5μm and >0.49 μm). Particle and gas phase concentrations of PCDD/Fs were determined to be 2337 fg/m^3 (129 fg I-TEQ/m^3) and 345 fg/m^3 (59 fg I-TEQ/m^3), respectively. PCDD/F compounds exhibited mono-modal size distribution. Particle phase concentration of PCDD/F$_s$ showed a tendency to accumulate in particles smaller than 1.5 μm diameter and 54% of the PCDD/F compounds were deposited in d_{ae}<0.49 μm particles. Higher chlorinated compounds have higher contribution to PCDD/F concentrations (88%) rather than lower chlorinated compounds. The gas phase concentration of PCBs (ind+dl PCB) was determined to be 82 pg/m^3 and the particle phase concentration was determined to be 5.6 pg/m^3. PCB compounds exhibited bi-modal size distribution. Mass median diameter (MMAD) for ind-PCBs and dl-PCBs were 1.6 and 0.95 μm, respectively. The ratio of the indicator PCB and dl-PCB in the particle size of <0.49 μm was 25% and 35%, respectively. The contribution of lower chlorinated homologues was higher (86%) than higher chlorinated PCB compounds. Combustion sources (motor vehicles, waste incineration, use of fossil fuels for warming) at high temperatures are considered to be the most important source for the region in terms of gas/particle partitioning, particle size distribution and homologous distribution of the compounds.

Keywords: *Dioxin, polychlorinated biphenyl, atmosphere, particle, size distribution*

INTRODUCTION

Polychlorinated dioxins/furans are toxic chemicals that naturally exist in the environment and can be released into the environment through forest fires, backyard burning of trash, certain industrial activities, and residue from past commercial burning of waste. When released into the atmosphere, dioxins may be transported long distances (Tseng et al., 2014a,b; Chandra Suryani et al., 2015). Because of this, dioxins are found in many parts of the world. Particle size is the most important factor determining the atmospheric behavior, residence time and removal mechanisms of particles in the atmosphere (Bidleman, 1988; Offenberg and Baker, 1999).

Size distribution influences atmospheric transport. For example larger particles settle close to their sources, while smaller ones have tendency to long-range transportation; both atmospheric wet and dry deposition are influenced by particle size (Lohmann and Jones, 1998). Information of the particle size distribution of organic compounds gives important clues about their behavior in environmental environments (transports, removal by storage mechanisms), resources, and effects on human health.

Particle size is one of the most important factors affecting human health. Atmospheric particles are classified in 3 different size ranges: Ultrafine (d_{ae}< 0.1 μm), accumulation (0.1<d_{ae}<2.0 μm) and coarse (d_{ae}>2μm) (Bidleman, 1998). Ultrafine particles are formed in the atmosphere by homogeneous nucleation and are emitted from incinerators and waste incineration plants. Accumulation particles are formed by coagulation and condensation. Coarse particles are formed mechanically and emitted as sea spray (Allen et al., 1996). For this reason, it is important to know the particle size distribution in order to determine the particle source. Therefore, knowing the particle size distribution allows to predict the particle source as well as the health risk. Studies have shown that PCDD/F compounds are mostly accumulated on fine particles in the atmosphere (Kaupp et al., 1994; Kurogawa et al., 1998; Kaupp and McLachlan, 1999, 2000). Oh et al., (2002) reported that the largest mass of particles was collected in the back-up filter (dae<0.41 μm) and >50% of particles were in the <1.4 μm size class. Zhang et al. (2016) investigated gas/particle distribution of PCDD/F compounds in ambient air during the haze days and normal days. They reported that higher concentrations of airborne PCDD/Fs were detected during all hazy days and 95% of PCDD/Fs were adsorbed in the d_{ae} < 2.5 μm particles on hazy days. Zhang et al., (2016) reported in another study that 70% of the 1-3 chlorinated congeners are deposited in d_{ae}> 1μm particles, while 78% of 4-8 chlorinated congeners deposited in d_{ae}< 1μm particles.

In this study, concentrations, gas/particle partitioning and particle size distributions of polychlorinated dibenzo-p-dioxins (PCDD), dibenzo furans (PCDF) and dioxin like-polychlorinated biphenyls (dl-PCB) and indicator PCB_s were investigated in Istanbul by two different samplers.

DATA AND METHODS

Sampling station is characterized by mixed source groups of industrial, residential and traffic. Sampling and analysis were conducted in accordance with the reference method of EPA TO-9A. Samples were taken from the ambient air in Istanbul in the spring season. Two different sampling devices were used in the study. Five-staged cascade impactor (Staplex Hi Vol Cascade Impactor, USA) and High Volume Air Sampler (Echo Hi Vol, TECORA, Italy) was used for sampling of particle size distribution and total suspended particle (TSP) and gas phase, respectively. High volume air sampler and cascade impactor were operated at 0.151 m^3/min and 1.1 m^3/min flow rates and total sampling volume 1521m^3 and 11000 m^3 respectively. The samplers were placed 10 m above the ground level. The particles were separated into the following size ranges: <0.49, 0.49-0.95, 0.95-1.5, 1.5-3.0, 3.0-7.2, >7.2μm. Glass fiber filters (GFF) of 10 cm diameter and polyurethane foam (PUF) cylindrical plugs (6.0 cm-dia) were used for particle and gas phase samplings, respectively. Glass fiber filters of a compatible shape to cascade impactor was used in particle size distribution sampling. Before sampling, GFF filters were conditioned at 450°C for 5 h and PUF plugs were pre-cleaned with acetone in a soxhlet extractor for 16 h. Extraction, clean up and fractionation were applied for GFF and PUF plugs after sampling. The collected particle mass was obtained from the difference between the weigh of the GFF before and after sampling. Detailed extraction, clean up and fractionation methods was described previously elsewhere (Gunes and Saral, 2014). PCDD/Fs and dl-PCBs were analyzed by high-resolution gas chromatography/high-resolution mass spectrometry (HRGC–HRMS, Thermo Gas Chromatograph Trace GC Ultra-HRMS). $^{13}C_{12}$-labeled sampling and extraction standards were used to determine the recovery efficiency of sampling and extraction processes. Recovery values were determined in the ranges of 71–94% and 64–114% for sampling and extraction standards, respectively.

APPLICATION AND RESULTS

PCDD/F AND DL-PCB LEVELS IN AMBIENT AIR

TSP concentration of $\sum_{17}$PCDD/F compounds was 2337 fg/m^3 (129 fg I-TEQ/m^3), while gas phase concentration was 345 fg m^{-3} (59 fg I-TEQ/m^3). The total I-TEQ concentration was 188 fg I-TEQ/m^3. This value is lower than the Japan Air Quality Standards (600 fg I-TEQ/m^3) (Government of Japan, 2005). Moreover, this value is within the criateria value (100-400 fg I-TEQ m^{-3}) for urban areas according to Lohmann and Jones (2000 a). Total (gas+particle) PCDD congener concentrations were 993 fg/m^3 (37 fg I-TEQ/m^3) and PCDF congener concentrations were 1344 fg/m^3 (152 fg I-TEQ/m^3). Measurements were conducted at the same location between May 2011 and October 2012. The average concentrations were found as 2906 fg/m^3 and 156 fg I-TEQ/m^3. Similar I-TEQ concentrations were observed in Hong Kong (152 fg I-TEQ/m^3) (Choi et al., 2008) and in an industrial area in Catalonia, Spain (140 fg I-TEQ/m^3) (Abad et al., 2007).

In this study, the total concentration of PCB (ind + dl-PCB) was 88 pg/m^3. The fraction of the indicator PCBs was 89% and the dl -PCB was 11%. The dl-PCB concentration was determined to be 1.658 pg/m^3 (4.0 fg I-TEQ/m^3) for the TSP and 7.878 pg/m^3 (21 fg I-TEQ/m^3) for the gas phase. The average concentration at the same sampling site was 6.130 pg/m^3 (10.7 fg I-TEQ/m^3) between May 2011 and October 2013. The gas phase concentration was 4.23 pg/m^3, while TSP concentration was 1.9 pg/m^3. As a result, the participation of dl-PCBs to total TEQ ($TEQ_{PCDD/F}$+TEQ_{dl-PCB}) was rather low (average 13%). In another study, the average concentration for the industrial plant (steel plant) was detected as 6 fg I-TEQ/m^3 and 2 fg I-TEQ/m^3 for residential areas (Li et al., 2010). Martinez et al. (2010) classified the concentrations according to wind sector. When the wind blown over the industrial area, the average concentration was 23 fg I-TEQ/m^3 and this value was reduced to 12 fg I-TEQ/m^3 when the wind blown over residential area. Choi et al. (2008 a) reported a dl-PCB concentration of 26.2 pg/m^3 in the vicinity of the iron and steel plant and 3.3 pg/m^3 in the urban area. In this study, concentration was 9.54 pg/m^3, in another study at the same location, covering two years, the same average concentration was 6.13 pg/m^3 (Gunes et al., 2015). These results are comparable with the concentrations observed in several studies as follows: in Toronto (city center 15.1 pg/m^3, suburban 5.4 pg/m^3) (Helm and Bidleman 2003), Chicago 13.3 pg/m^3 (Harner et al.1998), suburban area in Netherlands (5.4 pg/m^3), in a rural area in USA (1.2 pg/m^3) (Harner et al., 1998) in the Arctic region (2.4 pg/m^3) (Cleverly et al., 2007).
In this study, indicator-PCB concentration was 4 pg/m^3 and 74 pg/m^3 for TSP and gas phases, respectively. Gunes et al. (2015) reported 60 pg m^{-3} (24-407 pg m^{-3}) PCB concentration for the same sampling location between May 11 and October 2013. Gas phase concentration was 55 pg/m^3, whereas TSP concentration was 5 pg/m^3. Gas phase concentrations were reported as 21-72 pg/m^3 in Jimenez et al. (2009) and 35-163.8 pg/m^3 in Mandalakis and Stephanou (2002). Particle phase concentrations were 3-10 pg/m^3 in Jimenez et al. (2009) and 11 pg/m^3 in Gambaro et al. (2004). Indicator-PCBs show a wide variation in other studies (7-6800 pg/m^3). Reported concentrations were as follows: 7 pg/m^3 in Sweden (Backe et al., 2000), 86 pg/m^3 in Germany (Kaupp et al., 1996), 344.9 pg/m^3 in Greece (Mandalakis and Stephanou 2002), 370 pg/m^3 in England (Lohmann et al., 2000), 1600 pg/m^3 in USA (Simcik et al., 1999), 3300-6800 pg/m^3 in Sweden (Ishaq et al., 2003).

PARTICLE SIZE DISTRIBUTION

The total suspended particle (TSP) concentration was determined as 101 μg/m^3 during a 7-day measurement. In the sampling done by cascade separator, the total particulate matter concentration was determined as 66 μg/m^3. The concentration difference between the two devices can be explained by the difference between the sampling method and the filter paper.

This value is significantly higher than the limit value (50 µg/m^3) reported by the Air Quality Assessment and Management Regulation and the World Health Organization (2005). The TSP concentration was determined as 77 µg/m^3 at the same sampling site (Gunes and Saral, 2014) and 78 µg/m^3 (Kuzu, 2016) in previous monitoring studies. The particle size distribution is shown in Figure 1. 46% of the particles were deposited in particles smaller than 0.95 µm in diameter and 35% were smaller than 0.49 µm. Figure 2 shows the normalized distribution of particles sizes. Particles showed peak values in the 3-7.2 µm, 0.95-1.5 µm, and < 0.49 µm size ranges. In other sampling studies in Istanbul, particles exhibited bimodal distribution (Sahin et al., 2012; Kuzu et al., 2013). It was reported that atmospheric particles usually show 2 peaks in urban areas (Kurogawa et al., 1998). Fine particles (d_{ae} <1µm) are generally generated from combustion sources, such as waste incineration plants, fossil fuel combustion sources, etc., while coarse particles (d_{ae}> 2µm) are generated from the earth's crust, soil, and mechanical erosion. In this study, the particles showed 3 peaks.

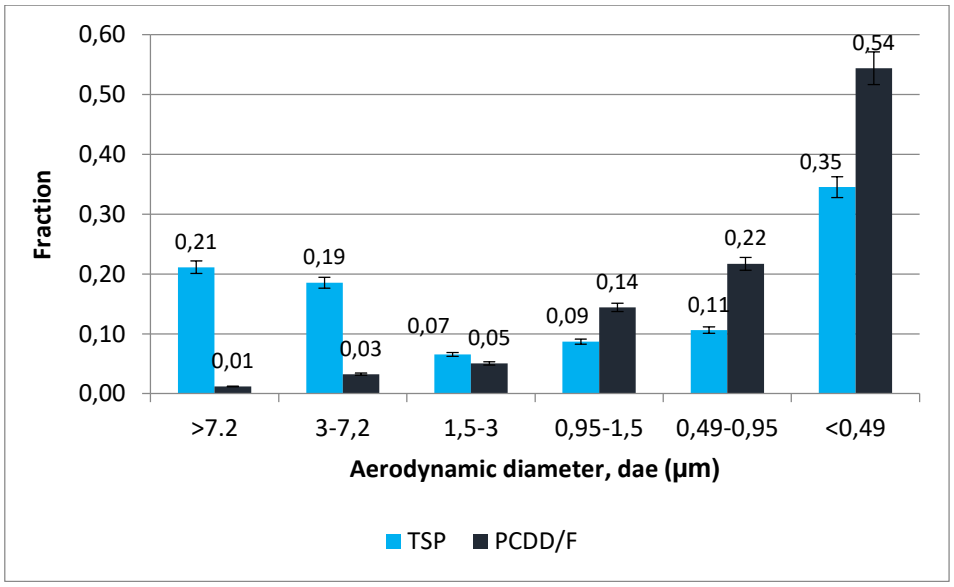

Figure 1. Particle size distribution of TSP and PCDD/Fs

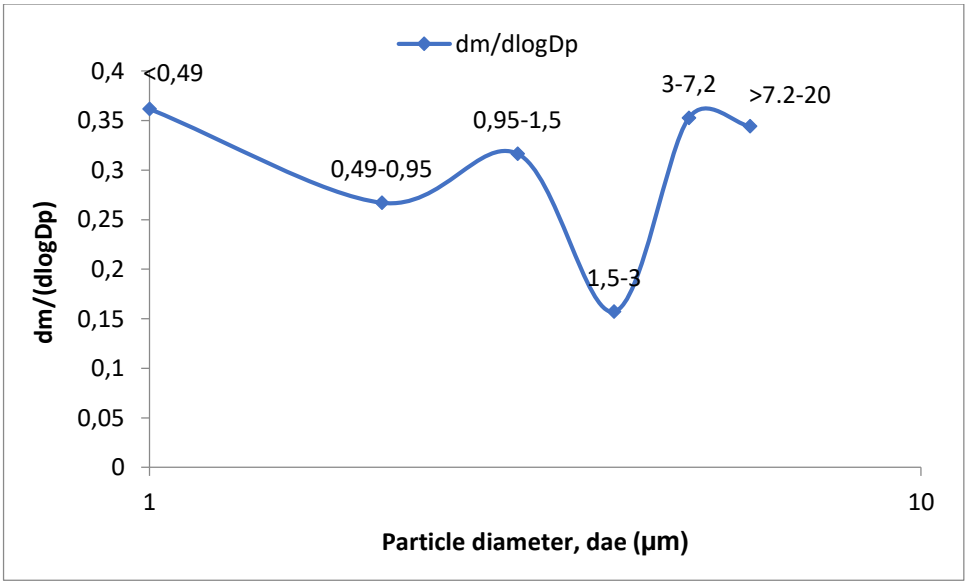

Figure 2. Normalized distribution of particle concentration with respect to their particle size

SIZE DISTRIBUTION OF PCDD/F COMPOUNDS

The normalized size distribution of PCDD/F compounds was shown in Figure 3. The PCDD/F compounds showed mono-modal size distribution and the peak value was determined at a diameter range of 0.95-1.5 µm. PCDD/F concentration continued to increase at smaller size ranges after this diameter interval. 54% of the PCDD/F compounds were accumulated in the particles of <0.49 µm. 90% accumulated in particles within the diameter of <1.5 µm. For PCDD/F compounds, MMAD was 0.39 µm and σ_g was 3.4. Similar results were reported in the literature. For example, Kurogawa et al. (1998) found that a very large amount of PCDD/F compounds accumulated in particles with a diameter of <1.1 µm, Kaupp et al. (1994) reported that those compounds accumulated in particles <1.35 µm. Oh et al. (2002) showed that 60% of particles are deposited in particles smaller than 0.41 µm and 90% are deposited in particles smaller than 2.1 µm in aerodynamic diameter.

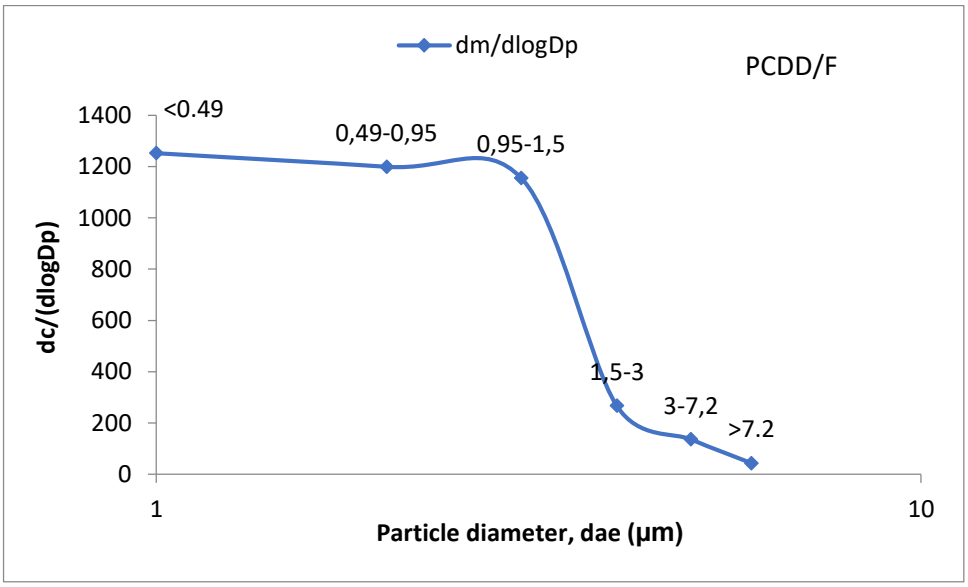

Figure 3. Normalized distribution of particle concentration with respect to their particle size

The contribution of lower chlorinated congeners to total PCDD/F concentration was 12%, while it was 88% for higher chlorinated congeners. The proportion of lower chlorinated homologues in the particulate phase is 10% and that of higher chlorinated was 90%. In the gas phase, the lower chlorinated homologues predominate and the ratio was 72%. Figure 4 shows the particle size distribution of the PCDD/F homologues of lower chlorinated congeners (4Cl, 5Cl), while and Figure 5 shows homologues of higher chlorinated congeners (6Cl, 7Cl, 8Cl). 51% of the lower chlorinated PCDD/F homologues were accumulated in the particles <0.49 µm, while this ratio was 55% for higher chlorinated homologues. 14% of the lower chlorinated homologues were accumulated in the particles larger than 1.5µm and this value was 9% for lower chlorinated homologues. The fractions of the lower chlorinated (4Cl and 5Cl) and higher chlorinated (6Cl, 7Cl, 8Cl) homologues in the particles smaller than 1.5µm were found to be 86% and 91%, respectively. As a result, all homologous groups tend to accumulate in the fine particles, but the fraction of less chlorinated homologues (4Cl and 5Cl) in the coarse particles was higher. For example, the fraction of lower chlorinated homologues in the particles > 3µm was 9%, while the fraction of higher chlorinated ones was 4%. This can be explained by the differences in vapor pressures of different congeners. Lower chlorinated congeners are in the range of $1.5x10^{-8}$ and $6.6x10^{-10}$ mm Hg and higher chlorinated congeners are in the range of ($1.5x10^{-9}$ and $8.2x10^{-13}$) (EPA, 2003). As lower chlorinated congeners have relatively higher vapor pressure, they have tendency to be present in the gaseous form. Oh et al. (2002) reported that PCDD/F

compounds weof re distributed in the range 1.4-2.1 µm and the proportion of veryhigher chlorinated (hexa, hepta, octa-CDD / F) homologues in the fine particles were higher.

Kurogawa et al. (1998) reported that higher chlorinated homologues exist in the particles < 1.1 µm and fraction of lower chlorinated congeners increased with the increasing diameter size. Similar results were reported by Kaupp and McLachlan (2000).

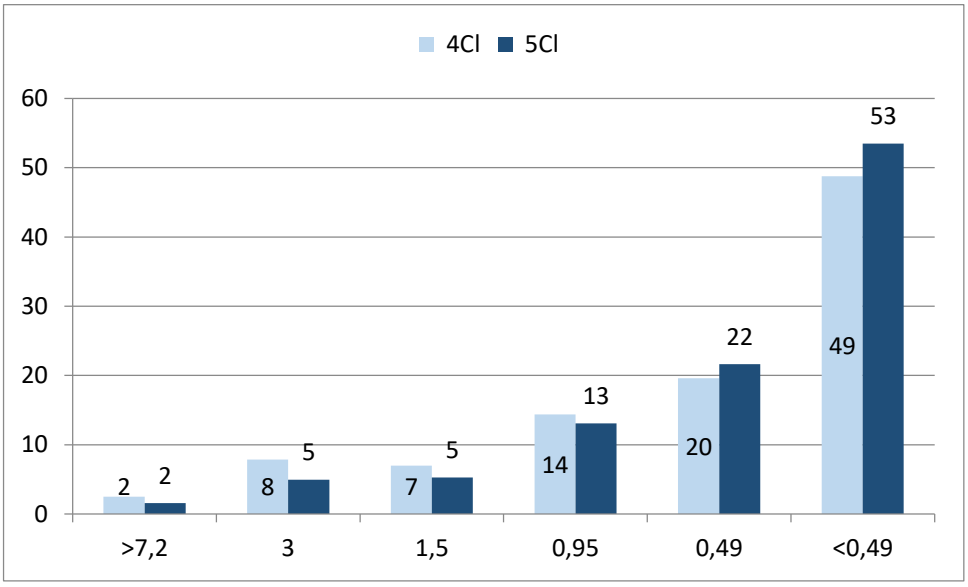

Figure 4. Distribution of lower chlorinated PCDD/F homologues with respect to their particle size

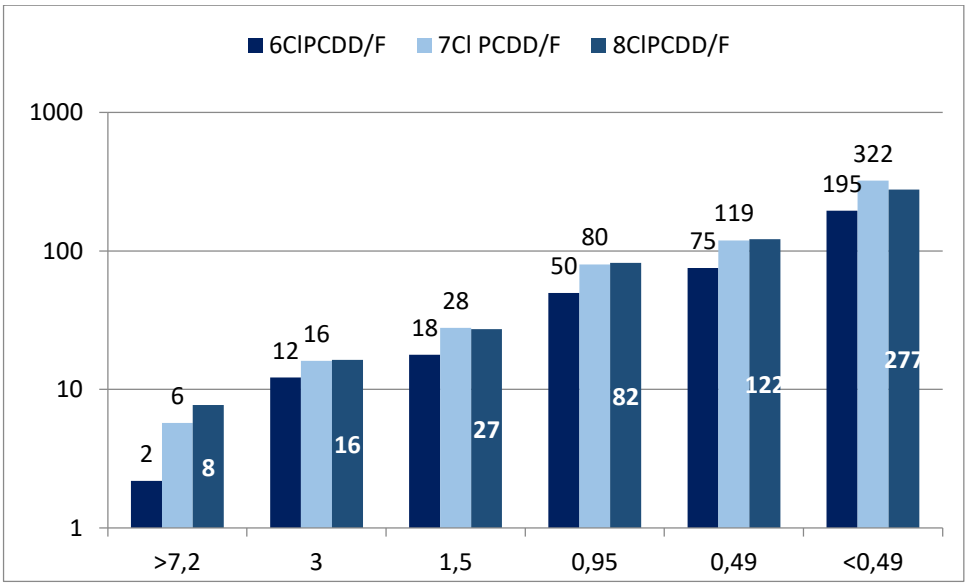

Figure 5. Distribution of higher chlorinated PCDD/F homologues with respect to their particle size

PARTICLE SIZE DISTRIBUTION OF PCB COMPOUNDS

The normalized size distribution of the indicator PCBs were shown in Figure 6. Ind-PCBs showed bimodal size distribution. Dominant peaks were determined in the range of 0.49-0.95 µm and dae> 7.2 µm. MMAD and geometric standard deviation were 1.59 µm and 7.3, respectively. The fraction of aerodynamic diameters greater than 7.2 µm and particles smaller

than 0.49 µm were 24% and 25%, respectively. The most significant difference between indicator PCBs and PCDD/F compounds was that PCDD/F had a fraction of 4.5% at >3 µm particles and indicator PCBs had 39%. This can be explained by the vapor pressures of PCDD/F and PCB and different formation mechanisms at source. In another study carried out at the same sampling site, MMAD was reported to be 1.14µm (Kuzu, S.L, 2016) where PCB compounds showed monomodal size distribution and the compounds accumulated in the 0.95-1.5 µm size range.

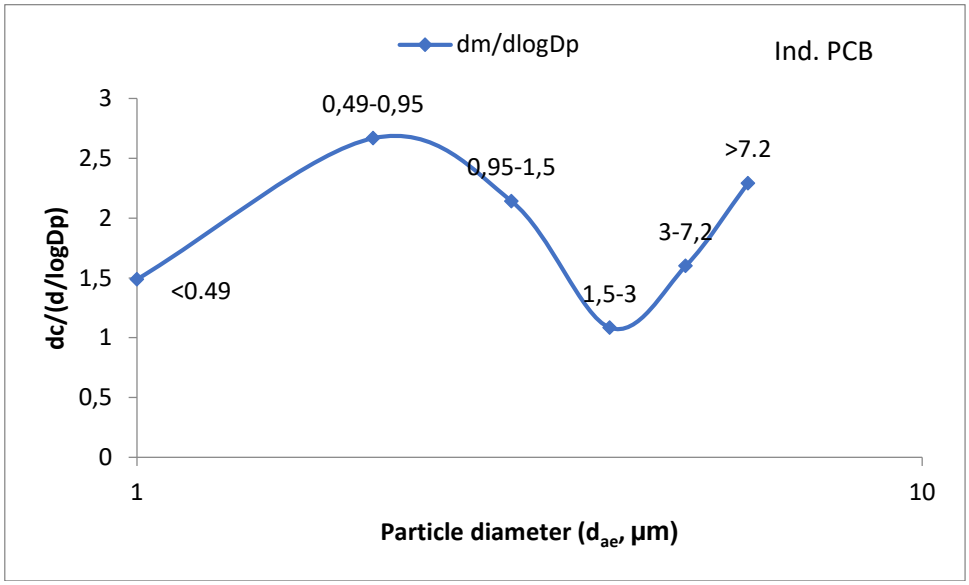

Figure 6. Normalized distribution of ind-PCB concentration with respect to their particle size

The normalized size distribution of dl-PCBs was shown in Fig 7. dl-PCBs showed bimodal distribution as with ind-PCBs. Peak concentrations were between 0.95 and 1.5 µm and 3.0 and 7.2 µm. MMAD and σ_g were determined to be 0.95 µm and 7.1, respectively. Unlike the indicator PCBs, Ddl-PCBs showed a greater tendency to accumulate (35%) in particles with a diameter of < 0.49 µm. However, the MMAD value (0.95 µm) of dl-PCBs was smaller than that of ind-PCBs (MMAD = 1.6 µm). This can be explained by the fact that the physicochemical properties of dl-PCBs are similar to those of PCDD/ Fs and are therefore found in smaller particles. The most important difference between dl-PCBs and PCDD/Fs was PCDD/F showed a mono-modal size distribution, whereas dl-PCBs exhibited bi-modal size distribution. When the MMAD values are compared, the MMAD value of PCDD/Fs (0.39 µm) is lower than dl-PCBs. Nevertheless, it was observed that both dl-PCBs and PCDD/Fs tend to accumulate in fine particles. The similarities are that the 0.95-1.5 µm diameter range is common for both compound groups. Concentration of PCDD/F compounds decreased as the size range increased, whereas dl-PCBs increased in the range of 3-7.2 µm. The fraction values for d_{ae}> 3 µm particles were determined to be 29% and 4.5% for dl-PCB and PCDD/F compounds, respectively. Similar results were observed for ind-PCBs and PCDD/F compounds as described in the previous section.

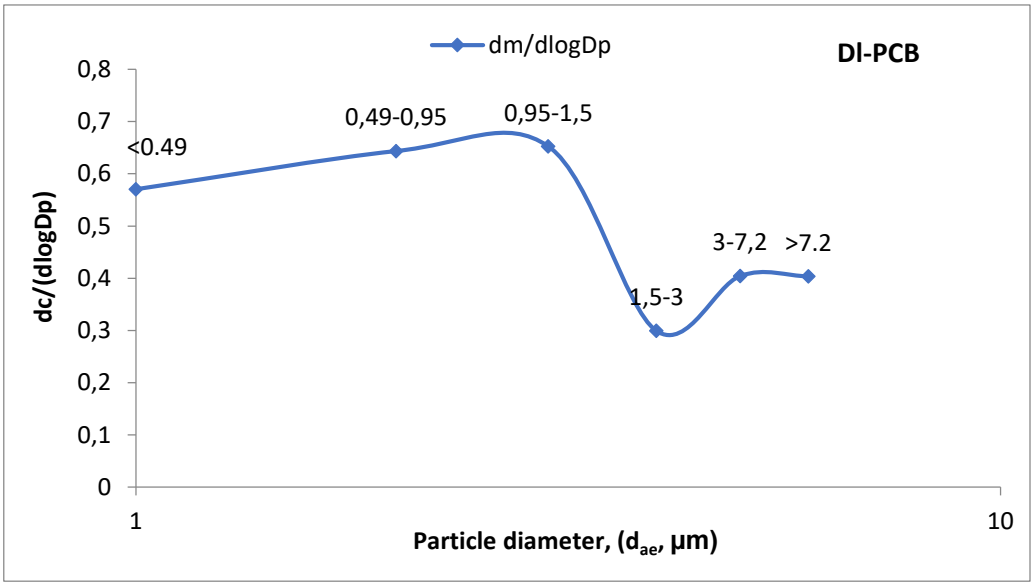

Figure 7. Normalized distribution of dl-PCB concentration with respect to their particle size.

DISTRIBUTION OF PCB HOMOLOGUES ACCORDING TO PARTICLE SIZES

The proportion of lower chlorinated homologues in the total PCB (ind + dl) concentration was 86%, and the proportion of higher chlorinated homologues was 14%. The ratio of lower chlorinated homologues in the gas phase was 88% and that of higher chlorinated homologues was 12%. The ratio of lower chlorinated homologues in the particle phase was 56% and that of higher lower chlorinated homologues was 44%. The predominance of lower chlorinated PCB homologues suggests that PCBs are emitted from combustion sources. Combustion of hazardous wastes, domestic wastes (Alcock et al., 2000) and other thermal processes at high temperature (Aries et al., 2004, Choi et al., 2008) are some examples. Combustion conditions affect homologue distribution. Some burning conditions lead to the formation of lower chlorinated PCB congeners (Brown and Ganey, 1995). The predominance of lower chlorinated PCB homologues suggests that motor vehicles and combustion for heating point is the most important PCB source at the sampling.

Dl-PCBs

Figure 8 shows distribution of dl-PCB and ind-PCB homologues with respect to their particle size. The proportion of lower chlorides homologues in the total dl-PCB concentration was 77%, while it was 23% for higher chlorinated homologues. The fraction of lower and higher chlorinated dl-PCBs was 15% for particles with a diameter >7.2 µm and for d_{ae} <0.49 µm it was 40% and 33% for lower and higher chlorinated homologues, respectively. As a result, 65% of the lower chlorinated homologues and 63% of the higher chlorinated homologues were accumulated in the particles d_{ae}<1.5 µm. 31% of the lower chlorinated homologues and 27% of the higher chlorinated homologues were accumulated in particles of size > 3µm. Similar to the PCDD/F compounds, the concentration of lower chlorinated homologues increased with increasing particle size. It can be explained by the number of chlorine and vapor pressure relationship as explained in the previous section.

Indicator PCBs

Ind-PCBs have a lower chlorined content of 87% and higher chlorinated content of 13%. As a result, it was determined that lower chlorinated PCB homologues were more dominant than higher chlorinated ones. 54% of the lower chlorinated homologues (3Cl, 4Cl, 5Cl) and 49% of the higher chlorinated homologues (6Cl, 7Cl) accumulated in particles smaller than d_{ae} = 1.5µm.

The fraction of particles with a diameter of > 3 μm for lower and higher chlorinated homologues was 40% and 31%, respectively. The proportion of lower chlorinated ind-PCBs was 26% in particles with >7.2μm diameter and 14% for higher chlorinated ones. 45% of the lower chlorinated and 29% of the higher chlorinated ind-PCBs accumulated in the particles of dae <0.95 μm.

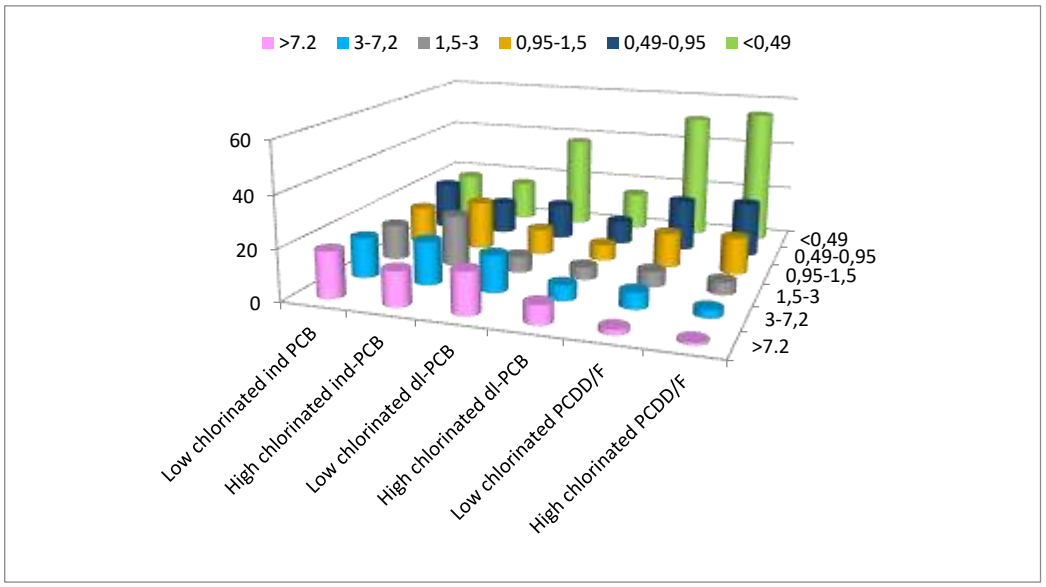

Figure 8. Distribution of dl-PCB and ind-PCB homologues with respect to their particle size

CONCLUSIONS AND RECOMMENDATIONS

In this study, gas/particle concentrations and particle size distributions of PCDD/F and PCB compounds were investigated. The total concentration of PCDD / F compounds (gas + particulate) was 2682 fg/m^3, 87% of the PCDD/F compounds (2337 fg/m^3) were determined in the particle phase and 13% (345 fg/m^3) in gas phase. In contrast to the PCDD/F compounds, 6% (5558 fg/m^3) of the PCB compounds were determined in the particle phase, 94% (81878 fg/m^3) was in the gas phase. 11% of the total PCB concentration was composed of dl-PCBs and 89% was ind-PCBs. When the size distribution of the compounds was evaluated, MMAD for PCDD/F compounds was 0.39 μm and 54% accumulated in the range of dae <0.49 μm. As a result, PCDD/Fs had tendency to accumulate in fine particles. Unlike PCDD / F compounds, PCBs showed bimodal distribution. The MMAD values for ind-PCBs and dl-PCBs were 1.6 μm and 0.95 μm, respectively. The proportion of lower chlorinated PCDD/F homologues was 12%, while the proportion of higher chlorinated PCDD/F homologues was 88%. The proportion of lower chlorinated homologues in the particulate phase is 10% and in the gas phase is 72%. 51% of the lower chlorinated PCDD/F compounds and 54% of the higher chlorinated PCDD/F compounds were deposited in the particles < 0.49 μm. The proportion of lower chlorinated homologues increases with the increasing particle size. Unlike PCDD/Fs, the percentage of lower chlorinated homologues in PCBs was 86%, and the proportion of higher chlorinated homologues was 14%. The proportion of lower chlorinated in the gas phase was 88%, and higher chlorinated was 12%. When the homologue distributions and particle size distributions of PCDD/F and PCB compounds are evaluated, it can be commented that combustion sources are effective in the sampling field.

REFERENCES

Abad, E., Martínez, K., Gustems, L., Gómez, R., Guinart, X., Hernández, I., Rivera, J., 2007. Ten years measuring PCDDs/PCDFs in ambient air in Catalonia (Spain). Chemosphere 67, 1709–1714

Allen, J.O., Dookeran, N.M., Smith, K.A., Sarofim, A.F., Taghizadeh, K., Lafleur, A.L., 1996. Measurement of PAHs associated with size-segregated atmospheric aerosols in Massachusetts. Environmental Science and Technology 30, 1023–1031.
Aries, E., Anderson, D.R., Ordsmith, N., Hall, K., Fisher, R., 2004. Development and validation of a method for analysis of ''dioxin-like'' PCBs in environmental samples from the steel industry. Chemosphere 54, 23–31.
Backe, C., Larsson, P., Okla, L., 2000. Polychlorinated biphenyls in the air of southern Sweden – spatial and temporal variation. Atmospheric Environment, 34, 1481-1486.
Bidleman, T.F., 1988. Atmospheric processes; wet and dry deposition of organic compounds are controlled by their vapor-particle partitioning. Environmental Science and Technology 22, 361–367.
Brown, A.P., Ganey, P.E. 1995. Neutrophil Degranulation and Superoxide Production Induced by Polychlorinated Biphenyls Are Calcium Dependent. Toxicology and Applied Pharmacology, 131, 198-205.
Chandra Suryani, R., Lee, W.-J., Endah Mutiara, M., Mwangi, J.K., Wang, L.-C., Lin, N.- H., Chang-Chien, G.-P., 2015. Atmospheric deposition of polychlorinated dibenzo-p-dioxins and dibenzofurans at coastal and high mountain areas in Taiwan. Aerosol Air Qual. Res. 15, 1390-1411
Choi, S.D., Baek, S.Y., Chang, Y.S., 2008. Atmospheric levels and distribution of dioxin-like polychlorinated biphenyls (PCBs) and polybrominated diphenyl ethers (PBDEs) in the vicinity of an iron and steel making plant. Atmos. Environ. 42, 2479–2488
Cleverly, D., Ferrario, J., Byrne, C., Riggs, K., Joseph, D., Hartford, P., 2007. A general indication of the contemporary background levels of PCDDs, PCDFs, and coplanar PCBs in the ambient air over rural and remote areas of the United States. Environmental Science and Technology 41, 1537–1544.
Gambaro A, Manodori L, Moret I, Capodaglio G, Cescon P, 2004. Determination of polychlorobiphenyls and polycyclic aromatic hydrocarbons in the atmospheric aerosol of the Venice Lagoon. Analytical and Bioanalytical Chemistry, 378(7): 1806–1814
Government of Japan. Information Brochure Dioxins, 2005.
Gunes, G., Saral, A (2014). Seasonal variation of PCDD/Fs in the metropolis of Istanbul, Turkey. Environ Sci Pollut Res. 21:8718–8729
Gunes, G., Saral, A., Kuzu, S.L., (2015). Seasonal Variation of Gas/Particle Partitioning of PCB Compounds In The Istanbul Atmosphere.
Harner, T., Kylin, H., Bidleman, T.F., Halsall, C., Strachan, W.M.J., Barrie, L.A., Fellin, P., 1998. Polychlorinated naphthalenes and coplanar polychlorinated biphenyls in arctic air. Environmental Science and Technology 32, 3257–3265.
Helm, P.A., Bidleman, T.F., 2003. Current combustion-related sources contribute to polychlorinated naphthalene and dioxin-like polychlorinated biphenyl levels and profiles in air in Toronto, Canada. Environmental Science and Technology 37, 1075–1082.
Ishaq, R., Näf, C., Zebühr, Y., UlfJärnberg, D., 2003. PCBs, PCNs, PCDD/Fs, PAHs and Cl-PAHs in air and water particulate samples—patterns and variations. Chemosphere, 50, 1131-1150.
Jiménez, J.C., Dueri, S., Eisenreich, S.J.,Mariani, G., Skejo, H., Umlauf, G., Zaldívarb, J.M. 2009. Polychlorinated biphenyls (PCBs) in the atmosphere of sub-alpine northern Italy. Environmental Pollution 157, 1024-1032.
Kaupp, H., Towara, J., McLachlan, M.S., 1994. Distribution of PCDD/Fs in atmospheric particulate matter with respect to particle size. Atmospheric Environment 28, 585–594.
Kaupp H. Atmospharische Eintragswege und Verhalten von ¨ polychlorierten Dibenzo-p-dioxinen und -furanen sowie polyzyklischen Aromaten in einem Maisbestand. Bayreuther Forum Okologie 1996; Band 38
Kaupp, H., McLachlan, M.S., 1999. Atmospheric particle size distributions of PCDD/Fs and PAHs and their implications for wet and dry deposition. Atmospheric Environment 33, 85–95.
Kaupp, H., McLachlan, M.S., 2000. Distribution of PCDD/Fs and PAHs within the full size range of atmospheric particles. Atmospheric Environment 34, 73–83.
Kurogawa, Y., Takahiko, M., Matayoshi, N., Satoshi, T., Kazumi, F., 1998. Distribution of PCDD/Fs in various sizes of airborne particles. Chemosphere 37, 2161–2171.
Kuzu, S.L (2016). Compositional Variation of PCBs, PAHs, and OCPs at Gas Phase and Size Segregated Particle Phase during Dust Incursion from the Saharan Desert in the Northwestern Anatolian Peninsula. Hindawi Publishing Corporation Advances in Meteorology. http://dx.doi.org/10.1155/2016/7153286
Kuzu, S. L., Saral, A., Demir, S., Summak, G., and Demir, G "A detailed investigation of ambient aerosol composition and size distribution in an urban atmosphere," Environmental Science and Pollution Research, vol. 20, no. 4, pp. 2556–2568, 2013.
Li Y, Wang P, Ding L, Li X, Wang T, Zhang Q, Yang H, Jiang G, Wei F (2010). Atmospheric distribution of polychlorinated dibenzo-pdioxins, dibenzofurans and dioxin-like polychlorinated biphenyls around a steel plant area, Northeast China. Chemosphere 79: 253–258
Lohmann, R., Jones, K.C., 2000a. Dioxins and furans in air and deposition: a review of levels, behavior and processes. Sci. Total Environ. 219, 53–81.

Lohmann, R., Harner, T., Thomas, G.O., Jones, K.C., 2000b. A comparative study of the gas-particle partitioning of PCDD/Fs, PCBs and PAH. Environ. Sci. Technol. 34,
4943–4951
Lohmann, R., Jones, K.C., 1998. Dioxins and furans in air and deposition: a review of levels, behaviour and processes. Science of the Total Environment 219, 53–81.
Mandalakis, M., Tsapakis, M., Tsoga, A., Stephanou, E.G., (2002). Gas-particle concentrations and distribution of aliphatic hydrocarbons, PAHs, PCBs and PCDD/Fs in the atmosphere of Athens (Greece), Atmospheric Environment 36, 4023–4035.
Martinez, K., Austrui, J.R., Jover, E., Ábalos, M., Rivera, J., Abad, E., 2010. Assessment of the emission of PCDD/Fs and dioxin-like PCBs from an industrial area over a nearby town using a selective wind direction sampling device. Environ. Pollut. 158, 764–769.
Offenberg, J.H., Baker, J.E., 1999. Aerosol size distributions of polycyclic aromatic hydrocarbons in urban and over-water atmospheres. Environmental Science and Technology 33, 3324–3331.
Oh, J.E., Choi, J.S., Chang, Y.S., 2002. PCDD/Fs monitoring of ambient air and soil near incinerators in Korea. Chemosphere, submitted for publication.
Simcik, M., Basu, I., Sweet, C.W., Hites, R.A., (1999). Temperature dependence and temporal trends of polychlorinated biphenyls congeners in the Great Lakes atmosphere, Environmental Science & Technology 33, 1991–1995.
Sahin, U.A., Scherbakova, K., and Onat, B "Size distribution and seasonal variation of airborne particulate matter in five areas in Istanbul, Turkey," Environmental Science and Pollution Research, vol. 19, no. 4, pp. 1198–1209, 2012.
Tseng, Y.-J., Mi, H.-H., Hsieh, L.-T., Liao, W.-T., Chang-Chien, G.-P., 2014a. Atmospheric deposition modeling of polychlorinated dibenzo-p-dioxins, dibenzofurans and polychlorinated biphenyls in the ambient air of Southern. Taiwan. Part I. Dry depositions. Aerosol Air Qual. Res. 14, 1950-1965.
Tseng, Y.-J., Mi, H.-H., Hsieh, L.-T., Liao, W.-T., Chang-Chien, G.-P., 2014b. Atmospheric deposition modeling of polychlorinated dibenzo-p-dioxins, dibenzofurans and polychlorinated biphenyls in the ambient air of Southern Taiwan. Part II. Wet depositions and total deposition fluxes. Aerosol Air Qual.
Res. 14, 1966-1985.
Zhang, X, Zheng, M., Liu, G., Zhu, Q., Dong, S., Zhang, H.,Wang, X., Xiao, K., Gao, L., Liu, W., 2016. A comparison of the levels and particle size distribution of lower chlorinated dioxin/furans (mono- to tri-chlorinated homologues) with those of tetra- to octa-chlorinated homologues in atmospheric samples. Chemosphere 151 (2016) 55-58

ATMOSPHERIC PCB CONCENTRATIONS AT TWO DIFFERENT SITES AND THEIR TIME TRENDS

Ahmet Egemen SAKIN, S. Sıddık CINDORUK, Yücel TASDEMIR*

Department of Environmental Engineering, Faculty of Engineering, Uludag University 16059 Nilüfer/Bursa, Turkey

esakin@uludag.edu.tr, cindoruk@uludag.edu.tr, tasdemir@uludag.edu.tr

ABSTRACT

This study was performed using passive air samplers (PASs), with the aim of examining the levels of the atmospheric PCB concentrations at 2 sites at different features, between 07.03.2014 and 07.05.2015 (14 months). At each site, PASs were collected once a month and analyzed for PCBs. The variations of the PCBs in the samples, depending on time and seasons were discussed. The average atmospheric PCB concentrations in the sites; urban and at the same time with heavy traffic and semi-rural, were calculated to be 190±136 pg/m^3 and 130±112 pg/m^3, respectively. It was determined that all of the obtained seasonal concentrations were increased at every site in hot seasons. When homolog distributions in the samples were examined, it was observed that the congeners with 2-, 3- and 4- chlorine were dominant. When the studies performed in the previous years were viewed, it was determined that the atmospheric concentrations at these sites tend to decrease over time.

Key Words: *PCBs, air concentration, passive sampling*

INTRODUCTION

Polychlorinated biphenyls (PCBs) are persistent organic pollutants (POPs) and in the Stockholm Convention, the participating countries have decided to take actions to reduce or eliminate POPs releases from the sources. These pollutants have adverse health effects. PCBs cause accumulations in the food chain since they are persistent and lipophilic and due to their biological accumulation properties (Gao, Zhang, Liu, Li, & Wang, 2014). PCBs are found in high concentrations at industrialized and urban sites since they are used as paint additives, in dielectric fluids, insulating liquids, flame retarders and etc. (Baek, Jurng, & Chang, 2013; Q. L. Li et al., 2012). Besides this, in the performed studies it was observed that the concentrations obtained at urban sites were higher in comparison with the rural sites (Cindoruk & Tasdemir, 2010). Even if the use of PCBs has been banned in the developed countries, they can mix with nature due to wrong or illegal discharge process of PCB containing wastes, burning of urban and industrial sludge, evaporations from the products containing PCB and leaks which may originate from old products (Aydin, Kara, Dumanoglu, Odabasi, & Elbir, 2014). One of the air samplers, which are used to determine the atmospheric concentrations of these pollutants mixing with nature, is passive air sampler (PAS) (Harner et al., 2006; Wilford, Harner, Zhu, Shoeib, & Jones, 2004). Atmospheric concentrations can be determined by converting the mass accumulated on the sampler in time into concentration. PASs provide an opportunity to examine local changes and pollutant sources since they give the chance to sample at several sites simultaneously (Harner, Shoeib, Diamond, Stern, & Rosenberg, 2004; Motelay-Massei et al., 2005). Passive samplers, having some advantages such as; easy to use, power supply free and low cost (Gouin, Shoeib, & Harner, 2008; Harner et al., 2004; Wania, Shen, Lei, Teixeira, & Muir, 2003), have recently become important in examining spatial and temporary trends of the concentrations of persistent organic pollutants. Polyurethane foam (PUF) discs are often used due to their high retention capacity. They are preferred in various implementations as they can be used at the sampling periods measured weekly or monthly (Jaward, Farrar, Harner, Sweetman, & Jones, 2004).

Aims of this study are;

(I) to determine the atmospheric PCB concentrations at the sites with different characteristics,

(II) to introduce time dependent changes in PCB concentrations,

(III) to compare with the concentrations obtained in the previous studies.

MATERIALS AND METHOD

Sampling Program

Atmospheric PCB samples were collected between 07.03.2014 and 07.05.2015 and passive air samplers (PASs) with PUF discs used in the samplings of PCBs and persistent organic pollutants (Gao et al., 2014; Y. M. Li et al., 2012; Motelay-Massei et al., 2005; Persoon & Hornbuckle, 2009; Pozo et al., 2012). The samples were collected at approximately one month retention time. A site with heavy traffic in Bursa and a university campus chosen as sampling points; BUTAL (BT) (N40°11'54",E29°02'55") and Uludağ University Campus (UUC) (40°13'55.3"N28°53'02.2"E) respectively.

BT sampling point is on a platform at 2 m high located at the nearest point to the road, in the garden of TUBİTAK-BUTAL, which is next to the street with heavy traffic. UUC is a campus with over 72,000 students and has human and traffic density with residential areas around, but away from the city and industries. Moreover, there is a highway 1.77 km away from the campus. The sampling point on UUC is on the roof of the single-storey sampling station at the entrance of the nature conservation center.

Materials and Method

The equipments used in samplings were washed with water, Methanol (MeOH) and dichloromethane (DCM) (Tasdemir, Odabasi, et al., 2004). PUFs used in samplings were cleaned using soxhlet extracted for overnight with distilled water, MeOH, DCM and acetone/hexane (ACE/HEX) mixture before using. After drying the cleaned PUF discs at 60 ^{o}C, they were kept in zip lock bags in the freezers. PUF discs were carried to and from the sampling point in these bags. After sampling PUFs were soxhlet extracted for 24 hours with ACE/HEX (1/1; v/v) mixture and before starting extraction, surrogate standards containing PCB #14, #65 and #166 were added (Cindoruk & Tasdemir, 2007c; Cotham & Bidleman, 1995; Odabasi, Sofuoglu, Vardar, Tasdemir, & Holsen, 1999; Vardar, Tasdemir, Odabasi, & Noll, 2004). The obtained extract was reduced to 5 mL with a rotary evaporator, 15 mL HEX was added and this process repeated twice (Cindoruk & Tasdemir, 2010). The obtained sample of 5 mL was reduced to 2 mL with a gentle nitrogen gas stream (Cindoruk & Tasdemir, 2007a). This sample was passed through the column containing silicic acid (%3 water), 2 g alumina (%6 water) and 2 g Na_2SO_4 and PCBs were collected from the column with 20 mL petroleum ether (PE) (Tasdemir, Vardar, Odabasi, & Holsen, 2004). Before the sample was passed through the column, the column was cleaned with 25 mL DCM and 25 mL PE. The extract of 20 mL containing PCB was reduced to 2 mL with a gentle nitrogen gas stream. The samples were washed with H_2SO_4 to avoid any organic pollution (Tasdemir, Vardar, et al., 2004). The samples, reduced to 1 mL with nitrogen gas stream, were transferred to vials and analyzed using GC. Before performing GC analysis, standard (PCB 204) was added to the samples to adjust volume (internal) (Cindoruk & Tasdemir, 2007c; Cotham & Bidleman, 1995; Gunindi & Tasdemir, 2010; Odabasi et al., 1999; Vardar et al., 2004).

The samples were analyzed using a gas chromatograph, Agilent 7890A model (containing ECD) having DB5-MS capillary column (30 m. x 0,250 mm. x 0,25 μm). In many studies, about 10-20 PCB congeners have been tried to identify, but in the study performed by our group 84 PCB congeners were searched. 84 PCB congeners aimed to identify were as follows; #4/10, #9/7, #6, #8/5, #18, #15/17, #16/32, #26, #31, #28, #21/53, #22, #45, #52, #47, #49/48, #44, #37/42, #71/41/64, #100, #74, #70/61, #66/95, #91, #56/60, #92, #84, #89/101, #119, #56/60, #92, #84, #89/101, #119, #83, #81/87, #86, #85, #77/110, #135/144, #114/149, #118, #123, #131, #153, #132/105, #163/138, #126, #128, #167, #174, #202/171/156, #172, #180, #200, #170/190, #169, #199, #207, #194, #205, #206. During the analysis a program, holding at 70 ^{o}C for 2 minutes, increasing to 150 ^{o}C with 25^{o}C /min. ramp rate, increasing to 200 ^{o}C with 3 ^{o}C /min. ramp rate, increasing to 280 ^{o}C with 8 ^{o}C /min. ramp rate and holding at this temperature for 8 minutes, increasing to 300 ^{o}C with 10 ^{o}C /min. ramp rate and holding at this temperature for 2 minutes, was used. The detector temperature was 320 ^{o}C and injector inlet temperature was 250 ^{o}C. As a carrier gas, helium gas (with 1,9 mL/min. flow rate) was used and as a make-up gas, high-purity nitrogen gas was used together with helium (Cindoruk & Tasdemir, 2007b; Cotham & Bidleman, 1995; Gunindi & Tasdemir, 2010).

Quality Assurance and Quality Control (QA/QC)

In order to determine the effects of the contaminations, which may occur during sample preparation, transportation and analysis, to the results; blank samples, at least 10% (n=5) of the total samples, were collected. The extraction and analysis procedures applied to the real samples were applied to blank samples, too. LODs (limit of detection) were determined with blank samples and reflected to the calculations. LOD values for each PCB congener were calculated by adding 3 standard deviations to the averages of the blank samples.

PCB#14, PCB#65 and PCB#166 congeners were added to the samples (as surrogate) to be able to calculate the extraction (recovery) efficiencies. Immediately before analyzing the samples, PCB#204 was injected into the vials (as internal standard) to be able to determine the net sample volume in the vials (Biterna & Voutsa, 2005; Gambaro, Manodori, Moret, Capodaglio, & Cescon, 2004; Gunindi & Tasdemir, 2010; Kim, Hirai, Kato, Urano, & Masunaga, 2004; Odabasi et al., 1999; Tasdemir, Odabasi, et al., 2004; Yeo, Choi, Chun, & Sunwoo, 2003).

RESULTS

Evaluation of Average Concentrations

In this study, atmospheric PCB concentrations at 2 different sites were measured using PASs for a year long. Concentrations were calculated by dividing the obtained masses by sampling period and sampling rate (R) (Persoon & Hornbuckle, 2009). In our previous study, R value for this sampler has been calculated for UUC. When the studies performed at different sites using this sampler were examined, it was observed that different R values were obtained (Chaemfa, Barber, Kim, Harner, & Jones, 2009; Choi et al., 2008; Klanova, Eupr, Kohoutek, & Harner, 2008; Q. L. Li et al., 2012). Therefore, R value was accepted as 3,5 m^3/day, which is the traditional acceptance as indicated in the study published by Chemfa in 2009 and accepted in many studies (Chaemfa et al., 2009; Jaward et al., 2004; Roots et al., 2010; Zhang et al., 2008). ∑PCB concentrations obtained at the measurements are shown in Figure 1. The obtained annual average concentrations for BT and UUC were calculated to be 190±136 pg/m^3 and 130±112 pg/m^3, respectively and plotted as average value in Figure 1. When the studies performed in Bursa province and in different regions of the world were examined (Table 1) it was observed that urban regions had higher concentrations (Baek, Choi, Park, Kang, & Chang, 2010; Baek et al., 2013; Cindoruk & Tasdemir, 2010; Halse, Schlabach, Sweetman, Jones, & Breivik, 2012; Melymuk, Robson, Helm, & Diamond, 2013). The values obtained from UUC were lower than

the concentrations from BT site is an expected situation. UUC is an area which has a rapid housing and crowded human activities with a population of university students. On the other hand, UUC is accepted as semi-urban as it is on the transport route of the pollutants from the Sea of Marmara, which is an inland sea with direct heavy ship traffic. For this reason, PCB concentrations measured at this site are higher in comparison with rural or semi-rural sites.

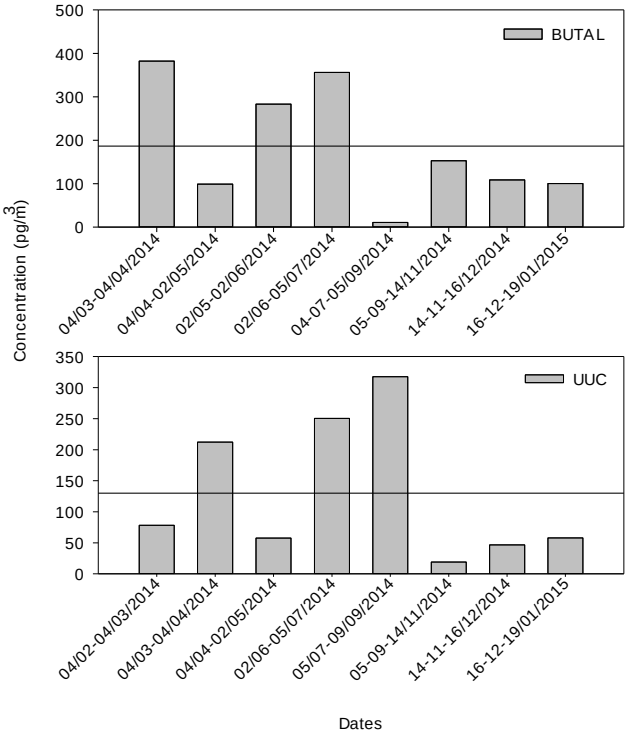

Figure 1. The PCB concentrations obtained at the sampling sites

Seasonal Variations of PCBs at the Sites

Seasonal variations of the concentrations measured at the sampling points are given in Figure 2. It was observed that PCB concentrations were higher in hot months generally. Maximum values obtained in the sites for BT and UUC were 320 pg/m^3 (Summer) and 251 pg/m^3 (Summer) respectively. Minimum values for BT and UUC were determined to be 82 pg/m^3 (Autumn) and 52 pg/m^3 (Winter) respectively. As is also understood from the lowest and the highest concentrations obtained, 4-5 times seasonal increase was observed at the sites. It is a usually determined that PCB concentrations in air reach to high levels with the evaporations in industrialized and crowded cities (Breivik, Sweetman, Pacyna, & Jones, 2002; Hsu, Holsen, & Hopke, 2003; Simcik, Zhang, Eisenreich, & Franz, 1997; Wethington & Hornbuckle, 2005).

In the sampling performed in UUC a year ago, correlations of the concentrations with temperature and wind velocity were examined. A correlation ($r=0.976$, $p<0.05$) was determined between atmospheric PCB concentrations and atmospheric temperature. When the concentrations obtained at maximum and minimum wind velocities were examined, no dilution increase with wind velocity was observed. In the light of this result, it was understood that the concentrations obtained from UUC, which is a semi-rural site, were due to transportation not from the local resources. Therefore, PCB levels in BT were found higher than in the other sampling points with the effect of traffic (Chrysikou, Gemenetzis, & Samara, 2009; Gueguen, Stille, & Millet, 2011).

Table 1. Some of the Atmospheric PCB Values Reported in Literature

Location	Date	PCB Number	Concentration (pg/m^3)	References
Aliağa, Türkiye	July –April 2010	35	349 - 94,363	(Aydin et al., 2014)
Bursa, Turkey	July 2004- May2005	28	287.27±174.80	(Cindoruk, Esen, & Tasdemir, 2007)
Bursa, Turkey	August 2004 –May 2005	37	491.8 _ 189.4	(Cindoruk & Tasdemir, 2007a)
Aliağa, Turkey	2-14 August 2004 20 March- 5 April 2005	41	3370_±1617 1164 ± 618	(Bozlaker, Odabasi, & Muezzinoglu, 2008)
Aliağa, Turkey	Winter, Spring, Summer, Fall)	41	8 727	(Kaya et al., 2012)
Bolu, Turkey	2007-2008	14	81 -87	(Yenisoy-Karakas, Oz, & Gaga, 2012)
Bursa, Turkey	July 2008-2009	82	360±210	(Yolsal, Salihoglu, & Tasdemir, 2014)
Bursa, Turkey	August 2004-2005	38	491.8 189.4	(Cindoruk & Tasdemir, 2007a)
Bursa, Turkey	June 2008-2009	29	311 ± 178	(Esen, 2013)
North Pacific-Atlantic Ocean	July- September 2012	26	19.116	(Wang, Na, Gao, Wang, & Yao, 2014)
Catalonia, /Spain	2010-2011	7	27.7	(Vilavert, Nadal, Schuhmacher, & Domingo, 2014)
Dalian, /China	November 2009 - 2010	18	50.9	(Xu et al., 2013)
Chicago, /USA	November 2006 - 2007	65	840	(Hu, Lehmler, Martinez, Wang, & Hornbuckle, 2010)
King George Island, the Antarctic	Summer of 2009	20	4.34	(Y. M. Li et al., 2012)
Serra dos Orgaos National Park /Rio de Janeiro	2007-2008	30	235 (geometrical average)	(Meire, Lee, Targino, Torres, & Harner, 2012)
Concepción/Chile	2007	48	160	(Pozo et al., 2012)

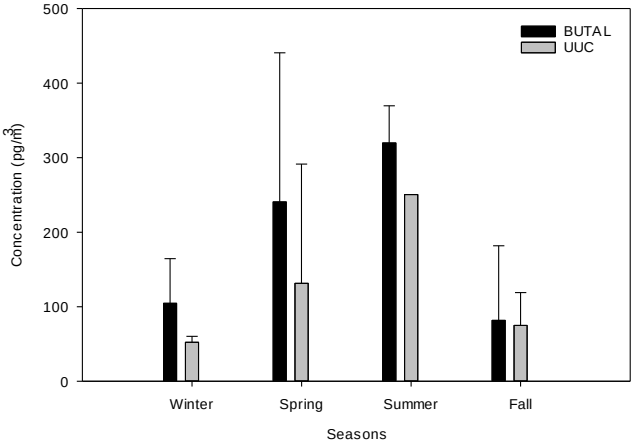

Figure 2. Seasonal variations of the concentrations

Examination of Homolog Group Distributions

Homolog distributions obtained from the sampling sites are presented in Figure 3. It was observed that the congeners' homologue with 3 chlorines in each of the sites was taken %40 and %41 values for BT and UUC, respectively and they were dominant congeners. Even if the homolog group distributions obtained at the sites were similar, the congeners with two chlorines in BT were higher in comparison to the other site.

When the studies in literature were examined, it was seen that traffic could create a source in terms of PCBs (Chrysikou et al., 2009; Gueguen et al., 2011). Besides the sampling point at BT site is in the city, it is also in a site with a heavy traffic. Furthermore, there are second-hand transformer suppliers, coil winding places, panel beaters and washing and oiling stations near the sampling point so; it is thought that the difference in homolog group distribution is because of these effects. In the study performed in 2010 by our group (Cindoruk & Tasdemir, 2010) it was informed that 3- and 4 chlorine congeners for BT was 60% of the total concentration. In our study, this value was calculated to be 57%. It was observed that the calculated gas-phase distribution was close to the previous values, but lower.

It was reported that in the study covering the years of 2004-2005 performed by our group (Cindoruk & Tasdemir, 2008), 3- and 4 chlorine congeners were 75% of the total and in the other study performed in 2008-2009 by our group (Cindoruk & Tasdemir, 2010) it was 57%. In our study, this value obtained for UUC was 69% and showed consistency with the studies performed at the same site. When the historical change of the 3- and 4 chlorine congeners were examined, it could be said that these congeners are in roll-off rate during the period up to our study. It can be said that the congener distribution is also affected from different samplers usage since in the previous studies the obtained results are the concentrations, which have been measured using an active sampling device (High volume air sampler, HVAS). But, the results of the PCB measurements performed using an active sampler from 2004 on, have also shown that there has been a decrease in the number and concentration of the congeners in time (Cindoruk & Tasdemir, 2007a, 2008, 2010; Gunindi & Tasdemir, 2011).

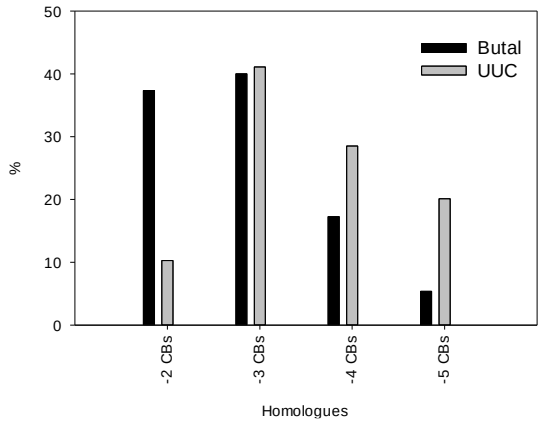

Figure 3. Homolog group distributions obtained at the sites

Temporally Changes at the Sites

In the previous years, outdoor PCB concentrations in BT and UUC have been measured by our group using HVAS (Cindoruk & Tasdemir, 2007a, 2008, 2010; Gunindi & Tasdemir, 2011). The comparison of the concentrations obtained in BT with the results obtained in the previous studies is given in Figure 4. It is seen that despite there is an increase in the number of the investigated PCB congeners, there is a decrease in the obtained concentrations in time. When

the common 22 congeners in these studies were examined, the PCB concentrations for 2004-2005, 2008-2009 and 2014-2015 periods were calculated to be 335 pg/m^3, 138 pg/m^3 and 89 pg/m^3, respectively.

Comparison of the concentrations obtained at UUC with the values obtained in the previous studies is given in Figure 4. In the studies the targeted PCB numbers vary therefore, the results were interpreted on the basis of the common PCB congeners in each sampling in order to determine the trend exactly. When the concentrations of the 22 PCB congeners common in the four studies examined, a decrease in the obtained PCB concentrations was observed as the time passes by.

In the studies in literature, it has been indicated that in the measurements performed using an active sampler introduced higher values in comparison with passive samplers (Ding et al., 2013; Melymuk, Robson, Helm, & Diamond, 2012). It is thought that the reason of the decrease seen at both sites is that it has been decided to get the PCBs under control with the Stockholm Convention and following that, the legal sanctions applied. On the other hand, they are still at the measurable level in the atmosphere although their usage has been banned. Therefore, since PCBs have a long atmospheric life, the PCB containing materials used previously could be disposed uncontrolledly and it is understood that they could still evaporate from the polluted surfaces, waters and plants to the atmosphere.

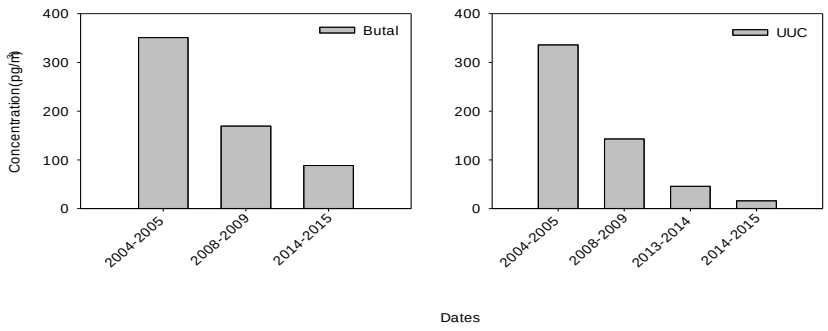

Figure 4. Historical Changes of the Concentrations Obtained at BUTAL and UUC Site

CONCLUSION

Atmospheric PCB concentrations were measured at 2 different sites using PASs. At the sites with traffic-urban and semi-urban features, a grading such as BT>UUC was obtained, respectively. It was observed that the concentrations had shown change with the site structure and it was understood that seasonal variations had also an influence on atmospheric PCB concentrations. Moreover, it has been considered that although UUC is a site with semi-urban characteristic feature, PCBs have been transported from the surfaces polluted with medium-range atmospheric transportation, especially from the Sea of Marmara. In this study it was observed that the concentrations at sampling sites were correlated with seasonal temperatures and homolog group distributions were similar. When the concentrations in this study compared with previous results it was determined that there was a time-dependent decrease in atmospheric PCB concentrations. It is considered that performing the next study on the congeners, whose measured atmospheric PCB concentration levels are common, and in terms of potential source and continuing with an active and a passive sampling simultaneously, will introduce helpful results.

ACKNOWLEDGEMENT

This study was supported by The Commission of Scientific Research Projects of Uludag University with Project number: OUAP (M) 2012/22

REFERENCES

Aydin, Y. M., Kara, M., Dumanoglu, Y., Odabasi, M., & Elbir, T. (2014). Source apportionment of polycyclic aromatic hydrocarbons (PAHs) and polychlorinated biphenyls (PCBs) in ambient air of an industrial region in Turkey. *Atmospheric Environment, 97*, 271-285. doi: DOI 10.1016/j.atmosenv.2014.08.032

Baek, S. Y., Choi, S. D., Park, H., Kang, J. H., & Chang, Y. S. (2010). Spatial and Seasonal Distribution of Polychlorinated Biphenyls (PCBs) in the Vicinity of an Iron and Steel Making Plant. *Environmental Science & Technology, 44*(8), 3035-3040. doi: 10.1021/es903251h

Baek, S. Y., Jurng, J., & Chang, Y. S. (2013). Spatial distribution of polychlorinated biphenyls, organochlorine pesticides, and dechlorane plus in Northeast Asia. *Atmospheric Environment, 64*, 40-46. doi: DOI 10.1016/j.atmosenv.2012.09.015

Biterna, M., & Voutsa, D. (2005). Polychlorinated biphenyls in ambient air of NW Greece and in particulate emissions. *Environment International, 31*(5), 671-677. doi: DOI 10.1016/j.envint.2004.11.004

Bozlaker, A., Odabasi, M., & Muezzinoglu, A. (2008). Dry deposition and soil-air gas exchange of polychlorinated biphenyls (PCBs) in an industrial area. *Environmental Pollution, 156*(3), 784-793. doi: DOI 10.1016/j.envpol.2008.06.008

Breivik, K., Sweetman, A., Pacyna, J. M., & Jones, K. C. (2002). Towards a global historical emission inventory for selected PCB congeners - a mass balance approach 1. Global production and consumption. *Science of the Total Environment, 290*(1-3), 181-198. doi: Pii S0048-9697(01)01075-0

Doi 10.1016/S0048-9697(01)01075-0

Chaemfa, C., Barber, J. L., Kim, K. S., Harner, T., & Jones, K. C. (2009). Further studies on the uptake of persistent organic pollutants (POPs) by polyurethane foam disk passive air samplers. *Atmospheric Environment, 43*(25), 3843-3849. doi: DOI 10.1016/j.atmosenv.2009.05.020

Choi, S. D., Baek, S. Y., Chang, Y. S., Wania, F., Ikonomou, M. G., Yoon, Y. J., . . . Hong, S. (2008). Passive air sampling of polychlorinated biphenyls and organochlorine pesticides at the Korean Arctic and Antarctic research stations: Implications for long-range transport and local pollution. *Environmental Science & Technology, 42*(19), 7125-7131. doi: Doi 10.1021/Es801004p

Chrysikou, L. P., Gemenetzis, P. G., & Samara, C. A. (2009). Wintertime size distribution of polycyclic aromatic hydrocarbons (PAHs), polychlorinated biphenyls (PCBs) and organochlorine pesticides (OCPs) in the urban environment: Street- vs rooftop-level measurements. *Atmospheric Environment, 43*(2), 290-300. doi: DOI 10.1016/j.atmosenv.2008.09.048

Cindoruk, S. S., Esen, F., & Tasdemir, Y. (2007). Concentration and gas/particle partitioning of polychlorinated biphenyls (PCBs) at an industrial site at Bursa, Turkey. *Atmospheric Research, 85*(3-4), 338-350. doi: 10.1016/j.atmosres.2007.02.004

Cindoruk, S. S., & Tasdemir, Y. (2007a). Characterization of gas/particle concentrations and partitioning of polychlorinated biphenyls (PCBs) measured in an urban site of Turkey. *Environmental Pollution, 148*(1), 325-333. doi: DOI 10.1016/j.envpol.2006.10.018

Cindoruk, S. S., & Tasdemir, Y. (2007b). Deposition of atmospheric particulate PCBs in suburban site of Turkey. *Atmospheric Research, 85*(3-4), 300-309. doi: 10.1016/j.atmosres.2007.02.002

Cindoruk, S. S., & Tasdemir, Y. (2007c). The determination of gas phase dry deposition fluxes and mass transfer coefficients (MTCs) of polychlorinated biphenyls (PCBs) using a modified water surface sampler (WSS). *Science of the Total Environment, 381*(1-3), 212-221. doi: DOI 10.1016/j.scitotenv.2007.03.011

Cindoruk, S. S., & Tasdemir, Y. (2008). Atmospheric gas and particle phase concentrations of polychlorinated biphenyls (PCBs) in a suburban site of Bursa, Turkey. *Environmental Forensics, 9*(2-3), 153-165. doi: 10.1080/15275920801888442

Cindoruk, S. S., & Tasdemir, Y. (2010). Ambient Air Levels and Trends of Polychlorinated Biphenyls at Four Different Sites. *Archives of Environmental Contamination and Toxicology, 59*(4), 542-554. doi: 10.1007/s00244-010-9507-4

Cotham, W. E., & Bidleman, T. F. (1995). Polycyclic Aromatic-Hydrocarbons and Polychlorinated-Biphenyls in Air at an Urban and a Rural Site near Lake-Michigan. *Environmental Science & Technology, 29*(11), 2782-2789. doi: Doi 10.1021/Es00011a013

Ding, L., Li, Y. M., Wang, P., Li, X. M., Zhao, Z. S., Ruan, T., & Zhang, Q. H. (2013). Spatial concentration, congener profiles and inhalation risk assessment of PCDD/Fs and PCBs in the atmosphere of Tianjin, China. *Chinese Science Bulletin, 58*(9), 971-978. doi: DOI 10.1007/s11434-013-5694-5

Esen, F. (2013). Development of a Passive Sampling Device Using Polyurethane Foam (PUF) to Measure Polychlorinated Biphenyls (PCBs) and Organochlorine Pesticides (OCPs) near Landfills. *Environmental Forensics, 14*(1), 1-8. doi: 10.1080/15275922.2012.729008
Gambaro, A., Manodori, L., Moret, I., Capodaglio, G., & Cescon, P. (2004). Determination of polychlorobiphenyls and polycyclic aromatic hydrocarbons in the atmospheric aerosol of the Venice Lagoon. *Analytical and Bioanalytical Chemistry, 378*(7), 1806-1814. doi: DOI 10.1007/s00216-004-2498-0
Gao, L. R., Zhang, Q., Liu, L. D., Li, C. L., & Wang, Y. W. (2014). Spatial and seasonal distributions of polychlorinated dibenzo-p-dioxins and dibenzofurans and polychlorinated biphenyls around a municipal solid waste incinerator, determined using polyurethane foam passive air samplers. *Chemosphere, 114*, 317-326. doi: 10.1016/j.chemosphere.2014.04.100
Gouin, T., Shoeib, M., & Harner, T. (2008). Atmospheric concentrations of current-use pesticides across south-central Ontario using monthly-resolved passive air samplers. *Atmospheric Environment, 42*(34), 8096-8104. doi: DOI 10.1016/j.atmosenv.2008.05.070
Gueguen, F., Stille, P., & Millet, M. (2011). Air quality assessment by tree bark biomonitoring in urban, industrial and rural environments of the Rhine Valley: PCDD/Fs, PCBs and trace metal evidence. *Chemosphere, 85*(2), 195-202. doi: DOI 10.1016/j.chemosphere.2011.06.032
Gunindi, M., & Tasdemir, Y. (2010). Atmospheric polychlorinated biphenyl (pcb) inputs to a coastal city near the marmara sea. *Marine Pollution Bulletin, 60*(12), 2242-2250. doi: 10.1016/j.marpolbul.2010.08.012
Gunindi, M., & Tasdemir, Y. (2011). Wet and Dry Deposition Fluxes of Polychlorinated Biphenyls (PCBs) in an Urban Area of Turkey. *Water Air and Soil Pollution, 215*(1-4), 427-439. doi: DOI 10.1007/s11270-010-0488-8
Halse, A. K., Schlabach, M., Sweetman, A., Jones, K. C., & Breivik, K. (2012). Using passive air samplers to assess local sources versus long range atmospheric transport of POPs. *Journal of Environmental Monitoring, 14*(10), 2580-2590. doi: Doi 10.1039/C2em30378g
Harner, T., Pozo, K., Gouin, T., Macdonald, A. M., Hung, H., Cainey, J., & Peters, A. (2006). Global pilot study for persistent organic pollutants (POPs) using PUF disk passive air samplers. *Environmental Pollution, 144*(2), 445-452. doi: DOI 10.1016/j.envpol.2005.12.053
Harner, T., Shoeib, M., Diamond, M., Stern, G., & Rosenberg, B. (2004). Using passive air samplers to assess urban - Rural trends for persistent organic pollutants. 1. Polychlorinated biphenyls and organochlorine pesticides. *Environmental Science & Technology, 38*(17), 4474-4483. doi: Doi 10.1021/Es040302r
Hsu, Y. K., Holsen, T. M., & Hopke, P. K. (2003). Locating and quantifying PCB sources in Chicago: Receptor modeling and field sampling. *Environmental Science & Technology, 37*(4), 681-690. doi: Doi 10.1021/Es025531x
Hu, D. F., Lehmler, H. J., Martinez, A., Wang, K., & Hornbuckle, K. C. (2010). Atmospheric PCB congeners across Chicago. *Atmospheric Environment, 44*(12), 1550-1557. doi: DOI 10.1016/j.atmosenv.2010.01.006
Jaward, F. M., Farrar, N. J., Harner, T., Sweetman, A. J., & Jones, K. C. (2004). Passive air sampling of polycyclic aromatic hydrocarbons and polychlorinated naphthalenes across Europe. *Environmental Toxicology and Chemistry, 23*(6), 1355-1364. doi: Doi 10.1897/03-420
Kaya, E., Dumanoglu, Y., Kara, M., Altiok, H., Bayram, A., Elbir, T., & Odabasi, M. (2012). Spatial and temporal variation and air-soil exchange of atmospheric PAHs and PCBs in an industrial region. *Atmospheric Pollution Research, 3*(4), 435-449. doi: Doi 10.5094/Apr.2012.050
Kim, K. S., Hirai, Y., Kato, M., Urano, K., & Masunaga, S. (2004). Detailed PCB congener patterns in incinerator flue gas and commercial PCB formulations (Kanechlor). *Chemosphere, 55*(4), 539-553. doi: DOI 10.1016/j.chemosphere.2003.11.056
Klanova, J., Eupr, P., Kohoutek, J., & Harner, T. (2008). Assessing the influence of meteorological parameters on the performance of polyurethane foam-based passive air samplers. *Environmental Science & Technology, 42*(2), 550-555. doi: Doi 10.1021/Es072098o
Li, Q. L., Xu, Y., Li, J., Pan, X. H., Liu, X., & Zhang, G. (2012). Levels and spatial distribution of gaseous polychlorinated biphenyls and polychlorinated naphthalenes in the air over the northern South China Sea. *Atmospheric Environment, 56*, 228-235. doi: DOI 10.1016/j.atmosenv.2012.03.074
Li, Y. M., Geng, D. W., Liu, F. B., Wang, T., Wang, P., Zhang, Q. H., & Jiang, G. B. (2012). Study of PCBs and PBDEs in King George Island, Antarctica, using PUF passive air sampling. *Atmospheric Environment, 51*, 140-145. doi: 10.1016/j.atmosenv.2012.01.034
Meire, R. O., Lee, S. C., Targino, A. C., Torres, J. P. M., & Harner, T. (2012). Air concentrations and transport of persistent organic pollutants (POPs) in mountains of southeast and southern Brazil. *Atmospheric Pollution Research, 3*(4), 417-425. doi: Doi 10.5094/Apr.2012.048
Melymuk, L., Robson, M., Helm, P. A., & Diamond, M. L. (2012). PCBs, PBDEs, and PAHs in Toronto air: Spatial and seasonal trends and implications for contaminant transport. *Science of the Total Environment, 429*, 272-280. doi: DOI 10.1016/j.scitotenv.2012.04.022
Melymuk, L., Robson, M., Helm, P. A., & Diamond, M. L. (2013). Application of Land Use Regression to Identify Sources and Assess Spatial Variation in Urban SVOC Concentrations. *Environmental Science & Technology, 47*(4), 1887-1895. doi: Doi 10.1021/Es3043609

Motelay-Massei, A., Harner, T., Shoeib, M., Diamond, M., Stern, G., & Rosenberg, B. (2005). Using passive air samplers to assess urban-rural trends for persistent organic pollutants and polycyclic aromatic hydrocarbons. 2. Seasonal trends for PAHs, PCBs, and organochlorine pesticides. *Environmental Science & Technology, 39*(15), 5763-5773. doi: Doi 10.1021/Es0504183

Odabasi, M., Sofuoglu, A., Vardar, N., Tasdemir, Y., & Holsen, T. M. (1999). Measurement of dry deposition and air-water exchange of polycyclic aromatic hydrocarbons with the water surface sampler. *Environmental Science & Technology, 33*(3), 426-434. doi: Doi 10.1021/Es9801846

Persoon, C., & Hornbuckle, K. C. (2009). Calculation of passive sampling rates from both native PCBs and depuration compounds in indoor and outdoor environments. *Chemosphere, 74*(7), 917-923. doi: 10.1016/j.chemosphere.2008.10.011

Pozo, K., Harner, T., Rudolph, A., Oyola, G., Estellano, V. H., Ahumada-Rudolph, R., . . . Focardi, S. (2012). Survey of persistent organic pollutants (POPs) and polycyclic aromatic hydrocarbons (PAHs) in the atmosphere of rural, urban and industrial areas of Concepcion, Chile, using passive air samplers. *Atmospheric Pollution Research, 3*(4), 426-434. doi: Doi 10.5094/Apr.2012.049

Roots, O., Roose, A., Kull, A., Holoubek, I., Cupr, P., & Klanova, J. (2010). Distribution pattern of PCBs, HCB and PeCB using passive air and soil sampling in Estonia. *Environmental Science and Pollution Research, 17*(3), 740-749. doi: DOI 10.1007/s11356-009-0147-z

Simcik, M. F., Zhang, H. X., Eisenreich, S. J., & Franz, T. P. (1997). Urban contamination of the Chicago coastal Lake Michigan atmosphere by PCBs and PAHs during AEOLOS. *Environmental Science & Technology, 31*(7), 2141-2147. doi: Doi 10.1021/Es9609765

Tasdemir, Y., Odabasi, M., Vardar, N., Sofuoglu, A., Murphy, T. J., & Holsen, T. M. (2004). Dry deposition fluxes and velocities of polychlorinated biphenyls (PCBs) associated with particles. *Atmospheric Environment, 38*(16), 2447-2456. doi: DOI 10.1016/j.atmosenv.2004.02.006

Tasdemir, Y., Vardar, N., Odabasi, M., & Holsen, T. M. (2004). Concentrations and gas/particle partitioning of PCBs in Chicago. *Environmental Pollution, 131*(1), 35-44. doi: DOI 10.1016/j.envpol.2004.02.031

Vardar, N., Tasdemir, Y., Odabasi, M., & Noll, K. E. (2004). Characterization of atmospheric concentrations and partitioning of PAHs in the Chicago atmosphere. *Science of the Total Environment, 327*(1-3), 163-174. doi: 10.1016/j.scitotenv.2003.05.002

Vilavert, L., Nadal, M., Schuhmacher, M., & Domingo, J. L. (2014). Seasonal surveillance of airborne PCDD/Fs, PCBs and PCNs using passive samplers to assess human health risks. *Science of the Total Environment, 466*, 733-740. doi: DOI 10.1016/j.scitotenv.2013.07.124

Wang, Z., Na, G. S., Gao, H., Wang, Y. J., & Yao, Z. W. (2014). Atmospheric concentration characteristics and gas/particle partitioning of PCBs from the North Pacific to the Arctic Ocean. *Acta Oceanologica Sinica, 33*(12), 32-39. doi: DOI 10.1007/s13131-014-0531-5

Wania, F., Shen, L., Lei, Y. D., Teixeira, C., & Muir, D. C. G. (2003). Development and calibration of a resin-based passive sampling system for monitoring persistent organic pollutants in the atmosphere. *Environmental Science & Technology, 37*(7), 1352-1359. doi: Doi 10.1021/Es026166c

Wethington, D. M., & Hornbuckle, K. C. (2005). Milwaukee, WI, as a source of atmospheric PCBs to Lake Michigan. *Environmental Science & Technology, 39*(1), 57-63. doi: Doi 10.1021/Es048902d

Wilford, B. H., Harner, T., Zhu, J. P., Shoeib, M., & Jones, K. C. (2004). Passive sampling survey of polybrominated diphenyl ether flame retardants in indoor and outdoor air in Ottawa, Canada: Implications for sources and exposure. *Environmental Science & Technology, 38*(20), 5312-5318. doi: Doi 10.1021/Es049260x

Xu, Q., Zhu, X. H., Henkelmann, B., Schramm, K. W., Chen, J. P., Ni, Y. W., . . . Li, Y. (2013). Simultaneous monitoring of PCB profiles in the urban air of Dalian, China with active and passive samplings. *Journal of Environmental Sciences-China, 25*(1), 133-143. doi: Doi 10.1016/S1001-0742(12)60030-8

Yenisoy-Karakas, S., Oz, M., & Gaga, E. O. (2012). Seasonal variation, sources, and gas/particle concentrations of PCBs and OCPs at high altitude suburban site in Western Black Sea Region of Turkey. *Journal of Environmental Monitoring, 14*(5), 1365-1374. doi: Doi 10.1039/C2em30038a

Yeo, H. G., Choi, M., Chun, M. Y., & Sunwoo, Y. (2003). Concentration distribution of polychlorinated biphenyls and organochlorine pesticides and their relationship with temperature in rural air of Korea. *Atmospheric Environment, 37*(27), 3831-3839. doi: 10.1016/S1352-2310(03)00456-4

Yolsal, D., Salihoglu, G., & Tasdemir, Y. (2014). Air-soil exchange of PCBs: levels and temporal variations at two sites in Turkey. *Environmental Science and Pollution Research, 21*(5), 3920-3935. doi: DOI 10.1007/s11356-013-2353-y

Zhang, G., Chakraborty, P., Li, J., Sampathkumar, P., Balasubramanian, T., Kathiresan, K., . . . Jones, K. C. (2008). Passive Atmospheric Sampling of Organochlorine Pesticides, Polychlorinated Biphenyls, and Polybrominated Diphenyl Ethers in Urban, Rural, and Wetland Sites along the Coastal Length of India. *Environmental Science & Technology, 42*(22), 8218-8223. doi: Doi 10.1021/Es8016667

EVAPORATION OF POLYCYCLIC AROMATIC HYDROCARBONS (PAHs) FROM THE AUTOMOTIVE TREATMENT SLUDGE DURING PAH PHOTODEGRADATION APPLICATIONS

Gizem EKER, Yücel TASDEMIR
Department of Environmental Engineering, Faculty of Engineering, Uludag University, 16059, Nilüfer/Bursa, TURKEY
geker@uludag.edu.tr, tasdemir@uludag.edu.tr

ABSTRACT
Restriction of polycyclic aromatic hydrocarbon (PAH) migration is a significant issue for minimizing transport of PAHs into air. This study focuses on the evaporation ratios of PAHs from automotive treatment sludge to air during UV- titanium dioxide (TiO_2) and UV-diethyl amine (DEA) application. Experiments were performed on a specially-designed apparatus. At the end of the 24 hr photodegradation experiment periods, residual and evaporated PAH amounts were determined. The PAH concentrations were measured by a gas-chromatography mass-spectrometer (GC-MS). It was found that 3-ring PAH compounds (Phe, Ant) were the most evaporated species. More than 75% of evaporated PAHs comprise 3 ring species during photodegradation experiments at 15 ^oC and 40 ^oC. PAH evaporation ratios increased with increasing temperature. While 71% of PAHs in the sludge evaporated during the UV application, this value increased to 100% during the UV-TiO_2 and UV-DEA applications. At the conclusion of the mass balance studies, it was revealed that the PAHs evaporation during the sludge processes could be an important source for PAHs to spread around.

Key Words: *PAH removal, Temperature, TiO_2, Diethyl amine, Mass balance*

INTRODUCTION
Automotive sector is one of the important industrial segments and approximately 30% of the market share in this segment in Turkey is held by companies operating in the Bursa province. The amount of automotive industry wastewater, and thus the sludge volume, increases every year due to increasing production. PAHs exist in automotive treatment sludge along with other pollutants (Karaca, 2013a; Salihoglu et al., 2010). Due to hydrophobic and lipophilic structures of PAHs, they are expected to remain in the body of sludge (Beck et al., 1996; Trably and Patureau, 2006). Some PAH species have the potential to cause mutagenic and/or carcinogenic effects when they are taken to human body (IARC, 1986). For this reason, it is necessary to remove these pollutants from all environments such as air, water, sludge. PAHs in treatment sludge can widely be removed using several chemical and biological methods (Flotron et al., 2005; Trably and Patureau, 2006; Zheng et al., 2007). However, studies on the PAH removal from sludge via UV applications, as an advanced oxidation method, have been performed only recently (da Rocha et al., 2010; Dong et al., 2010; Karaca and Tasdemir, 2011; Salihoglu et al., 2012).

The evaporation quantities of PAHs from solid matrices have not been determined in studies on the removal of PAHs by degradation through biological, chemical or photolytic methods (Cornelissen et al., 1998; Sayles et al., 1999; Trably and Patureau, 2006; Zhang et al., 2008). However, understanding not only the removal of PAHs through degradation but also the quantities of evaporated PAHs during the removal applications is important to evaluate the environmental movement and fate of PAHs (Hawthorne and Grabanski, 2000). In fact, Bamford et al. (1999) showed that the amount of evaporated PAHs from water to air found to closely

resemble the amount of PAH removed by photo-degradation. When the boiling points of PAH compounds are examined, it has been found that Naphtlene, a 2-ring species, boils at 218°C, 3-ring species such as Phe and Ant boil at approximately 350°C, and 4-ring species boil at approximately 400°C. At first sight, PAHs are often thought not to evaporate at a remarkable ratio because of their high boiling rates (Hawthorne and Grabanski, 2000). However, it is known that PAHs evaporate even at atmospheric temperatures. Several researchers showed that 2-, 3- and 4-ring PAH species were found in the vapor phase in the atmosphere (Esen et al., 2008; Tasdemir and Esen, 2007; Vardar et al., 2004). Even heavier PAHs (5-6-ring PAHs) were reported in the atmosphere (Esen et al., 2008). These results indicate the possibility of PAH evaporation at high ratios during PAH removal applications performed in open or closed environments.

In the present study, the PAH levels in automotive treatment sludge were determined and the PAH amounts evaporating from the sludge to the air during the UV, UV-Diethylamine (DEA) and UV-Titanium Dioxide (TiO_2) applications were investigated. The evaporated PAHs species distributions were examined. Mass distributions of PAHs in the automotive treatment sludge during PAH removal applications were also examined.

MATERIALS AND METHODS

Sludge Sampling

Sludge samples were taken from the sludge stabilization unit of an automotive factory wastewater treatment plant, located in Bursa, with the capacity to produce 360,000 automobiles per year. Detailed information about treatment plant and wastewater characteristics can be seen in (Karaca and Tasdemir, 2013a). Total annual amount of sludge generated in the plant was approximately 162,000 kg. The pH and solid matter (SM) values were determined according to the standard methods and their values were 7.5 and 25%, respectively. Total PAH ($\sum_9$ PAH) concentration in the sludge was measured using GC-MS. $\sum_9$ PAH concentration was approximately 3220 ng/g of dry matter (DM). The solid matter content of the sludge was 25%, its total organic carbon content (TOC) (Standard Method 5310B) was approximately 3%. TOC measurements were carried out by using SSM-5000 Shimadzu TOC Analyzer TOC-V CPN.

The UV Apparatus

The apparatus was specially designed for PAH photodegradation experiments from the treatment sludge. It was manufactured from stainless steel. The apparatus was mounted in a cabinet to prevent heat and light interactions. The air taken into the apparatus was purified from PAHs by employing inlet polyurethane foam (PUF) column. The purified air entering the apparatus remained inside for ~6 seconds. It is known from the literature that PUFs are successfully used for the collection of semi-volatile organic compounds (SVOCs) in air (Bozlaker et al., 2008; Demircioglu et al., 2011; Karaca and Tasdemir, 2011; Sun et al., 2006; Tasdemir and Esen, 2007). This feature differentiated the designed apparatus from other apparatuses described in the literature (Zhang et al., 2008; Zhao et al., 2004). Three lamps (254 nm UV-C, Philips TUV G8T5) with a total power output of 24 W were installed on the top of the apparatus. Sludge samples were laid onto the petri plates with a diameter of 8 cm and placed on the rack with a grid design. The sludge height was about 5 mm. The distance between the rack and the UV source was 18 cm. Temperature in the apparatus was measured using a Hobo-S-Thb M002 sensor, and data was collected with an H21-002 Hobo logging microstation. Experimental apparatus (Figure 1) used in this study can be seen elsewhere in detail (Karaca, 2013a; Salihoglu et al., 2012). Experimental flow chart can be seen in Figure 1.

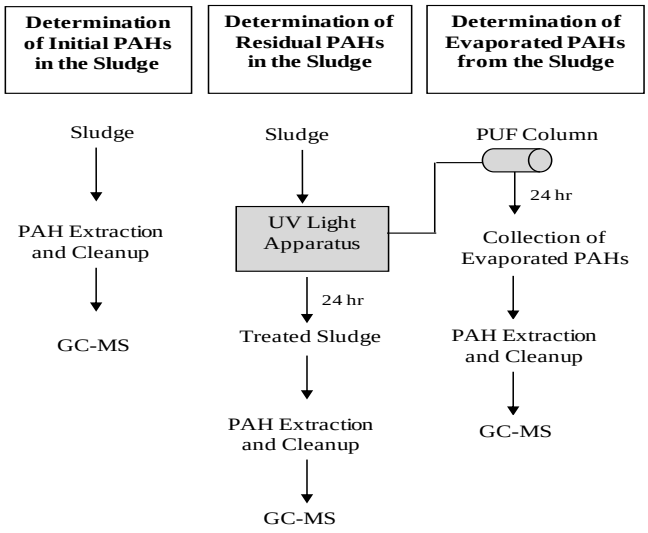

Figure 1. Experimental Flow Char

PAH Removal Experiments

UV, UV-DEA and UV-TiO_2 Applications

In the UV, UV-DEA and UV-TiO_2 applications, the UV-C light intensity to which the sludge samples were exposed was 0.6 mW/cm^2. The DEA and TiO_2 doses were added to the sludge at ratios of 5% and 20% of the dry sludge weight. In the present study, nano-crystalline powder form of TiO_2 (Degussa, P-25) with a pH: 4, specific surface area (BET): 50 m^2/g and loss on ignation (LOI):2% was used. In our experiments, GC grade DEA (Merck 8.03010.2500) was employed. Twenty grams of wet sludge was laid on each Petri dish. The photodegradation experiments were completed within the 24 hr. The samples were taken from the apparatus at the end of the 24 hr and PAH concentrations were measured using GC-MS.

Sampling of Evaporated PAHs from the Sludge

The PUF columns were placed on the inlet and outlet of the apparatus. Dimensions of the PUFs were 5.5 x 6.5 cm (diameter x height). The air was vacuumed at a rate of 0.8 m^3/h for 24 hours in order to remove any evaporated PAHs. % PAH evaporation ratios were calculated and compared with % PAH removal ratios. By this way, PAH migration from sludge to the air and possible transformation of PAHs were evaluated. Following equation (Equation 1) was used to calculate the evaporated PAH ratios at the end of the PAH removal applications:

$$\%\text{PAH Evaporation} = \frac{(\text{Evaporated conc.}\,(\text{ng/m}^3) * \text{Vacuumed air volume}\ (\text{m}^3)) * 100}{\text{Input}_{\text{sludge}}\ (\text{ng})}$$

(Equation1)

PAH Extraction and Cleanup

Extraction of sludge samples: The PAH amounts that remained in the sludge after the PAH removal applications were determined. The aim of this study was to determine the following 9 PAH compounds included in the list of primary pollutants issued by the US EPA: phenanthrene (Phe), anthracene (Ant), fluoranthene (Fl), pyrene (Pyr), benzo[a]anthracene (BaA), chrysene (Chr), benzo[b]fluoranthene (BbF), benzo[k]fluoranthene (BkF) and benzo[a]pyrene (BaP). The raw sludge samples (before the PAH removal experiments) and the sludge samples taken out from the apparatus after the PAH removal experiments were extracted in an ultrasonic bath

by adding 20 mL of DCM/Petroleum ether (PE) (1/1:v/v) for 30 minutes. The extracted samples were filtered and 20 mL DCM/PE (1/1) was added again to the residual sample in the bottle and it was extracted to 30 minutes and filtered. 20 mL DCM/PE was added to the sample for a third time. Then, the sample was extracted for 30 minutes with an ultrasonic bath.

Extraction of PUF samples: Before their first usage, the PUFs used were extracted with distilled water, MeOH, acetone/hexane (ACE/HEX 1:1), and dichloromethane (DCM) in Soxhlet extractor for 24 hr and then dried under 60°C (Cindoruk and Tasdemir, 2007; Esen et al., 2006). PUF cartridges were kept in glass jars with Teflon covers until usage. PUF samples taken from the inlet and outlet of the apparatus were subjected to the Soxhlet extraction for 24 hr with ACE/HEX (v/v, 1:1). After extraction, same procedures were applied to the sludge and PUF samples.

Other steps for both sludge and PUF samples: Sludge and PUF extracts were concentrated to 5 mL in a rotary evaporator. The sample volume was reduced to 2 mL under a gentle nitrogen stream (Karaca, 2013b; Karaca and Tasdemir, 2011; Salihoglu et al., 2012). The fractionating process was applied to the samples. After fractionating, the volumes of the PAH samples were reduced to 1 mL with using N_2 gas. Detailed experimental procedure can be seen in our previous publications (Karaca and Tasdemir, 2013c; Salihoglu et al., 2010).

Mass Balance Calculations

Mass balances were calculated with Equation 2 for each PAH compounds. In the first step, the quantities of the 9 PAH species in the sludge (ng) were determined prior to the PAH removal applications. In the second step, the PAH masses (ng) remaining in the sludge and evaporating to the air were determined at the end of each experiment. When the indoor air, cleaned from PAHs by using inlet PUF column was considered, it could be accepted that the sludge was the only PAH source in the apparatus. The evaporated PAHs were collected with an outlet PUF column. At the end of each 24-hr experimental period, the PAHs were expected to disappear due to our applications, remain in the sludge or evaporate to the air. For this reason, the sum of the PAH contents remaining in the sludge and evaporating to the inside air yielded the total PAH content ($\sum_{Output}$ PUF) at the end of 24 hr. The total PAH content in the environment prior to the PAH removal application is shown as ($\sum_{Input}$ PAH) in Equation 2.

$$\sum_{Input} PAH = \sum_{Output} PAH \qquad \text{(Equation 2)}$$

$$P1 + P2 = P3 + P4$$

(P1)PAH content in the inside air at the beginning=0 ng (P2)PAH content in the sludge at the beginning (ng)
(P3)PAH content remained in the sludge after 24 hr (ng) (P4)PAH content evaporated to the air during 24 hr (ng)

Total PAH removal ratios according to (Output sludge) and (Output sludge + Output PUF) were calculated as below (Equation 3 and Equation 4):

$$\%PAH\ Removal_{(Sludge)} = \frac{InputPAH_{sludge}\ (ng) - OutputPAH_{sludge}\ (ng)}{InputPAH_{sludge}\ (ng)} * 100 \qquad \text{(Equation 3)}$$

$$\%PAH\ Removal_{(Sludge+PUF)} = \frac{InputPAH_{sludge}\ (ng) - OutputPAH_{sludge+PUF}\ (ng)}{InputPAH_{sludge}\ (ng)} * 100 \qquad \text{(Equation 4)}$$

Quality Assurance / Quality Control
Field blanks were taken to determine any contamination during the sample handling, transportation, and analyses (Salihoglu et al., 2010). They were prepared by filling thimbles with 5 gr of sodium sulfate (Na_2SO_4). The PAH tests that were applied to the sludge samples were also applied to the field blanks. The limit of determinations (LODs) were calculated for each PAH species by adding 3 standard deviations to the mean of the blank (Stevens et al., 2003; Tasdemir et al., 2004).

Prior to the extraction, the samples were spiked with Standard Mix A PAH surrogate standard (including Naphthalene-d10, Acenaphthene-d10, Phenanthrene-d10, Chrysene-d12 and Perylene-d12). Pyrene d-10 volume correction standard (internal standard) was added to the samples before the PAH analysis (Salihoglu et al., 2012; Salihoglu et al., 2010). The PAH concentrations were measured using an Agilent 7890 Model Gas Chromatograph (GC) equipped with an Agilent 5975C inert XL mass selective with a triple axis detector (MSD). Detailed information on the measurement of the PAH concentrations can be found in the elsewhere (Karaca and Tasdemir, 2013b; Salihoglu et al., 2012).

RESULTS AND DISCUSSION
PAH concentrations and species distribution in the automotive treatment sludge are shown in Figure 2. The $\sum_9$ PAH amount in the sludge samples was 3220±310 ng/g DM. Total concentrations of BbF, BkF and BaP compounds were very low levels.

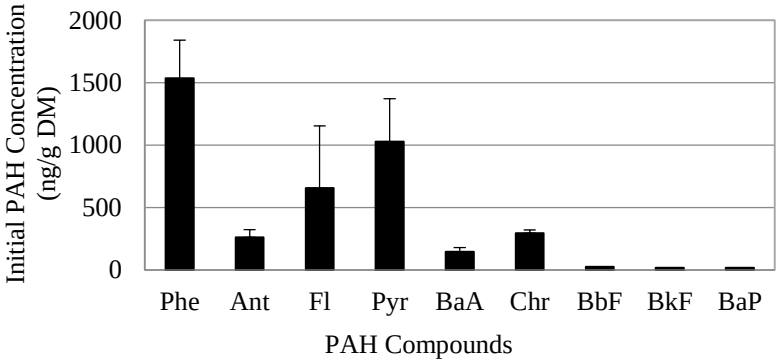

Figure 2. PAH Concentrations in the Automotive Treatment Sludge

UV Applications
Σ_9 PAH removal efficiencies at 10°C and 40°C (without TiO_2 and DEA) were found to be 48% and 65%, respectively after the UV applications. We explained the removal of PAHs from automotive industry treatment sludge via photodegradation in our previous publication (Karaca and Tasdemir, 2013a). Effect of UV to evaporation of PAH are given in Figure 3. During the UV applications, 12% and 79% of the PAHs originally present in the sludge evaporated to the air at 10°C and 40°C, respectively. It was determined that an increase in temperature caused higher PAH content in the air due to bigger evaporation rates. It can be concluded that the increase in temperature and photo-degradation showed a synergistic effect for the removal and evaporation of PAHs (Nadal et al., 2006).

When the UV applications were performed, it was observed that the 3-ring PAH compounds were the dominant in evaporated air from the sludge for both temperature ranges (10 ^oC, 40 ^oC). While the 3-, 4- and 5-ring compounds were found with percentages of 75%, 24% and 1%,

respectively in the PUF samples at 10 °C, these percentages were 88%, 11% and 1 %, respectively at 40 °C. It can be stated that the increasing amount of 3- ring compounds rather than the 4-,5-ring ones, is due to higher evaporation tendency than the 4-,5-ring ones (Huang et al., 2004).

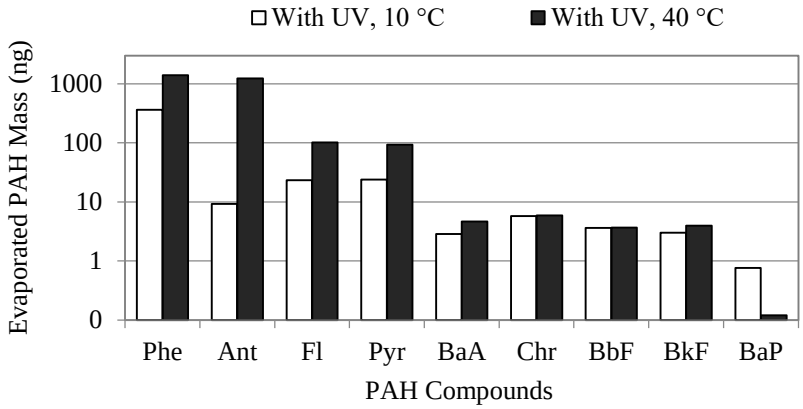

Figure 3. Effect of UV on the Evaporation of PAHs from the Sludge to the Air

UV-DEA Applications

During UV-DEA applications PAH removal ratios increased with increasing temperature and increasing DEA dose. At 40°C, 50% decrease was achieved in the sludge with 5% DEA addition, while Σ_9 PAH species were totally (100%) removed from the sludge with using 20% DEA. Σ_9 PAH removal efficiency after the UV application was 65% in the samples without DEA. Therefore, DEA can be considered an effective photo-sensitizer only at a dose of 20%. A detailed explanation about PAH removal efficiencies during UV-DEA applicaitons can be found elsewhere (Karaca and Tasdemir, 2013a).

The amounts of PAHs evaporating from the sludge to the air during the UV-DEA applications are given in Figure 4. Average 85% of PAHs in the air consisted of 3-ring compounds during UV-DEA experiments at 15 ^{o}C and 40 ^{o}C. Increasing DEA dose and temperature enhanced the evaporation of Σ_9 PAH compounds. Evaporation ratios in the samples including 5% and 20% DEA were 20% and 80%, respectively, at 15°C. These values did not exceed removal ratios (68%, 80%). At 40°C, evaporated PAH ratio was 64% in the samples containing 5% DEA which was higher than the removal ratio (50%). In the samples including 20% DEA, the ratio of PAH evaporating to the air over 100%. In the other words, in the apparatus, $\sum_9$ PAH amounts in the indoor air at the end of the 24 hr (after experiment) was higher than $\sum_9$ PAH amounts in the sludge at the beginning (before experiment). Possible reason for this can be explained as follows: PAH species other than targeted 9 PAHs or other organic compounds might have transformed into light PAH species via photo-degradation and then evaporated. Several researchers emphasized that heavy PAHs could be transformed into light species during PAH photodegradation (Guieysse et al., 2004; Ireland et al., 1995; Salihoglu et al., 2012). Sludge was unique PAH source in the apparatus and there was no other PAH source present. Also, samples were prevented from contamination by strict quality assurance/quality control procedure. Therefore, these results support the species transformation.

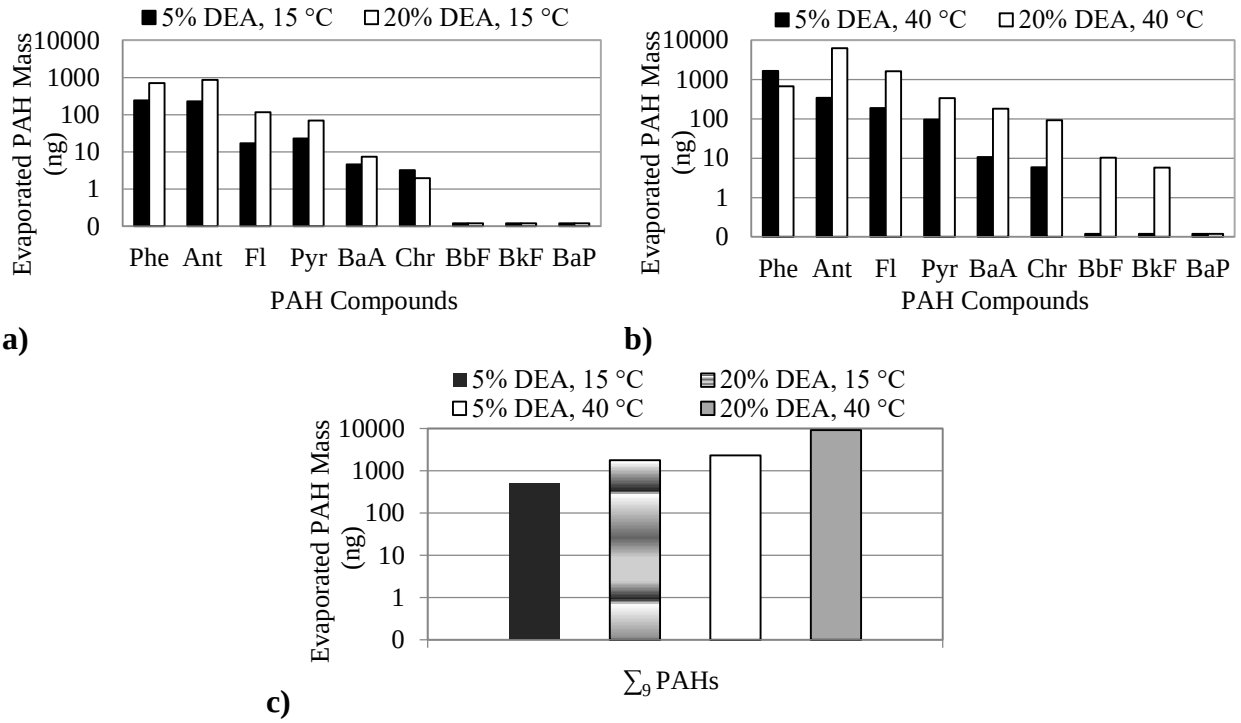

Figure 4. Evaporation of PAHs from the Sludge to the Air during UV-DEA Applications
a) 15°C b) 40°C c) $\sum_9$ Evaporated PAHs

UV-TiO_2 Applications

At 15°C and 40°C with the addition of 5% TiO_2, $\sum_9$ PAH removal efficiencies were 5% and 37%, respectively, and it was observed that 5% TiO_2 addition was not sufficient for the removal of PAHs. In the samples including 20% TiO_2, $\sum_9$ PAH removal ratios were determined as 40% and 98%, at 15°C and 40°C, respectively.

The changes in PAH concentrations evaporated from the sludge during the UV-TiO_2 applications are shown in Figure 5. It was observed that the 3-ring PAH compounds were the dominant (average 89%) in evaporated air from the sludge for both temperature ranges (15 ^oC, 40 ^oC). The increase in the TiO_2 dose and temperature caused the PAH photo-degradation and evaporation to increase. It was concluded that the photo-degradation process of PAHs was facilitated at high temperatures due to the increase in the dosage of the catalyst (Karaca and Tasdemir, 2013a). At 15°C, while 5% of the $\sum_9$ PAH were removed with 5% TiO_2 addition, 35% of the PAH in the sludge evaporated. At 40^{o}C, when TiO_2 was added to samples at 5% and 20% dose, $\sum_9$ PAH evaporation ratios in the sludge samples were 100% and 102%, respectively. PAH content evaporating to the air was determined to be even greater than the PAH quantities present in the sludge at the beginning of the experiment. Several researchers emphasized that PAHs can be transformed into different compounds with hydroxylation reaction at the end of the photo-degradation reactions in studies where TiO_2 was used as a photo-catalyst (Kot-Wasik et al., 2004; Wen et al., 2003; Woo et al., 2009). In the present study, if only hydroxylation reaction became effective during the photodegradation, the evaporated PAH amounts were expected to be low. In reality, it was found that the quantities of PAH evaporating to the air were at very high levels. Based on these data, it was thought that not only hydroxylation reactions but also species transformations occurred at great extent in the UV-TiO_2 applications.

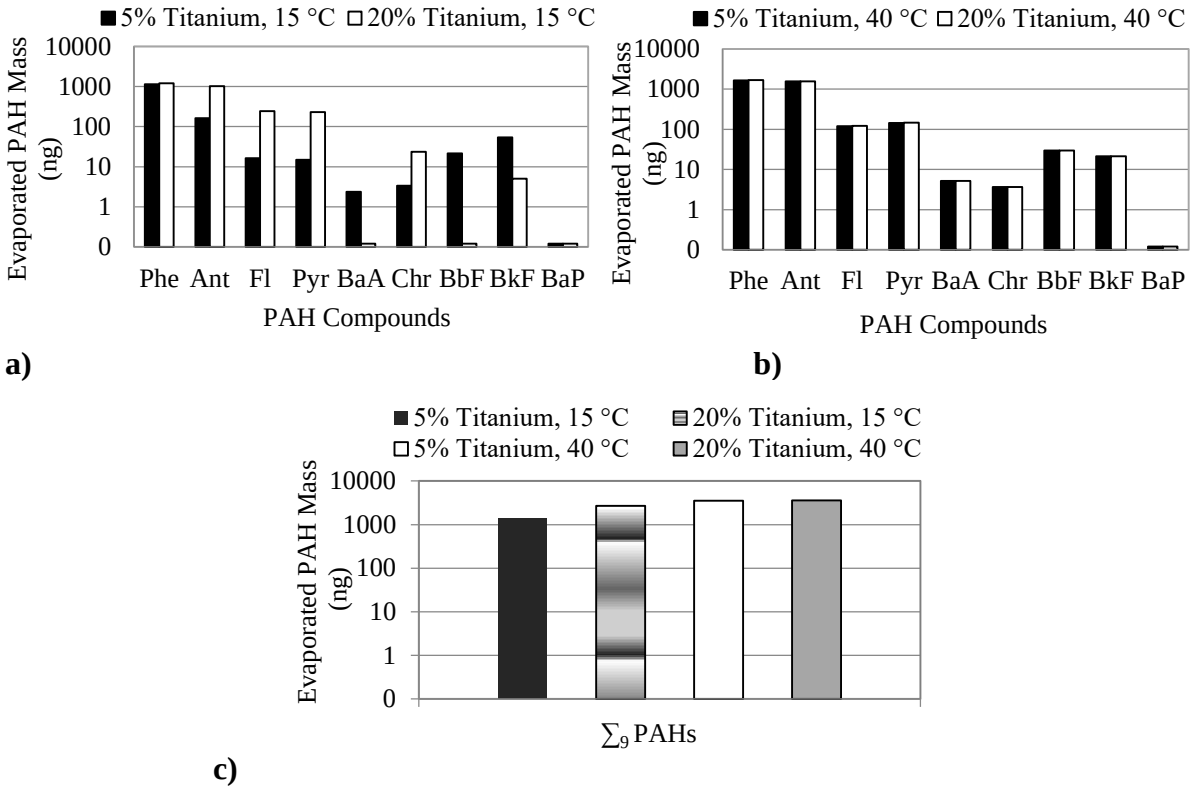

Figure 5. Evaporation of PAHs from the Sludge during UV-TiO_2 Applications
a) 15°C b) 40°C c) $\sum_9$ Evaporated PAHs

Mass Distributions of PAHs during the Removal Applications

In the PAH removal calculations (% PAH $removal_{(sludge)}$) made by only considering the PAH contents remaining in the sludge after experiments, it was found that removal was achieved at certain ratios for the 3-, 4- and 5-ring PAH species (Table 1). However, when the quantities of PAH evaporating to the air at the end of the experiments were included in the calculations (% PAH $removal_{(sludge+PUF)}$) the total 3-ring PAH content (sludge+PUF) at the end of the experiments became more than the total 3-ring PAH content in the sludge at the beginning. Therefore, negative removal efficiency values were obtained (Table 1). In light of this information, it was concluded that in the PAH quantities evaporating from sludge to the air had to be considered to correctly evaluate the fate of PAHs.

Mass balances were calculated with Equation 2. It was found that the total quantities of 3-ring PAHs (sludge+PUF) increased significantly after the UV-TiO_2 and UV-DEA applications (Table 1). In all PAH removal applications, it was determined that the content of 3-ring, Ant species in particular, increased. After the UV-DEA applications, total 3-ring PAH content (sludge+PUF) was found to measure 391% more than the beginning 3-ring PAH content (i.e., -391% removal). After the UV-TiO_2 applications, this value increased to 537% (i.e., -537% removal). These data appear to support the hypothesis that heavy PAH species and/or other organic compounds transformed into 3-ring PAH species caused the contents of the 3-ring PAH species in the environment to increase through photodegradation and evaporation (Guieysse et al., 2004; Salihoglu et al., 2012).

Table 1. Mass Distributions of PAHs in the Automotive Sludge Before and After Removal Applications

WITH UV, 10 °C							WITH UV, 40 °C						
Ring	Input Sludge	Output Sludge	Output PUF	Total Output	% Removal (Sludge)	% Removal (Sludge+PUF)	Ring	Input Sludge	Output Sludge	Output PUF	Total Output	% Removal (Sludge)	% Removal (Sludge+PUF)
3	1853	1100	371	1471	41	21	3	1797	1527	2626	4152	15	-131
4	1674	676	47	723	60	57	4	1684	0	195	195	100	88
5	74	0	7	7	100	90	5	58	0	8	8	100	87
5% DEA, 15 °C							**20% DEA, 15 °C**						
Ring	Input Sludge	Output Sludge	Output PUF	Total Output	% Removal (Sludge)	% Removal (Sludge+PUF)	Ring	Input Sludge	Output Sludge	Output PUF	Total Output	% Removal (Sludge)	% Removal (Sludge+PUF)
3	1410	673	468	1142	52	19	3	1410	999	1577	2577	29	-83
4	1153	140	40	180	88	84	4	1153	350	187	536	70	53
5	60	0	0	0	100	100	5	60	0	0	0	100	100
5% DEA, 40 °C							**20% DEA, 40 °C**						
Ring	Input Sludge	Output Sludge	Output PUF	Total Output	% Removal (Sludge)	% Removal (Sludge+PUF)	Ring	Input Sludge	Output Sludge	Output PUF	Total Output	% Removal (Sludge)	% Removal (Sludge+PUF)
3	1410	1613	2002	3615	-14	-156	3	1410	0	6925	6925	100	-391
4	1153	0	281	281	100	76	4	1153	0	1957	1957	100	-70
5	60	0	0	0	100	100	5	60	0	16	16	100	73
5% TiO_2, 15 °C							**20% TiO_2, 15 °C**						
Ring	Input Sludge	Output Sludge	Output PUF	Total Output	% Removal (Sludge)	% Removal (Sludge+PUF)	Ring	Input Sludge	Output Sludge	Output PUF	Total Output	% Removal (Sludge)	% Removal (Sludge+PUF)
3	1797	2558	1302	3860	-42	-115	3	1797	49	11400	11448	97	-537
4	1684	1638	31	1669	3	1	4	1684	474	474	948	72	44
5	58	0	75	75	100	-30	5	58	0	5	5	100	91
5% TiO_2, 40 °C							**20% TiO_2, 40 °C**						
Ring	Input Sludge	Output Sludge	Output PUF	Total Output	% Removal (Sludge)	% Removal (Sludge+PUF)	Ring	Input Sludge	Output Sludge	Output PUF	Total Output	% Removal (Sludge)	% Removal (Sludge+PUF)
3	1797	40	3253	3293	98	-83	3	1797	40	3253	3293	98	-83
4	2125	0	276	276	100	87	4	2125	0	276	276	100	87
5	24	0	24	23	100	4	5	24	0	30	30	100	-25

Total Input= Input sludge: PAH amounts (ng) in the sludge at the beginning (P2)
Output sludge: PAH amounts (ng) remained in the sludge after 24 hr (P3)
Output PUF: PAH content evaporated to the air during 24 hr (P4)
Total Output: Output sludge + Output PUF

CONCLUSIONS

Alternative methods are available for removal of PAHs from treatment sludge. However, the extent to which the environmental movement of PAHs through evaporation takes place during removal applications is not precisely known. The aim of the present study was to contribute to the relevant existing literature by determining the evaporation ratios of PAHs in automotive industry treatment sludge during PAH photodegradation experiments.

PAH content evaporating to the air increased while the PAH content in the sludge decreased indicated that the pollution altered the environment. Environmental movement of the PAHs (from the sludge to the air) occurred at significant levels in all of the removal applications.

It was determined that the temperature rise in experimrents increases the amount of PAH evaporating into air. Three ring compounds accounted for more than 75% of evaporated PAHs. It can be stated that the increasing amount of 3- ring compounds rather than the 4-,5-ring ones is due to higher evaporation tendency than the 4-,5-ring ones.

The automotive factory examined within the scope of this study produces 142 dry tons of treatment sludge per year. Assuming that all of this sludge is exposed to UV application, the $\sum_9$ PAH content evaporating to the air is expected to be approximately 0.4 kg/year. Moreover, these values will be approximately 0.3 and 0.6 kg/year after the UV-DEA and UV-TiO_2 applications, respectively. These results represent the $\sum_9$ PAH contents released from only one automotive factory to the air. The total quantity of industrial treatment sludge produced by Bursa's industries is enormous. According to 2008 data, the annual quantity of urban sludge produced in Bursa was approximately 600,000 dry tons, and 1,700 kg of PAH will be released to the atmosphere every year due only to the treatment of urban sludge. When considering the effects of industrial sludge, this value could reach much higher levels. These data highlight the need for the removal of PAHs in treatment sludge via methods that limit their evaporation to the air. Otherwise, treatment sludge will be a significant source of PAHs in the atmosphere.

ACKNOWLEDGEMENTS

This study was supported by the UAP (M) 2009/20 numbered project of the Uludag University Scientific Research Projects Commission. We would like to thank Melike BALLICA for her devoted work in the laboratory.

REFERENCES

Bamford, H.A., Offenberg, J.H., Larsen, R.K., Ko, F.C., Baker, J.E., 1999. Diffusive exchange of polycyclic aromatic hydrocarbons across the air-water interface of the Patapsco River, an urbanized subestuary of the Chesapeake Bay. Environ Sci Technol 33, 2138-2144.

Beck, A.J., Johnson, D.L., Jones, K.C., 1996. The form and bioavailability of non-ionic organic chemicals in sewage sludge-amended agricultural soils. Sci Total Environ 185, 125-149.

Bozlaker, A., Muezzinoglu, A., Odabasi, M., 2008. Atmospheric concentrations, dry deposition and air-soil exchange of polycyclic aromatic hydrocarbons (PAHs) in an industrial region in Turkey. Journal of Hazardous Materials 153, 1093-1102.

Cindoruk, S.S., Tasdemir, Y., 2007. Deposition of atmospheric particulate PCBs in suburban site of Turkey. Atmospheric Research 85, 300-309.

Cornelissen, G., Rigterink, H., Ferdinandy, M.M.A., Van Noort, P.C.M., 1998. Rapidly desorbing fractions of PAHs in contaminated sediments as a predictor of the extent of bioremediation. Environ Sci Technol 32, 966-970.

da Rocha, O.R.S., Dantas, R.F., Duarte, M.M.M.B., Duarte, M.M.L., da Silva, V.L., 2010. sludge treatment by photocatalysis applying black and white light. Chem Eng J 157, 80-85.

Demircioglu, E., Sofuoglu, A., Odabasi, M., 2011. Atmospheric Concentrations and Phase Partitioning of Polycyclic Aromatic Hydrocarbons in Izmir, Turkey. Clean-Soil Air Water 39, 319-327.

Dong, D.B., Li, P.J., Li, X.J., Xu, C.B., Gong, D.W., Zhang, Y.Q., Zhao, Q., Li, P., 2010. Photocatalytic degradation of phenanthrene and pyrene on soil surfaces in the presence of nanometer rutile TiO2 under UV-irradiation. Chemical Engineering Journal 158, 378-383.

Esen, F., Cindoruk, S.S., Tasdemir, Y., 2006. Ambient concentrations and gas/particle partitioning of polycyclic aromatic hydrocarbons in an urban site in Turkey. Environmental Forensics 7, 303-312.

Esen, F., Tasdemir, Y., Vardar, N., 2008. Atmospheric concentrations of PAHs, their possible sources and gas-to-particle partitioning at a residential site of Bursa, Turkey. Atmospheric Research 88, 243-255.

Flotron, V., Delteil, C., Padellec, Y., Camel, V., 2005. Removal of sorbed polycyclic aromatic hydrocarbons from soil, sludge and sediment samples using the Fenton's reagent process. Chemosphere 59, 1427-1437.

Guieysse, B., Viklund, G., Toes, A.C., Mattiasson, B., 2004. Combined UV-biological degradation of PAHs. Chemosphere 55, 1493-1499.

Hawthorne, S.B., Grabanski, C.B., 2000. Vaporization of polycyclic aromatic hydrocarbons (PAHs) from sediments at ambient conditions. Environmental Science & Technology 34, 4348-4353.

Huang, X.Y., Chen, J.W., Gao, L.N., Ding, G.H., Zhao, Y., Schramm, K.W., 2004. Data evaluations and quantitative predictive models for vapor pressures of polycyclic aromatic hydrocarbons at different temperatures. Sar and Qsar in Environmental Research 15, 115-125.

IARC, 1986. PAH as occupational carcinogens, in: Bjorseth, A., Becker, G. (Eds.), PAH work atmosphere occurrence and determination. CRC Press, Boca Raton, FL, .

Ireland, J.C., Davila, B., Moreno, H., Fink, S.K., Tassos, S., 1995. Heterogeneous Photocatalytic Decomposition of Polyaromatic Hydrocarbons over Titanium-Dioxide. Chemosphere 30, 965-984.

Karaca, G., 2013a. Determination of PAHs levels ın the treatment sludge, Nılufer Creek sediment and invesatigation of removal methods Ph.D. dissertation, Uludag University.
Karaca, G., 2013b. Determination of PAHs levels ın the treatment sludge, Nılufer Creek sediment and invesatigation of removal methods. Environmental Engineering, PhD Thesis, Uludag University.
Karaca, G., Tasdemir, Y., 2011. Effect of Diethylamine on Pah Removal from Municipal Sludge under Uv Light. Fresenius Environmental Bulletin 20, 1777-1784.
Karaca, G., Tasdemir, Y., 2013a. Effects of Temperature and Photocatalysts on Removal of Polycyclic Aromatic Hydrocarbons (PAHs) from Automotive Industry Sludge. Polycyclic Aromatic Compounds 33, 380-395.
Karaca, G., Tasdemir, Y., 2013b. Effects of Temperature and Photocatalysts on Removal of Polycyclic Aromatic Hydrocarbons (PAHs) from Automotive Industry Sludge. Polycycl Aromat Comp 33, 380-395.
Karaca, G., Tasdemir, Y., 2013c. Removal of polycyclic aromatic hydrocarbons (PAHs) from industrial sludges in the ambient air conditions: Automotive Industry. Journal of Environmental Science and Health Part a-Toxic/Hazardous Substances & Environmental Engineering 48, 855-861.
Kot-Wasik, A., Dabrowska, D., Namiesnik, J., 2004. Photodegradation and biodegradation study of benzo(a)pyrene in different liquid media. Journal of Photochemistry and Photobiology a-Chemistry 168, 109-115.
Nadal, M., Wargent, J.J., Jones, K.C., Paul, N.D., Schuhmacher, M., Domingo, J.L., 2006. Influence of UV-B radiation and temperature on photodegradation of PAHs: Preliminary results. Journal of Atmospheric Chemistry 55, 241-252.
Salihoglu, N.K., Karaca, G., Salihoglu, G., Tasdemir, Y., 2012. Removal of polycyclic aromatic hydrocarbons from municipal sludge using UV light. Desalination and Water Treatment 44, 324-333.
Salihoglu, N.K., Salihoglu, G., Tasdemir, Y., Cindoruk, S.S., Yolsal, D., Ogulmus, R., Karaca, G., 2010. Comparison of Polycyclic Aromatic Hydrocarbons Levels in Sludges from Municipal and Industrial Wastewater Treatment Plants. Archives of Environmental Contamination and Toxicology 58, 523-534.
Sayles, G.D., Acheson, C.M., Kupferle, M.J., Shan, Y., Zhou, Q., Meier, J.R., Chang, L., Brenner, R.C., 1999. Land treatment of PAH contaminated soil: Performance measured by chemical and toxicity assays. Environ Sci Technol 33, 4310-4317.
Stevens, J.L., Northcott, G.L., Stern, G.A., Tomy, G.T., Jones, K.C., 2003. PAHs, PCBs, PCNs, organochlorine pesticides, synthetic musks, and polychlorinated n-alkanes in UK sewage sludge: Survey results and implications. Environmental Science & Technology 37, 462-467.
Sun, P., Blanchard, P., Brice, K.A., Hites, R.A., 2006. Trends in polycyclic aromatic hydrocarbon concentrations in the Great Lakes atmosphere. Environ Sci Technol 40, 6221-6227.
Tasdemir, Y., Esen, F., 2007. Urban air PAHs: Concentrations, temporal changes and gas/particle partitioning at a traffic site in Turkey. Atmospheric Research 84, 1-12.
Tasdemir, Y., Vardar, N., Odabasi, M., Holsen, T.M., 2004. Concentrations and gas/particle partitioning of PCBs in Chicago. Environmental Pollution 131, 35-44.
Trably, E., Patureau, D., 2006. Successful treatment of low PAH-contaminated sewage sludge in aerobic bioreactors. Environmental Science and Pollution Research 13, 170-176.
Vardar, N., Tasdemir, Y., Odabasi, M., Noll, K.E., 2004. Characterization of atmospheric concentrations and partitioning of PAHs in the Chicago atmosphere. Science of the Total Environment 327, 163-174.
Wen, S., Zhao, J.C., Sheng, G.Y., Fu, J.M., Peng, P.A., 2003. Photocatalytic reactions of pyrene at TiO2/water interfaces. Chemosphere 50, 111-119.
Woo, O.T., Chung, W.K., Wong, K.H., Chow, A.T., Wong, P.K., 2009. Photocatalytic oxidation of polycyclic aromatic hydrocarbons: Intermediates identification and toxicity testing. Journal of Hazardous Materials 168, 1192-1199.
Zhang, L.H., Li, P.J., Gong, Z.Q., Li, X.M., 2008. Photocatalytic degradation of polycyclic aromatic hydrocarbons on soil surfaces using TiO2 under UV light. Journal of Hazardous Materials 158, 478-484.
Zhao, X., Quan, M., Zhao, H.M., Chen, S., Zhao, Y.Z., Chen, J.W., 2004. Different effects of humic substances on photodegradation of p,p'-DDT on soil surfaces in the presence of TiO2 under UV and visible light. Journal of Photochemistry and Photobiology a-Chemistry 167, 177-183.
Zheng, X.J., Blais, J.F., Mercier, G., Bergeron, M., Drogui, P., 2007. PAH removal from spiked municipal wastewater sewage sludge using biological, chemical and electrochemical treatments. Chemosphere 68, 1143-1152.

AIR QUALITY ANALYSIS STUDIES OF ATAŞEHİR IN ISTANBUL

Ayten Bağdatlıoğlu Kartal[1], İpek Önder[1], Feyza Dişli[1], Ozan Melih Direk[1], Çiğdem KARA[1], Mikdat Kadıoğlu[2], Hüseyin Toros[2]

[1] Ataşehir Municipality, Directorate of Environmental Protection and Control, Barbaros Mah., Şebboy Sok., No:4/A, Ataşehir, İstanbul, Turkey. ayten.kartal@atasehir.bel.tr, ipek.onder@atasehir.bel.tr, feyza.disli@atasehir.bel.tr , ozan.direk@atasehir.bel.tr, cigdem.kara@atasehir.bel.tr

[2] Department of Meteorology, Faculty of Aeronautics and Astronautics, Istanbul Technical University, İstanbul, Turkey. kadioglu@itu.edu.tr, toros@itu.edu.tr

Abstract

Today, the air quality of a place is one of the most important indicators of social and economic development needed to ensure the standard of living and sustainability. Ataşehir Municipality has cooperated with Istanbul Technical University, Faculty of Meteorology Engineering Teaching Members for the current state of air pollution and improvement works. In the preliminary study, three main sources of pollution, heat, transportation and industry were found to exist in the region. Due to the heterogeneous nature of the pollution sources in the region and surrounding area and the complex topographic structure of the region, it is planned to carry out measurements at different locations at different times by establishing a mobile air quality station. In order to measure pollutants from three main sources of pollution, wind speed, direction, temperature, pressure and humidity measurement devices are installed beside the station PM_{10}, $PM_{2.5}$, NO, NO_2, SO_2, O_3 and CO. These devices can be upgraded if needed. The measurement station that was commissioned on January 2016 was first established in the Küçükbakkalköy District, which is a part of the midpoint to obtain Ataşehir air pollution values, and test measurements were made. The station was placed in this area in the direction of the demands of the public in the Fatih district located within the borders of our municipality. In this study, the measurement results of 14 April 2 July 2017 were evaluated. A meeting was held in the neighborhood and the results of the measurements were presented to the people of the neighborhood. Action plans to increase air quality have been discussed. One of these action plans is to cover both sides of the roads with green and leafy plants in summer and winter, and to create to make less noise pollution and drain pollution.

Keywords: *Ataşehir, air quality, measurement, analysis*

INTRODUCTION

With the measurement and evaluation of the rapidly increasing air quality in the modern world, work is increasingly being undertaken to contribute to the socio-economic development and quality of life of the inhabitants of the region. It is known that the relationship between industrialization, urbanization and air pollution is high. The levels of urbanization vary widely in different regions of the world. The proportion of people living in cities all over the world is increasing. Urbanization brings new physical, social and economic processes together. According to the statistics of the United Nations Environment Program, in the last 60 years the population of the city has increased at an incredible rate. In the 1950s, only 30 percent of the world's population lives in cities, while 54 percent of the world's population lives in cities globally, compared to 2014 data. It is estimated that this ratio will increase to 66 percent in the 2050s.

The pollutants released into the eventual atmosphere of people's activities come from many different sources, but most of them come from transportation, industrial activities and warming (Guenther and the others, 2006).

Air pollution is increasing especially in developing country cities. For example, 16 of the 20 most polluted cities in the world are located in China, (Shu ve Zhu, 2009). İncecik and İm (2012) have studied the values of air pollution in Istanbul and the big cities in the world and it is stated that pollution is a problem in some periods. The growing population density in the major cities poses a health risk for those living with air pollution due to economic, demographic, social policy and ecological processes. It is inevitable to adopt new visions of city planning and innovative management tools to enhance life satisfaction in cities (İncecik ve İm, 2012). These studies aimed at improving air quality by examining air pollution measurement values with the methods used in developed countries and sharing the results with the public, administrators and lawmakers are high-value projects.

The Atasehir Municipality Environmental Protection and Control Department aims to contribute to the healthy living environment by determining the quality of air quality, management and air quality correctly within the scope of Environmental Legislation. The metering station will assist in action plans for air quality improvement work by decision makers by measuring pollution from the metering station transportation, heating and industry to measure the mobile air pollution measurement cabinet located in the area or to make a certain period of time in areas complaining about air quality. Work will continue to inform residents of the city of Ataşehir about the quality of the air and to determine the precautions that must be taken in order to survive in a healthy environment. By contributing to the solution of air pollution which is a global problem and by taking responsibility for us and future generations by measuring the air pollution values in our region and by making clean action plans and keeping our climate clean, we will help to protect the environment where we use our natural resources sensitively and consciously.

Data and Method

The Directorate of Environmental Protection and Control of Ataşehir District decided to establish an air quality station in the region within the framework of regional air quality improvement works. The air quality measurement station is designed to be portable so that measurements can be made at the related sites in the direction of public requests for air pollution.

In addition to PM10, PM2.5, NO, NO2, SO2, O3 and CO, wind speed, direction, temperature, pressure and humidity measurement devices have been installed to measure pollution levels from heating, The data obtained from the measurement stations can be monitored by transferring them to the data collection computers via the municipal Data Operation Center via GSM modems. The designed interface is also shared with the public via the web.

Measurements are made at different points in Ataşehir. In the direction of requests from the public, the air quality measurement station has been moved to the position given below as of April 13, 2017 (Figure 1, Figure 2). Site residents in this location asked for information on pollutant levels and possible sources. As you can see in the figure, TEM and D100 highway pass from the north of the station. The altitude of the station is about 80 meters. The station is located on a hill with a radius of 3 km and a vertical cross-section in the east-west direction. According to the vertical section in the north-south direction, the station is located on a sloping slope.

Figure 1. Air quality station location and east-west vertical section

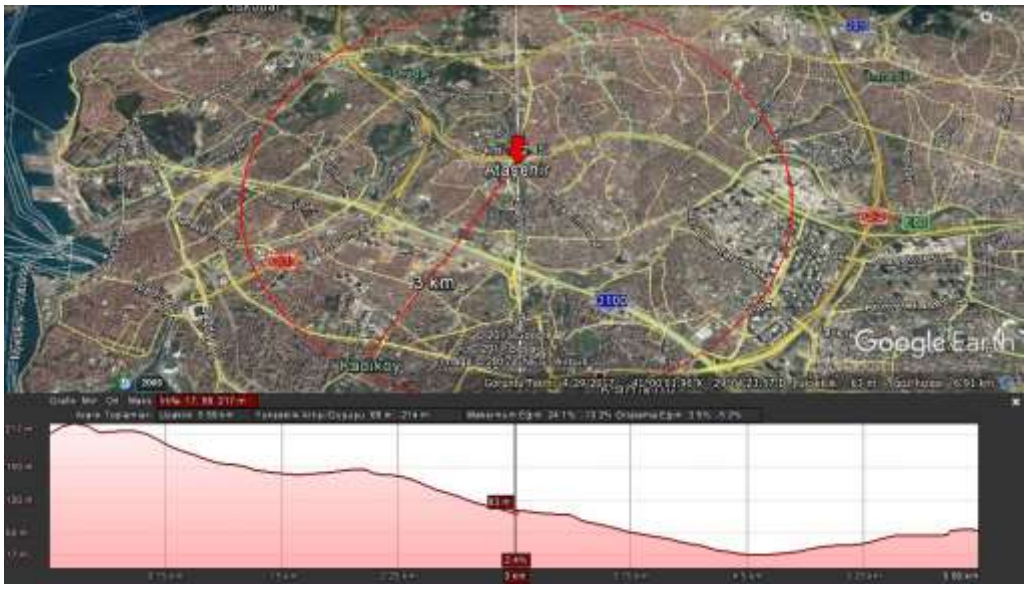

Figure 2. Air quality station location and north-south vertical section

Results

As the most important stakeholder in improving air quality is the people and workers in the region, it is planned to be supported by air quality information and awareness building seminars in the public, civil society and educational institutions in the region. Seminars have been planned to be given to different communities (eg muhtars) and by academic staff specializing in the subject, so as to make air quality awareness and awareness more effective.

Assessment of the measurement results of air quality data that can be obtained at the station and in the surrounding region will be evaluated by analyzing the air quality measurement results in terms of air quality standards and air quality index. This stage is a big factor in the research project. Within the parameters that are analyzed, it is possible to reach the parameters that cause the most pollution. Analysis of air quality measurement results The air quality level of the Ataşehir district will assist both public and decision makers in their plans and programs and in

future projects. Obtained findings are directly related to the occurrence of air quality enhancement.
- Information will be collected about the level and type of pollution by measuring in the region / regions that have complained with the mobile station.
- Based on the information obtained, the solution proposal will be investigated.
- As the information about the source of pollution is obtained, solutions will be sought in the district of Ataşehir within the framework of the legislation and solutions in the world.
- In addition to the effect of meteorological conditions in the district as a whole, it is necessary to identify those who use low quality or unfavorable fuels together with installations of facilities and buildings individually causing air pollution.

Daily Mean Values of Pollutants

The daily mean changes of pollutants measured at Ataşehir Municipality Air Quality Station between April 14 and July 2, 2017 are given in Figure 3. The average daily average PM2.5 reached the maximum of 54 μg / m³ on April 21, 2017. The average of the periods examined is 16 μg / m³. The observed mean PM10 was 51 μg / m³ and the highest daily average observed during the period was 175 μg / m³ on 14 April 2017. NO daily mean density values are given. The daily average value of the NO value at the measurement period is 74 μg / m³. The highest daily releases were 342 μg / m³ on 12.05.2017. The average daily NO2 value is 168 μg / m³. The highest value was reached on June 2, 2017 during the measurement period. The NOx average value was measured at 241 μg / m³ and the highest value was measured at 2 June 2017 at 849 μg / m³. The O3 average was 46 μg / m³ and the highest was 93 μg / m³ on June 26, 2017. CO values were generally observed to be low and were measured above 2600 g / m³ on 26-28 April and 26-27 May 2017.

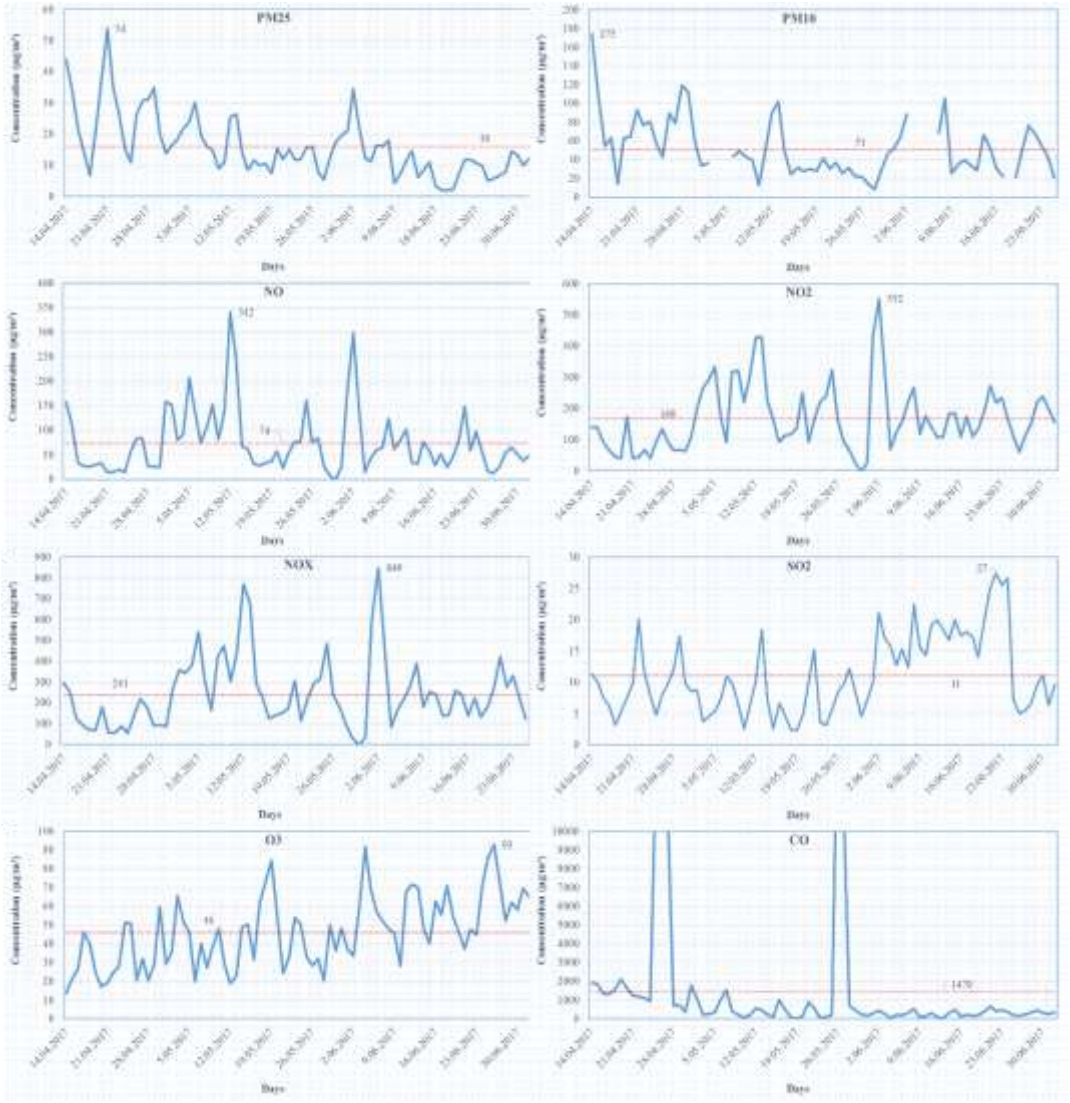

Figure 3. Time-series plots of daily pollutant concentrations, µg/m³.

Change of Polluters in the Day

The releases of pollutants during the day according to the measurement data are given in Fig. 4. PM2.5 reaches the highest value of 23 µg / m³ during the day to 14.00 hours . The smallest values are at 15 and 19 o'clock. The lowest measured PM2.5 value is 13 µg / m³. NO values increased rapidly with morning traffic during the day, reaching the highest value of 115 µg / m³ in the morning. It decreases during the day and the lowest value reaches around 18 hours 47 µg / m³. After this hour, the night continues to increase until 12, and after midnight it decreases again and falls to 05. NO2 values decrease by 5 o'clock in the morning during the night. An increase of up to 08 'in the morning hours shows a slight decrease. The NO2 values that continue to increase after lunchtime reach a maximum of 222 µg / m³ at around 12 noon. NOx values are highest at 336 µg / m³ during the day and around 12 at night. It falls until 5 o'clock in the morning and then increases until 8 o'clock. It decreases again after this hour and the lowest value of 186 is reached around 14:00 after lunch. SO2 values start to increase at 4 o'clock in the morning and reach around 10 o'clock at 10 o'clock with a maximum value of 13 µg / m³. It falls to 04 in the morning from this hour and reaches 9 µg / m³ at 4 o'clock in the morning. The increase and decrease of O3 values need to be investigated in more detail. Because O3 values increase rapidly from midnight to 6 o'clock in the morning and reach 71 µg / m³ at 6 o'clock. At 7 o'clock the value is falling rapidly. Increasing O3 values at 8 o'clock in the morning

continue to increase until 15 o'clock. Starting at 18 o'clock, O3 reaches its minimum value of 26 µg / m³ at 12 o'clock. When CO release is examined within days, an increase is observed from 5 o'clock in the morning. Co reaches the highest value of 1969 at around 9 o'clock in the morning. Then it gradually decreases to reach the lowest value of 1264 around 17 o'clock. After this time the clock continues to increase until 12.

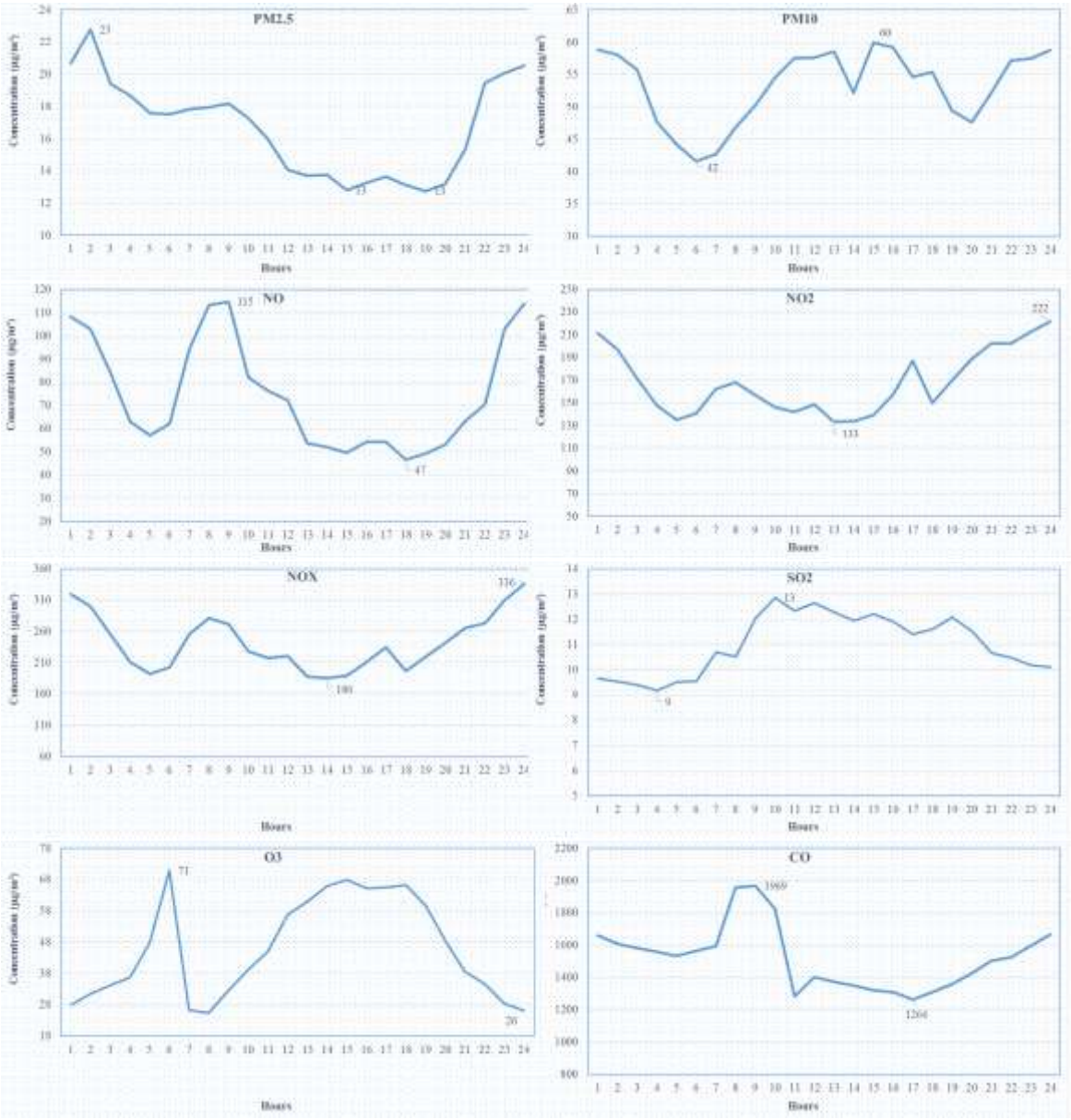

Figure 4. Diurnal variation of pollutant concentrations, µg/m³.

The percentage of the pollutants to which the pollutants are carried out is given in Table 1 according to the National Air Quality Index values of the pollutant parameters according to the average values of PM10 for 24 hours, SO2 and NO2 for 1 hour, O3 and CO 8 hours. The AQI values of the PM10 data are given in the following chart. The AQI values of the PM10 data are given in the following chart. The measured hourly mean data were 57% good, 27% moderate and 5%. The AUC values of SO2 data are given in the following chart. The measured hourly average is in good class. The AQI values of NO2 data are given in the following chart. The measured hourly mean values were 36% good, 34% moderate, 27% sensitive and 2% unhealthy.

All values of O3 were in good group. 6% of the CO values are good, 1% is unhealthy, and 3% is poor.

Table 1. Percent realization rates of pollutants by National Air Quality Index values

İndeks	PM10 [µg/m³] 24 hour average	Percentage	SO2 [µg/m³] 1 hour average	Percentage	NO2 [µg/m³] 1 hour average	Percentage	O3 [µg/m³] 8 hour average	Percentage	CO [µg/m³] 8 hour average	Percentage
Good	0-50	0,57	0-100	1,00	0-100	0,36	0-120	1,00	0-5500	0,96
Moderate	51-100	0,37	101-250	0,00	101-200	0,34	121-160	0,00	5501-10000	0,00
Unhealthy for Sensitive Groups	101-260	0,05	251-500	0,00	201-500	0,27	161-180	0,00	10001-16000	0,00
Unhealthy	261-400	0,00	501-850	0,00	501-1000	0,02	181-240	0,00	16001-24000	0,01
Very Unhealthy	401-520	0,00	851-1100	0,00	1001-2000	0,00	241-700	0,00	24001-32000	0,03
Hazardous	>521	0,00	>1101	0,00	>2001	0,00	>701	0,00	>32001	0,00

Pollution Direction Distribution

The distribution of the PM10 and SO2 concentrations is given in Figure 5 in order to be able to obtain information on possible sources of pollution at the measuring point depending on the pollutant wind speed and direction . When the wind is over 4 m / s and the direction is south-west, the PM10 density is above 100 µg / m³. The wind speed ranges from 0-2 m / s and the PM10 values range from 60-100 µg / m³ when exposed to the south-west direction. When the density of SO2 is observed above 12 µg / m³, it is observed that the wind speed is 0-2.3 m / s and the direction is from south-west direction. When the pollutant density is around 10 µg / m³, the wind speed is 2-3 m / s and the direction is south-west.

The potential sources of SO2 pollutants need to be investigated in order to determine the source that affects them.

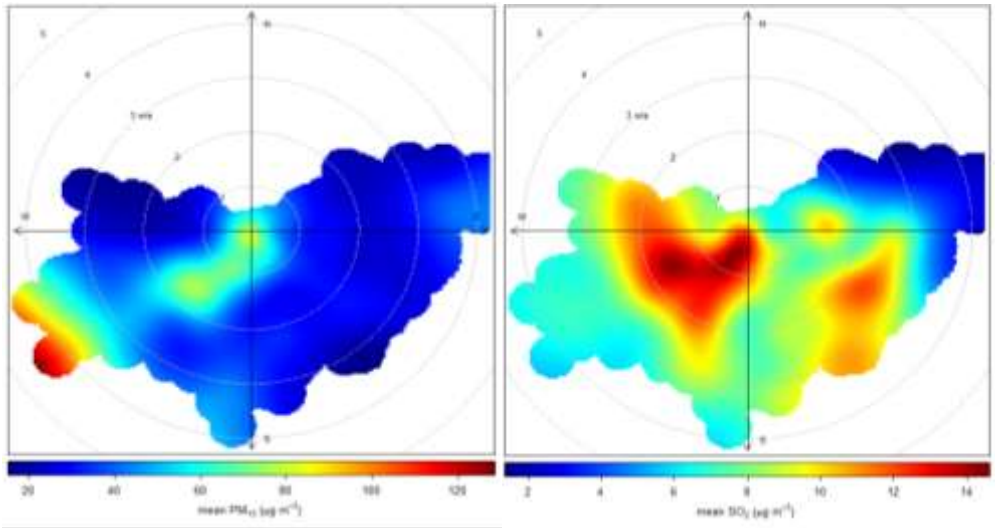

Figure 5. PM10 and SO2 pollution rose

According to the PM10 measurement data, the intensity increases on weekdays and the highest value reaches on Friday. The SO2 intensity is highest on weekdays, reaching on Saturday (Figure 6).

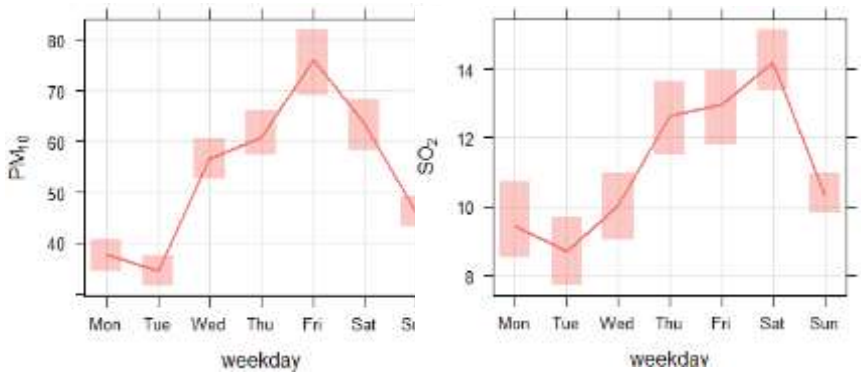

Figure 6. Change of pollutant intensity according to days

References

ARL (Air Resources Laboratory), 2015. Alıntı tarihi: 12.09.2015, Alıntı Adresi: http://www.arl.noaa.gov/

ARL (Air Resources Laboratory), 2015. "Hybrid Single-Particle Lagrangian Integrated Trajectory, (HYSPLIT) Model". Alıntı tarihi: 10.09.2015, Alıntı Adresi: http://www.arl.noaa.gov/HYSPLIT_info.php

CSB (Çevre ve Şehircilik Bakanlığı), 2009. "Hava Kalitesi Değerlendirme Ve Yönetimi Yönetmeliği", Türkiye.

MTHM (Marmara Temiz Hava Merkezi Müdürlüğü), 2016. "HKDY Yönetmeliği EK-I A, Geçiş Dönemi Uzun Vadeli ve Kısa Vadeli Sınır Değerlerinde Kademeli Azaltım", Alıntı tarihi: 09.01.2016, Alıntı Adresi: http://mthm.havaizleme.gov.tr/secure/index2.htm.

Ulusal Hava Kalitesi İzleme Ağı, 2015, alıntı tarihi: 14.10.2015, alıntı adresi: http://www.havaizleme.gov.tr/hava.html

ANALYSIS OF AIR POLLUTION CAUSED BY MOTOR VEHICLES PASSING FROM BRIDGES ON THE BOSPHORUS OVER ISTANBUL

Birkan Kilic and Orhan Sen

İstanbul Technical University, Faculty of Aeronautics and Astronautics, Deparartment of Meteorological Engineering, Maslak, Istanbul, Turkey. seno@itu.edu.tr.

Abstract

Industrial activities, fuels for heating purposes and transportation vehicles are the main causes of air pollution. Emissions gases are released by vehicles that play an important role in air pollution. The change of living standards and economic developments with the increase in Istanbul population cause increasing number of vehicles participating in traffic every year. Motor vehicles used in transport are the sources of air pollutants. Consequently this increase, it is normal to expect that emissions produced by motorway vehicles will rise. Bridges over Istanbul are traffic center . Bridges connect Asia and Europe Continents. Therefore, hundreds of thousands of vehicles use these bridges. A major part of the air pollution is caused by motor vehicles. These gases directly affect human health. According to figures released by the World Health Organization in September, 9 out of every 10 people in the world live in places where air pollution reaches dangerous dimensions.

This study that it is has been investigated the air pollution from bridges over Istanbul that is resulted by transportation. First, air pollutant sources, formation and properties are explained. It is mentioned that these emissions are related to the weather conditions, operating conditions of the engine and fuel types. Numbers of vehicles were taken from the T.C. 1st Regional Directorate of Highways. The NOx, CO, HC, SOx and PM pollutants emitted from vehicles are released to the atmosphere at different emission values. The emission value for each pollutant is calculated on an annual basis and according to the classes of vehicles. In 2016, emission analysis for Yavuz Sultan Selim Bridge was taken with reference to the decrease of passing vehicles in comparison with other year.

Keywords: *Bosphorus Bridges, Motor Vehical, Air Pollution.*

INTRODUCTION

Istanbul has most crowded city in Turkey and Europe connectes like bridge with Asia and Europe continents. The importance of Istanbul's geopolitical position as well as it draws attention with the increase of trade activities such as finance, industry and tourism. Marmara coast and along the Bosphorus, Golden Horn was established area inside Istanbul. Bosphorus is center of Europa. Location of İstanbul is Çatalca in the west, Kocaeli in the east, Black Sea in the north, Marmara Sea in the south.

There are 3 bridges on the Istanbul Bosphorus. These are 15 July Martyrs Bridge opened on October 29, 1973 , the Fatih Sultan Mehmet Bridge opened on July 3, 1988, and finally Yavuz Sultan Selim opened on August 26, 2016. 15 Martyrs Bridge is the first name of the Bosphorus Bridge that was sufficient for the circumstances of the time and it was not able to respond to the needs of the day by day. The number of vehicles passing through the bridge has exceeded its carrying capacity. Therefore, it was decided to build a new bridge. Fatih Sultan Mehmet Bridge was not enough against the rapidly growing population (4).

Northern Marmara Motorway project, both to ease traffic and transit passengers are prevented to enter the center of Istanbul. These bridges are used not only the Turkish people but also all nations as it is an international trade route. It is evidenced by the fact that Istanbul is carrying out international shipment with the ports it owns and Turkey doing export and import. So, traffic on bridges is continuously increasing, insufficient and affects human health (6).

Air pollution occurs when natural, plant, animals or human acticity (anthropogenic) sources of gas, dust or liquid are interacted with the atmosphere directly or indirectly by reaction with other particles [1]. Research emphasizes that motor vehicles cause more than 50% of air pollution. In a metropolis like Istanbul, population growth is increasing in parallel with the number of vehicles. Emission increase due to the increase in the number of vehicles is a very important issue affecting air pollution in Istanbul. Sea, air, and roads are the sources of air pollution caused by transportation. In motor vehicles, pollutants such as carbon monoxide, hydrocarbons, nitrogen oxides, sulfur oxides, lead oxides and particulate matter present in the exhaust gases are harmful to human health in areas with density traffic. This work is based on petrol and diesel fuels. Carbon monoxide, which is the colorless gas released from exhausts of gasoline vehicles. Diesel engine vehicles release most NOx than other gases (2).

In the first part, the sources of air pollution and air pollution are mentioned. Then, emissions from motor vehicles, factors affecting vehicle emissions, and exhaust emissions are included. In addition, the emissions and the emissions of gasoline and diesel engines are compared (3). Finally, the effects of exhaust gases on human health were examined. In the analysis part, pollution due to the number of vehicles was detected at the bridges. For each pollutants a specific area calculation was made. As a result of the annual evaluations, the emission amounts were reached. Annual evaluations were made within 3 bridges and to look at difference results. Millions of vehicles using bridges emit tons of pollutants. In particular, heavy traffic on bridges increases the amount of emissions and increases the amount of gases. Electric vehicles, the product of developing technology, will play a role in the fight against air pollution (5).

DATA AND METHODS

The locations referenced in the study include 3 km distance for the 15 July Martyrs Bridge, Fatih Sultan Mehmet Bridge and Yavuz Sultan Selim Bridge. Between 2007 and 2016, the number of vehicles passing on the was obtained from 15 July Martyrs Bridge and Fatih Sultan Mehmet Bridge the 1st Regional Directorate of Highways [7] . Vehicle numbers are provided in sorted order on a 5 class basis.

Table 1. Types of Vehicles Crossing the Bridge [7]

1.CLASS	VEHICLES WITH 2 AXLES WITH A DISTANCE LESS THEN 3,20 m (CARS, MOTOBIKES, TRUCKS, VANS, MINIBUS)
2.CLASS	VEHICLES WITH 2 AXLES WITH A DISTANCE EQUAL AND MORE THAN 3,20 m(TRUCKS, VANS, PUBLIC BUSES JEEP, PICK UP, AMBULANCE, FUNERAL VANS)
3.CLASS	ALL VEHICLES WITH 3 AXLES (1st & 2nd CLASS WITH 1 ADDITIONAL AXLE)
4.CLASS	ALL VEHICLES WITH 4 & 5 AXLES (2nd CLASS WITH 1 ADDITIONAL AXLE), (1st CLASS WITH 2 ADDITIONAL AXLES)
5.CLASS	TRUCKS WITH 6 AND MORE THAN 6 AXLES

All types of vehicles have been included in the calculations. The distance of 3 km is accepted between the entry and exit points of the bridges. In this study, emission values were calculated according to the number of vehicles passing through the bridge.

It is accepted that 2nd, 3rd, 4th and 5th class vehicles use diesel, 1st class vehicles use both gasoline and diesel fuel. The information about how much fuel the 1 st class vehicles used is reached from the automotive distributors magazine. it is accepted that there are 61% diesel and 39% gasoline cars (9).

Emission values are not only related to fuel types, but also to the operating conditions of the engine. The air excess coefficient is dependent on the operating conditions of the engine, such as ignition advance, number of rotations of the motor, valve thrusts and valve timing. In this study, these conditions are mentioned but neglected. Because it is not possible to assess these conditions one by one for all the vehicles passing through the bridge, these characteristics of the vehicles are considered constant.

Emission Calculation Method

Table 2. Vehicle Emission Value (g/km) [11]

Vehicle Fuel Type	CO	HC	NOx	PM	SOx
Gasoline	16,1	1,8	3	0,05	0,05
Diesel	0,72	2,2	16,5	1,5	2

Emission values were calculated based on vehicle numbers on the bridge. This study was carried out at a distance of 3 km determined on the Bridge. With the information received from the automotive distributors association magazine; In traffic, 61% diesel, 39% gasoline was considered to have a car [9]. Annual emission amounts of all pollutants were calculated by multiplying emission values (g / km), determination distance (km) and vehicle numbers.

15 July Martyrs Bridge

This project was carried out between the D 100 Kuzguncuk and the O1 Balmumcu Connection at a distance of 3 km covering the 15 July Martyrs Bridge.

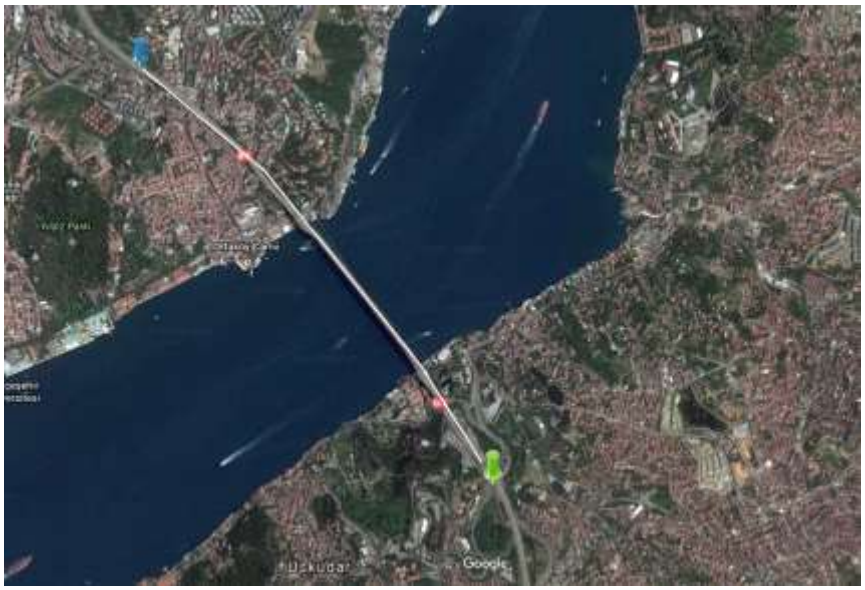

Figure 1. Road Used for the 15 July Martyrs Bridge [8]

Measurements Figure 1. As indicated in the picture, it was made at 3 km distance between blue and green points. The total length of the bridge is 1560 meters, and the length between two towers is 1074 meters. The existence of the idea of easily crossing the Bosphorus, which

separates the European and Asian continents, has preserved its existence. There are 6 strips in total and 3 strips in the direction of arrival and departure. The bridge linking the European and Asian continents is a very important ring of the Turkish transportation network.

15 July Martyrs Bridge Vehicle Distribution

Number of vehicles of 15 July Martyrs Bridge owned by 15 July Martyrs Bridge Operation Directorate.

Table 3. Number of Vehicles Passing through the 15 July Martyrs Bridge (7)

	Vehicle Class					
Years	**1.Class**	**2.Class**	**3.Class**	**4.Class**	**5.Class**	**Total**
2007	30240565	1670188	109625	402	46	32020826
2008	30726611	1741006	102054	885	72	32570628
2009	29922718	1632619	75533	151872	114	31782856
2010	30742444	1807406	51705	238827	40	32840422
2011	31180174	1958981	57489	292484	81	33489209
2012	28543625	1884418	81979	278797	36	30788855
2013	29720806	1966520	305176	136991	33	32129526
2014	29237016	1904699	338196	98529	119	31578559
2015	29246765	1924297	384493	74881	151	31630587
2016	28488815	1818666	328438	127141	165	30763225

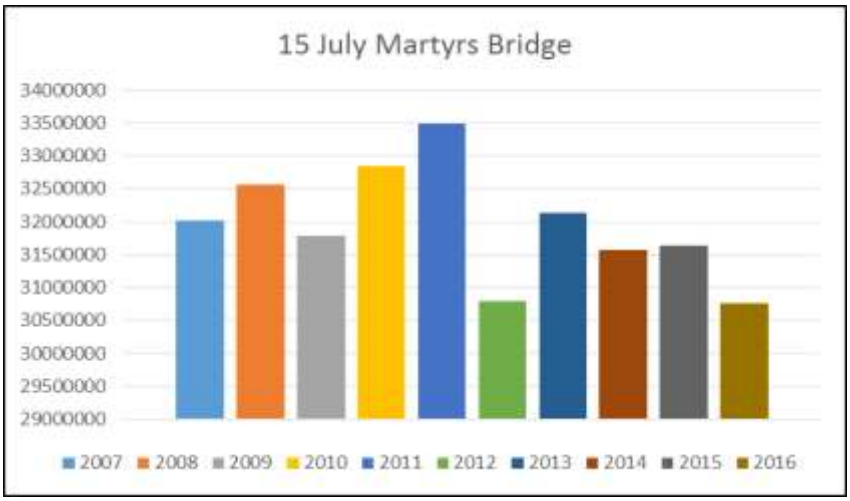

Figure 2. Vehicle Number Distribution by Years for 15 July Martyrs Bridge

Figure 2, shows that the maximum number of vehicles in 2011 and the decline in 2012 and 2016 are noteworthy This may be due to the increase in bridge transit in 2012 and the transition to the KGS system. The decline in 2016 may have been influenced by the opening of Yavuz Sultan Selim Bridge. The number of vehicles that have decreased in the last 5 years may not be preferred by automobile users depending on the bridge operating conditions.

Fatih Sultan Mehmet Bridge
This project was carried out between the D 80 Etiler and the D 80 Anadolu Hisarı at a distance of 3 km covering the Fatih Sultan Mehmet Bridge.

Figure 3. Road Used for the Fatih Sultan Mehmet Bridge [8]

Measurements Figure 3. As indicated in the picture, it was made at 3 km distance between blue and green points. The Fatih Sultan Mehmet Bridge, which began construction on December 4, 1985, was completed on July 3, 1988 and opened for use. The total length of the bridge is 1510 meters, and the length between two towers is 1090 meters. Heavy traffic due to the increase in the number of vehicles in Turkey has prevented the Bosphorus Bridge from responding to the needs and systematically flowing traffic. Fatih Sultan Mehmet Bridge, which combines the two sides of the Istanbul Bosphorus, will alleviate the burden of the traffic on the existing bridge and also increase the capacity of Europe and Anatolia Motorways and connect it with the ring road.

Fatih Sultan Mehmet Bridge Vehicle Distribution
Number of vehicles of Fatih Sultan Mehmet Bridge owned by 15 July Martyrs Bridge Operation Directorate.

Table 4. Number of Vehicles Passing through the Fatih Sultan Mehmet Bridge (7)

	Vehicle Class					
Years	**1.Class**	**2.Class**	**3.Class**	**4.Class**	**5.Class**	**Total**
2007	32130044	4516546	1331463	1021760	10854	39010667
2008	30909771	4833612	1358348	1072060	12044	38185835
2009	30541541	4732303	1253766	1000003	8880	37536493
2010	30437887	5378112	1368141	1193589	8516	38386245
2011	31240166	5735501	1371717	1538988	17782	39904154
2012	29013609	5652276	1315099	1663117	24875	37668976
2013	29969214	5612648	1164987	1695153	31957	38473959
2014	32319373	6181776	1197415	1867051	51667	41617282
2015	31717233	5784983	1032020	1766154	19373	40319763
2016	29753490	4859095	616601	1124493	10374	36364053

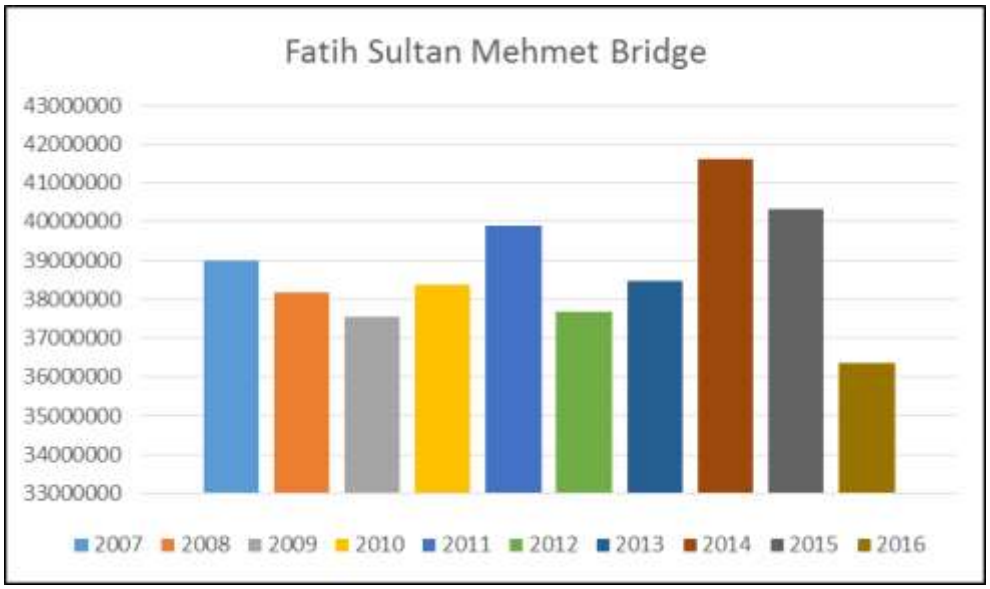

Figure 4. Vehicle Number Distribution by Years for Fatih Sultan Mehmet Bridge

Figure 4. The maximum number of vehicles in 2014 has passed and the decline in 2015 and 2016 is remarkable. 2010 was box office maintenance due to KGS. As the bridge in 2012 is closed for traffic for 32 days due to maintenance, the number of vehicles decreased. The decline in 2016 may have been influenced by the opening of Yavuz Sultan Selim Bridge. Especially in the 3rd, 4th and 5th class vehicles of these classes with the prohibition of passing through Fatih Sultan Mehmet Bridge.The number of cars has increased in the last 4 years except 2016 .

Yavuz Sultan Selim Bridge

The Yavuz Sultan Selim Bridge, which began construction on May, 2013, was completed on August 26, 2016 and opened for use. The total length of the bridge is 2682 meters. It has an 8 lane highway over the 3rd Bosphorus Bridge which is made against the unresolved traffic problem in Istanbul. It is one of the few bridges in the world with its aesthetic and technical features.

Table 5. Number of Vehicles Passing through the Yavuz Sultan Selim Bridge (7)

	Vehicle Class					
Years	**1.Class**	**2.Class**	**3.Class**	**4.Class**	**5.Class**	**Total**
2016	1963743	925888	415419	641661	8999	3955710

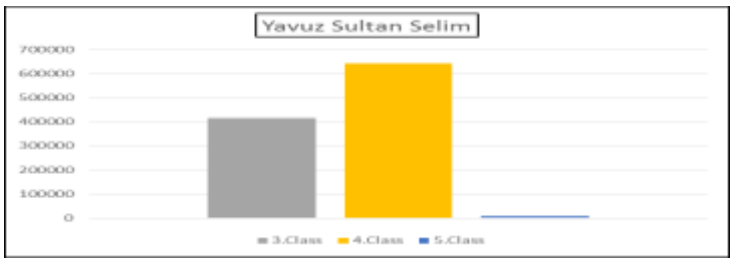

Figure 5. Vehicle Number Distribution for Yavuz Sultan Bridge

At Yavuz Sultan Selim Bridge The percentage of 3rd, 4th and 5th grade vehicles is higher than other bridges. This is due to the prohibition of passing heavy buses and pessenger and less trafic from other bridges. In addition, at North Marmara Motorway transit passengers and less trafic are favorable for 1st and 2nd class vehicles than at other bridges.

ANALYSIS RESULTS AND EVALUATION

Calculation of Emission Amount

This content of study; Emission amounts for Fatih Sultan Mehmet Bridge and the 15th of July Martyrs Bridge were calculated for a period of 10 years including 2007 and 2016 years. With this data, the air pollution caused by the vehicles passing over the Istanbul's bridges has been examined and vehicles passing by Yavuz Sultan Selim Bridge were analysed for air pollution. Later, using statistical methods, amount of emissions are found by vehicle types. Thus, pollutant quantities have been obtained on vehicle basis.

July Martyrs Bridge 10 Years Emission Values

For the 15 July Martyrs Bridge, it is seen that the NOx emission is the highest in the emission values. NOx emissions are respectively followed by CO, HC, SOx and PM emissions. The following table shows full values.

Table 6. Annual Emission Amounts for 15 July Martyrs Bridge (ton)

Year	CO	HC	NOx	PM	SOx
2007	613,33	197,18	1107,38	92,79	123,13
2008	623,27	200,59	1126,92	94,44	125,32
2009	607,10	195,76	1100,62	92,26	122,43
2010	624,13	202,36	1140,02	95,63	126,90
2011	633,41	206,44	1165,22	97,80	129,80
2012	580,14	189,85	1073,20	90,13	119,61
2013	604,21	198,15	1120,97	94,16	124,97
2014	594,32	194,74	1101,34	92,50	122,77
2015	594,61	195,07	1103,76	92,72	123,06
2016	579,09	189,70	1072,80	90,10	119,58
Total	6053,61	1969,84	11112,24	932,54	1237,57

Table 7. Average CO Emission Amounts (ton) for 15 July Martyrs Bridge

2007 -2011 Ave.	620,25	Max.	633,41
2012 - 2016 Ave.	590,47	Min.	579,09
Difference	29,78	**Difference**	54,32

It is observed that the CO emission values are at very high levels until 2012, but the values for 2012 and thereafter are showing a decline. An average of CO emissions in the last 5 years

have decreased by 29.80 tons. The highest CO emission is 633.41 tons in 2011 while the lowest is 579.09 tons in 2016. CO value is 16 g / km for gasoline and 0.72 g / km for diesel. CO emissions are affected the increase in the quantity of diesel vehicles as well as the number of vehicles in traffic.

Table 8. Average HC Emission Amounts (ton) for 15 July Martyrs Bridge

2007 -2011 Average	200,47	Max.	206,44
2012 - 2016 Average	190,53	Min.	189,7
Difference	9,94	**Difference**	16,74

HC emission values are close each other for a period of 10 years. Average HC emissions have decreased by 9.94 tons over the last 5 years. The highest HC emissions in 2011 were 206.44 tons, while the lowest level was 189.07 tons in 2016. The gasoline HC emission value is slightly lower than the diesel value. HC emissions are associated with an increasing amount of diesel vehicles and a decreasing in the number of vehicles using bridges.

Table 9. Average NOx Emission Amounts (ton) for 15 July Martyrs Bridge

2007 -2011 Average	1128,03	Max.	1165,22
2012 - 2016 Average	1094,41	Min.	1072,8
Difference	33,62		92,42

NOx emission values have remained low for the past 5 years compared to previous years. The average NOx emission in the last 5 years has decreased by 33.62 tons. The highest NOx emission in 2011 was 1165.22 tons, while the lowest level was 1072.8 tons in 2016. NOx emission is released the highest value by vehicles. 16.5 g / km for diesel and 3 g / km for gasoline. The NOx emission value is higher because NOx gases are spread more in diesel vehicles.

Table 10. Average PM Emission Amounts (ton) for 15 July Martyrs Bridge

2007 -2011 Ave	94,58	Max.	97,8
2012 - 2016 Ave	91,92	Min.	90,1
Difference	2,66	**Difference**	7,7

PM emission values are close each other for a period of 10 years. Average PM emissions have decreased by 2,66 tons over the last 5 years. The highest PM emissions in 2011 were 97,08 tons, while the lowest level was 90,01 tons in 2016. The gasoline PM emission value is lower than the diesel value. PM emissions are associated with an increasing amount of diesel vehicles and a decreasing in the number of vehicles using bridges. It is also observed that the PM pollutant amount is from pollutants with the least amount of emission when compared to other pollutants.

Table 11. Average SOx Emission Amounts (ton) for 15 July Martyrs Bridge

2007 -2011 Ave	124,53	Max.	129,8
2012 - 2016 Ave	122	Min.	119,58
Difference	2,53	**Difference**	10,22

The SOx gas has like emission values and dispersion to the PM gas. Average SOx emissions have decreased by 2,53 tons over the last 5 years. The highest SOx emissions in 2011 were 129,08 tons, while the lowest level was 119,58 tons in 2016.

Fatih Sultan Mehmet Bridge 10 Years Emission Values

For the Fatih Sultan Mehmet Bridge, it is seen that the NOx emission is the highest in the emission values. NOx emissions are respectively followed by CO, HC, SOx and PM emissions. The following table shows full values.

Table 12. Annual Emission Amounts (ton) for FSM Bridge

Yıl	**CO**	**HC**	**NOx**	**PM**	**SOx**
2007	662,43	242,43	1423,53	121,04	160,76
2008	638,69	237,56	1401,98	119,40	158,59
2009	630,66	233,45	1375,65	117,10	155,54
2010	630,63	239,10	1419,35	121,10	160,87
2011	648,35	248,75	1481,82	126,57	168,15
2012	603,45	235,04	1406,34	120,29	159,82
2013	622,39	239,90	1431,10	122,29	162,47
2014	671,47	259,55	1549,57	132,45	175,97
2015	657,83	251,27	1494,85	127,63	169,56
2016	613,95	226,08	1330,06	113,16	150,30
Total	6379,85	2413,13	14314,27	1221,03	1622,03

Table 13. Average CO Emission Amounts (ton) for FSM Bridge

2007 -2011 Ave	642,15	Max.	671,47
2012 - 2016 Ave	633,82	Min.	603,45
Difference	8,33	**Difference**	68,02

It is detected that the generally, CO emissions are at high levels, but values have declined in recent years. An average of CO emissions in the last 5 years have decreased by 8,33 tons. The highest CO emission is 671.47 tons in 2014 while the lowest is 603,45 tons in 2012. CO value is 16 g / km for gasoline and 0.72 g / km for diesel. CO emissions are affected the increase in the quantity of diesel vehicles as well as the number of vehicles in traffic.

Table 14. Average HC Emission Amounts (ton) for FSM Bridge

2007 -2011 Ave	240,26	Max.	259,55
2012 - 2016 Ave	242,37	Min.	226,28
Difference	2,11	**Difference**	33,27

HC emission values are similar for a period of 10 years. Average HC emissions have increased by 2,11 tonnes over the last 5 years. The highest HC emissions in 2014 were 259,55 tons, while the lowest level was 226,28 tons in 2016. The gasoline HC emission value is slightly lower than the diesel value. HC emissions are associated with an increasing amount of diesel vehicles and a decreasing in the number of vehicles using bridges.

Table 15. Average NOx Emission Amounts (ton) for FSM Bridge

2007 -2011 Ave	1420,47	Max.	1549,57
2012 - 2016 Ave	1442,39	Min.	1330,06
Difference	21,92	**Difference**	219,51

NOx emission values have increased over the past 5 years compared to the past years. The average NOx emission in the last 5 years has rised by 21,92 tons. The highest NOx emission in 2014 was 1549,57 tons, while the lowest level was 1330,06 tons in 2016. NOx emission is released the highest value by vehicles. 16.5 g / km for diesel and 3 g / km for gasoline. The NOx emission value is higher because NOx gases are spread more in diesel vehicles.

Table 16. Average PM Emission Amounts for FSM Bridge (ton)

2007 -2011 Ave	121,04	Max.	132,45
2012 - 2016 Ave	123,16	Min.	113,16
Difference	2,12	**Difference**	19,29

PM emission values are similar for a period of 10 years. Average PM emissions have increased by 2,12 tons over the last 5 years. The highest PM emissions in 2014 were 132,45 tons, while the lowest level was 113,16 tons in 2016. The gasoline PM emission value is lower than the diesel value. PM emissions are associated with an increasing amount of diesel vehicles and a decreasing in the number of vehicles using bridges. It is also observed that the PM pollutant amount is from pollutants with the least amount of emission when compared to other pollutants.

Table 17. Average SOx Emission Amounts for FSM Bridge (ton)

2007 -2011 Ave	160,78	Max.	175,97
2012 - 2016 Ave	163,62	Min.	150,3
Difference	2,84	**Difference**	25,67

The SOx gas has like emission values and dispersion to the PM gas. Average SOx emissions have rised by 2,84 tons over the last 5 years. The highest SOx emissions in 2014 were 175,97 tons, while the lowest level was 150,3 tons in 2016.

Yavuz Sultan Selim Bridge Emission Values

For the Yavuz Sultan Selim Bridge, it is seen that the NOx emission is the highest in the emission values. NOx emissions are respectively followed by CO, HC, SOx and PM emissions. The following table shows full values.

Table 18. Emission Amounts for Yavuz Sultan Selim Bridge (ton)

CO	**HC**	**NOx**	**PM**	**SOx**
59,39	30,56	195,75	17,09	22,73

Results

According to the number of vehicles passing through the 15 July Martyrs Bridge, the emission values are lower in the last 5 years. In 2011, the most cars pass and have the maximum pollution values. Metrobus services were taken on March 3, 2009, connecting the two shortest routes of Istanbul to each other [29]. In addition, on 29 October 2013, Marmaray entered service. The Marmaray and Metrobus lines were an alternative to the traffic on the 15 July Martyrs' Bridge and led to tend people to public transport. In 2009, the number of vehicles in the 4th class vehicle category increased by 150,000 due to the Metrobus service. Transport Minister Yildirim said that the number of vehicles passing through the Bosporus bridges decreased due to the influence of Marmaray (10). Development of the transport system contributed to the decline in the number of vehicles and emission values.

According to the number of vehicles passing by Fatih Sultan Mehmet Bridge, the emission values have increased in the last 5 years. In 2014, the most cars passed and the level of pollution is high. There is a decrease in the amount of emissions due to the decrease in the number of vehicles passing by because there is maintenance work on the bridge in 2012.

With the opening of Yavuz Sultan Selim Bridge, which was put into service on August 26, 2016, there has been a change in the amount of pollutants that are released in other bridges, especially in the number of vehicles in Fatih Sultan Mehmet Bridge. The air pollution rate in the Fatih Sultan Bridge has decreased with the passing of the vehicles passing by Yavuz Sultan Selim Bridge, which are passing by the Fatih Sultan Bridge, especially 3,4 and 5 class vehicles, as a legal obligation.

Furthermore, in the formation of photochemical smog, which is one of the important consequences of vehicle pollution. NOx and HC play a role. At the highest values of these two pollutants, it is estimated that the amount of O3 (Ozone), the product of the photochemical smog reactions, will increase. As a result of heavy traffic on the bridges, the amount of CO can reach the health-hazardous values for the people sitting around the Bosphorus.

REFERENCES

[1] Al-Hassen, A., Sultan, A. & Alhello, A., 2015. Spatial Analysis on the Concentrations of Air Pollutants in Basra Province . Int. J. Climatol. 16: 1057-1076.

[2] Mayer, H., 1999: Air Pollution in Cities, Atmospheric Environment, 33(24), 4029-4037, Meteorological Institute, University of Freiburg, Germany

[3] Sakarya Üniversitesi Mühendislik Fakültesi Çevre Mühendisliği Bölümü, 2010. İçten Yanmalı Motorda Temel Kavram ve Çalışma Prensipleri, Sakarya.

[4] Deniz, O. " İstanbul Boğaz Köprüleri'nde Taşıtların Yarattığı Kirliliğin Copert Iıı Ve Mobıle 6 Modelleri İle Hesaplanması." Thesis. Istanbul Technical University, 2007. Print.
[5] Faiz, A., Walsh, M. P., & Weaver, C. S. (1996). Air Pollution From Motor Vehicles: Standards and Technologies for Controlling Emissions. Washington, D.C.: The World Bank.
[6] Brunekreef, B. (2009). Effects of long-term exposure to traffic-related air pollution on respiratory cardiovascular mortality in the Netherlands: the NLCS-AIR study. Boston, MA: Health Effects Institute.
[7] 1st Regional Directorate of Highways, 2017: Istanbul, Türkiye
[8] Turkey, Istanbul, Bridges, 2017 : *http://maps.google.com/*
[9] Automotive Distributors Association, 2011; Market Assessment, Istanbul
[10] Saatçioglu, T. " Marmaray Projesi İle Trafikten Çekilecek Otomobil Sayısının İstanbul'da Hava Kalitesine Yapacağı Etkinin Ive Model İle Tespiti." Thesis. Istanbul Technical University, 2010. Print.
[11] Şen O., 2015. Air Pollution Course Notes, Istanbul Technical University, İstanbul

BACK TRAJECTORY ANALYSIS of PARTICULATE MATTER DEPOSITIONS in DENİZLİ, TURKEY

Sibel Cukurluoglu[1], Ulker Guner Bacanli[2]

[1]*Pamukkale University, Faculty of Engineering, Environmental Engineering Department, 20070, Denizli, Turkey*
scukurluoglu@pau.edu.tr

[2]*Pamukkale University, Faculty of Engineering, Civil Engineering Department, 20070, Denizli, Turkey*
ugbacanli@pau.edu.tr

Abstract

Particulate matters in ambient air were sampled using Bergerhoff method in Pamukkale, Denizli, Turkey in April 2015 and May 2015. Dry deposition fluxes of particulate matters were calculated. The average dry deposition flux was calculated as 217.1 ± 37.8 mg m^{-2} day^{-1}. The minimum flux was determined as 165.4 mg m^{-2} day^{-1} between May 18-20, 2015, while the maximum flux was observed as 269.2 mg m^{-2} day^{-1} between May 14-16, 2015. The hybrid single-particle Lagrangian integrated trajectory (HYSPLIT) model was used to calculate seven-day back trajectories. It can be assumed that the high amounts of particulate matters in dry deposition samples were influenced by the air masses in the Baltic Sea-eastern Europe-Balkans route based on back-trajectory analysis. The air masses originated from the northern Europe-Mediterranean-northern African-Mediterranean route transport less particulate matter.

Keywords: *Back trajectory analysis, Bergerhoff method, particulate matter, dry deposition, flux.*

INTRODUCTION

Particulate matter (PM) exists as a complex mixture of extremely small particles and liquid droplets including acids, metals, organic chemicals, etc. The extent of its pollution in the atmosphere can thus be affected by a number of variables including the number, size, shape, surface area, chemical composition, solubility, and origin. PM can be classified into $PM_{2.5}$ (PM with an aerodynamic diameter < 2.5 μm), PM_{10} (PM with an aerodynamic diameter < 10 μm), and total suspended particles based on the aerodynamic diameter of particles (Kim et al., 2010).

The physical and chemical patterns of PM emissions may vary considerably by the factors controlling their source characteristics because it is emitted into the atmosphere by the combined effects of anthropogenic and natural sources. A large-scale dust storm frequently occurring in association with strong winds and exposed soils (namely Asian dust) is a common phenomenon in China and surrounding countries from winter to spring. As such, Asian dust events have the great potential to alter the PM concentrations and the air quality (Ahmed et al., 2015).

Urban outdoor air pollution is estimated to cause deaths, and even low concentrations of air pollutants have been related to a variety of harmful health effects. Fine particulate matter is an air pollutant that causes major environmental problems and has a disproportionately harmful impact on human cardiovascular and respiratory systems (WHO, 2008).

Wet deposition and dry deposition are the ultimate paths by which particulate matters and trace gases are removed from the atmosphere. The process of dry deposition of particles and gases is generally represented as consisting of three steps: (1) aerodynamic transport down through the atmospheric surface layer to a very thin layer of stagnant air just adjacent to the surface; (2) molecular (for gases) or Brownian (for particles) transport across this thin stagnant layer of air

to the surface itself; and (3) uptake at the surface. Each of these steps contributes to the value of the deposition velocity (Seinfeld and Pandis, 2006).

The aim of this study is to perform back trajectory analysis of particulate matter depositions using the HYSPLIT model. Dry deposition fluxes of particulate matters in ambient air were determined using Bergerhoff method in Pamukkale, Denizli, Turkey in April 2015 and May 2015. Analyses of the deposition samples were carried out at the Environmental Engineering Research Laboratory, Environmental Engineering Department, Pamukkale University and dry deposition fluxes were calculated.

DATA AND METHODS

Dry Deposition Sampling

Dry deposition sampling of particulate matters was performed in Pamukkale, Denizli, Turkey in April 2015 and May 2015. The sampling site was an urban region, Kinikli, Denizli under the traffic effect. Dry deposition sampling of particulate matters was performed using Bergerhoff method. The dimensions of sampler were 13 cm of diameter and 26 cm of height. The sampler was transparent, polyethylene and cylindrical. The sampler was placed in a stand at a height of about 0.5 m above the ground in the garden. Ultra-pure water of 500 mL was put to the sampler. The sampler was hold on throughout 2 days. At the end of the dry deposition sampling, dry deposition samples were transferred to the cleaned sample storage containers and brought immediately to the Environmental Engineering Research Laboratory, Environmental Engineering Department, Pamukkale University.

The sampler and laboratory materials were washed with 1:1 HNO_3 acid, then rinsed with tap water and deionized water and dried prior to use. The same procedure was replicate using 1:1 HCl acid (USEPA, 2007).

Analysis of Suspended and Dissolved Solids in Dry Deposition Samples

The analysis of suspended and dissolved solids in dry deposition samples were carried out at the Environmental Engineering Research Laboratory, Environmental Engineering Department, Pamukkale University. The volumes of the samples were measured and recorded. The amount of total suspended solids (TSS) and the amount of total dissolved solids (TDS) were added to each other to determine the total solid matter in the sample.

To analyze suspended solids, the conditioned 0.45 μm cellulose acetate filters (Sartorius) were weighed with analytical balance. The deposition samples of 50 mL were filtered by filtration apparatus. The filter was put to the oven at 103-105 ^{0}C for one hour. Then the filter was cooled for half an hour in the desiccator and weighed with the analytical balance. TSS value was calculated by the following formula:

$$TSS = \frac{A-B}{V} \quad (1)$$

A: Weight of the filter paper and the residue (mg)
B: Weight of the clean filter paper (mg)
V: Volume of sample (L)

To measure total dissolved solids, a clean evaporating dish was conditioned and weighed with analytical balance.

After the sample has been filtered, the filtrate was transferred to the evaporating dish and weighed with analytical balance. The filtrate was put to the oven at 103-105 ^{0}C for one hour. Then it was cooled for half an hour in the desiccator and weighed with the analytical balance. TDS value was calculated as follows:

$$TDS = \frac{A-B}{V} \quad (2)$$

A: Weight of the evaporating dish and the residue (mg)
B: Weight of the clean porcelain evaporating dish (mg)
V: Volume of sample (L)

Calculation of Dry Deposition Fluxes

The dry deposition fluxes of the samples were calculated by the following formula:

$$F = \frac{m}{A \times t} \quad (3)$$

F: Flux (mg m^{-2} day^{-1})
m: Mass of total solid matter (mg)
A: Surface area of the sampler (m^2)
t: Sampling time (day)

Quality Control

Field and laboratory blanks were collected along with the dry deposition samples to determine the contaminants occurred during the sampling, handling, and filtration steps. The particulate matter analyses of these samples were also performed.

Back Trajectory Analysis

The U.S. National Oceanic and Atmospheric Administration (NOAA) HYSPLIT model (Stein et al., 2015; Rolph, 2016) was used to determine back trajectories. Seven-day back trajectories were computed for 500, 1000, and 1500 m above average ground level. The seven-day intervals provide adequate time to follow the movement of air masses coming from other parts of the world.

RESULTS

Dry Deposition Fluxes

The average dry deposition flux of particulate matters was determined as 217.1 ± 27.8 mg m^{-2} day^{-1} in Pamukkale, Denizli, Turkey. The minimum flux was determined as 165.4 mg m^{-2} day^{-1} between May 18-20, 2015, while the maximum flux was observed as 269.2 mg m^{-2} day^{-1} between May 14-16, 2015 (Figure 1).

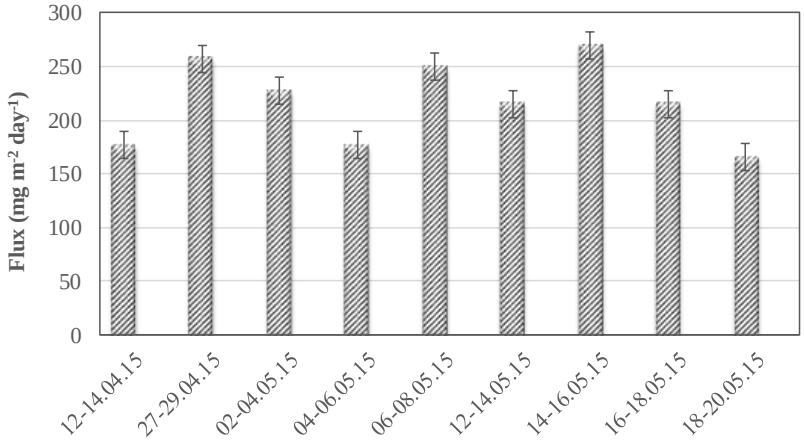

Figure 1. Dry deposition fluxes in Pamukkale, Denizli, Turkey

The flux values at Uludag University, Bursa, Turkey by Bergerhoff method were ranged from 300 to 7860 mg m^{-2} day^{-1} the period of April to June 2001. The daytime flux values (3078 ± 2412 mg m^{-2} day^{-1}) were more than six times the value for nighttime (524 ± 149 mg m^{-2} day^{-1}) (Tasdemir et al., 2004).

Dust samples were collected at monthly intervals from three different sites (commercial, residential, and control) of the Jharia coal mining area, India by Rout et al. (2014). The yearly average dust fall was higher for the commercial site (15.5 t km^{-2} $month^{-1}$) than the residential site (10.7 t km^{-2} $month^{-1}$) of Jharia coal mining area. The dust deposition rate was highest during summer (March–June), followed by winter (October-February) and lowest in the monsoon season (July-September).

Differences between the dry deposition fluxes may be due to regional pollution sources, traffic intensity, and meteorological parameters such as wind speed and wind direction.

Evaluation of Back Trajectory Analysis

The dry deposition events were placed into five classes according to the direction of the seven-day back trajectories of the dominant air masses using the NOAA HYSPLIT model.

The high amounts of particulate matters in dry deposition samples were influenced by the air masses in the Baltic Sea-eastern Europe-Balkans route. It can be assumed that the air masses originated from the northern Europe-Mediterranean-northern African-Mediterranean route transport less particulate matter.

Dry deposition sampling performed between April 12-14, 2015 may be under the influence emissions from the North Atlantic Ocean-northern Europe-Black Sea (Figure 2).

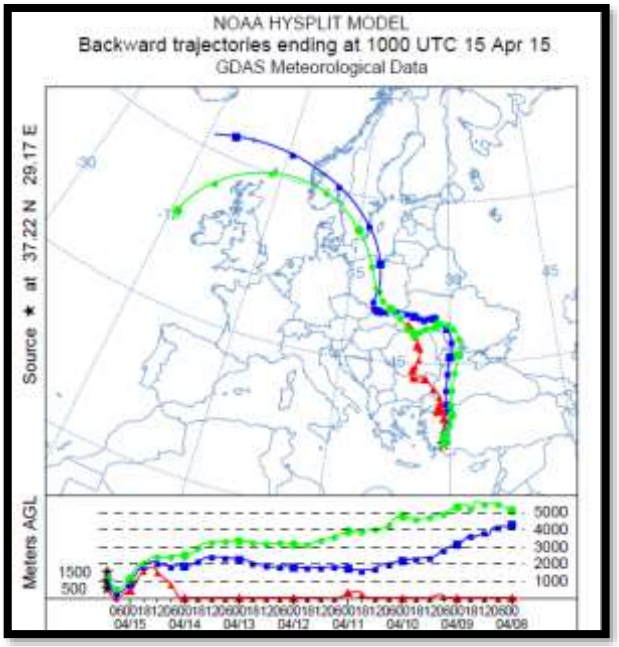

Figure 2. Seven-day back trajectories of the air masses between April 12-14, 2015

Air masses transported from the North Atlantic Ocean-southern Europe-Mediterranean route could affected the dry deposition sampling between April 27-29, 2015 (Figure 3).

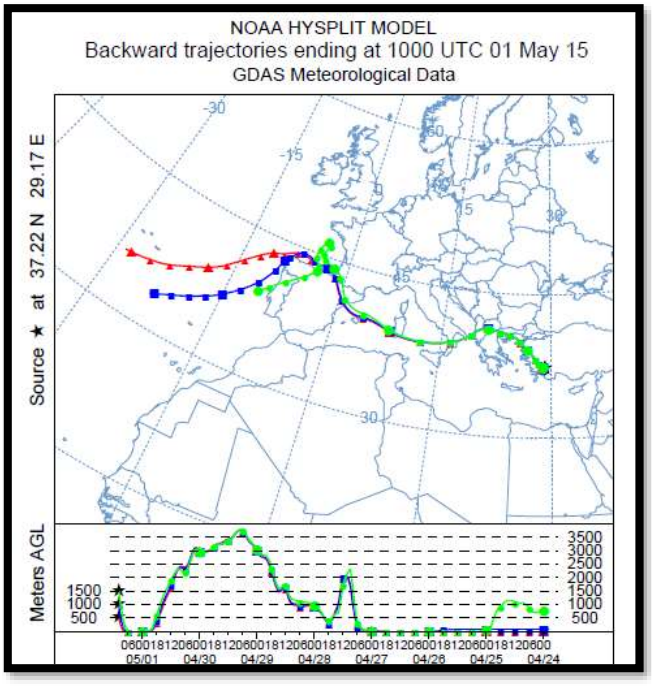

Figure 3. Seven-day back trajectories of the air masses between April 27-29, 2015

Deposition samplings carried out between May 2-4, 2015, May 4-6, 2015, and May 6-8, 2015 may be affected the air masses sourced from the North Atlantic Ocean-Europe (Figure 4).

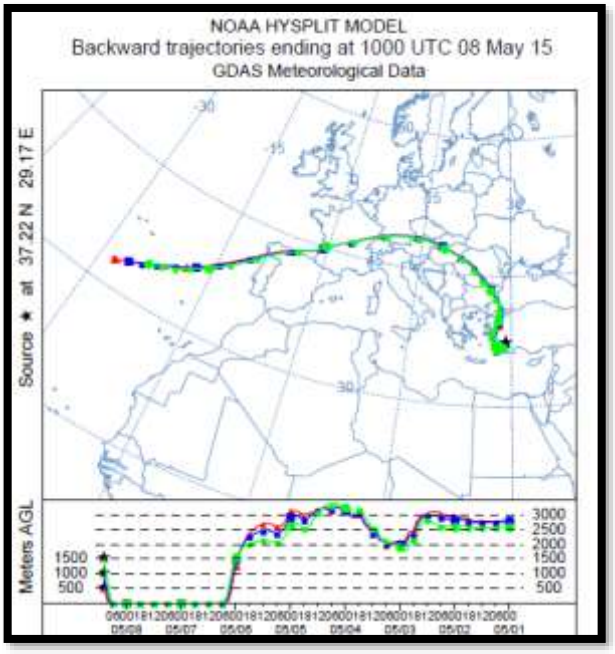

Figure 4. Seven-day back trajectories of the air masses between May 2-8, 2015

Emissions from the Baltic Sea-eastern Europe-Balkans could be effective in the high dry deposition fluxes observed between May 12-14, 2015, and May 14-16, 2015 (Figure 5).

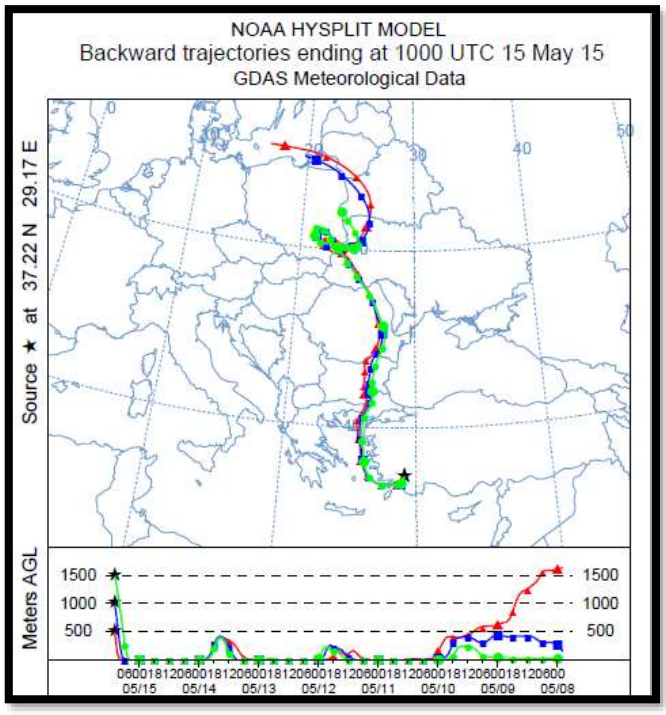

Figure 5. Seven-day back trajectories of the air masses between May 12-16, 2015

Air masses from northern Europe-Mediterranean-northern African-Mediterranean might affected the dry deposition samples determined between May 16-18, 2015, and May 18-20, 2015 (Figure 6).

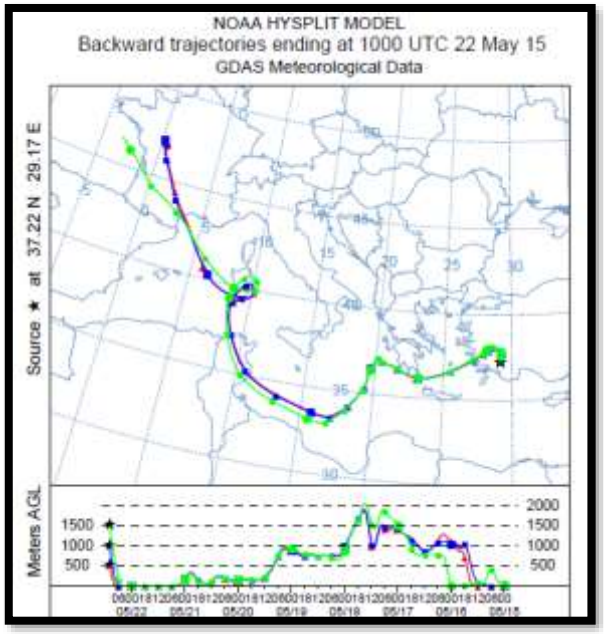

Figure 6. Seven-day back trajectories of the air masses between May 16-20, 2015

The back trajectory analysis was performed for PM_{10} concentrations for the sampling periods in addition to the dry deposition fluxes. The results of this analysis confirmed the results of the back trajectory analysis carried out with flux values. PM_{10} values were obtained from Denizli Air Pollution Measurement Station of the Ministry of Environment and Urban Planning which is closest to the sampling area.

CONCLUSIONS

The backward trajectories of particulate matter depositions were investigated using the HYSPLIT model for the first time in Pamukkale, Denizli, Turkey. It can be assumed that the air masses from the northern Europe-Mediterranean-northern African-Mediterranean route transport less particulate matter while the high fluxes in dry deposition samples may be influenced by air masses in the North Atlantic Ocean-northern Europe-Balkans route.

REFERENCES

Ahmed, E., Kim, K., Shon, Z., and Song, S. 2015. Long-term trend of airborne particulate matter in Seoul, Korea from 2004 to 2013. Atmospheric Environment, 101, 125-133.

Kim, K.H., Pandey, S.K., Nguyen, H.T., Chung, S.Y., Cho, S.J., Kim, M.Y., Oh, J.M., and Sunwoo, Y. 2010. Long-term behavior of particulate matters at urban roadside and background locations in Seoul, Korea. Transportation Research Part D: Transport and Environment, 15, 168-174.

Rolph, G.D. 2016. Real-time environmental applications and display system (READY). College Park, MD: NOAA Air Resources Laboratory. http://www.ready.noaa.gov/hypubbin/trajtype.pl.

Rout, T.K., Masto, R.E., Padhy, P.K., and George, J. 2014. Dust fall and elemental flux in a coal mining area. Journal of Geochemical Exploration, 144, 443-455, 2014.

Seinfeld, J.H., and Pandis, S.N. 2006. Atmospheric Chemistry and Physics, from Air Pollution to Climate Change. 2nd ed., 900-931, New Jersey: John Wiley & Sons Inc.

Stein, A.F., Draxler, R.R., Rolph, G.D., Stunder, B.J.B., Cohen, M.D., and Ngan, F. 2015. NOAA's HYSPLIT atmospheric transport and dispersion modelling system. Bulletin of the American Meteorological Society, 96, 2059–2077.

Tasdemir, Y., Erbaslar, T., and Gunez, H. 2004. Measurement of dry deposition fluxes of atmospheric particulate matters: Application of Bergerhoff method. Journal of Engineering and Natural Sciences, 1, 64-72.

USEPA. 2007. Inorganic Analytes, EPA, Wastes, Hazardous Wastes, Test Methods, SW846. Chapter 3, Revision 4, Washington, DC.

WHO. 2008. Air Quality and Health Questions and Answers. Available from: http://www.who.int/phe/air_quality_q&a.pdf.

CHARACTERIZATION OF A BASIN THROUGH ITS ENVIRONMENTAL SIGNATURE TO IDENTIFY POSSIBLE SOURCES OF POLLUTION; HIGH ATOYAC BASIN, PUEBLA-TLAXCALA, MEXICO

E. Martinez-Tavera[1,2], P.F. Rodriguez-Espinosa[1], G. Rosano-Ortega[2]

1 Centro Interdisciplinario de Investigaciones y Estudios sobre Medio Ambiente y Desarrollo (CIIEMAD), Instituto Politécnico Nacional (IPN), Calle 30 de junio de 1520, Barrio d la Laguna Ticomán, Del. Gustavo A. Madero, C.P.07340 Ciudad de México, México.

2 Universidad Popular Autónoma del Estado de Puebla (UPAEP), 17 sur no. 901 Barrio de Santiago, Puebla, Puebla, México, C.P. 72410, México.

estefmtzt@hotmail.com; pedrof44@hotmail.com; genoveva.rosano@upaep.mx

ABSTRACT

The characterization of an urban river through the integration of physicochemical parameters (Environmental signature) enables us deduce potential sources of contamination, as well as determine the behavior across the basin as a tool for the measurement and monitoring of water quality and management of water resources in one of the most polluted rivers in México. As a result of this work environmental critical points were found and distinguished: agricultural, residential and Industrial discharges. The determination of eleven physicochemical parameters; seven of them instrumental: temperature (T), potential hydrogen (pH), dissolved oxygen (DO), spectral absorption coefficient (SAC), oxide reduction potential (ORP), turbidity (TURB),conductivity (λ), and four from laboratory: biochemical oxygen demand in 5 days (BOD_5), chemical oxygen demand(COD), total suspended solids (TSS) and total dissolved solids (TDS), were evaluated in 65 sites for the dry season in Atoyac, Zahuapan and Alseseca river, High Atoyac Basin, Puebla - Tlaxcala, Mexico. The integration of these physicochemical parameters in an algorithm represent an important tool for environmental interpretation in the different region in these rivers. The geographical localization of the treatment plants and the most important discharges were correlated in space through a water quality index which for dry season denoted a great contamination in four diferent sites whith values since 1055, 1035, 1028 and 1209 of COD (mg/L), until values of 23 and 25 of COD (mg/L) in the pristine sites in the upper of the basin. This project supports the cleanup actions Atoyac, Zahupan and Alseseca river, through the values of water quality parameters in real time, measured and sampled, in the urban area of Puebla and Tlaxcala Cities.

Keywords: *water quality, physicochemical parameters, water management*

INTRODUCTION

Population growth, the rapid process of urbanization and industrialization, the expansion of agriculture, tourism and climate change, put increasing pressure on water availability and pollution. Due to this growing tension, proper management of this vital resource is of crucial importance. The pressure on water resources reveals the hydrological, social, economic and ecological interdependencies that exist in watersheds, lakes and aquifers. Such interdependence requires more integrated approaches to identifying sources of contaminants, as well as developing and managing water and land resources (GWP 2009).

In Mexico, there is not adequate monitoring of water bodies throughout the country due to insufficient economic resources and, therefore, personnel and materials. Due to the above, the total of water bodies of national importance is not sampled (CONAGUA 2010), resulting in a problem of water quality monitoring. This should be continuous in order to record the changes by seasonal and seasonal variation in the different sites, which is fundamental to detect early

alarms in water pollution events. One of the most polluted basins in Mexico is the "Alto Atoyac" in which the rivers Atoyac, Zahuapan and Alseseca are located (CONAGUA 2016, CNA 2003). Within the basin are three volcanoes: Malinche, Iztaccihuatl and Popocatépetl, the latter being an active volcano. In it is the 4th largest metropolitan area of the country, bordering on the west with the megalopolis of Mexico City, has 3,303,6079 inhabitants and more than 24,000 industries in 4,395 km^2 of territory (INEGI 2010).

The objective of the present work is to use an algorithm that allows to characterize the basin, through physicochemical parameters of in situ determination and allows the water managers in the Upper Atoyac Basin to make decisions in time and in a economic way to improve water quality of the rivers, as well as to establish the possible origins of contaminants. This algorithm can be implemented through multi-parameter field or real-time measurement equipment.

MATERIALS AND METHODS

Study area

The "Upper Atoyac Basin" is located in the states of Puebla and Tlaxcala, which are located 120 km from the megalopolis of the City of Méixco, where the fourth largest metropolitan area of the country is located. It is a worldwide automotive manufacturing and assembly center and the site where the Textile Industry begins in Latin America. This, favored an important population growth and of services in the last 20 years in an unplanned way, generating an imbalance in the use of the natural resources and especially of the water.

The region is framed by the presence of an active volcano (Popocatépetl) and two inactive volcanoes (Iztaccíhuatl and La Malinche). Popocatépetl is classified as a stratovolcano, which often erupts from ash and lava, which is composed of andesite, dacite, or rhyolite (Atlas et al. 2006). Recent volcanic eruptions are the continuation of volcanic activity initiated in 1992, where ash eruptions have occurred continuously since 1996 (Mendoza-Rosas and Servando de la Cruz-Reyna 2008). In continental regions, high concentrations of detransition metals in the ash released during volcanic eruptions can directly affect human health (Horwell et al., 2003). Recent studies on trace elements deposition in humans, animals and plants indicate that leachable elements are easily transferred to the water column through which they later directly enter the biological cycle (Rodríguez-Espinosa et al., 2015).

The Alto Atoyac Basin is formed by the rivers Atoyac, Zahuapan and Alseseca which flow into the Manuel Ávila Camacho Dam (Fig. 1). It has 4395 km^2 and has rural, industrial and urban areas. It is composed of the Atoyac River with an extension of 200 km, born in the Sierra Nevada at an altitude of 5000 m, is flanked by the east side by the volcanoes Iztaccihuatl and Popocatepetl (active) and to the west by the Malinche and finally drain in Manuel Ávila Camacho (Valsequillo) dam. Zahuapan river born in the Tlaxco mountains at 3000 m height and has 120 km length until its confluence with Atoyac river (IMTA 2005). Alseseca river born in Malinche volcano at 1086 km elevation and measurement 30.5 km until its drain in Valsequillo dam. The dry season corresponds to the months of March-May, the rainy season from June-September and winter during October-February (National Meteorological Service 2010).

Finally, the basin has a mainly agricultural land use (63.6%), followed by a relatively low forest area (22.0%) and grassland (4.95%); the urban area occupies 7.6 percent, Fig. 1 (INEGI 2010, Martinez-Tavera 2016).

Sampling and analytical techniques

Sixty samples were taken in the dry season; 9 sites on the Zahuapan River, 10 on the Atoyac River before its confluence with the Zahuapan, 10 after its confluence, 13 in Alseseca and 23 in Valsequillo dam. Sampling was designed to cover residencial and industrial discharges, natural soil erosion and the influence of volcanoes.

Sampling, preservation and transportation of water samples to the laboratory was performed according to the methods standardized by APHA (1992).

The physicochemical parameters that were measured *in situ* were: temperature (T), hydrogen potential (pH), conductivity (□). dissolved oxygen (DO), spectral absortion coefficient (SAC), oxidation reduction potential (ORP) and tubidity (TURB), while those measured in the laboratory were: 5-day biochemical oxygen demand (BOD_5), chemical oxygen demand (COD) and total suspended solids (TSS).

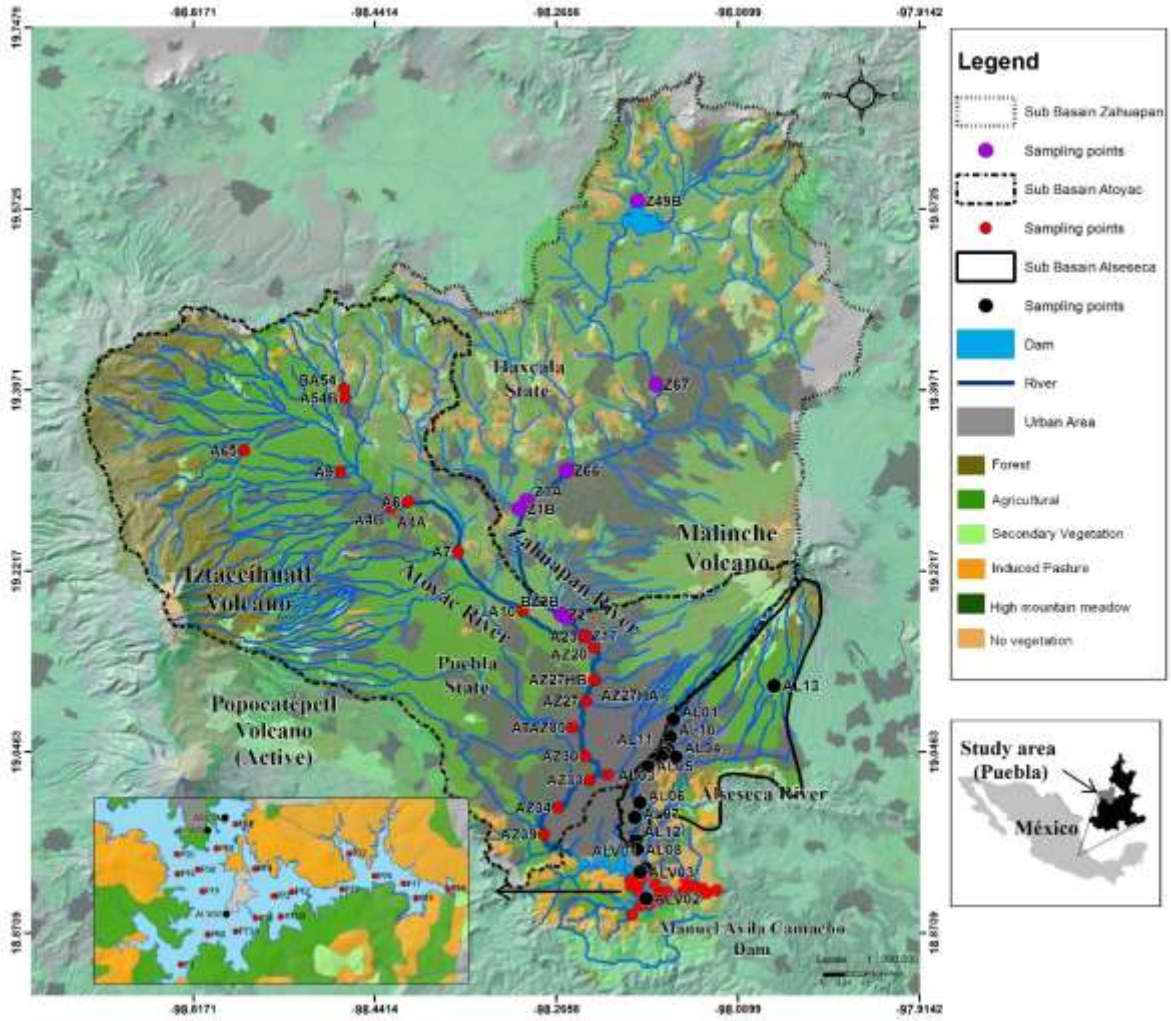

Figure. 1 Study area illustrating sampling locations from Zahuapan, Atoyac, Alseseca and Manuel Ávila Camacho Dam

Algorithms for evaluation of water quality

The proposed mathematical algorithms for the Atoyac River (Martinez-Tavera et al., 2017) were used in the Zahuapan, Alseseca and Valsequillo dam, in order to generate the

environmental signature of the entire basin and to establish the possible sources of contaminants.

The algorithms are:
Algorithm for field recorded physicochemical parameters (AFRPP)

$$\mathbf{APPFR}= \sum_{i=1}^{n} \left(\left|\frac{pH_0-pH_n}{pH_0}\right|\right) + \left(\left|\frac{\lambda_0-\lambda_n}{\lambda_0}\right|\right) + \left(\left|\frac{SAC_0-SAC_n}{SAC_0}\right|\right) + \left(\left|\frac{T_0-T_n}{T_0}\right|\right) + \left(\left|\frac{ORP_0-ORP_n}{ORP_0}\right|\right) + \left(\left|\frac{OD_0-OD_n}{OD_0}\right|\right) + \left(\left|\frac{TURB_0-TURB_n}{TURB_0}\right|\right)$$

Algorithm for laboratory-based physicochemical parameters (ALPP)

$$\mathbf{APPL}= \sum_{i=1}^{n} \left(\left|\frac{\boldsymbol{DBO_{50}-DBO_{5n}}}{\boldsymbol{DBO_{50}}}\right|\right) + \left(\left|\frac{\boldsymbol{DQO_0-DQO_n}}{\boldsymbol{DQO_0}}\right|\right) + \left(\left|\frac{\boldsymbol{SST_0-SST_n}}{\boldsymbol{SST_0}}\right|\right)$$

RESULTS AND DISCUSSION

To characterize the water quality of the Atoyac river through measuring the parameters *in situ* and to infer the parameters that can only be measured in the laboratory, a mathematical algorithm has been proposed(Martinez-Tavera et al. 2017). In the scientific literature, there are mathematical integration proposals that combine in-field and laboratory physicochemical parameters and assign weights to each of the parameters (Wu and Chen 2013). In addition, there are different state-of-the-art proposals for which water quality indexes are used for characterization and to establish policies to adequately manage water quality (Akkoyunlu and Akiner 2012; Bonanno and Giudice 2010; Boyacioglu 2010; Dede et al. 2013; Gazzaz et al. 2012; Golge et al. 2013; Hurley et al. 2012; Kannel et al. 2007; Liu et al. 2011; Lumb et al. 2011; Pesce and Wunderlin 2000; Rahman et al. 2011; Sedeño-Díaz and López-López 2007; Song and Kim 2009; Terrado el al. 2010; Torres et al. 2009).

The results presented here for the algorithm AFRPP and ALPP (Fig. 2 and 3) correspond to samples taken in the dry season; for the Zahuapan River, Atoyac and Valsequillo Dam in 2013 and for the Alseseca River in 2017. As observed in Fig. 2(A and B) and Fig. 3 (A and B), the behaviors of the assimilated and plotted data are similar. In the Fig. 2 (A and B) the upstream regions I and II in the basin, points with similar characteristics to the pristine or low-contamination sites (COD of 40 – 60 mg/L) are observed, as well as in the Manuel Ávila Camacho Dam (region III). In region II, from the confluence with the Zahuapan River, sites with moderated pollution can be observed (COD of 170 – 400 mg/L) and points of maximum value (AZ27HA) is observed, which represents a severe contamination site: COD of 1055 mg/l, BOD_5 of 480 mg/l and pH of 10.25 in the dry season.

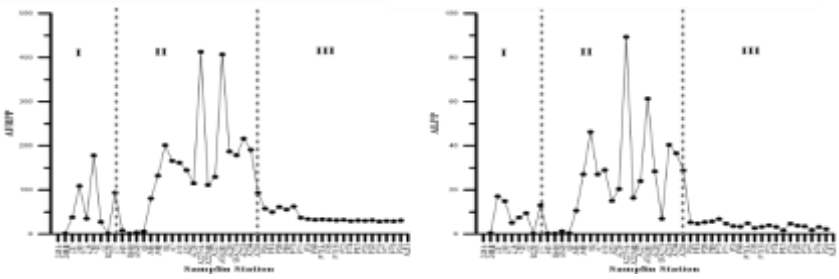

Figure 2 Algorithm for field recorded physicochemical parameters (AFRPP) (A) and Algorithm for laboratory-based physicochemical parameters (ALPP) (B) for Zahuapan (I) and Atoyac (II) river and Valsequillo dam (III). 2013 dry season

The results observed for the Alseseca River through the AFPPP and ALPP algorithms show us not only the similarity between both, but also the sites with the most pollution problems such as point AL09 that corresponds to the industrial zone "Puebla 2000" with a COD (1204 mg/L), BOD_5 (652 mg/L), TDS (2,580 mg/L) and □ (3290 □S/cm). The observed and measurements characteristics of the water sampled at this site reflect the processes of contamination by industrial discharges. Like in the Fig. 2 the high basin has a similar behavior like Valsequillo dam where pollution levels decrease due to sediment deposition and bio filtration performed by the macrophyte consortium present. In figures 2 and 3 we can see that in the upper part of the basin we have predominantly rural areas, as well as in the lower part of the Valsequillo dam generating regions with the lowest pollution. In these same figures, we can observe in the middle part of the basin, the highest concentrations of pollutants due to the industrial zones, as well as to the most populated sites of the basin.

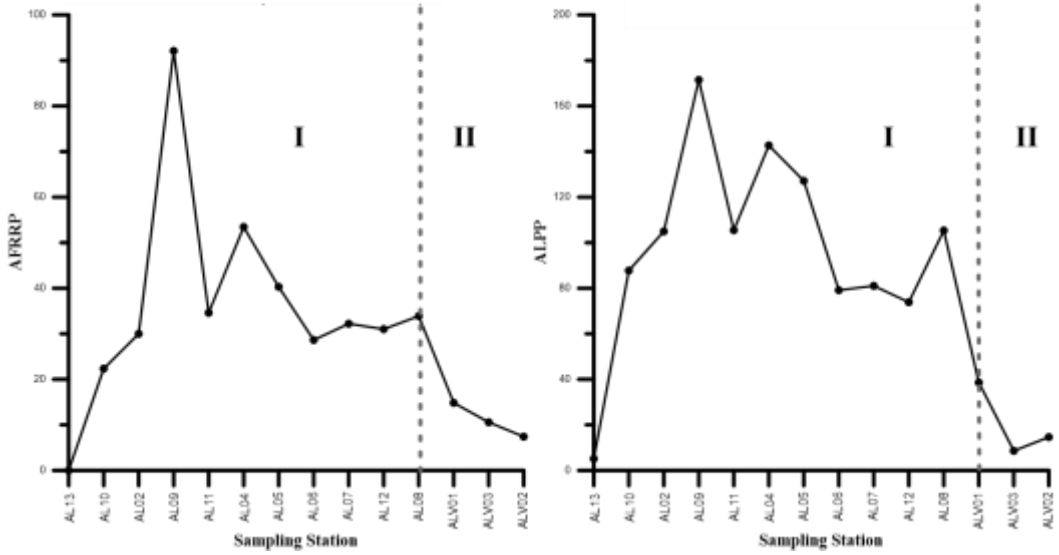

Figure 3 Algorithm for field recorded physicochemical parameters (AFRPP) (A) and Algorithm for laboratory-based physicochemical parameters (ALPP) (B) for Alseseca (I) river and Valsequillo (II) dam. 2017 dry season

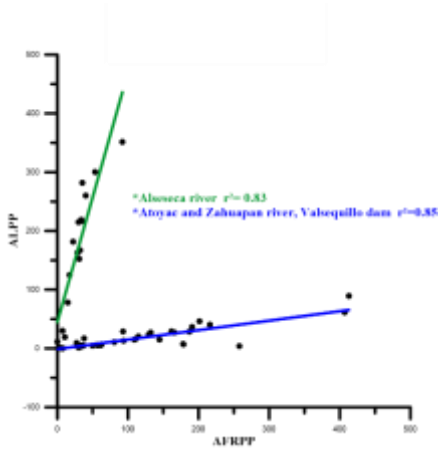

Figure 4 Correlation of AFRPP and ALPP, "High Atoyac Basin" (Zahuapan, Atoyac and Alseseca river and Valsequillo dam), Puebla-Tlaxcala, Mexico

A strong positive correlation was observed between AFRPP and ALPP for Zahuapan, Atoyac river and Valsequillo dam with r^2=0.85 and Alseseca river with a r^2 =0.83. This different slope observed in the correlation of the AFPPP and ALPP algorithm is because the pristine water characteristics are slightly different, since they present a different geology. On the one hand, the river Alseseca is strongly influenced by the volcano La Malinche and on the other the Zahuapan and Atoyac by the Iztaccíhuatl and Popócatepetl (active).

CONCLUSION

"High Atoyac Basin" is a heavily contaminated watershed by not only the Atoyac River, but the Alseseca River. However, the environmental function that develops the Valsequillo dam is an efficient wastewater treatment plant, since although the area in which drains the river Alseseca is very short and does not have different ponds as it happens for the river Atoyac, is enough to significantly improve the quality of water poured into this important reservoir.The physicochemical characteristics of the river basin revealed the influence of the small-scale changes associated with the active Popocatepetl Volcano, as well as by intense human activities. The mathematical algorithms used to characterize the Atoyac River are also suitable for the Alseseca River, which can become an important and economic tool for water quality management in the basin for federal, state and municipal authorities.

REFERENCES

Akkoyunlu, A. and Akiner, M. E. (2012). Pollution evaluation in streams using water quality indices: A case study from Turkey's Sapanca Lake Basin. Ecological Indicators, 18, 501-511. doi:10.1016/j.ecolind.2011.12.018.

Atlas, Z.D., Dixon, J.E., Sen, G., Finny, M., Martin-Del Pozzo, A.L. (2006) Melt inclusions from Volcán Popocatépetl and Volcán de Colima, Mexico: Melt evolution due to vapor-saturated crystallization during ascent. Journal of Volcanology and Geothermal Research, 153: 221-240.

Bonanno, G. and Giudice, R. L. (2010). Application of two Quality índices as monitoring and management tools of rivers. Case Study: the Imera Meridionale River, Italy. Environmental Management, 45(4), 856-867. doi:10.1007/s00267-010-9450-1.

Boyacioglu, H. (2010). Utilization of the wáter quality index method as a classification tool. Environmental Monitoring and Assessment, 167(1–4), 115-124. doi:10.1007/s10661-009-1035-1.

CONAGUA (2010). Estadísticas del Agua en México edición 2010. 10 años de presentar el agua en cifras. México D.F. Secretaría de Medio Ambiente y Recursos naturales.

CNA (2003). Estadísticas del Agua en México 2003. México, D.F.: Comisión Nacional del Agua

Dede, O., Telci, I. T., & Aral, M. M. (2013). The use of water Quality index models for the evaluation of surface water Quality: A Case study for Kirmir Basin, Ankara, Turkey. Water Quality, Exposure and Health, 5(1), 41-56. doi:10.1007/s12403-013-0085-3.

Gazzaz, N. M., Yusoff, M. K., Aris, A. Z., Juahir, H., & Ramli, M. F. (2012). Artificial neural network modeling of the water quality index for Kinta River (Malaysia) using water quality variables as predictors. Marine Pollution Bulletin, 64(11), 2409-2420. doi:10.1016/j.marpolbul.2012.08.005.

Global Water Partnership (2009). Manual para la Gestión Integrada de Recursos Hídricos en Cuencas. Consulted on: http://www.gwp.org/globalassets/global/toolbox/references/a-handbook-for-integrated-water-resources-management-in-basins-inbo-gwp-2009-spanish.pdf (08/10/2017)

Golge, M., Yenilmez, F., Aksoy, A. (2013). Development of pollution indices for the middle section of the lower Seyhan basin (turkey). *Ecological Indicators*, 29, 6-17. doi:10.1016/j.ecolind.2012.11.021.

Horwell, C., Fenoglio, I., Ragnarsdottir, K.V., Sparks, K.S., Fubini, B. (2003). Surface reativity of volcanic ash from the eruption of Sufriere hills volcano, Montserrat, West Indies with implications for health hazards. Environmental Research, 93:20-215

Hurley, T., Sadiq, R., Mazumder, A. (2012). Adaptation and evaluation of the Canadian Council of Ministers of the Environment Water Quality Index (CCME WQI) for use as an effective tool to characterize drinking source water quality. Water Research, 46(11), 3544-3552. doi:10.1016/j.watres.2012.03.061.

IMTA (2005) Estudio de Clasificación del río Atoyac, Puebla-Tlaxcala. México D.F., CONAGUA

INEGI (2010) Censo de Población y Vivienda, 2010. Consulted on (08/10/2017): http://censo2010.org.mx

Kannel, P. R., Lee, S., Lee, Y., Kanel, S. R., & Khan, S. P. (2007). Application of water Quality indices and dissolved oxygen as indicators for river water classification and Urban impact assessment. Environmental Monitoring and Assessment, 132(1–3), 93-110. doi:10.1007/s10661-006-9505-1.

Liu, S., Lou, S., Kuang, C., Huang, W., Chen, W., Zhang, J. *et al.* (2011). Water quality assessment by pollution-index method in the coastal waters of Hebei Province in western Bohai Sea, China. Marine Pollution Bulletin, 62(10), 2220-2229. doi:10.1016/j.marpolbul.2011.06.021.
Lumb, A., Sharma, T. C., Bibeault, J. (2011). A review of Genesis and evolution ofWater Quality Index (WQI) and some future directions. Water Quality, Exposure and Health, 3(1), 11-24. doi:10.1007/s12403-011-0040-0.
Martinez Tavera, E. (2016). Variación Espacio-Temporal de la Calidad del Agua del Río Atoyac, (2013-2014), Puebla, México. phD Tesis. Centro Interdisciplinario de Investigaciones y Estudios sobre Medio Ambiente y Desarrollo del Instituto Politécnico Nacional.
Mendoza-Rosas, A. and Servando de la Cruz-Reyna (2008). A statistical method linking geological and historical eruption time series for volcanic hazard estimations: Applications to active polygenetic volcanoes. Journal of Volacanology and Geothermal Research, 176:227-290.
National Meteorological Service (2010). Consulte don (08/10/2017) http://smn.conagua.gob.mx/es/
Pesce, S., & Wunderlin, D. A. (2000). Use of water quality indices to verify the impact of Córdoba city (Argentina) on Suquía river. Water Research, 34(11), 2915-2926. doi:10.1016/S0043-1354(00)00036-1.
Rahman, I. M. M., Islam, M. M., Hossain, M. M., Hossain, M. S., Begum, Z. A., Chowdhury, D. A. *et al.* (2011). Stagnant surface water bodies (SSWBs) as an alternative water resource for the Chittagong metropolitan area of Bangladesh: physicochemical characterization in terms of water quality indices. Environmental Monitoring and Assessment, 173(1–4), 669-684. doi:10.1007/s10661-010-1414-7.
Rodríguez-Espinosa, P.F., Jonathan, M.P., Morales-García, S.S., Campos Villegas, L.E., Martinez-Tavera, E., Muñoz-Sevilla, N.P., Alvarado Cardona, M. (2015). Metal enrichment of soils following the April 2012-2013 eruptive activity of the Popocatépetl volcano, Puebla, Mexico.
Sedeño-Díaz, J. E. and López-López, E. (2007). Water Quality in the Río Lerma, Mexico: an overview of the last quarter of the twentieth century. Water Resources Management, 21(10), 1797-1812. doi:10.1007/s11269-006-9128-x.
Song, T. and Kim, K. (2009). Development of a water quality loading index based on water quality modeling. Journal of Environmental Management, 90(3), 1534-1543. doi:10.1016/j.jenvman.2008.11.008.
Terrado, M., Barceló, D., Tauler, R., Borrell, E., Campos, S. d, & Barceló, D. (2010). Surface-water-quality indices for the analysis of data generated by automated sampling networks. Trends in Analytical Chemistry, 29(1), 40-52. doi:10.1016/j.trac.2009.10.001.
Torres, P., Cruz, C. H., Patiño, P. J. (2009). Water Quality Index in Surface Sources Used in Water Production for Human Consuption. A Critical Review. Revista Ingenierías Universidad de Medellin, 8(15), 79-94.
Wu, Y. and Chen, J. (2013). Investigating the effects of point source and nonpoint source pollution on the water quality of the East River (Dongjiang) in South China. Ecological Indicators, 32, 294-304. doi:10.1016/j.ecolind.2013.04.002.

TURKEY'S TOTAL OZONE PROJECTIONS USING CMIP5 OZONE DATABASE BASED ON TWO DIFFERENT RCP SCENARIOS (2.6 AND 4.5)

Yılmaz AÇAR[1], Serpil YAĞAN[1], Mithat EKİCİ[1], Osman ESKİOĞLU[1], Hüdaverdi GÜRKAN[1], Ali Ümran KÖMÜŞCÜ[1], Mustafa COŞKUN[1], Yusuf ÇALIK[2]

[1]Turkish State Meteorological Service, Research Department, ANKARA

[2]Turkish State Meteorological Service Meteorological Data Processing Department, ANKARA

yacar@mgm.gov.tr, syagan@mgm.gov.tr, mekici@mgm.gov.tr, oeskioglu@mgm.gov.tr, hgurkan@mgm.gov.tr, aukomuscu@mgm.gov.tr, mustafacoskun@mgm.gov.tr, ycalik@mgm.gov.tr

ABSTRACT

Ozone is a greenhouse gas that has considerable impact in climate change, and therefore it is vital to project future trends in ozone to assess its probable effects on future climate change. In this study, total ozone projections were obtained by using the Coupled Model Intercomparison Project (CMIP5) outputs for Europe and Turkey domain for RCP2.6 and RCP4.5. The fifth phase of the Coupled Model Intercomparison Project (CMIP5) has been developed to ensure that the ozone is represented realistically by obtaining a continuous time series. For the projections, the CMIP5 datasets were obtained with reference to 1971-2000 period. We used the satellite and CMIP5 ozone analysis data for the verification to determine the Mean Error (ME), Mean Absolute Error (MAE), Standard Deviation Error (SDE) and Correlation (r). For the selected domain (30-50 °N latitude, 10-50 °E longitude), projections were produced for the future trends of ozone for the period 2011-2099, namely for 2011-2040, 2041-2070 and 2071-2099 periods. It was observed that there are 6 Dobson Unit (DU) decrease as compared to the reference period for the first period. It is expected that these negative values in 2029 for RCP2.6 and in 2025 for RCP4.5 will be close to zero in other words equal to the reference period values. At the last period, ozone anomalies in all scenarios are predicted to increase as 4 DU and 9 DU respectively for the each scenario.

Keywords: *Ozone, Climate change, CMIP5, IPCC, RCPs.*

INTRODUCTION

Ozone is one of the greenhouse gases that cause climate change although its effect is less than that of CO_2. Continuous ozone time series, which does not involve any interactive chemistry, allow ozone to be represented more realistically in CMIP5 simulations (Cionni et al., 2011). CMIP5 ozone data set are obtained from Ozone database of Atmospheric Chemistry and Climate/Stratospheric Processes and their Role in Climate (AC&C/SPARC). The ozone database covers the period from 1850 to 2099 at global scale (Cionni et al., 2011). We used the satellite ozone data and CMIP5 ozone analysis data for the verification to determine the Mean Error (ME), Mean Absolute Error (MAE), Standard Deviation Error (SDE) and Correlation (r). For the selected domains, projections were produced for the future trends of ozone, with reference period from 1971 to 2000 and for the period 2011-2099, namely for 2011-2040, 2041-2070 and 2071-2099 periods. For the verification, 1979-2008 satellite ozone data and CMIP5 ozone analysis data were used.

In this study, we aimed at putting forward a different view on the current measurement of the ozone data and generated future model scenarios considering the effect of ozone on climate change.

DATA AND METHOD

As stated in the IPCC reports, Turkey is located in the Eastern Mediterranean basin that is one of the most vulnerable regions to climate change. In this study, first step was to determine the next generation scenarios agreed by the IPCC, and then low resolution downscaling of climate models were developed on a global scale (Gürkan, H., et al.). In global climate projections published in IPCC 5th Assessment Report (AR5), 32 for RCP 2.6 and 42 for RCP 4.5 different global model studies were carried out. The most preferred scenarios on a global scale were RCP 4.5 and RCP 8.5 (IPCC, 2013). In this study, a global scale prepared ozone database was used under the Unified Model Comparison Project (CMIP5).

Our study area covers 30-50 °N latitude, 10-50 °E longitude for Europe and a total of forty-five grid intervals and 35-45 °N latitude, 25-45 °E longitude for Turkey and fifteen grids of the domain covers Turkey (see Figure 1).

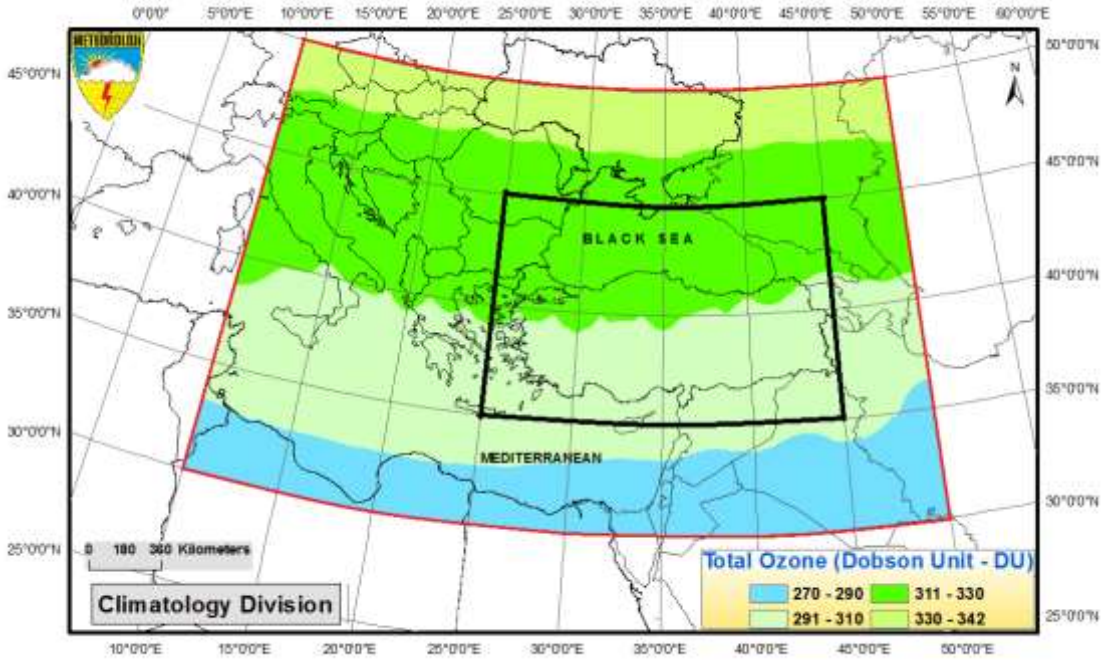

Figure 1. The Europe (red line) and Turkey (black line) domain area.

Anomaly values of the whole data set were obtained with reference to 1971-2000 period. For the verification, satellite data between 1979-2008 were used, CMIP5 total ozone data were analyzed based on the ten grids covering Turkey.

Historical part of the ozone database (from 1850 to 2009) consists of combining stratospheric and tropospheric data sources, which are in separate states (URL 1, http://cmip-pcmdi.llnl.gov/index.html). Stratospheric data is constructed using Polar SAGE I + II satellite observations and polar ozonsonde measurements for the period 1979-2005 using multiple linear regression analysis (Cionni et al., 2011). Tropospheric ozone simulations were carried out using the Chemistry-Climate Models Community Atmosphere Model (CAM) version 3.5 and the NASA-GISS PUCCINI model (Cionni et al., 2011). For the CAM 3.5, a full transient simulation was carried out between 1850-2005 (with a 10-year spin-up after 1850). In NASA-GISS model, between 1850 and 1930, a time slice experiment was taken every 20 years. Every 10 years thereafter, calculations were made in the last 6 years of 8 year simulations for the climatological mean (URL 1, http://cmip-pcmdi.llnl.gov/index.html).

Future part of the ozone database covering the years 2010-2099 is combined with the historical time series up to 2009 to form a single database. The simulations were carried out four different Representative Concentration Pathways (RCPs) up to 2099. The preferred RCP scenarios for the CAM3.5 include RCP 8.5, RCP 6.0, RCP 4.5 and RCP 2.6. These scenarios are not an estimate of future, but they aim to identify possible alternative emission levels (IPCC, 2000).

Satellite ozone data used in this study date back to TOMS measurements in 1978 and are available today with OMI data since 2004 (Ekici, M., et al., 2013). In order to investigate the relation between the CMIP5 model ozone analysis data and satellite total ozone measurements, 30 years of data covering 1979-2008 period were taken into consideration. Ten common grid representing Turkey and the closest grid representing Ankara (40 °N, 35 °E) were selected in the satellite and CMIP5 ozone analysis data for the verification. As for the verification, Mean Error (ME), Mean Absolute Error (MAE), Standard Deviation Errors (SDE) and Correlation (r) values were calculated.

Level-based (1000-1 mb) mixing rates in the NC format are resolved and inserted into the database. Total ozone data sets in Dobson Unit (DU) were obtained from the level-based data. Average level thicknesses and temperatures used for total ozone calculation are calculated from the geopotential elevation and temperature at standard level for high atmospheric observations in Turkey between 1980 and 2016 and the standard atmosphere (Anderson, John D. 2001). In the total ozone calculation, the average main level thicknesses and temperatures from the surface up to 10 mb were taken from standard-level average geopotential heights and temperatures of high atmospheric observations between 1980 and 2016 in Turkey. Average level thicknesses and temperatures above 10 MB were obtained from the geopotential elevation and temperatures of the standard atmosphere (SI) according to international measurement units (SI) (Anderson, John D. 2001).

Anomaly values of the whole data set were obtained with reference to 1971-2000 year. For the verification, satellite data between 1979-2008 and total ozone data of CMIP5 were evaluated for the ten grids covering Turkey.

HISTORICAL DIVISION OF OZONE DATABASE (1850-2009)

The historical part of the ozone database (from 1850 to 2009) consists of combining stratospheric and tropospheric data sources which exist in separate forms. The most appropriate option for producing radiation forces that chancing according to the past is to create a three dimensional (latitude, longitude, elevation) ozone time series based on observations. However, observations are not available for all atmosphere and all periods. For this reason, regression data completion or CCM output were used to obtain the data set covering the entire area (URL 1, http://cmip-pcmdi.llnl.gov/index.html).

As described in Randel and Wu (JGR, 2007), polarized SAGE I + II satellite observations and polar osonsonde measurements were constructed using multiple linear regression analysis for the period 1979-2005. The regression contains terms equivalent to the Equivalent Effective Stratospheric Chlorine (EESC) and 11-year solar cycle variability. The stratospheric time series dating back to the 1850s were constructed using EESC and solar variability and adapted to regression (Cionni et al., 2011).

Tropospheric data are derived from model simulations. Tropospheric ozone simulations were conducted using the Chemistry-Climate Models Community Atmosphere Model (CAM)

version 3.5 and the NASA-GISS PUCCINI model. Both tropospheric and stratospheric model chemistry simulated by radiation and the feedback of recent historical emissions at hand are briefly described by Lamarque et al. (IGAC Newsletter, May 2009). In addition, while CAM NASA-GISS PUCCINI mode, used the observed SSTs, the previous CCSM3 simulation used SSTs (Rayner et al., JGR, 2003 Hadley Center dataset), Cionni et al., 2011).

For CAM3.5, a full transient simulation was carried out between 1850 and 2005 (with a 10-year turnaround after 1850). In the NASA-GISS model, however, imaging was performed between 1850 and 1930, every 20 years instant, and after 1930, imaging was carried out every 10 years for the last 6 years of 8 year simulations. For climatology, a 10-year annual average was obtained for each model, then the NASA-GISS results were interpolated with the CAM 3.5 vertical grid and the averages of both were taken. For climatology, a 10-year annual average was obtained for each model, then the NASA-GISS results were interpolated with the CAM 3.5 vertical grid and the averages of both were taken. This average area represents the area of tropospheric ozone in climatology. A simple data set has been produced as a result of the simple integration of stratospheric and tropospheric data throughout the climatological tropopause (URL 1, http://cmip-pcmdi.llnl.gov/index.html).

FUTURE PART OF OZONE DATA BASE (2010 - 2099)

The future part of the ozone database covering the years 2010-2099 was merged with the historical time series until 2009. Future three-dimensional (latitude, longitude, elevation) tropospheric ozone time series continues in the historical CAM3.5 model, but it does not continue in the NASA GISS-PUCCINI model. RCP emissions were produced in both amplitudes and geographical distribution by the Integrated Assessment Models (IAMs). The RCP emissions have been harmonized with historical emissions. The preferred RCP scenarios for CAM3.5 include: RCP 2.6, RCP 4.5, RCP 6.0, and RCP 8.5. These scenarios are not an estimate of future, but rather they are the identification of possible alternative emission situations (IPCC, 2000). Here, the RCP shows the radiation enforcement in W / m², which comes from long-lived greenhouse gases for each scenario and reaches up to 2100 years. Since the RCPs for the simulation starting dates of the combined climate models are not defined, sea surface temperature (SST) of the nearest SRES (Emission Scenario Special Report) scenarios belong to this period were used (Cionni et al., 2011).

TOMS (OMI) SATELLITE OZONE DATA

Total Ozone Mapping Spectrometer (TOMS) is an ozone sensor used by NASA in observing ozone. Observations are made spectrometers placed in satellites and the obtained data is called TOMS ozone data. Current measurements under the TOMS program began in November 1978 using the TOMS module on the Nimbus-7 spacecraft, and ended in May 1993. Instead, the Meteor-3 TOMS began to transmit data in August 1991 and ended its operation in December 1994. Initially, the data obtained with the Earth Probe (EP) TOMS was completed with the data obtained from the ADEOS TOMS due to its high orbital and full equatorial characteristics. OMI is a NADIR imaging system with NASA's Earth Observation System Aura Satellite deck UV / Visible CCD Spectrometer. Aura satellite has been sending data since August 9, 2004 (Ekici, M., et al., 2013).

MODEL DATA VERIFICATION AND RESULTS

In order to identify the relation between the CMIP5 ozone analysis data and the satellite total ozone measurement data, 30 years data between 1979 and 2008, which are common in both data sets, were taken into consideration. In the satellite and CMIP5 ozone analysis data for the verification, 10 joint grids representing Turkey and the closest grid representing Ankara (40°

N, 35° E) were selected. During the evaluation of the verification, The Mean of Errors (ME), the Mean Absolute Mean of Errors (MAE), the Standard Deviation of Errors (SDE), and the Correlation (r) were examined.

The Mean of Errors (ME) indicates the direction of the error that occurred in the positive or negative direction of the predicted value. When ME values are examined, it is noticed that the values of all grids vary between -9.6 and -23.6, and the grid value representing Ankara was -14.5. These negative ME values can be expressed as CMIP5 projections producing lower estimates than those of the satellite data (Figure 2 and Table 1).

The Absolute Average of Errors (MAE) shows the average size of the errors. When MAE values are examined, it is noticed that the values of all grids fluctuate between 12.3 and 23.7, and the grid value representing Ankara is 15.9 (Table 1). According to satellite ozone measurements, the average of long years in Turkey is 318 (Ekici, M., et al., 2013), and it is seen that these two absolute error values in all grids correspond to 3.9% and 7.4%.

The Standard Deviation of Errors (SDE) is the measure of the spread of the ME value. It can be clearly seen how the ME values are deviating from the estimation and observation bases. When the SDE value is examined, it is observed that the values of all grids are changed between 12.4 and 14.2, and the grid value representing Ankara is 13.3. The SDE value close to zero indicates the accuracy of the model results (Table 1).

R value changes between 0.86 and 0.91 for all grids, and the grid value representing Ankara is 0.91. That indicates that the satellite measurement and the model estimates are statistically compatible with each other.

Table 1. Standard Deviation of Seasonal Errors (SDE) and Correlation Coefficient (r) values for Turkey and for Ankara in the comparison study of CMIP5 ozone analysis data with satellite ozone data.

	WINTER		**SPRING**		**SUMMER**		**FALL**		**Annual AVERAGE**	
	SDE	r	SDE	r	SDE	r	SDE	r	SDE	r
TURKEY	13.7-16.6	0.67-0.77	14.3-17.7	0.30-0.56	5.58-8.35	0.79-0.88	8.02-9.40	0.11-0.41	12.4-14.2	0.86-0.91
ANKARA	15.7	0.76	17.3	0.47	8.1	0.88	8.7	0.23	13.3	0.91

When analyzing the seasonal variation of the SDE, it is noticed that they are higher than the values in the summer and autumn seasons, because of ozone-rich air masses affect our country during the winter and spring seasons (Acar, Y., et al., 2013). The SDE values are also lower because ozone-poor air masses affect our country during the summer and autumn seasons. When the seasonal variation of the correlation coefficient is examined, it is seen that the correlation values in the spring and autumn seasons are low, while the winter and summer seasons correlations are high (Table 1).

CMIP5 ozone analysis data is generally lower than satellite ozone measurement data (Figure 2). This is seen especially in spring and autumn seasons (Table 1). It is concluded that CMIP5 ozone analysis data can not well represent the effect of air masses on ozone in spring and autumn.

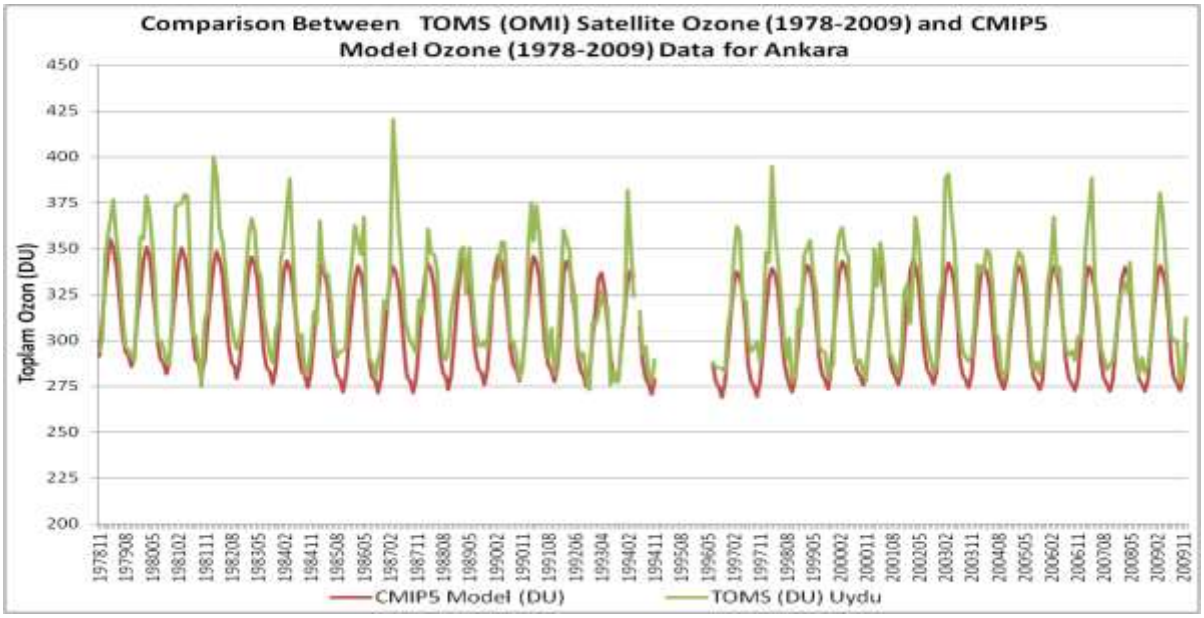

Figure 2. Change in TOMS (OMI) satellite ozone and CMIP5 ozone analysis data of Ankara (1978-2009).

CHANGE BEFORE RCP SCENARIOS

The simulations covering 2010-2099 period of the ozone database and forming the future part are followed by four different Concentration Concentration Routes (RCP 2.6, RCP 4.5, RCP 6.0 and RCP 8.5). 15 grid representing Turkey from CMIP5 ozone database and the closest grid (40 ° N, 35 ° E) representing Ankara were selected. Projections were produced during 2011-2099 period based on the 1971-2000 reference period. For the periods 2011-2040, 2041-2070, 2071-2099, projection outputs of ozone data were obtained.

OZONE PROJECTION FOR EUROPE, TURKEY AND ANKARA (2010-2099 PERIOD)

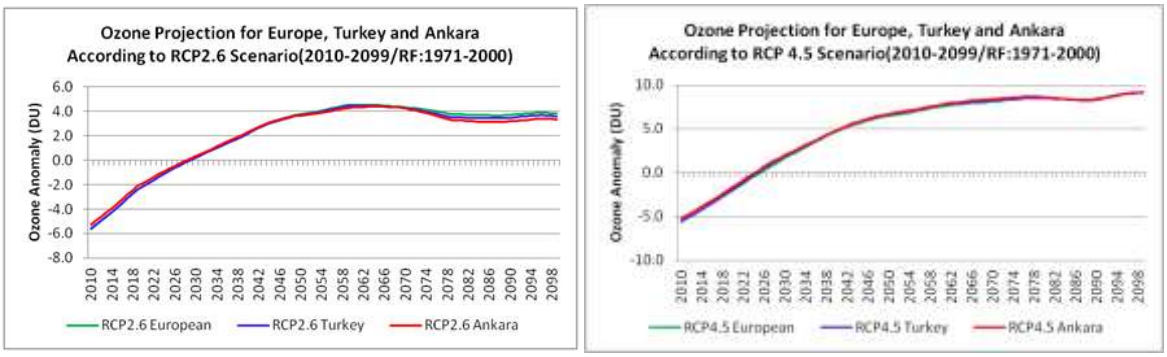

Figure 3. RCP 2.6 and RCP 4.5 ozone projections of Europe, Turkey and Ankara during 2010-2099 period according to 1971-2000 normal.

In Europe, Turkey and Ankara during the 2010-2099 period, the change of all RCP ozone projections seems to be very close to each other and even some years they are equal.

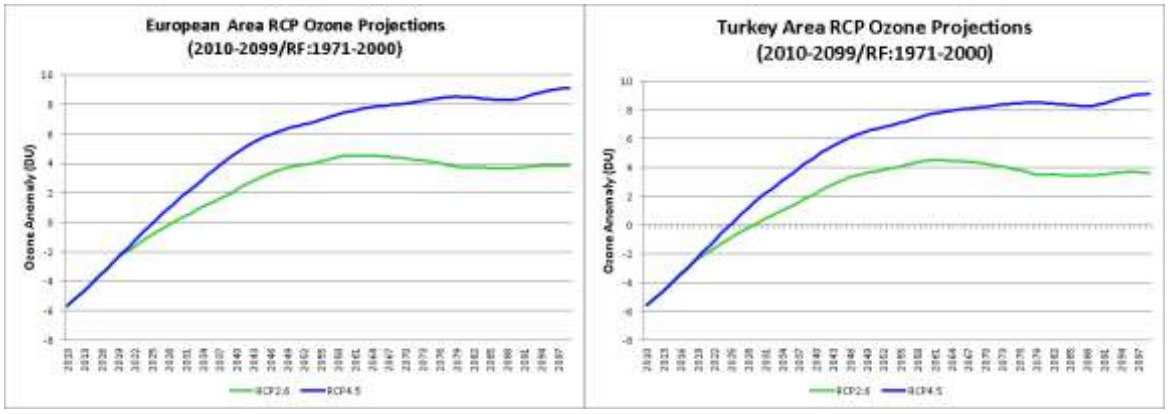

Figure 4. Europe and Turkey area ozone anomaly change in both projections during 2010-2099 period according to 1971-2000 normal.

At the beginning of the period, there are projections for Europe, Turkey and Ankara to be close to 6 Dobson Unit which shows decreasing trends in accordance withthe 1971-2000 reference period.

It is expected that those negative values in 2029 for RCP2.6 and 2025 for RCP4.5 will be close to zer. In other words they are equal to the reference period values. At the end of the period, ozone anomalies are predicted to increase in both scenarios as 4 DU and 9 DU respectively (Figure 3 and Figure 4). Based on the ozone projections of different models, WMO's 2014 Ozone Analysis Review Report stated the total ozone projected for the 2017-2026 period will come back to 1980's levels in the northern hemisphere mid-latitudes (WMO, 2014).

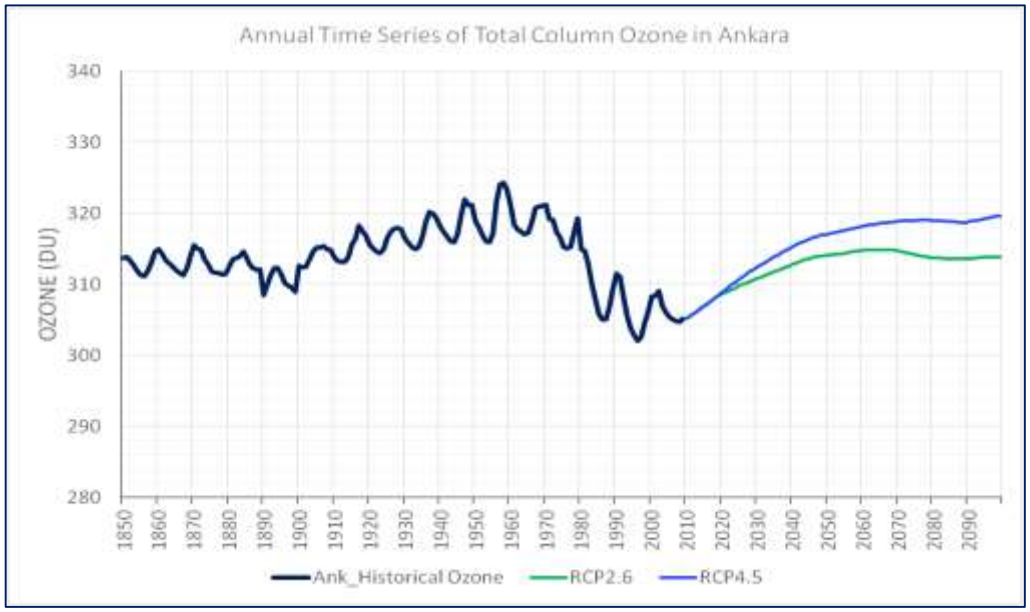

Figure 5. Ankara's annual average total ozone (DU) time series (1850-2099).

When the annual average total ozone time series of Ankara in the CMIP5 ozone database is analyzed, it is seen that historical historical data (1850-2009) vary between approximately 300 and 325. In the total ozone time series, there is a rise from 1850 to 1958 and there was a decline between 1959-1980 years. There is also a sharp downward trend between 1981-1997. From the beginning of the 2000s a tendency for recovery and the start of an upward trend began

again. It was seen that the highest annual average ozone value in the time series was 324.3 in 1958, also the lowest ozone value was 302.1 in 1996 (Figure 5). When total ozone (DU) values of two different RCP scenarios related to the future period of Ankara (2010-2099) are examined, it is predicted that at the beginning of the period starting values at about 305 DU and at the end of the period for RCP 2.6 will reach 314 (0.0%) while RCP 4.5 the values will reach 320 (1.9%) (Figure 5).

MONTHLY AND SEASONAL OZONE PROJECTION FOR RCP 2.6 SCENARIO TURKEY AND ANKARA 2011-2040 PERIOD

When taking the 1971-2000 reference period, for, the highest monthly ozone anomaly value is estimated to be 3.2 DU in March and the lowest monthly ozone anomaly value is estimated to be -4.7 DU in August for Turkey for 2011-2040 period of RCP2.6 scenario. For Ankara, it is predicted that the highest monthly ozone anomaly value will be 5.0 DU in March and the lowest ozone anomaly value will be -5.5 DU in September (Fig. 6).

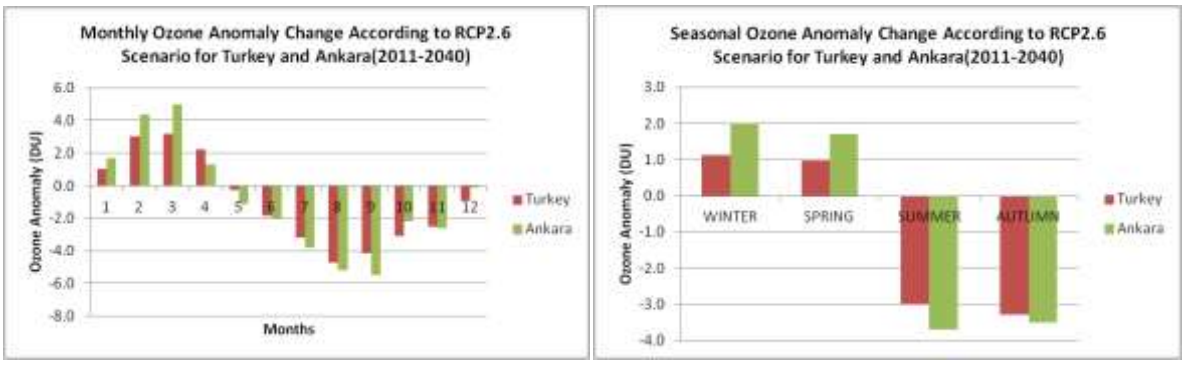

Figure 6. According to RCP 2.6 scenario,monthly and seasonal ozone anomaly values expected in the period of 2011-2040 in Turkey and Ankara (RF: 1971-2000).

It is predicted that seasonal ozone anomaly values for Turkey and Ankara are 1.1 DU and 2.0 DU in the winter, 1.0 DU and 1.7 DU in the spring, -3.0 DU and -3.7 DU in the summer, and -3.3 DU and -3.5 DU in the autumn (Figure. 6).

2041-2070 Period

When taking the 1971-2000 reference period, it is predicted that the highest monthly ozone anomaly value for Turkey will be 14.0 DU in February and the lowest ozone anomaly value will be -5.0 DU in September for 2041-2070 period of the RCP2.6 scenario. For Ankara, it is predicted that the highest monthly ozone anomaly value will be 15.9 DU in March and the lowest ozone anomaly value will be -6.8 DU in September (Figure 7).

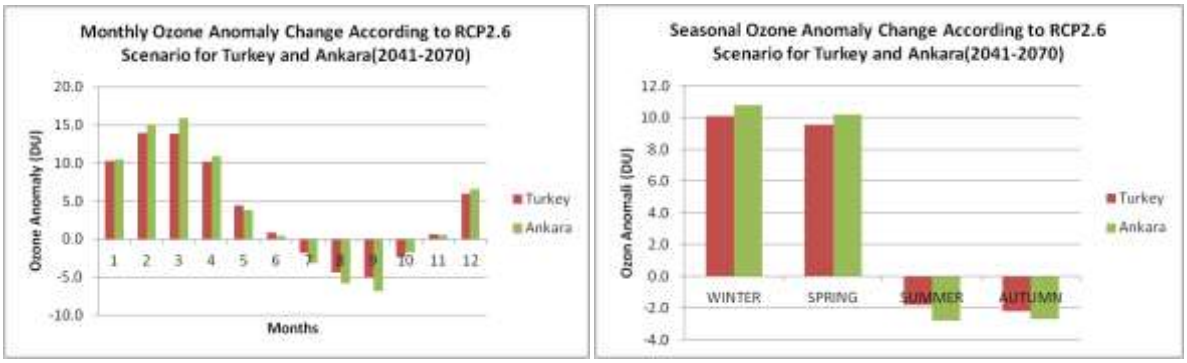

Figure 7. According to RCP 2.6 scenario,monthly and seasonal ozone anomaly values expected in the period of 2041-2070 in Turkey and Ankara (RF:1971-2000).

For Turkey and Ankara, it is predicted that seasonal ozone anomalies will be 10.1 DU and 10.8 DU in the winter, 9.5 DU and 10.2 DU in the spring, -2.2 DU and -2.7 DU in the autumn, and -1.8 DU and -2.8 DU in the summer (Figure 7).

2071-2099 Period

When taking the 1971-2000 reference period, it is predicted that the highest monthly ozone anomaly value for Turkey general will be 17.6 DU in February and the lowest ozone anomaly value will be -9.0 DU in September for 2071-2099 period of the RCP 2.6 scenario.

For Ankara, it is predicted that the highest monthly ozone anomaly value will be 19.0 DU in March and the lowest ozone anomaly value will be -11.6 DU in September (Figure 8).

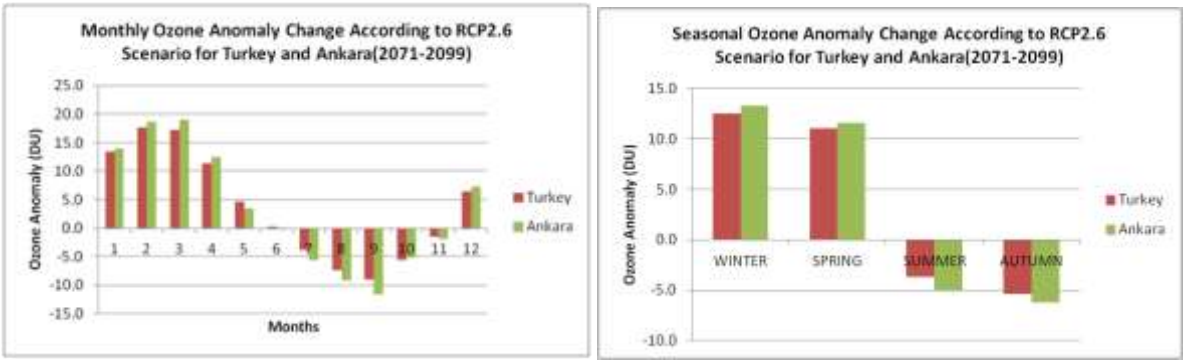

Figure 8. According to RCP 2.6 scenario, monthly and seasonal ozone anomaly values expected in the period of 2071-2099 in Turkey and Ankara (RF:1971-2000).

For Turkey and Ankara, it is predicted that seasonal ozone anomalies will be 12.5 DU and 13.3 DU in the winter, 11.1 DU and 11.6 DU in the spring, -5.4 DU and -6.2 DU in the autumn -3.7 DU and -5.0 DU in the summer (Figure 8).

MONTHLY AND SEASONAL OZONE PROJECTION FOR RCP 4.5 SCENARIO TURKEY AND ANKARA 2011-2040 PERIOD

According to the norms of 1971-2000, for 2011-2040 period of RCP 4.5 scenario, the highest monthly ozone anomaly value is estimated to be 3.8 DU in March and the lowest monthly ozone anomaly value is estimated to be -3.5 DU in September for Turkey. For Ankara, it is predicted that the highest monthly ozone anomaly value will be 5.6 DU in March and the lowest ozone anomaly value will be -4.4 DU in September (Figure. 9).

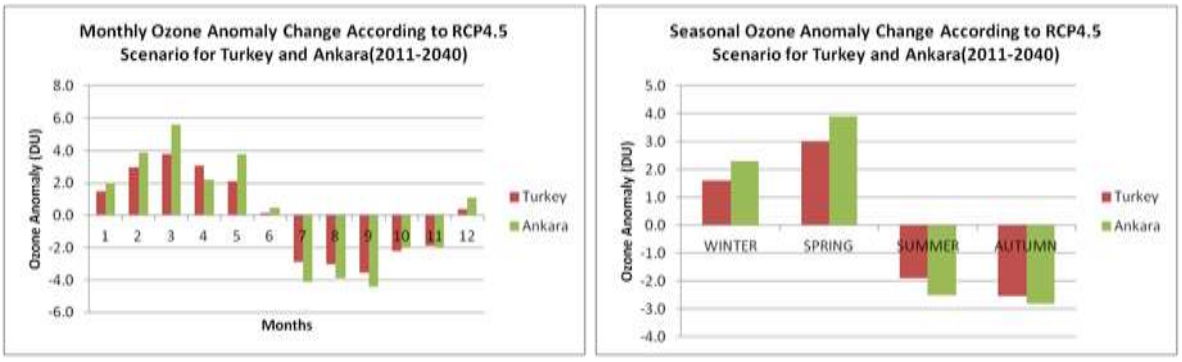

Figure 9. According to RCP 4.5 scenario, monthly and seasonal ozone anomaly values expected in the period of 2011-2040 in Turkey and Ankara (RF:1971-2000).

It is predicted that seasonal ozone anomaly values for Turkey and Ankara are 1.6 DU and 2.3 DU in the winter, 3.0 DU and 3.9 DU in the spring, -1.9 DU and -2.5 DU in the summer, -2.5 DU and -2.8 DU in the autumn (Figure. 9).

2041-2070 Period

When taking the 1971-2000 reference period, it is predicted that the highest monthly ozone anomaly value for Turkey will be 16.3 DU in March and the lowest ozone anomaly value will be -1.8 DU in September for 2041-2070 period of the RCP4.5 scenario. For Ankara, it is predicted that the highest monthly ozone anomaly value will be 18.1 DU in March and the lowest ozone anomaly value will be -3.0 DU in September (Figure 10).

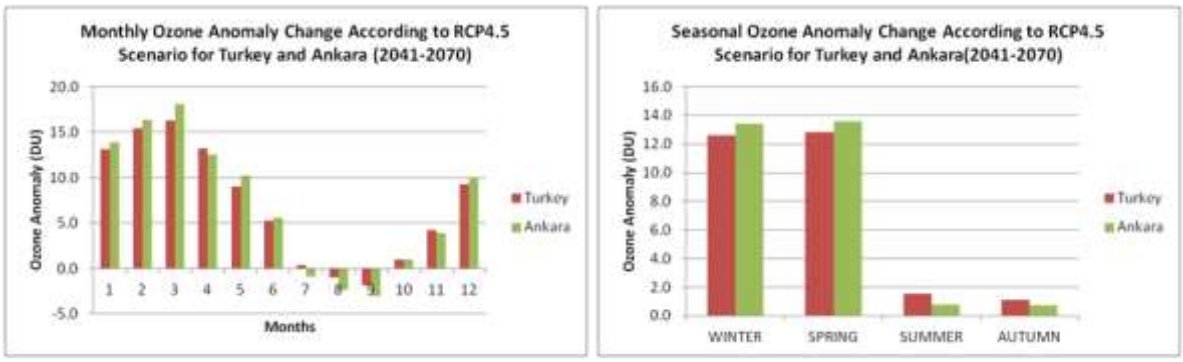

Figure10. According to RCP 4.5 scenario, monthly and seasonal ozone anomaly values expected in the period of 2041-2070 in Turkey and Ankara (RF:1971-2000).

For Turkey and Ankara, it is predicted that seasonal ozone anomalies will be 12.6 DU and 13.4 DU in the winter, 12.8 DU and 13.6 DU in the spring, 1.1 DU and 0.7 DU in the autumn, and 1.5 DU and 0.8 DU in the summer (Figure 10).

2071-2099 Period

When taking the 1971-2000 reference period, it is predicted that the highest monthly ozone anomaly value for Turkey will be 21.3 DU in February, and the lowest ozone anomaly value will be -4.1 DU in September for 2071-2099 period of the RCP4.5 scenario. For Ankara, it is predicted that the highest monthly ozone anomaly value will be 22.7 DU in March and the lowest ozone anomaly value will be -5.6 DU in September (Figure 11).

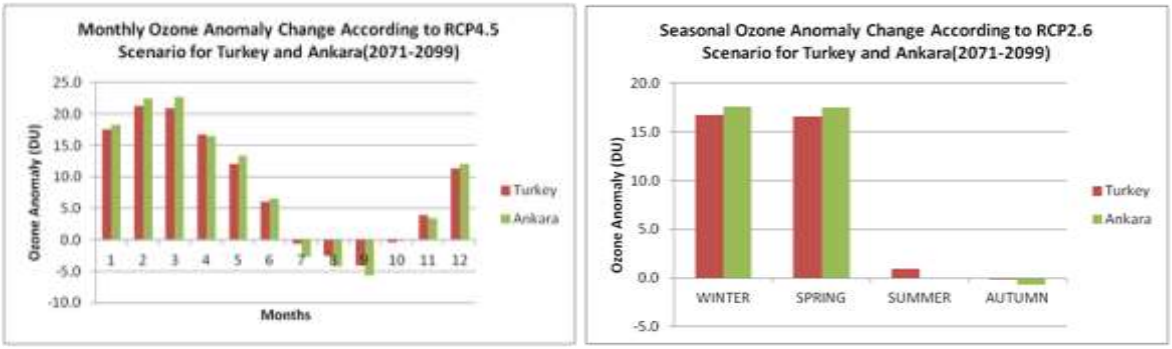

Figure11. According to RCP 4.5 scenario, monthly and seasonal ozone anomaly values expected in the period of 2071-2099 in Turkey and Ankara (RF:1971-2000).

For Turkey and Ankara, it is predicted that seasonal ozone anomalies will be 16.7 DU and 17.6 DU in the winter, 16.6 DU and 17.5 DU in the spring, -0.2 DU and -0.7 DU in the autumn, and

0.9 DU and -0.1 DU in the summer (Figure 11). Ozone anomaly values for Turkey and Ankara are predicted to decrease for RCP2.6 and RCP4.5 in 2011-2040 period, and increase in 2041-2070 and 2071-2099 periods. The highest monthly positive anomalies for all periods of ozone in Turkey and Ankara are predicted in March (2041-2070 and February 2071-2099) and the lowest negative anomalies in September (August and September 2011-2040, 2041-2070 in August).

CONCLUSION

The CMIP5 ozone analysis values are generally lower than those of satellite ozone measurements. This is especially evident in the spring and autumn seasons. It is seen that the CMIP5 ozone analysis data can not represent the effect of air masses on ozone in spring and autumn very well. In the 2010-2099 period, the change in all RCP ozone projections seems to be very close to each other and equal in some years for Europe, Turkey and Ankara. At the beginning of the period, for Europe, Turkey and Ankara the projection foresee approximately 6 Dobson Unit decrease according to the 1971-2000 reference period. It is expected that those negative values in 2029 for RCP2.6 and 2025 for RCP4.5 will be close to zero in other words equal to the reference period values. At the end of the period, ozone anomalies are predicted to increase in both scenarios as 4 DU and 9 DU respectively. Ozone anomaly values for Turkey and Ankara decreased in RCP 2.6 and 4.5 in 2011-2040 period. It is predicted that the values will rise in both scenarios for 2041-2070 and 2071-2099 periods. For Turkey and Ankara, it is predicted that the biggest monthly positive ozone anomaly in all periods will be in March and the lowest negative ozone anomaly will be in September in RCP 2.6 and RCP 4.5. Similarly, it is predicted that the biggest seasonal positive ozone anomalies in all periods will be in spring and the lowest negative ozone anomaly will be in the fall in RCP 2.6 and RCP 4.5.

REFERENCES:

Acar, Y., Yağan, S., Ekici, M., Ersoy, S., Akçakaya, A., ve Eskioğlu, O. 2013, Türkiye Üzerine Gelen Hava Kütlelerinin Ankara'nın Toplam Ozon Kalınlığı Üzerine Etkisi, III. Türkiye İklim Değişikliği Kongresi, TİKDEK 2013, İstanbul.

Anderson, John D. Jr. Fundamentals of Aerodynamics, 3rd edition, 2001. Appendix D, URL: http://highered.mheducation.com/sites/dl/free/0073398101/834219/and50463_appD.pdf.

Cionni, I., V. Eyring, J. F. Lamarque, W. J. Randel, D. S. Stevenson, F. Wu, G. E. Bodeker, T. G. Shepherd, D. T. Shindell, and D. W. Waugh. 2011, Ozone database in support of CMIP5 simulations: results and corresponding radiative forcing, Atmos. Chem. Phys. Discuss., 11, 10875-10933, doi:10.5194/acpd-11-10875-2011.

Ekici, M., Eskioğlu, O., Acar, Y., Demircan, M., ve Akçakaya, A. 2013, TOMS ve OMI Uydu Türkiye Ozon Verilerinin CBS Ürünleriyle Analizi (1979-2012), III. Türkiye İklim Değişikliği Kongresi, TİKDEK 2013, İstanbul.

Gürkan, H., Arabacı, H., Demircan, M., Eskioğlu, O., Şensoy, S., Yazıcı, B. 2016, "GFDL-ESM2M Modeli Temelinde RCP4.5 ve RCP8.5 Senaryolarına Göre Türkiye İçin Sıcaklık ve Yağış Projeksiyonları", Coğrafi Bilimler Dergisi, 14(2): 77-88. DOI:10.1501/Cogbil_0000000174 http://dergiler.ankara.edu.tr/dergiler/33/2149/22251.pdf.

Gürkan, H., Demir,Ö., Atay, H., Eskioğlu, O., Demircan, M., Yazıcı, B., Kocatürk, A., Akçakaya, A. 2015, "MPI-ESM-MR Modelinin RCP4.5 ve RCP8.5 Senaryolarına Göre Sıcaklık ve Yağış Projeksiyonları", VII. Uluslararası Katılımlı Atmosfer Bilimleri Sempozyumu, 28-30 Nisan 2015, İstanbul Teknik Üniversitesi İstanbul Aydın Üniversitesi, İstanbul, Türkiye, http://www.atmosfer.itu.edu.tr/wp-content/uploads/2015/05/Cilt2.rar.

IPCC, 2000, Special Report on Emissions Scenarios, Cambridge University Press.

IPCC, 2013, Climate Change 2013, The Physical Science Basis, Working Group I Contribution to the Fifth Assessment Report of the Intergovernmental Panel on Climate Change, Cambridge University Press. http://www.climatechange2013.org/images/report/WG1AR5_ALL_FINAL.pdf

Taylor, K. E., Stouffer, R. J., and Meehl, G. A. 2009, A Summary of the CMIP5 Experiment Design, available at: http://cmip.llnl.gov/cmip5/docs/Taylor CMIP5 design.pdf.

URL 1, (http://cmip-pcmdi.llnl.gov/index.html)

URL 2, (https://www.mgm.gov.tr/FILES/arastirma/ozonuv/OveUveri-analizi.pdf).

WMO, 2014, Scientific Assessment of Ozone Depletion: 2014, Global Ozone Research and Monitoring Project–Report No. 55, Geneva, Switzerland.

ASSESSMENT OF AIR POLLUTION REDUCTION AND ECONOMIC BENEFITS OF BIOETHANOL-BLENDED GASOLINE USE IN TURKEY

Özge ÖSTÜRK[1], Orhan SEVİMOĞLU[2]
[1]*Department of Environmental Engineering, Gebze Technical University, Gebze, Kocaeli, 41400, Turkey*
osturk@gtu.edu.tr
[2]*Department of Environmental Engineering, Gebze Technical University, Gebze, Kocaeli, 41400, Turkey*
sevimoglu@gtu.edu.tr

Abstract
Exhaust emissions from vehicles impact on the decreasing of the urban air quality due to mainly emission of Particle Matter (PM) and Hydro Carbons (HC). Gasoline enrichment with ethanol has been considered for a decade. The main purposes for use of ethanol in gasoline is to increase oxygen content while burning fuel, and decreasing of emission for PM, CO and HC. The other promoting is that the depletion of fossil fuels in the World promotes the consumption of alternative fuel in vehicles.In this study, the concentrations of pollutants emitted in the atmosphere in Turkey were calculated using the emission values obtained from the literature for gasoline and ethanol fuels. Also, the selling price of E10 and E85 was found using the selling price of gasoline and ethanol. According to obtained results, E10 and E85 are more economical than the gasoline by 2.6% and 29% respectively.

Keywords: *Bioethanol, gasoline, air pollution, Economic benefit.*

INTRODUCTION

In recent years, as an alternative to fossil fuels, the search for energy sources has increased. Moreover, the adverse effect of existing fossil energy sources on the environment reveals the importance of renewable energy sources day by day.As an alternative fuel, ethanol is the most widely used alcohol [1]. It can be pooled combined with gasoline as its simple chemical structure, high octane number and oxygen content, and accelerated flame propagation [2].

Traditionally, bioethanol has been produced from starch and sugar crops (e.g., cassava, rice, wheat, barley, corn grain or sugarcane) as first generation biofuels. Turkey is a country that supplies oil demand from the outside to produce gasoline, diesel and other products to supply the fuel to the public. It constitutes a significant proportion of the foreign trade budget of the country. Turkey has a large bioethanol production capacity as agricultural and available plants. However, ıt is not very common to mix Bioethanol with gasoline in Turkey. Legislation allows the ethanol blend with gasoline only up to 3%.According to the results of Bayrakci and Kocar, 2014 the number of vehicles increasing every year in turkey increases the dependency on petrol fuels. Also, when taxes on fuel cost are added, Turkey is one of the countries paying the highest price per liter of gas in the world [3].

In a study by Melikoglu, 2014, Turkey's supply-demand forecasts of road transportation fuels containing gasoline, diesel, LPG, bioethanol and biodiesel were examined. The results have shown that the addition of biofuels to the fuel increases rather than reduces dependence on petroleum-based fuels. For the solution of this situation, the use of biofuels must to be promoted with tax favours and incentives. Also, the biofuels must be used as a first alternative road transportation fuels instead of adding to current fuels at certain rates [4].

In the literature, ethanol is added at different ratios of benzene. However, higher ethanol concentration blend increased emissions of organic compounds such as acetaldehyde and formaldehyde. A study by Susana et. al., 2014 is determined that CO_2, NO_x and exhaust emissions were estimated to decrease by 19%, 50% and 90%, respectively. But, acetaldehyde emissions were estimated to increase by 233% for E85-vehicles compared to petrol/diesel vehicles [5].

The Turkish Government plans to reduce the country's dependence on petrol-based fuels. In this context, the authoritiesdecided to add biofuels to fuels such as gasoline and diesel. But studies on this subject are limited. In this study, air pollution reduction and economic benefits of bioethanol-blended gasoline use in Turkey were evaluated.

DATA AND METHODS

Nowadays, for sustainable development in urban areas, gasoline mixed with ethanol can be used widely as an alternative fuel for the vehicle to reduce the emission rate of pollutants (PM, HC, NOx, CO), reduction fossil fuel consumption and cost of gasoline/ethanol per unit. The schematic view of the experimental set up generally used in the literature is shown in Figure 1. A gas analyser is used to measure the CO, HC, PM and NOx emissions. Results for parameters such as different engine speeds and bioethanol/gasoline mixture ratios are evaluated pollution reduction and economic benefits.

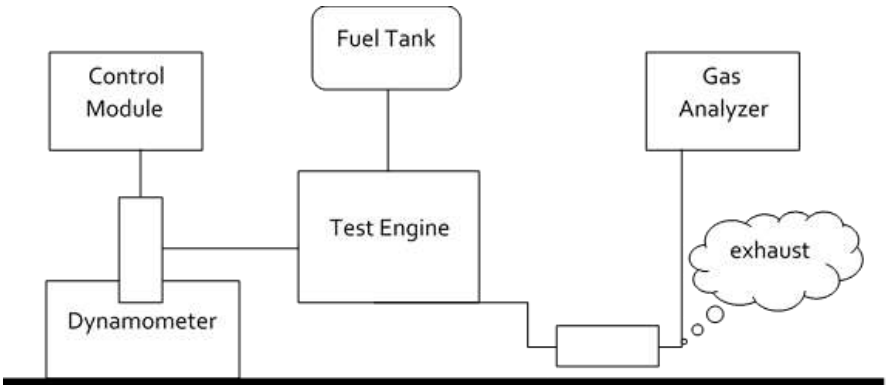

Figure 1. Schematic view of the engine test bed.

APPLICATION AND RESULTS

Assessment of Air Pollution Reduction

A number of studies published in the literature indicate that. The air pollutant emissions are reduced as a result of the use of bioethanol/gasoline in transport vehicles. In reference to General Directorate of Security As of March 2017, there are 11.493.249 cars registered to traffic in Turkey. About 3.049.193 of these vehicles use gasoline as fuel. Assuming that each car has a distance of 15 km per day, a total of 47.737.895 kilometers per day is taken throughout Turkey. Using the data given in Table 1 [6], how much pollutant assaults have been obtained for cars using gasoline, E10 and E85 per day in the atmosphere.The results presented are shown in figure 2.As a result of bioethanol use, the concentrations of NH_3, N_2O, NO_x and CH_4 increased while the concentrations of CO, CO_2, NMVOC and SO_2 concentrations decreased in the atmosphere.

Table 1. Air emissions over the life cycle of each fuel based on a travel distance oriented FU perspective (1 km driving distance).

Fuel	CO_2 (g/km)	CO (mg/km)	NMVOC (mg/km)	NO_x (mg/km)	NH_3 (mg/km)	SO_2 (mg/km)	N_2O (mg/km)	CH_4 (mg/km)
Gasoline	273	522	107	198	0.43	420	0.65	135
E10	259	284	109	224	1.7	411	0.67	185
E85	129	341	63	237	15	227	0.84	670

Reference: Daylan and Ciliz, 2016.

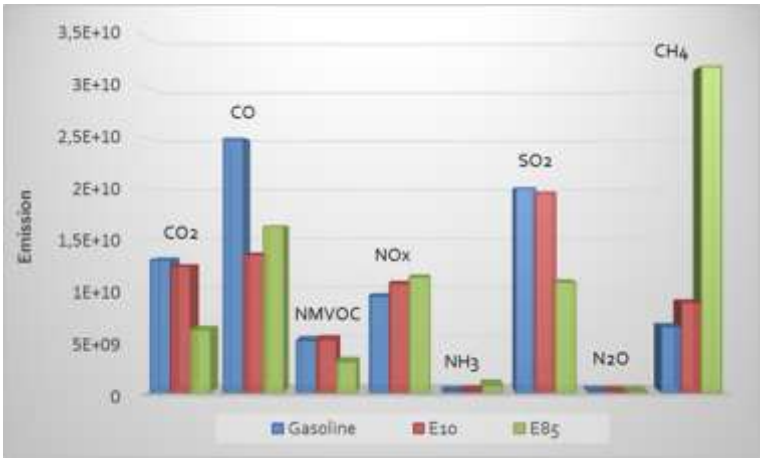

Figure 2. Amounts of emissions emitted from automobiles to the atmosphere in a day in Turkey.

Economic Benefits

In the real market, the prices of fuels are highly dependent on the taxes and subsidies. Gasoline sales price ws determined by Energy Market Regulatory Authority (EMRA) in January, 2016 report. Bioethanol selling price was calculated as $0.725 (2.55 TL) from in different studies [7,8]. The final selling prices shown in table 2 for E10 and E85 were calculated using these sales prices. For this reason, the selling prices of E10 and E85 are more economical than the gasoline by 2.6% and 29% respectively.

Table 2. Fuel Types Price Formation (TL / LT)

Fuel	Fuel price	Wholesale margin	Portion of income	Distributor and dealer margin	Total tax	Final selling price
Gasoline	0.94	0.05	0.00268	0.43	2.83	4.25
Bioethanol	-	-	-	-	-	2.55
E10	0.846	0.05	0.002412	0.43	2.55	4.14
E85	0.141	0.05	0.000402	0.43	0.496	3.29

CONCLUSIONS AND RECOMMENDATIONS

his study will give direction to application of ethanol blended gasoline use in Turkey. The results have shown that E10 and E85 are both better economically and environmentally friendly than gasoline. Today, 3% ethanol is added to the volume of gasoline in Turkey. Further studies are needed to increase this ratio and even to direct biofuels.In this context, the first step is to increase support for the agriculture and biofuel sectors. Also, the use of biofuels should to be encouraged with tax favours and incentives.

REFERENCES

[1] A. Demirbas, Biofuels securing the planet's future energy needs, Energy Convers. Manag., 50, 2239-2249, 2009.
[2] B.M. Masum, M.A. Kalam, H.H. Masjuki, S.M. Palash, Study on the effect of adiabatic flame temperature on Nox formation using ethanol gasoline blend in SI engine, Adv. Mater. Res., 781, 2471-2475, 2013.
[3] A. Gul Bayrakci and G. Kocar, Second generation bioethanol (SGB) production potential in Turkey, Inter. J. of Energy Research, 38, 822-826, 2014.
[4] M. Melikoglu, Demand forecast for road transportation fuels including gasoline, diesel, LPG, bioethanol and biodiesel for Turkey between 2013 and 2023, Renewable Energy, 64, 164-171, 2014.
[5] S. Lopez-Aparicio, C. Hak, I. Sundvor, K. Sundseth, Understanding effects of bioethanol fuel use on urban air quality: An integrative approach, Energy Procedia, 58, 215-220, 2014.
[6] B. Daylan, N. Ciliz, Life cycle assessment and environmental life cycle costing analysis of lignocellulosic bioethanol as an alternative transportation fuel, Renewable Energy, 89, 578-587, 2016.
[7] L. Luo, E. Van Der Voet, G. Huppes, Life cycle assessment and life cycle costing of bioethanol from sugarcane in Brazil, Renew. Sustain. Energy 13, 1613-1619, 2009.
[8] S. Chovau, D. Degrauwe, B. Van der Bruggen, Critical analysis of technoeconomic estimates for the production cost of lignocellulosic bio-ethanol, Renew. Sustain. Energy Rev. 26, 307-321, 2013.

ICING IN EXTREME WEATHER CONDITIONS AND IMPACT ON FLIGHTS

Ismail Gultepe[1,2], Martin Agelin-Chaab[2], John Komar[3], and Gary Elfstrom[3].
[1,*]Environment and Climate Change Canada, MRD, MRD, Toronto, Ontario, Canada
[2]Faculty of Engineering and Applied Science, UOIT, Oshawa, Ontario, Canada
[3]ACE, UOIT, Oshawa, Ontario, Canada

Abstract
Observations and prediction of icing in extreme weather conditions are important for aviation, transportation, and shipping applications that can adversely affect the economy. Icing environment can be studied using observations collected either in the atmosphere or in cloud chambers. There have been several aircraft based in-situ studies related to weather conditions affecting aviation operations, transportation, and marine shipping that include icing events. However, studying severe weather conditions from aircraft observations is limited due to safety and sampling issues. Remote sensing based techniques (e.g. retrieval techniques) usually cannot represent the important icing scales, and also represents indirect observations. Therefore, weather simulations of atmospheric processes in the cloud or climate chambers can help us better evaluate the interactions among microphysical and dynamical processes. The Climatic Wind Tunnel (CWT) in ACE at the University of Ontario Institute of Technology (UOIT) has a large 3/4 open jet test chamber with nozzle area that varies from 7 to 13 m^2. The temperature can be precisely controlled from 60ºC down to -40ºC, and wind speed up to 250 km hr^{-1}, similar to ones observed in the Arctic and cold climate regions, or at high altitude aeronautical conditions. In this study, using the ACE CWT a spray nozzle array system suspended in the CWT settling chamber and fed by pressurized water, various supercooled droplet sizes from a few microns up to mm size range were obtained to characterize icing event conditions. This array system, together with cold temperature and high wind speed conditions, enabled simulation of various severe icing conditions. In this study, the icing conditions created by various microphysical conditions are summarized, and their application to aircraft icing is provided. Overall, it is concluded that, icing environments can create significant challenges for flight conditions in the Arctic and cold environments, and these are emphasized for future studies.

Keywords: *aircraft icing, cloud chamber, aviation weather*

Introduction
Observations and prediction of icing in extreme weather conditions are important for aviation, transportation, and shipping applications that can adversely affect safety and the economy. Icing environment can be studied using observations collected either in the atmosphere or in the cloud chambers. There have been several aircraft based in-situ studies related to weather conditions affecting aviation operations, transportation, and marine shipping that include icing events. However, studying severe weather conditions from aircraft observations is limited due to safety and sampling issues. Remote sensing based techniques (e.g. retrieval techniques) usually cannot represent the important icing scales, and also represents indirect observations. Therefore, weather simulations of atmospheric processes in the cloud or climate chambers can help us better evaluate the interactions among microphysical and dynamical processes. The objectives of the study are: 1) To develop new icing envelopes for various icing conditions, 2) explore the feasibility of developing an icing system for the ACE CWT capable of producing an icing cloud typically experienced by aircraft at medium/low altitudes, 3) evaluate aircraft-based microphysical probes for characterizing icing conditions, 4) evaluate resulting icing

build-up on representative objects in ACE CWT, and 5) summarize microphysical conditions leading to various icing types.

Observations

The Climatic Wind Tunnel (CWT) in ACE at the University of Ontario Institute of Technology (UOIT) has a large 3/4 open jet test chamber with nozzle area that varies from 7 to 13 m^2. The temperature can be precisely controlled from 60ºC down to -40ºC, and wind speed up to 250 km hr^{-1}, similar to ones observed in the Arctic and cold climate regions, or at high altitude aeronautical conditions. Measurements collected in the CWT on Aug 26 2016 and May 2 2017 are used in this work. The key differences between the August 2016 and May 2017 tests were related to heated water and new spray nozzle array system used in the May 2 2017 tests. In this study, using the ACE CWT, a spray nozzle array system suspended in the CWT settling chamber and fed by pressurized water, various supercooled droplet sizes from a few microns up to mm size range were obtained to characterize icing event conditions (Fig. 1). This array system, together with cold temperature and high wind speed conditions, enabled simulation of various severe icing conditions.

Figure 1: Microphysical sensors in the CWT from left to right used in the analysis; GCIP probe (10-960 micron), WXT, LPM (100 micron-1 cm), and Gondola sensors that include CDP (2-50 micron) and BCP sensors (5-100 micron).

Microphysical probes developed for ground and aircraft icing condition measurements (Fig. 1), such as droplet spectra and precipitating particles characteristics as a function of temperature and wind were used to characterize the water particles distribution properties in the airstream during CWT experiments. An example of droplets images measured with GCIP probe is shown in Fig. 2 on May 2 2017 where the distance between vertical lines is about 960 μm.

The following subsections briefly summarize sensors and set-up system used in the CWT experiments performed on Aug 26 2016 for regular water case and May 2 2017 for heated water case.

UOIT Icing Spray Bar System

The new spray bar system consists of an array of pipes and nozzles:

- 10 rows of horizontal pipes each with 13 spray nozzles located every 18 inches (457 mm)
- Distance between pipes: 24 inches (610 mm)

- Nozzles: McMaster Carr Model No. 32885K103, rated 2 GPM @ 40 psi, orifice diameter 3 mm, 90° round cone spray pattern
- The entire Row 1 and Row 10 nozzles shut off; elsewhere every other nozzle shut off to create a diamond pattern of 49 nozzles. This pattern was chosen after observing the spray cone pattern when the array was tested outside the settling chamber.
- The overall spray nozzle array size was W5.5 m × H5.5 m, active areas W4.6 m × H4.9 m

The entire array was suspended in the settling chamber such that Row 1 was 457 mm down from the ceiling.

Microphysics Icing Probes

The following probes on loan from ECCC PanAm UOIT Meteorological Supersite (PUMS) were used for measuring the droplet size spectral characteristics:

- GCIP Ground cloud imaging probe (0-940 μm)
- Gondola CDP and BCP (cloud droplet probe and backscatter probe, respectively) probe (10-100 μm)
- LPM (Laser Precip Monitor) precipitation probe (0.1 mm-1 cm in diameter)
- RID (Rosemount Icing Detector) for icing rate (was not functional)
- MiniVis (mini visibility sensor) for visibility estimation (data was lost)
- WXT (meteorological compact sensor) for T, RH, and wind speed.

The probes were located about 1.5 m downstream of the nozzle exit, as shown in Figure 1.

Analysis and Results

The icing cloud characterization testing was carried out at 80 kph and 180 kph air speeds with the air temperature of -20^{o}C in all the cases. For May 2017 case, the heated water spray system was operated for 2 minutes, once every 10 minutes. This enabled quick checks of the microphysics probes to verify that they were operating properly and not iced up. Tests were done with wind speeds of Uh=80 km/hr, and Uh=180 km hr^{-1} at T= -20 ^{o}C. The water temperature used in the nozzle was 80 ^{o}C. 600 gallons of water was used with 10 bar pressure and 130 nozzles were placed over 18 inch intervals in the horizontal and 2 ft in the vertical. The top 2 bars, bottom bar and side bars of the spray system were not used. Only staggered positions of nozzles were used. The flow rate of Qv=3 GPM was used in the analysis.

Figure 2: GCIP images taken on May 2 2017 at 152014 UTC. Distance between top and bottom lines is about 960 μm.

The observations during icing experiments suggested that increasing air speed in colder temperatures (T) play an important role for icing prediction during flights and characterizing icing conditions. Both T and Uh, as well as droplet number concentration (Nd) and mean volume diameter (MVD) (representing droplet microphysical parameters), should be considered for icing predictions for various durations of flights.

Icing can also be produced on an airfoil with changing patterns which differ with air speed and build-up (Figure 3). The rain rig suspended in the settling chamber is safe and capable of producing icing. Icing can be produced over a range of air speeds: 60 kph to 180 kph; and depends on air speed. At low air speeds the patterns are striped in nature and spread across the y-axis (Fig. 3a). As air speed increases, the pattern becomes more circular in nature with

increased build-up in the center of a pattern (Fig. 3b). The accumulation pattern shifts upward with increasing wind speed. This is presumed to be the result of reduced acceleration of droplets downwards due to gravity.

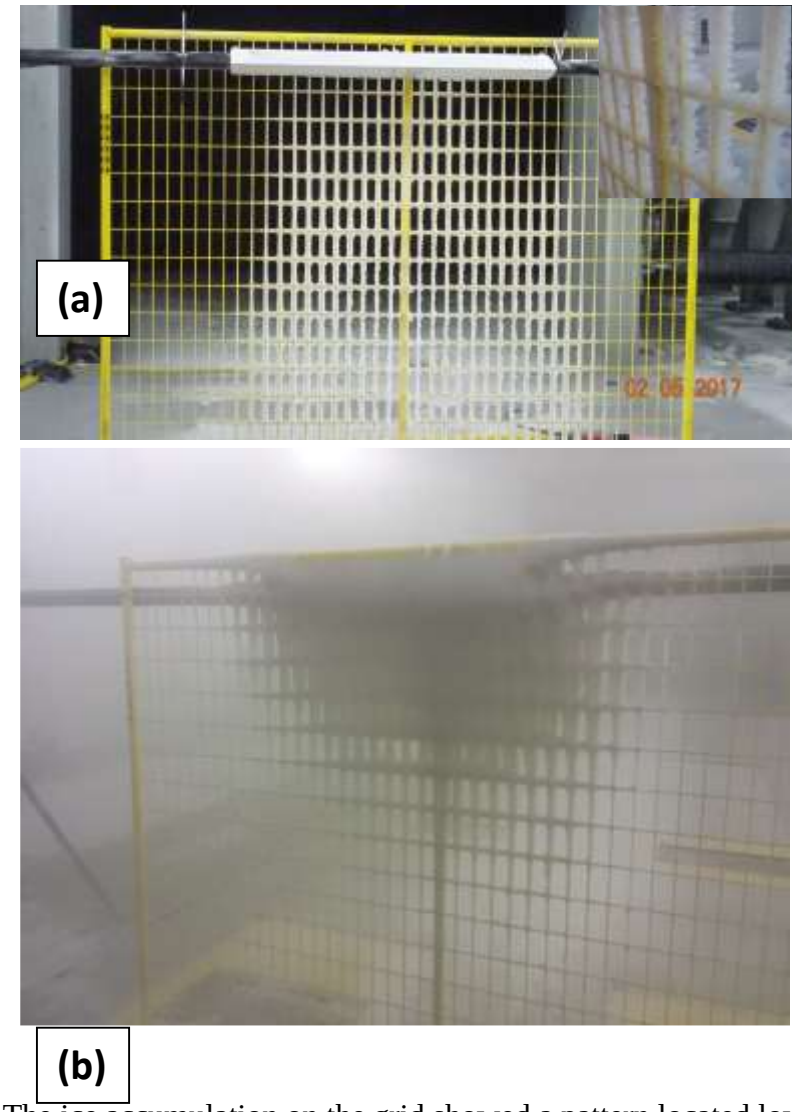

Figure 3: The ice accumulation on the grid showed a pattern located lower and covered a larger area at 60 kph as shown in (a) and as air speed increases, the pattern becomes more circular in nature with increased build-up in the center of a pattern at 180 kph (b) for May 2 2017 case.

Figure 4 shows increasing LWC with increasing MVD when Uh>45 m s^{-1} and smaller LWC are seen for Uh<20 m s^{-1} on August 26 2016 case. Observations from the May 2 2017 icing study case indicate that LWC increases with increasing Nd (Fig. 5a). A lot of small droplets with diameter < 200 μm existed (Fig. 5b). As indicated, large droplets (D >300 μm) are also measured with the LPM sensor (Fig. 5c). Figure 5c shows droplet falling velocity (y-axis) versus diameter (D, x-axis) where color squares represent number concentration of particles. Figure 5d shows LWC versus MVD taken on May 2 2017 where color lines are for various Nd values. Icing occurred on the Gondola platform on May 2 2017 experiment is shown in Fig. 6 where test duration was about 6 minutes.

Ice accumulation on the airfoil for Aug 26 and May 2 cases are shown in Fig. 7a and Fig. 7b, respectively. The May 2 case is quite different compared to August 26 case. Specifically, there

is clear"run-back" icing which is indicative of large droplets being supercooled or at least impacting in a partially liquid state. For May 2 case, the water supply was an insulated stainless steel 600 gallon storage tank filled with city water and heated to 80°C and nominal water pressure of 120 psi by pump at tank outlet, and heated water entered at bottom of array. These conditions indicate that heated water likely played an important role for run-back icing on the air foil.

Figure 8 suggests that icing rates on the aircraft surfaces are strong functions of Nd, LWC, MVD, as well as PR. The PR on the plot shows the possible icing rates indicated by Newton's work (Newton 1978; Lewis 1969) that represent light icing rate, moderate icing rate, and severe icing rates. Severe icing conditions based on PR value suggested by FAA icing envelopes shown on this figure can occur beyond the conventional envelops and further research is needed on this issue.

The overall results demonstrated feasibility of developing an icing cloud conditions in the ACE CWT which covers a wide range of atmospheric microphysical and dynamical conditions. Therefore, Figue 8 can be applicable to various icing evaluations but it needs to be further improved. Note that this figure is for the Aug. 26 2016 test and it doesn't show the results from May 2 2017 case.

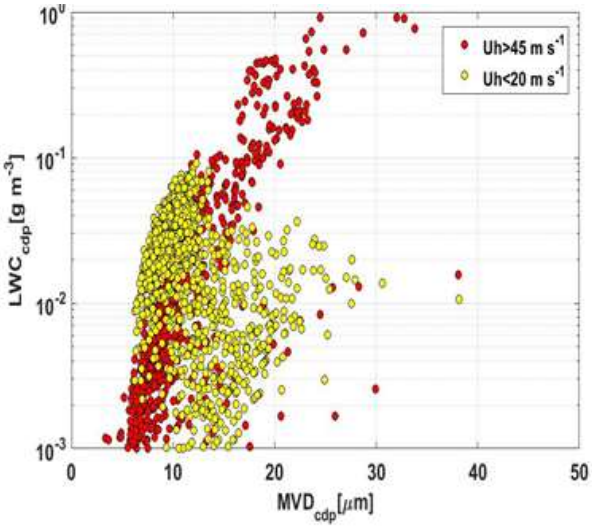

Figure 4: LWC versus MVD for Uh>45 m s^{-1} and <20 m s^{-1} taken on Aug 26 2016.

Conclusions

The results suggest following conclusions from this work:

1. Microphysical sensors measured icing parameters properly.
2. Nozzle physical characteristics such as flow rate and volume pressure can affect icing amounts strongly and this is left for future studies
3. Rain rig suspended in settling chamber is stable and capable of providing icing at different speeds.
4. Icing patterns change depending on air speed and water temperature (differences between 2 cases studies) This will be documented in future works.
5. Lower speeds patterns are more striped and spread across the y-axis.
6. Higher speeds produce circular patterns with more build up in centre of patterns.
7. Icing can be accumulated on an air foil and characterized.

8. There is more even ice buildup on the air foil at 180 kph.
9. Icing intensity can be important beyond the previously described icing envelops (Fig. 8).

Overall, further analyses are required to obtain well defined droplet size and LWC conditions that lead to certain icing intensity conditions.

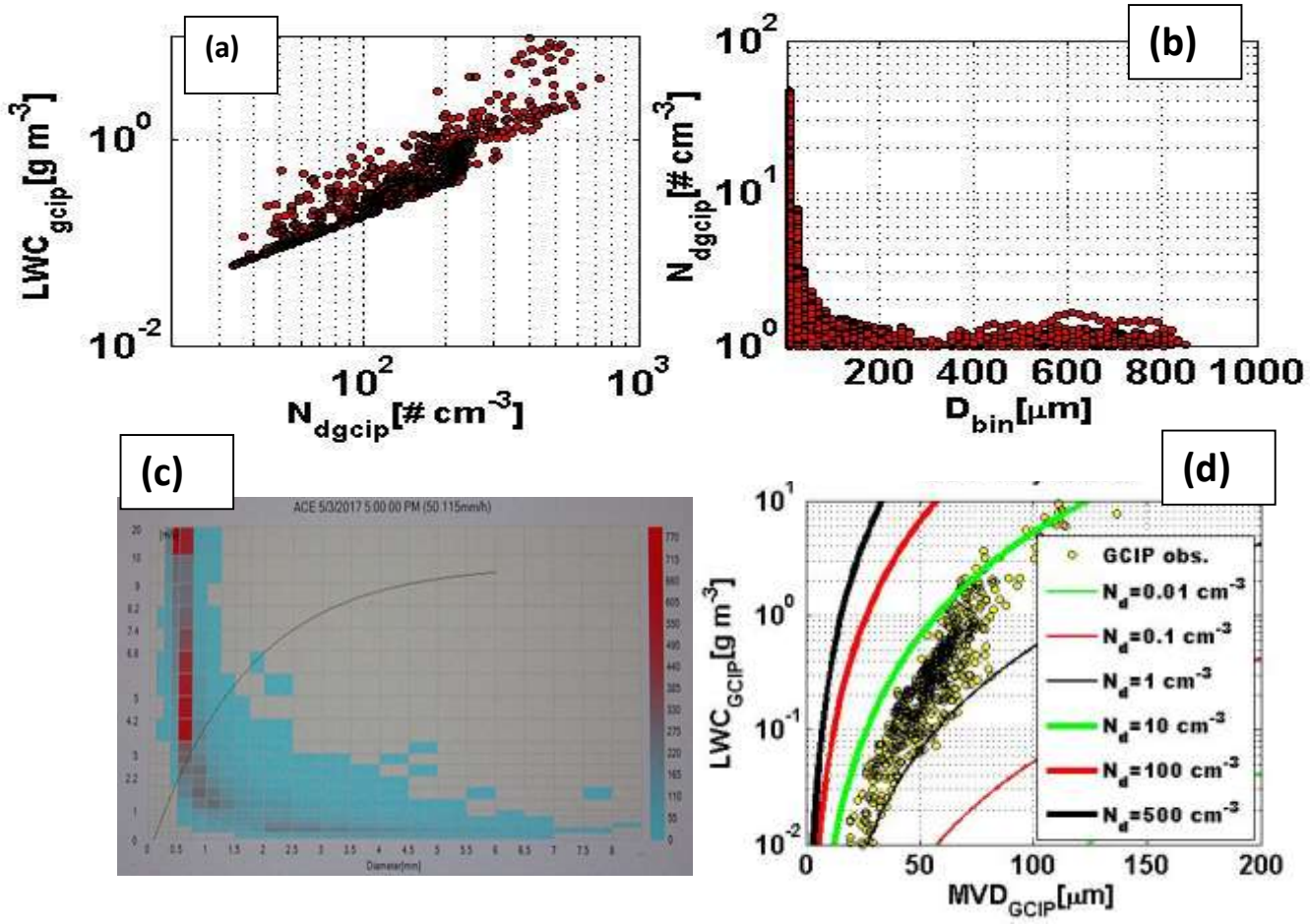

Figure 5: LWC versus Nd (a) and Nd versus D (b) from GCIP probe measurements, fall velocity (Vf) versus D with counts in colored squares from LPM probe. The black line is for droplets. LWC versus MVD is shown on (d) from GCIP probe where lines are for theoretical relationships for fixed Nd values.

Figure 6: Icing occurred on Aug 26 2016 case on the Gondola platform.

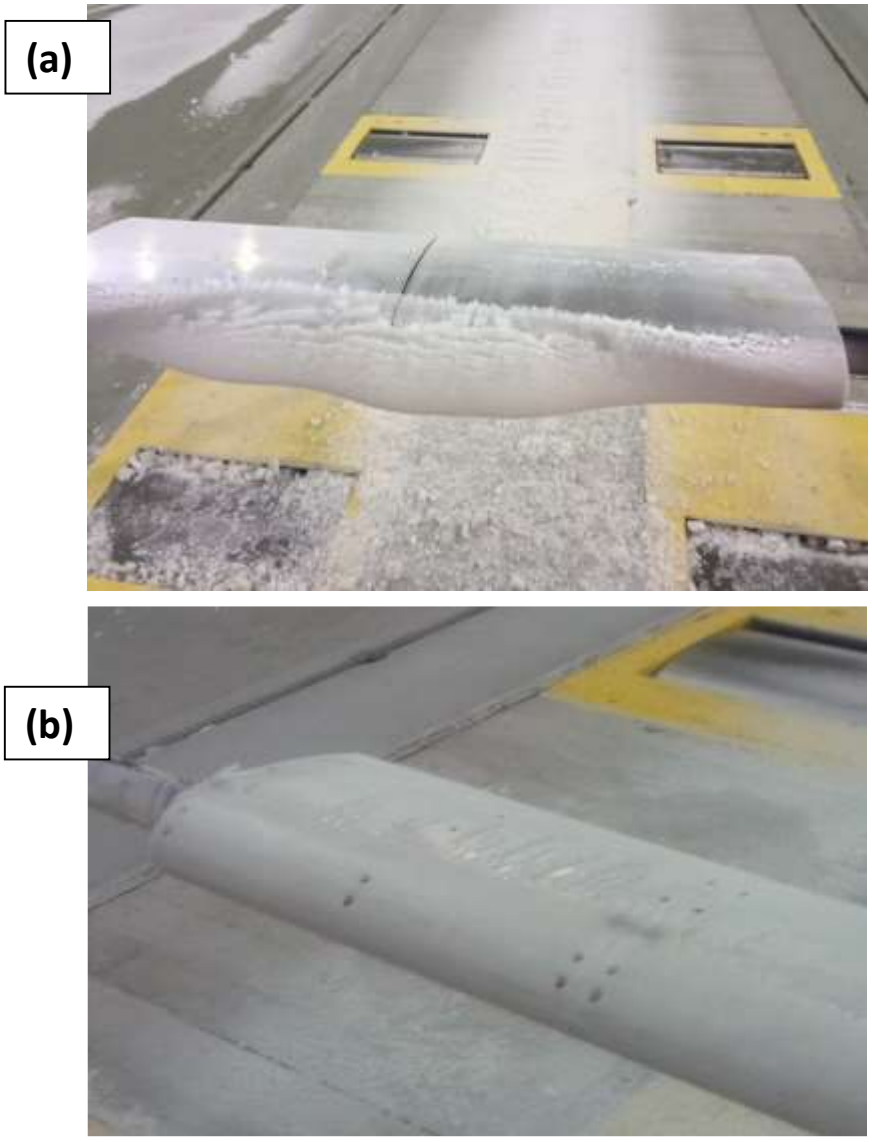

Figure 7: Icing occurrence over air foil with horizontal wind speed (Uh) = 60 m s^{-1}: Clear runback icing with riming in the leading edge of air foil on May 2 2017 that used warm water at 80 ºC to delay icing (a) and using same conditions with cooler water at about 18ºC on Aug 16 2016 (b).

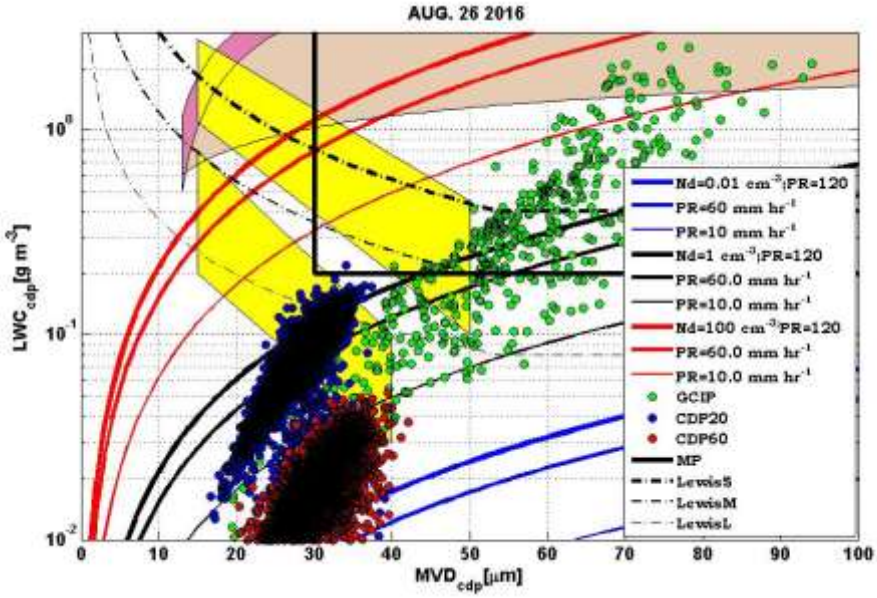

Figure 8: ACE CWT icing microphysical parameters (blue circles for CDP probe and green circles for GCIP probe) in comparison to FAA (yellow boxes) and others (pink colored areas for nozzle testing (Steen et al. 2015); solid dark lines for extreme icing conditions (Politovich 1996), dashed lines (theoretical curves from Newton 1978). Theoretical lines from the concept of microphysical relationships are shown by 3 solid lines representing conditions of precipitation rates (PR) for various Nd values and changing MVD.

References

Lewis W., 1969: "Review of icing criteria, Aircraft ice protection report of symposium ". Federal Aviation Administration (FAA), Flight Standards Service.

Newton, D. W., 1978: An integrated approach to the problem of aircraft icing. *J. Aircraft*, 374-381.

Esposito, B. M. et al, 2002: *Cloud calibration update of the CIRA icing wind tunnel*, SAE. Paper 2002-01-2132

Steen, L. E., R. F. Ide, J. F. V. Zante, and W. J. Acosta, 2015: *NASA Glenn icing Research Tunnel: 2014 and 2015 cloud calibration procedures and results.* NASA/TM-2015-218758. 22 pp.

Politovich, M.K., 1996: Response of a research aircraft to icing and evaluation of severity indices. J. *Aircraft*, 33, 291-297.

INVESTIGATION OF THE AERODROME WARNING BELONG TO ATATURK INTERNATIONAL AIRPORT METEOROLOGY OFFICE

Emrah Tuncay ÖZDEMİR
Turkish State Meteorological Service, Ataturk International Airport Meteorology Office
34149 Yeşilköy İstanbul Türkiye
etozdemir@gmail.com; etozdemir@mgm.gov.tr

Abstract
In this study, the aerodrome warning prepared by Atatürk International Airport Meteorology Office were searched for between 1 April 2016 and 31 March 2017. 60 aerodrome warning and 9 meteorological evaluations were prepared by the Atatürk International Airport Meteorology Office for a period of 1 year and delivered to the users at the airport. 60 aerodrome warning were categorized into 8 different event or events. The highest number of oraj was done with 45 %. Thunderstorm event consistency is 77.8%. Only snow and the average wind and gust with snow was consistent with 100%. The consistency of all these 8 event or events is 83.3%. The consistency of meteorological evaluations is 88.9%.

Key Words: *Atatürk International Airport, Aerodrome Warning, Thunderstorm, Snow*

Introduction
Aerodrome Warnings are made in the case one or more of the major meteorological phenomenons occur or are predicted to occur at the airport or in the vicinity of the airport. The purpose of this warning is to ensure that the competent authorities at the airport take the necessary precuations on time. Scope of warnings, airport services and aircraft in the park that are expected to be affected or expected to be adversely affected are informed about important meteorological events

According to the data of the State Airports Authority (DHMİ)'s 2015; Turkey Overall (excluding transit), all aircraft traffic is 1,456,673 and Atatürk International Airport accounts for 31,9% (464,774 units) of this traffic. Istanbul Sabiha Gökçen International Airport, which is 2nd, accounts for 15.1% (219,158) of all aircraft traffic. (DHMİ, 2017). According to this, Atatürk International Airport is the airport with the busiest passenger and aircraft traffic in Turkey. Atatürk International Airport (40 ° 58'34 "N, 28 ° 48'50" E) is located on the southwest of the most populous city of Istanbul (population: 14.804.116; source: TUİK, 2017). It is the largest of the 3 airports in Istanbul. The Ataturk International Airport is located in the south of the Marmara Sea. The terminal building of the airport is 345.270 m2. The airport has a modern passenger terminal and its elevation is 49.75 m (AMSL) (Özdemir et al., 2016, DHMİ, 2017, Ozdemir et al., 2017, Sirdas et al., 2017).

Yavuz et al. (2015) examined the accident-crime reports between 2005 and 2014 and investigated the causes of 527 deadly accidents in the European Region. The technical reasons with 40% were the most effective, while pilotage was 31%, meteorology 15%, fire 6%, passenger 4%, tower 2% and other reasons 2%. The meteorological causes with 15% are very important. Studies on meteorological canvases affecting aviation are increasing day by day in our country (Annanurov et al., 2014, Yazmuhammedov et al., 2014, Özdemir ve Deniz, 2015). The purpose of this study is to investigate the consistency of these warnings by evaluating the warnings of the Ataturk International Airport, which is the biggest airport in the country and located in the most crowded city of Turkey.

DATA AND METHOD

Aerodrome warnings at airports are prepared and published by meteorological offices in charge at airports. These warnings should include information on concise / short meteorological conditions. Aerodrome warnings, including aircraft parked on the runway and parking area should include adverse meteorological conditions to cover areas where the airports facilities and services. At the airport, the warnings are prepared and distributed by the operators or by the airport services as required (Annex 3 ICAO, 2016), in accordance with a specific template (taking into account local regulations).

In Turkey, 30 kt or more is used for the wind gust, while in the UK, 28 kt or more is used (Metoffice, 2017). It is recommended that airports be set up between meteorology offices and users to determine the values, such as the expected maximum wind speed, estimated total snow depth, etc. (Annex 3 ICAO, 2016).

In this study, the information about the notices of the courts belonging to Atatürk International Airport was obtained in digital environment and evaluated for the period from 1 April 2016 to 31 March 2017. The meteorological warnings obtained from the Atatürk International Airport Meteorological Station connected to the Turkish State General Directorate of Meteorology were classified according to the meteorological processes. Meteorological assessments have been assessed within themselves.

Meteorological Terminal Air Report (Metar) observations made every half hour belonging to Atatürk International Airport and Aviation Selected Special Weather Report (Speci) observations made outside of Metar observations but in directed with meteorological rules, and daily maximum wind values were used to investigate the consistency of square denunciations. When it is expected that more than one meteorological events will come to the warning of the square, the consistency is calculated by evaluating that the warning is 100% when any event observed in the observation period at the estimated period. In addition, the thunderstorm report which is not on the airport at the time of the receipt of the aerodrome warning, but within 16 km has been accepted as 100% consistent.

ANALYSIS, RESULTS AND DISCUSSION

Between April 1, 2016 and March 31, 2017, aerodrome warning information from the Meteorological Office of the Atatürk International Airport and the meteorological assessment information were used in this study. A total of 90 aerodrome warning and 9 meteorological evaluations were made for a period of 1 year.

In the 1-year period, 27 aerodrome warning (45%) which is the highest number of aerodrome were given for the thunderstorm event. The second most notifiable warning is 21.7% (13 aerodrome warning) that the ground wind is 20 kt or more and / or 30 km or more of the move. The aerodrome warning is required for the events where the wind is at least 20 kt or more and/or 30 kt or more at the start, should not be in the meteorological evaluation of the Ataturk International Airport Meteorological Office, have not been made and this expactations were given at meteorological evaluation.

There is no need to done so much before the thunderstorm aerodrome warnings which can now be completely done in the nowcasting application, monitoring of radar, lightning and satellite observations.

The information that should not be included in the aerodrome warning is shown in the these documents. These includes low-speed winds, temperature forecasts, and light rainfall forecasts. It is also necessary for the Thunderstorms to be given over 2 hours if the expected duration of the 2-hour periods is expected to be longer. Ozdemir et al. (2017), 8-9 September 2009 and 23 June 2010 for the period of 2008-2012 years in the study carried out 7 hours and 30 minutes of the arrest was found.

CONCLUSIONS

In this study, the aerodrome warnings prepared by Atatürk International Airport Meteorology Office were searched for between 1 April 2016 and 31 March 2017. 60 aerodrome warnings in 1-year period and 9 meteorological evaluations were prepared by Atatürk International Airport Meteorology Office and delivered to the users at the airport. 60 aerodrome warnings were grouped to cover 8 different events or events, and 45% (27 aerodrome warning) of the aerodrome warnings had the highest number of thunderstorm events. The consistency of the thunderstorm events were 77.8%, just snow and snow with the average wind and gust were 100%. The consistency of all these 8 event/events is 83,3%. The consistency of meteorological evaluations is 88.9% (8).

ACKNOWLEDGEMENT

The author would like to thank the General Directorate of Meteorology for the aerodrome warnings of the Ataturk International Airport.

REFERENCES

Annanurov, S., Deniz, A., Özdemir, E. T. (2014). İstanbul Fır Sahası İçin Sigmet ve Airmet Analizi. *V. National Aviation and Space Conference*, 8-10 September 2014, Erciyes University, Kayseri. UHUK-2014-082.ISBN: 978-605-86838-3-9. (in Turkish).

Annex 3 ICAO (International Civil Aviation Organization) (2016). Meteorological Service for International Air Navigation, Nineteenth Edition, July 2016.

DHMİ (Devlet Hava Meydanları İşletmesi) (2017). <http://www.dhmi.gov.tr/istatistik.aspx>, Retrieved date: 04.04.2017;

< http://www.ataturk.dhmi.gov.tr/havaalanlari/sayfa.aspx?hv=1&mnu=4996#.WPUn-GkT6Uk>, Retrieved date: 17.04.2017.

Aviation Meteorology Book (2016). Repuclic of Turkey, Ministry of Foresty and Water Affairs, Meteorology General Directorate, Directorate of Aviation Meteorology. page:146. (in Turkish)

Metoffice (2017). <http://www.metoffice.gov.uk/aviation/aerodrome-warnings/faq>, Retrieved date: 22.04.2017.

Ozdemir, E. T., Deniz, A., Sezen, I., Aslan, Z., & Yavuz, V. (2017). Investigation Of Thunderstorms Over Ataturk International Airport (Ltba), Istanbul. *Mausam*, *68*(1), 175-180.

Özdemir, E. T., Deniz, A., Sezen, İ., Menteş, Ş. S., & Yavuz, V. (2016). Fog analysis at Istanbul Ataturk International Airport. *Weather*, *71*(11), 279-284.

Özdemir, E. T., Deniz, A. (2015). Yanardağ Patlamalarının Türkiye'deki FIR Sahaları Üzerine Etkisi: Volkanik Kül İçin 14 Nisan 2010 Örnek Olay İncelemesi. *Ejosat*, Volume. 2, Number. 5, Page: 149-154, December, 2015. (in Turkish).

Sirdas, S. A., Özdemir, E. T., Sezen, İ., Efe, B., & Kumar, V. (2017). Devastating extreme Mediterranean cyclone's impacts in Turkey. *Natural Hazards*, *87*(1), 255-286.

TUİK (Türkiye İstatistik Kurumu) (2017). <http://www.tuik.gov.tr/UstMenu.do?metod=temelist>, alıntılanma tarihi: 17.04.2017

Yavuz, V., Temiz, C., Özdemir, E. T., Deniz, A. (2015). Avrupa Bölgesi için Kaza-Kırım Raporlarının İncelenmesi. *Ejosat*. Volume. 2, Number. 5, Page:155-160, December, 2015. (in Turkish).

Yazmuhammedov, S., Deniz, A., Özdemir, E. T. (2014). İstanbul Havalimanlarinin Cb ve Oraj Analizi. *V. National Aviation and Space Conference*, 8-10 September 2014, Erciyes University, Kayseri. UHUK-2014-084. ISBN: 978-605-86838-3-9. (in Turkish).

CLIMATOLOGICALLY FOG CHARACTERISTICS AT AIRPORTS IN TURKEY

Mahmut Müslüm[1], Ahmet Duran Şahin[2]
[1]*Turkish State Meteorological Service, mmuslum@mgm.gov.tr*
[2]*Istanbul Technical University, sahind@itu.edu.tr*

Abstract
A statistical approach to fog events in all airports in Turkey is presented in this study by classifying fog events according to their occurrence. METAR (Aerodrome Routine Meteorological Report) and SPECI (Aerodrome Special Meteorological Report) for aviation has been analyzed using the historical hourly observations data for 2008-2016. Frequency and duration analysis of fog events; mean annual, monthly and daytime variability in each airport are presented. Fog events are also classified based on the types and examined temporal frequencies that characterizes with their duration and intensity. Classifying fog types; along with the objective criteria set out by using meteorological parameters (wind, cloud-base lowering) affecting the fog formation process, are taken into account in some geographical features of the airports. As a result, it has been determined that airports in the Marmara region are more affected by fog events than airports in other regions. However, when considered locally, the LTCJ-Batman airport with an annual average of 39.22 days/year has the dense fog events and the longest consecutive events occurred at the LTBF-Balikesir airport for 71 hours.

Keywords: *Fog events, Climatology, Airports, Turkey*

INTRODUCTION

Poor visibility at airports has always been one of the main problems that prevent flights from being carried out normally. This problem, disrupt regular landings and take-off aircrafts. Poor visibility conditions causes to flight to be unsafety, to disorder air traffic, to delay and diverting, and even to related fatal accidents. Such problems in flight planning lead to great financial losses to airways companies. Fog is the most important meteorological phenomenon that associate with poor visibility. Fog is the phenomenon in which atmospheric suspended water droplets or ice crystals the visibility decrease to less than 1 km (WMO 1996; NOAA Glossary 2009). With a physical description, the poor visibility associated with the fog is that droplets and ice crystals suspended in air become visible.

According to Akimoto Y. and Kusaka H. (2014), the most common methodology used in fog studies is to analyze the average annual or monthly foggy days of the studied area. Recent studies have been done frequency analysis by detecting the types of fog that occur under different atmospheric conditions (Tardif and Rassmussen 2007; Stolaki S.N. et al. 2009; Akimoto, Y. and Kusaka, H. 2015). Tardif and Rasmussen (2007) have determined the frequency of fog types by using a simple algorithm based on atmospheric conditions that triggering fog events to using hourly data from ground observations in New York City. They also took into account the geographical characteristics of the ground observation stations (Tardif and Rasmussen 2007). Çamalan et al. 2009; Esenboğa airport examined the fog events that took place between 2000 and 2009 and found that the total number of foggy days in the 10-year period was 221 days and that these fog events were observed as 77% supercooled fog and 23% warm fog according to the formation conditions. Ozdemir et al.2014; identified the fog events that took place between 2008 and 2012 at the Atatürk Airport as frequency and duration of fog events and the percentage of fog events that have occurred has changed the CAT category of the airport. This study will analyze the annual monthly and hourly in daily variability of fog

events observed at Turkish airports. Another important point to focus on in this study is the frequency analysis of the fog types classified by each fog event using a simple classification algorithm based on the trigger mechanisms of fog occurrences. It is determined that fog mostly observes in Batman-LTCJ, Balıkesir-LTBF, Erzurum-LTCE and Bursa-LTBR airports in Turkey.

DATA AND METHODS

In this study observations during 2008-2016 period of Aviation Route Weather Report (METAR) and SPECİ Aviation Selected Special Weather Report (SPECI) in the Turkish State Meteorological Service (MGM) are used as dataset. The Turkish State Meteorological Service (MGM) classified the airports as A, B and C according to the operating conditions of the airports. Class C airports make observation only during working hours. For this reason, Class C airports, which are lack much of their observational data, are not included in the study. This study will analyze the annual monthly and hourly in daily variability of fog events observed in METAR reports at airports. Another important point to focus on in this study is the frequency analysis of the fog types classified by each fog event using a simple classification algorithm based on the trigger mechanisms of fog occurrences. In earlier studies, Willet (1928) and Byers (1959), 11 fog types are defined by taking into account the fog formation mechanism and fog forming weather events by Willet (1928) and Byers (1959). Recently, Tardif and Rasmussen (2007) introduced a classification algorithm that recognizes five types of fog. Tardif and Rasmussen (2007) set out the primary mechanisms that make up the fog types used in the classification algorithm and the definitions based on the morphology of the fog formation are given in Table 1. Also in this study, fog events are classified according to temperature and visibility. Classification of fog by temperature, warm fog; the temperature is above 0 ° C, the freezing fog temperature is below 0 ° C and the ice fog temperature is below -29 ° C.

Table 1. List fog types the primary mechanism and morphology considered in classified in the algorithm.

Fog type	***Primary physical mechanism***	***Definition/morphology of fog formation***	***References***
Precipitation (PCP)	*Thermodynamical influence of evaporating precipitation*	*Precipitation observed at the onset of fog or the hour prior*	*Petterssen (1969)*
Radiation (RAD)	*Radiative cooling over land*	*Onset during the night with an observed wind speed below 2.5 m/s and cooling during the hour prior in absence of a cloud ceiling, or with a cloud base rising concurrently or slight warming in the hour leading to onset if preceded by cooling period (e.g., fog forming between two hourly observations) or cloud ceiling below 100 m if followed shortly by fog at surface (e.g., elevated fog formation)*	*Taylor (1917), Pilié et al. (1975), Roach et al. (1976), Roach (1995a), Meyer et al. (1986), Meyer and Lala (1990), Baker et al. (2002)*
Advection (ADV)	*Shear-induced mixing of air parcels of contrasting temperatures as moist, warm air flows over a colder (water, land, or snow) surface*	*Onset as a "wall" of fog reaches a station, with an observed wind speed greater than 2.5 m/s and an associated sudden decrease in visibility or sudden appearance of a cloud ceiling below 200 m, followed by fog onset within next 2 h*	*Roach (1995b), Baars et al. (2003)*
Cloud-base	*Moistening and/or cooling of the layer*	*Gradual lowering of a cloud ceiling within a 5-h period prior to fog onset, with initial ceiling*	*Pilié et al. (1979), Duynkerke and*

lowering (CBL)	*below boundary layer stratiform clouds and/or prolonged subsidence*	*height below 1 km*	*Hignett (1993), Korac˙in et al. (2001), Baker et al. (2002)*
Morning evaporation (EVP)	*Evaporation of surface water and mixing in the surface layer*	*Increasing temperature and greater increase in dewpoint leading to saturation, within 1 h of sunrise*	*Arya (2001), Brutsaert (1982)*

Tardif and Rassmusen (2007)

This algorithm fog types classes are determined by meteorological conditions before the onset of the fog and at the fog onset Fig.1 (Tardif and Rasmussen 2007). In this study; the algorithm has classified the fog events by examining the meteorological conditions fog onset to at least 1 hours prior or at least three METAR or SPECİ observations Fig 1.

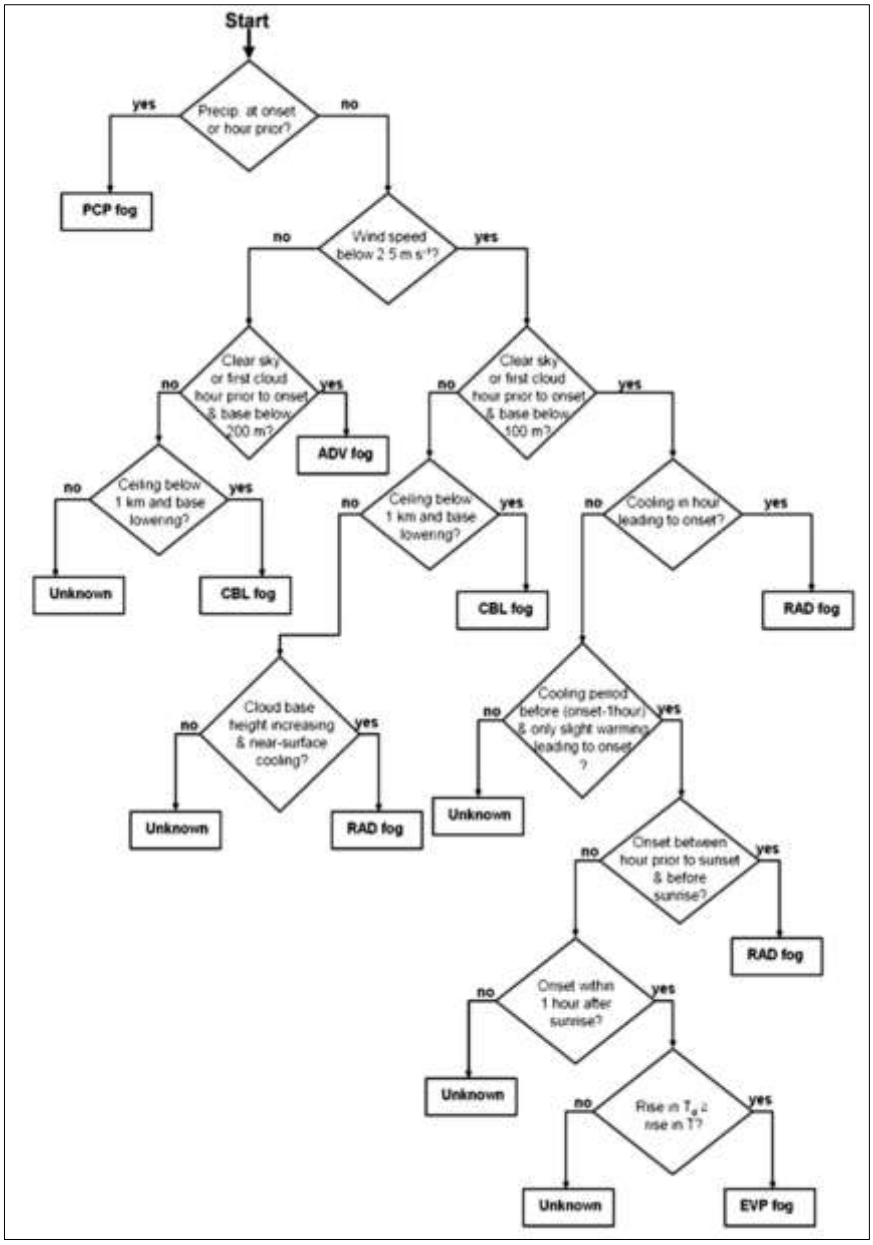

Figure 1. Flow diagram for fog type classification (Tardif and Rasmussen 2007).

Table 2 gives information about each station's the geographical location, height, city and region information and physiographic character information such as density of buildings in the vicinity (urban, suburban or rural) and sea, lake and dam (coastal or inland) closeness. Because of the physiographic characteristics of stations, land-sea (coastal) and land surface (urban, suburban and rural) and topography are important influences in fog formation. According to the physiographic characteristics of stations, most stations are suburban and inland (Table 1).

Table 2. List of stations, their geographical information and physiographic character.

Station Icao Code	Station Synoptic Code	City	Region	Lat (∘)	Lon (∘)	Elev (m)	Station Geographic Character
LTAB	17131	Ankara	Central Anatolia	39.939	32.74	823	Urban-Inland
LTAC	17128	Ankara	Central Anatolia	40.121	32.994	949	Urban-Inland
LTAD	17129	Ankara	Central Anatolia	39.955	32.686	800	Urban-Inland
LTAE	17127	Ankara	Central Anatolia	40.081	32.558	841	Urban-Inland
LTAF	17352	Adana	Mediterranean	36.989	35.296	20	Urban-Inland&Near Dam
LTAG	17350	Adana	Mediterranean	37.002	35.432	66	Suburban-Inland&Near Dam
LTAH	17189	Afyon	Aegean	38.725	30.597	1001	Suburban-Inland
LTAI	17300	Antalya	Mediterranean	36.895	30.798	51	Urban-Coastal
LTAJ	17260	Gaziantep	Southeastern A.	36.94	37.47	699	Rural-Inland
LTAN	17244	Konya	Central Anatolia	37.967	32.55	1031	Urban-Inland
LTAP	17082	Amasya	Black Sea	40.826	35.522	535	Rural-Inland
LTAT	17200	Malatya	Eastern Anatolia	38.435	38.095	848	Rural-Inland&Near Dam
LTAU	17195	Kayseri	Central Anatolia	38.773	35.489	1054	SubUrban-Inland
LTAY	17257	Denizli	Aegean	37.789	29.7	848	Rural-Inland&Near Lake
LTAZ	17194	Nevşehir	Central Anatolia	38.773	34.522	942	Suburban-Inland&Near River
LTBA	17060	İstanbul	Marmara	40.974	28.815	33	Urban-Coastal
LTBF	17150	Balıkesir	Marmara	39.618	27.92	102	Suburban-Inland
LTBG	17115	Balıkesir	Marmara	40.318	27.973	58	SubUrban-Inland
LTBI	17124	Eskişehir	Central Anatolia	39.78	30.587	786	Suburban-Inland
LTBJ	17219	İzmir	Aegean	38.287	27.152	124	Urban-Inland
LTBL	17218	İzmir	Aegean	38.513	27.012	6	Suburban-Coastal
LTBQ	17068	Kocaeli	Marmara	40.73	30.1	65	Urban-Coastal
LTBR	17118	Bursa	Marmara	40.252	29.563	232	Rural-Inland
LTBS	17295	Muğla	Aegean	36.719	28.788	5	Suburban-Coastal
LTBU	17051	Tekirdağ	Marmara	41.142	27.914	160	Rural-Inland
LTBY	17123	Eskişehir	Central Anatolia	39.817	30.517	801	Suburban-Inland
LTCA	17202	Elazığ	Eastern Anatolia	38.606	39.298	881	Suburban-Inland&Near Dam
LTCB	17616	Ordu	Black Sea	40.96	38.08	0	Rural-Coastal
LTCC	17280	Diyarbakır	Southeastern A.	37.897	40.202	677	Suburban-Inland
LTCD	17092	Erzincan	Eastern Anatolia	39.716	39.525	1154	Suburban-Inland
LTCE	17096	Erzurum	Eastern Anatolia	39.954	41.177	1757	Rural-Inland
LTCF	17098	Kars	Eastern Anatolia	40.564	43.112	1795	Rural-Inland
LTCG	17038	Trabzon	Black Sea	40.99	39.78	33	Suburban-Coastal

LTCI	17170	Van	Eastern Anatolia	38.468	43.337	1665	Suburban-Coastal
LTCJ	17284	Batman	Southeastern A.	37.926	41.122	554	Suburban-Inland
LTCS	17271	Şanlıurfa	Southeastern A.	37.44	38.9	817	Rural-Inland
LTDA	17371	Hatay	Mediterranean	36.36	36.27	78	Rural-Inland
LTFC	17241	Isparta	Mediterranean	37.859	30.366	870	Rural-Inland&Near Lake
LTFE	17291	Muğla	Aegean	37.245	27.671	11	SubUrban-Coastal
LTFH	17031	Samsun	Black Sea	41.254	36.568	7	Rural-Coastal
LTFJ	17063	İstanbul	Marmara	40.896	29.313	99	Urban-Coastal

ANALYSIS AND DISCUSSION

Firstly, foggy observations are analyzed with hourly, monthly and annual distributions of fog events at airports. Figure 2 shows the hourly distribution of foggy observations in the airports. As can be seen in Figure 2, the most frequent foggy observations have been observed respectively in BAT-LTCJ (Batman), BAL-LTCF (Balıkesir), ERZ-LTCE (Erzurum) and BUR-LTBR (Bursa) airports.

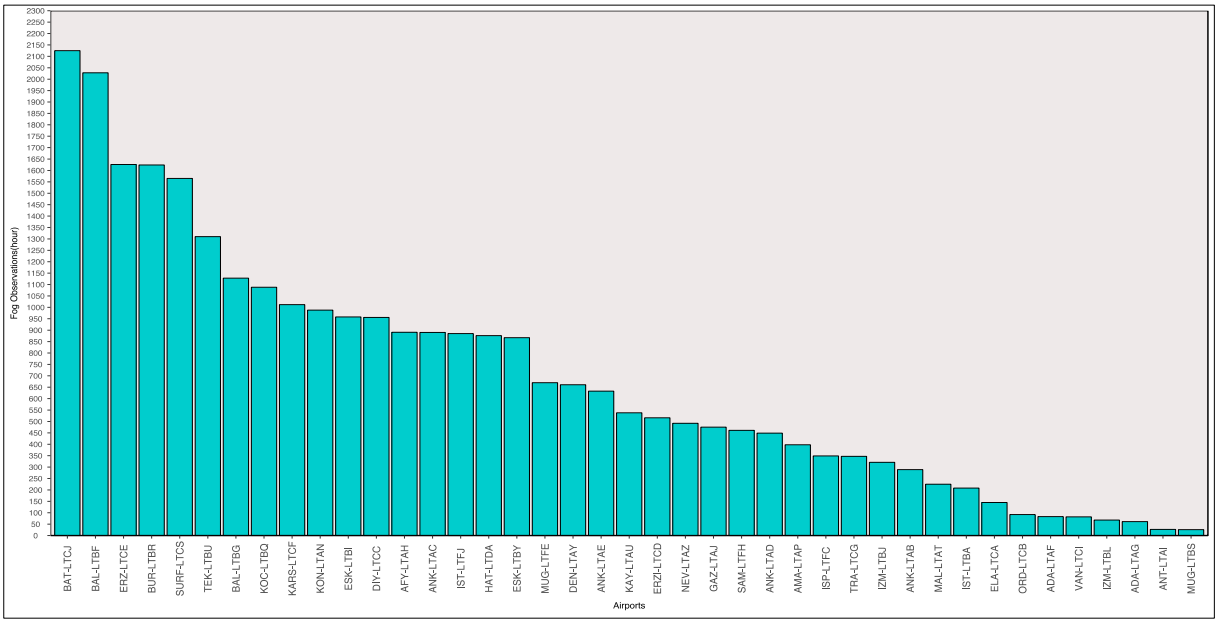

Figure 2. Number of observations of fog events between 2008 and 2016 in METAR or SPECI

The fog events that occur especially at the airports of rural-inland, urban-inland and suburban-inland are mostly occur during middle of the fall and early of the spring. (October, November, December January, February and March) Figure 3. But ın contrast the frequency of fog events is generally low in the summer months (Fig.3).

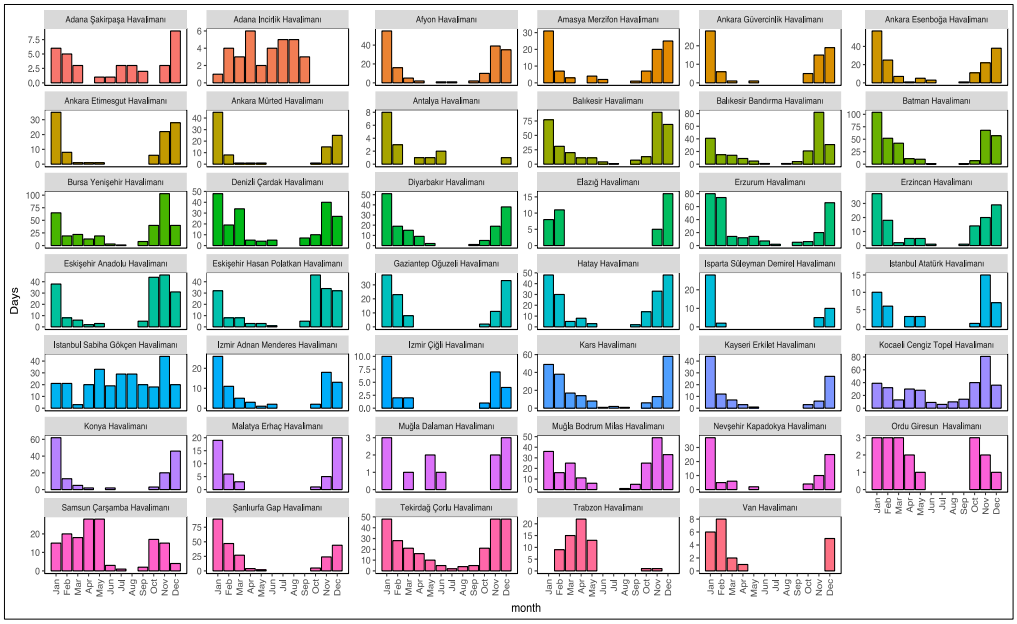

Figure 3. Monthly distribution of fog events between 2008 and 2016

It is shown in Figure 3 that it is possible to observe the fog event every month in the coastal airports such as IST-LTFJ (Istanbul Sabiha Gökçen), KOC-LTBQ (Kocaeli), TEK-LTBU (Tekirdağ) and BAL-LTBF (Balıkesir) airports. IST-LTBA (Istanbul Atatürk), ANK-LTAC (Ankara Esenboğa) and IST-LTFJ (Istanbul Sabiha Gökçen) are the three largest airports in Turkey. Most of the fog events in these airports were observed in November, January and November, respectively (Fig.3). OZDEMIR et all. (2014) determined that most of the fog events at Ataturk Airport were observed in November. Also, Camalan et all. (2009) found that the maximum number of foggy days in the study they conducted for Esenboğa Airport was in January.

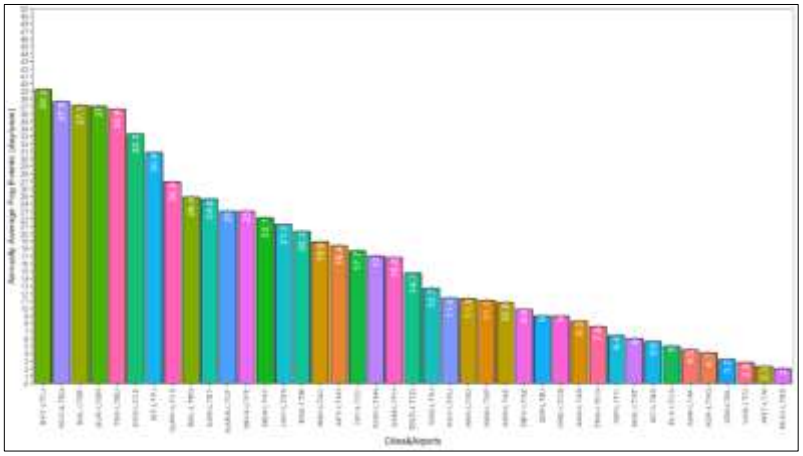
Figure 4. Average number of fog events per year determined from METAR&SPECI

As shown in Figure 4, which is annually average foggy days 39.2, 37.6, and 37.1day year^{-1} in BAT-LTCJ (Batman), KOC-LTBQ (Kocaeli) and BAL-LTBF (Balıkesir) Airports respectively. It is determined that the minimum number of foggy days annually is at MUG-LTBS (Muğla Dalaman) airport (Figure 4).

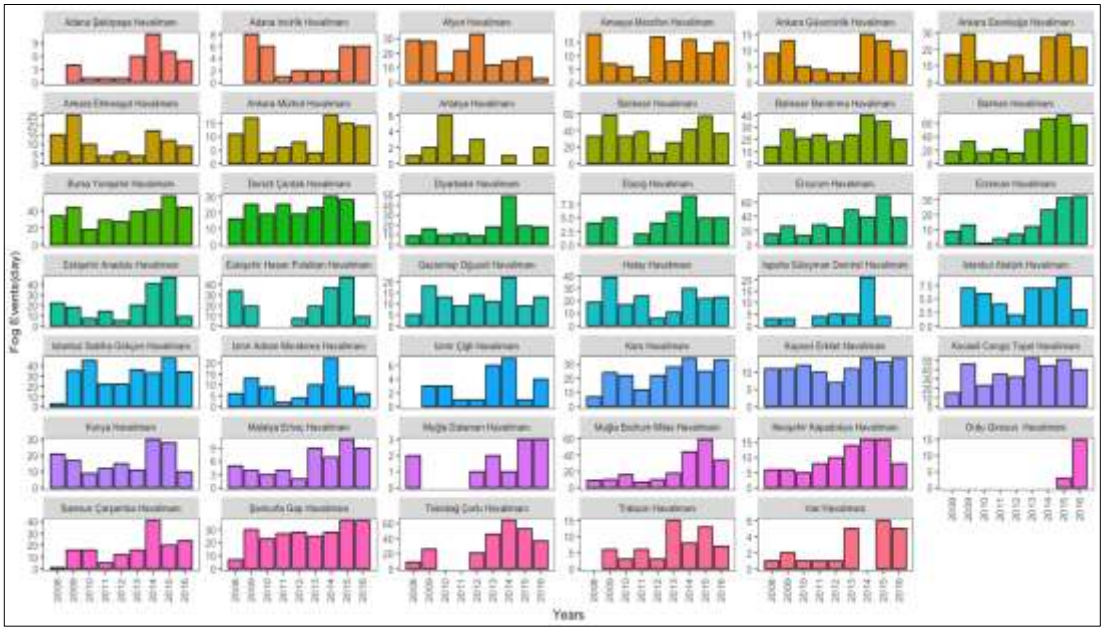

Figure 5. Total number of fog events per year determined from METAR&SPECI

ADA-LTAF (Adana Şakirpaşa), BAT-LTCJ (Batman), ERZI-LTCD (Erzincan), MAL-LTAT (Malatya Erhaç), MUG-LTBS (Muğla Dalaman) and NEV-LTAZ (Nevşehir Kapadokya) airports at the number of foggy days are increase in recent years (Figure 5). IST-LTBA Istanbul Ataturk Airport has been determined to be the most foggy year in 2015 that was recorded with 9 days fog events. In the same year, IST-LTFJ Istanbul Sabiha Gökçen airport also observed the most frequent fog events in 47 days.

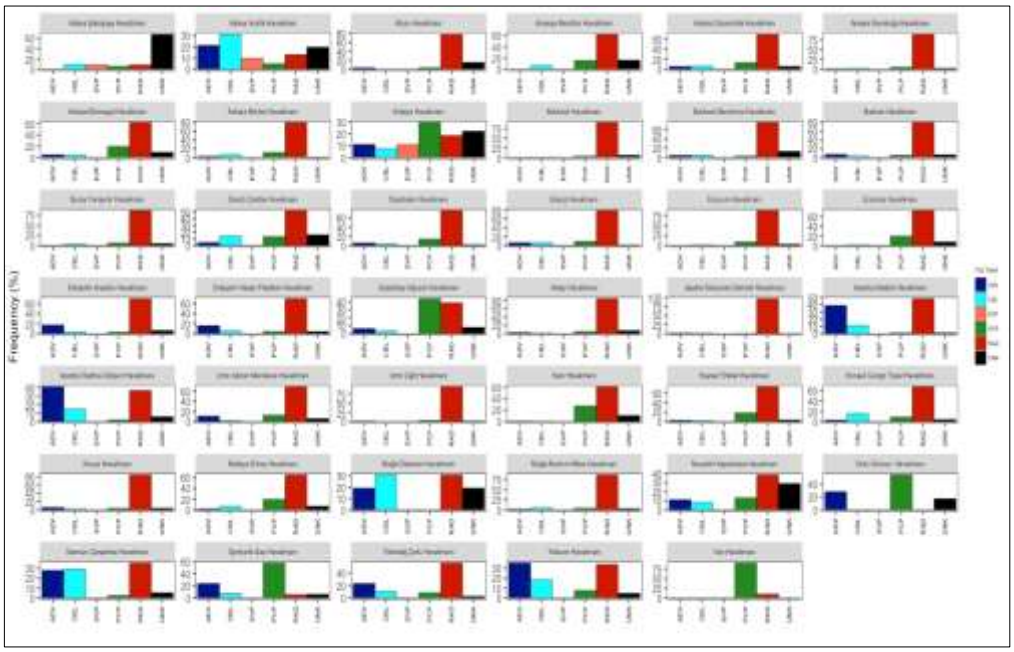

Figure 6. Frequency of occurrence of fog types for airports

The fog type classification algorithm explain in Fig. 1 is implemented to every fog event in each station. Approximately 92% of all identified fog events have been accomplished classified into one of five types determined. When the results are examined (Figure 6), it is seen that the

most prevalent scenario of radiation fog formation and 31 of 41 stations have the highest rate of events in this category. Precipitation fog formation appears to have the highest rate of occurrence in this category in 5 stations (Figure 6). Istanbul Sabiha Gökçen and Trabzon Airports are the fog types with the highest frequency of advection fog types. Moreover, at the airports of Adana Incirlik and Muğla Dalaman, CBL has the highest frequency of occurrence (Figure 6). However, the frequency of occurrence of fog that is not related to the fog types-UNK (unknown) determined in Adana, Afyon, Antalya, Amasya, Denizli, Nevşehir, Muğla Dalaman and Ordu-Giresun airports is 15% or more. Many of the undefined fog types (UNK) have not been identified by the cause of missing data of fog onset. The types of fog events observed at Istanbul Atatürk Airport are 48.1% RAD, 38.9% ADV and 11.1% CBL. According to Ozdemir et al. (2007), fog types at Ataturk Airport were found as 52.17% radiation, 39.13% advection and 4.35% cloud base lowering.

CONCLUSIONS AND RECOMMENDATIONS

The subject addressed in this study was the identification of the general characteristics and observed frequency of the fog events during the 2008-2016 period, at airports. METAR and SPECI observations of fog events were identified and classified into a species using a simple classification algorithm, each based on basic mechanisms for the first occurrence of the fog event. Except Batman airport which is far from the coastal zone in the Southeast Anatolia region, the fog events in the Marmara region airports has been observed more than the other regions. Batman, Kocaeli and Balıkesir airports are the most frequent fog events occurrences. Van, Antalya and Muğla Dalaman are airports where the fog events are the least frequent occurrence. Depending on the physiographic character of the airport, variability in fog types is available. The advection fog events occur in more coastal regions, and the interaction between the cold air on the surface and the warmer and humid air from the sea surface depends. Radiation fog occurrences are more frequent in the inner regions and more frequent in the autumn and winter seasons.

REFERENCES

Akimoto, Y., & Kusaka, H. (2015). A climatological study of fog in Japan based on event data. Atmospheric research, 151, 200-211.

Byers, H. R., & Byers, H. R. (1959). General meteorology/Synoptic and aeronautical meteorology (No. 551.5). McGraw-Hill

Çamalan, G., Yağan, S., Akgün, N., (2010) T.C Çevre ve Orman Bakanlığı, Meteoroloji işleri Genel Müdürlüğü, "Esenboğa Havalimanı Sis Etüdü" Uluslararası Katılımlı 1. Meteoroloji Sempozyumu, 27-28 Mayıs 2010 Sempozyum Bildiri Kitabı, 317-327.

NOAA Glossary < http://w1.weather.gov/glossary/index.php?word=fog>, 05 August 2017

Özdemir, E. T., Sezen, İ., Deniz, A., & Mentes, S. ATATÜRK HAVALİMANI'NIN SİS ANALİZİ/ANALYSIS OF FOG FOR ATATURK INTERNATIONAL AIRPORT.

Stolaki, S. N., Kazadzis, S. A., Foris, D. V., & Karacostas, T. S. (2009). Fog characteristics at the airport of Thessaloniki, Greece. Natural hazards and earth system sciences, 9(5), 1541-1549.

Tardif, R., & Rasmussen, R. M. (2007). Event-based climatology and typology of fog in the New York City region. Journal of applied meteorology and climatology, 46(8), 1141-1168.

WMO (1966). International Meteorological Vocabulary. World Meteorological Organization, Geneva, 275 pp.

Willett, H. C. (1928). Fog and haze, their causes, distribution and forecasting. Monthly Weather Review.

ESTIMATION OF WIND POTENTIALS UNDER SEVERE WEATHER CONDITIONS IN SELECTED REGIONS USING THE WRF MODEL

Duygu AKYIL[1], S. Sibel MENTEŞ[1], Yasemin EZBER[2], Erkan YILMAZ[1], Yurdanur ÜNAL[1], Sema TOPÇU[1]

[1]Istanbul Technical University, Department of Meteorological Engineering, Maslak 34469 Istanbul, TURKEY
akyil.duygu@gmail.com, sentes@itu.edu.tr, ezber@itu.edu.tr, yilmazerkan1@itu.edu.tr, sunal@itu.edu.tr, stopcu@itu.edu.tr
[2]Istanbul Technical University, Eurasia Institute of Earth Sciences, Maslak 34469 Istanbul, TURKEY
eerten@itu.edu.tr

ABSTRACT

This work was supported by the Scientific and Technological Research Council of Turkey (TÜBİTAK) under the European Union ERANET + project titled New European Wind Atlas (NEWA) numbered 215M386 conducted by Prof Dr. Ş.Sibel MENTEŞ. Project is carried out modeling of wind energy source on Turkey under the scope of the "New European Wind Atlas (NEWA) Project ". The Weather Research Forecast (WRF) model is simulated for two different planetary boundary layer (PBL) shemes. which are called Mellor-Yamada-Nakanishi-Nino (MYNN) and Yonsei University Scheme (YSU) in this project. Performance of WRF model is investigated Afyon, Hatay, and Ordu,stations under strong meteorological events by using model and observation time series. Predictability of the model is crucial in extreme events such as storm, flood, tornado etc. Therefore, error analyzes are made by calculating correlation, absolute error, relative error, mean square error, root mean square error and normalized root mean square error. Two boundary layer conditions were used in the WRF model to examine which boundary layer condition best represents the observations in extreme weather events. Both boundary layer parametrizations of the model have deviations from observed datasets in extreme weather conditions. YSU indicates high correlation values for Afyon station while MYNN has higher correlation for Hatay and Ordu under severe weather events. Error is low in Afyon for YSU, however MYNN gives lower error statistics for Hatay and Ordu stations.

Keywords: *WRF Model, Wind Power Potential, Wind Atlas, Severe Weather Conditions*

Introduction

Nowadays, the energy sector is one of the most energy sectors since increase in population, urbanization and social welfare, and the rapid development of industrialization increase the energy demands. It is known that current traditional energy production and consumption technologies have adverse effects on human, environment and natural resources at regional and global level; therefore, producing and consuming energy without harming the environment become an important issue. There is an increasing interest and market in the renewable energy sector all over the world. Developing countries compete to take part of these market opportunities. Countries have accelerated the development of energy production technologies, the creation of various policies to encourage production and consumption, and the preparation of strategic renewable energy zones, in particular to bring economies of zero emission renewable energy sources without compromising on reliable, economical, quality and free market mechanisms and conditions.

The global wind industry has passed a record year in 2015, with annual installations over 54.6 GW, and by the end of 2016 as a whole it has grown to around 486.7 GW globally (GWEC Global Wind Report, 2016). Beyond the European Union, Turkey has become one of the largest

markets in Europe, with a total installed capacity 6145.5 MW at the end of May 2017 (GWEC Global Wind Report, 2017).

Additionally, interest in wind simulation is not only meteorological but also a topic of interest to the wind energy sector. Hence, there have been many model sensitivity studies in the literature. There several purposes to verify numerical models with observations. Why observations are important to verify numerical weather prediction is that observation is a recorded criterion of the progress of forecast skill in years; it is used compare to compare two versions of the forecasting system in order to decide which model is the best for certain operations, and it helps to understand where the problems and which part of the system needs to be improved, and it is also important for relative evaluations of two different systems for certain user category. Topographical features are also very crucial for the model verification. It is expected that the model has better performance over smooth regions since representation of simulation region is close to real topographic features. However model prediction is difficult over Turkey due to the its complex topography.

The best strategy for the verification is to choose a region which has a dense and qualified observation network and the used model with high horizontal resolution representation of the study area. There are a few indicators in order to evaluate the quality of a model. For instance, model forecast variance should be high and root mean square error should be reasonably small (Bougeault, 2003).

Data and Methodology

a) Data

ERA-Interim dataset, provided by The European Centre for Medium-Range Weather Forecasts (ECMWF), is used for simulations, ERA-Interim is daily 4 times dataset with 0.75° horizontal resolution, and 61 vertical levels from sea level to 10 mb. In this study, initial and boundary layer conditions were prepared by using 12 hours ERA-Interim data. Dataset contains u and v components of the wind, temperature, geopotential height, relative humidity, soil temperature and other atmospheric variables. Global 0.25° daily OISST (Optimum Interpolation Sea Surface Temperature) data provided by NOAA was used as a model SST input.

b) The Weather Research and Forecasting Model (WRF)

The Weather Research and Forecasting (WRF) Model is a next-generation mesoscale numerical weather prediction model designed for both atmospheric research and operational forecasting. It features two dynamical cores, a data assimilation system, and a software architecture facilitating parallel computation and system extensibility. WRF, which has a multi-centered dynamic code, has a data assimilation system called MM5 3DVAR (3 Dimensional Varitional) and uses an open software that allows parallel calculations (Barker et al., 2004). WRF domain setup in Figure 1. Three nested domains d01, d02 and d03 with 27 km x 27 km, 9 km x 9 km and 3 km x 3 km resolution respectively, over Turkey (in Figure 1). Only data from d03 were used in the study. The model field structure used is given in Fig.1. Model setup is given Table 1.

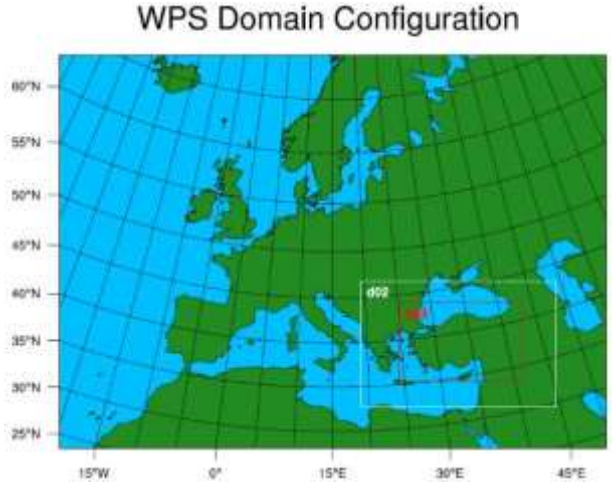

Figure 1. WRF simulation domain

As it seen Table 1 two different PBL schemes, YSU and MYNN are used for three nests. Turbulent kinetic energy is calculated based on local mixing in MYNN PBL scheme which uses improved formulation than YSU by taking more parameters into account.

Table 1. WRF Parametrizations

WRF	
Domain	3 km x 3 km
Vertical Level	61
Initial Data	ECMWF ERA-Interim
Elevation Data	USGS default 30 arc sec
Land Use	Corine Land Cover 250 m
Planeteary Boundary Parameterization	MYNN / YSU
Microphysic	WRF Single Moment 5
Radiation	RRMTG
Surface Scheme	Monin - Obukhov
Cumulus Parameterization	Kain - Fritsch

Results

a) Analyses for Afyon

Four grid points close to Afyon observation station, whose coordinates are shown in Figure 2, take into account for statistical analysis. It is clear that 1st grid point is the best representation based on error rates in YSU and MYNN PBL (Table 2-3).


Figure 2. Grid points belonging to Afyon.

Table 2. Error Analysis of Grid Points in YSU PBL in Afyon.

AFYON	YSU					
	Correlation	Absolute Error	Relative Error	MSE	RMSE	nRMSE
Grid 1	0,5538	1,2484	21,3495	14,8101	3,8484	13,6949
Grid 2	0,5476	2,1549	37,2255	19,2308	4,3853	15,6055
Grid 3	0,4552	1,0553	18,2386	17,6282	4,1986	14,9411
Grid 4	0,4804	2,2293	17,0759	23,0256	4,7985	17,0759

Table 3. Error Analysis of Grid Points in MYNN PBL in Afyon.

AFYON	MYNN					
	Correlation	Absolute Error	Relative Error	MSE	RMSE	nRMSE
Grid 1	0,4493	0,8211	14,1876	17,3435	4,1646	14,8201
Grid 2	0,467	1,9984	34,529	22,1124	4,7024	16,7339
Grid 3	0,5416	1,8996	32,823	17,9919	4,2417	15,0945
Grid 4	0,5283	0,9807	16,9448	14,0665	3,7505	13,3465

Error analysis indicates that 1st grid point, has better representation of Afyon station than the other grids for examined extreme weather days therefore Table 4 and Table 5 are prepared for 1st grid for both YSU and MYNN PBL schemes. According to these tables, the error rates for both PBL schemes are very high. Figure 3 shows the time series analysis of the model results for 1st grid point with annual wind intensity data of Afyon station at 80 m level. Our results show that extreme cause a significant difference between observation and model results.

Table 4. Error Analysis of 1stGrid Point in YSU PBL in Afyon Extreme Weather Days..

AFYON	YSU					
	Correlation	Absolute Error	Relative Error	MSE	RMSE	nRMSE
05.01.2015 - Snow	0.92	1.16	14.75	2.35	1.53	15.68
30.01.2015 - Storm	0.58	2.22	33.05	23.41	4.83	49.53
09.02.2015 - Snow	0.05	4.1	67.92	32.84	5.73	82.64
27.03.2015 - Heavy Rainfall	0.27	0.74	9.72	50.86	7.13	43.9
08.04.2015 - Snow	0.53	3.08	42.64	25.71	5.07	85.78
08.06.2015 - Heavy Rainfall	0.33	5.99	83.67	15.71	6.5	94.52
27.06.2015 - Heavy Rainfall	0.25	2.69	57.08	17.44	4.17	47.06
08.08.2015 - Heavy Rainfall	0.05	0.9	14.06	6.09	2.46	27.06

Table 5. Error Analysis of 1stGrid Point in MYNN PBL in Afyon Extreme Weather Days..

AFYON	MYNN					
	Correlation	Absolute Error	Relative Error	MSE	RMSE	nRMSE
05.01.2015 - Snow	0.93	1.02	12.9	2.66	1.63	16.71
30.01.2015 - Storm	0.59	4.32	64.26	11.15	3.33	34.15
09.02.2015 - Snow	0.09	6.94	81.64	61.69	7.85	96.72
27.03.2015 - Heavy Rainfall	0.23	0.78	10.26	39.02	6.24	38.42
08.04.2015 - Snow	0.76	1.78	23.52	25.53	5.05	85.44
08.06.2015 - Heavy Rainfall	0.31	2.37	67.05	42.25	3.96	69.23

27.06.2015 - Heavy Rainfall	0.12	1.29	27.48	12.77	3.57	40.29
08.08.2015 - Heavy Rainfall	0.22	1.29	20.07	9.42	3.06	33.66

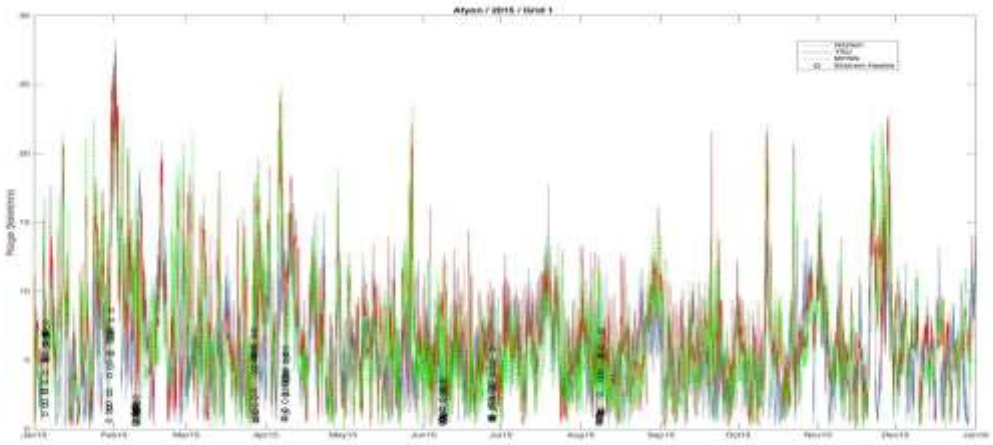

Figure 3. The time series of the model 1st grid point and the annual wind intensity for Afyon station at 80 m level

There are patterns in the synoptic scale that are effective on Afyon in the periods where the model results differ from the observed data. To explain this relationship, it is examined that the synoptic patterns of ground and upper level (500 hPa) 5 January 2015 are examined by using synoptic charts.on (Figure 4-6).

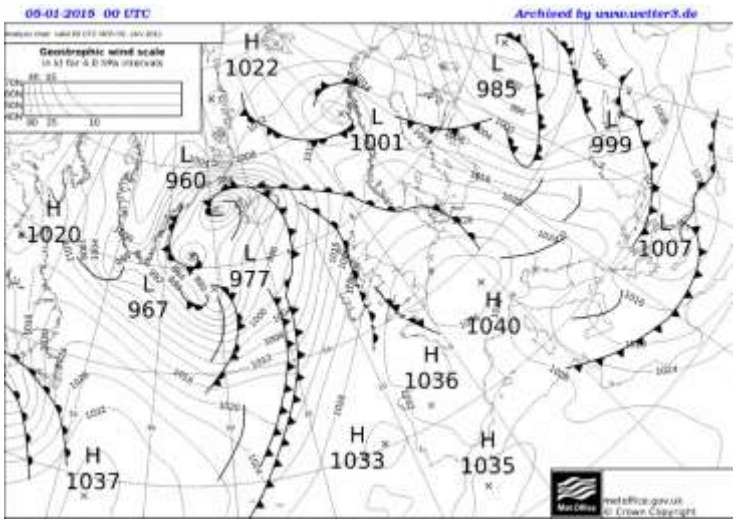

Figure 4. Synoptic chart of surface on 05-01-2015 at 00 UTC.(www.wetter3.de)

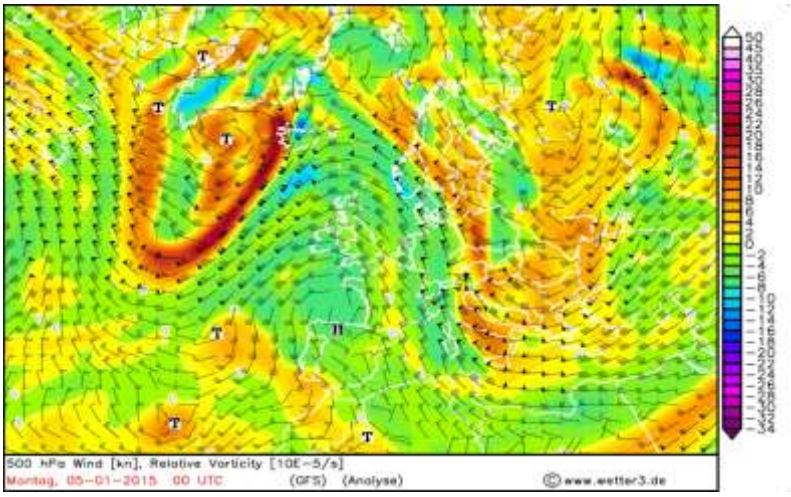

Figure 5. Map of Wind and Relative Vorticity at 500 hPa on 05-01-2015 at 00 UTC. (www.wetter3.de)

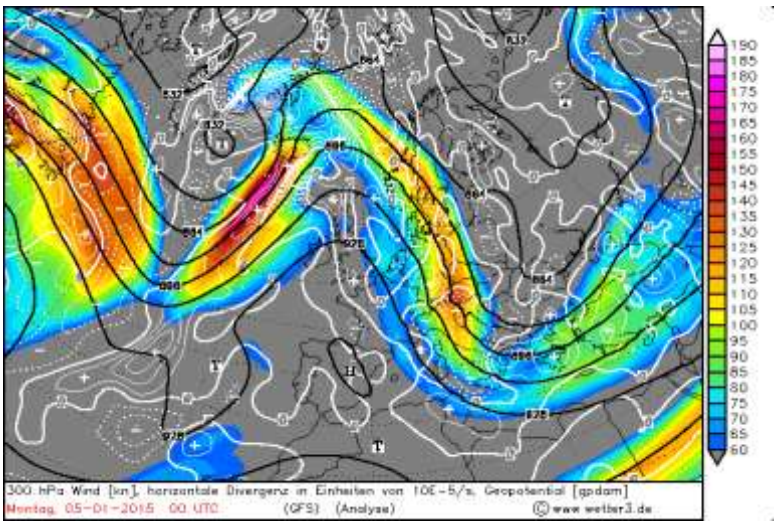

Figure 6. Map of Wind ve Jet Streams at 300 hPa on 05-01-2015 at 00 UTC. (www.wetter3.de)

Figure 4 shows that before before the cyclone occluded, a cold front passed over Afyon, and a low pressure center (with 1007 mb) affects the region. It is obviously seen from the 500hPa vorticity map that Afyon takes place east of a trough where positive vorticity and advection are observed (in Figure 5). Location of 300mb jet streams which reach up to 80knots influence the existence of the system as seen in Figure 6.

b) Analyses for Hatay

Four grid points close to Hatay observation station, whose coordinates are shown in Figure 7, take into account for statistical analysis. . It is clear that 2st grid point is the best representation based on error rates in YSU and MYNN PBL (Table 6-7).

Figure 7. Grid points belonging to Hatay.

Table 6. Error Analysis of Grid Points in YSU PBL in Hatay.

HATAY	YSU					
	Correlation	Absolute Error	Relative Error	MSE	RMSE	nRMSE
Grid 1	0,5167	0,7403	10,2248	15,2459	3,9046	15,6265
Grid 2	0,547	1,1777	16,2579	13,7937	3,714	14,8637
Grid 3	0,5464	1,044	14,4123	13,2597	3,6414	14,5732
Grid 4	0,5066	0,6837	9,4384	16,6553	4,0811	16,3329

Table 7. Error Analysis of Grid Points in MYNN PBL in Hatay.

HATAY	MYNN					
	Correlation	Absolute Error	Relative Error	MSE	RMSE	nRMSE
Grid 1	0,5812	1,1723	16,183	12,9815	3,603	14,4195
Grid 2	0,5817	0,9779	13,4989	12,3166	3,5095	14,0453
Grid 3	0,5321	0,6579	9,0817	16,2802	4,0349	16,148
Grid 4	0,545	0,7595	10,4839	14,9216	3,8629	15,4596

Error analysis indicates that 2stgrid point, has better representation of Hatay station than the other grids for examined extreme weather days therefore Table 6 and Table 7 are prepared for 2st grid for both YSU and MYNN PBL schemes. According to these tables, the error rates for both PBL schemes are very high. Figure 8 shows the time series analysis of the model results for 2st grid point with annual wind intensity data of Hatay station at 80 m level. Our results show that extreme cause a significant difference between observation and model results. The results of MYNN PBL is more consistent than YSU PBL with the observations for the observed extreme events. Error statistics indicate that RMSE and nRMSE values of MYNN lower than YSU for both extreme days given in Table 8 and 9.

Table 8. Error Analysis of 2st Grid Point in YSU PBL in Hatay Extreme Weather Days..

HATAY	YSU					
	Correlation	Absolute Error	Relative Error	MSE	RMSE	nRMSE
05.01.2015 - Storm and Heavy Rainfall	0.36	2.54	15.46	33.09	5.75	35.21
26.06.2015 - Heavy Rainfall	0.19	0.9	8.78	4.01	2.09	31.33

Table 9: Error Analysis of 2st Grid Point in MYNN PBL in Hatay Extreme Weather Days..

HATAY	MYNN					
	Correlation	Absolute Error	Relative Error	MSE	RMSE	nRMSE
05.01.2015 - Storm and Heavy Rainfall	0.58	2.75	16.72	25.9	5.08	31.1
26.06.2015 - Heavy Rainfall	0.3	0.31	3.05	3.18	1.78	26.68

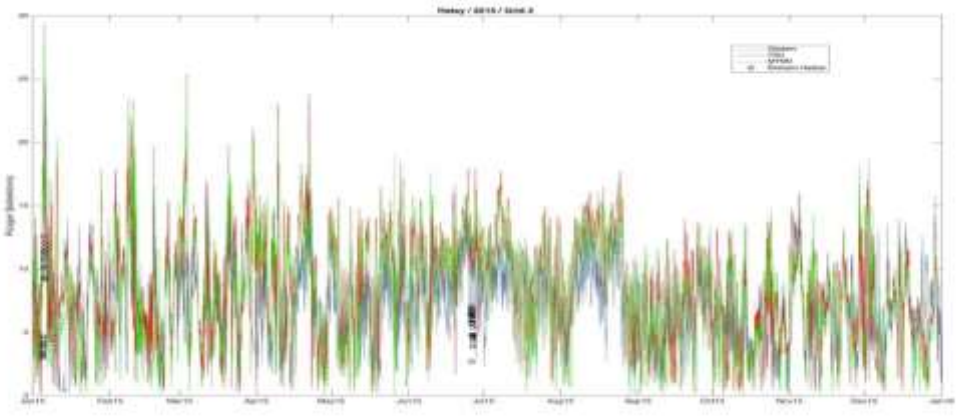

Figure 8. The time series of the model 2st grid point and the annual wind intensity for Hatay station at 80 m level

.

c) Analyses for Ordu

Four grid points close to Ordu observation station, whose coordinates are shown in Figure 9, take into account for statistical analysis. . It is clear that 4st grid point is the best representation based on error rates in YSU and MYNN PBL (Table 10-11).

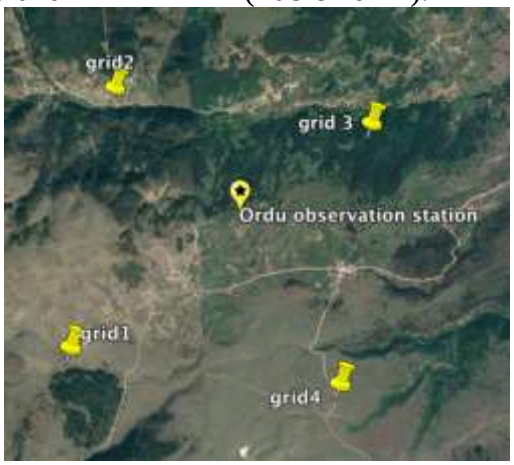

Figure 9. Grid points belonging to Ordu.

Table 10. Error Analysis of Grid Points in YSU PBL in Ordu.

ORDU	YSU					
	Correlation	Absolute Error	Relative Error	MSE	RMSE	nRMSE
Grid 1	0,5374	0,8681	16,8952	12,0214	3,4672	14,9706
Grid 2	0,4894	0,738	14,4571	11,9004	3,4497	14,8951
Grid 3	0,5124	0,7824	15,3266	11,8645	3,4445	14,9676
Grid 4	0,5312	0,6012	11,7774	10,8867	3,2995	14,2461

Table 11. Error Analysis of Grid Points in MYNN PBL in Ordu.

ORDU	MYNN					
	Correlation	Absolute Error	Relative Error	MSE	RMSE	nRMSE
Grid 1	0,5448	0,4357	8,5431	11,1381	3,3374	14,4102
Grid 2	0,521	0,3325	6,5201	10,9938	3,3157	14,3165
Grid 3	0,5424	0,4844	9,4998	11,1852	3,3444	14,4404
Grid 4	0,5587	0,2978	5,8393	10,2908	3,2079	13,851

Error analysis indicates that 4st grid point, has better representation of Ordu station than the other grids for examined extreme weather days therefore Table 12 and Table 13 are prepared for 4st grid for both YSU and MYNN PBL schemes. According to these tables, the error rates for both PBL schemes are very high. Figure 9 shows the time series analysis of the model results for 4st grid point with annual wind intensity data of Ordu station at 80 m level. Our results show that extreme cause a significant difference between observation and model results.

Table 12. Error Analysis of 4st Grid Point in YSU PBL in Ordu Extreme Weather Days.

ORDU	YSU					
	Correlation	Absolute Error	Relative Error	MSE	RMSE	nRMSE
28.03.2015 - Storm	0.29	2.23	16.11	20.39	4.51	24.4
19.06.2015 - Heavy Rainfall	0.07	0.92	22.83	11.47	3.38	39.57
07.10.2015 - Heavy Rainfall	0.27	0.81	19.88	5.09	2.25	36.34

Table 13. Error Analysis of 4st Grid Point in MYNN PBL in Ordu Extreme Weather Days.

ORDU	MYNN					
	Correlation	Absolute Error	Relative Error	MSE	RMSE	nRMSE
28.03.2015 - Storm	0.36	1.55	11.21	17.09	4.13	22.34
19.06.2015 - Heavy Rainfall	0.25	0.53	13.22	7.49	2.73	31.96
07.10.2015 - Heavy Rainfall	0.32	0.2	4.88	6.34	2.51	40.54

In general, when the extremes are observed, the error value of MYNN PBL is lower than the YSU PBL, but the correlation is low and the error rates are high. Correlation is the relatively high for the storm than heavy rainfall events and also errors for storm event is lower than heavy rainfall events.

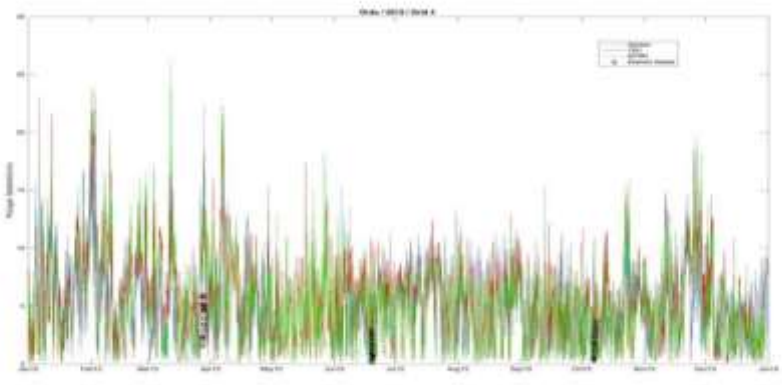

Fig 9. The time series of the model 4st grid point and the annual wind intensity for Hatay station at 80 m level

Conclusions and Discussion

In this study, performance of WRF under extreme weather events is investigated in year 2015 for selected regions Afyon, Hatay and Ordu, using two PBL schemes, YSU and MYNN. The consistency of the observed model outputs with the observed values is compared by making the necessary error analyzes and examining the time series analyzes. The relation between patterns in the synoptic scale, where periods are suddenly deviated in the model, is studied. The following conclusions were drawn from the study:

• Average wind speed is high both for YSU and MYNN than observations. However, average wind speed of MYNN is closer to observed one.

• Both boundary layer parametrizations of the model have deviations from observed datasets in extreme weather conditions.

• 1st grid point better represents the station in Afyon, which has high correlation on YSU simulation. Error of the YSU model data is lower while the average of the MYNN model data is closer to the average of the observation data. But there is not much difference between MYNN and YSU error.

• Correlation is higher for MYNN than YSU in Hatay, and Ordu. Error values of the MYNN are lower and the average of the MYNN model data is closer to the average of the observation data. But there is not much difference between MYNN and YSU error values.

• It is not anticipated that a grid closest to station provides the best representation of the model. It is very important to pay attention whether the selected grid point represents the topography for wind atlas studies in order to avoid miscalculations when acquiring data from the model.

• It is not possible to directly relate to error values and correlations between model outputs and observation data sets. Wind atlas studies should be conducted by considering average wind speeds, deviations from the mean, and error values.

• Model might be corrected by generating coefficients depending on model prediction above or below to observations.

Acknowledgement

We would like to thank to the Scientific and Technological Research Council of Turkey (TUBITAK) for supporting the Project on Modeling of Wind Energy Source on Turkey number 215M386 and thank the ITU National Center for High Performance Computing (UYBHM) (grant no. 5003652015) for the calculation time they have allocated to us.

References

Barker, D. M., W. Huang, Y.-R. Guo, and A. Bourgeois, 2003: A Three-Dimensional Variational (3DVAR) Data Assimilation System For Use With MM5. NCAR Tech Note, NCAR/TN- 453+STR, 68 pp. [Available from UCAR Communications, P.O. Box 3000, Boulder, CO, 80307.].

Bourgeault P. "The WGNE Survey of Verification Methods for Numerical Prediction of Weather Elements and Severe Weather Events." WGNE Assessment of Verification Methods. N.p., 2003. Web. 29 July 2017.

Global Wind Energy Council. (2016). Global Wind Report.

Global Wind Energy Council. (2017). Global Wind Report.

THE IMPACT OF SKYSCRAPERS AND WIND TURBINE FARMS ON ISTANBUL WEATHER RADAR DATA

Kurtuluş ÖZTÜRK, Alper ÇUBUK
Turkish State Meteorological Service, Remote Sensing Division
kozturk@mgm.gov.tr, acubuk@mgm.gov.tr

ABSTRACT
As a result of the increasing needs for renewable energy and smart-multiple floor tall buildings in crowded metropolitans, the number of wind turbines and skyscrapers is increasing rapidly day by day. In this study, the impact of wind turbine farms and skyscrapers built after Istanbul radar installation are investigated. It is seen that Istanbul single polarization Doppler radar can filter the clutter echoes caused by the targets such as skyscrapers and mountains; however, it may not completely remove the clutter from wind turbines due to their rotating blades. This may cause misestimates by forecasters and hydrologists. Partial Beam Blockage (PBB) and attenuation are the other error sources and this study shows that radar quantitative precipitation estimates (QPE) and NWP radar data assimilations are adversely affected by these error sources. PBB diagrams and beam blockage fractions are derived by using 30m resolution digital elevation database and modified open source wradlib code. It is stated that super refraction can occur due to the low-level inversion; hence the radar beam may bend more even if it is not seen in theoretical PBB diagrams when the standard atmospheric refraction applies. This study presents visual examples including radar products, Google maps and PBB diagrams to support the statements.

Keywords - *Radar, Anomalous Propagation, Partial Beam Blockage, Attenuation, Beam Width*

INTRODUCTION
The location of weather radar is very essential and should be carefully selected to avoid some environmental error sources. Before designating radar location, beam blockage maps and possible interference sources in the radar coverage should be identified. By evaluating many factors affecting cost and data quality, the best location is decided among the candidate locations. However, after radar installation, it may not be possible to control new constructions in the region such as wind turbine farms and skyscrapers. As a result of the increasing needs for renewable energy and smart-multiple floor tall buildings in crowded metropolitans, the number of wind turbines and skyscrapers is increasing rapidly. On the other hand, weather radars suffer from interference, clutter problem and partial beam blockage (PBB) caused by these constructions. Single polarization Doppler radars can filter the clutter echoes from the stationary targets; however, they may not remove the clutter from wind turbines due to their rotating blades.

In this study, the impact of wind turbine farms and skyscrapers installed after radar installation in 2003 are studied by means of radar products, Google maps and PBB diagrams. To study the affect of anomalous propagation, Skew-T diagrams are examined and the results are given in Result and Conclusion chapter.

METHODS
PBB diagrams and beam blockage fractions are derived by using 30m resolution digital elevation maps and modified open source wradlib code. To calculate theoretical PBB, the radar site and concerned site coordinates, number of rays, number of bins, the elevation, the beam width (See Figure 1) and the range resolution need to be known

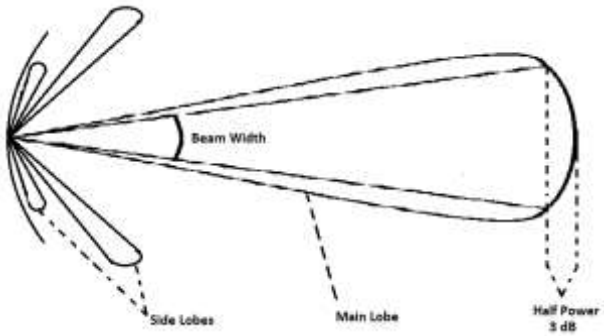

Figure 1. The 3-dB beam width of a radar antenna

The maximum height of the radar beam is given by the following equation when the standard atmospheric refraction applies (Rinehart, 2000).

$$H = \sqrt{r^2 + R'^2 + 2rR'\sin\phi} - R' + H_0 \quad (1)$$

where r is the distance between the radar and the point of interest, ϕ is the elevation angle of the radar beam, H_0 is the height of the radar antenna above mean sea level, $R' = 4R/3$ and R is the earth's radius. İstanbul weather radar has been operational since 2003. It is a single polarization Doppler radar at C-band. Bursa weather radar which is a dual polarization Doppler radar at C-band has been operational since 2015. Dense rain gauge networks that are operated in field campaigns help to determine the variability of rainfall within the scale of a radar pixel and satellite footprint (Tokay and Ozturk 2012). In order to have reliable ground observations, Turkish State Meteorological Service (TSMS) has been collecting rainfall observations from 50 sites containing triple collocated rain gauges since 2014.

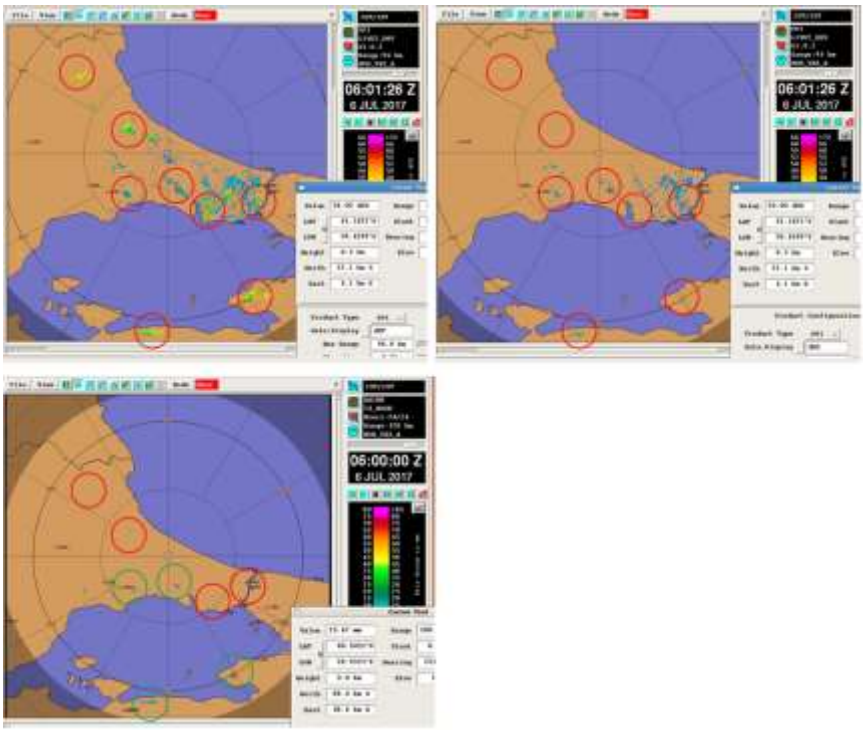

Figure 2. Comparison of unfiltered reflectivity (dBT), filtered reflectivity (dBZ) and 24-hour total rainf

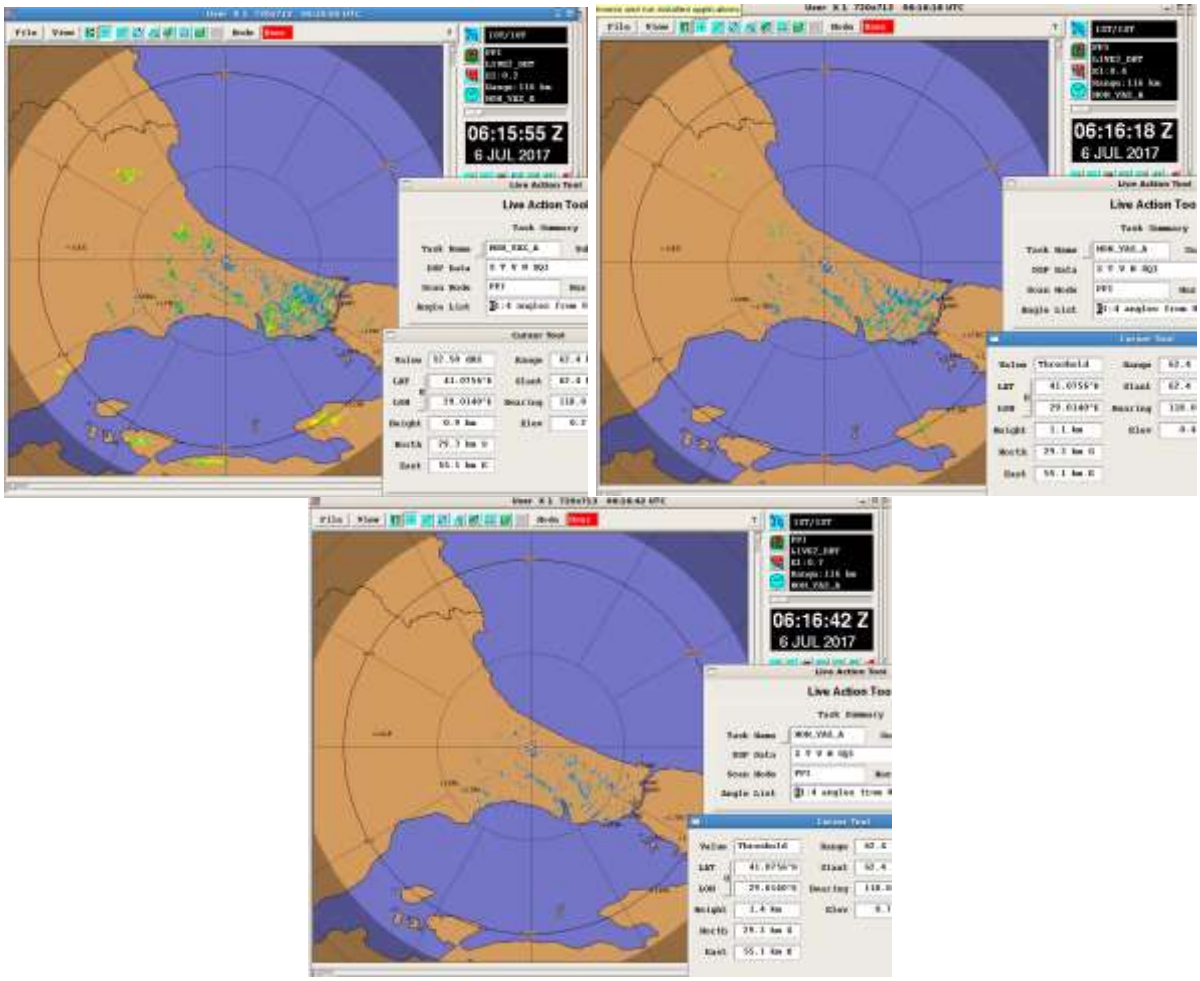

Figure 3. Comparison of reflectivity values in PPI dBT 0.2 deg, dBT 0.4 deg and dBT 0.7 deg

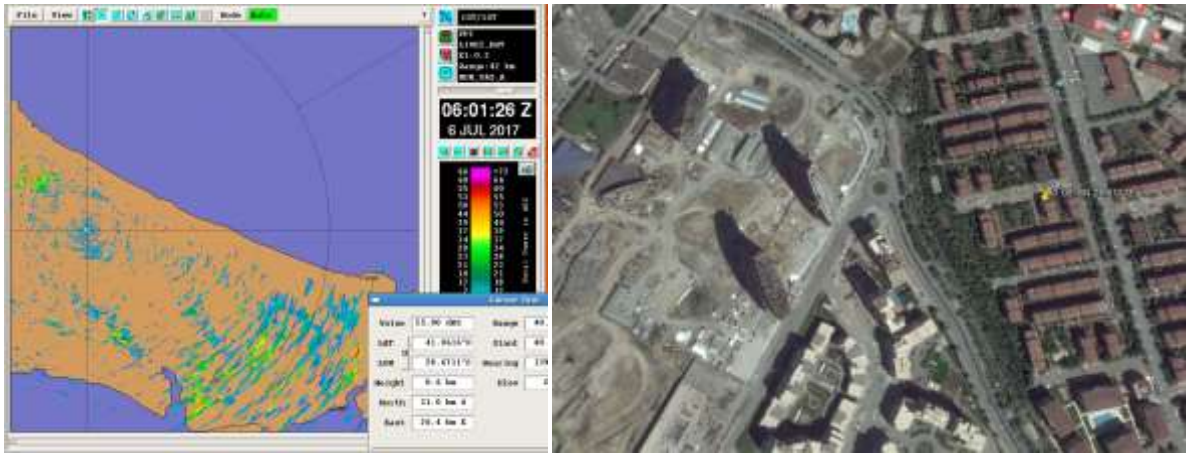

Figure 4. High reflectivity in PPI dBT product and corresponding coordinate in Google Maps showing Kozapark buildings

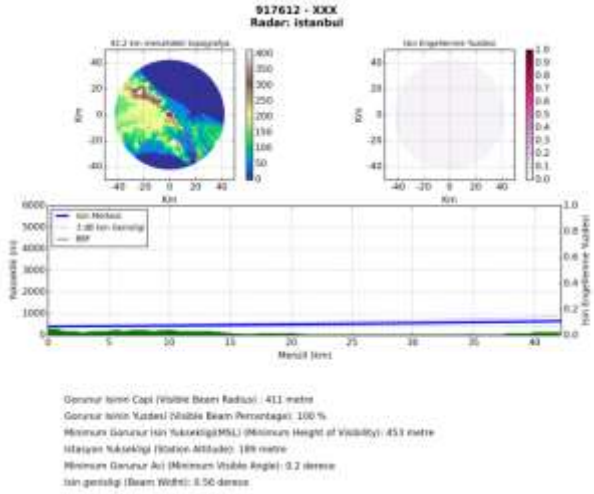

Figure 5. Partial beam blockage diagram between Kozapark buildings and İstanbul radar

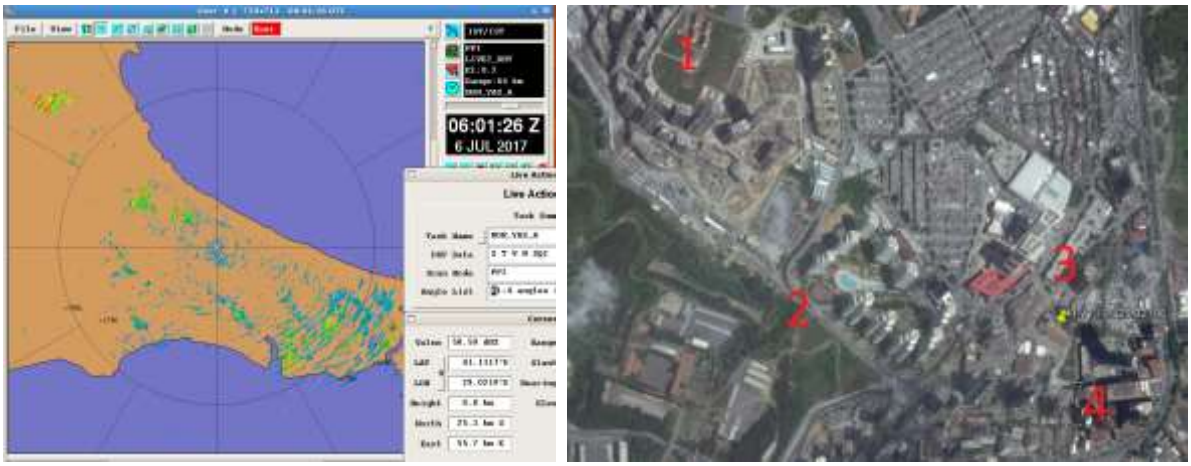

Figure 6. High reflectivity in PPI dBT product and corresponding coordinate in Google Maps showing the region including Maslak 1453 (1), Mashattan (2), Doğus Center (3) and Spine Tower (4) Buildings

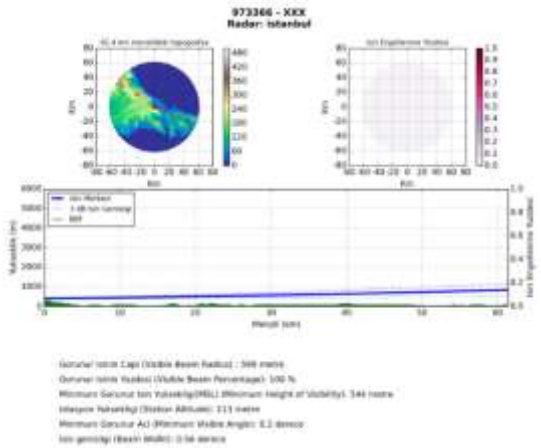

Figure 7. Partial beam blockage diagram between Spine Tower and İstanbul radar

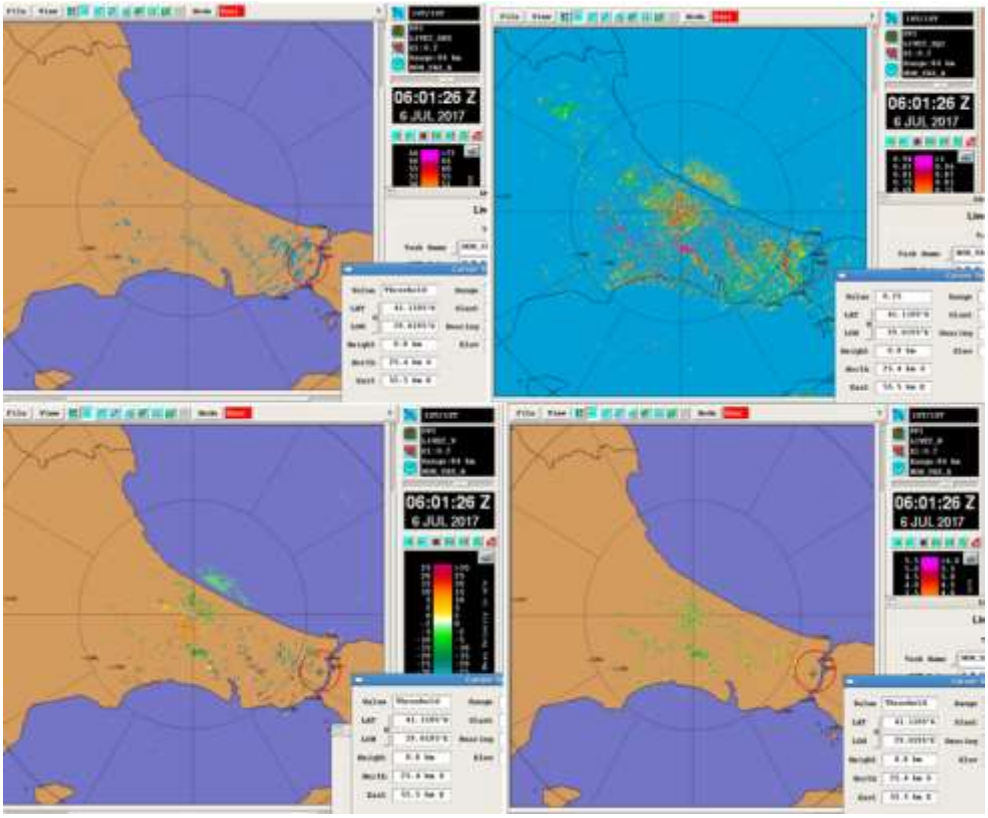

Figure 8. Compasion of PPI dBZ, SQI, Velocity and Spectral Width at Spine Tower location

.

Figure 9. The comparison of PPI dBT products in 2009 and 2017. Corresponding coordinate in Google Maps shows Sapphire Skyscraper location

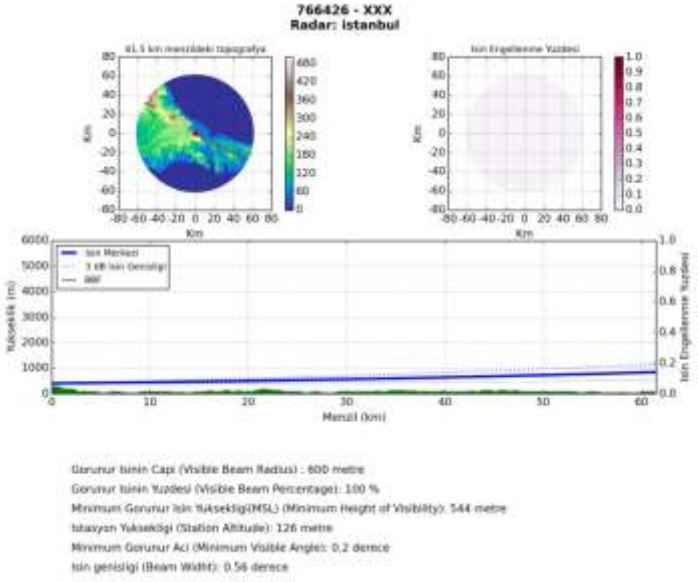

Figure 10. Partial beam blockage diagram between Sapphire Skyscraper and İstanbul radar

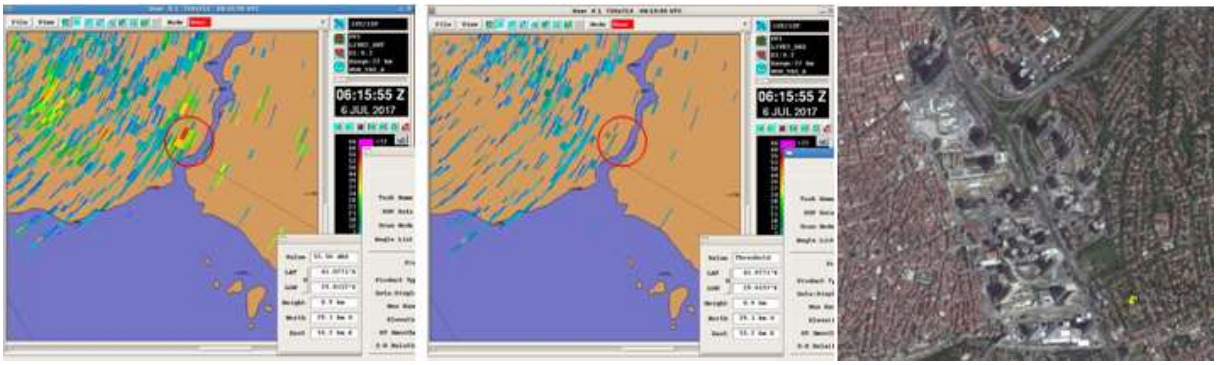

Figure 11. PPI dBT and dBZ product and corresponding coordinate in Google Maps showing the region including Sapphire Skyscraper and other high buildings located at downtown İstanbul, Maslak region.

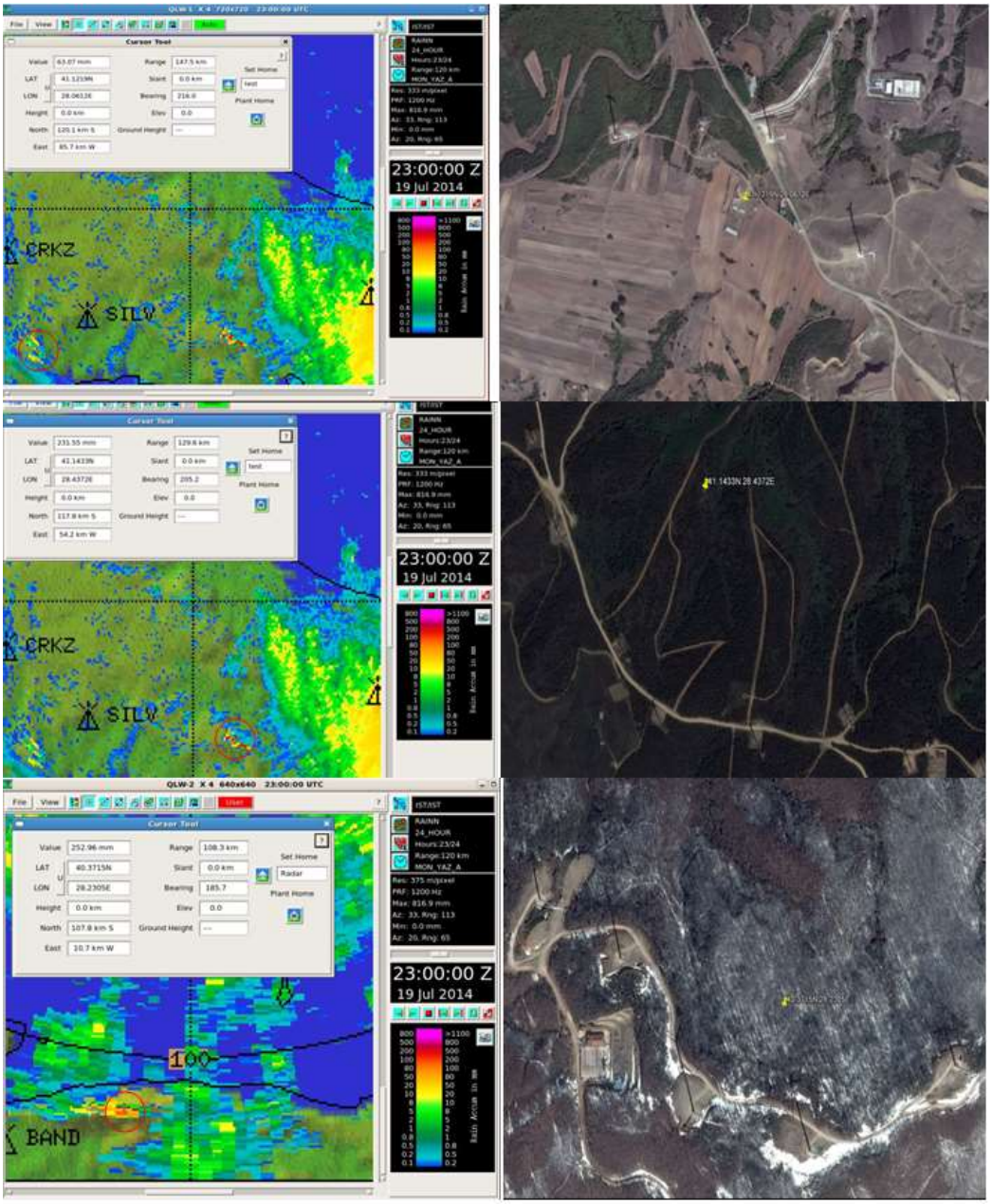

Figure 12. Unrealistic rain amounts in Vaisala RAIN product and corresponding coordinates in Google Maps showing Wind Farm Turbines

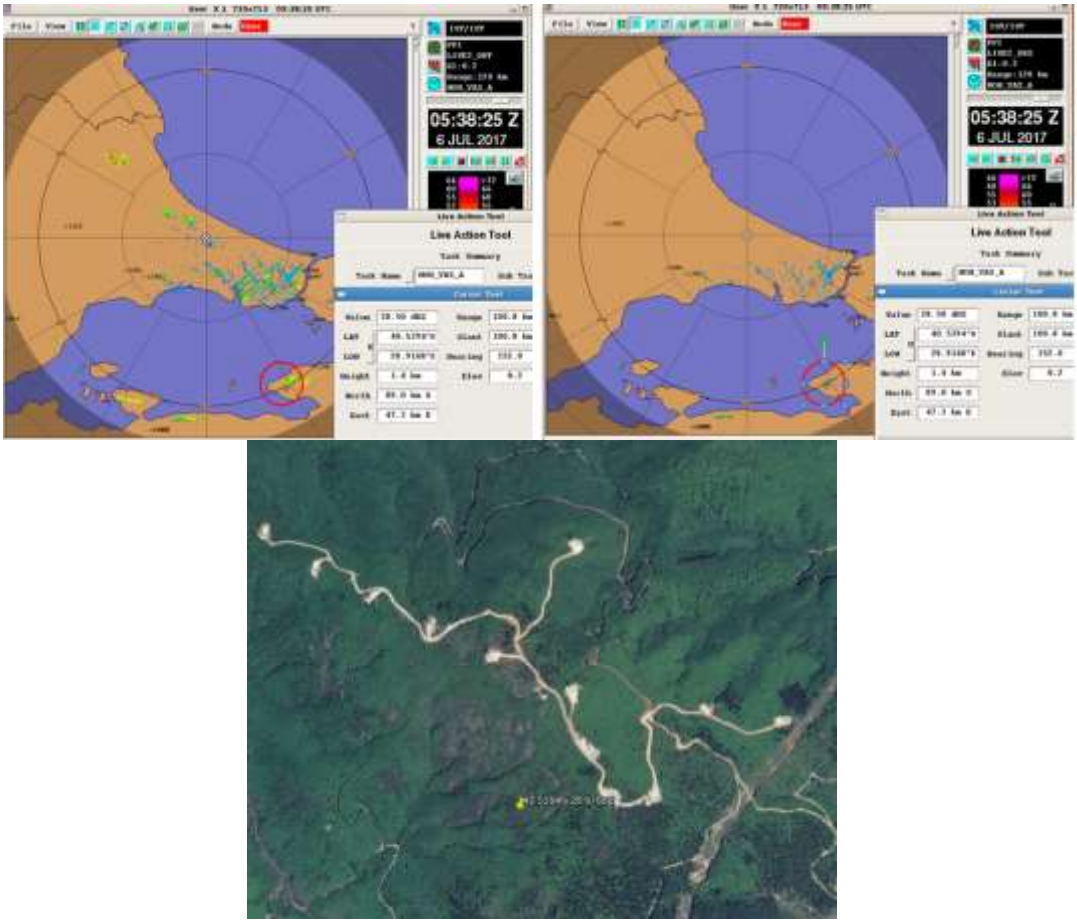

Figure 13. Compasion of reflectivity values in PPI dBT, PPI dBZ and corresponding coordinate in Google Maps showing Wind Turbine Farms located in Yalova.

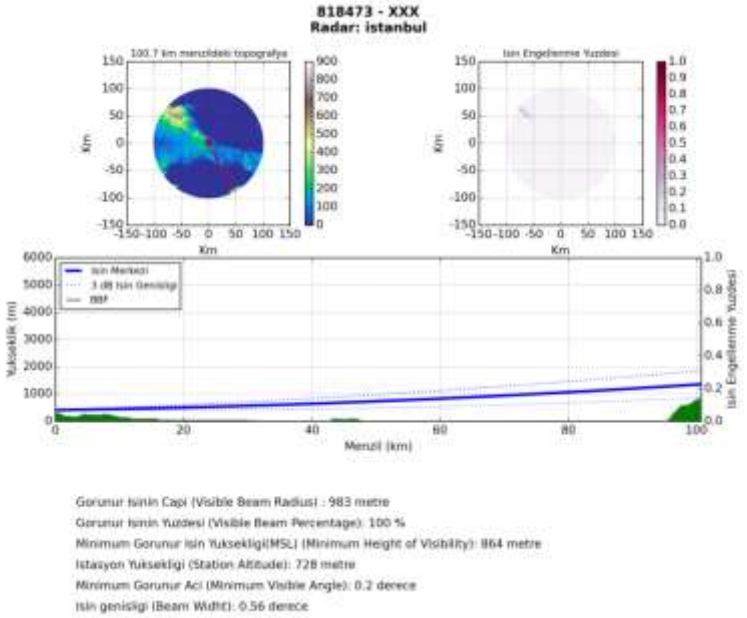

Figure 14. Partial beam blockage diagram between a wind turbine located at Yalova farm and İstanbul radar

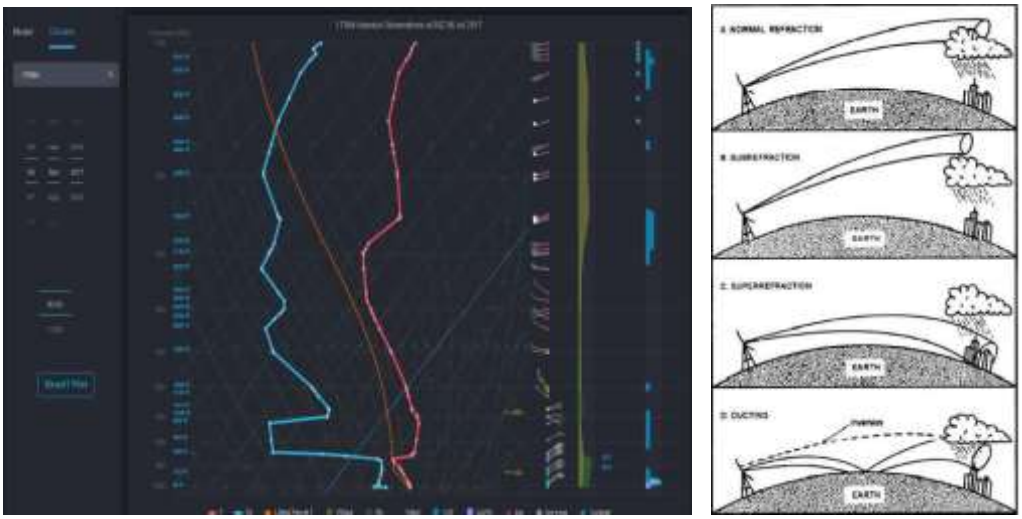

Figure 15. Skew-T Diagram on June 6, 2017 showing stable weather and inversion which may cause anomalous propagation

Table 1. Rain accumulation in 1 hour at Üsküdar site having 3 collocated rain gages (19.07.2017 08:00Z).

2014	7	15	20	0.10	0.00	0.10
2014	7	16	13	0.00	0.06	0.00
2014	7	17	9	0.00	0.07	0.00
2014	7	18	8	0.00	0.06	0.00
2014	7	19	6	6.60	6.68	6.80
2014	7	19	7	46.70	45.99	47.20
2014	7	19	8	0.70	0.73	0.70
2014	7	19	10	0.60	1.11	1.20
2014	7	19	11	0.00	0.00	0.10

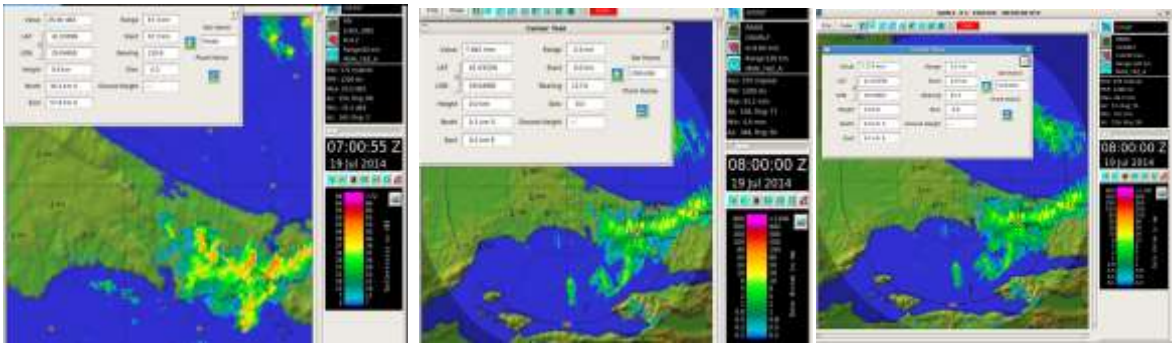

(a) (b) (c)

Figure 16. a-PPI Reflectivity, b-1 hour total RAIN (Marshall-Palmer), c-1 hour total RAIN ($300R^{1.4}$)

Table 2. Rain accumulation in 2 hours at Üsküdar site having 3 collocated rain gages (23.08.2015 at 09:00Z).

2015	8	23	2	10.50	10.74	10.50
2015	8	23	3	0.10	0.15	0.10
2015	8	23	4	0.80	0.68	0.70
2015	8	23	7	18.70	16.86	18.50
2015	8	23	8	10.20	10.05	10.30
2015	8	23	9	1.90	2.05	2.10
2015	8	23	10	0.10	0.14	0.20

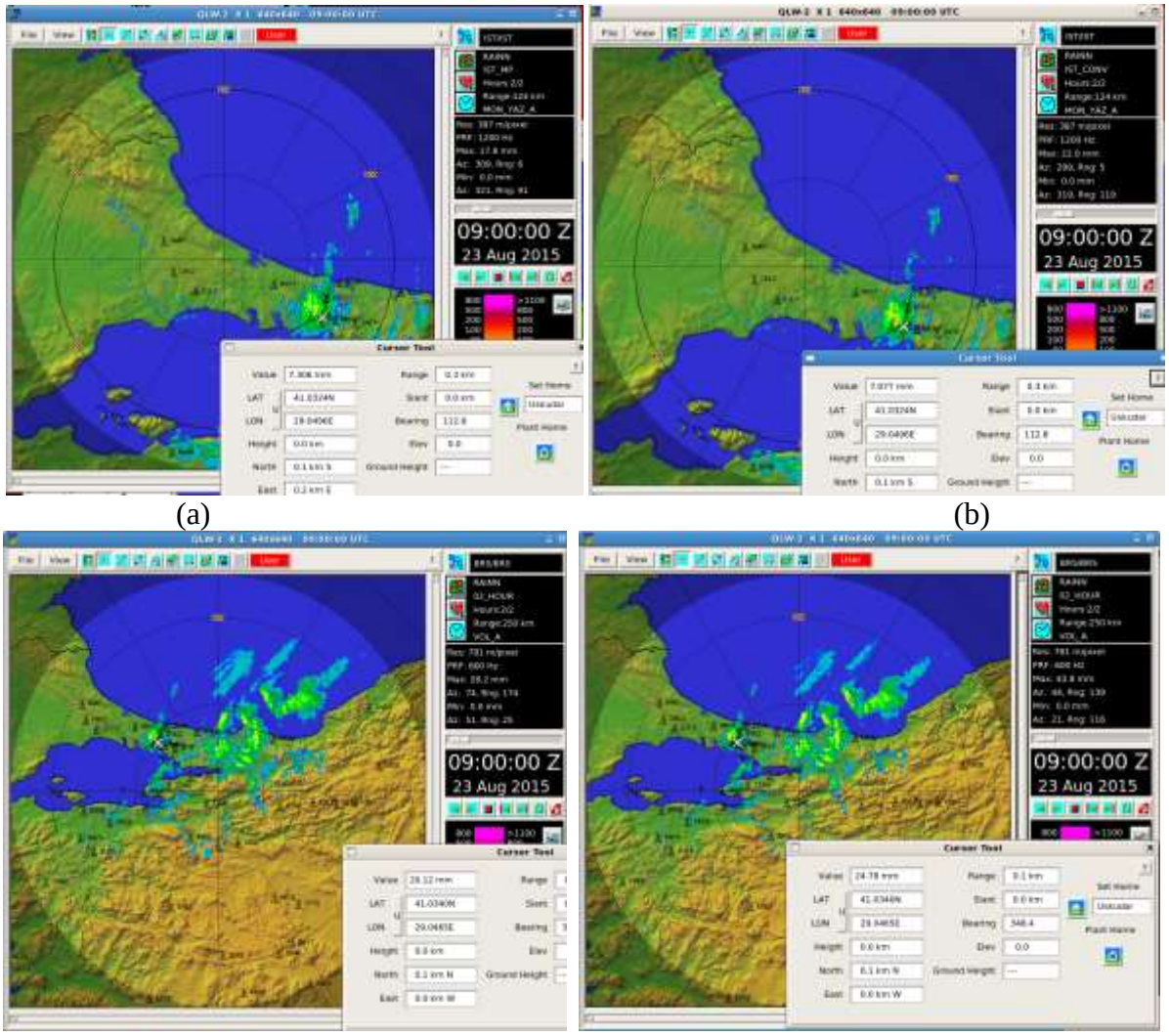

(a) (b)

(c) (d)

Figure 17. Radar rain accumulation in 2 hours at Üsküdar site (23.08.2015 at 09:00Z) , a) by Istanbul radar (Marshall-Palmer), b) by Istanbul radar ($300R^{1.4}$), c) by Bursa radar (Marshall-Palmer), d) by Bursa radar (R-KDP)

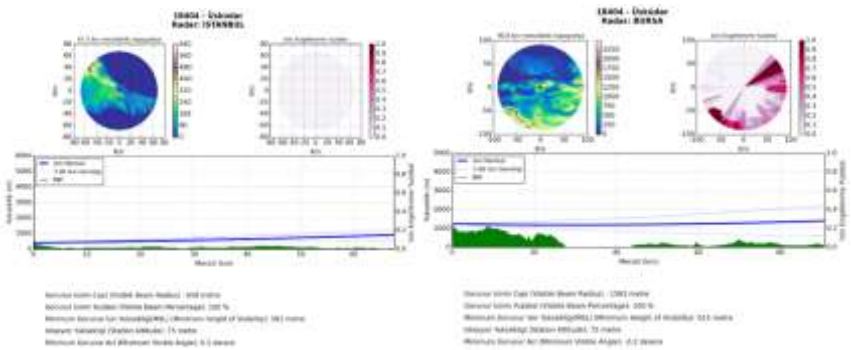

Figure 18. Partial beam blockage diagram between Üsküdar and İstanbul (0.2 deg) / Bursa radars (-0.2 deg)

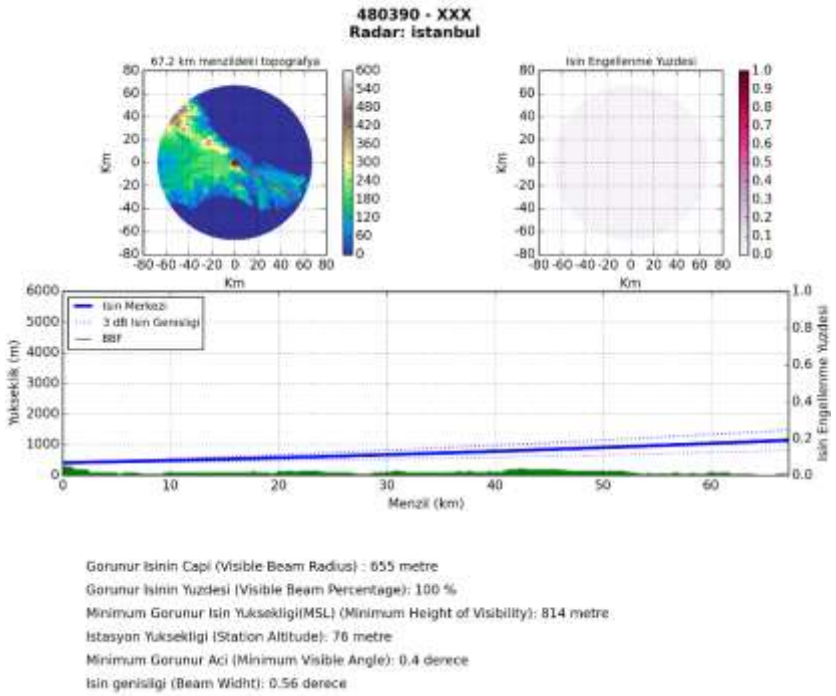

Figure 19. Partial beam blockage diagram between Üsküdar and İstanbul radar (0.4 deg)

RESULTS AND CONCLUSION

Comparison of total reflectivity (dBT), filtered reflectivity (dBZ) and 24-hour total rainfall (See Figure 2) indicates that some clutter data is filtered but there is still clutter data which cannot be filtered. By changing the elevation angles or looking at the filtered reflectivity, velocity and spectral width products also help user to identify clutters (Figure 3 and Figure 8). Unfiltered clutters may cause unrealistic rain estimates for QPE studies, erroneous input to NWP data assimilations and poor forecasts.

Comparison of two unfiltered reflectivity products İstanbul radar before and after Sapphire Skyscraper construction, it is clearly seen that there were no clutter at Sapphire location before its construction. PBB diagrams and beam blockage fractions are derived by using 30m resolution digital elevation database and modified open source wradlib code. This code uses 3 dB half-power beam width (Figure 1) and employs Equation 1 to find the height of the radar beam at a given distance when normal atmosphere refraction conditions apply. However, the real atmosphere may differ from theory and digital elevation databases do not include skyscrapers and wind turbines. The Kozapark buildings are located at 189 m above MSL and the heights of the buildings are around 150 m (total height is 339 m above MSL). The PBB diagrams indicate that the minimum height of visibility is 453 m above MSL (See Figure 4). The Spine Tower is located at 113 m above MSL and the height of the building is 211 m (total height is 324 m above MSL). The PBB diagrams indicate that the minimum height of visibility is 544 m above MSL (Figure 6 and 7). Another tall building is Sapphire Skyscraper It is the tallest building in city of İstanbul and was constructed in 2011. It is located at 387 m above MSL (including 261 m building height). The PBB diagrams indicate that the minimum height of visibility is 544 m above MSL (Figure 9, 10 and 11). All of these results suggest that radar beams should not hit these skyscrapers according to theoretical calculations, but reflectivity in these points is observed in radar products.

If the temperature of the atmosphere increases with height and/or the water vapor content decreases rapidly with height, the refractivity decreases from the standard. This situation

is called as super refraction and low-level inversions can cause more bending towards the earth surface (See Figure 15). Even though Istanbul radar beam must not hit to skyscrapers according to the PBB diagrams (should be around 200 m above), clutters are seen in radar images at skyscraper's coordinates. Single polarization Doppler radars can filter the clutter echoes from stationary targets such as skyscrapers or mountains; however, they cannot eliminate the effect of PBB. Weather radars may not remove the clutter from wind turbines completely due to their rotating blades. The total height (including blades) of a wind turbine installed at Yalova wind turbine farm is 147 m. The PBB diagrams indicate that the minimum height of visibility is 864 m above MSL while the turbine is located at 728 m above MSL. These situations yield clutter at 100 km distance from Istanbul radar. Similar situations produce clutter 108 km away from radar at Bandırma wind turbine farm. Since these clutters cannot be filtered, they cause unrealistic rain calculations.

Theoretical PBB calculations between Üsküdar and İstanbul radar (first elevation angle: 0.2 deg) / Bursa radar (first elevation angle: -0.2 deg) (See Figure 18) look quite similar. Since digital elevation databases do not include skyscrapers and wind turbines and the wradlib code employs standard refraction model, Üsküdar is 100% visible from both radars according to wradlib PBB calculations, but it is not in reality. Istanbul radar beam hits skyscrapers especially located at Maslak region (See Figure 4, 5, 6, 9 and 11) and this causes PBB over Üsküdar and underestimation of rainfall. Anomalous propagation is investigated by means of Skew-T diagram in order to understand the effect of inversion on the beam geometry (See Figure 15). It is stated that super refraction can occur due to low-level inversion, then radar beam may bend more than standard even if it cannot be seen in theoretical PBB diagrams when the standard atmospheric refraction applies.

This study also shows that quantitative precipitation estimates (QPE) are adversely affected by PBB and attenuation, even if the clutters are filtered. Unrealistic rainfall amounts can be seen in radar rainfall products (See Figure 2 and Figure 12). A convective storm occurred in 19.07.2014 08:00 Z. Three collocated rain gages installed at Üsküdar site recorded very close rain amounts in 1 hour (See Table 1). Another convective storm occurred in 23.08.2015 09:00 Z and observations of 3 rain gages were consistent during 2 hours-rainfalls (See Table 2). Comparison of Istanbul radar rainfall estimates with these reliable ground observations indicates that Istanbul radar underestimates rainfall significantly (See Figure 16b and 16c). The reason for underestimation can be attenuation (See Figure 16a) or PBB or empirical reflectivity-rainfall calculations. All the factors may affect this underestimation at the same time. Bursa radar is polarimetric radar and does not suffer from PBB at Üsküdar. During the event in 23.08.2015, there was no attenuation problem between Bursa radar and Üsküdar site. Bursa radar can estimate rainfall by employing polarimetric rainfall relationships such as R-KDP. KDP parameter is immune to beam blockage. Figure 17 shows that Bursa radar estimates rain at Üsküdar better than Istanbul radar, polarimetric estimate is the best. In order to mitigate the clutter problem due to skyscrapers and wind farms, the first elevation angle of radar can be shifted up from 0.2 deg to 0.4 deg (Figure 3). In this case, most of the clutter echo can be removed but the minimum height of visibility increases from 581 m to 814 m (See Figure 19). This may cause underestimation of rainfall especially during convective rain storms.

REFERENCES

Rinehart, R. 2000. Radar for meteorologists, Rinehart Publications, Columbia, 62-63.

Tokay, A., and Ozturk, K., 2012: An experimental study of the small-scale variability of rainfall. J. Hydrometeor., 13, 351–365.

EXTREME DISCHARGE EVENTS IN THE EARLY SPRING OF 2004 IN EASTERN ANATOLIA: IMPACT OF THE EAST ASIAN TROUGH

Deniz Bozkurt[1], Yasemin Ezber[2], Ömer Lütfi Şen[2]
[1]Center for Climate and Resilience Research, University of Chile, Santiago, Chile
dbozkurt@dgf.ıchile.cl
[2]Eurasia Institute of Earth Sciences, Istanbul Technical University, Istanbul, Turkey
ezber@itu.edu.tr, senomer@itu.edu.tr

Abstract
The eastern Anatolia, which lies in the east of the Mediterranean Basin, hosts important snow-fed rivers, and its water resources are critical for the irrigation, domestic use and hydroelectric power generation for the region. The climate of the region is largely controlled by the large-scale circulations and teleconnection patterns. An extreme temperature increase and snow melting resulted in anomalous discharge events in the early spring of 2004 in the region of interest. In this study, we aim to explore how unusual the river discharges during the early spring of 2004 and to investigate the underlying surface and atmospheric mechanisms by linking the EAT impact on regional temperature pattern over eastern Anatolia. For that aim, we used streamflow measurements, gridded observed dataset of temperature as well as ERA-Interim reanalysis. The discharges values in the first week of March 2004 for both Palu and Uzumcu gauging sites stand out very clearly from the background values observed in the last 41 years indicating extreme surface and atmospheric conditions. Large scale temperature anomalies indicate a marked dipole pattern of warmer and colder temperatures over eastern Turkey and western Europe, respectively. The dipole pattern of temperature anomalies is characterized by a ridge-trough system over Euro-Mediterranean region. Large scale atmospheric circulation anomalies indicate a high-amplitude Rossby waves propagating eastward in the Northern Hemisphere during the early spring of 2004. Further analysis of the EAT strength and the zonal shifts of the Mediterranean trough at pentad resolution shows that the 13th pentad corresponding to early March has the highest correlation leading to warmer temperature anomalies over eastern Mediterranean.

Keywords: *Atmospheric teleconnections, Euro-Mediterranean, EAT, Rossby waves, extreme events*

INTRODUCTION
The eastern Anatolia, which lies in the east of the Mediterranean Basin, hosts important snow-fed rivers, and its water resources are critical for the irrigation, domestic use and hydroelectric power generation for the region (Fig. 1). The climate of the region is largely controlled by the large-scale circulations and teleconnection patterns (Bozkurt and Sen, 2013). Previous studies have mainly focused on climate change impacts in the eastern Anatolia by analyzing atmospheric model outputs and river discharge models (Bozkurt and Sen, 2013; Bozkurt et al., 2015). To date, only a limited number of studies have been carried out to investigate present large-scale climate variability and atmospheric teleconnection impacts on regional climate variability and extremes in the eastern Anatolia. Sen et al. (2011) studied the temporal changes in the discharges of the snow-fed rivers in the eastern Anatolia, namely the Euphrates and Tigris rivers. They highlighted a marked increase of discharges in the eastern Anatolia taking place during the first half of March, and they discussed that a pulse-type increase in the early spring was resulted from a long-term trend in atmospheric circulation patterns in recent years.

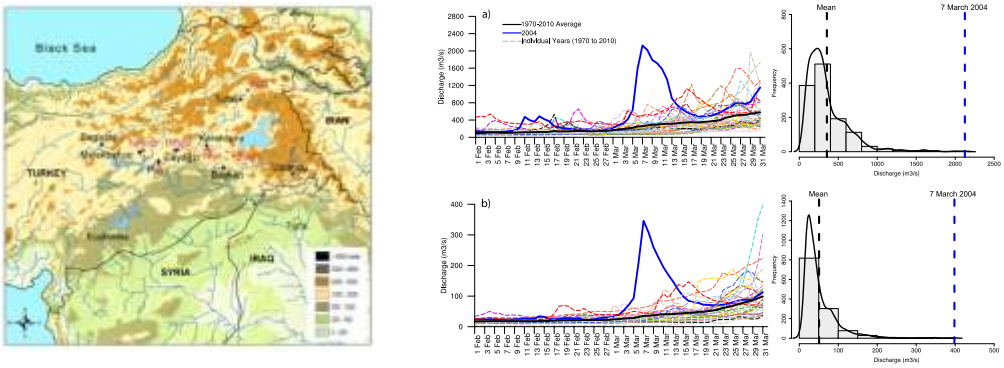

Figure 1. Topography of eastern Anatolia and the the locations of the streamflow gauging sites (left plot). Also shown is time series and frequency analyzes of the streamflow measurements of February and March from Palu and Uzumcu sites for 1970-2010 period.

In this study, we have presented that the pulse-type increase in the early spring is due to an anomalous increase of the discharges in 2004 rather than a long-term trend (Figure 1). Furthermore, Sen et al. (2017) and Ezber et al. (2017) have highlighted that there is a strong relationship between the East Asian Trough (EAT) strength and the zonal shifts of the Mediterranean upper layer trough in winter season and some pentads of the year controlling the temperature pattern over eastern Mediterranean and Anatolia. Ezber et al. (2017) have found the highest correlation between the EAT and temperature of Euro-Mediterranean region for the 13th pentad of the year corresponding to early March. This study, therefore, aims to explore how unusual the river discharges during the early spring of 2004 and to investigate the underlying surface and atmospheric mechanisms leading to this extreme event within the context of the EAT impact on regional temperature pattern over eastern Anatolia.

DATA AND APPROACH

We used streamflow measurements at Palu (Euphrates river) and Uzumcu (Tigris river) gauging sites obtained from the Turkish General Directorate of Electrical Power Resources Survey and Development Administration Hydro-Climatic Data Network. Both stations have 41-year continuous daily measurements between 1970 and 2010. Locations of the stations are given in Figure 1. We carried out time series and frequency analyzes of daily discharge records for two months (February-March) for the period 1970-2010.

In terms of gridded dataset, we used E-OBS daily gridded dataset of surface temperature at 0.25 x 0.25-degree spatial resolution spanning from 1950 to 2013 (Haylock et al., 2008). We calculated daily anomalies of surface temperature for each day between 28 February and 5 March 2004 with respect to long-term mean (1957-2010) of the same days. To further investigate the underlying surface and atmospheric mechanisms leading to the extreme discharge events, we used the European Center for Medium-Range Weather Forecast (ECMWF) ERA-Interim reanalysis dataset (Dee et al., 2011) at daily temporal resolution, which spans from 1979 to 2017. The spatial and vertical resolutions of the data are 0.75x0.75-degree and 60 vertical levels (surface to 0.1hPa), respectively. Particularly, we investigated surface temperature, 200-hPa geopotential heights, 200-hPa meridional components of wind as well as stream function derived from wind fields. We calculated 5-day (27 February-3 March 2004) average daily anomalies of 200-hPa geopotential heights and meridional components of wind as well as surface temperature with respect to 1979-2015 mean values of the same 5-day period. We calculated daily stream function anomalies between 20 February and 8 March 2004

with respect to long term mean (1979-2015) of the same days.

RESULTS

The time series and frequency analyzes of the streamflow measurements indicate high discharge values in the first week of March reaching to a maximum on 7 March 2004 (>2000 m^3/s, with a departure >1600 m^3/s from the mean field for Palu). The discharges values on 7 March 2004 for both Palu and Uzumcu gauging sites stand out very clearly from the background values observed in the last 41 years indicating extreme surface and atmospheric conditions. Figure 2 shows daily anomalies of surface temperature for each day between 28 February and 5 March 2004 with respect to long-term mean (1970-2010) of the same days. Temperature anomalies indicate a marked dipole pattern of warmer and colder temperatures. Warmer temperatures take place over eastern Europe, Turkey and western Russia, whereas colder temperatures take place over western Europe. It is clearly seen that the temperature increased well above 12 ºC over eastern Anatolia on 5 March, just before the extreme discharge events occurring on 7 March in this region.

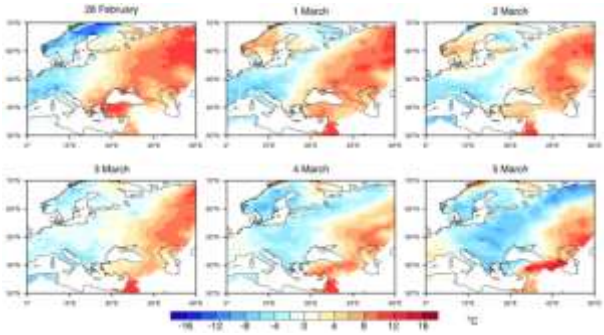

Figure 2. Daily anomalies of surface temperature for each day between 28 February and 5 March 2004 with respect to long-term mean (1970-2010) of the same days

Figure 3 presents 5-day (27 February-3 March 2004) averaged daily anomalies (with respect to 1979-2015) of ERA-Interim geopotential heights and meridional wind at 200-hPa (a, b) and surface temperature (c). In general, spatial plots of all the analyzed variables indicate the existence of a high-amplitude Rossby waves propagating eastward in the Northern Hemisphere. 200-hPa meridional wind and geopotential height anomalies show that the synoptic conditions of the dipole pattern are characterized by a ridge-trough system over Euro-Mediterranean region along a tilted axis between central north Africa to eastern Europe. The hemispheric surface temperature anomalies indicate a larger warming pattern (more than 6ºC anomaly) extending from northeastern Africa to Caucasus and Caspian regions to Siberia. A counter cooling pattern that extends from Europe to northwestern parts of Africa is also evident (Figure 3c).

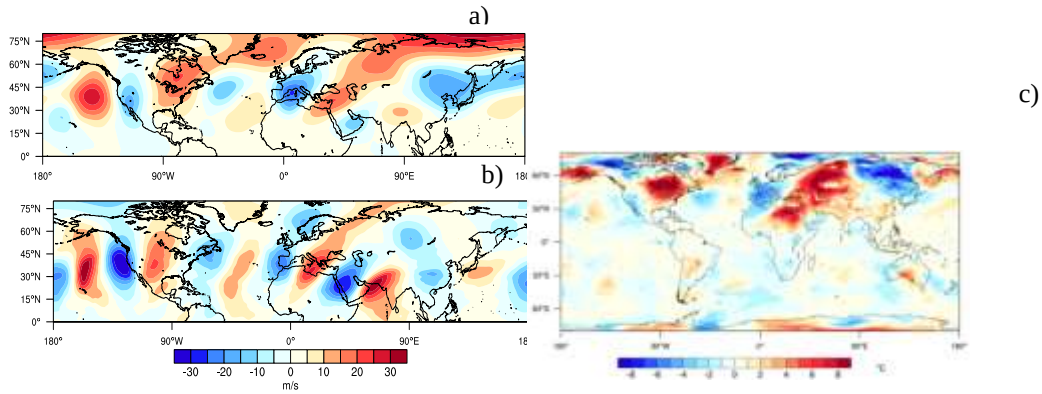

Figure 3. 5-day (27 February-3 March 2004) averaged daily anomalies (with respect to 1979-2015 period) of ERA-Interim geopotential heights and meridional wind at 200-hPa (a, b) and surface temperature (c).

Figure 4 exhibits a longitude-time cross section of 20°N and 40°N mean stream function anomalies at 200-hPa for the dates between 20 February and 8 March 2004. Temporal variability of the circulation indicates substantial longitudinal variations in the stream function anomalies, particularly at the end of February and first week of March. A strong anomalous anticyclone is evident between 45°E and 60°E occurring after 4th of March, and resulted in a persistent trough with warm air transported from northeastern Africa towards eastern Mediterranean.

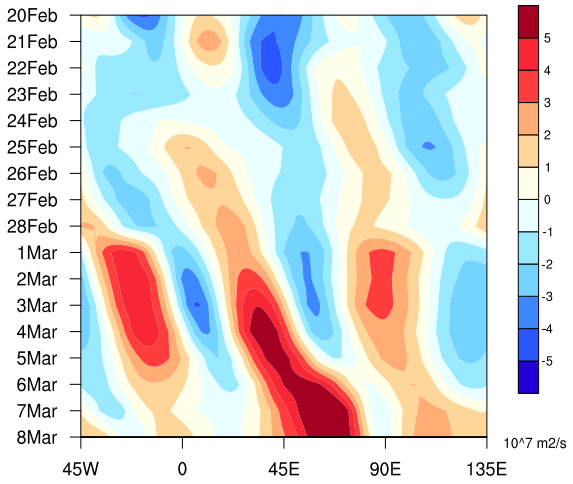

Figure 4. Longitude-time cross section of 20°N and 40°N mean stream function anomalies at 200-hPa for the dates between 20 February and 8 March 2004 with respect to 1979-2015 period.

CONCLUSIONS AND DISCUSSIONS

In this study, we aim to explore how unusual the river discharges during the early spring of 2004 and to investigate the underlying surface and atmospheric mechanisms leading to this extreme event within the context of the EAT impact on regional temperature pattern over eastern Anatolia. We used streamflow measurements, gridded observed dataset of temperature as well as ERA-Interim reanalysis. The discharges values in the first week of March 2004 for both Palu and Uzumcu gauging sites stand out very clearly from the background values observed in the last 41 years indicating extreme surface and atmospheric conditions. Large scale atmospheric circulation anomalies indicate the existence of the high-amplitude Rossby waves

propagating eastward in the Northern Hemisphere. Furthermore, a ridge-trough system over Euro-Mediterranean region along a tilted axis between central north Africa to eastern Europe resulted in a marked dipole pattern of warmer and colder temperatures over eastern Mediterranean and western Europe, respectively. We have hypothesized that the anomalous strengthening of the EAT leads to increase of the amplitudes of ridge trough system over Euro-Mediterranean region controlling the temperature pattern in eastern Mediterranean (Sen et al. 2017). Indeed, Sen et al. (2017) have performed a winter EOF analysis covering the region determined based on trough axis analysis of 38 years from ERA-Interim data and revealed that the first principal component is associated with the strength of the trough and the second with the zonal shift. Sen et al. (2017) have also highlighted that there is a strong (and significant) relation between the intensity of EAT and the zonal shifts of the Mediterranean trough. Furthermore, following the Sen et al. (2017), Ezber et al. (2017) have linked the EAT strength and the zonal shifts of the Mediterranean trough at pentad resolutions and found that the 13th pentad corresponding to early March has the highest correlation leading to warmer temperature anomalies over eastern Mediterranean. Therefore, our results exhibit a case study of extreme discharge events in eastern Anatolia as a result of the EAT impact on temperature pattern in the region of interest.

REFERENCES

Bozkurt, D. and O. L. Sen, 2013: Climate change impacts in the Euphrates-Tigris Basin based on different model and scenario simulations. J. Hydrol., 480:149-161.

Bozkurt, D., O. L. Sen and S. Hagemann, 2015: Projected river discharge in the Euphrates-Tigris Basin from a hydrological discharge model forced with RCM and GCM outputs. Clim. Res., 62:131-147

Dee, D. P. et al., 2011: The ERA-Interim reanalysis: configuration and performance of the data assimilation system. Q.J.R. Meteorol. Soc., 137: 553–597. doi: 10.1002/qj.828.

Ezber, Y., D. Bozkurt and O. L. Sen, 2017: Relation between the East Asian Trough and Euro-Mediterranean Climate at Pentad Resolution. ATMOS2017, these proceedings.

Haylock, M. R., N. Hofstra, A. M. G. Klein Tank, E. J. Klok, P. D. Jones and M. New, 2008: A European daily high-resolution gridded dataset of surface temperature and precipitation. J. Geophys. Res (Atmospheres), 113, D20119, doi:10.1029/2008JD10201.

Leung M.Y-T. and W. Zhou, 2015: Variation of circulation and East Asian climate associated with anomalous strength and displacement of the East Asian trough. Clim. Dyn, 45,2713–2732.

Sen, O. L., A. Unal, D. Bozkurt and T. Kindap, 2011: Temporal changes in the Euphrates and Tigris discharges and teleconnections. Environ. Res. Lett., 6, 024012.

Sen, O. L., Y. Ezber and D. Bozkurt, 2017: On the role of East Asian Trough on the Euro-Mediterranean climate variability. ATMOS2017, these proceedings.

THE INFLUENCE OF MADDEN-JULIAN OSCILLATION ON PRECIPITATION PATTERN IN MEDITERRANEAN REGION OF TURKEY

Hilal Erdem[1], Ercan Kahya[2]
[1]*Istanbul Technical University, Civil Engineering Department, Istanbul*
erdemhi@itu.edu.tr
[2] *Istanbul Technical University, Civil Engineering Department, Istanbul*
kahyae@itu.edu.tr

Abstract
The Madden-Julian Oscillation (MJO) is the most prominent form of tropical intra-seasonal variability in the climate system and has a significant influence on precipitation variability. The propagating path of the MJO over Indian and Pacific Ocean has been classified into 8 phases. Although equatorial parts of the Indian and western Pacific Oceans are known as the centers of action of the MJO, recent investigations have shown the significant impact of this oscillation on precipitation variability and hydro-climatic characteristics in extra-tropical regions. The aim of this study is to improve our understanding on the influence of the MJO over precipitation patterns in Mediterranean Region of Turkey using the composite analysis. Daily rainfall data set, including from 1979 to 2012, was used in this analysis. The available rainfall data sets were grouped according to the 8 MJO phases. The influence of each station is represented by a coefficient and achieved with calculating the total value of each phases by dividing the total annual cycle. These coefficients are assumed to represent the influence of MJO phases at each station in the region; therefore, we plotted the results on 8 maps and concluded that Phase 7 is the most prominent phase with 1,48 influence coefficient. The most effective phase after Phase 7 is Phase 3 as 1,20. Burdur and Antalya is the most affected cities.

Keywords: *Madden-Julian Oscillation, composite analysis, precipitation, Turkey,*

INTRODUCTION

MJO is the largest element of the intra-seasonal (generally 60 days) variability in the tropical atmosphere. It propagates eastwards at approximately 4 to 8 m/s, through the atmosphere above the warm parts of the Indian and Pacific oceans. Maloney and Hartmann (1998) and Maloney and Kiehl (2002) found out an MJO index for characterizing the intensity and state of the MJO. Wheeler and Hendon (2004) developed another index for monitoring and predicting the MJO. The influences of the MJO on precipitation variability of the global tropics have been studied on various areas. (e.g., Madden and Julian 1994; Maloney and Hartmann 2000a,b; Hall et al. 2001; Lorenz and Hartmann 2006; Pai et al. 2009; Klotzbach 2010). Some studies have shown that MJO affects extra-tropical weather and climate systems (Krishnamurti et al. 1997; Straus and Linzden 2000; Matthews 2006; Nazemosadat and Ghaedamini 2010). It has been increasing interest to investigate the relation between large-scale atmospheric oscillation and surface variable patterns for the last three decades. For example, North Atlantic Oscillation (NAO) and drought in mid-latitude regions; among others, Kahya (2011) and Şarlak et al. (2009) documented such relations for the Eastern Mediterranean and southern part of Turkey. In addition, Karabörk and Kahya (2009) documented the linkage between hydrologic and climate variables in Turkey and Southern Oscillation (SO). Kalayci et al. (2004) analyzed El Nino signals on Turkish streamflow and precipitation patterns using spectral analysis and found noticeable linkages. Following this trend, we intended to look at different oscillation mode the Madden–Julian Oscillation (MJO), which has yet studied in Turkey.

DATA AND METHODS

29 stations of daily precipitation (mm) data set from 1979 to 2012 was compiled by the Turkish State Meteorological Service (TSMS). These time series were determined to be the common years for all selected stations. The other data, MJO Indices, are satellite-based sets which is available in the Centre for Australian Government-Bureau of Meteorology (AGBM) website and are grouped into 8 MJO phases. Each rainfall data set was grouped considering these phases. The influence of each station is represented by a non-diamensional coefficient called 'R'. It is expressed with Equation 1 and represents a procedure to identify each phase influence rate.

$$R = \frac{(P_{cum})_{phase_i}}{(P_{cum})_{annual\ cycle}} \quad [1]$$

$(P_{cum})_{phase_i}$ and $(P_{cum})_{annual\ cycle}$ indicates the cumulative precipitation value of ith phase and the cumulative value of data set, respectively. These coefficients are assumed to represent the influence of MJO phases at each station over Mediterranean Region. If R is lower than 1, it means the weak influence and vice versa. The five steps of the methodological approach of the study is summarized in Figure 1.

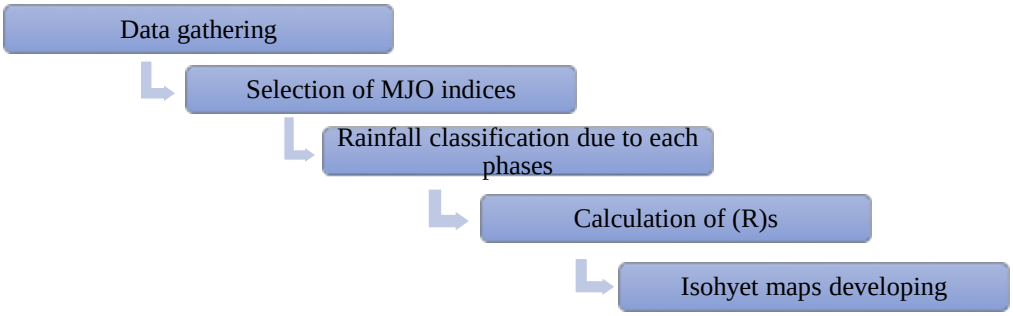

Figure 1. Methodological steps of the study

This algorithm mentioned in the above has been applied to each station rainfall data.

APPLICATION AND RESULTS

Using Equation 1, (R)s have been prepared separately for the time series. A modelling package Software (Surfer), has been applied for preparation of Isohyet maps using mentioned (R)s for all the stations. Figure 2(a) - (h) illustrate the above-mentioned isohyet maps prepared in this study presenting Phase 1 - 8 influences respectively. (R)s indicate weak or strong influence of MJO on rainfall over Mediterranean Region. Considering the maps in the Figure 2, every MJO phase includes minimum and maximum R value shown in Table 1. A weak interaction occurs at Erdemli station (SI#17958) at Phase 1 in Mersin and also strong interaction occurs at Eğirdir station (SI#17882) at Phase 7 in Isparta. Consequently, legend changes between 0,65 to 1,49 that is the minimum and maximum values of R in all phases respectively.

Table 1. R values and locations

Phase	Min. R	St. Code	Max. R	St. Code
1	0,65	17958	0,96	17926
2	0,69	17952	0,98	17300
3	0,92	17864	1,23	17981
4	0,81	17926	1,10	17986
5	0,70	17300	1,17	17340
6	0,93	17300	1,17	17954
7	1,09	17986	1,49	17882
8	0,88	17340	1,31	17952

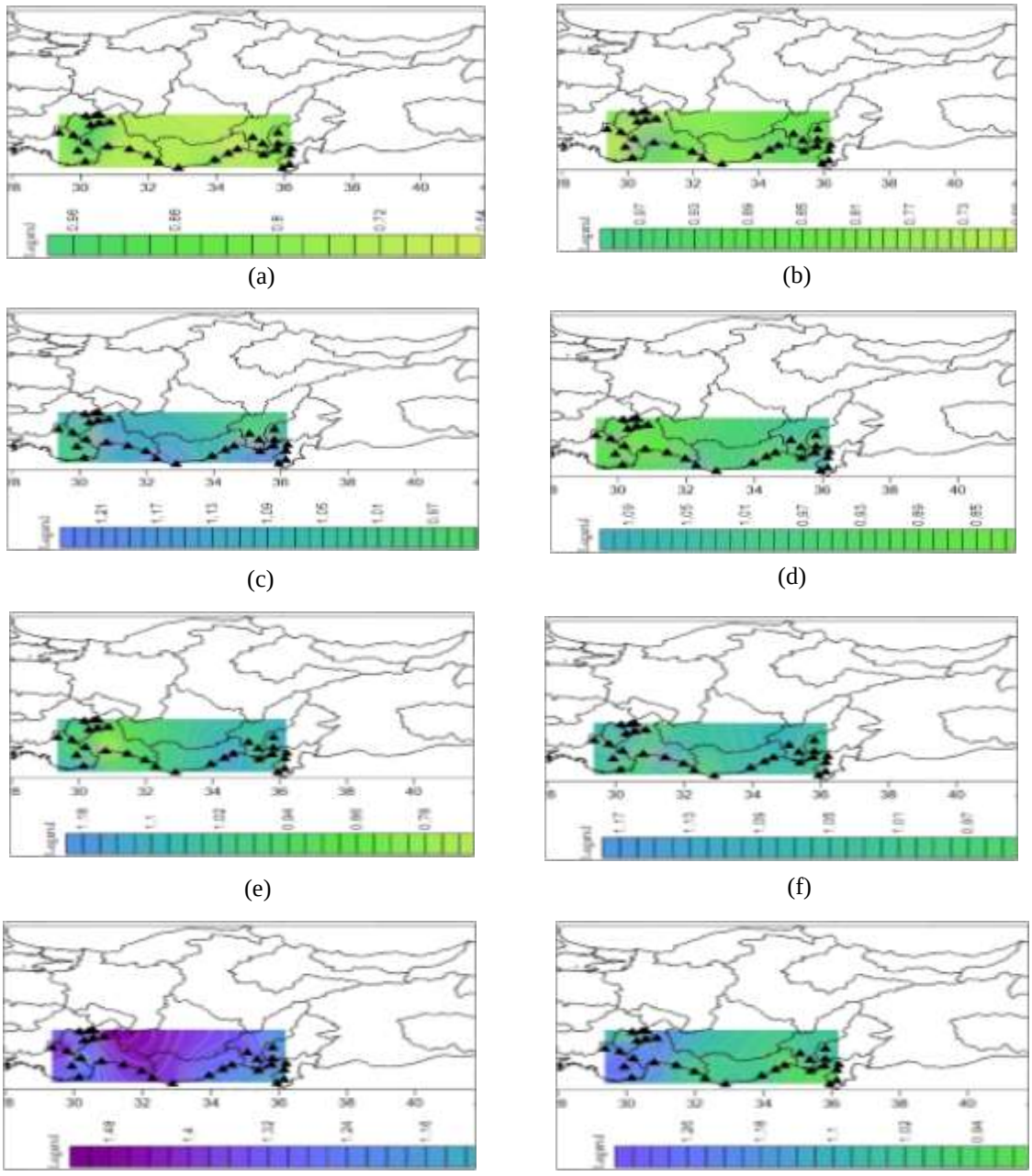

(a) (b) (c) (d) (e) (f) (g) (h)

Figure 2. Isohyet maps based on MJO Phases calculated for Mediterranean Region
*Same legend used to show the accurate differences among all phases in all figures.
**Numbered dots illustrates the location of stations.

CONCLUSIONS

MJO indices have been used to evaluate the impact of MJO over Mediterranean Region rainfall. The rainfall data sets were grouped into 8 MJO phases. The influence of each station is represented by a coefficient (R). It is assumed to represent the influence of MJO phases at each station, for this reason, the results were plotted on 8 maps that each shows one of the phase. Considering the maps at Figure 2; the strongest influence occurs at Phase 7 in Isparta and the most effective phase after Phase 7 is Phase 3 occurs in Adana.

REFERENCES

Hall, J.D., Matthews, A.J., Karoly, D.J., 2001: The modulation of tropical cyclone activity in the Australian region by the Madden-Julian Oscillation. Mon Weather Rev 129:2970–2982

Kahya, E, 2011: Impacts of the NAO on the Hydrology of the Eastern Mediterranean in "Hydrological, Socioeconomic and Ecological Impacts of the North Atlantic Oscillation in the Mediterranean Region", Eds: S. M. Vicente-Serrano and R. M. Trigo. Advances in Global Change Research, Vol. 46, p 57-71, Springer. 1st Edition., 2011, VIII, 236 p., DOI: 10.1007/978-94-007-1372-7

Kalaycı, S., M.Ç. Karabörk and E. Kahya, 2004: Analysis of El Nino Signals on Turkish Streamflow and Precipitation Patterns Using Spectral Analysis. Fresenius Environmental Bulletin, Vol. 13, No 8, 719-725

Karabörk, M. Ç. and E. Kahya, 2009: The Links between the Categorized Southern Oscillation Indicators and Climate and Hydrologic Variables in Turkey. Hydrological Processes, Vol. 23, No 13, 1927-1936, DOI: 10.1002/hyp.7331.

Krishnamurti, T. N., Sinha, M., Misra, C.V., and Sharma, O.P., 1997: Tropical–middle latitude interactions viewed via wave energy flux in the frequency domain. Dyn. Atmos. Oceans, 27, 383–412

Klotzbach, PJ., 2010: On the Madden-Julian Oscillation-Atlantic hurricane relationship. J Clim 23:282–293

Lorenz, D.J., Hartmann, D.L., 2006: The effect of the MJO on the North American monsoon. J Clim 19:333–343

Madden, R. A., and Julian, P.R., 1994: Observations of the 40-50 day tropical oscillation: A review. Mon. Wea. Rev., 112, 814-837

Maloney, E. D., and D. L. Hartmann, 1998: Frictional moisture convergence in a composite life cycle of the Madden–Julian oscillation. J. Climate, 11, 2387–2403

Maloney, E.D., and Hartmann, D.L., 2000a: Modulation of eastern North Pacific hurricanes by the Madden-Julian oscillation. J Clim 13:1451–1460

Maloney, E.D., and Hartmann, D.L., 2000b: Modulation of hurricane activity in the Gulf of Mexico by the Madden-Julian Oscillation. Science, 287:2002–2004

Maloney, E.D., and Kiehl, J.T., 2002: MJO-related SST variations over the tropical eastern Pacific during Northern Hemisphere summer. J. Climate, 15, 675–689

Matthews, A.J., 2006: Propagation mechanisms for the Madden-Julian oscillation. Q J Roy Meteor Soc 126:2637–2651

Nazemosadat, M. J., and Ghaedamini, H., 2010: On the Relationships between the Madden–Julian Oscillation and Precipitation Variability in Southern Iran and the Arabian Peninsula: Atmospheric Circulation Analysis, Journal of Climate, ISSN 0894-8755, 02/2010, Volume 23, Issue 4, p. 887

Pai, D.S., Bhate, J., Sreejith, O.P., and Hatwar, H.R., 2009: Impact of MJO on the intraseasonal variation of summer monsoon rainfall over India. Clim Dyn. doi:10.1007/s00382-009-0634-4

Straus, D.M., and Lindzen, R.S., 2000: Planetary-scale baroclinic instability and the MJO. J Atmos Sci 57:3609–3626

Şarlak, N., E. Kahya and A.O. Bég, 2009: Critical Drought Analysis: A Case Study of Göksu River (Turkey) and North Atlantic Oscillation Influences. Journal of Hydrologic Engineering, Vol. 14, No 8, 795-802, DOI:10.1061/(ASCE)HE.1943-5584.0000052

Wheeler, M., and H. Hendon, 2004: An all-season real-time multivariate MJO index: Development of an index for monitoring and prediction. Mon. Wea. Rev., 132, 1917–1932

http://www.bom.gov.au/climate/mjo/

THE ROLE OF THE EAST ASIAN TROUGH ON THE EURO-MEDITERRANEAN CLIMATE VARIABILITY

Ömer Lütfi Şen[1], Yasemin Ezber[1], Deniz Bozkurt[2]
[1]Eurasia Institute of Earth Sciences, Istanbul Technical University, Istanbul, Turkey
senomer@itu.edu.tr, ezber@itu.edu.tr
[2]Center for Climate and Resilience Research, University of Chile, Santiago, Chile
dbozkurt@dgf.uchile.cl

Abstract
The eastern Mediterranean upper layer trough plays an important role in the zonal climate variability in the Euro-Mediterranean region. Its zonal shifts switch the temperature and precipitation anomalies in this region. A winter EOF analysis based on trough axis determination of 38-year data from ERA-Interim dataset over the region revealed that the first principal component is associated with the zonal shift of the trough and the second with the strength. A similar EOF analysis of the East Asian Trough (EAT) yielded that most of the variation, which is explained by the first principal component, is associated with the strength of the trough. The correlation analysis between the principal components of the EAT and those of the Mediterranean trough suggests that there is a strong and significant relation between the strength of the EAT and the zonal shifts of the Mediterranean trough (the correlation is negative and about 0.50). It appears that when the EAT is strong, the Mediterranean trough shifts westward, and when the EAT is weak, then it tends to shift eastward. When it is strong, eastern side of Euro-Mediterranean region becomes warmer while western side gets cooler, and vice versa. Consequently, it can be said that the EAT has an important role on the zonal climate variability of the Euro-Mediterranean region.

***Keywords*:** *Euro-Mediterranean region, climate variability, Mediterranean trough, EOF analysis, East Asian Trough*

INTRODUCTION
Mediterranean climate variability is mostly associated with the North Atlantic Oscillation (NAO) / Arctic Oscillation (AO), Eastern Atlantic pattern and Eastern Atlantic/Western Russia pattern (Barnston and Livezey, 1987), and Scandinavian pattern (Barnston and Livezey, 1987). Lutherbacher et al. (2006) link warm and dry winters to positive NAO modes, cold and wet winters to Scandinavian blocking, cold and dry winters to different anticyclonic regimes, and warm and wet winters to different cyclonic regimes. Studies exist linking the El Niño Southern Oscillation (ENSO) to climate of southeastern Mediterranean (e.g., Yakir et al., 1996; Price et al., 1998), however, unlike the stable influence of NAO/AO on this region, the influence of ENSO is deemed nonstationary. The South Asia Monsoon (SAM) is also related with the climate variability in the central and eastern parts of Mediterranean (Ziv et al., 2004). It produces high variability in sea level pressure over the Middle East causing low pressures in summer and high pressures in winter. A recent study (Lolis and Türkeş, 2016) suggests that the extreme precipitation events over Turkey are largely caused by the west to east movement of strong upper air disturbances, mainly troughs with strong gradient toward or over Turkey. The Mediterranean upper layer trough is only secondary to major East Asian Trough (EAT) and U.S. East Coast Trough in the Northern Hemisphere. The EAT is an important component of the mid-tropospheric circulation in the Northern Hemisphere in winter and the strength of the East Asian Winter Monsoon is closely associated with the strength of this trough (Ding et al., 2014). The purpose of this study is to investigate the role of EAT on the Mediterranean upper layer trough that causes variability in the climate of the Euro-Mediterranean region.

DATA AND APPROACH

The main dataset used in the analysis is the European Center for Medium-Range Weather Forecast (ECMWF) ERA-Interim reanalysis (Dee et al, 2011). It is available from 1979 to present day, but we used data between 1979 and 2016. The current analysis considers only winter but we plan to extend the whole analysis to other seasons as well using the indices developed in this study. A pentad analysis of the EAT covering the whole year is given in a companion paper (Ezber et al., 2017), and a related impact case study of the EAT that investigates the early March 2004 extreme events in Turkey is given in another companion paper (Bozkurt et al., 2017). Some preliminary results of these studies including the present one were presented somewhere else earlier (Ezber et al., 2016). In the present study, we first developed an algorithm to track the winter trough axis lines of both EAT and Mediterranean upper layer trough for the 38 years. Based on the trough axis analysis, two domains are determined for the EOF analysis: one for EAT and one for the Mediterranean trough. We conducted EOF analysis for both domains to obtain the principal components of variability in the 500 hPa geopotential height data. After identifying the EOFs, we carried out a cross correlation analysis revealing which mode of the EAT has more influence on the Mediterranean trough that has a strong role on the Mediterranean climate variability.

RESULTS

There are two major troughs in the Northern Hemisphere: The U.S. East Coast Trough and the EAT. Both are well observed over regions featuring a large ocean-land temperature contrast in winter. In addition to these, the upper layer maps show a much weaker trough over the eastern Mediterranean region in the Northern Hemisphere (Figure 1). A year-to-year trough axis analysis reveals that this trough is quite unstable zonally and its yearly location shifts east-west direction substantially. The climatological position of the trough axis is along a line from Egypt to Turkey to Russia.

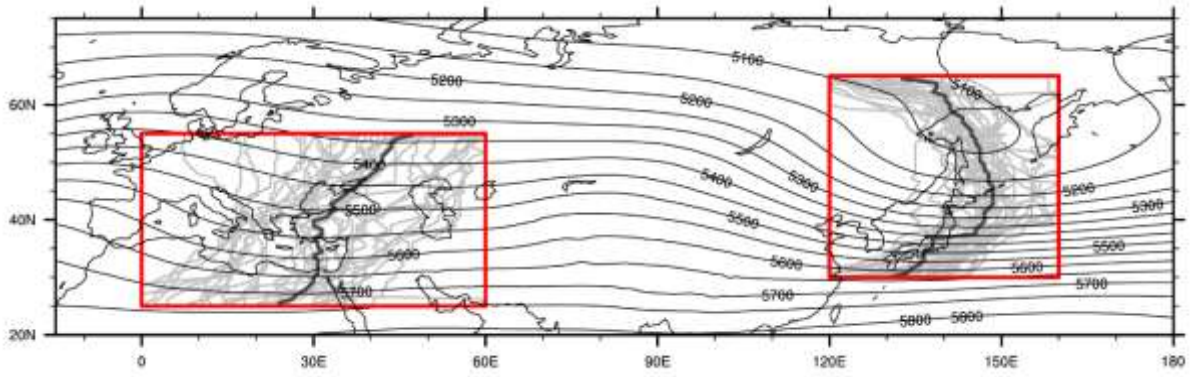

Figure 15. Winter climatology of 500 hPa geopotential heights. Light grey lines indicate yearly winter axis lines of Mediterranean trough and East Asian Trough (EAT) identified from the ERA-Interim 500 hPa geopotential height fields. Dark grey lines show the climatological axis lines. Red boxes depict the regions used in the EOF analysis.

An EOF analysis based on the trough axis determination for the considered regions is performed for both Mediterranean trough and EAT. The EOF analysis results of the EAT are found to be in agreement with previous studies. As with those, the first EOF points to the strength of the trough, the second to meridional shift and the third to zonal shift. There aren't such studies that identify the EOFs of the Mediterranean trough. In our analysis, we used a trough intensity index, simply the average of the 500 hPa height fields of a box in the eastern Mediterranean, and found over 90% correlation with the second principal component (PC). So, the second EOF in the Mediterranean analysis explains the yearly variability in the strength of the trough. We

developed another index, which is a measure of east-west movement of the trough (see Ezber et al., 2017). It turns out that this index is highly correlated (over 85%) with the first PC. So, the first EOF explains the variability due to zonal shift of the trough. We were unable to identify the physical meaning of the third EOF, but it could be related to meridional shifts as in EAT. Cross correlation analysis between the principal components associated with the EAT and Mediterranean trough reveals that there is a strong and significant relation between the strength of the EAT and the east-west movement of the Mediterranean trough. The correlation is -0.50. The correlation between the strengths of both troughs (i.e., PC1 of EAT and PC2 of Mediterranean trough) is also large (0.43).

Table 8. Correlations between the principal components of East Asian and Mediterranean troughs.

	PC1 EAT (strength)	PC2 EAT (meridional shift)	PC3 EAT (zonal shift)
PC1 Med (zonal shift)	-0.50	-0.14	0.27
PC2 Med (strength)	-0.43	-0.11	0.03
PC3 med (meridional shift?)	0.17	-0.22	-0.20

Figure 2 clearly exhibits the relation between the EAT and the Mediterranean trough. A composite analysis based on the positive and negative years of the first PC associated with the EAT (average of positive years minus average of negative years in 500 hPa geopotential height) indicates a dipole like structure over Euro-Mediterranean region. It seems that when the EAT is weak, the Mediterranean trough tends to shift eastward resulting in a positive anomaly over western Euro-Mediterranean region and a negative anomaly over the Middle East and eastern Europe. On the other hand, when the EAT is strong, it tends to shift westward causing a negative anomaly over western Euro-Mediterranean region and positive anomaly over the Middle East and eastern Europe.

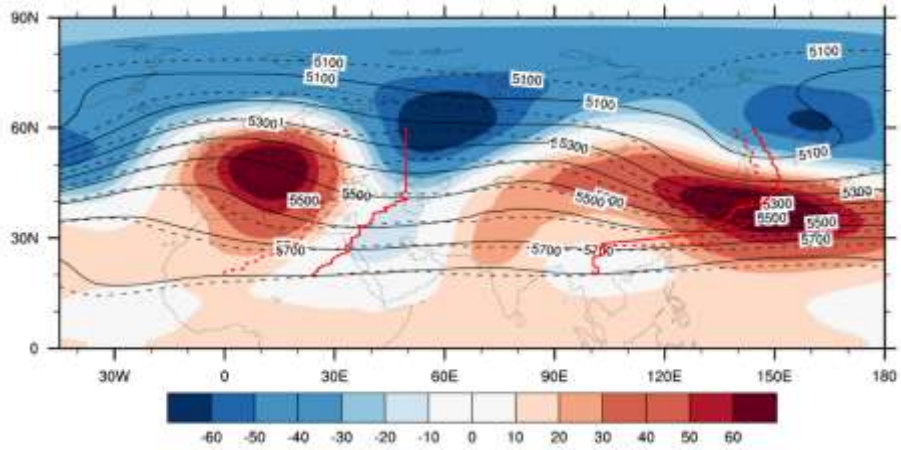

Figure 16. Difference (shade) of 500 hPa geopotential height in the positive and negative composites of the first principal component of East Asian Trough. Black solid lines are showing average 500 hPa geopotential heights of the positive years, and black dashed lines average of the negatives years. Red solid lines show the trough axis lines in positive years (composite), and red dashed lines in negative years (composite).

We computed correlations between the first PCs associated with both EAT and Mediterranean troughs with the 500 hPa geopotential heights and surface temperatures (Figure 3). It is intriguing to see that both PCs produce quite similar correlation patterns for the Northern Hemisphere for both 500 hPa geopotential height and surface temperature. The dipole like pattern over the Euro-Mediterranean region is evident for both variables. The temperature correlation map suggests that when the EAT is strong, then the eastern Euro-Mediterranean region, Middle East and northeastern Africa become warmer while western Euro-Mediterranean region and northwestern Africa become colder.

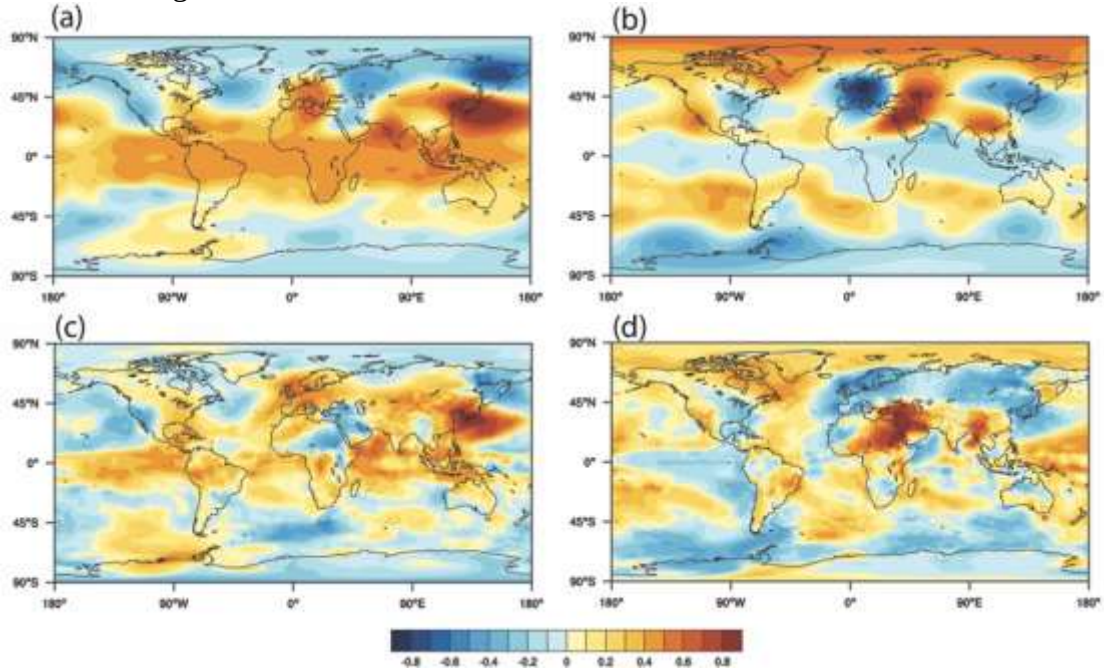

Figure 17. Correlation maps of the first principal components of East Asian (first column) and Mediterranean (second column) troughs with 500 hPa geopotential height (a and b) and surface temperature (c and d).

CONCLUSIONS AND DISCUSSIONS

This study explores the role of the East Asian Trough (EAT) on the variability of the Euro-Mediterranean climate. It is found that the Mediterranean upper layer trough plays an important role in the climate of this region. Lolis and Türkeş (2016) suggest that the east-west movement of this trough is one of the major factors affecting the severe precipitation events in Turkey. Our study shows that such a movement does not only affect the precipitation in Turkey but also zonal temperature and precipitation variability in the larger Euro-Mediterranean region. Our study also suggests that the east-west movement of Mediterranean upper layer trough is strongly associated with the strength of the East Asian Trough. When it is stronger, the Mediterranean upper layer trough tends to shift westward, and vice versa.

The zonal shift of the Mediterranean trough results in a dipole type temperature anomaly over the Euro-Mediterranean region. In case the trough is positioned in the western side, which is associated with a strong EAT, the eastern Mediterranean becomes warmer, and the western Mediterranean becomes colder. A pentad analysis revealed that the strongest relation between the EAT and the Mediterranean trough is in the 13th pentad, which coincides with early days of March (Ezber et al., 2017). Accordingly, it turns out that the severe flooding events in the first few days of March 2004 in eastern Anatolia is related with the strengthening of the EAT (Bozkurt et al., 2017). In this case, the Mediterranean upper layer trough positioned in the central Mediterranean is deepened and extended towards central Africa in these days. This

strong system carried warm tropical African air towards eastern Mediterranean and Turkey resulting in rapid melting of the snowpack as well as severe precipitation and flooding events in the eastern Anatolia. In the other side, it carried cold polar air over western Mediterranean and Africa, decreasing the temperatures significantly.

REFERENCES

Barnston, A. G., R. E. Livezey, 1987: Classification, seasonality and persistence of low frequency atmospheric circulation patterns. Mon. Weather Rev., 115**,** 18-25.

Bozkurt, D., Y. Ezber, Ö. L. Şen, 2017: Extreme discharge events in the early spring of 2004 in eastern Anatolia: Impact of the East Asian Trough. These proceedings.

Dee, D. P. et al., 2011: The ERA-Interim reanalysis: configuration and performance of the data assimilation system. Q.J.R. Meteorol. Soc., 137: 553–597. doi: 10.1002/qj.828.

Ding, Y., Y. Liu, S. Liang et al., 2014: Interdecadal variability of the East Asian winter monsoon and its possible links to global climate change. J. Meteor. Res., 28(5), 693-713. doi: 10.1007/s13351-014-4046-y.

Ezber, Y., D. Bozkurt and O. L. Sen, 2016: Effect of East Asian Trough on the temperature patterns in the Euro-Mediterranean region in the early spring and the extreme case of the year 2004. Proceedings of MEDCLIVAR 2016, http://www.medclivar2016conf.eu/index.php/book-abstracts.

Ezber, Y., D. Bozkurt and O. L. Sen, 2017: Relation between the East Asian Trough and Euro-Mediterranean Climate at Pentad Resolution. ATMOS2017, these proceedings.

Price, C., L. Stone, B. Rajagopalan, P. Alpert, 1998: A possible link between El Nino and precipitation in Israel. Geophys. Res. Lett., 25: 3963-3966.

Lolis, C. J., M. Türkeş, 2016: Atmospheric circulation characteristics favouring extreme precipitation in Turkey. Clim. Res., 71: 139–153.

Luterbacher, J., E. Xoplaki, C. Casty, H. Wanner, A. Pauling, M. Küttel, et al., 2006: Chapter 1 Mediterranean climate variability over the last centuries: a review. P. Malanotte-Rizzoli, R. Boscolo, P. Lionello (Eds.), Developments in Earth and Environmental Sciences: Mediterranean, vol. 4 (2006), pp. 27-148

Yakir, D., S. Lev-Yadun, A. Zangvil, 1996: El Nino and tree growth near Jerusalem over the last 20 years. Global Change Biology, 2: 101-105.

Ziv, B., H. Saaroni, P. Alpert, 2004: The factors governing the summer regime of the Eastern Mediterranean. Int. J. Clim., 24: 1859-1871.

COMPARISON BETWEEN DIFFERENT VEGETATION INDICES AND THEIR USE TO MONITORING HUMID PROTECTED AREAS

Alfredo Altobelli[1], Rossella Napolitano[1], Zafer Aslan[2], Gokhan Erdemir[3] and Enrico Feoli[1]

[1] University of Trieste, Italy
altobell@units.it, napolita@units.it, feoli@units.it
[2]Istanbul Aydin University, Turkey
zaferaslan@aydin.edu.tr
[2]Istanbul Sabahattin Zaim University, Turkey
gokhan.erdemir@izu.edu.tr

Abstract

Vegetation and ecosystem analyzes based on remote sensing (RS) and Geographical Information System (GIS) technology are of great importance in the planning of environmental protection and sustainability studies. It is possible to classify land, land use, wetlands based on these systems. Intensive urbanization plays an important role in biodiversity. In general, analyzes carried out are based on such factors as surface vegetation class, vegetation density and soil erosion risk of the area. Different indices have been developed for this purpose. These indices are not only sensitive on human activities, but also on climate and ecosystem changes. For this purpose, RS and GIS techniques provide great effective in analysis. These systems provide rapid and low cost analysis of data from large areas. In this paper, as a case study, the changes of different indices in Turkey are compared. Variations of industrial pollution, intensive urbanization in the selected areas have been discussed. Various suggestions for solution of environmental problems can be brought. For these purposes, it is often the normal use of indicators such as a vegetation cover or a leaf area index to be used for the calculation of relative plant mass, drought and erosion risks. In risky situations, forests can overcome problems on soil conservation. The creation of new urban plans, the preparation of slope class and roughness maps, and protection of deforestation problems can be carried out very usefully. The development of definition of vegetation indexes and the evaluation of their accuracy are required. Based on the findings, the use of the most appropriate indice for the study area would be selected. MODIS offers temporal and spatial variations of different vegetation indexes and monitoring of humidity by using MODIS terra evaporation.

Keywords: *Vegetation indices, remote sensing, humid areas, biosphere, degradation, evapotranspiration, GIS*

OBJECTIVE

The main objective of the paper is to present some preliminary analyses of NDVI, LAI and evapotranspiration of selected data.

DATA AND METHODS

The MODIS Normalized Difference Vegetation Index (NDVI) complements NOAA's Advanced Very High-Resolution Radiometer (AVHRR) NDVI products and provides continuity for time series historical applications [1]. Enhanced Vegetation Index (EVI) that also is supported by MODIS, minimizes canopy background variations and maintains sensitivity over dense vegetation conditions. The MODIS NDVI and EVI products are computed from atmospherically corrected bi-directional surface reflectance that have been masked for water, clouds, heavy aerosols, and cloud shadows. Vegetation indices (VI) are used for global monitoring of vegetation conditions and are used in products displaying land cover and land

cover changes. VI data can be used for wide range of climate modelling applications as not only input but also reference. In addition, VI data may be used for characterizing and classifying of different biophysical environments.

NDVI

The NDVI is a normalized transform of the NIR to red reflectance ratio. It is commonly expressed as:

$$NVDI = \frac{NIR - Red}{NIR + Red} \quad (1)$$

In equation (1), Red and NIR refer to the spectral reflectance measurements acquired in the visible red and near-infrared bands, respectively. NDVI can take a value between -1.0 and +1.0.

Vegetation Indices (VI)

Vegetation Indices (VI) are defined as measuring coverage of green vegetation areas. It is gathered from satellites to observe short-term and long-term characteristics of vegetation of the earth surface in green areas.

Enhanced Vegetation Index (EVI)

The Enhanced Vegetation Index (EVI) is used to normalize and to filter the vegetation signal, which has some distortions, and noise in the reflected light because of not only the some disturbances in the air but also vegetation cover. The EVI can be expressed as [1]:

$$EVI = \frac{NIR - Red}{NIR + C1Red - C2Red + L} \quad (2)$$

In equation (2), NIR, Red, and Blue are the full or partially atmospheric-corrected. Atmospheric correction covers Rayleigh scattering and ozone absorption. (Surface reflectance; L is the canopy background adjustment for correcting the nonlinear, differential NIR and red radiant transfer through a canopy; C1 and C2 are the coefficients of the aerosol resistance term which uses the blue band to correct for aerosol influences in the red band; and G is a gain or scaling factor). The coefficients adopted for the MODIS EVI algorithm are, L=1, C1=6, C2=7.5, and G=2.5.

The 2-band EVI equation used for the MODIS VI products is:

$$EVI2 = \frac{NIR - Red}{NIR + 2.4Red + 1}$$

RESULTS AND DISCUSSIONS

Some case studies on vegetation index and evapotranspiration are presented in this part of the paper.

Analysis of Temporal Variation of NDVI in and near vicinity of Tekirdağ

Product:	**MODIS/Terra Vegetation Indices (** NDVI/EVI **)**
Coordinates:	**Latitude: 40.98333, Longitude: 27.516667 (WGS84 datum)**
Areal Extent:	**Approximately 6.25 km Wide x 6.25 km High**

Subset Date Range:	**February 18, 2000 (2000049) to May 24, 2016 (2016145)**
Request ID:	**26Jun2016_08:29:07_398682867L40.983333L27.516667S25L25_MOD 13Q1**
Quality Control Conditions:	**As Specified by Science Team (See QC table tab)**

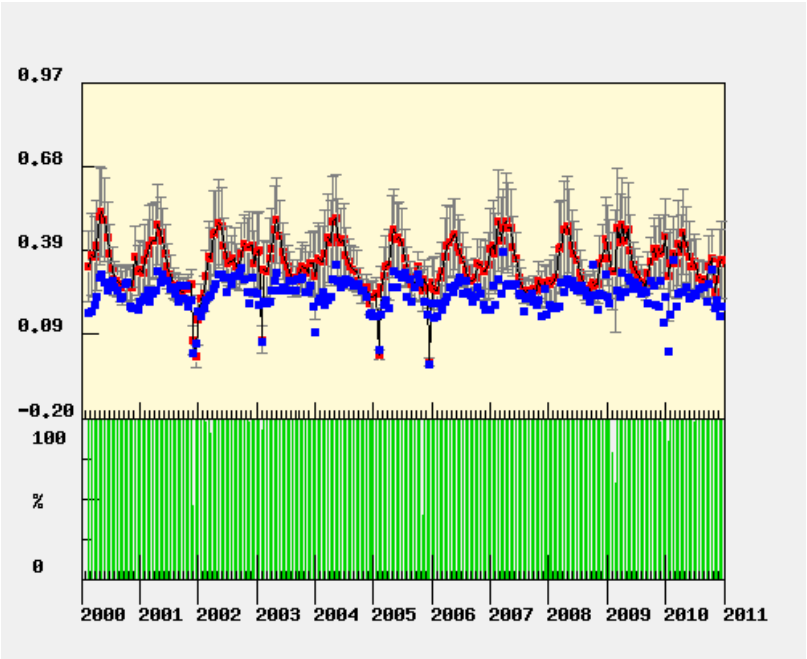

Figure 1 Temporal variation of NDVI, Tekirdağ, 2000-2010

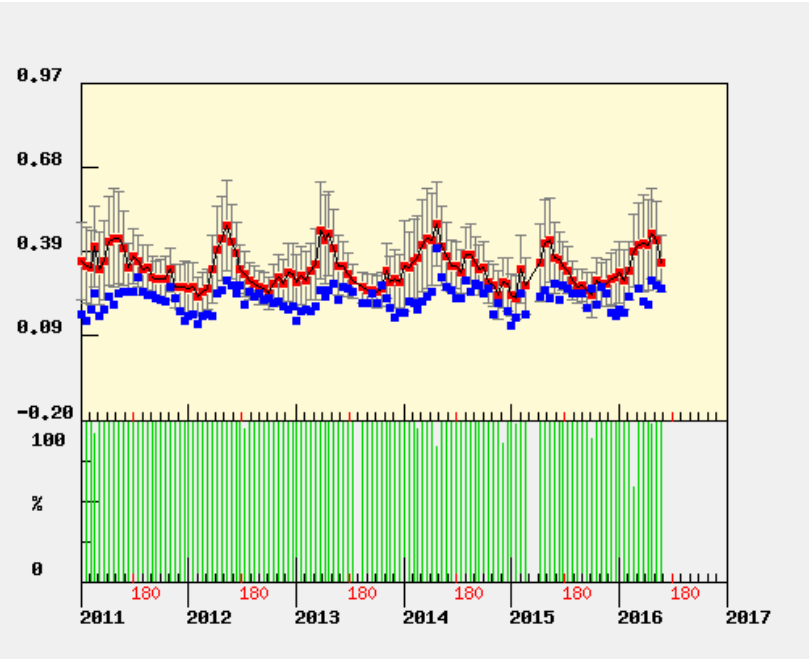

Figure 2 Temporal variation of NDVI, Tekirdağ, 2011-2016

Analysis of Temporal Variation of Evapotranspiration (ET) in and near vicinity of Tekirdağ

Product:	MODIS/Terra Evapotranspiration (ET)
Coordinates:	Latitude: 40.983333, Longitude: 27.516667 (WGS84 datum)
Areal Extent:	Approximately 7 km Wide x 7 km High
Subset Date Range:	January 01, 2000 (2000001) to December 27, 2014 (2014361)
Request ID:	29Jun2016_05:14:02_127392718L40.983333L27.516667S7L7_MOD16A2
Quality Control Conditions:	As Specified by Science Team (See QC table tab)

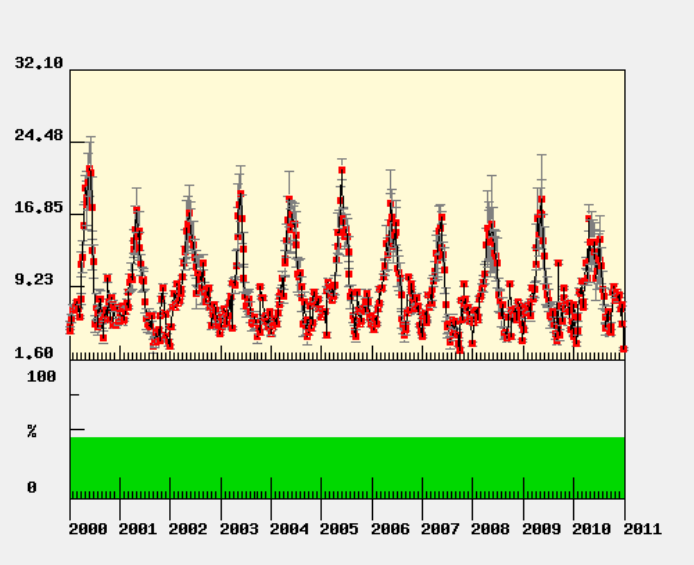

Figure 3 Temporal variation of Evapotranspiration, Tekirdağ, 2000-2010

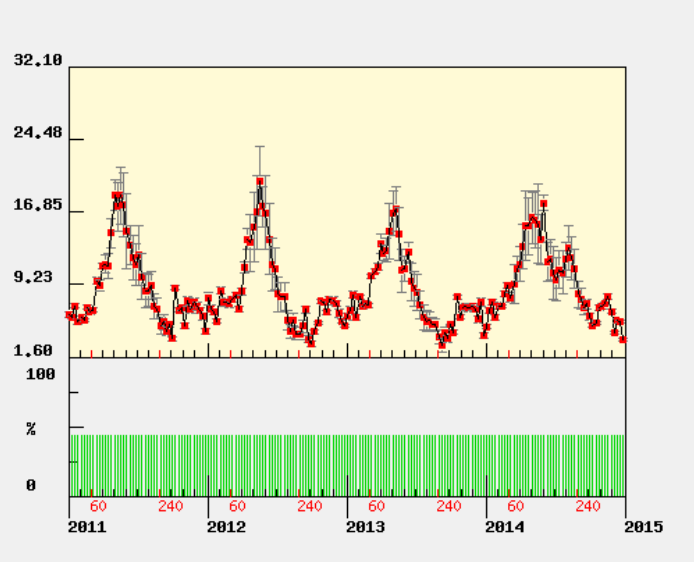

Figure 4 Temporal variation of Evapotranspiration, Tekirdağ, 2011-2014

There is a significant difference in temporal variation of NDVI extremes. Evapotranspiration values also show some slightly decreasing trend beginning in 2006.

ACKNOWLEDGEMENTS

This work was made possible thanks to ICTP Associateship and Earth System Physics Programs that have considerably improved the article. Special acknowledgements to our colleague M.S. Nilüfer ŞEN who helped in the data transferring process.

REFERENCES

Guido Incerti, Giuliano Bonanomi, Francesco Giannino, Flora Angela Rutigliano, Daniela Piermatteo, Simona Castaldi, Anna De Marco, Angelo Fierro, Antonietta Fioretto, Oriana Maggi, Stefania Papa, Anna Maria Persiani, Enrico Feoli, Amalia Virzo De Santo, Stefano Mazzoleni, "Litter decomposition in Mediterranean ecosystems: Modelling the controlling role of climatic conditions and litter quality", Applied Soil Ecology, Pages 148-157, Volume 49, September 2011.

Enrico Tordoni, Rossella Napolitano, Pierluigi Nimis, Miris Castello, Alfredo Altobelli, Daniele Da Re, Samanta Zago, Arianna Chines, Stefano Martellos, Simona Maccherini, Giovanni Bacaro, "Diversity patterns of alien and native plant species in Trieste port area: exploring the role of urban habitats in biodiversity conservation", Urban Ecosystems, Pages 1151-1160, Volume 20, Issue 5, pp 1151–1160, 2017.

Alfredo Altobelli, Tatsiana Hubina, Stefano Sponza, Alberto Sisto, "Effect of abiotic and biotic factors on the abundance of waterbird in Grado-Marano Lagoon (Italy)", Proceedings of SPIE - The International Society for Optical Engineering 7104, October 2008

Athos Agapiou, Diofantos G. Hadjimitsis and Dimitrios D. Alexakis, "Evaluation of Broadband and Narrowband Vegetation Indices for the Identification of Archaeological Crop Marks", Remote Sensing, Pages 3892-3919, Vol. 4, Issue 12, 2012

Altobelli A., Feoli E., Boglich Perasti B., "Application of Goodall's Affinity Index in Remote Sensing Image Classification", GW2-2nd Italian GRASS users meeting proceedings, Feb. 2001, Trento, Italy.

Altobelli A., Feoli E., Napolitano R., Cinco M., "Remote Sensing/GIS techniques for risk assessment of Borrelia burgdorferi infection", GW2-2nd Italian GRASS users meeting proceedings, Feb. 2001, Trento, Italy.

P. Almeida, A. Altobelli, L. D'Aietti, E. Feoli, P. Ganis, F. Giordano, R. Napolitano and C. Simonetti, "The role of vegetation analysis by remote sensing and GIS technology for planning sustainable development: A case study for the Santos estuary drainage basin (Brazil)", Plant Biosystems - An International Journal Dealing with all Aspects of Plant Biology , Pages 540-546,Vol. 1148, Issue 3, 2014.

Ramon Solano, Kamel Didan, Andree Jacobson and Alfredo Huete, "MODIS Vegetation Indices (MOD13) C5 User's Guide", Terrestrial Biophysics and Remote Sensing Lab. The University of Arizona, 2010.

Land Processes Distributed Active Archive Service,https://lpdaac.usgs.gov/dataset_discovery/modis/(Access Date:September 9, 2017).

USDA Risk Management Agency Rainfall and Vegetation Indices, https://www.rma.usda.gov/policies/ri-vi/ (Access Date: September 9, 2017).

CLIMATE CHANGE AND AGRICULTURAL SUSTAINABILITY IN TURKEY

Mikdat Kadıoğlu*, Yurdanur Ünal, Aslı İlhan, Cemre Yürük
ITU Meteorological Engineering Department,, İstanbul Turkey
**kadioglu@itu.edu.tr*

ABSTRACT

Agriculture in Turkey is an important sector both economically and socially. However, the delicate ecosystems, particularly the large industrial plant, the agricultural sector, are largely vulnerable to global climate change. For this reason, knowledge of climate conditions is important in all agriculture activities and plans for the future in Turkey. According to the Climate Services Global Framework (GFCS), agriculture and food security are among the priority sectors. On the other side, "poverty" and "zero hunger" constitute the first two of the United Nations Sustainable Development Targets (SDTs).

The increase in atmospheric carbon dioxide and the prolongation of the plant growth season are positive, but the temperature increases caused by climate change, changes in the amount and regime of precipitation, increasing frequency and severity of extreme weather events negatively affect agricultural activities. The agricultural system is already challenging today to respond to increasing food and renewable energy demands. The changing climate also causes resource problems beyond threatening food safety security, such as water scarcity, pollution, erosion and soil degradation. The effects of severe weather events on agricultural production in Turkey are increasingly significant and negative. It is anticipated that these impacts will increase further with global climate change in the coming years and that the opportunities to access safe food will decrease.

Turkish Ministry of Food, Agriculture and Livestock has also used past year climate data to identify agricultural production basins in Turkey to identify products that need to be supported on watershed basis. As is known, the existence of agricultural production basins and the types of products promoted in these basins, the boundaries of the present basins, the land and terrain classification in the basins, and so on, are changing with time, largely with global climate change. In other words, it is necessary to take into account global climate change projections, both in determining the agricultural production basins and in selecting and supporting appropriate products, in the course of determining future agricultural policies for sustainable agriculture in Turkey.

According to the IPCC reports, the characteristics of climate change must be understood very well in Turkey, which is located in a geographical region most affected by climate change, in order to formulate better policies and strategies in agriculture. For example, inadequate rainfall is known as the most important factor limiting agriculture and water resources. The policies and strategies needed to increase sustainable food production and water resources can only be established by knowing the characteristics of this parameter and the future situation in the best possible way.

According to the findings of the global climate models based on different emission scenarios based on the scale-down of their simulations using the regional climate model, as stated in the "Climate Change Impact Project of Climate Change Impact on Water Resources" Project, which was made by the Ministry of Forestry and the Ministry of Water, General Directorate of Water Management, The expected changes in air temperatures of our country during the 2100

projection period are briefly as follows:
• Mean air temperatures over Turkey will increase significantly at 2-3.5 ° C according to RCP 4.5 scenario and 4-6 ° C according to RCP 8.5 scenario and extreme values will be exacerbated towards the end of 2100,
• At the highest and lowest temperatures of the day, the highest temperature increases will occur along Turkey's south-east and the Mediterranean (with an increase of 1-2 ° C higher than in other regions)
• In the Southeast, Mediterranean and Aegean regions, the increase in air temperature will occur most in summer, with increases of 21 ° to 4 ° C,
• Hot weather waves will increase in the north from the southern latitudes of Turkey. Especially in the Eastern and Southeastern Anatolia Regions after 2041, increases in both frequency and intensity of hot air waves will be observed

Similarly, between 2015-2100 according to all scenarios;
• Turkey's total precipitation amounts are predicted to decrease by 250-300 mm, which is more evident from 2050 except Eastern Black Sea Region,
• Rainfall deficiency is predicted especially due to the expected significant reductions in the amount of precipitation in the Aegean and Mediterranean coasts, in the Southeast and East regions,
• In the east of the Black Sea, precipitation is expected due to increases in average precipitation and extreme precipitation events,
• The frequency of frost events is decreasing, the winters are warmer but the summers are warmer,
• It is estimated that there will be significant reductions in snow-covered areas and snowfall amounts throughout Turkey,
• Due to increasing population, climate change and declining water resources, it is expected that the amount of water available per capita in Turkey will fall to around the critical water stress limits of ~1.100 m3 / year.

In summary, while the winter and spring rains in the Aegean, Central Anatolia and Mediterranean are decreasing, both the increase in the temperature of summer and the increase in evapotranspiration, the increase of summer vegetation such as sunflower and corn and the rapid increase of clover plantation in Central Anatolia the amount of irrigation water required will be about twice as high as today. Even if irrigation is carried out, it is expected that the yields of summer plants will decrease especially because plants will be exposed to higher and extreme temperatures during flowering and grain filling.

In this preliminary study, the focus of the difference between rainfall and evaporation on the monthly changes during the growing season, together with how the global climate change could affect the balance of precipitation, evapotranspiration in agriculture basins in Turkey. For this, specific information on projections for changes in the global climate change up to 2100, for the current period for each basin and for three future periods, 2015-2039, 2040-2069 and 2070-2100, and then the future data obtained from global climate change models, frosty days, plant growth season and soil moisture balance analyzes were made for 30 farming basins.

The results show that in summer and spring a large part of Turkey will have limited water content, and the balance between precipitation and evapotranspiration will change. However, the greatest impact on ecosystem hydrology is the length of the plant growth season and the increasing growth days. And depending on this, changes in the vegetation cover may occur. At the same time more arid periods will cause the fire season to extend.

The increase in evapotranspiration rate along with the expected snow and rain deficiencies will increase stress in water resources and therefore in agriculture sector. Thus, with the rapid increase in hot weather waves and the decrease in precipitation, the climate projections period is expected to be high, or even very high, in the tourism, agriculture, textile manufacturing sectors and the drinking and utility sectors which are in competition for water starting from 2015.

In addition to global climate change, another problem in basins is agricultural policies that cause widespread water-demanding products and consequently water consumption to increase. Reducing the dependence on green and blue water and increasing the use of treated gray water is one of the solutions that each sector understands. However, new, comprehensive and integrated climate change adaptation methods such as water saving, widespread rainwater harvesting, and the treatment of seawater and salted irrigation water, should be developed and implemented for the short term solution of the water problem. The regions that will not be able to adapt to the global climate change and are no longer able to be developed with agriculture should be identified and invested and passed on to other sectors.

In order to ensure agricultural, social, economic and environmental sustainability in the basins and therefore in Turkey, it is necessary to take into consideration global climate change seriously already and to start adaptation works for each agricultural product. It is neither casual nor palliative; serious scientific and structural solutions / reforms to be implemented in the short, medium and long term are urgently needed. As a result of all of these, with changing climate conditions, water resources in the basins, product design, agricultural irrigation practices, water harvesting, purification, water footprint of import and export etc. integrated agriculture and watershed management, which will include all sectors that are all in common with each other and share water, must be deceived by a participatory approach.

In sum, solving the priority water problem of our large scale is very important for agriculture and therefore our country to be resistant to climate change. For this, renewable energy projects supported irrigation projects, irrigation infrastructure and land consolidation, infrastructure, and so on climate adaptation studies need to be completed first. Due to the vital importance of this issue, this preliminary study should be continually improved and updated with a more comprehensive team from different disciplines, renewed every few years.

Reference

Kadıoğlu, M., Y. S. Ünal, A. İlhan, C. Yürük, 2017: Türkiye'de İklim Değişikliği ve Tarımda Sürdürülebilirlik, Türkiye Gıda ve İçecek Sanayii Dernekleri Federasyonu Yayını, p. 168.

INVESTIGATION OF CANAKKALE FOREST FIRES BY CANADIAN FOREST FIRE WEATHER INDEX

Hasan TATLI[1], Mahir ÇEKMEK[1], Cengiz AKBULAK[1], Gürcü AYGÜN[1], Bülent SAĞLAM[2]

[1] Çanakkale Onsekiz Mart University, Department of Geography, 17100, Çanakkale
[2] Artvin Çoruh University, Faculty of Forestry, Artvin

ABSTRACT

In this study, the Canadian Forest Fire Weather Index (FWI), an index of which has been effectively used, was applied for the investigation of the wildland forest fires in Çanakkale. Because the area of Çanakkale is in the region of subtropical Mediterranean climate, it is arid in summer and semi-humid in the other seasons. Due to the geographical features of Çanakkale, forest fires here are very likely to occur and spread. Forest is an important component of both natural resource and ecosystem. Forests have become an important resource for humans throughout history, as well as being a ecological domain for many animal breeding and feeding. Forest fires, one of the most important causes of destruction of forests, are due to natural and human factors. Although the share of human activities in the beginning of the fires is high, the natural factors "meteorological and the conditions of the tree species, etc." are the most fundamental factors affecting the behavior and development of these fires. The FWI is an index expressed as a simple number for explaining and understanding the very complicated forest fire risk. This method, which accounts the factors that make up the forest fire, is basically composed of three main components. These include: i) meteorological conditions, ii) combustible material moisture codes, and iii) fire behavior index. Compared with the statistics of the past forest fires seen in Çanakkale, the results show that FWI can predict the forest fire risk for Çanakkale quite efficiently.

Keywords: *Çanakkale, Forest Fire, FWI, Meteorology, Risk*

INTRODUCTION

Forests are the vital natural resource for conservation of natural balance and sustainability of life. Those creatures of forests are both a source of life and a natural habitat which create ecosystem. It is also one of the important sources that have been actively utilized by people since ancient times (e.g., Akbulak and Özdemir, 2008). Forest fires, if the physical conditions are ready, often start with human factors, but some may be due to lightning.

Throughout the history, forests have become under the constant pressure of farmers to open more agricultural land, for industrial raw materials, or for human influences such as domestic fuel demand. In addition, forests have been constantly threatened by natural causes such as mass movements or climate change-induced drought. When the statistics of forest fires from 2010 to 2015 has been examined, one can see that a total of 35,227 issues of forest fires have occurred and 145631 hectares of forest areas have disappeared in these fires. It is seen that 3738 of these fires were due to intentional consequences, 17776 of them resulted in negligence-accident, 3916 of them were caused by natural causes (lightning etc.) and 9797 of them were due to the unsolved reasons (General Directorate of Forestry. OGM, 2015). Along with the rapid development of the technology, a early warning systems in which, satellite and meteorological forecasting data (calculating various forest fire weather indexes etc.) used together might give a great advantage in combating forest fires and its losses being minimized (e.g., Akbulak, 2010; Bouabdellah et al., 2013).

In many countries of the world (especially in wild-forest fires) intervention can be achieved without fire or fire-growth. In particular, very successful results have been achieved in many countries, especially in Canada, the USA and Australia. To give an example, this success rate is 90% in Canada (Ertuğrul, 2005). Hefeeda *et al*. (2007) used a Fire Weather Index (FWI) as an indicator in early warning systems they developed. They found the FWI approach widely used in many countries, such as Canada and the USA, provided very successful results. Dimitrakopoulos et al. (2011) found that the Canadian Forest Fire Index (CFWI) gave very good results on behalf of the eastern Mediterranean wildfire early warning system.

For a closer look at Australian wildland forest fire, Dowdy et al. (2009) compared the "McArthur Forest Fire Hazard Index (MFFHI)" with "CFWI." The comparison shows that the McArthur index is much more sensitive to temperature and relative humidity than the CFWI. On the other hand, the result of the study suggests that for Australia, both indexes would be much more successful if used together. For a closer look at the wildfire fires in Australia, Dowdy et al. (2009) have compared the "McArthur Forest Fire Danger Index (MFDI)" with CFWI. As a result, they found MFDI been much more sensitive to temperature and relative humidity than the CFWI, while CFWI been so sensitive to wind speed and amount of the precipitation. They suggested that better results could be obtained if both indices were used together in the early warning system of wildfire fires in Australia. Along with morphological and human structure variables, meteorological variables have an important influence on the wildland forest fires and behaviour patterns. Taking this into consideration, the FWI has more advantages because it is derived from meteorological variables unlike many other methods (Tian et al., 2011; Author, 2014).

In this study, it was aimed to set up a risk map of forest fires in Çanakkale with CFWI. After the Introduction section given above, the "data and methodology" section of the study is given in the second section. The third and fourth chapters cover "results" and "conclusions", respectively.

DATA AND METHODOLOGY

Data and Study Area

To show the validity of forest fire risk analysis, it is necessary to collect effective data as it relates to the validity and adequacy of the data obtained. For this purpose, the daily data from meteorological stations of Balıkesir, Bandırma, Biga, Bozcaada, Burhaniye, Çanakkale, Edremit, Enez, Erdek, Ezine, Gelibolu, Gökçeada, Gönen, Keşan, Malkara, Manyas, Savaştepe, Susurluk, Şarköy were used. This data set was obtained from the Turkish State of Meteorology (TSM). The data used in these stations are the total daily precipitation and maximum temperature, wind speed and relative humidity measured at 14:00 GMT, respectively.

The data used in the study are daily-scale data from 1970 to 2015. In addition to the stations listed above to calculate the CFWI, the missing points in the mountainous areas have been estimated by the means of spatial interpolation technique. The geostatistical method called Kriging was applied to complete data or gridding (Tatli and Dalfes, 2016).

In this study, the estimated values of temperature and wind at the grid points are obtained using the data of nearby stations in the vicinity so that the effect of changes that can be caused by the influence of the topography can be evaluated in this way.
During the application the Kriging method to the temperature data, the vertical temperature gradient was taken as 0.65 ° C / 100 meters. On the other hand, for interpolation of the relative humidity values, the data in the neighbours were not used. First, the dew point temperatures

(T_d) were found for each station, then these T_d values were interpolated to the grids by the Kriging method. Using the interpolated dew point temperatures, the actual vapor pressures and temperatures were used to obtain saturated vapor pressure values. At last, the relative humidity values were calculated from the ratio of these vapor pressures. Thus, the dew point and current temperature values of the topography effect were indirectly transferred to the gridded relative humidity values. All calculations were performed using an enhanced FORTRAN 2003 source code program and the maps obtained using by GIS program of the Arc-GIS 10.3 version.

The Çanakkale province is in the South Marmara Division of the Marmara Region. Its geographical position is between 27 ° 35'-27 ° 45'E longitudes and 39 ° 30'-40 ° 45' N latitudes and its surface area is about 9737 km^2. The Aegean Sea lies in the western part of the province, Edirne in the north part, Tekirdağ and Marmara Sea in the north, and Balikesir in the eastern and southern part. Çanakkale, including the central district, is made up of 12 districts and 568 villages.

The Ida (Kaz) Mountains in the southern part of the study area rise immediately after the coast and peak at 1774 meters on the Biga peninsula. The Ida Mountains and its surroundings has a form of steep slopes and deep valleys due to the influence of the rivers. The northern sections and the coastal areas of the study area are a slightly rugged appearance broken by rivers (Türkeş, 2007).

Despite it belongs to macro Mediterranean climate zone, Çanakkale has local-climatic features of Marmara region, which is locally distinctive characteristic and shows a transition climate between local Mediterranean and Black Seas. The seasonal rainfall and temperature distributions are different according to the macro Mediterranean climate (Turkes, 2010, Altan and Turkes, 2014). The Ida Mountain in the district behaves as a barrier to the seasonal air blowing from tropics and polar, subjecting these air masses rising along the mountain slopes, and to occur the orographic precipitation. This situation distinguishes the features from the characteristic macro-Mediterranean climate in terms of temperature and precipitation within the year (Turkes and Tatli, 2011; Turkes and Altan, 2008).

Çanakkale is one of the most forested provinces of Turkey with 54% of the province's overall forest cover. Due to the "summer drought" which is the main feature of Çanakkale's climate, there is a marked water-shortage from July to the end of October during the year (Altan and Turkes, 2011). In Çanakkale province, due to the meteorological variability and the topographical changes in a narrow area of the region, the variety of plant species is very helpful in terms of diversity and density, and in fact there are about 800 different plant species seen in the Ida Mountains, around 80 of which are endemic (Altan and Turkes, 2014).

In the period of seen in Figure 1 of the water budget of Çanakkale province, in the "fire season", the possibility of fire is high and the area of violence and influence can be wider. As seen in this figure, the water shortage is beginning from the beginning of July, with excess water accumulating during the winter with decreasing precipitation towards the end of April. Convective precipitations, which sometimes occur in the summer months, are not affected much in the prevention of summer drought because of short time and small amount of rainfall. The rains, which started from the beginning of October, can only return to the water-surplus conditions after mid-November with the reason of water-deficiency during the summer.

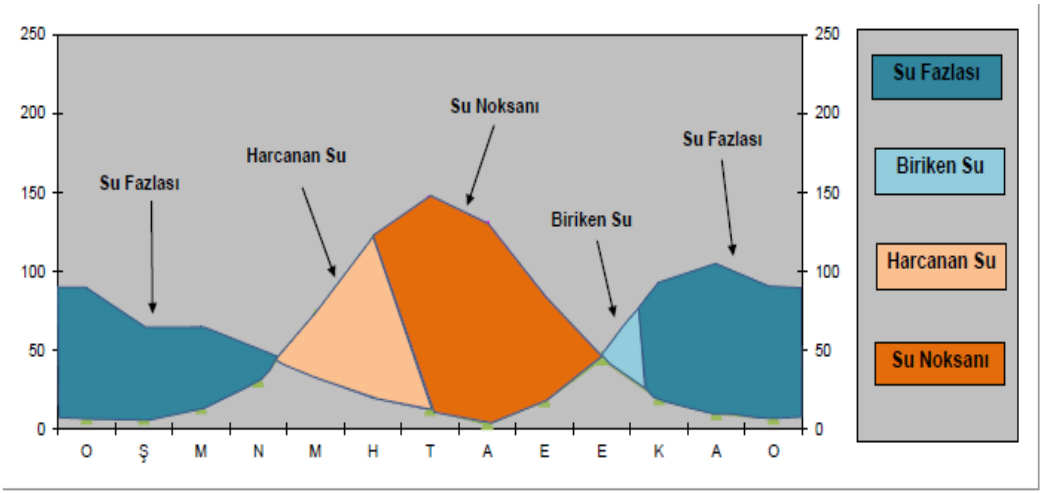

Figure 1. The annual water budget of Çanakkale

Methodology

The FWI is an index that has been used successfully in many parts of the world, combining the meteorological information with the combustible material on the surface (Van Wagner, 1974; Turner and Lawson, 1978; Lee et al., 2002; Sharples et al., 2009; Matthews, 2009) ; Dowdy et al., 2010; Clarke et al., 2013, Author, 2014; Camia et al., 2017). One of the main reasons for using this index is to estimate the forest fire formation, which is defined as highly complex, with a simple number in the potential sense.

In a study of Yamakin (2006), many fire hazard indexes using in many countries were compared by a software program named "fire danger processing" and test of "Mandallaz and Ye's Performance Score" method. Among the many fire hazard indexes evaluated according to the test results, CFWI was chosen as the "forest fire hazard index", as a good representation for Turkey and other Mediterranean countries. Because CFWI is used in this study, the formulas and algorithm are quite long and only the calculation steps describing the underlying logic are given in Figure 2. As seen from this figure; CFWI calculations involve meteorological conditions such as temperature, precipitation, relative humidity, wind speed and dew point temperature.

In Mediterranean countries, during the day, the most likely outbreak of forest fire is at 14:00 GMT (after lunch). Because the maximum temperature and the saturated vapor pressure take the greatest value at this time. Since humidity in atmosphere and in flammable material reaches its minimum value (dryness is the most) at this time, the possibility of a fire occurrence or the risk is very high. Combining meteorological observations with flammable material moisture, CFWI is obtained by integrating the Initial Spread Index (ISI) and Build Up Index (BUI), which describe fire behaviour.

According to the algorithm of Van Wagner (1987) given in the flow chart below (Figure 2), the daily FWI calculations were made for each station. There is no an obvious fire-meteorology pattern for the region in the normal literary sense because the entire region is in the "Very High" and "High" risk classes. However, the changes in topographic patterns and local seasonal recurrence of meteorological airflow should be accounted. From these concerns, it was again divided into categorical classes, so that a distinct fire-meteorology pattern would emerge. All calculations were done with the help of a program developed in FORTRAN 2003.

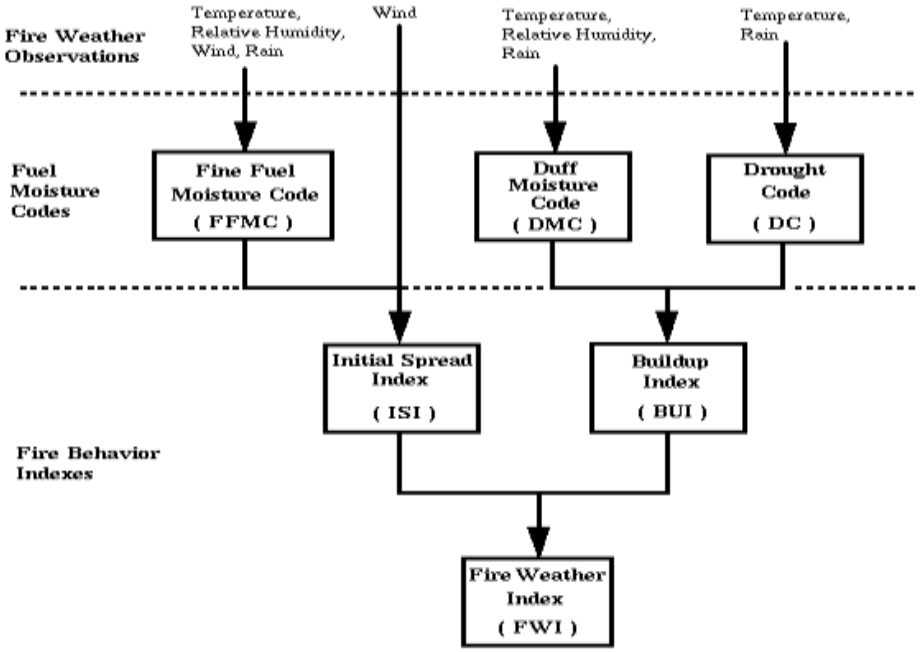

Figure 2. Canadian Fire Weather Index (CFWI) System and its components (modified from Van Wagner, 1987).

The evaluation of the CFWI components given above in Figure 2 is summarized in Table 1. DSR , which is the abbreviation given in this table, means "Daily Severity Rating", the meanings of other abbreviations are given in Figure 2.

According to Table 1, because the DSR values over Çanakkale are almost "High" and "Extremely High", the CFWI values divided into six classes again (mentioned just before) to display a definite fire-meteorology pattern. The "fire risk map" given in the Results section of the manuscript is drawn from this point of view Table 1.

Table 1. Danger classes of Canadian forest fire weather index

Index	Low	Moderate	High	Very High	Extreme
FFMC	0 - 80.9	81 - 87.9	88 - 90.4	90.5 - 92.4	92.5+
DMC	0 - 12.9	13 - 27.9	28 - 41.9	42 - 62.9	63+
DC	0 - 79.9	80 - 209.9	210 - 273.9	274 - 359.9	360+
ISI	0 - 3.9	4 - 7.9	8 - 10.9	11 - 18.9	19+
BUI	0 - 18.9	19 - 33.9	34 - 53.9	54 - 76.9	77+
DSR	0 - 0.47	0.48 - 2.91	2.92 - 5.96	5.97- 13.25	13.26+

RESULTS

In this study, the effects of meteorological factors on forest fires were analyzed using CFWI method. In the analysis of CFWI, temperature, precipitation, wind and relative humidity were taken from meteorological variables. These variables used in the FWI have significant effects on the behavior and growth rate of forest fires in the wildland (Wagner, 1987, Altan et al., 2011, Altan and Turkes, 2011, Sweet and Turkes, 2014).

The meteorological variables used to calculate CFWI are temperature, wind speed, precipitation and relative humidity. The effect of these variables on the occurrence of forest fires can be measured in the drying and humidification of the burning material in the forest, that is, if these

meteorological variables are in proper conditions, the risk of ignition of the fuel increases (Altan and Turkes, 2014).

When we look at the effect of wind speed, this variable has a drying effect on fuel like temperature at the beginning of the forest fire, as well as affecting the behaviour and growth rate of a fired fire (Wagner, 1974). Because the wind can cause a fire to bounce at distances and cause the fire to grow.

Another variable, the amount of precipitation (with relative humidity), has an adverse effect on the occurrence of forest fires in comparison with the effects of temperature and wind speed. Precipitation over the region reduces the risk of fire due to increased soil moisture and fuel moisture content. On the other hand, when the amount and frequency of rainfall in the region is low, it has a negative impact on the risk of fire, because it reduces the moisture content (Wagner, 1987). Another variable used in the calculation of CFWI is the relative humidity that decreases with temperature (for saturated vapor pressure increase), but the relative humidity in the environment increases with precipitation. That is, relative humidity is usually high in rainy conditions, low in times of high temperatures. Accordingly, low relative humidity also means that the fuel's humidity is low. Therefore, when the relative humidity is high, the forest is in the low risk of fire, while in the opposite case it increases the risk (Wagner, 1974, Wagner, 1987, Bilgili, 2014, Sweet and Turkes 2014, Tatli 2015).

The CFWI values obtained from the study were rated in terms of fire-extinguishing risk and mapped using the ArcGIS 10.3 GIS program. The map obtained is shown in Figure 3. When looking at the risk map given in Figure 3, the risk-ratio decreases markedly from the coast to the inner periphery, which can be explained as one of the main causes of the rise in precipitation and relative humidity as the precipitation increases towards the interior. As it is seen in this map, the places with the least risk are the eastern, western and northern parts of the eastern southern parts of Biga, Çan, Yenice and Bayramic and Ayvacık districts. There is higher fire risk in this part of the coast and aaccording to the Northern part, said that changing the topography of the local meteorological conditions. Due to be a rugged nature of the topography and the Ida Mountains of assets with extension line to see a barrier in terms of overall air circulation, southerly hot dryer air type namely Lodos the impact of the break and with the weather, with a mass forced to rise passing the Ida Mountains be leaving precipitation along the high slopes. This increases the relative humidity of the eastern and southern regions of the study area, thus reducing the risk of fire-extinguishment as the wind reduces the drying effect.

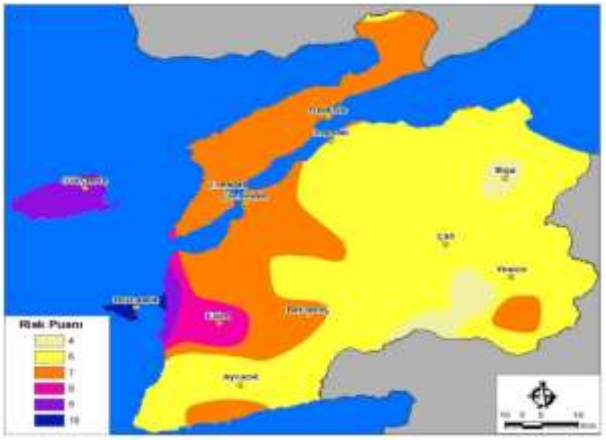

Figure 3. Forest fire air index classes as specified in a subjective manner

This study covers a part of a TUBITAK project that is still underway. In the related project, the risk map given in Figure 4 is obtained when many human and physical geographical factors take part in the account. This map is the most detailed risk map of forest-fire for this region, depending on the open literature. The reason for the awarding of this map is how much representation of the risk map obtained by the CFWI alone can be seen. Hence, the details were not given in this study.

When this last risk-map is examined, there is no low risk area on the entire land, which is in perfect agreement with the risk map obtained with CFWI. Moderately risky areas are observed in a few places. On the other hand, high and very-high risk areas cover the entire working area, except for non-forest areas. This risk seems to be risk-free because there is no forest in the settlement areas.

When the result map is taken into consideration, medium risk areas occupy very little locally between the Çanakkale-Lapseki-Bayramiç and Yenice-Çan-Biga districts. High risk areas are located over the high sections of the Ida Mountains, and the environment Biga, Çanakkale and Gallipoli Lapseki eastern covers the north-western part of the peninsula. Very high-risk areas located over the entire of Gökçeada, the southern parts of Bozcaada, along the Eceabat and Gelibolu shoreline, the entire forest area between Çanakkale-Ezine-Bayramic, Yenice and southern parts and Ayvacık surroundings. Extreme risk areas are locally located in the eastern parts of Gökçeada, northern parts of Bozcaada, between Bayramic and Ayvacık, around İntepe, in southern parts of Yenice, Northeast part of Bayramiç and northern parts of Saros Gulf (Figure 4).

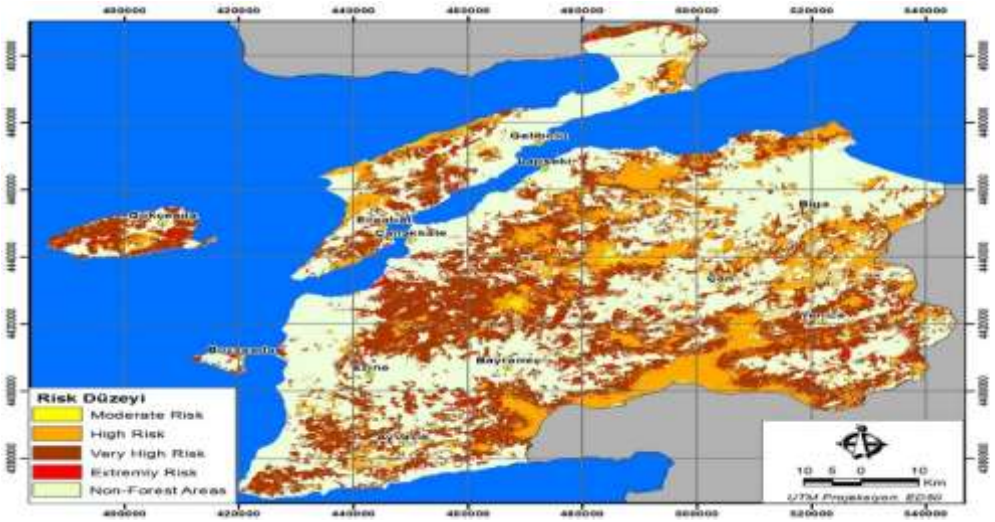

Figure 4. Forest fire-occurrence risk map resulting from all physical (including meteorology) and human geographical factors

CONCLUSIONS

The risk analysis of forest fire formation for Çanakkale was obtained by using the CFWI values given in Figure 3. This map can be seen as "high and very high risk" in terms of forest fire formation for Canakkale. As a result, it is thought that this study will provide great support in terms of forest fire fighting, minimizing fire-prevention and damages.

This study can be regarded as an important resource for the relevant institutions in terms of taking the necessary precautions in the field of work, especially for the very high risk areas covering large areas.It is recommended that these risky areas should be cleaned from

combustible fuels primarily in forest settlements, near agricultural areas and roads close to forest areas, and that the fire in these areas should be informed through direct training and media.

In addition, the related fire-information networking systems which using risk maps of forest fires. Accordingly, the related fire-intervention equipment must be put in the critical places selected from the risk maps in order to prevent the growth of fires. Prior to the occurrence of a possible fire, necessary safety measures can be taken, such as reducing the amount of fuel under the forest. If these and similar fire monitoring and intervention studies are given primarily high-risk and very high-risk field weight, both the number of fires and the magnitude of fires can be reduced. One of the noteworthy shortcomings of the study area is the lack of numbers of meteorological stations and the fact that they are not located in the prerequisite places for fire monitoring and follow-up to take more realistic and reliable data. The permanent meteorological stations can also be placed at suitable places where the necessary measures can be taken in the forest areas and informing the public as well as providing the necessary data.This study has shown that CFWI approach can be used in forest fire risk analysis to give good results. The application of this method in other areas will also benefit from the investigation of its validity. First of all, within the scope of combating forest fires, it is the high public benefit of the country that the necessary financial support of the relevant public institutions is provided for this and similar works.

ACKNOWLEGEMENTS

This study covers a part of the "The Scientific and Technological Research Council of Turkey (TUBITAK)" project of No. 12, and it is also a part of the Thesis of Mahir ÇEKMEK (conducted advisor Professor Hasan TATLI), who pursued his master's studies in the Department of Geography at Çanakkale Onsekiz Mart University. We would like to thank the General Directorate of State Meteorology for providing the meteorological data used in Master Thesis of Mahir ÇEKMEK.

REFERENCES

Akbulak, C. 2010. "Analitik Hiyerarşi Süreci ve Coğrafi Bilgi Sistemleri İle Yukarı Kara Menderes Havzası'nın Arazi Kullanımı Uygunluk Analizi", Uluslararası İnsan Bilimleri Dergisi, Cilt. 7, s. 557-576 (in Turkish).

Akbulak, C.; Özdemir, M. 2008. "The Application of the Visibility Analysis for Fire Observation Towers in the Gelibolu Peninsula (NW Turkey) Using GIS", Proceedings of the Conference on Water Observation and Information System for Decision Support, 27-31 May 2008, Ohird, Republic of Macedonia.

Altan G., Türkeş, M. 2014. "Çanakkale Yöresinde Oluşan Orman Yangınlarının Hidroklimatolojik Karakteristikleri ve İklim Değişimleriyle İlişkisi", Ege Coğrafya Dergisi, s:1-25 (in Turkish).

Altan, G.; Türkeş, M.; Tatlı, H. 2011. "Çanakkale ve Muğla 2009 Yılı Orman Yangınlarının Keetch-Byram Kuraklık İndisi ile Klimatolojik ve Meteorolojik Analizi", In *5th Atmospheric Science Symposium Proceedings Book*, Istanbul Technical University, 27-29 April 2011, 263-274, İstanbul (in Turkish).

Bilgili, E. "Orman Koruma Geçici Ders Notları". https://teyit.org/wp-content /uploads/2017/01/bilgili-ders-notu-2014.pdf (Son Erişim Tarihi: 07.07.2017)

Bouabdellah K., Noureddine H., Larbi S. 2013 "Using Wireless Sensor Networks for Reliable Forest Fires Detection", Published by Elsevier B.V. *Procedia Computer Science*, 19: 794 – 801.

Bozer, R. 2011. "COĞRAFİ VE METEOROLOJİK PARAMETRELERE BAĞLI OLARAK ORMAN YANGININ VERDİĞİ ZARARIN YAPAY ZEKÂ YÖNTEMLERİYLE TESPİTİ". Basılmamış Yüksek Lisans Tezi, Fen Bilimleri Enstitüsü, TOBB Ekonomi ve Teknoloji Üniversitesi.

Camia, A., Liberta, G., San-Miguel-Ayanz, J. 2017 "Modeling the impacts of climate change on forest fire danger in Europe", *JRC Technical Reports*, 10:2760/768481.

Clarkea H., Lucasc C., Smith P. 2013. "Changes in Australian fire weather between 1973 and 2010", Royal Meteorological Society, *International Journal of Cliamtology*, 33: 931–944.

Dimitrakopulos, A.P.; Bemmerzouk, A.M.; Mitsopoulos, I.D. 2011. "Evaluation of the Canadian Fire Weather Index System in an Eastern Mediterranean Environment", *Meteorological Applications* 18: 83-93.

Dowdy A. J., Mills G. A., Finkele K., Groot W. 2009 “Australian fire weather as represented by the McArthur Forest Fire Danger Index and the Canadian Forest Fire Weather Index”, Australian Weather and Climate Research. Australia. Bureau of Meteorology, CSIRO, 10: 1836-019X.
Dowdy A. J., Mills G. A., Finkele K., Groot W. 2010 “Index sensitivity analysis applied to the Canadian Forest Fire Weather Index and the McArthur Forest Fire Danger Index”. Royal Meteorological Society, Meteorological Applications, 17: 298–312.
Erol, O. 1992. “Çanakkale Yöresinin Jeomorfolojik ve Neotektonik Evrimi”. *Türkiye Petrol Jeologları Derneği Bülteni*, 4:147-165.
Ertuğrul, M. 2005. “Orman Yangınlarının Dünyadaki ve Türkiye’deki Durumu”, ZKÜ Bartın Orman Fakültesi Dergisi 7: 43-50 (in Turkish).
Hafeeda, M.; Bagheri, M. 2007 “Wireless Sensor Networks for Early Detection of Forest Fires”, School of Computing Science Simon Fraser University Surrey BC Canada, 1: 4244-1455.
Koç, Telat. “Kaz Dağı Kuzey Kesiminin (Bayramiç-Çanakkale) Jeomorfolojisi”, Coğrafi Bilimler Dergisi, 2007, s:1-27 (in Turkish).
Lee B. S., Alexander M.E., Hawkes B.C., Lynham T.J., Stocks B.J., Englefield P. 2002. “Information systems in support of wildland fire management decision making in Canada”, Published by Elsevier Science B.V. All rights reserved, Computers and Electronics in Agriculture, 37: 185-198.
OGM, 2015a. Orman Genel Müdürlüğü Yangın İstatistikleri, İnternet Adresi: https://www.ogm.gov.tr /ekutuphane/Sayfalar/Istatistikler.aspx?RootFolder=%2Fekutuphane%2FIstatistikler%2FOrmanc%C4%B1l%C4 %B1k%20%C4%B0statistikleri&FolderCTID=0x012000301D182F8CB9FC49963274E712A2DC00&View={4 B3B693B-B532-4C7F-A2D0-732F715C89CC}(Son Erişim Tarihi: 07.07.2017) (in Turkish).
Özden, S.; Üstüner, B. 2012. “Orman Yangını İnsan İlişkisi”, Türkiye Ormancılar Derneği Yayını, 978-9944 - 0048-7-9 (in Turkish).
Sharples J.J., McRae R.H.D., Weber R.O., Gill A.M. 2009. “A Simple Index For Assessing Fire Danger Rating”, Published by Elsevier Science B.V. All rights reserved, Environmental Modelling & Software, 24: 764–774.
Stuart Matthews. 2009 “A comparison of fire danger rating systems for use in forests”, Australian Meteorological and Oceanographic Journal, 58: 41-48.
Tatli H., Dalfes H.N., 2016. “Defining Holdridge’s Life Zones over Turkey”, *International Journal of Climatology*, 36:3864-3872.
Tatli, H. 2015. “Detecting Persistence of Meteorological Drought via The Hurst Exponent”. *Meteorological Application*s 22:763-769.
Tatli, H.; Türkeş, M. 2014. “Climatological Evaluation of Haines Forest Fire Weather Index Over the Mediterranean Basin”, Meteorological Applications, 21, 545- 552.
Tian Xiao-rui, Shu Li-fu, Zhao Feng-jun, Wang Ming-yu, Douglas J. McRae. 2011. “Future impacts of climate change on forest fire danger in northeastern China”, Journal of Forestry Research, 22, 437–446.
Türkeş, M. 2007. “Prof Dr. Oğuz Erol’a Göre Çanakkale Yöresinin Jeomorfolojik ve Neotektonik Evrimi”, Çanakkale Araştırmaları Türk Yıllığı Dergisi, 5, 129-145.
Türkeş, M. 2010. *Klimatoloji ve Meteoroloji* (1. Basım). İstanbul: Kriter Yayınevi.
Türkeş, M.; Altan, G. “Kaz Dağı Yöresi’nde Orman Yangınlarının Kuraklık İndisi ile Analizi ve İklim Değişimleriyle İlişkisi”, Kaz Dağı III. Ulusal Sempozyumu 2012 Bildirileri, 25 Mayıs 2012, Balıkesir (in Turkish).
Türkeş, M; Tatli H. 2011. “Use of the Spectral Clustering to Determine Coherent Precipitation Regions in Turkey for the Period 1929–2007”, International Journal of Climatology, 31, 2055-2067.
Turner J. A. and Lawson B. D. 1978. “Weather İn The Canadian Forest Fire Danger Rating System”, Department of The Environment, Canadian Forestry Service, Victoria, B. C. BC-X-77.
Van Wagner, C.E. 1974. “Structure Of The Canadian Forest Fire Weather Index”, Department of The Environment, Canadian Forestry Service, Ottawa Canada, Cataloge No. Fo47-1333.
Van Wagner, C.E. 1987. “Development and structure of the Canadian Forest Fire Weather Index”, Forestry Technical Report 35, 37. Canadian Forestry Service, Ottowa, Canada.
Yamak Ç. 2006. “Investigation Over a National Meteorological Fire Danger Approach For Turkey With Geographic Information Systems”, Middle East Technical University Graduate School of Natural and Applied Sciences, non-published Master Thesis.
Yetmen H. 2014 “Ardeşen (Rize)’de Mart 2014’te Meydana Gelen Orman Yangınının Meteorolojik Hazırlayıcıları”, Coğrafi Bilimler Dergisi, 12 (2), 133-148 (in Turkish).

DETERMINING RISK OF THE FOREST FIRES IN ÇANAKKALE VIA GEOGRAPHIC INFORMATION SYSTEMS AND *ANALYTIC HIERARCHY PROCESS*

Hasan TATLI[1], Cengiz AKBULAK[1], Gürcü AYGÜN[1], Mahir ÇEKMEK[1], Bülent SAĞLAM[2]

[1] *Çanakkale Onsekiz mart University, Faculty of Sciences and Arts, Department of Geography, 17100, Çannakkle, Turkey*

[2] Artvin Coruh University, Faculty of Forestry, 08000 Artvin, Turkey

ABSTRACT

Forest fires are one of the natural disasters that cause significant loss of life and property in our country as well as all over the world. Forest fires are one of the most important problems of the countries of the great Mediterranean climate (Portugal, Greece, Spain, Italy, France and Turkey in particular). Since Turkey is located in the Mediterranean Basin, a significant part of its forests is threatened by fire. In Turkey, starting from Kahramanmaraş, especially the parts of the 1700 km coastline extending from the Mediterranean Sea basin to the north part of Aegean Sea and 160 km deep constitute a very sensitive area in terms of forest fire danger. More than half of Turkey's forests (58%) are under the threat of forest fire. In this study, the risk analysis of the forest fires in the province of Çanakkale was examined by the Geographic Information Systems (GIS) and *Analytic Hierarchy Process* (AHP). Forest fire is one of the disasters that cause natural and economic losses in Turkey as well as in the whole world. Forecasting areas where forest fires can occur, in other words, forest fire risk analysis is very important for fire prevention. There have been many studies on forest fire risk analysis up to now, but in those studies, the variables involved in the forest fire weather index (FWI) and the physical and human factors affecting the fire have not been considered together. In this study, topographical (elevation, slope, orientation) and human factors (settlement areas, agricultural areas and distance to population and population density) and FWI (temperature, relative humidity, wind speed) were taken into consideration in Çanakkale. To determine the effects of variables on fire risk, the AHP technique was applied and the weight of each variable was determined. Then these variables were combined in a GIS (Arc-GIS 9.3.1 software) environment by the method of weighted overlay and a forest fire risk map was produced. According to the analysis results, there is no area where the risk of forest fires is low. Many significant parts of the forests in Çanakkale are identified as high and very high-risk areas in terms of forest fires. The high and very high-risk areas are seen in the corresponding areas where the pinus brutia and black pine forests and maquis and phrygana seen intensively.

Keywords: *AHP, Çanakkale, Fires, FWI, GIS, Meteorology*

INTRODUCTION

With the increasing population and industrialization, the pressure on the forests has increased to make more use of forest areas around the world, and sometimes has led to disasters. One of these disasters is forest fires. Forest fires are a destructive disaster that affects biodiversity (Carvalho et al., 2011). As in the world, in our country the vast majority of forest fires are the result of human activities, in addition, a very small percentage of fires occurs due to lightning and volcanic movements and other natural phenomena. When we look at the recorded data of the OGM for 2016, 88% of the forest fires are human-induced. It can be determined that 78% of them were caused by "negligence and carelessness" and 10% by "intentionally" fires. Forest fires originating from lightning occurred at 12% (OGM, 2017a). In Turkey, about 12.76 million hectares of the totaling 22.3 million hectares of forests are in 1st and 2nd degree level of fire-

sensitive areas. Approximately 58% of total forests are under the influence of the Mediterranean climate and risk of the forest-fire is very high in those forests. The forest-fire statistics of the last 10 years says that 8903 hectares of forests have been damaged of the 2330 forest fires. Only considering the forest fires occurred in 2016, approximately 9154 hectares of area were damaged due to a number of 3188 forest fires (OGM, 2017a). During those fires, besides the damage of forest areas, serious losses of life and property were occurred (Ertuğrul, 2005).

Forest fires in Turkey are mostly observed in the Aegean, Mediterranean and Marmara regions. Muğla, Antalya, İzmir and Çanakkale cities (study area of this project) are the most dangerous regions in terms of forest fires (DPT, 2001). Due to the very hot and arid weather in the summer months, which is the dominant feature of the Mediterranean climate large areas are damaged due to forest fires, especially in the Aegean and Mediterranean regions. In the Mediterranean and Aegean regions, forest areas of 0-400 meters above sea level are within the first vulnerable zone of the forest-fire. The maquis and red-eyed stalks in these forest areas are damaged due to settlement, agriculture and tourism activities of human (OGM, 2008). Majority parts of the forests of Çanakkale Regional Directorate of Forestry (CRDF) are in the first and second sensitive areas in terms of forest-fire. When the fire-sensitive areas in the CRDF are examined, the forests of Çanakkale, Keşan, Ayvacık and Bayramic are at the first sensitive level. On the other hand, the forests of Biga, Çan, Yenice and Kalkan are in the second degree. In addition, there are no third, fourth and fifth degree sensitive areas in the CRDF (Türkeş ve Altan, 2012). The study area of Çanakkale province is one of the forest-rich areas of the country in terms of forest assets. There are 2 national parks named Gelibolu Peninsula and Troy Historical National Parks. However, as mentioned above, the province is a priority place both in terms of forest fires and in the degree of fire sensitivity. Therefore, the aim of this study is to elaborate the risk of forest fires in this area and to identify a risk-map.

Prediction of forest fires is very difficult due to the complexity of forest fires as well as the effects of human factors. However, with the help of fire information systems and fire risk mapping tools, it may be possible to reduce most of the damage caused by fires (Erten et al., 2005). Though it is unlikely to completely prevent forest fires, the risk analysis may provide support for decision-makers for taking preventive and fire-fighting activities. As a matter of fact, the number of studies carried out in recent years in order to benefit from the results of risk analyzes on disasters both in the world and in the country, has increased considerably. Comprehensive studies have been undertaken in order to reveal the risk of forest fires, especially in forest fire sensitive countries, and various models have been proposed. For example, in the United States and Canada two models were developed for the "forest fires hazard rate system" in 1964, then in 1972 this number increased to nine. In 1978, the number of models reached 20 (Deeming et al., 1978). In a study by Hayes (1944), a "firefighting index" was developed, taking altitude and daylight hours into consideration. Van Wagner (1974) developed an index called "Canada forest fire weather index" and is currently implemented in Canada. Cheney (1976) examined the statistical distributions of forest fires in the period covering 1973-1974 in Izmit, Muğla and Antalya and created a daily fire "danger class" for July, August and September.

In recent studies, remote sensing tools and Geographic Information Systems (GIS) techniques have been used effectively. For example, Jaiswall et al. (2002) prepared maps of forest fire risk-sites for the Gorna basin in India using satellite imagery and GIS technology. Yin et al. (2004) have created forest fires risk zones using GIS in Hinngan Mountain, which is one of the mountainous areas in China. Chandra (2005) have developed "forest fire risk maps" using GIS and remote sensing (RS) methods in the Uttaranchal region of India. Erten et al. (2005) have

created a "forest fire risk map" for some of the Gallipoli Peninsula, using RS and GIS methods. Pradhan et al. (2007) have examined the forest fire sensitivity of the Kuala Lumpur environment in Malaysia using RS and GIS. Small et al. (2007) have applied GIS techniques in Korudağ Forestry area in Turkey, and they have revealed fire behavior depending on the characteristics of flammable substance types and weather conditions. Saglam et al. (2008) have identified forest fires in the forest area of Korudağ. Assaker et al. (2012) have analyzed the risk of forest fires in the Nahr Ibrahim Basin in Lebanon using RS and GIS. Sringeswara et al. (2012) have prepared a forest fire risk map and forest fire management plan for Kudremukh National Park in India. Karabulut et al. (2013) have determined the risk of fire in the Başkonuş Mountain (Kahramanmaraş) in Turkey by GIS. In a significant part of the studies, fire risk analyzes were carried out in different countries by using GIS and applying weighted cointegration method. To determine the risk of fire in these studies, it is generally necessary to determine slope, elevation, view, plant type, plant density, distance to settlement, distance to electric power lines, distance to agricultural areas and land use. In some studies, only a few meteorological data such as monthly rainfall, temperature change, sunshine duration and evaporation have been included in the analysis. However, meteorological parameters such as temperature, precipitation, relative humidity, wind speed and direction have important effects on the occurring and spreading of the wildland forest fires (Byram, 1954, Countryman, 1971, Ryan, 1977; Tatli, 2014).

On the other hand, according to the open literature, it was seen that "forest fire weather indexes" did not participate in the calculation of forest fire risk analyzes in Turkey. It is of great importance to participate in assessing meteorological parameters along with the constants such as "slope, elevation, distance to the settlement area and land use" in order to better evaluate wildland forest fires. These topics have been extensively investigated in this study.

DATA AND METHODOLOGY

Study Area

The province of Çanakkale is located in the South Marmara Region (Figure 1). The city's territory lies between 27°35' - 27°45'E longitudes and 19°30' - 40°45' N latitudes. The total surface area of Çanakkale which is composed of Biga and Gelibolu Peninsulas being 9737 km^2. Çanakkale is surrounded by Balikesir from east and south, Aegean Sea from the west, Edirne from the northwest and Tekirdağ and Marmara Sea from the north.

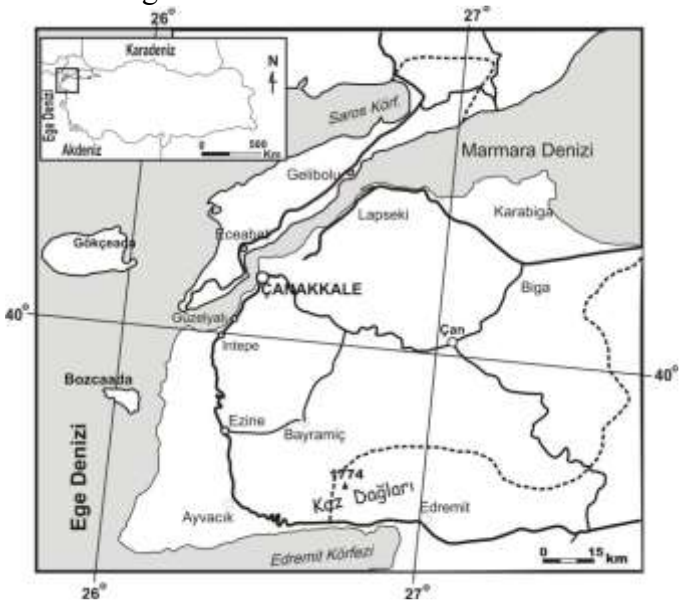

Figure 1. Location map of Çanakkale

There are different geological units formed in different periods. Çanakkale and its surroundings began to form on the Mesozoic rocks in the Paleotectonic period and continued to develop as sedimentation area in the Upper Cretaceous period. The present marine features have taken place in terrestrial features after the formation of the Biga and Yeniköy volcanic in the late Oligocene and early Miocene periods due to volcanic activity at Eocene (Erol, 1992; Türkeş, 2007). Çanakkale is a complex geological and geomorphological point of view. The most important geomorphological unit is undoubtedly the Kaz Mountains located in the peninsula of Biga. These mountains are the most important morphological unit of Biga Peninsula with a height of 1774 meters (Akbulak, 2010). The highest mountain on Gallipoli is Mount Koru (726 m). The lowlands located in the peninsula are Kavak, Cumalı, Yalova, Kilye, Eceabat and Piren. The other plains in the Biga peninsula are Ezine, Bayramic, Kumkale, Biga and Karabiga, Yenice, Kalkım, Umurbey and Sarıçay. Çanakkale, located in the south Marmara division has a local Marmara transition climate (Turkes, 2010).

The effects of polar and Tropical systems and the interaction of north-south air movements, different pressure generations have been observed in different periods. For example, terrestrial Tropical (cT) and marine Tropical (mT) air masses are dominant in summer, while terrestrial Polar (cP) and marine Polar (mP) air masses are more frequently observed in winter (Koç, 2001). In Çanakkale, the rainfall tends to decrease from south to north, and from coast line to interior areas. In general, transition-climate characteristics are observed in the field. The marine impact in the region is decreasing from the coast to the interior. The hottest and driest month is August. Due to the lack of precipitation and the evaporation-excess, August differs from other months in terms of drought. This explains why forest fires are frequently seen in this month. The current dominant directions are the north-northeastern (NNE) and northeastern (NE) winds. The dominant wind is due to the pressure systems of polar. After the northern winds, the second most important winds are the southern winds. The most effective winds in the area are easterly and South-westerly winds. In fact, the wind is not so effective in the beginning of the fire, but it is great importance during the growth and spread of the fire. Since Çanakkale is located between the Mediterranean and Euro-Siberia (Öksin) phytogeographical regions, he has transition characteristics of vegetation cover. That is, the Blacksea phyto-geography area being inhabited to the northern parts of the Kaz Mountains, the area to the south of the Blacksea phytogeographical region dominates the features of the Mediterranean phyto-geography. In some places, the forests seem to have risen after raising more than 150-200m, although they started just right by the coastal areas. Due to ascent, there are wrinkled plants with features of steppe (Kantarci, 1996). On the north-facing slopes of the study area, there are oak species in the areas where the red-headed, larch and forested areas are damaged, as well as alder (Alnus), Ihlamur (Tilia), and chestnut (Castanea) forests. There are also Pinus pinea, Maquie and Garig Juniper, Pinus nigra and Abies in the Mediterranean phytogeography area.

GIS Database

To check the validity of the proposed methods for forest fire risk analysis, the data set must be complete and accurate. In this context, a 1/25000 scale topographic map of the study area was produced using the maps from the cartography laboratory in the Geography Department of Çanakkale Onsekiz Mart University. The digital elevation model, slope and elevation maps were produced in a similar way. The meteorological data set used to calculate the Canadian Forest Fire Index (CFWI) was provided by the Türkish State of Meteorology. The Landsat (L8 OLI / TIRS) satellite images of November 18, 2016 were used to determine the NDVI values indicating the vegetation density classes of the study area. Current stand maps showing the distribution and closure of plant species were obtained from Çanakkale Forest Regional Directorate. The data related to the land use situation was obtained from Çanakkale 2012-

CORINE data base and numerical stand maps. In order to determine the population density of the settlements, the data of 2016 of the address-based population registration system (ADNKS) of the statistical institution of Turkey (TUIK) was used. The distribution of highways was obtained from the digital road data of the cartography laboratory in the Geography Department of Çanakkale Onsekiz Mart University, the data showing the start points of fires in 2007-2016 with coordinates were obtained from the Çanakkale Forest Regional Directorate.

Methodology

The GIS approach provides the opportunity for cheap, fast and error-free analysis of forest fires during the monitoring of the occurrence of the fires and subsequent damage (Erten *et al*., 2005). Because of these advantages, GIS is used as a very effective tool for forest fire risk analysis. Many physical and human factors were evaluated together in risk analysis. Of these, calculation steps the values of CFWI in Figure 2. The source code of the CFWI was written in FORTRAN 2003. Another component NDVI was obtained by using the images of the Landsat (L8 OLI / TIRS) satellite and they were classified in terms of vegetation density to form NDVI layer. In addition, the type of variables used in the risk analysis was selected by consideration the knowledge of literature and expert opinions (experts of the project team and Çanakkale Forest District Directorate Forest Fighting Branch Directorate). Considering the geographical conditions of the study area, the variables used in the study are slope, elevation, aspect, vegetation type, plant-cover (closure of the pavement), distance to previous-fire exit, distance to road, settlement areas and agricultural areas, population density and the values of CFWI as given in Table 1.

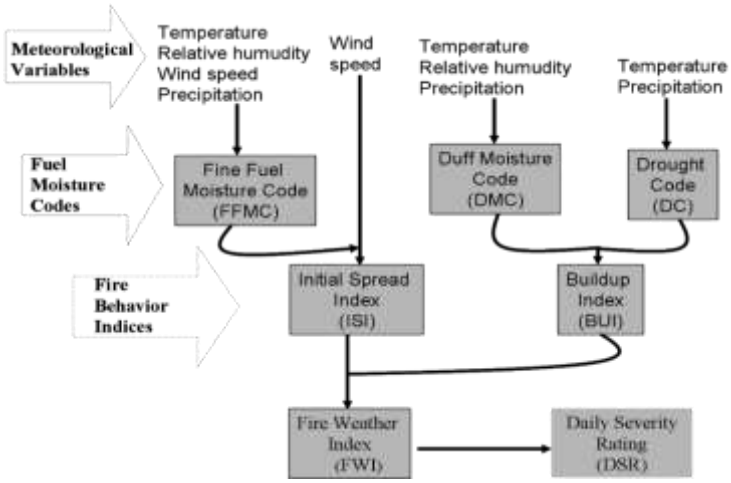

Figure 2. Canadian forest fire weather index system and its components (after Turner and Lawson, 1978)

To complete the necessary missing data and to generate data at the new grid points, a well-known geo-statistical model (Tatli and Dales, 2016) named kriging was used. The slope, elevation and elevation layers are produced from the Digital Elevation Model used in GIS. In order to be able to create a distance layer between the settlements, the point centres of the province centre, the districts and the villages were used.

In the study, the Analytical Hierarchy Process (AHS) method, one of the "Multi Criteria Decision Making" techniques (MCDM), was applied to determine the importance of each component in the fire risk formation (due the restriction of number of papers the details of AHP method were not given here). Within the scope of the study, a total of 12 variables were evaluated in the formation of forest fire risk. It is recommended that the number of variables should not exceed 9 to make the right decision while weighing by the AHS method (Saaty,

1980). For this reason, the 12 variables seen Table 1 were taken into consideration and divided into subgroups, so that the scores of the main variables and sub-variables could be separately determined. After determining the weights of the main and sub variables by the AHS method, the layers in the raster format of the corresponding variables were combined by weighted over layering method (considering the weights of the variables) in the GIS environment.

Table 1. The major and sub-variables used in the study

Main Variable	**Sub-Variable**
CFWI	--
Previous fires	--
Topography	Slope
	Altitude
	Aspect
Vegetation	Plant type
	Plant coverage
	NDVI
Human Factors	Population density
	Distance to settlement
	Distance to road
	Distance to agricultural

RESULTS

The forest fires in Turkey arise mainly due to human reasons, on the other hand topography, meteorological conditions and characteristics of the flammable material are also effective in formation of the fires (Altan and Turkes, 2011, Neyişçi et al., 1999). The "altitude steps" shown in Table 2 were divided into 9 classes with a maximum of 10 score point.

Table 2. Risk score according to altitude

Altitude (meter)	**Risk score**
0 - 200	10
201 - 400	9
401 - 600	8
601 - 800	7
801 - 1000	6
1001 - 1200	4
1201 - 1400	3
1401 - 1600	2
1600 +	1

Since the altitude values are low throughout the city, the high-risk of the fire category is so common. As given in Figure 3, it is observed that the scores are high in the coastal areas and low in the mountainous areas. The low risk scores are seen in the Ida Mountains and its surrounding, which is the highest part of the region.

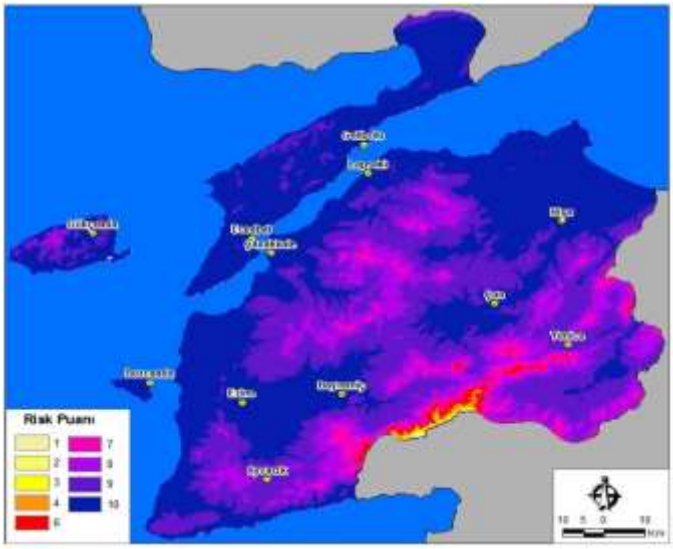

Figure 3. Risk scores according to the altitude

The slope is another important factor in the spread of fire as it affects the rate of accumulation of the flammable material (Bilgili, 2014; Başaran et al., 2004). The slope values were divided into 6 classes and the risk scores ranging from 1 to 10 assigned (the results are not given here due to the limitation of the number of pages). The "aspect" that affects the duration of sunshine and humidity was accounted in the risk analysis. Similarly, the aspect that affects the moisture content and temperature of the flammable material also determines the behaviour of the fire (OGM, 2017). In the study area, the aspect was divided into the classes shown in Table 3, and scores ranging from 1 to 10 are given. Especially the risk of fire is high on the southern slopes of mountainous and plateau areas (Figure 4).

Table 3. Risk scores according to aspect

Aspect	**Risk score**
Flat	5
North	1
Northeast	2
East	5
Southeast	7
South	10
Southwest	8
West	5
Northwest	2

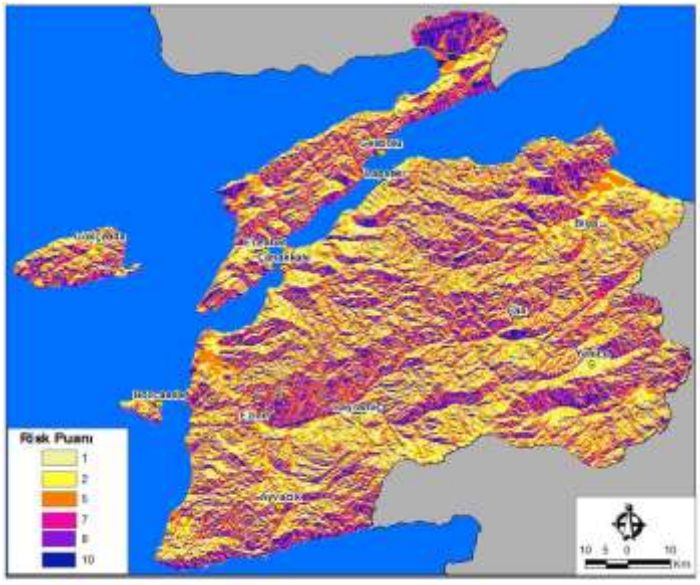

Figure 4. Risk scores according to aspect

The CFWI values have been included in the analysis in order to evaluate the effect of meteorological conditions on the forest fires. It is well-known that meteorological variables are very effective on the fire behaviour and spread of it (Başaran et al., 2004; OGM, 2008, Türkeş and Altan, 2012). Since Çanakkale experiences semi-arid Mediterranean climate features, the evaporation and precipitation values have balanced distribution (Tatli et al., 2004, 2005, Turkes and Tatli, 2011; Tatli and Turkes, 2014; Tatli, 2015). However, in some years, especially during the summer season, the water shortage reaches the drought level causes forest fires. The CFWI values have mainly "high" and "very high" risk throughout the region. However, in order to obtain a more pronounced meteorological pattern with a local-sense, the CFWI values were converted between 4 and 10 scores, and the map of the new scores is shown in Figure 5. Considering this figure, the CFWI pattern shows a gradient of decreasing risk from Bozcada and Gökçeada to northwest and east of the interesting area. Especially in the coastal areas, the risk seems to be significantly higher than the inner regions due to elevation of the inner areas. The fire risk observed around Gökçeada, Bozcada and Gelibolu Peninsula and Ezine is quite high. One of the reasons for the high fire risk values seen in these areas may be that the effect of hot-winds blowing from the Aegean Sea.

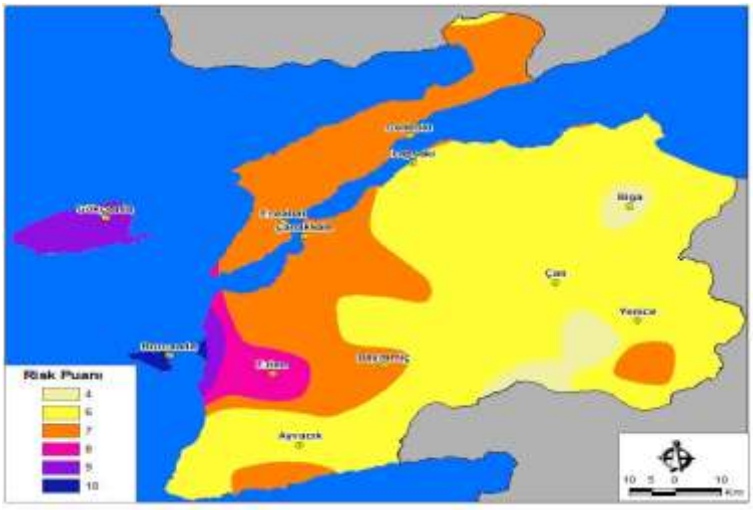

Figure 5. The risk pattern of the forest fire weather index

On the other hand, because of the limitation of the number of pages, the details of the risk analysis for the other variables given in Table 1 such as "vegetation cover", "plant type", "NDVI", "distance to settlement area", "distance to road", "population density" and "distance to the start points of previous fire occurred" were combined in order to obtain the risk map shown in Figure 6. The marginal risk maps of each component were not given here due to the number page limitation. The score of the risk values were classified as given Table 4. Accordingly, it is seen that the risk in Çanakkale province is quite high. There is no area where forest fire risk is low. A few moderately risky areas are observed in some narrow areas.

Table 4. Classification of the risk of forest fires in Çanakkale (in %)

State of risk	**Area (ha)**	**Ratio (%)**
Moderate	2549	0.53
High	153.317	32.13
Very high	302.802	63.46
Extreme	18.457	3.87
Total	**477.125**	**100**

The final risk map is given in Figure 6. According to this map, the high-risk and very high-risk areas are dominant. The high-risk areas are mostly concentrated around the Ida Mountains located in the south-east of the province, while high-risk areas are also found in the central areas. There are also high-risk areas in the area between Gelibolu Peninsula and Eceabat-Gelibolu. The part of the Ida Mountains, Ayvacık and Ezine-Canakkale lines are found in very high-risk areas. Gökçeada is another area where forest fire risk is very high. Similarly, there are areas in the Eceabat-Gelibolu line with very high risk. A few extremely high risk areas are seen on the edge points of Gökçeada, Bozcaada, Ida Mountains and its surrounding, Eceabat-Gelibolu line (Figure 6).

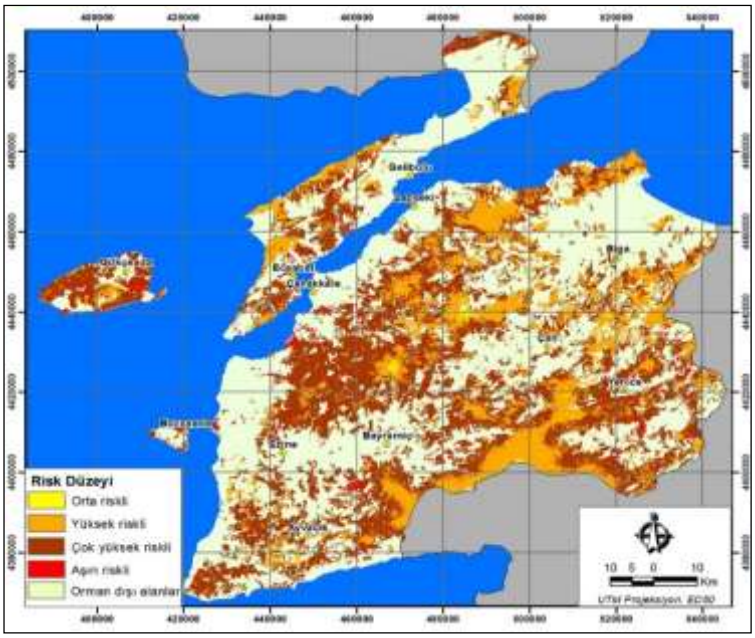

Figure 6. The risk map of fires over Çanakkale

CONCLUSIONS

In the risk analysis of predicting the areas where fires can occur is of great importance in combating forest-fires and preventing. The risk of forest fire of Çanakkale was carried out with the integration of remote sensing, GIS and AHP methods. The risk map was obtained by

merging the sensitive areas in a most accurate way. For example, the expert-knowledge was also utilized in order to calculate the risk situation. In study, the topography, vegetation and human factors, CFWI and distance to the starting points of previous fires were used as the main variables. However, the slope, altitude and aspect conditions were considered as the sub-variables of topography. Similarly, plant type, plant cover and NDVI variables were considered under the vegetation variable. Likewise, the population density, distance to road, residential areas and agricultural areas were taken as sub-variables of the human factor.

According to the fire risk map, it is seen that the risk of forest fire is quite high. There is no area with low risk. The medium risk areas are spreading in a very narrow area, especially, existing in the small spots around Çan. The high-risk areas are concentrated around the Ida Mountains located in the south-eastern part of the province. Moreover, there are high-risk areas in the area between Gallipoli and Eceabat-Gallipoli. It has been determined that there are very high-risk areas in Ida Mountains, Ayvacık-Ezine-Canakkale line and Gökçeada. According to high and very high-risk areas, extreme risk areas are located in the south of Gökçeada, in Bozcaada, around Ida Mountains and between Eceabat and Gelibolu line.

It is revealed that there are too many high and very high-risk areas in terms of forest fire in the province and that protective and preventive measures should be given much importance in the fight against fire in the region. It is suggested that the findings obtained should be taken into consideration in the possible management plans that can be formed within the fight against fire in Çanakkale province. In areas where fire risk is high, it may be planned to clean roadsides to reduce the load of combustible materials, to make regulations on the use of recreational areas, and to determine the rules to be followed by local people and to make necessary informed consent. It should also take advantage of risk maps to take a variety of preventive measures, such as training that will be useful in the fight against fire, planning fire safety roads and lanes, reducing the amount of flammable materials, identifying locations for placement of combat equipment, and construction of surveillance towers. Extinguishing vehicles, which have the ability to intervene quickly and effectively in fighting against fires, such as airplanes and helicopters, must be deployed at points that can reach high risk areas in a short time. Because fires that may occur in such areas may cause serious loss of life and property due to the severity of the fire, in this context, both the fire frequency and the burning area can be greatly reduced by precautionary trials. The study shows that the combined use of GIS, RS and AHP methods in forest fire risk analysis can produce positive results. Consequently, the application of the suggested method in other areas will also benefit from the investigation of its validity. It is thought that more accurate, effective and successful results can be obtained by taking into consideration the current data which can be converted into useful, fast and desired formations obtained from these types of studies, especially in decision stages to be taken within the scope of forest fire fighting activities.

ACKNOWLEDGEMENT

This study covers a part of the “The Scientific and Technological Research Council of Turkey (TUBITAK)” project with number of 116O011.

REFERENCES

Akbulak, C. 2010. “Analitik Hiyerarşi Süreci ve Coğrafi Bilgi Sistemleri İle Yukarı Kara Menderes Havzası“nın Arazi Kullanımı Uygunluk Analizi”, Uluslararası İnsan Bilimleri Dergisi, 7, 557-576 (in Turkish).

Akkaş, M. E., Bucak, C., Boza, Z., Erkonat, H., Bekereci, A., Erkan, A., Cebeci, C. 2008. “Büyük Orman Yangınlarının Meteorolojik Veriler Işığında İncelenmesi”, T.C. Çevre ve Orman Bakanlığı, Ege Ormancılık Araştırma Müdürlüğü, Teknik Bülten, 36, İzmir (in Turkish).

Altan, G., Türkeş, M. 2011. "Çanakkale Yöresinde Oluşan Orman Yangınlarının Hidroklimatolojik Karakteristikleri ve İklim Değişimleriyle İlişkisi", Ege Coğrafya Dergisi, 20, 1-25 (in Turkish).
Assaker, A. Darwish T. Faour G. Noun M. 2012. "Use of Remote Sensing and GIS to Assess the Anthropogenic İmpact on Forest Fires in Nahri Ibrahım Watersheed", Lebanon. Lebanese Science Journal,13, 15-28.
Başaran, M.A. Sarıbaşak, H. Cengiz,Y. 2004. "Yangın Söndürme Planı Temel Esaslarının Belirlenmesi (Manavgat Örneği)", Çevre ve Orman Bakanlığı Yayın No:225, Antalya (in Turkish).
Bilgili, E. "Orman Koruma Geçici Ders Notları". https://teyit.org/wp-content/uploads/2017/01/bilgili-ders-notu-2014.pdf . Son Erişim Tarihi: 12.04.2017 (in Turkish).
Bilgili, E., 2004. "Ülkemizde Orman Yangını Gerçeği", Orman Mühendisleri Odası Dergisi, Sayı 7-8-9, 14-19.
Bonneau LR, Shields KS, Civco DL, 1999. "Using Satellite Images to Classify and Analyze the Health of Hemlock Forests Infested by the Hemlock Woolly Adelgid". Biological Invasions 1, 255–267.
Byram, G.M., 1954. "Atmospheric Conditions Related to Blowup Fires", USDA Forest Service, Southeast Forest Expt. Sta. Pap.35. 31 pp.
Carvalho, A. C. Carvalho, A. Martins, H. Marques, C. Rocha, A. Borrego, C. Viegas, D. X, Miranda, A.I.2011. "Fire weather risk assesment under climate change using a dynamical downscaling approach", Enviromental Modelling and Software, 26, 1123-1133.
Çelik, M.A, Sönmez, M.E. 2013. "Kızıltepe İlçesi'nin Tarımsal Yapısındaki Değişimlerin MODIS NDVI Verileri Kullanılarak İzlenmesi ve İncelenmesi", Marmara Coğrafya Dergisi, 27, 262-281 (in Turkish).
Chandra, S. 2005. "Application of Remote Sensing and GIS technology in Forest Fire Risk Modelling and Managment of Forest Fires: A Case Study in the Gargwal Himalayan Region". *Geo-information for Disaster Management*, edt. Oosterom, P.V, Zlatanova, S., Fendel, E., M, Springer-Verlag Berlin Heidelberg New York,1239-1254.
Cheney, N.P. 1976. "Industrial Forestry Plantations, Turkey Forest Fire Protection. Working Document 14". United Nations Development Programme, 1976 FAO- FO--/DP/TUR/71/521.
Countryman, C. M. 1971, "This Humidity Business: What it is all about and its use in Fire Control". U.S Forest Service, Pasific Southwest Forest and Range Experiment Station, Berkeley, CA. Miscellaneous Publication.
Deeming, J.E., Burgan, R.E., Cohen, J.D., 1977. "The National Fire- danger Rating System -1978". U.S. Department of Agriculture, Forest Service, Intermountain Forest and Range Experiment Station, Ogde, UT. General Technical Report INT-39.
Devlet Planlama Teşkilatı, 2001. "8'inci Beş Yıllık Kalkınma Planı Ormancılık Özel İhtisas Raporu". www.kalkinma.gov.tr/Pages/OzelIhtisasKomisyonuRaporlari.aspx *Son ErişimTarihi :08. 04.2017* (in Turkish).
Dogan HM., Celep F., Karaer F. 2009. "Evaluation of ndvi in plant community composition mapping: a case study for Tersakan valley of Amasya county in Turkey". International Journal of Remote Sensing, 30, 3769 – 3798.
Doğanay, H., Doğanay, S. 2004. "Türkiye'de orman yangınları ve alınması gereken önlemler", Doğu Coğrafya Dergisi, 11, 31-48 (in Turkish).
Duran, C. 2014. "Mersin ilindeki orman yangınlarının başlangıç noktalarına göre mekansal analizi", Ormancılık Araştırma Dergisi, 1, 38-49 (in Turkish).
Edwards MC., Wellens J., Al-Eisawi D., 1999. "Monitoring the Grazing Resources of the Badia Region, Jordan, Using Remote Sensing". Applied Geography,19, 385–398.
Erol, O. 1992. "Çanakkale yöresinin jeomorfolojik ve neotektonik evrimi", Türkiye Petrol Jeologları Derneği Bülteni C 4/1, 147-165 (in Turkish).
Erten, E., Kurgu, V., Musaoğlu, N. 2005. "Uzaktan algılama ve coğrafi bilgi sistemleri kullanarak orman yangını bilgi sisteminin kurulması". TMMOB Harita ve Kadastro Mühendisleri Odası 10. Türkiye Harita Bilimsel Teknik Kurultayı-2005, Ankara (in Turkish).
Ertuğrul, M. 2005. "Orman yangınlarının dünyadaki ve Türkiye'deki durumu", ZKÜ Bartın Orman Fakültesi Dergisi, 7, 43-50 (in Turkish).
Gabban, A., Ayanz, S.M.G., Viegas, D.X. 2007. "On the Suitability of the Use of Normalized Difference Vegetation Index for Forest Fire Risk Assessment", International Journal of Remote Sensing, 27, 5095-5102.
Huete, A., Leeuwen, W.V., Justice, C. 1999. "MODIS Vegetation Index (MOD13) Algorithm Theoretical Basic Document". Arizona.
Ilgar, R. 2007. "Çanakkale Boğazı Fiziki Coğrafyası (1. Basım)", Ankara: Gazi Kitapevi (in Turkish).
Jaiswal, K., Mukherjee, S., Mukherjee, K.D, Saxena, R. 2002. "Forest fire risk zone mapping from satellite imagery and gis". International Journal of Applied Earth Observation and Geoinformation, 4,1-10.
Kantarcı, D. 1997. "Biga Yarımadasında Ekolojik Faktörler ile Ağaç ve Çalı Türlerinin Yayılışı Arasındaki İlişkiler ve Ormanlara Verebilecek Etkenler", Yerleşim ve Çevre Sorunları, Çanakkale, 9-13 Eylül Bildirileri, İzmir (in Turkish).
Karabulut, M. 2003. "An Examination of Relationship Between Vegetation and Rainfall Using Maximum Value Composite AVHRR- NDVI Data", Turkish Journal of Botanic, 27, 93-101.

Karabulut, M., Karakoç, A. 2013. "Coğrafi Bilgi Sistemleri Kullanarak Başkonuş Dağında (Kahramanmaraş) Orman Yangını Risk Alanlarının Belirlenmesi", Uluslararası Sosyal Araştırmalar Dergisi, 6, 171-179 (in Turkish).
Koç, T. 2001. Kuzeybatı Anadolu'da İklim ve Ortam Sinoptik, İstatistik ve Uygulama Boyutlarıyla (1. Basım), İstanbul: Çantay Kitapevi (in Turkish).
Küçük, Ö., Bilgili, E. 2007. "Yangın Davranışının Coğrafi Bilgi Sistemi (CBS) Yardımıyla Haritalanması: Korudağ Örneği", KSÜ Fen ve Mühendislik Dergisi,10, 64-71 (in Turkish).
Myneni, R.B., Keeling, C.D., Tucker, C.J., Aarar,G, Neamanı, R.R. 1997. "Increased Plant Growth in the Northern High Latitudes from 1981 to 1991", Nature, 698-702.
Neyişçi, T., Ayaşlıgil, Y., Ayaşlıgil, T., Sönmezışık, S. 1999. "Yangına Dirençli Orman Kurma İlkeleri", Tübitak-Togtag -1342, TMMOB Orman Müh. Odası Yayın No:21, Ankara.
OGM, 2008. "Baharlar Yanan Alanların Rehabilitasyonu ve Yangına Dirençli Ormanlar Tesisi Projesi", TC Çevre ve Şehircilik Bakanlığı, Orman Genel Müdürlüğü, Çanakkale Orman bölge Müdürlüğü, Silvikültür Şube Müdürlüğü (in Turkish).
OGM, 2017. Orman Genel Müdürlüğü Yangın İstatistikleri, İnternet Adresi: https://www.ogm.gov.tr/ekutuphane/Sayfalar/Istatistikler.aspx (Son Erişim Tarihi: 08.06.2017) (in Turkish).
Rouse, J. W., Haas, R. H., Schell, J. A., Deering, D. W., 1974. "Monitoring vegetation systems in the great plains with ERTS", 3rd ERTS Symposium", 309-317.
Ryan, B.C., 1977." A Mathematical Model for diagnosis and Prediction of Surface winds in Mountainous Terrain. J. Appl. MCT". 16, 571-584.
Saaty, T., 1980. "*The Analytic Hierarchy Process*", ISBN 0-07-054371-2, USA.
Sağlam, B., Bilgili, E., Durmaz, D.B., Kadıoğulları, İ.A., Küçük, Ö. 2008. "Spatio Temporal Analysis of Forest Fire Risk and Danger Using Landsat Imagery". Sensors 2008, 8,3970-3987.
Sringeswara, N.A., Shivanna, B.M., Gowda, B. 2012. "Forest fire and its management in Kudremukh National Park, Western Ghats", India Using Remote Sensing and GIS".13th Esri India User Conference, 1-9.
Tatlı H., Dalfes H.N., 2016. "Defining Holdridge's life zones over Turkey", International Journal of Climatology, 36, 3864-3872.
Tatli, H. 2015. "Detecting persistence of meteorological drought via the Hurst exponent", Meteorological Application, 22, 763-769.
Tatli, H., Dalfes, H,N., Menteş, Ş,S. 2004. "A statistical downscaling method for monthly total precipitation over Turkey", International Journal of Climatology, 24, 161-180.
Tatli, H., Dalfes, H.N., Menteş, Ş,S. 2005. "Surface air temperature variability over Turkey and its connection to large-scale upper air circulation via multivariate techniques", International Journal of Climatology, 25, 331-350.
Türkeş, M. 2007. "Prof Dr. Oğuz Erol"a göre çanakkale yöresinin jeomorfolojik ve neotektonik evrimi", Çanakkale Araştırmaları Türk Yıllığı Dergisi, 5, 129-145 (in Turkish).
Türkeş, M. 2010. "*Klimatoloji ve Meteoroloji (1. Basım*)". İstanbul: Kriter Yayınevi.
Türkeş, M., Altan, G. 2012. "Çanakkale'nin 2008 yılı Büyük Orman Yangınlarının Meteorolojik ve Hidroklimatolojik Analizi". Coğrafi Bilimler Dergisi. 10, 195-218.
Türkeş, M., Tatli H. 2011. "Use of the spectral clustering to determine coherent precipitation regions in Turkey for the Period 1929–2007". International Journal of Climatology, 31, 2055-2067.
Van Wagner, C.E. 1987. "Development and structure of the Canadian Forest Fire Weather Index". Forestry Technical Report 35, 37. Canadian Forestry Service, Ottowa, Canada.
Yın, Hai-Wei, Kong, Fan-Hua, Li, Xiu-Zhen. 2004. "RS and GIS-based forest fire risk zonem mapping in Da HINGGAN Mountains". Chınese Geographıcal Science,14, 251-257.

CLIMATE PROJECTIONS FOR THE CENTRAL ANATOLIAN AGRICULTURAL BASIN

Aslı İLHAN, Yurdanur ÜNAL, Mikdat KADIOĞLU and Cemre YÜRÜK
Istanbul Technical University, Department of Meteorology Engineering
ilhanas@itu.edu.tr

Abstract
The knowledge of climate change conditions is important for all agricultural activities and plans in Turkey since Turkey's geopolitical position makes it sensitive to atmospheric variations. According to researches there is a known consensus that climate change has increased the challenges about the agricultural sector. In this study, the effect of climate change on the precipitation and evapotranspiration in the Central Anatolian Agricultural Basin assessed. For this purpose, the present and future climate conditions over the basin is estimated by using MPI-ESM-MR+RegCM model chain under RCP8.5 emission scenario with 10 km resolution. Precipitation and evapotranspiration in plant growth season (March-October) are examined for periods of 2015-2039, 2040-2069, 2070-2099. The basin averaged cumulative growing degree-days with respect to 5°C and 10°C for plant growing season are studied. The changes are determined for the reference period and the next three future periods, separately.

Keywords: *Climate model, MPI-ESM-MR, RCP8.5, RegCM, agricultural basin, Central Anatolian Agricultural Basin*

INTRODUCTION

Turkey is located in a transition zone between the arid climate and the mild and rainy climate, in Mediterranean region. As Giorgi (2006) pointed out, the Mediterranean region is one of the primary hotspots which are very sensitive to climate change. Turkey is under the influence of various meteorological and climatic phenomenon at different scales as a result of variations in terrain, vegetation cover and water bodies. Hence, climate change is one of the biggest ecological, environmental, social and economic problems that Turkey faces with. Many modeling studies have been carried out to investigate climate variability and future projections in Turkey. For instance, Onol and Semazzi (2009), Unal et al. (2010), Bozkurt and Sen (2011), Bozkurt et al. (2012), Onol and Unal (2014), Demircan (2014), SYGM (2016) and Yuruk (2016) investigated climate change projections by using regional climate models over Turkey for old and new emission scenarios. All these studies point out that the temperatures are most likely to increase in the future for mild and severe emission scenarios. Also the results suggest that precipitation regime over Turkey is most likely to change and frequently drier conditions dominate most of the regions. Therefore, water scarcity is expected to affect many sectors. Changes in the frequency and severity of droughts and floods could pose challenges on the agriculture and threaten food safety. Many studies pointed out climate change effect on agriculture (Fisher et al., 2005, Nelson et al., 2009). Agriculture is one of the major source of income for Turkish economy. The purpose of this study is to estimate present and future climate conditions over the Central Anatolian Agricultural Basin by using MPI-ESM-MR+RegCM model chain under RCP8.5 emission scenario.

METHODOLOGY

In this study, high resolution dynamically downscaled results of the Earth System Model (ESM) MPI-ESM forced by RCP8.5 emission scenario are used to estimate present and future climate conditions over Central Anatolian Agricultural Basin. Climate simulations are obtained with resolution of 10 km (≈8000 grid) after 50x50 km by using regional climate model of RegCM4.3

for present climate and future. The future projections (from 2015 to 2100) are compared with reference period (from 1971 to 2000) and analysed for precipitation, evapotranspiration and soil temperature parameters by dividing the future into three periods (2015-2039, 2040-2069, 2070-2099). In Figure 18, the domain of RegCM4.3 simulations and the borders of the Central Anatolian Agricultural Basin are depicted along with the topography. The cumulative Growing Degree Days (GDD) for the thresholds of 5ºC and 10ºC are calculated between the last and first frozen days. The seasonal changes in water availability are investigated by superimposing the annual march of actual evapotranspiration on annual march of precipitation for reference and three future periods.

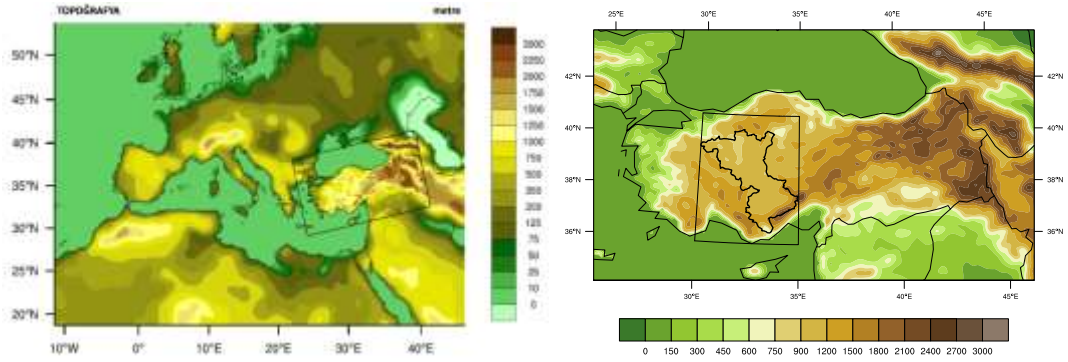

Fİgure 18. The domain of simulations on topographic map. The bold line (right panel) corresponds to the Central Anatolian Agricultural Basin

RESULTS

The average air temperature for the Central Anatolian Agricultural Basin is 9.3°C during the reference period. Basin averaged temperatures are expected to increases in the future with respect to the reference period around 0.9°C, 2.3°C and 3.8°C for the periods of 2015-2039, 2040-2069, 2070-2099, respectively (not shown). RCP8.5 emission scenario projects that the basin temperature first slowly increases but through the end of century, the warming will be expected to accelerate.

By using the average surface temperature over the basin, the last and the first frozen days are estimated. The last frozen days for the reference period (1971-2000), and the future periods (2015-2039, 2040-2069, 2070-2099) are 4th March, 2nd March, 1st February and 11th January, respectively. On the other hand, the first frozen days for the reference period and the future periods are 23th December, 16th December, 3rd January and 8th January, respectively. While the last average frozen days supervene almost two months relative to the reference period, the first ones predate roughly two weeks. Therefore, the growth season is expected to increase in the future.

The monthly cumulative GDD for the thresholds of 5°C and 10°C are calculated to estimate heat accumulation necessary for the plant development. Figure shows basin averaged cumulative GDD values between the last and first frozen days according to RCP8.5 emission scenario for the Central Anatolian Agricultural Basin. Significant increases are observed in the total growth season and the cumulative GDDs up to 2100 degree day with respect to the reference period (1971-2000) due to increasing air temperatures and the preceded last frozen date. The cumulative GDD is increasing approximately 200 ºC day from reference to 2015-2039, 300 ºC day to 2040-2069 and 400 ºC day to 2070-2099. 500 ºC day is reached in July in the reference period but it is reached in June in 2070-2099 period. The results indicate that if

the water scarcity is not a concern or overcome by diverting water from other areas, increasing water allocation systems or using irrigation, the crop yields is likely to increase and the growing period is likely to decrease in the future. On the other hand, these may elevate the rate of environmental degradation.

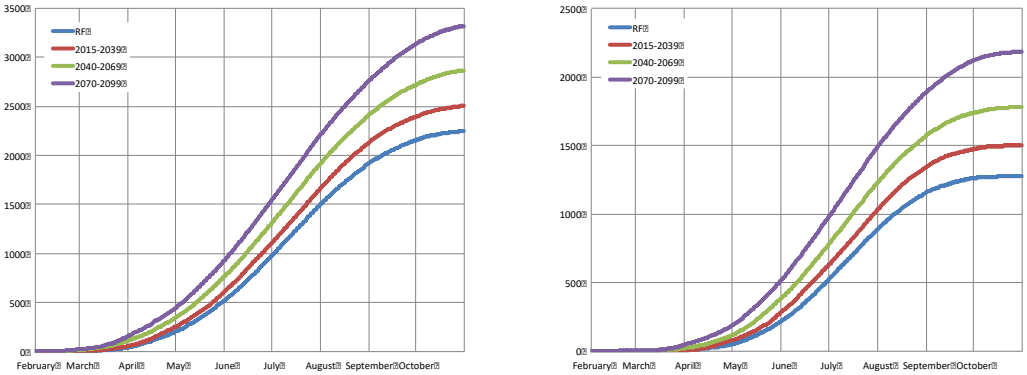

Figure 2. The cumulative growing degree-days (left; >5°C and right; >10°C) distributions during the year over the Central Anatolian Agricultural Basin for present and future periods; 1971-2000 (blue line), 2015-2039 (red line), 2040-2069 (green line) and 2070-2099 (purple line).

Climate change affects soil water balance by altering precipitation regime, soil evaporation and plant transpiration. The relative changes of simulated precipitation and actual evapotranspiration on the Central Anatolia Agricultural basin for each future period are analysed. The average monthly total precipitation and the average monthly actual evapotranspiration distributions are shown in Figure 3. The annual precipitation on the basin decreases from 648 mm for the reference to 539 mm for the last period of this century. Therefore, water availability will be one of the limiting constraints for agricultural production in the basin. In the current climate, the equilibrium between precipitation and evapotranspiration is established in May. However, the climate projection shows that this equilibrium might shift to March or April trough the end of century. The period which the soil mosture is used for the plant growth will enlarge and it will start one and a half month earlier during the period of 2070-2099 than the reference period. Thus, the time needed for plants to use soil moisture will enlarge.

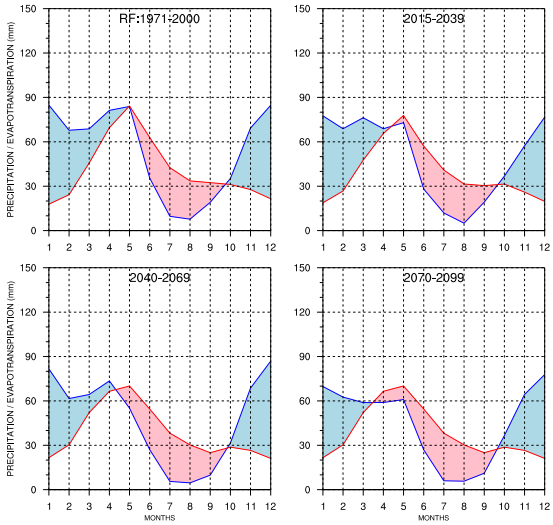

Figure 3. The changes of the average monthly total precipitation (blue line) and the average monthly actual evapotranspiration (red line) according to the RCP8.5 emission scenario over the Central Anatolian Agricultural Basin (basin average) in the reference period (1971-2000) and the future periods (2015-2039, 2040-2069 and 2070-2099).

Figure 4 shows the expected precipitation and actual evapotranspiration changes over the basin between March and October for future three periods. The significant decreases are estimated with respect to the reference period in the future for total precipitation in the plant growth season over most part of the basin. While the decreasing in precipitation was obtained during the first and the last future periods, the small increasing regions are simulated over the center of the basin during the second future period. Potential evapotranspiration increases due to the increasing temperatures. However, actual evapotranspiration is limited by the amount of soil moisture. The results shows decreasing tendency of actual evapotranspiration during the all future periods till 2100 because of the depletion of soil moisture in the earlier dates compared to reference period.

CONCLUSIONS

The following results were obtained due to the analysis of climate change in the Central Anatolian Agricultural Basin.

- The annual precipitation decreases up to 539 mm with respect to reference period. The precipitation reduction during the growth season over the central of the basin is relatively small to the northern and southern part of the basin. Maximum decreases are around 100 mm.
- Basin average temperatures for RCP8.5 scenario are expected to increase around 0.9°C, 2.3°C and 3.8°C for the periods of 2015-2039, 2040-2069, 2070-2099, respectively.
- While the last average frozen days supervene almost two months relative to the reference period, the first ones predate roughly two weeks. Therefore, the growing season is likely to start earlier and likely to expand in the future.
- The cumulative degree-days are increasing as a result of increasing temperatures. Eventually crop growth period might shorten.
- Even though potential evapotranspiration increases due to the warming till end of the century, the actual evapotranspiration is expected to decrease because of the soil moisture deficiency.
- The increasing potential evapotranspiration due to the decreasing precipitation and increasing temperatures most likely increase stress on water resources and agriculture.

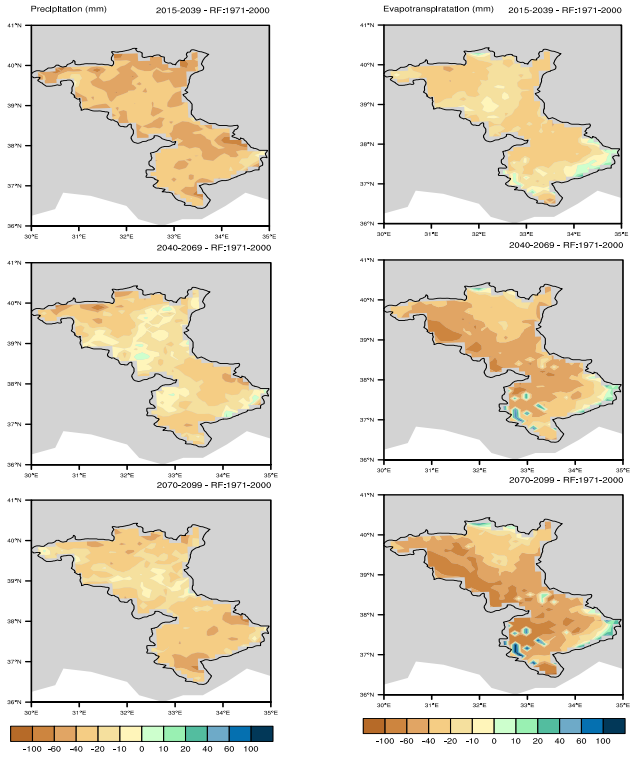

Figure 4. The differences between future periods and reference period for total precipitation (left) and total evapotranspiration (right) in the plant growth season (March-October) for 2015-2039, 2040-2069, 2070-2099 periods.

REFERENCES

Bozkurt, D., Sen, O. (2011). Precipitation in the Anatolian Peninsula: sensitivity to increased SSTs in the surrounding seas. *Climate Dynamics , 36* (3), 711-726.

Bozkurt, D., Turuncoglu, U., Sen, O. L., Onol, B., & Dalfez, H. N. (2012). Downscaled simulations of the ECHAM5, CCSM3 and HadCM3 global models for the eastern Mediterranean–Black Sea region: evaluation of the reference period. *Climate Dynamics , 39* (1), 207-225.

Demircan M., Demir, O., Atay, H., Yazici, B., Eskioglu, O., Tuvan, A., Akcakaya, A. (2014). Climate Change Projections For Turkey With New Scenarios

Fischer, G., Shah, M., Tubiello, F., & van Velhuizen, H., (2005). Socio-economic and climate change impacts on agriculture: an integrated assessment, 1990–2080. Philosophical Transactions of the Royal Society, B: Biological Sciences, 360(1463), 2067–2083, doi:10.1098/rstb. 2005.1744.

Giorgi, F. (2006). Climate change hot spots, doi: 10.1029/2006GL025734. From http://onlinelibrary.wiley.com/doi/10.1029/2006GL025734/full

Nelson, G. C., Rosegrant, M. W., Koo, J., Robertson, R., Sulser, T., Zhu, T., Ringler, C., Msangi, S., Palazzo, A., Batka, M., Magalhaes, M., Valmonte-Santos, R., Lee, D., (2009). In Climate change: impact on agriculture and costs of mitigation. Washington, DC: International Food Policy Research Institute. (doi:10.2495/ 0896295354)

Onol, B., Semazzi, F. H. M. (2008). Regionalization of Climate Change Simulations over the Eastern Mediterranean, *Journal of Climate , 22*, 1944-57.

Onol, B., Unal, Y. (2014). Assessment of climate change simulations over climate zones of Turkey. *Regional Environmental Change 14* , 1921-1935.

Smil, V., (2005). Do we need higher farm yields during the first half of the 21st century? In Yields of farmed species.

SGYM (2016). İklim Değişikliğinin Su Kaynaklarına Etkisi Projesi, Proje Nihai Raporu, T.C. Orman ve Su İşleri Bakanlığı Su Yönetimi Genel Müdürlüğü (SYGM) Taşkın ve Kuraklık Yönetimi Dairesi Başkanlığı, Ankara.

Yuruk C. (2016). COSMO-CLM (CCLM) climate simulations over Turkey: Performance evaluation and climate projections for the 21st century, ITU, Graduate School of Science Engineering and Technology, p. 73.

Unal Y.,Onol B., Menteş S., Borhan Y., Kahraman A., Ural D. (2010), Assessment of Global Climate Change Impact on Turkey by Regional Climate Model TUJJB-TUMEHAP-02-06, 2006-2010

DROUGHT STRESS DUE TO CLIMATE CHANGE AND EFFECTS ON PLANTS

Hüseyin Bulut[1], Hüdaverdi Gürkan[2]
[1]*Turkish State Meteorological Service, Information Technologies Department*
hbulut@mgm.gov.tr
[2]*Turkish State Meteorological Service, Research Department*
hgurkan@mgm.gov.tr

Abstract
The Climate comes first in the most important factors which effect of the life and the distribution of life forms on earth. For this reason, life plains of natural and cultural plants is formed by the effect of climatic factors. The observations of the World Meteorological Organization and lots of works show a global climate change. No doubt, the effects of this change is seen in Turkey. The effect of climate factors on agricultural production cannot be ignored. Plants encounter many stress factors which affect their growth and development throughout their lifecycles because of their nature. These stress conditions which can be originated by biotic and abiotic factors can adversely affect the quantity and quality of the product with leading to physiological and biochemical damage to crops. Drought stress, one of the most common environmental limitations affecting growth and productivity of plants, causes many mechanical, metabolic and photosynthetic changes in plants. This situation makes cultivation of plants tolerant to high stress more crucial. Therefore, current studies are mostly focused on the explaining the tolerance mechanisms of highly drought resistant plants and protecting and transforming of the plant genetic sources. In this paper, drought effects on the plants are explained by referring important researches done in the recent years.

Keywords: *Climate change, drought stress, mechanical, metabolic and photosynthetic changes.*

INTRODUCTION
Increasing temperatures due to climate change, changes in precipitation regime and record-increasing natural disasters due to meteorological changes every year, which we are beginning to feel more nowadays, negatively affect the vital activities of human beings. It is inevitable that crop production is also affected by climate changes. Climate change and associated meteorological disasters cause serious crop losses in crop production. Atmospheric evaporation losses are expected to increase as a result of drought events that are expected to increase due to climate change (Teuling, 2013). Increased temperatures due to climate change and irregularities in the precipitation regime cause drought to occur more and more every year.

In addition, drought stress has become increasingly important in plant breeding every day due to the declining nature and quantity of water resources around the world, leading to changes in the normal physiological functions of plants with economical preserve. This is especially important in the cultivation of crop plants, which require large amounts of water for their development and often cause water loss to yield deficiencies. Drought, which causes very serious decreases in crop production, causes serious economic losses all over the world Therefore, WMO provides guidance and scientific information to strengthen national services responsible for addressing drought risks to agriculture.

Plants encounter many stress factors during their lives. According to Levitt, stress factors are divided into biotic and abiotic (Levitt, 1980). Biotic factors; Infection of microorganisms (fungi, bacteria and viruses), and attack factors of harmful animals (Figure 1).

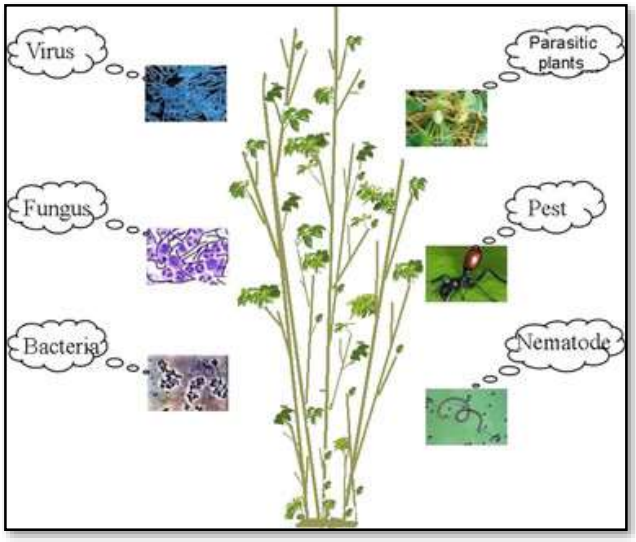

Figure 1: Biotic stress factors

Abiotic factors are environmental factors such as drought, water, radiation, chemicals, magnetic and electrical fields (Lichtenhaler, 1996). Climate and soil factors are at the top of the abiotic factors that plants have to cope with (Figure 2). Each of these factors affects the distribution of plant species and the genetic makeup of the population in different ways. Their effects are not independent of each other and they have a common effect on the plant. For example, it is possible to balance the resistance of the plant against high temperature stress, in part with the amount of available water in the soil (Burke, 1990). Climate factors include unpredictable properties such as the amount of precipitation or the number of days below zero, as well as predictable properties such as photoperiod. Soil properties vary very slowly over time according to climate characteristics.

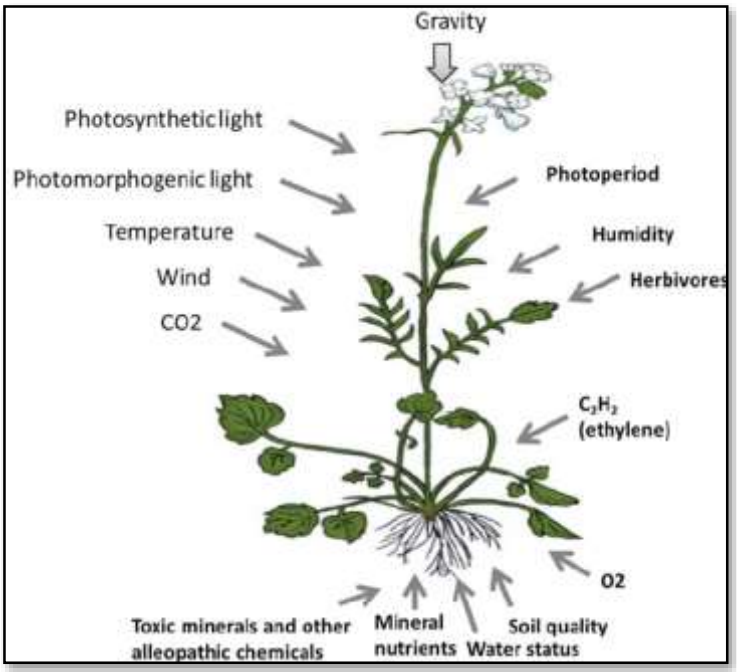

Figure 2: Abiotic stress factors

Drought stress, which is a natural stress factor, has the highest percentage with 26% part when the usable areas on the earth are classified in view of stress factors. It is followed by mineral stress with 20% part, cold and freezing stress with 15% part. The other stress get 29% part whereas only 10% area is not exposed any stress factors (Blum, 1986) (Figure 3). Therefore drought stress is one of the most widespread environmental stresses, which affects growing and productivity; it causes mechanical, metabolic and photosynthetic changes on plants.

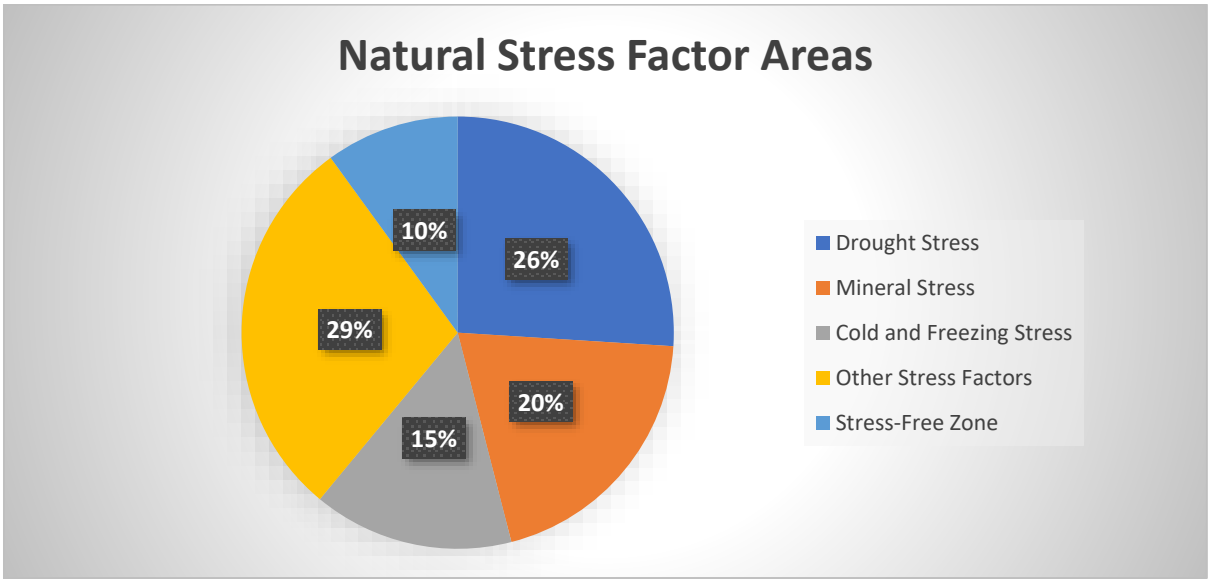

Figure 3: Natural stress factor areas.

DROUGHT STRESS

In the most general sense, drought can be defined as a meteorological phenomenon: a period without rain long enough to cause significant reduction in soil moisture content and plant growth. The period of time without rainfall actually needed to produce a drought depends mainly on the water holding capacity of the soil and rate of evapotranspiration by plants (Jones, 1992). There are significant differences in terms of physiological and metabolic changes between plant species and varieties, even their organs, in terms of their effect on drought stress (Belkhodja, 1994) (Figure 4). The degree of drought induced by different genotypes depends on the metabolic changes that the genotype develops under stress, that is, the physiological and biochemical reactions (Kayabaşı, 2011).

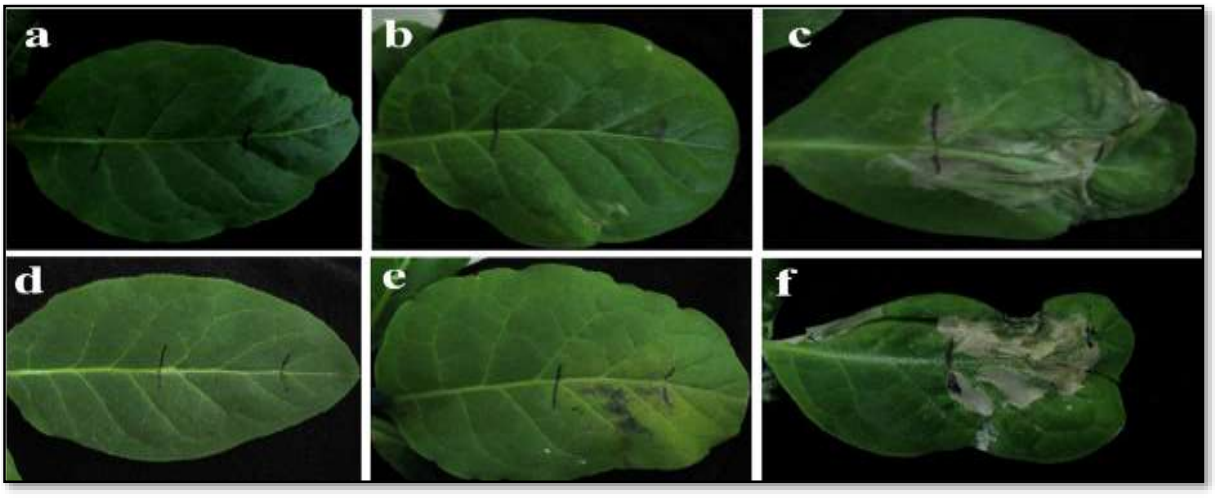

Figure 4: Grades affected by drought in different plants

Drought, which is the stress factor with the greatest effect on plant yield and quality, has recently caused yield losses in different plants and parts of Turkey. Loss of up to 30% in agricultural production has been determined that in regions with drought in 2007, 2008, 2012 and 2014. When the yield values of wheat, barley and oat were examined in the last 10 years period, there was a yield loss of 15% in wheat, 22% in barley and 12% in oat in 2014 (TUIK, 2017) (Figure 5).

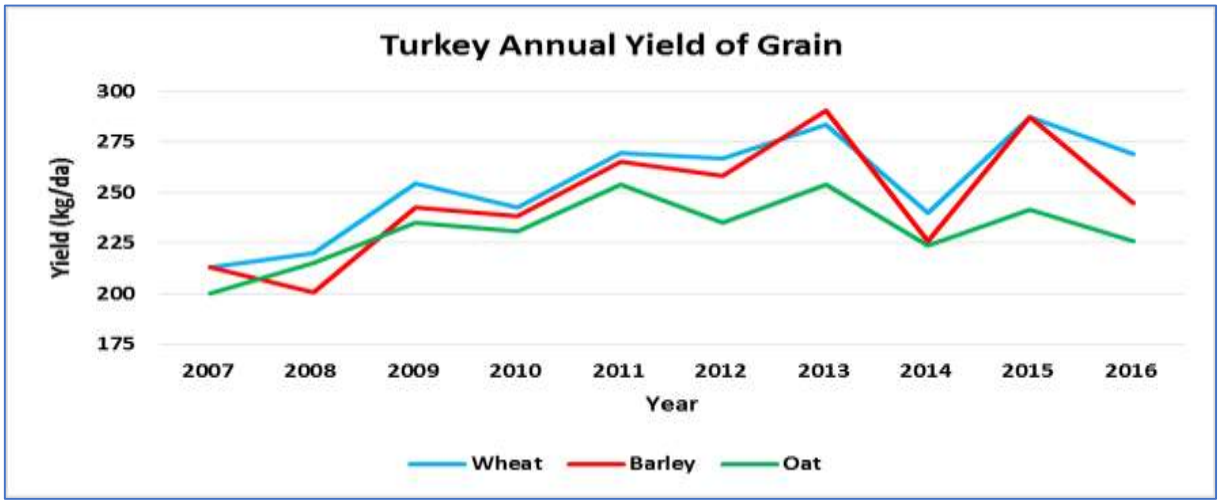

Figure 5: Turkey annual yield of grain.

Drought could be considered as water deficit and desiccation separately. Water deficit can be defined to be a moderate loss of water which leads to stomatal closure and limitation of gas exchange. In plants which are exposed to mild water deficits that relative water content (RWC) remains approximately 70%, carbon dioxide uptake is limited because of stomatal closure. Desiccation can be defined to be as an excessive loss of water which can potentially lead to entirely disruption of metabolism and cell structure and eventually to the cessation of enzyme-catalyzed reactions. As a general rule, most vegetative tissues of desiccation-sensitive vascular plants, cannot recover if dried to a RWC below 30% (Smirnoff, 1993).

THE EFFECTS OF DROUGHT STRESS ON PLANTS

MECHANICAL EFFECT

When water is lost in significant quantities from plant cells, the immediate stress experienced as turgor is lost by the plant, is mechanical (Levitt, 1980). The structure of the plasma membrane, Liquid-crystalline phase is consequence of the aqueous environment of the cell (Figure 6). As water leaves the cell, the structure of the membrane alters. Membranes pass into the Gel phase, which is a compact appearance. In this new construction, there is less mobility in the membrane than in the Liquid-crystalline phase. Due to water loss, the volume in the cell also decreases. Plasma membrane under tension may rupture (McKersie, 1994). This may result in the release of the hydrolytic enzymes located on the membranes and thus the autolysis of the cytoplasm (Salisbury, 1992). This harm usually permanently disrupts normal cellular metabolism.

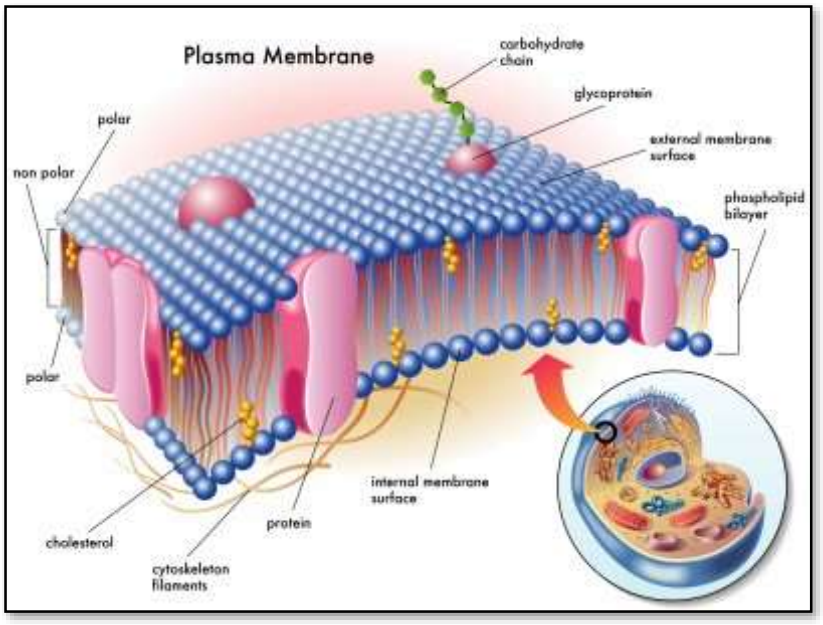

Figure 6: Structure of plasma membrane

METABOLIC EFFECT

When water is lost from cells, because of its functional characteristics of filling the most part of the cell volume, being a transport medium, playing the role as a solvent for the cellular reactions and processes, regulation in the cell and metabolism disrupts. Ion accumulation which is originating from the water loss of the cell, can damage the cell, disrupt membranes and cause protein denaturation. As a result of water loss; the interactions of amino acids in the structure of proteins with water disrupt (Campbell, 1991). Another damage to plant cells during drought stress is the degradation of nucleic acids such as DNA and RNA (Figure 7). According to Kessler, in foliage exposed to drought stress, enzymes shift from bound-state to free-state and cause destruction of nucleic acids (Kessler, 1961).

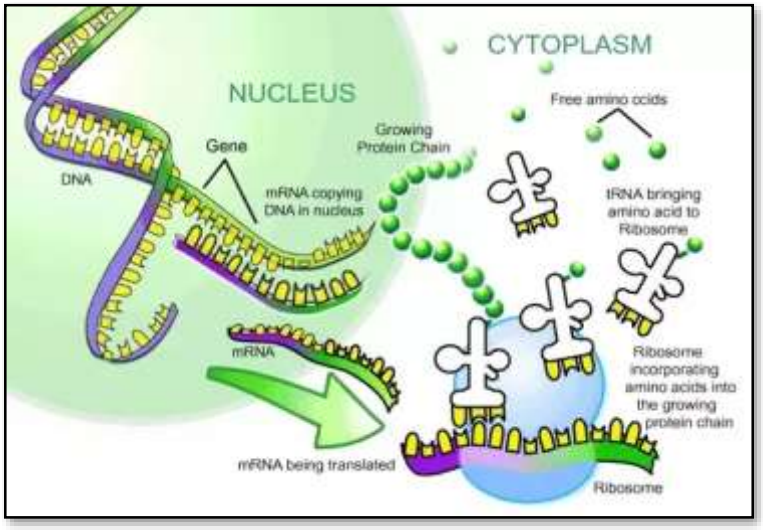

Figure 7: Structure of amino acids degraded by water loss

PHOTOSYNTHETIC EFFECT

During drought, photosynthesis decreases due mainly to two reasons; stomatal limitations that occur due to stomatal closure upon moderate water deficit conditions and other limitations that generally occurs upon longer and more severe water stresses (Figure 8). One of the earliest responses against drought is stomatal closure that limits CO2 diffusion towards chloroplasts (Lima, 2002). During drought two main reasons to cause plants to close their stomata are hydrolic signals (leaf water potential, cell turgor) and chemical signals (Abscisic acid; ABA). Abscisic acid (ABA), synthesized in the roots can also be transport via transpiration stream, induces stomatal closure under drought stress conditions (Teiz, 1998).

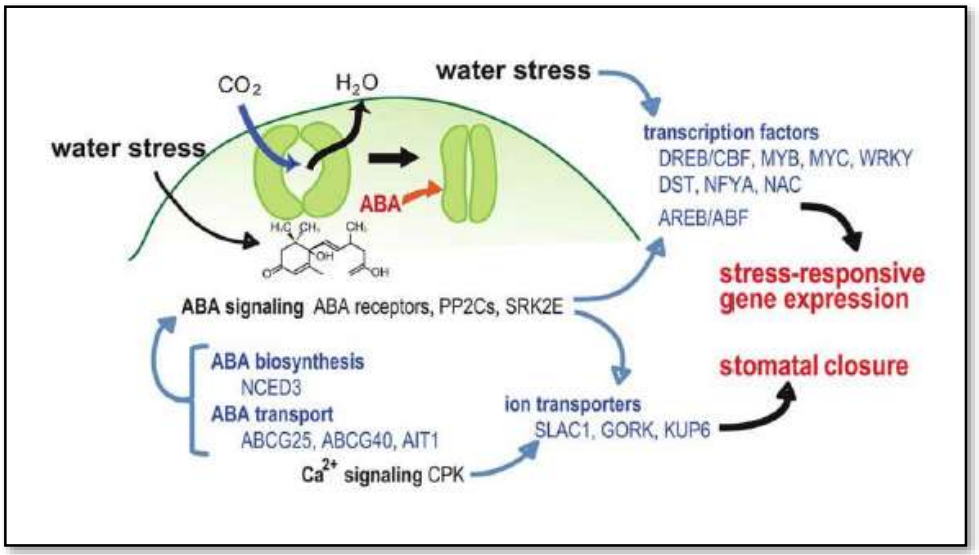

Figure 8: Closure of stomata by the effect of abscisic acid (ABA) in the plant exposed to the stress

It has been found that photosynthetic electron transport and photophosphorylation capacities decrease in chloroplasts of plants which are exposed to severe water deficit reduce (Smirnoff, 1993). Photosystems in chloroplasts, particularly PSII, are affected by drought stress (He, 1995). Other limitation of photosynthesis may be related to the oxidative damage to chloroplast lipids, pigments or proteins (Tambussi, 2000). Photosynthetic capacity in plants varies depending on the content of water within the cell.

CONCLUSIONS AND RECOMMENDATIONS

Drought, which is generally defined as the rainfall values below the average of underground and surface water values, is in the first place of the natural disasters in the world. Human activities like burning of fossil fuel, destroying forests, industrial activities cause increase of the “greenhouse gases” such as carbon dioxide, methane, ozone. As a result of the greenhouse effect created by these gases, there is also an increase in temperature on the surface of the earth. This phenomenon is called global warming resulted in changes in the climate and according to the research results in South Europe including Turkey will be under the influence of dry and hot climate in the middle of this century. Drought stress, which is mostly an oxidative damage at cellular level, mechanically, metabolically and photosensitically affects the plant and reduces yield and quality in arid and semi-arid regions.

Drought, which may cause reduction in feeding capacity of the natural resources and as a result of that millions of people may die due to starvation, is the major threat for all biologic life. For

this reason, research works on determination the plant species tolerant to drought, determining the tolerance mechanisms, conservation and transformation of the gene resources of the plants resistant to drought will play an important role in preventing the drought particularly caused by global warming, to become a major problem for all organisms in the future.

The mechanisms of plants that can survive in restricted water conditions and which show relatively low decreases in yields have become a field of interest. By examining these mechanisms, stress resistant genotypes have begun to be determined. It is important to change the production and irrigation methods depending on the physiological water requirements of the drought and the plants. The development of new varieties using biotechnological methods and drought tolerance and high water use efficiency characteristics can also provide important contributions to the provision of food for future years.

REFERENCES

Belkhodja, R. Morales, F., Abadia, A., & Gomez-Aparisi, J. 1994. Chlorophyll fluorescence as a possible tool for salinity tolerance screening in barley (Hordeum vulgare L.). Plant Physiology, 104: 667- 673.

Blum, A. 1986. Breeding Crop Varieties for Stress Environments. Critical Reviews in Plant Sciences, 199-237.

Burke, J. J. 1990. High temparature stress and adaptation in crops. In: R.G. ALSCHER and J. R. Cummings (Eds). Stress responses in plants: Adaptation and acclimation mechanisms, 295-309 s.

Campbell, M.K. 1991. Biochemistry, Harcourt Brace Jovanovich College Publishers, Fort Worth, USA.

He, J.X., Wang, J. and Liang H.G. 1995. Effects of water stress on photochemical function and protein metabolism of photosystem II in wheat leaves, Physiol. Plant., 93: 771-777.

Jones, H.G. 1992. Plants and Microclimate, Cambridge University Press, Cambridge.

Kayabaşı, S. 2011. Kuraklık stresinde yetiştirilen soyada (Glycine max L.) bazı fizyolojik parametreler ile prolin birikiminin araştırılması. Master Thesis, Harran University, Şanlıurfa.

Kessler, B. 1961. Nucleic acids as factors in drought resistance of higher plants. Recent Adv. Bot. 1153-1159.

Levitt, J. 1980. Responses of Plants to Environmental Stresses, Vol 1, Academic Press, New York.

Lichtenhaler, H.K. 1996. Vegetation stress: An introduction to the stress concept in plants. J Plant Physiol, 148: 4-14.

Lima, A.L.S., DaMatta, F.M., Pinheiro, H.A., Totola, M.R. and Loureiro, M.E. 2002. Photochemical responses and oxidative stress in two clones of Coffea canephora under water deficit conditions. Environ. Exp. Bot., 47: 239-247

McKersie, B.D. and Leshem, Y. 1994. Stress and Stress Coping in Cultivated Plants, Kluwer Academic Publishers, Netherlands.

Salisbury, F.B. and Ross, C.W. 1992. Plant Physiology, Wadsworth Publishing Co., California.

Smirnoff, N. 1993. The role of active oxygen in the response of plants to water deficit and desiccation. New Phytol, 125: 27-58.

Tambussi, E.A., Bartoli, C.G, Beltrano, J., Guiamet, J.J. and Araus, J.L. 2000. Oxidative damage to thylakoid proteins in water-stressed leaves of wheat (Triticum aestivum). Physiol. Plant., 108: 398-404.

Teiz, L. and Zeiger, S.C.E. 1998. Plant Physiology, University of California, Los Angeles Sinauer Associates, Inc., Publisher, 726-735.

Teuling, A.J., van Loon, A., Seneviratne, S.I., Lehner, I., Aubinet, M., Heinesch, B., Bernhofer, C., Grünwald, T., Prasse, H., & Spank, U. 2013. Evapotranspiration amplifies European summer drought. Geophysical Research Letters, 40 (10): 2071-2075.

TUIK. 2017. Statistics of Turkey annual yield of grain. Retrieved from www.tuik.gov.tr. Date: 15.07.2017.

THE SENSITIVITY OF WRF-ARW PARAMETERIZATIONS AND INITIALIZATIONS ON HEAVY PRECIPITATION PREDICTION: HOPA-ARTVIN CASE, AUGUST 2015

Onur Hakan Doğan[1], Barış Önol[1], Ufuk Utku Turunçoğlu[2], Abdullah Kahraman[3], Sezel Karayusufoğlu Uysal[4]

[1]Istanbul Technical University, Department of Meteorology doganonur@itu.edu.tr
[2] Istanbul Technical University, Department of Computational Science and Engineering
[3] Ondokuz Mayis University, Department of Meteorology
[4] Turkish State of Meteorological Service,Remote Sensing Office

Abstract

This study analysis the extreme summer precipitation sensitivity of the WRF-ARW model over the Eastern Black Sea region of Turkey. The simulations have been driven with three nested domains, the inner domain has 3 km resolution and covers all Black Sea. The simulations have been forced in the 3 days, 7 days, 14 days and 25 days time period for the August 23 and 24, 2015 heavy precipitation case, during which 255mm total precipitation was measured at the station in Hopa, Artvin. The simulation results have been produced by two different PBL schemes (YSU PBL and Mellor-Yamada-Janjic) and two different microphysics (Kessler and New-Thompson) which were then compared to the satellite data (Global Precipitation Measurement: GPM). Finally, root mean square error test, which was calculated by using satellite data and simulation results, has been analyzed.

Keywords: *Heavy precipitation, WRF, Sensitivity Analysis, the Black Sea Region*

INTRODUCTION

Together with the globally changing climate, extreme weather events have begun to be observed more frequently. Addressing the reasons and realizing their mechanisms are of great importance in terms of reducing damages with better predictions. As Dee et al. (2011) mentioned in their study, extreme convective precipitation events' occurrences have increased at the Mediterranean Sea and Black Sea because of increasing sea surface temperature. Increment at sea surface temperatures causes evaporation over the sea surfaces to increase as well, which results in much intense precipitation events. In this study, we analyzed the extreme precipitation case over the Eastern Black Sea region of Turkey by using WRF-ARW. Flood and landslides due to this extreme precipitation caused 11 people to lost their lives and many buildings to be damaged in Artvin province. According to ground observations, total precipitation measured at Hopa for two days (August 23 and 24, 2015) was 255 mm whereas with respect to satellite based data (Global Precipitation Measurement: GPM) (Jenner L. 2016), which used for validation, it was 150 mm for the same period. For the simulations, three nested domains, which have 27(d01)-9(d02)-3(d03) km resolutions, have been prepared. The inner domain includes all Black Sea and the surrounded sea coasts.

DATA AND METHODS

The simulations have been forced by ECMWF ERA-Interim data (Simmons *et al.*, 2006) with four different initializations, which were 3-days, 7-days, 15-days and 25-days before the case. WRF-ARW model physics parameters have been modified to develop simulation capability for extreme precipitation cases. Each simulation implemented separately according to microphysics ([Kessler, E., 1969] Kessler and New-Thompson [Thompson et all, 2008]) and PBL (YSU PBL[Hong, Song–You et al, 2006]) and Mellor-Yamada-Janjic[Janjic, Zavisa I. 1994]) options, and thus 16 sensitivity simulation produced by different parameterizations have been analyzed. Generally, all simulations underestimated the total precipitation amount for this

extreme precipitation case, which involved the interactions of large-scale air movement over warmer sea surface and complex terrain at the eastern Black Sea province. Simulation results and precipitation rates have been analyzed with respect to GPM and surface based observations.

APPLICATION AND RESULTS

The simulations have been forced by different initial timing and model physics. Analysis of the simulations proved that modifying initialization and model physics directly affects the precipitation pattern and rates for the selected case. According to the results of sensitivity simulations, all 3-days and 25-days simulations predict daily total precipitation amount better than other simulations. However, 7-days simulations failed to capture the extreme precipitation case. The 25-days simulation with New Thompson microphysics and Mellor-Yamada-Janjic PBL predicted 221 mm precipitation, which was the highest daily total precipitation among all the simulations. Additionally, simulations with Kessler microphysics and YSU PBL were more reliable in terms of spatial distribution of precipitation compared to the simulations produced by other microphysics in all simulation periods. 3-days Kessler Microphysics and YSU PBL precipitation amount was148 mm for corresponding station location (Fig.1).

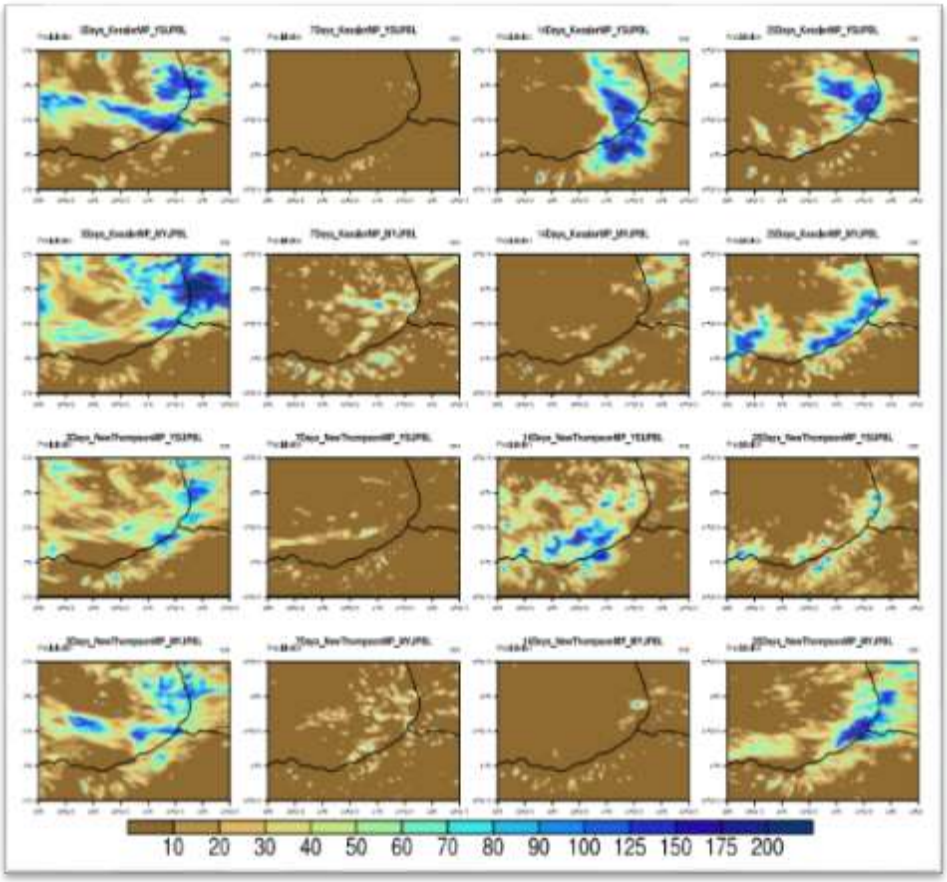

Figure1. Daily total precipitation results of the simulations that originated by discrete model physics (Microphysics: Kessler and New-Thompson and PBL: YSU and Mellor-Yamada-Janjic) and time periods (3, 7, 14 and 25 days)

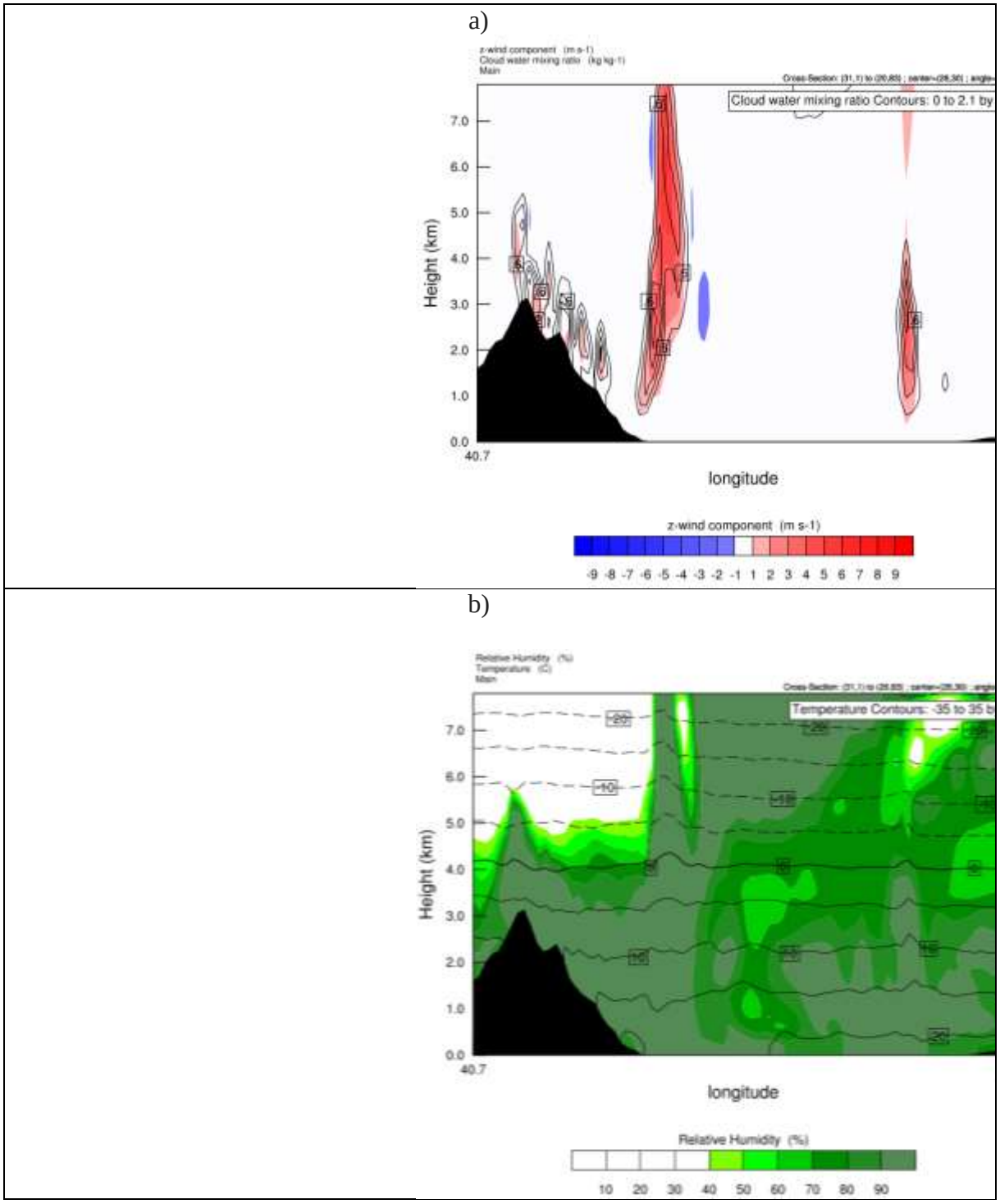

Figure2. Vertical wind component and cloud mixing ratio(a) and relative humidity and temperature(b) at 24.08.2015 06Z

We have also analyzed the vertical cross section of simulated atmospheric variables, such as the temperature, cloud mixing ratio, relative humidity and vertical wind. For 24.08.2015 06Z, the formation of cloud caused by strong updraft and vigorous vertical development over the coastal zone and steep mountains. In addition, relative humidity conditions were also favorable

for extreme precipitation case (Fig.2a and 2b). Finally, root mean square error test, which was calculated by using satellite data and simulation results, was applied. Results showed that the 3-days simulation with New Thompson microphysics and Mellor-Yamada-Janjic PBL provided the better approach than other simulations, root mean square error of this simulation is 15.41. On the other hand, the 25-days simulation with New Thompson microphysics and Mellor-Yamada-Janjic PBL had highest error, with respect to root mean square error test, which was 20.79.

CONCLUSIONS AND RECOMMENDATIONS

As a result, in this extreme precipitation sensitivity analysis, Kessler microphysics and YSU PBL with 3-days simulations predicted better-simulated precipitation compared to other simulations based on the location of meteorological station. In terms of spatial distribution of precipitation according to satellite data (GPM), 25-days simulation had better spatial coverage especially 25-days simulation with New Thompson microphysics and Mellor-Yamada-Janjic PBL according to root mean square error test. Finally, the WRF-ARW model needs to be tested with other extreme precipitation cases to expand the confidence on numerical weather prediction studies over the Black Sea region, which is dominated by complex topography, air-sea interactions and effect of the sea surface temperature increases.

REFERENCES

Dee DP, Uppala SM, Simmons AJ, Berrisford P, Poli P, Kobayashi S, Andrae U, Balmaseda MA, Balsamo G, Bauer P, Bechtold P, Beljaars ACM, van de Berg L, Bidlot J, Bormann N, Delsol C, Dragani R, Fuentes M, Geer AJ, Haimberger L, Healy SB, Hersbach H, Holm EV, Isaksen L, K ´ allberg P, K ˚ ohler M, ¨ Matricardi M, McNally AP, Monge-Sanz BM, Morcrette J-J, Park B-K, Peubey C, de Rosnay P, Tavolato C, Thepaut J-N, Vitart F. 2011. The ERA-Interim reanal ´ ysis: configuration and performance of the data assimilation system. Q. J. R. Meteorol. Soc. 137: 553–597. DOI:10.1002/qj.828

Hong, Song–You, Yign Noh, Jimy Dudhia, 2006: A new vertical diffusion package with an explicit treatment of entrainment processes. *Mon. Wea. Rev.*, **134**, 2318–2341.

Janjic, Zavisa I. 1994: The Step-Mountain Eta Coordinate Model: Further developments of the convection, viscous sublayer, and turbulence closure schemes. Mon. Wea. Rev., 122, 927-945

Jenner, L.(2016, February 13). Global Precipitation Measurement Missin. Retrieved from https://www.nasa.gov/mission_pages/GPM/overview/index.html

Kessler, E., 1969: On the distribution and continuity of water substance in atmoshperic circulations. *Meteor. Monogr.*, **32**, Amer. Meteor. Soc.

Simmons A, Uppala S, Dee D, Kobayashi S. 2006. ERA-Interim: New ECMWF reanalysis products from 1989 onwards. *ECMWF Newsletter* **110**: 26–35.

Thompson, Gregory, Paul R. Field, Roy M. Rasmussen, William D. Hall, 2008: Explicit Forecasts of Winter Precipitation Using an Improved Bulk Microphysics Scheme. Part II: Implementation of a New Snow Parameterization. *Mon. Wea. Rev.*, **136**, 5095–5115.

MONTHLY STREAMFLOW ESTIMATION MODEL: A STUDY OF PORSUK RIVER BASIN, TURKEY

Bülent SELEK[1], Bihrat ÖNÖZ[2], Mustafa Utku YILMAZ[3], Göksel Ezgi DİKER[4], Hakan AKSU[5], Bilal BEKTAŞOĞLU[6], Ahmed Faruk ÖZTÜRK[7], Osman KARAAHMETOĞLU[8], Semra SEZER[9]

[1]General Directorate of State Hydraulic Works (DSI), General Manager Assistant, Ankara, Turkey
bulent.selek@dsi.gov.tr
[2]Istanbul Technical University, Faculty of Civil Engineering, Istanbul, Turkey
onoz@itu.edu.tr
[3]Kirklareli University, Faculty of Engineering, Department of Civil Engineering, Kirklareli, Turkey
utkuyilmaz@klu.edu.tr
[4]Istanbul Technical University, Graduate School Of Science Engineering and Technology, Istanbul, Turkey
g.ezgiguzey@gmail.com
[5]General Directorate of State Hydraulic Works (DSI), Investigation, Planning and Allocation Department, Ankara, Turkey
hakana@dsi.gov.tr
[6]General Directorate of State Hydraulic Works (DSI), Operation and Maintenance Department, Ankara, Turkey
bilalb@dsi.gov.tr
[7]General Directorate of State Hydraulic Works (DSI), Investigation, Planning and Allocation Department, Ankara, Turkey
afozturk@dsi.gov.tr
[8]General Directorate of State Hydraulic Works (DSI), Technology Department, Ankara, Turkey
okaraahmetoglu@dsi.gov.tr
[7]General Directorate of State Hydraulic Works (DSI), Investigation, Planning and Allocation Department, Ankara, Turkey
semras@dsi.gov.tr

Abstract

Streamflow estimations in basins, which have no or limited recorded streamflow measurements is one of the biggest challenges faced by hydrologists. Uncertainties due to the variability of hydrological data and lack of adequate data for hydro-meteorological analyses cause hydrological research to be difficult and results to be untrustworthy. Thus, it is of utmost importance to make reliable flow estimations, especially in the planning and projecting of efficient systems designs of water resources. In this study, it was intended to evaluate the estimation strengths of the performance-weighted approach blended with three streamflow transfer methods by developing an application software to estimate monthly streamflows in Porsuk River Basin which was selected as a case study. During the study, three streamflow transfer methods are used. These include the most common method of standardization of the streamflows according to the drainage area (DAR), standardization of the streamflows with the mean flow (SM), standardization by mean and standard deviation (SMS). And also, during the study, stepwise regional regression method was used to estimate the streamflow statistics for SM and SMS methods. To develop an applicable method for the less developed areas, only easily available hydroclimatic variables were used. With this purpose, it was developed regional hydrological regression models that use the parameters such as precipitation, temperature, drought index, evapotranspiration and drainage area. In addition, the blended performance weighted approach which is the weighted average of the methods (DAR and SM or SMS) was also evaluated. Such blended approach provides weighting of the two techniques that maximizes the advantages of each method while minimizing their disadvantages. Standardizing monthly flows by drainage are is one of the most commonly used hydrostatistical techniques for transfering streamflow information from one site to another. The DAR method was compared with two classes of statistical regionalization techniques including

standardization by mean and standardization by mean and standart deviation. The statistics of prediction performance, namely the Nash-Sutcliffe efficiency (NSE) was performed for performance evaluation of estimation methods. According NSE values, performance of both SM and SMS was generally superior to DAR approach. As a result, it can be seen that SM, SMS and the blended methods can be applied successfully instead of the drainage area ratio (DAR) method, which is sometimes considered to be a very rough estimation approach. The study should be done in different basins where there are more stations. This study is important in terms of effective planning of water resources and sustainable use of water. Especially for developing countries such as Turkey, streamflow estimation models should be developed in ungauged basins in order to obtain more reliable estimates.

Keywords: *Drainage-area ratio, Monthly streamflow estimation, Porsuk River basin, Regional hydrology, Stepwise regression, Ungauged basins.*

EVALUATION OF STREAMFLOW ESTIMATION IN UNGAUGED BASINS USING INVERSE DISTANCE WEIGHTED (IDW)

Mustafa Utku YILMAZ[1], Bihrat ÖNÖZ[2]
[1]*Department of Civil Engineering, Kirklareli University, Kirklareli, Turkey*
utkuyilmaz@klu.edu.tr
[2]*Department of Civil Engineering, Istanbul Technical University, Istanbul, Turkey*
onoz@itu.edu.tr

Abstract

Nowadays, streamflow estimation in ungauged basins is one of the biggest challenges that the scientists who study hydrology and the practitioners who produce projects about the same subject face with. Especially for the practitioners, reliable streamflow estimation is very important during the planning and project designing of water resources. Streamflow time series should be known for the studies like project designing of dams, protection of fish and natural life, basin management and environment impact assessment. Streamflow is one of the most important parameters for the determination of the hydroelectrical energy potential. Streamflow is determined by streamflow gauging stations which are constructed in the particular points of the river by State Hydraulics Works in Turkey (DSİ in Turkish acronym). However, many streams and arms do not have streamflow gauging stations station and data can not be obtained in cases such as a failure in existing stations. Due to the limited number and insufficient current monitoring stations in Turkey, the donor station (source station) is usually chosen as the nearest station for the streamflow estimation in ungauged stations. In other words, the euclidean distance is the main selection criterion for donor streamflow station selection. Choosing the nearest streamflow station as the donor streamflow station is preferred in widespread practice, but acceptance of the distance as the primary donor streamflow station selection criterion may not always be correct. Although the distance is currently used as the selection criterion in Turkey for selecting a donor station, it may be possible to obtain better results by using the most correlated station as the donor station for estimation of ungauged basins. In order to determine the criteria for selection of the donor station, a sample application study was carried out by selecting 5 streamflow gauging stations on the Middle Euphrates basin. How the correlation between streamflow time series of stations change with the Euclidian distances between the streamgaging stations was investigated. For this purpose, Pearson correlation coefficients were calculated by using the area-normalized streamflow ($m^3/s/ km^2$) of the 5 selected stations. The drainage area ratio method (DAR) was used to estimate the monthly streamflow of each of the 5 stations to compare the estimation performances of the nearest and most relevant streamflow stations as the donor station. Each target station was estimated with its closest and most correlated donor stations. Nash-Sutcliffe Efficiency (NSE) values were calculated to test the appropriateness of donor streamflow station selection criteria for the study area. In order to test the success of the Inverse Distance Weighting (IDW) method for estimation of monthly streamflows, 5 stations selected in the Middle Euphrates basin were used. Euclidean distances between stations were used for weight calculation. Each station was initially considered ungauged in turn and monthly streamflow time series were estimated for all stations. In the conventional DAR method, streamflow values are transferred from a single donor station with the closest geographical proximity to ungauged (target) station. However, the IDW method is used for direct streamflow transfer to ungauged station from multiple donor stations In the application of the IDW method, all the stations in the basin were used as donor stations first in estimating any target station. Subsequently, donor stations were selected which gave the best NSE for each target station. Estimation performance of the IDW method is not as good as the DAR method when all other stations are used as donors in the estimation of a target station.

However, the performance of the IDW method is more successful than the DAR method when the most suitable donor stations are selected for target station.

Keywords: *Monthly streamflow estimation, Drainage area ratio method, Inverse distance weighting method, Donor station selection, Ungauged.*

Figure 1. Geographical locations of the gauging stations

Table 1. General information on the gauging stations.

Basin	Station Number	Observation year	Mean streamflow (m^3/s)	Drainage Area (km^2)	Basin Elevation (m)
Middle Euphrates	2102	1970-2000	239,34	25515,6	859
	2122		46,56	5882,4	1552
	2157		24,49	2098,4	1250
	2158		18,88	1577,6	1310
	2164		32,81	2232,0	998

Table 2. Correlation matrix (Pearson)

Station Number	2102	2122	2157	2158	2164
2102	1	0,948	0,929	0,962	**0,972**
2122	0,948	1	0,807	**0,967**	0,889
2157	0,929	0,807	1	0,823	**0,935**
2158	0,962	**0,967**	0,823	1	0,913
2164	**0,972**	0,889	0,935	0,913	1

Table 3. The nearest and the most correlated stations

Station Number	The nearest station	Euclidian distance	The most correlated station	Correlation coefficent
2102	2164	55	2164	0,972
2122	2158	120	2158	0,967
2157	2158	36	2164	0,935
2158	2157	36	2122	0,967
2164	2102	55	2102	0,972

Table 4. NSE values that are calculated from the nearest station and the most correlated station

Target station	The nearest station used as the donor station	The most correlated station used as the donor station
2102	0,126	0,126
2122	0,443	0,443
2157	0,652	**0,728**
2158	0,636	**0,770**
2164	0,719	0,719

Table 5. NSE values for DAR and IDW

Target station	Donor station	DAR	IDW
2102	2122	**0,878**	0,425
	2157	0,620	
	2158	0,728	
	2164	0,126	
2122	2102	**0,838**	0,363
	2157	-0,088	
	2158	0,443	
	2164	-0,916	
2157	2102	**0,802**	0,727
	2122	0,570	
	2158	0,652	
	2164	0,728	
2158	2102	**0,852**	0,727
	2122	0,770	
	2157	0,636	
	2164	0,655	
2164	2102	0,719	0,795
	2122	0,534	
	2157	**0,833**	
	2158	0,797	

Table 6. The best NSE values calculated according to the IDW method

Target station	Donor station	IDW
2102	2122	0,893
	2157	
	2158	
2122	2102	0,564
	2158	
2157	2102	0,837
	2164	
2158	2102	0,894
	2122	
	2164	
2164	2157	0,869
	2158	

USING SATELLITE-BASED INDICES FOR MONITORING DROUGHT EFFECTS ON THE BUYUK MENDERES RIVER BASIN

Semra Kocaaslan Karamzadeh[1], Nebiye Musaoğlu[2], Murat Türkeş[3], Ayşegül Tanık[4]

[1]Istanbul Technical University, Department of Applied Informatics, Geographical Information Technologies Program, 34469, Istanbul, Turkey, kocaaslan@itu.edu.tr

[2]Istanbul Technical University, Department of Geomatics Engineering, 34469, İstanbul, Turkey, musaoglune@itu.edu.tr

[3]Boğaziçi University, Center for Climate Change and Policy Studies, 34342, Istanbul, Turkey, murat.turkes@boun.edu.tr

[4]Istanbul Technical University, Department of Environmental Engineering, 34469, İstanbul, Turkey, tanika@itu.edu.tr

Abstract

In this study, the effectiveness of satellite-based drought indices as an indicator for monitoring drought impacts is investigated. The Büyük Menderes River Basin was selected as the pilot research area. For this purpose, Normalized Difference Vegetation Index (NDVI) data are utilized as the primary spectral indicator for monitoring vegetation health and Land Surface Temperature (LST) data, which are important since the surface temperature is sensitive to the drought events, were derived from the thermal channels of satellites and compiled from 2007 till 2016 during the growing seasons (May-June-July). By the aid of these data sets, satellite-based drought indices such as the Drought Severity Index (DEV_{NDVI}), the Vegetation Anomaly Index (VAI) and the Vegetation Condition Index (VCI), the Temperature Condition Index (TCI) and the Vegetation Health Index (VHI) have been applied and analyzed for the research area. According to the results achieved, these indices can be provided for near real-time drought monitoring at appropriate spatial and temporal resolution.

Keywords: *drought, satellite-based indices, VAI, VCI, VHI*

INTRODUCTION

Climate change has been playing a major role in human life by causing extreme weather and climate events together with disasters and other environmental reactions such as floods, heat waves, forest fires, drought etc. in the 21st century. Drought is separated from other climatic problems because of its complexity. It has a slow onset, and not easy to monitor its frequency, severity and spatial coverage. In addition, since drought commonly covers large areas, it is difficult to monitor using traditional systems. As remote sensing methods provide pixel-based monitoring of large areas near-real time in an accurate and economical way, they were widely used to examine drought impacts in the recent years.

Numerous indices were applied by many researchers from various disciplines in order to monitor drought impacts. Among them, satellite sensor data have been playing an increasingly significant role. Various satellite-based drought indices have been proposed; many of them based on vegetation indices (Ji and Peters, 2003; Martínez-Fernández et al., 2016). The most commonly used satellite-based vegetation index is the Normalized Difference Vegetation Index (NDVI; Rouse, 1974; Tucker, 1979) that was first applied to drought monitoring by Tucker and Choudhury (1987). Subsequently, this study triggered various NDVI-derived indices such as, the Vegetation Condition Index (VCI) based NDVI normalization suggested by Kogan (1990), deviation of NDVI called the Drought Severity Index (DEV_{NDVI}; Thenkabail et al., 2004) and anomaly of NDVI called the Vegetation Anomaly Index (VAI; Amri et al., 2011; Zribi et al., 2016). Besides NDVI-based drought indices, Land Surface Temperature (LST) parameters

derived from thermal bands were also utilized to develop drought indices as the Temperature Condition Index (TCI; Kogan, 1995). Furthermore, using the negative correlation between the NDVI and the LST (Karnieli et al., 2010) several combinations of these variables as drought indices have been applied across the globe. The most significant one is the Vegetation Health Index (VHI) that rely on the advantage of combining optical and thermal information proposed by Kogan (1997, 2001).

The main objective of this study is to investigate the effectiveness of satellite-derived drought indices mentioned above as an indicator for monitoring drought impacts. Since being part of the large Mediterranean Basin, especially western and southern part of Turkey has been frequently affected by drought conditions. For this purpose, the Büyük Menderes River Basin was chosen as the pilot research area.

DATA AND METHODOLOGY

STUDY AREA

The Büyük Menderes River Basin, located in the south-western part of Turkey between the latitude of 37°10'- 38° 49' north and longitude of 27° 11' - 30° 53' east, is characterised with a real dry and warm/hot summer subtropical Mediterranean climate (Türkeş, 2016), was selected as the study area. It is the largest river of the Aegean Region (with 592 km); it rises in the Anatolian plateau and flows westwards through a narrow valley and canyon. It then expands into a broad, flat-bottomed valley and from here this slow-moving river winds across the Aegean plains and empties into the sea. The geographical location and the topography of the basin are shown in Figure 1.

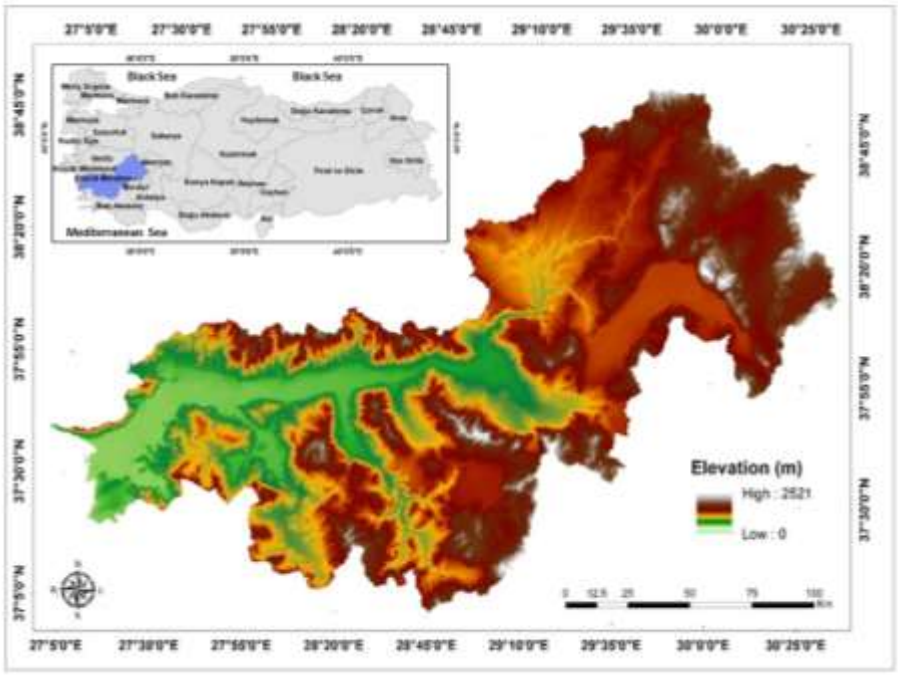

Figure 1. The location and topography of the Büyük Menderes River Basin. (SRTM-90 m spatial resolution Digital Elevation Model-DEM)

SATELLITE DATA

In this study, 250 m spatial resolution 16-day composite of NDVI (MOD13Q1, collection 5) and 1 km spatial resolution 8-day composite of Land Surface Temperature (LST) (MOD11A2, collection 5) retrieved from NASA's Moderate Resolution Imaging Spectroradiometer

(MODIS) Terra (EOS AM) products in the period of 2007-2016 May to July over the Büyük Menderes River Basin was utilized. All data sets were freely acquired from United States Geological Survey (USGS) Center for Earth Resources Observation and Science (EROS) via webmrt tool and reprojected from the Sinusoidal to World Geodetic System (WGS84).

METHODOLOGY

The methodology is based on satellite-based drought indices as presented below:

The Normalized Difference Vegetation Index (NDVI; Rouse, 1974; Tucker, 1979) is an index related to vegetation health and density. It is defined as:

$$NDVI = R_{NIR}-R_{RED}/R_{NIR}+R_{RED} \quad (1)$$

where R_{NIR} and R_{RED} are the reflectances in the near infrared and red bands portion of the electromagnetic spectrum, respectively. It varies in a range of (-1 to + 1) according to ranking from unhealthy to healthy vegetation conditions.

The Drought Severity Index (DEV_{NDVI}) is a deviation of NDVI from its long-term mean illustrated as the severity of a drought. It is defined accordingly:

$$DEV_{NDVI} = NDVI_i - NDVI_{mean,m} \quad (2)$$

where $NDVI_i$ is the NDVI value for each pixel in the period (month, week, 16-day etc.) and $NDVI_{mean,m}$ is the long-term mean NDVI for the same period m for the same pixel. If DEV_{NDVI} is negative, it indicates the below-normal vegetation condition/health (Thenkabail et al., 2004).

The Vegetation Anomaly Index (VAI) is based on statistics derived from the NDVI time series (Amri et al., 2011; Zribi et al., 2016). It is defined as:

$$VAI_i = NDVI_i - NDVI_{mean,m} / \sigma_i \quad (3)$$

where $NDVI_{mean,m}$ is the long-term mean NDVI for the same period m for the same pixel and σ_i corresponds to the standard deviation of the NDVI values estimated for period i, over the same period.

The Vegetation Condition Index (VCI) is a kind of normalization of NDVI developed by Kogan (1990). It is defined as:

$$VCI = 100*(NDVI_i-NDVI_{min})/(NDVI_{max}- NDVI_{min}) \quad (4)$$

where $NDVI_i$ is actual, $NDVI_{min}$, $NDVI_{max}$ are the multi-year minimum and maximum NDVI values for each pixel, respectively. The VCI values vary between (0 and 100). It was designed for improving the analysis of vegetation conditions with weather impact especially in non-homogeneous areas while removing the ecosystem signal from the NDVI (Kogan, 1990; Kogan, 2001).

The Temperature Condition Index (TCI) land surface temperature (LST) derived thermal infrared bands. It is related to the altered response of vegetation to temperature and defined as:

$$TCI = 100*(LST_{max} –LST_i)/(LST_{max}- LST_{min}) \quad (5)$$

where LST_i is actual, LST_{min} and LST_{max} are the multi-year minimum and maximum LST values for each pixel, respectively, calculated from multiyear time series data. While high temperature shows unfavorable or drought conditions, low temperature commonly presents favorable conditions (Kogan, 1995).

The Vegetation Health Index (VHI) was also proposed by Kogan (1997). It is based on the combination of VCI and TCI and defined as:

$$VHI = \alpha*VCI + (1- \alpha)* TCI \quad (6)$$

where α and (1- α) is related to the weight of VCI and TCI from 0 to 1. If contributions of indices are unknown, it is commonly used as 0.5. VHI values similarly vary between (0 and 100). If VCI, TCI, and VHI values are higher than 70, that means the conditions are favorable and the vegetation is healthy. On the contrary, if VHI values below 40, vegetation is stressed (Kogan, 1997; Kogan, 2001).

RESULTS AND DISCUSSION

The Drought Severity Index (DEV_{NDVI}), the Vegetation Anomaly Index (VAI) and the Vegetation Condition Index (VCI) have been computed using 250m spatial resolution 16-day composite temporal resolution NDVI data. In addition, the 8-day composite LST derived from the thermal channel of MODIS Terra satellite data was averaged into 16-day composite in order to be compatible with the NDVI data. Similarly, 250m spatial resolution NDVI data was resampled to 1 km spatial resolution by using nearest neighbor resampling method that uses the values of the closest pixel to assign to the output pixel value (Lillesand et. al, 2015). Thus, 1 km spatial resolution, 16-day composite Temperature Condition Index (TCI) and the Vegetation Health Index (VHI) based on the combination of TCI and VCI, have been acquired.

Detailed evaluation of spatial and temporal dynamic drought changes during growing seasons (May-June-July) have been carried out through the mentioned drought indices and corresponding maps were generated in Geographic Information Systems (GIS). As a result of the assessment, the initial 16-day period of May (09 – 24) was selected and presented as this period was less exposed to summer drought effects than the other terms.

VCI maps with 250 m spatial resolution in the stated period of (2007-2016) were demonstrated as an example in Figure 2. VCI values below 40 indicate that vegetation stress (with dark red color in Fig.2). As reflected in the results, 2007, 2010 and 2014 have been the years where this impact was observed more than the others. However, 2009 VCI values illustrate the least significant vegetation stress conditions.

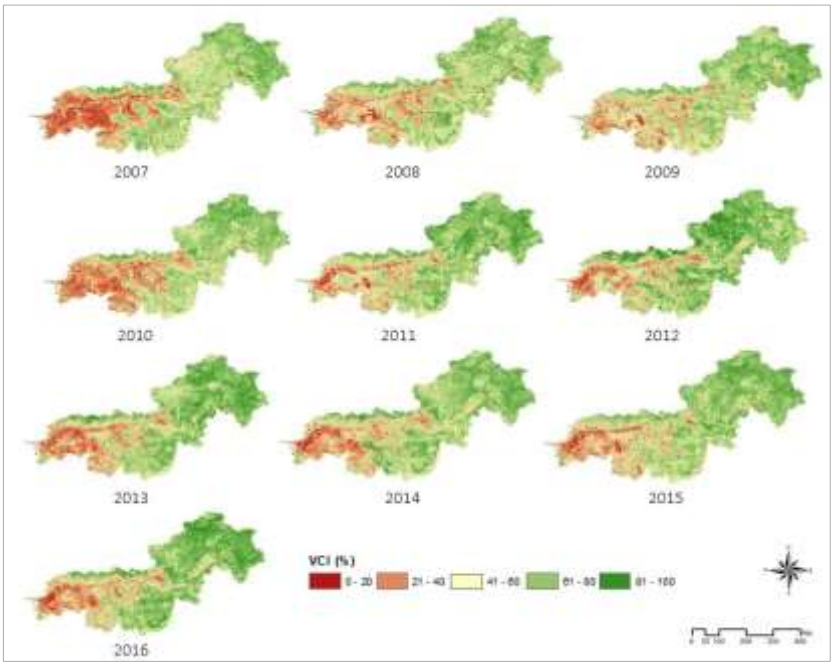

Figure 2. Spatio-temporal changes of the Vegetation Condition Index(VCI) during the last ten years (2007 to 2016).

As mentioned previously, DEV_{NDVI} and VAI indices were also applied to the selected data. All VCI results have been proven by these indices as well. 2007 as a drought year and 2009 as a non-drought year have been chosen for reflecting this consistency as shown in Figure 3 (a) and (b), respectively. Finally, the results of VHI for the stated period of May are given in Figure 3 (c). According to the figures, all results are in compliance with each other.

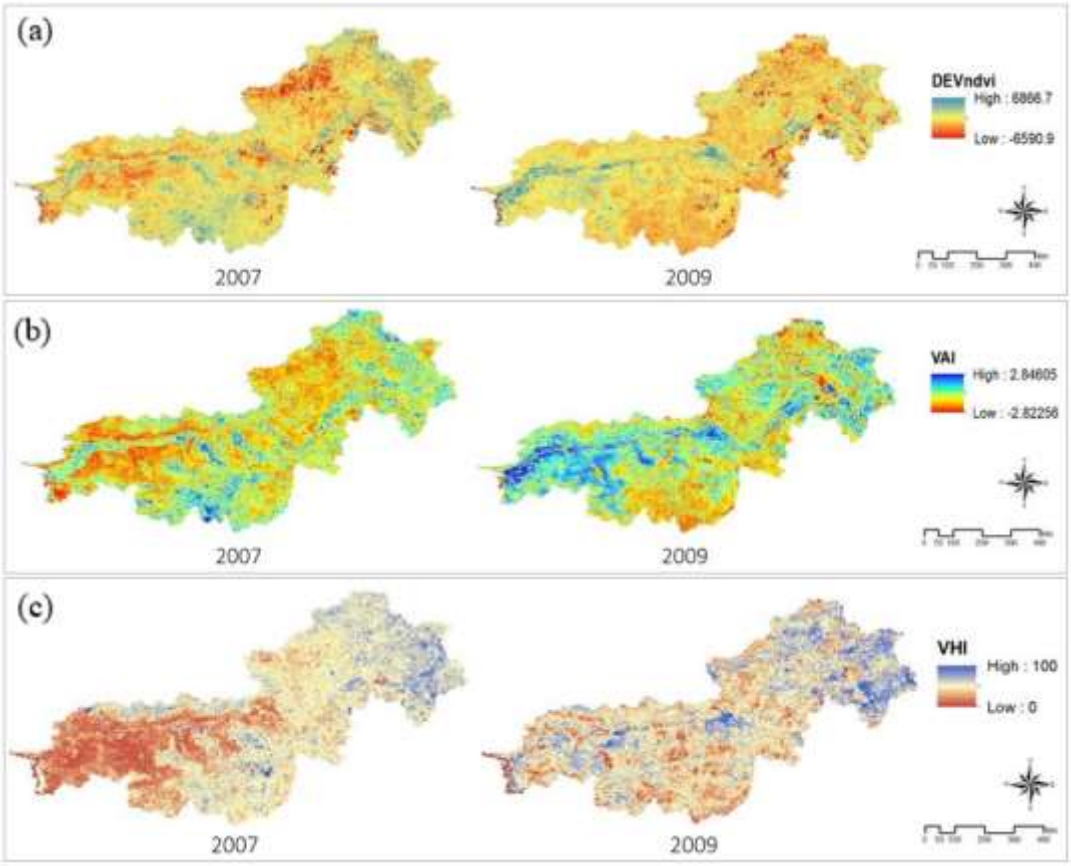

Figure 3. The comparison of satellite-based drought indices a) the Drought Severity Index (DEV_{NDVI}) b) the Vegetation Anomaly Index(VAI) c) the Vegetation Health Index(VHI).

CONCLUSIONS AND RECOMMENDATIONS

This paper attempts to indicate that satellite-based drought indices such as DEV_{NDVI}, VAI, VCI, TCI and VHI can be regarded as sensitive indicators of drought conditions. For this purpose, LST and NDVI of MODIS-Terra satellite data were utilized for retrieving these indices and monitoring drought impacts over the Büyük Menderes River Basin between 2007 and 2016 (May, June and July). It can be concluded that these indices are valuable tools and capable of providing near-real-time indicators of spatio-temporal drought assessment.

In further research, together with additional meteorological data, one may follow an improved evaluation of the impact of a drought. In addition, a combination of these data sets with land cover information such as CORINE may handle a more comprehensive assessment of the possible impact of drought events.

REFERENCES

Amri, R., Zribi, M., Chabaane, Z.L., Duchemin, B., Gruhier, C., and Chehbouni, A., 2011. Analysis of vegetation behavior in a North African semi-arid region using SPOT-Vegetation NDVI data, *Remote Sensing*, 3(12), 2568-2590.

Ji, L. and Peters, A., 2003. Assessing vegetation response to drought in the northern Great Plains using vegetation and drought indices. *Remote Sensing of Environment*, 87,85-98.
Karnieli, A., Agam, N., Pinker, R. T., Anderson, M., Imhoff, M. L., Gutman, G. G., and Goldberg, A., 2010. Use of NDVI and land surface temperature for drought assessment: merits and limitations. *Journal of Climate*, 23(3), 618-633.
Kogan, F.N., 1990. Remote sensing of weather impacts on vegetation in non-homogeneous areas. *International Journal of Remote Sensing*, 11, 1405–1419.
Kogan, F. N., 1995. Application of vegetation index and brightness temperature for drought detection. *Advances in Space Research*, 15,91–100.
Kogan, F.N., 1997. Global drought watch from space. *Bulletin of the American Meteorological Society*, 78, 621–636.
Kogan, F. N., 2001. Operational space technology for global vegetation assessment. *Bulletin of the American Meteorological Society*, 82(9), 1949–1964.
Lillesand, T., Kiefer, R. W., Chipman, J. 2015. Remote Sensing and Image Interpretation, 7th Edition, Wiley, USA
Rouse, J. W., Haas, R. H., Schell, J. A., and Deering, D. W., 1974. Monitoring Vegetation Systems in the Great Plains with ERTS in Proceedings of the Third Earth Resources Technology Satellite-1 Symposium, 1, 48–62.
Martínez-Fernández, J., González-Zamora, A., Sánchez, N., Gumuzzio, A., & Herrero-Jiménez, C. M. 2016. Satellite soil moisture for agricultural drought monitoring: Assessment of the SMOS derived Soil Water Deficit Index. *Remote Sensing of Environment*, 177, 277-286.
Thenkabail, P.S., Gamage, M.S.D.N., and Smakhtin, V.U., 2004. The use of remote sensing data for drought assessment and monitoring in Southwest Asia, International Water Management Institute (IWMI), 85, 25p.
Tucker, C. J., 1979. Red and photographic infrared linear combinations for monitoring vegetation, *Remote Sensing of Environment*, 8, 127–150.
Tucker, C. J., and Choudhury, B. J., 1987. Satellite remote sensing of drought conditions. *Remote Sensing of Environment*, 23(2), 243–251.
Türkeş, M. 2016. General Climatology: Fundamentals of Atmosphere, Weather and Climate. First Edition, Kriter Publisher Physical Geography Series No: 4, ISBN: 978-605-9336-28-4, xxii + 522 pp. Kriter Publisher, Berdan Matbaası: İstanbul. (in Turkish)
Zribi, M., Dridi, G., Amri, R. and Lili-Chabaane, Z., 2016. Analysis of the Effects of Drought on Vegetation Cover in a Mediterranean Region through the Use of SPOT-VGT and TERRA-MODIS Long Time Series. *Remote Sensing*, 8(12), 992,1-16.

COUPLING OF MESO SCALE MODEL RESULTS WITH MICRO SCALE MODELS, SENSITIVITY ANALYSIS STUDY FOR EDIRNE PROVINCE AT DIFFERENT ELEVATION DATA RESOLUTIONS

Gizem BUĞDAY[1], Erkan YILMAZ[1], Esra ERTEN[2], S. Sibel MENTEŞ[1], Yasemin EZBER[3]

[1]Istanbul Technical University,Department of Meteorological Engineering, Maslak Istanbul,TURKEY
bugday@itu.edu.tr, yilmazerkan1@itu.edu.tr, smentes@itu.edu.tr
[2]Istanbul Technical University, Department of Geomatic Engineering, Maslak Istanbul, TURKEY
eerten@itu.edu.tr
[3]Istanbul Technical University, Eurasia Institute of Earth Sciences, Maslak 34469 Istanbul, TURKEY
ezber@itu.edu.tr

Abstract

In this study, the meso scale model results of the NEWA project are coupled with the micro model, the model results of the land elevation maps with different resolutions and the changes on the topography were investigated. WAsP and WindSim Micro scale model application was made for the Edirne region which was chosen as the plot region. In these applications, sensitivity analysis using high resolution 12m field height data as well as the most commonly used land use and altitude data were carried out and the effect of change in land resolution on micro scale model results is examined. For this reason, the CORINE data, which is the land use model, is kept constant on both maps, and maps using with TanDEM-X (12m) and SRTM (90m) resolution altitude data are prepared by project team. The WAsP and WindSim micro-scale models were used to analyze the potential wind energy potential of the region in the best possible way. Statistical analysis was performed to compare the analyzed WAsP and WindSim results with the observed value. In the WAsP program, two different results were obtained for the SRTM and TanDEM-X topographic maps with different resolutions by moving the WRF hourly data to the observation point. CFD based WindSim program is also used. So that both the 2 different models and the 2 different land model results were moved to the observing point at the 80 m meteorological measurement spot in the field and the results were examined. While SRTM-WAsP model demonstrates the best approach to real value, WindSim-TanDEM-X model outputs have the worst results.

***Keywords**: NEWA, TanDEM-X, SRTM, WAsP, WindSim, Geomatic*

INTRODUCTION

Terrain features affect air movements and mechanical turbulence in the lower atmosphere. Landforms such as mountains, hills and valleys play incredibly important roles in controlling wind speed and wind direction. Studies are being undertaken to improve the prediction performance of digital models using high-resolution data on topographical features. But there is a lack of research on topographical heights and analyzes of urban land with complex land use data and vertical structure of the atmosphere. In order to improve the prediction performance of a numerical model, it is important to understand the effect of resolution by using topographic height and land use data at the same time in different resolutions.

In previous literature, Lombard A and Talayero [1] compared the performance of two models, WAsP and WindSim in predicting the power production of individual turbines. Zhang et al. [2] has conducted research into whether digital modeling (DEM) data of finer-scale models is more accurate than rough-scale digital models and that the improved expression of topography is not sufficient to improve weather-case simulation of high-resolution models. Joon-Bum Jee and

Sangil Kim [3] conduct research about sensitivity study on high-resolution numerical modeling of static topographic data. This study focused on the influence of multi-scale surface databases of topographical height and land use on the modeling of atmospheric circulation in a megacity. Lupaşcu A and Irıza A. [4] carry out project about the performance of the Weather Research and Forecast (WRF) model simulation was evaluated using different topographic data sets for the Southern Carpathians, Romania, and surrounding area, characterized by complex terrain.

In order to analyze the wind energy potential of the region in the best possible way, the sensitivity analysis with different resolution topographic maps for the Edirne province under the NEWA project was carried out using the WAsP and WindSim programs and the monthly wind data for the Edirne station data, which is taken as an example, was examined. A statistical analysis was conducted to compare how consistent WAsP and WindSim results are with observed values. In the WAsP program, two different results were obtained for the SRTM and TanDEM-X topographic maps at different resolutions by WRF hourly data interpolate to the observation point. In addition, using the SRTM (90m) terrain data and the high-resolution TanDEM-X (12 m) data in the WindSim micro-scale program, the WRF hourly wind data was moved to the observation point at the 80 m meteorological measurement pole within the site and two different results were obtained from this program. Model performance is evaluated by using four data points from these two models
The aim of this study is to compare the numerical forecasted data with that observed in the field in order to validate the model ability to reproduce the observed parameters using two topographical data bases by using two models WAsP and/or WindSim for calculation of wind resource maps.

DATA AND METHODS

In this study, land use model CORINE data was kept constant in both maps and maps were prepared by project team using TanDEM-X (12m) and SRTM (90m) altitude data. The Corine Land Cover is referring to a European program establishing a computerized inventory on land cover of the 27 European Unions and other European countries, at an original scale of 1: 100 000, using 44 classes of the 3-level Corine terminology (https://www.eea.europa.eu/). SRTM is being implemented by NASA in order to create a topographical map of the land. It has height values corresponding to approximately 150 million grid points spaced 90 x 90 m. It is a digital elevation model (DEM) supported by heights that are digitized using 1: 25000 scale topographical maps and produced by interpolation technique. Secondly, the primary mission of TanDEM-X is the generation of a world-wide, consistent, current, and high-precision DEM, with a spatial resolution of 0.4 arc seconds (12 m at the equator). It has vertical accuracy of 2 m (relative) and 10 m (absolute) and 12 m x 12 m raster(https://tandemx-science.dlr.de/).In this paper, to find the resolution effects of the terrain data of topographic height and land use on the model forecasting results over the Edirne domain, the topographic and land use data depending on the resolution of the data were categorized, into two groups which are TanDEM-X and SRTM. SRTM had a resolution of 90 m, the Tandem data had a resolution of 12 m. For the control of real observation value, SRTM based on the DEM (Digital Elevation Model) data developed by the United States Geological Survey (USGS) were used, and the default data set was generally used for many community models, such as the WRF model. For calculation of wind resource maps in relatively small areas we use the models WAsP and/or WindSim. In this context, SRTM (Shuttle Radar Topography Mission) and TadDEM-X (TerraSAR-X add-on for Digital Elevation Measurement) that are performed in WAsP and WindSim microscale programs provide four construction of sensitivity analyses for different land resolutions.
WAsP is a computation efficient model, making it possible to calculate the wind resources in a relatively large area in relatively short time. WAsP is using for predicting wind climates, wind

resources and power productions from wind turbines and wind farms. The predictions are based on wind data measured at stations in the same region. The program includes a complex terrain flow model, a roughness change model and a model for sheltering obstacles. SRTM data can be used to establish height contour maps for the WAsP flow model, though some editing may still be required. (http://www.WAsP.dk/). The WASP software assumes that wind speed data are distributed according to the two-parameter Weibull function when performing data analysis (Deaves et al., 1997). The Weibull probability density function is one of the most used statistical distributions for determining the wind energy potential. For the simulations, Vestas brand wind turbines were selected at 2MW power with a height of 90m. Coordinates of Observation and Model Points were determined with the help of Global Mapper.

WindSim uses CFD technology to optimize the placement of wind turbines. WindSim is based on a 3D Reynolds Averaged Navier Stokes (RANS) solver. Solving the non-linear transport equations for mass, momentum and energy makes WindSim a suitable tool for simulations in both complex terrain, and in situations with complex local climatology. Using SRTM and TanDEM-X topographic maps in WindSim, two different outputs is provided.

APPLICATION AND RESULTS

When a CFD model like WindSim are compared with the WAsP, the effects on the average flow of turbulence in the CFD model are directly calculated. The CFD model is particularly useful in a complex area where a complicated turbulence structure is encountered.In this study, two different results obtained from the SRTM and TANDEM topographic maps at different resolutions run in WindSim program. WindSim outputs run in the WAsP program to compare with same parameters and WindSim model outputs move to the observation point by using WAsP programming. When these model results were compared to the measured parameters which is in observation data, model success rate is calculated. The finding shows us 4 different models outputs. The data has been analyzed using WAsP, to get a statistical summary. The WAsP program gives the wind rose and the wind speed distributions for each sector and in total. it is divided into 12 sectors; each one represents 30degree. The mean wind speed is calculated from the Observed Mean Wind Climate as well as, k and a parameters of Weibull distribution and the power density for the location. We take wind blowing frequency and wind speed using with WAsP reports to compare measurement success in each sector among models. Wind frequency is an important parameter in wind distribution modelling. It is the distribution in function of wind direction especially in a complex terrain. Important changes in velocity could be due to eventual speed-ups created by orography. According to results, the best model approaching in four model outputs for observation outputs is SRTM-WAsP. When we look at frequency error and wind speed accuracy, underestimate values are smaller than other models. Wind speed seen much closer to observation values. The worst model outputs were found TanDEM-WindSim which has more underestimate values. Frequency error and wind speed misprediction seen much more than other models. On the other hand, we look art relative error at mean speed, best approach seen Tandem-WAsP with 0.037147 and SRTM-WAsP with 0.038633 and the worst approach to observation value is calculated to be 0.062407 in WindSim-Tandem-X.

Table 1. Model Frequency and Wind Speed Value

Sector		1	2	3	4	5	6	7	8	9	10	11	12
Angle		0	30	60	90	120	150	180	210	240	270	300	330
Observation	U1	5.67	6.35	6.16	7.26	7.09	5.72	5.21	9.11	8.90	3.20	3.40	4.70
	F1	9.70	17.00	14.90	13.60	8.80	3.60	2.50	11.40	9.20	1.80	2.30	5.30
mean speed	6.73												
SRTM-Windsim	U2	6.11	6.20	7.54	7.24	7.07	6.99	7.08	10.37	7.50	3.60	4.49	5.11
	F2	16.90	17.60	15.40	8.90	6.20	3.10	2.80	11.90	5.40	1.70	2.30	7.80
	(U2-U1)	0.44	-0.15	1.38	-0.02	-0.02	1.27	1.87	1.26	-1.40	0.40	1.09	0.41
	|(U2-U1)|	0.44	0.15	1.38	0.02	0.02	1.27	1.87	1.26	1.40	0.40	1.09	0.41
	(F2-F1)	7.20	0.60	0.50	-4.70	-2.60	-0.50	0.30	0.50	-3.80	-0.10	0.00	2.50
relative error		0.077601	0.023622	0.224026	0.002755	0.002821	0.222028	0.358925	0.13831	0.157303	0.125	0.320588	0.087234
mean speed	7.05		Relative error		0.047548								
TANDEM-Windsim	U3	6.26	6.32	7.62	7.24	7.08	6.99	7.33	10.50	7.53	3.59	4.52	5.20
	F3	17.30	17.60	15.30	8.70	6.10	3.20	2.80	12.10	5.20	1.70	2.20	7.80
	(U3-U1)	0.59	-0.03	1.46	-0.02	-0.01	1.27	2.12	1.39	-1.37	0.39	1.12	0.50
	|(U3-U1)|	0.59	0.03	1.46	0.02	0.01	1.27	2.12	1.39	1.37	0.39	1.12	0.50
	F3-F1	7.60	0.60	0.40	-4.90	-2.70	-0.40	0.30	0.70	-4.00	-0.10	-0.10	2.50
relative error		0.10	0.00	0.24	0.00	0.00	0.22	0.41	0.15	0.15	0.12	0.33	0.11
mean speed	7.15		Relative error		0.062407								
SRTM-Wasp	U4	6.06	6.19	7.55	7.44	7.37	7.16	7.62	10.15	7.66	4.02	4.69	5.25
	F4	15.80	16.94	15.69	9.53	6.46	3.29	3.11	10.82	5.34	1.92	2.95	8.15
	(U4-U1)	0.39	-0.16	1.39	0.18	0.28	1.44	2.41	1.04	-1.24	0.82	1.29	0.55
	|(U4-U1)|	0.39	0.16	1.39	0.18	0.28	1.44	2.41	1.04	1.24	0.82	1.29	0.55
	F4-F1	6.10	-0.06	0.79	-4.07	-2.34	-0.31	0.61	-0.58	-3.86	0.12	0.65	2.85
relative error		0.068783	0.025197	0.225649	0.024793	0.039492	0.251748	0.462572	0.11416	0.139326	0.25625	0.379412	0.117021
mean speed	6.99		Relative error		0.038633								
TANDEM-Wasp	U5	6.32	6.88	7.27	6.63	6.34	7.03	6.77	10.29	7.80	3.61	4.32	4.91
	F5	16.21	19.20	15.68	8.54	5.48	3.32	3.17	11.78	5.09	1.69	2.68	7.16
	(U5-U1)	0.65	0.53	1.11	-0.63	-0.75	1.31	1.56	1.18	-1.10	0.41	0.92	0.21
	|(U5-U1)|	0.65	0.53	1.11	0.63	0.75	1.31	1.56	1.18	1.10	0.41	0.92	0.21
	F5-F1	6.51	2.20	0.78	-5.06	-3.32	-0.28	0.67	0.38	-4.11	-0.11	0.38	1.86
relative error		0.114638	0.083465	0.180195	0.086777	0.105783	0.229021	0.299424	0.129528	0.123596	0.128125	0.270588	0.044681
mean speed	6.98		Relative error		0.037147								

CONCLUSIONS AND RECOMMENDATIONS

The micro-scale models WAsP and WindSim have been compared and evaluated for a complex terrain site in Edirne Province. This research was done to see which model is giving the best results. According to the real value approach of the models, SRTM-WAsP shows the best approach and Windsim-Tandem has the worst model values. Observation mean speed equal 6.73, WASP gave better results than WindSim, SRTM-WAsP wind speed with 6.99 and Tandem-WAsP wind speed with 6.98. If we look at WindSim results, SRTM-windsim wind speed equals 7.05 and Tandem-windsim wind speed with 7.15 has the worst approach. According to these mean wind speeds, relative error in these models are the same direction. In terms of expansion of research, another digital elevation model can be used except Tandem and SRTM in new research, or research can be extended using different roughness data.

ACKNOWLEDGEMENT

This research is funded by TUBITAK with the project ID 215M386. We would like to thank to ITU National Center for High Performance Computing (UHEM) for granting us (grant no. 5003652015) calculation time in their systems. This research is a part of NEWA New European Wind Atlas Project which is composed by 30 funding agencies from European. This work was supported by the Scientific and Technological Research Council of Turkey under 215M386, by the German Aerospace Center under Project XTILAND1476.

REFERENCES

De Meij A, Vinuesa J. F., 2014, Impact of SRTM and Corine Land Cover data on meteorological parameters using WRF, Atmospheric Research 143 (2014) 351–370

Elsner, P. ve Bonnici, M. (2007). Vertical accuracy of Shuttle Radar Topography Mission (SRTM) elevation and void-filled data in the Libyan Desert. International Journal of Ecology & Development, 8(F07):66–80.
Heni Kh. S., Khamees A.B., Raja O. H., 2015, Wind Power Density Estimation In The Middle of Iraq "Karbala Site", International Journal of Application or Innovation in Engineering & Management (IJAIEM), Volume 4.
Joon-Bum Jee and Sangil Kim, 2016, Sensitivity Study on High-Resolution Numerical Modeling of Static Topographic Data, Atmosphere 2016, 7, 86
Llombart A., Talayero A., Mallet A. and Telmo E ,2006, Performance analysis of wind resource assessment programs in complex terrain, RE&PQJ, Vol. 1, No.4
Lupaşcu A., Irıza A., Dumitrache C., 2013, Using a High resolution Topographic Data Set and Analysis of the İmpact on the Forecast of Meteorological Parameters, Romanian Reports in Physics, Vol. 67
Mortensen, N. G. (2016). Wind resource assessment using the WAsP software (DTU Wind Energy E-0135). Technical University of Denmark. (DTU Wind Energy E; No. 0135).

ATMOSPHERIC STABILITY ANALYSIS AND COMPARISON OF WIND PROFILES RELATED TO RADIONSODE MEASUREMENTS AND WRF MODEL OUTPUT

Tarık Kaytancı[1], Şükran Sibel Menteş[1], Yasemin Ezber[2], Erkan Yılmaz[1], Yurdanur Ünal[1], Sema Topçu[1], Selahattin İncecik[1]

[1]Istanbul Technical University, Department of Meteorological Engineering, Maslak 34469, Istanbul, Turkey
kaytanci@itu.edu.tr; smentes@itu.edu.tr; sunal@itu.edu.tr; stopcu@itu.edu.tr; incecik@itu.edu.tr
[2]Istanbul Technical University, Eurasia Institue of Earth Sciences, Maslak 34469, İstanbul, Turkey
ezber@itu.edu.tr

Abstract

In this study, the statistical analysis of atmospheric stability for 15 specific measurement locations over Turkey and for entire Turkey including all seas were studied using the output data of Weather Research and Forecasting (WRF) model. Besides that vertical wind profiles based on standard pressure levels were obtained from measurement data of seven different radiosonde measurement points, and model performance of WRF was tested. Overall performance of WRF model in terms of vertical wind profile was observed sufficiently. In seasonal analysis of atmospheric stability, stable condition was observed to have the highest percentage occurence in the seasons of autumn and winter and as unstable condition was observed to have the highest percentage occurence in spring and summer. In annual analysis of atmospheric stability, stable condition was observed to have the highest percentage occurence in land as unstable condition was observed to have the highest percentage occurence in seas. Neutral condition has lowest percentage occurrence in both seasonal and annual analysis with respect to stable and unstable condition.

Keywords: *Atmospheric stability, , Model performance, Percentage occurrence, Wind profile, WRF*

INTRODUCTION

Atmospheric stability has a important role in wind energy assessments because wind profiles have a significant effect on power production and loads on turbine. This study aims to test the performance of WRF model for stability conditions with respect to vertical wind profile obtained from radiosonde measurements in the standard pressure. This study also aims to show seasonal and annual percentage occurrence of every stability condition for 15 specific measurement locations (Aydın, Aksaray, Amasya, Afyon, Balıkesir, Çanakkale, Edirne, Hatay, Karaman, Kayseri, Kırklareli, Mersin, Mut, Ordu, Yozgat) over Turkey and entire Turkey including all seas, respectively. In this study, atmospheric stability was estimated by Obukhov length, a length scale, and classified by Obukhov length intervals.

There are some related studies carried out. In the study of Sakagami et al (2015), hourly and monthly percentage occurrence of seven stability conditions based on Obukhov length intervals was showed by estimating atmospheric stability with data obtained from lidar wind profiler in Pedra do Sal Wind Farm located in the northeast coast of Brazil. In the study of Sathe (2010), the statistics of atmospheric stability in terms of percentage occurrence of seven stability conditions, and also validation of theoretical non-dimenosinal wind profiles were studied using the standard surface-layer theory at Egmond aan Zee in the North Sea. Gryning et al (2011) studied the comparison of wind profile obtained from WRF with long-term lidar measurements at a coastal flat site at Hovsore, Denmark. Comparison is applied up to 600 m. They found that WRF model predicts very well, but its prediction capacity is poor in response to change in atmospheric stability.

In this study, overall performance of WRF model in terms of vertical wind profiles was observed sufficiently. In seasonal atmospheric stability analysis for 15 locations over Turkey, stable condition occurs in autumn and winter with the highest percentage as unstable condition occurs in spring and summer with highest percentage. Neutral condition has lowest percentage occurrence with respect to stable and unstable condition. In annual atmospheric stability analysis over entire Turkey including all seas, stable condition was observed in land mostly as unstable condition was observed in seas mostly.

DATA

WRF model was run using three nested domains which have resolutions 27 km, 9 km and 3 km covering Europe and Turkey, extended Turkey and only Turkey, respectively (Figure 1). In this study, model output data of the finest domain was used. Although there are runs for two different PBL schemes, that are YSU (Yonsei University Scheme) and MYNN (Mellor-Yamada-Nakanishi-Nino), MYNN pbl scheme was evaluated only. For all domains, Corine data with a horizontal resolution of 250 km is used for land use / cover as USGS data with a horizontal resolution of up to 1km is used for elevation data. Model run for year of 2015 as daily and weekly. However, daily results were used in this study. In daily model runs, initial data is obtained from ERA-Interim data at 00 UTC, and model is run for next 36 hours. First 12 hours was considered as a spinup period, and not included in the evaluation.

Figure 1 : WRF model domain areas

Radiosonde data was used to obtain vertical wind profile with respect to standard pressure levels, and to test the model performance with respect to measurement. Data of seven measurement stations of radiosonde was used, and the data was obtained from University of Wyoming.

In the section of stability analysis in terms of seasonal and annual percentage occurrence of each stability condition for 15 specific measurement points over Turkey and for entire Turkey including all seas, respectively. However, the measurement data related to these measurement points was not used in this study, because there is no multiple level temperature or related data to estimate stability conditions at those points. Model data was, therefore, used to estimate percentage occurrence of each atmospheric stability condition in these specific measurement points.

METHOD

In this study, atmospheric stability was classified according to Obukhov length (L). Obukhov length is given as,

$$L = -\frac{u_{*0}^3 T}{\kappa g \overline{\omega' \theta_v'}}$$

where is u_{*0}^3 the local friction velocity, $\kappa = 0.4$ is von Karman constant, T is the absolute temperature, θ_v is the virtual potential tempeature, $\overline{\omega'\theta_v'}$ is the virtual kinematic heat flux. Seven atmospheric stability conditions were classified in many studies. These are very stable, stable, near-neutral stable, neutral, near-neutral unstable, unstable and very unstable atmospheric stability conditions (Table 1). However, in this study, very stable, near-neutral stable, near-neutral unstable and very unstable conditions were considered as stable and unstable conditions, respectively (Table 2). Therefore, this study assumed and used just three atmospheric stability conditions, that are stable, neutral and unstable, according to Obukhov length intervals in classification of seven stabilities.

Table 1: Atmospheric stability classification according to Obukhov length intervals

Very Stable	$0 < L \leq 50$ m
Stable	$50 \leq L \leq 200$ m
Near-neutral Stable	$200 \leq L \leq 500$ m
Neutral	$\lvert L \rvert \geq 500$ m
Near-neutral Unstable	$-500 \leq L \leq -200$ m
Unstable	$-200 \leq L \leq -100$ m
Very Unstable	$100 \leq L < 0$ m

Table 2 : Atmospheric stability classification used in this study according to Table 1

Stable	$0 < L \leq 500$ m
Neutral	$\lvert L \rvert \geq 500$ m
Unstable	$-500 \leq L < 0$ m

For performance analysis, Root Mean Squrare Error (RMSE) was calculated and drawn as vertical profile in standard pressure levels. In the wind profile plot, all values, that are appointed based on stability condition in every standard pressure level were averaged to get a mean value for every pressure level.

RESULTS

Wind profiles obtained from WRF model generally agree very well with wind profiles obtained from rasdiosonde measurement (Figure 2). However, wind profile related to model at 00 GMT for stable and neutral atmospheric conditions agree better with measurement than wind profile related to at 12 GMT. For 12 GMT model exhibited poor performance with respect to RMSE profile especially in lower levels for stable and neutral atmospheric conditions (Figure 3). An interesting point that wind profiles related to model and radiosonde at 12 GMT and 00 GMT for unstable atmospheric condition were observed to be quite similar. As a result, overall performance of WRF model was observed sufficiently (Figure 3).

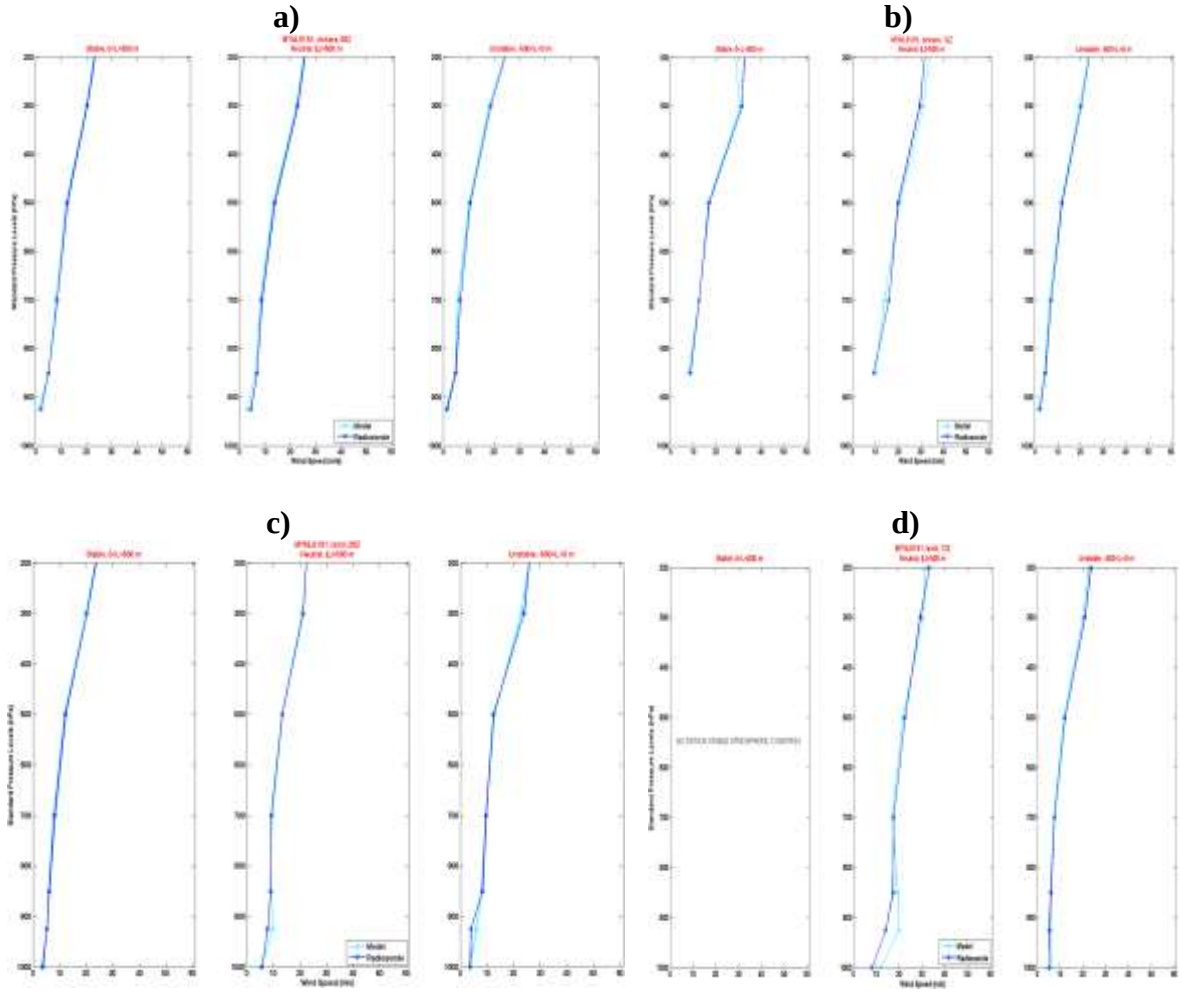

Figure 2 : Wind profiles obtained from WRF model and radiosonde measurements for a) Ankara for 00 GMT, b) Ankara for 12 GMT, c) İzmir for 00 GMT, d) İzmir for 12 GMT, e) Samsun for 00 GMT, f) Samsun for 12 GMT: radiosonde (blue), model (cyan), stable (left), neutral (middle), unstable (right)

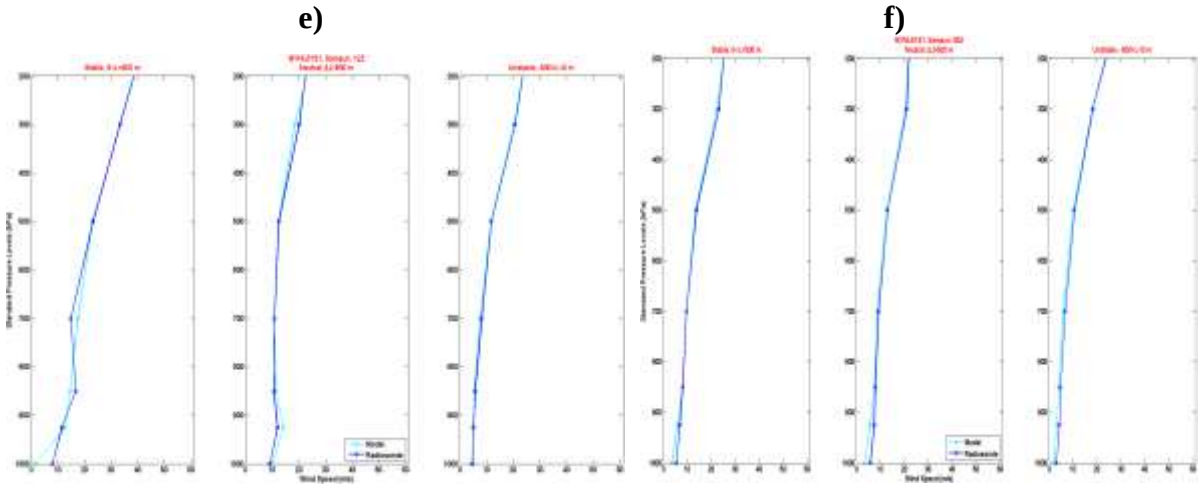

Figure 2 (Continue): Wind profiles obtained from WRF model and radiosonde measurements for a) Ankara for 00 GMT, b) Ankara for 12 GMT, c) İzmir for 00 GMT, d) İzmir for 12 GMT, e) Samsun for 00 GMT, f) Samsun for 12 GMT: radiosonde (blue), model (cyan), stable (left), neutral (middle), unstable (right)

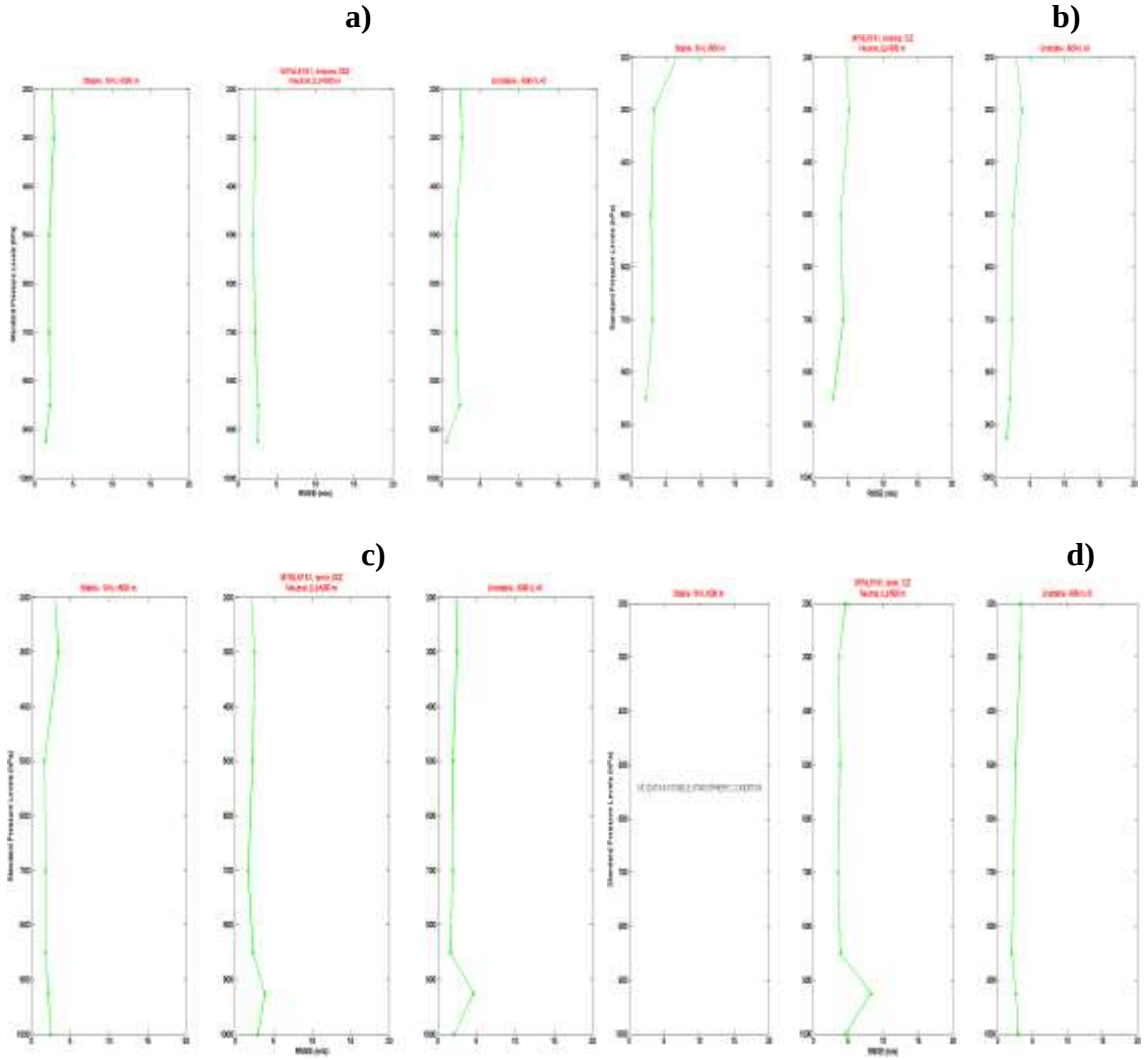

Figure 3 : RMSE plots for a) Ankara for 00 GMT, b) Ankara for 12 GMT, c) İzmir for 00 GMT, d) İzmir for 12 GMT, e) Samsun for 00 GMT, f) Samsun for 12 GMT: stable (left), neutral (middle), unstable (right)

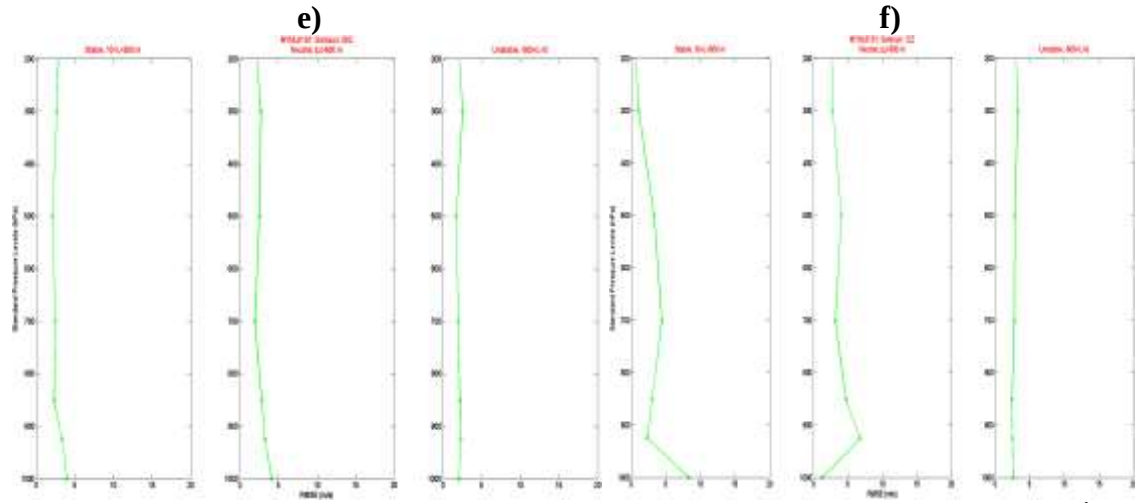

Figure 3 (Continue): RMSE plots for a) Ankara for 00 GMT, b) Ankara for 12 GMT, c) İzmir for 00 GMT, d) İzmir for 12 GMT, e) Samsun for 00 GMT, f) Samsun for 12 GMT: stable (left), neutral (middle), unstable (right)

In seasonal atmospheric stability analysis for 15 locations over Turkey, the highest percentage occurrence of stable atmospheric condition was generally observed in autumn and winter season, respectively (Figure 4). On the other hand the highest percentage occurrence of unstable atmospheric condition was observed in summer and spring, respectively (Figure 4). An interesting point that both Balıkesir and Çanakkale exhibited the highest percentage occurrence for stable atmospheric condition in spring and winter, respectively. According to figure 3, neutral condition was generally observed to have the lowest percentage occurrence with respect to stable and unstable condition, but in some locations the value of percentage occurrence was observed to reach up to 40 %. Winter and autumn are, respectively, seasons related to highest percentage occurrence for neutral condition.

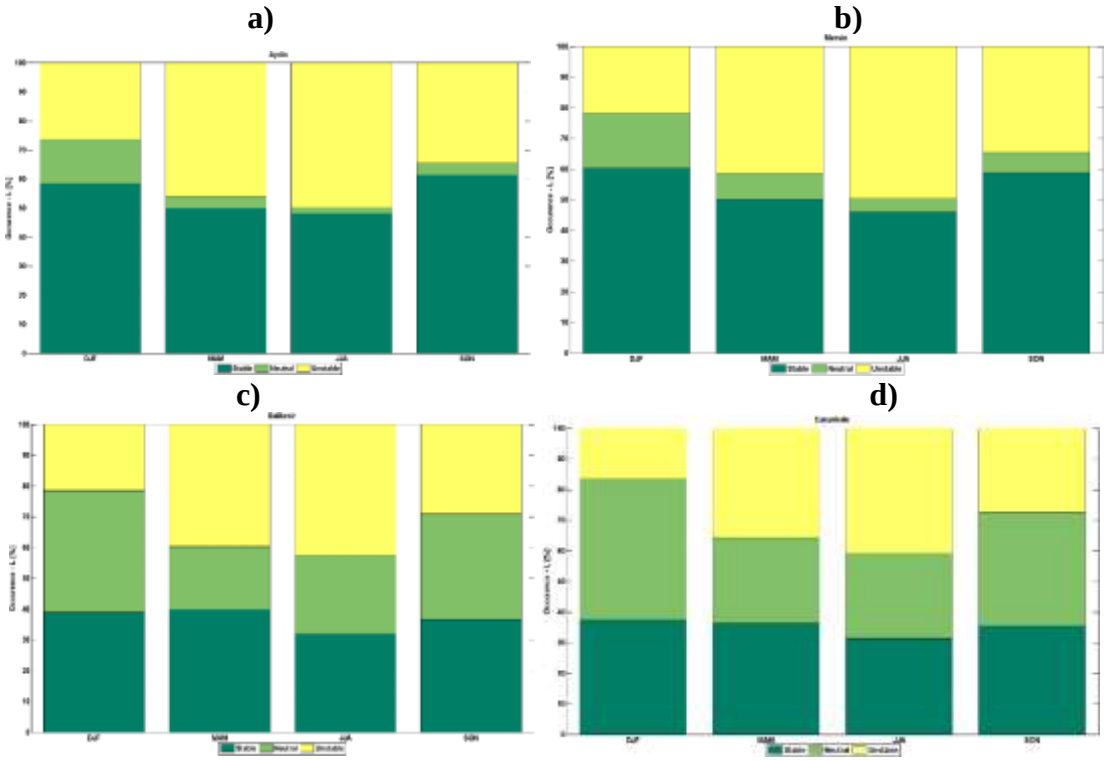

Figure 4 : Seasonal percentage occurrence of each stability condition for specific measurement points (a) Aydin, b) Mersin, c) Balikesir, d) Canakkale, e) Hatay, f) Ordu) over Turkey : stable (dark green), neutral (light green), unstable (yellow), winter (first bar), spring (second bar), summer (third bar), autumn (last bar).

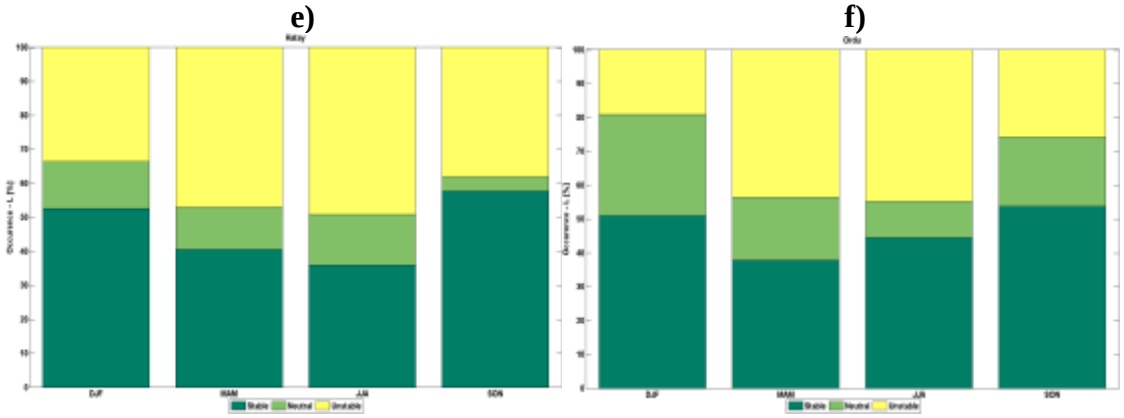

Figure 4 (Continue): Seasonal percentage occurrence of each stability condition for specific measurement points (a) Aydin, b) Mersin, c) Balikesir, d) Canakkale, e) Hatay, f) Ordu) over Turkey : stable (dark green), neutral (light green), unstable (yellow), winter (first bar), spring (second bar), summer (third bar), autumn (last bar).

In annual atmospheric stability analysis over entire Turkey including all seas, stable condition was observed to have its highest percentage occurrence (60-70 %) over land (Figure 5). In contrast to stable condition, unstable condition was observed to have its highest percentage occurrence (70-90 %) over seas. Neutral condition was observed as the stability condition that have the lowest percentage occurrence in both land and seas in comparison with other two stability conditions. However, its percentage occurrence value was observed to be higher in land, and Çanakkale is the location that have the highest percentage occurrence for neutral condition.

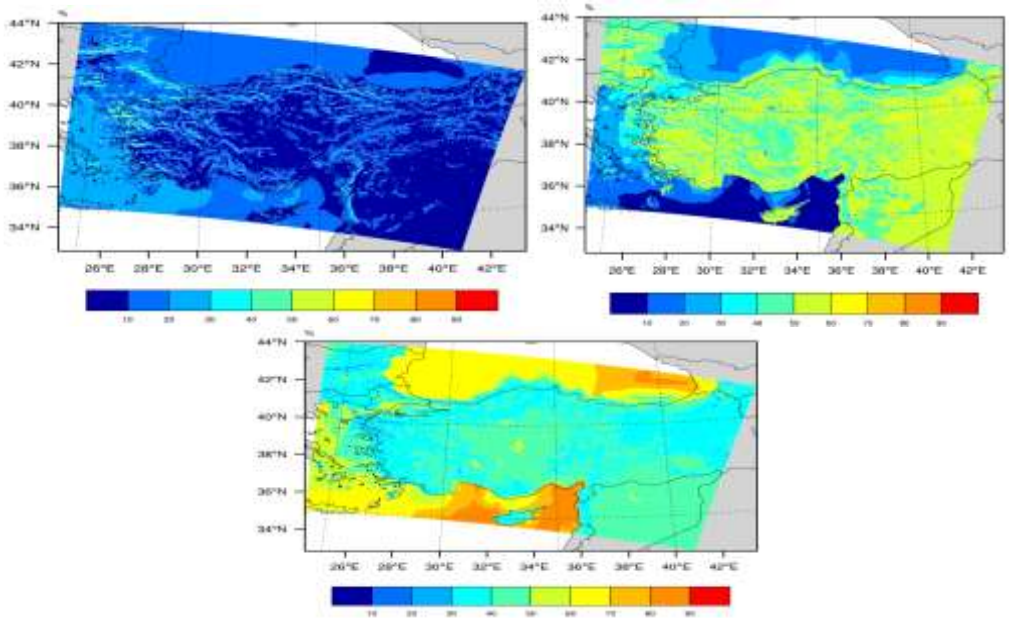

Figure 5 : Annual percentage occurrence of each stability condition over entire Turkey including all seas : Stable (upper right), neutral (upper left), unstable (bottom).

CONCLUSIONS

Statistics of atmospheric stability and WRF's model performance in terms of wind profiles obtained based on atmospheric stability were studied in Turkey. Overall performance of WRF model was observed sufficiently. In seasonal analysis for specif measurements points over Turkey, stable condition was observed to occur mostly in autumn and winter as unstable condition was observed to occur mostly in spring and summer. In annual analysis for entire Turkey including all seas, stable condition was observed to occur mostly in land as unstable condition was observed to occur mostly in seas. Neutral condition was generally observed to have lowest percentage occurence in both seasonal and annual analysis with respect to stable and unstale conditions.

ACKNOWLEGMENT

Computing resources used in this study were provided by the National Center for High Performance Computing of Turkey (UHeM) under grant number <5003652015>

REFERENCES

S.-E.Grying, E.Batchvarova, R. Floors, A.Hahmann, A. Pena, T. Mikkelsen, T.Mikkelsen. (2011). *Comparison of wind lidar profile sup to 600 meters and WRF modelling output; what can we see and what can we learn ?*, European Workshop COST ES-1002 'WIRE: Weather Intelligence for Renewable Energies', MINES ParisTech, Sophia Antipolis, France, 2011, March 22 – 24.

Ameya Sathe. (2010). *Atmospheric stability and wind profile climatology over the North Sea – Case study ay Egmond aan Zee*, TORQUE 2010 : The Science of Making Torque from Wind, 2010, June 28-30, Greece.

Y. Sakagami, P. A. Santos, R. Haas, J. C. Passos, F. F. Taves. (2015). *A simple method to estimate atmospheric stability using lidar wind profiler*, EWEA Offshore, 2015, March 10-12, Copenhangen, Denmark.

MODIS DATA TO KNOWLEDGE GENERATION BY INTEGRATING DIFFERENT DATABASES

Enrico Feoli[1], Alfredo Altobelli[1], Rossella Napolitano[1], Zafer Aslan[2] and Gokhan Erdemir[3]

[1] University of Trieste, Italy
{ feoli , altobell, napolita}@units.it
[2]Istanbul Aydin University, Turkey
zaferaslan@aydin.edu.tr
[3]Istanbul Sabahattin Zaim University, Turkey
gokhan.erdemir@izu.edu.tr

Abstract

NASA built an integrated data set under the Cloud and Earth Radiation Energy System (CERES) project. Data set using CERES scanners and Visible Tropical Rainfall Measurement Mission (TRMM) satellite system with Spectral and Terra and Aqua bands in Moderate Resolution Infrared Scanner (VIRS) and (MODIS) were utilized from high resolution visualizes. MODIS data are generally received twice a day. The VIRS data at two local time points are taken over a 46-day cycle between latitudes 37 ° N and 40 ° S. Thus, the daily cycle is made better with TRMM, Aqua, and Terra data. Cloud features are achieved using the latest imaging methods, including cloud height, optical thickness, emissivity and ice or liquid water phases. These cloud products are converted into CERES scan fields that are matched using the point spread functions of the scanners. Simultaneous cloud and radiation images provide high selectivity data. VIRS data can be accessed for at least three years, MODIS Terra MODIS data for one year. These data are compared with other climatological data and active remote sensing methods. The amount of cloud is very similar to climatologically surface observations, satellite data is 6-7% lower. Optical depths are found 2-3 times lower. However, in general, satellite data do not show a difference of more than 5% compared to surface data. Cloud droplet sizes are up to 10% of the surface results. The data obtained in this way is very valuable and provides the meaning of the relationship between clouds and radiation budget (radiation, clouds, cloud microfiche, climatology, MODIS, CERES, VIRS). It is one of the priority areas of the Earth Observing System (EOS) program and tries to understand how the earth functions as a system, examining the amount and role of terrestrial vegetation in large-scale global processes. This requires biophysical and structural properties as well as global distribution of vegetation types as well as spatial / temporal changes. Vegetation Indices (VI) are effective, empirical indicators of the vegetation cover on the land surface. They are usually designed to increase the power of the signal being measured by combining two (or more) wave bands in the red band zone (0.6-0.7 μm) and in the near infrared band zone (0.7-1.1 μm).

Keywords: *MODIS, database, GIS – Geographic Information System*

OBJECTIVE

The main objective of the paper is to present MODIS data to knowledge generation by integrating different databases and analyse MODIS data on selected area.

DATA AND METHODS

The MODIS VI (MOD13) observes spatio- temporal variations and comparisons of global vegetation conditions. Data would be used to monitor the Earth's terrestrial photosynthetic vegetation activity. It gives an opportunity to analyze phenologic and biophysical changes.The MODIS VI products are currently produced at 250 m, 500 m, 1 km and a special 0.05 deg. spatial resolutions. For data processing purposes, MODIS VIs are generated in square tile units

that are approximately 1200-by-1200 km (at the equator), and mapped in the Sinusoidal (SIN) grid projection (equal area projection). Only tiles containing land features are processed. When mosaicked, all tiles cover the Earth landmass and the global MODIS-VI can thus be generated each 16 days and each calendar month.

RESULTS AND DISCUSSIONS

Case studies on selected data are presented in this part.

TEKİRDAĞ

Product:	MODIS/Terra Land Surface Temperature/Emissivity (LST)
Coordinates:	Latitude: 40.983333, Longitude: 27.516667 (WGS84 datum)
Areal Extent:	Approximately 7 km Wide x 7 km High
Subset Date Range:	March 05, 2000 (2000065) to June 09, 2016 (2016161)
Request ID:	29Jun2016_05:13:07_337922846L40.983333L27.516667S7L7_MOD11A2
Quality Control Conditions:	As Specified by Science Team (See QC table tab)

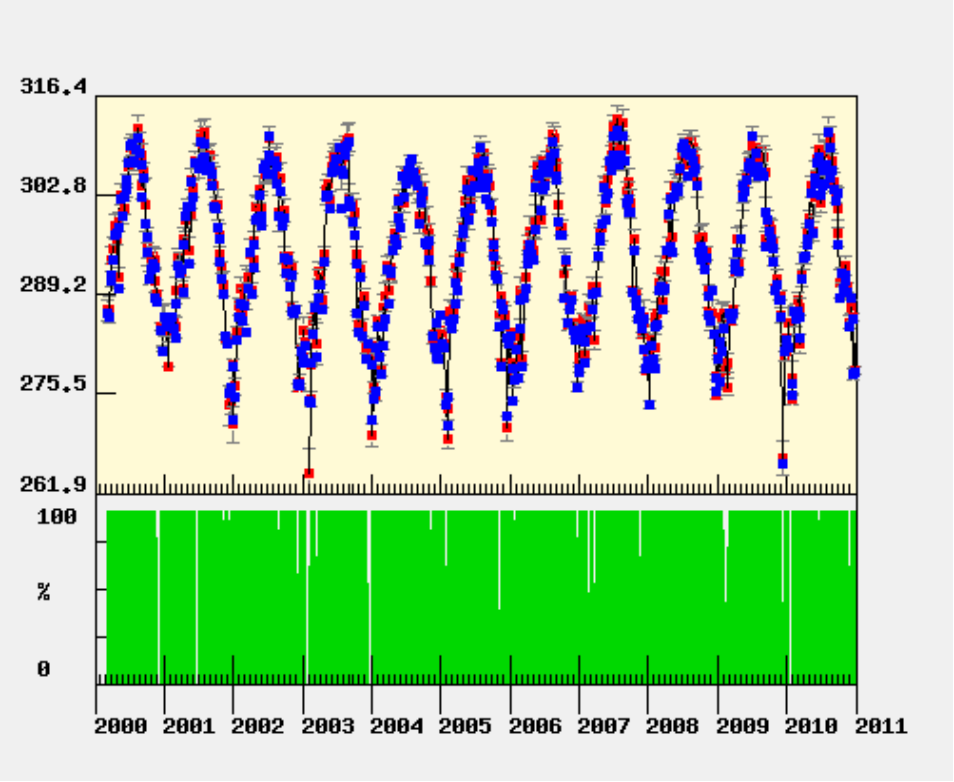

Figure 1- Land surface temperature, Tekirdağ, 2000-2010.

MOD11A2/LST_Day_1km [Scale Factor = 0.02, Units= Kelvin]
Pixels having the same land cover as the center pixel.
21 of 49 pixels [42.86%] have the same class as the center pixel
Center Pixel Class: (13) Urban and Built-Up

There is a decreasing trend at the first part of study period (Fig.1). Beginning from 2005, gradually increasing values of minimum and maximum surface temperature have been recorded. In general, this increasing has also been observed in the last term, (Fig. 2).

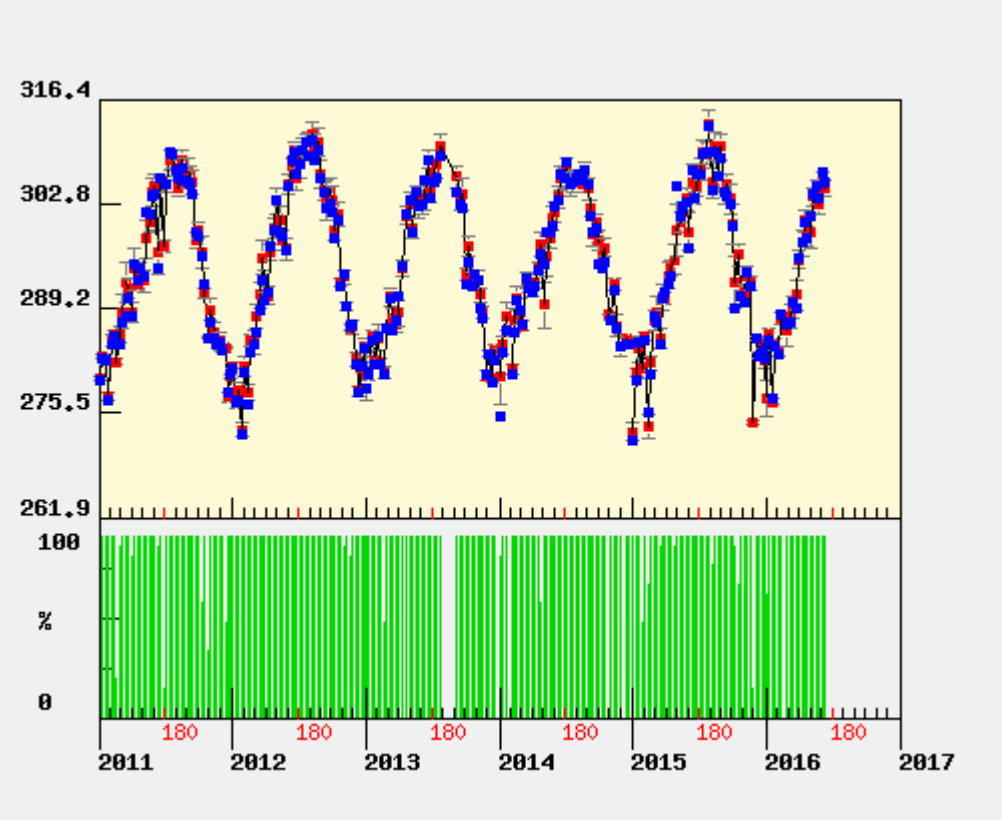

Figure. 8- Land surface temperature, Tekirdağ, 2011-2016.

MOD11A2/LST_Day_1km [Scale Factor = 0.02, Units= Kelvin]
Pixels having the same land cover as the center pixel.
21 of 49 pixels [42.86%] have the same class as the center pixel
Center Pixel Class: (13) Urban and Built-Up

ACKNOWLEDGEMENTS
This work was made possible thanks to ICTP Associateship Program that have considerably improved the article. Special acknowledgements to our colleague M.S. Nilüfer ŞEN who helped in the data transferring process.

REFERENCES

A. Altobelli, E. Bressan, E. Feoli, P. Ganis and F. Martini, "Digital representation of spatial variation of multivariate landscape data", Community Ecology, Vol. 7, No. 2 (2006), pp. 181-188
Patrick Minnis, David F. Young, Bruce A. Wielicki, Sunny Sun-Mack, Qing Z. Trepte, Yan Chen, Patrick W. Heck, Xiquan Dong,"Global cloud database from VIRS and MODIS for CERES", Third International Asia-Pacific Environmental Remote Sensing Remote Sensing of the Atmosphere, Ocean, Environment, and Space, 2002, Hangzhou, China
https://lpdaac.usgs.gov/sites/default/files/public/product_documentation/mod16_atbd.pdf (October 21,2017)

PERFORMANCE TEST OF WEATHER RESEARCH AND FORECASTİNG (WRF) MODEL FOR CENTRAL ANATOLİA AND BLACK SEA REGİONS OF TURKEY

Cem Özen[1], Emre Korkmaz[1], Serdar Bağış[2], Hüseyin Toros[1]

[1]*Department of Meteorology, Faculty of Aeronautics and Astronautics, Istanbul Technical University, İstanbul, Turkey.*

cemozen@live.com, kemik_87@hotmail.com, toros@itu.edu.tr

[2]*Computer Engineering Department, Institute of Science and Technology, Istanbul Technical University, İstanbul, Turkey.*

serdarbagis@gmail.com

Abstract

Weather forecasting is quite challenging and significant issue since atmosphere is very hard to determine due to its dynamical and nonlinear structure. Despite the complexity of atmosphere, there are several methods to overcome and achieve success in weather forecasting like statistical and numerical weather prediction methods (NWP). Furthermore, NWP models give much more realistic and accurate results since it struggles with the atmospheric equations when it's compare to the statistical methods. In this study, WRF – ARW model with 3.8.1 edition has been used as NWP model and its performance has been tested for Turkey. Two nested domains have been used for performance analysis and while the resolution of coarser domain has been set as 9 kilometers, inner domain has been set as 3 kilometers. On the other hand, Final Operational Global Analysis (FNL) data of National Centres for Environmental Prediction (NCEP) which has 1-degree by 1-degree resolution has been used as the initial and boundary condition for downscaling purposes. Besides, model has been runned for 4 months in 2016 and months have been chosen as the middle month of four different season in order to determine and investigate the seasonal dependence of model reliability. Furthermore, automatic weather observation stations which are located in the 13 provinces where especially in the northern and middle part of Turkey has been chosen for performance analysis of model. Consequently, two meter temperature variable has been chosen in order to make statistical comparisons which has been chosen as RMSE, Standart Deviation Error and Bias methods.

Keywords: *WRF, weather analysis, prediction, modeling*

Introduction

The modeling of the atmosphere with its constantly changing dynamic structure and chaotic processes is a very difficult and important phenomenon. Therefore, by accurately estimating how these variables will change in future processes, it becomes possible to model the atmosphere properly and thus the forecasting of the weather becomes meaningful. On the other hand, high performance weather forecasting is needed in a very large area such as energy, construction sectors and military purposes. Despite the chaotic nature, it is possible to model the atmosphere with certain approaches, but a model created in this way requires considerable processing power. Today, however, thanks to computers, the time it takes to perform these transactions has become more consistent than in the past. Nevertheless, there are some statistical methods that are shorter in terms of the calculation time for the weather forecast and emergency situations are also preferred (Li et al., 2013).

Carvalho et al. (2012) performed the performance of the WRF model in wind simulation in the complex area of Portugal, characterized by a significant source of wind energy. The effects of local terrain complexity and simulated field resolution on model results were also investigated. The data obtained from the three wind measurement stations selected were compared with the

model results in terms of Root Mean Square Error, Standard Deviation Error and Bias and Trends. The results emphasize the importance of error minimization in wind simulations, the use of high resolution field data, and the importance of an appropriate numerical and physical configuration for the region of interest. Tilev-Tanriover and Hero (2014) used the WRF-ARW 3.4 version to estimate the heavy snowfall in Turkey from 8 to 9 March 2011 with 2-way nesting using 24 and 8 km horizontal resolution and 35 vertical levels.

The contribution of working in the development of models and increasing their accuracy is great. Models vary in time and space. Therefore, it is important to operate the models with different options in order to increase the model accuracy for a region. Inspection of the sensitivity of a numerical model depending on the changes in the configuration options creates an important assessment exercise and this sensitivity analysis will give great contribution to the other studies to improve the knowledge of how numerical simulation models work and which model parameters will work better (Hirabayashi et al.,, 2011; Barnsley, 2007; Dudhia, 1989; Hong et al., 2004; Hong et al., 2006; Kain, 2004; Mlawer et al., 1997; Pielke Sr, 2002; Tewari et al., 2004). Sensitivity studies can give vital information to model users about the use and effects of various model parameters. Relations between air pollution forecasts and measurement results of atmospheric digital models in Turkey are also made by many researchers. Özelkan. et al. (2015) conducted consistency analysis of air pollution observation data and satellite images and model results in İzmir region. Toros et al. (2014) conducted consistency analyzes between air pollution and HIRLAM and HARMONIE model results.

In this study, it is aimed to provide a basis for the model success of the users of the WRF digital weather forecast model, which is increasingly used in our country as well as in the world. Achievement test; WRF model products to represent reasonable meteorological values during the modeling period. In this study, the temperature variation for 2 meters height was evaluated.

Data and Method

Model Review

In this study, a numerical weather prediction model named Weather Research and Forecasting Model (WRF) is used. Weather Research and Forecasting Model (WRF) is a next generation mid-scale digital weather forecasting system designed for both atmospheric research and operational forecasting needs. The two dynamic cores have a data assimilation system and a software architecture that facilitates parallel computation and system extensibility. With the model, a wide range of meteorological applications can be made from ten meters to thousands of kilometers. The WRF model, which was started to be developed in 1990, was developed by the National Atmospheric Research Center (NCAR), the National Oceanic and Atmospheric Administration (represented by the National Environment Prevention Center (NCEP)) and the Air Force Weather Agency (AFWA), Ocean Research Laboratories, Oklahoma University The Federal Aviation Administration (FAA) continues to be developed with (later) Forecasting Systems Laboratories (FSL) contributions. Because it is open source, it is contributed by all the world users. There are two different dynamic solvers, the WRF (ARW) and the Nonhydrostatic Mesoscale Model (NMM) core, and the WRF - ARW model with 3.8.1 slides is used in this study.

The microfiche option chosen for the physical configuration of the model has been the WSM 3-class simple ice scheme created by Hong, Dudia and Chen (2009). The atmospheric boundary layer scheme used in the model was YSU-Scheme (Hong et al., 2006), also known as Yonsei University Scheme.On the other hand, Dudhia (Dudhia, 1989) and RRTM (Mlawer et al., 1997) schemes were used for short and long wavelength radiations, respectively. Unmodified and the

default values that come with the model setup are used. On the other hand, Dudhia (Dudhia, 1989) and RRTM (Mlawer et al., 1997) schemes were used for short and long wavelength radiations, respectively. Unmodified and the default values that come with the model setup are used.Furthermore, the resolution of the geographical data used as the model is 10 minutes for the large area; 5 minutes for small area. In addition, the model is divided into 30 vertical levels. The information related to the model configuration is also shown in detail in the table below (Table 9).

Table 9. Model configuration information

Model	**WRF-ARW 3.8.1**
Working period	January, April, July, October 2017
Horizontal resolution (km)	9 and 3 km
Number of vertical levels	30
Projection	Lambert Conformal
Number of grids	322x202 ve 622x280
Reference coordinates (West-East, South-North)	ref_lat = 39, ref_lon = 32,
Time Frame	54, 18
Dynamic	Non-hydrostatic
Physics Microphysical Option Long Wavelength Radiation Short Wavelength Radiation Floor Surface Model Atmospheric Boundary LayerKümülüs Opsiyonu	 WRF Single–moment 3–class RRTM Longwave Scheme Dudhia Shortwave Scheme, Unified Noah Land Surface Model Yonsei University Scheme (YSU) Kain–Fritsch Scheme
Analysis	3DVAR
Boundary	NOAA/FNL

Domains and Working Area

In order to compare the model results with the measured values, a complex topography was chosen as the study area. The study area includes Ankara, Bartın, Bolu, Çankırı, Düzce, Eskişehir, Karabük, Kastamonu, Kırıkkale, Kırşehir, Kütahya, Yozgat and Zonguldak which are located in the North Central Anatolia region.

The model is run with two domains inside. The outdoor area has a resolution of 9 km; It is located within 3 km resolution and covers all of Turkey. Therefore, model results from this area with high resolution were used for analysis (Figure 19).

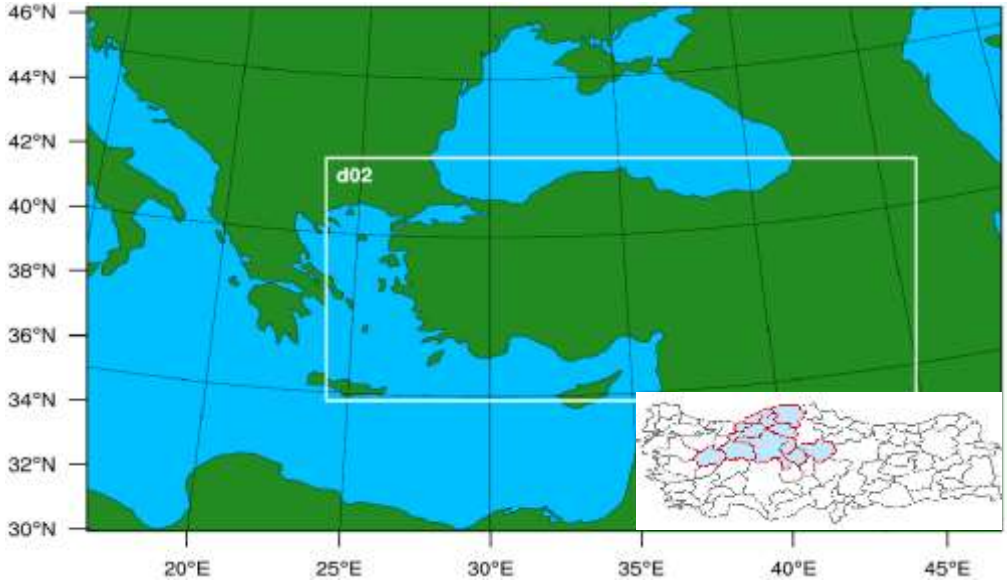

Figure 19. Model working areas.

Initial and Boundary Condition Data

NCEP based FNL global analysis data with 1 degree spherical resolution was used to determine the model start and boundary conditions. In order to be able to understand and test the seasonal performance of the WRF model used in the study, the model was run for the middle of each season. In this case, 2016, January, April, July and October months; The model was run for a total of 123 days. On the other hand, a 2-meter temperature data was selected to compare with model results. The observational data used for this are data from the Automatic Meteorological Observation Station (OMGİ) belonging to the General Directorate of State Meteorology and there are 199 OMGİ in total for the 13 provinces that are focusing on the study. In the study, the model results of each of the 199 stations were compared, but the provincial-based averaging method was used at stations to make the results more understandable.

Model Performance Test

Since accurate and frequent measurement of meteorological elements is expensive and troublesome, it is very easy to estimate intermediate values with the aid of models. It is socially economically beneficial to obtain products for both past and present time intervals and to obtain forecast products for the future with the model.

Digital weather forecast model results can be verified by different methodologies that complement each other (Pielke, 2002). Statistical methods are used to verify the validity of the model using meteorological observations that represent the true state of meteorological variables (Carvalho et al., 2012.). Knowing the accuracy of the model results or the accuracy of the model performance accuracy helps decision makers and researchers to make more accurate decisions in their plans, programs and calculations. Therefore, there is a need for researches for different time and space for knowing the accuracy percentages between observation and model results. Each result will contribute to the efficiency of new work. The relationships between observations and the results obtained from different performance tests will contribute to both the model developers and those using the model products. In this study, 3 different performance tests were applied for model correctness. These are Root Mean Squared Error (RMSE), Mean Error (BIAS) and Standard Deviation Error (STDE).

Root Mean Squared Error, (RMSE)

The RMSE is a measure of how far away the data points are from the relationship line, that is, the data propagation. As the forecast and observation data are separated from each other, the RMSE value becomes larger, and becomes smaller as they approach each other. The following formula is used for RMSE calculations.

$$RMSE = \sqrt{\frac{\sum_{i=1}^{n}(x_{g,i} - x_{m,i})^2}{n}}$$

Mean Error (BIAS)

The average error is obtained by dividing the sum of the differences between observations as statistically and model results by the number of observations. From the average error count, it helps to see the obvious, ie sided errors, between the measurement and the model results in general. The occurrence of systematic faults helps to uncover a constant effect, if any.

$$BIAS = \frac{1}{n}\sum_{i=1}^{n}(x_{g,i} - x_{m,i})$$

Standard Deviation Error, (STDE)

A high RMSE or BIAS indicates that the error is constant and can be viewed as a type if the STDE values are small. In the case of a high STDE, the error is random and shows a relatively low RMSE or Tendency, the simulation has a low physical meaning.

$$STDE = \left[\frac{1}{n}\sum_{i=1}^{n}\left((x_{g,i} - x_{m,i}) - \frac{1}{n}\sum_{i=1}^{n}(x_{g,i} - x_{m,i})\right)^2\right]^{1/2}$$

Analysis and Results

Model results For the January, April, July and October of 2016, the nearest model grid values were compared to the locations of the same stations with 2 meters of temperature data for 199 stations from which 248 stations of MGM data could be used. Results The RMSE, BIAS and STDE values were evaluated for each month. From these statistics, the values of RMSE values for 199 stations are categorized and given visually. As the number of stations is high, RMSE, BIAS and SHH statistical values are given in Table 2 by taking provincial basis averages.

Table 10. Mean accuracy test values for illusions in the study area.

	RMSE				**BIAS**				**STDE**			
County	**Jan**	**Apr**	**Jul**	**Oct**	**Jan**	**Apr**	**Jul**	**Oct**	**Jan**	**Apr**	**Jul**	**Oct**
Ankara	3.30	2.55	2.66	2.69	0.93	0.05	-0.89	0.30	2.82	2.18	1.74	2.34
Bartın	5.90	4.04	4.72	4.08	-4.09	-1.81	-3.44	-2.41	3.76	3.48	2.81	2.81
Bolu	3.92	4.04	3.85	4.08	1.89	2.62	2.13	2.69	2.98	2.66	2.47	2.75
Çankırı	3.90	3.05	3.19	3.25	0.04	0.58	-0.17	1.11	3.35	2.26	2.01	2.42
Düzce	4.47	3.94	3.48	3.35	-0.84	1.01	-0.43	0.49	3.14	3.10	2.31	2.62
Eskişehir	3.52	2.78	3.06	2.76	0.38	-0.58	-1.87	-0.25	2.92	2.27	1.74	2.34
Karabük	4.13	3.19	3.67	3.43	-1.14	-0.68	-2.07	-0.35	3.38	2.56	2.28	2.79
Kastamonu	4.47	3.44	3.51	3.38	-2.20	-0.88	-1.96	-0.27	3.15	3.06	2.50	2.57
Kırıkkale	3.34	2.64	2.87	2.40	-0.95	-1.31	-2.11	-0.75	3.04	2.14	1.55	2.14
Kırşehir	3.10	2.27	2.29	2.27	0.13	0.18	-0.09	0.53	2.87	2.04	1.80	2.08
Kütahya	4.34	3.44	3.56	3.71	0.78	0.73	1.07	1.71	3.21	2.47	2.13	2.69
Yozgat	3.37	2.51	2.53	2.66	-0.48	0.07	-0.83	0.39	3.08	2.18	1.88	2.32
Zonguldak	4.10	3.71	3.66	3.39	-0.77	0.03	-1.95	0.27	2.88	3.04	2.23	2.58
Average	**3.87**	**3.08**	**3.20**	**3.13**	**-0.17**	**0.04**	**-0.83**	**0.41**	**3.07**	**2.49**	**2.06**	**2.47**

In January, April, July and October, 199 station observations were compared with model results, and the distributions of station numbers according to the results obtained are given in Figure 1, according to the RMSE values, model performance errors generally appear to be concentrated between 3.5 and 4.5. According to BIAS results, there is no significant deviation in model outputs. STDE values range from 2 to 4. In general, the nearness of the BIAS values to zero indicates that the model results show trends and the error is 3 degrees. It is believed that the reason for the faults to arrive at these values may be due to the topographic subdivision used in the model. Besides, the resolution we have worked with is 3km, which is more likely to bring mistakes. In our next work we propose to increase the resolution of the topographic subdivision (from 5 min to 2 min). We also estimate that if we remove the dominance resolution from 3km to 1km, it will affect the results positively.

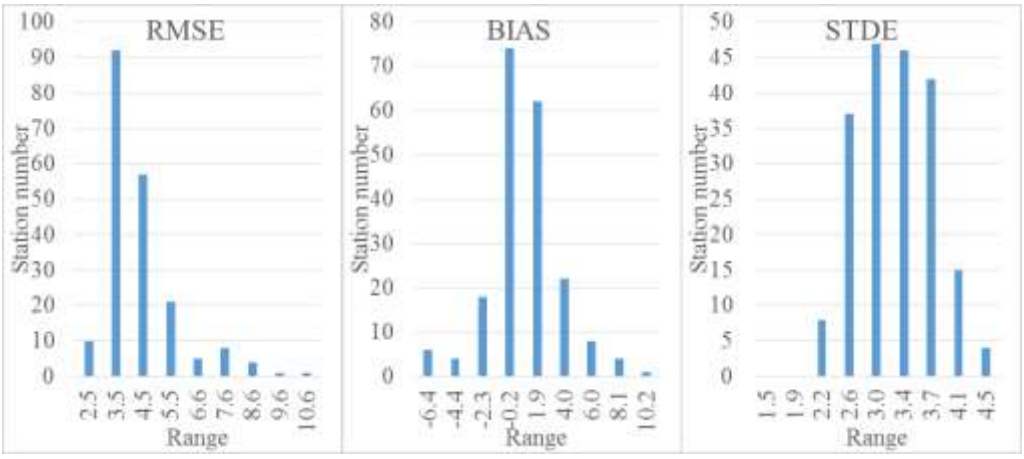

Figure 20. According to model and observation results, distribution range of stations

The distribution of RMSE values according to the observation and model results for all stations is given in Table 3. The RMSE values ranged from 2-4 in all months and in the majority of stations. There is no station whose RMSE value is less than 2 between January observation and model hourly temperature values. The RMSE value of 139 stations was 2-4, 4-6 in 44, 6-8 in 16, and the remaining 5 stations were above statistical value 8. When the RMSE value between April observations and model hourly temperature values were examined, the number of stations less than 2 was 26, 2-4 between 138, 4-6 between 31, 6-8 between 3 and the remaining 1 station value. When the RMSE value between July observation and model hourly temperature values were examined, the number of stations less than 2 was 33, 2-4, 121, 4-6, 35, 6-8, 7 and the remaining 1 station value. When the RMSE value between October observation and model hourly temperature values were examined, the number of stations less than 2 was increased from 25, 2-4 to 138, 4-6 to 29, 6-8 to 5 and the remaining 1 station value to 8.

Table 11. RMSE values between observations and model results for all stations.

Range	January	April	July	October
<2	0	26	33	25
4	139	138	121	138
6	44	31	35	29
8	11	3	7	5
>8	5	1	1	1

The spatial distribution of the RMSE values between the observation stations for four different months of 2016 and the model results for these points is given in Figure 3. Errors appear to have grown in the coastal area.

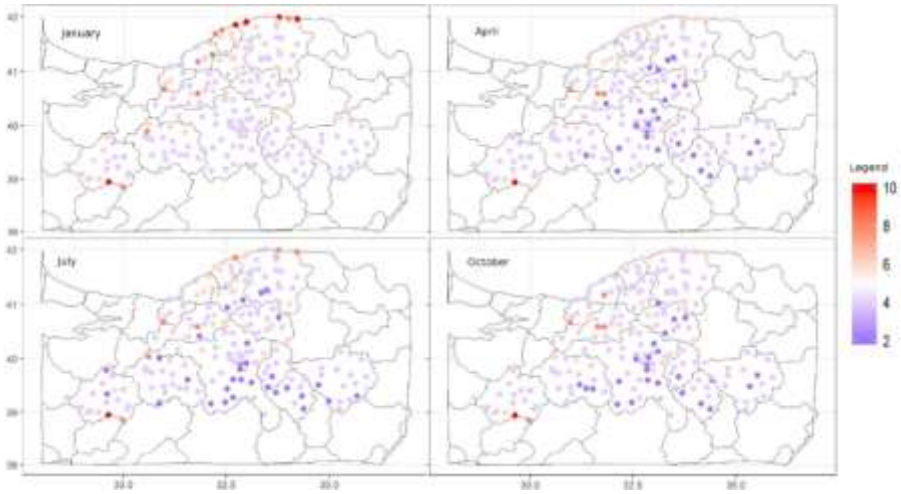

Figure 21. RMSE values between observation and model results.

Acknowledgments

We would also like to show our gratitude to the Turkish State Meteorological Service for sharing the data of the related stations.

References

Barnsley, M.J., 2007. Environmental Modeling: A Practical Introduction. CRC Press, Textbook, pp 432.

Carvalho D., Alfredo Rocha A., Gómez-Gesteira M., Santos C., 2012. A sensitivity study of the WRF model in wind simulation for an area of high wind energy, Environmental Modelling & Software, 33, 23-34.

Dudhia, J., 1989. Numerical study of convection observed during the winter monsoon experiment using a mesoscale two-dimensional model. Journal of the Atmospheric Sciences, 46(20), 3077-3107.

Hirabayashi, S., Kroll, C.N., Nowak, D.J., 2011. Component-based development and sensitivity analyses of an air pollutant dry deposition model. Environ. Modell. Softw. 26 (6), 804-816.

Hong, S. Y., Dudhia, J., & Chen, S. H. 2004. A revised approach to ice microphysical processes for the bulk parameterization of clouds and precipitation. Monthly Weather Review, 132(1), 103-120.

Hong, S. Y., Noh, Y., & Dudhia, J. 2006. A new vertical diffusion package with an explicit treatment of entrainment processes. Monthly weather review, 134(9), 2318-2341.

Kain, J. S., 2004. The Kain–Fritsch convective parameterization: an update. Journal of Applied Meteorology, 43(1), 170-181.

Li, Z., Yang, Z., Yao, Y., Chen, S., Zhang, X., Feng, T., 2013. Wind farm power forecast in mid-eastern coastline of china, International Journal of Recent Research and Applied Studies (IJRRAS), 14(2), 324-332.

Mlawer, E. J., Taubman, S. J., Brown, P. D., Iacono, M. J., & Clough, S. A., 1997. Radiative transfer for inhomogeneous atmospheres: RRTM, a validated correlated-k model for the longwave. Journal of Geophysical Research: Atmospheres, 102(D14), 16663-16682.

Özelkan E, Karaman M, Mostamandy S, Uça Avcı Z. D, Toros H, 2015. Derivation of PM10 Levels Using OBRA on Landsat-5TM Images: A Case Study in Izmir, Turkey, Fresenius Environmental Bulletin, Vol. 24, No. 4b, 1585-1596,

Pielke Sr., R.A., 2002. Mesoscale Meteorological Modeling, second ed. Academic Press, San Diego, CA.

Tewari, M., Chen, F., Wang, W., Dudhia, J., LeMone, M. A., Mitchell, K., ... & Cuenca, R. H., 2004. Implementation and verification of the unified NOAH land surface model in the WRF model. In 20th conference on weather analysis and forecasting/16th conference on numerical weather prediction, Vol. 1115.

Tilev-Tanriover S. and Kahraman A., 2014. Impact of Turkish ground-based GPS-PW data assimilation on regional forecast: 8–9 March 2011 heavy snow case, Atmos. Sci. Let. 15: 159–165.

Toros H, Geertsema G, Cats G, 2014. Evaluation of the HIRLAM and HARMONIE numerical weather prediction models during an air pollution episode over Greater İstanbul Area. CLEAN - Soil, Air, Water, 42(7), 863-870.

FLOOD RISK ANALYSES IN BLACK SEA REGION BY USING HadGEM2-ES CLIMATE PROJECTION

Erdem Odabaşı
Turkish State Meteorological Service, Department of Meteorological Disasters

Abstract
The number of rainy days for flood risk threshold were obtained with respect to RCPs 4,5 and 8,5 scenarios. Had-GEM-2 Projection outputs include in 2017-2046 periods. This HadGEM2-ES outputs have been compared with disasters reports and numbers of rainy days over threshold value on 24 hourly observed between 2006-2015 years.In this study, as a result, the data sets of flood risk percentage in 2017-2046 period have been created for every province in Black Sea Region, by calculating HadGEM2-ES rainfall outputs between 2017-2046 periods with rate of disaster reports to numbers of rainy days over threshold value on 24 hourly observed between 2006-2015 years. As a result, Flood risk areas and graphics have been detected as percent for every province in Black Sea Region by using these data between 2017-2046 periods.

Keywords: *Flood Disaster Risk, HadGEM2-ES Projections, Threshold Value.*

Introduction

Climate Projections produced by Turkish Meteorological Service for Turkey and its regions;Projections have been produced according to RCP 4,5 and RCP 8,5.The scenarios we have used are most prefered scenario in IPPC 5. evaluation report. 2016-2099 terms for projections and 1971-2000 terms as referans period have been chosen for projections produced on resolution 20 km.The outputs(**HadGEM2-ES,MPI-ESM-MR,ve GFDL-ESM2M**) properly producing conclusion for Turkey and itself region have been chosen.Regional Climate Projection(RCP) have bene obtained by means of RegCM4 (Regional Climate Model System) from this 3 model.

HadGEM2-ES is a coupled Earth System Model that was used by the Met Office Hadley Centre for the CMIP5 centennial simulations. HadGEM2-ES was the first Met Office Hadley Centre model to include Earth system components as standard.

Material and Method

The number of total rainy days over rain threshold on 24 hourly in 2006-2015 with flood disasters in 2006-2015 are calculated.By calculating this rate with The number Of days Over Threshold of rainy on 24 hourly obtained from HadGEM2-ES model,the data sets of flood risk percentage in 2017-2046 periods have been created.The calculation methodology for Trabzon city is belowzon.

1) The threshold value of precipitation on 24 hourly in Trabzon= 30 mm
The number Of total flood occurring in 2006-2015(as 10 years)= 5 day
The number of rainy days over 30 mm in 2006-2015= 29 day
100x5/29= %17
%17 is the rate of flood number and rainy day number in 2006-2015

2) The number of rainy day over 30 mm in 2017-2026 by RCP 4,5 in Trabzon= 100 day
100x17/100=17
100x17/5=%340 %340-%100=%240 increasing in 2017-2026

3) The number of rainy day over 30 mm in 2017-2026 by RCP 8,5 in Trabzon=115 day
115x17/100= 19,55
100x19,55/5=%391 %391-%100=%291 increasing in 2017-2026

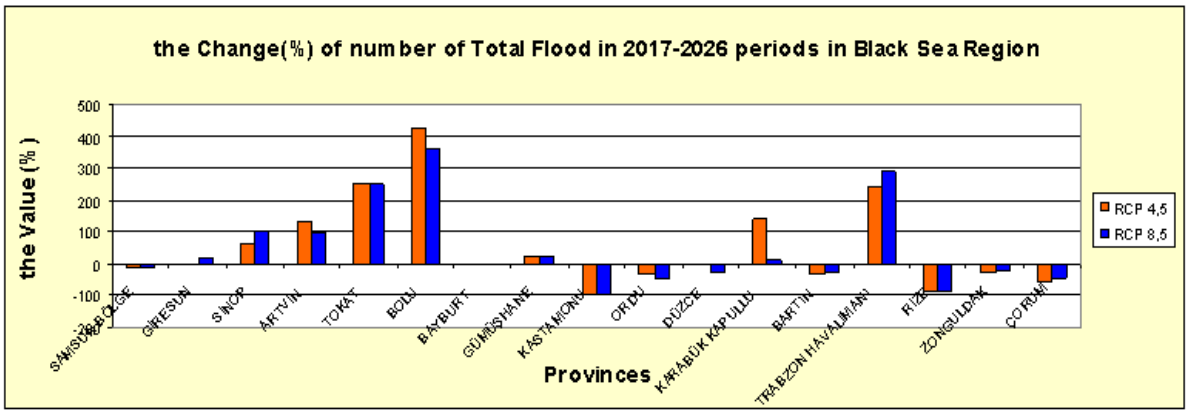

Figure 1.Flood Risk(%) in Black Sea Region in 2017-2026 periods

According to RCP 4,5 scenarios and RCP 8,5 scenarios in 2017-2026 periods,the maximum increase in Black Sea Region is expected in Bolu Province.As the increasing over percent 400 in Bolu is estimated by RCP 4,5,the increasing over percent 300 is expected by RCP 8,5 scenarios.İn the same time,the increasing over percent 200 in Tokat and Trabzon Province is expected by both RCP 4,5 and RCP 8,5.As have seen in Figure 1,the increasing in Sinop,Artvin and Kastamonu are expected by RCP 4,5 and RCP 8,5 scenarios.According to RCP 4,5 scenarios and RCP 8,5 scenarios in 2017-2026 periods,the maximum decreasing in Black Sea Region is estimated in Kastamonu and Rize province.As the decreasing percent 100 in Kastamonu is expected by both RCP 4,5 and RCP 8,5,the decreasing in Rize where is the place taking the most precipitation of Turkey and the place expericing the most flood event of Turkey is approximately percent 100.

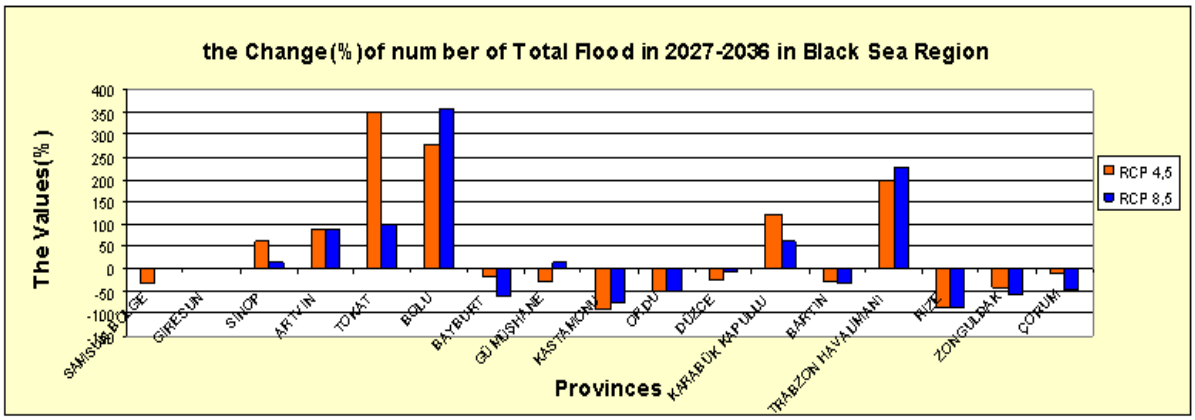

Figure 2. Flood Risk(%) in Black Sea Region in 2027-2036 periods

The maximum increasing in number of total flood in 2027-2036 periods is expected by RCP 4,5 and RCP 8,5 in Tokat and Bolu where is in Black Sea Region.While the increasing in Bolu is over %250 by RCP 4,5 and is over %350 by RCP 8,5,the increasing in Tokat is %350 by RCP 4,5.On the other hand,the increasing in Trabzon by RCP 4,5 and RCP 8,5 is %200 and over %200. The decreasing which is close %100 by RCP 4,5 and RCP 8,5 is expected in Rize where is the place taking most precipitation of Turkey. In the same time, while the increasing about %100 in Artvin is expected by RCP 4,5 and RCP 8,5,the more than %50 decreasing in Kastamonu is expected by RCP 4,5 and RCP 8,5.

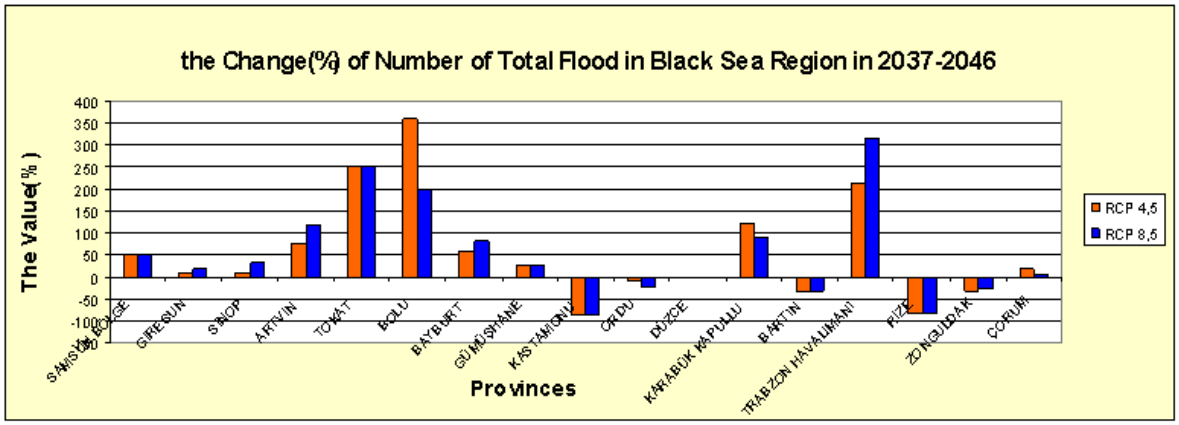

Figure 3.Flood Risk(%) in Black Sea Region in 2037-2046 periods

The maximum increasing number of total flood occurence in 2027-2036 periods is expected by RCP 4,5 and RCP 8,5 in Tokat,Bolu and Trabzon.While the increasing of total flood occurrence is about %200 in Tokat by RCP 4,5 and RCP 8,5. Increasing number of total flood occurence in Bolu is %360 by RCP 4,5 and %200 by RCP 8,5. In the same time,the increasing in number of total flood in Trabzon is %211 by RCP 4,5 and is %311 by RCP 8,5. The increasing in number of total flood occurence in 2037-2046 is expected by RCP 4,5 and RCP 8,5 in Artvin,Karabük,Samsun and Bayburt,again. While the increasing in Artvin is close %100 by RCP 4,5,it is % 100 by RCP 8,5. According to RCP 4,5 and RCP 8,5,the increasing in number of total flood is over %100 in Karabük and is %50 in Samsun,Bayburt. As have been seen in Figure 3,again,the maximum decreasing in number of total flood occurence in 2037-2046 periods in Black Sea Region is expected in Kastamonu and Rize.the decreasing in Kastamonu and Rize is close %100 by RCP 4,5 and RCP 8,5.

The Grapichs of Provinces with Maximum Flood Risk in Black Sea Region in 2017-2046

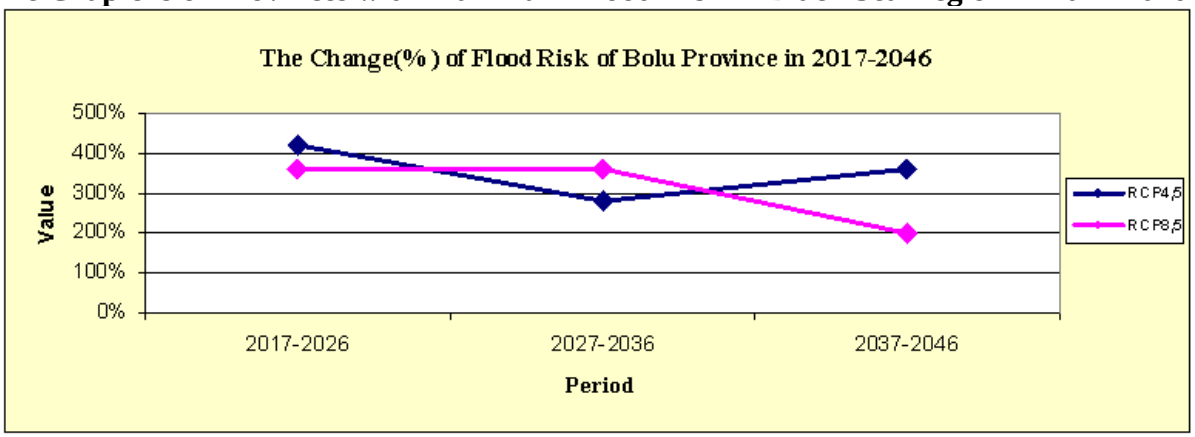

Figure 4.the Change(%) of Flood Risk of Bolu Province in 2017-2046 periods

The flood risk in Bolu is expected about %300-400 by RCP 4,5 and RCP 8,5 in 2017-2026 periods, after this period, the some decreasing on flood risk is expected in 2027-2036 period by RCP 4,5 and RCP 8,5 according to 2017-2026 period. The rate of Bolu in 2027-2036 is about %300-350 interval. On the other hand,while the rate of 2037-2046 is %200 by RCP 8,5,and is about %350 by RCP 4,5. As have seen in Figure 4,the most flood risk in 2017-2046 period is expected in 2017-2026 period.

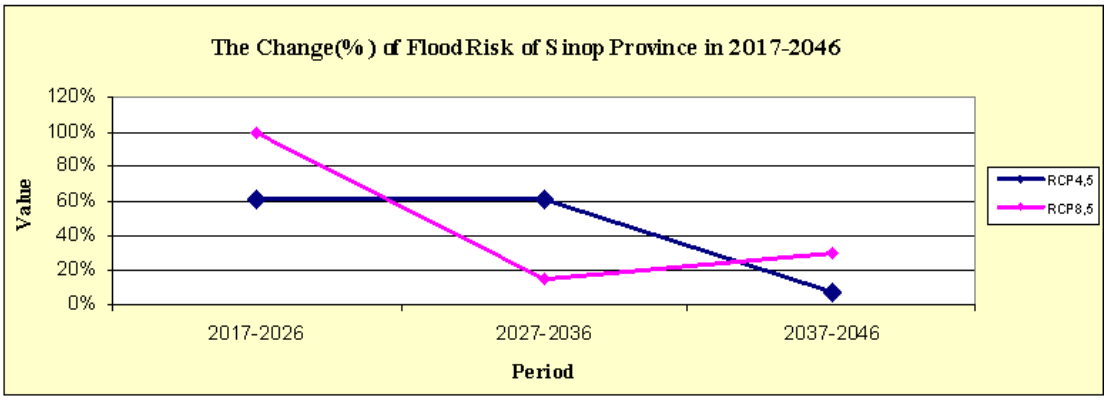

Figure 5.The Change(%) of Flood Risk of Sinop Province in 2017-2046 periods

As have been seen in Figure 5, the most flood risk in Sinop is expected in 2017-2026 periods,the rate in Sinop is %60 by RCP 4,5 and %100 by RCP 8,5. After 2017-2026 periods,while the value of flood risk in Sinop don't change by RCP 4,5 in 2027-2036,According to RCP 8,5,the flood risk in Sinop decreases about %20.On the other hand,while the value of flood risk in Sinop slightly increases by RCP 8,5 in 2037-2046,the decreasing on value of flood risk is expected by RCP 4,5 in 2037-2046.the value of RCP 8,5 is about %30, the value of RCP 8,5 is about %10.

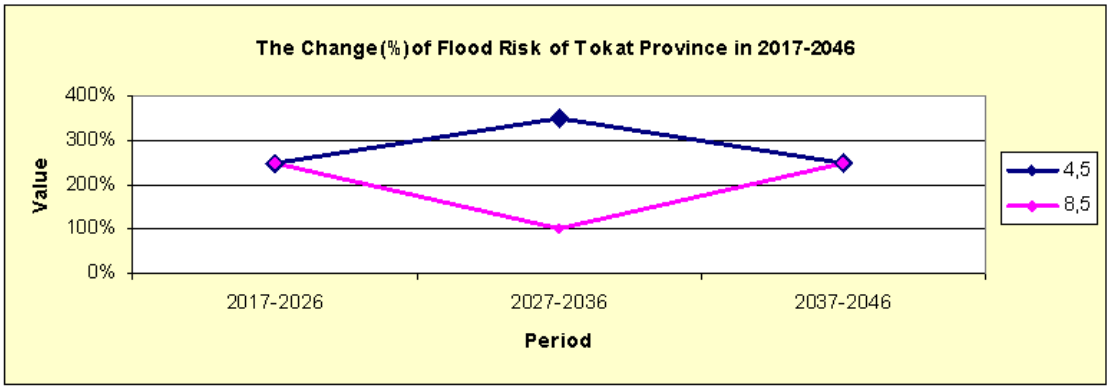

Figure 6.The Change(%) of Flood Risk of Tokat Province in 2017-2046 periods

The values of flood risk expected about %250 in Tokat is similar by RCP 4,5 and RCP 8,5 in 2017-2026 periods.After 2017-2026 periods,the difference among scenarios in 2027-2036 periods are too much in Tokat,while the value of RCP 4,5 in this period is about %350,the value of RCP 4,5 in this period is about %350,RCP 8,5 is % 100 as well.Also,as have been seen in chart ,while the increasing of flood risk from 2027-2036 to 2037-2046 is so expected by RCP 8,5 in Tokat,RCP 4,5 with decreasing close to %100 is about %250.

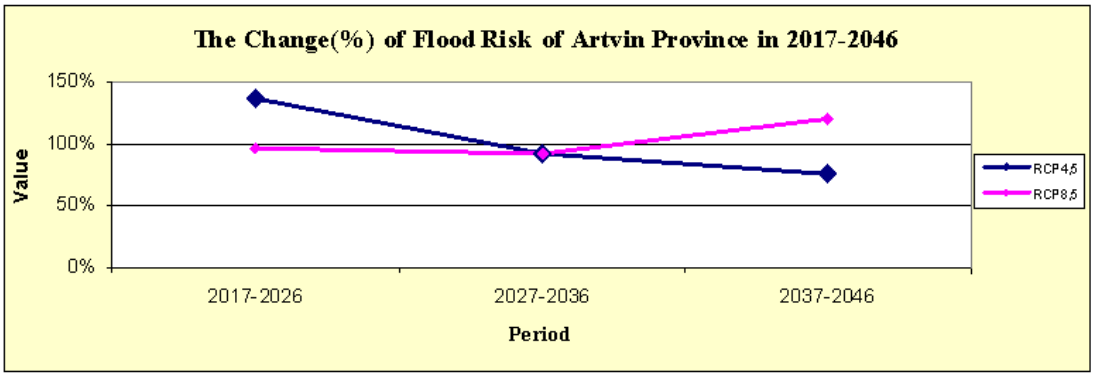

Figure 7.The Change(%) of Flood Risk of Artvin Province in 2017-2046 periods

According to the number of total flood occuring in 2006-2016 periods in Artvin,while the changing of the number of total flood in 2017-2026 periods is expected increasing close to %150 by RCP 4,5 in Artvin,RCP 8,5 expects about %100 in this period as well. After 2017-2026 period,the increasing on the number of total flood in Artvin is expected by RCP 4,5 and RCP 8,5 in 2027-2036 periods. As have been seen in chart,the changing of RCP 4,5 and RCP 8,5 is similar 2027-2036 peirods. The value of RCP 4,5 and RCP 8,5 is %92.the increasing in 2037-2046 periods is expected in Artvin again. The increasing on the number of total flood in Artvin is %120 by RCP 8,5 and is % 76 by RCP 4,5 sceneiro.

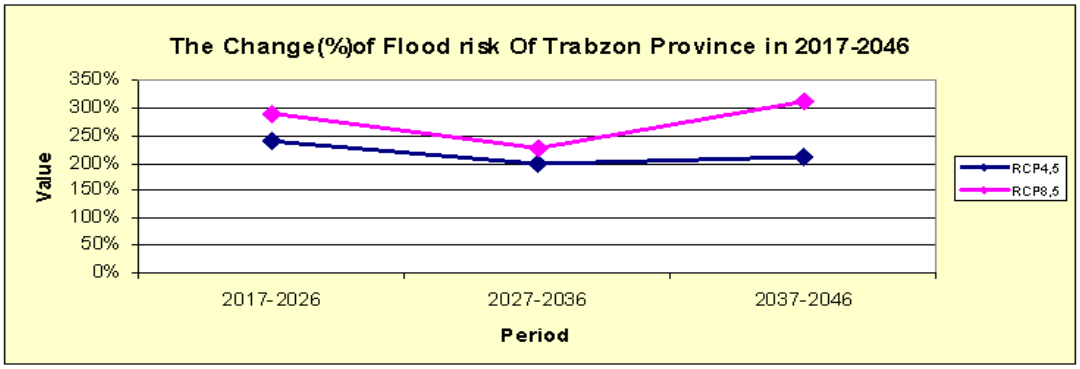

Figure 8.The Change(%) of Flood Risk of Trabzon Province in 2017-2046 periods

The increasing in all of 2017-2046 periods is generally estimated in the changing of number of total flood in Trabzon. As have been seen in chart,the increasing in 2017-2026 is %291 by RCP 8,5 and %241 by RCP 4,5 in Trabzon. After 2017-2026 periods,a slight decreas in 2027-2036 by comparison in 2017-2026 is estimated in Trabzon,the increasing in 2027-2036 periods is %226 by RCP 8,5 and %199 by RCP 4,5. After 2027-2036 periods in Trabzon,the increasing finnally in 2037-2046 is estimated that it is % 311 by RCP 8,5 and % 211 by RCP 4,5.

Conclusions

-The increase in the number of Total flood in 2017-2046 periods by comparison the number of total flood occurrence in 2006-2016 periods in Black Sea Region is estimated in Trabzon,Artvin,Bolu,Tokat,Sinop Provinces.
-The increase in Tokat,Trabzon and Bolu is over %100 by RCP 4,5 and RCP 8,5 scenario in 3 period from 2017 to 2046.
- The most increase in 2017-2036 periods is expected with a increase over %300 by RCP 4,5 and RCP 8,5 scenarios in Bolu in 2017-2026 periods.

References

Meteorological Disasters Division,Turkish State Meteorological Services Research Department.
-Akçakaya, A., Sümer, U.M., Demircan, M., Demir, Ö., Atay, H., Eskioğlu, O., Gürkan, H.,Yazıcı, B., Kocatürk, A., Şensoy S., Bölük, E., Arabacı, H., Açar, Y., Ekici,M., Yağan, S. ve Çukurçayır, F. (2015). Climate Projections and Climate Change For Turkey with New Scenarios-TR2015-CC. Published by Turkish State Meteorological Services , 149 s., Ankara.

HYDRODYNAMIC MODEL FOR KAĞITHANE WATERSHED VIA COMPARING WAVE ROUTING METHODS

Cevza Melek Kazezyılmaz-Alhan[1*], Sezar Gülbaz[2], Mohsen Mahmoody Vanolya[3], Emre Saraçoğlu[4], Rouhollah Nasirzadeh-Dizaji[5]

[1,2] Department of Civil Engineering, Istanbul University, Avcılar, Istanbul, Turkey,
[3,5] Department of Civil Engineering, Yıldız Technical University, Davutpaşa, Istanbul, Turkey,
[4] Department of Civil Engineering, Beykent University, Ayazağa, Istanbul, Turkey,
**Corresponding author e-mail: meleka@istanbul.edu.tr*

Abstract

Hydrologic and hydraulic models are used for solving water resources problems and selecting appropriate alternatives for flood management. Hydraulic models use continuity and momentum equations, which are kinematic, diffusion and dynamic water waves in watershed and streams. The aim of this study is to compare kinematic and dynamic wave routing methods by employing a hydrodynamic model for Kağıthane Stream Watershed located in Istanbul, Turkey. For this purpose, first, a hydrodynamic model is developed by using Environmental Protection Agency Storm Water Management Model (EPA SWMM) which is a dynamic simulation model for the surface runoff that develops on a watershed during a rainfall event. Then, by using the hydrodynamic model, the surface runoff generated over the watershed are simulated with different scenarios. Finally, the flow rate is calculated with dynamic and kinematic wave theories for the Kağıthane Watershed by using this model. Afterwards, results of different scenarios are compared with each other to observe the sensitivity that can affect the value of floods peak. Moreover, the sensitivity of the parameters on flow rates, such as Manning's roughness coefficient for both channels and subcatchments, infiltration parameters, i.e., hydraulic conductivity and initial soil moisture condition of the hydrodynamic model, are determined.

Keywords: *Kağıthane Stream watershed, Dynamic Wave Model, Kinematic Wave Model, Flood Routing, EPA SWMM.*

INTRODUCTION

Flood wave propagation is important to calculate overland flow and open channel flow. The numerical solutions of the Saint-Venant equations (St. Venant, 1871) are used to calculate overland flow. Hydrologists developed several analytical and numerical methods for the partial differential equation of Saint-Venant equations (Kazezyılmaz-Alhan, C.M. and Medina, M.A., Jr 2007; Ying et al. 2004; Crossley et al. 2003; Lackey and Sotiropoulos 2005). Kinematic-wave and diffusion-wave models can be derived from the dynamic wave equations by neglecting the acceleration and pressure terms in the momentum equation. The kinematic wave model (Lighthill and Whitham, 1955) substitutes a steady uniform flow (stage-discharge) relationship for the momentum equation. The diffusion waves are obtained by introducing physical diffusion into the kinematic wave continuity equation, which results mathematically in a second-order term. Cunge (1969) also obtained the diffusion wave equation by linearizing the dynamic wave equation around a perturbation and ignoring inertial terms. Diffusion occurs in most natural unsteady open channel flows and in overland flow (Ponce, 1989; Lighthill and Whitham, 1955). These three models are used to calculate the overland flow. As it is well known that there is strictly connection between surface runoff and infiltration through the soil surface. Therefore, it is necessary to develop mathematical models for simulating overland flow with infiltration.

MATERIALS AND METHODS

In this study, dynamic (Equations 1 and 2) and kinematic wave (Equations 3 and 4) routing methods are compared by employing a hydrodynamic model for Kağıthane Stream Watershed which has 58 km^2 area located in Istanbul, Turkey (Figure 1). For this purpose, first, a hydrodynamic model is developed by using Environmental Protection Agency Storm Water Management Model (EPA SWMM) which is a dynamic simulation model for the surface runoff that develops on a watershed during a rainfall event. Then, by using the hydrodynamic model, the surface runoff generated over the watershed are simulated with different scenarios (Table 1). Finally, the flow rate is calculated with dynamic and kinematic wave theories for the Kağıthane Watershed by using this model. Afterwards, results of different scenarios are compared with each other to observe the sensitivity that can affect the amount of floods peak (Table 2). Moreover, the sensitivity of the parameters on flow rates, such as Manning's roughness coefficient for both channels and sub catchments, infiltration parameters, i.e., hydraulic conductivity and initial soil moisture condition of the hydrodynamic model, are determined.

$$\frac{\partial y}{\partial t} + V\frac{\partial y}{\partial x} + y\frac{\partial V}{\partial x} = i - f \quad (1)$$

$$\frac{\partial V}{\partial t} + V\frac{\partial V}{\partial x} + g\frac{\partial y}{\partial x} = g(S_0 - S_f) + \left[(i-f)\frac{V}{y}\right] \quad (2)$$

$$\frac{\partial y}{\partial t} + \alpha\frac{\partial (y^m)}{\partial x} = i - f \quad (3)$$

$$q = \alpha y^m \quad (4)$$

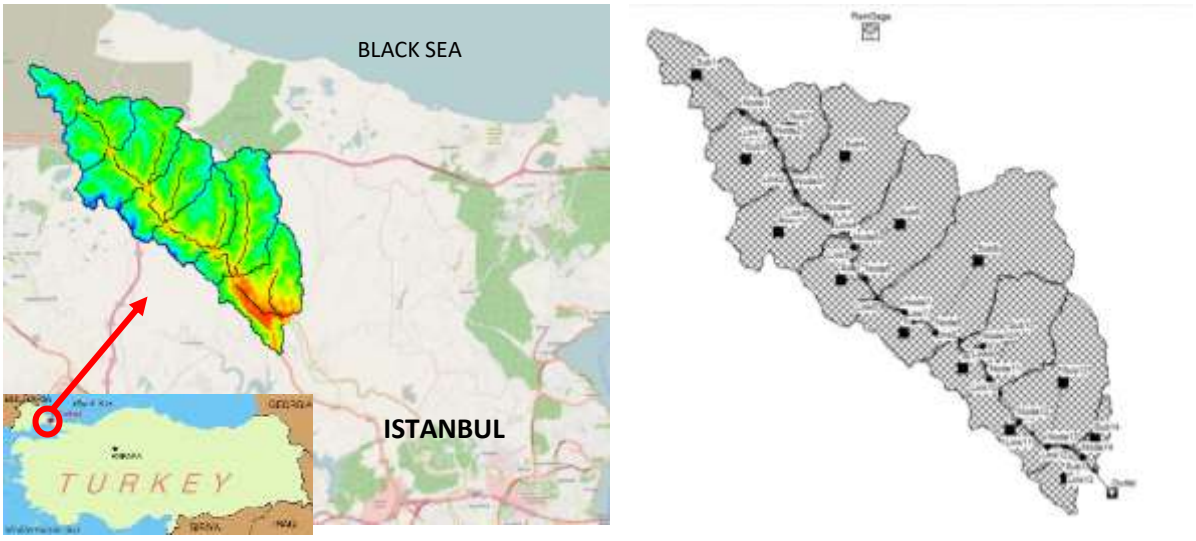

Figure 1. Location and watershed of Kağıthane Stream in Istanbul and its model in EPA-SWMM

RESULTS AND DISCUSSION

The most sensitive parameters of the hydrodynamic model are determined as Manning's roughness coefficient for both channels and sub catchments followed by the infiltration parameters, i.e., hydraulic conductivity and initial soil moisture condition. A decrease in Manning's roughness coefficient results in a crucial increase in the peak flow. In addition, Manning's roughness coefficient for channels affects also both the position and the shape of the hydrograph significantly. The infiltration parameters, namely hydraulic conductivity and initial soil moisture condition also affect the peak flow rates significantly. As a result of the analyses made, small differences were observed between the calculated Kinematic and

Dynamic wave equations. Table 2 shows that peak of flood depend on channel roughness, however, flood volume depend on accuracy of infiltration model. Change of channel from natural condition to lined channel increase peak of flow about 25 percent. Two methods of flood routing in channel show near result of peak respectly. This result shows Kinematic wave can be used instead of Dynamic wave method. However, flood flow is sensitive for roughness and infiltration methods.

Table 1. Scenarios for comparison Kinematic and Dynamic wave routing

Scenario No	Catchment loss	Channel Routing	Channel Condition
Scenario 1	Green-Ampt	Kinematic Wave	n=0.030
Scenario 2	Green-Ampt	Kinematic Wave	n=0.017
Scenario 3	Green-Ampt	Dynamic Wave	n=0.030
Scenario 4	Green-Ampt	Dynamic Wave	n=0.017
Scenario 5	Horton	Kinematic Wave	n=0.030
Scenario 6	Horton	Kinematic Wave	n=0.017
Scenario 7	Horton	Dynamic Wave	n=0.030
Scenario 8	Horton	Dynamic Wave	n=0.017

Table 2. Summary of results for Scenarios

Scenarios	KW-GA (0.030)	KW-GA (0.017)	DW-GA (0.030)	DW-GA (0.017)	KW-H (0.030)	KW-H (0.017)	DW-H (0.030)	DW-H (0.017)
	Green-Ampt				Horton			
	Kinematic Wave		Dynamic Wave		Kinematic Wave		Dynamic Wave	
	n=0.030	n=0.017	n=0.030	n=0.017	n=0.030	n=0.017	n=0.030	n=0.017
Runoff Depth (mm)	29.892	30.010	29.315	29.678	37.647	37.769	37.077	37.442
Runoff Peak (m^3/s)	84.02	104.92	77.03	107.66	84.96	104.15	78.14	105.98

CONCLUSIONS

Watershed models are interactive programs that utilize analytical methods, such as simulation and optimization algorithms, to help decision-makers formulate water resources alternatives, analyze their impacts, and interpret and select appropriate options for implementation. Moreover, hydraulic models use different forms of continuity and momentum equations, which are kinematic, diffusion and dynamic waves and represent wave routing of the surface. As a result of this study, it is concluded that two methods of flood routing in channel show near result of peak. This result shows Kinematic wave can be used instead of Dynamic wave method. However, flood flow is sensitive for roughness and infiltration methods.

REFERENCES

CROSSLEY, A.J., WRIGHT, N.G. and WHITLOW, C.D., 2003, Local time stepping for modeling open channel flows, Journal of Hydraulic Engineering-ASCE, 129(6), 455-462.

Cunge, J.A. 1969. On the subject of a flood propagation method (Muskinghum Method), J. Hydrol. Res., Vol. 7, No.2, 205-230.

LACKEY, T.C., and SOTIROPOULOS, F., 2005, Role of artificial dissipation scaling and multigrid acceleration in numerical solutions of the depth-averaged free-surface flow equations, Journal of Hydraulic Engineering-ASCE, 131(9), 755-769.

LIGHTHILL, M.J., WHITHAM, G.B. 1955. On kinematic waves. I. Flood movement in long rivers, Proceedings, Royal Society of London, London, England, Series A, Vol.229, No.1178, 281-316.
KAZEZYILMAZ-ALHAN, C.M. and MEDINA Jr, M.A., 2007, Kinematic and Diffusion Waves: Analytical and Numerical Solutions to Overland and Channel Flow, Journal of Hydraulic Engineering-ASCE, 133 (2), 217-228.
Lighthill, M.J., Whitham, G.B. 1955. On kinematic waves. I. Flood movement in long rivers, Proceedings, Royal Society of London, London, England, Series A, Vol.229, No.1178, 281-316.
Ponce, V.M. 1989. Engineering Hydrology: Principles and Practices, Prentice Hall, Inc, Englewood Cliffs, New Jersey 07632.
Saint-Venant, Barre de. 1871. Theory of unsteady water flow, with application to river floods and to propagation of tides in river channels, French Academy of Science, Vol. 73, 148-154, 237-240.
YING, X., KHAN, A.A., and WANG, S.S.Y., 2004, Upwind conservative scheme for the Saint Venant equations, Journal of Hydraulic Engineering-ASCE, 130 (10), 977-987.

ACCORDING TO THE SPEI DROUGHT INDEX, THE DROUGHT TREND PROJECTION IN TURKEY FOR THE NEXT CENTURY

Gülten ÇAMALAN[1], A.Serap AKGÜNDÜZ[1], Hanifi AYVACI[1], S.ÇETİN[1], H.ARABACI[1], M.ÇOŞKUN[1]

General Directorate of Meteorology-Ankara

gcamalan@mgm.gov.tr[1]; sakgunduz@mgm.gov.tr[1]; hayvaci@mgm.gov.tr[1]; harabaci@mgm.gov.tr[1]; mustafacoskun@mgm.gov.tr[1]

ABSTRACT

In this study, the monthly average temperature and monthly total rainfall data of the 1971-2015 period of the 123 meteorology observation stations with different climate characteristics selected from Turkey, and the regional climate projection data of the RCP 4.5 scenario of HADGEM2-ES model for 2016-2098 period were used. SPEI drought severity indices were calculated at 1, 3 and 12 month time scales with this data and the frequency of occurrence according to drought classes was obtained. The temporal and spatial changes of the frequency of occurrence of drought with the calculated SPEI values were examined and it was aimed to evaluate the climatic tendency which may exist in the future with reference to the climatology in the past periods. In this way, it is aimed to use projection models as a useful tool in the management of drought in order to provide scientific support for managers, researchers, public institutions and all interested parties, especially for agriculture, animal husbandry, agricultural production and environment.

***Keywords**: SPEI, Drought, HadGEM2-ES*

INTRODUCTION

Disasters have very important role in human life for a long time. One of the most important disasters is drought which is affecting widespread human populations. Although drought is a disaster which starts and develops slowly, it is the most difficult climatologic phenomenon to forecast. It is also continuous with its adverse effects by accumulating long time periods.

Drought could be defined as natural phenomena which causes degradation on hydrological balance and adverse effect over terrain and water resources as a result of significant decreasing of recorded normal levels of precipitation [1]. As well as many types of drought in literature, there are 4 significant type of drought which are meteorological drought, agricultural drought, hydrological drought and social-economical drought. [2]

All drought types begin firstly as a meteorological drought which means insufficient precipitation. Agricultural droughts follow this situation with decreasing soil moisture and decreasing evapotranspiration levels. Hydrological drought follows that by decreasing levels of river and dam water and this situation finally results in socio-economic droughts.

Drought is an important reason for agricultural, economic and environmental damages. Since the effects of drought have been slowly appear after a long time with lack of rainfall, it is difficult to determine beginning, content and end of drought. For this reason, it is hard to measure objectively period of droughts with regard to scope of density, magnitude, duration and areal. It has been made an effort for developing techniques about drought analysis and monitoring. Definition of quantative indexes is the most widespread approach among this, however subjectivity in definition of drought has made difficult to generate unique and universal drought index definition.

Many of studies about drought analysis and monitoring systems has been planned for two approaches:

1. Palmer Drought Severity Index (PDSI) which based on soil water balance equation [3]
2. Standardized Precipitation Index. (SPI) [4],

Drought indices are acknowledged as an efficient approach and method for monitoring and measuring of droughts, because the indexes provide to understanding of complicate interactions between climatic variables and climate related processes by summarizing.

The use of drought indices permits quantitative assessment of climatic anomalies in terms of severity, geographical spread and frequency of occurrence, as well as exchange of information on both the decision makers and between society and citizens about the drought conditions [5]. Standard Precipitation Index (SPI), that will be used to characterize meteorological drought by national meteorological and hydrological services, has been accepted by World Meteorological Organization (WMO). Besides, SPI only depends on precipitation data, which doesn'ttake into account other meteorological variables determining temperature, relative humidity, evaporation, winds speed etc...However some studies show that the precipitation is the main factor for determining the intensity of drought, period of drought and end of drought. As a result of increasing global temperatures at last 150 years, significant temperature increase has foreseen at 21st century by climate change models. The trends of increasing global temperatures show that the possibility of dramatic results on drought conditions. Increasing greenhouse gas levels such as CO_2 at Earth since the industrial revolution is a triggering factor for global warming. To slow this increases at global warming there are taken precautions for decreasing carbon emissions. On the other hand, severity of the drought and effects of drought are tried to predict by using statistical and amprical approaches. Usage of drought indices which include temperature data such as Palmer Drought Index (PDSI) are particularly prefered for applications that inculde climate scenarios. However PDSI is insufficient neither evaluating of drought that is related to different hydrological systems nor multi-scalar criterias which is neccesary to distinguish different types of drought. Therefore Normalized Precipitation-Evaporation İndex (SPEI) are formuleted that based on the precipitation and PET. SPI could not determine the role of increasing temperature values at drought conditions and the role of temperature variables and warm air currents independently of global warming scenarios, in response to this SPEI could explain the possible effects of temperature variability and extreme temperatures with the difference of global warming. SPEI has sensibility of PDSI against the fluctuations of latent heat and natural spatial distribution of SPI. The index had been developed by Vincente-Serrano at al. [6].

SPI is especially effective at determination and monitoring of drought and also explaining the results of global warming at drought conditions. [7;8;9]

The calculation and identification of the probabilities of various drought index classes (briefly drought) in drought determination, evaluation and monitoring studies to be carried out within the framework of a comprehensive and large-scale Drought Management Plan is very important in terms of the success of the management plan.

The primary purpose for evaluation of drought quality is determining and evaluating time of drought events and severity of droughts which occurs probabilistic terms in a particular location, region or basin. Thus, such a scientific assessment is very useful for describing droughts that have a certain time of return (frequency of occurrence) in terms of solving the

former drought events that have occurred in those areas in the past according to the existing evidence.

METHODS and DATA

In this study, that has been examined observation data which belongs to 123 Meteorological Observation Station in between 1971-2015 years by using SPEI method. In addition, it has been examined spatial variations in the frequency of occurrence of drought at 1,3,12 month scale and time dependent variations of SPEI values by using regional climate projection data at 2016-2098 years of HadGEM2-ES RCP4.5 scenario which is a global climate model. (Time-dependent variations could not be showed this paper due to the page limitation).

Climate projections for 2016-2098 years (monthly mean temperature and monthly total precipitation) has been produced by adding 1971-2000 period anomalies which is an observation reference period of stations that is used when the models runned to the anomaly values of the nearest grid points to the stations. The time interval of projections has been examined in terms of three periods (2016-2040, 2041-2070, and 2071-2098).

Application data for each period has been runned with observation data. The aim of this is to procure continuous for drought analysis. Although the future data hasn't got any effect at examined working period, initial data is important. However, series for calculating SPEI drought indices has been runned and examined in terms of three different period which is 1971-2040 period for 2016-2040 period, 1971-2070 period for 2041-2070 period and at 1971-2098 period for 2071-2098 period just in case future predictions could affect observation data.

After calculating the SPEI drought severity indices, the occurrence of frequency of drought categories (frequency possibilities) has been determined and possible tendency of drought in the future has been evaluated by referencing historical climatology of drought.

SPEI is based on climatic water balance (precipitation and evaporation) and it has been advised for determination of drought periods. 3 parameter log logistic distribution has been used by taking into consideration excess of negative values. Evaporation has been calculated by Thorntwaite Method [10]. Analysis of SPEI has been calculated according to distribution of Pearson Type III. The parameters of α, β and γ which belongs to this distribution has also been obtained by using L-Moment Method. L-Moments is a linear combination of probability weighted moments given by Greenwood [11] and that has been obtained by increasing or decreasing the observations

The simplest approach in PET calculations is the Thorntwaite method. The formula of the method, which uses average monthly temperature only, is like the following.

$$i = \left(\frac{t}{5}\right)^{1.514}$$

where i is the monthly temperature index and t is the average monthly temperature. The sum of "i" values for 12 months gives the annual temperature coefficient of I.

A= 6.75*10-7 *I3 -7.71*10-5 *I2 + 1.79*10-2 *I +0.492 multiplied by sunshine durations by the latitude of the stations for PET.

$$PET = 16 * K * \left[\frac{10 * T(I)}{I}\right]^{A}$$

K= correction coefficient calculated for the latitudes of the stations and months.

The difference between PET values for a given month and precipitation provides the amount of excess or deficiency of water.

$$Di = Pi - PETi$$

Tsakiris et al. (2007) showed that the P/PET ratio (the ratio of total monthly precipitation to potential monthly evapotranspiration) is also a suitable parameter to obtain a drought index which takes the process of global warming into account. However, considering the P/PET ratios, especially in winter months, the cases with PET values of "0" were undefined. The Di values can be calculated in different time scales (such as monthly, for 3, 6, 12, 18, 24 months). For example, the January 3-month Di value of a given year is the sum of the values of previous year's November and December, and that year's January.

While 2-parameter gamma distribution is used in SPI calculations, SPEI calculations use 3-parameter distribution. The L-moment method was used in parameter estimations of 3-parameter distributions.

L-moments of the Di series were obtained from probability weighted moments.
Probability weighted moments are obtained using the following formula;

$$w_s = \frac{1}{N} \sum_{i=1}^{N} (1 - F_i)^s * D_i$$

$\lambda 1 = w0$; $\lambda 2 = w0 - 2w1$; $\lambda 3 = w0 - 6w1 + 6w2$; $\lambda 4 = w0 - 12w1 + 30w2 - 20w3$

$$F_i = \frac{i - 0.35}{N}$$ (Hosking 1990).

Fi → Frequency estimator

i → Order numbers given by ordering D_i values in a way to obtain an increasing sequence
N→ Number of observations
3-parameter log-logistic distribution was used to standardize the Di = (Pi – PETi) series of 12 stations in the study area. The probability density function of the 3-parameter log-logistic distribution;

$$f(x) = \frac{\beta}{\alpha} \left(\frac{x-\gamma}{\alpha}\right)^{\beta-1} \left[1 + \left(\frac{x-\gamma}{\alpha}\right)^{\beta}\right]^{-2}$$

In this distribution function, α is the scale, β is the shape and γ is the position parameter (γ >Di < α)
The parameters of the log-logistic distribution can be obtained in various ways. However, the l-moment method is the simplest approach (Ahmad et al. 1998).
The parameters of Pearson type III distribution are obtained after calculating the l-moments.

$$\beta = \frac{2w_1 - w_0}{6w_1 - w_0 - 6w_2} \; ; \qquad \alpha = \frac{(w_0 - 2w_1) * \beta}{\Gamma\left(1+\frac{1}{\beta}\right)\Gamma\left(1-\frac{1}{\beta}\right)} \; ; \; \gamma = w_0 - \alpha\, \Gamma\left(1 + \frac{1}{\beta}\right)\Gamma\left(1 - \frac{1}{\beta}\right)$$

Here, Γ(β) is the gamma function of beta.
Log-logistic distribution represents the Di series very well in all time scales.
The probability distribution function of the Di series based on log-logistic distribution;

$$F(x) = \left[1 + \left(\frac{\alpha}{x-\gamma}\right)^{\beta}\right]^{-1}$$

while with F(x), SPEI is calculated as the standardized variable of F(x) like the following;

$$SPEI = w - \frac{C_0 + C_1 w + C_2 w^2}{1 + d_1 w + d_2 w^2 + d_3 w^3}$$

where $w = \sqrt{-2\, ln(P)}$ → for P≤0.5
While P is the probability of exceeding a certain D value, P= 1-F(x).

If P>0.5, then P is replaced by 1-p and the sign of SPEI is reversed. In this formulation, the constants are;
C0 = 2.515517; C1 = 0.802853; C2 = 0.010328
d1 = 1.432788; d2 = 0.189269; d3 = 0.01308
SPEI's mean is 0 and standard deviation is 1. As SPEI is a standardized variable, it is related to other SPEI variables in the area time dimension.

After the calculation of SPEI drought index, frequency probabilities has been calculated for each station according to drought classes. Probablities have been obtained by rating each drought class over total occurance of droughts [12].
$P(A) = \lim_{n\to\infty} \frac{n_a}{n} P(A)$: Relative probability (probability of frequency), n_a :Number of occurrence desired event , n:number of all events.

In fact, normal drought class shows the sum of moderately wet drought and moderately dry. For this reason this class interval has been regulated Figure 1, in accordance with the purpose of this study.

Table:1 SPEI category of drought intervals

SPEI	Class of Drought
≥ 2.00	Extremely wet
1.50 –1.99	Severely wet
1.00 – 1.49	Moderately wet
0.99-(-0.99)	Normal wet
(-1.00) – (-1.49)	Moderately drought
(-1.50) – (-1.99)	Severely drought
(-2.00) ≥	Extremely drought
(-2.00) ≥	Extremely drought

Table:2 Fixed SPEI category of drought intervals

SPEI	Class of Drought
≥ 2.00	Extremely wet
1.50 –1.99	Severely wet
1.00 – 1.49	Moderately wet
0.0 – 0.99	Lightly wet
0.0 – (-0.99)	Lightly drought
(-1.00) – (-1.49)	Moderately drought
(-1.50) – (-1.99)	Severely drought

RESULTS AND DISCUSSION

The analyses show that if the period of time increases the frequency of drought is less but it is also long-acting effective. In the period of 1-3 months, drought gets more frequent but the duration of its effect shortens; however, as the time period enlarges, the duration of drought effect increases, while its occurrence frequency decreases in especially the period of 12 months.

Although the issues that has been faced on short term severe drought periods are same with the issues which is long duration drought, the damages that occurs in droughts which last longer periods will be more effective. Therefore, precautions which will take for drought, should be generated by taking into account the severity of drought events, areal consistency of drought and duration of drought.

On the basis of 12-months-scale, it is estimated that SPEI drought severity frequency possibilities that concentrate on Damp Dry part of normal class have the tendency [13] to slip through a higher drought class as being lightly drought (Figure: 1-3) at 2016-2040 and 2071-2098 periods and as being drought at medium level at 2041-2070 period regarding the drought severity classes with the increase on heat and decrease on rain for 2041-2070 period at HadGEM2-ES RCP4.5 model projection climate data according to the existing observations all around Turkey (Figure: 2).

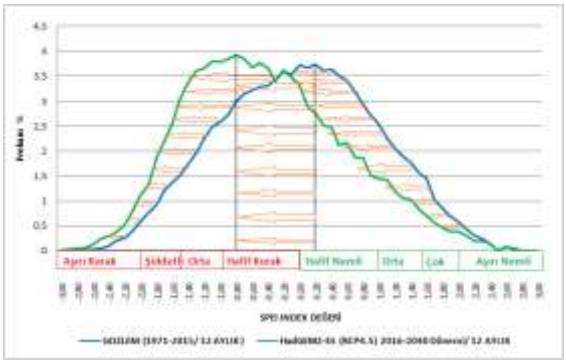

Figure-1 Turkey-Wide Observation (1971-2015) and SPEI Frequency Possibility Change at HadGEM2-ES RCP4.5(2016-2040)Period on 12-Months Basis

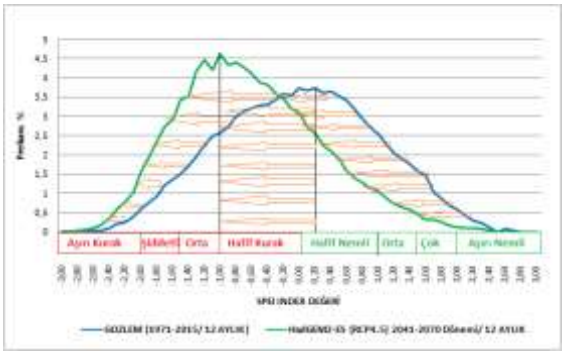

Figure-2 Turkey-Wide Observation (1971-2015) and SPEI Frequency Possibility Change at HadGEM2-ES RCP4.5(2041-2070)Period on 12-Months Basis

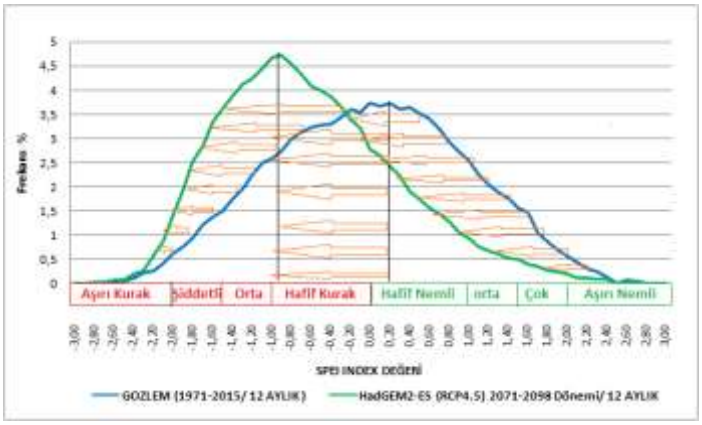

Figure-3 Turkey-Wide Observation (1971-2015) and SPEI Frequency Possibility Change at HadGEM2-ES RCP4.5(2071-2098)Period on 12-Months Basis

The current evaluations and predictions of drought periods are been given in the following Figures based on 12 months and on spatial distribution.

The distributions of the increases and decreases has also been examined by adding the difference maps of HagGEM2-ES 4.5 scenario from the observations with the observation data's and model predictions.

The possibilities of frequency at normal class which includes lightly drought and lightly wet class have been mostly seen in Turkey. As it is expected that the extreme drought frequency possibilities, which range on 0-4% scale within observations (Figure: 4a), increase (5-9%) at 2016-2040 period of projection, in around Central Black Sea, the eastern part of Aegean Region, the western part of Central Anatolia, West Thrace, Eastern Mediterranean and in Igdir, Gumushane, Batman and Siirt it is also expected to protect the current situation in around Mugla and Mersin and to have a decrease in Erzurum (Figure: 4b-e).

Northern Marmara, Western Black Sea and Central Black Sea shores are foreseen to keep their current situation on observations at 2041-2070 period while regions other than those are predicted to have an increase as the highest increase is envisaged to be in Artvin, Ardahan and Kars (9%). (Figure: 4c-f). It is foreseen that a decrease at 2071-2098 period in Central Anatolia and Central Black Sea shores and interiors is expected while other places are expected to have an increase. (1-6%) (Figure: 4d-g).

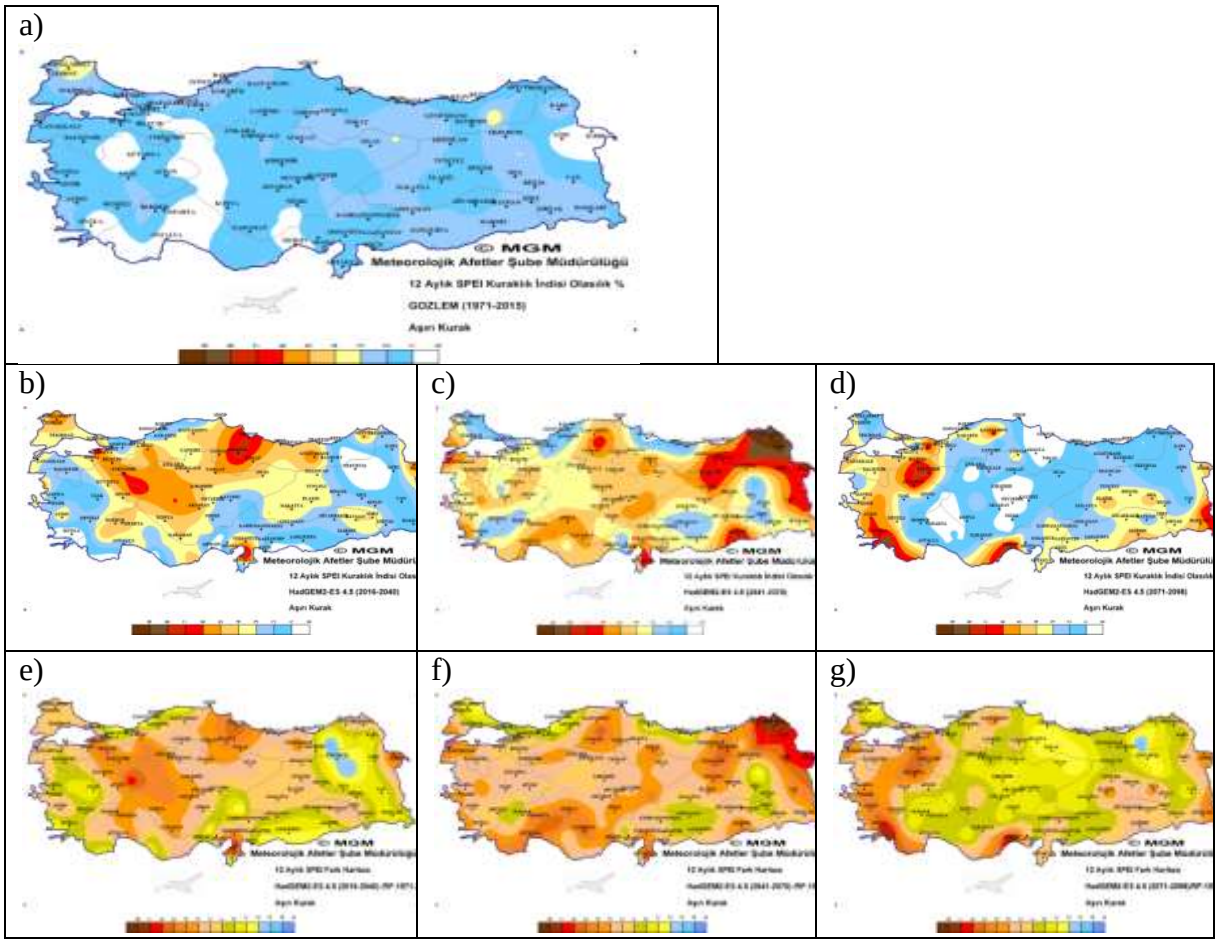

Figure-4 Geographical distribution of frequency possibilities of extremely drought class over Turkey

a. Observation
b. HagGEM2-ES 4.5 (2016-2040)
c. HagGEM2-ES 4.5 (2041-2070)
d. HagGEM2-ES 4.5 (2071-2098)
e. HagGEM2-ES 4.5 (2016-2040)/(RF: 1971-2015) The Difference Map
f. HagGEM2-ES 4.5 (2041-2070)/(RF: 1971-2015) The Difference Map
g. HagGEM2-ES 4.5 (2071-2098)/(RF: 1971-2015) The Difference Map

Severity drought probability frequencies has been reached the highest values for observations at Southern Marmara, Inner Aegean Region, West and East Mediterranean Region, Eastern part of Central Anatolia, Eastern part of Southeastern Anatolia Region, middle part of Eastern Anatolia Region and around the Igdir (Figure 5a). During the period of 2016-2040 of projection, coastal regions of Thrace, West and East Black Sea and coastal regions of Western and Eastern Black Sea in 2041-2070 / 2071-2098 periods are predicted to protect the situation in the observations. It is predicted that other places outside these regions will show an increase in the period of 2016-2040 and the highest increase will be around Şanlıurfa, Uşak and Giresun (Figure 5b-e). In the period of 2041-2070, an increasing trend is predicted, with the Central Black Sea (Samsun), Göller Region (Burdur), Niğde, Kahramanmaraş, Malatya and Batman circles being higher. (%18-20) (Şekil:5c-f). It is predicted that increases in the period of 2071-2098 will be continued in Göller Region (Isparta, Burdur) (22%) (Figure: 5d-g).

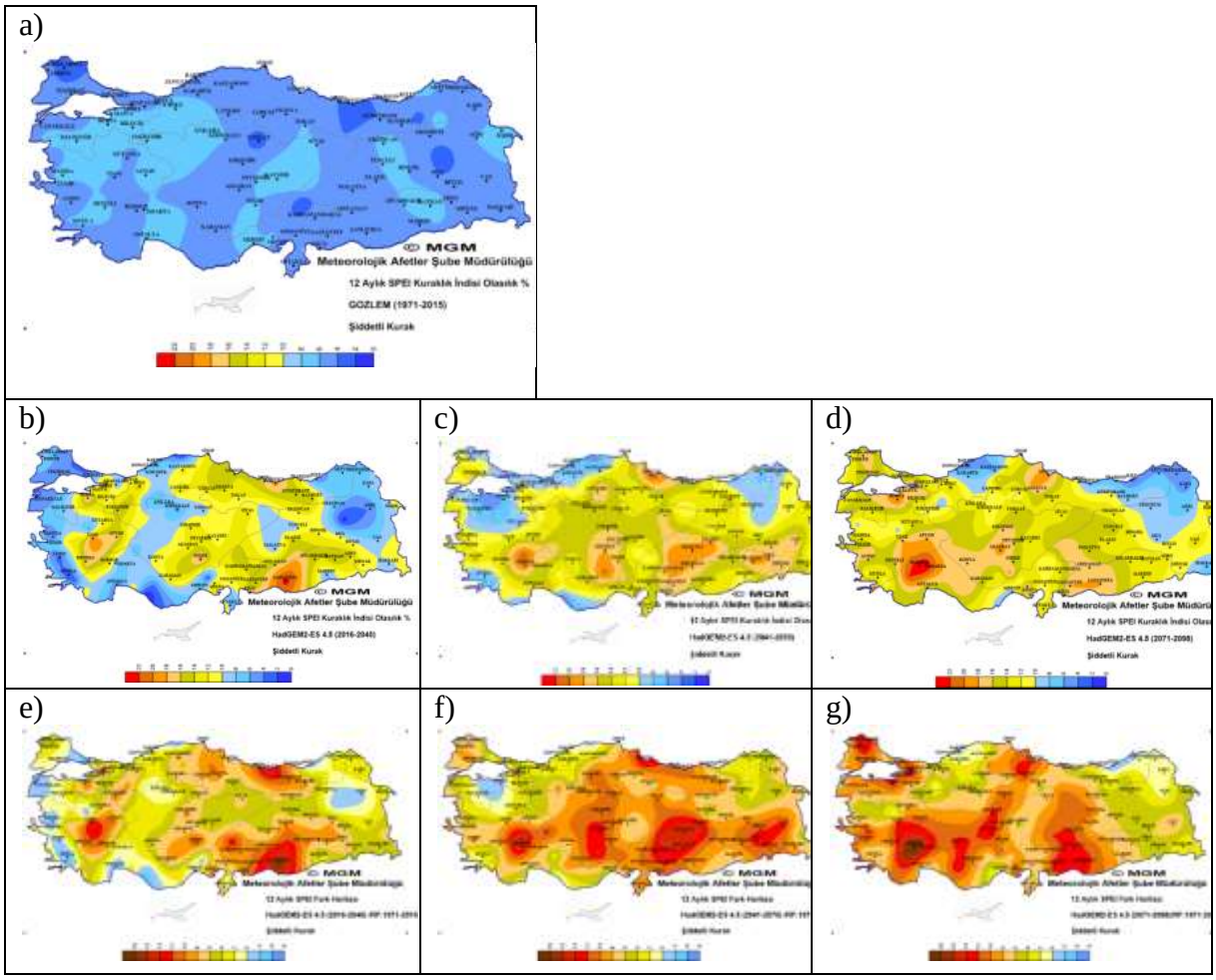

Figure:5 Geographical distribution of frequency possibilities of extremely drought class over Turkey for 12 months

a. Observation
b. HagGEM2-ES 4.5 (2016-2040)
c. HagGEM2-ES 4.5 (2041-2070)
d. HagGEM2-ES 4.5 (2071-2098)
e. HagGEM2-ES 4.5 (2016-2040)/(RF: 1971-2015) The Difference Map
f. HagGEM2-ES 4.5 (2041-2070)/(RF: 1971-2015) The Difference Map
g. HagGEM2-ES 4.5 (2071-2098)/(RF: 1971-2015) The Difference Map

Moderately dry frequency probabilities for observations are higher in the Aegean coastal areas, coastal and inland parts of the Central and Eastern Black Sea, Mediterranean, Southeastern Anatolia and around Ağrı, and lower in other places (6-14%). In the 2016-2040 period of the projection, while the Southern Marmara region is expected to protect the situation, in the western observations, Turkey shows an increase trend in other regions (12-34%), higher in Ankara and its vicinity (Figure: 6b-e). It is also expected this increasing trend will continue in 2041-2070 period and it will be more pronounced in Southeastern Anatolia (12-36%). Similarly, in the 2071-2098 period, higher increasing trend is expected to continue especially in Southeastern Region of Turkey (%12-30) (Figure:6d-g).

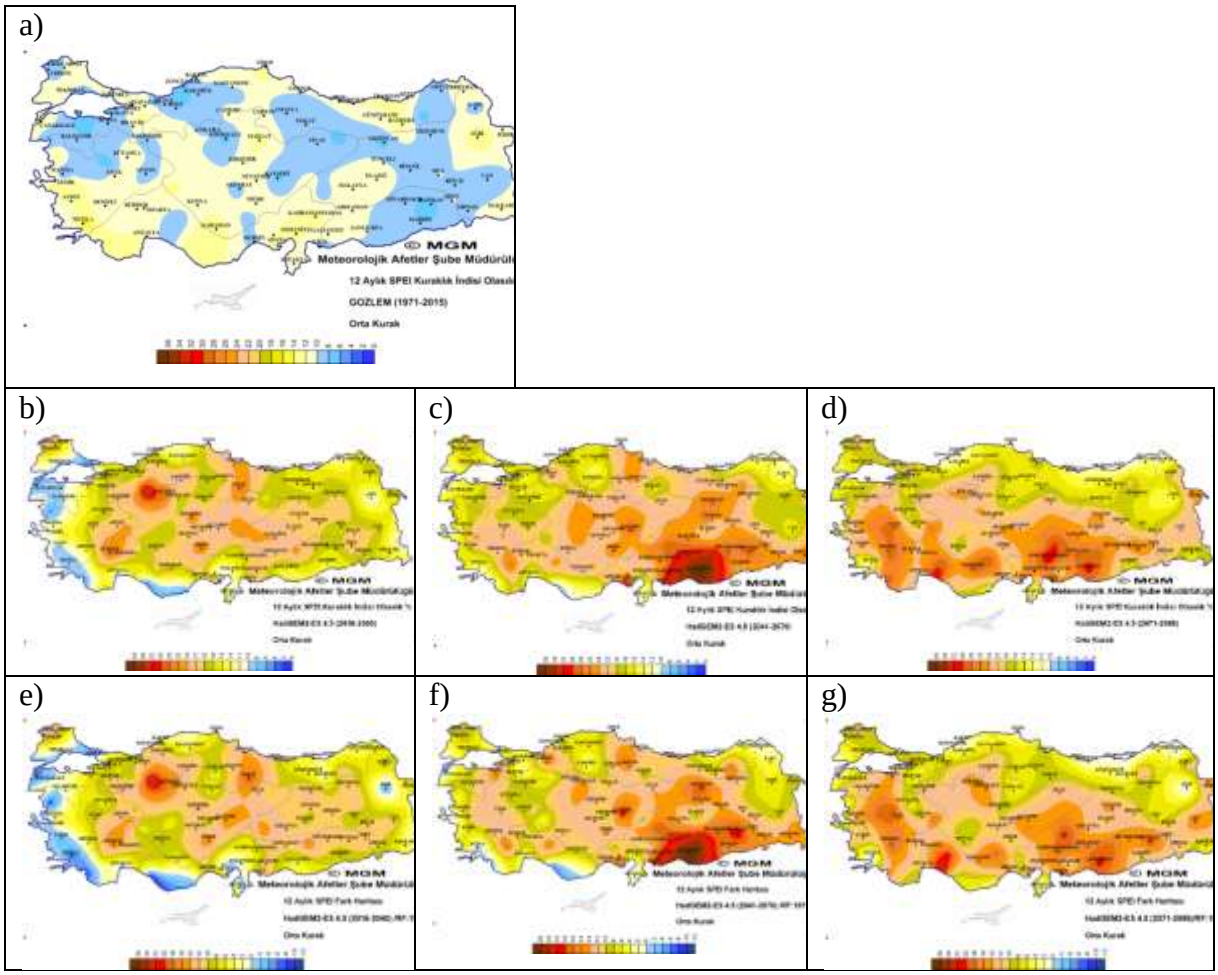

Figure:6 Geographical distribution of frequency possibilities of moderately drought class over Turkey for 12 months

a. Observation
b. HagGEM2-ES 4.5 (2016-2040)
c. HagGEM2-ES 4.5 (2041-2070)
d. HagGEM2-ES 4.5 (2071-2098)
e. HagGEM2-ES 4.5 (2016-2040)/(RF: 1971-2015) The Difference Map
f. HagGEM2-ES 4.5 (2041-2070)/(RF: 1971-2015) The Difference Map
g. HagGEM2-ES 4.5 (2071-2098)/(RF: 1971-2015) The Difference Map

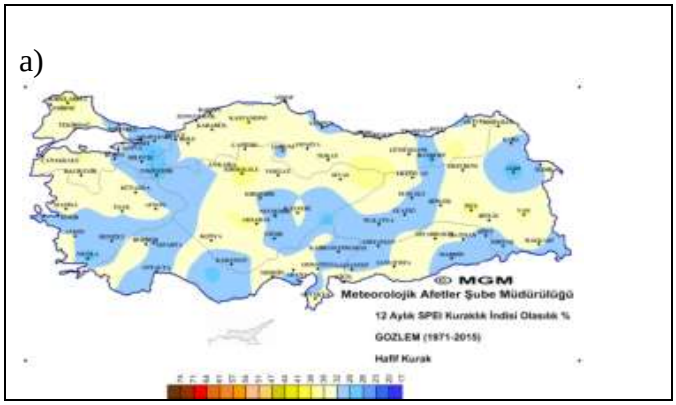

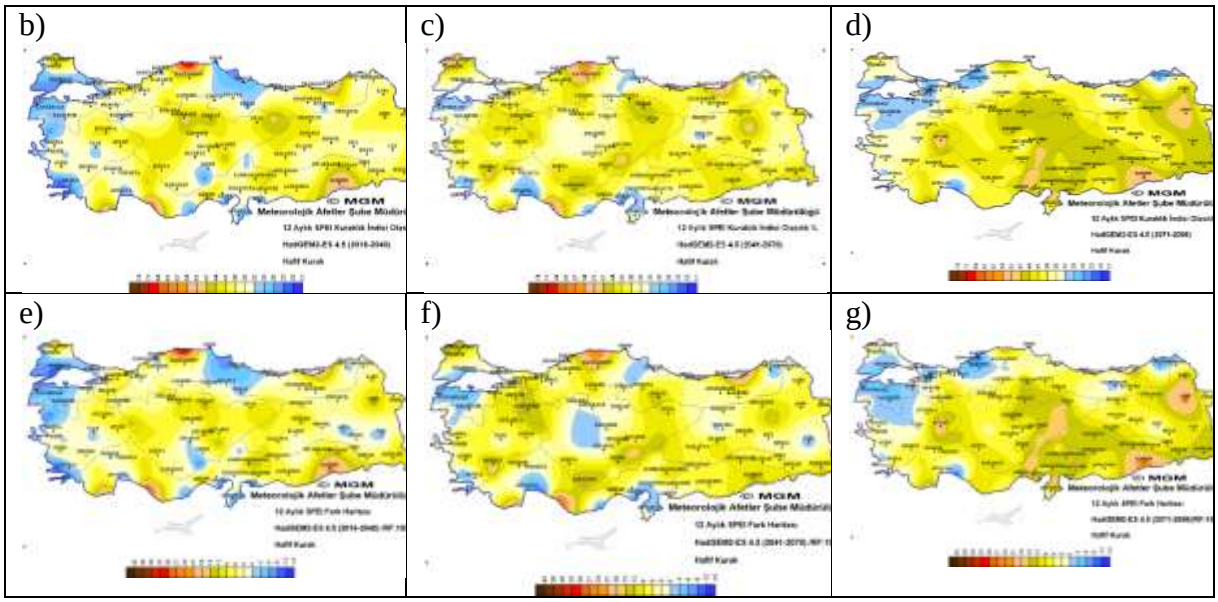

Figure:7 Geographical distribution of frequency possibilities of lightly drought class over Turkey for 12 months

a. Observation
b. HagGEM2-ES 4.5 (2016-2040)
c. HagGEM2-ES 4.5 (2041-2070)
d. HagGEM2-ES 4.5 (2071-2098)
e. HagGEM2-ES 4.5 (2016-2040)/(RF: 1971-2015) The Difference Map
f. HagGEM2-ES 4.5 (2041-2070)/(RF: 1971-2015) The Difference Map
g. HagGEM2-ES 4.5 (2071-2098)/(RF: 1971-2015) The Difference Map

Moderately drought frequency probabilities are approximately 22-38 % (Figure:7a). In the 2016-2040 period of the projection, observations are expected to protect their situation for the coastal and inland parts of the Central Black Sea and the northern part of the Marmara region and western part of Istanbul and Tekirdağ and the west part of Southern Marmara region. It is also predicted that all regions will show an increase trend with the coastal side of Western Black Sea being higher. This values which belongs to 2016-2040 period of the projection, will be expected to decrease in the 2041-2070 period of the projection. In the period of 2071-2098, it is foreseen that while the increase will be seen in Central Anatolia, Inner Aegean, Eastern and Southeastern Anatolia Regions, there is an expected lower tendency than the situation for the Western Black Sea, Southern Marmara Region and Thrace regions show a lower tendency than observed situation (Figure: 7d-g).

REFERENCES

Birleşmiş Milletler Çölleşme ile Mücadele Sözleşmesi - BMÇMS (1997). Çevre Bakanlığı Yayınları. Ankara.

Wilhite, David, and Glantz, M.R.(1987). Understanding the drought phenomenon-The role of definitions, in Wilhite, David, Easterling, William, and Wood, David, eds., Planning for drought: Boulder, Colo., Westview Press, p. 11-27.

Palmer, W.C., (1965). Meteorological Drought Research Paper No. 45. Office of Climatology U.S. Weather Bureau, Washington.

Mckee,T.B.,N.J.Doesken, and J.Kleist, 1993: The relationship of drought frequency and duration to time scales. Eight of Con.on Applied Climatology, Anaheim,CA, Amer.Met.Soc. 179-184

Türkeş, M. ve Tatlı , H. (2010). "Kuraklık ve Yağış Etkinliği indislerinin Çölleşmenin Belirlenmesi, Nitelenmesi ve izlenmesindeki Rolü" Çölleşme ile Mücadele Sempozyumu Bildiriler Kitabı, 245-263, Çorum.

Vicente-Serrano, Sergio M. A Multi-Scalar Drought Index Sensitive to Global Warming: The Standardized Precipitation Evapotranspiration Index–SPEI,2009

https://climatedataguide.ucar.edu/climate-data/standardized-precipitation-evapotranspiration-index-spei

http://spei.csic.es/index.html

http://spei.csic.es/home.html

Thorntwaite, C.W.1948: an approach toward a rational classification of climate. Geogr.Rev.328,55-94

Hosking J.R.M.,1990: L-Moments: Analysis and estimation of distributions using lineer combination of order statistics. J.Roy.Stat.Soc. 52B, 105-124

Chow , V. T., D.R.Maidment , ve L.R. Mays , Applied Hydrology, McGraw-Hill Inc., Newyork,1988.

Yeni Senaryolar ile Türkiye İklim Projeksiyonları ve İklim Değişikliği, MGM Yayınları, Ankara,2015

REGIONAL LOW FLOW AND DROUGHT ANALYSIS FOR EASTERN BLACK SEA BASIN

Dilara Karınca[1], Elif Kartal[1], Cemre Yürük[2], Aslı İlhan[2], Ahmet Nuri Şahin[2], Bihrat Önöz[1]

[1] Istanbul Technical University, Department of Hydraulics and Water Resources Engineering, Istanbul, Turkey
[2] Istanbul Technical University, Department of Meteorological Engineering, Istanbul, Turkey
dilara.karinca@hotmail.com

Abstract

In this study, regional low flow analysis was carried out by using data of five flow stations located in Eastern Black Sea Basin. In order to verify flow stations are in homogeneous region, statistical consistency between data of flow stations was defined. According to estimated confidence interval, it was found that flow stations belong homogeneous region except for station numbered 2228. Weighted averages of L moments of dimensionless flow data set of flow stations that are in same homogeneous area were calculated. General Extreme Value (GEV) distribution was deemed compatible for regional low flow analysis. Dimensionless low flow values were estimated for every station and 10, 50 and 100 year recurrence intervals. Due to the dimensionless flow data, the estimated values of the regional 7-day minimum flow were obtained for each station. Mean annual flow data of hydro metric stations during 1968 and 1999 were used for regional drought analysis. According to selected threshold value and critical area percentage, runs analysis was applied. The mean and standard deviations of observed regional drought periods and total water deficiencies were calculated. According to the findings obtained; it has been found that average and standard deviation of drought duration is three years.

Keywords: *Regional Low Flow Analysis, Regional Drought Analysis, Runs Analysis.*

INTRODUCTION

Low flows are randomly changing hydrological processes that occur during rainless periods. Analysis of low flows and drought is important in reducing the adverse effects of dry periods. In this study, regional low flow analysis and drought analysis were carried out using the data of 2202, 2218, 2228, 2232 and 2247 flow monitoring stations within the Eastern Black Sea Basin. Low flow analysis was performed with 7-day minimum flow data between 1963 and 1999. Drought analysis was carried out between 1968 and 1999 with daily flow data.

For low flow analysis, it was investigated whether the data of the stations belong to a statistically significant group. According to statistically significant group, regional L-moments and General Extreme Value distribution parameters were determined. Low flow values were estimated for every station and 10, 50 and 100 year recurrence intervals by using GEV.

Runs analysis was used for regional drought analysis. The weight coefficients of the stations were determined as the ratio of the drainage area to the total drainage area. The average duration of drought is 3 years for the selected threshold level ($q = 0.5$) and the critical area percentage ($A_c = 0.33$).

METHODOLOGY

Before performing a regional analysis, it is necessary to statistically define the compatibility between all stations. C_{vx} (coefficient of variation) obtained separately from each station data were used to identify the stations that constitute a meaningful group and to define homogeneous

regions. Due to weighted average C_{vx} based on the number of annual data of flow observation stations, maximum and minimum values (confidence interval) were calculated for homogeneous region. In this example, since the variation coefficients of all flow observation stations are not within the confidence interval, the stations are divided into two regions. After separation, the homogeneity of the each region was retested and the homogeneity was verified. After the station data is divided into its own average and made dimensionless, the variation coefficients (C_{vx}) and the skewness coefficients (C_s) of each station are calculated by using L-moments. Regional variation coefficient was computed using weighted average of C_{vx} of stations data with observation periods. The regional variation coefficient (C_s) and L moments parameters were calculated by similar calculation method. The regional L_3/L_2 and L_4/L_2 values for the three parameter distributions are shown in Figure 1. It is accepted that the General Extreme Value (GEV) distribution is proper because the marked point is closest to the curve of the GEV distribution. Since the three-parameter general extreme value (GEV) distribution is selected as the regional distribution function by the L-moment diagram method, k, α and u parameters were determined and dimensionless low flow values were estimated for every station and 10, 50 and 100 year recurrence intervals. The averages of the stations' own flow values were multiplied by the calculated dimensionless estimated values. Thus, estimated low flows were calculated by regional analysis of the stations.

For regional drought analysis, annual averages of daily flow values of flow monitoring stations are used. The values of 1968 and 1999 are taken into consideration as the common data range at all stations. All the auxiliary variables and drought characteristics were defined by Santos (1983). As to the critical area (A_c=0.33) it will be defined as a significant proportion of the region area. Drainage basin areas, selected threshold value (q = 0.5), total local water deficiencies below this threshold (negative run sums), maximum drought run intensities (maximum point deficiency) were used as drought parameters. The mean and standard deviations of regional drought duration (L) and total regional areal deficit (U), proportion of temporal drought area (A), temporal total regional areal deficit (I) were obtained.

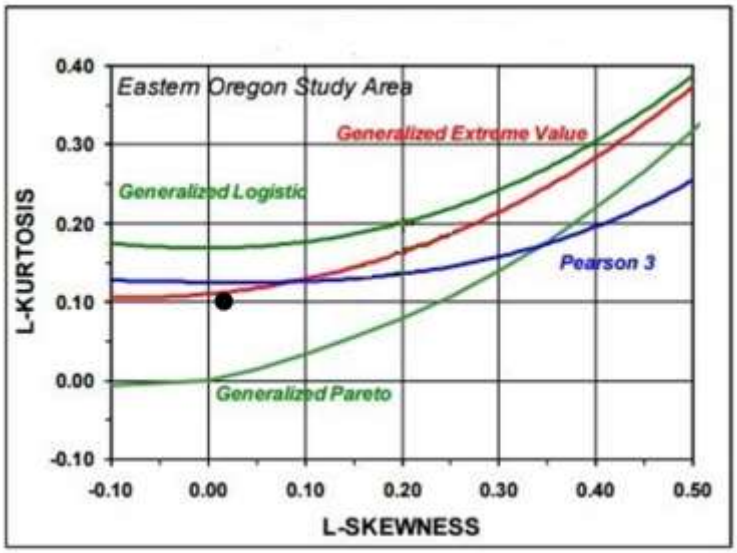

Figure 1. L-moment ratio diagrams for three parameters distributions

FINDINGS

The expression of the general extreme value (GEV) distribution, which is the theoretical asymptotic distribution for minima, was obtained by Önöz and Bayazıt (1999). Using L moments, we calculated the parameters of the distribution as k = 0.35, α = 0.23 and u = -1.07.

After the parameters of the distributions have been determined, non-dimensional regional 7-day minimum flows for 10, 50 and 100 year recurrence intervals were calculated as 0.71, 0.58, and 0.54 respectively. Regional minimum flows estimates (see Table 1) are obtained by multiplying non-dimensional regional 7-day minimum flows by average of stations own flows. Average of daily flow values were annualized for regional drought analysis. The common time period of data range was carried out as 1968 and 1999. The weight coefficients of the stations were determined as the ratio of the drainage area to the total drainage area. The weight coefficients were 14.8%, 19.5%, 4.5%, 17.8%, and 43.4% for the flow monitoring stations 2202, 2218, 2228, 2232, 2247 respectively. According to these weight coefficients, regional average annual water volume was computed as $676.7*10^6$ (m^3). The selected threshold level (q) is the average, in other words 0.5. Percentage of critical area (Ac) of observed drought was determined as 0.33. In these premises, mean and standard deviations of observed proportion of instantaneous deficit-area (As), proportion of instantaneous drought affected area (Ad), instantaneous regional areal deficit (D), instantaneous drought areal deficit (Dd), regional drought duration (L), total regional areal deficit (U), proportion of temporal drought area (A), temporal total regional areal deficit (I) (see Table 2) were figured out.

Table 1. Regional 7-day minimum flow estimates of the stations according to various recurrence intervals

T (year)	Q/Q_{mean}	2202 (m^3/s)	2218 (m^3/s)	2232 (m^3/s)	2247 (m^3/s)
10	0.71	1.37	6.24	5.79	2.29
50	0.58	1.12	5.09	4.72	1.86
100	0.54	1.05	4.77	4.42	1.75

Table 2. Parameters of observed droughty periods

Auxiliary variables and drought characteristics	A_s	A_d (%)	D	D_d (10^6 m^3)	L (Year)	U (10^6 m^3)	A (%)	I (10^6 m^3/year)
Average	0.53	0.48	53	74	2.8	202	0.7	75
Standard deviation	0.30	0.37	58	59	2.6	164	0.2	47

CONCLUSIONS

The following results were obtained from the regional low-flow and drought analysis for the Eastern Black Sea Region. Except for 2228 flow station, the other stations constitute a meaningful group for homogeneous regions. For the regional analysis on the remaining stations, it was determined that the proper distribution is the 3 parameter GEV distribution. Non-dimensional regional 7-day minimum flows for 10, 50 and 100 year recurrence intervals were calculated as 0.71, 0.58, and 0.54 respectively. Local drought analysis has examined the situation in which at least 33% of the system is below the average flow. Low flow (below average value) will be seen on average 48% of the system in a dry year. In dry years. the average water volume deficit in the system is $73.61x10^6$ m^3. Average duration of drought was found 3 years.

REFERENCES

Önöz. B. and Bayazıt. M. "GEV-PWM Model for Distribution of Minimum flows". J. Hydr. Engrg.. ASCE. Vol.4(3) (1999):289–292.

Santos. M.A. "Regional droughts: A stochastic characterization" J. Hydrol.. 66 (1983): 183—211

REGIONAL FLOOD FREQUENCY ANALYSIS FOR EASTERN BLACK SEA BASIN

Cemre Yürük[1], Aslı İlhan[1], Dilara Karınca[2], Elif Kartal[2], Ahmet Nuri Şahin[1] and Bihrat Önöz[2]

[1]Istanbul Technical University, Department of Meteorological Engineering, Istanbul, Turkey
[2] Istanbul Technical University, Department of Hydraulics and Water Resources Engineering, Istanbul, Turkey
yurukc@itu.edu.tr

Abstract

In a regional flood frequency analysis, data from all stations in a region where has statistically similar characteristics are evaluated together. In this study, regional flood frequency analysis was performed by using high flows of Ağnas, Şimşirli, Bahadırlı, Topluca ve Gocallı stations that locates in Eastern Black Sea Basin. It was confirmed that the stations locate in the same homogenous region with respect to confidence interval test. Thus, the frequency analysis was applied by considering the area as a single region. General Extreme Value (GEV) Distribution was selected for the calculation of frequency analysis. Due to the calculation of Xp quantile, the parameters of GEV were determined by using regional coefficients. Therefore, Q/Qavg ratios for the 10, 25, 50, 100, 200, and 500 return intervals in Eastern Black Sea Basin were calculated. The dimensionless flood values are representative for all stations in the homogeneous region. Thus, the flood values of any station can be easily determined by using an average maximum current in the homogeneous region. The flood values obtained by collecting data from all the stations in the region give more reliable results than the flood values calculated for the individual stations.

Keywords: *GEV distribution, maximum flows, regional flood frequency analysis*

INTRODUCTION

The Eastern Black Sea Basin is a region of high flood risk in Turkey due to its rich water resources and heavy rainfall during the year. The floods that have taken place in the past years have caused the loss of life, property and land in the region. It is important that flood analyzes of Eastern Black Sea Basin are perform correctly in order to carry out reigional agricultural policies, water projects and urbanization planning. Regional analysis is based on homogeneity. Since the available records are usually short, the flood forecasts made for long return intervals based on data from a single station can not be reliable. Therefore, using all the datasets of the stations together in the homogeneous region can make more meaningful estimations. The purpose of the flood frequency analysis is to predict the flood that corresponds to a certain return interval (such as 50, 100, 500 years) in the region. For this reason, general extreme value (GEV) distribution estimated by L-moments method was selected as the regional distribution function and it was aimed to find the expected flow values exceeded every 10, 25, 50, 100, 200, 500 years in the region.

DATA AND METHODS

This study covers the analysis of annual high flows provided from five different stations. The locations of stations that are situated in Eastern Black Sea Basin are shown with red circles in Figure 22. Şimşirli station (2218) has the highest elevation with 308 meters whereas Bahadırlı station (2228) is at the lowest altitude with 17 meters. Gocallı station, which is numbered as 2247 and locates at the westernmost part of the basin, has the maximum water collecting capacity with the drainage area of approximately 1860 km^2 and is still open. However, the drainage area of Bahadırlı station is 191.4 km^2, which corresponds to minimum water collecting

capacity within the stations. L-moments are considered for regional frequency analysis, while product moments (variation coefficients) are used to determine the homogeneous region. The data of all stations are rendered dimensionless and used together for regional flood analysis. The stations data are divided into its average in order to make dimensionless. Therefore, the average of high flows for each station is calculated. The average current values for 2202, 2218, 2228, 2232 and 2247 stations are 95.8 m^3s^{-1}, 166.2 m^3s^{-1}, 80.7 m^3s^{-1}, 179.4 m^3s^{-1} and 398.0 m^3s^{-1}, respectively.

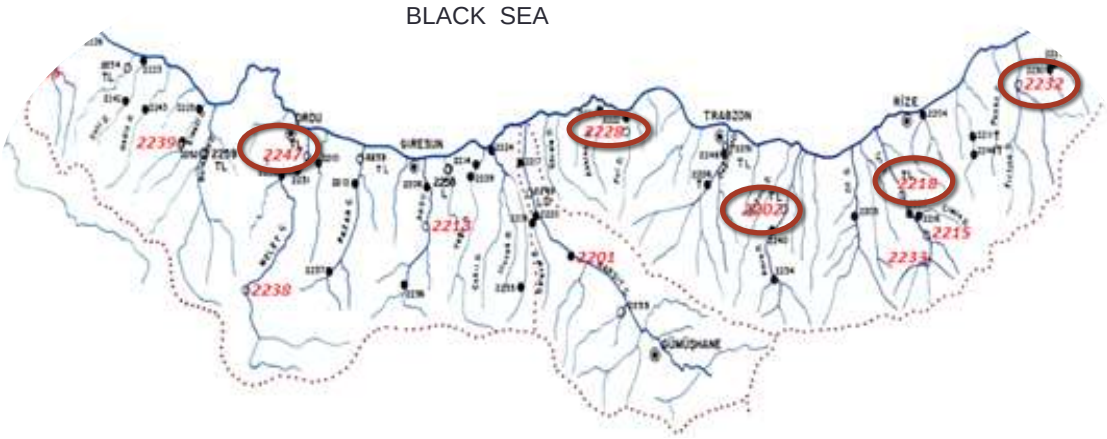

Figure 22. The locations of stations (shown with red circles) in Eastern Black Sea Basin.

APPLICATION AND RESULTS

The confidence interval test indicates whether the entire basin can be considered as a homogeneous zone or not. The confidence interval was set between 0.63 and 0.38 by using the average variation coefficient (Cv_x=0.5) of the basin and the average recording period (n=47.6) of stations. Since the largest and smallest coefficients of variation shown in Table 12 are within this confidence interval, it has been statistically confirmed that the stations fall in the same homogeneous region. Therefore, the region did not need to be divided into different areas for the frequency analysis. To find the best distribution function for basin, various distribution functions for each station were performed and General Extreme Value (GEV) was selected as best fitted distribution for the basin. The stations data was divided into its average to make dimensionless and then, the variation coefficients (L-Cv_x) and the skewness coefficients (L-Cs_x) of each station were calculated by L-moments method in order to calculate the parameters of the GEV distribution. The weighted averages of these coefficients (given in Table 12) were taken to represent the basin. Thus, the regional variation coefficient and the regional skewness coefficient were determined as 0.25 and 0.29, respectively. These regional coefficients were used in calculation of GEV parameters, which are ξ=154.89 and α=8.91. X_p quantile corresponding to a probability of p was drived from following formula (Önöz & Bayazıt, 2008) and the ratios Q/Q_{avg} for the 10, 25, 50, 100, 200, and 500 return intervals in Eastern Black Sea Basin were calculated as 1.79, 2.32, 3.24, 5.17, 9.18 and 21.85, respectively.

$$X_p = \xi + \frac{\alpha}{k}\{1 - [-\ln(F)]^k\}$$

Table 12. Calculated statistical moments and L-moments for the stations.

Station No	Record Period (Years)	Variation Coefficient (Cv_x)	L-Variation Coefficient (L-Cv)	L-Skewness Coefficient (L-Cs)
2202	47	0.44	0.22	0.13
2218	47	0.51	0.25	0.41
2228	48	0.58	0.31	0.24
2232	50	0.43	0.19	0.40
2247	46	0.55	0.30	0.25

The flood values can be determined after multiplying Q/Q_{avg} ratios by the average of maximum current of any station in the homogeneous region. The flood values for the 10, 25, 50, 100, 200, and 500 return intervals in Eastern Black Sea Basin are given in Figure 23. The flood corresponds to 500 return interval is excluded from Figure 23 because of its high value (8695.03 m^3s^{-1}).

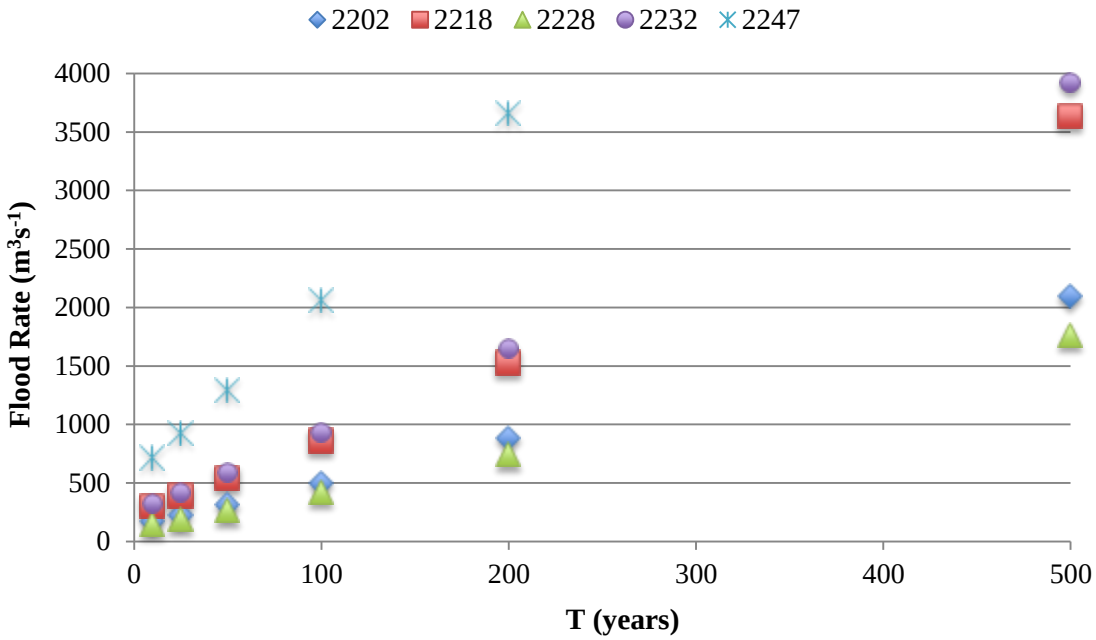

Figure 23. The flood values for the 10, 25, 50, 100, 200, and 500 return intervals in Eastern Black Sea Basin.

CONCLUSIONS

The following findings were obtained from the regional flood frequency analysis for Eastern Black Sea Basin.

1. By means of the variation coefficients (Cv_x) calculated separately from the each station data, it was determined that the stations constitute a meaningful group and a homogeneous region.
2. GEV distribution was obtained as the appropriate distribution for the regional analysis.
3. Q/Q_{avg} ratios for the 10, 25, 50, 100, 200, and 500 return intervals in Eastern Black Sea Basin were calculated as 1.79, 2.32, 3.24, 5.17, 9.18 and 21.85, respectively.

REFERENCES

Önöz, B., & Bayazıt, M. (2008). *Taşkın ve Kuraklık Hidrolojisi.* Nobel Akademik Yayıncılık.

LONG TERM DROUGHT ANALYSIS IN AEGEAN REGION, TURKEY

Ülker Güner Bacanlı[1], Sibel Çukurluoğlu[2]
[1]*Pamukkale University, Engineering Faculty, Department of Civil Engineering*
ugbacanli@pau.edu.tr
[2]*Pamukkale University, Engineering Faculty, Department of Environmental Engineering, Denizli, Turkey*
scukurluoglu@pau.edu.tr

Abstract
Drought analysis take part a significant role in the for the future development and sustainable management of water resources.This paper is were analyzed meteorological drought for long time. Standardized Precipitation Index (SPI) were investigated variability on monthly 24, 36 and 48 monthly SPI. Meteorological data from 8 meteorological stations in Aegean region of Turkey for the period 1960–2013 was used. The total relative frequencies of the drought vary between 12.8 % and 21.3 % for the periods of 24, 36 and 48 months in 8 meteorological stations, Aegean region of Turkey. The important droughts occurred in 1970-1974, 1986-1992, 2003-2006 in Aegean Region on 24, 36 and 48 months time scale. In drought analysis by SPI; in the long time period (as 24,36,48 months) drought is more frequent but taller. Knowing the processes of this drought, It is possible to plan better by knowing the potential of water resources in the region.

Keywords: *Drought, Trend Analysis, Standardized Precipitation Index(SPI), Aegean Region, Turkey.*

INTRODUCTION
Drought is known as a regional recurring feature of the climate. Drought can be classified as meteorological, agricultural, hydrological, socio-economic and groundwater drought (Dracup et al., 1980, Wilhite and Glantz, 1985, Mishra and Singh, 2010). Droughts has result in long-term a lot of (social, economic and environmental) effects. Droughts are difficult to detect. Many indices are widely used in drought studies. Different some drought indices as the Palmer Drought Severity Index (PDSI) (Palmer, 1965; Liu et al., 2015), the vegetation drought response index (Brown et al. 2008), the multivariate standardized drought index (MSDI) (Hao and Aghakouchak 2013), crop moisture index (CMI), soil moisture drought index (SMDI), vegetation condition index (VCI) (Madadgar and Moradkhani 2013), drought severity index (DRI) (Mu et al., 2013), Surface Water Supply Index (SWSI) (Shafer and Dezman, 1982), Standardized Precipittion Index (SPI) (McKee et al., 1993; Ganguli and Reddy, 2014) are the most common tools for detecting from past to the present.

Researchers by using the SPI index have done a lot of work from past to the present. Selection of a proper timescale, which will be used in the drought assessment, is a critical issue, since the SPI was designed to quantify the precipitation deficit for multiple timescales, reflecting the impacts of drought on different forms of water resources (Meshram et al., 2017). Standardized precipitation index method and Geographic Information System (GIS) is used. Turkes and Tatlı (2009) presented a new methodology for the Standardized Precipitation Index (SPI).

Meteorological and soil moisture conditions (agriculture) respond to precipitation anomalies on relatively short timescales (e.g., 1 to 6 months), whereas streamflow, reservoirs, and groundwater respond to longer term precipitation anomalies (e.g., 6 to 24 months or longer), as noted in WMO (2012). Therefore, if a meteorological drought is concerned, a 1- or 2-month

SPI may be a better choice; if an agricultural drought is concerned, anywhere from 1- to 6-month SPI can be a choice. For hydrological drought analyses and applications, one could select a timescale something like 6-month up to 24-month SPI or more. It is important to note that the shorter the timescale SPIs (e.g., 1, 2, or 3 months), the higher the stakes that we can provide early warning of drought and assess drought severity (WMO 2012; Meshram et al., 2017).

The goal of this study are to assess the temporal and spatial characteristics of meteorological droughts in the Aegean region of Turkey to generate a guide for sustainable water resources management. The main objectives of this study are: (1) to investigate the drought in Aegean Region between 1960-2013, and (2) to investigate variability on monthly 24, 36 and 48 monthly SPI.

STUDY AREA AND DATA

Turkey's diverse regions have different climates because of irregular topography. The Aegean region occupies 11% of the total area of Turkey (Figure 1). The Aegean coastal plain has an exceptionally mild climate. The Aegean region has perpendicular mountains to its shores and many valleys between them, thus permitting the sea climate reach inner parts of the region. Although some of the provinces inland show also characteristics of continental climate [Erinç, 1957; Bacanli, 2011; 2017].

Observed monthly rainfall data records from 8 meteorological stations located in Aegean Anatolia, Turkey, have been selected for this study. The length of available records at these stations is between 1960 and 2010. The evaluated monthly rainfall data were measured by the Turkish State Meteorological Services [DMI]. The SPI drought indices for this study have been calculated on the basis of these rainfall data records.

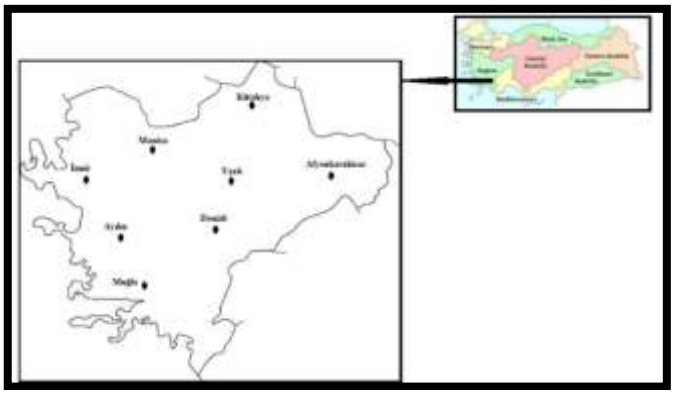

Figure 1 Aegean Region

Table I shows the geographic coordinates of the synoptic stations chosen in the Aegean Anatolia regions. The precipitation and temperature data of these stations for the 54 years between 1960 and 2013 were obtained from the Turkish State Meteorological Service [DMI].

Table I. Raingauge Stations in the Aegean Regions

Raingauge Stations	Geographic coordinates			Raingauge Stations	Geographic coordinates		
	Latitude	Longitude	Elevation (m)		Latitude	Longitude	Elevation (m)
Afyon	38.44	30.34	1034	Kütahya	39.25	29.59	969
Aydın	37.50	27.50	56	Manisa	38.36	27.24	71
Denizli	37.45	29.5	425	Muğla	37.17	28.22	646
İzmir	38.23	27.40	29	Uşak	38.40	29.24	919

The monthly precipitation series's statistical parameters at seven stations during the 1960-2013 period are presented in Table II. The mean monthly precipitation is limited from 34.41 to 97.81 mm.

Table II. Statistical parameters of monthly precipitation series at seven stations during the 1960-2013 period.

Station Name	**Afyon**	**Aydın**	**Izmir**	**Kutahya**	**Manisa**	**Mugla**	**Usak**
Mean (mm)	34,41	52,66	57,39	46,86	61,31	97,81	45,63
Standard Deviation (mm)	26,10	57,09	68,76	37,71	67,67	114,43	38,77
Skewness	0,99	1,40	1,60	1,34	1,63	1,66	1,14
Min (mm)	0,10	0,10	0,10	0,10	0,10	0,10	0,10
Max (mm)	165,80	344,10	380,30	255,80	393,80	645,30	211,70
Kurtosis	1,45	2,07	2,60	2,70	3,07	2,92	1,44

METHOD

STANDARD PRECIPITATION INDEX (SPI)

The Standardized Precipitation Index (SPI) Method is commonly accepted and used in research. The SPI was developed by McKee et. al. [1993, 1995]. SPI estimation is further to long term precipitation data. SPI is obtained by dividing the difference between precipitation and mean to standard deviation in a specific duration (McKee et al 1993).

$$SPI = \frac{x_i - \bar{x}_i}{\sigma} \tag{1}$$

The SPI is produced by standardizing the probability of observed precipitation for any duration. The magnitude, length and duration of drought can be calculated with SPI. The studies have expressed that precipitation is subject to law of gamma distribution (Zhang et al., 2015; Ganguli and Reddy, 2014). The calculation of SPI is complex. The SPI index classes are shown in the Table III.

Table III. Classification According to SPI Values

SPI	**Drought Category**	**SPI**	**Drought Category**
2 ≤	Extremely Wet	(-1.0) ~(-1.49)	Moderately Dry
1.99~1.5	Very Wet	(-1.5) ~ (-1.99)	Severely Dry
1.49 ~ 1.0	Moderately Wet	-2≥	Extremely Dry
0.99 ~ (-0.99)	Near Normal		

The data sets are organized for a period (3, 6, 9, 12, 24 or 48 months). Later, presume x is the cumulated monthly precipitation in the time period of research which fits a gamma probability density function g(x) as follows:

$$g(x) = \frac{1}{\beta^{\alpha}\Gamma(\alpha)} x^{\alpha-1} e^{x/\beta} \qquad \text{for x > 0.} \tag{2}$$

Where, x is the precipitation amount, and $\Gamma(\alpha)$ is the Gamma function. α *and* β are the shape and scale parameter respectively.

$$\alpha = \frac{1}{4A}\left(1+\sqrt{1+\frac{4A}{3}}\right) \quad (3)$$

$$\beta = \frac{\bar{x}}{\alpha} \quad (4)$$

$$A = \ln(\bar{x}) - \frac{\sum \ln(x)}{n} \quad (5)$$

In these equations *n* is the number of precipitation observations. The cumulative probability distribution function is defined as follows:

$$G(x) = \int_0^x g(x)dx = \frac{1}{\beta^{\alpha}\Gamma(\alpha)}\int_0^x x^{\alpha-1}e^{-x/\beta}dx \quad (6)$$

The Gamma function is undefined for x = 0 and precipitation distribution can have zero values. When this is the case, the cumulative probability distribution is defined as follows:

$$H(x) = q + (1-q)\cdot G(x) \quad (7)$$

In the equation above, *q* represents the probability for zero value. If *m* is used for denoting the zero values in a precipitation series then the following definition can be made: q = m /n. The cumulative probability value *H(x)* is converted to *Z* variable with a standard normal random value denoting the SPI value having zero mean value and variance equal to 1. *H(x)* is the value of SPI. Normalization of SPI values enables the consideration of the variations of precipitation series of that station by both time and place (McKee et al. 1993; Guttman 1999).

RESULTS AND DISCUSSION

STANDARD PRECIPITATION INDEX ANALYSIS ASSESMENT

The SPI values were calculated separately for all 8 rain gauge stations on 24, 36 and 48 months time scale conditions. The graphs of different stations which selected as example Denizli stations from the Aegean Region with different altitudes are plotted as Figure 2. As can be seen, there are differences between regions. The important droughts also occurred in 1969-1974, 1979-1980, 1986-1992, 1994, 1988-1999, 2001-2006 in Aegean Region on 24 months time scale. The important droughts also occurred in 1969-1975, 1983-1992, 1999, 2002-2007 in Aegean Region on 36 months time scale. The important droughts also occurred in 1970-1975, 1984-1992, 2003-2007 in Aegean Region on 48 months time scale. As the SPI time increases, The drought periods increase.

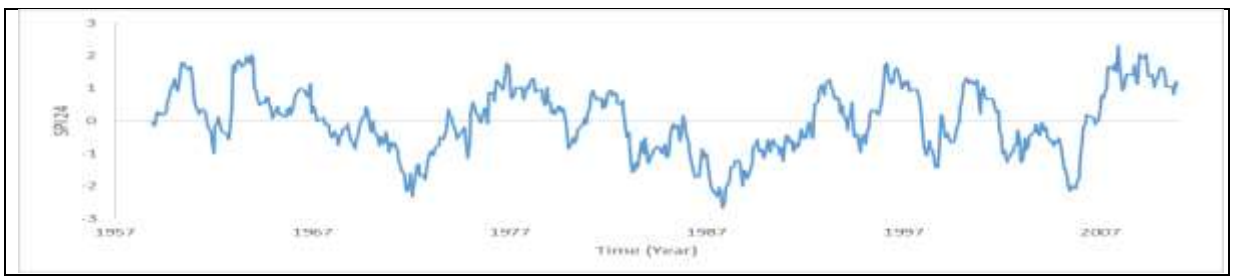

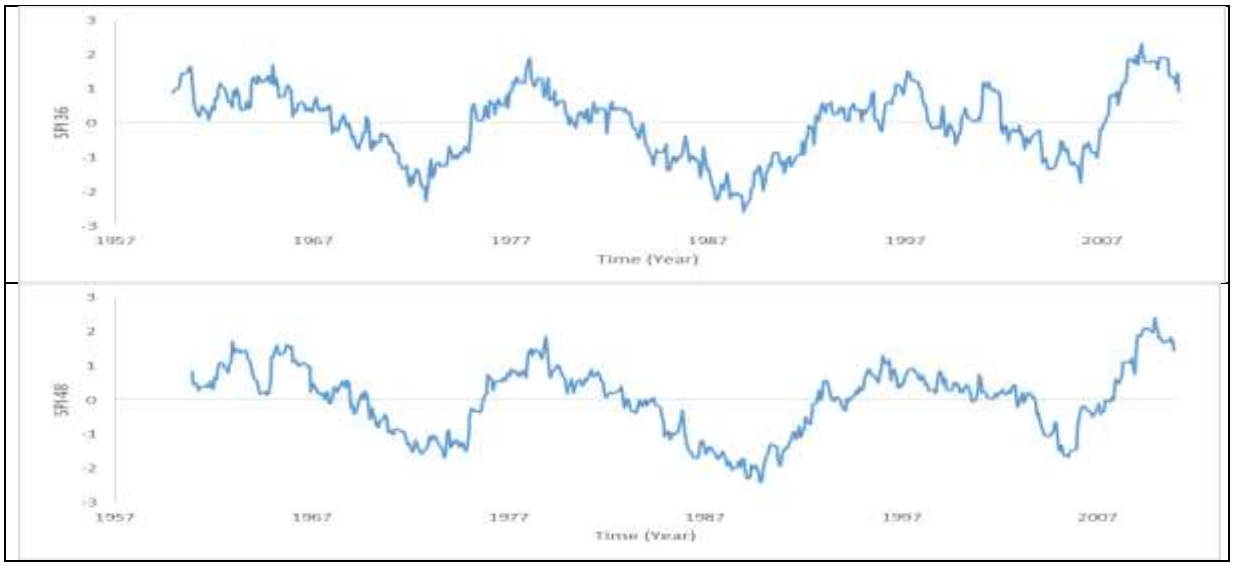

Figure 2 SPI values of Denizli city for 24, 36 and 48 months period

The SPI relative frequencies values were calculated separately for all 8 rain gauge stations on 24, 36 and 48 months time scale conditions and were given Table IV and Table VII. For Aegean region, Moderate degree drought distribution varies between 7.2 % and 11.8 % for the periods of 24 months, between 4.6 % and 12.1 % for the periods of 36 months, between 6.0 % and 18 % for the periods of 48 months.

Table IV. The relative frequencies of Denizli and Izmir city SPI values for 24, 36 and 48 months time

SPI range		Denizli Months			Izmir Months		
		24	36	48	24	36	48
2 or more	Extremely wet	0,005	0,003	0,013	0,011	0,002	0,002
1,5 to 1,99	Very wet	0,042	0,049	0,040	0,046	0,051	0,050
1 to 1,49	Moderately Wet	0,132	0,129	0,092	0,109	0,090	0,125
0,99 to -0,99	Near normal	0,657	0,628	0,642	0,664	0,682	0,639
-1 to -1,49	Moderately dry	0,08	0,121	0,117	0,093	0,067	0,113
-1,5 to -1,99	Severely dry	0,041	0,042	0,079	0,038	0,078	0,035
-2 and less	Extremely dry	0,042	0,028	0,017	0,038	0,031	0,037

Table V. The relative frequencies of Afyon and Aydın city SPI values for 24, 36 and 48 months time

SPI range		Afyon Months			Aydın Months		
		24	36	48	24	36	48
2 or more	Extremely wet	0,021	0,007	0,007	0,010	0,002	0,000
1,5 to 1,99	Very wet	0,030	0,055	0,062	0,040	0,018	0,020
1 to 1,49	Moderately Wet	0,094	0,101	0,118	0,106	0,132	0,141
0,99 to -0,99	Near normal	0,694	0,710	0,674	0,661	0,669	0,681
-1 to -1,49	Moderately dry	0,083	0,046	0,060	0,072	0,069	0,062
-1,5 to -1,99	Severely dry	0,035	0,033	0,038	0,083	0,057	0,037
-2 and less	Extremely dry	0,042	0,049	0,042	0,029	0,054	0,060

Table VI. The relative frequencies of Manisa and Mugla city SPI values for 24, 36 and 48 months time

SPI range		Manisa Months			Mugla Months		
		24	36	48	24	36	48
2 or more	Extremely wet	0,018	0,003	0,000	0,002	0,000	0,000
1,5 to 1,99	Very wet	0,027	0,036	0,042	0,030	0,011	0,027
1 to 1,49	Moderately Wet	0,123	0,124	0,133	0,154	0,184	0,168
0,99 to -0,99	Near normal	0,654	0,674	0,669	0,640	0,602	0,631
-1 to -1,49	Moderately dry	0,080	0,055	0,068	0,080	0,106	0,098
-1,5 to -1,99	Severely dry	0,064	0,086	0,055	0,059	0,070	0,047
-2 and less	Extremely dry	0,034	0,021	0,033	0,035	0,026	0,030

Table VII. The relative frequencies of Kutahya and Usak city SPI values for 24, 36 and 48 months time

SPI range		Kutahya Months			Usak Months		
		24	36	48	24	36	48
2 or more	Extremely wet	0,003	0,003	0,002	0,019	0,005	0,005
1,5 to 1,99	Very wet	0,054	0,039	0,052	0,046	0,055	0,047
1 to 1,49	Moderately Wet	0,144	0,157	0,106	0,120	0,114	0,097
0,99 to -0,99	Near normal	0,606	0,608	0,586	0,645	0,670	0,694
-1 to -1,49	Moderately dry	0,118	0,103	0,180	0,096	0,064	0,082
-1,5 to -1,99	Severely dry	0,069	0,086	0,075	0,061	0,052	0,027
-2 and less	Extremely dry	0,005	0,003	0,000	0,013	0,039	0,050

Severe degree drought distribution varies between 3.5 % and 8.3 % for the periods of 24 months, between 3.3 % and 8.6 % for the periods of 36 months, between 2.7 % and 7.9 % for the periods of 48 months.. Extremely level drought distribution varies between 0.5 % and 8.3 % for the periods of 24 months, between 0.3 % and 5.4 % for the periods of 36 months, between 0.0 % and 6.0 % for the periods of 48 months.

Table VIII. Drought events according to several time steps for Denizli and Izmir stations

Station	**Year**	**24SPI**	**36SPI**	**48SPI**	**Station**	**Year**	**24SPI**	**36SPI**	**48SPI**
Denizli	1962	-1,01	-	-	**Izmir**	1961	-1,67	-	-
	1972	-2,33	-2,28	-1,69		1965	-0,99	-	-
	1983	-1,59	-	-		1970	-1,67	-1,74	-1,5
	1987	-2,68	-2,26	-1,72		1988	-2,1	-1,98	-2,53
	1988	-2,01	-2,09	-2,41		1989	-2,39	-2,54	-2,66
	1998	-1,43	-	-		1997	-1,59	-	-
	2005	-2,15	-1,73	-1,67		2004	-3,49	-2,2	-1,6

In this study, the meteorological drought was evaluated using the SPI approach based on several timescales. These timescales detected several intense drought events in numerous years as shown in Table VIII. The results are illustrated for two stations namely Denizli and İzmir as a sample calculation. These results of SPI show the advantage of using several time steps when applying the SPI approach. Sometimes, one of these timescales may detect a drought that cannot be observed by another timescale. For example, a drought event was detected in Izmir station by 24SPI in 1965; however, this event was not detected by any other SPI timescales (Table VIII).

CONCLUSION

In this study was to analyze monthly SPI trends in the Aegean region of Turkey for the year of 1960 to 2013. In this study, the SPI for meteorological drought analysis was considered as a long term drought index for 24, 36 and 48 months period. Assessments for each station were made according to the SPI classifications in these periods. The total relative frequencies of the drought vary between 12.8 % and 21.3 % for the periods of 24, 36 and 48 months in all cities. The important droughts occurred in 1970-1974, 1986-1992, 2003-2006 in Aegean Region on 24, 36 and 48 months time scale. Knowing the processes of this drought, It is possible to plan better by knowing the potential of water resources in the region. Monitoring drought needs different indicators or indices. The drought management plans should immediately be get ready for the region which is basin management and agriculturally important. Futher, the drought analysis will have important contribution in the determination of the priorities for planning, design and construction of water structures.

REFERENCES

Bacanli, U.G. 2011. Dryness Characterization: A Climatic Water Deficit Approach In Turkey. *Fresenius Environmental Bulletin* 20/3: 665-677. ISSN: 1018-4619

Bacanli, U.G. 2017. Trend analysis of precipitation and drought in the Aegean region, Turkey. *Meteorological Application* 24/2: 239-249

Brown J.F., Wardlow B.D., Tadesse T., Hayes M.J., Reed B.,2008. The Vegetation Drought Response Index (VegDRI): A New Integrated Approach for Monitoring Drought Stress in Vegetation. *GIScicence&Remote Sensing* 45/1: 16-46.

DMI (State Meteorological Service) http://www.dmi.gov.tr/files/en-US/climateof turkey.pdf , Last Access : November 2009.

Dracup JA, Lee KS, Paulson EG. 1980. On the statistical characteristics of drought events. *Water Resources Research* 16:289–296. DOI: 10.1029/WR016i002p00289

Erinç S. 1957. *Applied Climatology and the Climate of Turkey (in Turkish)* İstanbul Technical University, Hydrogeology Institute, İstanbul, Turkey.

Ganguli P, Reddy MJ. 2014. Evaluation of trends and multivariate frequency analysis of droughts in three meteorological subdivisions of western India. *International Journal of Climatology* 34/3: 911-928. DOI: 10.1002/joc.3742

Guttman NB, 1999. Accepting the Standardized Precipitation Index: A Calculation Algoritm. *Journal of the American Water Resources Association* 35/2: 311-322.

Hao Z, AghaKouchak A., 2013. Multivariate Standardized Drought Index: A parametric multi-index model *Advances in Water Resources* 57: 12-18.

Li Q, Li P, Li H, Yu M, 2015. Drought assessment using a multivariate drought index in the Luanhe River basin of Northern China. *Stochastic Environmental Reseorces and Risk Assessment.* 29: 1509-1520. DOI: 10.1007/s00477-014-0982-4

Madadgar S, Moradkhani H, 2013. Drought analysis under climate change using copula. J Hydrol Eng 18(7):746–759

McKee TB, Doesken NJ, Kleist J, 1993. The relationship of drought frequency and duration to time steps. *8th Conference on Applied Climatology, January 17–22* 1993. 179–184 pp., Anaheim, California.

McKee TB, Doesken NJ, Kleist J, 1995. Drought monitoring with multiple time scales. the *Ninth Conference on Applied Climatology*. American Meteorological Society: Dallas, TX; 233–236.

Meshram S.G., Gautam R. and Kahya E. (2017). Drought analysis in the Tons River Basin, India during 1969-2008. Theoretical and Applied Climatology. pp 1–13

Mishra AK, Singh VP, 2010. A review of drought concepts. *Journal of Hydrology* 391: 202-216. DOI: 10.1016/j.jhydrol.2011.03.049

Mu Q, Zhao M, Kimball JS, McDowell NG, Running SW, 2013. A Remotely Sensed Global Terrestrial Drought Severity Index. *American Meteorological Society* 94/1: 83-98.

Palmer, W. C., 1965. Meteorological Drought. Research Paper No.45. Washington, DC: US Weather Bureau.

Palmer WC, 1968. Keeping Track of Crop Moisture Conditions, Nationwide: The New Crop Moisture Index. *Weatherwise* 21/4: 156-161.

Shafer BA, Dezman LE, 1982. Development of a Surface Water Supply Index (SWSI) to assess the severity of drought conditions in snowpack runoff areas. *In Proceedings of the Western Snow Conference*, 164–175pp. Colorado State University, Fort Collins, Colorado.

Turkes M, Tatlı H, 2009. Use of the standardized precipitation index (SPI) and a modified SPI for shaping the drought probabilities over Turkey. *International Journal of Climatology*. 29: 2270-2282. DOI: 10.1002/joc.1862

Wilhite DA, Glantz MH, 1985. Understanding of the drought phenomenon: The role and definition. *Water International* 10/3: 111–120. DOI: 10.1080/02508068508686328

WMO (2012) WMO: standardized precipitation index user guide, edited by: Svoboda, M., Hayes, M., and Wood, D. A., published by WMO, Geneva, 2012.

Zhang Y, Cai W, Chen Q, Yao Y, Liu K, 2015. Analysis of Changes in Precipitation and Drought in Aksu River Basin, Northwest China. *Advances in Meteorology*. doi.org/10.1155/2015/215840

RECENT TRENDS IN METEOROLOGICAL DROUGTH IN TURKEY: 1980-2015

Filiz Dadaser-Celik[1], Ali Ümran Kömüscü[2], Ertan Turgu[2], Rabia Ucar[1], Mete Celik[3]
[1]Dept. of Environmental Engineering, Erciyes University
fdadaser@erciyes.edu.tr, rabia.ucar@outlook.com.tr
[2]State Meteorological Service
aukomuscu@mgm.gov.tr, eturgu@mgm.gov.tr
[3]Dept. of Computer Engineering, Erciyes University
mcelik@erciyes.edu.tr

Abstract
Standardized Precipitation Index (SPI) is one of the widely used meteorological drought indices to assess and monitor drought events. It helps quantify precipitation deficit for multiple time scales. In this study, monthly precipitation data from 195 meteorology stations in Turkey were used to estimate the SPI for multiple timescales (1, 3, 6, 12, 24, and 48 months). Trends in the SPI were analyzed using the Mann– Kendall test with the trend-free prewhitening procedure. The results showed that 8, 4, 6, 8, 10, 28% of stations had statistically significant trends (at the 0.05 level) for 1-, 3-, 6-, 12-, 24-, and 48- month timescales, respectively. The long-term timescale series showed more significant trends compared to the short-term timescale series. Significant upward trends were observed particularly in western Turkey, indicating that western Turkey getting wetter. In eastern and southeastern Turkey, on the other hand, significant downward trends and longer-duration droughts were detected.

Keywords: *drought, standardized precipitation index (SPI), trend analysis, Turkey*

INTRODUCTION

Drought is a natural phenomenon that has important economic, social, and environmental implications. A meteorological drought occurs primarily due to the precipitation deficit in comparison to some "normal" or average amount (Keyantash and Dracup 2002). It is also defined on the basis of duration of the dry period. Many different indices can be found in the literature to assess meteorological droughts (Keyantash and Dracup 2002). Standardized Precipitation Index (SPI) is one of the most widely used methods in assessing and monitoring drought occurrences. It was designed to quantify the precipitation deficit for multiple timescales, which reflect the impact of drought on the availability of the different water resources. In order to reflect the impact of precipitation anomalies on different water resources, McKee and others (1993) originally calculated the SPI for 3-, 6-,12-, 24- and 48-month timescales.

Many local and regional examples of SPI application for drought analysis exist in literature (e.g., Cancelliere et al. 2007, Livada and Assimakopoulos 2007). Previously, Kömüşcü (1999) calculated SPI for 40 stations for the 1940-1997 period to assess historical drought occurrences in Turkey. Kömüşcü et al. (2004) and Sönmez et al. (2005) calculated SPI using long-term precipitation data at 101 stations for 1951–2001 period. Türkes and Tatlı (2009) used classical SPI and a modified SPI method to estimate long-term probabilities for dryness and wetness for 96 stations over Turkey. In some other studies SPI was used to evaluate regional drought events (e.g., Tonkaz 2006, Sirdaş and Şen 2003, Karabulut 2015, Gumus and Algin 2017).

In this study, the objective is to assess and understand how drought conditions evolved in Turkey in the last 26 years (1980-2015) by identifying trends in the SPI series.

DATA AND METHODS

SPI is a meteorological drought index developed by (McKee et al. 1993). In simple terms, SPI is based on the probability of precipitation for any time scale. It is calculated by using long-term precipitation data series where the series is fitted to a gamma distribution, and the cumulative probability of an observed precipitation event for each timescale of interest is calculated. The value of SPI can be obtained by transforming cumulative probability gamma function into a standard normal random variable Z with mean of zero and standard deviation of one. If a particular precipitation event gives a low probability on the cumulative probability function, then this is indicative of a likely drought event. Alternatively, a precipitation event which gives a high probability on the cumulative probability function is an anomalously wet event. Positive SPI values indicate wetter conditions, and negative values indicate drier conditions (McKee et al. 1993). Because the SPI is normalized, wetter and drier climates can be represented in the same way; thus, wet periods can also be monitored using the SPI.

Table 1. SPI values and their description (McKee et al. 1993)

SPI	Description
>2	Extremely wet
1.5-1.99	Severely wet
1.0-1.49	Moderately wet
-0.99-0.99	Near normal
-1.0- -1.5	Moderately dry
-1.5- -.199	Severely dry
<-2.0	Extremely dry

In this study, SPI values were calculated for 1-, 3-, 6-, 12-, 24- and 48-month timescales for 195 stations across Turkey (Figure 1). The stations were selected among 238 stations based on homogeneity tests conducted with Pettitt test, Standard normal homogeneity test (SNHT), Buishand range test and Von Neumann ratio test (Wijngaard et al. 2003).

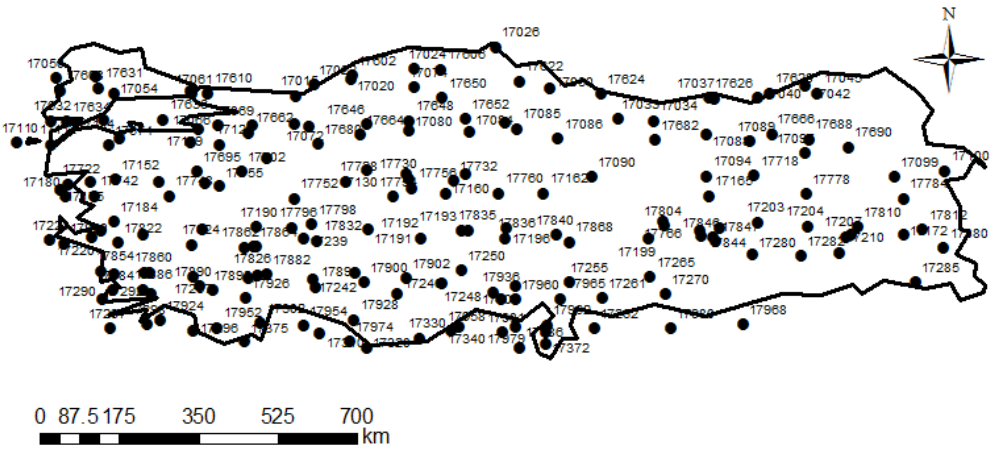

Figure 1. Location of 195 stations which have homogeneous precipitation records for the 1980-2015 period

The Mann-Kendall trend test (Kendall 1975, Mann 1945) with the trend-free prewhitening procedure (Yue et al. 2002) was used for trend analysis. The statistical significance of the trends were evaluated at the 0.05 level.

RESULTS

Average 1-, 3-, 6-, 12-, 24-, and 48-month SPI values were calculated and depicted in Figure 2. As can be seen, the drought frequency changes as the time scale changes. On longer time scales, drought becomes less frequent, but lasts longer. The variation of average SPI values for 195 stations shows that only the year 1989 had extreme drought event (SPI<-2) for 3- month SPI and 6-month SPI but the event of extreme wet is not observed within these variations. Although there is alternating periods of wet and dry periods in recent decades, the wetter conditions are dominating the trends.

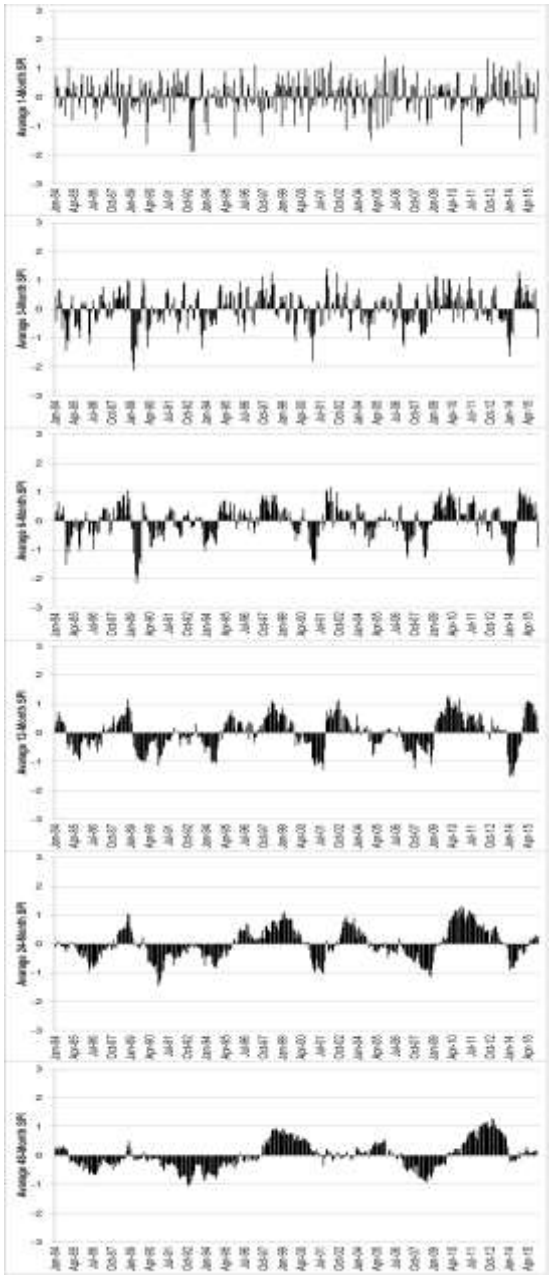

Figure 2. Average 1-, 3-, 6-, 12-, 24-, and 48-month SPI values for 195 stations.

Trends in SPI values of 195 stations were summarized in Table 1. A total of 57, 70, 69, 68, 67, and 73% of stations showed upward trends for 1-, 3-, 6-, 12-, 24-, and 48-month SPI time series, respectively (Table 2). Statistically significant trends were detected 8, 4, 6, 8, 10, 28% of stations, respectively (Table 2). Upward trends indicate a decrease in dry conditions or increase

in wet conditions while the downward trends indicate increase in dry conditions. These results suggest that drought events decrease at majority of stations. In other words, wetter conditions are dominating in at least 2/3 of the stations in Turkey in recent decades. It is noticed that the number of stations with downward trends did not show a major change among different timescales while it increased significantly from short timescale (1-month) to longer timescales (48-month) for upward trends. While only 15 stations were characterized with upward trends at 1-month timescale, this figure increased to 55 stations at 48-month timescale. In other words, more stations are characterized with upward trends (wetter conditions) as we shift from short timescale to longer timescale. As can be seen, the long-term time series showed more significant trends compared to the short-term series.

Table 1. Number (%) of stations with downward (negative) or upward (positive) trends in 1-, 3-, 6-, 12-, 24-, and 48-month SPI and the number (%) of stations for which these trends are statistically significant at the 0.05 level.

Timescale	Number (%) of stations with downward trends	Number (%) of stations with upward trends	Number (%) of stations with downward trends (significant at the 0.05 level)	Number (%) of stations with upward trends (significant at the 0.05 level)
1-month SPI	64 (33)	112 (57)	4 (2)	15 (8)
3-month SPI	53 (27)	137 (70)	3 (2)	8 (4)
6-month SPI	54 (28)	134 (69)	4 (2)	12 (6)
12-month SPI	59 (30)	133 (68)	2 (1)	15 (8)
24-month SPI	62 (32)	131 (67)	4 (2)	19 (10)
48-month SPI	53 (27)	142 (73)	11 (6)	55 (28)

Spatial characteristics of trends were shown in Figure 3. Upward trends were prevalent in Marmara, Aegean and Black Sea regions, while downward trends were detected in eastern and southeastern Turkey. The upward trends became more dominant especially at 24-month and 48-month time scales in western Turkey while some downward trends are detected at southeastern corner of the eastern Anatolia. In central regions, no trends in SPI values were detected, indicating that there is no significant change in drought conditions.

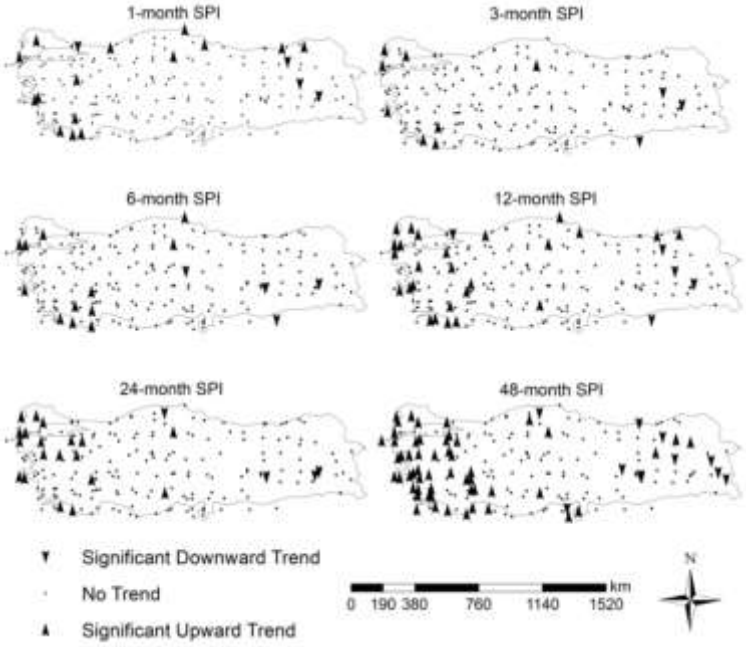

Figure 3. Trends in SPI at 195 stations.

CONCLUSIONS AND RECOMMENDATIONS

In this study, trends in meteorological droughts over Turkey were analyzed based on SPI values, calculated using monthly precipitation data collected at 195 stations. From 1980 to 2015, the drought occurrences tended to decrease in western Turkey and increase in eastern and southeastern Turkey at all timescales. It was concluded that the trends were more apparent on longer timescales. More stations are characterized with upward trends (wetter conditions) as we shift from short timescale to longer timescale. Overall, the results suggest that drought events decrease at majority of stations. In other words, wetter conditions are dominating in most of the stations in Turkey in recent decades.

REFERENCES

Keyantash, J. and Dracup, J.A. (2002) The Quantification of Drought: An Evaluation of Drought Indices. Bulletin of the American Meteorological Society 83(8), 1167-1180.

McKee, T.B., Doesken, N.J. and John Kleist, J. (1993) The relationship of drought frequency and duration to time scales, Anaheim, California.

Cancelliere, A., Mauro, G.D., Bonaccorso, B. and Rossi, G. (2007) Drought forecasting using the Standardized Precipitation Index. Water Resources Management 21(5), 801-819.

Livada, I. and Assimakopoulos, V.D. (2007) Spatial and temporal analysis of drought in greece using the Standardized Precipitation Index (SPI). Theoretical and Applied Climatology 89(3), 143-153.

Kömüşcü, A.Ü. (1999) Using the SPI to Analyze Spatial and Temporal Patterns of Drought in Turkey, http://digitalcommons.unl.edu/droughtnetnews/49.

Kömüsçü, A.Ü., Erkan, A., Turgu, E. and Sönmez, F.K. (2004) A new insight into Drought Vulnerability in Turkey using the Standardized Precipitation Index. Journal of Environmenal Hydrology 12, 18.

Sönmez, F.K., Kömüscü, A.Ü., Erkan, A. and Turgu, E. (2005) An Analysis of Spatial and Temporal Dimension of Drought Vulnerability in Turkey Using the Standardized Precipitation Index. Natural Hazards 35(2), 243-264.

Türkeş, M. and Tatlı, H. (2009) Use of the standardized precipitation index (SPI) and a modified SPI for shaping the drought probabilities over Turkey. International Journal of Climatology 29(15), 2270-2282.

Tonkaz, T. (2006) Spatio-Temporal Assessment of Historical Droughts using SPI with GIS in GAP Region, Turkey. Journal of Applied Sciences 6(12), 2565-2571.

Sirdaş, S. and Şen, Z. (2003) Spatio-temporal drought analysis in the Trakya region, Turkey. Hydrological Sciences Journal 48(5), 809-820.

Karabulut, M. (2015) Drought analysis in Antakya-Kahramanmaraş Graben, Turkey Journal of Arid Land.

Gumus, V. and Algin, H.M. (2017) Meteorological and hydrological drought analysis of the Seyhan−Ceyhan River Basins, Turkey. Meteorological Applications 24(1), 62-73.

Wijngaard, J.B., Klein Tank, A.M.G. and Können, G.P. (2003) Homogeneity of 20th century European daily temperature and precipitation series. International Journal of Climatology 23(6), 679-692.

Kendall, M.G. (1975) Rank Correlation Methods. Griffin London.

Mann, H.B. (1945) Non-Parametric tests against trend. Econometrica 13, 245–259.

Yue, S., Pilon, P., Phinney, B. and Cavadias, G. (2002) The influence of correlation on the ability to detect trend in hydrological series. Hydrological Processes 16, 1808-1829.

EVALUATION OF DIFFERENT FLOW ROUTING METHODS IN WATERSHED MODELING

Kebir Emre Saraçoğlu[1,2], Cevza Melek Kazezyılmaz-Alhan [1], Sezar Gülbaz[1]
[1]*Istanbul University, Civil Engineering Department, Istanbul, Avcılar, Turkey*
[2]*Beykent University, Civil Engineering Department, Istanbul, Ayazağa, Turkey*

Abstract
The aim of this study is to evaluate and compare kinematic, diffusion and dynamic wave routing methods in watershed modeling using **E**nvironmental **P**rotection **A**gency **S**torm **W**ater **M**anagement **M**odel (EPA SWMM). For this purpose, the hydrologic and hydraulic model of Sazlıdere Watershed is employed and simulations are made using different Manning's coefficients under heavy and typical rainfall events. Results are compared to each other to determine the influence of selected flow routing methods on outflow rates.

Keywords*: Dynamic Wave Model, Diffusion Wave Model, Kinematic Wave Model, Watershed Modeling, EPA SWMM*

INTRODUCTION

Flood has become more prominent due to climate change in recent years and causes serious damages in urban, industrial and agricultural areas. In order to prevent damages, surface runoff should be estimated accurately. In the computation of flow rate, rainfall-runoff relations are described by wave routing methods, which can be categorized as kinematic, diffusion and dynamic waves. The routing methods are based on continuity and momentum equations. Dynamic waves are valid for unsteady nonuniform flow, first presented by St. Venant (1871). The theory of the kinematic wave was given by Lighthill and Whitham (1955) whereas the diffusive wave theory was presented by Hayami (1951).

EPA SWMM is a comprehensive watershed simulation model that can simulate rainfall/runoff relations and can be used in flow prediction and urban drainage system design. SWMM involves the three wave routing methods as options in surface runoff calculation. SWMM is employed in many studies related to hydrologic and hydraulic watershed modeling [Gülbaz and Kazezyılmaz-Alhan (2013)]. These studies show that SWMM can simulate overall hydrological characteristics of watersheds with an acceptable margin of error.

The Sazlıdere Watershed is one of the most important water resources to meet potable water demand of Istanbul. Therefore, a calibrated hydrodynamic model for Sazlıdere Watershed is developed by Gülbaz and Kazezyılmaz-Alhan (2013). And, this hydrodynamic model is employed in this study to investigate the effect of different wave routing methods on surface runoff. Analyses are carried out to determine the effect of kinematic, diffusion and dynamic wave routing methods on flow rates over a watershed using different Manning's roughness coefficients and under different storm events.

MATERIALS and METHODOLOGY

Site Description

Sazlıdere Watershed is located on the continental Europe of Istanbul. The location of the study area is given in Fig. 1.

Figure 1. Location of the Sazlıdere Watershed

The Sazlıdere Watershed has an overall drainage area of approximately 165 km^2 and consists of pasture and agricultural land (58%), residential and industrial area (18.22%), forested land (18%) and dam area (5.78%). The Sazlıdere Dam in the watershed area meets Istanbul's water demand of 55 million m^3/year [Gülbaz and Kazezyılmaz-Alhan (2011)].

Wave Routing Methods

The dynamic wave equations for overland flow consist of continuity and momentum equations, as follows:

$$\frac{\partial y}{\partial t} + V\frac{\partial y}{\partial x} + y\frac{\partial V}{\partial x} = i - f \quad (1)$$

$$\frac{\partial V}{\partial t} + V\frac{\partial V}{\partial x} + g\frac{\partial y}{\partial x} = g(S_0 - S_f) + \left[(i-f)\frac{V}{y}\right] \quad (2)$$

Where; y is depth of water [L], S_f is friction slope [L/L], S_0 is bed slope [L/L], V is water velocity [L/T], i is rainfall intensity [L/T], f is infiltration rate [L/T], g is accelaration of gravity [L/T^2], t is time [T] and x represents distance [L].

These equations are for moderately wide overland flow and small bottom slope. The diffusion wave model neglects only the local and convective accelerations in the dynamic wave momentum equation whereas the kinematic wave model neglects both the local and convective acceleration and pressure terms in Equation (2). Thus, friction and gravity forces essentially balance each other, $S_f = S_0$ [Kazezyılmaz-Alhan (2010)].

Hydrological and Hydraulic Watershed Model of Sazlıdere with EPA SWMM and Test of Flow Routing Methods

The EPA SWMM is a dynamic rainfall-runoff simulation model used for single event or long-term (continuous) simulation of runoff quantity and quality from primarily urban areas. [EPA (2015)]. The SWMM model consists of four routing options, which are steady flow, kinematic, diffusion and dynamic waves and five infiltration options, which are Horton, Modified Horton, Green-Ampt, Modified Green-Ampt and Curve Number.

The hydrological and hydraulic model of Sazlıdere Watershed [Gülbaz and Kazezyılmaz-Alhan (2013)] developed with EPA SWMM is used to test the effect of different flow routing methods. The hydrological watershed model consists of 177 subcathments and 173 open channels (See Fig. 2).

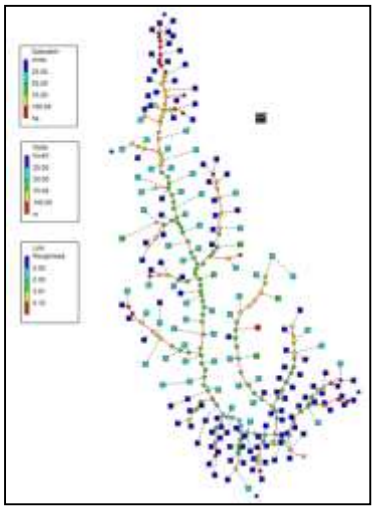

Figure 2. Numerical Model Area of the Sazlıdere Watershed

In this part of the study, a number of scenarios is used to present differences in flow rates by using different flow routing methods, which are kinematic, diffusion and dynamic waves, along with two types of Manning's coefficients under heavy and typical rainfall events. Rainfall data collected at the rain gauges set in the study area is used for testing of the flow routing methods. Rainfall data used for the numerical modeling comprises 4 days of time span from September 7, 2009 to September 11, 2009 which represents a heavy rainfall event. Another rainfall dataset comprises 3 days of time span from March 2, 2010 to March 6, 2010. which is referred as the typical rainfall. Detailed information with regard to selected 4 scenarios is provided in Tab. 1.

Table 1. Modeling Scenarios

Scenario No.		**Wave Routing Method**	**Manning's Coefficient**	**Rainfall**
Scenario 1	1-1	Dynamic	0.12	Heavy
	1-2	Diffusion	0.12	Heavy
	1-3	Kinematic	0.12	Heavy
Scenario 2	2-1	Dynamic	0.20	Heavy
	2-2	Diffusion	0.20	Heavy
	2-3	Kinematic	0.20	Heavy
Scenario 3	3-1	Dynamic	0.12	Typical
	3-2	Diffusion	0.12	Typical
	3-3	Kinematic	0.12	Typical
Scenario 4	4-1	Dynamic	0.20	Typical
	4-2	Diffusion	0.20	Typical
	4-3	Kinematic	0.20	Typical

RESULTS and DISCUSSION

The calculated flow rates for scenarios 1-4 using the Sazlıdere Watershed model are presented in Fig. 3-6, respectively

.

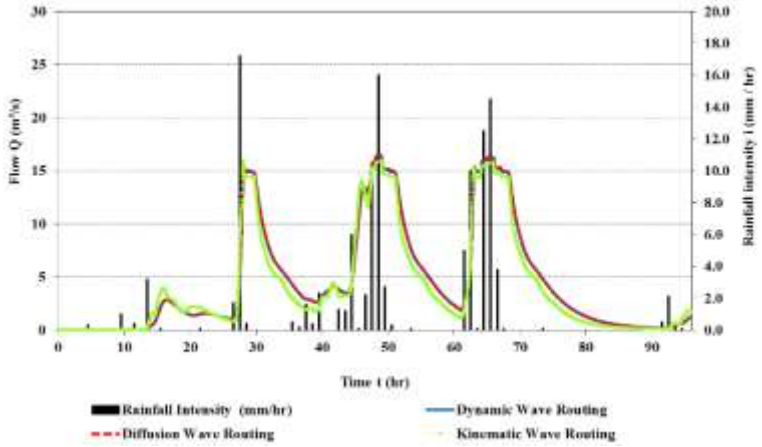

Figure 3. Calculated Flow Rates for the Scenario 1

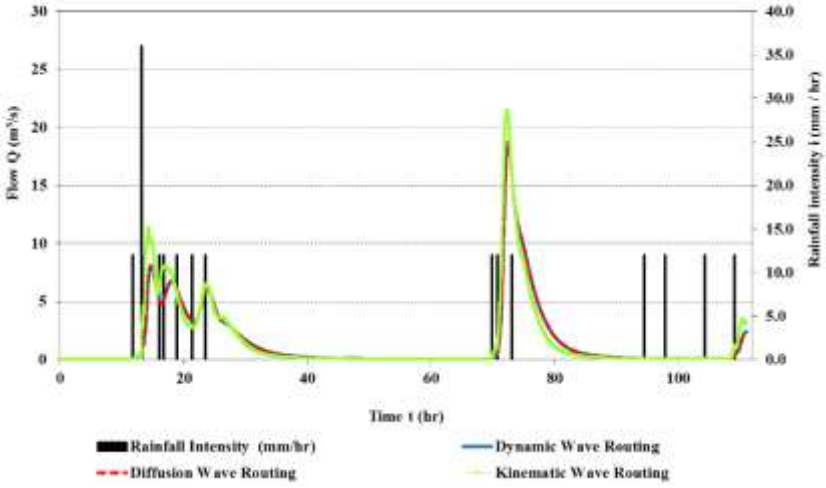

Figure 4. Calculated Flow Rates for the Scenario 2

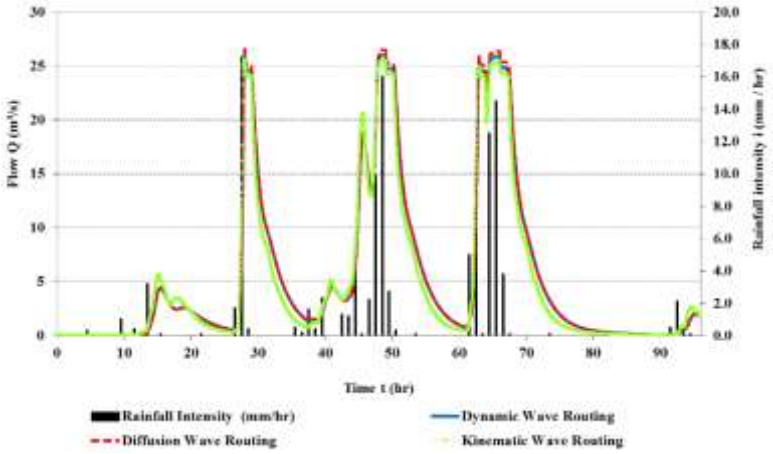

Figure 5. Calculated Flow Rates for the Scenario 3

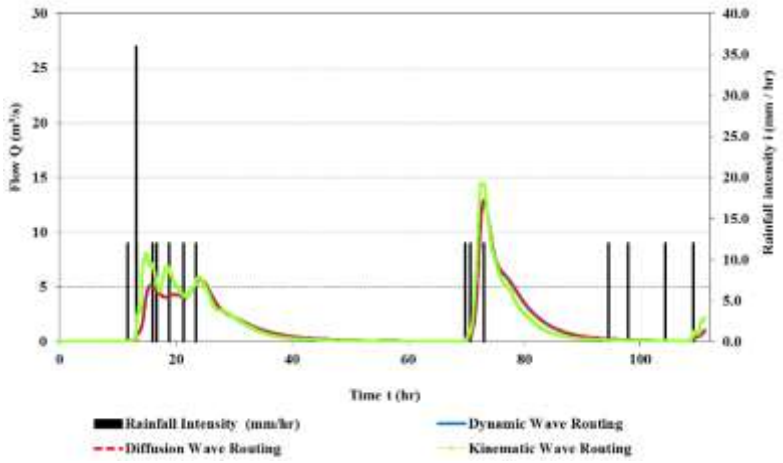

Figure 6. Calculated Flow Rates for the Scenario 4

In order to examine effects of different Manning's coefficients, Scenario 1 is compared to Scenario 2 and found that as Manning's roughness coefficients rise, the peak flow rates decrease from 26 m^3/s to 16 m^3/s. In order to investigate flow rate changes under typical and heavy rainfall events, Scenario 1 is compared to Scenario 3. It is observed that peak flow rates calculated with kinematic wave routing are higher than the ones calculated with diffusion and dynamic wave routing methods under typical rainfall. On the other hand, the opposite situation is observed in case of heavy rainfall. Thus, peak flow rates calculated with kinematic wave routing are lower than the ones calculated with the two other methods. The difference between kinematic and dynamic wave method is more dominant under typical rainfall with big Manning's coefficient. In general, all three routing methods in EPA SWMM work well for all scenarios.

CONCLUSIONS

In this study, dynamic, diffusion and kinematic wave routing methods are evaluated and compared. For this purpose, Sazlıdere hydrological and hydraulic watershed model developed with Environmental Protection Agency Storm Water Management Model (EPA SWMM) is employed in evaluation of different routing methods. The routing methods are tested using different Manning's coefficients and rainfall events. Two rainfall data measured at the field site are used in simulation to represent typical and heavy storm events. Model results show that EPA SWMM performs well and calculated flow rates with all three different routing methods are in general in good agreement.

References

EPA (The United States Environmental Protection Agency), 2015. Storm Water Management Model User's Manual Version 5.1.

Gülbaz S. and Kazezyılmaz-Alhan C.M. (2013) — Calibrated Hydrodynamic Model for Sazlıdere Watershed in Istanbul and Investigation of Urbanization Effects. Journal of Hydrologic Engineering. 18 (1) 75–84.

Gülbaz, S., Kazezyılmaz-Alhan, C. M., 2011. Hydrodynamic Model of the Sazlıdere Watershed. In: 5. National Water Engineering Symposium, September 12-16, Istanbul/Turkey.

Hayami, S., 1951. On the Propagation of Flood Waves, Bull. 1, Disaster Prevention Research Institute, Kyoto University, pp. 1–16.

Kazezyılmaz-Alhan, C. M., 2010. An Improved Solution for Diffusion Waves to Overland Flow. Applied Mathematical Modeling, 4165-4172.

Lighthill, M.J., Whitham, G.B., 1955. On kinematic waves, I: Flood movement in long rivers. Proceedings of the Royal Society of London, Series A 229, 281–316.

Saint-Venant, Barre de, 1871. Theory of unsteady water flow, with application to river floods and to propagation of tides in river channels, French Academy of Science, vol. 73. pp. 148-154, 237-240.

A COMPARISON OF FLOOD VULNERABILITY USING DIFFERENT RESOLUTION DIGITAL ELEVATION MODELS

V. S. Ozgur Kirca, Hafzullah Aksoy, H. Ibrahim Burgan*
Istanbul Technical University, Civil Engineering Department, Hydraulics Division, Istanbul, Turkey
*kircave@itu.edu.tr; haksoy@itu.edu.tr; burgan@itu.edu.tr**

ABSTRACT
Geographic Information System (GIS) technology is widely used in hydrological modeling studies. GIS based hydrological models always need Digital Elevation Models (DEM) data. This study is based on a comparative flood vulnerability defined by wetness indices using different resolution DEMs. Study area is selected as Guneskaya Catchment in Meric (Evros) River Basin, Turkey. DEMs were obtained from General Command of Mapping of Turkey as 1/25000 scale map and the free-access ASTER GDEM. The former has a 10-15 m mean accuracy while the latter has 30 m horizontal-20 m vertical accuracy at 90% confidence level. The wetness indices are defining according to basin morphology. Based on results of the implementation, it is concluded that scale of maps should be selected according to the importance and scope of the study. Also, the higher resolution of utilized DEMs, the more detailed flood vulnerability maps can be prepared.

Keywords: *Digital Elevation Model (DEM), Flood Vulnerability, Geographic Information Systems (GIS), SAGA Wetness Index (SAGAWI), Topographic Wetness Index (TWI).*

INTRODUCTION
In order to control flood disaster, various struggle and prediction methods related to flood are investigated and applied. Floods cannot be expressed only by meteorological phenomena. In the areas where economic and social development activity continues, the urbanization increasing due to the increasing population with industrialization increases the risk of overflow in the river basin.

Flood has remained the second deadliest of all weather related hazards and has been detrimental to many other societies in most parts of the world because of the large numbers of fatalities and the costly damages to properties and human lives (Adewumi et al., 2017). Flooding is also a part of the complex processes, which need to be assessed accurately to know the accurate spatial and temporal changes of flooding and their causes. Hydrological modelling has been used by several researchers in river and floodplain modelling for flood analysis (Anees et al., 2017).

For most rivers sufficient observations of flood extent are not available to determine inundation areas and recourse must be made to some of predictive models. These can range in complexity from simply intersecting a plane representing the water surface with a Digital Elevation Model (DEM) of sufficient resolution to give the flooded area (Bates & De Roo, 2000). Lack of gauged flow data most of the time, flood hazard extent determination is difficult. So, topographical and morphological characteristics can be used in these ungauged basins. Some morphologic indices can be used to produce these flood vulnerability maps. One of them is TWI which is proposed by Kirkby (1975) and is widely used in the studies such as Schmidt & Persson (2003), Manfreda et al. (2011, 2014, 2015), Qin et al. (2011), Maduako et al. (2016), Wu et al. (2016), De Risi et al. (2017), Giri et al. (2017). Also there are a lot of studies to determine flood risks using DEM data by Saksena & Merwade (2015), Hsu et al. (2016), Samela et al. (2017).

In this study, topographic wetness index and SAGA wetness index are used to assess the flood vulnerability. There are a lot of ungauged basins in Turkey so, the study will be very useful in terms of preliminary assessment of flood risks without flow data. Also the study presents a comparison of two different scaled DEM data on wetness indices.

DATA AND STUDY AREA

Data

Digital Elevation Model (DEM) data is used in the study. DEM data is classified as low and high resolution DEM. Low resolution DEM is acquired from ASTER-GDEM (Advanced Spaceborne Thermal Emission and Reflection Radiometer-Global Digital Elevation Model) data. It can be freely and easily downloaded from NASA-USGS Global Data Explorer website. The ASTER-GDEM data is developed by NASA and the Ministry of Economy, Trade and Industry (METI) of Japan.

High resolution maps are obtained from General Command of Mapping of Turkey as 1/25000 scale. For the purpose of the study, E19c3, E20d4, F19b2 and F20a1 sheets are merged and these merged contour line shapefiles are converted to DEM in QGIS software. The characteristics of commonly used DEM data are presented in Figure 1.

Comparison with other DEMs

	ASTER GDEM	SRTM3*	GTOPO30**	10 m mesh digital elevation data
Data source	ASTER	Space shuttle radar	From organizations around the world that have DEM data	1:25,000 topographic map
Generation and distribution	METI/NASA	NASA/USGS	USGS	GSI
Release year	2009 ~	2003 ~	1996 ~	2006~
Data acquisition period	2000 ~ ongoing	11 days (in 2000)		
Posting interval	30m	90m	1000m	about 10m
DEM accuracy (stdev.)	7~14m	10m	30m	5m
DEM coverage	83 degrees north ~ 83 degrees south	60 degrees north ~ 56 degrees south	Global	Japan only
Area of missing data	Areas with no ASTER data due to constant cloud cover (supplied by other DEM)	Topographically steep area (due to radar characteristics)	None	None

Other examples of available DEMs
- NED: with a resolution of 30 m, covering the entire U.S.A., provided by USGS

*SRTM3: Shuttle Radar Topography Mission Data at 3 Arc-Seconds
**GTOPO30: Global 30 Arc-Second Elevation Data Set

Figure 1. Comparison map scales of DEM data (ASTER G-DEM, 2017)

Study Area

The study area is selected as Guneskaya Catchment in Meric (Evros) River Basin, Turkey. Ergene River joins to Meric River which is a transboundary river and comes from Bulgaria to Saros, Aegean Sea, Greece. The output of the catchment is coordinated at 27°55'20" E-41°28'30" N. The catchment boundary is inside of Saray County, Tekirdag Province (Figure 2). The drainage area is 59.2 km^2 and the elevation at the output of the catchment is 149 m.

Guneskaya is the upstream zone of Ergene River. Also it is understood from historical ruins that Guneskaya is an historical place. Settlement traces in Guneskaya cave from Palaeolithic

(Old Stone Age) and Chalcolithic periods were found. The population is approximately 20000 in the region. Yildiz mountains encircling the basin have expansive forested areas. The study area has cold-wet winters and hot-dry summers. Mean annual precipitation is 678.2 mm.

Figure 2. 1/500000 scaled location map of Guneskaya Catchment (red colored).

METHOD AND APPLICATION

In this study, wetness indices are used to define flood vulnerability areas in Guneskaya Catchment in Meric (Evros) River Basin, Turkey. For identification of flood vulnerability in the catchment, two indices are used. To produce maps of these indices, two software packages are used; Quantum GIS (QGIS) and System for Automated Geoscientific Analyses GIS (SAGA GIS), both of which are fully supported by GIS. Both GIS software packages are freely available and user-friendly. The methods to map flood vulnerability areas are based on the Topographic Wetness Index (TWI) approach and its variant, the SAGAWI, respectively.

TWI used in QGIS was suggested by Beven & Kirkby (1979) as

$$\mathrm{TWI} = ln\left(\frac{A_s}{tan\,\beta}\right) \qquad (1)$$

where A_s is the (upslope) flow accumulation area (or drainage area) per unit contour length (Wilson & Gallant, 2000) and β is the angle of the slope. *TWI* has found a wide range of application in hydrology (Moore et al., 1991; Quinn et al., 1995; Sorenson et al., 2005). Although TWI assumes that the soil in the watershed is homogeneous and isotropic as a constraint, it was found that topographical changes become much more significant in flood-related analyses, therefore, the drawback of this assumption becomes negligible compared to the change in the topography of the watershed. This allows one to use TWI in the hydrological analysis such as this study.

The SAGA WI used in SAGA-GIS is based on a modified catchment area calculation which does not consider the flow as a very thin film. As a result, it predicts, for cells situated in valley floors with a small vertical distance to a channel, a more realistic and with higher potential soil

moisture as compared to TWI. This fact is translated to a wider area calculated as potentially covered with water during a flood event.

The TWI can be effectively used to reveal the flooding susceptibility by mapping the flood vulnerability areas. The procedure to calculate the TWI and the SAGA WI in order to define the susceptibility to flooding (the flood-vulnerability areas) is very straight forward since the selected open source software Quantum GIS (QGIS) incorporates the respective routines built into the SAGA-GIS. In the literature, no study exists dealing with the problem as in the way used here other than a case study performed very recently by Samela et al. (2015) for delineation of flood-prone areas in ungauged basins.

RESULTS

TWI and SAGA WI maps resulted from low and high resolution DEM data are presented in Figure 3-6. According to SAGA WI results, the output of Guneskaya catchment, Ayvacik, Kavacik and Gungormez, which are old settlements as Guneskaya, have flood vulnerability. In addition to this preliminary assessment, hydraulic models should be developed in the region to produce detailed flood hazard maps using hydrological, meteorological and topographical data.

Figure 3. Topographic wetness index map using low resolution DEM data.

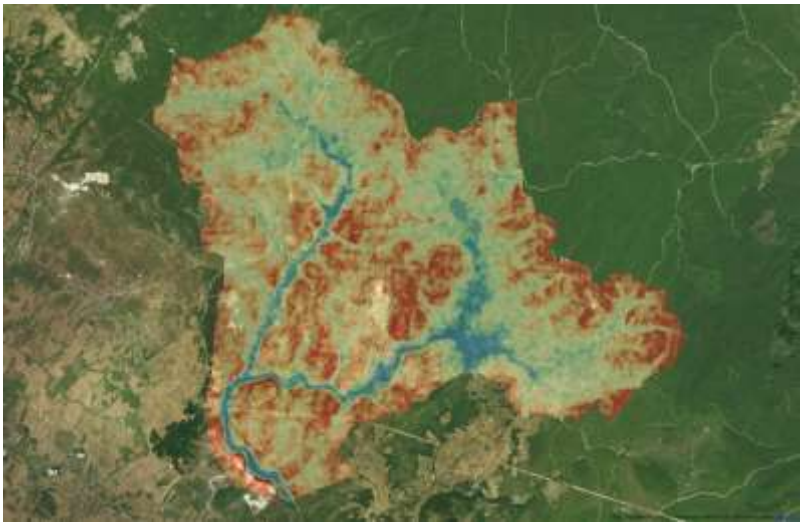

Figure 4. SAGA wetness index map using low resolution DEM data.

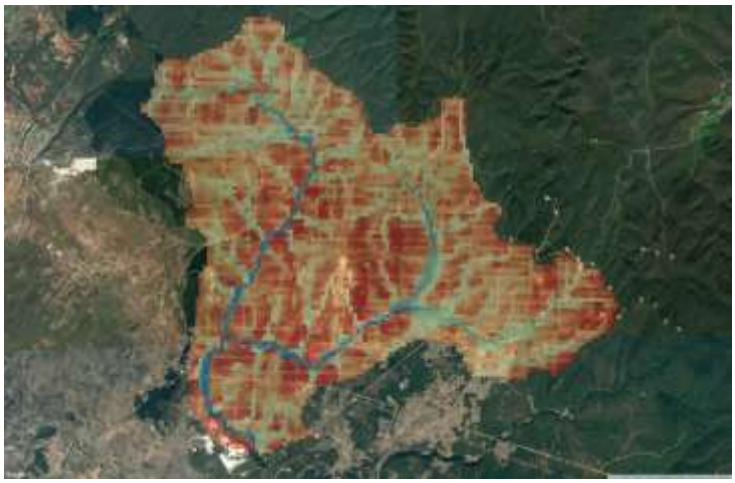

Figure 5. Topographic wetness index map using high resolution DEM data.

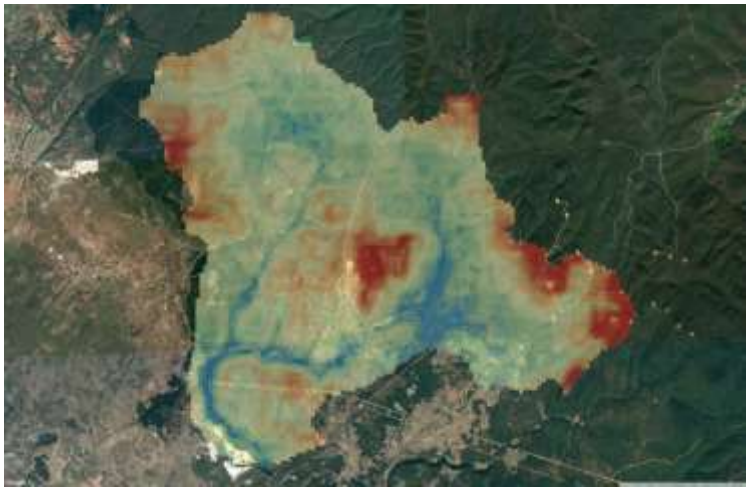

Figure 6. SAGA wetness index map using high resolution DEM data.

C**ONCLUSIONS**

This study provides a convenient method for the preliminary assessment of flood vulnerability in a selected study area practically. For this analysis, the only required data is DEM, which can be obtained freely and easily in the form of ASTER GDEM data, as mentioned above. However, for specific purposes like the planning of protection structures against flood, high resolution maps are needed. It is shown that higher the 1/25000 scale maps provided a much refined spatial output of flood vulnerability compared to ASTER GDEM data (which roughly corresponds to 1/150000~1/100000 scale). When it comes to hydraulic calculations to yield the spatial distribution of flow depth and velocity as a function of the return period of extreme events, at least 1/5000 (or even higher) scale maps are required for utilizing 1D or 2D hydraulic models by use of software packages such as HEC-RAS. When the two wetness indices applied in this study are compared, TWI results present us a more optimistic (or less risky) flooded area distribution compared to the results of SAGA WI. This finding is in compliance with the results of past studies by Aksoy et al. (2015, 2016), Burgan et al. (2015, 2016). The results of high resolution maps give higher and more detailed flood vulnerability maps for both TWI and SAGA WI. As the next step, other characteristics of the catchment area (such as land-use, surface texture, soil characteristics, urbanization, precipitation features, etc.) can be used in more refined hydraulic model. As an alternative approach, historical floods can be considered to assess flood risks in such study areas.

REFERENCES

Adewumi, J.R., Akomolafe, J.K., Ajibade, F.O. (2017). Development of flood prone area map for Igbokoda Township using geospatial technique. Journal of Applied Science & Process Engineering, 4(2), 158-178.

Aksoy, H., Kirca, V. S. O., Burgan, H. I., Kellecioglu, D., Ermis, I. S. (2015). Determination of flood-prone areas by soil wetness index in river basins. The 8th National Hydrology Congress, 08-10 October 2015, p. 424-429, Harran University, Sanliurfa, Turkey (*in Turkish*).

Aksoy, H., Kirca, V.S.O., Burgan, H.I., Kellecioglu, D. (2016). Hydrological and hydraulic models for determination of flood-prone and flood inundation areas. The 7th International Water Resources Management Conference of ICWRS, 18-20 May 2016, vol: 373, p. 137-141, Proceedings of the International Association of Hydrological Sciences (IAHS), Bochum, Germany.

Anees, M.T., Abdullah, K., Nordin, M.N.M., Ab Rahman, N.N.N., Syakir, M.I., & Kadir, M.O.A. (2017). One-and two-dimensional hydrological modelling and their uncertainties. Chapter 11, Flood Risk Management, InTech.

ASTER G-DEM website "Comparison with other DEMs." *Features of ASTER G-DEM*, METI, www.jspacesystems.or.jp/ersdac/GDEM/E/2.html, Access date: 09/10/2017.

Bates, P.D., De Roo, A.P.J. (2000). A simple raster-based model for flood inundation simulation. Journal of Hydrology, 236, 54-77.

Beven, K.J., Kirkby, M.J. (1979). A physically-based variable contributing area model of basin hydrology. Hydrol. Sci. Bull., 24, 43-69.

Burgan, H. I., Kellecioglu, D., Aksoy, H., Kirca, V. S. O., 2015. Flood hydraulics model based on geographic information systems. The 4th Water Structures Symposium, 19-20 November 2015, p. 260-267, The Chamber of Civil Engineers, Antalya, Turkey (*in Turkish*).

Burgan, H. I., Kirca, V. S. O., Aksoy, H., 2016. The effects of sea level on flooded area. The 4th National Flood Symposium, Recep Tayyip Erdogan University, 23-25 November 2016, p. 749-755, Rize, Turkey (*in Turkish*).

De Risi, R., Jalayer, F., De Paola, F., Lindley, S. (2017). Delineation of flooding risk hotspots based on digital elevation model, calculated and historical flooding extents: the case of Ouagadougou. Stochastic Environmental Research and Risk Assessment, 1-15.

Giri, S., Qiu, Z., Zhang, Z. (2017). A novel technique for establishing soil topographic index thresholds in defining hydrologically sensitive areas in landscapes. Journal of Environmental Management, 200, 391-399.

Hsu, Y.-C., Prinsen, G., Bouaziz, L., Lin, Y.-J., Dahm, R. (2016). An investigation of DEM resolution influence on flood inundation simulation. Procedia Engineering, 154, 826–834.

Kirkby, M.J. (1975). Hydrograph modelling strategies. In: Peel R.F., Chisholm M.D., Haggett P. (eds.) Progress in physical and human geography. Heinemann, London, 69–90.

Maduako, I.N., Ndukwu, R.I., Ifeanyichukwu, C., Igbokwe, O. (2016). Multi-index soil moisture estimation from satellite earth observations: comparative evaluation of the Topographic Wetness Index (TWI), the Temperature Vegetation Dryness Index (TVDI) and the improved TVDI (iTVDI). Journal of the Indian Society of Remote Sensing, 45(4), 631-642.

Manfreda, S., Di Leo, M., Sole, A., (2011). Detection of flood prone areas using digital elevation models. Journal of Hydrologic Engineering, 16 (10), 781–790.

Manfreda, S., Samela, C., Sole, A., Fiorentino, M. (2014). Flood-prone areas assessment using linear binary classifiers based on morphological indices. Second International Conference on Vulnerability and Risk Analysis and Management (ICVRAM), 13-16 July 2014, p. 2002-2011, University of Liverpool, UK.

Manfreda, S., Samela, C., Gioia, A., Consoli, G.G., Iacobellis, V. Giuzio, L., Cantisani, A., Sole, A. (2015). Flood-prone areas assessment using linear binary classifiers based on flood maps obtained from 1D and 2D hydraulic models. Natural Hazards, 79, 735-754.

Moore, I. D., Grayson, R.B., Ladson, A.R. (1991). Digital terrain modeling: A review of hydrological, geomorphological and biological applications. Hydrological Processes, 5, 3-30.

Qin, C.-Z., Zhu, AX., Pei, T., Li, B.-L., Scholten, T., Behrens, T., Zhou, C.-H. (2011). An approach to computing topographic wetness index based on maximum downslope gradient. Precision Agriculture, 12(1), 32–43.

Saksena, S., Merwade, V. (2015). Incorporating the effect of DEM resolution and accuracy for improved flood inundation mapping. Journal of Hydrology, 530, 180–194.

Samela, C., Manfreda, S., Paola, F. D., Giugni, M., Sole, A., Fiorentino, M. (2015). DEM-based approaches for the delineation of flood-prone areas in an ungauged basin in Africa. Journal of Hydrologic Engineering, 06015010.

Samela, C., Troy, T.J., Manfreda, S. (2017). Geomorphic classifiers for flood-prone areas delineation for data-scarce environments. Advances in Water Resources, 102, 13-28.

Schmidt, F., Persson, A. (2003). Comparison of DEM data capture and topographic wetness indices. Precision Agriculture, 4, 179-192.

Sorenson, R., Zinko, U., Seibert, J. (2005). On the calculation of the topographic wetness index: evaluation of different methods based on field observations. Hydrology and Earth Systems Sciences Discussions, 2, 1807–1834.

Wilson, J.P. and Gallant, J.C. (2000). Terrain Analyses: Principles and Applications. John Wiley & Sons Inc.

Wu, Y., Giri, S., Qiu, S. (2016). Understanding the spatial distribution of hydrologic sensitive areas in the landscape using soil topographic index approach. International Soil and Water Conservation Research 4, 278–283.

ANALYSIS OF URBAN VOLNERABILITY FROM EXTREM PRECIPITATION INDICES OVER IRAN (1981-2010)

Manuchehr Farajzadeh[1], Amir Gandomkar[2] Hamideh Dalaei[3]
[1]-Tarbiat Modares University, Tehran, Iran
farajzam@modares.ac.ir
[2]- Islamic Azad University, Najafabad Branch, Najafabad, Iran
aagandomkar@yahoo.com
[3]-Expert of Iran meteorological organization (IRIMO)
h-dalaei@irimo.ir

Abstract
Cities due to changes in hydrological conditions in the areas and their large critical infrastructures are increasingly vulnerable to the changes in patterns of rainfall events arising from climate change and resulting floods. In this study, by identifying the extreme indices of precipitation recommended by the Climatology Commission of World Meteorology Organization, we have carried out zoning and weighting these indices in ArcGIS, and finally Vulnerability zones of Iran were classified into 5 categories. The result found that frequency of precipitation indices decreased and trend of them had increased.

***Keywords**: Urban, Extreme Climate Indices, Precipitation Indices, Iran.*

INTRODUCTION
Climate change as one of the major threats to interpret some researchers as the most serious threat in the 21st century. This is a threat for global commons such as oceans, seas, ozone and weather. In recent years climate change, affect all regions of the world problems and crises. One of the most damaging effects of climate change, extreme events and changes in the intensity and frequency of their formation (Dalaei et al., 2009). Although limit events happen rarely but have direct effect people, countries and vulnerable regions (Farajzadeh, 2013). The climate occurrence depends on Extreme temperature and Precipitation. Therefore, consider of Extreme climate data is necessary (Taghavi et al., 2014). The causes of extreme events weather and climate due to the destruction of human life and increased costs associated with it in the past few years that have been extremely (Easterling and et al., 2000), that Can be cause a major impact on society, the economy and the environment (Manton et al., 2001). Commission of Climate (CCL / CLIVAR) in associate with research program variability and predictability (WCRP) to monitor climate change and its profile of them proposed special formulas to calculate the various indexes (Peterson, 2001). The result of this effort has been the production of software's such as ClimDEX (Rahimzadeh et al., 2007). Results of above study showed that percent of the number of days that minimum the temperature of them is more than 95th percentile have increased and the percent days with minimum temperature less than the 5th percentile fallen cold nights, thus the desire for reduce the number of temperature anomalies days was decreased across the Russia (Bulygina et al., 2007). Also, with development and application of some climate indexes, scaling based on monitoring extreme climate events and the social and economic effects in South Asian countries (Bangladesh, India, Nepal, Sri Lanka and Pakistan) with 27 profile part evaluated by ETCCDMI5 expert team. For this purpose extreme events were evaluate by temperature index of 210 stations and for precipitation was used from 265 stations. The results showed that both temperature and precipitation indices indicated trends increased in South Asia. The performed studies for the indexes point to the average regional temperature and precipitation in South America for the period 1950-2010 and 1969- 2009 showed that heating and cooling throughout of South America increased from the second half of the twentieth century indicate minimum temperature profile showed warming

rates, if the daytime maximum temperature shows warming. Severe and moderate trends index obtained by means of regional means and often mentioned to cold declining in South America during the warm days and nights (Milagros Skansi et al., 2013).
Therefore, the aim of this study is identify of climate behavior and analysis of the precipitation indices of Iran to explain the opportunities and challenges of climate change in order to achieve deal environmental security in Iran.

METHODS

Considering that the criteria for the recognition of climate behavior based on WMO standards is a 30-year-old climate, where climatic parameters, shows their behavior. In this paper used as the basis period of 1981 to 2010. Daily synoptic stations data, since 1981 had been investigated and 52 stations were extracted. After reviewing the station data select stations that have heterogeneity due to natural problems only. In order to calculate the values of 11 degree temperature profile indices used RCLIMDEX software and daily minimum and maximum data daily for daily temperature and precipitation selected by used of Fortran90 program in RCLLMDEX input file (Table1). Missing data showed as -99.9 that isolate them from zero and the option that daily missing of them is lower than World Meteorological Organization standards were used. After indices and trend calculate significance of trend considered by Kendall Tau test, After this, zoned areas with frequency of high precipitation and these areas exactly coincide to internal threats and are unsafe. By identifying those areas can improve crisis management.

APPLICATION AND RESULTS

Climatological studies about Iran shows that the North, West and South-West regions with an area of about 31 percent constitute 52 percent of precipitation and 69 percent of runoff; While 69 percent of the country produce 44% of precipitation and 31% of runoff. According to the forecasts of climate change in Iran's precipitation, Northwestern, West and Southwestern regions will faced with decreased rate of precipitation compared with the current status and average precipitation and East, Southeast and Central regions will have an increase in the amount of precipitation. According to the trend maps and the precipitation slope in the cold months, it is concluded that in these months the percentage of land area with negative trend in the trend of rainy days has been increased. This means that the intensity of rainfall for the cold season in these areas has been increased during recent years. This is a proof of the impact of global climate change on the country's climate. Figure 1 shows venerability of Iran based on extreme precipitations indices.

CONCLUSION AND RECOMENDATION

All the trends were calculated at 95% and their significance was investigated using the Mann-Kendall's test. The results show that the indicators of heavy precipitation in most of the stations of Iran (Bandar Abbas, Kish, Bam, Tabas, Mashhad, and Shahroud) have been decreased from -0.02 to -0.01 and the stations in Abali and Noshahr had experienced an increasing trend in the heavy precipitation days from 0.4 to 0.9. The precipitation indices have had decreasing trends that is in line with the results of global warming. These indices can lead to two basic strategies, defensive and attack strategy. Countries that have the resources have to have fortified for protection of their sources. However, this country may also have long-standing enemies in neighborhood with climate change, access to food, water or energy. Also, may be have a alliance far from the mind in order to make a defensive formed. This scenario poses new challenges for all countries.

Table 1. The data used to analysis of vulnerability based on RCLLMDEX input

RX1day	Max 1-day precipitation amount	Monthly maximum 1-day precipitation	Mm
R10	Number of heavy precipitation days	Annual count of days when PRCP>=10mm	Days
R20	Number of very heavy precipitation days	Annual count of days when PRCP>=20mm	Days
Rnn	Number of days above nn mm	Annual count of days when PRCP>=nn mm, nn is user defined threshold	Days
CDD	Consecutive dry days	Maximum number of consecutive days with RR<1mm	Days
CWD	Consecutive wet days	Maximum number of consecutive days with RR>=1mm	Days
PRCPTOT	Annual total wet-day precipitation	Annual total PRCP in wet days (RR>=1mm)	mm

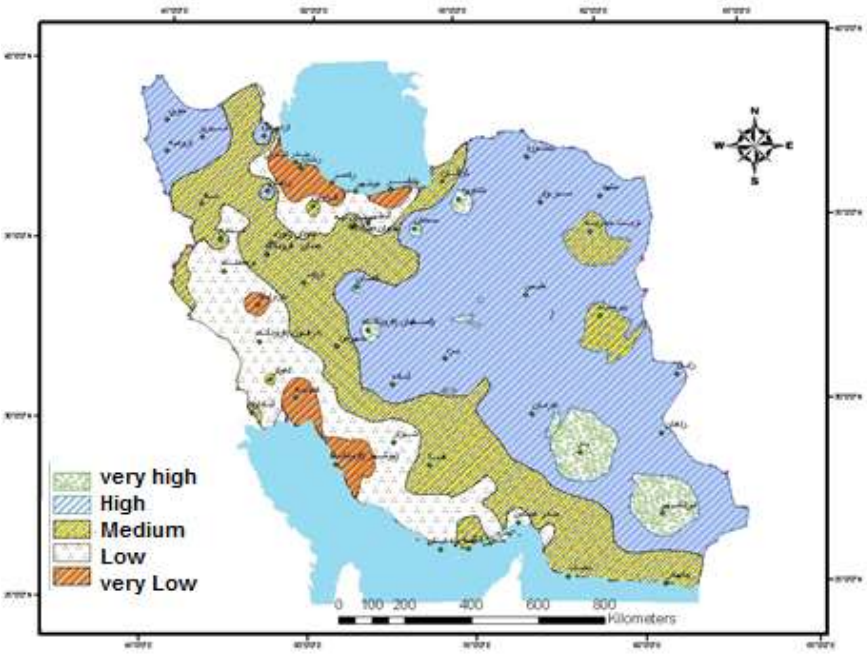

Figure 1. The vulnerability of Iran based on extreme precipitation indices

REFERENCES

Bulygina., O N, Razuvaev., V N , Korshunova., N N and P YaGroisman, 2007, Climate variations and changes in extreme climate events in Russia, IOP PUBLISHING ENVIRONMENTAL RESEARCH LETTERS , Environ. Res. Letters. No 2. P 1-7.

Dalaei, H. Alijani, B. and Ahmadi, M. 2009. Statistical analysis of the risk management approach freezing temperatures and ice road in the province of Lorestan and Bakhtiari. Transportation Engineering Research Journal. 2(2):122-129. [In Persian].

Easterling D.R., J.L. Evans, P.Ya. Groisman, T.R. Karl,K.E. Kunkel, and P.Ambenje,2000, Observed Variability and Trends in Extreme Climate Events: A brief review. Bulletin of the American Meteorological Society, 81(3), 417-425.

Farajzadeh Manuchehr, 20013, Climatic disaster of IRAN, SAMY publisher, p. 12 [In Persian].

Manton MJ, Della-marta PM, Haylock MR, Hennessy KJ, Nicholls N, Chambers LE,Collins DA, Daw G, Finet A, Gunawan D, Inape K, Isobe H, Kestin TS, Lefale P, LeyuCH, Lwin T, Maitrepierre L, Ouprasitwong N, Page CM, Pahalad J, Plummer N,Salinger MJ, Suppiah R, Tran VJ, Trewin B, Tibig I and Yee D., 2001, Trend in Extreme Daily Rainfall and Temperature in Southeast Asia and South Pacific:1961-1998, Int. J. Clim. Vol. 21, pp 269-284.

Milagros Skansi, D., Manola Brunet , Javier Sigró , Enric Aguilar ,Juan Andrés Arevalo Groening , Oscar J. Bentancur , Yaruska Rosa Castellón Geier ,Ruth Leonor Correa Amaya , Homero Jácome , Andrea Malheiros Ramos , Clara Oria Rojas ,Alejandro Max Pasten , Sukarni Sallons Mitro , Claudia Villaroel Jiménez , Rodney

Martínez , Lisa V. Alexander , P.D. Jones 2013, Warming and wetting signals emerging from analysis of changes in climate extreme indices over South America, Global and Planetary Change 100 (2013) 295–307.
Peterson,T.C., C.Folland,G. Gruza, W.Hogg, A.Mokssit, and N.Plummer, 2001, Report of the Activities of the Working Group on Climate Change Detection and Related Rapporteurs, World Meteorological Organization Technical Document No.1071, WMO Geneva,146PP.
Rahimzadeh, F. Dezfuli, H. Poorasgharian, M.,2007, Assessment of the extent of the mutation profile of temperature and precipitation in the province of Hormozgan. Geography and Development Journal. 21:97-116. [In Persian]
Robeson SM. 2002. Inareasing Growing – Season Length in Illinoise During the 20th Century, Climate Change ,52, 219-238.
Taghavi, F and Mohammadi, H. , 2005, Trends of temperature and precipitation indices in Tehran. Geographically Research. 53:151-172. [In Persian]

6-9 JANUARY 2017 SNOW STORM OVER ISTANBUL-TURKEY

Meral Demirtaş[1]
[1]*University of Ondokuz Mayıs, Department of Meteorological Eng.*
mdemirtas@omu.edu.tr

Abstract
Turkey was affected by a very heavy snowstorm during 6–9 January 2017 that resulted in high societal impacts. The snowstorm was not exceptional but remarkable for its intensity. It was associated with an eastern Atlantic ridge that intensified the northeast-southwest tilted trough to create favourable conditions for cold-air outbreaks and snowstorms. The composite analysis shows that the location of cold temperatures depends strongly on the position and strength of the atmospheric blocking. The blocking is associated with an arching-type low-frequency wave train that spans the Eastern Atlantic and Western Europe. This positioning has the most favourable structure for cold air outbreaks over the south Eastern Europe because it leads to an intense downstream trough over this region. The juxtaposition of these flow patterns promoted the occurrence of cold temperatures and snowstorm. Analysis of atmospheric model products indicated that the remarkable snowstorm was strongly modulated by meso-scale effects induced on the synoptic-scale flow. There was a sustained co-alignment of an upper-tropospheric tongue of high potential vorticity (PV) over a pre-existing low-level baroclinic region. Interaction between the PV-streamer and conditions at low-levels set the scene for an enhanced dynamical feedback between the low-levels and upper levels, and the tighter coupling led to further reinforcement of low-level moist advection. A south-westerly low level jet transported conditionally unstable and moist air from the relatively warm Mediterranean Sea and north easterly flow carried moist air from the Black Sea, and the sustained moisture flux.

Keywords**:** *January 2017 snowstorm, potential vorticity, atmospheric blocking, İstanbul-Turkey*

INTRODUCTION
At the first week of January 2017 (hereafter January 2017), the north-eastern and south-eastern parts of Europe was hit by a cold spell resulting in temperatures below 40°C in Sweden and in Finland, and temperatures below 30°C in the various parts of Europe. In concurrently, some countries in southern and south-eastern Europe (*e.g.* Italy, Poland, Hungary, Romania, Bulgaria, Bosnia, Greece and Turkey) were hit by severe snow storms. Although the January 2017 winter storm was not the most severe of the twenty-first century, but it can be considered for the high-impact weather category. The snow storm caused many accidents on roads, school closures, and cancelled flights. The Danube River and the Bosporus Sea Strait were closed for shipping. Turkish Airlines cancelled 192 domestic and international flights that were scheduled for 7 January 2017. About 600 flights were cancelled on 8 January 2017. After the heavy snow, icy conditions and strong winds were forecast for Istanbul. Ferry services between the European and Asian sides of the city were stopped and schools across the city were also closed. The snowfall has also caused hundreds of village roads to be blocked in the eastern provinces of Turkey.

The January 2017 snow storm in some ways resembles the persistent severe snow storm of March 1987 (Tayanç *et al.*, 1998) which significantly disrupted everyday life over a very large area covering the Balkans and eastern Mediterranean. The January 2017 snow storm was much more extensive and abundant and the heavy snowfall paralyzed many parts of the city. İstanbul Municipality (hereafter İM) reported that 7,000 staff with 350 heavy-duty vehicles was in duty throughout day and night, and around 9,000 tons of salt and related solutions were used to keep

roads open to traffic. İM's snow height observations are: on 8 January 2017, snow covers of 20-50 cm over central parts of Istanbul, and values above 100 cm over Asian side of the city. The January 2017 outbreak is the first of its kind since February 2012 (Demirtaş, 2017) when there was a similar Atlantic-Europe upper air pattern with blocking high extending from the Atlantic into Western Europe and intense Siberian cold extending south to the Mediterranean on the rear of a large, deep cyclone which dropped out of Scandinavia.

The wintry January 2017 weather set in across much of Central and Eastern Europe. It was the result of a strong area of stationary high pressure over mid-Atlantic and Western Europe, resulting in strong winds circulating from Russia and Scandinavia towards Eastern Europe. The location of the high-pressure system implied that the past few days had seen a cold northerly winds extend from Scandinavia to south eastern European countries. Further south, an area of low pressure dominated the weather, which brought relatively mild, moist air across the Mediterranean. This feed of moisture led to snow as it moved over Italy, the Balkans and across the Black Sea. In addition, heavy snow in central and Southern Italy was the result of cold air flowing across the warmer Adriatic Sea.

Some parts of Greece and Turkey received sea-impact snowfall from the Aegean Sea and the Black Sea. Various islands and mainland coast of the Aegean Sea in Greece and western Turkey as well as the Marmara region received large amounts of snow. Snow height in some places exceeded 100 cm. The intense snowfall was caused by the large, persisting cut-off low, which formed during the intense polar air intrusion across eastern into south Eastern Europe and eastern Mediterranean. Northerly and north easterly winds advected cold air mass across the Black sea, the Marmara Sea and the Aegean Sea caused locally intense convective snow showers.

A high-pressure system moving slowly eastwards over Europe advected cold air to south Eastern Europe. The largest surface temperature deviations from the climatological means were on the Balkans: Montenegro, Serbia, the republic of Macedonia and Bulgaria were much colder than climatological means, with temperatures as low as -15 ºC over five consecutive days. It was also cold in eastern Italy, Romania, Greece and western Turkey with 5-day mean temperatures of 5- 10 ºC below climatological means of January. The freezing temperatures with a low over the Mediterranean caused large amounts of snow to many places. This study investigates the salient features of the 6-9 January 2017 snow storm and the influence of large-scale concurring atmospheric circulation patterns. For this purpose: (i) observations, (ii) prominent synoptic and dynamic precursors and (iii) atmospheric blocking are examined.

DATA AND METHODS

This study uses operational European Centre for Medium-Range Weather Forecast (ECMWF) high-resolution analysis data, interpolated on a 0.25° × 0.25° latitude-longitude grid. The structure, time and space evolution of the case presented in here is based mainly on the ECMWF operational analyses. The ERA-Interim (EI) reanalysis data of the ECMWF (Dee *et al.,* 2011) are employed with a 1°x1° longitude-latitude grid horizontal resolution to compute atmospheric blocking parameters.

Atmospheric blocking detection method

Objective detection of atmospheric blocking is very desirable for weather forecasting, since it exerts a strong influence on the upstream, *in-situ*, and downstream weather. Thus, it is necessary to employ an objective blocking detection method. A two-dimensional index based on the reversal of the meridional gradient of geopotential height at 500 hPa is implemented (Tibaldi

and Molteni, 1990; Scherrer *et al.,* 2006; Davini *et al.,* 2012; Demirtaş, 2017). For every grid point, the following metric is defined:

$$GHGS(\lambda_0,\Phi_0)=\frac{Z500(\lambda_0,\Phi_0)-Z500(\lambda_0,\Phi_S)}{\Phi_0-\Phi_S} \quad (1)$$

$$GHGN(\lambda_0,\Phi_0)=\frac{Z500(\lambda_0,\Phi_N)-Z500(\lambda_0,\Phi_0)}{\Phi_N-\Phi_0} \quad (2)$$

$$\Phi_s=\Phi_0-15° \quad (3)$$

$$\Phi_N=\Phi_0+15° \quad (4)$$

where $Z500(\lambda_0,\Phi_0)$ represents the grid point 500 hPa geopotential height at longitude (λ_0) which ranges from 0° to 360° and latitude (Φ_0) which ranges from 30° to 70°N. An instantaneous local blocking (LIB) is assigned for a grid point, if both of the following conditions are satisfied:

$$GHGS(\lambda_0,\phi_0)\succ 0 \quad (5)$$

$$GHGN(\lambda_0,\phi_0)\prec -10\,\text{m/°latitude} \quad (6)$$

A grid point is assigned for instant atmospheric blocking if conditions given in Equations (5-6) are satisfied. A sector is defined as large-scale blocking, if the above criteria are satisfied for at least 15 continuous longitudes. A time-scale of 4 days is used to define a blocking episode. A blocking event is considered as large scale episode of blocking if afore mentioned both spatial and temporal conditions are satisfied.

OBSERVATIONAL AND DYNAMICAL ANALYSIS OF THE EVENT

Observational Overview

Precipitation is modulated by topography and this poses great variability throughout İstanbul. The State Meteorological Service snow height measurements are presented in Table 1. As it can be inferred from the Table 1, the heavy snow fell during the 6–9 January 2017 period and was followed by snowy weather with short intermissions.

Table 1. Turkish State Meteorological Service's snow measurements (cm) in İstanbul.

Station name	*06.01.2017*	*07.01.2017*	*08.01.2017*	*09.01.2017*
Sarıyer	12	5	50	55
Kilyos	8	13	15	24
İstanbul Atatürk Int. Airport	17	23	15	25
İstanbul Sabiha Gökçen Int. Airport	20	22	16	33
Kartal	13	12	14	30

Surface air temperatures rapidly decreased during 6-9 January 2017 period. Table 2 presents minimum temperature measurements for the selected İstanbul stations. Temperatures are below zero throughout the period, except at the Sabiha Gökçen Int. Airport on 6 January, but at the

same station, the minimum temperature is -2.5°C on 7 January, and it is -5.8°C on 8 January. It can be inferred from Table 2 that 7-8 January are the coldest days which provided conditions for icy roads.

Table 2. Turkish State Meteorological Service's 2 m minimum temperature measurements (°C) in İstanbul.

Station name	*06.01.2017*	*07.01.2017*	*08.01.2017*	*09.01.2017*
Sarıyer	-1.7	-4.7	-4.9	-3.1
Kilyos	-1.0	-4.1	-3.7	-2.6
İstanbul Atatürk Int. Airport	-4.2	-5.5	-3.6	-1.4
İstanbul Sabiha Gökçen Int. Airport	9.4	-2.5	-5.8	-2.8
Kartal	-1.0	-4.5	-4.6	-1.8

The development of snow clouds can be inferred from the Meteosat-10 water vapour imagery. The exceptional moist air-mass seclusion appears to be one of the main factors that led to the high concentration of moist air which made possible the unprecedented snow over north-western part of Turkey Figure 1(a)–(b). The convective system stayed over the same region for many hours.

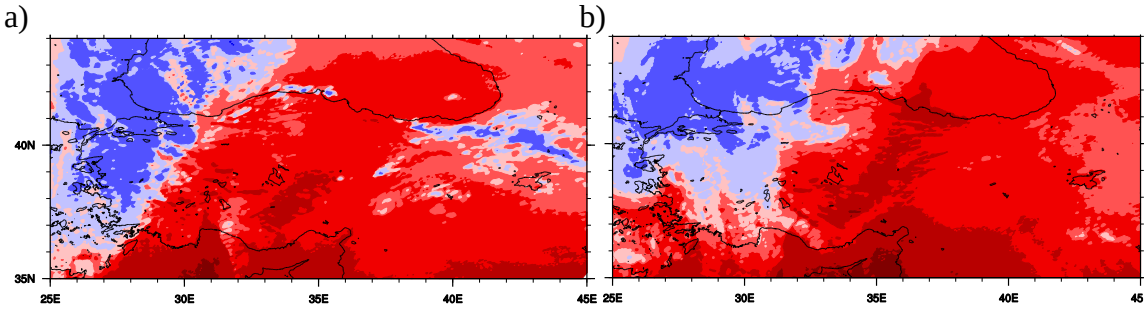

Figure 1. Meteosat-10 water vapour imagery: a) 1700 UTC 6 January 2017; b) 0300 UTC 7 January 2017

Turkish State Meteorological Service's İstanbul radar images were also examined. According to radar images considered, the 24-h total precipitation amounts were underestimated (Figure 2 (a-b)). These images are based on the raw data, no further calibration and/or Z-R relationship modifications are applied.

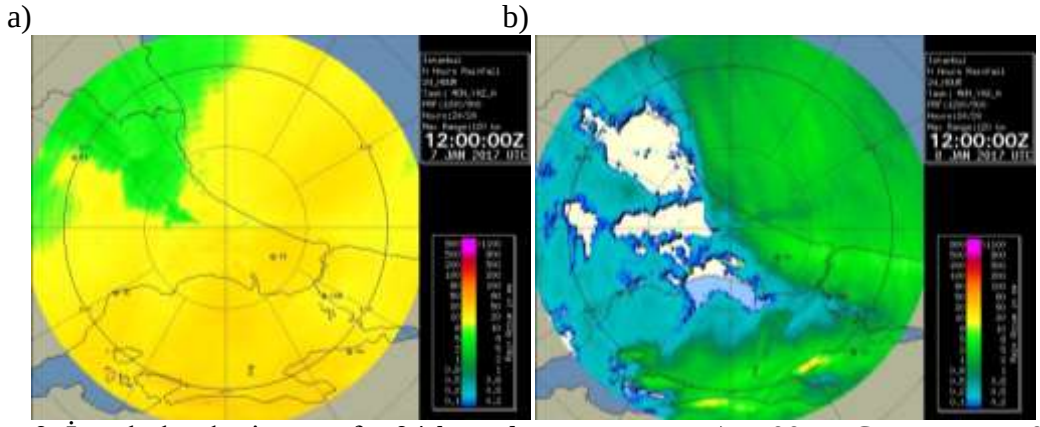

Figure 2. İstanbul radar images for 24-h total precipitation: a) 1200 UTC 7 January 2017; b) 1200 UTC 8 January 2017

Synoptic and Dynamical Precursors

The formation of a high pressure system over eastern Atlantic steered the low toward the Mediterranean region. Due to the atmospheric blocking which is caused by the persistent high pressure system, a cold core cyclone formed over the eastern Mediterranean and the Balkans. The amplification of the large-scale flow during the development phase of the cyclone advected cold air to very low latitudes.

At 006 UTC 6 January 2017, a surface low is centred over north-west of Turkey (Figure 3 (a)), and a cold front extending from the low centre, turning anti-cyclonically and spanning from north to south over the north of Spain (not shown). Another cold front is over north-west of Turkey (not shown). The multiple front structures are consistent with the November 1994 Piedmont Flood case (Buzzi *et al.*, 1998) and the October 2011 Antalya case (Demirtaş, 2016).

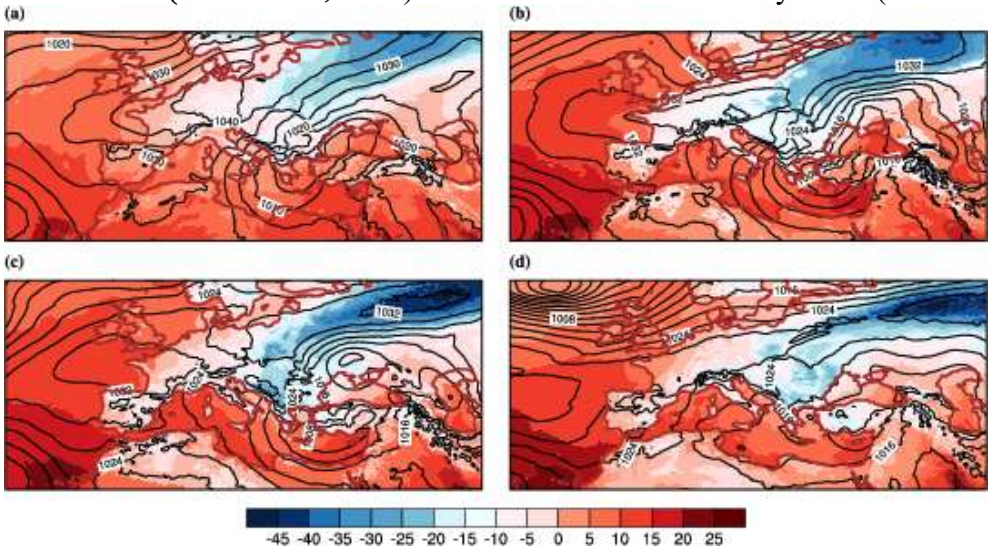

Figure 3. Temperature at 2 m (°C) and mean sea level pressure (hPa) in contours. a) 0600 UTC on 6 January 2017; b) 0600 UTC on 7 January 2017; c) 0600 UTC on 8 January 2017; d) 0600 UTC on 9 January 2017

The upper level northeast - southwest tilted trough is over southern Italy (Figure 4 (a)). At the 300-hPa, the Polar jet with strong (50 m s^{-1}) jet cores are noted on both sides of the upper level trough and there is also a strong zonal sub-tropical jet with 55 m s^{-1} maxima (Figure 4 (a)).

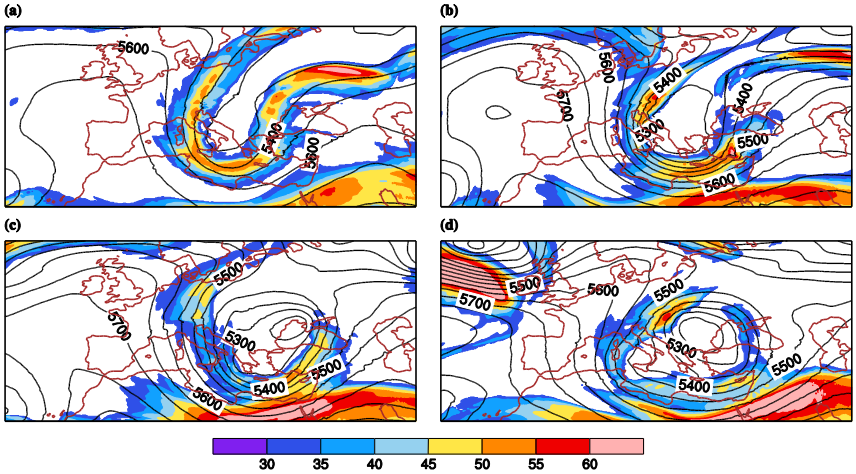

Figure 4. 500 hPa geopotential height (gpm) and wind (ms^{-1}) at 300 hPa. a) 0600 UTC on 6 January; b) 0600 UTC on 7 January 2017; c) 0600 UTC on 8 January 2017; d) 0600 UTC on 9 January 2017

Another synoptic scale ingredient conducive to snow-storms is the potential vorticity (PV)-streamer -which is related with high-PV stratospheric air that intrudes into lower levels of the atmosphere in a filamentary structure (Massacant *et al.*, 1998). These PV structures are usually considered as upper-tropospheric dynamical precursors of Mediterranean cyclogenesis, and they also play a pivotal role in the development and intensification of these cyclones (Massacant *et al.*, 1998; Demirtaş, 2016). A broad high-PV area prevails in the northeast and southwest direction (Figure 5 (a)) and coincides well with the upper-level trough (Figure 4(a)). Multiple fronts are aligned parallel to, and ahead of, the PV-streamer.

During the following 24-h, the surface low (Figure 3 (b)) and the short-wave trough at 500 hPa (Figure 4 (b)) are both tilted in northeast – southwest direction, and cover a large area with very tight height gradients. At 300-hPa, the Polar Jets and the sub-tropical jet are more intense and merged on the forward flank of the trough (Figure 6 (b)). At this time, the broad high PV structure is over Italy and broad filament of PV is over the Balkans (Figure 5(b)), and the elongated filament of intruded stratospheric air with some sub-structures at its southern tip is associated with short-wave troughs circulating around the main low. The surface low plunges further southwest toward southern Turkey.

At 06 UTC 8 January 2017, the upper level trough -which has a cut-off low at this stage- is over northwest of the Black Sea (Figure 4 (c)). One of the merged Polar jets and the sub-tropical jet are further intensified (more than 60 m s^{-1}). It may be of interest to note that a similar jet merging event was noted during the December 2001 floods in Israel (Krichak *et al.*, 2007) and the October 2011 Antalya flash-flood event (Demirtaş, 2016). The PV-streamer swung further southeast towards Greece and over Turkey (Figure 5 (c)). Circulating around it, a cut-off low at 500 hPa level, characterized by the substructure of intruded stratospheric air, translated south-eastward above the Aegean Sea; this resulted in an increase of the upper-level divergent flow over the west of Turkey.

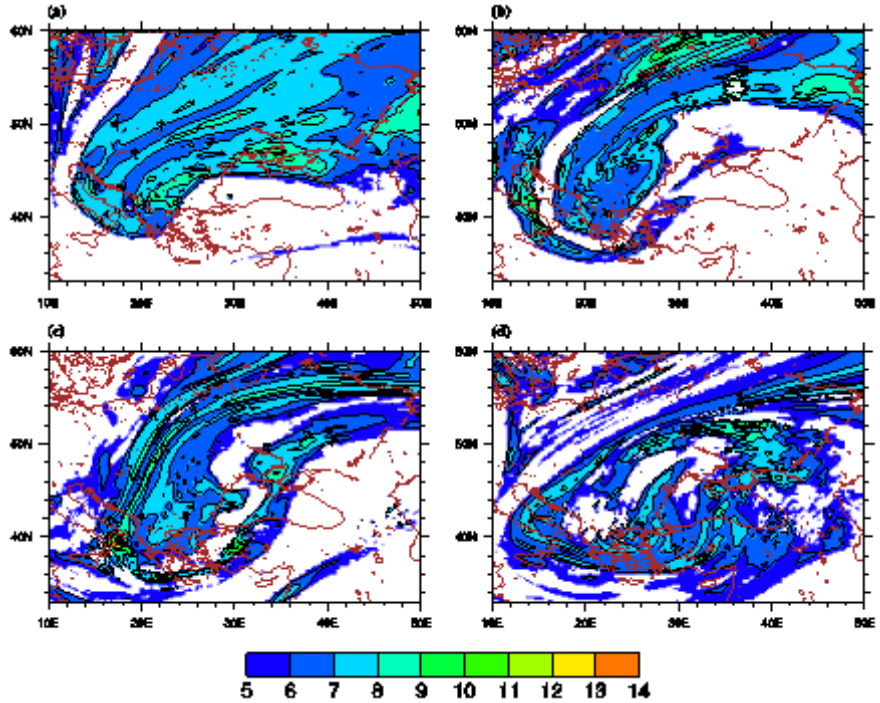

Figure 5. Potential vorticity (in pvu) at 330-K surface. a) 0600 UTC on 6 January 2017; b) 0600 UTC on 7 January 2017; c) 0600 UTC on 8 January 2017; d) 0600 UTC on 9 January 2017

At 06 UTC 9 January 2017, the surface low (Figure 3 (d)) and the upper level cut-off low (Figure 4 (d)) slowly move towards the east. This implies intensification of geopotential height gradient and westerly flow on the eastern side of the upper level trough (Figure 4 (d)). The tongue of high PV (8-10 PVU) (Figure 5 (d)) moves further southeast and arrives over southern Turkey, and the subtropical jet maximum (60 ms^{-1}) is located over the Aegean Sea and western Turkey (Figure 4(d)). This may illustrate the role of upper-tropospheric processes – which are orchestrated by the PV streamer – in enhancing the south-westerly flow component. At the surface, a cut-off low oriented in the northeast – southwest direction is located coherently below the PV-streamer (Figure 3 (d)). The structure and progression of the PV-streamer, its influence on the Polar jet and sub-Tropical jet streams, and the surface development resemble the climatological analysis of cyclones in the Eastern Mediterranean (Raveh-Rubin and Wernli, 2015) and the October 2011 Antalya flash-flood event (Demirtaş, 2016). The upper-level ridge located to the east of the deep cut-off low expands in north easterly direction (Figure 4 (c-d)).

The flow at low levels maintains cold and moist south-westerly and south-easterly winds over Turkey. The upper-level PV or short-wave trough at 500-hPa helps to induce the south-westerly low-level jet (Figure 6 (a-d)), which reaches a maximum value of about 20-25 ms^{-1} at 1000-hPa. The atypical eastward progression of the surface low, the low-level jets that are enhanced by upper level dynamical precursors and possible frontal forcing, together they maintain low-level jets over south-west Turkey (Figure 4 (b)), where abundant moisture is advected by both the south-westerly flows at low levels 1000 hPa and 925 hPa (not shown). The north easterly flow advects moist air from the Black Sea to over northwest of Turkey.

The conveyor belt of warm-moist air while advected by the low-level jets over colder Europe and relatively warm Mediterranean Sea induces a quasi-stationary precipitation system causing heavy precipitation, similar to the Western Mediterranean storms (Buzzi *et al.*, 1998; Nuissier *et al.*, 2008; Davolio *et al.*, 2009; Demirtaş, 2016). Air parcels translate rapidly north-eastwards, and then ascend sharply and become saturated. The rapid translation is consistent with an increasing influence of the tongue of high PV as it advects into the Eastern Mediterranean (Figure 5 (d)). Prominent features of the low levels are consistent with earlier inferences regarding the influence of the tongue of high PV: (i) a strong south-westerly flow is located ahead of the upper level PV and the surface cold front; (ii) the areas of ascent lie on the forward flank of the PV within the south-westerly flow.

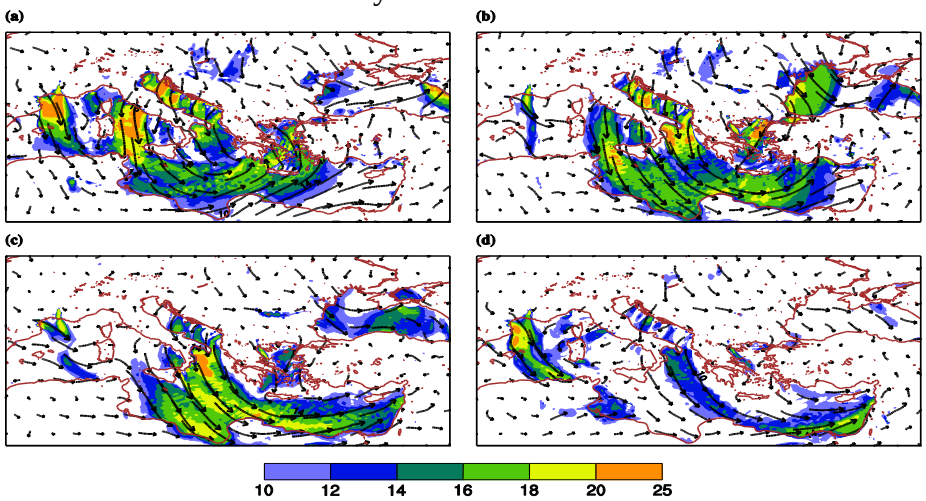

Figure 6. Wind speed (m/s) and direction at 1000 hPa. a) 0600 UTC on 6 January 2017; b) 0600 UTC on 7 January 2017; c) 0600 UTC on 8 January 2017; d) 0600 UTC on 9 January 2017

Analysis of Atmospheric Blocking

Wintry conditions and snow storms in Europe are usually related to upstream blocking events over the North Atlantic. The 2009/2010 winter was noted to have exhibited the second highest blocking frequency (33%) since 1949 (Cattiaux *et al.,* 2010). The winter 2012 prolonged cold wave events were noted to be related to the persistent upstream and downstream atmospheric blocking events which were reported to exhibit instantaneous atmospheric blocking frequency of 50% to the west of Spain and 75% over Siberia (Demirtaş, 2017). The December 2013 Middle East snowstorm was found to be associated with the upstream omega (Ω) type of European blocking that transported cold air into the Middle East and produced snowfall within the downstream trough over the Middle East (Luo *et al.,* 2015). Downstream impacts of atmospheric blocking on extreme winter temperatures over North America (Carrera *et al.,* 2004; Whan and Zwiers, 2016), China (Lu and Chang, 2009; Zhou *et al.,* 2009) and Japan (Kitano and Yamada, 2016) have also been documented.

The atmospheric blocking detection method highlighted in Section 2.1 is applied to the 1-9 January 2017 period. The analysis indicates that the instantaneous atmospheric blocking area extends from mid-Atlantic to Scandinavia region Figure 7 (a-b). Instantaneous atmospheric blocking frequency is above 40-50% over mid-Atlantic (Figure 7 (b)). If episode of blocking is considered, it is 4-5 days which satisfies the condition for total number of consecutive blocking days for an episode of blocking (Figure 7 (c)). Episode of large scale blocking is 4-5 days over the mid-Atlantic (Figure 7 (d)).

The duration of atmospheric blocking plays a very important role in maintaining the impact of its downstream effects. The total duration of atmospheric blocking which takes into account at least 4-days of uninterrupted blocking reveal that anticyclonic conditions persisted over the eastern Atlantic for 4-5 days (Figure 7 (c)). The large scale episode of blocking manifests itself over the mid-Atlantic as depicted in Figure 7 (d).

It can be inferred from the analysis that upstream atmospheric blocking over the mid-Atlantic plays an important role in maintaining not only cold conditions but also inhibiting movement of upcoming weather systems towards eastern Mediterranean.

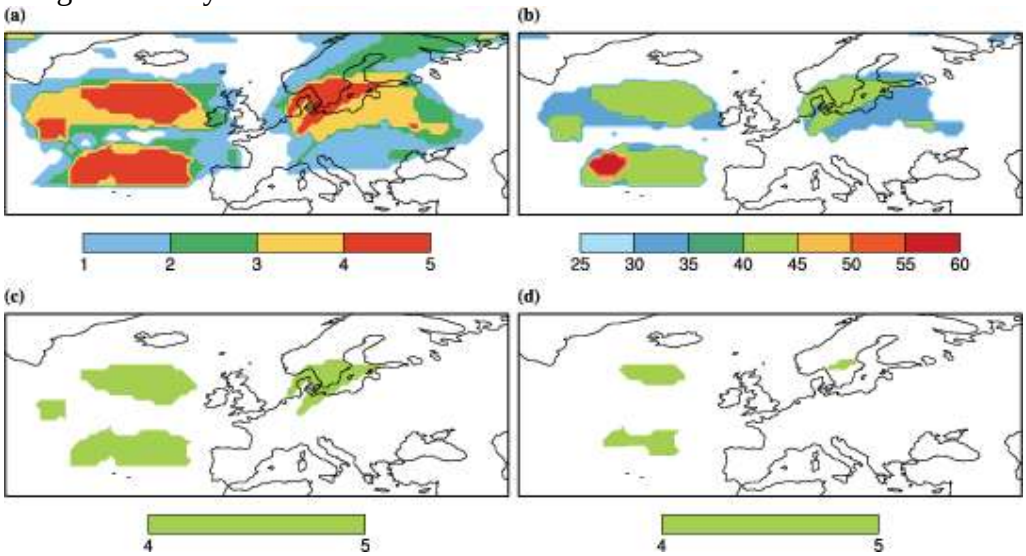

Figure 7. For the 1-9 January 2017 period: (a) Total number of instantaneous atmospheric blocking days (# days), (b) frequency of instantaneous atmospheric blocking days (%), (c) total number of episode of atmospheric blocking days (# days), (d) total number of episode of large scale atmospheric blocking days (# days).

CONCLUDING REMARKS

The wintry January 2017 weather set in across much of Central and Eastern Europe. It was the result of a strong area of persistent high pressure over the mid-Atlantic and Western Europe, resulting in strong winds circulating from Russia and Scandinavia towards Eastern Europe. Further south, an area of low pressure dominated the weather, which brought relatively mild, moist air across the Mediterranean. This feed of moisture led to snow as it moved over Italy, the Balkans and across the Black Sea. In addition, heavy snow in central and Southern Italy was the result of cold air flowing across the warmer Adriatic Sea. The formation of a high pressure system over eastern Atlantic steered the low toward the Mediterranean region. Due to the persistent atmospheric blocking, a cold core cyclone formed over the eastern Mediterranean and the Balkans. The amplification of the large-scale flow during the development phase of the cyclone advected cold air to lower latitudes. The heavy snow fell during the 7–9 January 2017 period and reached as high as 50 cm height, and it was followed by snowy weather with short intermissions. Surface air temperatures rapidly decreased during 6-9 January 2017 period. Minimum temperature measurements for the selected İstanbul stations showed below zero temperatures throughout the study period. The period of 7-8 January 2017 was the coldest. The development of snow clouds were inferred from the Meteosat-10 water vapour imagery. The exceptional moist air-mass seclusion was one of the main factors that led to the high concentration of moist air which made possible the heavy snow over north-western part of Turkey. The convective system stayed over the same region for many hours. Turkish State Meteorological Service's İstanbul radar images were also examined, but the 24-h total precipitation amounts were underestimated. Prominent synoptic and meso-scale ingredients conducive to high impact storms, as indicated by previous studies (Massacand *et al.*, 1998; Lin *et al.*, 2001; Nuissier *et al.*, 2008; Demirtaş, 2016), were present to more or less the same extent for the case studied: upper level dynamical precursors (a tongue of high PV at 330 K and the short-wave trough at 500-hPa) to the west of the threat area and a strong low-level jet. There was a sustained co-alignment of an upper-tropospheric tongue of high PV with a cold front to the west of the affected area. This was accompanied by a significant and sustained north-eastward moisture flux ahead of the cold front and resulted in a period of intense precipitation. The PV streamer was associated with a low-level wind field and thereby promoted convergence of very moist air masses. It is noted that the northeast-southwest tilted trough is made quasi-stationary by the ridge over the Eastern Atlantic. The analysed relationship between the January 2017 wintry conditions and atmospheric blocking is consistent with the previous Mediterranean case studies (Pfahl, 2014; Bieli *et al.*, 2014; Luo *et al.*, 2015; Demirtaş, 2017). The location of atmospheric blocking remotely influences the strength of cold weather and snow conditions. The atmospheric blocking indicator used in this study has emerged as a valuable tool for representing the geographical distribution of the atmospheric blocking phenomenon. This indicator can be useful for investigating the spatial dimension, geographical location, and time persistence of atmospheric blocking events which are important for the occurrence of some weather extremes. The findings have the following implications. (i) High impact snow storms are related to their identifiable and predictable synoptic precursors, which establish the meso-scale environment favourable for large precipitation as well as serving as the primary triggering agents; (ii) Application of the PV-perspective appears to be useful for diagnosing and predicting small scale intense systems over the Eastern Mediterranean; (iii) Additional research efforts are required for a deeper investigation of the role of the PV-streamer in the development and maintenance of high impact snow storms over the Eastern Mediterranean, and to quantify the role of PV by employing the powerful invertibility principle that relates the PV to the flow and thermal structure (Hoskins *et al.*, 1985); (iv) Prediction of atmospheric blocking well in advance may help to point possible downstream high impact cyclone developments and associated extreme weather events.

Acknowledgements. Meteorological data were obtained from the Turkish State Meteorological Service (TSMS) and the European Centre for Medium-Range Weather Forecasts. Data for satellite images were gathered from the EUMETSAT. Plots were created using the NCAR Command Language (NCL, 2016). The author is very grateful to TSMS, ECMWF, EUMETSAT and NCAR.

REFERENCES

Bieli M, Pfahl S, Wernli H. (2014): A Lagrangian investigation of hot and cold temperature extremes in Europe. *Q. J. R. Meteorol. Soc*., doi:10.1002/qj.2339

Buzzi A, Tartaglione N, Malguzzi P. (1998): Numerical simulations of the 1994 Piedmont flood: Role of orography and moist processes. *Mon. Weather Rev.* 126: 2369–2383.

Carrera ML, Higgins RW, Kousky VE. 2004. Downstream Weather Impacts Associated with Atmospheric Blocking over the Northeast Pacific. *J. Climate*, 17: 4823–4839.

Cattiaux J, Vautard R, Cassou C, Yiou P, Masson-Delmotte V, Codron F. (2010): Winter 2010 in Europe: a cold extreme in a warming climate. *Geophys. Res. Lett.*, 37:L20704. doi:10.1029/2010GL044613

Dee DP, *et al.* (2011): The ERA-Interim reanalysis: Configuration and performance of the data assimilation system. *Q. J. R. Meteorol. Soc*., 137: 553–597, doi:10.1002/qj.828.

Demirtaş, M. (2017): The large scale environment of the European 2012 high-impact cold wave: prolonged upstream and downstream atmospheric blocking. *Weather*, doi:10.1002/wea.3020.

Demirtaş, M. (2016): The October 2011 Devastating Flash Flood Event of Antalya: Triggering Mechanisms and Quantitative Precipitation Forecasting, *Q. J. R. Meteorol. Soc.*, 142, 699, 2336-2346, doi:10.1002/qj.2827

Davini P, Cagnazzo C, Neale R, Tribbia J. (2012): Coupling between Greenland blocking and the North Atlantic Oscillation pattern. *Geophys. Res. Lett.*, 39:L14701, doi:10.1029/2012GL052315.

Davolio S, Mastrangelo D, Miglietta MM, Drofa O, Buzzi A, Malguzzi P. (2009): High resolution simulations of a flash flood near Venice. *Hazards Earth Syst. Sci*., 9: 1671–1678.

Hoskins BJ, McIntyre ME, Robertson AW. (1985): On the use of and significance of isentropic potential vorticity maps. *Q. J. R. Meteorol. Soc.*, 111: 877–948.

Kitano Y, Yamada TJ. (2016): Relationship between atmospheric blocking and cold day extremes in current and RCP8.5 future climate conditions over Japan and the surrounding area. *Atmos. Sci. Let.*, 17: 616–622 (2016), doi: 10.1002/asl.711

Krichak SO, Alpert P, Dayan M. (2007): A south-eastern Mediterranean PV streamer and its role in December 2001 case with torrential rains in Israel. *Nat. Hazards Earth Syst., Sci.*7: 21–32.

Lin Y-L, Chiao S, Wang T-A, Kaplan ML, Weglarz RP. (2001): Some common ingredients for heavy orographic rainfall. *Weather and Forecasting*, 16: 633–659.

Lu M-M, Chang C-P. 2009. Unusual late-season cold surges during the 2005 Asian Winter Monsoon: roles of Atlantic blocking and the Central Asian Anticyclone. J. Clim. 22: 5205-5217, https://doi.org/10.1175/2009JCLI2935.1.

Luo D, Yao Y, Dai A, Feldstein SB. (2015): The Positive North Atlantic Oscillation with Downstream Blocking and Middle East Snowstorms: The Large-Scale Environment. *J. Climate*, 28: 6398-6418, doi: 10.1175/JCLI-D-15-0184.1

Massacand AC, Wernli H, Davies HC. (1998): Heavy precipitation on the Alpine south-side: An upper-level precursor. *Geophys. Res. Lett.*, 25: 1435–1438, doi10.1029/98GL50869.

Nuissier O, Ducrocq V, Ricard D, Lebeaupin C, Anquetin S. (2008): A numerical study of three catastrophic precipitating events over Southern France. I: Numerical framework and synoptic ingredients. *Q. J. R. Meteorol. Soc.*, 134: 111–130.

Pfahl S. (2014): Characterising the relationship between weather extremes in Europe and synoptic circulation features. *Nat. Hazards Earth Syst. Sci.*, 14: 1461-1475, doi:10.5194/nhess-14-1461-2014

Raveh-Rubin S, Wernli H. (2015): Large-scale wind and precipitation extremes in theMediterranean: a climatological analysis for 1979–2012. *Q. J. R. Meteorol. Soc.*, DOI:10.1002/qj.2531

Scherrer S, Croci-Maspoli M, Schwierz C, Appenzeller C. (2006): Two-dimensional indices of atmospheric blocking and their statistical relationship with winter climate patterns in the Euro-Atlantic region. *Int. J. Climatol.*, 26: 233–249.

Tayanç, M., M. Karaca, and H. N. Dalfes (1998): March 1987 cyclone (blizzard) over the eastern Mediterranean and Balkan region associated with blocking. *Mon. Wea. Rev.*, 126, 3036–3047.

Tibaldi, S. and Molteni F. (1990): On the operational predictability of blocking. *Tellus*, Ser. A, 42:343-365.

The NCAR Command Language (Version 6.3.0) [Software]. (2016): Boulder, Colorado: UCAR/NCAR/CISL/TDD. doi:10.5065/D6WD3XH5

Whan K and Zwiers F. (2016): The Influence of Atmospheric Blocking on Extreme Winter Minimum Temperatures in North America. *J. Climate*, 29: 4361–4381. DOI: 10.1175/JCLI-D-15-0493.1

Zhou W, Johnny CL, Chen W, Ling J, Pinto JG, Shao Y. (2009): Synoptic-Scale Controls of Persistent Low Temperature and Icy Weather over Southern China in January 2008. *Mon. Wea. Rev*., DOI: 10.1175/2009MWR2952.1

29 JUNE – 3 JULY 2017 HEATWAVE OVER TURKEY

Meral Demirtaş[1]
[1]*University of Ondokuz Mayıs, Department of Meteorological Eng.*
mdemirtas@omu.edu.tr

Abstract
During 29 June – 3 July 2017, very high temperatures were recorded over the south east Europe. In Turkey, several locations experienced temperatures over 35°C - 45°C, and temperatures were 10°C-14°C above climatological mean. The present study investigated this heat wave event in concert with some meteorological anomalies and atmospheric blocking highs, and focused on heat wave analysis on a grid point base. This study employed a recently developed heat wave detection method and a two dimensional atmospheric blocking detection method. The recently developed heat wave detection method provided an objective analysis of the heat wave of the study period throughout different regions of Turkey. The two-dimensional atmospheric blocking detection method has emerged as a valuable tool for examining the phenomenon. Examination of the spatial distribution of the composite anomalies of the 500 hPa geopotential height anomaly field showed that the Azores anticyclone was shifted towards the north. The positive anomaly over north-west of Turkey exceeded 100 gpm. The analysis of the total number of contiguous heat wave days revealed that the north west of Turkey was under hot summer conditions for about 3-4 days. Instant atmospheric blocking frequency was around 25-35% over the eastern Atlantic and over northern parts of Turkey. The results indicate that summer climate might experience a pronounced increase in year-to-year variability, and they may also contribute to a better understanding of heat waves in context of climate variability.

Keywords**:** *Climate variability, Heat waves, Atmospheric blocking, High impact weather, Turkey*

INTRODUCTION

Climate change affects also climate variability which refers to deviations in the mean state of the climate on temporal and spatial scales. Climate variability is measured by underlying deviations, which are usually termed anomalies. It is not spatially and temporally uniform. The modes of climate variability can affect weather and climate on various spatial and temporal scales. The well-known and most periodic climate variability mode is the seasonal cycle. Modes of climate variability and their influence on regional climates are usually diagnosed through spatial teleconnections.

Heat waves are good examples to impacts of climate variability. Heat wave events have discernible impacts; on health, wellbeing, efficiency, rise in mortality and morbidity (Basu, 2009), an increased demand on energy and water supply (Fink *et al.*, 2004), agricultural resources, the retail industry, ecology and tourism (Ciais *et al.*, 2005), increased air pollution (Vautard *et al.*, 2005), and consequences on economy due to crop failure and wild forest fires (IPCC, 2012).

Several heat waves affected parts of Europe in the last decade (Coumou *et al.*, 2012): the 2003 European mega heat wave (Schär *et al.*, 2004), the 2006 heat wave of Central Europe (Rebetez *et al.*, 2006), the 2007 summer heat wave of South–Eastern Europe (Founda *et al.*, 2009; Demirtaş, 2017a), and the 2010 mega heat wave of Russia (Barriopedro *et al.*, 2011). The mega heat wave of 2003 led to about 70,000 deaths, and the mega heat wave of 2010 caused a death toll of 55,000 due to high heat and poor air quality caused by wildfires, an annual crop failure of about 25%, around 1 million ha of burned areas, and ~US$15 billion of total economic loss

(Barriopedro *et al.,* 2011). Research studies (IPCC, 2012; Schär *et al.,* 2004; Meehl and Tebaldi, 2004; Diffenbaugh *et al.,* 2007; Sillmann *et al.,* 2013) indicate that heat waves may be more frequent and intense in coming decades.

According to a report by the Intergovernmental Panel on Climate Change (IPCC, 2012), the 1983-2012 period was the warmest 30-yr period of the past 1400 years in the Northern Hemisphere. An observed increase of summer air temperatures of around 4°C is noted in a region stretching from the Atlantic across the Central Europe to over the Black Sea (Beniston, 2004). The IPCC report noted that in the period of 2016-2025 air temperatures are expected to rise by 0.3-0.7°C compared to the 1985-2005 period. Considering various climate projection scenarios, the report also remarks that air temperatures may rise by 2.6-4.8°C. Global anthropogenic greenhouse gas (GHG) emissions have been on increase since the pre-industrial era. Studies on the impact of continued emissions of GHG imply that the Mediterranean region is among the sensitive and positively responsive regions; rise in temperature, large decrease in precipitation and increases in inter-annual warm-season variability (Diffenbaugh *et al.,* 2007; Giorgi, 2006). Future climate projection studies suggest an increase in the number of hot days in the Mediterranean zone and the Eastern Europe, with an additional 60 days or more above 30°C than under current climatic conditions (Beniston, 2004).

The year-to-year high fluctuations in summer air temperature are related to the meridional pattern, which suggests a northward shift of classic climate zones. Dynamical factors depend on pole ward shifts of climatological storm tracks and associated cyclones and anticyclones, baroclinic zones, and jets as descending Hadley cell branches and subtropical dry zones enlarge north ward, and as mid-latitude flows adjust to a less pronounced equator-to-pole temperature gradient (Polade *et al.,* 2012).

Common ingredients leading to severe heat waves can serve as guidance and yield insights into their most important triggering and driving mechanisms. The common dynamical and physical factors works in concert are given below (Demirtaş, 2017a):

i. Persistent high pressure systems. Heat waves mainly depend on large-scale atmospheric circulation patterns. Persistent high pressure systems are considered to be the major dynamical factor (Black *et al.,* 2004; Pfahl *et al.,* 2012; Miralles *et al.,* 2014). The interaction between persistent high pressure systems and land-surface might be the reason why they are so important for hot extremes over land. Quasi-stationary anticyclonic atmospheric circulation patterns are usually characterized by the persistent 500 hPa geopotential height anomalies that dynamically cause subsidence which leads to clear-sky, adiabatic warming and inhibits cloud formation which, in turn, increases incoming solar radiation, warm-air advection and prolonged hot weather conditions at the surface. The absence of clouds causes strong radiative anomalies. These anomalies enhance surface evaporation, and cause a gradual depletion of soil moisture, which, in turn, leads to larger sensible heat (SH) fluxes from the ground in to the atmospheric boundary layer and thus increasing surface air temperature (Fischer *et al.,* 2007). Persistent high pressure systems may also directly be responsible for establishing and maintaining warm Mediterranean Sea surface temperature anomalies (Black *et al.,* 2004; Feudale *et al.,* 2007). The duration of the persistent high pressure system is a key factor for heat waves contributing dynamical and physical processes work in concert.

ii. Atmospheric boundary layer (ABL). The surface plays a very important role in severe heat waves by accumulating heat during the day. The warmed ABL may persist

throughout the night (Miralles *et al.,* 2014). This situation can offset night time cooling which is driven by upward radiation under clear sky conditions, keeping the nocturnal ABL warm, thus slowing the decrease in surface air temperature before sunrise (Black *et al.,* 2004; Miralles *et al.,* 2014; Fischer *et al.,* 2007). Therefore, the following day starts off in a warmer state than the previous day and, as this positive feedback cycle repeats, the heat continues to build up in ABL. In response to these progressive processes, ABL becomes much warmer and deeper (Fischer, 2014). The studies of mega heat waves of 2003 and 2010 revealed that ABL changed from 500 m to 4 km in some places (Black *et al.,* 2004; Miralles *et al.,* 2014). The heat built-up during prolonged intensive heat waves is the key mechanism for the escalation of surface air temperature throughout the event. These progressive processes shed light on why temperatures continue to increase from one day to the next. The heat built-up ABL interact strongly with the underlying soil, which continuously dries out. As a result, cooling of the land surface by evaporation decreases and the land surface is further warmed-up, which, in turn, causes increased SH flux from the surface into ABL. The progressive cycle of pronounced heat storage and soil desiccation were found in both 2003 and 2010 mega heat waves and increased temperatures to record-breaking levels (Miralles *et al.,* 2014; Fischer, 2014).

iii. Soil moisture (SM). It varies very slowly, on the time scale of weeks to months (Diffenbaugh *et al.,* 2007; Vautard *et al.,* 2007) and thus carries potential of the previous months/season's storage until summertime. Precipitation deficit in winter and/or in early spring leads to SM deficit. The anomalous clear skies and very strong radiative anomalies contribute to loss of SM reservoirs, and in subsequent days, SM depletion and soil desiccation take place. The early phenology green-up caused by spring time warmness, together with dry weather conditions, can result in early season moisture depletion too (Zaitchik *et al.,* 2006). Under persistent anticyclonic conditions, exposed to sunnier and drier air, plants evaporate more water. Subsequently, dried soils emit more SH flux and less latent heat (LH) flux, then this leads to reduced cloudiness and hence further increasing diurnal surface air temperature. An increase of air temperature is further amplified when the inability of LH fluxes to transfer heat upwards due to the depleted SM. The land radiation budget and water resources are interrelated via the LH flux associated with evaporation (Lorenz *et al.,* 2010). In SM poor areas, the surface radiation budget is dominated by SH (Diffenbaugh *et al.,* 2007) which is strongly determined by SM. Dry soils inhibit cloud formation, thus increasing incoming solar radiation, and hence amplifying evaporation. Lack of SM enhances diurnal hot air entrainment and causes the formation of persistent residual layers that produce the heat built-up (Miralles *et al.,* 2014). Modeling studies of 2003 mega heat wave showed a high sensitivity to SM conditions (Miralles *et al.,* 2014; Fischer *et al.,* 2007; Vautard *et al.,* 2007; Ferranti *et al.,* 2007).

iv. Sea surface temperature (SST). It is well-known that SST is a critical component which influences the exchange of energy between the atmosphere and ocean. A warm SST anomaly can modify air temperature which, in turn, can cause a reduction of the meridional temperature gradient. This may shift the polar jet and the sub-tropical jet northward –which brings warm and dry air from subtropics- further north than its climatological position, allowing the expansion of the anticyclone; in turn, this atmospheric circulation can induce SST anomalies (Feudale *et al.,* 2007). When the anticyclone persists over the area, it can block and divert the transient weather coming from the Atlantic Ocean and thus prevent cooling of the Mediterranean SST. Since anticyclones are characterized with downward motion, they can suppress convection and

thus increase solar radiation over the Mediterranean Sea. The positive feedback processes between the atmospheric circulation and sea can establish/maintain/sustain very warm Mediterranean SST for some weeks. High SSTs also have the potential to generate and sustain anticyclones. The 2003 mega heat wave period was shown to be associated with record breaking warm SST of the Mediterranean Sea (Black *et al.,* 2004; Feudale *et al.,* 2007; Grazzini and Viterbo, 2003).

Atmospheric simulation models have shortcomings in simulating some of the key heat wave triggering and driving mechanisms, such as the persistence of anticyclonic circulations, variability of SM and related positive feedback mechanisms between the atmosphere and land-surface (Fischer *et al.,* 2014). Comprehensive treatments of land-surface hydrology, radiation and convection play a vital role in simulating and predicting heat waves properly (Weisheimer *et al.,* 2011).

Heat waves over the Balkans and Turkey were noted to be associated with prolonged high pressure systems by previous studies (Türkeş and Sümer, 2002-2004; Founda *et al.,* 2009; Erlat and Türkeş, 2013; Unal *et al.,* 2013), but this relationship has not yet been investigated explicitly. This study is tailored to associate heat waves and atmospheric dynamics in an event-based approach on a grid point basis. Heat waves occur under the influence of large scale atmospheric circulation factors, and they are not localized events, therefore this study examines heat waves in spatial context not on certain observational points (Türkeş and Sümer, 2002-2004; Founda *et al.,* 2009; Erlat and Türkeş, 2013; Unal *et al.,* 2013).
This study aims to examine the event by including in: (i) a recently developed heat wave detection method which is based on spatially and temporally varying maximum temperature threshold; (ii) a 500 hPa geopotential height based two-dimensional atmospheric blocking detection method; (iii) the episode mean and composite anomalies of the 500 hPa geopotential height and surface temperature at 2 m height.

DATA AND METHODS

This study uses operational European Centre for Medium-Range Weather Forecast (ECMWF) high-resolution analysis data and the ECMWF ERA-Interim (EI) (Dee *et al*., 2011) reanalysis data. Both data are employed with a 1°x1° longitude-latitude grid horizontal resolution.

The study period (25 June – 5 July 2017) mean of the 500 hPa geopotential height and temperature at 2 m height were computed. Composite anomalies (with respect to 1979-2009) of geopotential height at 500 hPa and temperature anomalies at 2 m height are computed by removing the June-July 1979–2009 climatological mean.

Heat Wave Detection Method

Historical record breaking temperatures should not be misled for heat waves. The definition of heat waves is not quite straightforward (Robinson, 2001), and there is no objective and uniform heat wave definition (Meehl and Tebaldi, 2004). One of ways to identify heat wave is based on daily maximum temperature being above a fixed absolute threshold. A detection based on the exceeding a fixed temperature threshold cannot be implemented to all regions, because each region is usually characterized by different micro-climatic conditions. For example, in relatively cooler regions absolute thresholds may not be reached, and temperatures may have to be much higher in hotter regions.

In order to reduce the degree of arbitrariness involved in the selection of a threshold temperature and to provide an objective definition, which may also be easily transferable to other places,

percentiles turns out to be more appropriate. This study deals with spatial distributions and utilizes a nonparametric method to determine a spatially and temporally varying maximum temperature threshold, which is based on a 90th percentile from a 7-day time window (Demirtaş, 2017a). The 90th percentile temperature threshold is computed on a grid point basis as outlined below.

v. **Spatially and daily varying maximum temperature threshold:** For a given grid point, a temperature value with respect to the climatology (1979–2009) is considered to be extreme when its value exceeds the 90th percentile. The threshold is computed for a respective calendar day (RCD) using the temperature data of the 1979–2009 period between *d-3* and *d+3* days. For each day, a 90th percentile is computed from a sample of seven days (three days on each side of the RCD). For example, on 3 July, the temperature values between 30 June and 6 July of the years 1979-2009 are used.

$$T_{(i,j,y,d)threshold,90^{th}} = \bigcup_{y=1979}^{2009} \bigcup_{t=d-3}^{d+3} T_{(i,j,y,d)}$$

where ⋃ denotes the union of sets and $T_{i,j,y,d}$ is the daily maximum temperature at 2 m height belonging to the RCD in the year (*y*). The indices *i,j,y,d* represent latitude, longitude, year and day, respectively.

vi. **Temporal threshold*:*** The above described temperature threshold is to be satisfied on three consecutive days**.**

vii. **Heat wave detection:** A heat spell that satisfies (i) and (ii) is identified as heat wave.

viii. **Heat wave intensity:** It is computed by summing up the absolute differences between the temperature values and the percentile temperature threshold for the duration of the event, and then the sum is divided by the duration of the heat wave (Shevchenko *et al.,* 2014; Spinoni *et al.,* 2015; Demirtaş, 2017a).

Atmospheric Blocking Detection Method

Objective detection of atmospheric blocking is necessary for weather forecasting, since it exerts a strong influence on the upstream, *in-situ,* and downstream weather. A two dimensional index based on the reversal of the meridional gradient of geopotential height at 500 hPa is applied (Tibaldi and Molteni, 1990; Scherrer *et al.,* 2006; Davini *et al.,* 2012). For each grid point, the following metric is defined:

$$GHGS(\lambda_0,\Phi_0) = \frac{Z500(\lambda_0,\Phi_0) - Z500(\lambda_0,\Phi_S)}{\Phi_0 - \Phi_S} \quad (1)$$

$$GHGN(\lambda_0,\Phi_0) = \frac{Z500(\lambda_0,\Phi_N) - Z500(\lambda_0,\Phi_0)}{\Phi_N - \Phi_0} \quad (2)$$

$$\Phi_s = \Phi_0 - 15° \quad (3)$$

$$\Phi_N = \Phi_0 + 15° \quad (4)$$

where $Z500(\lambda_0, \Phi_0)$ represents the grid point 500 hPa geopotential height at longitude (λ_0) which ranges from 0° to 360° and latitude (Φ_0) which ranges from 30° to 70°N. An instantaneous local blocking (LIB) is assigned for a grid point, if both of the following conditions are satisfied:

$$GHGS(\lambda_0, \phi_0) \succ 0 \tag{5}$$

$$GHGN(\lambda_0, \phi_0) \prec -10\,\text{m/°latitude} \tag{6}$$

A grid point is assigned for instant blocking if conditions given in Equations (5-6) are satisfied. A sector is defined as large-scale blocking, if the above criteria are satisfied for at least 15 continuous longitudes. A time-scale of 4 days is used to define a blocking episode. A blocking event is considered as large scale episode of blocking if afore mentioned both spatial and temporal conditions are satisfied.

ANALYSIS OF THE HEAT WAVE EVENT

The 29 June – 3 July 2017 period was very hot for the south-eastern Europe. A ridge of high pressure from the North Africa brought a scorching heat wave to southeast Europe. Observed temperature anomalies over southeast Europe were between 6°C and 10°C. In Turkey, several locations experienced temperatures over 35-45°C, and temperatures were 10°C-14°C above climatological mean. In many places, temperatures were above 37°C on three consecutive days from 30 June to 3 July 2017. Heat wave period prompted forest fires in İzmir/Menderes, Antalya/Alanya and Mersin/Anamur. The total burnt area was 3,100 ha.

Overview of Atmospheric Circulation Mean and Anomalies

The nature and origins of heat waves are closely related to the underlying atmospheric circulation dynamics. Figure 1(a) depicts the mean 500 hPa geopotential height of the study period of 25 June – 5 July 2017, which highlights the panoply of large-scale weather systems. The prevalence of an upstream northward shifted ridge over the eastern Mediterranean dominates the atmospheric circulation. The south westerly winds associated with the ridge advect dry air from lower southern latitudes to over southeast Europe and warm-moist Mediterranean air towards northerly latitudes.

Examination of the spatial distribution of the composite anomalies (with respect to the 1979–2009 climatological mean) of the 500 hPa geopotential height field implies that the Azores anticyclone is shifted towards the north (Figure 1(a)). The positive anomaly over north-west of Turkey exceeds 100 gpm, while the negative anomaly over north exceeds −60 gpm (Figure 1(b)). The nature of these anomalies indicates that they may be due to the steady residence of the same prevailing atmospheric circulation.

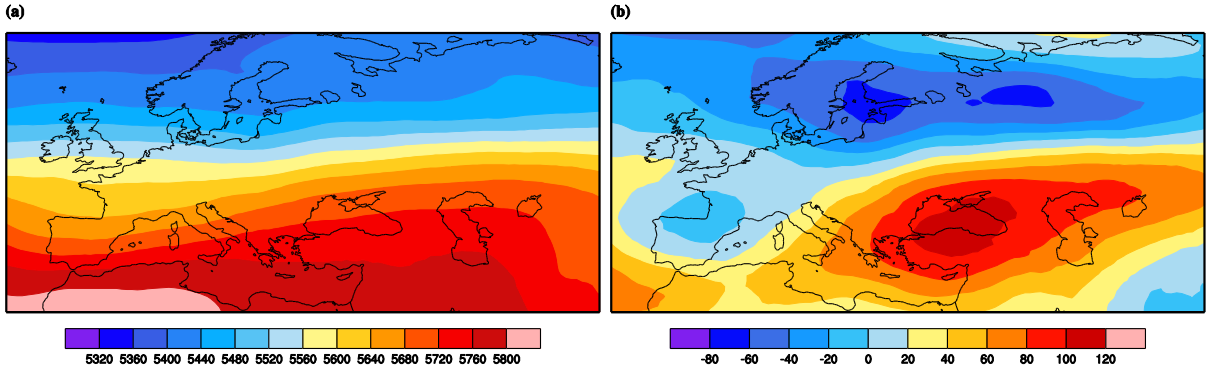

Figure 1. For the 25 June – 5 July 2017 period: (a) Time-mean 500 hPa geopotential height (in gpm), (b) The composite 500 hPa geopotential height anomaly.

The spatial distribution of the surface air temperature at 2 m height shows that the warmest regions, with high temperatures ranging from 34°C to 40°C, were located over south west and south east of Turkey (Figure 2(a)). It should be noted that temperatures shown here are grid-point values at 1° × 1° resolution, and they represent the time-mean of the study period. (It should be kept in mind that station-based daily maximum temperatures may show higher values compared to area averaged grid values.)

Inspection of the spatial distribution of the composite anomalies (with respect to the 1979–2009 climatological mean) of the study period surface temperature at 2 m suggests that temperature anomalies are pronounced over most part of Turkey (up to 12-14 degC; Figure 2(b)). The surface air temperature anomalies correspond to roughly 1σ (with respect to the 1979–2009 ECMWF-EI) in some places (not shown).

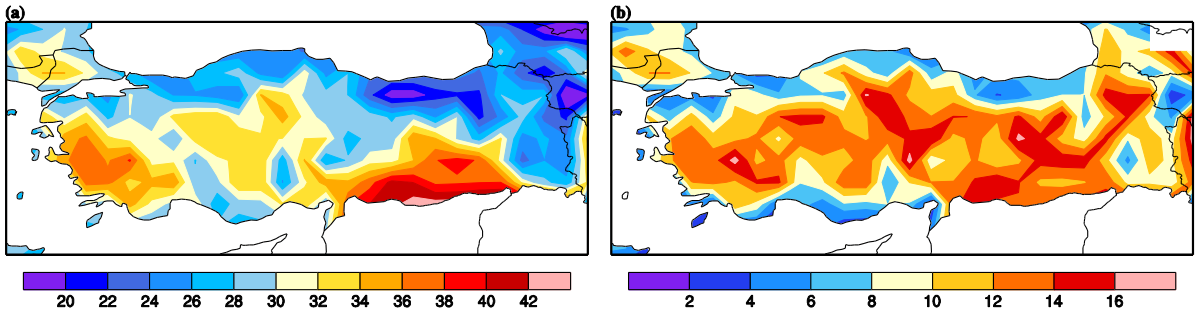

Figure 2. For the 25 June – 5 July 2017 period: (a) Time-mean temperature at 2 m (°C), (b) The composite temperature at 2 m anomaly (degC).

Heat Wave Analysis

The heat wave detection technique outlined in Section 2.1 is applied to 25 June – 5 July 2017 period. It should be kept in mind that maximum reference threshold temperature changes spatially and temporally, therefore impact of hot summer conditions on surface air temperature differs throughout the country. An analysis of the total number of contiguous heat wave days shows that the north west of Turkey is under hot summer conditions for about 3-4 days, and the eastern part of Turkey is under such conditions for more than 5 days (Figure 3a), these results can be expected since 2 m temperature anomalies are also located over the same area (Figure 2(b)). The intensity of the heat wave is higher over the western and eastern parts of Turkey (Figure 3b) which is again coincides well with the composite 2 m temperature anomaly map of the region (Figure 2(b)).

It should be noted this heat wave was not unprecedented or exceptional compared to the high impact heat waves of 2000, 2007, 2010 and 2012 (Demirtaş, 2017a-b) – which were long lived, very intense and accompanied by high frequency atmospheric blocking periods. This heat wave was short lived, because the associated high pressure system did not stay over the affected area much longer.

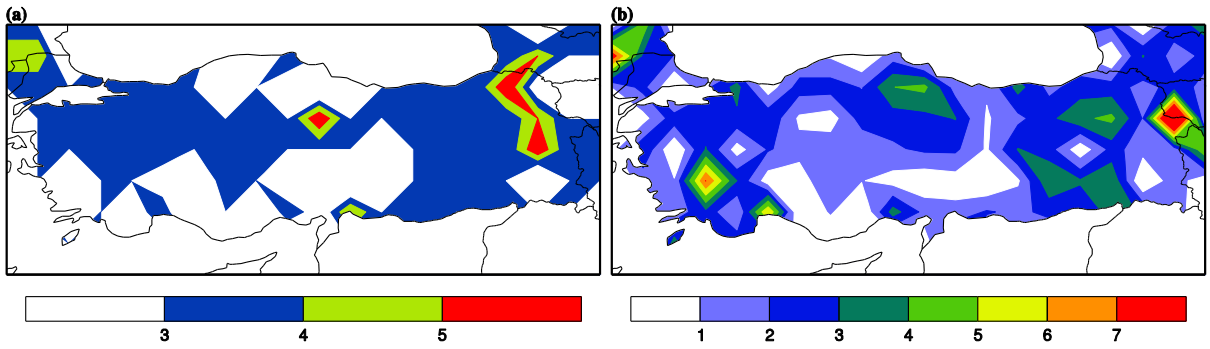

Figure **3.** For the 25 June – 5 July 2017: a) Total number of heat wave days, b) Heat wave intensity (°C).

Atmospheric Blocking Analysis

The atmospheric detection technique outlined in Section 2.2 is applied to 25 June – 5 July 2017 period. Analysis of atmospheric blocking of the study period indicates two major blocking areas: (i) over the eastern Atlantic, (ii) over the eastern Mediterranean and the Black Sea (Figure 4a-b). The total duration of atmospheric blocking -which considers at least 4-days of uninterrupted blocking- shows that anticyclonic conditions persisted over north of the UK and over northern parts of Turkey (Figure 4a). Instant atmospheric blocking frequency is around 25-35% over the eastern Atlantic and over northern parts of Turkey (Figure 4b).

Duration and instant atmospheric blocking frequencies of this event are lower compared to atmospheric blocking events of the recent past events (Demirtaş, 2017a-b). This may be because the blocking high in question was short lived; it might have not sufficient feedback physical and dynamical mechanisms to maintain it.

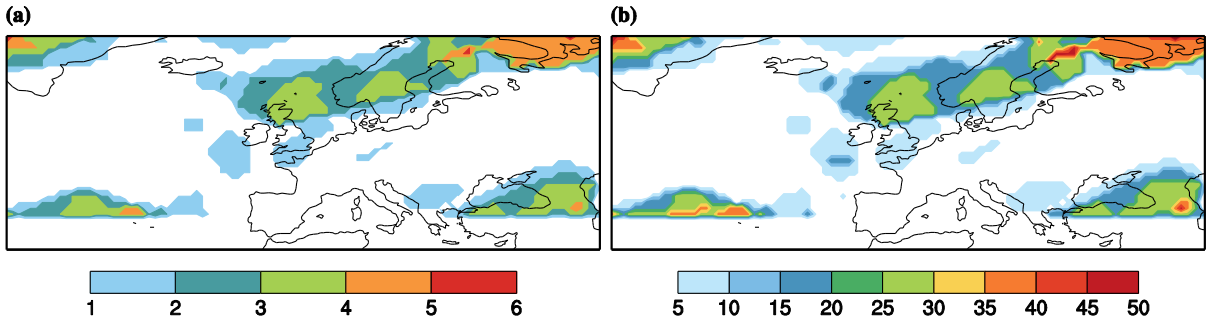

Figure 4. For the 25 June – 5 July 2017: a) Total episode of blocking days, b) Frequency of instant atmospheric blocking in (%).

CONCLUDING REMARKS

A ridge of high pressure from the North Africa brought a scorching heat wave to southeast Europe. This study examined the connection between the heat wave and atmospheric blocking, using an objective heat wave detection method and a two-dimensional atmospheric blocking detection method. Examination of the spatial distribution of the composite anomalies of the 500

hPa geopotential height field showed that the Azores anticyclone was shifted towards the north. The positive anomaly over north-west of Turkey exceeds 100 gpm. The analysis of the total number of contiguous heat wave days revealed that the north west of Turkey was under hot summer conditions for about 3-4 days. Instant atmospheric blocking frequency was around 25-35% over the eastern Atlantic and over northern parts of Turkey. Results indicated that this heat wave was not exceptional compared to the high impact heat waves of 2000, 2007, 2010 and 2012 (Demirtaş, 2017a-b) – which were long lived, very intense and accompanied by high frequency atmospheric blocking. This heat wave was short lived, because the associated high pressure system did not stay over the affected area much longer. Duration and instant atmospheric blocking frequencies were lower compared to the recent past events (Demirtaş, 2017a-b). This may be because the blocking high in question was short lived; it is beyond the scope of this study to address underlying physical and dynamical reasons behind it.

The heat wave detection method provided an objective analysis of the heat wave throughout different regions of Turkey which otherwise would have required the use of spatially varying temperature threshold due to the variation in topography and micro-climatic features across the country. This detection method can be useful for investigating main features of heat waves; their spatial distribution, duration, number and intensity. The objective atmospheric blocking detection method has emerged as a valuable tool for representing the phenomenon. This method can be useful for investigating the spatial coverage and time persistence of blocking events important for the occurrence of temperature extremes. Results from this analysis indicate that the atmospheric blocking was likely to be responsible for establishing and maintaining the hot summer conditions.

This heat wave can be thought of as an example of a heat wave superimposed on a warming climate. Since climate projection studies suggest that the European warming may continue in the twenty first century, a further increase in the frequency of heat waves can be expected. The association between heat waves and atmospheric blocking is important both for weather prediction and for the investigation of temperature extremes in the frame work of climate variability. The results imply that summer climate might experience year-to-year variability. Increase in climate variability might be able to explain the high impact heat waves, and would strongly affect their incidence in the future. Society is faced not only with addressing current climate variability, but also with finding ways to adapt to future changes relating to high impact heat waves, such as the one described here, and their societal and environmental impacts.

Acknowledgements. Meteorological data were obtained from the Turkish State Meteorological Service and the European Centre for Medium-Range Weather Forecasts. Plots were created using the NCAR Command Language (NCL, 2016). The author is very grateful to these organizations.

REFERENCES

Basu R. High ambient temperature and mortality: a review of epidemiologic studies from 2001 to 2008. Environmental Health 2009; 8:40, DOI: 10.1186/1476-069X-8-40.

Barriopedro D, Fischer EM, J. Luterbacher, Trigo RM, García-Herrera R. The hot summer of 2010: Redrawing the temperature record map of Europe. Science 2011; 332: 220–224.

Beniston M. The 2003 heat wave in Europe: A shape of things to come? An analysis based on Swiss climatological data and model simulations. Geophys. Res. Lett. 2004; 31: L02202, doi:10.1029/2003GL018857.

Black E, Blackburn M, Harrison G, Hoskins BJ, Methven J. Factors contributing to the summer 2003 European heatwave. Weather 2004; 59: 217–223.

Blunden J, Arndt DS, Baringer MO. Eds. State of the Climate in 2010. Bull. Amer. Meteor. Soc. 2011; 92(6): S1–S266.

Ciais P., et al. Europe wide reduction in primary productivity caused by the heat and drought in 2003.Nature 2005; 437: 529–533, doi:10.1038/nature03972.
Coumou D, Rahmstorf S. A decade of weather extremes. Nat. Clim. Change 2012; 2(7): 491–496.
Dee D P, et al. The ERA-Interim reanalysis: Configuration and performance of the data assimilation system. Q. J. R. Meteorol. Soc. 2011; 137: 553–597, doi:10.1002/qj.828.
Demirtaş, M. 2017a. High Impact Heat Waves Over the Euro-Mediterranean Region and Turkey - In Concert with Atmospheric Blocking and Large Dynamical and Physical Anomalies, Anadolu Univ. J. of Sci. and Technology A– Appl. Sci. and Eng. 18 (1) , 97-114. doi: 10.18038/aubtda.300426
Demirtaş, M. 2017b. Şiddetli sıcak hava dalgaları: dinamik-fiziksel etkenler ve bu sıcak hava dalgalarının özellikleri, Sakarya Üniversitesi Fen Bilimleri Enstitüsü Dergisi, 21(2), 2017, 190-202. doi: 10.16984/saufenbilder.297005
Diffenbaugh NS, Pal JS, Giorgi F, Xuejie G. Heat stress intensification in the Mediterranean climate change hotspots. Geophys. Res. Lett. 2007; 34: L11706, doi:10.1029/2007GL030000.
Erlat E, Türkeş M. Observed changes and trends in numbers of summer and tropical days, and the 2010 hot summer in Turkey. International Journal of Climatology 2013; 33(8): 1898–1908. DOI: 10.1002/joc.3556
Ferranti L, Viterbo P. The European summer of 2003: Sensitivity to soil water initial conditions. J. Clim. 2006; 19: 3659– 3680.
Feudale L, Shukla J. Role of Mediterranean SST in enhancing the European heat wave of summer 2003. Geophys Res Lett. 2007; 34: L03811
Fink A, Brücher T, Krüger A, Leckebusch G, Pinto J, Ulbrich U. The 2003 European summer heatwaves and drought – synoptic diagnosis and impacts. Weather 2004; 59: 209–216.
Fischer EM, Seneviratne SI, Vidale PL, Lüthi D, Schär C. Soil moisture–atmosphere interactions during the 2003 European summer heat wave. J. Clim. 2007; 20: 5081–5099
Fischer EM. Autopsy of two mega-heatwaves. Nature Geoscience 2014; 7: 332–33, doi:10.1038/ngeo2148
Founda D, Giannakopoulos C. The exceptionally hot summer of 2007 in Athens, Greece. Global Planet Change 2009; 67: 227-236.
Giorgi F. Climate change hot-spots. Geophys. Res. Lett. 2006; 33: L08707, doi:10.1029/2006GL025734.
Grazzini F, Viterbo P. Record-breaking warm sea surface temperature of the Mediterranean Sea. ECMWF Newsletter 98, ECMWF, Reading, United Kingdom, 2003. pp. 30-31
IPCC Summary for policymakers. In Climate Change: Impacts, Adaptation, and Vulnerability. Part A: Global and Sectoral Aspects. Contribution of Working Group II to the Fifth Assessment Report of the Intergovernmental Panel on Climate Change, Field CB, Barros VR, Dokken DJ, Mach KJ, Mastrandrea MD, Bilir TE, Chatterjee M, Ebi KL, Estrada YO, Genova RC, Girma B, Kissel ES, Levy AN, MacCracken S, Mastrandrea PR, White LL, editors. Cambridge University Press, 2014. Cambridge, UK and New York, NY, 2012. pp. 1–32.
Kuglitsch F G, Toreti A, Xoplaki E, Della-Marta PM, Zerefos CS, Türkeş M, Luterbacher J. Heat wave changes in the eastern Mediterranean since 1960. Geophys. Res. Lett. 2010; 37: L04802, doi:10.1029/2009GL041841.
Lorenz R, Jaeger EB, Seneviratne SI. Persistence of heat waves and its link to soil moisture memory. Geophys. Res. Lett. 2010; 37: L09703, doi:10.1029/2010GL042764.
Meehl GA, Tebaldi C. More intense, more frequent, and longer lasting heat waves in the 21st century. Science 2004; 305: 994–997, doi:10.1126/science.1098704.
Miralles D G, Teuling AJ, van Heerwaarden CC, de Arel- lano VG. Mega-heatwave temperatures due to combined soil desiccation and atmospheric heat accumulation. Nat. Geosci. 2014; 7: 345–349
Pfahl S, Wernli H. Quantifying the relevance of atmospheric blocking for co-located temperature extremes in the Northern Hemisphere on (sub-)daily time scales. Geophys. Res. Lett. 2012; 39: L12807, doi:10.1029/2012GL052261
Polade SD, Cayan DWPDR, Gershunov A, Dettinger MD. The key role of dry days in changing regional climate and precipitation regimes. Sci Rep 2012; 4:4364, DOI 10.1038/srep04364
Rebetez M, Dupont O, Giroud M. An analysis of the July 2006 heatwave extent in Europe compared to the record year of 2003. Theor. Appl. Climatol. 2009; 95: 1–7.
Robinson PJ. On the definition of a heat wave. J. Appl. Meteorol. 2001; 40: 762–775
Russo S, Dosio A, Graversen AR, Sillmann J, Carrao H, Dunbar MB, Singleton A, Montagna P, Barbolam P, Vogt JV. Magnitude of extreme heat waves in present climate and their projection in a warming world. J. Geophys. Res. Atmos. 2014; 119: 12,500–12,512, doi:10.1002/2014JD022098.
Schär C, Vidal PL, Luthi D, Frei C, Haberli C, Liniger MA, Appenzeller C. The role of increasing temperature variability in European summer heatwaves. Nature 2004; 427: 332– 336.
Scherrer S, Croci-Maspoli M, Schwierz C, Appenzeller C. Two-dimensional indices of atmospheric blocking and their statistical relationship with winter climate patterns in the Euro-Atlantic region. Int. J. Climatol. 2006; 26: 233–249.

Sillmann J, Kharin VV, Zwiers FW, Zhang X, Bronaugh D. Climate extremes indices in the CMIP5 multimodel ensemble: Part 2. Future climate projections. J. Geophys. Res. 2013; 118(6): 2473–2493.
Stefanon M, D'Andrea F, Drobinski P. Heatwave classification over Europe and the Mediterranean region. Environ. Res. Lett. 2012; 7: L014023, doi:10.1088/1748-9326/7/1/014023
Spinoni J, Lakatos M, Szentimrey T, Bihari Z, Szalai S, Vogta J, Antofiea T. Heat and cold waves trends in the Carpathian Region from 1961 to 2010. Int. J. Climatol. 2015; 35: 4197–4209, DOI: 10.1002/joc.4279
Tibaldi T, Molteni F. On the operational predictability of blocking. Tellus 1990; 42A: 34-365.
Türkeş M, Sümer UM. Spatial and temporal patterns of trends and variability in diurnal temperature ranges of Turkey. Theor. Appl. Climatol. 2004; 77: 195–227.
Türkeş M, Sümer UM, Demir I. Re-evaluation of trends and changes in mean, maximum and minimum temperatures of Turkey for the period 1929–1999. Int. J. Climatol. 2002; 22: 947–977, doi:10.1002/joc.777.
Unal, YS, Tan E, Mentes SS, Summer heat waves over western Turkey between 1965 and 2006. Theor. Appl. Climatol. 2013; 112: 339–350, doi:10.1007/s00704-012-0704-0
Vautard R, Yiou P, D'Andrea F, de Noblet N, Viovy N, Cassou C, Polcher J, Ciais P, Kageyama M, Fan Y. Summertime European heat and drought waves induced by wintertime Mediterranean rainfall deficit. Geophys. Res. Lett. 2007; 34: L07711, doi:10.1029/2006GL028001.
Vautard R, Honore C, Beekmann M, Rouil L. Simulation of ozone during the August 2003 heat wave and emission control scenarios. Atmos. Environ. 2005; 39: 2957– 2967.
Weisheimer A, Doblas-Reyes AJ, Jung T, Palmer TN. On the predictability of the extreme summer 2003 over Europe. Geophys. Res. Lett. 2011; 38, L05704, doi:10.1029/2010GL046455
Zaitchik B, Macalady AK, Bonneau LR, Smith RB. Europe's 2003 heat wave: A satellite view of impacts and land-atmosphere feedbacks. Int. J. Climatol. 2006; 26: 743–769.

CLIMATE CHANGES, WEATHER EVENTS BECOME EXTREMER

Seyfullah Çelik, Erdoğan Bölük, Ali İhsan Akbaş, Aziz Deniz
Turkish State Meteorological Service
scelik@mgm.gov.tr

Abstract
The global warming, which is the main indicator of climate change, continues, and the weather events in the world become extremer correspondingly. The last consecutive years have become warmer worldwide. The hottest year is 2016, the previous one is 2015. The expectations are that the year 2017 will be even hotter. The situation in Turkey looks a bit different. 2010 is the hottest year and 2014 is the second. The geographical location and topographical features of our country prevent the increase of temperature in parallel with the world. This difference is sometimes seen between European countries and our country as well. In general, the temperature of the air in our country continues to increase due to years, becoming more pronounced in summer. The increase in temperature brings with it evaporation and humidity increase. This has caused heavy rains in recent years. When large-scale heavy rains causing loss of life and property in our country are analyzed, it has been observed that the precipitation has been more effective for a short time and has released large quantities. 50 mm of rainfall in 30 minutes was used in this study. The centers of all the automatic observation stations after 2000 and 50 mm per 30 minutes obtained from the printing rainfall instruments measured in the previous years were uncovered and the map and frequency values of the country were obtained as a result of the study. As a result; areas of extreme rainfall are expanding. Furthermore, have come to the conclusion that not only the centers in the Eastern Black Sea and Western Mediterranean regions, but also Istanbul and Ankara have entered the areas where extreme rainfall occurs.

Keywords: *Temperature, precipitation, flash flood, global warming, extreme rainfall*

A CASE STUDY: ANALYSIS of FLASH FLOOD USING FFGS PRODUCTS on 17 JANUARY 2016 in CESME, DIKILI, IZMIR and MANISA

Ertan TURGU, Mustafa COŞKUN, Seyfullah ÇELİK, Mehmet AKSOY
[1]Turkish State Meteorological Service(TSMS), Hydrometeorology Division of Research Department, Ankara
eturgu@mgm.gov.tr, mustafacoskun@mgm.gov.tr, scelik@mgm.gov.tr, mehmetaksoy@mgm.gov.tr

Abstract
Flash floods are among the world's deadliest natural disasters and result in significant social, economic and environmental impacts. Damages to the infrastructure were found in İzmir's Çeşme, Dikili and Konak districts and in Manisa on January 17, 2016 as a result of heavy precipitation of 101.8 mm, 90.5 mm 84.4 mm and 87.4 mm respectively within 24 hours. The Polar Jet Stream, which was associated with the frontal system, stretched down over France was very strong. The image on the right shows that the jet stream axis was divided into two over Çeşme. This formation induces heavier precipitation and stronger storm at the separation area. This was the important mechanism that determined the heavy precipitation over Çeşme. 500 hPa Chart on 17 January 2016 at 00:00 UTC shows a trough that was expanding over the southern Italy. Behind trough, geopotential height contours were very close to each other indicating the presence of very strong winds. Here, the northern and north western wind streams caused subsidence and convergence space. But, in front of trough, atmospheric upward vertical motion with the south and south western winds were pronounced, which was called divergence space. When the wind speed behind the trough is higher than the wind speed in front of the trough, the trough descends further south. Strong winds on divergenge area in front of the trough caused the system to become stronger. Meteorological conditions in terms of rainfall intensity, synoptic scale, mesoscale, radar and sounding, that caused the Flash Flood event on 17 January 2016 in Çeşme, Dikili, İzmir, and Manisa was examined. It was taken into consideration of the effect of precipitation either increasing or decreasing in the next 24 hours. This information and knowledge with the support of FFGS products were investigated particularly soil moisture saturation (ASM), FFG and Flash Flood Threat (FFT) products to ensure the success of decision making process on Flash Flood occurrence. The Flash Flood Guidance component is used to estimate the amount of rainfall that is required to cause bankfull flow for a given duration (e.g., one, three and six hours) at the outlet of each sub-basin taking into account of current soil moisture conditions.As aresult, The FFGS provided the necessary products to support the development of warnings for flash floods from rainfall events through the use of remote sensed precipitation (e.g., radar and satellite-based rainfall estimates) and hydrological models.

***Keywords**: Flash flood early warning system*

INTRODUCTION

To address the issues associated with flash floods, especially to address the lack of capacity to develop effective flash flood warnings, the Flash Flood Guidance System (FFGS) was designed and developed for interactive use by meteorological and hydrologic forecasters throughout the world (WMO,2016). In support of the FFGS programme, a Memorandum of Understanding was signed among the World Meteorological Organization, the U.S. Agency for International Development/Office of U.S. Foreign Disaster Assistance, the U.S. National Oceanic and Atmospheric Administration/National Weather Service and the Hydrologic Research Center (a U.S. non-profit corporation) to work together under a cooperative initiative to implement the FFGS worldwide.

FFGS is an important tool necessary to provide operational forecasters and disaster management agencies with real-time informational guidance products pertaining to the threat of small-scale flash flooding. The FFGS is a robust system designed to provide the necessary products to support the development of warnings for flash floods from rainfall events through the use of remote-sensed precipitation (e.g., radar and satellite-based rainfall estimates) and hydrologic models. To assess the threat of a local flash flood, the FFGS is designed to allow product adjustments based on the forecaster's experience with local conditions, incorporation of other information (e.g., Numerical Weather Prediction outputs) and any last minute local observations (e.g.,non-traditional rain gauge data) or local observer reports.

MATERIAL AND METHOD

The purpose of this study is first, to examine meteorological conditions in terms of rainfall intensity, synoptic scale, mesoscale, radar and sounding, that caused the FF event on 17 January 2016 in Çeşme, Dikili, İzmir, and Manisa; second,to take into consideration of the effect of precipitation either increasing or decreasing in the next 24 hours; third, to examine this information and knowledge with the support of FFGS products particularly soil moisture saturation (ASM), FFG and FFT products to ensure the success of decision making process on FF occurrence. Figure 1 shows location of FFGS subbasins over Çeşme, İzmir, Manisa and Dikili.

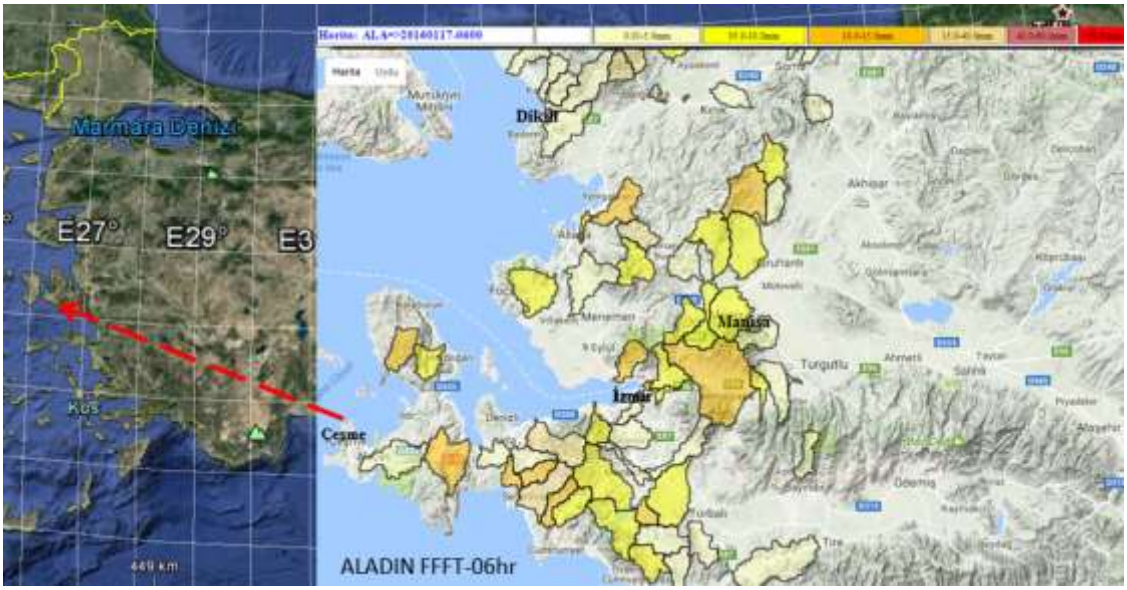

Figure 1. Region of Study Source: https://212.175.180.79/ERTFFT from BSMEFFGS

Station Name	WMO Synoptic Station No	ICAO Name	ELEVATION (m)	LAT	LON
Çeşme:	17221	CESM	5	38.3036	26.3724
Dikili:	17180	DIKL	3	39.0737	26.8880
İzmir(Konak)	17220	GUZL	29	38.3949	27.0819
Manisa:	17186	MANS	71	38.6153	27.4049

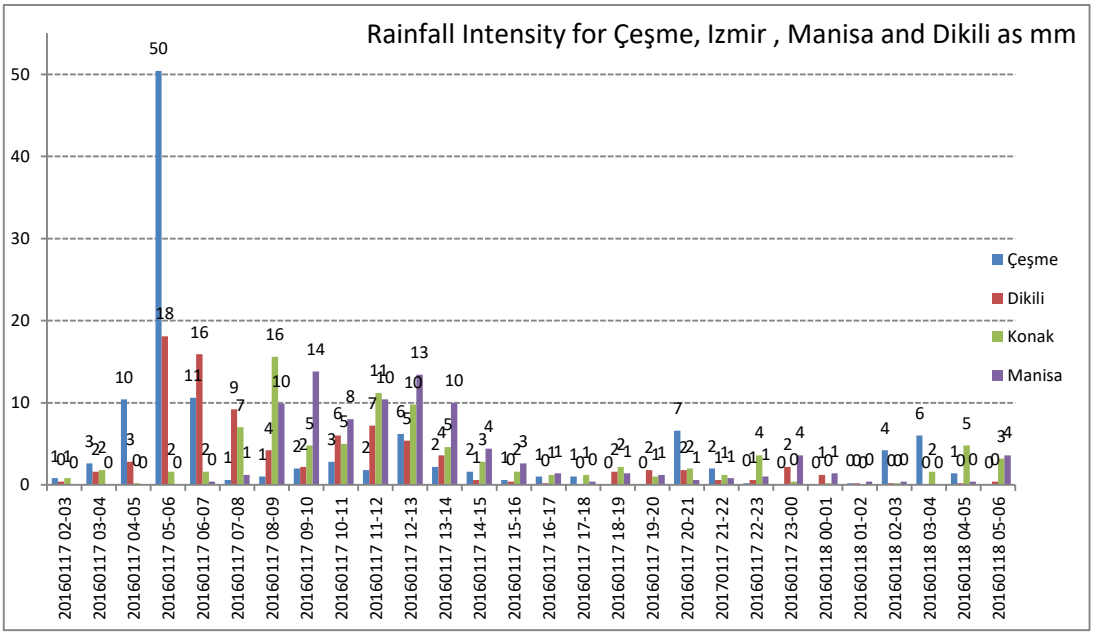

Figure 2. Rainfall Intensity for Cesme, Dikili, Izmir and Manisa.

Rainfall intensity graph shows maximum precipitation (or distinctive peaks) measured at Çeşme between 05-06UTC with **50** mm/hr and at Dikili between 05-06UTC with **18** mm/hr and at İzmir (Konak) between 08-09UTC with **16** mm/hr and at Manisa between 09-10UTC with **14** mm/hr on 17 January 2016.

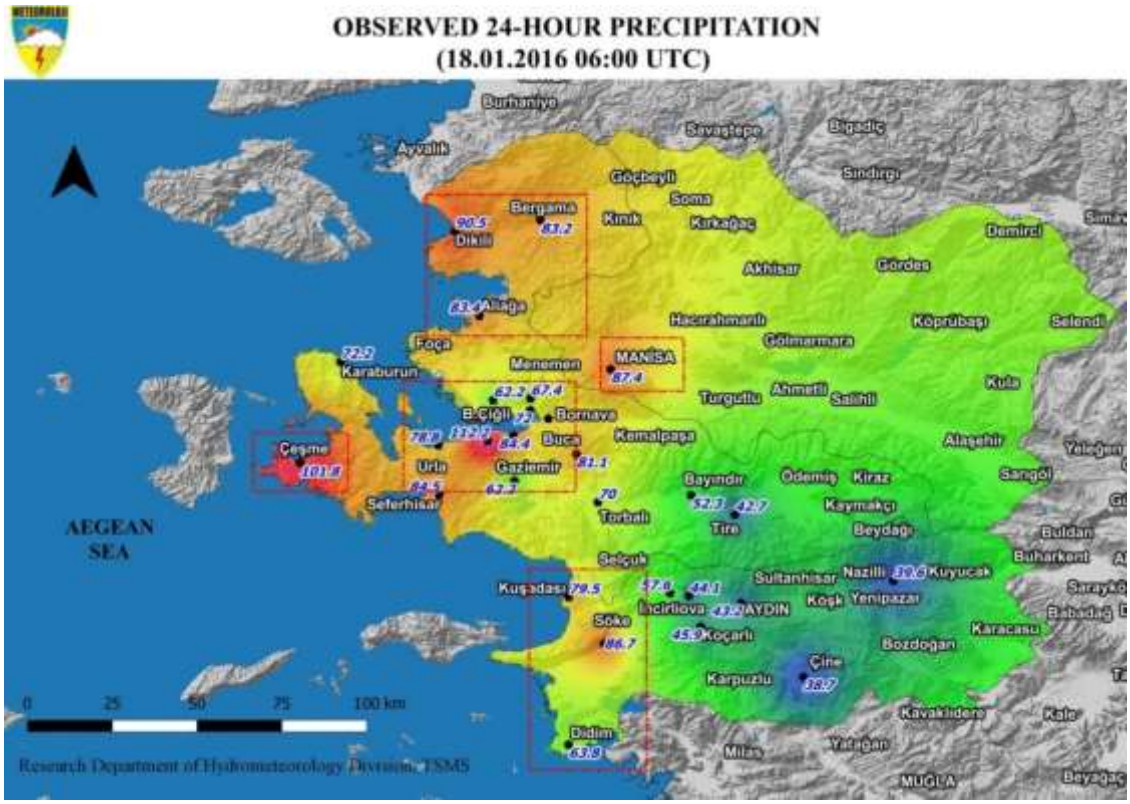

Figure 3. Observed 24 hour Precipitation.

Accumulations of precipitation as measured by AWOS over the last 24 hour ending on 18 January 2016 at 06:00 UTC were **101.8**mm for Çeşme; **90.5**mm for Dikili; **84.4**mm for İzmir and **87.4**mm for Manisa.

Methods used in this study include:

- analysing meteorological conditions that caused flash flood event on 17 January 2016 in Çeşme, Dikili, İzmir and Manisa for synoptic scale weather patterns at surface, 850 hPa, 500 hPa and 300 hPa charts.
- analysing satellite product using ECMWF surface chart for 24 hours precipitation (T+24) valid from 00:00UTC on 17 January 2016.
- analysing radar product using İzmir radar which is the nearest radar to the study region.
- analysing instability product using Skew T and Log P diagramme generated by University of Wyoming.
- evaluating FFGS products (particularly ASM and FFTs) to decide the possibility of flash flood.

SURFACE CHART ANALYSIS

On the 17th of January at 00:00UTC, isobars were shown at 3 hPa intervals. There was a deep Low Pressure Center (A) with 998 hPa value over Greece. This frontal system associated with (A) affected western Turkey when surface pressure tendencies had negative values toward the northeast and the east of (A).

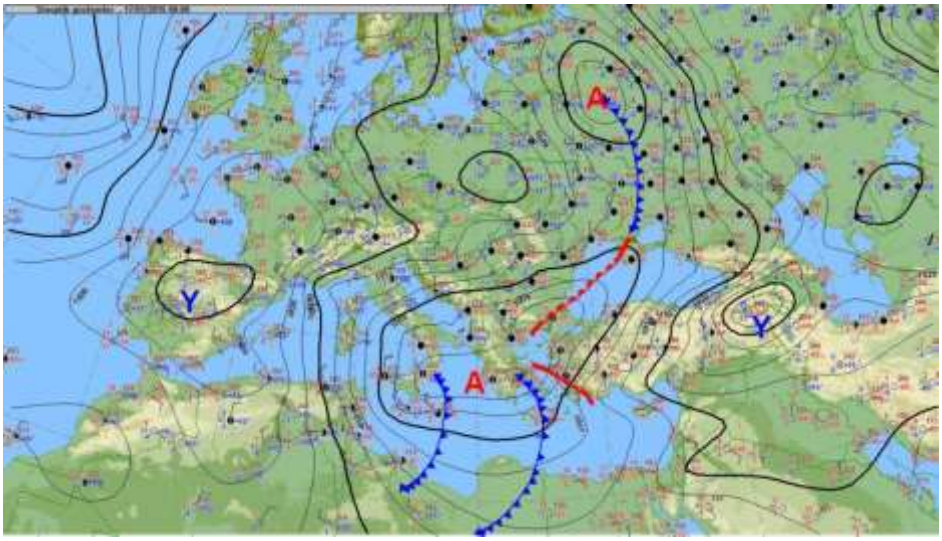

Figure 4. Surface Chart for 17 January at 00:00 UTC (Source:METCAP)

850 hPa CHART ANALYSIS

Strong cold air advection over Athens from southwest and also Low Level Jet (LLJ) from southeast brought high humidity and warm air towards Çeşme. There were strong winds having 50-70 kt between Athens and Çeşme. So, this frontal system generated heavy rainfall.

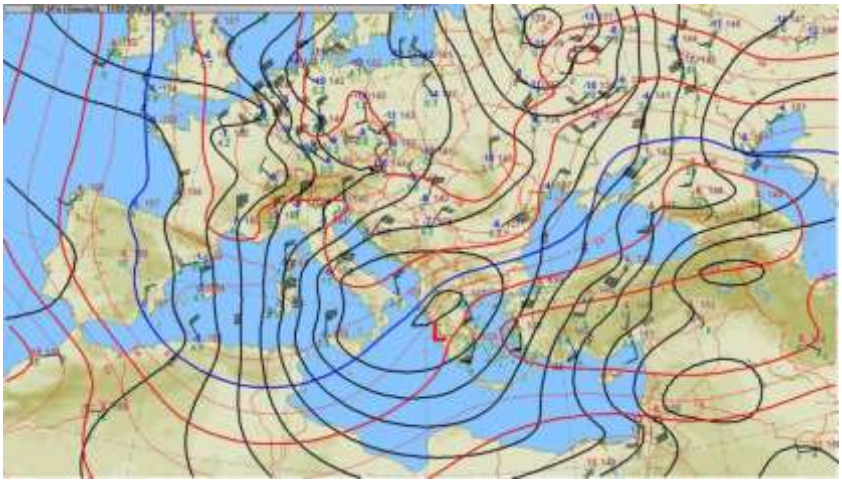

Figure 5. 850 hPa Chart for 17 January at 00:00 UTC (Source:METCAP)

500 hPa CHART ANALYSIS

A trough was expanding over the southern Italy. On the left side of the trough (behind trough), geopotential height contours were very close to each other indicating the presence of very strong winds.Here,the northern and north western wind streams caused subsidence and convergence space. But, in front of trough, atmospheric upward vertical motion with the south and south western winds were pronounced, which was called divergence space. Temperature at the surface chart over Çeşme was 16ºC while -19ºC at 500 hPa level on 17 January 2016 at 00UTC. In general, when the wind speed behind the trough is higher than the wind speed in front of the trough, the trough descends further south. Strong winds on divergenge area in front of the trough caused the system to become stronger.

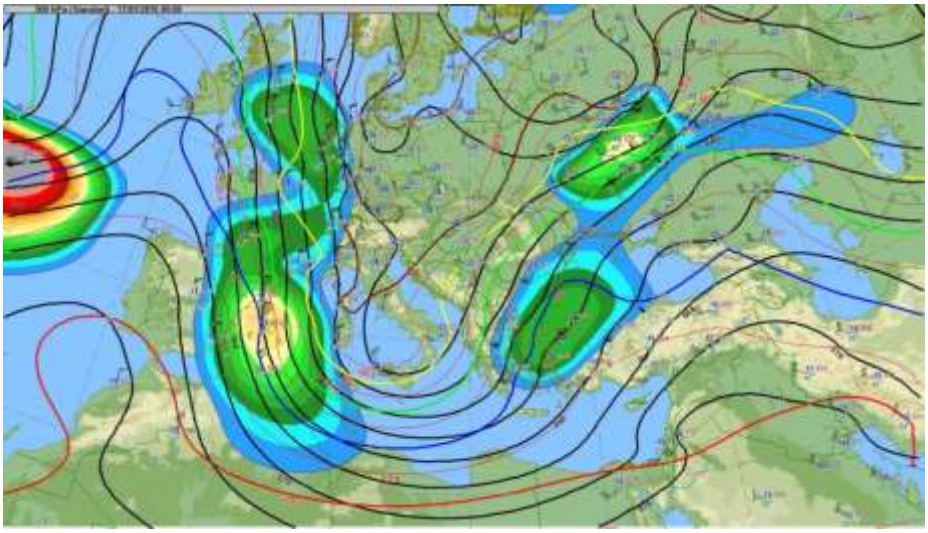

Figure 6. 500 hPa Chart for 17 January at 00:00 UTC (Source:METCAP)

MAXIMUM WIND SPEED AT 300 hPa CHART ANALYSIS

The image on the left shows that the Polar Jet Stream, which was associated with the frontal system, stretched down over France was very strong.

The image on the right shows that the jet stream axis was divided into two over Çeşme. This formation induces heavier precipitation and stronger storm at the separation area (Maddox and Crisp,1999). The composite chart on the right shows **500** hPa features in blue, **850** hPa features

in red and green and **surface** frontal analyses in black. This was the important mechanism that determined the heavy precipitation over Çeşme.

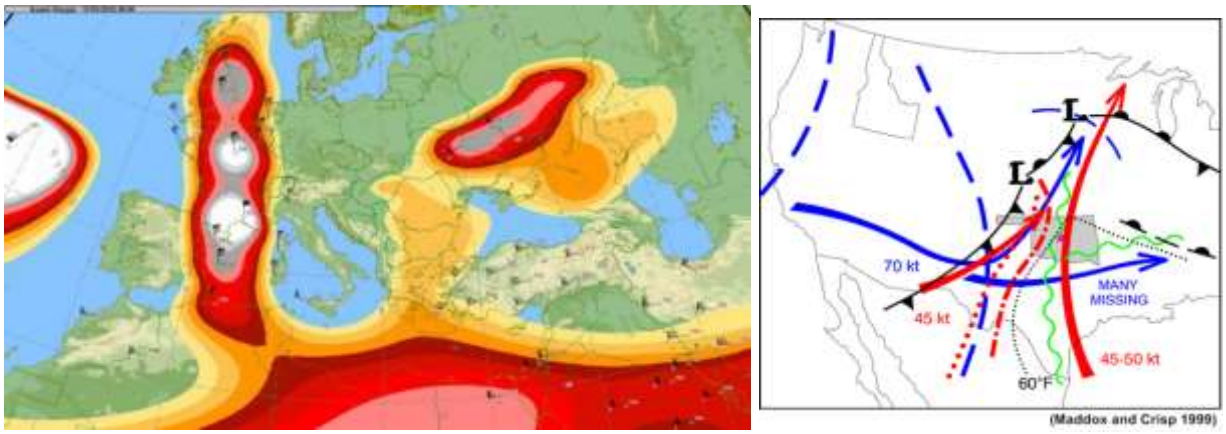

Figure 7. 500 hPa Chart for 17 January at 00:00 UTC on the left and jet stream axis on the right (Source:METCAP)

ECMWF PRECIPITATION FORECAST CHART ANALYSIS

ECMWF map predicted rainfall of 151 mm/24 hour over Çeşme on 17 January 2016 at 00:00UTC.

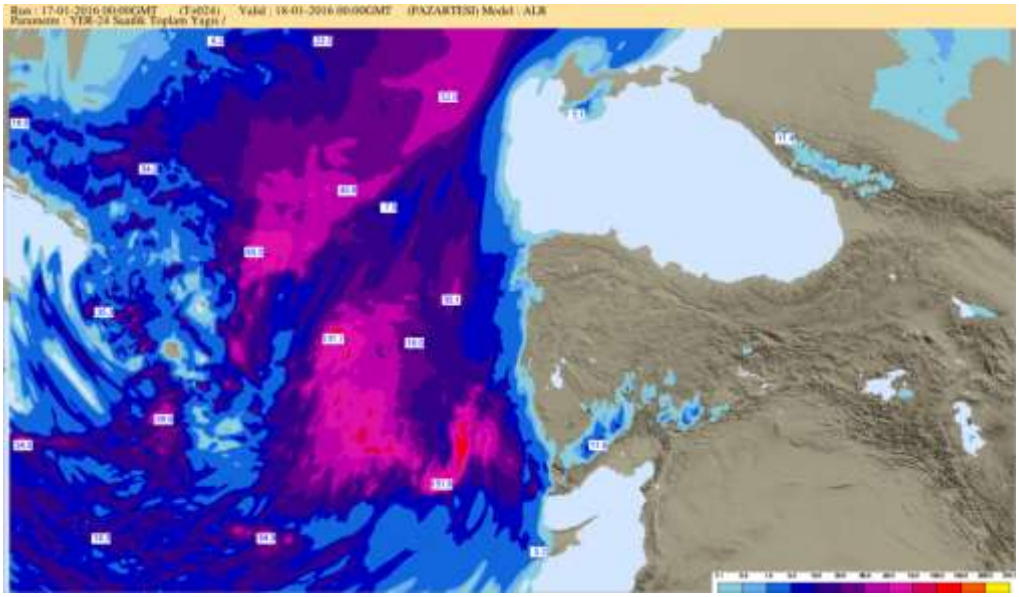

Figure 8. ECMWF Operational Analysis and Foracast Map on 17 January 2016 at 00:00UTC T+24hr (Total precipitation for the next 24 hours).
Source:http://sht.mgm.gov.tr/sht/meteor.php

SATELLITE IMAGE ANALYSIS

Figure 9. EUMETSAT MSG WV channel 5 on 17 January 2016 at 00:00UTC

Satellite image shows that the frontal system was more visible and pronounced over Crete island. Here, the Water Vapour (WV) absorption band (5.35 to 7.15 μm) is used in determining the amount of water vapour in the upper troposphere.

RADAR IMAGE

(a) (b) (c)

(d)

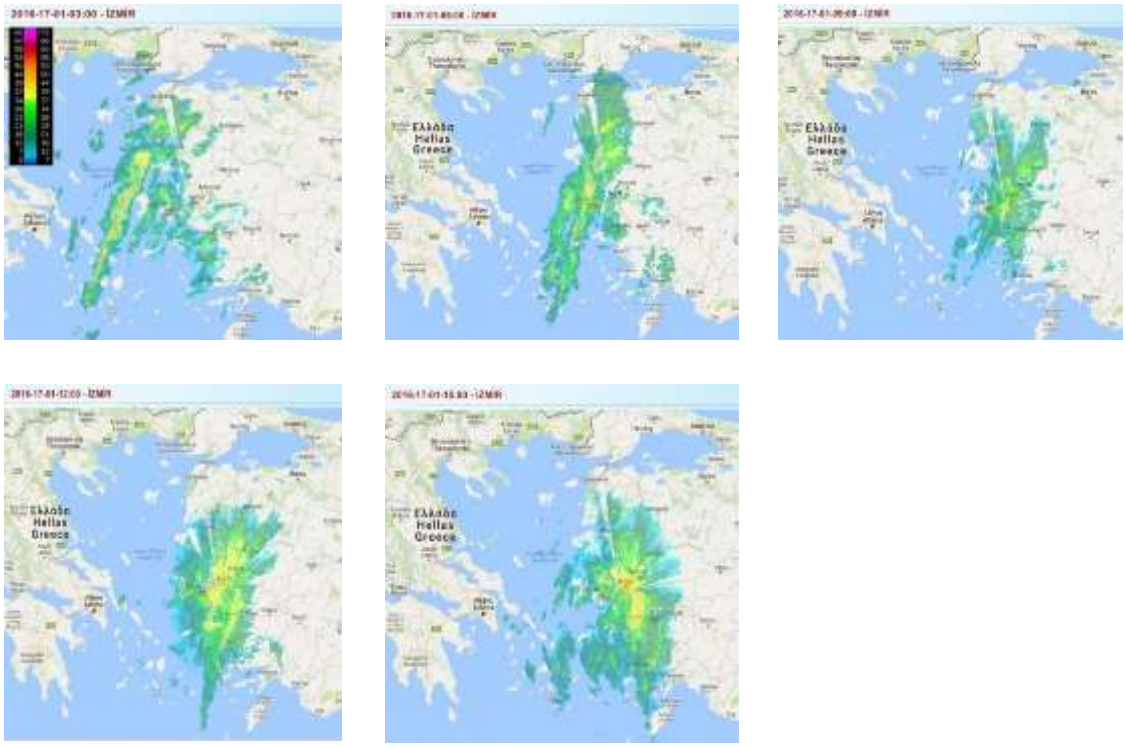

Figure 10. IZMIR RADAR PPI REFLECTIVITY on 17 January 2016 at 03:00UTC, at 06:00UTC, at 09:00UTC, at 12:00UTC and at 15:00UTC Source:TSMS

Izmir RADAR shows the evolution of precipitation along a cold front first over Çeşme, then Dikili, İzmir and Manisa. Radar reflectivity was greater than 40 dBz which indicated heavy precipitation in the winter season.

SKEW-T LOG-P DIAGRAM

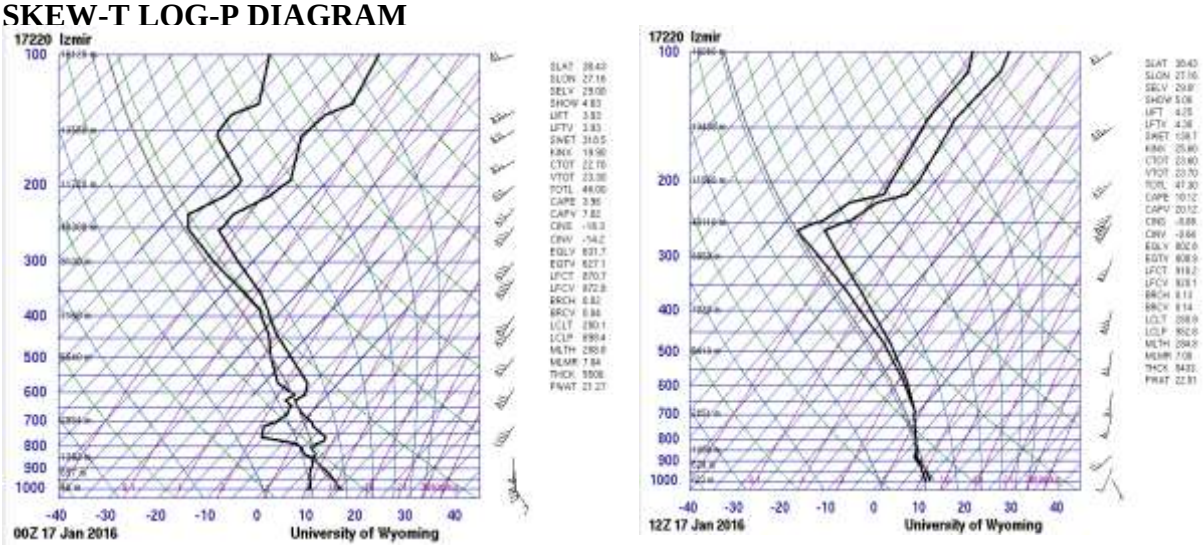

Figure 11.Instability index in the vertical profile of the atmosphere for İzmir 17220 Radiosonde Station Observation on 17 January 2016 at 00UTC(on the left) and 12UTC(on the right). Source:University of Wyoming

The sounding image (Figure 11) on the left shows a **veering wind** which turns clockwise with height. This veering wind is associated with **warm air advection** and **dynamic lifting**. Furthermore, temperature and dew point temperature lines became closer on the image which refers to a saturated or moist air. South and south east wind associated with warmer and moist air can be seen **up to 850 hPa**. Figure 11 on the right shows the sounding data indicating up to 100 hPa (approximately 16000 m) geopotential height from the ground as very moist and cloudiness where air temperature and dew point temperature values were very close to each other. Strong south western jet stream was seen above 650 hPa.

BSMEFFG PRODUCTS: Average Soil Moisture (ASM-06)

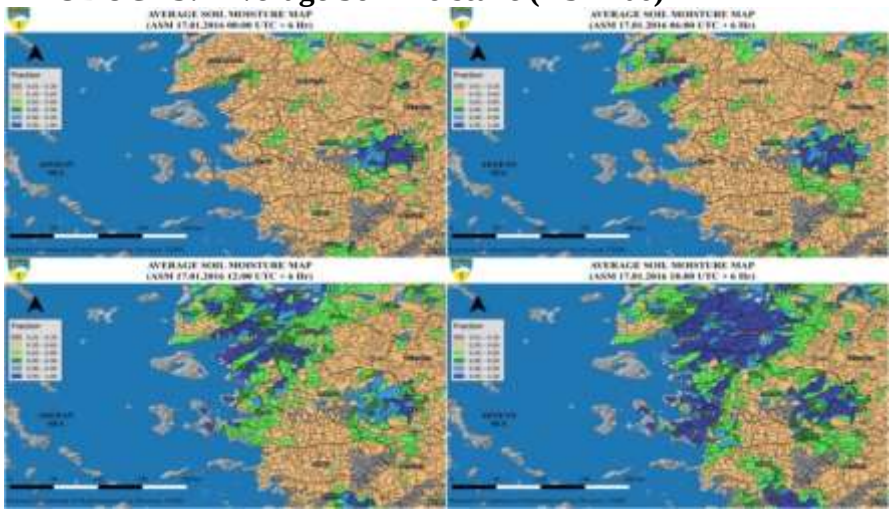

Figure 12. Average Soil Moisture (ASM-06) Source:BSMEFFGS at TSMS

ASM provides soil water saturation fraction (dimensionless ratio of contents over capacity) for the upper zone (approximately 20-30 cm depth) of the Sacramento Soil Moisture Accounting Model for each of the sub-basins (Georgakakos,2005 and 2002). Average Soil Moisture map is changing in time (00-06-12-18UTC) as shown in the images. The color of sub-basins turns from dark yellow to green and finally blue on 17 January 2016 at 18:00UTC. Soil becomes more saturated where subbasins are blue thus it can be interpreted as flash flood threat is increasing.

BSMEFFG PRODUCTS: ALADIN FORECAST MEAN AREAL PRECIPITATION FMAP-06 and FMAP-24

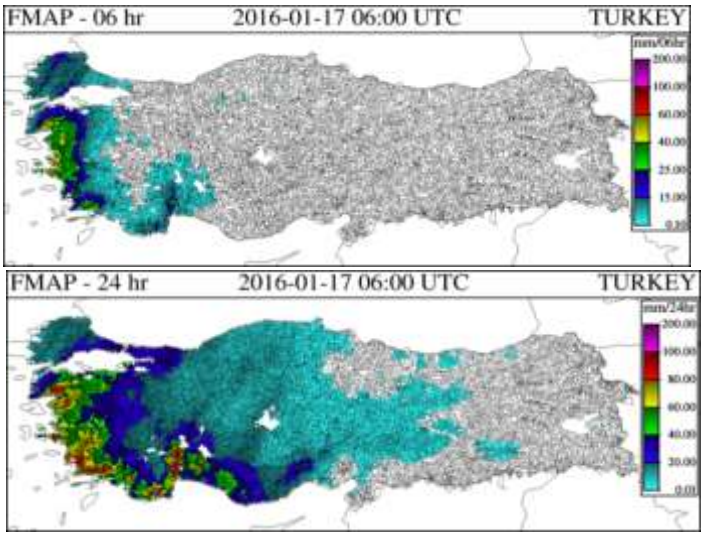

Figure 13. FMAP-06 and FMAP-24 Source:BSMEFFGS at TSMS

FMAP provides 1-hour, 3-hour, 6-hour and 24-hour totals of forecast precipitation (mm) produced by using numerical forecasts from the ALADIN Model (Georgakakos,1987). FMAP-06hr (above) and FMAP-24hr(below) on 17 January 2016 at 06UTC show that a prolonged and intensifiying precipitation was forecasted in Çeşme, Dikili, İzmir and Manisa.over 6 hr and 24hr beginning from the 06:00UTC.

BSMEFFG PRODUCTS: FFG-06hr at 00, 06, 12, 18 UTC

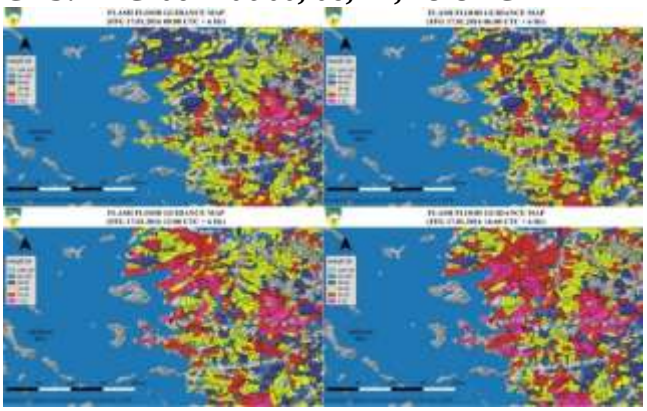

Figure 14.FFG-06hr at 00,06,12 and 18 UTC Source:BSMEFFGS at TSMS

FFG value indicates the total volume of rainfall of a given duration (1,3 or 6-hr) over the given sub-basin which is just enough to cause bankfull flow at the outlet of the draining stream.

(Carpenter at all,1999) In this case, color of sub-basins gradually turn from **blue** and **yellow** into **red** and **purple** which means flash flood threat is rising.

BSMEFFG PRODUCTS: Merged MAP-06

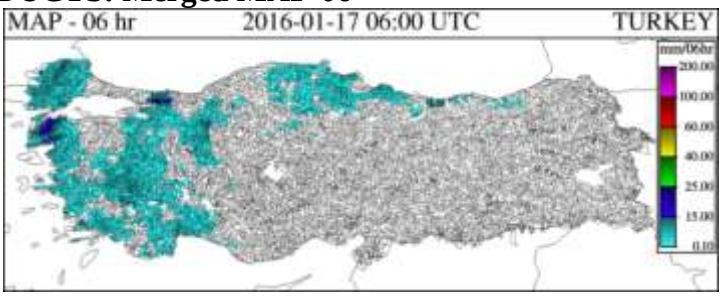

Figure 15.MERGED MAP-06hr Source:BSMEFFGS at TSMS

Merged MAP provides 1-hour, 3-hour, 6-hour and 24-hour totals of the Merged Mean Areal Precipitation (mm) for each system sub-basin. Merged MAP 06hr expresses accumulations of mean areal precipitation estimates for a sub-basin over the last 6 hours ending on the current navigation hour using best available mean areal precipitation estimates from bias-adjusted RADAR or bias-adjusted MWGHE or bias-adjusted GHE or the gauge-interpolations. (mm/6hr). Merged MAP is main input to the Snow17 and SAC-SMA. Note that bias is corrected with rain gauge data (Georgakakos,1987).

BSMEFFG PRODUCTS: PFFT-06hr

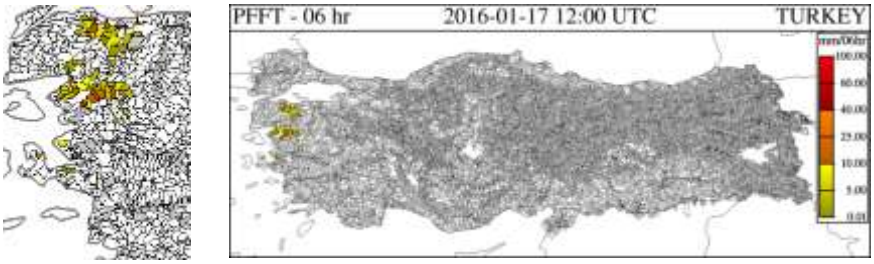

Figure 16.PFFT-06 Source:BSMEFFGS at TSMS

PFFT values indicate the difference of recent persisted Merged MAP of the given duration and the corresponding current FFG of the same duration for a given sub-basin. PFFT-06 (Figure 15) shows yellow coloured sub-basins with the value of approximately 5 mm/6hr as excess water from bankfull level for Çeşme.

BSMEFFG PRODUCTS: FFFT-06hr

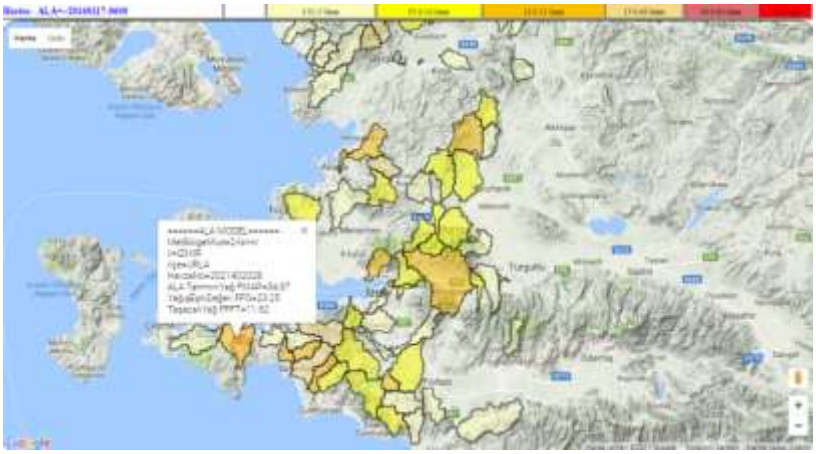

Figure 17.FFFT-06 from BSMEFFGS, Source: https://212.175.180.79/ERTFFT

The FFFT values indicate the difference of the FMAP of the given duration and the corresponding current FFG of the same duration. ALADIN FFFT-06 shows orange coloured sub-basins with the value of approximately 60 mm/6 hr as excess water from bankfull level on 17 January 2016 at 06:00UTC for Çeşme.

FFG CHECK LIST ASSESSMENT

Table 1. Check List for FFG

Date of Warning: 20160117-0600					ALADIN FFFT	ALADIN FMAP		Gauge MAP	MERGED MAP	ASM	FFG
Model	Region	City	County	BasinID	mm/6sa	mm/6sa	mm/24sa	mm/6sa	mm/6sa	%	mm/6sa
ALA	2-İzmir	IZMIR	CESME	2021402031	0.15	26.93(<-2)	39.48(<-2)	7.46	3.29	0.51	26.78
ALA	2-İzmir	IZMIR	URLA	2021402028	11.62	34.87(3)	52.83(4)	0.42	2.26	0.59	23.25
ALA	2-İzmir	IZMIR	DIKILI	2021401571	0.24	31.52(<-2)	56.41(2)	0.56	3.66	0.55	31.28
ALA	2-İzmir	IZMIR	DIKILI	2021401573	0.83	32.90(<-2)	65.15(4)	0	2.7	0.46	32.07
ALA	2-İzmir	IZMIR	DIKILI	2021401574	4.26	34.80(<-2)	73.45(5)	0	4.65	0.54	30.54
ALA	2-İzmir	IZMIR	DIKILI	2021401579	3.65	34.14(<-2)	68.97(4)	0	4.48	0.51	30.49
ALA	2-İzmir	IZMIR	KONAK	2021402021	3.95	42.27(3)	63.67(3)	1.57	0.97	0.55	38.32
ALA	2-İzmir	IZMIR	KONAK	2021402024	6.62	43.62(3)	72.16(4)	1.26	2.93	0.6	37
ALA	2-İzmir	MANISA	MANISA_M	2021401635	16.34	43.12(4)	63.57(3)	0	1.47	0.54	26.78
ALA	2-İzmir	MANISA	MANISA_M	2021401835	3.23	36.21(<-2)	55.80(2)	0	0.06	0.65	32.98
ALA	2-İzmir	MANISA	MANISA_M	2021401838	5.31	29.63(<-2)	48.38(<-2)	0	0.03	0.66	24.32
ALA	2-İzmir	MANISA	MANISA_M	2021401841	9.75	29.57(<-2)	47.52(<-2)	0	0	0.73	19.82
ALA	2-İzmir	MANISA	MANISA_M	2021401913	2.45	32.59(<-2)	63.24(3)	0	0.38	0.53	30.14
ALA	2-İzmir	MANISA	MANISA_M	2021402005	9.03	33.39(<-2)	62.27(3)	0	0.14	0.56	24.36
ALA	2-İzmir	MANISA	MANISA_M	2021402006	6.87	33.40(<-2)	56.61(2)	0	0.17	0.59	26.53
ALA	2-İzmir	MANISA	MANISA_M	2021402007	6.91	34.53(<-2)	60.42(3)	0.01	0.39	0.54	27.62

Reference: https://212.175.180.79/ERTFFT/ software program developed by Ertan Turgu at TSMS

Forecaster Opinion: According to check list (Table 1) given above, FF warning is advise for the next 6 hours. In the next 24 hours heavy rainfall was highly expected for Çeşme.

TSMS EXTREME WEATHER EVENT OBSERVATION

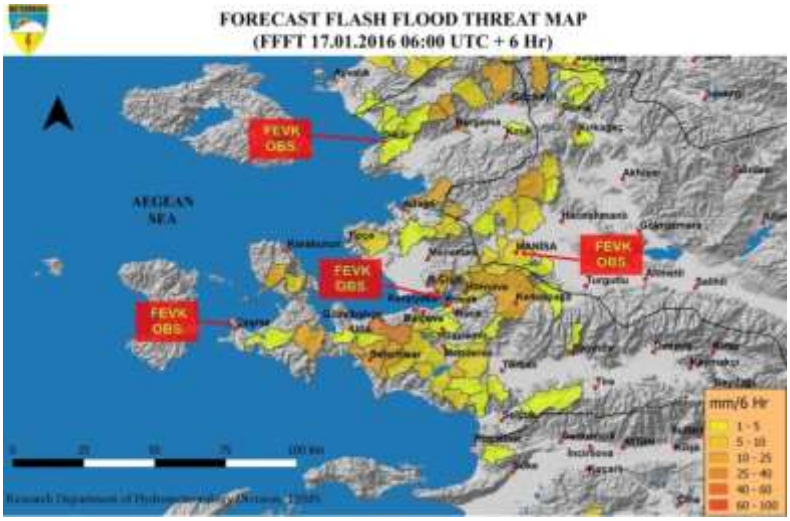

Figure 18.FFFT MAP Source:TSMS

FEVK observations are performed by TSMS for extreme weather events such as flood, hail, storm, high temperature etc. There were four FEVK reports for flash flood as indicated on the map which were prepared for Çeşme, Dikili, Izmir and Manisa.

CONCLUSIONS AND RECOMMENDATIONS

Fevk Raporu (CESM - 17221)			
Başlama Tarihi	17 Ocak 2016 Pazar 04:00		
Bitiş Tarihi	18 Ocak 2016 Pazartesi 01:15		
Olay Tanımı	43- Şiddetli yağış _ Sel _ Su baskını		
Zarar Tanımı	05- Yerleşim yerleri zarar gördü		
Rüzgar Yönü			
Rüzgar Hızı	7777.0		
Yağış Miktarı	109.0		
Yağış Periyodu	24		
Olay Şiddeti	03- Kuvvetli	Ölü Var=Hayır	Yaralı Var=Hayır

Hasar Raporu

Meydana gelen kuvvetli yağış neticesinde; Çeşme merkez, Alaçatı,Ilıca ve Ovacık' ta alt yapının yetersiz kalması sonucu yollarda su birikintisi oluştu ev ve işyerlerinin alt katlarını su bastı. Yetkililerden aldığımız bilgilere göre 600.000 TL maddi hasar oluşmuştur. Abdulkerim KARATAŞ

Figure 19.DAMAGE REPORT

- Meteorological conditions that caused flash flood event have been analysed for 17 January 2016 in Çeşme, İzmir, Manisa and Dikili in terms of synoptic scale weather patterns, satellite product, ECMWF surface chart, radar product and sounding analysis.
- A Mediterranean cyclone developed over Greece produced heavy precipitation and caused flash flood event on 17 January 2016 in Çeşme, Dikili, İzmir and Manisa.
- In this study, a top-down approach has been used for the analysis. In other words, We started with synoptic scale, mesoscale and nowcasting analyses and finally FFGS products were investigated and analyzed.
- Figure 19 shows damage report that was recorded in extreme weather event database at TSMS
- As a result, the use of FFGS products to issue flash flood watches / warning report and bulletin was shown to be very effective and useful.

REFERENCES

*Carpenter T. M, Sperfslage J. A, Georgakakos K.P, Sweeneyc T, Fread D.L., (1999). "National Threshold Runoff Estimation Utilizing GIS in Support of Operational Flash Flood Warning Systems", Journal of Hydrology.

*Georgakakos Konstantine P., (1987). "Realtime Flash Flood Predictions", Journal of Geophysical Research.

*Georgakakos Konstantine P., (2002). "Hydrometeorological Models for Realtime Rainfall and Flow Forecasting", Water Resources Publications.

*Georgakakos Konstantine P., (2005). "Analytical results for operational flash flood guidance", Journal of Hydrology.

*Maddox,R.A., and C.A., Crisp (1999). The Tinker AFB tornadoes of March 1948.Wea.Forecasting,14:492-499.

*WMO,FLASH FLOOD GUIDANCE SYSTEM (FFGS) with GLOBAL COVERAGE (2016), http://www.wmo.int/pages/prog/hwrp/flood/ffgs/documents/2016_ffgs-brochure_en.pdf

CLIMATIC VARIABILITY OF NORTHERN HEMISPHERIC STATIONARY WAVES IN ERA-INTERIM

Deniz Demirhan Barı

The recent changes in climate is effecting not only the troposphere but also the middle and upper stratosphere. It has been long known that the middle atmospheric circulation in the Northern Hemisphere have shifted signifying an increase in the amplitude of planetary waves due to the climate change. The long-term evolvement of zonally asymmetric atmospheric transport is analyzed using ECMWF ERA-INTERIM data from 1979 to 2013. The atmospheric circulation defined by the residual circulation is induced by vertically propagating planetary waves and gravity waves. Thus the longest and most powerful planetary waves, such as waves with zonal wave number 1, are capable of changing the structure of the 3D residual circulation in the middle atmosphere, which is characterized by downwelling in the area of the polar low anomaly and upwelling in the area of the Aleutian high anomaly. In this study the long term variability in the amplitude of the vertical and horizontal residual winds in the Northern Hemispheric winter Stratosphere is investigated. In this study, it is clear that there is an increase in the planetary wave one structure of the residual circulation which associates with an increase in middle atmospheric temperatures in the area of the polar low over Europe and Russia and a decrease in the area of the Aleutian high.

Keywords:*Stationary waves, ERA-Interim, residual winds*

Introduction

The changes in the middle stationary atmospheric wave pattern created via large scale waves and the topography. 3D transformed Eulerian mean equations formulated by Kinoshita et al. (2010) is used in to analyse the stationary waves. The regional differences in tropospheric wave activity due to land-sea contrasts, orography and ocean currents suggest strong zonal asymmetries of the wave driving in the whole middle atmosphere. Therefore, the long-term changes in the 3D BDC might be stronger and more significant than those identified by the 2D approach. The zonal asymmetries in the 3D BDC might largely determine the stationary waves and local changes of various quantities in the middle atmosphere, e.g., the observed local ozone trends which are different from the zonal mean and not fully understood (Tereao and Logan, 2007). The 3D stationary waves and local changes in the troposphere effect also the middle atmospheric transport processes. For example, the radiative effects of the stationary wave-one in stratospheric O_3 (largely produced by the 3D BDC) can significantly alter the stratospheric and tropospheric circulation, and wind-driven ocean currents (Gabriel et al., 2012). Stationary waves largely control various aspects of regional climate change (IPCC, 2007, Chapter 3) but their amplitudes are too weak in the model simulations (Boer and Lambert, 2008). An examination of the 3D stationary waves might help to improve this deficiency.

Data and Method

In this study, ERA-Interim which is provided by the European Centre of Medium Weather Forecasts (ECMWF) between 1979 and 2012 is used. ERA-Interim is the latest ECMWF global atmospheric reanalysis data set starting in 1979 (Dee et al., 2011). The project will use the data provided on a 1.5°x1.5° longitude-latitude grid and 37 standard pressure levels up to 1 hPa (50km) with a time increment of 6h.

ERA-Interim data is used to analyse the recent changes in middle atmospheric stationary waves. Recently Kinoshita et al. (2010) have formulated a 3D transformed Eulerian mean equations by

using the time-mean 3D eddy fluxes in the transformation, as proposed earlier for investigating wave-mean flow interactions in a 3D framework (Hoskins et al., 1983; Plumb, 1986; Trenberth, 1986).

According to Kinoshita et al. (2010) the time-mean residual wind components are given by:

$u_{res} = u - \square(RH^{-1} \langle u \square T \square \rangle / N^2) / \square z + \square(S/f) / \square y$ (1a)

$v_{res} = v - \square(RH^{-1} \langle v \square T \square \rangle / N^2) / \square z + \square(S/f) / \square x$ (1b)

$w_{res} = w + \square(RH^{-1} \langle u \square T \square \rangle / N^2) / \square x + \square(RH^{-1} \langle v \square T \square \rangle / N^2) / \square y$ (1c)

Here f is the Coriolis parameter, S is a wave energy perturbation, N^2 is the Brunt-Vaisala frequency, R is the ideal gas constant, H is the scale height, and $\square\square/\square z = RTH^{-1}$ ($\square$: geopotential); for convenience the time means denoted by brackets <> are only shown for the eddy heat flux terms; x and y denote eastward and northward directions as usual, and $z=\log(p/p_s)$ (p_s: surface pressure).

Diagnosis of stationary waves

Time and latitude averaged residual wind vectors indicates significant wave-one structure with a positive meridional residual wind over the Aleutian high and negative winds over the polar vortex at the middle stratosphere. Such a wave-1 structure is a result of the stationary waves in the middle atmosphere (Figure 1).

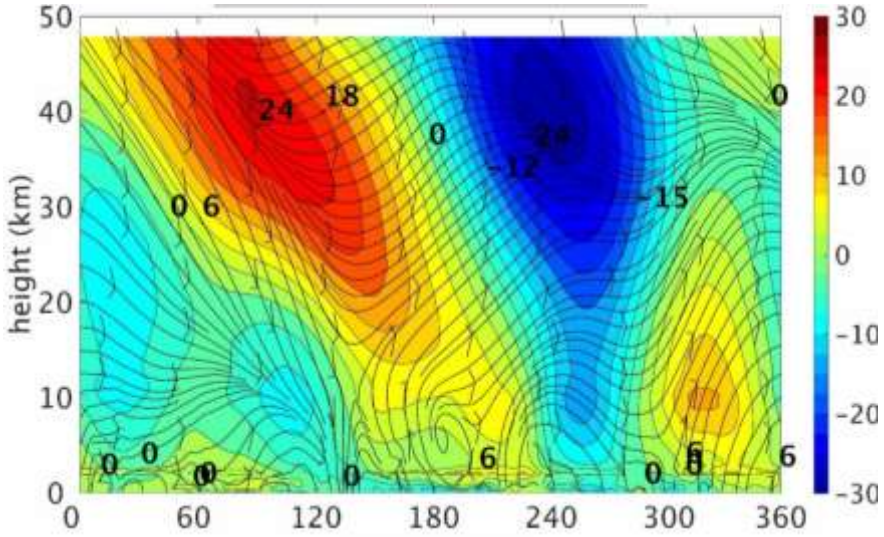

Figure 1. Residual winds averaged over 55-65°N and the from 1979 to 2012. Shaded area : v_{res} contours: u_{res}*w_{res} vectors

Longitudinal and time distribution of the vertical residual winds averaged over 55°- 65° N shows that between the longitudes 0°E and 120°E (Northen Europe and Southern Russia) shows a clear downward motion in January and over 120°E and 0° (North Pacific and North Atlantic) there is an upward motion (Figure 2).

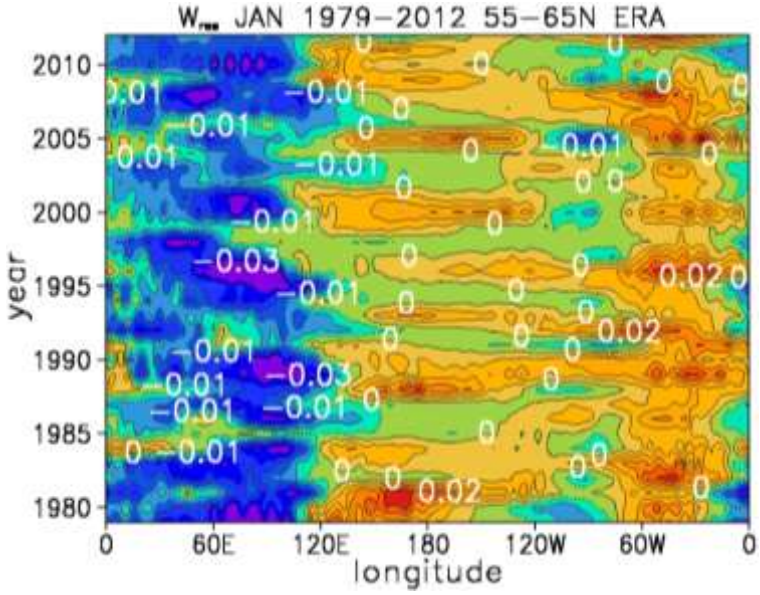

Figure 2. Residual vertical winds averaged over 55-65°N and from 1979 to 2012.

However the year by year variability in the vertical wind is more significant in figure 3. Figure 3 indicates the 12 months running mean of the vertical residual winds (x1000) averaged over latitudes 55-65°N and 0-180°E (Figure 3 a) and 180°W-0 (Figure 3 b). Over Northern Europe and mid-Russia (0-180°E) where a downward motion is observed in January, the vertical residual winds gain strength. But on the other side the upward motion over North Pacific and North Atlantic weaken during January.

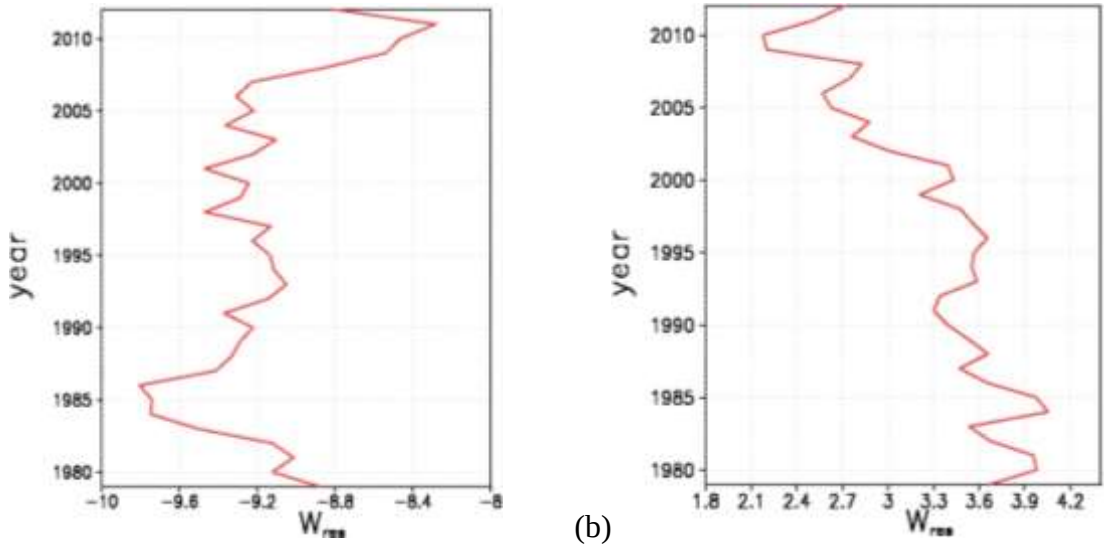

(a) (b)

Figure 3. 12 moths running mean of residual vertical winds averaged over latitudes 55-65°N and from 1979 to 2012. (a) averaged over longitudes 0°-180°E (b) 180°W-0°

Results and Discussions

Long term variability in middle atmospheric residual winds over 55-65°N is investigated by using ERA-Interim reanalysis data between 1979-2012. In this study the zonal asymmetries indicate a wave-1 structure in the wind patterns in January. An upward and southward movement is observed over Atlantic region and a downward and northward movement over Pacific region. It is found that there is a decrease in the speed of the residual meridional and vertical winds from 1979 to 2012 in January.

RELATION BETWEEN THE EAST ASIAN TROUGH AND EURO-MEDITERRANEAN CLIMATE AT PENTAD RESOLUTION

Yasemin Ezber [1], Deniz Bozkurt[2] and Ömer L. Şen[1]
[1] ITU Eurasia Institute of Earth Sciences
ezber@itu.edu.tr, senomer@itu.edu.tr
[2] University of Chile, Center for Climate and Resilience Research
dbozkurt@dgf.uchile.cl

Abstract
Euro-Mediterranean climate variability is mostly associated with different modes of teleconnection patterns such as North Atlantic Oscillation (NAO), Scandinavian Pattern, and Eastern Atlantic Pattern. In this study, relation of the Euro-Mediterranean climate variability with the strength of the East Asian trough (EAT) is investigated using 500hPa geopotential height composites of Trough Axis Index (TAI) at high temporal resolution (pentad). For that purpose, pentad time series obtained from 38-year daily ERA-Interim reanalysis data are used in the analysis. The pentad analysis shows that TAI is strong for the 3rd, 13th, 60th, 65th, and 71st pentads corresponding mostly to winter and spring seasons. EOF analysis indicates that all of the strong pentads have similar EOF patterns, except for the 3rd pentad. A negative correlation between TAI and temperature of Euro-Mediterranean region is found for the 3rd, 13th, 60th and 71st pentads based on the composite analysis.

Keywords: *EAT, TAI, pentad, ERA-Interim, surface temperature.*

INTRODUCTION
The Northern Hemisphere (NH) features two marked trough zones, one is located over Northern US and another one is located over Eastern Asia. The East Asian Trough (EAT) is a zonally asymmetric circulation characterized by strong negative deviation from the zonal mean over East Asia during boreal winter (Zhang et al., 1997; Wang et al., 2009; Song et al., 2016). Planetary waves are strong in the NH where large land surfaces are present (Nakamura et al., 2010). Orography (e.g. the Himalayas) and thermal contrast between the Pacific Ocean and large cold Eurasian continent enhances Rossby waves (Nakamura et al., 2010).

Many studies focus on the relation of climate over East Asia to the strength and position of the Siberian High (Ding and Krishnamurti 1987; Zhang et al. 1997). Strong radiative cooling due to sinking motion behind the EAT influences the buildup of the Siberian high (Ding and Krishnamurti 1987; Zhang et al. 1997). Pacific storm track activities are also affected by meridional temperature gradient due to the encounter of the cold monsoonal air with warm air over the western pacific (Nakamura et al., 2002). The development of the Aleutian Low is also associated with the EAT (Jhun and Lee, 2004).

The EAT contributes to the interdecadal variation of planetary wave activities (Huang et al., 2012). An upper-level short wave builds up from the western Eurasian continent, when the intensity of the Siberian High and EAT reaches a certain level. At that level, the wave moves and deepens towards east, then forms the original trough (Song et al., 2016). Propagation of the wave to the south results in outbreak of cold surge (Zhang et al., 1997). Yang et al. (2002) links spatial variability of the East Asian Jet to climate variability in Asia-Pasific-American region, illustrating that the impact region of the EAT might be large.

In this study, we investigated the relation of the EAT to the Euro-Mediterranean region at

pentad temporal resolution using daily ERA-Interim data.

DATA AND METHODS

We used the European Center for Medium-Range Weather Forecast (ECMWF) ERA-Interim reanalysis dataset (Dee et al, 2011) at daily temporal resolution, which spans from 1979 to 2017, The spatial and vertical resolutions of the data are 0.75x0.75 degree and 60 vertical levels (surface to 0.1hPa), respectively. We used 500hPa geopotential height in order to construct 38 years pentad time series from 1979 to 2016.

Trough Axis Index (TAI) is adopted from the description of Sun (1997). It is calculated by averaging 500 hPa geopotential height for the area between 30-45^{o}N and 125-145^{o}E. In addition, we developed another index for a secondary trough over the Euro-Mediterranean region using 500hPa geopotential height to further investigate the effect of intensity of the EAT on the Euro-Mediterranean climate. The index is basically based on 500hPa geopotential height differences at two points at the same latitude (39^{o}N), and it reflects the zonal shifts of the upper layer trough over the Euro-Mediterranean region. The index, which is called as TI_med, is calculated as follows;

$$TI\_med = Z_{(39^{o}N,10^{o}E)} - Z_{(39^{o}N,50^{o}E)}$$

where Z is the geopotential height at 500hPa.

Pentad correlations between TAI (defining the EAT strength) and TI_med (defining the zonal shifts of Mediterranean trough) yield significant values for some pentads at 99% significance level (Figure 1). Accordingly, correlations for 3rd, 13th, 31st, 37th, 60th, 65th, and 71st pentads are significant at this level. Therefore, EOF analysis is applied to the 500hPa geopotential height of these pentads. Composite analysis is used to determine the spatial pattern of the strength of the EAT.

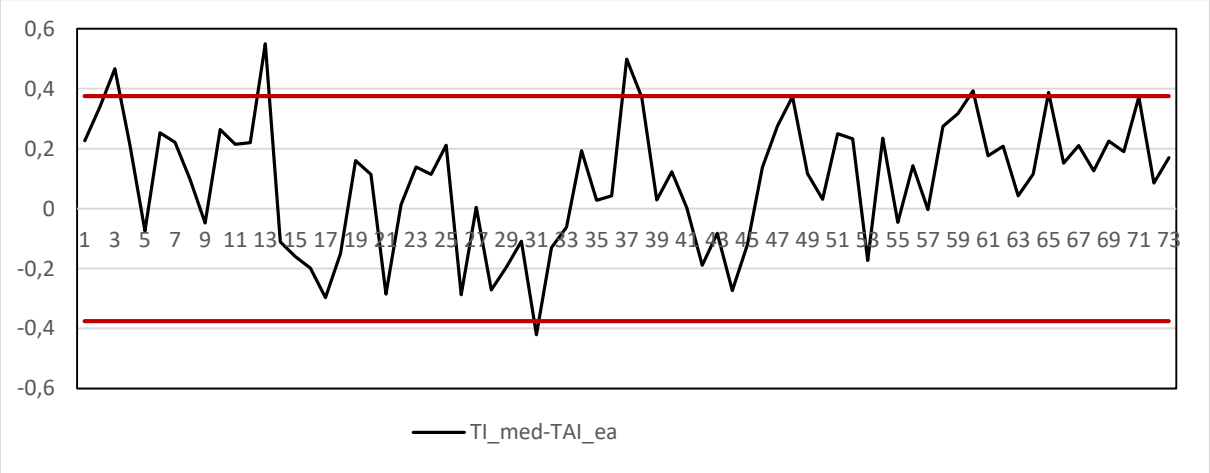

Figure 1. Pentad correlations between TI_med and TAI for pentads (red lines represent 99% significance level).

RESULTS

Average 500hPa geopotential height contours exhibit the two marked troughs over eastern North America and East Asia (Figure 2). A comparatively less marked trough is observed over Turkey (Figure 2). It is known that there is a relation between the strength of the EAT and the east-west movement of trough over the Mediterranean (Şen et al., 2017). When the EAT is

strong, the Mediterranean upper level trough tends to shift to the westward, and vice versa. The axis of the EAT is tilted to the west with narrow impact area in pentads corresponding to winter or spring seasons. However, trough axis of the EAT for the 31st and 37th pentads –corresponding to summer season- is tilted to the west, yet these are weak troughs like the one forming over the Mediterranean (Figure 2). Figure 2 indicates that strong EAT is observed in winter and spring seasons in which a strong East Asian jet stream takes place.

EOF analysis is applied to 500 hPa geopotential height ERA-Interim data to determine the first three EOF patterns. In general, the first EOF shows the strength of the troughs whereas the second EOF explains meridional changes of the geopotential height for almost all the pentads. However, in the 3rd pentad, it is the first EOF (41% of variation) that explains the strength of EAT. The second EOF of the 3rd pentad explains the meridional changes of the pattern. The third EOF explains the meridional movement of the pattern for all pentads.

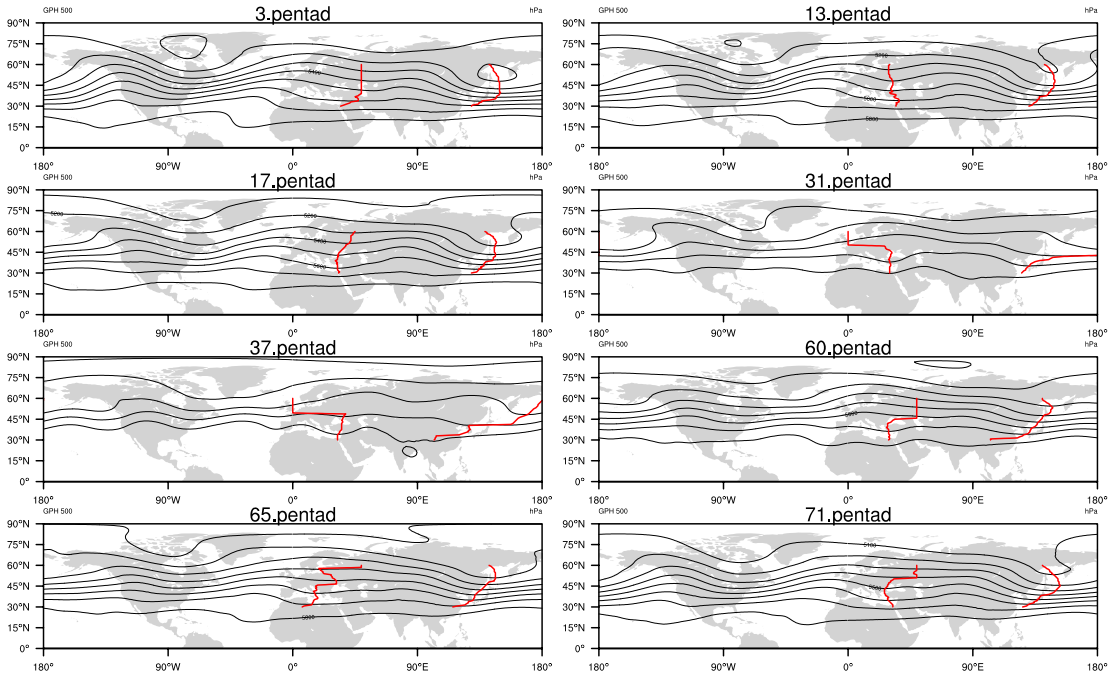

Figure 2. Climatology of 500hPa geopotential height for defined pentads (red lines shows trough axis over Mediterranean and East Asia).

Composite analysis is used to understand effect of the EAT on Mediterranean temperature pattern. For this analysis, a standard deviation equaling to 1 is used as the criterion to split the TAI into negative, positive or normal composites. We pay more attention to the difference between the negative and positive composites, since they clearly show a marked temperature pattern. Figure 3 exhibits a distinct temperature pattern over the Euro-Mediterranean region with contrasting anomalies between the eastern and western sides. In this regard, previously defined pentads behave differently depending on the season. For instance, the 3rd, 13th, 60th, 65th and 71st pentads have a cooling pattern over western Europe and the EAT region, whereas, a warming pattern is observed over Turkey towards Siberia (in Figure 3). This warming is strong in 3rd and 13th pentads, and it extends from eastern Africa and Middle East towards Turkey. On the other hand, the 17th, 31st, and 37th pentads illustrate a warming pattern over western Europe and a cooling pattern over eastern Mediterranean. A relatively weak cooling pattern is observed over the EAT region in these pentads (Figure 3).

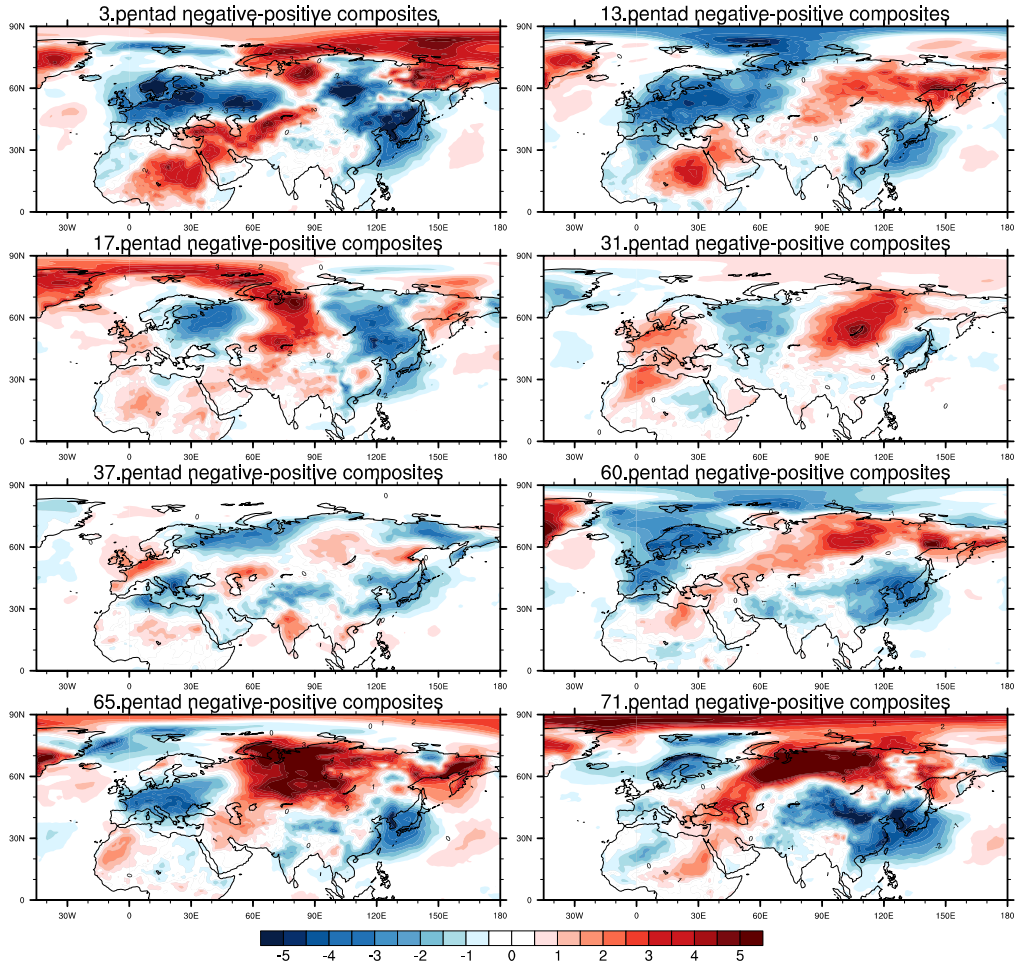

Figure 3. Temperature difference of negative and positive composites (defined by TAI) for selected (statistically significant at 99% level) pentads.

CONCLUSIONS

This study shows preliminary results of our research on the relation of the EAT to the Euro-Mediterranean climate. It suggests that there is a strong relationship between the EAT strength and the zonal shifts of the Mediterranean upper layer trough in some pentads of the year. The highest correlation is found for the 13th pentad corresponding to early March. Temperature composite analysis shows that the EAT has an impact on temperature distribution over the Euro-Mediterranean region. There is a positive temperature pattern over eastern Mediterranean up to Siberia and negative temperature pattern over Europe for winter pentads. The same negative temperature composite difference is also observed over the East Asian coast. In other words, difference of temperature composite over the East Asian coast is positively correlated with Europe, while the correlation is negative over a region lying between east Africa and Siberia.

REFERENCES

Dee, D. P., Uppala, S. M., Simmons, A. J., Berrisford, P., Poli, P., Kobayashi, S., Andrae, U., Balmaseda, M. A., Balsamo, G., Bauer, P., Bechtold, P., Beljaars, A. C. M., van de Berg, L., Bidlot, J., Bormann, N., Delsol, C., Dragani, R., Fuentes, M., Geer, A. J., Haimberger, L., Healy, S. B., Hersbach, H., Hólm, E. V., Isaksen, L., Kållberg, P., Köhler, M., Matricardi, M., McNally, A. P., Monge-Sanz, B. M., Morcrette, J.-J., Park, B.-K., Peubey, C., de Rosnay, P., Tavolato, C., Thépaut, J.-N. and Vitart, F. , 2011. "The ERA-Interim reanalysis: configuration and performance of the data assimilation system", Q.J.R. Meteorol. Soc., **137**: 553–597. doi: 10.1002/qj.828.

Ding, Y., and T. N. Krishnamurti, 1987: Heat budget of the Siberian high and the winter monsoon. Mon. Wea.

Rev., 115, 2428–2449, doi:10.1175/1520-0493(1987)115,2428: HBOTSH.2.0.CO;2.
Huang, R. H., J. L. Chen, L. Wang, and Z. D. Lin, 2012: Characteristics, processes and causes of the spatio-temporal variabilities of the East Asian monsoon system. Adv. Atmos. Sci., 29, 910–942, doi:10.1007/s00376-012-2015-x.
Jhun, J.-G., and E.-J. Lee, 2004: A new East Asian winter monsoon index and associated characteristics of the winter monsoon. J. Climate, 17, 711–726, doi:10.1175/1520-0442(2004)017,0711: ANEAWM.2.0.CO;2.
Nakamura, H., T. Miyasaka, Y. Kosaka, K. Takaya, and M. Honda, 2010: Northern Hemisphere extratropical tropospheric planetary waves and their low-frequency variability: Their vertical structure and interaction with transient eddies and surface thermal contrasts. Climate Dynamics: Why Does Climate Vary? Geophys. Monogr., Vol. 189, Amer. Geophys. Union, 149–179.
Song, L., L. Wang, W. Chen, Y. Zhang, 2016: Intraseasonal Variation of the Strength of the East Asian Trough and Its Climatic Impacts in Boreal Winter. J. Climate, 29, 2557–2577, doi: 10.1175/JCLI-D-14-00834.1.
Sun, B.M., and C. Y. Li, 1997: Relationship between the disturbances of East Asian trough and tropical convective activities in boreal winter (in Chinese). Chin. Sci. Bull., 42, 500–504.
Şen, Ö.L., Y. Ezber, and D. Bozkurt, 2017: On the role of East Asian Trough on the Euro-Mediterranean climate variability, ATMOS2017, these proceedings.
Wang, L., W. Chen, W. Zhou, and R. Huang, 2009: Interannual variations of East Asian trough axis at 500 hPa and its association with the East Asian winter monsoon pathway. J. Climate, 22, 600– 614, doi:10.1175/2008JCLI2295.1.
Yang, S., K. M. Lau, and K. M. Kim, 2002: Variations of the East Asian jet stream and Asian–Pacific–American winter climate anomalies. J. Climate, 15, 306–325, doi:10.1175/ 1520-0442(2002)015,0306: VOTEAJ.2.0.CO;2.
Zhang, Y., K. R. Sperber, and J. S. Boyle, 1997: Climatology and interannual variation of the East Asian winter monsoon: Re- sults from the 1979–95 NCEP/NCAR reanalysis. Mon. Wea. Rev., 125, 2605–2619, doi:10.1175/1520-0493(1997)125,2605: CAIVOT.2.0.CO;2.

ANALYSIS OF CLIMATE EXTREMES INDEX OVER TURKEY

Mehmet Barış Kelebek[1], Fulden Batıbeniz[1,2], Barış Önol[1]
Istanbul Technical University, Meteorological Engineering Department[1]
Oak Ridge National Laboratory, Climate Change Science Institute[2]
kelebek15@itu.edu.tr
batibenizf@ornl.gov
onolba@itu.edu.tr

Abstract
This study presents to quantify observed changes in the climate of Turkey from 1979 to 2015 through analysis of Climate Extremes Index (CEI). Original CEI calculation has been defined and applied over United States in order to show the impacts of climate change more obvious (Karl et al., 1996). In this study, we adapted the calculations for Turkey and the results show that the south part of Turkey has experienced extreme events more than the north part of Turkey and the Central Anatolia. Trend analysis of the CEI reveals that extreme events are on rise in terms of occurrence over Turkey.

Keywords**:** *climate change, turkey, climate extremes index, observation, Anatolia*

INTRODUCTION

Extreme meteorological events are important parts of the climate studies. Each event can be examined individually but, it is important to know the overall situation in order to understand the effects of climate change. The Climate Extremes Index (CEI), which comprises several indicators, has been designated and calculated over United States in effort to represent the impacts of climate change more obvious (Karl et al. 1996). CEI is an implementation of five indicators those measure extremes in monthly maximum/minimum temperatures, drought or moisture surplus (PDSI) (Palmer,1965), extremes in 1-day precipitation and days with/without precipitation based on a reference value. Recently, similar calculations have been applied for the Eastern Mediterranean region by using high resolution climate model outputs for the period of 1961-2008 (Batıbeniz et al., 2015). In this study, we have expanded their research to calculate the CEI over Turkey for the period of 1979-2015 by adapting indicators and using the observational data sets. CEI shows that the Marmara Region and the south of Turkey have experienced extreme events in range of 35%-40% more than the Black Sea Region and the Central Anatolia spanning from 31% to 35% on average. The minimum values have appeared over the northeast of Turkey, which is about 29%. Trend analysis of the CEI indicates that there is a positive decadal trend (1.33%) over Turkey in terms of occurrence of extreme events.

DATA AND METHODS

CEI represents individual extreme events in a single frame spanning from 0% to 100% as a set of different indicators where greater values mean that more extremes have occurred. 20% is expected average extreme value for each indicator. Extremes have been defined as the percentage of each indicator that existed above/below 90^{th}/10^{th} percentile of reference value which was calculated on the period of 1981-2010. The sum of the following five indicators is divided by five in order to express the CEI:

i. The sum of percentage of daily maximum temperatures above 90^{th} percentile and percentage of maximum temperatures below 10^{th} percentile.
ii. The sum of percentage of daily minimum temperatures above 90^{th} percentile and percentage of minimum temperatures below 10^{th} percentile.

iii. The sum of percentage of monthly scPDSI above 90th percentile and percentage of monthly scPDSI below 10th percentile.
iv. The sum of percentage of daily precipitation amount above 90th percentile and percentage of daily precipitation amount below 10th percentile.
v. The sum of percentage of days with precipitation above 90th percentile and percentage of days with precipitation below 10th percentile (percentage of dry days).

We applied calculations with E-OBS 0.25°x0.25° daily maximum and minimum temperature data set (Haylock et al., 2008) using 5-days running mean, Climate Prediction Center (CPC) 0.5°x0.5° gridded daily precipitation observation data (Chen et al., 2008) and Climate Research Unit (CRU) 0.5°x0.5° monthly self-calibrating Palmer Drought Severity Index (scPDSI) data set (Schrier et al., 2013). scPDSI was defined by Wells et al. (2004). Resolution of temperature data set has been reduced to 0.5°x0.5° so as to match with other data set's grid points by using bilinear interpolation.

APPLICATION AND RESULTS

CEI spans from 29% to 43% on account of long-term areal average over Turkey and the least extremes have occurred over the northeast of Turkey which is about 29%. The Marmara Region, the Aegean Region and the south of Turkey have experienced extremes in range of 35%-40% supported by percentage of dry days and moisture surplus. Extremes over the Black Sea Region are more related to extreme precipitation events above 90th percentile which is about 35%. In order to see the variability, decadal anomalies have been calculated based on the period of 1981-2010. CEI variates between 29%-35% from 1979 to 1987. In 1989, CEI made a peak 43% and in 1990-1999 period demonstrates rising signal over the west parts of Turkey.

Between 2000-2009 the southwest of Turkey has experienced extremes ranging from 36% to 40% which is 2%-4% more than normal. After 2010, increase signal reached to 10% over most parts of Turkey but, extreme events took place less than reference over the eastern regions. Trend analysis reveals that there is up to 4% positive decadal trend over the west and the Central Anatolia while decrease tendency over the northeastern parts of Turkey was indicated. Overall, there is 1.33% upward decadal trend over Turkey in point of extreme events.

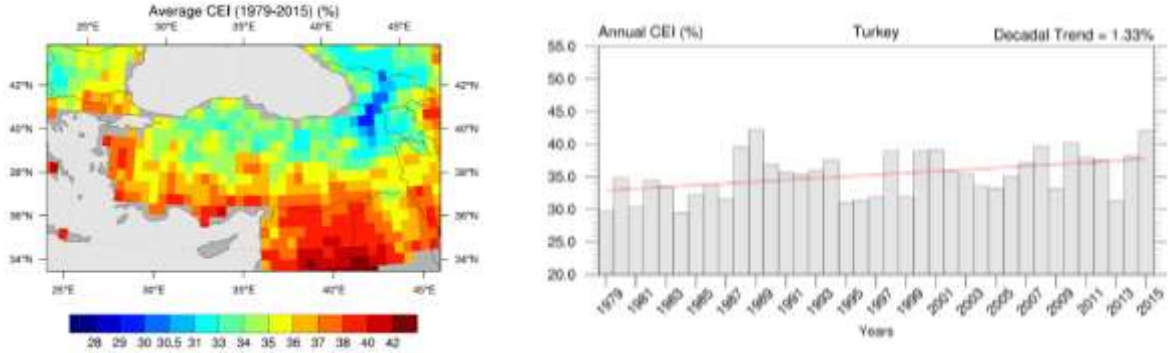

a) **b)**

Figure 1. a) Long-term average of CEI. b) Annual areal average of CEI and decadal trend.

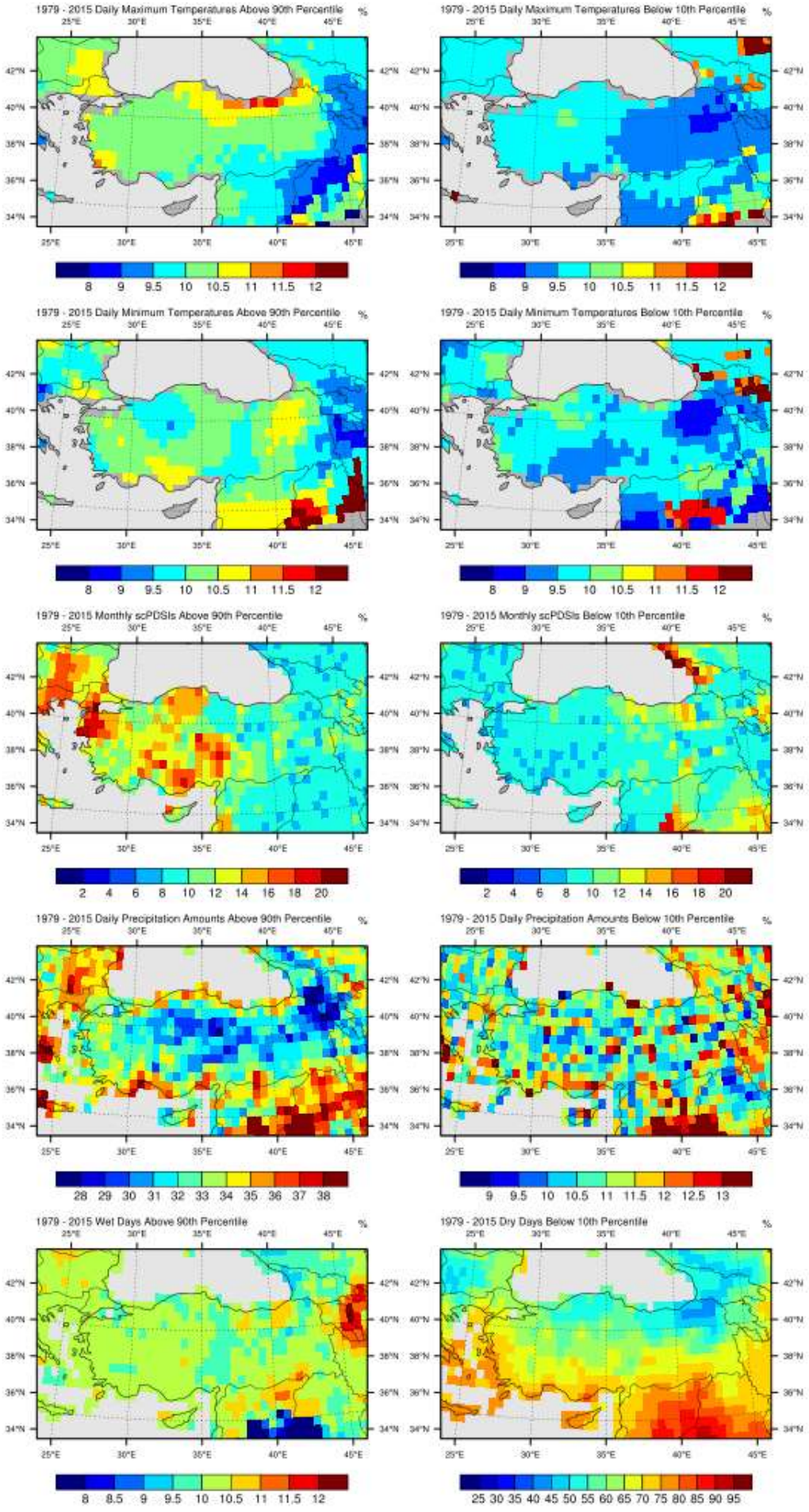

Figure 2. Long-term average of each CEI indicator.

CONCLUSIONS AND RECOMMENDATIONS

CEI is a useful implementation to understand the effects of extreme events on climate change in a single frame. In this study we applied calculations using observations and the results indicate that extreme events are on rise over Turkey. CEI variates between 29%-43% from 1979 to 2015 as the areal average. Greater values have been calculated over the southern and the western parts of Turkey due to percentage of dry days and moisture surplus whereas the CEI was supported by extreme precipitation events over the Black Sea region. The least values have been calculated over the northeast of Turkey. This study could be a good reference for future regional analysis and could be expanded to whole Europe which is still being studied.

REFERENCES

Batıbeniz F., Önol B., Turunçoğlu U. U., 2015: Climate Extremes Index Analysis Based on High Resolution Regional Climate Simulation. European Geosciences Union, April 12-17, 2015 Vienna, Austria.

Chen, M., W. Shi, P. Xie, V. B. S. Silva, V E. Kousky, R. Wayne Higgins, and J. E. Janowiak (2008), Assessing objective techniques for gauge-based analyses of global daily precipitation, J. Geophys. Res., 113, D04110, doi:10.1029/2007JD009132.

Haylock, M.R., N. Hofstra, A.M.G. Klein Tank, E.J. Klok, P.D. Jones and M. New. 2008: A European daily high-resolution gridded dataset of surface temperature and precipitation. J. Geophys. Res (Atmospheres), 113, D20119, doi:10.1029/2008JD10201

Karl, T.R., R.W. Knight, D.R. Easterling, and R.G. Quayle, 1996: Indices of Climate Change for the United States. Bull. Amer. Meteor. Soc., 77, 279–292, https://doi.org/10.1175/1520-0477(1996)077<0279:IOCCFT>2.0.CO;2

Palmer, W. C. (1965) Meteorological Drought, Weather Bureau Research Paper No. 45, U.S. Department of Commerce, Washington, D.C.

van der Schrier G, Barichivich J, Briffa KR and Jones PD (2013) A scPDSI-based global data set of dry and wet spells for 1901-2009. J. Geophys. Res. Atmos. 118, 4025-4048 [10.1002/jgrd.50355).

Wells, N., S. Goddard, and M.J. Hayes, 2004: A Self-Calibrating Palmer Drought Severity Index. J. Climate, 17, 2335–2351, https://doi.org/10.1175/1520-0442(2004)017<2335:ASPDSI>2.0.CO;2

CONSTRUCTION OF PREDICTION INTERVALS FOR PALMER DROUGHT SEVERITY INDEX USING BOOTSTRAP

Ufuk Beyaztas[1], Bugrayhan Bickici Arikan[2,3], Beste Hamiye Beyaztas[1], Ercan Kahya[3]
[1]Department of Statistics, Istanbul Medeniyet University, Istanbul/TURKEY
ufuk.beyaztas@medeniyet.edu.tr, beste.sertdemir@medeniyet.edu.tr
[2]Department of Civil Engineering, Istanbul Medeniyet University, Istanbul/TURKEY
bugrayhan.bickici@medeniyet.edu.tr
[2]Department of Civil Engineering, Istanbul Technical University, Istanbul/TURKEY
kahyae@itu.edu.tr

Abstract
In this study, we propose an approach based on the residual-based bootstrap method to obtain valid prediction intervals using monthly drought observations. The effects of North Atlantic and Arctic Oscillation indexes on the constructed prediction intervals are also examined. Performance of the proposed approach is evaluated for the Palmer Drought Severity Index (PDSI) obtained from Konya closed basin located in Central Anatolia, Turkey. Our results revealed that our proposed approach produces valid prediction intervals for future PDSI values.

Keywords: *Bootstrap, drought, prediction, Konya Closed Basin.*

INTRODUCTION
Drought is a temporary and recurring meteorological event, originating from the lack of precipitation over an extended period of time. Early indication of droughts can provide valuable information to help mitigate some of the consequences of drought. For instance, decision makers may plan and manage the water resource systems. In arid and semi-arid regions, drought has also a negative effect on the crops. Its detrimental effects to the society may reduce by storing sufficient water from available sources. Hence, forecasting the drought duration in the growing season is vital for farmers. It is important to note that the success of drought preparedness and mitigation depends upon timely information on the drought onset and development in time and space. This information may be obtained through continuous drought monitoring, which is normally generated using drought indices.

Over a region, many drought indices have been developed for monitoring and examining of meteorological drought. Among those, the Palmer Drought Severity Index (PDSI), which provides a standardized measurement of moisture conditions to compare between locations and over time, is widely used. It uses readily available temperature and precipitation data to estimate relative dryness, and has been reasonably successful at quantifying long-term drought. As it uses temperature data and a physical water balance model, it can capture the basic effect of global warming on drought through changes in potential evapotranspiration. For these reasons, PDSI is used as a drought indicator in this study. It has been increasing interest to investigate the relation between North Atlantic Oscillation (NAO) and drought in mid-latitude regions; among others, Kahya (2011) and Şarlak et al. (2009) documented such relations for the Eastern Mediterranean and southern part of Turkey. Following this trend, we intended to use NAO index (NAOI) and Arctic Oscillation Index (AOI) as exogenous variables since drought events are assumed to connected to large-scale atmosphere and ocean interactions even in mid-latitude regions. The intensity and spatial extent of droughts are also generally quantified by drought indices.

Drought forecast is an important problem and it has received great attention in the literature. Mishra and Desai (2005), Mishra and Desai (2006), Kim and Valdes (2003) and Morid et al.

(2007) provide an excellent overview of research on drought forecasting. However, those works only consider point forecasts even though prediction intervals provide better inferences taking into account uncertainty in the model. Technically, construction of such prediction intervals requires some distributional assumptions which are generally unknown in practice. Moreover, the constructed prediction intervals along with the estimated parameter values can be affected due to any departure from the assumptions and may lead us to unreliable results. One of the remedy to construct prediction intervals without considering distributional assumptions is to use the well-known resampling methods, e.g., the bootstrap.

DATA AND METHODS

The monthly PDSI data which is consisted a total of 552 observations were obtained starting from January, 1970 and ending on December, 2015. Konya Closed Basin is located between $36^{o}\,51^{'}$ and $39^{o}\,29^{'}$ north latitudes and $31^{o}\,36^{'}$ and $34^{o}\,52^{'}$ east longitudes in Central Anatolia Region of Turkey. Its surface area is roughly 54.000 km^2 and it constitutes approximately 7% of Turkey. The climate indexes data from 1970 to 2015 were obtained from NOAA Earth System Research Laboratory. NAOI is based on the surface sea-level pressure difference between the Subtropical (Azores) High and the Subpolar Low. The Arctic Oscillation (AO) is a large scale mode of climate variability, also referred to as the Northern Hemisphere annular mode.

We checked the stationary status of the PDSI values by applying Ljung-Box (LB) and augmented Dickey-Fuller (ADF) *t*-statistic tests, and small *p*-values (*p*- value = 0.000 for the LB test and *p*-value = 0.010 for the ADF test) suggest that the PDSI series are mean zero stationary processes. The time series plots and ACF-PACF plots suggest that the autoregressive (AR) model could be appropriate to model the PDSI series. To find the optimal lag, we defined many possible subsets of the AR(*p*) models with different *p*-values. To choose the best model, we used Akaike information criterion (AIC) (since it is proposed to determine the best model for forecasting), and the results show that AR(1) model is optimal according to AIC for all the PDSI series.

Let $\chi_n = \{X_1,\dots,X_n\}$ be a sequence of stationary dependent random variables of size n having an unknown common distribution function F, whose parameter $\theta_0 = g(\mu)$ is of our interest, where $g: R^d \to R$ is a smooth function. We further assume that the distribution has a finite mean and a finite variance σ^2, both unknown. Let $\hat{\theta}_n = g(\bar{X}_n)$, $\bar{X}_n = n^{-1}\sum X_i$, be the estimator of θ_0 based on χ_n. Then the bootstrap estimator of $\hat{\theta}_n$ is obtained by $\hat{\theta}_n^{*} = g(\bar{X}_n^{*})$, where $\bar{X}_n^{*} = n^{-1}\sum X_i^{*}$ is calculated from the bootstrap sample $\chi_n^{*} = \{X_1^{*},\dots,X_n^{*}\}$.

The autoregressive model of order 1 is defined by $X_t = \varphi_0 + \varphi_1 X_{t-1} + \varepsilon_t$, $t = 1,\dots,n.$ where ε_t is a sequence of i.i.d. random variables with zero mean and unit variance and φ_0 and φ_1 are the model parameters. We use the oscillation indexes mentioned as predictors in the AR model to see their effects on the constructed prediction intervals for future observations. To this end, we use the following autoregressive with exogenous terms (ARX(1)) model: $X_t = \varphi_0 + \varphi_1 X_{t-1} + \gamma^{\iota} F_{t-1} + \varepsilon_t$, $t = 1,\dots,n.$ where F_{t-1} represents an *v* times *u* vector of exogenous variables.

Let$h = 1,\dots,s$, $s \geq 1$ be defined as the lead time. Then, the complete algorithm used in this study to construct prediction interval for AR(1) model is as follows.

Step 1. Obtain the least squares estimators $\hat{\theta}_n$.

Step 2. Calculate the fitted residuals as $\hat{\varepsilon}_t = x_t - \hat{x}_t$where $\hat{x}_t = \hat{\phi}_0 + \hat{\phi}_1 x_{t-1}$ for $t = 2, \dots, n$.

Step 3. Center the fitted residuals as $r_t = \hat{\varepsilon}_t - \hat{\bar{\varepsilon}}$ for $t = 2, \ldots, n$, where $\hat{\bar{\varepsilon}}$ is the mean of the fitted residuals. Let $\hat{F}_n$ represents the empirical distribution function of r_t.
Step 4. Construct bootstrap residuals $\{\varepsilon_t\}_{t\geq 1}$ i.i.d. with replacement from $\hat{F}_n$.
Step 5. Calculate the bootstrap observations, x_t , as follows,

$$x_t = \phi_0 + \phi_1 x_{t-1} + \varepsilon_t \ , t = 2, \ldots, n$$

where x_1 is chosen at random from *y*. In practice, to ensure stationary of the generated bootstrap series, *n+m* bootstrap observations are generated for some large positive *m* and the first *m* observations are discarded.
Step 6. Compute the LS estimators of AR(1) coefficients based on the bootstrapped data obtained in Step 5., ϕ_0 and ϕ_1 .
Step 7. Obtain the future bootstrap predicted values by using recursion formula given below,

$$\hat{x}_{n+1} = \phi_0 + \phi_1 \hat{x}_{n+t-1}, t = 1, \ldots, h$$

where $\hat{x}_{n+t-1} = x_{n+t-1}$ when $t \leq 1$.
Step 8. Generate the future bootstrap observations as follows,

$$x_{n+t} = \phi_0 + \phi_1 x_{n+t-1} + \varepsilon_{n+t}, t = 1, \ldots, h$$

where $x_{n+t-1} = x_{n+t-1}$ when $t \leq 1$.
Step 9. Calculate the bootstrap root-replicate $x_{n+h} - \hat{x}_{n+h}$.
Step 10. Repeat Steps 4-9 *B* times, where *B* denotes the number of bootstrap simulation, for each *h*. Let αrepresents the αth quantile of the constructed distribution of the bootstrap root-replicates.
Then the 100(1-α)\% bootstrap prediction interval for x_{n+h} is calculated as follows.

$$[\hat{x}_{n+h} + q(\alpha/2), \hat{x}_{n+h} + q(1-\alpha/2)]$$

where $\hat{x}_{n+h} = \phi_0 + \phi_1 x_{n+t-1}$ for $t = 1, \ldots, h$ and $\hat{x}_{n+t-1} = x_{n+t-1}$ when $t \leq 1$.

APPLICATION AND RESULTS

To obtain out-of-sample prediction intervals for the real data we divide the full data into the following two parts: the model is constructed based on the observations from January, 1970 to December, 2013 (528 observations in total) to calculate 24 steps ahead (monthly), 8 steps ahead (short-term) and 4 steps ahead (mid-term) predictions, from January, 2014 to December, 2015, and compare with the actual values. For each series, *B* = 1000 bootstrap simulations were performed, and we set the significance level to 0.05 to obtain 95% bootstrap prediction intervals for future PDSI values.

The constructed prediction intervals for monthly drought (PDSI) observations, together with the true values, are presented in fig. 1. Our findings show that the bootstrap method with AR(1) and ARX(1) models provides reasonable prediction intervals for future PDSI values. It is clear that the bootstrap method produces narrower prediction intervals for short-term forecasts compared to prediction intervals constructed for long-term forecasts. This is because long-term forecasts are more uncertain. It is clear from our results that, the effects of the oscillation indexes on the constructed prediction intervals are not statistically significant, which means that the AO and NAO indexes do not play an important role for the PDSI values in Konya basin.

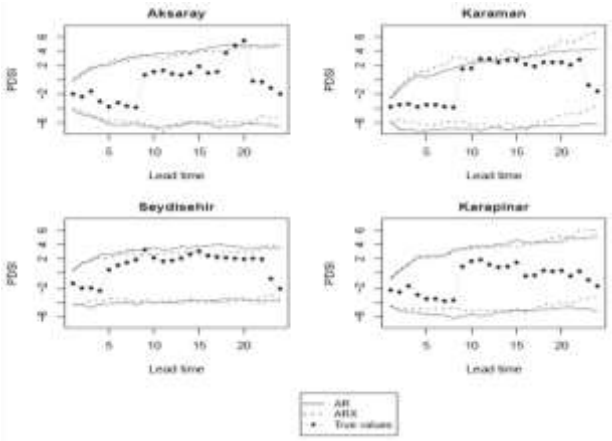

Figure 1. 95% prediction intervals for future monthly PDSI values from January, 2014 to December, 2015

CONCLUSIONS AND RECOMMENDATIONS

In this study, we propose to use the residual-bootstrap method to construct prediction intervals for future PDSI based drought observations under autoregressive time series model. Also, we analyze the effects of North Atlantic Oscillation and Arctic Oscillation indexes on the constructed prediction intervals. Our findings show that: (*i*) the bootstrap method produces valid prediction intervals for future PDSI values. The interval lengths are considerably narrower for short-term forecast than the one obtained for long term forecasts. Hence, consideration of short-term forecasts such as three months may be more useful for future plans. (*ii*) The oscillation indexes considered in this paper have a valuable but slight effect on the prediction intervals. But, the bootstrap method with oscillation indexes may produce considerably better prediction intervals for the areas where the oscillation indexes have significant effects such as Spain and Portugal. As a future research, the performances of the bootstrap methods can also be studied for other drought indices, or it can also be used in other meteorological-hydrological areas where the prediction is important. Finally, it should be noted that all the calculations in this study are performed under the assumption that the considered model forms are correct.

ACKNOWLEDGEMENTS

The second author would like to thank TUBITAK (Scientific and Technological Research Council of Turkey) for financial support. The authors acknowledge MGM (Turkish State Meteorological Service) authorities for providing data.

REFERENCES

Kahya, E, 2011: *Impacts of the NAO on the Hydrology of the Eastern Mediterranean* in "Hydrological, Socioeconomic and Ecological Impacts of the North Atlantic Oscillation in the Mediterranean Region", Eds: S. M. Vicente-Serrano and R. M. Trigo. Advances in Global Change Research, Vol. 46, p 57-71, Springer. 1st Edition., 2011, VIII, 236 p., DOI: 10.1007/978-94-007-1372-7.

Kim T, Valdes J. (2003). Nonlinear model for drought forecasting based on a conjuction of wavelet transforms and neural networks. *Journal of Hydrologic Engineering*, 8, 319-328.

Mishra A, Desai V. (2005). Drought forecasting using stochastic models. *Stochastic Environmental Research and Risk Assessment*, 19, 326-339.

Mishra A, Desai V. (2006). Drought forecasting using feed forward recursive neural network. *Ecological Modelling*, 198, 127-138.

Morid S, Smakhtin V, Bagherzadeh K. (2007). Drought forecasting using artificial neural networks and time series of drought indices. *International Journal of Climatology*. 27, 2103-2111.

Şarlak, N., E. Kahya and A.O. Bég, 2009: Critical Drought Analysis: A Case Study of Göksu River (Turkey) and North Atlantic Oscillation Influences. *Journal of Hydrologic Engineering*, Vol. 14, No 8, 795-802, DOI:10.1061/(ASCE)HE.1943-5584.0000052.

IMPACTS OF CLIMATE NONSTATIONARITIES ON HYDROCLIMATOLOGICAL EXTREMES IN TURKEY

Rizwan Aziz, Ismail Yucel
Civil Eng. Middle East Technical University, Ankara
rizwan.aziz@metu.edu.tr, iyucel@metu.edu.tr

Abstract
The study aims to assess the impacts of hydroclimatological nonstationarities on return periods/return levels of hydroclimatological extremes. The study comprises of two parts. The impact of nonstationarites on hydroclimatological variables 1) - considering the historical data and 2) - considering the RCMs projected data. Initially Mann Kendall trend test was used to detect any trend in the observed data on seasonal basis. Four probability distributions (Generalized Extreme Value, Gumbel, lognormal and normal distribution) were used with and without nonstationarity considerations to analyze the difference between stationary and nonstationary return levels for observed data. After that, bias corrected CORDEX RCM simulation data is used for similar stationary and nonstationary return level estimations for future time periods.

Keywords: *Hydroclimatological Extremes, nonstationarity, CORDEX, Trends*

INTRODUCTION

Presence of climate change and land use conditions may change the probabilities of hydrological extreme events, which further means that the parameters (of location, shape and scale) of underlying distributions may change with the passage of time and assumption of stationarity becomes invalid. Kartz and Brown (1992) studied hydrological extreme events under changing climate and concluded that climate change can have an effect on location and scale parameters, which in result can change the tail distribution. This change can a)-increase extreme events, b)-decrease extreme events or c) - randomly shift the extreme events. These changes in hydrological extreme events, like floods and droughts can be a matter of big concern for the decision makers. So the literature suggested using such flood frequency analysis where the distribution parameters change with time. Salas and Obeysekera (2014) summarised that these methods can be a) - probability distribution having trend component, b)- probabilistic models with considerations of pattern shifting, c)- using covariates and d)- use of probability distributions with mixed components.

In a recent study, it was found that there are significant increases in temperature with an average of 1.3°C across the stations over eastern Anatolia of Turkey (Yucel et al. 2015). They also found increases in total annual precipitation of average 7.5 % across stations. Şen (2013) presented a holistic view of climate change in Turkey and its impacts. By taking into consideration the results and recommendations of previous studies for Turkey, the hydroclimatological variables can no more considered as stationary. The probabilities of extremes are changing. So it is very important to incorporate this non-stationarity in decision making process, like estimation of return levels for given return periods etc

DATA AND METHODS

The data used in this study includes minimum, maximum temperatures and daily precipitation for 77 metrological stations throughout Turkey. In addition to the observed data, the climate data from 10 CORDEX GCM-RCM (http://www.euro-cordex.net/) combinations is used to

analyse the nonstationarities for future time period. The CORDEX GCM-RCM combinationas used are given in table 1.

Table 1. CORDEX GCM-RCM combinationas use

GIVEN NAME	GCM	RCM
MODEL1	CNRM-CERFACS-CNRM-CM5	CLMcom-CCLM4
MODEL2	CNRM-CERFACS-CNRM-CM5	CNRM-ALADIN53
MODEL3	CNRM-CERFACS-CNRM-CM5	SMHI-RCA4
MODEL4	ICHEC-EC-EARTH	KNMI-RACMO22E
MODEL5	ICHEC-EC-EARTH	DMI-HIRHAM5
MODEL6	ICHEC-EC-EARTH	CLMcom-CCLM4
MODEL7	IPSL-IPSL-CM5A-MR	IPSL-INERIS-WRF331F
MODEL8	IPSL-IPSL-CM5A-MR	SMHI-RCA4
MODEL9	MOHC-HadGEM2-ES	KNMI-RACMO22E
MODEL10	MOHC-HadGEM2-ES	SMHI-RCA4

Trend Analysis

Before studying the potential impacts on non-stationarities, it is good idea to detect the significance of trends in data. Mann-Kendall trend test is used for minimum and maximum temperature extremes for winter and summer season to find any trend significancy throughout Turkey.

Stationary and nonstationary frequency distributions

Four stationary and nonstationary distributions (GEV, Gumbel, lognormal and normal) are used in this study. Katz, 2013 formulated the GEV distribution under nonstationary condition

$$\text{as, } F(z,\theta_t) = exp\left\{-\left[1+\varepsilon\left(\frac{z-\mu_t}{\sigma_t}\right)\right]^{\frac{-1}{\varepsilon}}\right\}$$

In the above equation, θ_t represents time-varying set of parameters which includes location (μ_t), scale (σ_t) and shape (ε) parameters. When ε approaches to zero, the above expression reduce to Gumbel extreme value distribution and are given as,

$$F(z,\theta_t) = exp\left[-exp\left(-\frac{z-\mu_t}{\sigma_t}\right)\right]$$

In addition, following the similar procedure normal and lognormal distributions are also included in this study. The parameters are estimated by using maximum likelihood method. Akaike and Bayesian information criterion Model selection criterion are used for model selection. The best selected model is used in estimation of return values for different return periods.

APPLICATION AND RESULTS

After getting CORDEX RCM data and performance evaluation the bias correction is done for both temperature and precipitation data. For temperature data, mean and variance correction method is used as described in Chen et al. 2011. For precipitation data, Empirical Quantile Mapping method was used. The results of the bias correction shows great improvement in RCM data.

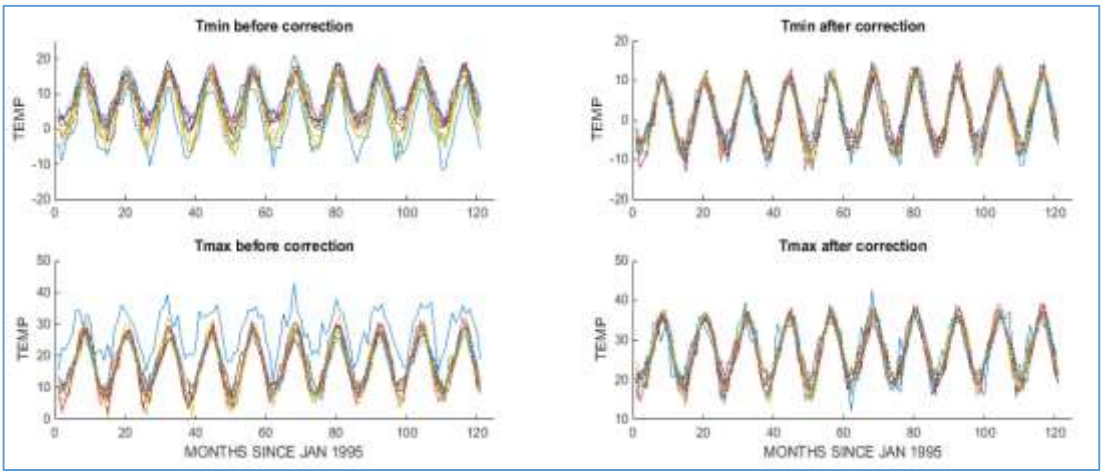

Figure.1 Observed vs RCM simulation data of Bartin station for Tmin and Tmax before and after bias correction (blue lines represents the oberved while colored are for different RCMs

The trend test results shows increase in temperatures for all seasons throughout stations with few exceptions giving the signs of the presence of nonstationarities. The positives trends are found to be more evident for daily average temperatures for summer seasons. For precipitation the trends both increasing and decreasing trends were found. After estimating the parameters of stationary and selected nonstationary distribution**,** the 100-year return levels are estimated for temperature and precipitation extremes for all seasons for observed and RCM projected data.

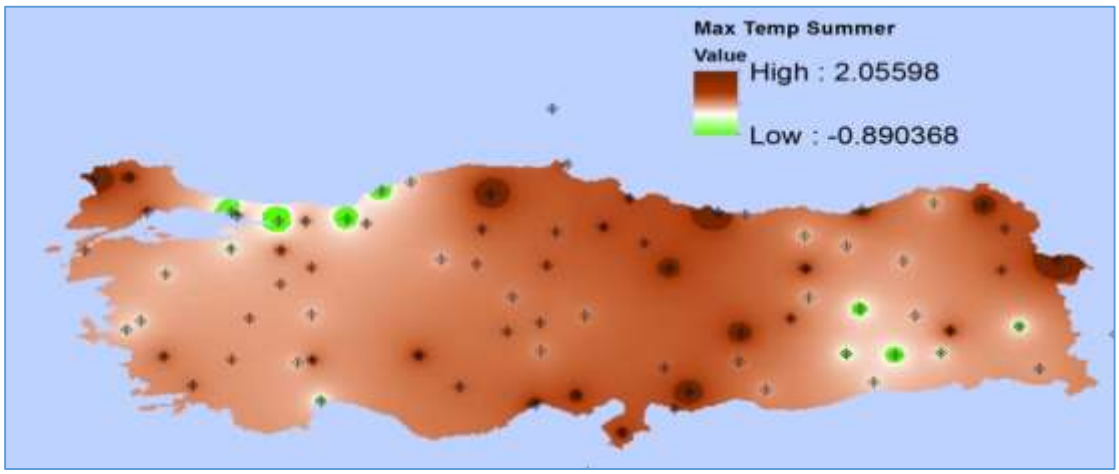

Figure 2 Difference between 100-year stationary and nonstationary return levels for seasonal maxima of daily temperature in summer.

The above given map of the different between 100-year stationary and nonstationary return level for temperature extremes shows that in most part of Turkey the summer maximum temperatures are going to be more extreme especially in central part of Turkey. Same was the case with the maximum tempratures in winter season so the winter extremes are going to be smaller in magnitude. Similar results for precipitation shows that 100-year daily precipitation are going to be decreased while considering the nonstationarity.

CONCLUSIONS AND RECOMMENDATIONS

The results conclude the evident presence of non-stationarities in hydroclimatological variables in Turkey. The changing behaviour of hydroclimatological extremes especially in winter can

alter the snow fall pattern and so snow melt runoff. One of the major recommendations based on this research is to consider these non-stationarities in hydroclimatological variables in the process of planning and designing of water resources.

REFERENCES

Chen, J., Brissette, F. P., and Leconte, R.: Uncertainty of downscaling method in quantifying the impact of climate change on hydrology, J. Hydrol., 401, 190–202, doi:10.1016/j.jhydrol.2011.02.020, 2011.

Kartz R.W., and B.G. Brown (1992), Extreme events in changing climate:variability is more important than averages, Clim. Change, 21(3), 289-302

Ömer Lütfi Şen. "A Holistic View Of Climate Change and Its Impacts in Turkey" Istanbul Policy Center 2013

Salas, J.D., Obeysekera, J., 2014. Revisiting the concepts of return period and risk for non-stationary hydrologic extreme events. J. Hydrol. Eng. 19, 554–568. http:// dx.doi.org/10.1061/(ASCE)HE.1943-5584.0000820.

Yucel, I., Güventürk, A. and Sen, O. L. (2015), Climate change impacts on snowmelt runoff for mountainous transboundary basins in eastern Turkey. Int. J. Climatol., 35: 215–228. doi:10.1002/joc.3974

TREND ANALYSIS OF EXTREME TEMPERATURE INDICES FOR MARMARA REGION OF TURKEY

Hüseyin Toros[1], Mohsen Abbasnia[2]

[1-] Department of Meteorology, Istanbul Technical University, Maslak Istanbul 34469, Turkey. Toros@itu.edu.tr

[2-] Postdoctoral Researcher, Department of Meteorology, Istanbul Technical University, Maslak Istanbul 34469, Turkey. Abbasnia@itu.edu.tr

Abstract

Impacts of extreme weather events are relevant for regional economies and in particular societies. In this study, Fifteen extreme temperature indices are selected and analyzed from the recommended list of the expert group CCL/CLIVAR and for the period of 1961 to 2016 which characterizing a long-term period and with high-quality data. The software used to process the data was the RClimdex 1.1. The trend results at 5% significant level showed that warm spell duration, numbers of summer days, tropical nights, warm nights and warm days have increased, while cold spell duration, ice days, frost days, cool nights and cool days decreased all over Marmara. Summer days have increased on average between 4 to 5 days per decades, While, ice days have decreased on average about 1 day during the whole studied period. Maximum of maximum, minimum of maximum, maximum of minimum and minimum of minimum temperatures have had a positive trend at station scales. Also, diurnal temperature range has slightly increased in most stations, except two southern stations, over the study area. Thus, a large number of stations show significant warming trends for warm days and nights throughout the study area, whereas warm extremes and night-time based temperature indices show greater trends than cold extremes and day-time indices. Overall, the warm extreme temperature events have increased in Marmara during the last decades and it is expected to pronounce by the potential of constant moisture in the Marmara's atmosphere. This is regionally evidencing the importance of the ongoing research on climate change.

Keywords: *Extreme events, climate monitoring, temperature extremes, warming trend, Marmara-Turkey*

Introduction

Global warming is a real fact. Temperature is the most important issue of climate change and extreme temperatures affect our lives the most. Many researchers found warming trends in surface temperature over the world, but the magnitude of changes is not uniform (e.g., Jones and Moberg 2003; Solomon et al. 2007; Kerr 2009; Abbasnia et al. 2016). Recently, global average temperature has shown a 0.85 °C increase over the last century (IPCC, 2013). Temperature fluctuation has both natural and anthropogenic origins, but the IPCC has concluded that most of the observed warming in global average surface temperature that has occurred since the mid-twentieth century is very likely a result of human activities (IPCC, 2007). A small change in the mean condition can cause a large change in the likelihood of an extreme. Any change in the frequency or severity of extreme climate events could have profound impacts on nature and society. There has been a clear tendency towards an increase in extreme temperatures in global land areas. There are numerous regional and national studies of recent trends and variability in monthly climate globally (e.g., Fauchereau et al., 2003; Hulme et al., 2001; Zhang et al., 2005; New et al., 2006; Caloiero, T. 2017; Toros et al., 2012). In this case, the analyses conducted by different researchers in different countries may not seamlessly merge together to form a global map because the analyses might have been conducted on different indices (e.g., Bonsal et al., 2001) and/or using different methods. To address this issue, the WMO expert team on climate change has, therefore, defined several

indices for climate change analysis. The Intergovernmental Panel on Climate Change (IPCC), Working Group on Climate Change Detection together with the Joint World Meteorological Commission for Climatology/World Climate Research Program (WCPRP) project on Climate Variability and Predictability (CLIVAR) has helped to bridge this gap by way of developing climate indices that describe climate change in more profound dimensions (New et al., 2006). All of these indices are created with a specific purpose for measuring and monitoring climate variability and change. Turkey has warmed up during the last 25 years, and warming is more concentrated in maximum than in minimum temperatures. There has been a strong warming in the warm period compared to the temperatures of the annual and cold period (Toros, 2012). In this regard, in turkey, many attempts have been made by some researchers to analyze trend of temperature parameters throughout Turkey area **(**e.g., Tayanç et al., 1997; Karabulut et al., 2008; Dogan et al., 2015; Acar-Deniz and Gönençgil, 2015**),** while, these studies are not much enough to assess the temperature extremes changes over variety topography in regional and local scales. In a recent research that has conducted by SENSOY et al (2013) to analysis trend of climatic indices, the results showed that numbers of summer days, warm days, warm nights and tropical nights have been increasing, while, frost days, cool days and cool nights have been decreasing in Turkey from 1960 to 2010.

These climate-related events have the potential to affect the country's national development plans, and retard the strategies for the Sustainable Development Goals (SDGs). Thus, temperature-related disasters should be carefully investigated since many of the historical, industrial, and commercial structures are situated near the coastal areas of Marmara region (GoK, 2007). These can cause excessive damage as a consequence of their vulnerability against such forces and may, in turn, cause not just loss of life, but also the loss of property resulting in a negative economic effect on the region and even the country. The objective of this study, therefore, is to detect extreme temperature events and then subsequently monitor and analyses its occurrence from observed temperature for seven meteorological stations of the Marmara region in north-western of Turkey during a long period of 1961-2016. The information on these trends is critical for decision-making with regard to water resources, human health, agriculture sectors, and practice.

Study area

Marmara region (Fig. 1) on a total area of 67.306 square kilometers is located in the most industrialized part of Turkey with the highest population density (Özhan, 2004). There aren't many altitudes in Marmara region so low altitude valleys and plateaus occupy a great percentage of the area. The Marmara region has a hybrid Mediterranean climate/humid subtropical climate on the Aegean Sea coast and the south Marmara Sea coast, an oceanic climate on the Black Sea coast and a humid continental climate in the interior. Summers are warm to hot, humid and moderately dry whereas winters are cold and wet and sometimes snowy. The coastal climate keeps the temperatures relatively mild. Average annual precipitation in the region ranges between 440 and 800 mm. Among the all seven geographical regions of Turkey, the Marmara region has the second-smallest area, yet the largest population; it is the most densely populated region in the country (Ref. Wikipedia website). Also, Because of its geographical location to Europe, ports on the Black Sea and the Aegean Sea, and many other advantageous factors make this region heavily advanced in the industry, commerce, tourism, and transportation.

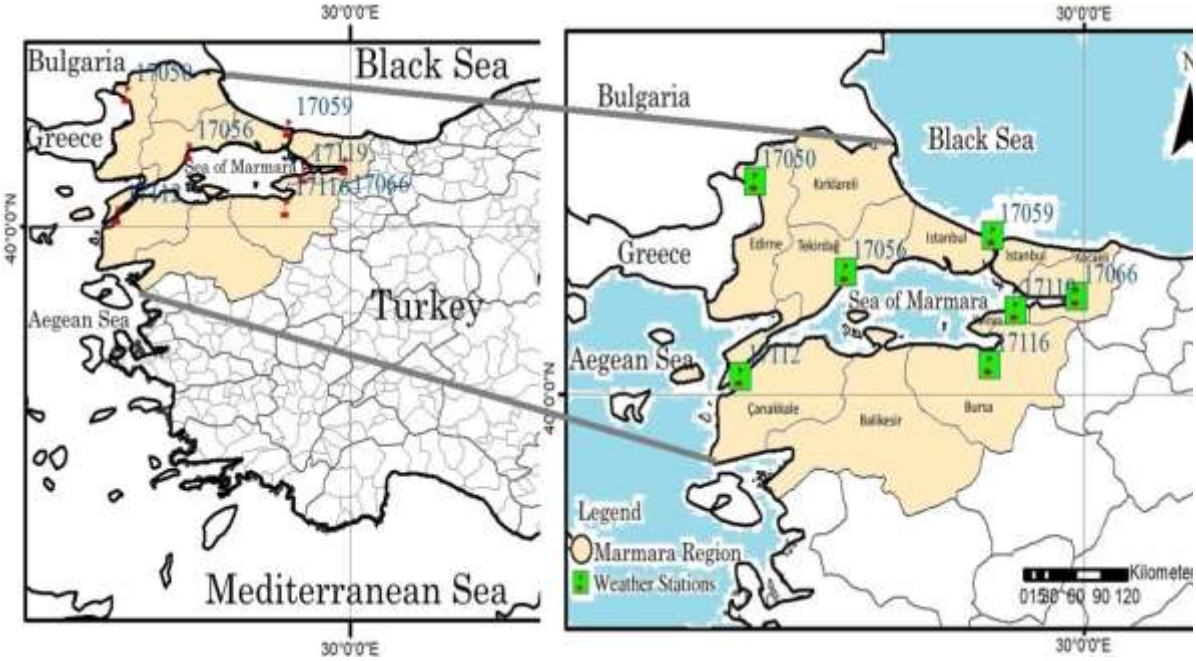

Figure 1. Map of Marmara region and distribution of the study stations

Data and Methodology

In this study, long-term daily average, maximum and minimum temperature data were taken from 7 meteorological stations across the Marmara (see Fig. 1) for the same period of 1961 to 2016. Data time series were analyzed to obtain the climatic extremes indices using the RClimDex software developed by Zhang and Yang (2004) at the Canadian Meteorological Service that software, documentation and RClimDex software and users guide are available for download from http://cccma.seos.uvic.ca/ETCCDMI. The RClimDex software provides 27 indices in total including temperature and precipitation indices. In Tables 1, we provide only summary information about 15 extreme temperature indices which were chosen for discussion here. The RClimDex software has an inbuilt system of checking data quality through: replaces all missing values into internal software's format of -99.9, automated checking for erroneous data, automated searches for outliers, where thresholds are defined by the user in terms of standard deviations from the long-term, data plot outputs enabling visual inspection of the time series. After the first step for quality control of the data, RClimDex had run to calculate climate indices from the daily data. Finally, the resulting series were analyzed through trends. The slopes of the annual trends and their statistical significance to climate indices were calculated based on non-parametric Mann–Kendall test and least square method in order to detect trends assuming a 95% confidence level within the time series.

Table 1. List of the 15 climate indices of ETCCDMI

ID	Indicator name	Definitions	Unit
FD0	Frost days	Annual count when TN(daily minimum)<0ºC	Days
SU25	Summer days	Annual count when TX(daily maximum)>25ºC	Days
ID0	Ice days	Annual count when TX(daily maximum)<0ºC	Days
TR20	Tropical nights	Annual count when TN(daily minimum)>20ºC	Days
TXx	Max Tmax	Monthly maximum value of daily maximum temp	ºC

TNx	Max Tmin	Monthly maximum value of daily minimum temp	ºC
TXn	Min Tmax	Monthly minimum value of daily maximum temp	ºC
TNn	Min Tmin	Monthly minimum value of daily minimum temp	ºC
TN10p	Cool nights	Percentage of days when TN<10th percentile	Days
TX10p	Cool days	Percentage of days when TX<10th percentile	Days
TN90p	Warm nights	Percentage of days when TN>90th percentile	Days
TX90p	Warm days	Percentage of days when TX>90th percentile	Days
WSDI	Warm spell duration indicator	Annual count of days with at least 6 consecutive days when TX>90th percentile	Days
CSDI	Cold spell duration indicator	Annual count of days with at least 6 consecutive days when TN<10th percentile	Days
DTR	Diurnal temperature range	Monthly mean difference between TX and TN	ºC

Results and Discussions

Analyzed temperature trends indicated that the frequency and intensity of warm temperature extremes have continued to increase in Marmara from 1961 to 2016. While the frequency and intensity of cold temperature extremes have continued to decrease in Marmara from 1961 to 2016. This trend is statistically significant at 95% level of confidence because of P-Value is less than 0.05. In this regard, analysis of extreme temperature trend of all stations revealed that the days are warmer as indicated by the index "summer days". The examples provided for Kumköy (ID; 17059) and Yalova (ID; 17119) stations clearly show the most positive trends of the count of "summer days" when the temperature exceeds 25˚C at 5% significant level. Numbers of "summer days" or "hot days" have been increasing all over the study area especially metropolitan area stations have greatest trends. Kendall's tau-based estimated trend indicates increasing from 4 to 50 days/56 years. The average increase is 25 days in 56 years or 4.5 days per decades (Fig. 2). In other hand, numbers of "frost days" have slightly decreased in Marmara region. All stations have had the negative trend, except the station of Bursa (ID; 17116) where is located in the southeastern inland portions of the study area has had a positive trend (Fig. 13). Numbers of "tropical nights" have been increasing for all stations; especially southern coastal stations such as Çanakkale (ID; 17112) and Tekirdag (ID; 17056) have greatest trends (Fig. 3). A decreasing trend in the frequency of "cool nights" was also revealed as depicted in the examples provided for Çanakkale (ID; 17112) and Bursa (ID; 17116) stations at 5% level of significance (Fig. 8). For the index of "Cold days" or "Ice days", all stations show statistically significant decreasing trends from 0.1 to 15 days during the whole studied period. In this regard, the southern coastal station of Çanakkale (ID; 17112) has had the lowest negative trend during the whole studied period (Fig. 12).

Analysis of the percentage of days when the maximum temperature is less than 10th percentiles (TX10p) during the whole studied period of the 1961–2016 indicated that the number of "cool days" has decreased in all station. The regionally averaged linear trends for two stations of Yalova (ID; 17119) and Kumköy (ID; 17059) by the greatest decreasing trends are 2.1 and1.7 days per decade, respectively (Fig. 11). However, for "warm days", an increasing trend was revealed throughout the study area and the highest positive trend has happened for the stations of Kumköy (ID; 17059) and Tekirdag (ID; 17056) at 5% significant level (Fig. 10). Significant increasing trends are in Istanbul city as well as inland portions of Marmara. Significant trends

at 5% significance level are displayed for the hottest day over the inland and southern part of Marmara. This means that inland and metropolitan area stations have mostly influenced extreme warm days. In the case of "warm nights", a broad increasing trend at 5% level of significance was evident in all station of the study area especially for two stations of Yalova (ID; 17119) and Çanakkale (ID; 17112) during whole studied period (Fig. 9). Approximately, there is a broad increasing trend in the annual count of "warm spell duration index", especially for the northwestern coastal station of Edirne (ID; 17050) at 5% significant level (Fig. 14). The increasing trend in the warm spell duration index is a good indicator of the persistence of the warm conditions in the region. In other hand, decreases in the number of "cold spell duration index" are spatially consistent (Fig. 15). In this case, all of the stations show statistically significant negative trends. The stations characterized by greatest decreasing trend are mostly located in southern part of the Sea of Marmara. The trend analysis of "diurnal temperature range index" indicated that the general tendency in most stations of study area is negligible or even slight increasing, but for two stations of Çanakkale (ID; 17112) and Bursa (ID; 17116) which have negative trend in the frequency of "cool nights", there is also a decreasing trend in the monthly mean difference between maximum and minimum temperature at 5% significant level. (Fig. 16). These results of "DTR" are in agreement with the results obtained for "TXx", "TXn", "TNx" and "TNn" indices. Most of the stations show significant positive trends at the 95% level for all the indices of "TXx", "TXn", "TNx" and "TNn". The averages of anomalies for annual maximum and minimum values of daily maximum temperatures (referred to as "TXx" and "TXn" respectively) are have shown upward but weak trends during the whole period of 1961–2016 (Fig 4 and 5). The long-term changes in the annual maximum and minimum values of daily minimum temperatures (referred to as "TNx" and "TNn" respectively) are similar to those of TXx and TXn, but the positive trends are stronger (Fig. 6 and 7).

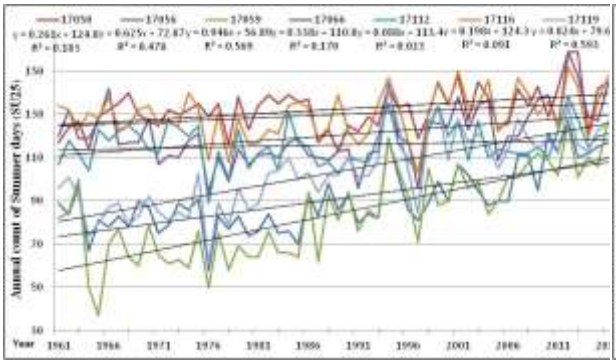

Figure 2. trend in Summer days index

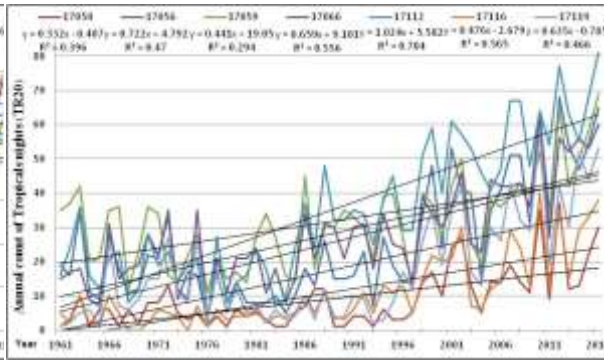

Figure 3. trend in Tropical nights index

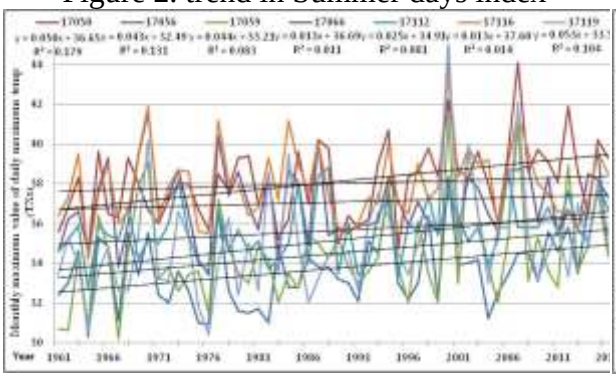

Figure 4. trend in Max-Tmax index

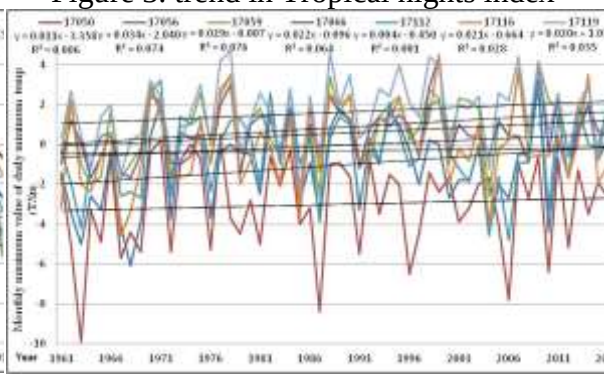

Figure 5. trend in Min-Tmax index

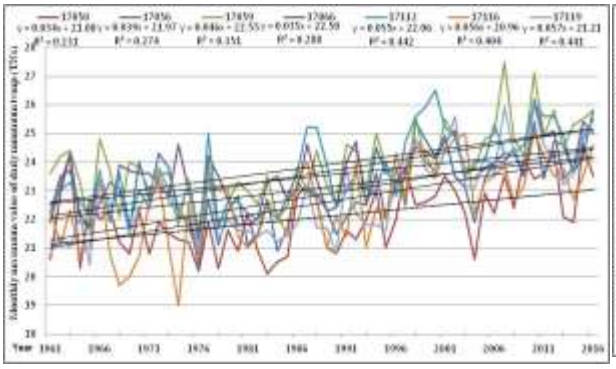

Figure 6. trend in Max-Tmin index

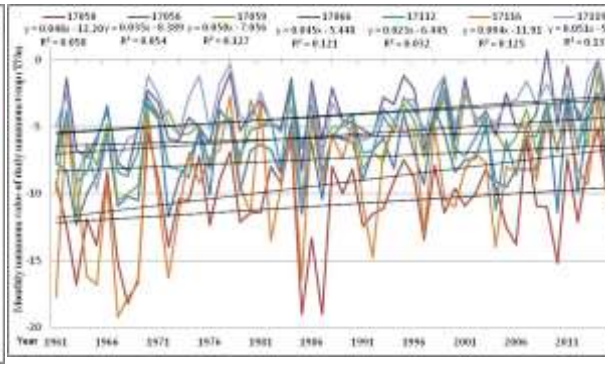

Figure 7. trend in Min-Tmin index

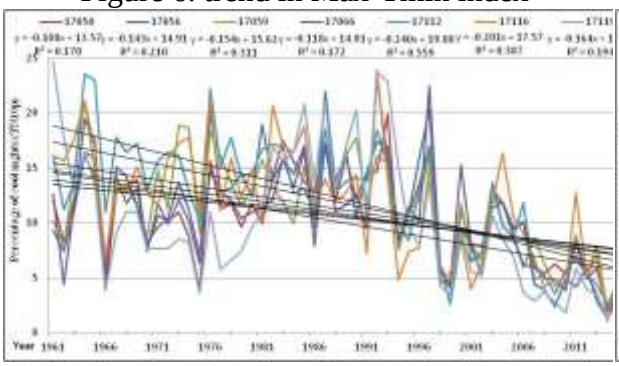

Figure 8. trend in Cool nights index

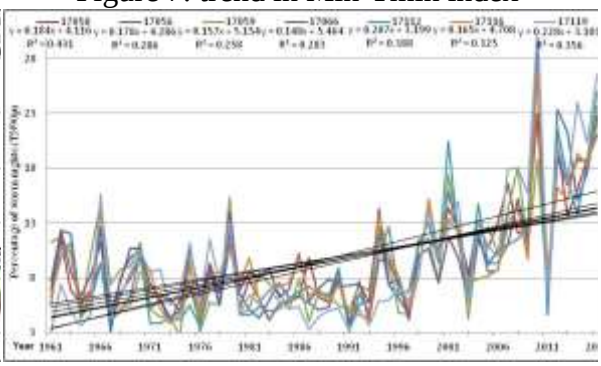

Figure 9. trend in Warm nights index

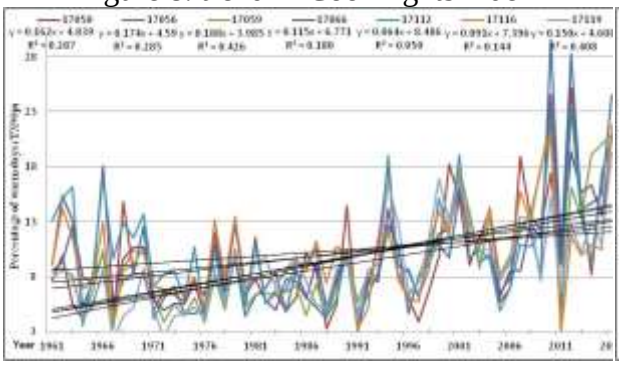

Figure 10. trend in Warm days index

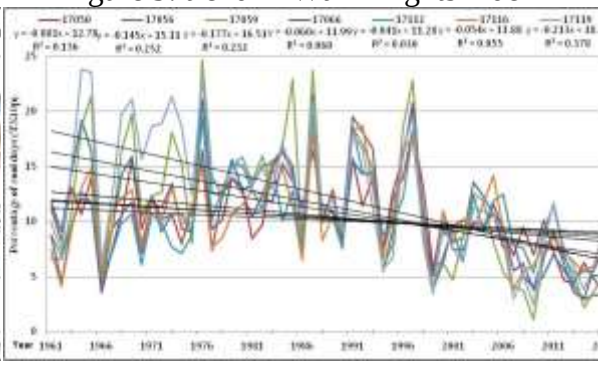

Figure 11. trend in Cool days index

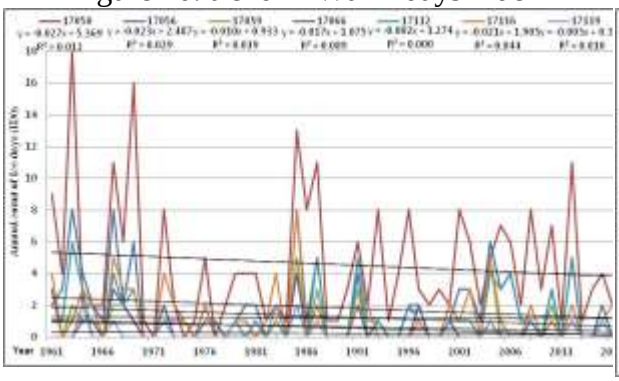

Figure 12. trend in Ice days index

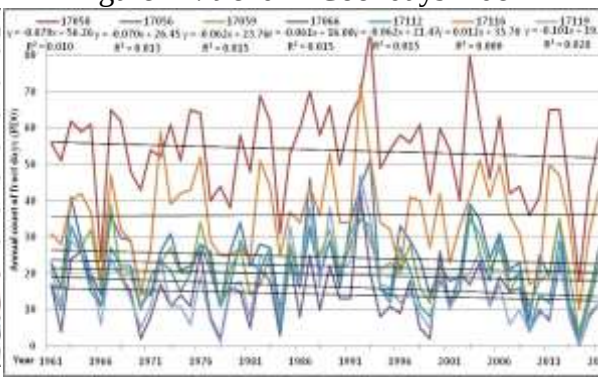

Figure 13. trend in Frost days index

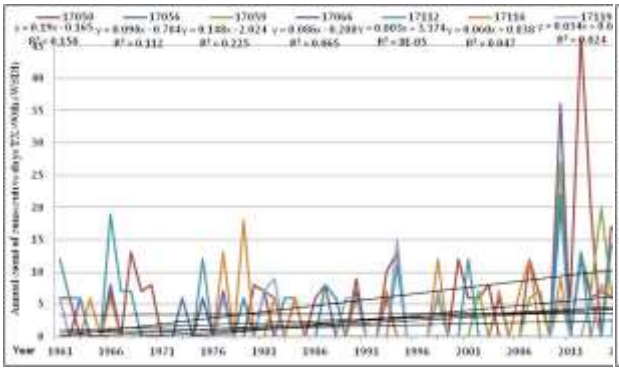

Figure 14. trend in Warm spell duration index

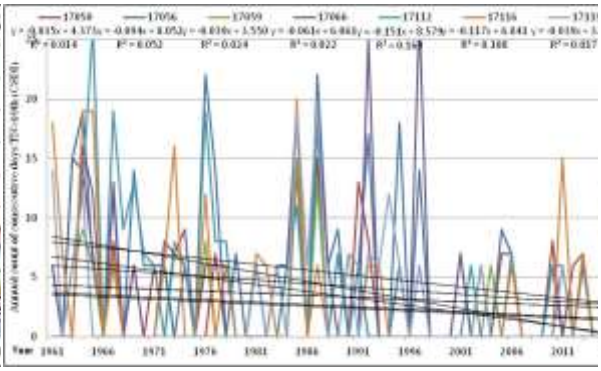

Figure 15. trend in Cold spell duration index

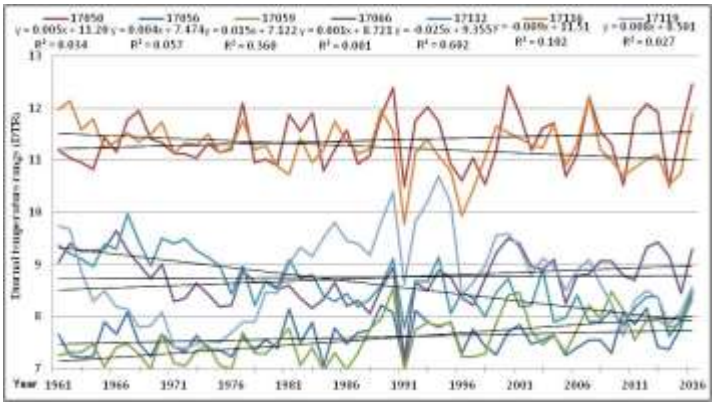

Figure 16. trend in Diurnal temperature range index

Conclusion

The risks associated with extreme weather/climate events have a great impact on the socio-economic activities in anywhere. This study presents analyses of the trends in fifteen annual extreme indices of air temperature over Marmara, Turkey. The trend results of these indices over 7 meteorological stations for a period between 1961 and 2016 showed that widespread changes in temperature extremes associated with warming warm and hot events. The results also showed numbers of summer days, tropical nights, warm nights, warm days and warm spell duration have increased all over the study area while ice days, frost days, cool nights, cool days and cold spell duration have decreased at 5% significance level for all stations in the study area. Overall, there are consistent patterns of warming across in the Marmara affecting both of the maximum and minimum temperatures series. In this regard, diurnal temperature range shows slightly positive trends to 5 stations and negative trends to 2 stations evidencing that the monthly mean difference between the maximum and minimum temperature is increasing almost for all stations which are affected by urbanization around Istanbul metropolitan and is decreasing for lower latitude stations in the Marmara region. These results obtained for diurnal temperature range index in most of the stations are in agreement with the results of general positive trends obtained at 5% significant level for TXx, TXn, TNx and TNn indices. It is worthwhile to note that the occurrence of extreme temperature is expected to be pronounced in favor of warm events along with more capacity of water vapor in the atmosphere than the cold events over the study area. Since the magnitude of change in the indices can be a factor which may contribute to the limitations in the ability of society and the fragile environment to cope with climate extremes, these results can be helpful in planning and decision-making for light of future climate projection and potential impacts on health, agriculture, environment and water resource.

Acknowledgements

The authors would like to thank the Turkish State Meteorological Service for availing the data used in this study.

References

Abbasnia, M., T. Tavousi, and M. Khosravi. "Assessment of future changes in the maximum temperature at selected stations in Iran based on HADCM3 and CGCM3 models." Asia-Pacific Journal of Atmospheric Sciences 52, no. 4 (2016): 371-377.

Acar-Deniz., Z, and B. Gönençgil. "Trends of summer daily maximum temperature extremes in Turkey." Physical Geography 36, no. 4 (2015): 268-281.

Bonsal, B. R., X. Zhang, L. A. Vincent, and W. D. Hogg. "Characteristics of daily and extreme temperatures over Canada." Journal of Climate 14, no. 9 (2001): 1959-1976.

Caloiero, T. "Trend of monthly temperature and daily extreme temperature during 1951–2012 in New Zealand." Theoretical and Applied Climatology 129, no. 1-2 (2017): 111-127.

Dogan, M., A. Ulke, and H. K. Cigizoglu. "Trend direction changes of Turkish temperature series in the first half of the 1990s." Theoretical and applied climatology 121, no. 1-2 (2015): 23-39.

Fauchereau, N., S. Trzaska., M. Rouault, and Y. Richard. "Rainfall variability and changes in southern Africa during the 20th century in the global warming context." Natural Hazards 29, no. 2 (2003): 139-154.

The government of Marmara (GoK). "Marmara Vision 2030". Marmara Government Blue Print Development Plan. The Popular Version, Ministry of Planning and National Development, (2007): 32 p.

Hulme, M., R. Doherty., T. Ngara., M. New, and D. Lister. "African climate change: 1900–2100." Climate Research 17, no. 2 (2001): 145-168.

IPCC 2007. "Fourth Assessment Report, Climate Change, The AR4 Synthesis Report". (2007): p. 73.

IPCC 2013. "Climate Change: The Physical Science Basis. The contribution of Working Group I to the Fifth Assessment", Report of the Intergovernmental Panel on Climate Change. Cambridge University Press, Cambridge, UK, and New York USA, (2013): 1550 p.

Jones, P. D, and A. Moberg. "Hemispheric and large-scale surface air temperature variations: An extensive revision and an update to 2001." Journal of Climate 16, no. 2 (2003): 206-223.

Karabulut, M., M. Gürbüz, and H. Korkmaz. "Precipitation and temperature trend analyses in Samsun." Journal International Environmental Application & Science 3, no. 5 (2008): 399-408.

Kerr, R. A. "What happened to global warming? Scientists say just wait a bit." (2009): 28-29.

New, M., B. Hewitson., D. B. Stephenson., A. Tsiga., A. Kruger, A. Manhique., B. Gomez et al. "Evidence of trends in daily climate extremes over southern and West Africa." Journal of Geophysical Research: Atmospheres 111, no. D14 (2006).

Özhan S (2004). "Watershed management". Publication no. 481, IU Faculty of Forestry Publications, Istanbul, pp. 384. [In Turkish]

SENSOY, S., N. TÜRKOĞLU., A. AKÇAKAYA., M. EKİCİ., M. DEMİRCAN., Y. ULUPINAR., H. ATAY., A. TÜVAN, and H. DEMİRBAŞ. "Trends in Turkey climate indices from 1960 to 2010." In 6th Atmospheric Science Symposium, ITU, Istanbul. Turkey State Meteorological Service, Ankara, Turkey, pp. 24-26. 2013.

Solomon, S. ed. "Climate change 2007-the physical science basis: Working group I contribution to the fourth assessment report of the IPCC". Vol. 4. Cambridge University Press, 2007.

Tayanç, M., M. Karaca, and O. Yenigün. "Annual and seasonal air temperature trend patterns of climate change and urbanization effects in relation to air pollutants in Turkey." Journal of Geophysical Research: Atmospheres 102, no. D2 (1997): 1909-1919.

Toros, H. "Spatio-temporal variation of daily extreme temperatures over Turkey." International Journal of Climatology 32, no. 7 (2012): 1047-1055.

Unal, Y. S., A. Deniz, H. Toros, and S. Incecik. "Temporal and spatial patterns of precipitation variability for annual, wet, and dry seasons in Turkey." International Journal of Climatology 32, no. 3 (2012): 392-405.

Wikipedia website; (https://en.wikipedia.org/wiki/Marmara_Region)

Zhang, X., and F. Yang. "RClimDex (1.0) User Guide: Climate Research Branch Environment Canada." RClimDex (1.0) User Guide: Climate Research Branch Environment Canada (2004).

Zhang, X., E. Aguilar., S. Sensoy., H. Melkonyan., U. Tagiyeva., N. Ahmed., N. Kutaladze et al. "Trends in Middle East climate extreme indices from 1950 to 2003." Journal of Geophysical Research: Atmospheres 110, no. D22 (2005).

ANALYSIS OF CHANGES IN PRECIPITATION EXTREMES OVER MARMARA REGION, TURKEY

Mohsen Abbasnia[1], Serdar Bağış[2], Hüseyin Toros[3]

[1-] Postdoctoral Researcher, Department of Meteorology, Istanbul Technical University, Maslak Istanbul 34469, Turkey. Abbasnia@itu.edu.tr

[2-] Department of Computer Engineering, Institute of Science and Technology, Istanbul Technical University, Maslak Istanbul 34469, Turkeyserdarbagis@gmail.com

[3-] Department of Meteorology, Istanbul Technical University, Maslak Istanbul 34469, Turkey Toros@itu.edu.tr

Abstract

In this study, we have run the RClimDex software to calculate 7 precipitation extreme indices at 6 stations in the Marmara region for the period from 1960 to 2016. These indices have shown decreasing trends in consecutive dry days and increasing trends in annual rainfall, rainfall intensity. The wet spell duration shows an insignificant positive trend over the most study stations of the Marmara which are affected by the fast rate of urbanization such as Istanbul, Bursa, and Tekirdag, while it is decreased for the stations of Kocaeli and Çanakkale. The trend of annual total precipitation indicator shows an insignificant positive trend all over the Marmara region except for the Çanakkale station. Annual precipitation trend was significant only for two urban stations of Sarier and Bursa at 90% level of confidence. The maximum one-day and 5 days and the heavy precipitation revealed a significant positive trend at 5% significant level for Edirne and Tekirdag by a mean rate of 2.8 and 5.4 mm per decades and for Bursa by a mean rate of 0.6 day per decades, respectively. Therefore, a large proportion of study stations have experienced an increase in the annual precipitation, heavy precipitation events, although the percentage of significant trend values was very low. In the Marmara region is expected that the rainfall events tend to change toward shorter and more intense spells of rainfall. Overall, there is a much more mixed pattern of changes in precipitation extreme trends at the station scales.

Keywords: *Climate change, RClimDex, precipitation extremes, climatic trends, Marmara region*

Introduction

Climate change is one of the biggest issues confronting humanity in the 21st century. This will give rise to changes in weather patterns, and an increase in the frequency and severity of extreme events. Extremes are defined with the maximum and minimum values of climatic variables that can be expected to occur at a certain place and time (Rohli and Vega, 2012), for places with a long period of observations. Climate extremes events have the potential to affect the country's national development plans, and retard the strategies for the sustainable development. In this case, precipitation variability influences both water resources and occurrence of extreme events such as droughts and floods, and consequently, it has a significant impact on agriculture, economy, and energy production (Unal et al., 2012). From climate models, some types of precipitation extremes are expected to become more frequent in the future because of anthropogenic influences on climate (e.g., Semenov and Bengtsson, 2002; Groisman et al., 2005). It is thus of great interest to analyze the occurrence of past precipitation extremes, to see if changes are already apparent. A great number of research papers have been analyzed extreme precipitation variability on global, regional and national scales. There is remarkable consistency among the results obtained from regional precipitation studies that showed patterns of precipitation differ for different regions, e.g. the Caribbean (Peterson et al., 2002), Africa (Mokssit, 2003), the Middle East (Zhang et al., 2005; Hamidianpour et al., 2016; Balling et al., 2016), Central America and northern South America (Aguilar et al., 2005), southern South America (Haylock et al., 2006), southern and western Africa (New et al., 2006),

central and southern Asia (Klein Tanket al., 2006). Also, many attempts have been investigated by some researchers to analysis the precipitation variability in Turkey for different periods, and stations focusing on seasonality, trend, and periodic behavior (e.g. Turkes, 1996; Kadioğlu, 2000; Türkeş et al., 2009; Deniz et al., 2010; Unal et al., 2012; Öztopal, 2017). The majority of these studies based on observational data indicate a general increase in extreme heavy precipitation events, which is attributed to anthropogenic forcing caused by increased levels of moisture in the atmosphere and warmer temperatures overall (Bindoff et al., 2013). However, most analyses of these studies have relied on changes in mean values or old data time series that may not be quite representing for the latest trends of such precipitation extremes in concerning to differences characteristics of these extreme events under the faster rate of climate change in coming years.

In general, the joint scientist group of WMO, CCl and CLIVAR Expert Team (ET) on Climate Change Detection, Monitoring and Indices (ETCCDMI) has defined several climatic extreme indices for showing the same research way in climate change analysis (Zhang et al., 2005). In this regard, the results of a workshop about analysis of climatic trends in 27 extreme indices extracted from (ETCCDMI) for 15 countries of the Middle East between the period 1950 to 2003 using the RClimDex software which be held in Antalya, Turkey, in 2004, showed that trends of extreme temperature indices were significant and coherent with other regional results but trends of extreme precipitation indices were weak and mostly non-significant (Rahimzadeh et al., 2009). Any change in the frequency or severity of extreme precipitation events, particularly drought and floods could have profound impacts on nature and society of the Marmara region which is characterized by high climatic variability among all geographical regions of Turkey. The objective of this study, therefore, was to examine trends in extreme precipitation indices derived from observed rainfall for 6 meteorological stations in the Marmara region of Turkey. It is hoped that this effort will result in an improved the latest monitoring of precipitation extreme change for decision making with regard to agricultural planning and practice. This, therefore, formed the fundamental basis of this study.

Data and Methodology

Study area

Marmara region in northwestern of Turkey covers a total area of 67.306 km2 and located between 25.40°–31.33° Eastern longitude and 38.85°– 42.50° Northern latitude. The Marmara by Greece and the Aegean Sea to the west, Bulgaria and the Black Sea to the north, the Black Sea Region to the east, the Central Anatolia Region to the southeast and the Aegean Region to the south (Özhan, 2004). The region is surrounded by mountains up to 2500 m.a.s.l. in the south and south-east, and up to 1000 m.a.s.l. in the north-west. Although the geographical region of Marmara is the smallest region in geographic size, also it has the highest density of population and also is economically the most developed part of the country (Kömüşcü et al., 2013). While the industrial activities are concentrated in the central and eastern parts of the region, agriculture remains to be the main source of income in the western and southern parts of the region. From the climate perspective, the Marmara region has a hybrid Mediterranean on the Aegean Sea coast and the south Marmara Sea coast, an oceanic climate on the Black Sea coast and a humid continental climate in the interior (Wikipedia website). The region receives an average of 595 mm rainfall annually with high spatial variability. The annual rainfall reaches exceeds 800 mm in the eastern part of the region while the central and western parts reach values of less than 600 mm. The Marmara region has diverse vegetation cover, consisting of forests grassland and some aquatic flora. The coastal belt of the region is covered by broadleaf forests (Atalay and Efe, 2010). the In this study, long-term daily precipitation, maximum and minimum

temperature data are prepared at six weather stations over the Marmara region which consistent the same data period and cover all parts of the region geographically (Table 1).

Table 1. List of selected synoptic stations in the Marmara region of Turkey

WMO no.	Station name	Latitude	Longitude	Altitude (m)
17050	Edirne	41.67	26.57	51
17056	Tekirdag	40.98	27.55	4
17061	Sarıyer	41.17	29.04	58
17066	Kocaeli	40.77	29.92	74
17112	Çanakkale	40.15	26.42	6
17116	Bursa	40.18	29.07	100

Methodology:

In this study, we have run the RClimDex software to calculate precipitation extreme indices in the Marmara region of Turkey for the period from 1961 to 2016. The software has an inbuilt system of checking data quality based on thresholds of relevant parameters and is flexible enough with the capability to compare 27 different standard climatic indicators. In this case, long-term daily precipitation, maximum and minimum temperature data as input of the RClimDex was prepared for six stations in the Marmara which have the same data period in order to compare station's outputs for the same climatic period. Before the indices calculation, quality of the data was tested and controlled via the RClimDex software and users guide are available from the web address of "http://etccdi.pacificclimate.org/RClimDex/RClimDexUserManual.doc". The quality control (QC) step in the RClimDex involved carefully evaluating numerous detailed graphs of daily data to detect evidence of possible quality issues with the data as well as statistically identifying outliers. Each outlier or potential data problem was manually validated using metadata information of our climate data with each change or acceptance of an outlier, a record of the decision and the reason behind it was made in the QC log file. QC procedures are; 1- If precipitation value is (–), it is assumed as missing value (-99.9); 2- If Tmax < Tmin both are assumed as missing value (-99.9) and, 3- If the data outside of threshold (mean ±4*STD) it is assumed as problematic value. After the data had been quality controlled, they were ready for calculation of 7 selected precipitation extreme indices (Table 2) out of all climate indices in RClimDex. For interpreting the outputs of RClimDex, Kendall's tau based slope estimator has been used to compute the trends since this method does not assume a distribution for the residuals and is robust to the effect of outliers in the series. If slope error is greater than slope estimate, then the slope estimate cannot be trusted. If P Value is less than 0.05, the trend is significant at 95% level of confidence. Also, as it shows in the all output's graphs of any station, the dash line shows "locally weighted regression" and the solid line shows "liner least square fit". Overall, in this research, he trends which were found to be statistically significant at 0.05% level were considered for more analysis.

Table 2. List of the 7 selected precipitation extreme indices of ETCCDMI

ID	Indicator name	Definitions	UNITS
RX1day	Max 1-day precipitation amount	Monthly maximum 1-day precipitation	Mm
Rx5day	Max 5-day precipitation amount	Monthly maximum consecutive 5-day precipitation	Mm
R10	Number of heavy precipitation days	Annual count of days when PRCP>=10mm	Days
R20	Number of very heavy precipitation days	Annual count of days when PRCP>=20mm	Days

CDD	Consecutive dry days	Maximum number of consecutive days with RR<1mm	Days
CWD	Consecutive wet days	Maximum number of consecutive days with RR>=1mm	Days
PRCPTOT	Annual total wet-day precipitation	Annual total PRCP in wet days (RR>=1mm)	mm

Results and Discussions

Rainfall is the most important climatic parameter for rain-fed agriculture economies in Marmara region. In this regard, consecutive dry days (CDD) are a good indication of the risk of inadequate water for agriculture systems. Trend in maximum number of consecutive dry days between the period from 1960 to 2016 showed decreased in the total number of dry days as depicted in the output's graphs provided for the stations of Tekirdag (Id: 17056), Sarıyer (Id: 17061) and Bursa (Id: 17116) by a rate of 2.9, 1.3 and 14.1 days in 100 years, respectively, while it is increased for the stations of Kocaeli (Id: 17066) and Edirne (Id: 17050) by a rate of 2.2 and 15.9 days in 100 years, respectively. The wet spell duration indicator (CWD) is increased over the most study stations of the Marmara (Fig. 3 and 4). Increasing trend in consecutive wet days (CWD) was evident as showed in the graphs provided for the stations of Tekirdag, Sarier and Bursa by a rate of 0.3, 3.3 and 0.6 days in 100 years, respectively, while it is decreased for the stations of Kocaeli (Id: 17066) and Çanakkale (Id: 17112) by a rate of 0.9 and 2.1 days in 100 years, respectively. But, none of these trends at the station scales showed significance at 95% level of confidence because of P Value is more than 0.05. Overall, the general tendency of number of wet days than dry days throughout Marmara region has increased specially for the any area which is affected by fast rate of urbanization such as Istanbul, Bursa and Tekirdag. Trend of annual total precipitation indicator (PRCPTOT) shows an insignificant positive trend all over the Marmara region except for the Çanakkale station. Only, total wet-day precipitation for two urban stations of Sarier and Bursa is significant by a rate of 203 and 190 mm in 100 years at 90% level of confidence (Fig. 7). In addition, the trend analysis in the Çanakkale station revealed that there was a negative trend in both indices of the annual total precipitation and consecutive wet days by a rate of 5 mm and 0.2 day per decades for the study period from 1960 to 2016, respectively. In this case, the trend specific behavior in the Çanakkale station among all stations could be affected from environmental and geographical factors of its location. Both indices of the maximum 1-day precipitation amount (RX1day) and the maximum consecutive 5-day precipitation amount (RX5day) indicated a significant increasing trend at 95% level of confidence by a mean rate of 2.8 and 5.4 mm per decades for the stations of Edirne and Tekirdag during whole the studied period of 1960-2016, respectively. Also, these indices showed insignificant increasing trend for most of all stations (Fig. 5 and 6).

The trend of these indices is showed an insignificant negative trend for the Kocaeli station by a mean decreasing rate of 2.1 mm per decades during the whole studied period. In addition, the trend analysis in the Kocaeli station revealed that there was a negative trend in the number of dry days and a positive trend in the annual total rainfall. Thus, this is proving that daily rainfall events are expected to occur by a high rate of intensity and a shorter wet period during the year. Heavy precipitation days are represented by the number of heavy or very heavy precipitation days with daily rain amount more than10 mm (R10), 20 mm (R20), respectively. Significant positive trend in the very heavy precipitation index is only observed for the Bursa station by an increasing rate of 0.7 day per decades at 5% significant level. Generally, trend analysis of the number of heavy precipitation days when PRCP>=10 mm and the number of very heavy precipitation days when PRCP>=20 mm in most of the studied stations such as; Edirne, Sarier, Kocaeli, and Bursa are indicated an insignificant positive trend by a mean rate of 0.52, 0.21, 0.55, and 0.7 day per decades during whole the studied period of 1960-2016, respectively (Fig.

1 and 2). Similarly, an increase in rain intensity as heavy rain could result from a decrease in rainfall days while the total amount of annual rainfall remains relatively unchanged or from a greater increase (smaller decrease) in the annual rainfall compared to the increase (decrease) in the number of rainfall days. Therefore, on average, total number of daily rain during the year is expected to falling if the rain intensity increases. Overall, what is important in most station's trends of precipitation extreme indices over Marmara is that the number and amount of rainfall along with annual total precipitation has increased during the period from 1960 to 2016, slightly. Thus, it is expected that the general tendency of rainfall events changes towards shorter and more intense spells of rainfall in future decades, especially for some parts of the region such as; Çanakkale and Bursa due to having decreasing trends in the number of consecutive wet days. Therefore, these parts of the Marmara will face by more vulnerable position at risk of landslides, floods, land degradation, etc.

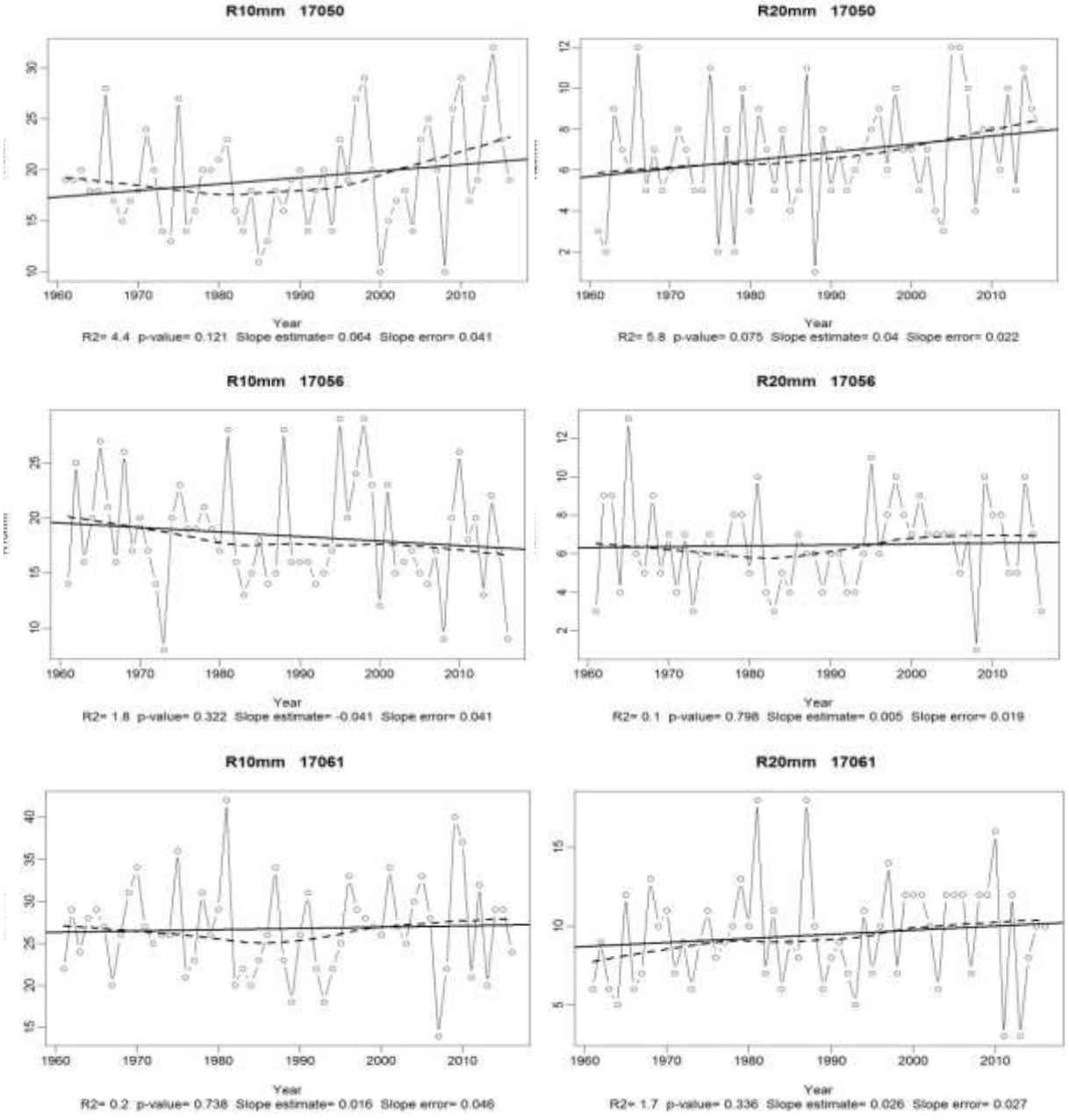

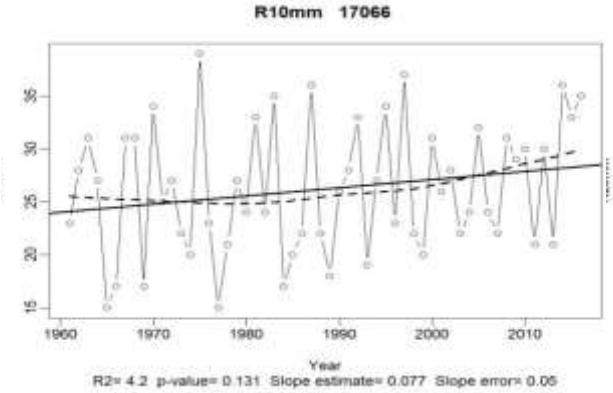

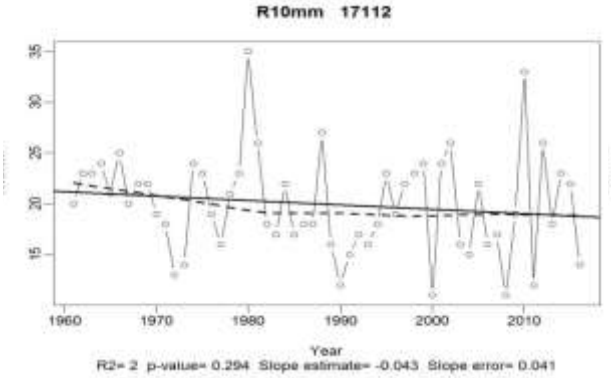

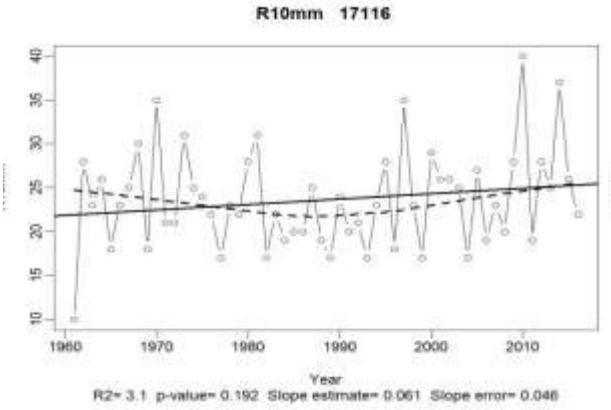

Figure 1. Annual count of days for each station when PRCP>=10mm

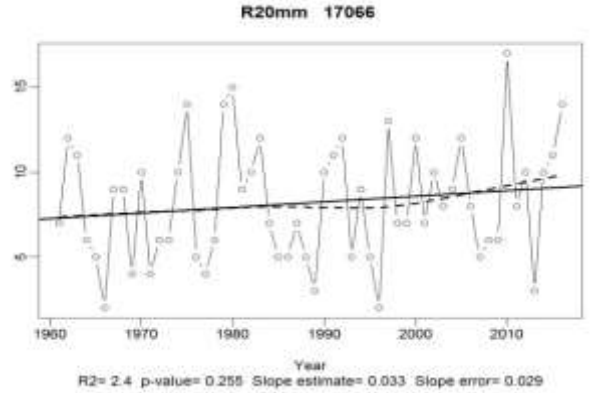

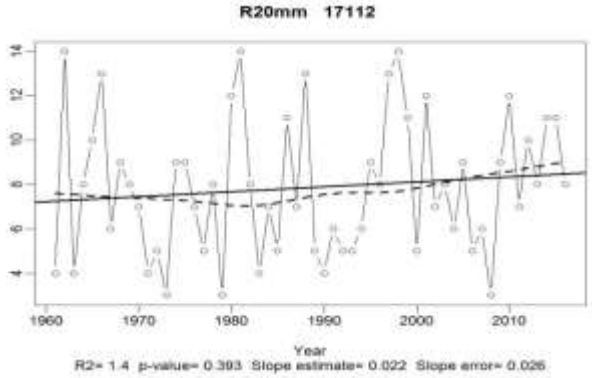

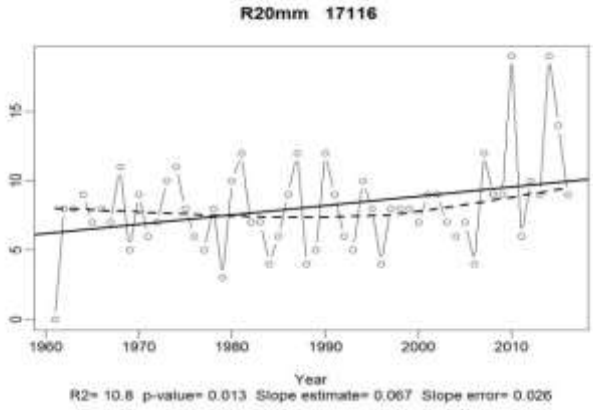

Figure 2. Annual count of days for each station when PRCP>=20mm

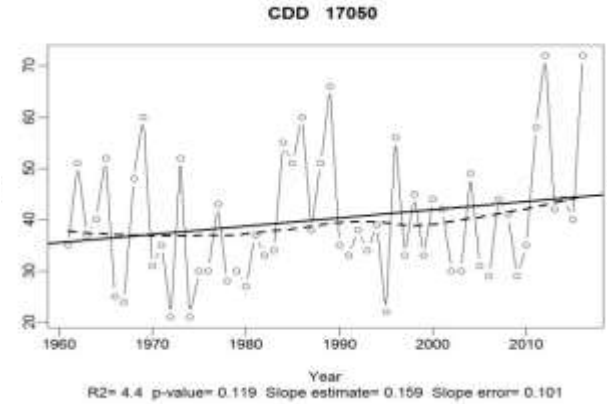

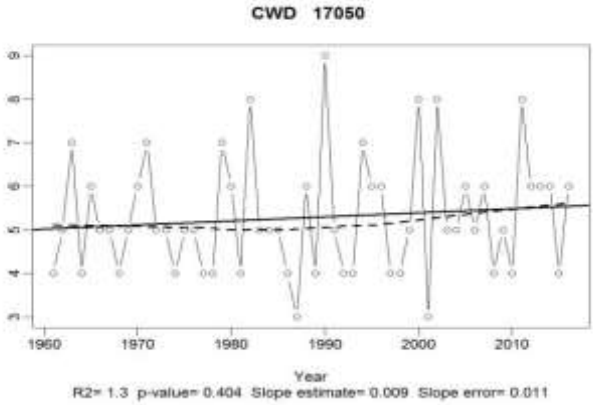

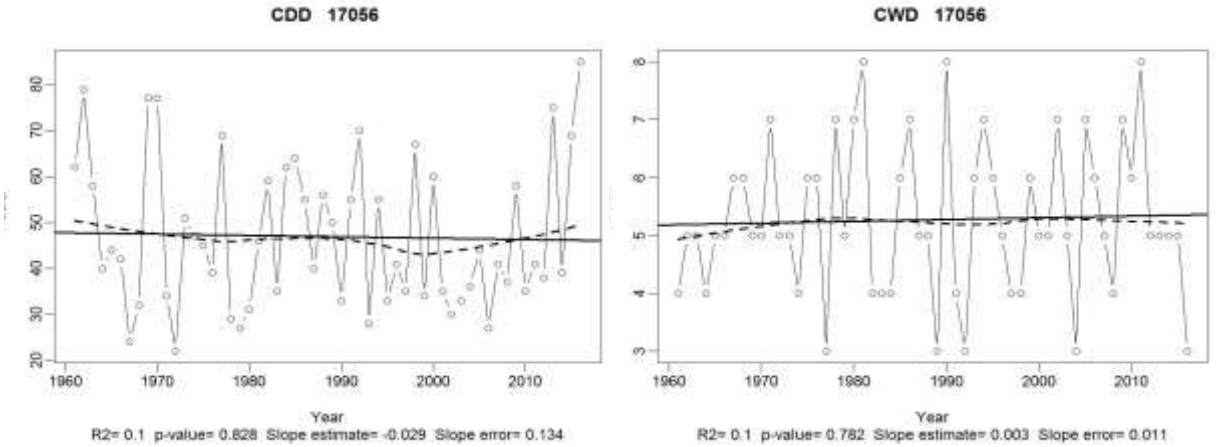
CDD 17056
Year
R2= 0.1 p-value= 0.828 Slope estimate= -0.029 Slope error= 0.134

CWD 17056
Year
R2= 0.1 p-value= 0.782 Slope estimate= 0.003 Slope error= 0.011

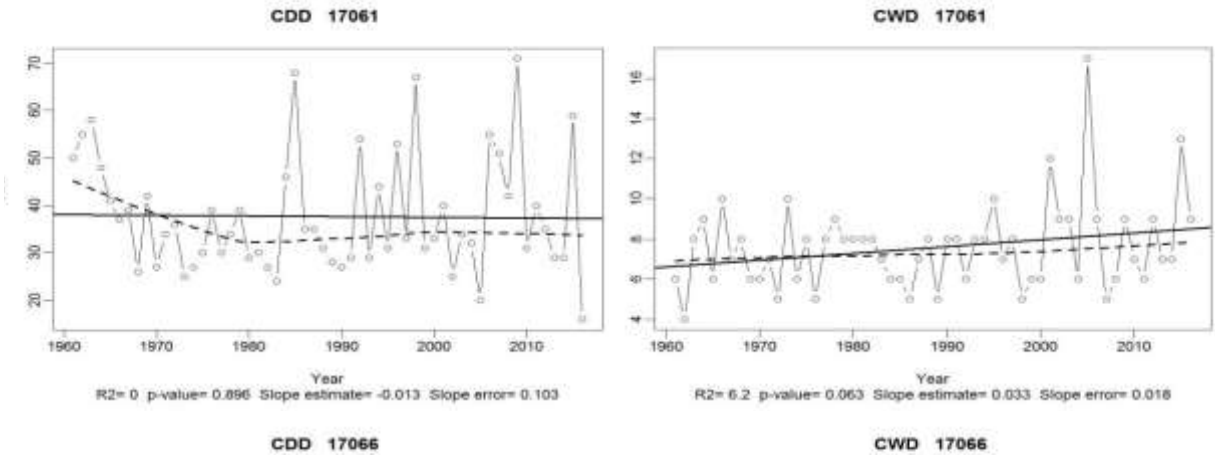
CDD 17061
Year
R2= 0 p-value= 0.896 Slope estimate= -0.013 Slope error= 0.103

CWD 17061
Year
R2= 6.2 p-value= 0.063 Slope estimate= 0.033 Slope error= 0.018

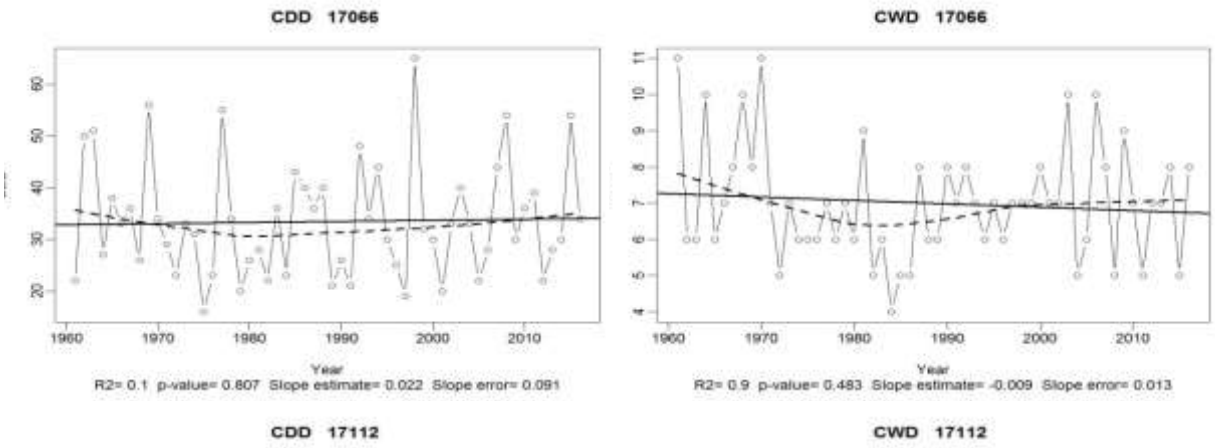
CDD 17066
Year
R2= 0.1 p-value= 0.807 Slope estimate= 0.022 Slope error= 0.091

CWD 17066
Year
R2= 0.9 p-value= 0.483 Slope estimate= -0.009 Slope error= 0.013

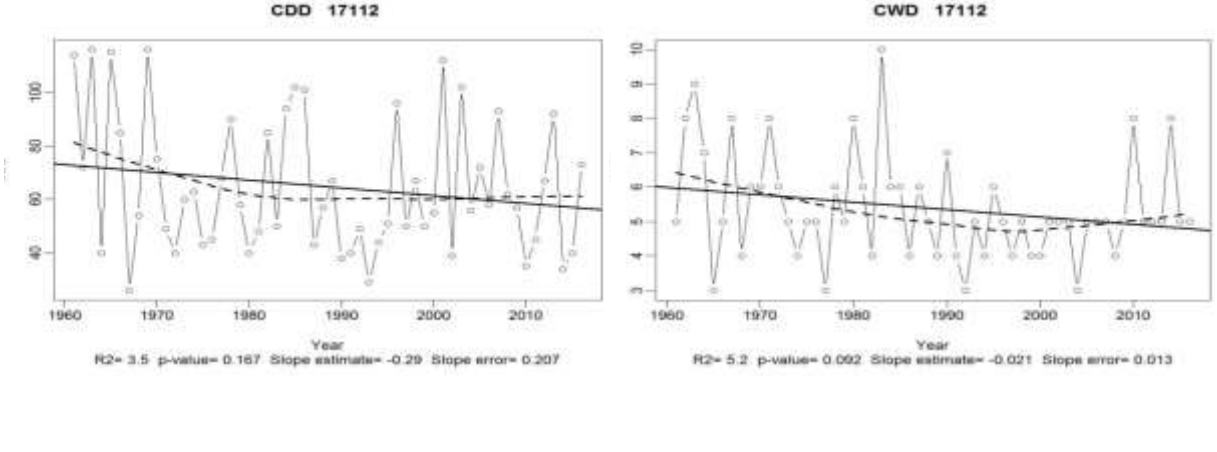
CDD 17112
Year
R2= 3.5 p-value= 0.167 Slope estimate= -0.29 Slope error= 0.207

CWD 17112
Year
R2= 5.2 p-value= 0.092 Slope estimate= -0.021 Slope error= 0.013

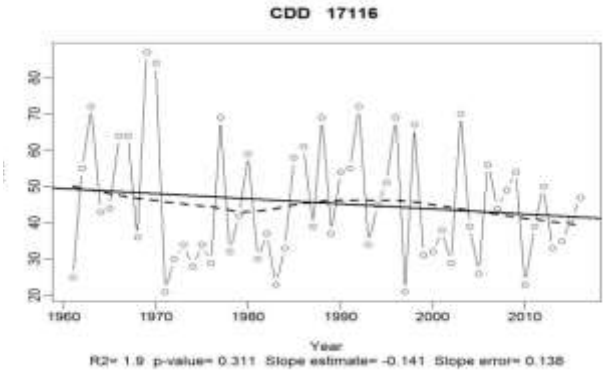

Figure 3. Total annual number of consecutive dry days for each station when RR<1mm

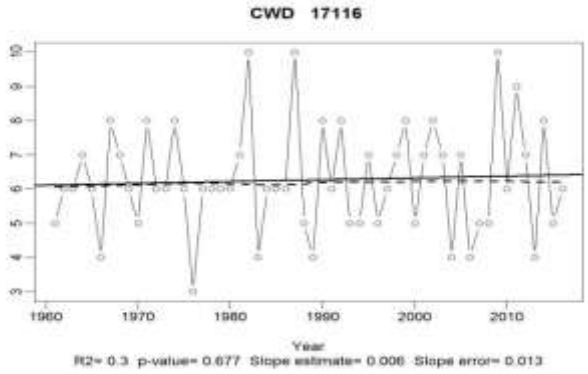

Figure 4. Total annual number of consecutive wet days for each station when RR>=1mm

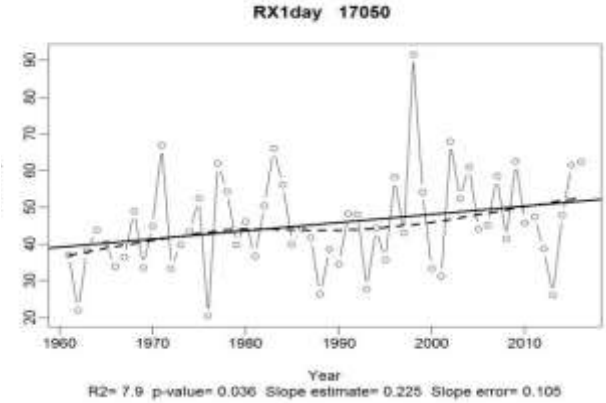

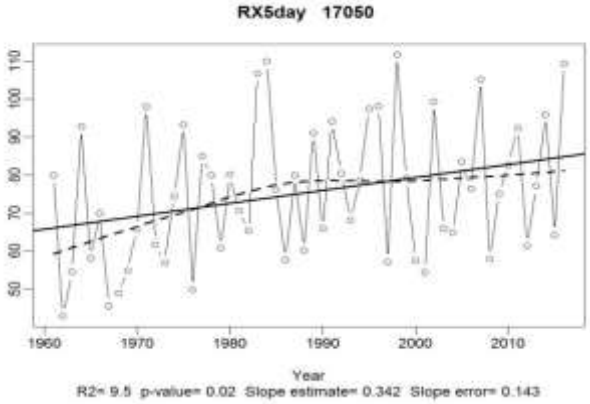

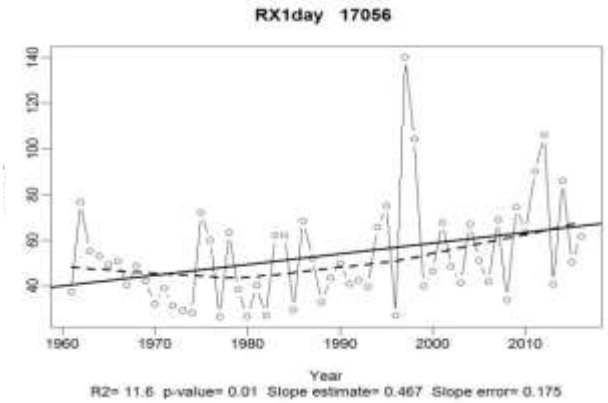

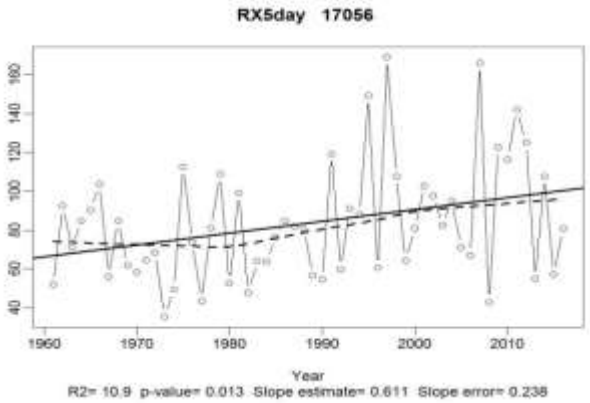

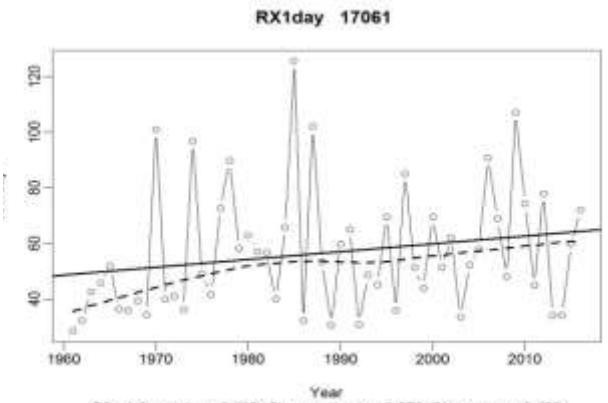

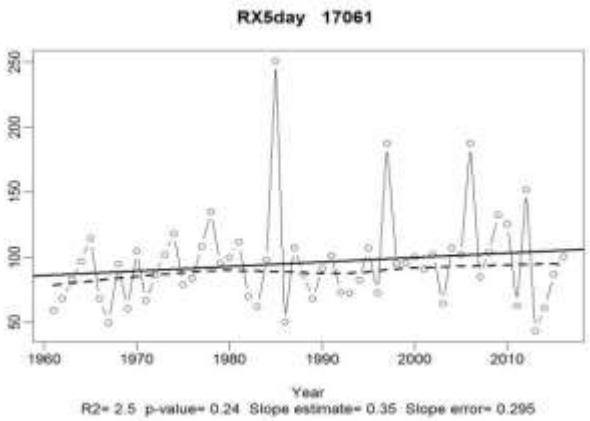

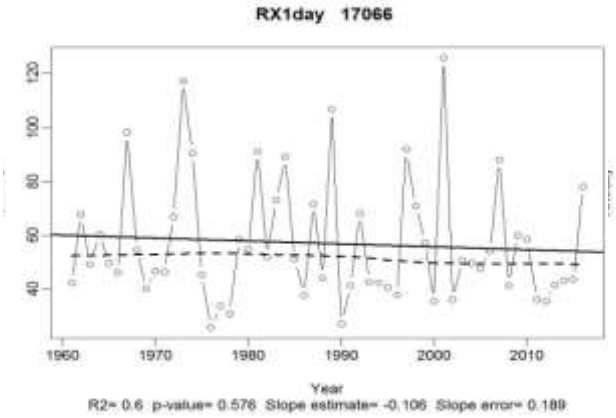

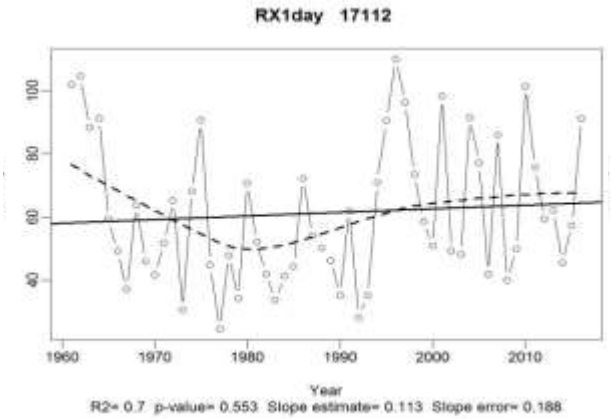

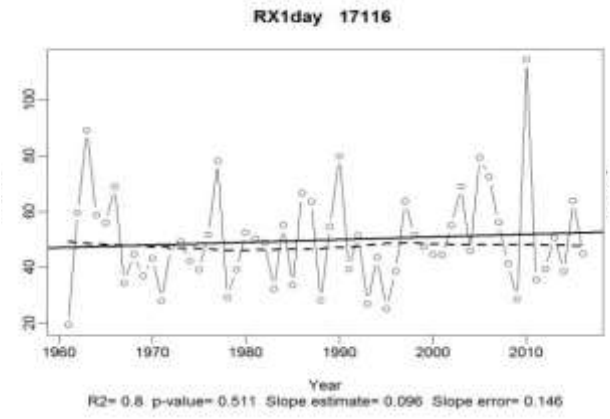

Figure 5. Annual amount of monthly maximum 1-day precipitation (mm) for each station

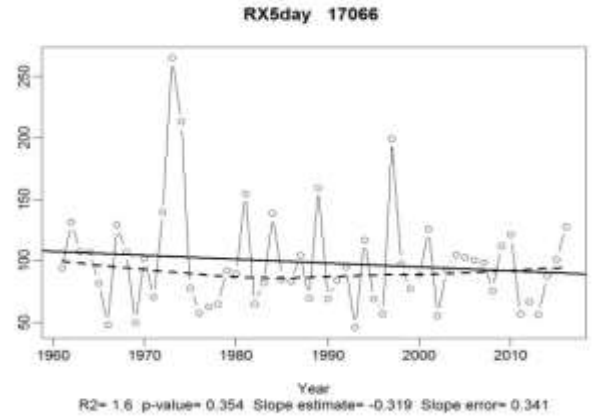

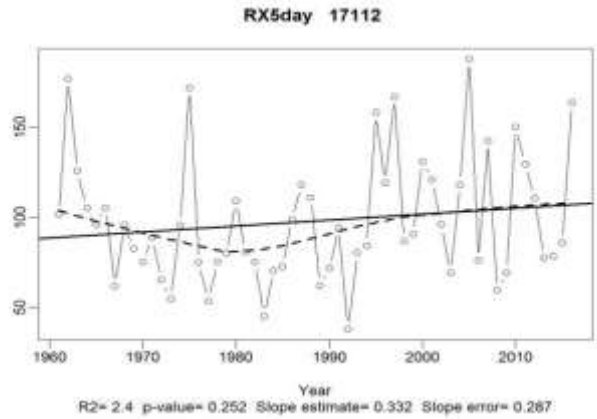

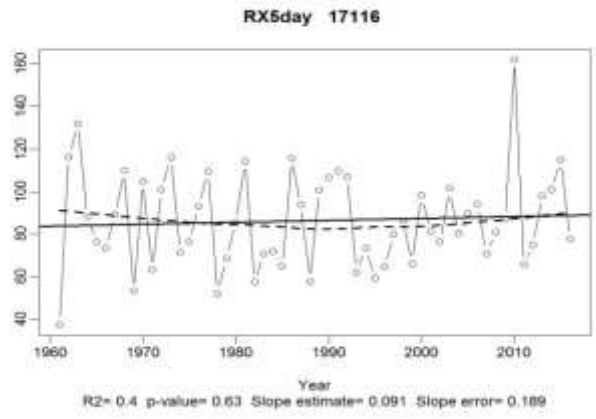

Figure 6. Annual amount of monthly maximum 1-day precipitation (mm) for each station

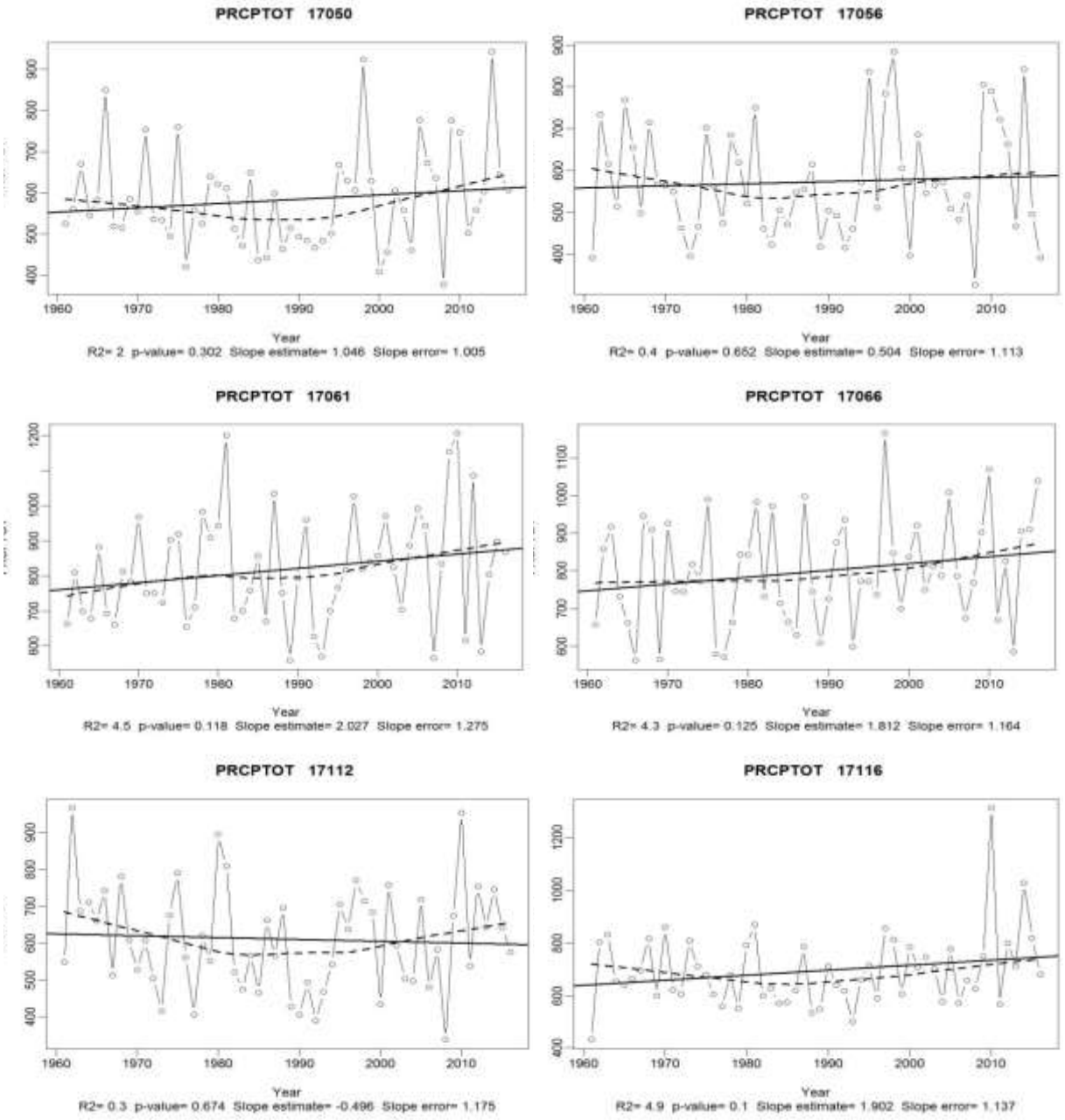

Figure 7. Annual total precipitation in wet days for each station when RR>=1mm

Conclusion

Precipitation is one of the most important climatic parameters in Turkey, due to its importance in water supply, agriculture, energy generation, and economic activities. Also, the risks associated with precipitation extreme events have a great impact on the county's socio-economic activities. The study looked at the long-term trends and patterns in precipitation extremes and average values over the Marmara region for the period from 1960 to 2016. The most results of the precipitation extreme indices at station scales showed a decreasing trend in the maximum number of consecutive dry days and an increasing trend in the maximum 1-day and 5-day precipitation amount, annual total number of heavy and very heavy precipitation days and annual total precipitation. In summary, there is a much more mixed pattern of changes in precipitation extreme trends at the station scales. In this regard, trend in maximum number of consecutive dry days showed negative trends for the weather stations of Tekirdag, Sarıyer and Bursa, while it is increased for the weather stations of Kocaeli and Edirne. In contrast, the wet

spell duration is increased over the most study stations of the Marmara such as; Tekirdag, Sarier and Bursa, while it is decreased for the stations of Kocaeli and Çanakkale. But, none of these trends at the station scales showed significance at 95% level of confidence. Thus, the increasing tendency in the number of wet days than dry days has happened in any area which is affected by fast rate of urbanization such as Istanbul, Bursa and Tekirdag. Trend of annual total precipitation indicator shows an insignificant positive trend all over the Marmara region except for the Çanakkale station. Annual total precipitation was significant only for two urban stations of Sarier and Bursa at 90% level of confidence. The maximum 1-day and 5-day precipitation showed a significant increasing trend at 95% level of confidence for the stations of Edirne and Tekirdag by a mean rate of 2.8 and 5.4 mm per decades, respectively. Also, these indices showed insignificant increasing trend for other stations except for the Kocaeli station in Marmara region. The trend analysis in the Kocaeli station revealed that there was a negative trend in the number of dry days and a positive trend in the annual total rainfall. Thus, this is proving that daily rainfall events are expected to occur by a high rate of intensity and a shorter wet period during the year. Trend in heavy and very heavy precipitation showed an insignificant positive trend for most of the stations and significant positive trend for the Bursa station at 5% significant level. Therefore, large proportion of study stations has experienced an increase for the annual total precipitation, the number of heavy precipitation days and maximum 1-day and 5-day precipitation, although the percentage of significant trend values was very low. It is expected that the rain changes towards shorter and more intense spells of rainfall, especially for the stations of Çanakkale and Bursa due to having decreasing trends in the number of consecutive wet days. However, knowing the magnitude of changes in the precipitation extremes is important as it reveals the limitations in the ability of society and the area's fragile environment to cope with climate extremes. The trends, as observed for the Marmara, call for a re-thinking of planning and practice of rain-fed agriculture in the rest of the country.

Acknowledgements
The authors would like to thank the Turkish State Meteorological Service for providing the raw meteorological data used in this study.

References

Aguilar, E., Peterson, T. C., Obando, P. R., Frutos, R., Retana, J. A., Solera, M., ... & Valle, V. E. (2005). Changes in precipitation and temperature extremes in Central America and northern South America, 1961–2003. Journal of Geophysical Research: Atmospheres, 110(D23).

Atalay, I., & Efe, R. (2010). Structural and distributional evaluation of forest ecosystems in Turkey.

Balling, R. C., Keikhosravi Kiany, M. S., Sen Roy, S., & Khoshhal, J. (2016). Trends in extreme precipitation indices in Iran: 1951–2007. Advances in Meteorology, 2016.

Bindoff, N. L., Stott, P. A., AchutaRao, K. M., Allen, M. R., Gillett, N., Gutzler, D., ... & Mokhov, I. I. (2013). Detection and attribution of climate change: from global to regional.

Deniz, A., Toros, H., & Incecik, S. (2011). Spatial variations of climate indices in Turkey. International Journal of Climatology, 31(3), 394-403.

Groisman, P. Y., Knight, R. W., Easterling, D. R., Karl, T. R., Hegerl, G. C., & Razuvaev, V. N. (2005). Trends in intense precipitation in the climate record. Journal of climate, 18(9), 1326-1350.

Hamidianpour, M., Baaghideh, M., & Abbasnia, M. (2016). Assessment of the precipitation and temperature changes over south east Iran using downscaling of general circulation models outputs. Physical Geography Research Quarterly, 48(1), 107-123.

Haylock, M. R., Peterson, T. C., Alves, L. M., Ambrizzi, T., Anunciação, Y. M. T., Baez, J., ... & Corradi, V. (2006). Trends in total and extreme South American rainfall in 1960–2000 and links with sea surface temperature. Journal of climate, 19(8), 1490-1512.

Kadioğlu, M. (2000). Regional variability of seasonal precipitation over Turkey. International Journal of Climatology, 20(14), 1743-1760.

Klein Tank, A. M. G., Peterson, T. C., Quadir, D. A., Dorji, S., Zou, X., Tang, H., ... & Sikder, A. B. (2006). Changes in daily temperature and precipitation extremes in central and south Asia. Journal of Geophysical Research: Atmospheres, 111(D16).

Kömüşcü, A. Ü., & Çelik, S. (2013). Analysis of the Marmara flood in Turkey, 7–10 September 2009: an assessment from hydrometeorological perspective. Natural hazards, 66(2), 781-808.
Mokssit, A. (2003). Development of priority climate indices for Africa: A CCI/CLIVAR workshop of the World Meteorological Organization. Mediterranean climate: variability and trends, 116-123.
New, M., Hewitson, B., Stephenson, D. B., Tsiga, A., Kruger, A., Manhique, A., ... & Mbambalala, E. (2006). Evidence of trends in daily climate extremes over southern and west Africa. Journal of Geophysical Research: Atmospheres, 111(D14).
Özhan S (2004). Watershed management. Publication no. 481, IU Faculty of Forestry Publications, Istanbul, pp. 384. [In Turkish]
Öztopal, A. (2017). Extreme precipitation climate change scenario evaluation over Turkey. International Journal of Global Warming, 11(4), 479-494.
Peterson, T. C., Taylor, M. A., Demeritte, R., Duncombe, D. L., Burton, S., Thompson, F., ... & Klein Tank, A. (2002). Recent changes in climate extremes in the Caribbean region. Journal of Geophysical Research: Atmospheres, 107(D21).
Rahimzadeh, F., Asgari, A., & Fattahi, E. (2009). Variability of extreme temperature and precipitation in Iran during recent decades. International Journal of Climatology, 29(3), 329-343.
Rohli, R. V., & Vega, A. J. (2012). Climatology (2nd ed.). Burlington, MA: Jones & Bartlett Learning LLC. ISBN 978-0-7637-9101-8.
Semenov, V., & Bengtsson, L. (2002). Secular trends in daily precipitation characteristics: greenhouse gas simulation with a coupled AOGCM. Climate Dynamics, 19(2), 123-140.
Türkeş, M., Koç, T., & Sariş, F. (2009). Spatiotemporal variability of precipitation total series over Turkey. International Journal of Climatology, 29(8), 1056-1074.
Turkes, M. U. R. A. T. (1996). Spatial and temporal analysis of annual rainfall variations in Turkey. International Journal of Climatology, 16(9), 1057-1076.
Unal, Y. S., Deniz, A., Toros, H., & Incecik, S. (2012). Temporal and spatial patterns of precipitation variability for annual, wet, and dry seasons in Turkey. International Journal of Climatology, 32(3), 392-405.
Wikipedia website. 2016. “https://en.wikipedia.org/wiki/Marmara_Region”.
Zhang, X., Aguilar, E., Sensoy, S., Melkonyan, H., Tagiyeva, U., Ahmed, N., ... & Albert, P. (2005). Trends in Middle East climate extreme indices from 1950 to 2003. Journal of Geophysical Research: Atmospheres, 110(D22).

STATISTICAL LONG-TERM PREDICTABILITY OF TURKISH SURFACE TEMPERATURES FROM GLOBAL SEA SURFACE TEMPERATURES

Ozan Mert Göktürk[1], Ömer Lütfi Şen[2], Tuğçe Şenel[3] and Nursel Çetin[4]
[1]Ondokuz Mayıs University, Department of Meteorology
ozan.gokturk@omu.edu.tr
[2]Istanbul Technical University, Eurasia Institute of Earth Sciences
senomer@itu.edu.tr
[3]Istanbul Technical University, Eurasia Institute of Earth Sciences
tugcesnl@hotmail.com
[4]Turkish State Meteorological Service, Department of Research
ncetin@mgm.gov.tr

Abstract
We present the first results of an ongoing, comprehensive analysis; in which monthly and seasonal land surface temperatures in Turkey are statistically related to global SSTs of the preceding seasons. The ultimate aim is to assess the statistical long-term predictability of Turkish temperatures by using appropriate subsets of global SST anomalies. For this purpose, cross correlations between each monthly mean temperature time series (predictand) from 41 stations in Turkey and monthly mean SSTs (predictor) from every grid point on the globe were computed for the period 1950-2015. This was done for numerous combinations (time averages) of both the predictor and predictand time series; with lags up to 7 months and predictor series averaged over up to 12 months, backwards from the most recent predictor month. All series were detrended prior to the analysis. The outcome is 9.5×10^8 correlation coefficients showing the time-lagged relationship (if any) between global SSTs and Turkish temperatures. Results unsurprisingly indicate that the North Atlantic SSTs have the strongest lagged relationship with temperatures in Turkey, especially when the predicted seasons are summer and fall. Generally, the more the number of predictor (SST) months, the higher the correlations; hinting at the role of SST persistence in monthly and seasonal climate. Two other, less expected and interesting results are, 1) some correlations are higher as the lag-time increases, implying potential long term predictability, 2) there are signals of moderate relationship between Turkish temperatures and the SSTs of remote regions such as the southern Indian Ocean or the western Pacific. These first results will help determine the best predictor (SST) regions for each prediction effort, which will be performed using more advanced regression methods.

Keywords: *predictability, SST, Turkey, statistical, temperature*

INTRODUCTION
Having the potential to shape long term logistic plans and investments, monthly and seasonal climate forecasts are products which are demanded by a variety of business sectors; agriculture, energy and tourism being the foremost. However, the long range (1 to 6 months in advance) predictability of seasonal climate, especially for mid and high latitudes, is quite low (van Oldenborgh vd., 2005; Weisheimer ve Palmer, 2014). In order to increase predictability, statistical models are constructed using lagged relationships between climate parameters (NRC, 2010); in addition to the continuous development of dynamical/physical models. This current work is a part of a project to construct a purely statistical model to predict monthly and seasonal climate in Turkey up to 6 months in advance. Gridded global monthly SST data and surface temperature data from Turkish meteorological stations were used, respectively, as the predictor and the predictand variables. Time-lagged cross correlations between numerous time averages of these predictors and predictands were computed; in order to determine the SST regions and

the lead-lag times implying the highest predictive power. North Atlantic SSTs were found to have the strongest time-lagged relationship with Turkish surface temperatures on various lead-lag times, signals becoming stronger as higher number of predictor months are used. Some correlations are stronger as the lead time increases, implying potential long term predictability. Moreover, a number of moderate correlations with regions far away from Turkey are observed.

DATA AND METHODS

As the predictor, *NOAA Extended Reconstructed SST Version 4* data provided by the NOAA/OAR/ESRL PSD (Huang et. al., 2016) were used. This is a global data set on 2^o x 2^o grids, composed of monthly average SSTs on each grid point. Monthly mean temperatures from 41 stations in Turkey were used as the predictand variables, and the data were obtained from the Turkish State Meteorological Service. The analysis period is 1950-2015, during which a reasonably high number (41) of Turkish stations with continuous data is available. For each meteorological station, 24 distinct predictand (temperature) series were created: 12 of them are individual months, and the remaining 12 are each consecutive 3-month average within the year. 84 predictor variables were constructed for each SST grid point: Starting from 1 to 7 months before the first *predicted* month, 1 to 12-monthly averages (backwards from the most recent *predictor* month) were computed as the predictor SST time series. For example, if the *predictor* number is ***407***; it means that the *predictor* begins **4** months before the least recent of the *predictand* months, and are composed of a ***7***-monthly average backwards, including the most recent predictor month. All predictor and predictands were detrended from their linear trends prior to the analysis, in order to avoid inflated correlations resulting from common trends. 9.5 x 10^8 correlation values were obtained by cross-correlating each predictand time series of each station by all predictor SSTs. Correlation coefficients which are significant at the 90% level were considered as 'statistically significant', with the purpose of taking into the account even the small predictive signals.

RESULTS AND OUTLOOK

According to the first results obtained from the analysis, potential predictability of Turkish surface temperatures implied by the computed correlations is the highest for fall and summer, and the strongest relationship is with the SSTs of the North Atlantic (e.g. Fig. 1). Interestingly however, there are also significant, spatially coherent correlations at far away regions such as SE or W Pacific (Fig. 1), results which are yet to be investigated. Correlations of individual grid points' SSTs is promising as well. For instance, the potential predictive power of a grid point in NW Atlantic, judging by the strength of cross correlations (Fig. 2); peaks at 6-month lag time for spring (MAM) and summer (JJA), and at 7-month lag time for fall (SON). Moreover, the peak of the average correlation for summer is at *predictor* no. 605 (Fig. 2), which means that a backward 5-month average yields the best predictive power, and implies the role and influence of SST persistence on regional climates.

The next step in the work will be to determine, using the huge number of correlation values obtained, the -potentially- best predictor regions and time series for each of the 24 predictands. These select predictors will then be the inputs of more advanced regression techniques such as multiple linear regression or canonical correlation analysis.

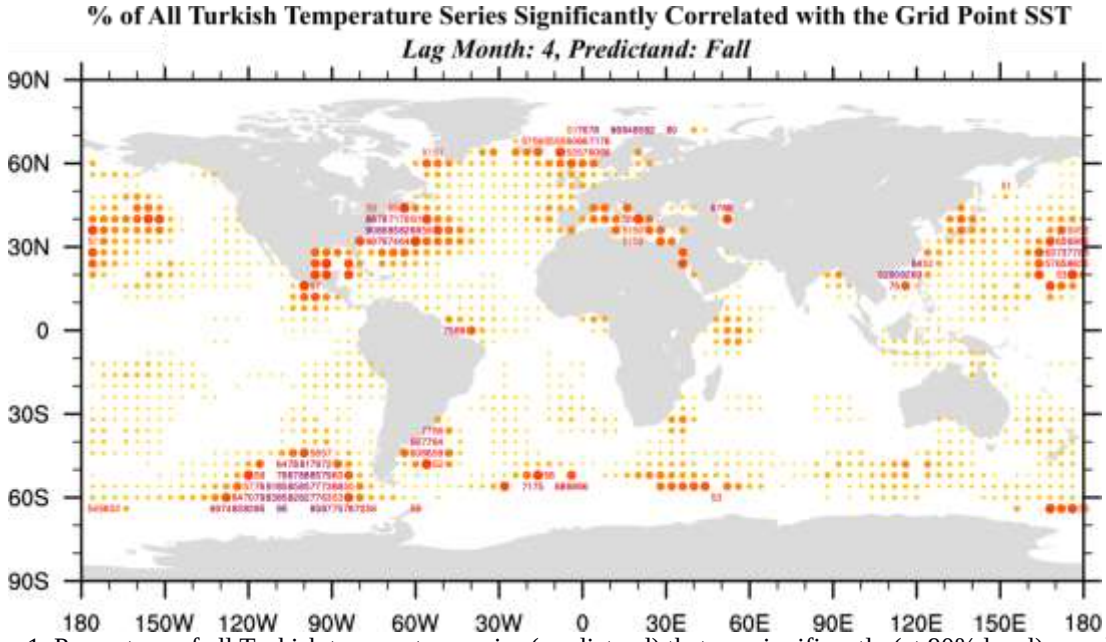

Figure 1. Percentage of all Turkish temperature series (predictand) that are significantly (at 90% level) correlated with the grid point's SST series (predictor). In this particular case, the predictands are fall (SON) mean temperature series; while the predictors are SSTs of lag time 4: that is, 4 months before the first *predictand* month. These percentages are mean values for the 12 distinct predictor series of lag time 4, which are constructed by averaging over one extra month for each predictor, backwards in time from the first *predictor* month. Darker and bigger dots are used for higher percentage values. Numbers indicate values greater than 50%. Signs of the correlations are not indicated here.

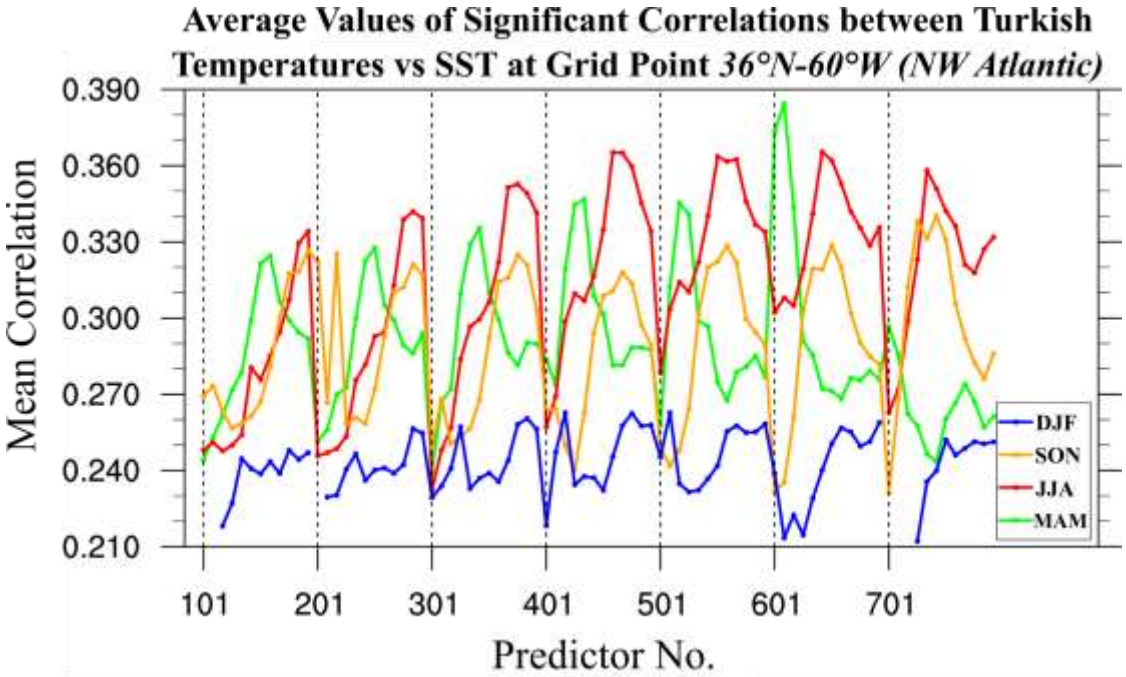

Figure 2. Average values of significant correlations between all Turkish temperature (predictand) time series and the SSTs at the specified grid point. Colors denote the correlations for 4 main *predictands*, namely the seasonal temperature averages. See *Data and Methods* for the explanation of *predictor* number.

ACKNOWLEDGEMENTS

This work was supported by the Turkish National Research Council (TÜBİTAK, grant no. 115Y664)

REFERENCES

Huang, B., Thorne, P., Smith, T., Liu, W., Lawrimore, J., Banzon, V., Zhang, H., Peterson, T., Menne, M. 2016. "Further Exploring and Quantifying Uncertainties for Extended Reconstructed Sea Surface Temperature (ERSST) Version 4 (v4)", Journal of Climate, 29, 3119-3142, https://doi.org/10.1175/JCLI-D-15-0430.1

NRC (National Research Council, ABD) Committee on Assessment of Intraseasonal to Interannual Climate Prediction and Predictability. 2010. "Assessment of Intraseasonal to Interannual Climate Prediction and Predictability". http://www.nap.edu/catalog/12878.html Last accessed: 04.08.2017. Full text: https://goo.gl/iqEkzx

van Oldenborgh, G.J., Balmaseda, M.A., Ferranti, L., Stockdale, T.N., Anderson, D.L.T. 2005. "Evaluation of atmospheric fields from the ECMWF seasonal forecasts over a 15 year period", Journal of Climate, 18, 5188–5198.

Weisheimer, A., Palmer, T.N. 2014. "On the reliability of seasonal climate forecasts", Journal of the Royal Society Interface, 11, http://dx.doi.org/10.1098/rsif.2013.1162

THE IMPACTS OF CLIMATE CHANGE ON EXTREME PRECIPITATION EVENTS IN KARADENIZ EREĞLİ STATION (TURKEY)

Mustafa NURI BALOV[1], Abdüsselam ALTUNKAYNAK[2]

[1]*Faculty of Civil Engineering, Hydraulics and Water Resources Division, Istanbul Technical Univ., Maslak 34469, Istanbul, Turkey,* mustafanuribalov@gmail.com;

[2] *Faculty of Civil Engineering, Hydraulics and Water Resources Division, Istanbul Technical Univ., Maslak 34469, Istanbul, Turkey, altunkay@itu.edu.tr*

Abstract

In this study the impacts of climate change on extreme precipitation events were investigated for reference period (1971-2000) and future period (2020-2099) in Karadeniz Ereğli Station where located in Western Black Sea Basin in the north of Turkey. The daily observed rainfall data together with projected precipitation data from GFDL-ESM2M and HadGEM2-ES global circulation models under RCP4.5 and RCP8.5 scenarios were used. The first part of the study was about the detection of the trend in eight precipitation indices during the reference period and future period by using Mann-Kendall (MK) trend test. In the second part the maximum 24-hr storm with return periods of 2, 5, 10, 20, 50, 100 and 500 years were generate by Peaks Over Threshold (POT) method for reference period and late future (2070-2099). The results of trend analyses show a non-significant trend during the reference period, in contrast to the future period which an increasing significant trend will be predicted in most of indices based on the outputs of the GCMs. Frequency analyses of 24-hr rainfall intensity depicted that the amount of huge precipitation events by the end of the century will be increased notably in the station. As a whole, the evaluation of precipitation pattern shows that the total amount of the precipitation will not be changed during the coming years, whereas the number of dray days and the number of days with heavy precipitation will increase significantly, which can be remarkable in terms of flood risk and water resources management.

Keywords: *Climate Change Impact, Global Circulation Model, Extreme precipitation events, Trend Analyses, Peaks Over Threshold Method.*

INTRODUCTION

Recently, a dramatic increase was observed in the number and intensity of hazardous floods caused by extreme precipitation events all around the world. This increase can be explained by the fact that growth in the water holding capacity of the atmosphere (by 7% per C) and global mean precipitation (2-3 %) as a results of global warming. The change in global precipitation amount is not in a spatial uniformity and cause to variation in the nature of hydrological cycle and the properties of precipitation like frequency, intensity and distribution (Held and Soden, 2006; Wentz et al., 2007; Lambert et al., 2008; Trenberth, 2011; Siswanto et al., 2016).

According to Intergovernmental Panel on Climate Change (IPCC, 2013) notwithstanding of possible decreases in annual total precipitation amount for some regions, extreme precipitation events will increase in future particularly in mid-latitude regions compared to average changes throughout 1951-2003 period. The results of analyses based on Global Circulation Models (GCM) also were approved this issue in spite of some differences between several model outputs (Frei et al., 2006).

IPCC has considered extreme precipitation events as an indicator of the climate change (IPCC, 2013). As a result, several studies focused on the variations in frequency and magnitude of extremes in the previous years in order to understanding and measuring the climate change (e.g.

Booth et al., 2012; de Lima et al., 2015; Bharti et al., 2016; Tian et al., 2017). Moreover, as a result of the insufficiency of proper meteorological station in some regions, using of high resolution gridded reanalysis data is an obligation for researchers in order to investigation of past and future precipitation events (Ren et al., 2015). The understanding climate change in south-western parts of India were investigated by considering the trends in seasonal precipitation extremes as indicator in a study by Pal and Al-Tabbaa (2009). They indicated that the changes were not be seasonally uniform spatially. They also found that the number of dry days in regions with the scarcity of water were increased. Yazid and Humphries (2015) concluded that there was an increasing trend in the number of days with huge precipitation amount in study on extreme precipitation events in Indochina Peninsula between 1960 and 2007 by using APHRODITE high resolution data.

Recently the number of studies based on projected climate variable from Coupled Model Intercomparison Project Phase 5 (CMIP5) global circulation models under new Representative Concentration Pathways (RCP) scenarios which introduced by IPCC in the Fifth Assessment Report (AR5) (IPCC,2013) have been increased (e.g. Cho et al., 2016; Xiao et al., 2016; Li et al., 2016; Wang et al., 2017; Chattopadhyay et al., 2017; Wen et al., 2017; Peng et al., 2017; Mohan and Rajeevan, 2017). In a study by Chattopadhyay et al. (2017) existence of the trend in precipitation indices from observed (from 16 station between 1976-2015) and projected data (from 10 GCMs outputs under RCP4.5 and RCP8.5 between 2070-2099), was investigated by utilization of Mann-Kendal test of precipitation indices in the Kentucky River Basin. They found a significant trend in 11% of station-index combinations. Mohan and Rajeevan (2017) made a research on investigation of trend in hydroclimatic intensity by using ensemble of 10 GCMs results under RCP4.5 scenario in Indian monsoon region. They generated hydroclimatic intensity index (HY-INT), intensity during wet days (PINT), and dry spell length (DSL) indicators by using GCMs' outputs for future period (2010-2100) and gridded observed data for reference period (1951-2010). The results of the study showed that increasing in precipitation intensity cause to increase in HY-INT, while there will not be any change in DSL during the current century.

In the recent years the downscaled outputs of Global Circulation Models (GCMs) have been utilized widely in the analyses of extreme precipitation events under the effects of climate change (Bartholy and Pongrácz, 2010; Yan et al., 2015; Devkota and Gyawali, 2015; Kara and Yucel, 2015) . Kara et al. (2015) investigated the future impacts of climate change on extreme precipitation events in Omerli catchment (Istanbul, Turkey) based on the geo-statistically downscaled outputs of five GCMs under A1B scenario. Considering the projected data, they found that by the end of the century (2071-2100) the extreme precipitation events will be increased for winter, spring and summer seasons while for fall there will be decreased.

For Turkey, based on the results of several studies, it can be inferred that there was an increasing trend in the number of extreme precipitation events during the past decades which will be continued during the coming years under the effects of climate change for different parts of the country (Türkeş and Tatlı, 2009; Deniz et al., 2011; Acer and Senocak, 2012; Yucel and Onen, 2014; Kara and Yucel, 2015; Baloch et al., 2015; Yilmaz, 2015). According to Paxian et al., (2015) over the Mediterranean basin which Turkey is a part of it, there will be a change in the magnitude and intensity of extreme precipitation events during the current century (Paxian et al., 2015). The more considerable increase will be occurred in winter for eastern Europe and Turkey in spite of decreasing in the total precipitation amount (Paxian et al., 2015).

In this study the magnitude and frequency of the past and future extreme precipitation events under the effects of climate change for Ereğli Karadeniz Station where located in Western Black Sea Basin ,Turkey, were investigated in two different ways. Firstly the existence of the trend in eight precipitation indices were analyzed by using the Mann-Kendall trend test and in the second part the frequency analyses of extreme precipitation events for different return period were established considering the Peaks Over Threshold (POT) method. The observed daily precipitation data between 1971 and 2000 were used for reference period analysis and for future period (2020-2099) the dynamically downscaled outputs of GFDL-ESM2M (Geophysical Fluid Dynamics Laboratory, USA) and HadGEM2-ES (Met Office Hadley Center, UK) global circulation models under RCP4.5 and RCP8.5 emission scenarios (Chaturvedi et al.,2012; Demir, 2012) were utilized. All data were obtained from Turkish State Meteorological Service.

DATA AND METHODS

STUDY AREA

In this study the analyses were undertaken based on the observed and projected daily precipitation data in Karadeniz Ereğli station (Station number:17611) where located in Western Black Sea Basin in Turkey. The station is located in Zonguldak province and 41.2691° N and 31.4328 ° E coordinates with elevation of 19 meters from sea surface. The position of the station was depicted in Figure 1.

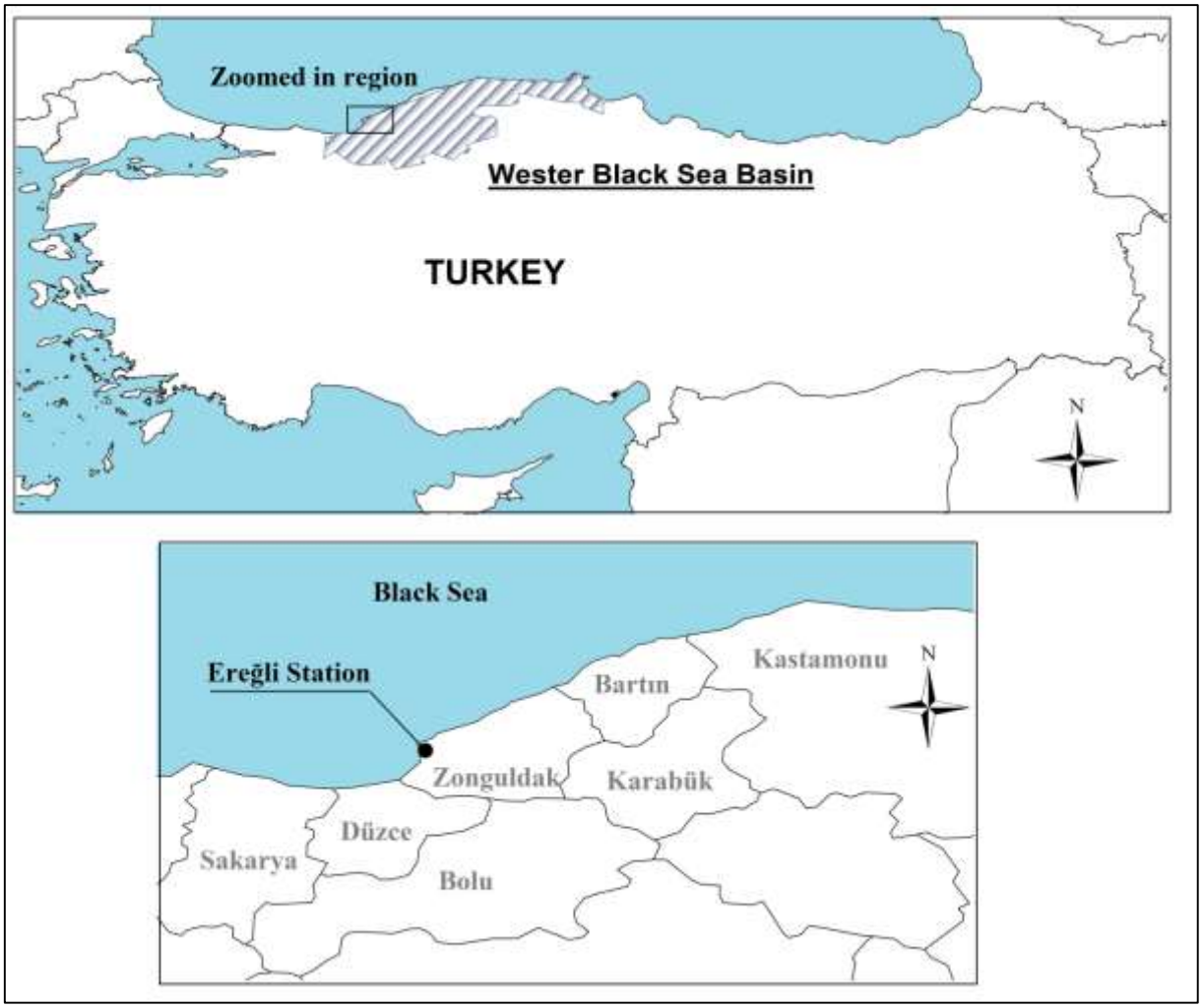

Figure 1: The position of Ereğli Station.

DATA COLLECTION AND STUDY APPROACH

In this study the existence of trend was investigated in eight precipitation indices (clarified by the Joint CCl/CLIVAR/JCOMM Expert Team on Climate Change Detection and Indices (ETCCDI), (WMO,2009)) of daily precipitation values which observed between 1971 and 2000. Additionally the outputs of GFDL-ESM2M and HadGEM2-ES global circulation models which were downscaled using a regional climate model named ICTP-RegCM4 (described in Giorgi et al., 2012) under RCP4.5 and RCP8.5 emission scenarios were used as the reference period (1971-2000) and future period (2020-2099). These indices can be listed as following:

PRCPTOT: total precipitation in wet days (> 1 mm)

RX1day, maximum one-day precipitation: highest precipitation amount in one-day period

RX5day, maximum five-day precipitation: highest precipitation amount in five-day period

SDII, simple daily intensity index: mean precipitation amount on a wet day

R10mm, heavy precipitation days: count of days where RR (daily precipitation amount) ≥ 10 mm

R20mm, very heavy precipitation days: count of days where RR ≥ 20 mm

CDD, consecutive dry days: maximum length of dry spell (RR < 1 mm)

CWD, consecutive wet days: maximum length of wet spell (RR ≥ 1 mm)

For frequency analysis projected daily precipitation data for reference period were utilized together with future period between 2070 and 2099 for calculation of maximum 24-hr rainfall intensity by POT method with 2, 5, 10, 20, 50, 100 and 500 years return periods.

MANN-KENDALL TREND TEST

For a given time series like $P=\{P_1, P_2, \ldots, P_n\}$ the statistics of the Mann-Kendall (MK) test (Mann, 1945; Kendall, 1975) can be calculated as:

$$S = \sum_{i<j} sign(P_j - P_i) \tag{1}$$

in which

$$sign(P_j - P_i) = sign(R_j - R_i) = \begin{cases} 1 & for \quad P_i < P_j \\ 0 & for \quad P_i = P_j \\ -1 & for \quad P_i > P_j \end{cases} \tag{2}$$

where R_i and R_j show the rank of P_i and P_j observation of the time series respectively (Hamed, 2008). By assuming that the data are independent and identically distributed, the mean (E) and variance (V) of the S statistic can be defined as below (Kendall, 1975):

$$E(S) = 0 \tag{3}$$

$$V(S) = \left[n(n-1)(2n+5) - \sum_{p=1}^{g} t_p (t_p - 1)(2t_p + 5) \right] \frac{1}{18} \tag{4}$$

where n is the number of data points, g is number of tied groups - a set of data with the same value- and t_p is the number of data points in the p^{th} group (Hamed, 2008). As a result, one can inferred the significance of the trend with comparing the standard normal density of probability and the standardized variable Z for any level of significance. The standardized variable Z can be determined as:

$$Z = \begin{cases} (S-1)/\sqrt{V(S)} & if \quad S > 0 \\ 0 & if \quad S = 0 \\ (S+1)/\sqrt{V(S)} & if \quad S < 0 \end{cases} \tag{5}$$

Finally the positive or negative values of Z can be used for determination of increasing or decreasing trend respectively.

PEAKS OVER THRESHOLD

In this study, for frequency analyses of past and future extreme precipitation events the Peaks Over Threshold (POT) method was used in order to generate partial duration series. In this method, only the values which exceed a certain threshold will selected under the assumption of independency and identically distribution of data for analyses. This time series can be fitted to Generalized Pareto Distribution (GPD) (Balkema and de Haan, 1974; Pickands, 1975) according to Coles (2001). According to the theorem of GPD, the cumulative distribution function can be defined as:

$$F(x) = 1 - \left\{1 + \frac{\gamma}{8}(x-u)\right\}^{-\frac{1}{\gamma}}, \qquad \gamma \neq 0 \tag{6}$$

$$F(x) = 1 - \exp(-\frac{x-u}{8}), \qquad \gamma = 0 \tag{7}$$

where u is location parameter (threshold), σ is scale parameter, γ is scale parameter, $x \in [u, \infty)$ for $\gamma \geq 0$ and $x \in [u, u - \sigma/\gamma]$(Um et al., 2010).

In this study the L-moment method (Hosking, 1990) was used for determination of GPD parameters. Graphical (The probability (P–P) and the quintile (Q–Q) plots) and statistical (Kolmogorov–Smirnov (KS)) tests were also used for evaluation of fitting. The P-P plot can be obtained by setting the x-axis as empirical and y-axis as theoretical cumulative distribution function (CDF) values, whereas for Q-Q plot observed data values and fitted distribution quintiles were used as x and y axises respectively. Finally from the scattering data points around the perfect fit (1:1) line, one can understand the goodness of fit. On the other hand in statistical test (KS test) which is a nonparametric test, for any random variable X and a sample series of $\{x_1, x_2, x_3, ..., x_n\}$, the empirical CDF of x can be obtained as:

$$F(x) = \frac{1}{n}\sum_{i=1}^{n} I \quad (x_i \leq x) \tag{8}$$

where, condition I is 1 for true and 0 for false (Salarpour et al., 2012). The statistic tests of KS (D_+ and D_-) for two CDF (F_x and F_y) can be calculated as (Salarpour et al., 2012):

$$D_+ = \max(F_x(x) - F_y(x)) \tag{9}$$

$$D_- = \max(F_y(x) - F_x(x)) \tag{10}$$

In this study the mean residual life plot (MRLP) (Lechner et al. 1992) was used for determination of the threshold (Kyselý and Beranová, 2009; Beguería et al, 2011; Shang et al., 2011; Tramblay et al., 2012; Anagnostopoulou and Tolika, 2012; Jahanbaksh Asl et al., 2013; Li et al., 2014; Yilmaz et al., 2014; Burn et al., 2016). The MRLP can be generated by plotting the average of differences between threshold and excesses versus thresholds and the position of the points can be obtained by:

$$\left\{(u, \frac{1}{n_u}\sum_{i=1}^{n_u}(x_{(i)} - u)) : u < x_{\max}\right\} \tag{11}$$

in which $x_{(1)}, ...,x_{(nu)}$ are the partial duration series of observed data (data which exceed threshold u). There are two main criteria for selecting the threshold. Firstly the plot should be approximately linear around the selected point and secondly the generated partial duration series should be satisfyingly fitted to GPD (Coles, 2001). The number of data in partial duration series should be between 1.65 to 3.0 extreme values per block (Yilmaz et al., 2014). Additionally consecutive values will be removed from data for independency of the extremes. Finally, the generated series of extreme precipitation events will be used for calculation of

maximum 24-hr rainfall intensity for 2, 5, 10, 20, 50, 100 and 500 by using the from inverse cumulative distribution function.

APPLICATION AND RESULTS

TREND ANALYSES

Table 1 presents the 30-year mean values of extreme precipitation indices for reference period (1971-2000) and late future (2070-2099) based on GCM results. As we can interpret from the table there will not be any prominent difference between reference period and the end of the current century. On the other hand, during the current century (2020-2099), most of trends in precipitation indices based on projected data will not be significant. The results of trend test of extreme precipitation indices for observed and projected data by MK test is depicted in Table 2. The critical values for MK test at the 0.1, 0.05 and 0.01 significance levels are 1.645, 1.96 and 2.576, respectively. In Table 2, the bolded values were found to be significant considering the critical value for 0.1 level of significance. In term of PRCPTOT there will be a positive trend during the century expect of those GFDL-ESM2M model under RCP8.5 scenario, in which the trend is negative, but non-significant. For RX1day and RX5day the trend will be prominently positive. These two indices are more important in term of flooding and the positive trend can be concerning.

Table 1**.** The 30-year mean values of precipitation indices for reference period (1971-2000) and late future (2070-2099) from GCMs outputs.

	Indices							
Model-scenario	*PRCPTOT (mm)*	*RX1day (mm)*	*RX5day (mm)*	*SDII (mm/day)*	*R10mm*	*R20mm*	*CDD*	*CWD*
GFDL-ESM2M-Ref.	*589.06*	*43.49*	*81.07*	*6.27*	*16.37*	*4.97*	*27.27*	*7.30*
GFDL-ESM2M-RCP4.5	*643.52*	*56.73*	*98.70*	*7.02*	*17.80*	*5.53*	*27.17*	*6.57*
GFDL-ESM2M-RCP8.5	*582.56*	*52.01*	*84.71*	*6.67*	*16.17*	*5.03*	*28.77*	*6.27*
HadGEM2-ES-Ref.	*692.33*	*63.35*	*102.17*	*8.22*	*20.07*	*7.63*	*68.73*	*7.73*
HadGEM2-ES-RCP4.5	*855.03*	*79.28*	*151.41*	*9.55*	*24.43*	*9.87*	*61.37*	*7.43*
HadGEM2-ES-RCP8.5	*809.96*	*78.95*	*132.60*	*9.78*	*23.33*	*9.37*	*64.47*	*7.83*

Table 2**.** The results of trend tests for precipitation indices of observation data.

Dataset	*Precipitation Indices*							
	PRCPTOT	*RX1day*	*RX5day*	*SDII*	*R10mm*	*R20mm*	*CDD*	*CWD*
Obs.	*1.463*	*-0.178*	*0.678*	*0.821*	*1.624*	*1.534*	*0.607*	*-0.607*
GFDL-ESM2M-RCP4.5	***2.646***	***1.719***	*1.232*	***2.26***	***2.132***	***2.078***	*0.07*	*0.923*
GFDL-ESM2M-RCP8.5	*-0.437*	***2.059***	***1.781***	*0.035*	*0.236*	*-0.773*	*0.962*	*-0.185*
HadGEM2-ES-RCP4.5	*1.248*	*0.429*	*0.753*	*0.220*	*1.008*	*-0.066*	*-1.078*	*1.070*
HadGEM2-ES-RCP8.5	*1.626*	*0.668*	*-0.143*	***1.951***	*1.611*	*0.738*	*0.587*	*-0.699*

During the reference period there was a non-strong increasing trend in SDII. While, during the coming years the trends were projected to be strong and positive especially for GFDL-ESM2M under RCP4.5 and HadGEM2-ES under RCP8.5. The trends in R10mm and R20mm were not found to be strong, but only for GFDL-ESM2M under RCP4.5 scenario the trend will be significant considering 0.1 level of significance. In terms of CDD and CWD all trends tests were found as non-significant for past and future projections. Finally, as a whole, the most of trends will be positive without considering of significance, which means that there will be an increasing in the magnitude of the future precipitation.

FREQUENCY ANALYSIS

In this study, the frequency of extreme precipitation events for past and future periods were analyzed by using the peaks over threshold method. The magnitude of probable maximum 24-hr rainfall intensity was calculated from inverse cumulative distribution function which was GPD in this study. The goodness-of-fit of GPD on partial duration datasets which were obtained from past data - including observed and simulated data of GCMs for reference period between 1971 and 2000 - and projected data for 2070-2099 based on the outputs of GCMs, can be inferred from the results of KS test which is presented in Table 3. In the table, the results of KS test for Gamma distribution are also presented in order to making comparison.

Table 3: The results of statistical test (KS test) for goodness of fit of GPD and Gamma distribution for peaks over threshold approach of observed and projected precipitation data.

period	*Reference period (1971-2000)*			*Late future (2070-2099)*			
Dataset	*Obs.*	*GFDL-ESM2M*	*HadGEM2-ES*	*GFDL-ESM2M*		*HadGEM2-ES*	
scenario	---	---	---	*RCP4.5*	*RCP8.5*	*RCP4.5*	*RCP8.5*
GPD	*0.0620*	*0.0606*	*0.0537*	*0.0454*	*0.0728*	*0.0719*	*0.0517*
Gamma	*0.1697*	*0.1519*	*0.2327*	*0.1608*	*0.1458*	*0.1407*	*0.2265*

Table 4 presents the calculated values of maximum 24-hr rainfall intensity for late future period (2070-2099) based on projected data for different return periods. The results are also depicted graphically in Figure 2 and Figure 3 for RCP4.5 and RCP8.5 scenarios respectively. The rainfall intensity were generated by HadGEM2-ES model found to be more than of those GFDL-ESM2M model as can be inferred from the table and figures.

Table 4: Calculated values of rainfall intensity (mm/day) for late future (2070-2099) based on GFDL-ESM2M and HadGEM2-ES data under RCP4.5 and RCP8.5 scenarios by peaks over threshold method.

	return period						
Dataset	*2yr*	*5yr*	*10yr*	*20yr*	*50yr*	*100yr*	*500yr*
GFDL-ESM2M-RCP4.5	*40.61*	*56.88*	*69.46*	*82.28*	*99.60*	*113.00*	*145.11*
GFDL-ESM2M-RCP8.5	*40.06*	*54.84*	*65.15*	*74.75*	*86.46*	*94.62*	*111.51*
HadGEM2-ES-RCP4.5	*65.60*	*92.71*	*111.94*	*130.14*	*152.70*	*168.71*	*202.65*
HadGEM2-ES-RCP8.5	*56.35*	*76.64*	*95.71*	*118.73*	*156.63*	*192.26*	*306.04*

As we can see in the Figure 2 and 3, the magnitude of extreme precipitation by the end of the century will be more than the reference period by approximately 30 % and 40 % under RCP4.5 and RCP8.5 emission scenarios respectively. On the other hand, the percentage of increase for GFDL-ESM2M and HadGEM2-ES models in compare with the observed data found to be 27 % and 43 % respectively. All these results show that the magnitude and intensity of the extreme and hazardous precipitation events will be increased remarkably during the coming years. The other important task in frequency analyses of extreme precipitation events is to select appropriate return period. In this selection one has to investigate the importance of the projects in economic, social and other important concerns.

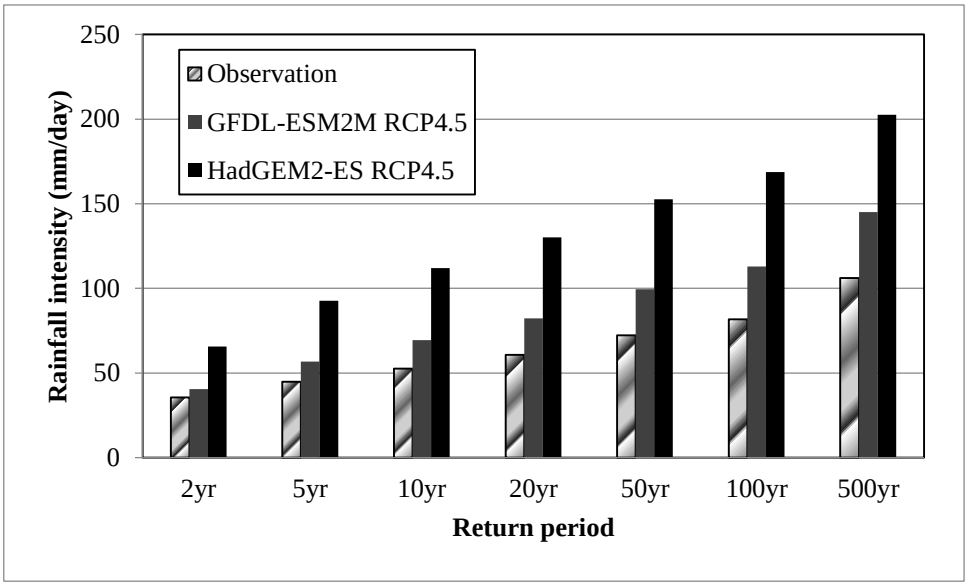

Figure 2: The comparative illustration of results of frequency analyses by peak over threshold method for reference period and late future based on GCMs outputs under RCP4.5 scenario.

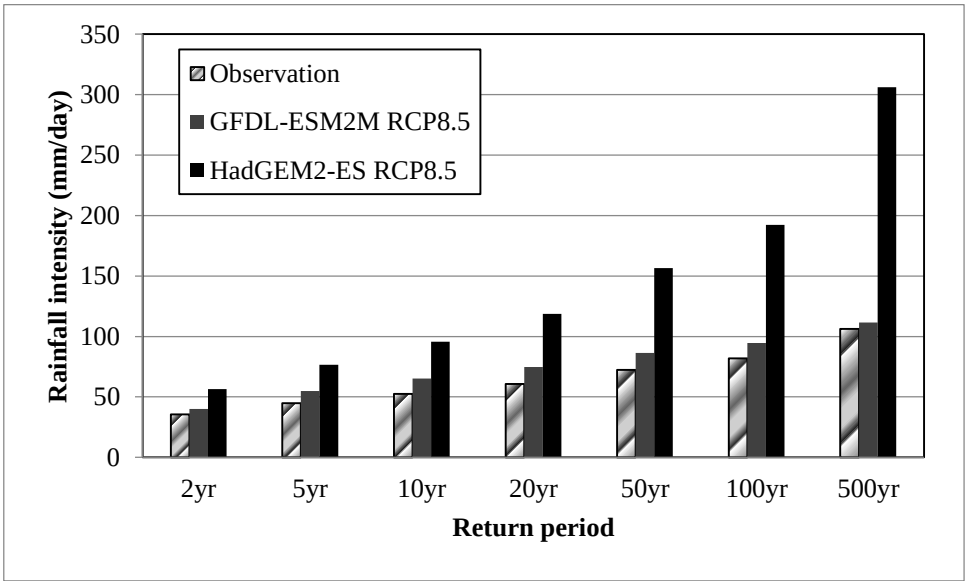

Figure 3: The comparative illustration of results of frequency analyses by peak over threshold method for reference period and late future based on GCMs outputs under RCP8.5 scenario.

SUMMARY AND CONCLUSION

In this study, the impacts of climate change on frequency and magnitude of extreme precipitation events were investigated based on observed and projected data of Karadeniz Ereğli station in Turkey. For projected data dynamically downscaled outputs of GFDL-ESM2M and HadGEM2-ES global circulation models under RCP4.5 and RCP8.5 emission scenarios. The Mann-Kendall test was used in order to trend detection in eight precipitation indices. The frequency analyses of the maximum 24-hr rainfall intensity were established on peaks over threshold method for 2, 5, 10, 20, 50, 100, 500 years return periods. The results of the study show that the trend -especially positive one- for some indices will be significant and remarkable. On the other hand the magnitude of future extreme precipitation events based on the projected values of HadGEM2-ES model will be remarkably increased by the end of the century. As the changes in the total amount of precipitation will not be significant (it inferred

from the results of trend test for PRCPTOT), the increase in extreme precipitation events can be explain as more dry days and more floods in the coming years.

ACKNOWLEDGMENT

The authors wish to thank Turkish State Meteorological Service for providing precipitation data and İTÜ-BAP (39550) for their supports.

REFERENCES

Acar, R., and Senocak, S.(2012). Annual extreme precipitation trends for western Turkey in associated with north Atlantic oscillation (NAO) index. ENERGY EDUCATION SCIENCE AND TECHNOLOGY PART A-ENERGY SCIENCE AND RESEARCH. 29 (1), 475-486.

Anagnostopoulou, C., and Tolika, K. (2012). Extreme precipitation in Europe: statistical threshold selection based on climatological criteria. Theor Appl Climatol. 107:479–489. DOI 10.1007/s00704-011-0487-8.

Balkema AA, de Haan L (1974) Residual life time at great age. Ann Prob. 2:792–804.

Baloch, MA., Ames, DP., and Tanik, A. (2015). Hydrologic impacts of climate and land-use change on Namnam Stream in Koycegiz Watershed, Turkey. Int. J. Environ. Sci. Technol. 12:1481–1494
DOI 10.1007/s13762-014-0527-x.

Bartholy, J., and Pongrácz, R. (2010). Analysis of precipitation conditions for the Carpathian Basin based on extreme indices in the 20th century and climate simulations for 2050 and 2100. Physics and Chemistry of the Earth. 35,43–51.

Beguería, S., Angulo-Martínez, M., Vicente-Serrano, SM., López-Moreno, JI., and El-Kenawy, A. (2011). Assessing trends in extreme precipitation events intensity and magnitude using non-stationary peaks-over-threshold analysis: a case study in northeast Spain from 1930 to 2006 *Int. J. Climatol.* 31: 2102–2114. DOI: 10.1002/joc.2218

Bharti, V., Singh, C., Ettema, J., and Turkington TAR. (2016). Spatiotemporal characteristics of extreme rainfall events over the Northwest Himalaya using satellite data. Int. J. Climatol. 36: 3949–3962.

Booth, ELJ., Byrne, JM., and Johnson, DL. (2012). Climatic changes in western North America, 1950–2005. Int. J. Climatol. 32: 2283–2300.

Burn, DH., Whitfield, PH., and Sharif, M. (2016). Identification of changes in floods and flood regimes in Canada using a peaks over threshold approach Hydrol. Process. 30, 3303–3314. DOI: 10.1002/hyp.10861.

Chattopadhyay, S., Edwards, D. R., and Yu, Y. (2017) Contemporary and Future Characteristics of Precipitation Indices in the Kentucky River Basin Water. 9, 109; doi:10.3390/w9020109.

Chatuverdi, R.K., Joshi, J., Jayaraman, M., Bala, G. and Ravindranath, N.H. (2012). Multi-model climate change projections for India under representative concentration pathways. Current science, 103: 1-12.

Cho, J., Ko, G., Kim, K., and OH. C. (2016) Climate Change Impacts On Agricultural Drought With Consideration Of Uncertainty In Cmip5 Scenarios. Irrig. and Drain. 65: 7–15. DOI: 10.1002/ird.2035.

Coles, S. (2001). An introduction to statistical modeling of extreme values. Springer, Berlin, Heidelberg, London, pp 208.

de Lima, MIP., Santo, FE., Ramos, AM., and Trigo, RM. (2015) Trends and correlations in annual extreme precipitation indices for mainland Portugal, 1941–2007. Theor Appl Climatol. 119:55–75 DOI 10.1007/s00704-013-1079-6.

Deniz, A., Toros, H., and Incecik. S. (2011). Spatial variations of climate indices in Turkey. Int. J. Climatol. 31: 394–403.

Devkota, LP., and Gyawali, DR. (2015). Impacts of climate change on hydrological regime and water resources management of the Koshi River Basin, Nepal. Journal of Hydrology: Regional Studies 4. 502–515.

Demir, O. (2012). Climate Assessment of Turkey in 2012 and Expected Climate Change for Eastern Mediterranean According to HadGEM2 RCP4.5 Scenario. Turkish State Meteorological Service. http://medcof.aemet.es/images/doc_events/scoping/presentations/Demir.pdf (15/09/2017).

Frei, C., Schóll, R., Fukutome, S., Schmidli, J., and Pier Luigi Vidale, P.L. (2006) Future change of precipitation extremes in Europe: Intercomparison of scenarios from regional climate models JOURNAL OF GEOPHYSICAL RESEARCH, VOL. 111, D06105, doi:10.1029/2005JD005965.

Giorgi, F., Coppola, E., Solmon, F., Mariotti, L., Sylla, M.B., Bi, X., Elguindi, N., Diro, G.T., Nair, V., Giuliani, G., Turuncoglu, U.U., Cozzini, S., Güttler, I., O'Brien, T.A., Tawfik, A.B., Shalaby, A., Zakey, A.S., Steiner, A.L., Stordal, F., Sloan, L.C., Brankovic, C., (2012). RegCM4: model description and preliminary tests over multiple CORDEX domains. Clim. Res. 52, 7–29. http://dx.doi.org/10.3354/cr01018.

Hamed, K.H. (2008) Trend detection in hydrologic data: The Mann–Kendall trend test under the scaling Hypothesis. Journal of Hydrology. 349, 350–363. doi:10.1016/j.jhydrol.2007.11.009.

Held IM, and Soden BJ. (2006). Robust responses of the hydrological cycle to global warming. J. Clim. 19: 5686–5699, doi: 10.1175/JCLI3990.1.
Hosking, J. R. M. (1990). L-moments: analysis and estimation of distributions using linear combinations of order statistics, J. Roy. Stat. Soc. B Met., 52, 105–124.
IPCC. 2013. Climate Change 2013: The Physical Science Basis. Contribution of Working Group I to the Fifth Assessment Report of the Intergovernmental Panel on Climate Change, Stocker TF, Qin D, Plattner G-K, Tignor M, Allen SK, Boschung J, Nauels A, Xia Y, Bex V, Midgley PM (eds). Cambridge University Press: Cambridge, UK and New York, USA, doi: 10.1017/CBO9781107415324, 1535 pp.
Jahanbaksh Asl, S., Khorshiddoust, AM., Dinpashoh, Y., and Sarafrouzeh, F. (2013). Frequency analysis of climate extreme events in Zanjan, Iran. Stoch Environ Res Risk Assess. 27:1637–1650. doi 10.1007/s00477-013-0701-6.
Kara, F., and Yucel, I. (2015). Climate change effects on extreme flows of water supply area in Istanbul: utility of regional climate models and downscaling method. Environ Monit Assess. 187: 580. DOI 10.1007/s10661-015-4808-8
Kendall, M.G., 1975. Rank Correlation Methods. Griffin, London.
Kyselý, J. and Beranová, R. (2009). Climate-change effects on extreme precipitation in central Europe: uncertainties of scenarios based on regional climate models Theor Appl Climatol. 95:361–374. DOI 10.1007/s00704-008-0014-8.
Lambert FH, Stine AR, Krakauer NY, and Chiang JCH. (2008). How much will precipitation increase with global warming? EOS Trans. AGU 89(21), 193–194, doi: 10.1029/2008EO210001.
Lechner, JA., Leigh, SD., and Simiu, E. (1992) Recent approaches to extreme value estimation with application to wind speeds. Part I: the Pickands Method. J Wind Eng Ind Aerodyn 41–44:509–519.
Li, Z., Li, C., Xu, Z., and Zhou, X. (2014). Frequency analysis of precipitation extremes in Heihe River basin based on generalized Pareto distribution. Stoch Environ Res Risk Assess. 28:1709–1721. DOI 10.1007/s00477-013-0828-5.
Li, X., Hu, Z., Jiang, X., Li, Y., Gao, Z., Yang, S., Zhu, J., and Jha, B. (2016) Trend and seasonality of land precipitation in observations and CMIP5 model simulations Int. J. Climatol. 36: 3781–3793, DOI: 10.1002/joc.4592.
Mann, H.B., 1945. Nonparametric tests against trend. Econometrica. 13, 245–259.
Mohan, T. S., and M. Rajeevan (2017), Past and future trends of hydroclimatic intensity over the Indian monsoon region, J. Geophys. Res. Atmos., 122, 896–909, doi:10.1002/2016JD025301.
Pal, I., and Al-Tabbaa, A. (2009). Trends in seasonal precipitation extremes – An indicator of 'climate change' in Kerala, India. Journal of Hydrology, 367, 62–69.
Paxian, A., Hertig, E., Seubert, S., Vogt, G., Jacobeit, J., and Paeth, H. (2015). Present-day and future mediterranean precipitation extremes assessed by different statistical approaches. Clim Dyn. 44:845–860 DOI 10.1007/s00382-014-2428-6
Peng, S., Ding, Y., Wen, Z., Chen, Y., Cao, Y., and Ren, J. (2017) Spatiotemporal change and trend analysis of potential evapotranspiration over the Loess Plateau of China during 2011–2100. Agricultural and Forest Meteorology. 233, 183–194.
Pickands J (1975) Statistical inference using extreme order statistics. Ann Stat. 3:119–131.
Ren, Z., Zhang, M., Wang, S., Qiang, F., Zhu, X., and Dong, L. (2015). Changes in daily extreme precipitation events in South China from 1961 to 2011. J. Geogr. Sci. 25(1): 58-68.
Salarpour, M., Yusop, Z., and Yusof, F. (2012). Modeling the Distributions of Flood Characteristics for a Tropical River Basin, Journal of Environmental Science and Technology. 5, 419–429.
Shang, H., Yan, J., Gebremichael, M., and Ayalew, SM. (2011). Trend analysis of extreme precipitation in the Northwestern Highlands of Ethiopia with a case study of Debre Markos Hydrol. Earth Syst. Sci., 15, 1937–1944. doi:10.5194/hess-15-1937-2011
Siswanto, S., van Oldenborgh, G.J., van der Schrier, G., Jilderda, R., and van den Hurk, B. (2016). Temperature, extreme precipitation, and diurnal rainfall changes in the urbanized Jakarta city during the past 130 years. Int. J. Climatol. 36: 3207–3225.
Tian, J., Liu, J., Wang, J., Li, C., Nie, H., and Yu, F. (2017) Trend analysis of temperature and precipitation extremes in major grain producing area of China , Int. J. Climatol. 37: 672–687.
Tramblay, Y., Neppel, L., Carreau, J., and Sanchez-Gomez, E. (2012). Extreme value modelling of daily areal rainfall over Mediterranean catchments in a changing climate Hydrol. Process. 26, 3934–3944. DOI: 10.1002/hyp.8417.
Trenberth KE. (2011). Changes in precipitation with climate change. Clim.Res. 47(4): 123–138, doi: 10.3354/cr00953.
Türkeş, M. and Tatlı, H. (2009) Use of the standardized precipitation index (SPI) and a modified SPI for shaping the drought probabilities over Turkey. Int. J. Climatol. 29: 2270–2282.

Um, MJ., Cho, W., and Heo, JH. (2010). A comparative study of the adaptive choice of thresholds in extreme hydrologic events Stoch Environ Res Risk Assess. 24:611–623. DOI 10.1007/s00477-009-0348-5.
Wang, Y., Zhou, B., Qin, D., Wu, J., Gao, R., and Song, L. (2017) Changes in Mean and Extreme Temperature and Precipitation over the Arid Region of Northwestern China: Observation and Projection ADVANCES IN ATMOSPHERIC SCIENCES. 34, 289–305.
Wen, X., Fang, G., Qi, H., Zhou, L., and Gao, Y. (2016) Changes of temperature and precipitation extremes in China: past and future. Theor Appl Climatol. 126:369–383 DOI 10.1007/s00704-015-1584-x
Wentz FJ, Ricciardulli L, Hilburn K, and Mears C. (2007). How much more rain will global warming bring? Science 317(5835): 233–235, doi: 10.1126/science.1140746.
(WMO) World Meteorological Organization (2009) Guidelines on Analysis of extremes in a changing climate in support of informed decisions for adaptation. Climate Data and Monitoring WCDMP-No. 72.
Xiao, Z., Zhou, X., Yang, P. and Liu, H. (2016) Variation and future trends in precipitation over summer and autumn across the Yunnan region Front. Earth Sci. 10(3): 498–512, DOI 10.1007/s11707-015-0523-6.
Yan, D., Werners, SE., Ludwig, F. and Huang, HQ. (2015) Hydrological response to climate change: The Pearl River, China under different RCP scenarios. Journal of Hydrology: Regional Studies 4 228–245.
Yazid, M. and Usa Humphries, U. (2015). Regional Observed Trends in Daily Rainfall Indices of Extremes over the Indochina Peninsula from 1960 to 2007. Climate, 3, 168-192; doi:10.3390/cli3010168.
Yilmaz, AG., Hossain, I., and Perera, BJC. (2014). Effect of climate change and variability on extreme rainfall intensity–frequency–duration relationships: a case study of Melbourne. Hydrol. Earth Syst. Sci. 18, 4065–4076. doi:10.5194/hess-18-4065-2014
Yilmaz, AG. (2015). The effects of climate change on historical and future extreme rainfall in Antalya, Turkey. Hydrological Sciences Journal – Journal des Sciences Hydrologiques. 60 (12) ,2148-2162
Yucel, I., and Onen, A. (2014). Evaluating a mesoscale atmosphere model and a satellite-based algorithm in estimating extreme rainfall events in northwestern Turkey. Nat. Hazards Earth Syst. Sci., 14, 611–624.

THE EFFECT OF CLIMATE CHANGE ON ATMOSPHERIC WATER VAPOR

Deniz Demirhan Barı

Abstract
Water vapor (WV) is a vital component of the atmosphere and has a pronounced effect on many atmospheric processes. The change in water vapor explains also the change in the greenhouse effect. Hence in the recent years spatial and temporal variability of humidity attracts attention of the scientists. Total precipitable water vapor (PWV) is the whole water, condensed to a liquid phase from the surface to the top of the atmosphere. Evolution of total precipitable water in the atmosphere over Eastern Europe is analyzed by using Coupled Model Intercomparison Project Phase 5 (*CMIP5*), Max Planck Institute for Meteorology (*MPI*-M)-ESM-MR model output RCP4.5 scenario simulations from 2006 to 2099. Seasonal variability in PWV indicates that there is a significant increasing trend in the all seasons. Spatial distribution of PWV shows that by the year 2050, maximum increase is observed over Lithuania, Poland and Moldova and Romania. The increase in the amplitude of PWV slows down between 2050 and 2099 around the study area.

Keywords: *CMIP5 MPI, RCP4.5, Precipitable water vapor, Europe*

Introduction
The atmosphere contains a great amount of moisture. However whole amount of water vapor does not condense into rain or snow because the correct balance of pressure and temperature are needed to create precipitation. Total precipitable water (TPW) in the atmosphere is the amount of water that can be obtained from the surface to the "top" of the atmosphere if all of the water and water vapor were condensed to a liquid phase. The goal of the study is to investigate the past and future long-term changes of the total precipitable water. For this purpose the project will use the projections of Coupled Model Intercomparison Project (CMIP5) and model sensitivity studies with the MPI-ESM. The study will investigate the effect of the climate change on the preciptation and local changes over Eastern Europe from 2006 to 2100.

Data and Method
The data that is used for the present study are the consortia simulations with the Earth-System-Model MPI-ESM performed in the framework of the Climate Modelling Intercomparison Project Phase 5 (CMIP5) were recently presented by MPI-Met/DKRZ (2012). The MPI-ESM includes the general circulation model ECHAM6, the ocean model MPI-OM, the land-biosphere model JSBACH, and the bio-geochemical model HAMMOC describing the ocean's bio-geochemical processes (for details see www.mpimet.mpg.de/en/science/models.html). The study will use provided data of the model version MPI-ESM MR, which includes the ECHAM6 with triangular truncation at wavenumber 63 (horizontal resolution: 1.875° or ~200km) and 95 layers up to a level of 0.01 hPa (~80km), and the MPI-OM with a horizontally varying resolution of 0.4° (~40km) at a mean value and 40 layers for describing the ocean's circulation (MPI-Met/DKRZ, 2012). These simulations are performed for the time period 1960-2005, and for the projections up to the year 2100 based on the scenarios RCP4.5 used for the next IPCC Assessment Report AR5 as described in detail by van Vuuren et al. (2011). RCP4.5 specifies an increase to 4.5 W/m² (~650 ppm CO_2) up to the year 2060, and remaining at this level up to the year 2100. RCP8.5 specifies a constant increase to 8.5 W/m² (~1370 ppm CO_2) up to the year 2100. The CMIP5 data are available at the World Data Centre (WDC) and the Climate and

Environmental Retrieval and Archive (CERA) Gateway (as presented by MPI-Met/DKRZ, 2012). The source code of the MPI-ESM is provided by the MPI-Met, Hamburg.
The total water vapor content, and total horizontal mean flux of water vapor can be obtained by vertical integration:

$$\overline{PW} = \frac{1}{g}\int_{p_s}^{0} M_r dp \qquad (1)$$

The formula (1), M_r indicates the specific humidity, (¯) shows the monthly mean, p is the pressure and g is the gravitational acceleration.
Total precipitable water is calculated for the study area given in Figure 1.

Figure 1. Study area.

Future changes in total preciptable water content

Monthly mean total precipitable water content is analyzed (Figure 2). Figure 2 shows that there is a prominent increase in total water vapor content of the atmosphere in all seasons and it is gradually increasing year by year until 2099. Such an increase is mainly observed over Eastern Turkey, Ukraine and Belarus in January between 2025 and 2050. The seasonal mean precipitable water is averaged longitudinally and deviation from yearly mean is examined for western and the eastern parts of the study area. Western part includes the latitudes averaged between 34°- 46°N and the Eastern part are the averaged latitudes of 46° - 54.5°N. Percantage of deviations from yearly mean total precipitable water increases at the eastern part in January. The deviations at the eastern part is between -30 and +30 percent (Figure 3). On the other hand in the all other seasons the deviations from mean is increasing gradually until the year 2099 but the fluctuations do not exceed -10 and +10 percent.

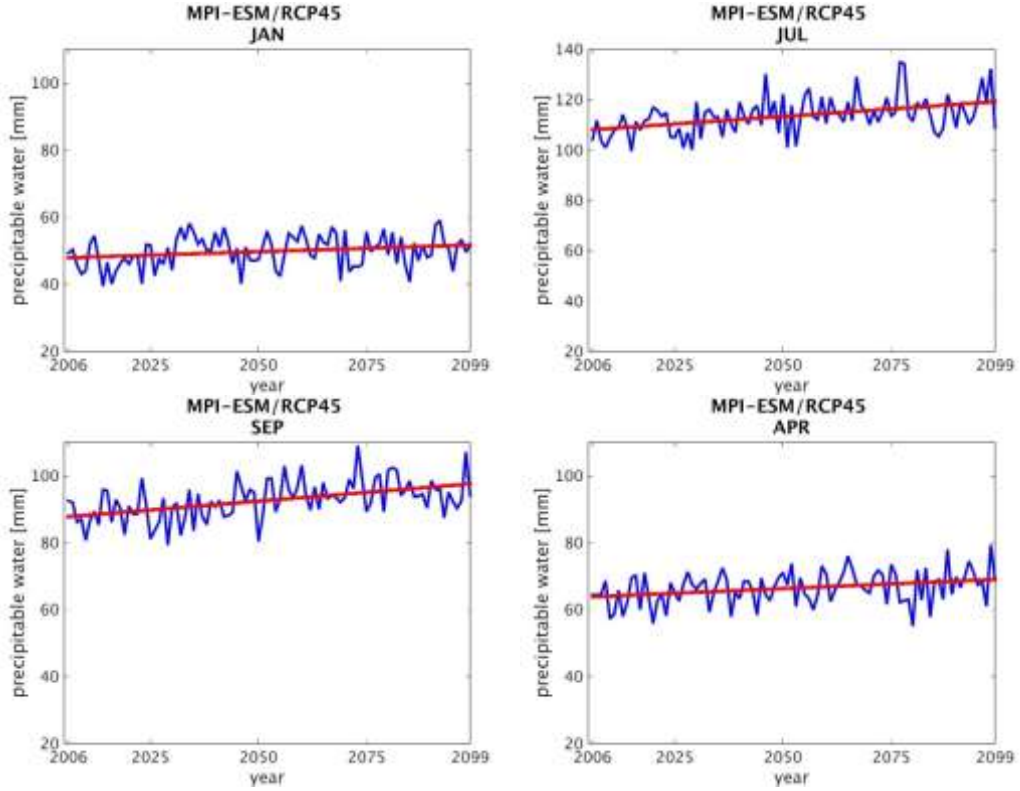

Figure 2. Total precipitable water content from 2006 to 2099 for January, July, September and April.

The trend of the deviation from yearly mean is mainly increased in the summer season. The deviations showed a clear increase from negative deviation values to positive values. Such a trend indicates a significant variation in precipitation until the year 2099.

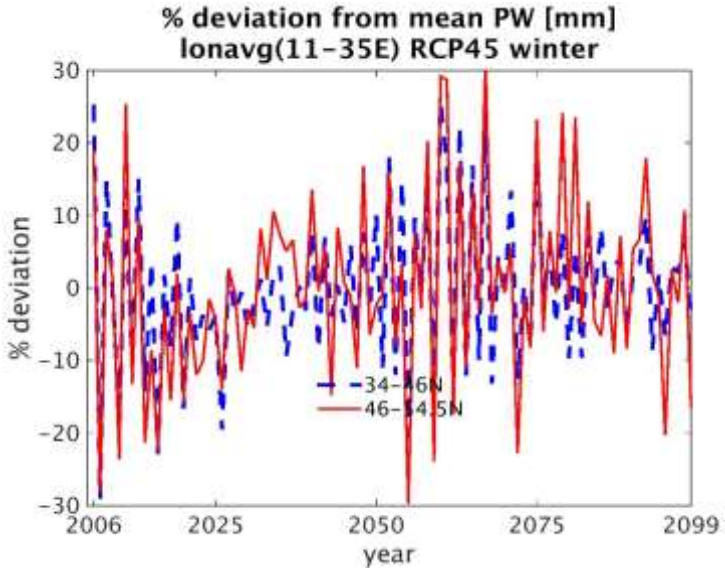

Figure 2. Percantage of deviations from winter yearly mean averaged over longitudes and seperated into 2 different latitudinal sections.

Results and Discussion

The total precipitable water is examined using CMIP5 MPI-MR RCP4.5 data over Eastern Europe. A significant increase in precipitable water in the atmosphere until 2099. Especially

over Turkey and Ukraine, total precipitable water is expected to increase arounf 14% in winter. But over Italy, Germany and Poland, it is around 4%. Such a result shows that future simulations indicate a strong spatial changes in winter.

REFERENCES

MPI-Met and DKRZ, Hamburg (2012): CMIP5-Workshop – "Von der Vergangenheit bis in die Zukunft: Neue Klimasimulationen für Wissenschaft und Gesellschaft", Informationsveranstaltung zum Abschluss der vom BMBF geförderten Konsortialrechnungen im Rahmen des CMIP5 (Coupled Modelling Intercomparison Project Phase 5) und Workshop für Nutzer, 23.-24. Februar 2012, ZMAW, Hamburg, s. http://www.dkrz.de/Klimaforschung/konsortial/ipcc-ar5/daten/workshop_02_12.

Van Vuuren, D.P., and co-authors (2011): The representative concentration pathways: an overview. *Climatic Change*, Volume 109, Numbers 1-2 (2011), 5-31, DOI: 10.1007/s10584-011-0148-z.

CLIMATE CHANGE: MONTHLY PATTERNS OF MINIMUM TEMPERATURES AND THEIR CHANGE

Mesut DEMİRCAN[1], Hüseyin ARABACI[1], Mustafa COŞKUN[1], Necla TÜRKOĞLU[2], İhsan ÇİÇEK[2]

[1]Turkish State Meteorological Service, Ankara, Turkey
mdemircan@mgm.gov.tr, harabaci@mgm.gov.tr, mustafacoskun@mgm.gov.tr,
[2]Ankara University, Faculty of Languages, History and Geography, Ankara, Turkey
Necla.Turkoglu@ankara.edu.tr, ihsan.cicek@ankara.edu.tr

Abstract

Climate change, in other word global warming, is one of the most serious environmental, economic, and social threats that this world faces. A change in the Earth's surface temperature also leads to increase in extreme events as well as extreme temperatures. Climate is the average weather conditions experienced in a particular place over a long period. The standard averaging period is 30 years but other periods may be used depending on the purpose. Climate also includes statistics other than the average, such as the magnitudes of day-to-day, month to month or year-to-year variations. Temperature is analysed with its mean, maximum and minimum values as climate and meteorological aspects. And also temperature has got an oscillation depending on time scale. In this study, it is intend to analysis monthly distributions pattern of minimum temperatures. For this purpose daily minimum temperature values are used from eight stations data with periods of 1971 to 2015 from Turkish State Meteorological Service which are Sarıyer, Sinop, Rize, Aydın, Ankara, Kars, Anamur and Hakkari. Extreme values of minimum temperatures are determined for 1971 to 2015 period, 1971 to 2000 period and 1981 to 2010 period. To determine monthly distribution patterns, it is calculated daily anomalies for each periods according to monthly mean values of extreme minimum temperatures of 1981 and 2010 period. As a result, probability of occurring minimum temperature or maximum temperature in certain time interval in a month may show a pattern in month. Moreover, the pattern is compatible with folk calendar and also the pattern is inclined to change with increasing temperature trend due to climate change. The minimum temperatures have increased with a different number of days according to different months after 1981. These figures changes from 1 day in March to 25 days in August.

Keywords: *Temperature, Maximum, Monthly pattern, Climate change, Folk calendar.*

INTRODUCTION

Climate change, in other word global warming, is one of the most serious environmental, economic, and social threats that this world faces. There are many assessments to monitor climate and to estimate climate variability over many regions and also globally by national and international institutions. A change in the Earth's surface temperature also leads to increase in extreme events as well as extreme temperatures.

Climate is the average weather conditions experienced in a particular place over a long period. Climatological normals are averages for consecutive periods of 30 years which are calculated from climatological data (Demircan et al. 2013; Demircan et al., 2014 [a],[b],[c],[d], Demircan et al., 2017 [a], [b]). Using climate normals are very important tool to provide a standard base for preparing global assessment and climate monitoring studies. The reference period of Climate; 1961-1990, 1971-2000 and 1981-2010 as climate normals are used by scientists, national climate services and international institutions and organizations in international, national and regional-based climate monitoring, climate trends, climate change and climate modelling studies.

Climate also includes statistics other than the average, such as the magnitudes of day-to-day, month to month or year-to-year variations. Temperature is one of the climate parameters and is most interested by the public and the sectors. The temperature is related to the solar energy which, in turn, is absorbed by the Earth's surface and heats the Earth's surface and then the Earth emits it as long wave radiation through the atmosphere into space and determines the climate and weather of the Earth. Greenhouse gases absorbs long wave radiation, thereby trapping and holding heat in the atmosphere. As a result of this, global temperature increases while amount of greenhouse gases increase. Temperature change occurs depending on the factors such as The Earth's rotation around its own axis and Sun, sun radiation and duration, latitude, altitude, distance to water sources, vegetation cover. At the same time it is a continuous climate parameter on the topography. Temperature is analysed with its mean, maximum and minimum values as climate and meteorological aspects. And also temperature has got an oscillation depending on time scale.

DATA AND METHODS

Daily minimum temperature values are used from eight stations data with periods of 1971 to 2015 from Turkish State Meteorological Service which are Sarıyer, Sinop, Rize, Aydın, Ankara, Kars, Anamur and Hakkari. Stations are selected as surrounding the Turkey and also according to direction of air masses which are entering to the Turkey. Extreme values of minimum temperatures are determined for 1971 to 2015 period, 1971 to 2000 period and 1981 to 2010 period from station's daily minimum temperatures data. Monthly mean minimum temperatures are calculated from extreme minimum temperatures of 1981-2010 period. Differences are calculated between daily extreme minimum temperatures of 1971-2000, 1981-2010 and 1971-2015 periods and monthly mean minimum temperatures of 1981-2010 period. Difference graphics are prepared per every months and every stations (Fig.1). Monthly distribution patterns are determined from difference values of 1971-2000 period. Changing in minimum temperatures are determined by comparing of difference values of 1971-2000 period and difference values of other two periods.

APPLICATION AND RESULTS

If the difference values are negative it is accepted as cold and if they are positive accepted as warm. Difference graphics show a pattern that some weeks are cold and some weeks are warm for the 1971-2000, 1981-2000 and 1971-2015 periods as summary (Fig.1). In generally difference values are equal for all periods. For this reason we can expect to occur a heatwave or cold wave according to warm or cold periods of the month as a probabilistic method. By the way, in some days values of 1981-2010 and 1971-2015 periods are bigger or smaller than 1971-2000 period's values which shows changing in climate.

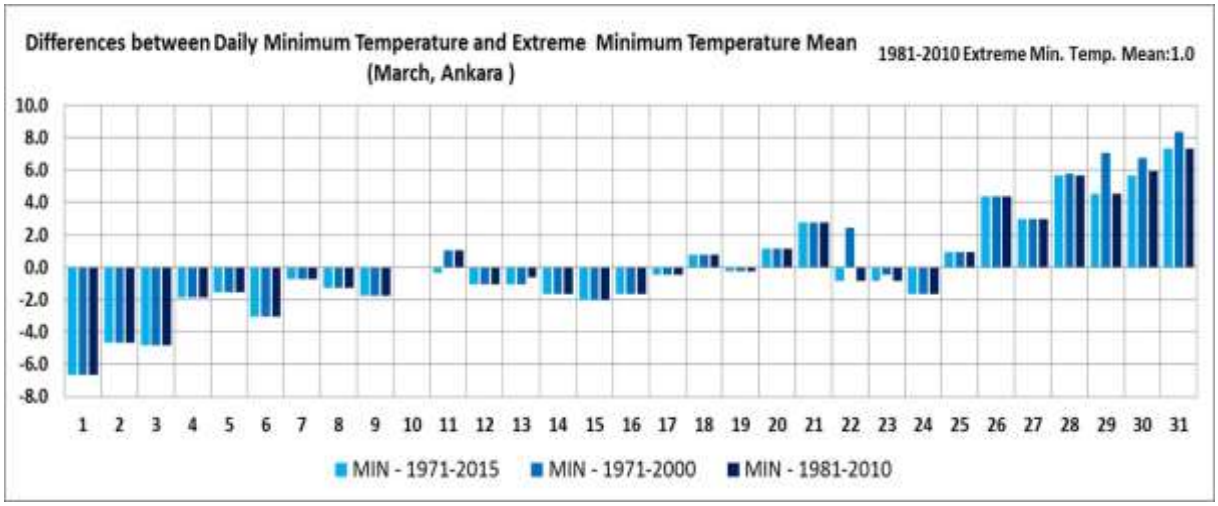

Figure 1. Differences between daily minimum temperature and extreme minimum temperature mean

We are using data sets and graphics and preparing a summary figure (Fig.3) to show monthly pattern and its change in all stations and months together. In this manner, regional and temporal compatibility could easily be seen. In the figure, daily minimum temperatures pattern according to 1971-2000 period are shown as red for warm differences and blue for cold differences. Change in pattern according to 1981-2010 and 1971-2015 periods are shown with figures (△) for increase and (▽) for decrease. In here increasing's meaning is daily extreme minimum temperature is higher than 1971-2000 period's value, in other term is warmer than 1971-2000 period's value and decreasing's meaning is vice versa. The number of increasing, decreasing and no changing days are showed in tables 1 to 12 for each month. The maximum, mean and minimum differences values from mean of 1981-2010 daily extreme minimum temperature are also showed for three periods. Minimum difference value is indicated bottom point of pattern and maximum difference value is indicated top point of pattern. Mean difference value is indicate mean of daily difference values of month.

Daily extreme minimum temperatures were increased 9 to 16 days and decreasing 1 to 11 days in January according to stations (Table 1; Fig. 2). The most increase is seen in two stations which are Ankara and Kars. While minimum difference between monthly mean and daily minimum temperature was -7.8°C in 1971-2000 period, it was increase to -5.5°C in 1981-2010 period in Ankara. In generally it is about 0.5 to 2°C increase in all stations in January is assumed one of the colder months.

Table 1. Daily extra minimum temperatures changes in January.

Stations	Months	Increasing	Decreasing	No changing	1971-2015			1971-2000			1981-2010		
					Diferences from Mean of 1981-2010 Daily Extreme Temperatures (MDET)								
					Maks.	Min.	Mean	Maks.	Min.	Mean	Maks.	Min.	MDET
SARIYER	January	10	11	10	1.7	-6.9	-1.0	2.3	-6.9	-0.4	3.1	-3.9	-2.9
SİNOP		11	8	12	2.1	-3.2	-0.8	2.1	-3.2	-0.5	2.1	-3.2	-1.3
RİZE		11	9	11	1.2	-3.6	-0.8	1.8	-3.6	-0.4	1.6	-2.8	-1.8
AYDIN		9	11	11	1.2	-3.4	-0.9	1.6	-3.4	-0.5	2.0	-2.2	-2.6
ANKARA		16	5	10	2.4	-7.8	-2.0	2.4	-7.8	-1.6	3.4	-5.5	-13.4
KARS		16	5	10	1.9	-8.4	-1.8	2.2	-8.4	-1.5	4.0	-3.6	-28.2
ANAMUR		11	1	19	1.0	-2.0	-0.3	2.0	-2.0	-0.3	1.6	-2.0	2.9
HAKKARİ		12	8	11	2.4	-5.5	-0.6	2.8	-3.5	-0.2	2.8	-5.5	-17.9

Daily extreme minimum temperatures were increased 3 to 19 days and decreasing 4 to 7 days in February according to stations (Table 2; Fig. 2). The most increase is seen in Kars. While minimum difference between monthly mean and daily minimum temperature was -5.8°C in 1971-2000 period, it was increase to -4.9°C in 1981-2010 period in Kars. Minimum difference values are equal for 1971-2000 and 1981-2010 periods due to cold wave occurred in 1985

between 19 to 23 February in Sarıyer, Sinop, Aydın, Ankara, Anamur and in 1984 between 17 to 28 February in Rize and in 1997 between 6 to 11 February in Hakkari.

Table 2. Daily extra minimum temperatures changes in February.

Stations	Months	Increasing	Decreasing	No changing	1971-2015			1971-2000			1981-2010		
					Diferences from Mean of 1981-2010 Daily Extreme Temperatures (MDET)								
					Maks.	Min.	Mean	Maks.	Min.	Mean	Maks.	Min.	MDET
SARIYER	February	6	5	20	1.7	-4.1	-0.4	2.4	-4.1	0.0	3.0	-4.1	-4.3
SİNOP		6	4	21	2.0	-4.6	-0.5	2.0	-4.6	-0.3	2.7	-4.6	-2.9
RİZE		3	4	24	2.6	-3.6	-0.3	3.2	-3.6	0.0	2.6	-3.6	-2.8
AYDIN		4	4	23	1.8	-1.8	-0.3	1.9	-1.8	0.0	1.8	-1.8	-3.4
ANKARA		12	5	14	4.6	-7.6	-1.3	5.9	-7.6	-0.9	4.6	-7.6	-13.9
KARS		19	0	12	2.1	-5.8	-2.5	2.1	-5.8	-2.5	3.3	-4.9	-27.3
ANAMUR		3	7	21	1.8	-2.6	-0.2	2.6	-2.6	0.0	2.0	-2.6	1.8
HAKKARİ		6	4	21	3.5	-4.8	-0.4	5.3	-4.8	-0.2	4.8	-4.8	-17.9

Daily extreme minimum temperatures were increased 1 to 6 days and decreasing 4 to 13 days in March according to stations (Table 3; Fig. 2). The most increase is seen in Kars. While minimum difference between monthly mean and daily minimum temperature was -7.4°C in 1971-2000 period, it was increase to -6.4°C in 1981-2010 period in Kars. Minimum difference values are equal for 1971-2000 and 1981-2010 periods due to cold wave occurred in 1985 between 1 to 13 February in generally.

Table 3. Daily extra minimum temperatures changes in March.

Stations	Months	Increasing	Decreasing	No changing	1971-2015			1971-2000			1981-2010		
					Diferences from Mean of 1981-2010 Daily Extreme Temperatures (MDET)								
					Maks.	Min.	Mean	Maks.	Min.	Mean	Maks.	Min.	MDET
SARIYER	March	3	10	18	3.0	-4.0	-0.1	5.0	-4.0	0.3	3.0	-4.0	-1.8
SİNOP		2	7	22	3.1	-4.4	-0.1	4.0	-4.4	0.2	4.2	-4.4	-0.4
RİZE		0	13	18	2.2	-4.3	-0.1	4.0	-4.3	0.4	2.5	-4.3	-1.8
AYDIN		6	6	19	3.7	-4.4	-0.3	4.8	-4.4	-0.1	4.4	-4.4	-0.6
ANKARA		1	7	23	7.4	-6.6	-0.1	8.4	-6.6	0.2	7.4	-6.6	1.0
KARS		5	4	22	7.3	-7.4	-0.5	13.6	-7.4	0.5	8.8	-6.4	-22.8
ANAMUR		3	4	24	3.4	-2.5	-0.1	3.4	-2.5	0.0	3.4	-2.5	4.5
HAKKARİ		1	5	25	5.2	-7.0	0.0	6.0	-7.0	0.3	5.2	-7.0	-12.0

Daily extreme minimum temperatures were increased 2 to 10 days and decreasing 4 to 12 days in April according to stations (Table 4; Fig. 2). The most increase is seen in Anamur. While minimum difference between monthly mean and daily minimum temperature was -1.7, -2.4, -5.7, -5.1 and -3.9°C in 1971-2000 period, it was decrease to -2.3, -5.4, -6.8, -10.3 and -5.7°C in 1981-2010 period in Sarıyer, Rize Ankara, Kars and Hakkari, respectively. Minimum difference values decrease in these stations due to cold wave in first week of April in 2003. The results suggest that there could be a cooling trend for April.

Table 4. Daily extra minimum temperatures changes in April.

Stations	Months	Increasing	Decreasing	No changing	1971-2015			1971-2000			1981-2010		
					Diferences from Mean of 1981-2010 Daily Extreme Temperatures (MDET)								
					Maks.	Min.	Mean	Maks.	Min.	Mean	Maks.	Min.	MDET
SARIYER	April	3	6	22	2.4	-2.3	-0.2	2.4	-1.7	0.1	2.6	-2.3	2.4
SİNOP		2	7	22	2.5	-3.0	-0.2	2.5	-3.0	0.2	2.5	-3.0	3.5
RİZE		7	9	15	2.2	-5.4	-0.4	3.2	-2.4	0.0	2.2	-5.4	2.6
AYDIN		8	4	19	2.6	-4.4	-0.4	2.6	-4.4	-0.2	3.4	-4.4	3.6
ANKARA		8	5	18	4.9	-6.8	-0.5	4.9	-5.7	-0.2	4.9	-6.8	8.4
KARS		6	12	13	3.8	-10.3	-0.9	4.1	-5.1	0.0	5.0	-10.3	-8.1
ANAMUR		10	0	21	2.3	-4.3	-0.4	2.3	-4.3	-0.4	2.7	-4.3	7.9
HAKKARİ		7	8	16	3.8	-5.7	-0.4	4.4	-3.9	0.0	5.2	-5.7	-2.4

Daily extreme minimum temperatures were increased 1 to 8 days and decreasing 4 to 9 days in May according to stations (Table 5; Fig. 2). The most increase is seen in Hakkari. The results suggest that there could be a cooling trend for May.

Table 5. Daily extra minimum temperatures changes in May.

Stations	Months	Increasing	Decreasing	No changing	1971-2015			1971-2000			1981-2010		
					Diferences from Mean of 1981-2010 Daily Extreme Temperatures (MDET)								
					Maks.	Min.	Mean	Maks.	Min.	Mean	Maks.	Min.	MDET
SARIYER	May	7	5	19	3.0	-4.6	-0.3	3.0	-4.6	-0.2	3.0	-4.6	7.6
SİNOP		2	4	25	3.2	-9.3	-0.6	3.2	-3.8	-0.2	3.2	-3.8	8.6
RİZE		5	5	21	3.5	-8.8	-0.6	3.5	-3.9	-0.1	3.7	-3.9	8.1
AYDIN		1	4	26	2.0	-4.0	-0.2	2.6	-4.0	-0.1	2.0	-4.0	8.6
ANKARA		3	4	24	4.7	-7.4	-0.1	4.7	-7.4	0.0	4.7	-7.4	12.6
KARS		5	9	17	2.8	-3.7	-0.4	5.3	-3.7	0.3	3.5	-3.7	-2.3
ANAMUR		7	4	20	3.0	-3.2	-0.4	3.0	-3.2	-0.3	3.0	-3.2	11.8
HAKKARİ		8	7	16	4.3	-4.1	-0.4	4.3	-4.1	-0.1	5.3	-4.1	3.7

Daily extreme minimum temperatures were increased 5 to 19 days and decreasing 1 to 7 days in June according to stations (Table 6; Fig. 2). The most increase is seen in Anamur. While minimum difference between monthly mean and daily minimum temperature was -4.4, -2.8, -4.5 and -3.7°C in 1971-2000 period, it was increase to -2.6, -2.5, -3.0 and -2.8°C in 1981-2010 period in Sinop, Rize, Anamur and Hakkari, respectively.

Table 6. Daily extra minimum temperatures changes in June.

Stations	Months	Increasing	Decreasing	No changing	1971-2015			1971-2000			1981-2010		
					Diferences from Mean of 1981-2010 Daily Extreme Temperatures (MDET)								
					Maks.	Min.	Mean	Maks.	Min.	Mean	Maks.	Min.	MDET
SARIYER	June	11	5	15	2.5	-4.0	-0.5	2.9	-4.0	-0.4	2.5	-4.0	12.5
SİNOP		11	1	19	1.6	-4.4	-0.5	1.6	-4.4	-0.5	3.2	-2.6	13.2
RİZE		9	6	16	2.1	-2.8	-0.4	2.5	-2.8	-0.2	2.3	-2.5	12.5
AYDIN		5	2	24	2.1	-5.3	-0.3	2.2	-5.3	-0.3	2.2	-5.3	13.7
ANKARA		6	4	21	3.2	-4.4	-0.1	3.8	-4.4	0.1	5.5	-4.4	8.4
KARS		12	7	12	2.8	-4.2	-0.5	2.8	-4.2	-0.2	2.8	-4.2	1.4
ANAMUR		19	0	12	2.0	-4.5	-1.1	2.0	-4.5	-1.1	2.5	-3.0	16.7
HAKKARİ		12	3	16	3.3	-3.7	-0.6	3.3	-3.7	-0.5	3.3	-2.8	9.1

Daily extreme minimum temperatures were increased 6 to 21 days and decreasing 1 to 9 days in July according to stations (Table 7; Fig. 2). The most increase is seen in Anamur. While minimum difference between monthly mean and daily minimum temperature was -2.3, -2.8, and -3.2°C in 1971-2000 period, it was increase to -2.2, -2.6, and -2.5°C in 1981-2010 period in Sinop, Aydın and Anamur, respectively. It was decrease -2.8 and -2.0°C to -3.4 and -3.6°C in Kars and Hakkari, respectively.

Table 7. Daily extra minimum temperatures changes in July.

Stations	Months	Increasing	Decreasing	No changing	1971-2015			1971-2000			1981-2010		
					Diferences from Mean of 1981-2010 Daily Extreme Temperatures (MDET)								
					Maks.	Min.	Mean	Maks.	Min.	Mean	Maks.	Min.	MDET
SARIYER	July	13	3	15	1.4	-3.2	-0.5	1.4	-3.2	-0.5	2.8	-3.2	15.2
SİNOP		8	1	22	1.7	-2.3	-0.3	1.7	-2.3	-0.3	2.1	-2.2	15.9
RİZE		11	1	19	1.3	-3.7	-0.6	1.3	-3.7	-0.6	2.9	-3.7	15.7
AYDIN		11	3	17	1.8	-2.8	-0.7	2.0	-2.8	-0.5	2.6	-2.6	16.2
ANKARA		6	4	21	2.7	-4.0	-0.3	2.8	-4.0	0.0	3.4	-4.0	22.2
KARS		14	9	8	3.4	-3.4	-0.6	3.6	-2.8	-0.3	3.5	-3.4	4.6
ANAMUR		21	0	10	0.8	-3.2	-0.9	0.8	-3.2	-0.9	1.6	-2.5	19.4
HAKKARİ		8	7	16	1.9	-3.6	-0.3	2.2	-2.0	-0.2	2.4	-3.6	13.6

Daily extreme minimum temperatures were increased 3 to 25 days and decreasing 1 to 8 days in August according to stations (Table 8; Fig. 2). The most increase is seen in Anamur. While minimum difference between monthly mean and daily minimum temperature was -2.0, -2.7, and -3.7°C in 1971-2000 period, it was increase to -1.7, -2.1, and -2.0°C in 1981-2010 period in Sinop, Aydın and Anamur, respectively.

Table 8. Daily extra minimum temperatures changes in August.

Stations	Months	Increasing	Decreasing	No changing	1971-2015			1971-2000			1981-2010		
					Diferences from Mean of 1981-2010 Daily Extreme Temperatures (MDET)								
					Maks.	Min.	Mean	Maks.	Min.	Mean	Maks.	Min.	MDET
SARIYER	August	13	1	17	1.2	-3.0	-0.7	1.2	-3.0	-0.6	2.8	-3.0	15.8
SİNOP		10	4	17	1.3	-2.3	-0.3	1.5	-2.0	-0.2	1.3	-1.7	16.5
RİZE		8	3	20	1.0	-2.0	-0.2	1.6	-2.0	-0.2	1.9	-2.0	15.8
AYDIN		15	2	14	1.2	-2.7	-0.7	1.2	-2.7	-0.6	2.1	-2.1	16.4
ANKARA		10	0	21	3.1	-3.9	-0.4	3.1	-3.9	-0.4	3.1	-3.9	22.9
KARS		9	8	14	1.8	-2.7	-0.4	2.7	-2.7	0.0	3.7	-2.7	4.3
ANAMUR		25	1	5	0.9	-3.7	-1.6	0.9	-3.7	-1.6	2.0	-2.0	19.5
HAKKARİ		3	4	24	2.9	-3.4	-0.2	2.9	-3.4	0.0	2.9	-3.4	13.1

Daily extreme minimum temperatures were increased 3 to 19 days and decreasing 2 to 11 days in September according to stations (Table 9; Fig. 2). The most increase is seen in Anamur. While minimum difference between monthly mean and daily minimum temperature was -2.8, -6.3 and -4.3°C in 1971-2000 period, it was increase to -2.2, -3.5, and -2.3°C in 1981-2010 period in Aydın, Ankara and Anamur, respectively. It was decrease -3.5°C to -3.9°C in Kars.

Table 9. Daily extra minimum temperatures changes in September.

Stations	Months	Increasing	Decreasing	No changing	1971-2015			1971-2000			1981-2010		
					Diferences from Mean of 1981-2010 Daily Extreme Temperatures (MDET)								
					Maks.	Min.	Mean	Maks.	Min.	Mean	Maks.	Min.	MDET
SARIYER	September	9	7	15	2.5	-4.8	-0.5	2.8	-2.4	-0.2	2.5	-2.4	11.9
SİNOP		7	8	16	2.9	-5.0	-0.4	3.5	-5.0	-0.1	3.1	-5.0	12.7
RİZE		7	2	22	3.9	-3.2	-0.1	3.9	-3.2	-0.1	3.9	-3.2	12.4
AYDIN		14	4	13	2.5	-4.2	-0.8	2.5	-2.8	-0.6	2.8	-2.2	11.8
ANKARA		5	11	15	3.7	-6.7	-0.4	4.7	-6.3	0.1	3.7	-3.5	8.4
KARS		3	10	18	5.4	-3.9	-0.4	5.4	-3.5	0.0	5.4	-3.9	-0.3
ANAMUR		19	4	8	1.6	-4.3	-1.1	1.6	-4.3	-1.0	2.3	-2.3	16.9
HAKKARİ		8	3	20	4.8	-4.5	-0.4	4.8	-4.5	-0.3	5.0	-4.5	8.8

Daily extreme minimum temperatures were increased 1 to 15 days and decreasing 2 to 11 days in October according to stations (Table 10; Fig. 2). The most increase is seen in Sinop. While minimum difference between monthly mean and daily minimum temperature was -4.4, -9.5 and -4.9°C in 1971-2000 period, it was increase to -4.0, -3.7, and -4.7°C in 1981-2010 period in Sarıyer, Kars and Anamur, respectively. It was decrease -3.8°C to -4.0 °C in Sinop.

Table 10. Daily extra minimum temperatures changes in October.

Stations	Months	Increasing	Decreasing	No changing	1971-2015			1971-2000			1981-2010		
					Diferences from Mean of 1981-2010 Daily Extreme Temperatures (MDET)								
					Maks.	Min.	Mean	Maks.	Min.	Mean	Maks.	Min.	MDET
SARIYER	October	8	17	6	2.2	-4.4	-1.5	2.3	-4.4	-0.7	3.2	-4.0	7.8
SİNOP		15	8	8	2.0	-4.4	-1.2	2.2	-3.8	-0.8	2.0	-4.4	8.6
RİZE		12	8	11	1.8	-4.7	-1.0	2.5	-4.7	-0.8	2.9	-4.7	7.9
AYDIN		8	8	15	2.3	-4.7	-1.1	3.1	-4.7	-0.7	4.4	-4.7	6.7
ANKARA		7	9	15	3.9	-5.6	-0.9	5.4	-5.6	-0.1	5.4	-5.6	10.8
KARS		14	3	14	3.3	-9.5	-1.5	3.3	-9.5	-1.5	3.7	-3.7	-6.3
ANAMUR		15	10	6	1.4	-4.9	-1.4	1.6	-4.9	-1.0	1.7	-4.7	13.1
HAKKARİ		1	6	24	3.6	-4.9	-0.1	4.6	-4.9	0.1	4.6	-4.9	1.8

Daily extreme minimum temperatures were increased 3 to 9 days and decreasing 4 to 7 days in November according to stations (Table 11; Fig. 2). The most increase is seen in Hakkari. While minimum difference between monthly mean and daily minimum temperature was -5.4°C in 1971-2000 period, it was increase to -5.2°C in 1981-2010 period in Ankara. It was decrease -1.8°C to -2.0 °C in Rize.

Table 11. Daily extra minimum temperatures changes in November.

Stations	Months	Increasing	Decreasing	No changing	1971-2015			1971-2000			1981-2010		
					Diferences from Mean of 1981-2010 Daily Extreme Temperatures (MDET)								
					Maks.	Min.	Mean	Maks.	Min.	Mean	Maks.	Min.	MDET
SARIYER	November	6	6	19	2.2	-2.8	-0.4	3.3	-2.8	0.0	4.4	-2.8	1.4
SİNOP		4	7	20	2.2	-3.1	-0.3	2.3	-3.1	-0.2	4.7	-3.1	2.7
RİZE		7	6	18	2.3	-2.0	-0.2	2.3	-1.8	0.0	3.4	-2.0	2.4
AYDIN		5	5	21	4.4	-2.4	-0.3	4.6	-2.4	0.0	4.4	-2.4	0.4
ANKARA		3	6	22	3.3	-5.4	-0.4	4.0	-5.4	-0.2	4.4	-5.2	2.2
KARS		8	6	17	5.9	-13.1	-2.2	7.1	-13.1	-1.5	9.1	-13.1	-16.3
ANAMUR		7	4	20	2.7	-5.0	-0.4	3.7	-5.0	-0.2	3.3	-5.0	7.3
HAKKARİ		9	5	17	6.6	-7.4	-0.4	6.6	-7.4	-0.1	6.6	-7.4	-7.6

Daily extreme minimum temperatures were increased 1 to 9 days and decreasing 5 to 17 days in December according to stations (Table 12; Fig. 2). The most increase is seen in Ankara. While minimum difference between monthly mean and daily minimum temperature was -1.8°C in 1971-2000 period, it was increase to -1.9°C in 1981-2010 period in Aydın. It was decrease -2.6 and -4.5°C to -3.4 and -5.1°C in Rize and Kars, respectively. The results suggest that there could be a cooling trend for December.

Table 12. Daily extra minimum temperatures changes in December.

Stations	Months	Increasing	Decreasing	No changing	1971-2015			1971-2000			1981-2010		
					Diferences from Mean of 1981-2010 Daily Extreme Temperatures (MDET)								
					Maks.	Min.	Mean	Maks.	Min.	Mean	Maks.	Min.	MDET
SARIYER	December	7	9	15	1.7	-2.8	-0.4	1.7	-2.8	-0.1	2.4	-2.8	-1.0
SİNOP		3	17	11	1.3	-2.5	-0.2	2.7	-2.5	0.6	2.3	-2.5	0.3
RİZE		1	12	18	2.2	-3.4	-0.2	2.6	-2.6	0.1	2.6	-3.4	-0.6
AYDIN		4	6	21	1.7	-1.9	-0.2	1.7	-1.8	0.0	1.9	-1.9	-1.9
ANKARA		9	11	11	2.1	-5.5	-0.9	2.1	-3.6	-0.5	5.1	-3.6	-1.5
KARS		4	12	15	6.9	-5.1	-0.3	6.9	-4.5	0.5	6.9	-5.1	-25.3
ANAMUR		6	5	20	2.2	-3.3	-0.5	2.2	-3.3	-0.3	2.2	-3.3	4.5
HAKKARİ		5	9	17	5.5	-5.3	-0.5	5.5	-5.3	-0.1	5.5	-5.3	-16.0

Extreme minimum temperatures were increased 9 to 16 days in January, 3-19 days in February, 1 to 6 days in March, 2 to 10 days in April, 1 to 8 days in May, 5 to 19 days in June, 8 to 21 in July, 3 to 25 days in August, in 3 to 19 days in September, 1 to 15 days in October, 3 to 9 days in November and 1 to 9 days in December since the year 1981. Extreme minimum temperatures were decreased 1 to 11 days in January, 0-7 days in February, 4 to 13 days in March, 0 to 12 days in April, 4 to 9 days in May, 0 to 7 days in June, 0 to 9 in July, 0 to 8 days in August, in 2 to 11 days in September, 3 to 17 days in October, 4 to 7 days in November and 5 to 17 days in December since the year 1981.

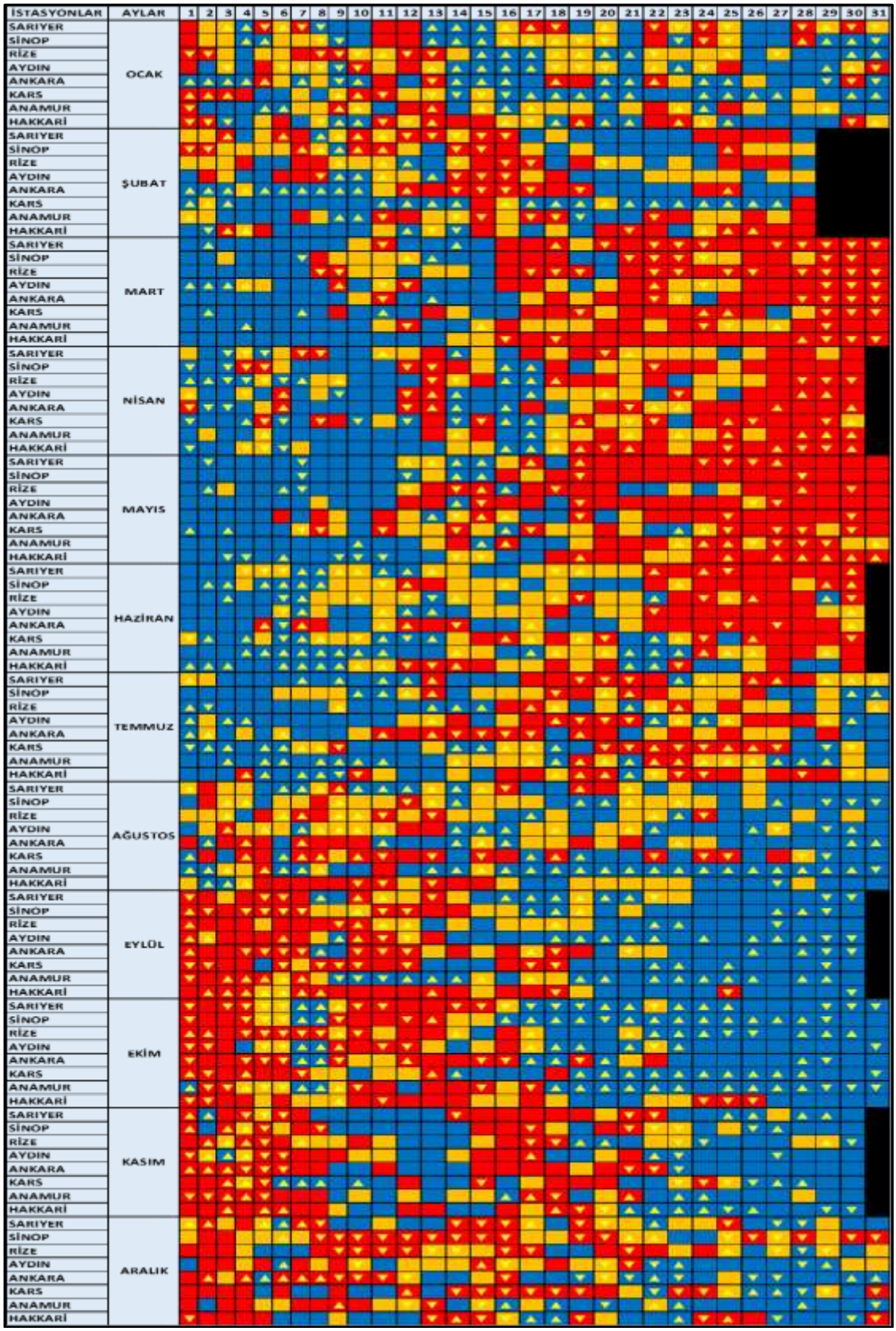

Figure 2. Daily minimum temperatures pattern and its change (warm–red, cold–blue; increase–△, decrease–▽).

CONCLUSIONS AND RECOMMENDATIONS

We've investigate daily extreme minimum temperature for its pattern and change with 8 stations which are located east to west and south to north in Turkey. Daily distribution of daily extreme minimum temperatures in a month shows a pattern which reflects warm and cold periods. Moreover, in generally stations monthly patterns are very similarly even though they are located in different geography. Additionally, this monthly pattern, warm and cold days, are generally compatible with public calendar which is familiar for Turkish people and based on long time public experience and knowledge on climate. Demircan et al. (2017) concluded that extreme maximum temperatures shows a pattern in month and also this pattern shows probability of occurring maximum temperature in certain time interval in a month. Moreover, the pattern is compatible with folk calendar and also the pattern is inclined to change with increasing temperature trend due to climate change. They found an increase in daily extreme temperature about 12-23 days and about 1-6 days in all months. Furthermore monthly patterns are compatible with occurring heatwaves in 2015 and February 2016. Extreme minimum temperatures are increased about 1 to 25 days and decreasing 1 to 17 days in months. Number of increasing days are more than decreasing days. Respectively, station's mean increasing and decreasing days are 12 and 7 in January, 7 and 4 days in February, 3 and 7 in March, 6 and 6 in April, 4 and 5 in May, 10 and 3 in June, 11 and 3 in July, 11 and 3 in August, 9 to 6 in September, 10 and 8 in October, 6 and 6 in November and 4 to 10 in December. The results suggest that there is a changing temperature pattern of months. While January, February, July, August, September and October are warming, March, April, May, June and December are cooling. This suggests needs to deeply researches on changing trends of these months separately. On the other hand these changing are signals of the new pattern. It is assumed that until new patterns are occurred by climate change, numbers and severity of extreme events are also increased rather than our familiar climate conditions.

REFERENCES

Demircan,M, Arabaci, H., Bölük, E., Akçakaya, A., And Ekici, M., Climate Normal's: Relationship and Spatial Distribution of Three Normal's, III. Turkey Climate Change Conference (TİKDEK 2013), 3 - 5 June, 2013, İstanbul, Turkey (Turkish).

Demircan, M., Demir, Ö., Atay, H., Eskioğlu, O., Tüvan, A. ve Akçakaya, A., (8-10 Ekim 2014). Climate Change Projections for Turkey with New Scenarios. The Climate Change and Climate Dynamics Conference-2014 – CCCD2014, İstanbul, Türkiye [a].

Demircan, M., Demir,Ö., Atay,H., Eskioğlu, O., Tüvan, A., Gürkan., H. and Akçakaya, A., Climate Change Projections in Turkey with New Scenarios,TUCAUM VIII. Geography Symposium, Ankara University Turkey Geography Research Center, October 23 to 24 in 2014, Ankara, Turkey (Turkish) [b].

Demircan, M., Demir,Ö., Atay,H., Eskioğlu, O., Tüvan, A., Gürkan., H. and Akçakaya, A., Climate Change Projections in Turkey's River Basin with New Scenarios, TUCAUM VIII. Geography Symposium, Ankara University Turkey Geography Research Center, October 23 to 24 in 2014, Ankara, Turkey (Turkish) [c].

Demircan, M., Çiçek, İ., Türkoğlu,N., Ekici, M., and Arabacı, H., Relationship Between Homogeneity Breaking Points in Average Temperatures And Climate Index, TUCAUM VIII. Geography Symposium, Ankara University Turkey Geography Research Center, October 23 to 24 in 2014, Ankara, Turkey (Turkish) [d].

Demircan, M., Arabacı, H., Gürkan, H., Eskioğlu, O., Coşkun, M., Climate Change Projections for Turkey: Three Models and Two Scenarios, Türkiye Su Bilimi ve Yönetimi Dergisi (Turkish Journal Of Water Science & Management), ISSN: 2536 474X Publication number:6777, Volume: 1 Issue: 1, January 2017, Ankara [a].

Demircan, M., Arabaci, H., Coskun, M., Turkoglu, N., Cicek, I., Climate Change and Public Calendar: Maximum Temperature Patterns and It's Change, Turkey Climate Change Congress - TCLCC'2017 5-7 July 2017, Istanbul, Turkey [b]

Demircan, M., Arabacı, H., Coşkun, M., Türkoğlu, N., ve Çiçek, İ., Sıcaklıkların Aylık Dağılım Desenleri, TUCAUM 2016 Uluslararası Coğrafya Sempozyumu, 13-14 Ekim 2016, Ankara

Özdemir, M., A., Bozyurt, O., Afyonkarahisar Halk Takviminin Sıcaklık Verileri ile Karşılaştırılması, Doğu Coğrafya Dergisi, Cilt 11, Sayı 15, Sayfa 53-82, 2006

CLIMATE CHANGE AND URBANIZATION: MINIMUM TEMPERATURE TRENDS

Mesut Demircan, Hüseyin Arabacı, Alper Akçakaya, Serhat Sensoy, Erdoğan Bölük, Ali Ümran Kömüşcü, Mustafa Coşkun

[1]Turkish State Meteorological Service, Ankara, Turkey

mdemircan@mgm.gov.tr, harabaci@mgm.gov.tr, aakcakaya@mgm.gov.tr, ssensoy@mgm.gov.tr, , aukomuscu@mgm.gov.tr, eboluk@mgm.gov.tr, mustafacoskun@mgm.gov.tr

Abstract

Human influence has also led to significant regional temperature increases at the continental and subcontinental levels. Warming continued in 2016, setting a new temperature record of approximately 1.1°C above the pre-industrial period (WMO, 2016). Understanding the long-term change of temperature events is important to the detection and attribution of climate change. However, it's unclear how much effect coming from the urbanization. In this study Adana, Kayseri, Rize, Sanliurfa and Van have been selected as an urban stations which show the city characteristic and Akcakale, Gevas, Karaisali, Pazar, Pinarbasi and Tomarza have been selected as rural stations which show rural characteristic. Cities were determined as rural area, if the population is less than 100 thousand. Turkish State Meteorological Service's mean minimum temperature data with the periods 1971-2014 and Mann-Kendall rank correlation statistics for trend analysis were used in study. All city stations and Pazar from rural stations have showed significant increasing trend in their mean minimum temperatures. Other rural stations haven't showed increasing or decreasing trend. And also stations couples have been created between urban and rural stations by taking the differences from their mean minimum temperatures. These station couples' data have also showed significant increasing trend.

Keywords: *Urbanization, mean minimum temperature, Mann-Kendall, trend*

INTRODUCTION

One of the main problems of urban residents is "urban heat island" which occurs depending on the horizontal and vertical development of cities. Formed by structuring and the increasing of impermeable surfaces, urban heat island causes cities to be hotter than the rural areas around the city (Bilgili and Sahin, 2013). "Urban heat island - UHI" was firstly defined by Luke Howard in 1820 for London, and it has been researched for several different cities in the world. Urban heat island is one of most significant climate indications of modern day civilization (Duman Yüksel and Yılmaz 2008; Bilgili and Sahin, 2013).

WMO (1983) defines urban climate as local climate that is modified by interactions between the builtup area including waste heat and the emission of air pollutants and regional climate. The climate of a city is a local mesoclimate (spatial extension about 250 km).The city affects both physical and chemical processes in the atmospheric boundary layer (the lowest 1000 m of the atmosphere) (Mayer,1992;Fezer, 1995; WHO, 2004; Duman Yüksel and Yılmaz 2008).

Temperatures are generally higher in urban areas, exposure to heat may be greater in large cities due to the UHI effect, which may amplify the regional heat load during heatwave events. UHI is caused by many factors, including less radiant heat loss in the urban canopy layer, changes in the energy and water balances and lower wind velocities compared to rural environs (Arnfield, 2003; WMO-NO.1142). Accordingly, local and regional climates can be modified significantly by urbanization and other land-use changes.

According to population; urban stations are defined in regions having population over 500.000 and rural stations with population of less than 100.000 (Hua et al., 2007; Kındap et al., 2012)

There were many studies on effect of urbanization on climate (Çiçek, 2004, Kindap et al. 2012, Taha, 1992, Tanrıkulu, 2006, Sensoy, 2015, and Demircan 2017) in Turkey. They all investigated differences in climate between urban and rural cities with different climatological parameters such as temperature, precipitation, albedo, evapotranspiration etc. In generally they found an urbanisation effect on climate.

Urban–nonurban differences in minimum temperature serve as the primary indicator of the magnitude of the heat island effect because urban–nonurban temperature differences are normally most pronounced at night (Rosenzweig et al., 2005).

In 2016, the mean global temperature was 0.94°C above the 20th century average of 14.0°C and 2016 becomes the warmest year since observation stated in the world. Turkey annual mean temperature in 2016 was 14.5°C. This value is 1.0°C above from 1981-2010 normal (13.5°C). 2016 was the fourth warmest year since 1971 and still 2010 is warmest year with 2.0°C above from normal.

DATA AND METHODS

We have used criteria of Hua et al., 2007 and Kındap et al., 2012 to select urban and rural stations. Urban stations have been selected in cities having population over 500.000 and rural stations with population of less than 100.000. Adana, Kayseri, Rize, Sanliurfa and Van have been selected as urban stations which show the urban characteristic and Akcakale, Gevas, Karaisali, Pazar, Pinarbasi and Tomarza stations have been selected as rural stations which show rural characteristic. Minimum temperature is the primary indicator of UHI (Rosenzweig et al., 2005). We have, therefore, used mean minimum temperatures of stations mentioned in above. Turkish State Meteorological Service's mean minimum temperature data with the periods 1971-2014 have been used in the study.

The UHI effect refers to an increase in urban air temperatures as compared to surrounding suburban and rural temperatures (Oke, 1982; Quattrochi et al., 2000). UHI effect is defined as:

$$\Delta T_{u-r} = T_u - T_r \quad (1)$$

Where; T_u is the urban station temperature, T_r is the rural station temperature, ΔT_{u-r} is the effect of UHI.

We have prepared mean minimum time series for all stations and also time series of mean minimum temperatures differences for city-rural pairs for UHI effect. City-rural pairs are Adana-Karaisali, Kayseri-Pinarbasi, Kayseri-Tomarza, Rize-Pazar, Sanliurfa-Akcakale and Van-Gevas. Mann-Kendall rank correlation statistics for trend analysis have been used for stations time series trends analysis and also time series of mean minimum temperatures differences for city-rural pairs.

APPLICATION AND RESULTS

Adana has been selected as urban station and Karaisali has been selected as rural station for station's pair Adana-Karaisali. The population is 2.165.595 in Adana with 7.9% increasing rate and 21.682 in Karaisali with -24.6 decreasing rate since 2007 (URL 1). The yearly mean temperature is increasing in both station according to 1971 and there is a difference between

stations' temperature (Fig. 1). While there is a significant increasing trend in mean minimum temperatures of Adana, there is not increasing or decreasing trend in Karaisali's mean minimum temperatures (Fig. 2; Table 1; Table 1). Mean minimum temperatures difference of Adana-Karaisali pair is showed an increasing trend with 95% of statistically significant level (Fig. 2; Table 1; Table 2).

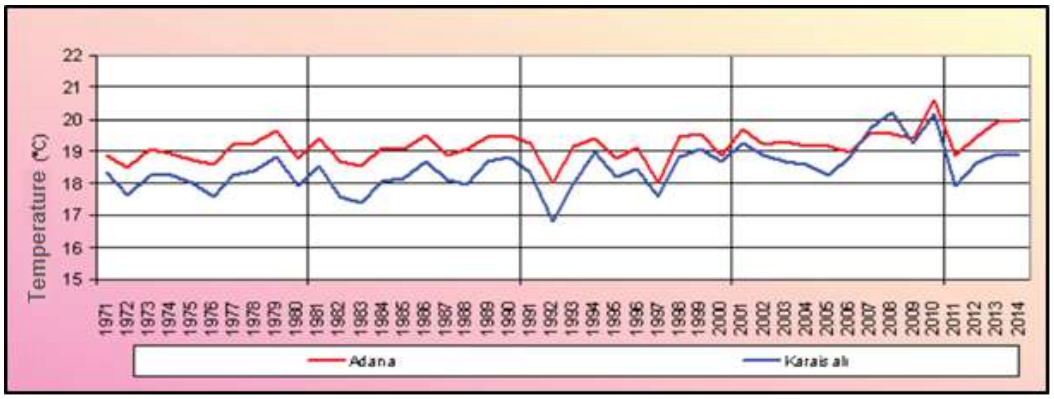

Figure 1. Time series of mean temperatures of Adana and Karaisali.

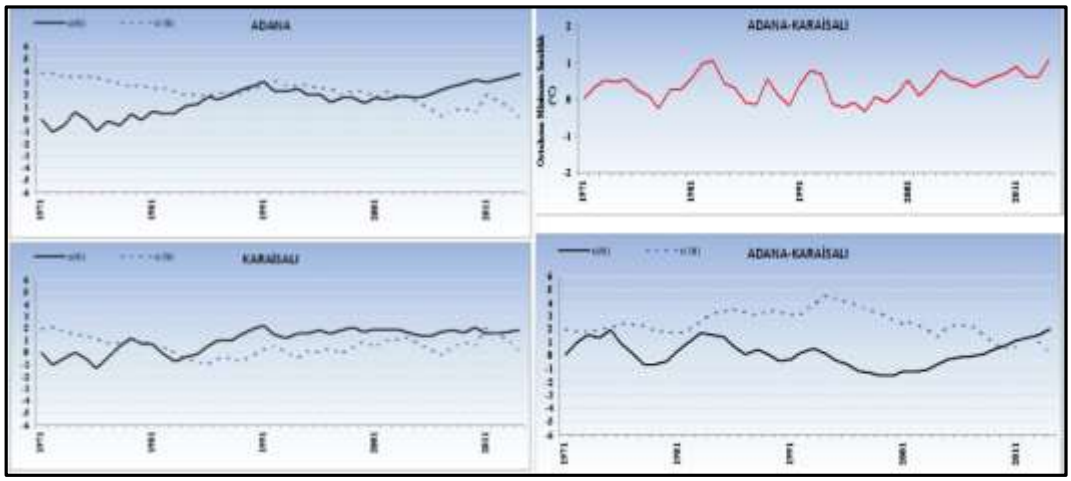

Figure 2. Mann-Kendal graphics for mean minimum temperatures of Adana and Karaisali (on the left), mean minimum temperatures difference of Adana-Karaisali pair (on right upper) and Mann-Kendal graphic for mean minimum temperatures difference of Adana-Karaisali pair (on right bottom)

Table 1. Mann-Kendal result for mean minimum temperatures of Adana and Karaisali. (*statistically significant)

Station Name	Mann-Kendall Test
Adana	3,80*
Karaisalı	1,88

Table 2. Mann-Kendal result for mean minimum temperatures difference of Adana-Karaisali pair

Station's Pair	Mann-Kendall Test
Adana–Karaisalı	2,00*

Kayseri has been selected as urban station. Pinarbasi and Tomarza have been selected as rural station for station's pairs Kayseri-Pinarbasi and Kayseri-Tomarza. The population is 1.322.376 in Kayseri with 13.5% increasing rate and 25.293 in Pinarbasi with -15.9 decreasing rate and 24.131 in Tomarza with -11.9 decreasing rate since 2007 (URL 1). The yearly mean temperature is increasing in all station according to 1971 and there is a difference between urban and rural stations' temperature while two rural stations' temperatures are too close (Fig. 3). While there is a significant increasing trend in mean minimum temperatures of Kayseri, there are not increasing or decreasing trend in mean minimum temperatures of Pinarbasi and Tomarza (Fig. 4; Table 3). Mean minimum temperatures difference of Kayseri-Pinarbasi and Kayseri-Tomarza pairs are showed an increasing trend with 95% of significant level (Fig. 4; Table 4).

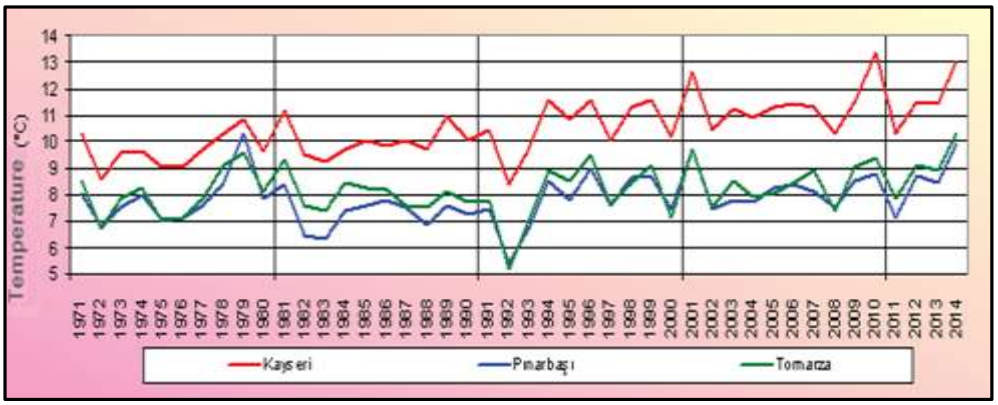

Figure 3. Time series of mean temperatures of Kayseri, Pinarbasi and Tomarza

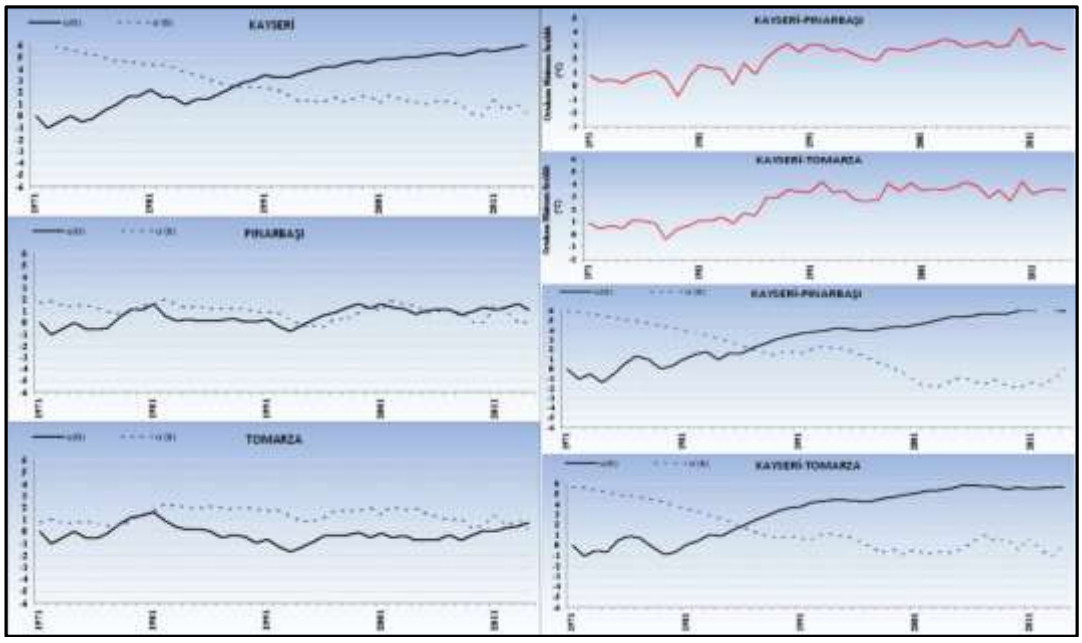

Figure 4**.** Mann-Kendal graphics for mean minimum temperatures of Kayseri, Pinarbasi and Tomarza (on the left), mean minimum temperatures difference of Kayseri-Pinarbasi and Kayseri- Tomarza pair (on right upper) and Mann-Kendal graphic for mean minimum temperatures difference of Kayseri and Pinarbasi pair and Mann-Kendal graphic for mean minimum temperatures difference of Kayseri and Tomarza pair (on right bottom)

Table 3. Mann-Kendal result for mean minimum temperatures of Kayseri, Pinarbasi and Tomarza. (*statistically significant)

Station Name	Mann-Kendall Test
Kayseri	6,05*
Pınarbaşı	1,66
Tomarza	0,77

Table 4. Mann-Kendal result for mean minimum temperatures difference of Kayseri-Pinarbasi and Kayseri-Tomarza pairs

Station's Pairs	Mann-Kendall Test
Kayseri–Pınarbaşı	5,91*
Kayseri–Tomarza	5,62*

Rize has been selected as urban station and Pazar has been selected as rural station for station's pair Rize-Pazar. The population is 329.779 in Rize with 4.3% increasing rate and 30.824 in Pazar with a slightly decreasing rate since 2007 (URL 1). The yearly mean temperature is increasing in both station according to 1971 and there is a difference between stations' temperature (Fig. 5).There are significant increasing trend in both of mean minimum temperatures of Rize and Pazar. However Rize's trend is higher than Pazar's trend (Fig. 6; Table 5). Mean minimum temperatures difference of Rize-Pazar pair is showed a significant increasing trend with 95% of significant level (Fig. 6; Table 6).

Figure 5. Time series of mean temperatures of Rize and Pazar.

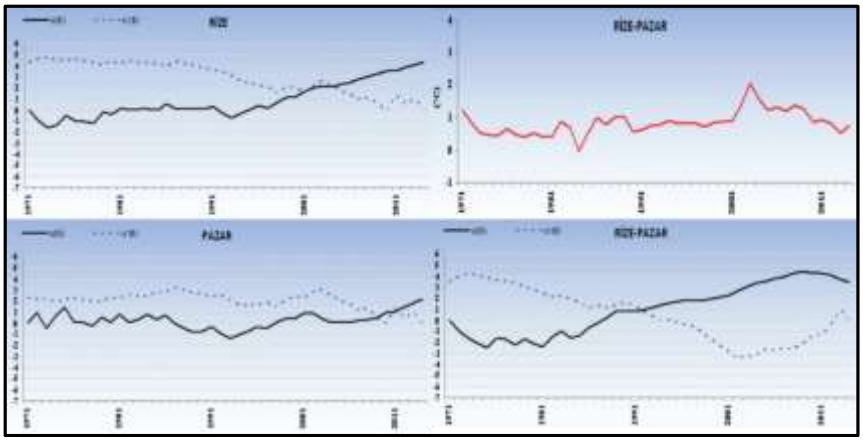

Figure 6. Mann-Kendal graphics for mean minimum temperatures of Rize and Pazar (on the left), mean minimum temperatures difference of Rize and Pazar pair (on right upper) and Mann-Kendal graphic for mean minimum temperatures difference of Rize and Pazar pair (on right bottom)

Table 5. Mann-Kendal result for mean minimum temperatures of Rize and Pazar. (*statistically significant)

Station Name	Mann-Kendall Test
Rize	4,37*
Pazar	2,18*

Table 6. Mann-Kendal result for mean minimum temperatures difference of station's Rize-Pazar pair.

Station's Pair	Mann-Kendall Test
Rize–Pazar	3,48*

Sanliurfa has selected as urban station and Akcakale has selected as rural station for station's pair Sanliurfa-Akcakale. The population is 1.845.667 in Sanliurfa with 21.2% increasing rate and 98.897 in Akcakale with 28.8 increasing rate since 2007 (URL 1). The yearly mean temperature is increasing in both station according to 1971 and there is a difference between stations' temperature (Fig. 7). While there is a significant increasing trend in mean minimum temperatures of Sanliurfa, there is not increasing or decreasing trend in Akcakale's mean minimum temperatures (Fig. 8; Table 7). Mean minimum temperatures difference of Sanliurfa-Akcakale pair is showed a significant increasing trend with 95% of significant level (Fig. 8; Table 8).

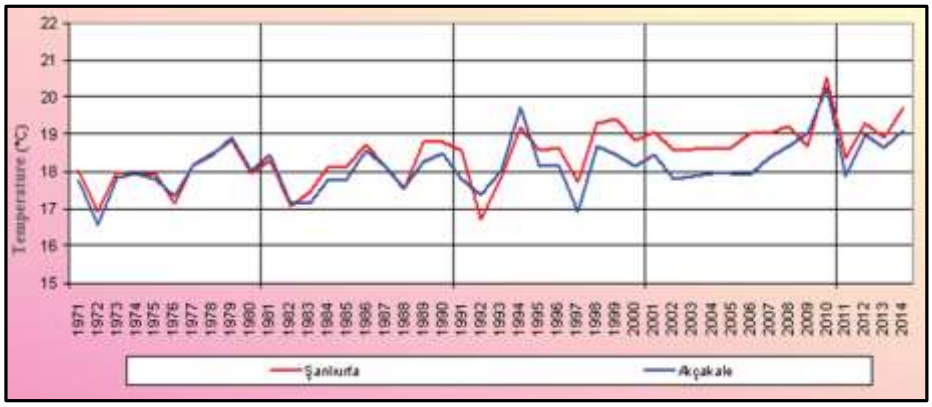

Figure 7. Time series of mean temperatures of Sanliurfa and Akcakale

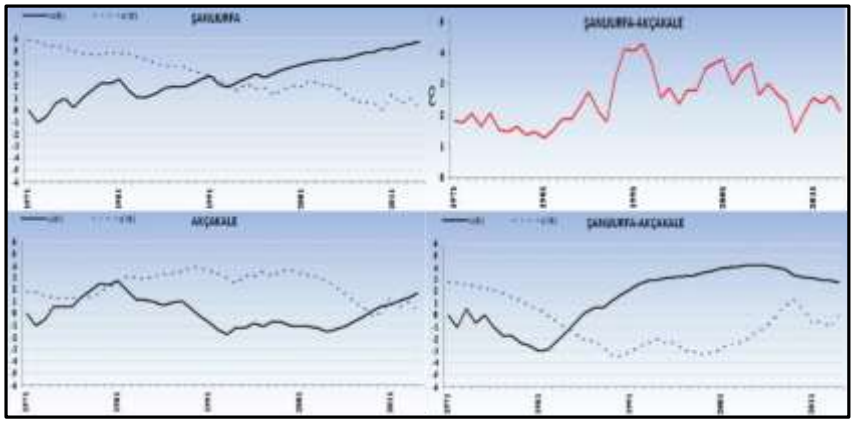

Figure 8. Mann-Kendal graphics for mean minimum temperatures of Sanliurfa and Akcakale (on the left), mean minimum temperatures difference of Sanliurfa and Akcakale pair (on right upper) and Mann-Kendal graphic for mean minimum temperatures difference of Sanliurfa and Akcakale pair (on right bottom)

Table 7. Mann-Kendal result for mean minimum temperatures of Sanliurfa and Akcakale. (*statistically significant)

Station Name	Mann-Kendall Test
Şanlıurfa	5,79*
Akçakale	1,76

Table 8. Mann-Kendal result for mean minimum temperatures difference of Sanliurfa-Akcakale pair

Station's Pair	Mann-Kendall Test
Şanlıurfa–Akçakale	2,75*

Van has selected as urban station and Gevas has selected as rural station for station's pair Van-Gevas. The population is 1.085.542 in Van with 10.8% increasing rate and 28.982 in Gevas with -2.7 decreasing rate since 2007 (URL 1). The yearly mean temperature is increasing in both station according to 1971 and there is a difference between stations' temperature (Fig. 9). While there is a significant increasing trend in mean minimum temperatures of Van, there is not increasing or decreasing trend in Gevas's mean minimum temperatures (Fig. 10; Table 9). Mean minimum temperatures difference of Van-Gevas pair is showed a significant increasing trend with 95% of significant level (Fig. 10; Table 10).

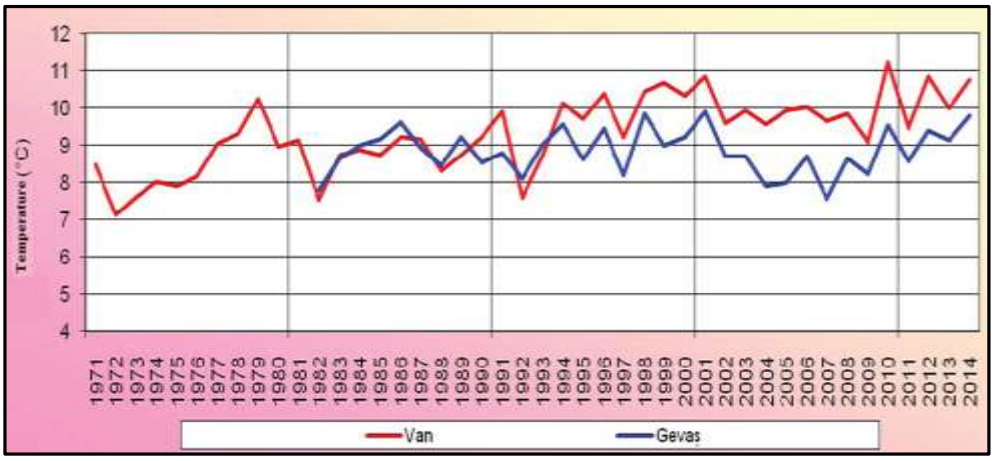

Figure 9. Time series of mean temperatures of Van and Gevas.

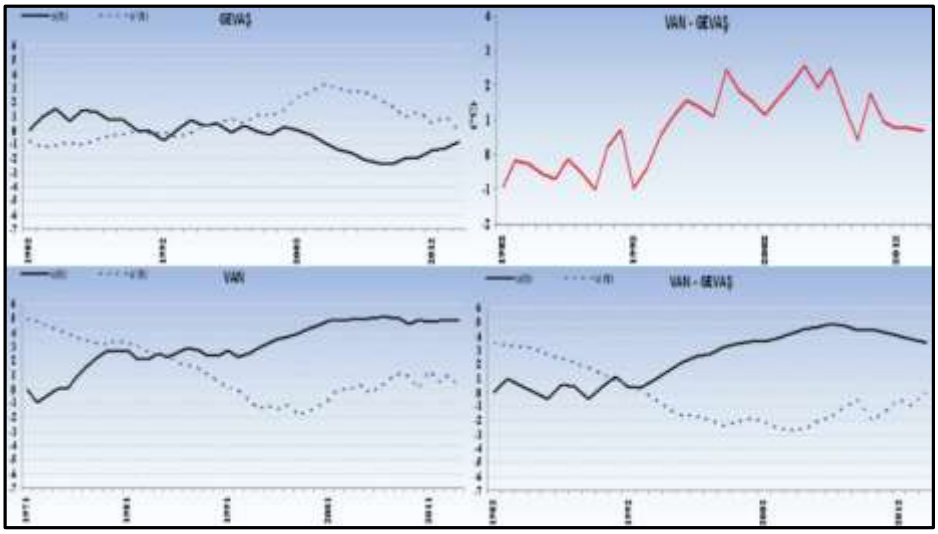

Figure 10. Mann-Kendal grafics for mean minimum temperatures of Van and Gevas (on the left), mean minimum temperatures difference of Van and Gevas pair (on right upper) and Mann-Kendal graphic for mean minimum temperatures difference of Van and Gevas pair (on right bottom)

Table 9. Mann-Kendal result for mean minimum temperatures of Van and Gevas. (*statistically significant)

Station Name	Mann-Kendall Test
Van	4,90*
Gevaş	-0,81

Table 10. Mann-Kendal result for mean minimum temperatures difference of Van-Gevas pair

Station's Pair	Mann-Kendall Test
Van–Gevaş	3,56*

CONCLUSIONS AND RECOMMENDATIONS

Global temperature has risen caused by climate change due to greenhouse gases produced by human activities in last century on Earth. In a similar manner, temperature has also risen in Turkey. However, increase in temperature is not same in everywhere as well as between cities and rural. Human activities is one of the important force to change land use and land cover in Earth to be categorized in either urbanization or cultivation. Urbans are the best sample to these due to vegetation-cover are replaced with highly impervious reconstruction in cities such as asphalts, concrete, and building. Furthermore, urban facilities are absorbing solar energy during the day and emitting during the night and thus preventing cooling in the cities surface and atmosphere. Urban–nonurban differences in minimum temperature serve as the primary indicator of the magnitude of the heat island effect because urban–nonurban temperature differences are normally most pronounced at night (Rosenzweig et al., 2005). In this study, urbanization effects on the mean minimum temperature trends are investigated at the selected stations which are Adana, Kayseri, Rize, Sanliurfa and Van as urban stations and Akcakale, Gevas, Karaisali, Pazar, Pinarbasi and Tomarza as rural stations for the period between. Urban stations have been selected in cities having population over 500.000 and rural stations with population of less than 100.000. While selected urbans' populations are increasing rural settlements' populations are decreasing except Akcakale. We aim to quantify the UHI effect by contrasting the temperatures between urban–rural areas and to this end we study on mean

minimum time series for all stations and also time series of mean minimum temperatures differences for urban-rural pairs for UHI effect. Due to climate change and rising temperature in the Earth, in parallel with this, mean temperatures of selected stations are increasing with difference between urban and rural stations. It is assumed that these differences caused by urbanization. This study's findings suggest that there is no statistically significant increase in rural mean minimum temperatures trends except Pazar for the period between 1971 and 2014. However, all the urban sites show statistically significant increase in mean minimum temperatures trends. Furthermore, urban-rural pairs show statistically significant increase in mean minimum temperatures trends. We assumed that this is a strong indication for the existence of UHI effect over these cities.

REFERENCES

WMO-No. 1189, WMO Statement on the State of the Global Climate in 2016, World Meteorological Organization, 2017

WMO-NO.1142, "Heatwaves and Health: Guidance on Warning-System Development", World Meteorological Organization and World Health Organization, 2015

World Health Organization (WHO), "Urban Bioclimatoloy", Heat-Waves: Risks and Responses, Health and Global Environmental Change Series, No. 2, WHO Regional Office for Europe, Denmark, 2004.

Bayram Cemil Bilgili and Şükran Şahin, Evaluation of Urban Green Areas on "The City Climate; Case Study of Ataturk Forest Farm, International Caucasian Forestry Symposium, October 24 – 26, 2013, Artvin

Ü. Duman Yüksel., O. Yılmaz. 2008. A study on determining and evaluating summertime urban heat islands in ankara at regional and local scale utilizing Remote sensing and meteorological data. Journal of The Faculty of Engineering and Architecture of Gazi Universty 23 (4), 937-952

Hua, L.J.; MA, Z.G. & Guo, W.D. (2007). The impact of urbanization on air temperature across China. Theoretical and Applied Climatology. Doi:10.1007/s00704-007-0339-8

Tayfun Kindap, Alper Unal, Huseyin Ozdemir, Deniz Bozkurt, Ufuk Utku Turuncoglu, Goksel Demir, Mete Tayanc and Mehmet Karaca, Quantification of the Urban Heat Island Under a Changing Climate over Anatolian Peninsula, Theor Appl Climatol (2012) 108:31–38, DOI 10.1007/s00704-011-0515-8

Çiçek, İ., 2004, Ankara'da şehirleşmenin yağış üzerine etkisi, Fırat Üniversitesi Sosyal Bilimler Dergisi, Cilt: 14, Sayı: 1, Sayfa: 1-17, Elazığ

Rosenzweig, C. Solecki, W.D.; Parshall, L.; Chopping, M.; Pope, G. & Goldberg, R. (2005). Characterizing the urban heat island in current and future climates in New Jersey. Environmental Hazards, 6: 51-62

Coşkun, M., Sümer, U.M., Ulupınar, Y., Şensoy, S., Demircan, M., Bölük, E., Arabacı, H., Eskioğlu, O., Kervankıran, S., 2017, State of the Climate in Turkey in 2016.

Demircan, M., Arabacı, H., Akçakaya, A., Şensoy, S., Bölük, E., Coşkun , M., 2017, İklim ve Şehirleşme: Minimum Sıcaklık Trendleri, III. Türkiye İklim Değişikliği Kongresi, TİKDEK 2017 3 – 5 Haziran 2017, İstanbul

Oke, T. R. (1982): "The Energetic Basis of the Urban Heat Island." Q. Jl. R. Met. Soc., 108, s:1-22.

Sensoy, S., Turkoglu, N., Cicek I., Demircan, M., Arabacı, H., Bölük, E., 2014, Urbanization Effect on Trends of Extreme Temperature Indices in Ankara, 7th Atmospheric Science Symposium, 28-30 April 2015, İstanbul

Taha, H., 1992, Urban Climates and heat islands: albedo, evapotranspiration and anthropogenic heat, Energy Buildings 25, s: 99-103

Tanrıkulu, M. , 2006, İzmir'de şehirleşmenin sicaklik ve yağiş üzerine etkisi, Yüksek Lisans Tezi, A.Ü. Sosyal Bilimler Enstitüsü, Fiziki Coğrafya Bölümü.

URL1: http://www.nufusu.com erişim tarihi : 28.09.2017

PROJECTED TRENDS IN HEAT AND COLD WAVES UNDER EFFECT OF CLIMATE CHANGE

Hüdaverdi Gürkan[1], Osman Eskioğlu[1], Başak Yazıcı[1], Serhat Şensoy[1], Ali Ümran Kömüşçü[1], Yusuf Çalık[2]

[1]Turkish State Meteorological Service, Research Department, Climatology Division, ANKARA
hgurkan@mgm.gov.tr[1], oeskioglu@mgm.gov.tr[1], byazici@mgm.gov.tr[1], ssensoy@mgm.gov.tr[1], aukomuscu@mgm.gov.tr[1]
[2]Turkish State Meteorological Service, Electronic and Information Processing Department, ANKARA
ycalik@mgm.gov.tr[2]

Abstract

Global average temperatures increased by 0.8°C in 2016 as compared to the period of 1961-1990 and 1.1°C from the pre-industrial period (1850-1899).They hit records for three consecutive years in 2014, 2015 and 2016, and the year 2016 ranks as the warmest on record. Climate models expect a temperature increase between 1.5°C-2.5°C and between 2.5°C-3.6°C based on RCP4.5 and RCP8.5 scenarios respectively by end of the century. It is projected that the increased temperatures may cause increases in the frequency and severity of some meteorological extreme events. Heat waves accounted for 43% of meteorological disasters in 2016 in Turkey. In this study, future trends of periods of heat and cold waves are studied with respect to RCP4.5 and RCP8.5 scenarios of HadGEM2-ES Global Climate Model. The results showed while number of heat waves are expected to increase, a decreasing trend of cold waves will dominate in future periods in Turkey.

Keywords: *Heat wave, cold wave, climate change*

INTRODUCTION

The global average surface temperature has risen about 1.1 °C since the late 19th century, a change driven largely by anthropogenic emissions into the atmosphere. Most of the warming occurred during the last three decades, with 16 of the 17 warmest years on record occurring since 2001. Scientists agree that global temperatures will continue to rise for decades to come, largely due to greenhouse gases produced by human activities. The IPCC predicts that increases in global mean temperature of less than 1 to 3 °C above 1990 levels will produce beneficial impacts in some regions and harmful ones in others (IPCC, 2013). Global warming is expected to bring more frequent and severe heat waves, which could impact vulnerable populations. Last quarter of the 20th century already witnessed negative effects of climate change probably more than any other period during the same century. Global warming has serious negative effects on all human activities such as health, agriculture, urbanization and tourism. WMO reported 2014, 2015 and 2016 as the warmest years since instrumental measurement of temperatures began (WMO, 2017). With the increasing global surface temperatures, the possibility of more droughts and increased intensity of storms will likely occur. If global climate change causes the global average temperature to rise as projected by climate models, there will be fewer cases of cold wave and a greater probability of more intense and frequent heat waves.

Heat waves are among the most dangerous of natural hazards, but rarely receive adequate attention (WMO, 2015b). Heat-cold waves cause serious health problems and lead to deaths. In the last 10 - 15 years, many severe heat waves have occurred in the world. One of the most severe was the European heat wave of July and August 2003, which occurred during an unusually dry summer (Black et al., 2004). Due to heat wave incidents in Europe, 14,800 people lost their lives in Germany, Spain, France and England in July and August 2003 (Bölük et al., 2013). The 2003 European heat wave was followed in 2010 by an even more intense and

widespread heatwave, which scorched enormous areas across Eastern Europe (Barriopedro et al., 2011). A number of major heat wave events have occurred over the past decade, some of which have had devastating effects, such as that of Europe in 2003 and that of the Russian Federation in 2010 (WMO, 2015a; Robine et al., 2008; Osborn, 2010). A heat wave has various definitions, depending on regional climate, among other factors. WMO defines a heat wave as five or more consecutive days in which the average daily maximum temperature is exceeded by at least 5 °C from normal (Alexander et al 2006; WMO, 2015b).

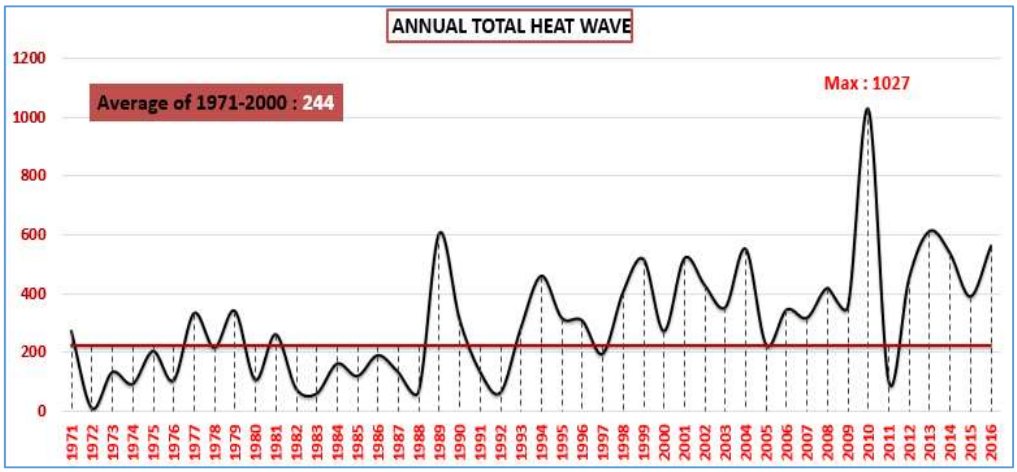

Figure 24 The number of annual total heat wave

The frequency of heat waves are increasing by year by year in Turkey. According to the data from 224 meteorological stations, the annual average number of heat waves is 224 in the period 1971-2000, and there have been just 2 years of heat wave below normal since 1993 (Figure 1).

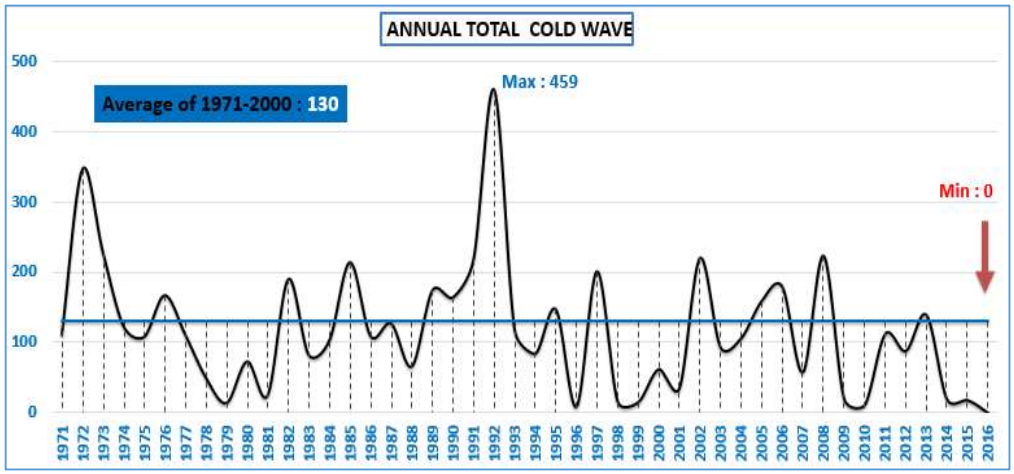

Figure 25 The number of annual total cold wave

There has been a decrease trend in the number of cold waves compared to the average of 1971-2000 period in recent years. 2016 was recorded as first year with no cold wave in the period of 1971-2016. In the period of 46 years (1971-2016), a cold wave was observed above the average in 16 years and below the average in 30 years (Figure 2). In this study, the trends of heat-cold wave occurrences were studied based on climate model projections for Turkey.

DATA AND METHODS

Initially three GCM models were considered for the study, and then after performing verification on temperature parameter, HadGEM2-ES Global Climate Model has been chosen

along with RCP4.5 and RCP8.5 scenarios. HadGEM2 stands for the Hadley Centre Global Environment Model version 2. Members of the HadGEM2 family were used in the Fifth Assessment Report of the Intergovernmental Panel on Climate Change (IPCC). The standard atmospheric component has 38 levels, with a horizontal resolution of 1.25 degrees of latitude by 1.875 degrees of longitude. This is equivalent to a surface resolution of about 208 km x 139 km at the Equator, reducing to 120 km x 139 km at 55 degrees of latitude. (MetOffice, 2014; Demircan et al., 2014)

In order to obtain high-resolution climatic parameters from the low-resolution global model data, nesting method (Nested simulations) was employed with Regional Climate Model (RegCM4). In next step, temperature projections were produced for 2016-2040, 2041-2070, 2071-2099 periods, relative to the 1971-2000 reference period at 20 km resolution. The results were mapped separately for the each period.

APPLICATION AND RESULTS

The HadGEM2-ES global climate model data were used in the study for the future projections of the heat-cold waves. The results are mapped on the basis of scenario and period selected. The results show that an increase of heat wave occurrences in Turkey in all the future periods (2013-2040, 2041-2070, 2071-2098). During the period of 2013-2098 based on RCP 4.5 scenario; the number of days with heat wave per year is expected to increase between 20-110 days with an average of 42 days.

Results of change of the heat waves days based on RCP4.5;

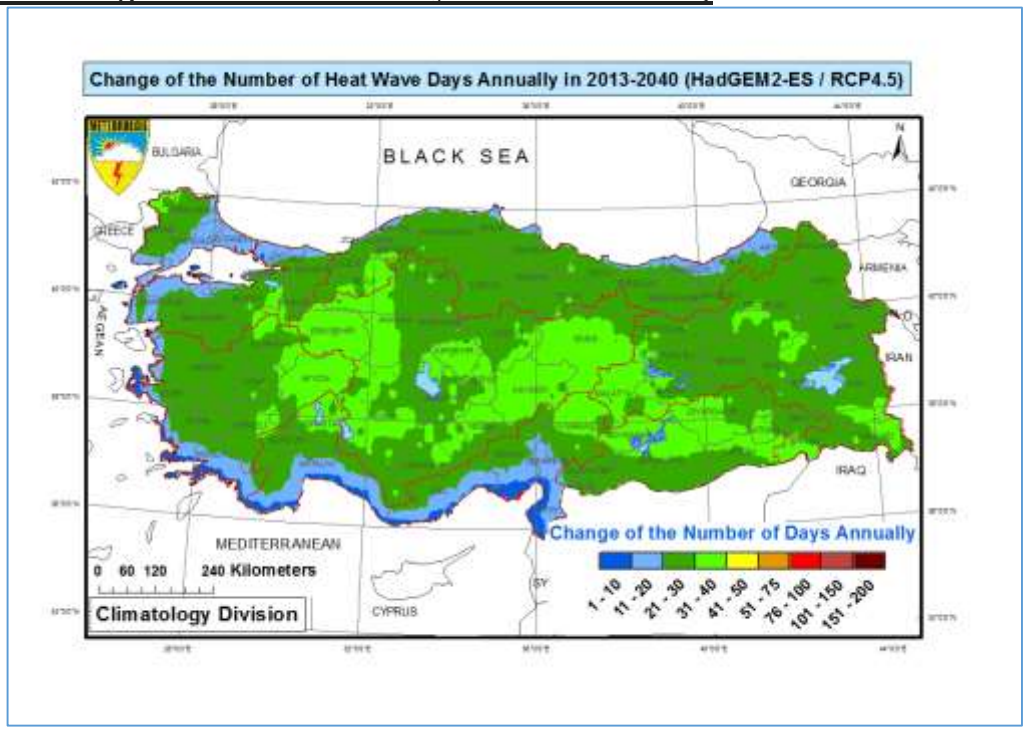

Figure 26 Change of the number of heat wave days annually in 2013-2040 (HadGEM2-ES / RCP4.5)

In the period of 2013-2040, increases in the number of heat waves are expected to attain nearly 40 days. Especially, in inland regions expected increases are significant (Figure 3).

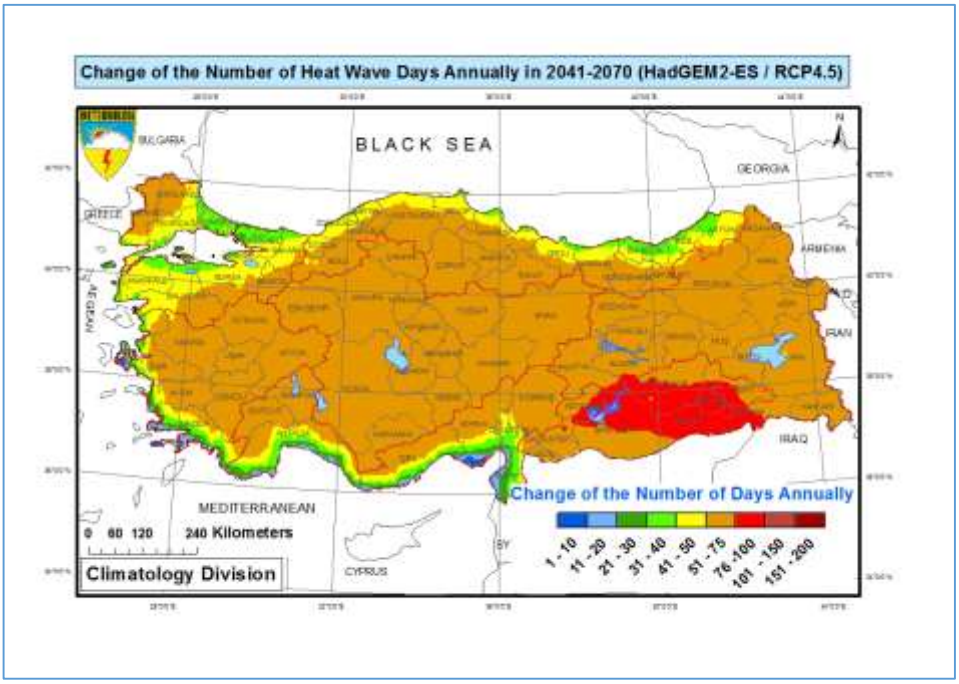

Figure 27 Change of the number of heat wave days annually in 2041-2070 (HadGEM2-ES / RCP4.5)

In the period of 2041-2070, increases in the number of heat waves are expected to reach nearly to 100 days. In the large part of the country, the increase is expected to take place around 51-75 days and in the southeast region 75 - 100 days (Figure 4).

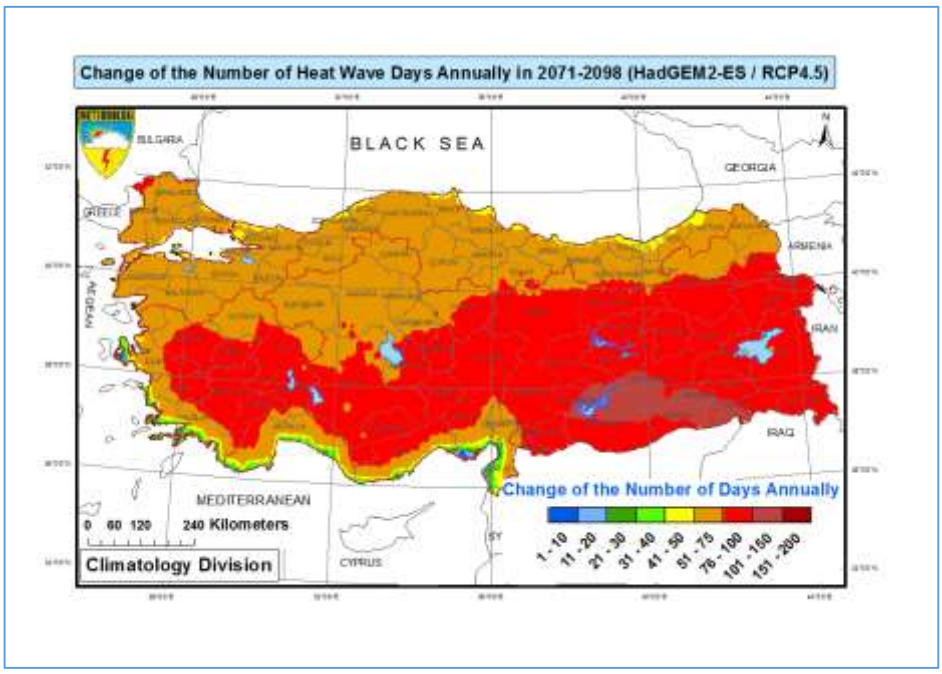

Figure 28 Change of the number of heat wave days annually in 2071-2098 (HadGEM2-ES / RCP4.5)

In the last period, southern regions are expected to be most vulnerable parts of Turkey. Especially in part of south eastern region, number of heat waves days are expected to change 101-150 days (Figure 5).

Results of change of the heat waves days based on RCP8.5;

According to RCP 8.5 scenario; the number of days of heat wave per year is expected to increase between 27-204 days with an average of 78 days during the period of 2013-2098.

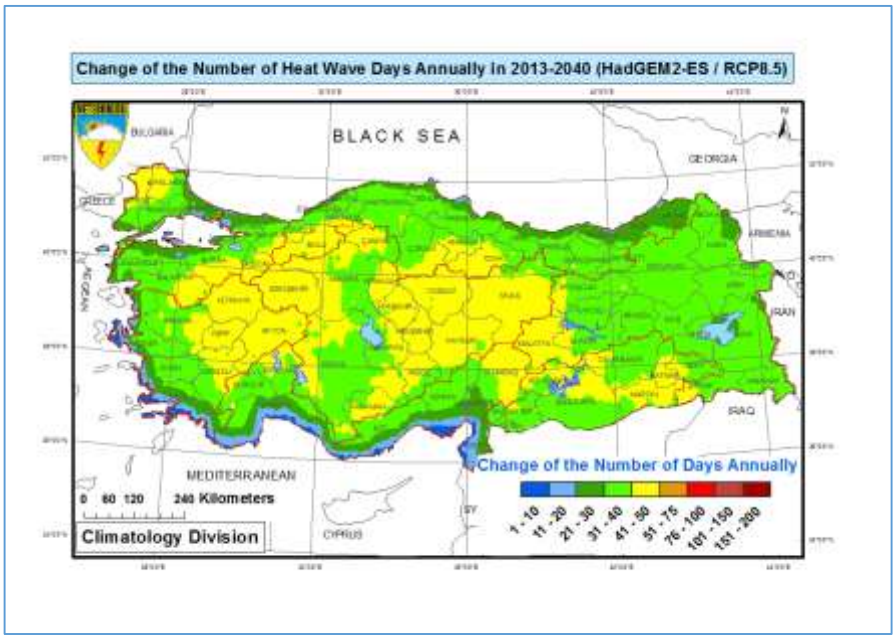

Figure 29 Change of the number of heat wave days annually in 2013-2040 (HadGEM2-ES / RCP8.5)

Sensitive regions during the period 2013-2040 are similar to RCP4.5 in the same period. Increasing trend in the number of heat waves days are expected to reach up to 50 days (Figure 6).

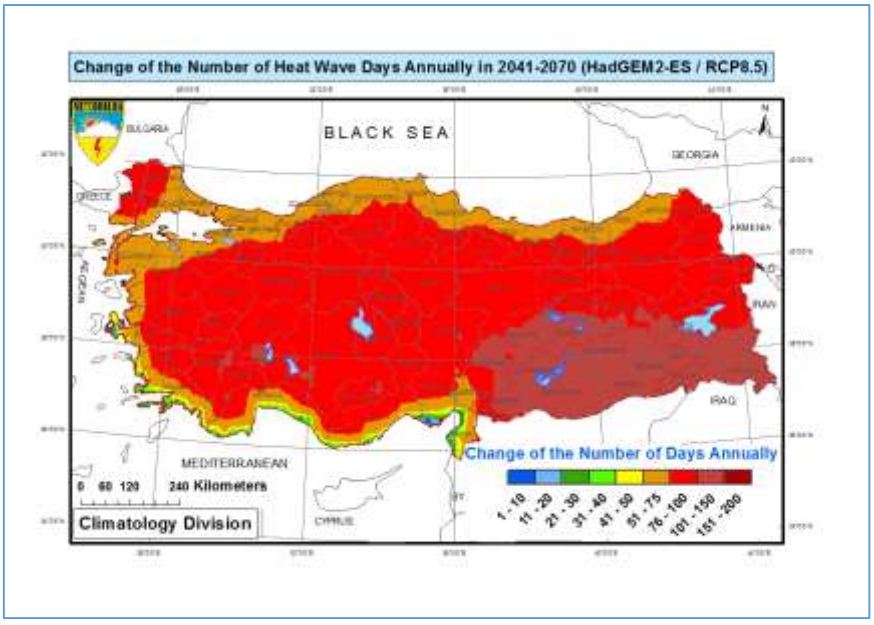

Figure 30 Change of the number of heat wave days annually in 2041-2070 (HadGEM2-ES / RCP8.5)

According to the projections of the period of 2041-2070, change of the number of days are expected to vary between 76-100 days. In addition, more than 100 days (101-150) of increasing trend is expected in the Southern East Anatolia region (Figure 7).

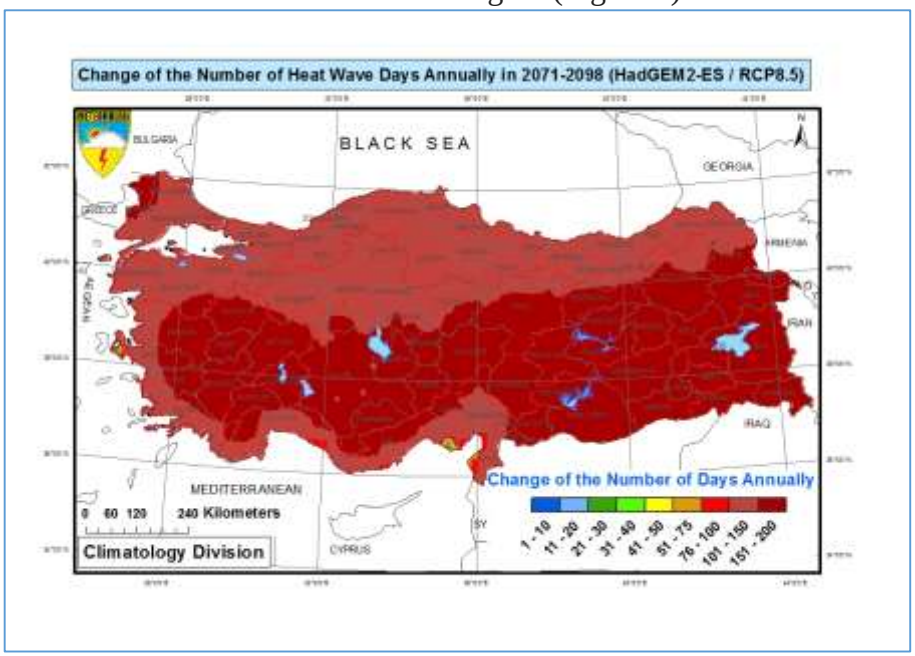

Figure 31 Change of the number of heat wave days annually in 2071-2098 (HadGEM2-ES / RCP8.5)

Projections of the last quarter of the century, shows that the change in the number of heat wave days exceed 100 days in the entire country. East Anatolia, South Eastern Anatolia, inland part of the Aegean region and southern part of Central Anatolia are expected to be affected seriously. In these regions, change in the number of heat wave days are expected to be between 151 and 200 days (Figure 8).

Results of change of the cold waves days based on RCP4.5;

Due to climate change and global warming, it is expected that the frequency of cold waves will decrease in future periods. Obtain results from the both scenarios (RCP4.5 and RCP8.5) indicate that no increase in the number of cold waves are expected throughout the country. RCP4.5 shows a decrease between 3-10 days per year for the entire period is projected. According to RCP8.5 scenario the number of days of cold wave per year is expected to decrease between 2 - 14 days. These results can have a positive impact on various sectors, especially human health and agriculture.

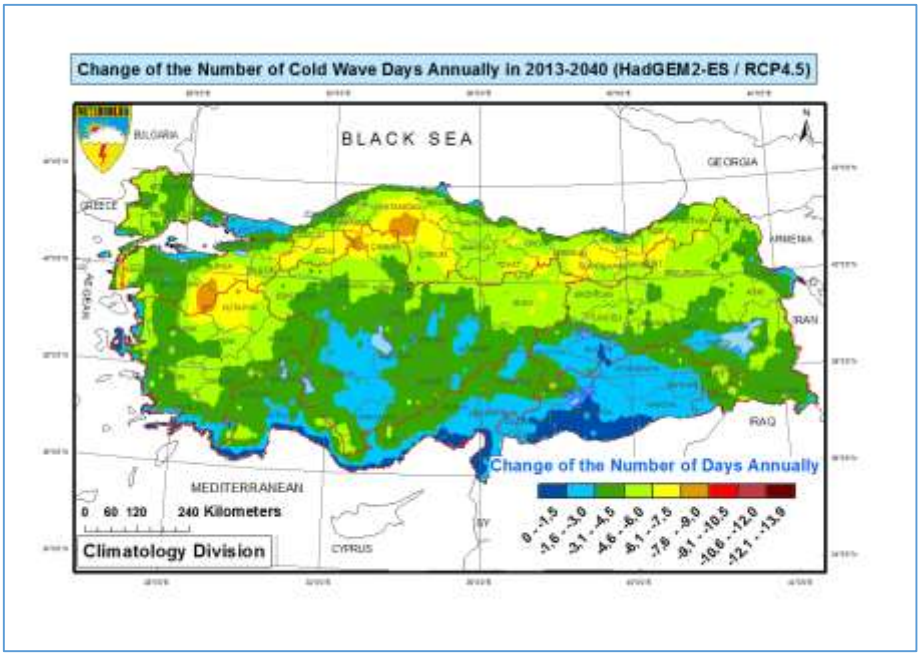

Figure 32 Change of the number of cold wave days annually in 2013-2040 (HadGEM2-ES / RCP4.5)

In the first future period, there is no significant change throughout the coastal parts of Mediterranean region and some southern border of country. The regions where maximum declines are expected in inner parts of the Black Sea Region and the southern parts of Marmara region (Figure 9).

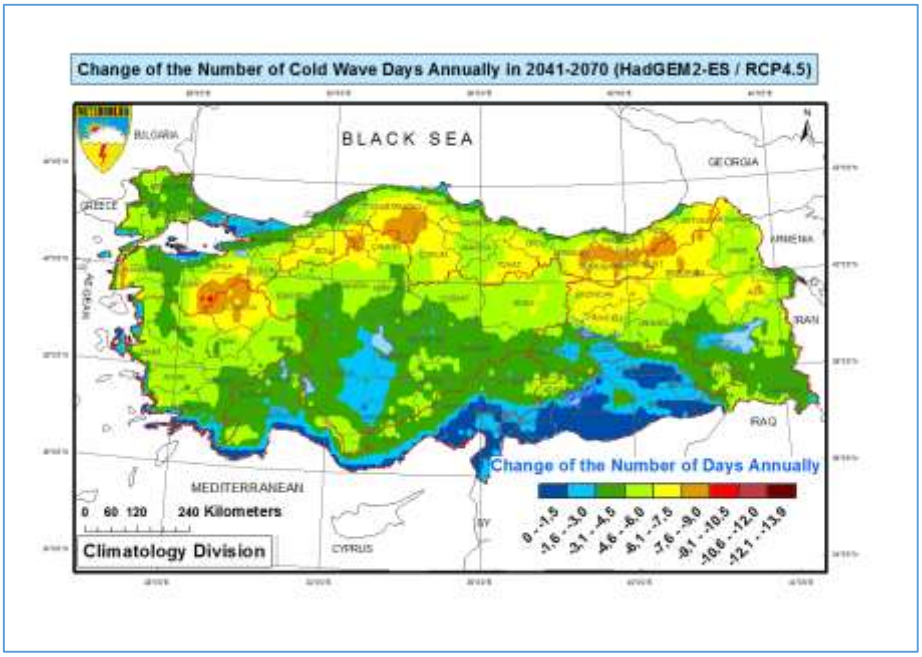

Figure 33 Change of the number of cold wave days annually in 2041-2070 (HadGEM2-ES / RCP4.5)

In the period of 2041-2070, the decrease in the northern regions of the country is expected to be more. As well as a decline up to 10 days is expected in the south of Marmara region (Figure 10).

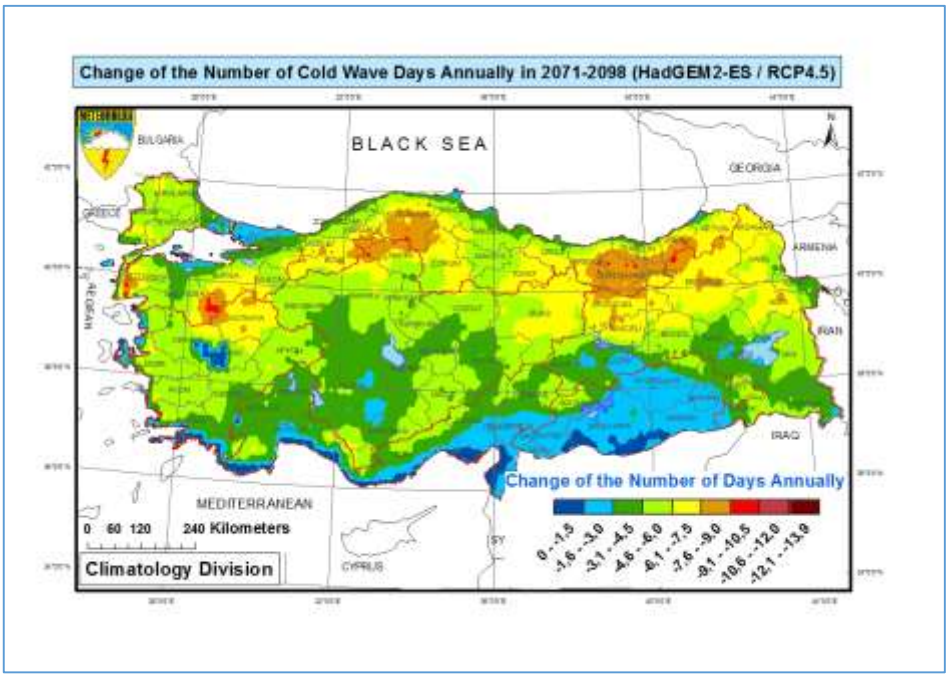

Figure 34 Change of the number of cold wave days annually in 2071-2098 (HadGEM2-ES / RCP4.5)

According to projections of last period (2071-2098), the regions to be affected positively due to decrease in the number of cold wave days are mostly the inner parts of the Black Sea Region and the southern parts of the Marmara Region (Figure 11).

Results of change of the cold waves days based on RCP8.5;

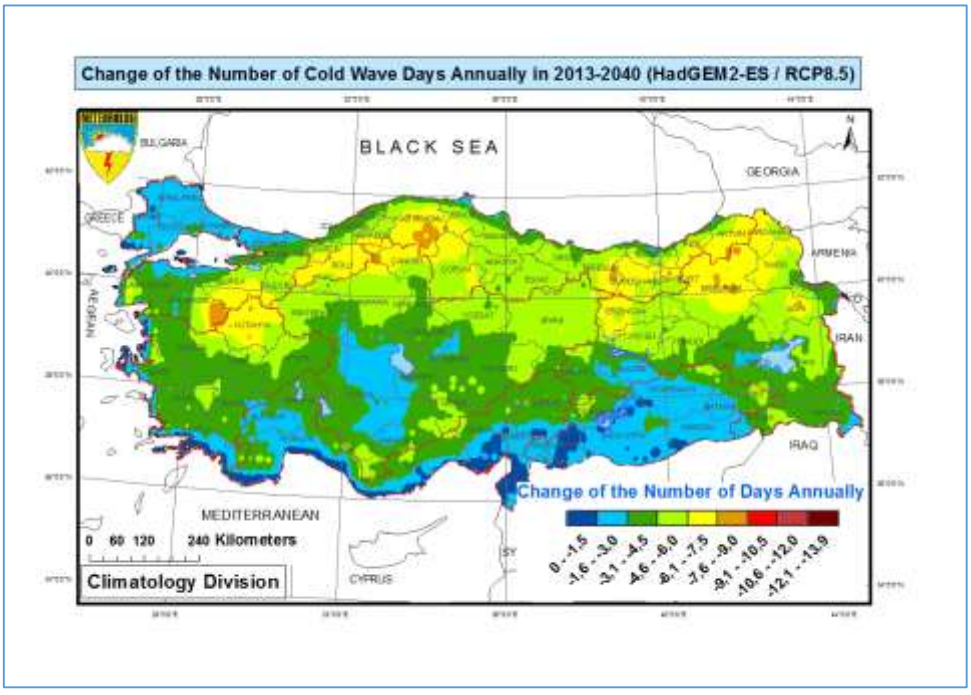

Figure 35 Change of the number of cold wave days annually in 2013-2040 (HadGEM2-ES / RCP8.5)

In the period of 2013-2040, it is noteworthy that the number of declines in the northern regions will be higher (Figure 12).

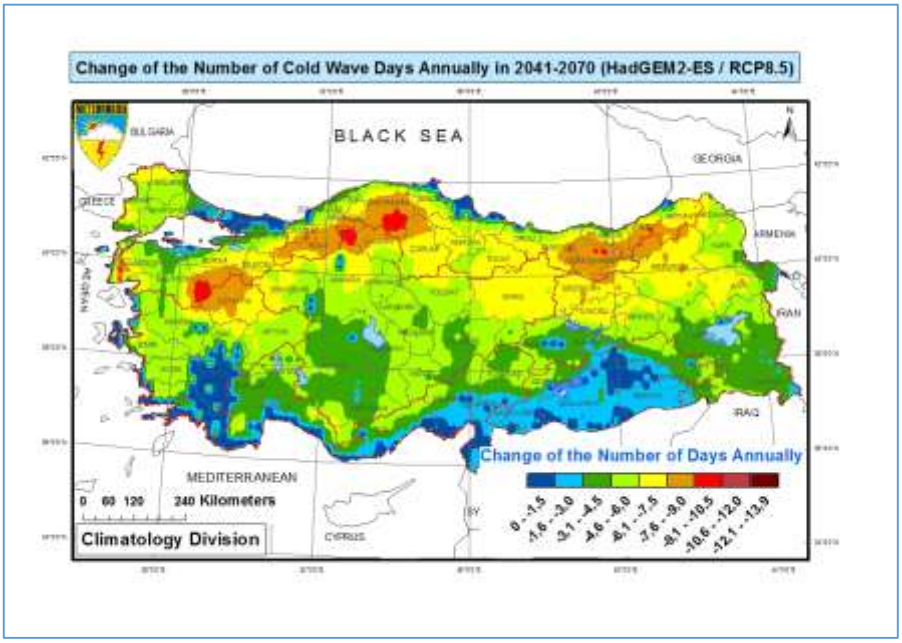

Figure 36 Change of the number of cold wave days annually in 2041-2070 (HadGEM2-ES / RCP8.5)

According to projections of 2041-2070 period, it is expected that the decrease in cold wave days will be over 10 days in the inner parts of the Black Sea Region and south of the Marmara Region. The change is very few in the southern regions (Figure 13).

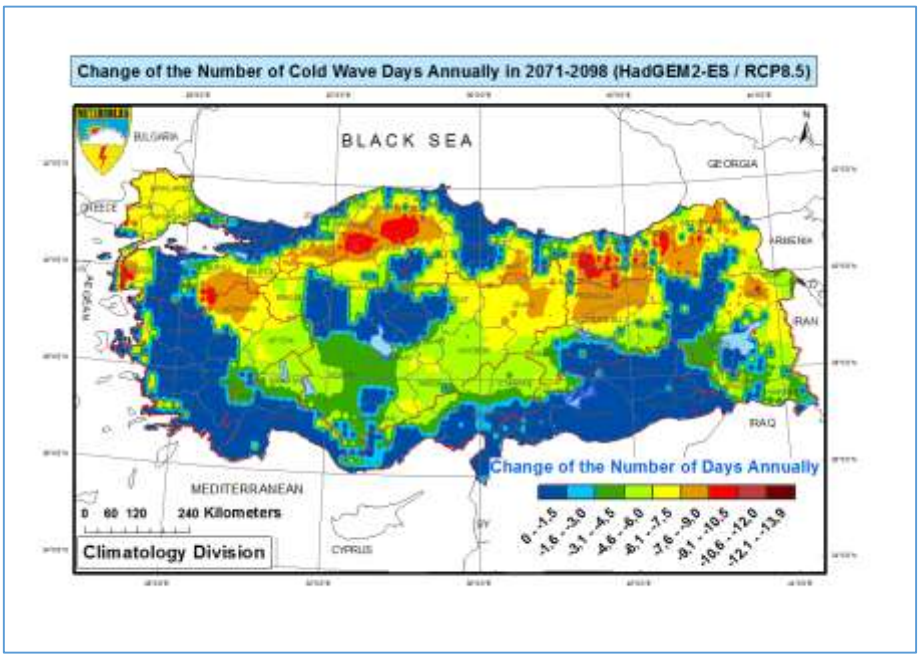

Figure 37 Change of the number of cold wave days annually in 2071-2098 (HadGEM2-ES / RCP8.5)

In the last period of the century (2071-2098), it is expected that the decreases will reach up to 14 days in northern regions. At the same time, it is also noteworthy that regions of no significant change in the number of days of cold wave days cover wider region (Figure 14).

CONCLUSIONS AND RECOMMENDATIONS

Climate change causes adverse impacts on human activities in many parts of the world. Temperature increases associated with global warming are among the main causes for the increase in frequency of meteorological disasters, and the most frequent increase in meteorological disasters in recent years is the heat wave. It is expected that climate change will make heat waves worse in terms of their impacts on people, property, communities and the environment. Heatwaves have widespread impacts, ranging from direct impacts on our health to damage to ecosystems, agriculture and infrastructure (Anonymous, 2014). In this study, projections were generated for the possible future trends of heat-cold waves. According to the results of the projections, the number of days of heat wave is expected to increase significantly. It is envisaged that the increase will be both for RCP4.5 and RCP8.5 scenarios especially after 2040s. Our study concludes that Central Anatolia, Eastern Anatolia and Southeastern Anatolia regions will be more sensitive in terms of increases in the heat waves. In the case of cold wave days, similar changes are expected in the both scenarios. The results indicate that the number of days of cold waves will decrease. The projection results reveal an optimistic situation in terms of cold waves throughout Turkey. It is expected that the change in cold waves is expected to be less than the change in heat waves. According to RCP 4.5 and RCP 8.5 scenarios, the change in heat waves is between 0 - 110 days and 0 - 200 days respectively; the change in the cold wave remains at 0 - (-11) days and 0 - (-14) days. The increase in the number of days of heat wave is in a level that can cause serious problems throughout the country. According to the average of the reference period (1971-2000), increases of up to 200 days may cause adverse effects on human life throughout the year. Heat wave is projected to become more frequent throughout the century. It is inevitable that that will cause negative effects on many sectors such as agriculture, energy and urbanization. According to the projection results, the number of cold wave days is expected to decrease. Declines are expected to occur mostly in the northern part of the country, on the contrary no significant change is expected in the southern parts of country. Because in the current climate conditions, the frequency of cold waves in southern regions is very low. Decreasing the number of cold wave days can be considered as one of the rare positive effects of climate change. Heat & cold waves also cause record temperatures. Mega-heatwaves' such as the 2003 and 2010 events likely broke the 500-year-long seasonal temperature records over approximately 50% of Europe (Barriopedro et al., 2011). The projections of change in the number of heat wave days reveal that Turkey is located in one of the most vulnerable geographical regions in terms of climate change and associated increases of temperatures. It is inevitable that the resulting figures would lead to negative effects on human activities if they occur as projected. The projection results show that Turkey will encounter hotter, more frequent and more severe heatwaves in the future. For this reason, necessary precautions must be taken to adapt to heat waves. Mitigation, early warning and public awareness of all meteorological disasters are important for adaptation to climate change. Heat waves can cause serious problems especially in elderly and children. In many countries early warning systems for heat-cold waves are being developed and trainings are held on what people should do in case of an emergency. It is important to plan to mitigate adverse impacts of heat waves that we are exposed to more and more every year.

REFERENCES

Anonymous. 2014. Heatwaves: Hotter, Longer, More Often. Climate Council of Australian. 70p.

Alexander, L.V., X. Zhang, T.C. Peterson, J. Caesar, B. Gleason, A.M.G. Klein Tank, M. Haylock, D. Collins, B. 1382 Trewin, F. Rahimzadeh, A. Tagipour, K. Rupa Kumar, J. Revadekar, G. Griffiths, L. Vincent, D.B. Stephenson, J. 1383 Burn, E. Aguilar, M. Brunet, M. Taylor, M. New, P. Zhai, M. Rusticucci and J.L. Vazquez-Aguirre. 2006. Global 1384 Observed Changes In Daily Climate Extremes Of Temperature And Precipitation, J. Geophys. Res. 111, DO5109 doi: 1385 10.1029/2005JD00690.

Barriopedro D., Fischer EM., Luterbacher J., Trigo RM. and García-Herrera R. 2011. The Hot Summer of 2010: Redrawing the Temperature Record Map of Europe. Science 332:220-224.
Black E., Blackburn M., Harrison G, Hoskins B and Methven J. 2004. Factors Contributing to the Summer 2003 European Heatwave. Weather 59:217-223.
Bölük, E., Akçakaya, A., Arabacı, H. 2013. 2012 Temmuz Ayında Yaşanan Sıcak Hava Dalgası. 6th Atmospheric Science Symposium-ATMOS 2013, İstanbul, Turkey.
Demircan M., Demir Ö., Atay, H., Eskioğlu O., Yazıcı, B., Tuvan, A., ve Akçakaya, A. 2014. Climate Change Projections for Turkey with New Scenarios, The Climate Change and Climate Dynamics Conference, CCCD, Istanbul, 8–10 September 2014.
IPCC. 2013. Climate Change 2013, The Physical Science Basis, Working Group I Contribution to the Fifth Assessment Report of the Intergovernmental Panel on Climate Change, Cambridge University Press, England. http://www.climatechange2013.org/images/report/WG1AR5_ALL_FINAL.pdf
MetOficce 2014. MetOffice Climate Prediction Model: HadGEM2 family, http://www.metoffice.gov.uk/research/modelling-systems/unified-model/climate-models/hadgem2 [Date of access: 25.07.2017].
Osborn, A. 2010. Moscow Smog and Nationwide Heat Wave Claim Thousands of Lives. Brit. Med. J., 10, 341,c4360.
Robine, J.M., S.L.K. Cheung, S. Le Roy, H. Van Oyen, C. Griffiths, J.P. Michel and F.R. Herrmann. 2008. Death toll exceeded 70,000 in Europe During the Summer of 2003. Comptes Rendus Biologies, 331(2):171–178.
WMO. 2015a. Guidelines on the Definition and Monitoring of Extreme Weather and Climate Events, Draft Version – First Review By Tt-Dewce December 2015, Geneva.
WMO. 2015b. Heatwaves and Health: Guidance on Warning-System Development, WMO-No: 1142, Geneva.
WMO. 2017. Climate Breaks Multiple Records in 2016, With Global Impacts, https://public.wmo.int/en/media/press-release/climate-breaks-multiple-records-2016-global-impacts [Date of access: 25.07.2017].

IMPACT OF URBANIZATION ON MEAN TEMPERATURE ANOMALIES AND CLIMATE INDICES IN TURKEY

Serhat Sensoy[1], Mustafa Coşkun[1], Ali Ümran Kömüşcü[1], Mesut Demircan[1], Erdoğan Bölük[1] Necla Türkoğlu[2], İhsan Çiçek[2]

[1]Turkish State Meteorological Service, Ankara, Turkey
ssensoy@mgm.gov.tr, mustafacoskun@mgm.gov.tr, aukomuscu@mgm.gov.tr, mdemircan@mgm.gov.tr, eboluk@mgm.gov.tr
[2]Ankara University, Faculty of Languages, History and Geography, Ankara, Turkey
nturkoglu@ankara.edu.tr, ihsan.cicek@ankara.edu.tr

Abstract

Understanding the long-term change of temperature events is important to the detection and attribution of climate change. However, it's unclear how much effect coming from the urbanization. According to the law issued in 2012, the city with population 750,000 and more was called as metropolis. If the population is less than 100 thousand it's determined as rural area. In this study we tried to eliminate urbanization effects on temperature anomalies by removing 30 metropolitan cities from the anomaly assessment. Also we have been calculated temperature indices for Ankara and Istanbul city centers and their rural areas in order to determine their trend differences. 1971-2016 annual temperature data of the 99 rural stations were used for temperature anomaly analysis. Extraction of metropolises from analysis caused to reduce the long term mean temperature from 13.5 to 13.1°C based on 1981-2010 but did not cause any change in positive temperature trend. Still positive temperature anomalies have been found since 1998. Frost Days (FD0), Cool Nights (TN10p), Cold Spell Duration Index (CSDI). Warm Nights (TN90p), Tropical Nights (TR20) and Growing Season Lengths (GSL) trends are greater in the Ankara and Istanbul city than their rural. We have clearly noticed that the minimum temperatures have great increasing trends in the city centers. But in both analyzes, it was observed that the positive temperature trends in Turkey were affected by global climate drivers, rather than the urbanizations.

Keywords: *Urbanization, temperature anomaly, impact, indices*

INTRODUCTION

There were many studies on effect of urbanization on climate (Çiçek, 2004, Hua et al., 2007, Kindap et al., 2012, Oke, 1982), Taha., 1992, Tanrıkulu., 2006, Sensoy et al., 2015, Demircan et al., 2017 and Georgescu et al., 2012). But this is new study on impact of urbanization on mean temperature anomalies. In Turkey we have been used 130 stations data to detect mean temperature anomaly including metropolitan. We wanted to eliminate impact of urbanization on this analysis. We extracted 30 metropolitan data in mean temperature analysis and we do same analysis with 99 rural station data. Also we have been calculated temperature indices for Ankara and Istanbul city centres and their rural areas (Table 1). Extraction of metropolises from analysis decreased the long term mean temperature from 13.5 to 13.1°C but did not cause any change in increasing trend (Fig 1). FD0 and TN10p have more declining trends in the Ankara and Istanbul city centre than their rural while TN90p and TR20 have increasing it. As the rural population declines, the urban population is increasing rapidly (Fig. 1).

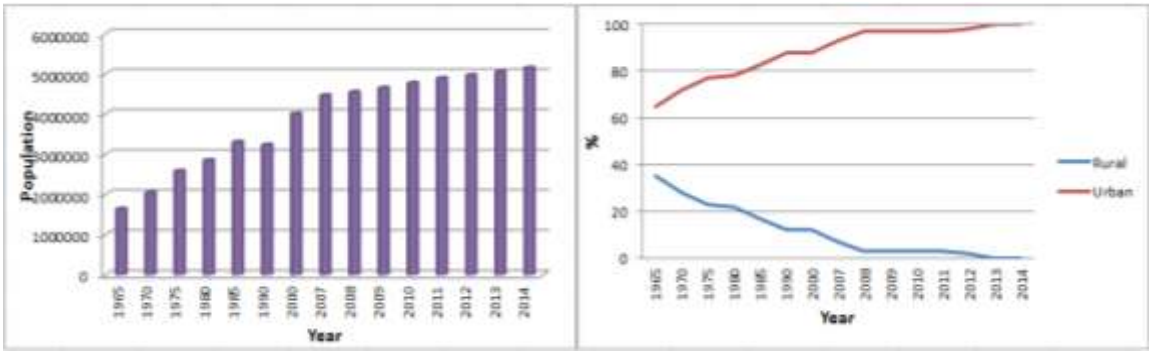

Figure 1. Ankara population (left), Ankara rural and urban population ratio (right) (TUİK)

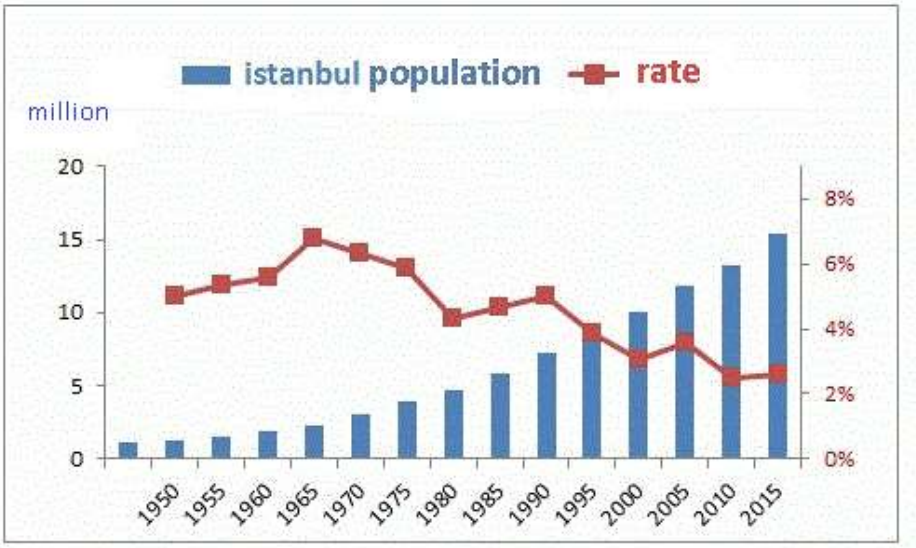

Figure 2. Istanbul population and rate of increase (TUİK)

Although population increase rate has been decreased, Istanbul population reached 14,804,116 by 2016 census. % 18,55 of Turkey population live in Istanbul.

DATA AND METHODS

Annual mean temperature belong to 130 stations from 1971 to 2016 has been used for anomaly detection. Climatic normal has been calculated from 1981-2010 base periods. After this analysis 30 metropolitan cities (population greater than 750,000) and Afyonkarahisar (714,523) have been extracted from the database. Mean temperature and anomalies have been recalculated again (Table 2.).

RClimdex software has been used to produce climate indices. Ankara and Göztepe stations have been selected to represent urban areas and Esenboğa and Şile have been selected to represent rural. 1961-2010 daily maximum and minimum temperature and precipitation data of these four stations have been used in order to calculate climate related temperature indices. All the indices were calculated *(Table 1)*, but only four of them (FD0, TN10p, TN90p and TR20) were shown due to limited places. Software user guide are available at: http://etccdi.pacificclimate.org/software.shtml.

APPLICATION AND RESULTS

Annual mean temperature anomalies have been calculated including major cities (130 stations, Fig. 1a) and without major cities (99 stations, Fig. 1b) based on 1981 to 2010 period.

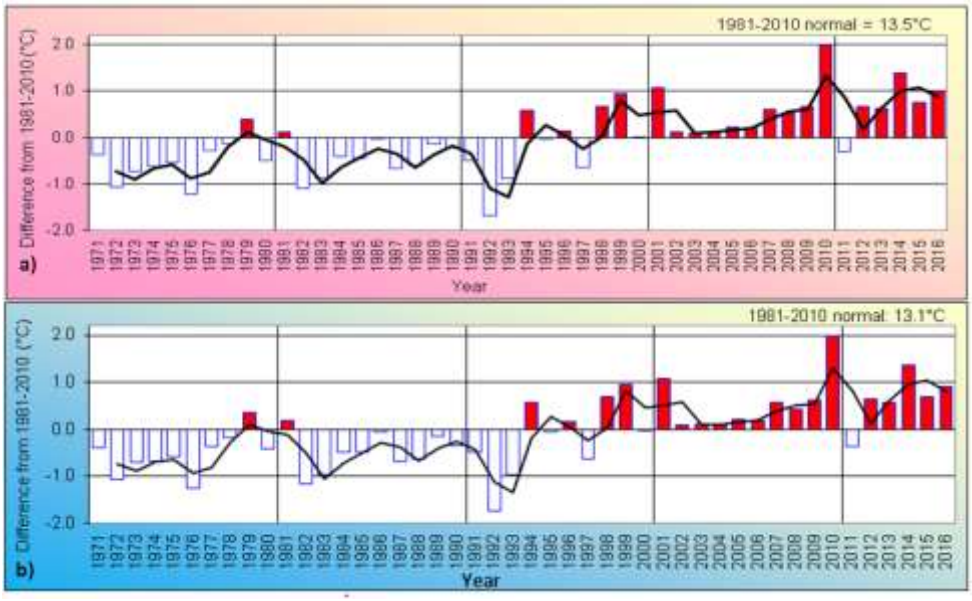

Figure 3. Mean Temperature anomalies of Turkey with (a) and without major cities (b) (Coşkun et al, 2017)

Extraction of metropolises from anomaly detection decreased the long term mean temperature from 13.5 to 13.1°C based on 1981-2010 normal, but did not cause any change in increasing trend. There are increasing trends in Turkey temperature since 1988 except 2011. It is observed that the positive temperature anomalies in Turkey are not only the effects of urbanization but also the effects of global climate drivers.

Table 1 Kendall's tau based slope estimate in temperature related climate indices in Ankara and İstanbul

Indice	Esenboğa, Ankara	Kalaba, Ankara	Şile, İstanbul	Göztepe, İstanbul
CSDI	-0.013	-0.077	0.011	-0.045
FD0	0.177	-0.120	0.204 *	-0.086
GSL	0.081	0.334	-0.134	0.028
ID0	-0.030	-0.020	-0.004	-0.009
TR20	0.028 *	0.206 *	0.114	0.462 *
TN10p	-0.025	-0.113 *	0.075	-0.102 *
TN90p	0.093	0.209 *	-0.057	0.129 *
TNx	0.037 *	0.048 *	0.035 *	0.037 *
TNn	0.105 *	0.088 *	0.043	0.071 *
SU25	0.368 *	0.190	0.692 *	0.837 *
TX10p	-0.015	-0.005	-0.011	-0.036
TX90p	0.124 *	0.069	0.115 *	0.124 *
TXx	0.039 *	0.026	0.069 *	0.018
TXn	0.081 *	0.051 *	0.027	0.021
WSDI	0.247 *	0.133	0.019	0.108
DTR	0.009	-0.013 *	0.019 *	0.003

(*) Trends are statistically significant at 95% level (p value < 0.0.5)

Table 2. Populations of Metropolises greater than 750.000 (TUIK,2016)

Metropolis	Total Population	Male population	Female Population	Population%
İstanbul	14,804,116	7,424,390	7,379,726	% 18,55
Ankara	5,346,518	2,653,431	2,693,087	% 6,70
İzmir	4,223,545	2,104,632	2,118,913	% 5,29
Bursa	2,901,396	1,454,059	1,447,337	% 3,64
Antalya	2,328,555	1,174,936	1,153,619	% 2,92
Adana	2,201,670	1,101,340	1,100,330	% 2,76
Konya	2,161,303	1,073,631	1,087,672	% 2,71
Gaziantep	1,974,244	998,926	975,318	% 2,47
Şanlıurfa	1,940,627	976,938	963,689	% 2,43
Kocaeli	1,830,772	927,157	903,615	% 2,29
Mersin	1,773,852	885,583	888,269	% 2,22
Diyarbakır	1,673,119	844,011	829,108	% 2,10
Hatay	1,555,165	780,854	774,311	% 1,95
Manisa	1,396,945	701,094	695,851	% 1,75
Kayseri	1,358,980	681,269	677,711	% 1,70
Samsun	1,295,927	640,699	655,228	% 1,62
Balıkesir	1,196,176	596,896	599,280	% 1,50
Kahramanmaraş	1,112,634	565,816	546,818	% 1,39
Van	1,100,190	561,592	538,598	% 1,38
Aydın	1,068,260	533,004	535,256	% 1,34
Denizli	1,005,687	500,398	505,289	% 1,26
Sakarya	976,948	490,935	486,013	% 1,22
Tekirdağ	972,875	499,819	473,056	% 1,22
Muğla	923,773	470,404	453,369	% 1,16
Eskişehir	844,842	421,580	423,262	% 1,06
Mardin	796,237	400,475	395,762	% 1,00
Malatya	781,305	389,572	391,733	% 0,98
Trabzon	779,379	385,009	394,370	% 0,98
Erzurum	762,021	381,138	380,883	% 0,95
Ordu	750,588	376,243	374,345	% 0,94
Afyonkarahisar *	**714,523**	354,458	360,065	% 0,90

* Afyonkarahisar is not a metropolis but it's candidate to become

Comparison of temperature related climate indices in the city and rural conditions

The most decisive climate indices which show urbanization effects are related with minimum temperature which are CSDI, FD0, GSL, ID0, TR20, TN10p, TN90p,TNx, TNn. However, SU25, TX10p, TX90p, TXx, TXn, WSDI are related with maximum temperature and haven't found decisive for urbanization effect due to include sun radiation in daytime. DTR is decreasing in the city centers due to increasing minimum temperature.

Comparison of Cold Spell Duration Indices (CSDI) Trends

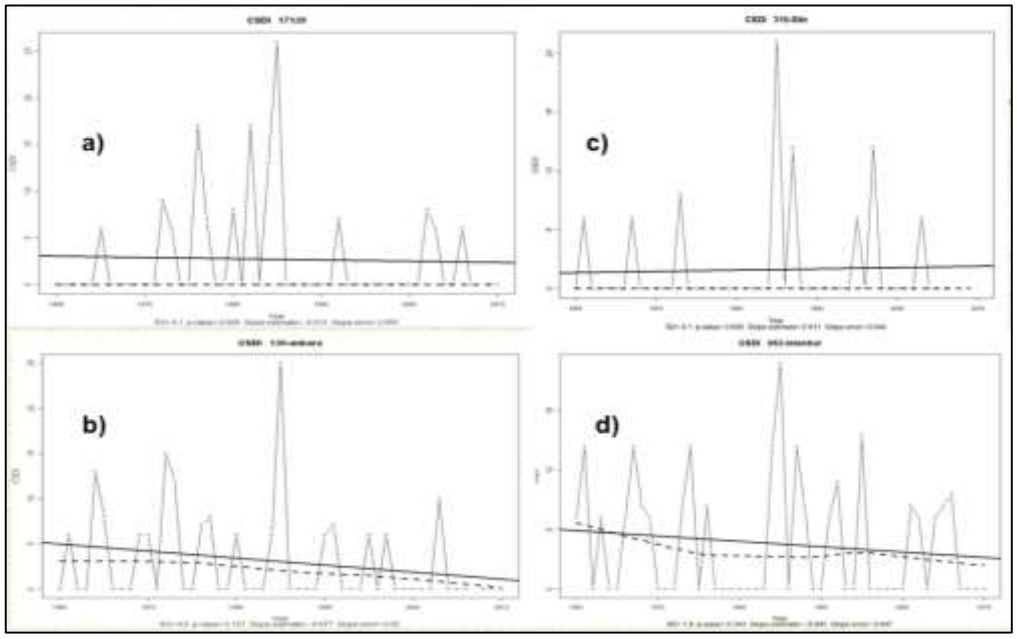

Figure 4. Cold Spell Duration indices of Esenboğa (a), Ankara (b), Şile(c), Istanbul (d) (Sensoy et al, 2013)

Cold Spell Duration Indices has more decreasing trends in the city centers (Figure 4).

Comparison of Frost Day (FD0) Trends

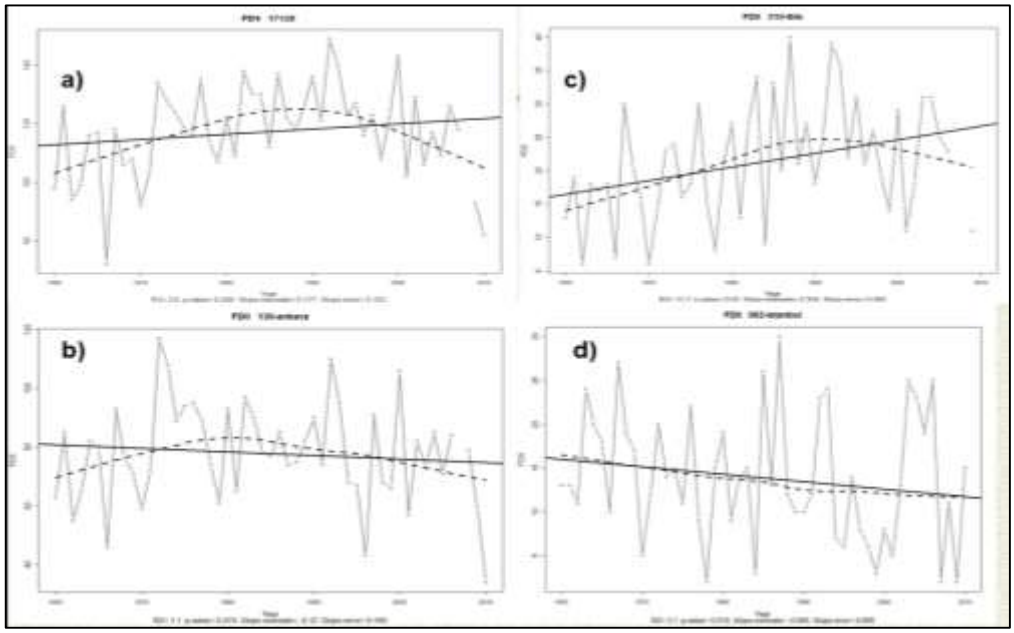

Figure 5. Frost Day Indices of Esenboğa (a), Ankara (b), Şile(c), Istanbul (d) (Sensoy et al, 2013)

Frost Days has more decreasing trends in the city centers.

Comparison of Tropical Nights (TR20) Trends

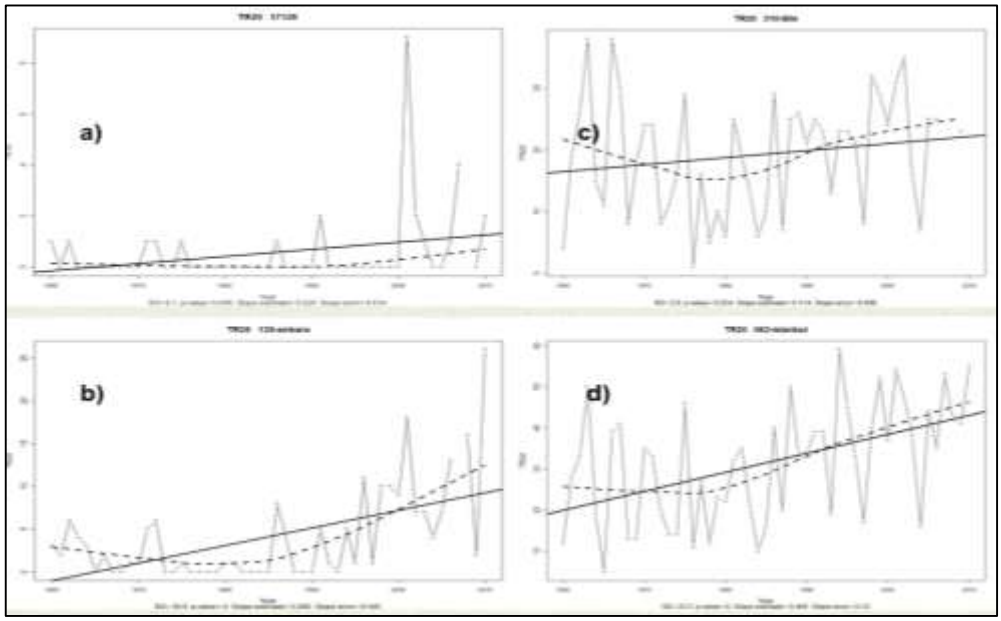

Figure 6. Tropical Nights indices of Esenboğa (a), Ankara (b), Şile(c), Istanbul (d) (Sensoy et al, 2013)

Tropical Nights has more increasing trends in the city centers

Comparison of Cool Nights (TN10p) Trends

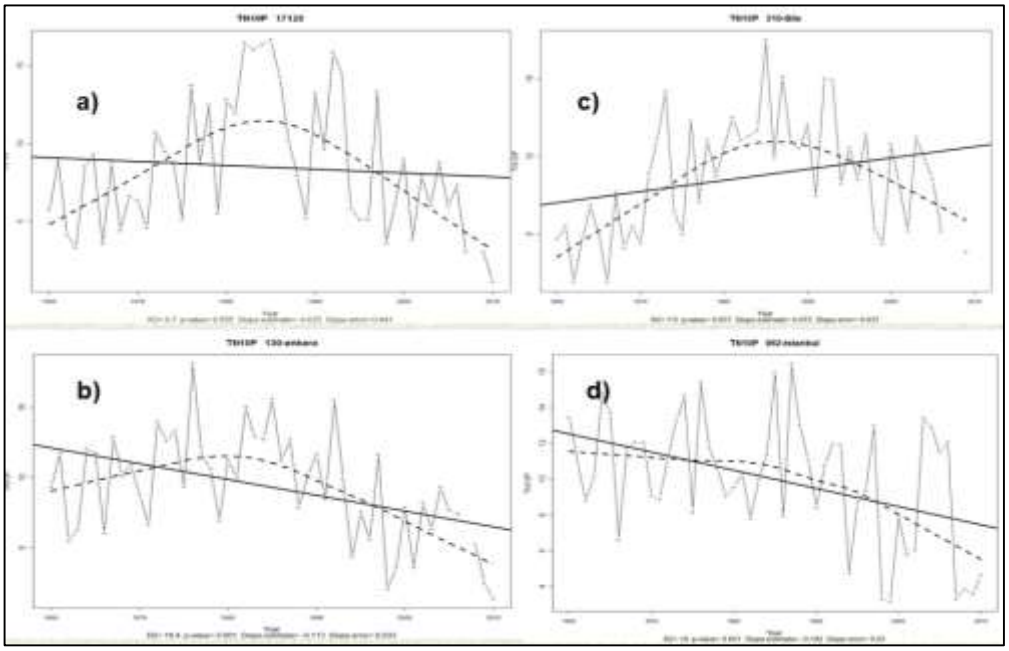

Figure7. Cool Nights indices of Esenboğa (a), Ankara (b), Şile(c), Istanbul (d) (Sensoy et al, 2013)

Cool Nights has more decreasing trends in the city centers.

Comparison of Warm Nights (TN90p) Trends

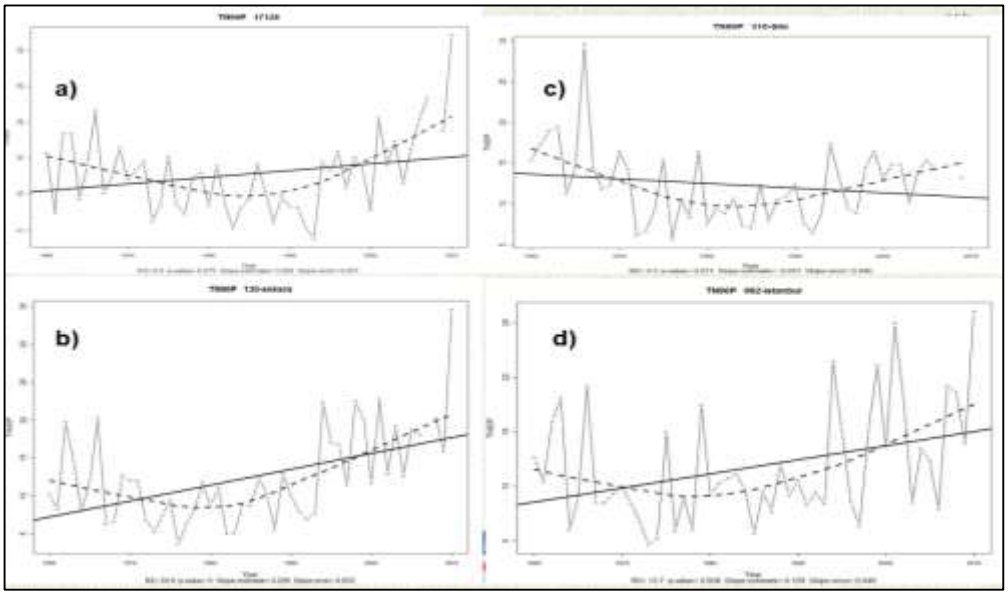

Figure 8. Warm Night Indices of Esenboğa (a), Ankara (b), Şile(c), Istanbul (d) (Sensoy et al, 2013)

Warm Nights has more increasing trends in the city centers.

Comparison of Summer Days (SU25) Trends

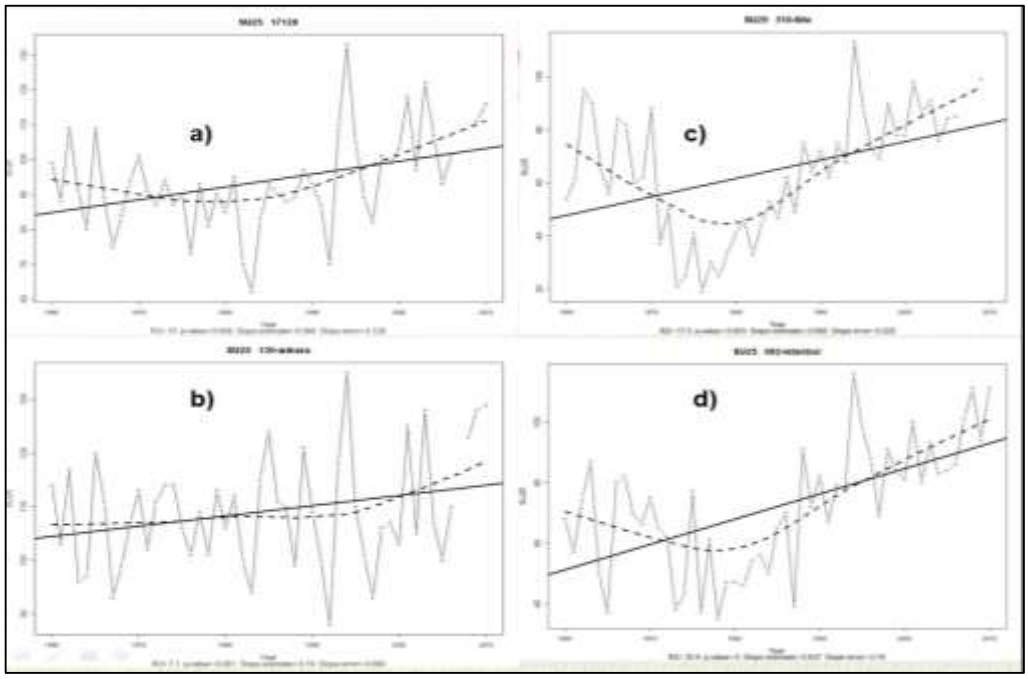

Figure 9. Summer Days Indices of Esenboğa (a), Ankara (b), Şile(c), Istanbul (d) (Sensoy et al, 2013)

Summer Days has increasing trends both in the city centers and rural areas.

Comparison of Warm Spell Duration Indices (WSDI) Trends

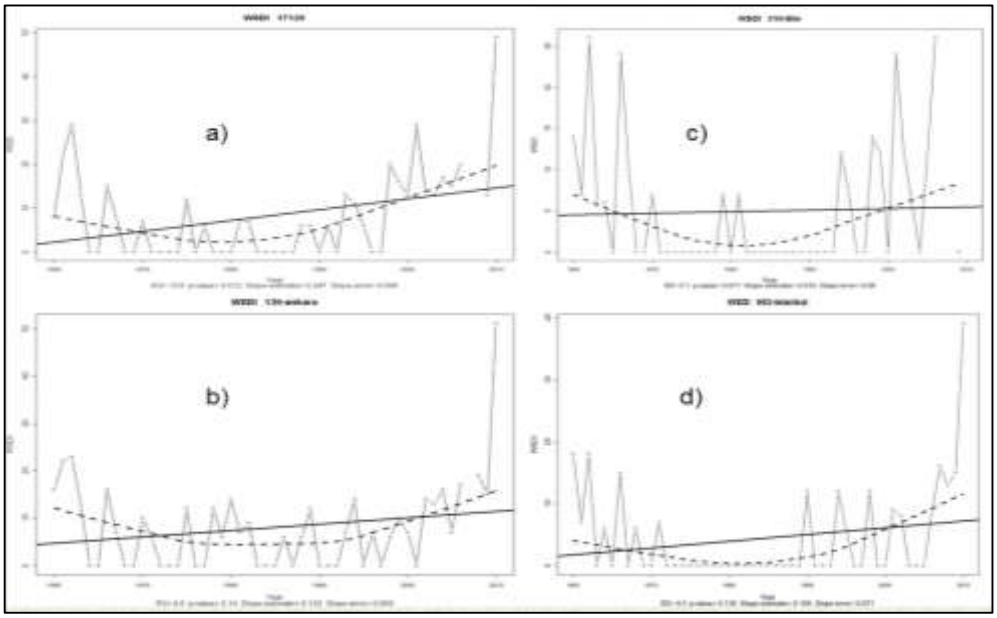

Figure 10. Warm Spell Duration Indices of Esenboğa (a), Ankara (b), Şile(c), Istanbul (d) (Sensoy et al, 2013)

Warm Spell has increasing trends both in the city centers and rural areas.

Comparison of Day Temperature Range (DTR) Trends

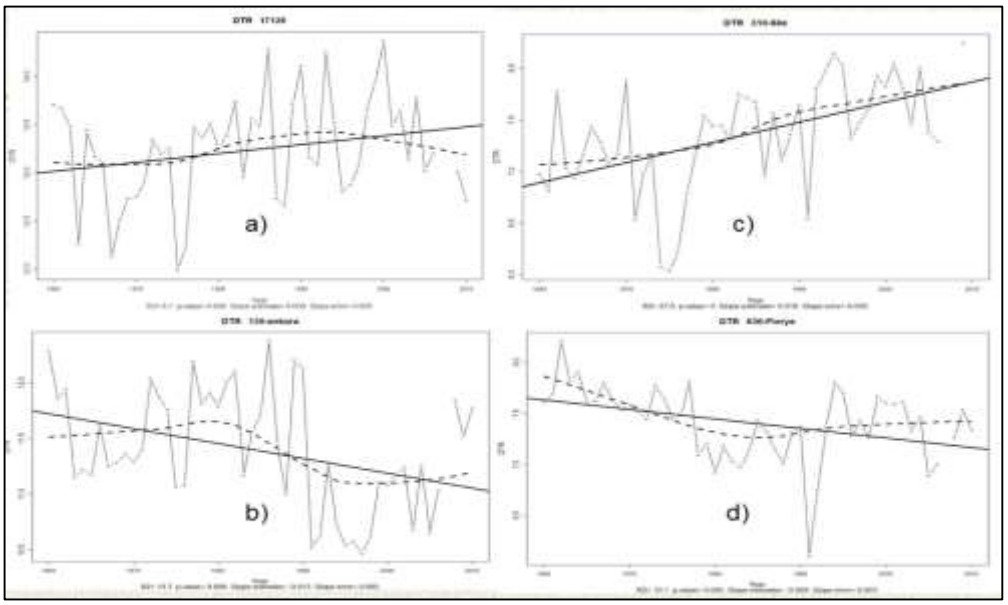

Figure 11 Day temperature range Indices of Esenboğa (a), Ankara (b), Şile(c), Istanbul (d) (Sensoy et al, 2013)

DTR has increasing trend in the rural area while decreasing in the city centers.

CONCLUSIONS AND RECOMMENDATIONS

In this study we tried to investigate urbanization effects on temperature anomaly and trends of extreme temperature indices in Ankara and İstanbul. Extraction of major cities from anomaly detection caused a decrease in long term mean temperature from 13.5 to 13.1°C. But again there are still increasing trends in Turkey temperature since 1988 except 2011. It is observed that the positive temperature anomalies in Turkey are not only the effects of urbanization but also the effects of global climatic drivers. Urbanization alone could increase local temperatures (Georgescu et al, 2012). The most decisive climate indices which show urbanization effects are related with minimum temperature. FD0 and TN10p have more declining trends in the Ankara and Istanbul city center than their rural while TN90p and TR20 have increasing it. However, Summer Days (SU25), Warm Days (TX90p) and Warm Spell Duration Indices (WSDI) are related with maximum temperature and haven't found decisive for urbanization effect due to include sun radiation in daytime. The results show that the most obvious effect of urbanization on climate is on minimum temperature. This causes decrease in Diurnal Temperature Range (DTR=Tmax-Tmin) especially in continental station like Ankara. Most of these trends found statistically significant at 95% level. These results show stronger urbanization effect in Ankara and İstanbul city center. Due to the increasing greenhouse gases, temperatures in Turkey are increasing in line with the world.

REFERENCES

Çiçek, İ., 2004, Ankara'da şehirleşmenin yağış üzerine etkisi, Fırat Üniversitesi Sosyal Bilimler Dergisi, Cilt: 14, Sayı: 1, Sayfa: 1-17, Elazığ

Coşkun, M., Sümer, U.M., Ulupınar, Y., Şensoy, S., Demircan, M., Bölük, E., Arabacı, H., Eskioğlu, O., Kervankıran, S., 2017, State of the Climate in Turkey in 2016.

Demircan, M., Arabacı, H., Akçakaya, A., Şensoy, S., Bölük, E., Coşkun , M., 2017, İklim Ve Şehirleşme: Minimum Sıcaklık Trendleri, III. Türkiye İklim Değişikliği Kongresi, TİKDEK 2013 3 – 5 Haziran 2013, İstanbul

Georgescu, M., M. Moustaoui, M., A. Mahalov, A., Dudhia , J., 2012, Summer-time climate impacts of projected megapolitan expansion in Arizona, Nature Climate Change 3,37–41(2013), doi:10.1038/nclimate1656

Hua, L.J.; MA, Z.G. & Guo, W.D.,2007, The impact of urbanization on air temperature across China. Theoretical and Applied Climatology

Kındap, T., Unal, A.,Ozdemir, H., Bozkurt D., Turuncoğlu, U.U., Demir, G., Tayanç, M., Karaca, M., 2012, Quantification of the Urban Heat Island Under a Changing Climate over Anatolian Peninsula.

Oke, T. R. (1982): "The Energetic Basis of the Urban Heat Island." Q. Jl. R. Met. Soc., 108, s:1-22.

Sensoy, S., 2006, Türkiye iklim sınıflandırması, www.mgm.gov.tr/FILES/iklim/iklim_siniflandirmalari.pdf

Sensoy S., Türkoğlu N., Akçakaya A., Ulupınar Y., Ekici M., Demircan M., Atay H., Tüvan A., Demirbaş, H., 2013: Trends in Turkey Climate Indices From 1960 to 2010, 6th Atmospheric Science Symposium, 24 - 26 April 2013, ITU, Istanbul, Turkey.

Sensoy, S., Turkoglu, N., Cicek I., Demircan, M., Arabacı, H., Bölük, E., 2014, Urbanization Effect on Trends of Extreme Temperature Indices in Ankara, 7th Atmospheric Science Symposium, 28-30 April 2015, İstanbul

Taha, H., 1992, Urban Climates and heat islands: albedo, evapotranspiration and anthropogenic heat, Energy Buildings 25, s:99-103

Tanrıkulu, M., 2006, İzmir'de şehirleşmenin sıcaklık ve yağış üzerine etkisi. Yüksek Lisans Tezi, A.Ü. Sosyal Bilimler Enstitüsü, Fiziki Coğrafya Bölümü.

Zhang, X., Aguilar, E., Sensoy, S., et al, 2005, Trends in Middle East climate extreme indices from 1950 to 2003, J. Geophys. Res., 110, D22104, doi:10.1029/2005JD006181.

HOVMÖLLER ANALYSIS OF TOTAL MONTHLY PRECIPITATION ANOMALIES FOR TURKEY

Mahir Aydın[1], İrem Özmen[1], Mikdat Kadıoğlu[1]
İstanbul Technical University, Faculty of Aeronautics and Astronautics, Meteorological Engineering, İstanbul[1]
aydinma@itu.edu.tr, ozmenir@itu.edu.tr, kadioglu@itu.edu.tr

ABSTRACT
Climate change in today's conditions can be considered at the top of the environmental problems that threaten Turkey as well as the whole world. Given the impacts on issues such as agriculture, forests, fresh water resources, sea level, energy and human health; the change in meteorological parameters due to climate change has a considerable precaution for future projections. In this study, the effect of climate change on the seasonal distribution of monthly total rainfall in Turkey is analysed by means of reanalysis. Monthly total rainfall and seasonal precipitation averages between 1980 and 2010 were considered to be meteorological normal of latitudes and longitudes. According to the meteorological normals, Hovmöller analysis of annual total rainfall anomaly and seasonal total rainfall anomaly between 1980 and 2016 has been prepared. In this context, it has been observed that the long-term droughts in our country that we keep the latitudes constant are primarily in the east of Turkey and also in the west. In addition, a decrease is observed in the precipitation in Turkey, while the western coast of the country is particularly noticeable in the precipitation during the last fifteen years. When the longitudes are kept constant, it is observed that rainfall below normal or near normal in autumn and winter gradually increases its effect in spring and summer. No regular periodicities have been encountered when considering the oscillations of precipitation in Turkey.

Keywords: *Climate Change, Precipitation, Seasonal, Turkey, Hovmöller*

INTRODUCTION
With the industrial revolution starting in 18th century, greenhouse gas has started to pollute the atmosphere in a great extent as a result of industrial production and population growth in settlements. As a consequence, temperature on a global scale tend to increase and precipitation has started to change.

It is observed in the study of "global climate change and its possible effects" that precipitation has tendency to decrease and drought increases more specifically in winter in Turkey. It can be also added that there is an increase in spring and summer precipitation in some stations with continental antecedent precipitation. The article "Global climate change and Turkey" suggests that winter precipitation in Aegean, Mediterranean and Southeastern Anatolia will decrease in %20-50 while there will be a precipitation increase that reaches to %50 in autumn in Southeastern and East Anatolia.

When the vital importance of human-climate interaction was taken into consideration, the determination of the areal and temporal precipitation change has been getting a great importance day by day. That's why, this study tries to determine the latitudinal and longitudinal change of precipitation in Turkey by accepting the amount of precipitation between 1890-2010 as normal, and by using Hovmöller diagram of total annual and total seasonal precipitation anomalies between 1980-2016.

MATERIAL AND METHOD

Hovmöller diagram used in this study which analysis the areal and temporal change of total precipitation in Turkey is a very effective method in determining the change and periodicity of some various meteorological parameters in time scale. While one axis of a typical Hovmöller diagram represents latitude and longitude, the other one stands for time. This type of diagram found by Ernest Hovmöller was firstly used for the determination of trough and ridge. Precipitation rates for diagram are the reanalysis rates taken from ECMWF. The data was converted by MATLAB and regulations were done on EXCEL. ORIGINLAB was used to generate the diagrams.

FINDINGS AND DISCUSSION

Constant Longitude

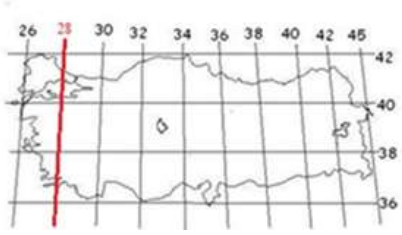

28E Longitude Constant: It is observed that precipitation in southwest of Turkey has increased in last eight years. The precipitation anomaly which is negative in autumn has changed as positive in summer and spring.
Figure 1. Longitude 28E

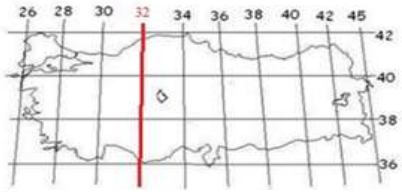

32E Longitude Constant: Precipitation emission in winter is lower than in summer. While precipitation between the years of 1990-2000 decreases in winter, it increases in summer. This is also the case for 2014.
Figure 2. Longitude 32E

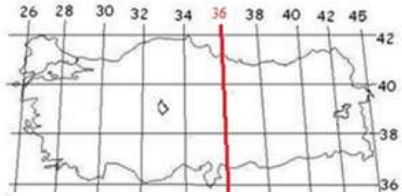

36E Longitude Constant: the decrease of precipitation between the years of 2000-2010 occurred in summer and spring. A drought season from the north of Turkey to the south is also observed in this longitude.
Figure 3. Longitude 36E

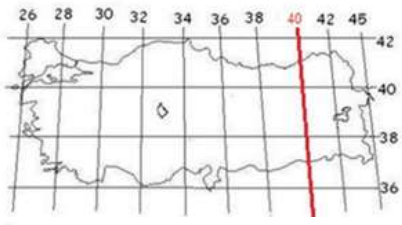

40E Longitude Constant: It is observed that precipitation in northeast of Turkey increases in summer and reaches near to seasonal normals in winter. Precipitation in southeast of Turkey is near to normal value in summer.
Figure 4. Longitude 40E

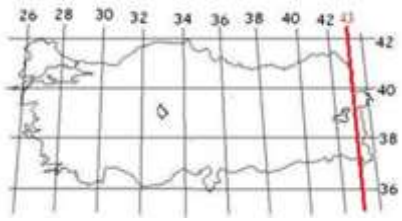

43E Longitude Constant: The profile of precipitation in west of Turkey depends on the changes of precipitation in spring and autumn as the precipitation in summer and winter is very close to each other.
Figure 5. Longitude 43E

Constant Latitude

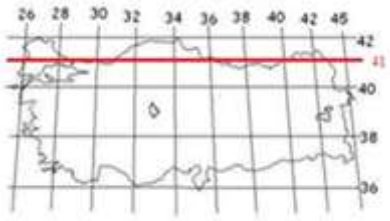

Latitude Constant: 41N Latitude Constant: It is observed that the precipitation in northwest of Turkey is lower than in northeast. It can be also added that there is an increase in rainfall in west while there is a decrease in east in recent years.
Figure 6. Latitude 41N

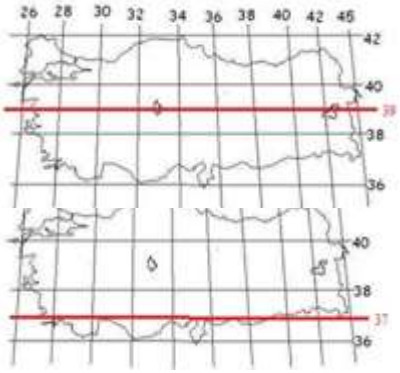

39N Latitude Constant: the decrease of precipitation about 1995 in east of Turkey become effective in west in 2008.
Figure 7. Latitude 39N

37N Latitude Constant: while the precipitation values are close to normals in summer, precipitation emission reaches its utmost in winter and spring.
Figure 8. Latitude 37N

Constant Longitude of 28E

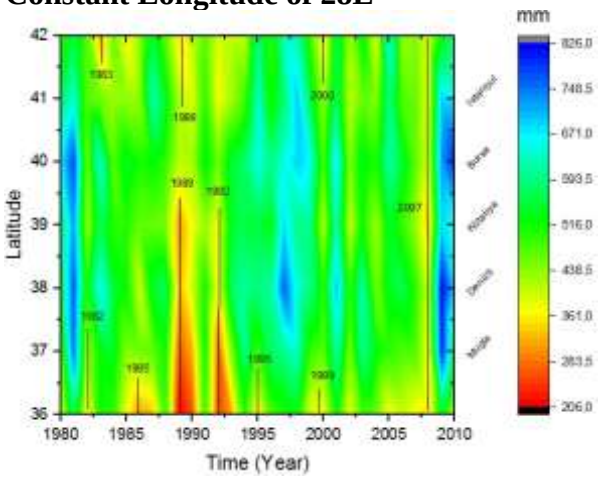

Diagram 1. 28E Longitude Climatology

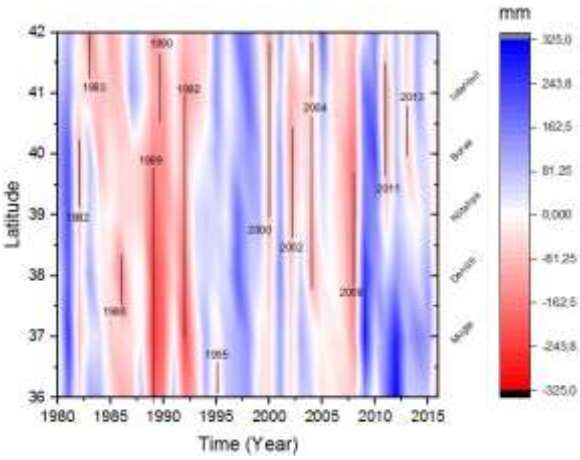

Diagram 2. 28E Longitude Anomaly

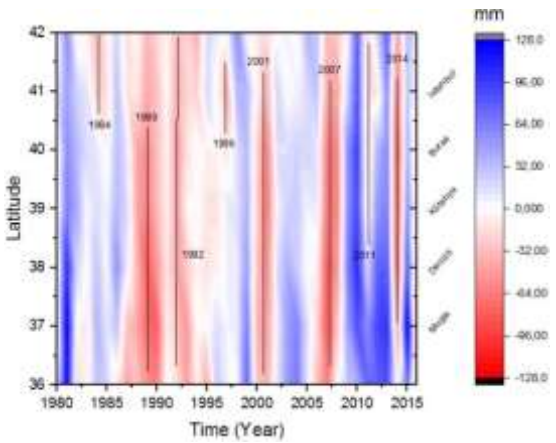

Diagram 3. 28E Longitude Winter Anomaly

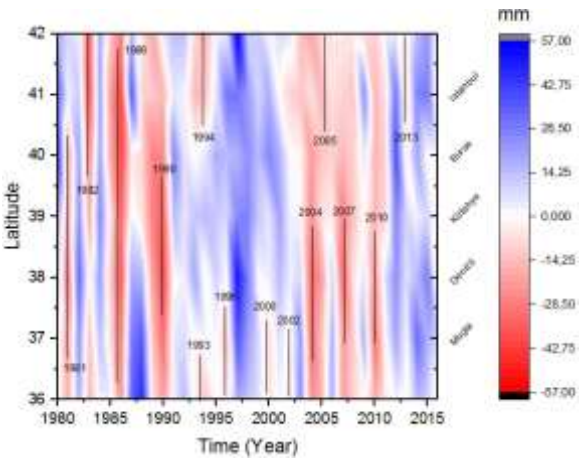

Diagram4. 28E Longitude Spring Anomaly

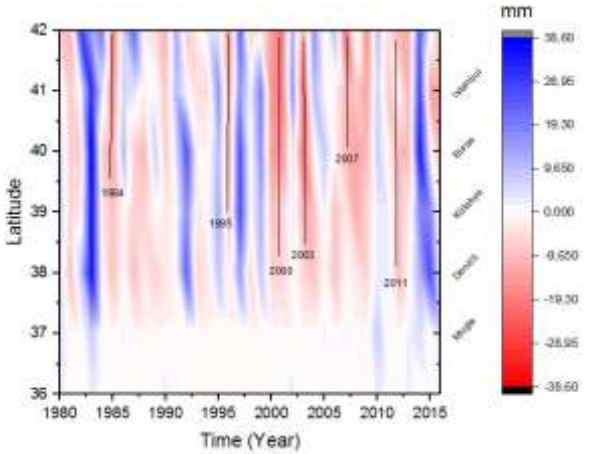

Diagram 5. 28E Longitude Summer Anomaly

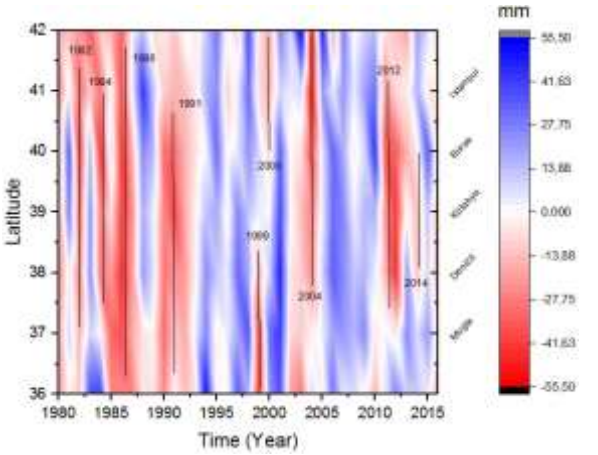

Diagram 6. 28E Longitude Autumn Anomaly

Constant Longitude

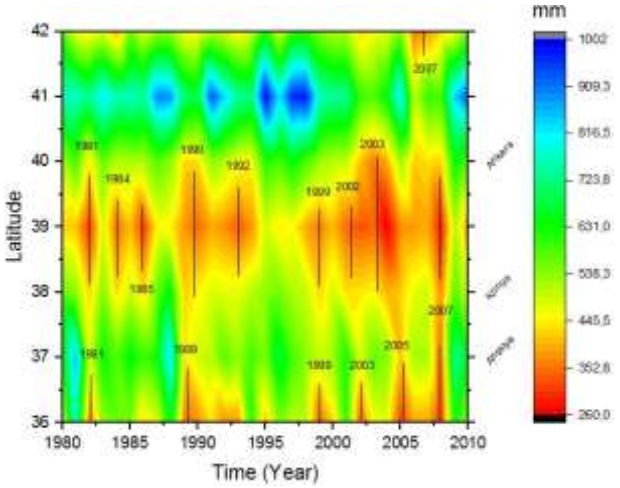

Diagram 7. 32E Longitude Climatology

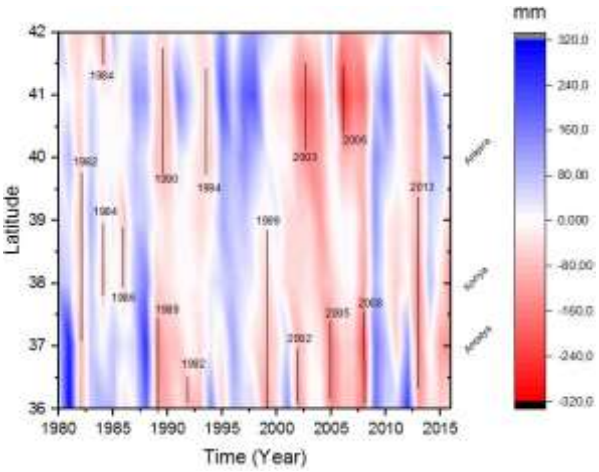

Diagram 8. 32E Longitude Anomaly

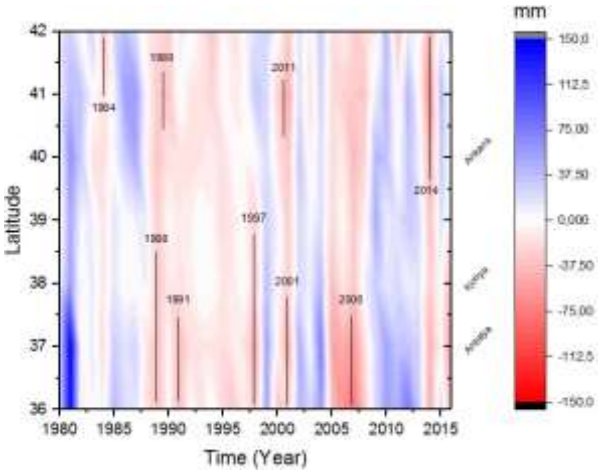

Diagram 9. 32E Longitude Winter Anomaly

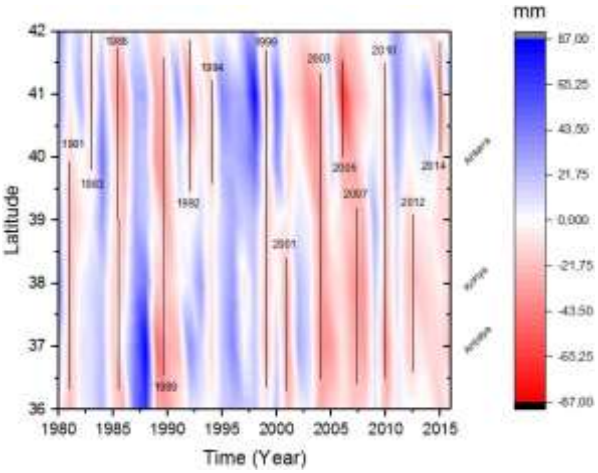

Diagram 10. 32E Longitude Spring Anomaly

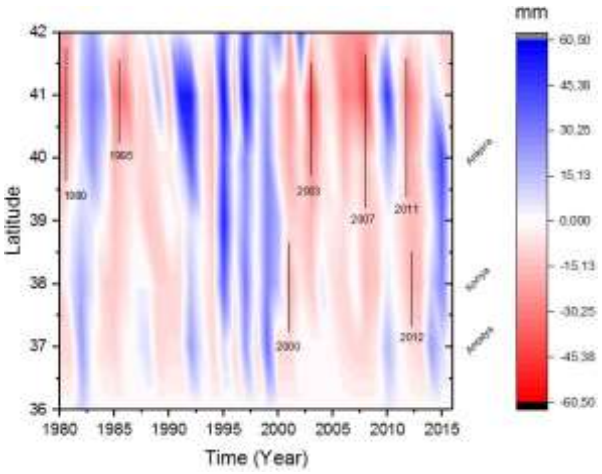

Diagram 11.32E Longitude Summer Anomaly

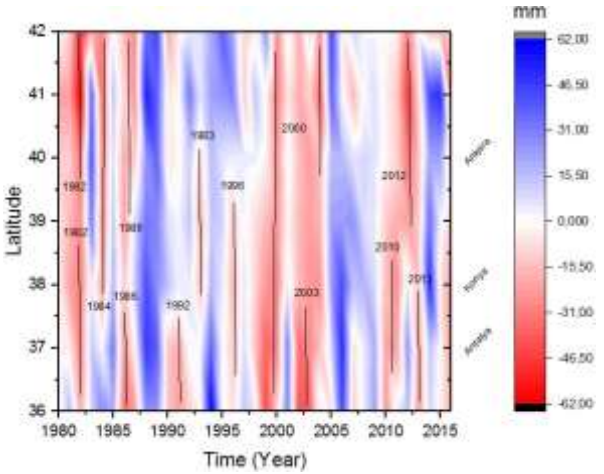

Diagram 12. 32E Longitude Autumn Anomaly

Constant Longitude of 36E

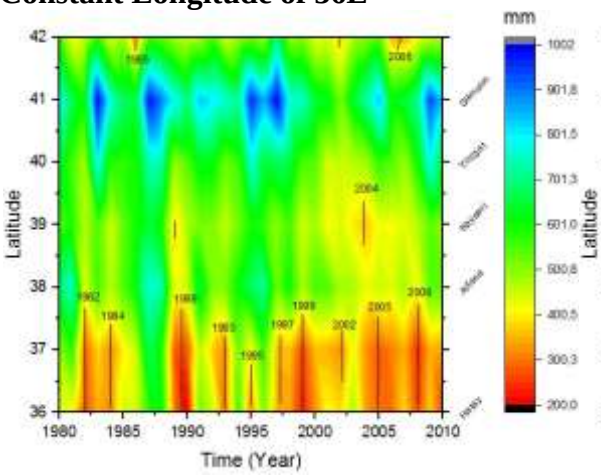

Diagram 13. 36E Longitude Climatology

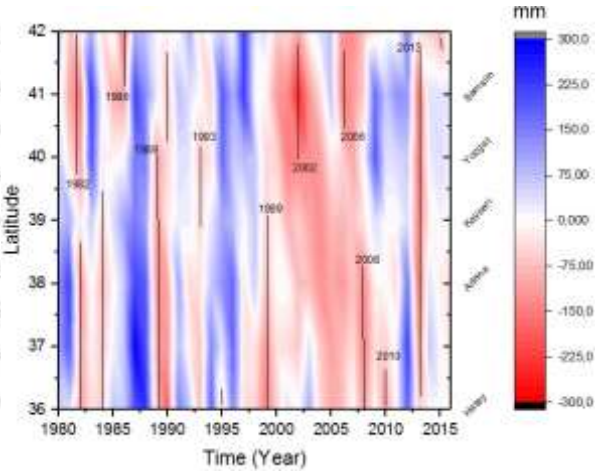

Diagram 14 36E Longitude Anomaly

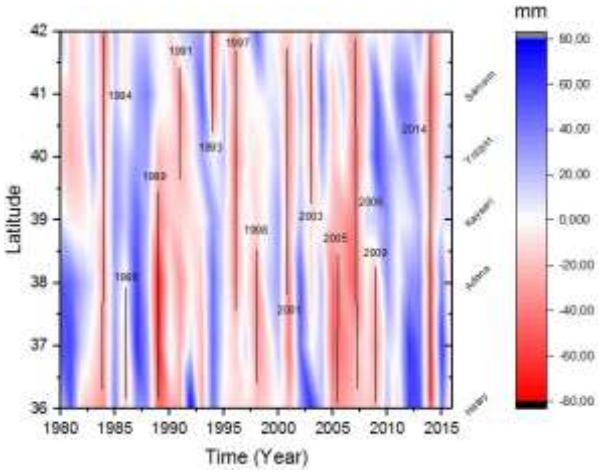

Diagram 15. 36E Longitude Winter Anomaly

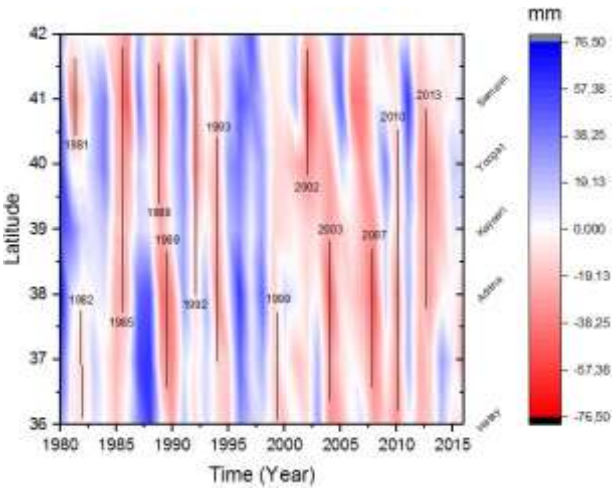

Diagram 16. 36E Longitude Spring Anomaly

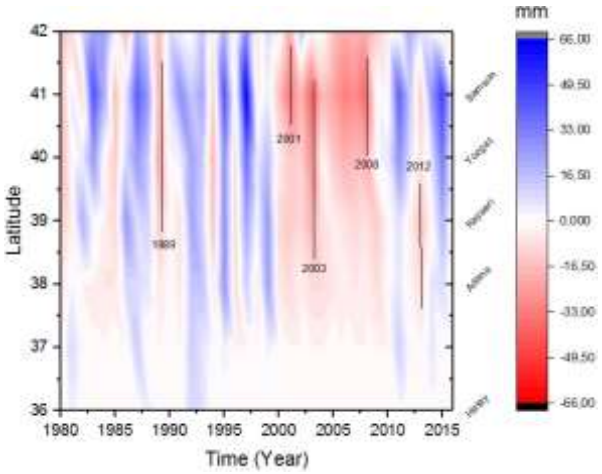

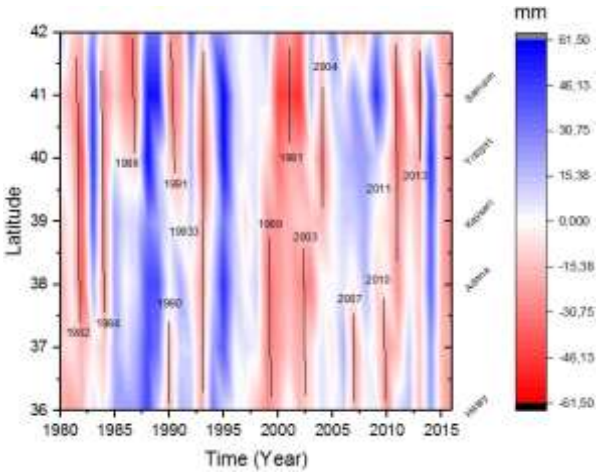

Diagram 17. 36E Longitude Summer Anomaly Diagram18. 36E Longitude Autumn Anomaly

Constant Longitude of 40E

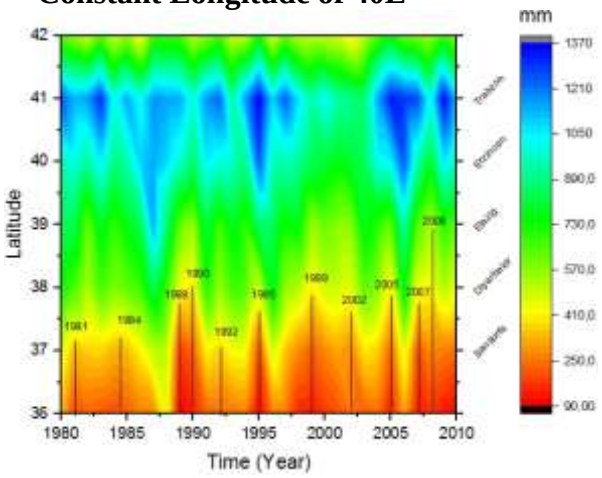

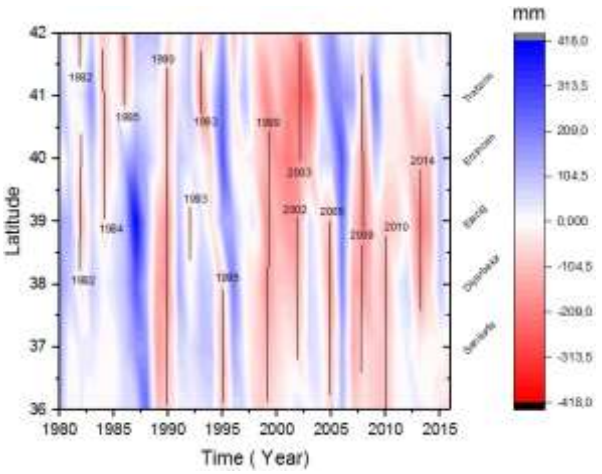

Diagram 19. 40E Longitude Climatology Diagram 20. 40E Longitude Anomaly

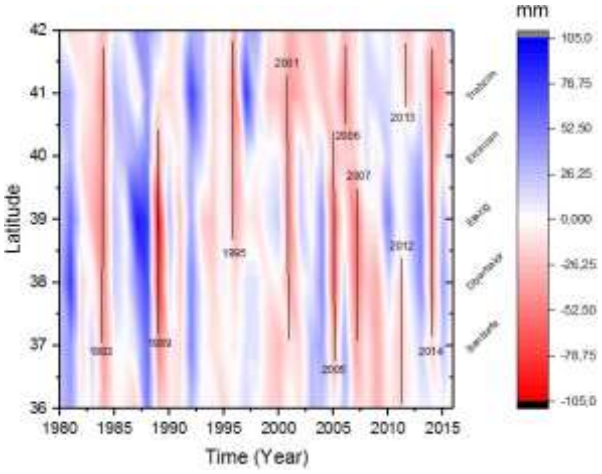

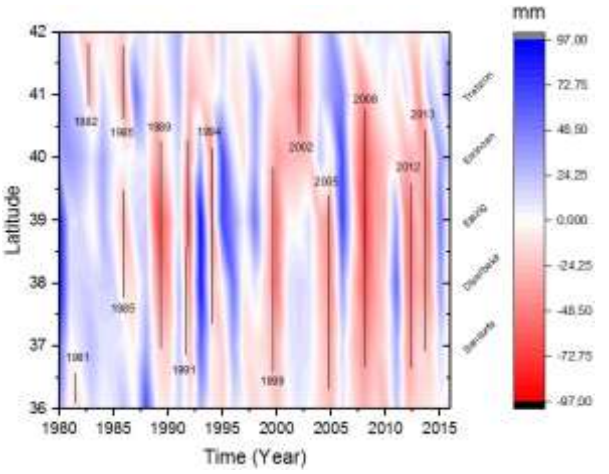

Diagram 21. 40E Longitude Winter Anomaly Diagram 22. 40E Longitude Spring Anomaly

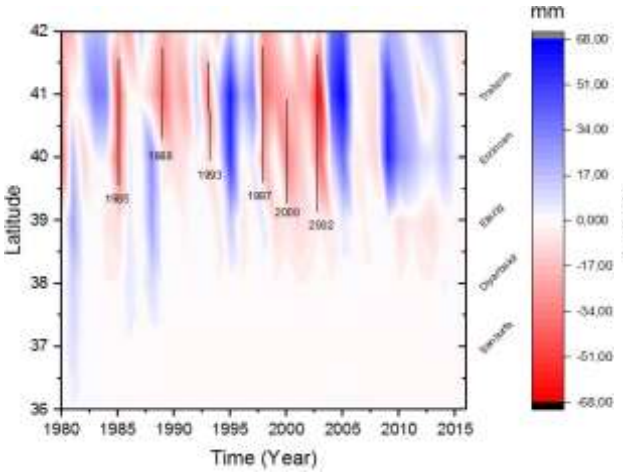

Diagram 23. 40E Longitude Summer Anomaly

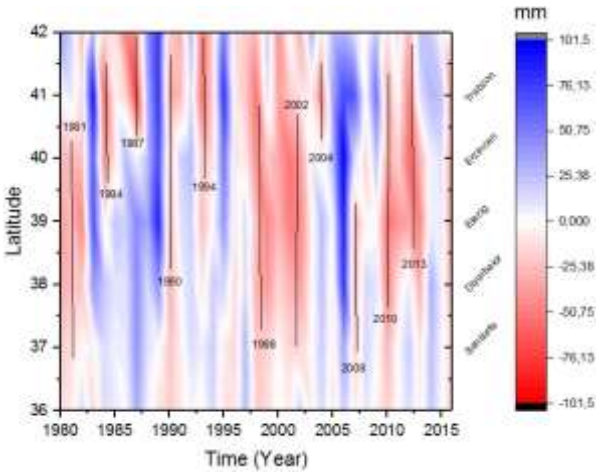

Diagram 24. Longitude Autumn Anomaly

Constant Longitude of 43E

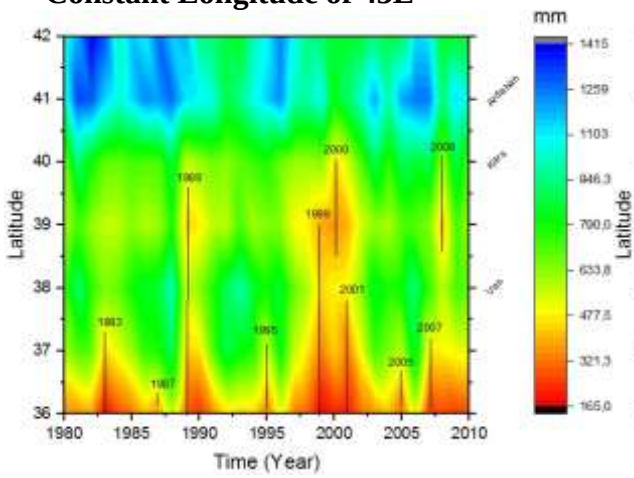

Diagram 25. 43E Longitude Climatology

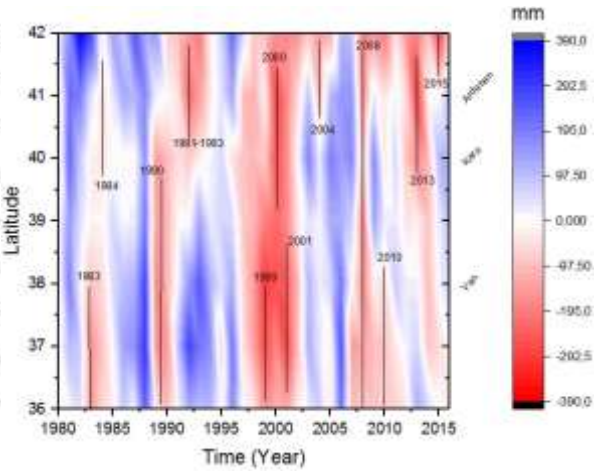

Diagram 26. 43E Longitude Anomaly

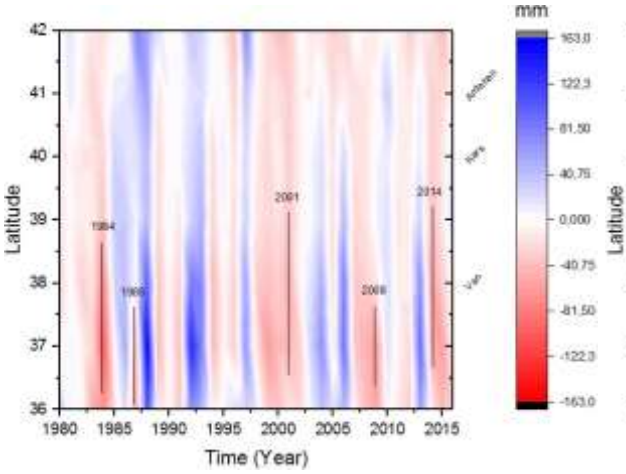

Diagram 27. 43E Longitude Winter Anomaly

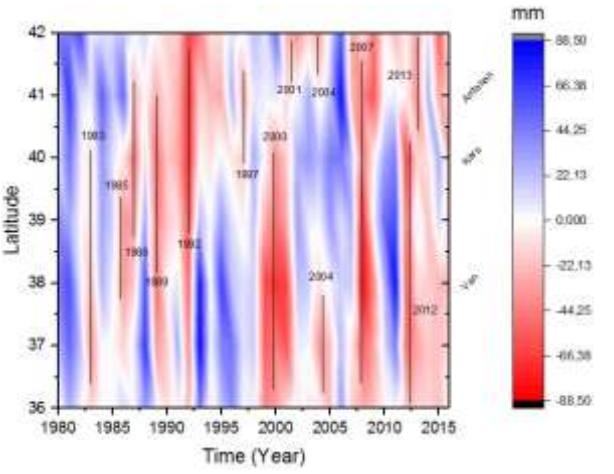

Diagram 28. 43E Longitude Spring Anomaly

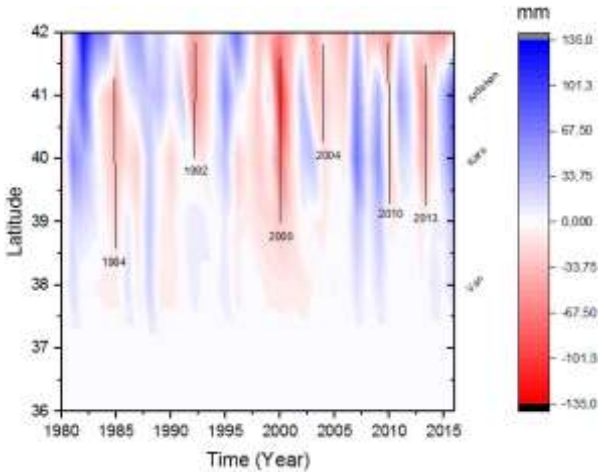

Diagram 29. 43E Longitude Summer Anomaly

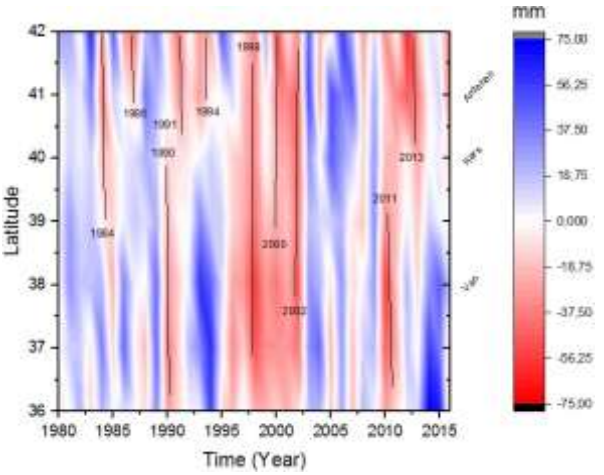

Diagram 30. 43E Longitude Autumn Anomaly

Constant Latitude of 41N

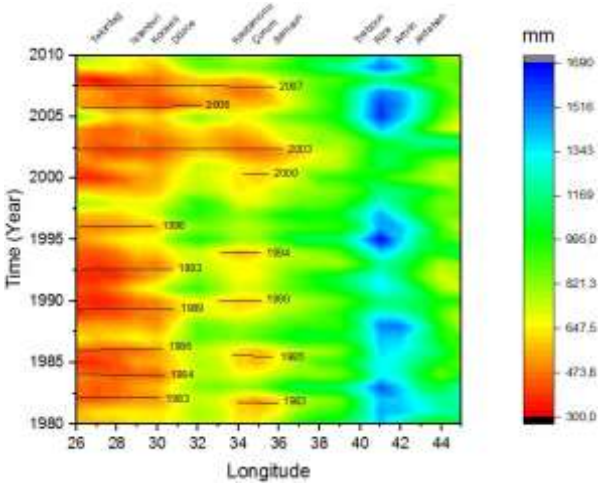

Diagram 31. 41N Latitude Climatology

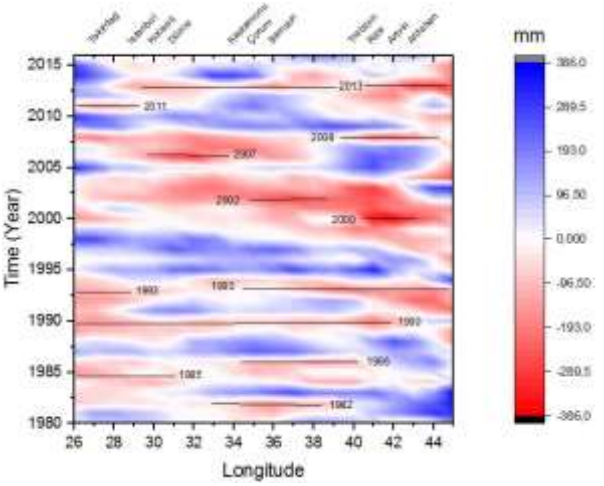

Diagram 32. 41N Latitude Anomaly

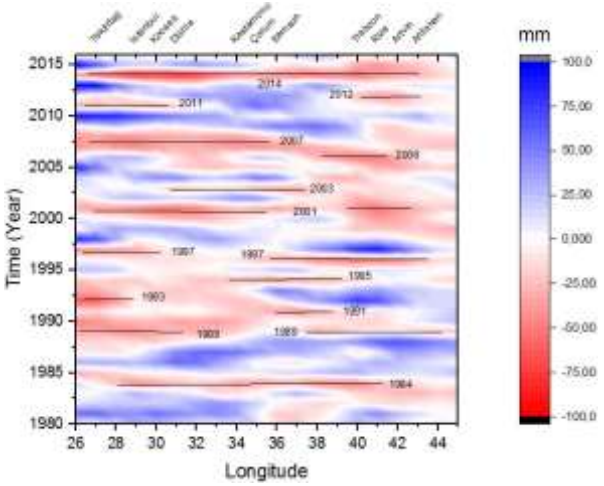

Diagram 33. 41N Latitude Winter Anomaly

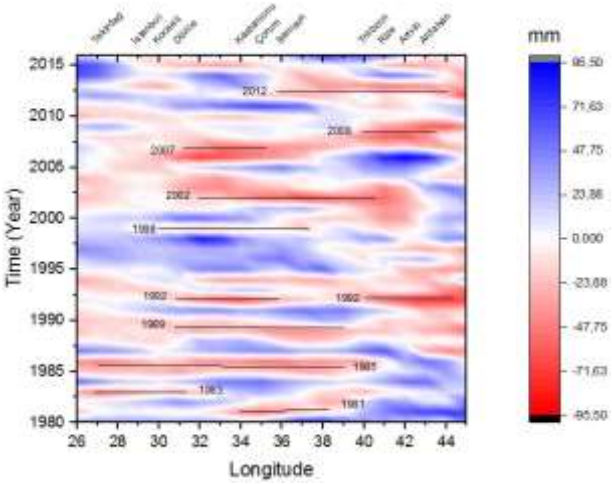

Diagram 34. 41N Latitude Spring Anomaly

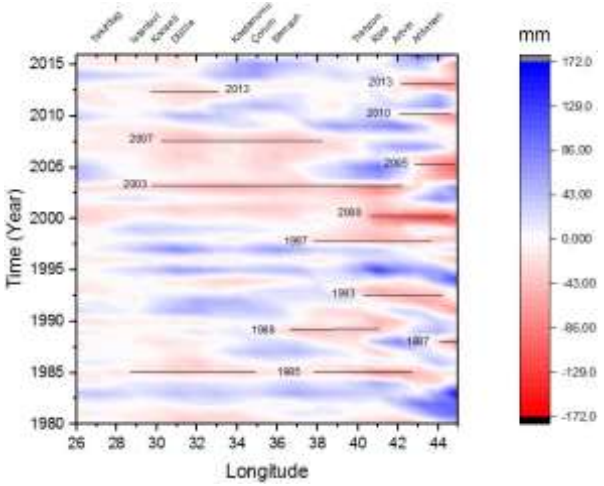

Diagram 35. 41N Latitude Summer Anomaly

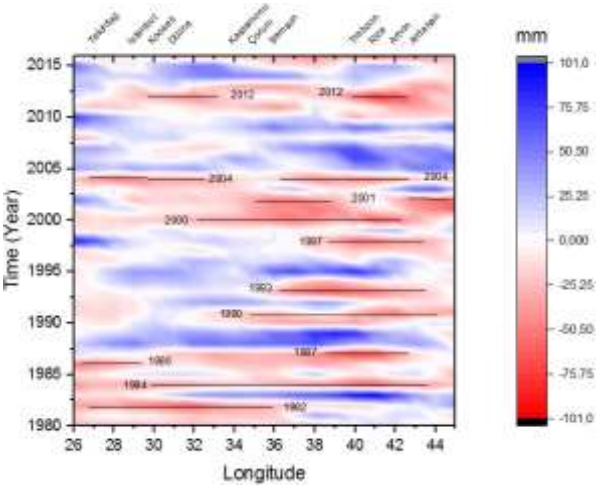

Diagram 36. 41N Latitude Autumn Anomaly

Constant Latitude of 39N

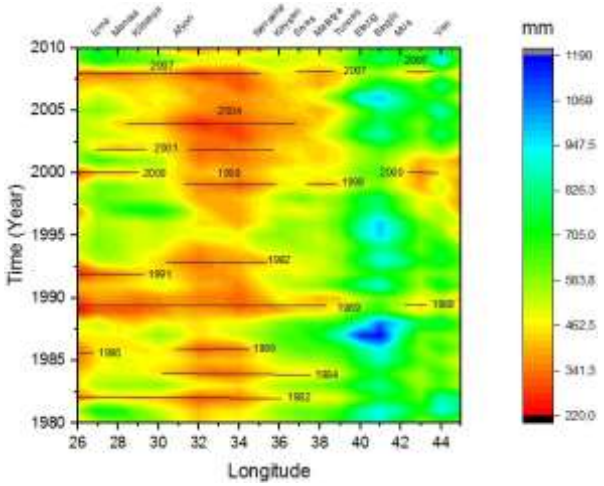

Diagram 37. 39N Latitude Climatology

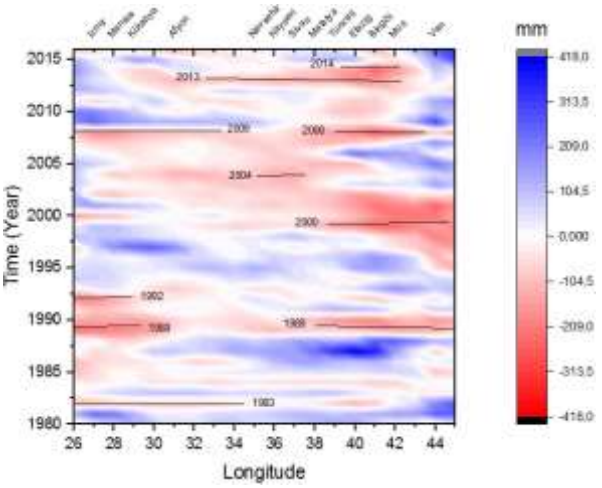

Diagram 38. 39N Latitude Anomaly

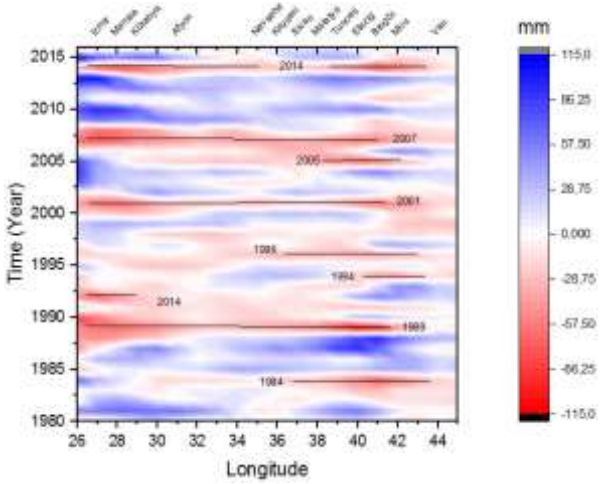

Diagram 39. 39N Latitude Winter Anomaly

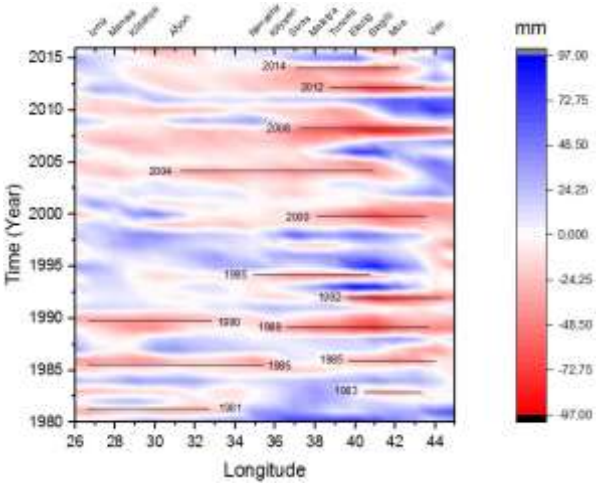

Diagram 40. 39N Latitude Spring Anomaly

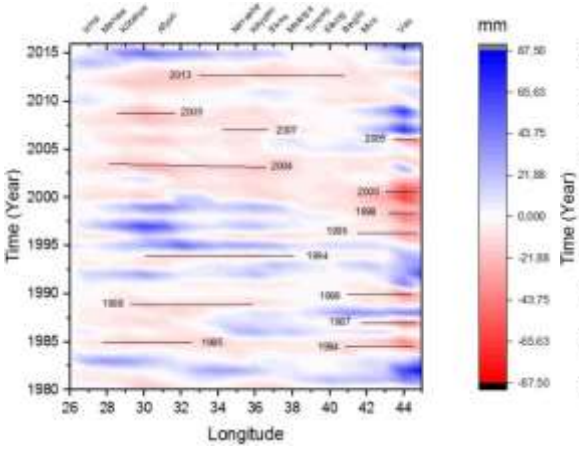

Diagram 41. 39N Latitude Summer Anomaly

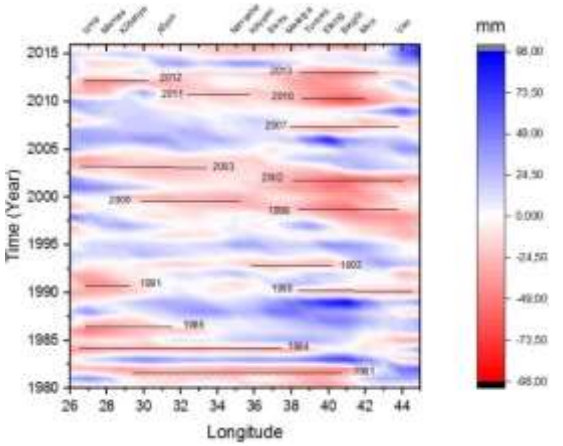

Diagram 42. 39N Latitude Autumn Anomaly

Constant Latitude of 37N

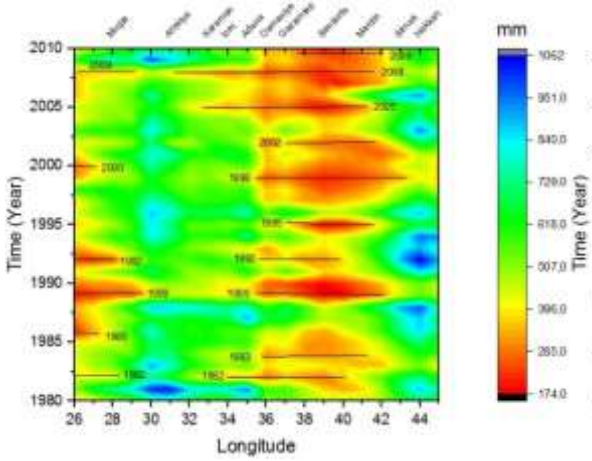

Diagram 43. 37N Latitude Climatology

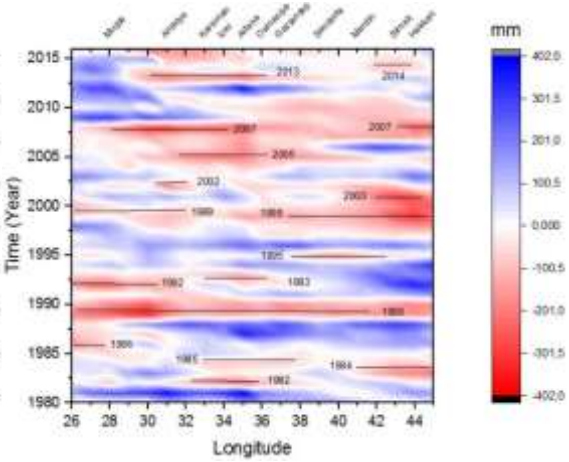

Diagram 44. 37N Latitude Anomaly

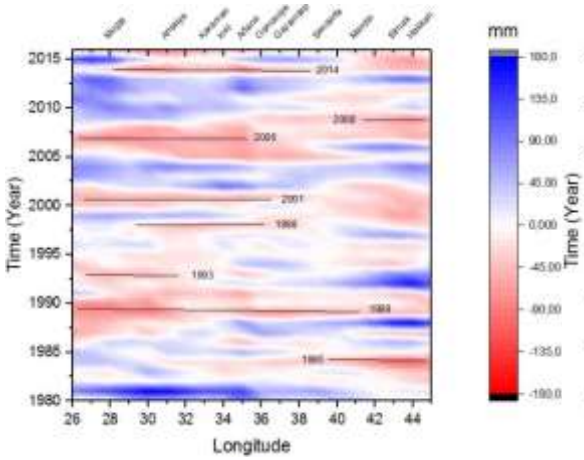

Diagram 45. 37N Latitude Winter Anomaly

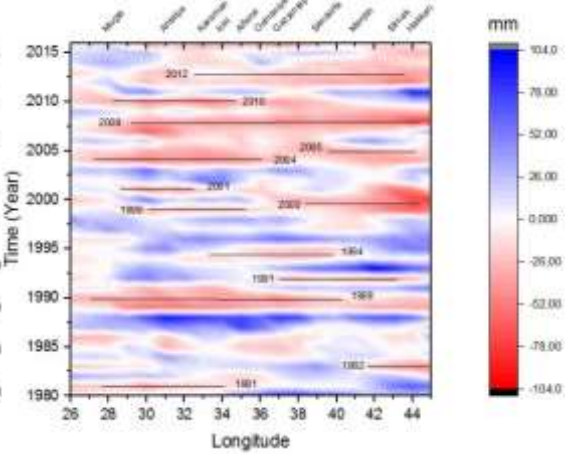

Diagram 46. 37N Latitude Spring Anomaly

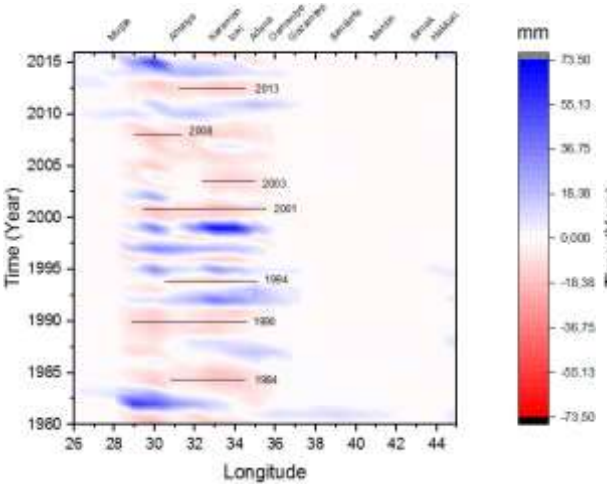

Diagram 47. 37N Latitude Summer Anomaly

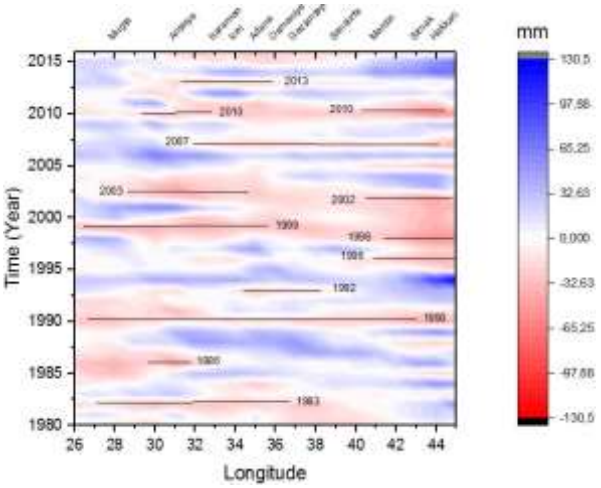

Diagram 48. 37N Latitude Autumn Anomaly

RESULTS

It can be clearly seen on the study that there is no regular periodicities have been encountered when considering the oscillations of precipitation in Turkey. When the altitudes are kept constant, Howmöller analysis suggests that:

- Except the areas where 36E altitude is kept constant and the emission is high, precipitation in the east of Turkey is close to normal in summer.
- It is observed that summer precipitation is higher than normal and winter precipitation is lower than normal in the last five years of periods.
- When the latitude are kept constant, The drought in the east of Turkey in 1995 has started to occur in the west in 2008.

It is observed that precipitation in southeast of Turkey decreases but summer precipitation is higher than normal. Although there are some small differences in some regions of Turkey, precipitation is too low in the years of 1989-1990, 1999-2003,2013-2014. The observed anomaly values are shown in Hovmöller diagram.

REFERENCES

Hovmöller, E. 1949. The Trough-and-Ridge Diagram, Swedish Meteorological and Hydrological Institute, Stockholm.

Kadıoğlu, M. tarih yok. Küresel İklim Değişikliği ve Türkiye. Mühendislik ve Makina, 22.

Türkeş, M., Sümer, U. M. ve Çetiner, G. 2000. 'Küresel İklim Değişikliği ve Olası Etkileri', Çevre Bakanlığı, Birleşmiş Milletler İklim Değişikliği Çerçeve Sözleşmesi Seminer Notları (13 Nisan 2000, İstanbul Sanayi Odası), 7-24, ÇKÖK Gn. Md., Ankara.

DETECTING CLIMATE-CHANGE FROM A SEASONAL PERSPECTIVE OVER TURKEY

Hasan TATLI

Canakkale Onsekiz Mart University, Faculty of Sciences and Arts, Department of Geography, Physical Geography Division, 17020, Canakkale, Turkey, tatli@comu.edu.tr

ABSTRACT

This study suggests a seasonal perspective to detect climate change. For this purpose, the Mann-Kendall (MK) trend method was applied to the seasonal values of maximum, minimum, average temperatures and precipitation totals of Turkey. To see the advantages of using seasonal-scale perspective, the results were also compared with those obtained from annual values, since several important traces of the climate change may be masked due to the smoothed annual data. In the study, the MK-trend test calculations were made by writing a source code of Fortran 95, and the homogeneity in data values was checked by a toolbox of the so called "Climtrends" written in R-language. In addition to being homogeneous of the data, the meteorological stations with less than 7% ratio of the missing records were selected. One of the important results is that the trends masked in the annual data, undoubtedly become clear in the seasonal-scale domain. In the study, another important result is the negative trend-patterns obtained from the precipitation series overlap the same areas of the several river-basins of Turkey, where the agricultural activities are so intense. In addition to global warming, determining the possible trends in the minimum temperatures under the influence of physical geographical factors observed in the southern coast of the country and the rain-shadows contribution to the precipitations in the north-east areas of the country are such important results of this study. This is the fact that an increasing of water demand due to increasing of the population is a very important problem needs to be solved by the policy makers.

Keywords: *Climate-Change, Mann-Kendall, Season, Trend, Turkey*

INTRODUCTION

Trends seen in slow components of temperature and precipitation values could be assessed as evidences of the climate change. Particularly, rainfall or water has been attracting so much from the past to present day. From the date of the Sumerians to present day, water has been perceived as an operable commodity. Due to the negative effects of climate-change on fresh water sources, our water related problems are becoming an inevitable spiral. In short, water crises are likely to emerge in many parts of the world in near future.

In this study, the MK-trend test was applied to detect a significant increase (or a decrease) in the slow components of the temperatures and precipitation values between 1970 and 2014 over Turkey. The country is located in the eastern Mediterranean basin, and mainly influenced from the westerly winds of the pressure disturbances especially in winter. There is a very humid region located in the northern coast of the country, where the precipitation shadows are also visible. Besides the fact that three sides of the country are covered by seas and mountainous over the eastern parts are cold and snowy in winter, and the summers are dry and hot. In other words, the typical real Mediterranean climate prevails in the country (Tatli and Dalfes, 2016). Since the southeastern region of the country is the hottest and moisture-poor place, the additional problem for agricultural activities could be overcome by the construction of various hydraulic power plants and dams. On the other hand, the Marmara Region, which is the most industrial region located in the north-west of the country has the most populous population, and therefore the demand for fresh-water have increased over time leads hydro-meteorological and environmental problems. One way to monitor these problems is to run a general circulation

model (GCM) linked to various socio-economic scenarios (Tatli *et al*., 2004, 2005; Tatli, 2015; IPCC, 2013). Another way is to have a look at the near past climate. The important issue in this context is the climate-change rather its natural variability. Correspondingly, one of the easy methods to detect climate change is finding trends in the variables, especially in temperature and precipitation values.

If one looks at the literature one many find studies on this topic. Some of them are summarized as: Partal and Kahya (2006) have applied Mann-Kendall-Sen to determine trend in the annual precipitation values over Turkey. Norrant and Douguédroit (2006) have investigated the identification of linear trends in monthly, seasonal and annual timescales in the Mediterranean. Jentsch *et al*. (2007) have underlined the evidences of the "event-based", not the "trend-based". Sousa *et al.* (2011) have analysed the trends and extremes of the drought indices throughout in the Mediterranean by using the average monthly precipitation and the Palmer Drought Severity Index (PDSI) during the 20th century. Tatli (2015) has suggested the Hurst exponent for determining the persistence of meteorological drought and using it in combination with the trends and jumps. Iqbal *et al.* (2016) have a recent study of changes in the maximum and minimum temperatures in Pakistan. Colombani *et al.* (2016) have found a relationship between the trend of heavy metal release and climate change. Chattopadhyay and Edwards (2016) have studied to determine the long-term trends in annual precipitation and mean annual air temperature for the state of Kentucky. Shi *et al.* (2016) have investigated the potential effects of climate change on energy demand in the household sector by determining the trends of heating and cooling days in China.

METHODS AND DATA

Data

In this study, the data set of monthly total precipitation and average temperature, maximum, minimum temperature values of the 212 meteorological stations belonging to the Turkish State Meteorological Service was used for the period 1970-2014. In addition, the homogeneity of the data was checked by cross applying the Pettit (Pettitt, 1979), Standard Normal Homogeneity (SNHT) (Alexandersson, 1986) and von Neumann ratio (Von Neumann, 1941) tests with the help of a statistical toolbox written in R-language of the so called "Statistical Methods for Climate Sciences (Climtrends)" (Gama, 2016). A confidence level of 95% was chosen while employing the tests. Consequently, in addition to homogenous stations and the number of stations with an incomplete-data ratio of less than 7% were chosen. Wijngaard *et al.* (2003) have studied the homogeneity characteristics of the climate series over Europe that one may find more detailed information of the corresponding tests in their study.

Mann-Kendall Trend Test

The Mann-Kendall trend (MK) test was first suggested by Mann (1945), and later it has been enhanced by Kendall (1975) and Hirsch *et al*. (1991). The application steps of the MK test follow as:

$$\left.\begin{array}{l} \mathrm{H}_0 : \text{There is no trend in the series} \\ \mathrm{H}_\mathrm{a} : \text{There is a trend in the series} \end{array}\right\} \quad (1)$$

To assess the null hypothesis, a required quantity of the test, *s*, is calculated by

$$s = \sum_{i=1}^{N-1} \sum_{j=i+1}^{N} \mathrm{sgn}(x_j - x_i) \quad (2)$$

Where *sgn* indicates the abbreviation of the Signum (or Sign) function. Let $x, y \in \mathbf{R}$, the sgn function is defined by

$$\operatorname{sgn}(x-y)=\begin{cases}1, & \text{if } x>y\\ 0, & \text{if } x=y\\ -1, & \text{if } x<y\end{cases} \tag{3}$$

The average of the statistic, $\bar{s}$, is assumed to be zero and follows the normal probability distribution, and its variance of σ^2 is acquired by

$$\sigma^2=\frac{N(N-1)(2N+5)-\sum_{i=1}^{p}h_i(i)(i-1)(2i+5)}{18} \tag{4}$$

Here, h_i, represents the number of ties up to sample i, and the test-statistic is calculated as follows,

$$Z=\begin{cases}\dfrac{s-1}{\sigma^2}, & \text{for } s>0\\ 0, & \text{for } s=0\\ \dfrac{s+1}{\sigma^2}, & \text{for } s<0\end{cases} \tag{5}$$

The probability density function of the Z also follows the standard normal distribution. If Z is greater than the critical value of $Z_{1-\alpha/2}$ then the alternative hypothesis, H_a, is accepted by a statistical significance level of $1-\alpha/2$, where "α" is generally taken as 0.01, 0.05 and 0.1.

RESULTS AND DISCUSSION

The results of the MK-trend analysis were transferred to the related Geographic Information Systems (GIS) program for shaping the patterns of trends in the climatic variables over the country. The unmarked areas indicate that there are no significant trends while the "+" and "-" signs on the maps show statistically significant trends in these areas, respectively. In this section, at first, the maps obtained from the annual data shown in Fig.1 were interpreted, and later the maps of the seasonal data were analysed.

Annual Patterns

Thus, the trend patterns of the annual mean temperatures are given in Fig.1a. As seen in this figure, the significant positive trends show a significant distribution across the northern, western and southern coasts of the country, as well as the ignificant positive trends are also observed on the southern part of Eastern Anatolia, one of the most mountainous regions of the country. Like the mean temperatures, the minimum temperatures have significant positive trends observed on the southern and southern-western regions of the country, which are distributed along the coasts of the country adjacent to the sea. Certainly, the changes seen in the minimum temperatures usually represent the local-climate conditions.

The very interesting patterns those given in Figure 1.d are seen in the trends obtained from the annual precipitation totals. As can be seen in this figure, there are two trend patterns of decreasing in the precipitations around the eastern Marmara and Van Lake. On the other hand, there is an increase in the precipitation throughout the belt of Agri-Ardahan-Artvin of the Eastern Anatolia, as well as in the coastal region of the Middle-Black Sea.

Seasonal Patterns

Spring

We have provided a collection of information about the geographic distribution of the trends from the annual data, but we are now detecting that the distribution of trends in the seasonal variables have been changed in a great deal. If we take each of the variables one by one, the

positive trends of the annual mean-temperatures as given in Fig.1a, previously were seen in the Mid-Black Sea and the entire Marmara region.

However, in the new situation as shown in Figure 2a, the positive trends of the mean-temperatures are only observed over the coasts of the south Aegean and Mediterranean seas of the country. Since the tourism activities in this region are very important, the possible changes in the climate are of great importance, as well as this region is known a centre of producing industry of the citrus-fruits and orangeries. Accordingly, the positive trends of the temperature values in these regions would also affect the population of the diversity of living species, perhaps it will lead to occurrence of possible proliferation of the new pests.

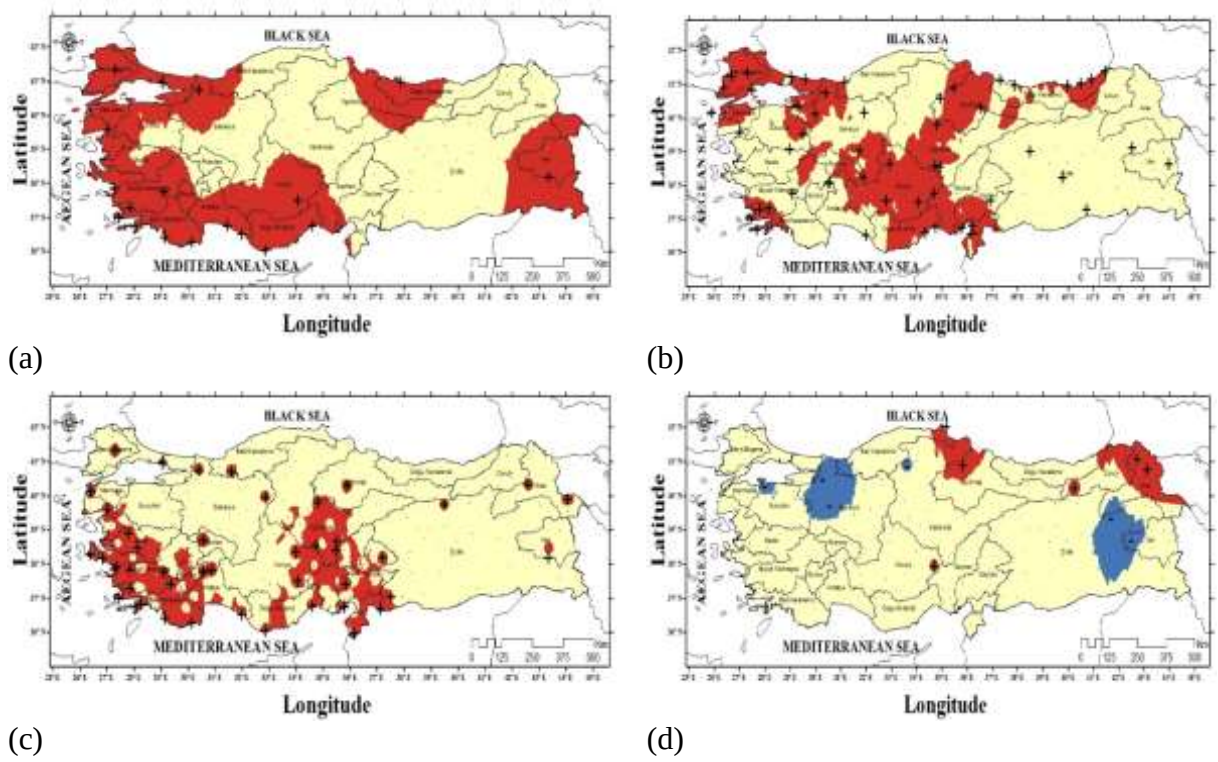

Figure 1. Spatial distributions of MK-trend in the annual data: Average temperature (a); Maximum temperature (b); Minimum temperature (c); and Total precipitation (d).

Similar situations are observed in the trends of the maximum temperatures as given in Fig.2b. As we can see from this figure that, the positive trends are observed on the entire Thrace region (except the west parts), the South-eastern Anatolia and Eastern Anatolia regions. Furthermore, a similar a positive trend pattern is also observed over the city of Konya and its surrounding. The grain production is very rich in Konya, but the underground water resources be so poor. When we examine the patterns of the minimum temperature as given in Fig.2c, they seem the patterns of those previously observed in the annual minimum-temperatures. However, the positive trends now are scattering over the coasts of the southern and southern Aegean of the country, are much more intense. This density is partly because of global warming, as well as the local-climate effects. In recent years, on these territories, it is a fact that summers have started early. This situation feels itself with the positive trend patterns observed in the minimum temperatures as seen in Fig.2c. When we look at the patterns at both maximum and minimum temperatures, we can see the significant positive trends in Istanbul, which is the most populous and financial city of the country. These positive trends, which are absorbed both in the annual and spring seasons, are the result of “urbanization” in Istanbul, i.e., the "heat island" reality.

Indeed, with the global warming, early precipitations are expected to increase due to acceleration of evaporation rate in the hydrologic cycle. However, this situation cannot be generalized. The negative trends of the spring rainfalls as given in Fig.2d are observed over the areas where the amount of agricultural produce being very economically important. Only on the north-eastern part of the country, the precipitations have a positive trend on a narrow-band area, which is influenced by the northly moist-cool air.

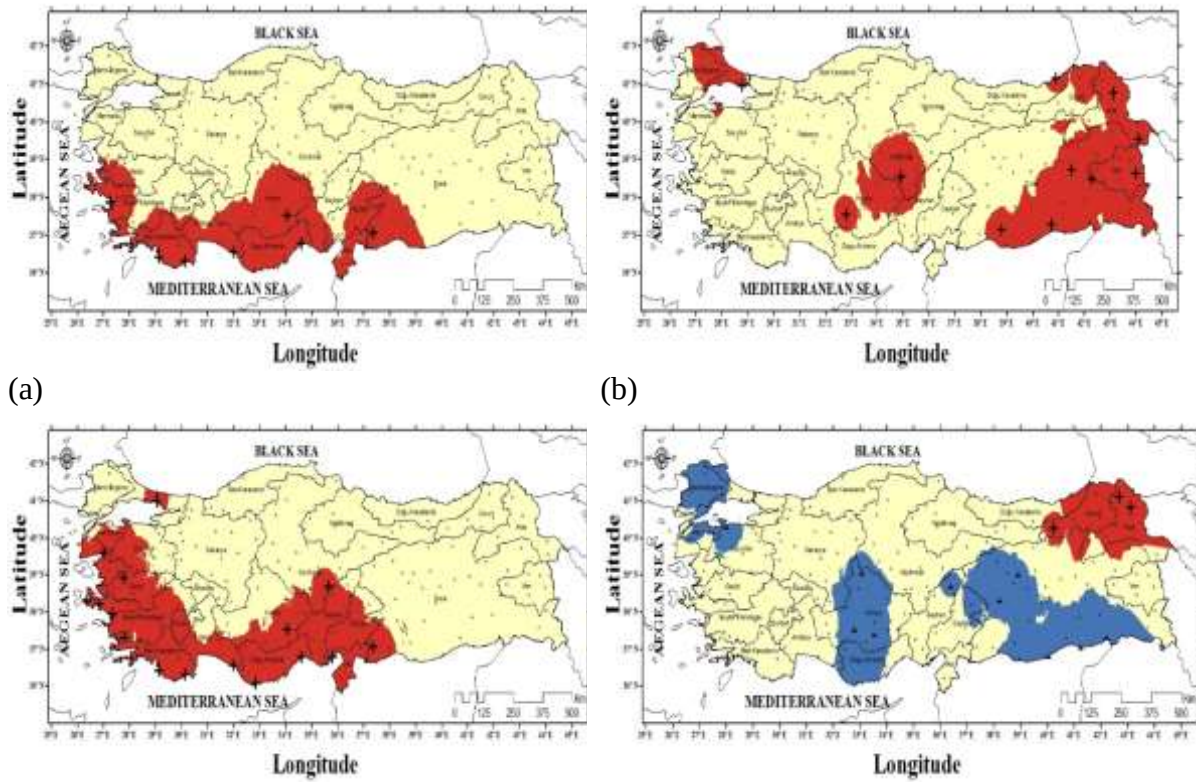

Figure 2. Spatial distributions of MK-trend in the spring: Average temperature (a); Maximum temperature (b); Minimum temperature (c); and Total precipitation (d).

Winter

As shown in Fig.3a, the positive trends in the mean temperatures of winter months have a pattern which is extending from the southern parts to north-eastern regions of the country. In other regions, there is an increase in the average-temperatures predominantly in some large cities. The global warming is felt much more in the southern regions; interestingly in the mountainous regions, several positive trends are seen in the places with high altitude and very cold weather can turn this into a more pleasant and comfortable region. On the contrary, the southern regions could be affected negatively. The increase in the winter average-temperatures may affect the snowfall in mountainous areas, so shortening the period of snow-cover on surface might have increased the frequency of extreme events such as various erosion and floods. It is obvious that many land-studies are needed to determine how living creatures adapting to the climatic conditions in that region and their diversity react to the new situation. The trends of the maximum temperature for the winter months are given in Fig.3b. This figure is very important in terms of revealing the gravity of the event. Because of the nature of the true Mediterranean climate, the winters must be cold and wet. In addition, a new study by Tatli and Dalfes (2016) have showed that the Holdridge based classification of the vegetation-types seen in the southern part of the country tended to resemble the tropical ones, and a shifting from the dominant cold-step vegetation structure to the warm-step vegetation, particularly in the inner regions of the country. This study clearly supports their work.

The trend patterns of the minimum temperatures are shown in Fig.3c, there are several significant positive trends of those predominantly seen in the eastern and southern of the central Anatolia, and southern parts of the Aegean. When the minimum temperatures and average-maximum temperatures are compared, we cannot see dominant trends except for the high mountainous and a narrow band area in the south-eastern Mediterranean Sea. Therefore, we can arrive at a conclusion that the minimum temperatures that reflect the characteristics of local effects are not effective in winter, but rather the effect of global (or regional) climate. One reason for not seeing the certain positive trends in the northern regions of the country in winter, we can link these conditions seen in these regions to the effects of the cold weather blowing by the Siberian high pressure and Arctic Oscillations bringing the cold air of North Pole (Cohen *et al*., 2001).

When we examine the winter precipitation, we observe that a decrease and increase in the precipitation values over the narrow areas (Fig.3d), in contrast to the trends observed in the temperatures. Likewise, there are positive trends seen in the precipitations only in a few narrow areas of the country such as north-east, middle and western parts of the Black Sea basin, because the northly air is fed with moisture and leaves much rainfall over there.

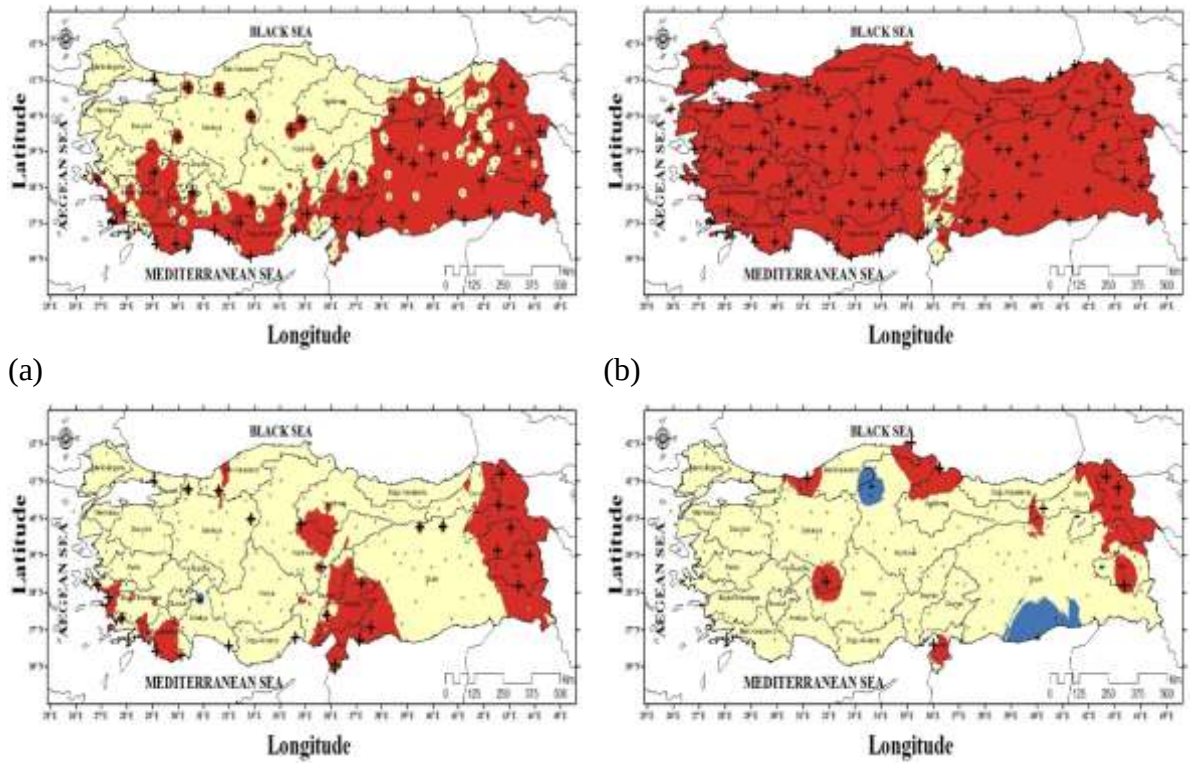

Figure 3. Spatial distributions of MK-trend in the winter: Average temperature (a); Maximum temperature (b); Minimum temperature (c); and Total Precipitation (d).

Autumn

When we look at the trends of the autumn temperatures and precipitation as given in Fig.4, we observe the typical local-climate effects. In no map, we have examined before, we have not found climate situations that reflect such local characteristics. There is a positive trend pattern in the warmest region of the country experienced the temperatures over the southern areas of the sea-coasts of the Mediterranean (Fig.4a).

Similarly, a positive trend of the maximum temperatures is seen in the eastern Black Sea region. Since this region of the country has rainy in all seasons, the released heat energy after rainfalls (Fig.4b) may have increased the temperatures.

The physical quantity that best describes the local effects is the minimum temperature (Fig. 4c). As can be seen, starting from the Central Anatolia region of the country, positive trends are detected in all the southern and western regions near the sea. A negative trend appears in the southern and round region between the south and the west positive trends.

As seen in Fig.4d, a negative trend of the precipitations is observed in the region, which is slightly in the west of the middle Black Sea basin. There is a positively contradictory pattern located to the south of this pattern.

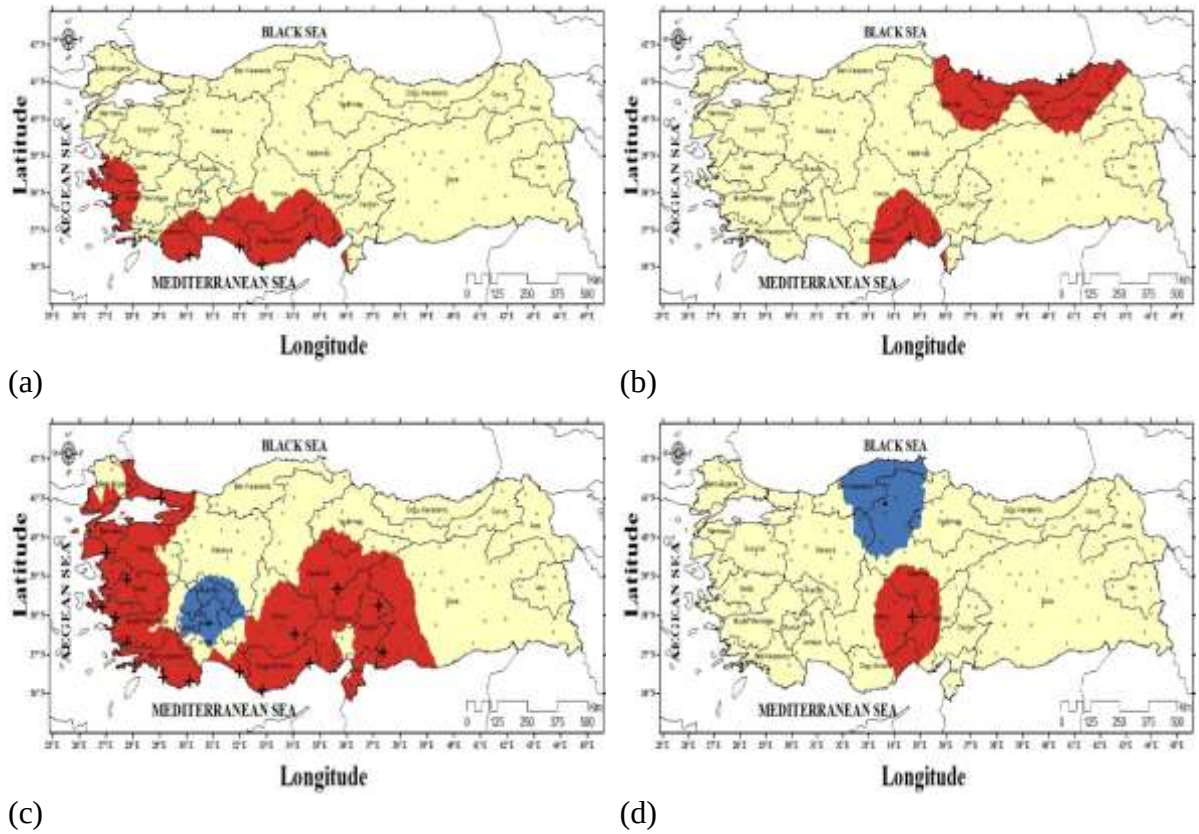

Figure 4. Spatial distributions of MK-trend in the autumn: Average temperature (a); Maximum temperature (b); Minimum temperature (c); and Total Precipitation (d).

Summer

When all types of temperature given in Fig.5abc are examined, positive temperature trends are observed in all areas except a few local points. Those local spots are probably preventing it from getting too warming due to its high altitude. In the summer season, global warming is the most felt. One of the negative conditions brought about by the warming is the increase of wild forest fires because of the increase of the drought. In the north Aegean, a decrease in summer precipitation is striking. In this case, as we have underlined previously, possible wild forest fires in this region are expected.

Likewise, although there is a positive trend due to sudden summer precipitation in the south-east region of the country, it is negligible in terms of the amount of precipitation observed there. Similarly, there is an increase in the summer-precipitation over an area of the north-east

part of the country. One of the reasons of this trend may be the rain-shadows observed there. In the summer, as seen in Fig.5abc, the country seems to be burning in a circle of fire. The most basic physical reason for these positive trends of the temperatures is, of course, the moving of the Inter Tropical Convergence Zone (ITCZ) to the northern regions, and the centre of the Asian low pressure, and the African temperatures brought by the Arabic low are such examples.

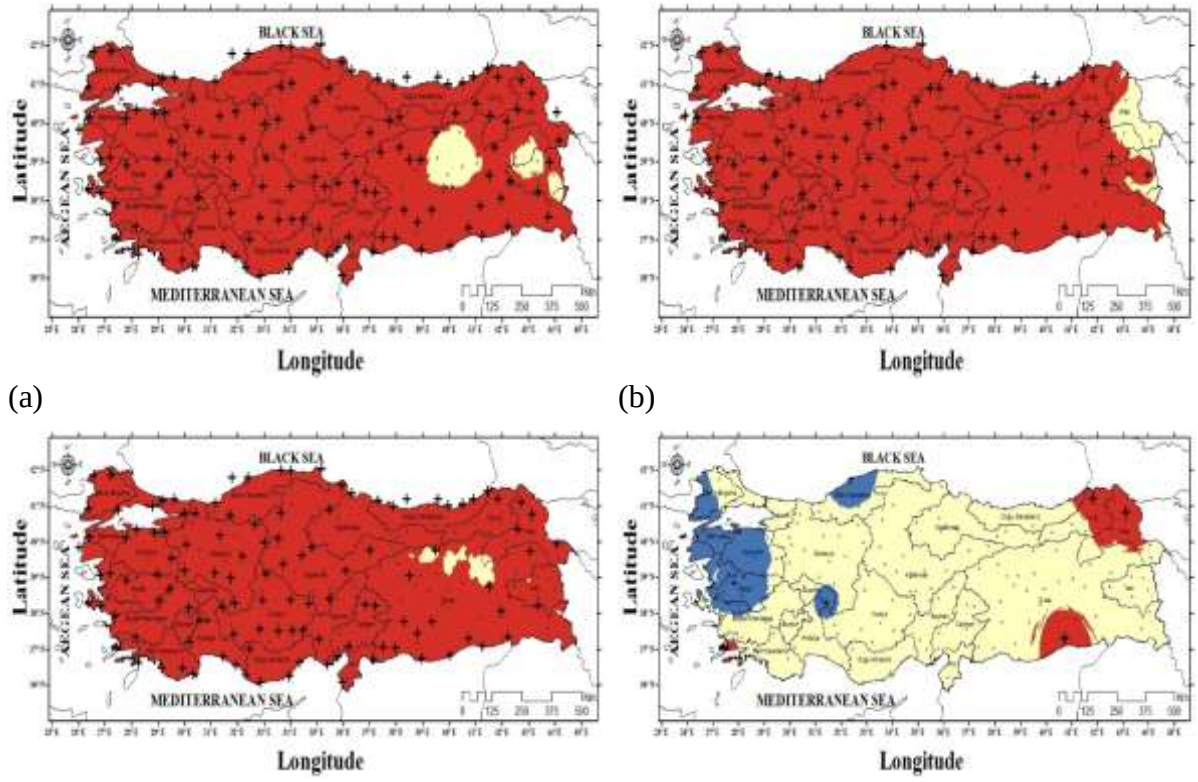

Figure 5. Spatial distributions of MK-trend in summer: Average temperature (a); Maximum temperature (b); Minimum temperature (c); and Total Precipitation (d).

CONCLUSIONS

These positive trends seen in the temperatures may cause more health problems as it will lead to an increase in the frequency of heat waves. When seasonal and annual trends are compared, a lot of detailed information and masked patterns have become much more transparent. In a large country like Turkey, where Mediterranean climate prevails, every season has produced its own patterns and many different classes of temperature and precipitation have emerged. The most important reasons for these differences are the physical geographical factors in the region concerned, that is, the most important in the minimum temperatures and partly in the rainfall are these geographical factors. On the other hand, the temperature values have been significantly increased due to the influence of the Arabic Low (an extension of the Monsoon Low), as well as the Central Asian Low, one of the large-scale pressure systems, because of global warming. Considering the method applied in this study, it consists of only a simple trend analysis which is quite simple and not complicated. However, the results of our study are not lower in the quality than those of the most complex methods. For example, the climate models that are very expensive in time-money gives only very smoothed information, indeed not the forecast, since the projections are not forecasts as in the daily weather forecasting. As a result, this work presents a photograph of the Turkey climate at a seasonal scale. As open points of this study, the results are not compared with the results of the previous studies in the literature. This is particularly preferred because it involves many differences from the quality of the data

used in the studies. For example, the preferred method of interpolation may create different maps. Secondly, since the length of data considered may change the results of the applied statistical method, the comparisons may lead the study to the wrong direction.

For future work in this topic, for example, for hydrological purposes, it may be advisable to examine possible trends of the rivers. It is possible to investigate the effects of these changes, for example, on the amount of agricultural production. Or it can be investigated whether there will be a positive contribution to tourism activities or not.

REFERENCES

Alexandersson H. 1986. A homogeneity test applied to precipitation data. *Journal of Climatology* 6: 661–675.

Chattopadhyay S, Edwards DR. 2016. Long-term trend analysis of precipitation and air temperature for Kentucky, United States. *Climate* 4:1-15.

Cohen J, Saito K, Entekhabi D. 2001. The role of the Siberian high in Northern Hemisphere climate variability. *Geophysical Research Letters* 28*:*299-302.

Colombani N, Dinelli E, Mastrocicco M. 2016. Trend of heavy metal release according to forecasted climate change in the Po Delta. *Environmental Processes* 3: 553. doi:10. 1007/s40710-016-0146-2.

Gama J. 2016. CRAN-Package Climtrends. *Available from* https://cran.r-project.Org/package = climtrends (Accessed 26 September 2016).

Hirsch RM, Alexander RB, Smith RA. 1991. Selection of methods for the detection and estimation of trends in water quality. *Water Resources Research* 27: 803-813.

Iqbal MA, Penas A, Cano-Ortiz A, Kersebaum KC, Herrero L, del Río S. 2016. Analysis of recent changes in maximum and minimum temperatures in Pakistan. *Atmospheric Research* 168: 234-249.

IPCC. 2013. Climate Change 2013: The Physical Science Basis (Stocker TF. *et al*. Eds.) Cambridge University Press.

Jentsch A, Kreyling J, Beierkuhnlein C. 2007. A new generation of climate-change experiments: events, not trends. *Frontiers in Ecology and the Environment* 5: 365-374.

Kendall MG. 1975. Rank Correlation Methods. 4th Ed. Charles Griffin. London.

Mann HB. 1945. Non-parametric test against trend. *Econometrica* 13: 245-259.

Norrant C, Douguédroit A. 2006. Monthly and daily precipitation trends in the Mediterranean (1950–2000). *Theoretical and Applied Climatology* 83: 89-106.

Partal T, Kahya E. 2006. Trend analysis in Turkish precipitation data. *Hydrological Processes* 20: 2011-2026.

Pettitt AN. 1979. A non-parametric approach to the change-point detection. *Applied Statistics* 28: 126–135.

Shi Y, Gao X, Xu Y, Giorgi F, Chen D. 2016. Effects of climate change on heating and cooling degree days and potential energy demand in the household sector of China. *Climate Research* 67: 135-149.

Sousa PM, Trigo RM, Aizpurua P, Nieto R, Gimeno L, García HR. 2011. Trends and extremes of drought indices throughout the 20th century in the Mediterranean. *Natural Hazards and Earth System Sciences* 11: 33-51.

Tatli H, Dalfes HN, Mentes SS. 2004. A statistical downscaling method for monthly total precipitation over Turkey. *International Journal of Climatology* 24: 161-180.

Tatli H, Dalfes HN, Mentes SS. 2005. Surface air temperature variability over Turkey and its connection to large-scale upper air circulation via multivariate techniques. *International Journal of Climatology* 25: 331-350.

Tatli H. 2014. Statistical complexity in seasonal precipitation of NCEP/NCAR reanalysis over the Mediterranean basin. *International Journal of Climatology* 34: 155–161.

Tatli H. 2015. Detecting persistence of meteorological drought via the Hurst exponent. *Meteorological Applications* 22: 763-769.

Tatli H, Dalfes HN. 2016. Defining Holdridge's life zones over Turkey. *International Journal of Climatology* 36:3864-3872.

Turkes M, Tatli H. 2011. Use of the spectral clustering to determine coherent precipitation regions in Turkey for the period 1929-2007. *International Journal of Climatology* 31: 2055-2067.

Von Neumann J. 1941. Distribution of the ratio of the mean square successive difference to the variance. *Annals of Mathematical Statistics* 13: 367–395.

Wijngaard JB, Klein Tank AMG, Können GP. 2003. Homogeneity of 20th century European daily temperature and precipitation series. *International Journal of Climatology* 23: 679–692.

RECENT TRENDS IN PRECIPITATION IN TURKEY: 1980-2015

Filiz Dadaser-Celik[1], Ali Ümran Kömüscü[2], Rabia Ucar[3], Mete Celik[4]
[1]*Dept. of Environmental Engineering, Erciyes University, fdadaser@erciyes.edu.tr*
[2]*State Meteorological Service, aukomuscu@mgm.gov.tr*
[3]*Dept. of Environmental Engineering, Erciyes University, rabia.ucar@outlook.com.tr*
[4]*Dept. of Computer Engineering, Erciyes University, mcelik@erciyes.edu.tr*

Abstract
This study examines spatial and temporal dynamics of monthly and annual precipitation over Turkey by analyzing data from 195 meteorological stations for a 26-year period (1980 to 2015). The stations were selected among 238 meteorological stations based on homogeneity analyses conducted with Pettitt test, Standart normal homojeneity test, Buishand range test and Von Neumann ratio test. Trends in annual and monthly totals were determined using Mann-Kendall trend test with the trend-free prewhitening procedure. Strengths of the trends were estimated by calculating the Sen's slope. During the 1980-2015 period, annual average precipitation was in the range of 263-2264 mm with an average of 642 mm. From 1980 to 2015, annual precipitation is characterized with upward trends at majority of the stations. Downward and upward trends were detected at 77 (39%) and 118 (61%) stations, respectively. However, most of these trends were not statistically significant. The analysis showed that at the annual timescale only 17 stations presented significant trends at the 0.05 level. Majority of significant trends were positive. The significant trends were detected in March, July, September, and October. In months of March, September, October, majority of significant trends were positive while they were negative in July. Overall the trend analysis suggested that the changes in annual and monthly precipitation series were minor from 1980 to 2015.

Keywords: *Precipitation, Trend analysis, Mann-Kendall Trend Test, Sen's Slope, Turkey*

INTRODUCTION
Recent trends in precipitation are of interest not only to climatologists but also to hydrologists. Many global and regional climate studies indicated downward trends in precipitation in the Mediterranean region. Even climate model projections for Turkey signal continuation of the downward trends in precipitation and irregular precipitation regime, especially in southern and inner parts of Turkey during upcoming decades (Demircan et al. 2017). Some previous studies, which analyzed historical precipitation records, also pointed to downward trends in some regions in Turkey (Partal and Kahya 2006; Tayanç et al. 2009; Tayanç and Toros 1997; Türkeş 1996; Türkeş et al. 2009). The latest of these studies investigated the trends up to 2009. The objective of this study is to fill in the existing knowledge gap by examining the recent trends in precipitation. For this purpose, we analyzed the trends in annual and monthly data from 1980 to 2015.

DATA AND METHODS
Precipitation data are collected by a dense network of meteorological stations in Turkey by the State Meteorological Service (MGM). In this study, the monthly precipitation data collected at 238 stations operated by MGM were used. Data period covered 26-year from 1980 to 2015.

Initially, the data were examined for incomplete records. There were only a few stations that had incomplete records, and they were excluded from further analyses. Also, precipitation data can include inhomogeneity due to the instrumentation changes, relocation of stations, or changes in the environment surrounding the stations. In this study, we used four different tests for homogeneity analysis namely, Pettitt test, Standard normal homogeneity test (SNHT),

Buishand range test and Von Neumann ratio test. The homogeneity of data series was investigated at significance level of 1% (0.01). Previously, Wijngaard et al. (2003) used the tests to evaluate the homogeneity of meteorological parameters and concluded that data the series can be used if two or more tests show that the data series are homogeneous. In this study, the usability of data analyzed as in Wijngaard et al. (2003) and the analysis revealed 195 homogeneous stations (Figure 1).

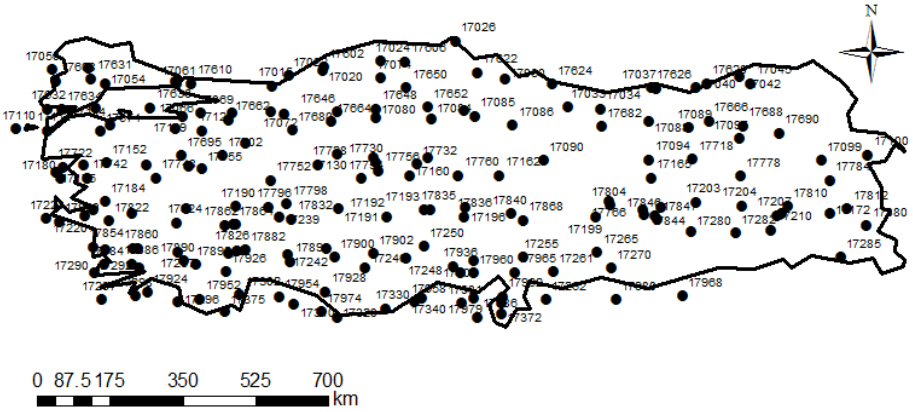

Figure 1. Location of 195 stations which have homogeneous precipitation records for the 1980-2015 period

In this study, we used the Mann-Kendall trend test (Kendall 1975; Mann 1945), which is a non-parametric method frequently used for detection of trends in climate data (e.g., Brunetti et al. 2000). Sen's slope (Sen 1968) was calculated to estimate the strengths of trends, if they exist. Sen's slope is also a non-parametric method and provides a measure of the slope if a trend is present in data. For non-parametric tests, the data must be serially independent because the existence of serial correlation will increase the probability for significant trend detection (Kulkarni and Storch 1995; Yue et al. 2002). In this study, we used the trend-free prewhitening procedure (Yue et al. 2002) to remove the influence of serial correlation.

RESULTS

Minimum, maximum, average, and standard deviation of annual precipitation in Turkey were calculated for 195 stations for the 1980-2015 period (Figure 2). Average annual precipitation for 195 stations was in the range of 263 mm and 2264 mm, with an average of 642 mm with a standard deviation of 300 mm. For 73 stations (37%), annual precipitation was smaller than 500 mm and for 148 stations (65%), it was smaller than 750 mm. 43 stations (21%) had annual precipitation between 750 mm and 1250 mm. Only 4 stations had annual precipitation over 1250 mm.

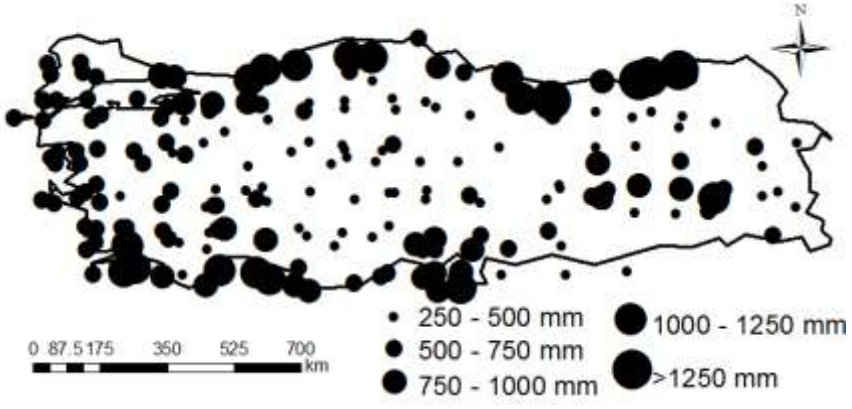

Figure 2. Annual average precipitation at 195 stations during the 1980-2015 period

Trends in precipitation data for 195 stations were determined using the Mann-Kendall trend test together with trend-free prewhitening method. The statistical significance of the trends was evaluated at the 0.05 level. The strengths of trends were evaluated by calculating the Sen's slope. The directions of trends in annual and monthly data at individual stations were presented in Figure 1. Statistical properties of the trends in monthly and annual precipitation data were summarized in Table 1.

Table 1. Number (%) of stations with downward (negative) or upward (positive) trends in monthly and annual precipitation and the number (%) of stations for which these trends are statistically significant at the 0.05 level.

Timescale	Number (%) of stations with downward trends	Number (%) of stations with upward trends	Number (%) of stations with downward trends (significant at the 0.05 level)	Number (%) of stations with upward trends (significant at the 0.05 level)
January	70 (36)	125 (64)	1 (1)	8 (4)
February	52 (27)	143 (73)	2 (1)	1 (1)
March	87 (45)	108 (55)	1 (1)	24 (12)
April	93 (48)	102 (52)	2 (1)	3 (2)
May	127 (65)	68 (35)	7 (3)	0 (0)
June	59 (30)	115 (59)	11 (6)	4 (2)
July	90 (46)	31(16)	24 (12)	7 (4)
August	43 (22)	70 (36)	2 (1)	6 (3)
September	1 (1)	180 (92)	0 (0)	70 (36)
October	38 (19)	157 (81)	2 (1)	37 (19)
November	190 (97)	5 (3)	22 (11)	0 (0)
December	159 (82)	36 (18)	1 (1)	1 (1)
Annual	77 (39)	118 (61)	5 (3)	12 (6)

From 1980 to 2015, annual precipitation is characterized with upward trends at majority of the stations. Downward and upward trends were detected at 77 (39%) and 118 (61%) stations, respectively (Table 1). However, most of these trends were not statistically significant. The downward trends were found to be statistically significant at only 5 stations (3%) and upward trends were significant at 12 stations (6%) (Table 1). Changes were also identified in monthly precipitation data (Table 1, Figure 1). Upward trends were prevalent in monthly data in all months except for March, July, November, and December. The number of stations with significant upward trends was also higher than those stations with significant downward trends. The most interesting results were obtained for September and October. Almost all stations showed upward trends in precipitation in these months. 70 (36%) and 37 (19%) stations had upward trends significant at the 0.05 level. As can be seen from Figure 1, in September and October significant trends were accumulated in western Turkey. Similarly precipitation in March also showed upward trends where 24 (12%) stations had statistically significant changes. In March significant trends were detected at northern Turkey stations along Black Sea coast (Figure 3). Downward trends in July were statistically significant at 24 (12%) stations

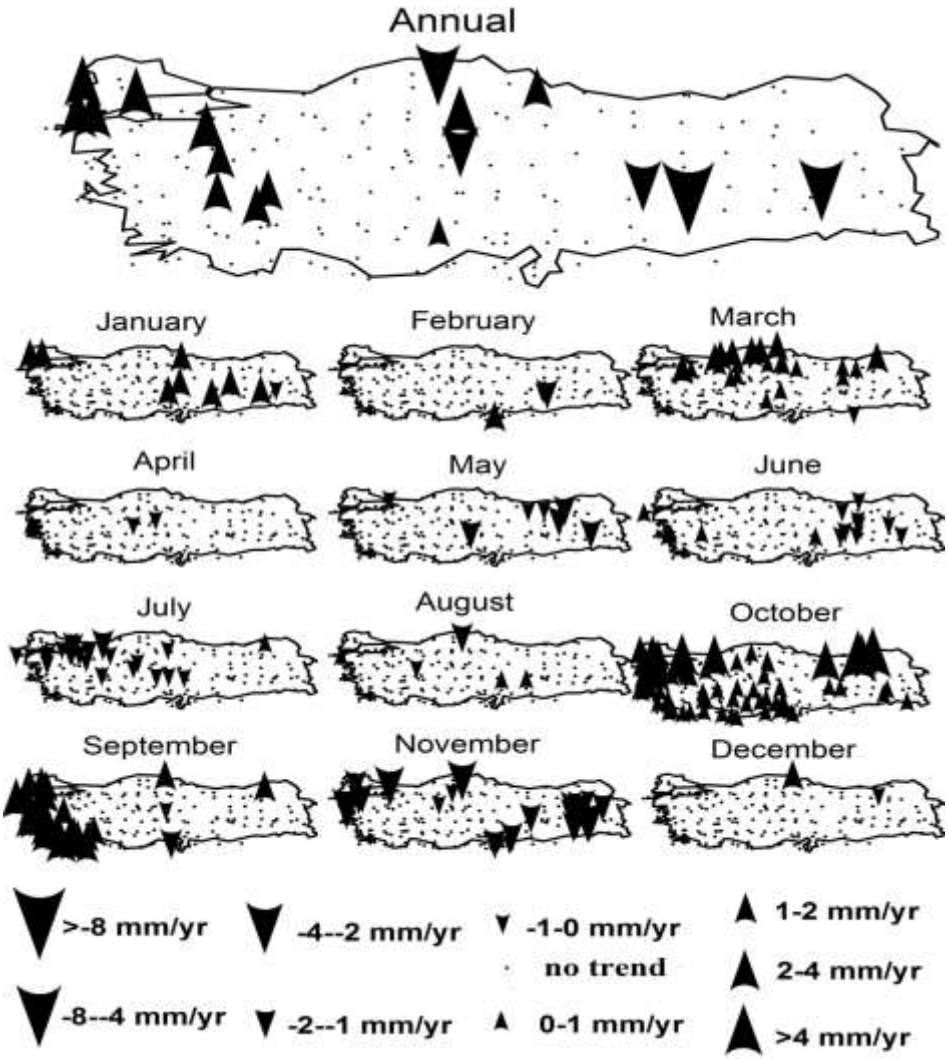

Figure 3. Trends in and annual and monthly precipitation data at 195 stations from 1980 to 2015. Only statistically significant trends were shown.

The magnitudes of trends in the annual timescale for 195 stations changed between -8.08 mm yr^{-1} and 8.81 mm yr^{-1} with an average of 2.81 mm yr^{-1} (Table 2). At the monthly timescale, average trend in November and December was negative and were -0.86 mm yr^{-1} and -0.35 mm yr^{-1}, respectively. Average trend was positive and 0.46 and 0.53 mm yr^{-1} for September and October, respectively. The strongest upward trend was detected in September (4.86 mm yr^{-1}) and the strongest negative trend was detected in November (-3.72 mm yr^{-1}).

Table 2. Minimum, maximum, average, and standard deviations the strengths of trends in mm yr^{-1} detected in annual and monthly precipitation data at 195 stations.

Timescale	Minimum	Maximum	Average	Standard Deviation
January	-2.00	3.85	0.23	0.74
February	-2.38	2.62	0.34	0.64
March	-1.68	1.63	0.00	0.67
April	-1.68	1.19	0.00	0.45
May	-1.24	0.90	-0.16	0.39
June	-0.76	1.81	0.09	0.34
July	-1.27	1.69	-0.08	0.28
August	-1.56	1.47	-0.01	0.23

September	-0.05	4.86	0.46	0.66
October	-1.66	3.79	0.53	0.75
November	-3.72	0.61	-0.86	0.63
December	-2.28	1.88	-0.35	0.62
Annual	-8.08	8.81	0.62	2.81

Figure 4 and 5 show the annual precipitation data from stations which had significant upward and downward trends in their precipitation record, respectively. As can be seen we see a gradual upward/downward trend and the stations located close to each other had similar change patterns.

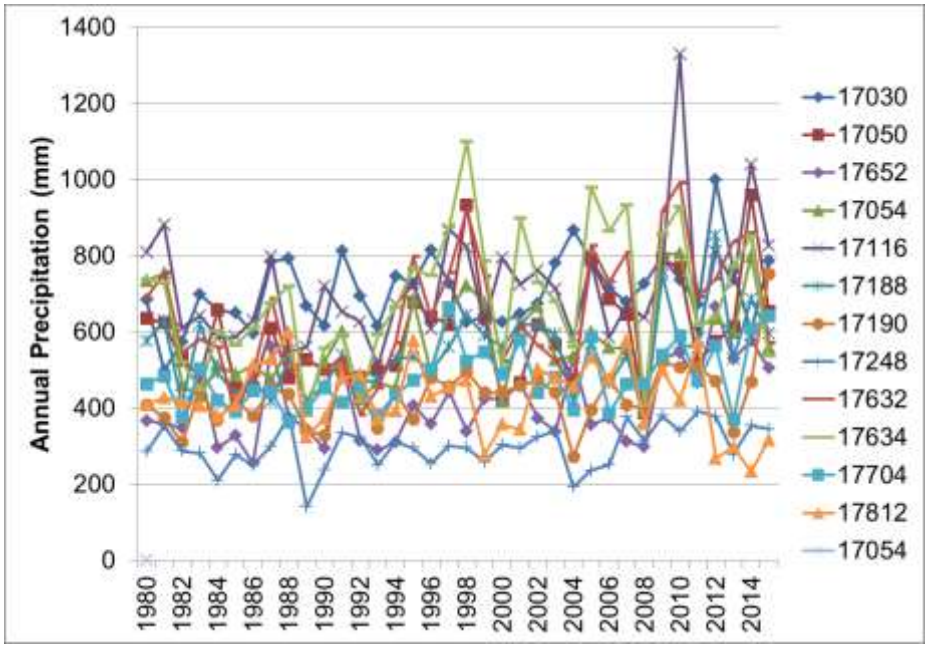

Figure 4. Annual precipitation at 12 stations which showed significant upward trend during the 1980-2015 period.

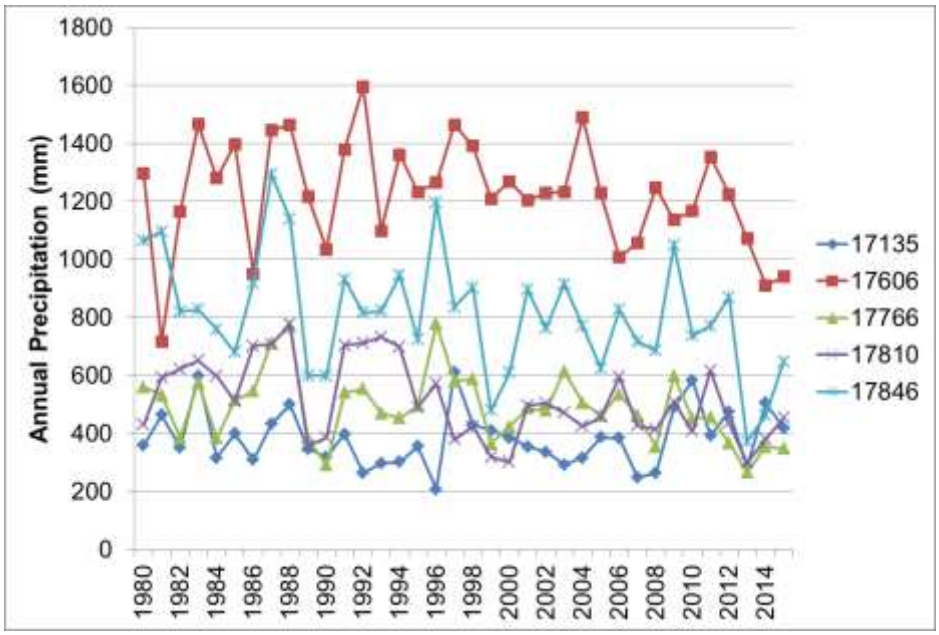

Figure 5. Annual precipitation at 5 stations which showed significant downward trend during the 1980-2015 period.

CONCLUSION

In this study, we examined the recent trends in Turkish precipitation data from 1980 to 2015. The downward trends were found to be statistically significant at only 5 stations (3%) and upward trends were significant at 12 stations (6%).It was concluded that although annual precipitation is characterized with upward trends at majority of the stations, they were not statistically significant. At the monthly time scale, significant upward trends were detected at western Turkey in September and October and in northern Turkey in March. Major downward changes were observed in precipitation in July. Overall, our analysis demonstrated that the changes in annual and monthly precipitation series were minor from 1980 to 2015.

REFERENCES

Brunetti M, Maugeri M, Nanni T (2000) Long-Term Trends in Extreme Precipitation Events over the Conterminous United States and Canada Theoratical and Applied Climatology 65:165-175

Demircan M, Gürkan H, Eskioğlu O, Arabacı H, Çoşkun M (2017) Climate Change Projections for Turkey: Three Models and Two Scenarios Turkish Journal of Water Science and Management 1:22-43

Kendall MG (1975) Rank Correlation Methods Griffin London

Kulkarni A, Storch Hv (1995) Monte Carlo experiments on the effect of serial correlation on the Mann-Kendall test of trend Meteorologixal Zeitschrift 4:82-85

Mann HB (1945) Non-Parametric tests against trend Econometrica 13:245–259

Partal T, Kahya E (2006) Trend analysis in Turkish precipitation data Hydrological Processes 20:2011-2026

Sen PK (1968) Estimates of the regression coefficient based on Kendall's tau Journal of American Statistical Association 39:1379-1389

Tayanç M, Im U, Doğruel M, Karaca M (2009) Climate change in Turkey for the last half century Climatic Change 94:483-502

Tayanç M, Toros H (1997) -Urbanization effects on regional climate change in the case of four large cities of Turkey Climatic Change 35:501-524

Türkeş M (1996) Spatial and temporal analysis of annual rainfall variations in Turkey International Journal of Climatology 16:1057-1076

Türkeş M, Koc T, Sariş F (2009) Spatiotemporal variability of precipitation total series over Turkey International Journal of Climatology 29:1056-1074

Yue S, Pilon P, Phinney B, Cavadias G (2002) The influence of correlation on the ability to detect trend in hydrological series Hydrological Processes 16:1808-1829

CLASSIFICATION OF THE KÖPPEN AND HOLDRIDGE LIFE ZONES WITH RESPECT TO THE CLIMATE SCENARIOS-RCP4.5 OVER TURKEY

Hasan TATLI

Physical Geography Division, Department of Geography, Faculty of Sciences and Arts, Çanakkale Onsekiz Mart University 17020 Çanakkale, Turkey, tatli@comu.edu.tr; tatli.hasan@gmail.com

ABSTRACT

This study is suggesting a new perspective for monitoring the climate zones of Holdridge and Köppen by employing the 30-year moving average since 2006 to 2100 with respect to the climate scenarios. The aim of the both climate classification systems of Holdridge and Köppen is to group climatic quantities of temperature and precipitation at the local-scales according to some pre-defined restrictions such as vegetation index (cover). Holdridge uses bio-temperature, precipitation and evapotranspiration ratio; on the other hand, the long-term means of temperature and precipitation variables are used in the Köppen's system. The Holdridge system is mostly used to understand the possible biome (vegetation) characteristics. A computer program based on FORTRAN 2003 was developed for climate classification systems. In addition, the large-scale variables of the General Circulation Models (GCMs) used in the study were obtained from the 6 type ensemble simulations of the model entitled "ESM2M" of the Geophysical Fluid Dynamics Laboratory (GFDL) based on the scenario-RCP4.5 (Representative Concentration Pathways. RCP). The RCPs are the four-greenhouse gas concentration (not emissions) trajectories adopted by the IPCC for its fifth Assessment Report (AR5). The results of the study show that the sub-classes from both classification systems of Köppen and Holdridge show that there will be noticeable changes in the northeastern parts of the country, and particularly in the southeastern parts of the country. According to the models, the south-eastern regions will have been almost completely faced with deep dry climate and/or desertification. In terms of water resources and management, it can be suggested that a new policy is needed to reduce the adaptation and mitigation of the climate change for Turkey.

***Key Words**: AR5, Climate Change, GFDL, Holdridge, Köppen, RCP4.5*

INTRODUCTION

In this study, the historical changes in vegetation cover in Turkey were quantified according to Köppen and Holdridge climate classifications based on climatic change scenario Representative Concentration Pathway (RCP) 4.5. It is a scenario of long-term, global emissions of greenhouse gases, short-lived species, and land-use-land-cover which stabilizes radiative forcing at 4.5 watts per meter squared (wm^{-2}), and approximately 650 ppm CO2-equivalent in the year 2100 without ever exceeding that value (Moss et al. 2010; Thomson *et al.* 2011). Climate change and its impacts could be brought together all the research fields contributing to a deep understanding of the ways in which we organize our lives with respective the new perspective.

A recent paper written by Chen and Chen (2013) looked at the change in spatial coverage of the major and minor Köppen categories across the entire earth as a metric for measuring climate change between 1900 and 2010. Köppen (Köppen, 1900) was trained as a plant physiologist and realized that plants are indicators for many climatic elements. His effective classification was constructed based on five vegetation groups determined by the French botanist De Candolle referring to the climate zones of the ancient Greeks (Sanderson, 1999). The five

vegetation groups of Köppen distinguish between plants of the equatorial zone (**A**), the arid zone (**B**), the warm temperate zone (**C**), the snow zone (**D**) and the polar zone (**E**). A second letter in the classification considers the precipitation (e.g. Df for snow and fully humid), a third letter the air temperature (*e.g.* Dfc for snow, fully humid with cool summer). Although various authors have published enhanced Köppen classifications or developed new classifications, the climate classification was originally developed by Köppen (here referred to as Köppen-Geiger classification) is still the most frequently used climate classification.

According to open literature, the Holdridge life zone (HLZ) system (Holdridge, 1967) can be regarded as the model considers some basic laws of plant physiology. For example, Lugo *et al.* (1999) have applied the HLZ to the conterminous United States. Chen *et al.* (2003) and Yue *et al.* (2015) have examined the possible responses of ecosystems to the climate change over China through the HLZ approach. Tatli and Dalfes (2016) have applied the HLZ to classify the vegetation zones associated with the surface climatic variables over Turkey. They have obtained fourteen types of the HLZ classes where the frequent zones are cool temperate steppe and warm temperate dry forests. On the other hand, the HLZ system was first suggested by Emanuel et al. (1985) to evaluate the effects of climate change on vegetation cover. Szelepcsényi et al. (2016) have applied HLZ by the temperature and precipitation values obtaining from 11 regional climate simulations to assess the possible ecological impacts of future climate change for the Carpathian region. In this study, the possible expected shifts in the spatial distribution of the HLZ types are investigated for Turkey, in accordance with the above-mentioned studies (Tatli and Dalfes, 2016).

DATA AND METHODOLOGY

Data

The global data set of climate simulations have been selected to update the historical world maps for both the Köppen-Geiger and Holdridge climate classes. The maps are generated from a large dataset of climate simulations by the data set obtained from the ensemble values of 6 "General Circulation Models" (GCMs) of so called "ESM2M (Dunne et al., 2012)" of the Geophysical Fluid Dynamics Laboratory for the 5th Assessment Report (AR5) of the Intergovernmental Panel on Climate Change (IPCC).

The data set used in this study is obtained from the GCM based on the scenario of Representative Concentration Pathway (RCP) 4.5. It is a scenario of long-term, global emissions of greenhouse gases, short-lived species, and land-use-land-cover which stabilizes radiative forcing at 4.5 Watts per meter squared (w/m^2), approximately 650 ppm CO2-equivalent) in the year 2100 without ever exceeding that value. The RCP4.5 scenario in the set of experiments is described by Taylor *et a*l. (2012). These climate model data are freely accessible at the Program for Climate Model Diagnosis and Intercomparing website https://www.gfdl.noaa.gov/ipcc-ar5-data/.

Köppen-Geiger Climate Classification

According to the literature there are various versions of Köppen's climate classification have been faced. The calculation scheme for the Köppen-Geiger classes applied in this study will now be briefly described. The key points of this classification scheme are described in Table 1. The key to the main climates is characterized by the first two letters. The annual mean near-surface (2 m) temperature is denoted by *Tann* and the monthly mean temperatures of the warmest and coldest months by Tmax and Tmin, respectively. P*ann* is the accumulated annual precipitation and Pmin is the precipitation of the driest month.

Additionally, Psmin, Psmax, Pwmin and Pwmax are defined as the lowest and highest monthly precipitation values for the summer and winter half-years on the hemisphere considered. All temperatures are given in ^{o}C, monthly and annual precipitations in mm. In addition to these temperature and precipitation values a dryness threshold Pth in mm is introduced for the arid climates (B), which depends on "Tann", the absolute measure of the annual mean temperature in ^{o}C, and on the annual cycle of precipitation. Furthermore, the scheme how to determine the additional temperature conditions (third letter) for the arid climates (B) as well as for the warm temperate and snow climates (C) and (D), respectively, is given in Table 2, where Tmon denotes the mean monthly temperature in ^{o}C.

Table 1. The basics of the Köppen-Geiger Classification

Type	Description	Criterion
A	**Equatorial climates**	Tmin ≥ 18 ◦C
Af	Equatorial rainforest, fully humid	Pmin ≥ 60 mm
Am	Equatorial monsoon	Pann ≥ 25 (100 − Pmin)
As	Equatorial savannah with dry summer	Pmin < 60 mm in summer
Aw	Equatorial savannah with dry winter	Pmin < 60 mm in winter
B	**Arid climates**	Pann < 10 Pth
BS	Steppe climate	Pann > 5 Pth
BW	Desert climate	Pann ≤ 5 Pth
C	**Warm temperate climates**	−3 ◦C < Tmin < +18 ◦C
Cs	Warm temperate climate with dry summer	Psmin < Pwmin, Pwmax > 3 Psmin and Psmin < 40 mm
Cw	Warm temperate climate with dry winter	Pwmin < Psmin and Psmax > 10 Pwmin
Cf	Warm temperate climate, fully humid neither	Cs nor Cw
D	**Snow climates**	Tmin ≤ −3 ◦C
Ds	Snow climate with dry summer	Psmin < Pwmin, Pwmax > 3 Psmin and Psmin < 40 mm
Dw	Snow climate with dry winter	Pwmin < Psmin and Psmax > 10Pwmin
Df	Snow climate, fully humid neither	Ds nor Dw
E	**Polar climates**	Tmax < +10 ◦C
ET	Tundra climate	0 ◦C ≤ Tmax < +10 ◦C
EF	Frost climate	Tmax < 0 ◦C

Table 2. Key to calculate the third letter temperature classification (note that for type (b), warm summer, a threshold temperature value of +10 ^{o}C should occur for at least four months).

Type	Description	Criterion
h	Hot steppe / desert	Tann ≥ +18 ◦C
K	Cold steppe /desert	Tann < +18 ◦C
a	Hot summer	Tmax ≥ +22 ◦C
b	Warm summer	not (a) and at least 4 Tmon ≥ +10 ◦C
c	Cool summer and cold winter	not (b) and Tmin > −38 ◦C
d	Extremely continental	like (c) but Tmin ≤ −38 ◦C

Holdridge Life Zones

The Holdridge Life Zones (Holdridge, 1967) scheme is specified in Figure 1. In the HLZ algorithm, there are two hypothesizes: (i) The temperature and precipitation values are chief factors shaping life zones (or biomes). (ii) The vegetation is assumed to be independent of animals. The model practices three bioclimatic indices: mean annual bio-temperature (*BT*), total annual precipitation (*R*), potential evapotranspiration ratio *(PER*). It is central to know that the indices are depicted on logarithmic scale in the so-called life zone chart. As stated by the assumptions, the main influences on life zones are those aspects that structure climate of the Holdridge system. In this respect, it is not related the systems of Köppen (1931) and Thornthwaite (1948).

Holdridge (1967) defines BT as the temperature in the interval of [0 - 30ºC].

$$BT = \frac{1}{N}\left(\frac{1}{12}\sum_{i}^{12} T_i \quad \text{for } 0^{\circ}C < T_i < 30^{\circ}C\right) \tag{1}$$

where T_i is the temperature of *i-th* month and *N* indicates number of years, respectively. The *R* and *PER* values are obtained as in the following.

$$R = \frac{1}{N}\left(\sum_{i}^{12} P_i\right) \tag{2}$$

where P_i is the total precipitation of the *i*-th month.

$$PER = \frac{BT \cdot 58.93}{R} \tag{3}$$

After the values of *BT, R* and *PER* calculated, the HLZ classes can be determined by using the geometric model given in Figure 1.

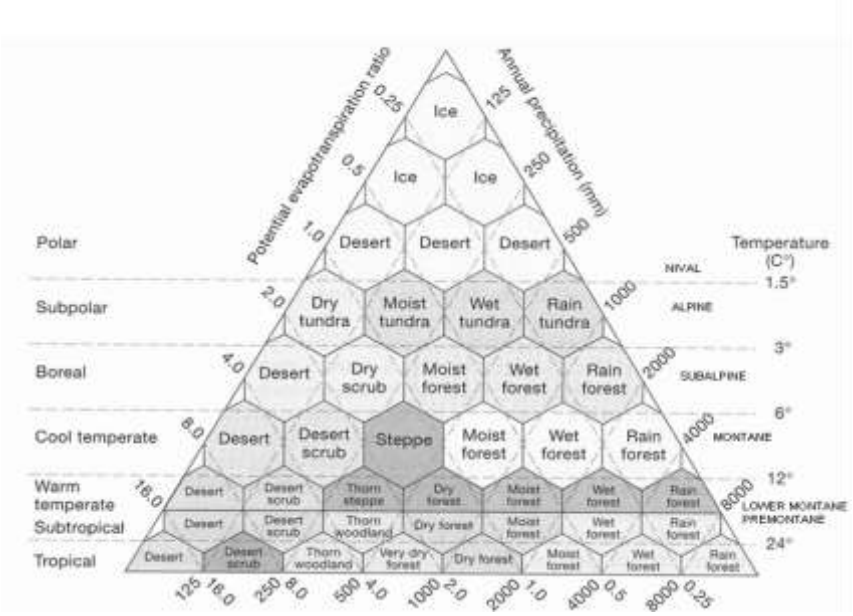

Figure 1 Holdridge's life zone system is one of most widespread for classification of climate-based vegetation types (after, Holdridge, 1967; Tatli and Dalfes, 2016).

RESULTS

Climatic classes were determined by taking 30-year moving-averages. That is, the averages are calculated for time intervals of moving windows such as 2000-2019, 2001-2030, ..., 2060-2089, 2061-2090, and so on. The map of the climate classes for 2006-2035 is shown in Figure 2. When this shape is closely diluted, a total of 5 sub-climate classes are observed over 2 basic Köppen climate of the "B nd C" types. As seen from this figure, there is a "C" type climate in

the Black Sea, Mediterranean, Aegean Sea borders and Central Anatolia region. On the other hand, "B" type climate is observed in the southeast part of the country and the westernmost part of the north-western part (including Çanakkale and Edremit Gulf).

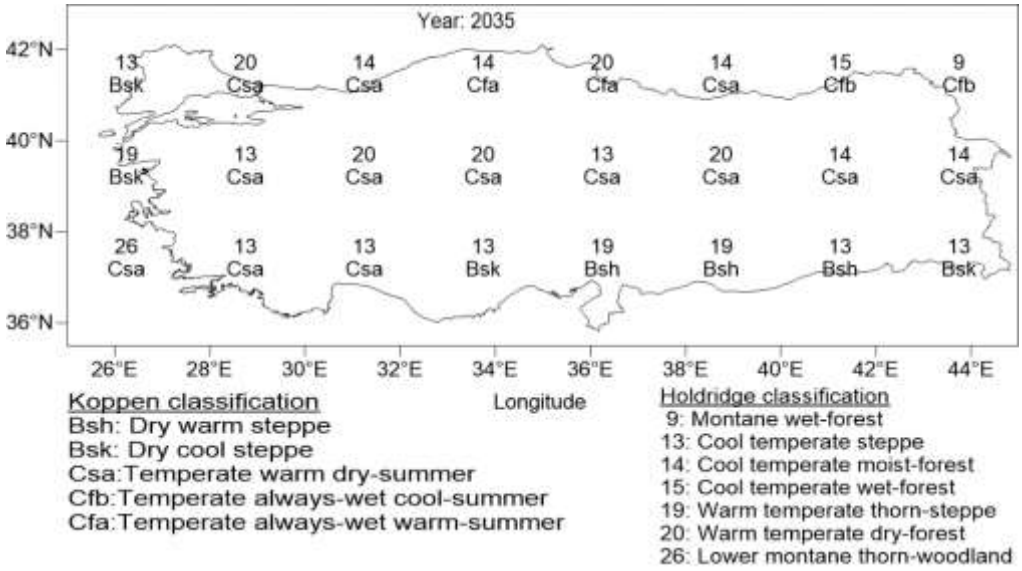

Figure 2. Distribution of the Köppen and Holdridge climate classes between the time interval of 2006 and 2035.

Similarly, when Holdridge climate classes are examined, it appears that there are 6 type climate classes in the country. As expected, the rainfall-forests in the Black Sea Region and more steppe species in the inner region are noteworthy. “Cool temperature” sub-climates are seen due to the grids located in the south of the country, and in the continental section of the Toros Mountains range. The reason for the lack of the marine effect is that the geographical coordinates of the model grids do not fall on to the shore. Southeastern Anatolia, as expected, has a climatic steppe that dominates the temperature. On the Çukurova region, where the effect of the mountains is partially diminished, war-temperate thorn-steppe climatic classes are seen.

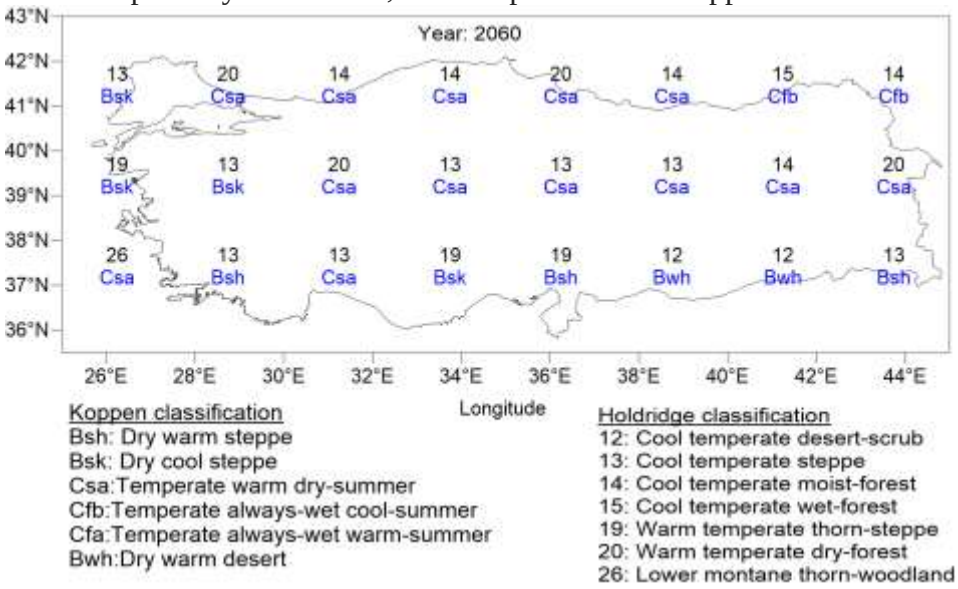

Figure 3. Distribution of the Köppen and Holdridge climate classes between the time interval of 2036 and 2060.

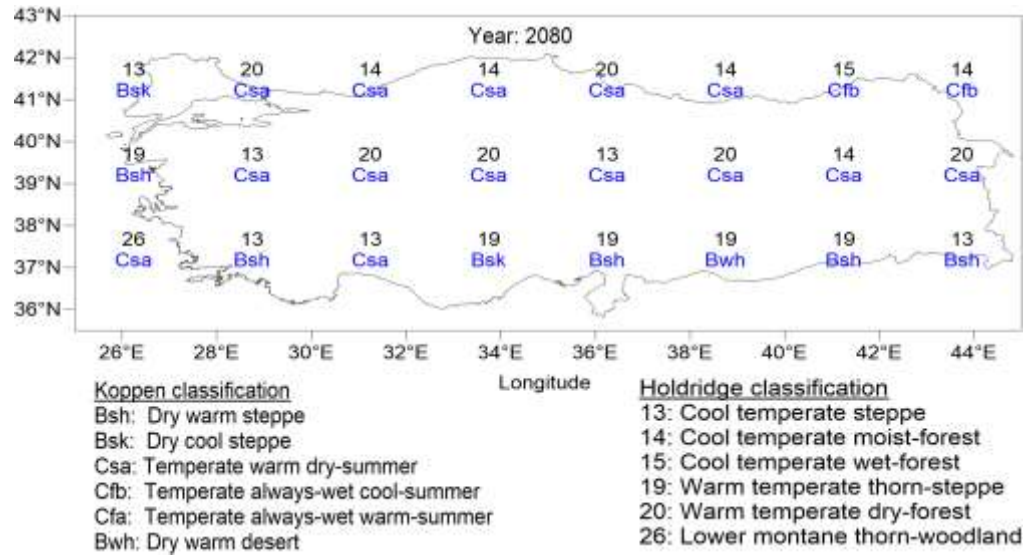

Figure 4. Distribution of the Köppen and Holdridge climate classes between the time interval of 2061 and 2080.

Correspondingly, from Figures 3 to 5, the distribution of Köppen climate types over the country mostly show that Subtropical Summer (Cs) will be deepen, turning into warm and dry summer. Those turning will lead to decrease crop yield. The Dry Semi-Arid (Bs) and Subtropical Summer-Dry (Cs) over the coastal regions. The Cs type, except southeastern and northwestern parts of the country dominates entire areas as well, while the always -wet cool summer (Csb) will be seen only in the eastern Black Sea basin.

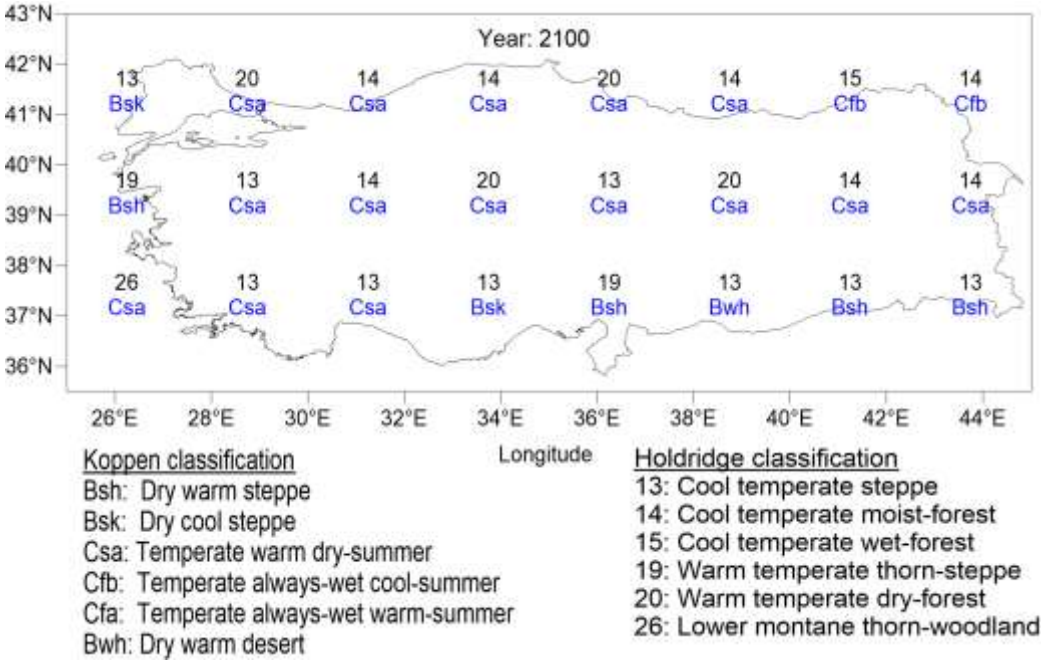

Figure 5. Distribution of the Köppen and Holdridge climate classes between the time interval of 2081 and 2100.

According to the distribution of HLZ classes as seen from Figure 3 to 5, there will be a shift towards dry and hot steppes, particularly in the southeastern part of the country. The RCP 4.5 scenario is an optimistic mode that corresponds to the old synchronized B1 middle level

optimistic scenario. Therefore, there will be little change in both Köppen and HLZ climate classes is expected.

CONCLUSIONS

In this study, the sub climate classes of Köppen and Holdridge types in Turkey were analyzed by generated from the ensemble values of GCMs of so called "ESM2M (Dunne et al., 2012)" of the Geophysical Fluid Dynamics Laboratory for AR5. The investigation focused on the large-scale spatial distribution of 30-year moving windows from the date of 2005 to 2100. The RCP4.5 scenario is a mid-level optimistic scenario. In other words, large-difference climates in the country were not achieved because the world countries were supposed to assume their duties on climate change. A pathway for "stabilization of radiative forcing" by 2100. In that case, since the climate change cannot be completely prevented for decision-makers, it can be suggested that the best scenario for Turkey (the good of the evil) is the RCP4.5. In this case, studies can be done based on this scenario in the country's climate change and damage prevention and international policies.

For future studies, determining changes in biomes under consideration of the climate scenarios in Turkey will be useful, and the biomes-changes could be verified with historical observations and data from remote sensing imagery.

REFERENCES

Chen D, Chen HW. (2013). Using the Köppen classification to quantify climate variation and change: an example for 1901–2010. *Environmental Development* 6:69-79.

Chen, X, Zhang XS, Li, BL. (2003). The possible response of life zones in China under global climate change. *Global and Planetary Change* 38:327-337.

Dunne JP, John JG, Adcroft AJ, Griffies SM, Hallberg RW, Shevliakova E, Krasting JP. (2012). GFDL's ESM2 global coupled climate–carbon earth system models. Part I: Physical formulation and baseline simulation characteristics. *Journal of Climate* 25: 6646-6665.

Emanuel WR, Shugart HH, Stevenson MP. (1985). Climatic change and the broad-scale distribution of terrestrial ecosystem complexes. *Climatic Change* 7:29-43.

Essenwanger OM. (2001). *Classification of Climates*, World Survey of Climatology 1C, General Climatology. Elsevier, Amsterdam, 102 pp.

Holdridge LR. (1967). *Life Zone Ecology*, Tropical Science Center, San Jose, Costa Rica, 206 pp.

Kharin VV, Zwiers FW, Zhang X, Wehner M. (2013). Changes in temperature and precipitation extremes in the CMIP5 ensemble. *Climatic Change 119:* 345-357.

Köppen W. (1900). *Versuch einer Klassifikation der Klimate*, vorzugsweise nach ihren Beziehungen zur Pflanzenwelt Geographische Zeitschrift, 6, pp. 657-679 (in German).

Köppen W. (1931). *The Climates of the Earth*. DeGruyter, Berlin, p. 388 (in German).

Lugo AE, Brown SL., Dodson R, Smith TS., Shugart HH. (1999). The Holdridge life zones of the conterminous United States in relation to ecosystem mapping. *Journal of Biogeography* 26*:* 1025-1038.

Moss RH, Edmonds JA, Hibbard KA, Manning MR, Rose SK, Van Vuuren DP, ..., Meehl GA. (2010). The next generation of scenarios for climate change research and assessment. *Nature* 463:747.

Sanderson M. (1999). The classification of climates from Pythagoras to Koeppen. *Bulletin of the American Meteorological Society* 80: 669–673.

Szelepcsényi Z, Breuer H, Kis A, Pongrácz R, Sümegi P. (2016). Assessment of projected climate change in the Carpathian Region using the Holdridge life zone system. *Theoretical and Applied Climatology* 1:1-18.

Tatli H, Dalfes HN. (2016). Defining Holdridge's life zones over Turkey. *International Journal of Climatology*, 36: 3864-3872.

Taylor KE, Stouffer RJ, Meehl GA. (2012). An overview of CMIP5 and the experiment design. *Bulletin of the American Meteorological Society* 93:485–498

Thomson AM, Calvin KV, Smith SJ, Kyle GP, Volke A, Patel P, ..., Edmonds JA. (2011). RCP4. 5: a pathway for stabilization of radiative forcing by 2100. *Climatic Change* 109:77.

Thornthwaite CW. (1948). An approach toward a rational classification of climate. *Geographical Review* 38: 55-94.

Yue TX, Du ZP, Lu M, Fan ZM, Wang CL, Tian YZ, Xu B. (2015). Surface modeling of ecosystem responses to climatic change in Poyang Lake Basin of China. *Ecological Modelling*, 306:16-23.

THERMAL CLIMATIC CHANGE WITH TREES IN URBAN CENTER: A MODELING APPROACH USING ENVI-MET

Sevgi Yilmaz*[1], M. Akif Irmak[1], Emral Mutlu[1] Hasan Yilmaz[1]

[1] *Ataturk Univ., Architecture and Design Fac., Dept. of Landscape Architecture, 25240, Erzurum/ Turkey*

**Corresponding author: Dr. Sevgi YILMAZ, Ataturk Univ., Architecture and Design, Dept. of Landscape Architecture, 25240, sevgiy@atauni.edu.tr; syilmaz_68@hotmail.com*

Abstract

Rapid population growth in urban centers around the world has forced us to focus on the climatic factors in these areas. For this study, Erzurum, an urban center in eastern Turkey was selected. The measurements were taken during the warmest month (August 2016) and the coldest month (January 2017) for 24 hours. Humidity level, temperature, wind speed and direction were recorded for the outdoors. Humidity and temperature were recorded on an hourly basis inside the buildings. All measurements were obtained at 1.5 meters above the ground level. The climate parameters obtained were used to create micro-scale **ENVI-Met** model 4.1. The current situation was created using the Space Module of the program. The Leonardo module was utilized to compare the different levels of suggested forestation. It is suggested that different species of trees (*Acer negundo* and P*inus sylvestris* L.) for the summer and winter months. The resulting scenarios were interpreted. The simulation of planting proposal showed that the temperature fell by 1^0C in August thus improving the comfort level. The suggested planting proposal increased the January temperature between 0.75^0C and 1^0 C. In this study, the urban space scenarios in which planting trees is carried out were considered for both summer and winter periods. The results indicated that with plants, comfort level improved compared to non-plant scenarios. The findings indicate that more livable and energy-focused urban centers can be created if the climatic factors are considered during the planning stage.

Keywords: *ENVI-Met, Thermal Comfort, Trees, climate parameters*

INTRODUCTION

In order plan urban spaces that provide better thermal comfort through the usage of climatic variables, **ENVI–met** 4.1. modeling scenarios can be utilized. This software was developed by Bruse and Fleer in 1998. This software enables helps the planners to determine the location of buildings as well as considering the appropriate selection of trees and other vegetation that will create suitable micro-climatic environments (Bruse, 2017). Jamei and Rajagopala (2017) have taken measurements in Melbourne, Australia during the summer months. The variables used included street direction, street width and floor heights. Yilmaz et al., (2017) determined that the most comfortable street directions for cold cities are ordinal directions. Particularly, in terms of pedestrian comfort, the streets extending in the north-south direction appeared to be more comfortable. Again, according to SVF values; narrow streets (deep canyon) were found more comfortable in winter months This study has compared different ratios using ENVI-met 3.1. As the above examples illustrate, there is an abundance of studies to assess the current situation as well as making city planning recommendations for the future. Other researchers have looked into the design aspects of new building structures and investigated the relationship between thermal comfort level and the use of different types of trees/plants (Ng et al., 2012; Lee et al., 2016; Tan et al., 2016). The roof structures and roof covering materials (Jänicke et al., 2015), materials used on the ground including grass cover (Ketterer and Matzarakis, 2014; Lobacarro and Acero, 2015; Kim et al., 2016) and the role of different building direction, urban density and building heights (Maggiotto et al., 2014; Perini and Magliocco, 2014; Taaleghani et al., 2015; Yilmaz et al., 2017a), were also investigated.

MATERIALS AND METHODS

The meteorological measurement station where the data was obtain for this study is located between residence areas and workplaces, and is set up in the backyard of a school in the city center (Figure 1). The latitude of this school is 39°54'18.05"N and the longitude is 41°16'23.62"E (Figure 2). This location best represents the city. The data was obtained by "Vantage Pro2 Meteorological Station, EU version" device (Figure 3). A three-dimensional microclimatic modelling tool ENVI-met 4.1 was used to evaluate meteorological data.

Figure 1. Backyard and courtyard of Gunes High School

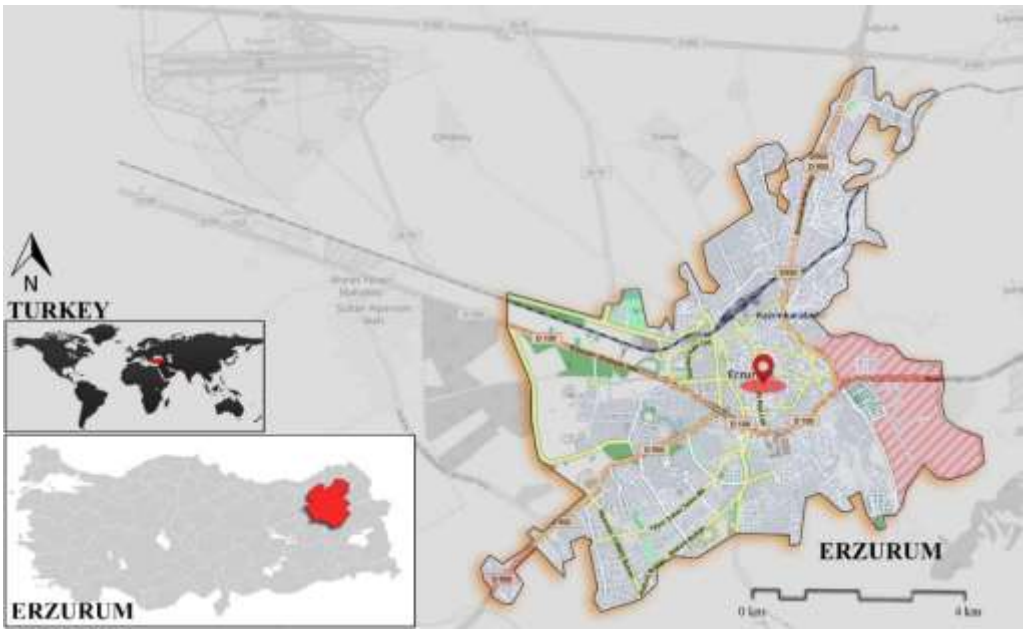

Figure 2. Location of study area (Gunes High School)

Figure 3. Vantage Pro 2 Meteorological Station

ENVI-met version 4.1 was used to enter the climate data. Although different versions of this software is available, the underlying logic is always the same. On the micro-climatic scale, ENVI-MET creates 3D models and has a horizontal resolution of 0.5 -10 meters (Yang et al., 2013; Lobaccaro and Acero, 2015). In this study time interval of 1 hour is used. With this software, the air temperature, vapor pressure, relative humidity, wind velocity, and the mean radiant temperature of the receptors can be calculated (Bruce, 2000; Huttner, 2012; Qaid et al., 2016; Bruse, 2017).

Data Obtained and ENVI-MET Model Simulated

Long term meteorological data indicates that the highest average temperature in Erzurum is in August while the lowest temperature is in January. Keeping this mind, hourly data was obtained for 24 hours in August 15, 2016 and January 15, 2017. Humidity, temperature, wind speed and direction of wind data were obtained in outdoor areas. Also humidity and temperature measurements were obtained inside the buildings. As part of the TUBITAK project, Vantage Pro 2 weather station was established in the yard at 1.5 meters above the ground level. Wireless was used to measure dry bulb air temperature with 5-minute intervals. In this study, the analysis was conducted using 90x90x30 grid system. Each grid was defined as 2mx2m and data was measured for 24 hours. For the current and recommended situations, Leonardo Module under the Space Module was used to obtain 24-hour evaluation maps. At the end of the analysis, 2 different tree species were used to create mixed trees scenario model. Also suitability for summer and winter months were considered.

ENVI-MET analysis scenarios

In this schoolyard, which is part of the city's residential and commercial area, different species of trees were introduced into the ENVI-MET model to create better thermal comfort levels. In the scenario, winter and summer conditions were considered. For this purpose, two types of trees, which grow widely in the city and has adapted to local urban conditions were selected. These were maple tree (*Acer negundo*) and Scots pine (*Pinus sylvestris* L). The analysis was conducted for summer and winter months. All analysis were conducted for 15:00 hour.

APPLICATION AND RESULTS

Analysis for mixed trees with ENVI-met model

Trees that are widely grown and adapted themselves to the city center environment were selected for modeling. These trees typical plants that are found in the landscape of the area

because their visual value. These trees were maple (*Acer negundo*) and The analaysis were carried out for the summer and winter months. Best growing and best adapted pine tree to the city where winters are long was selected for the analysis. This was scots pine (*Pinus sylvestris L*). Pine trees are very durable under harsh winter conditions. At the same time, they are quite high in visual value when it snows. They also provide intense shadow in the winter. On the negative side, they may cause icing conditions on the roadsides during the winter. Also, because of low branches, they may hinder pedestrian traffic.

Comparison of Existing Situation and Recommendation

In this study, two different usage proposals were analyzed for both summer and winter (Figure 4). These are:

- Current state,
- Mixed trees scenario.

Figure 4. The current model for the 90x90x30 grid system in the city center where the Gunes High School is located

Current situation simulation for August 15, 2016 at 13:00 hour
Proposed model simulation for August 15, 2016 at 13:00 hour
Current situation simulation for January 15, 2017 at 13:00 hour
Proposed model simulation for January15, 2017 at 13:00 hour

CONCLUSIONS

In conclusion, the models indicated that urban areas with trees provided much better thermal comfort compared to models without trees. These results were applicable to both summer and winter months. It is believed that the results of this study will help policy makers in designing healthy urbanization and determining the location of new settlements. Areas with trees are very important for the city. Because, these places are like the lungs of the city with the oxygen they produce. It is important for planning corret choise and correct place. There is a great need for climate-focused work which transferred to eco-plan decisions especially. All planner aims to provide physically and psychologically comfortable environment for people.

ACKNOWLEDGMENTS

It was benefited from the data of the station established within the scope of the project and the devices taken from the project (Scientific and Technological Research Council of Turkey,

TÜBİTAK as Project No: 215O627). The authors express their gratitude to Michael Bruse for providing the ENVI-met software from internet.

REFERENCES

Bruse, M., 2017. ENVI-met 4: A Microscale Urban Climate Model. http://www.envi-met.info. [Accessed on February 2017].

Huttner S., 2012. Further development and application of the 3D microclimate simulation ENVI-met PhD Thesis Johannes Gutenberg-University Mainz , p. 135

Jänicke, B., Meier, F., Hoelscher, M.-T., Scherer, D., 2015. Evaluating the effects offacade greening on human bioclimate in a complex urban environment. Adv.Meteorol. 15, http://dx.doi.org/10.1155/2015

Jamei E., Rajagopalan P., 2017. Urban development and pedestrian thermal comfort in Melbourne. Solar Energy 144, 681–698

Ketterer, C.; Matzarakis, A., 2014. Human-biometeorological assessment of heat stress reduction by replanning measures in Stuttgart, Germany. Lands. Urban Planning,122, 78–88

Kim Y., An S.M., Eum J.H., Woo J.H ., 2016. Analysis of Thermal Environment over a Small-Scale Landscape in a Densely Built-Up Asian Megacity. Sustainability , 8(4), 358; doi:10.3390/su8040358

Lobaccaro, G., Acero, J.A., 2015. Comparative analysis of green actions to improve outdoor thermal comfort inside typical urban street canyons. Urban Climate 14, 251–267.

Lee, H., Mayer, H., Chen, L., 2016. Contribution of trees and grasslands to themitigation of human heat stress in a residential district of Freiburg, SouthwestGermany. Landscape Urban Planning, 148, 37–50,

Maggiotto, G., Buccolieri, R., Santo, M. A., Leo, L. S., & Di Sabatino, S. (2014). Validation of temperature-perturbation and CFD-based modelling for the prediction of the thermal urban environment: The Lecce (IT) case study. Environmental Modelling and Software, 60, 69–83.

Ng, E., Chen, L., Wang, Y., Yuan, C., 2012. A study on the cooling effects of greening in a high-density city: an experience from Hong Kong. Build. Environ. 47, 256–271.

Qaid A., Lamit H.B., Ossen D.R., Shahminan R.N.R., 2016. Urban heat island and thermal comfort conditions at micro-climate scale in a tropical planned city. Energy and Buildings, 133,577-595

Perini, K.; Magliocco, A., 2014. Effects of vegetation, urban density, building height, and atmospheric conditions on local temperatures and thermal comfort. Urban For. Urban Green, 13, 495–506.

Taleghani, M., Kleerekoper, L., Tenpierik, M., van den Dobbelsteen, A., 2015. Outdoor thermal comfort within five different urban forms in the Netherlands. Build. Environment, 83, 65–78

Tan, Z., Lau, K.K., Ng, E.1, 2016. Urban tree design approaches for mitigatingdaytime urban heat island effects in a high-density urban environment. Energy Building, 114, 265–274.

Yang, X., Zhao, L., Bruse, M., Meng, Q., 2013. Evaluation of a microclimate model forpredicting the thermal behavior of different ground surfaces. Build. Environment, 60, 93–104.

Yilmaz S., Mutlu E., and Yilmaz H., 2017. Quantification of thermal comfort of based on different Street orientation in winter months of urban city Dadaskent. GREEN CITIES 2017 International Symposium on greener cities for more efficient ecosystem services in a climate changing world - Oral presentation, 12/15 September Bologna, ITALY

Yilmaz S., Dursun D., Yavaş M., 2017a. Analysis of climate sensitivity of public space in cold climate zone:The case of Yakudiye square, Erzurum. EDRA48 Madison, oral presentation , VOICES of Place – Empower, Engage, Energize, May 31-June 3, 2017, Madison, WI,USA

NUMERICAL STUDY OF TURBULENT FLOW IN CIRCULAR-SECTIONED PIPES

Tahir Karasu
Department of Mechanical Engineering, Eskişehir Osmangazi University, Meşelik, 26480 Eskişehir, Turkey, tahirkarasu26@gmail.com

Abstract
This original research work presents the results of an extensive study of numerical solution of steady, incompressible and axisymmetric developing turbulent flow in circular-sectioned pipes at two different Reynolds numbers. Employing the finite-volume method, a computer program based on the SIMPLE (Semi-Implicit Method for Pressure Linked Equations) algorithm has been developed. Numerical solution of the conservation equations of mass and momentum, together with the standard k-ε turbulence model, are obtained using an iterative numerical solution technique. Near the solid boundary, wall-functions are employed. Computational predictions for radial profiles of axial velocity, turbulence kinetic energy, turbulence kinetic energy dissipation rate, effective viscosity, centre-line velocity variation, wall-shear stress and friction coefficient distributions along axisymmetric pipe flow geometry are presented and compared with experimental data. The results of numerical study are generally in very good agreement with experimental measurements.

Keywords: *Turbulence, Flow, Pipes, Predictions.*

INTRODUCTION
Numerical study of developing turbulent flow in pipes of circular cross-section is one of the basic flow studies. This flow is basically a transition from a boundary layer-type flow at the entrance to a fully developed flow downstream. The free stream in the inlet region is completely surrounded by the boundary layer, which by diffusion of momentum through laminar and turbulent mechanisms grows in thickness as the distance from the pipe inlet increases. The growing boundary layer accelerates the free stream which eventually loses its identity as the boundary layer merges with it. Following the disappearance of the free stream, further changes occur in the velocity distribution and turbulence structure until the flow attains a fully developed state. Developing turbulent pipe flow has wide application in the field of engineering. The ability to compute the detailed nature of the behaviour of developing turbulent flow in pipes would lead to the improved design of engineering equipment. In practice, turbulent pipe flow is mostly encountered in: transportation of various liquids and gases in long pipes, heat exchangers, coolant passages of electrical generators, combustion chamber systems and air conditioning and heating systems. Considerable experimental and theoretical works on turbulent flow in pipes have been reported in the literature. Among the most interesting ones are the works of Barbin and Jones (1963), Den Toonder and Nieuwstadt (1997), Eggels et al. (1994), Kikuyama et al. (1983), Karasu (1980, 1993, 1995, 2016), Karasu et al. (1988), Pompeo and Matievic (1986/87), Richman and Azad (1973), Schildknecht et al. (1979), Wenger and Devenport (1999), and Wittmer et al. (1998). In the present numerical study, the experimental measurements of Kikuyama et al. (1983), and Pompeo and Matievic (1986/87) have been used for comparison with the numerical computations. The main objective of this investigation is to obtain computational predictions of steady, incompressible and axisymmetric developing turbulent flow in pipes using the standard k-ε turbulence model (Launder and Spalding, 1974) with a wall-functions boundary condition, and to compare the results of numerical study with available experimental measurements in the literature for validation.

MATHEMATICAL AND PHYSICAL MODEL

Governing Equations and Turbulence Model

With reference to Figure 1, the mathematical and physical model employed in the numerical study of incompressible and axisymmetric developing turbulent flow in circular-sectioned pipes, requires the simultaneous solution of the governing equations, together with the turbulence model equations. The transport equations representing the conservation of mass, momentum, turbulence kinetic energy and its dissipation rate are cast into a general form of steady state and axisymmetric cylindrical coordinates as follows:

$$\frac{\partial}{\partial x}(\rho u \phi) + \frac{1}{r}\frac{\partial}{\partial r}(\rho r v \phi) - \frac{\partial}{\partial x}\left(\Gamma_\phi \frac{\partial \phi}{\partial x}\right) - \frac{1}{r}\frac{\partial}{\partial r}\left(r\Gamma_\phi \frac{\partial \phi}{\partial r}\right) = S_\phi \qquad (1)$$

This equation represents a transport equation for a general variable ϕ. The flow is assumed to remain in radial planes. The variables u and v are axial and radial velocity components, ρ is the fluid density and Γ_ϕ is the transport coefficient. The final term, S_ϕ , is the source term. The variables, ϕ, necessary in this computational investigation are u, v, k and ε. Here, k and ε stand for the kinetic energy of turbulence and its dissipation rate, respectively. The turbulence model employed in the present study is the k-ε model of Launder and Spalding (1974). If ϕ is set equal to unity and Γ_ϕ and S_ϕ to zero, (1) also represents the equation of continuity. Pressure is derived from the pressure correction equation (Patankar, 1980). The transport equations, coefficients and the source terms are summarised in Table 1.

Table 1. Transport equations, coefficients and source terms

ϕ	Γ_ϕ	S_ϕ
1	**0**	**0**
u	$\mu_e = \mu + \mu_t$	$-\frac{\partial P}{\partial x} + \frac{\partial}{\partial x}\left(\mu_e \frac{\partial u}{\partial x}\right) + \frac{1}{r}\frac{\partial}{\partial r}\left(r\,\mu_e \frac{\partial v}{\partial x}\right)$
v	μ_e	$-\frac{\partial P}{\partial r} + \frac{\partial}{\partial x}\left(\mu_e \frac{\partial u}{\partial r}\right) + \frac{1}{r}\frac{\partial}{\partial r}\left(r\,\mu_e \frac{\partial v}{\partial r}\right) - 2\,\mu_e \frac{v}{r^2}$
k	$\frac{\mu_e}{\sigma_k}$	$G - \rho\,\varepsilon$
ε	$\frac{\mu_e}{\sigma_\varepsilon}$	$\frac{\varepsilon}{k}(C_1 G - C_2\,\rho\,\varepsilon)$

Note : 1. $\mu_t = C_\mu \rho\, k^2/\varepsilon$

2. Turbulence model constants are assigned the following values (Launder and Spalding, 1974)**:**
$C_\mu = 0.09, C_1 = 1.44, C_2 = 1.92, \sigma_k = 1.0, \sigma_\varepsilon = 1.3$

3. $G = \mu_t \left\{ 2\left[\left(\frac{\partial u}{\partial x}\right)^2 + \left(\frac{\partial v}{\partial r}\right)^2 + \left(\frac{v}{r}\right)^2\right] + \left(\frac{\partial u}{\partial r} + \frac{\partial v}{\partial x}\right)^2 \right\}$

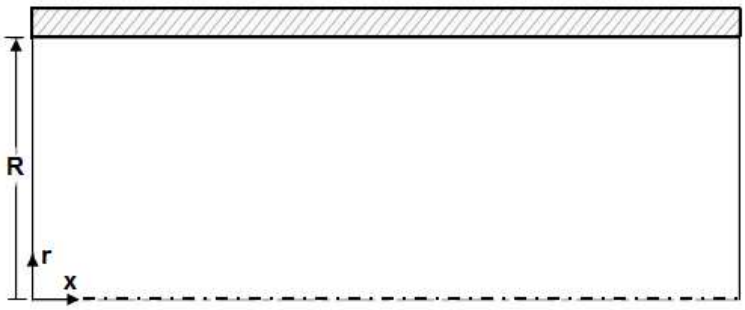

Figure 1. Axisymmetric cylindrical coordinate system and geometry of the pipe flow.

Boundary Conditions

With reference to Figure 1, the boundary conditions for turbulent flow in the pipes studied are given below. At the inlet to the pipe, a uniform axial velocity corresponding to the experimental condition is specified, while the radial velocity is assumed zero. Empirical relationships are employed to assign uniform entrance values to turbulence quantities k and ε; that is, k=(0.001-0.0015) u_b^2 and ε=($C_\mu k^{3/2}$ / 0.03R), where u_b is the bulk velocity and R is the radius of the pipe. The pipe section was chosen to be sufficiently long so that fully developed conditions could be assumed to prevail at the outlet; that is, all axial derivatives were assumed to vanish and the radial velocity was assumed zero. At the pipe axis, symmetry is assumed: $(\partial\phi/\partial r) = v = 0$, where ϕ can be any of u, k or ε. At the pipe wall, velocity components u, v and turbulence quantities k and ε are set to zero. The values of k and ε at the near-wall grid points are calculated using the wall-functions of Launder and Spalding (1974). Initial field values throughout the computational domain were specified properly so as not to cause numerical divergence.

Numerical Solution Procedure

In this computational investigation, employing the finite-volume approach, a computer program based on the SIMPLE algorithm of Patankar (1980) has been developed. The partial differential equations (1) are discretised by a control-volume-based finite-difference method with a hybrid scheme. The finite-volume forms of the partial differential equations coupled with the boundary conditions are solved iteratively using a line-by-line solution procedure in conjunction with a tridiagonal matrix form (Spalding, 1981).

Computational Details

The numerical computations were performed on an Intel(R) Core(TM) i5-2400 CPU @ 3.10GHz 3.40GHz personal computer. The computational grid distributions for two of the pipe-flow cases studied are depicted in Figures 2 and 11. All the computational grids employed were non-uniformly distributed with finer spacings in the regions of large spatial gradients, i.e., the near-wall region and inlet region of the pipe. Staggered control volumes were used for axial and radial velocity components. All other quantities of interest were calculated at the grid points. The line-by-line method was employed to obtain converged solutions iteratively. Under-relaxation factors were used to promote numerical stability with values of 0.6, 0.6, 0.8, 0.8, 0.5 and 0.3 for u, v, k, ε, P and μ_e, respectively. The convergence criterion adopted in the present computations was that the summation of the absolute values of the mass residual in the entire computational domain be less than a prescribed value of 10^{-5}. Grid tests were performed with different grid sizes to obtain an optimum grid-independent solution for each flow case studied. All the computations presented in this study are grid-independent. Table 2 summarises details of the computational requirements for the flow cases investigated. In this table, Re is

the Reynolds number and N is the number of iterations performed to obtain a converged solution.

Table 2. Flow case, Reynolds number, grid size and number of iterations.

Flow case of	Re	Grid Size (**x**) × (**r**)	N
Kikuyama et al. (1983)	**60 000**	40 × 30	206
Pompeo and Matievic (1986/87)	**180 000**	40 × 30	257

PRESENTATION AND DISCUSSION OF RESULTS

Numerical computations were carried out for developing turbulent flow in circular-sectioned pipes at two different Reynolds numbers, and the results of computations were compared with the experimental data of Kikuyama et al. (1983) and Pompeo and Matievic (1986/87). With air used as the working fluid in the pipe, the experimental study of turbulent pipe flow conducted by Kikuyama et al. (1983) is firstly selected as the test case for this numerical study. The Reynolds number based on the pipe diameter and bulk velocity is $Re=6 \times 10^4$ ($Re=u_b\, d/\nu$, where u_b is the bulk velocity). For this flow case, the computational domain is extended to an axial distance of 50 diameters downstream from the inlet plane of the pipe. The computational grid distribution for the pipe flow of Kikuyama et al. (1983) is shown in Figure 2. The predicted radial profiles of axial velocity along the pipe in dimensionless form u/u_c, and radial distance r/R, at axial locations ranging from x/d=0.4 to 50 are plotted in Figure 3, and compared with the experimental data of Kikuyama et al. (1983). As seen from the figure, the predicted axial velocity profile develops along the pipe, and at cross-sections x/d=2.7, 9.7, 15.5, and 28.7, the agreement obtained between the predictions and experimental data is excellent. In Figure 4, the predicted axial variation of centre-line velocity is presented in terms of u_c/u_b and axial distance x/d. Here, the centre-line velocity (u_c) is normalised with the bulk velocity (u_b), and the axial distance is normalised with respect to pipe diameter (d). As can be seen from the figure, the predicted axial variation of centre-line velocity increases first until it attains its maximum value and then decreases slightly to its fully-developed value downstream after which it remains constant.

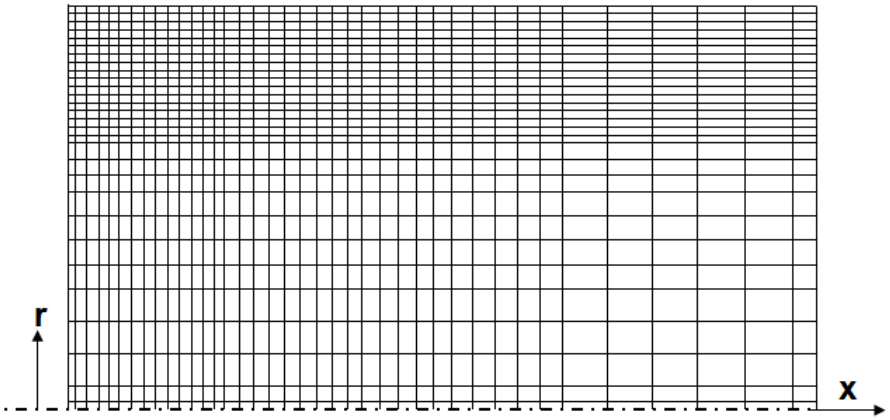

Figure 2. Computational grid distribution for pipe flow geometry of Kikuyama et al. (1983).

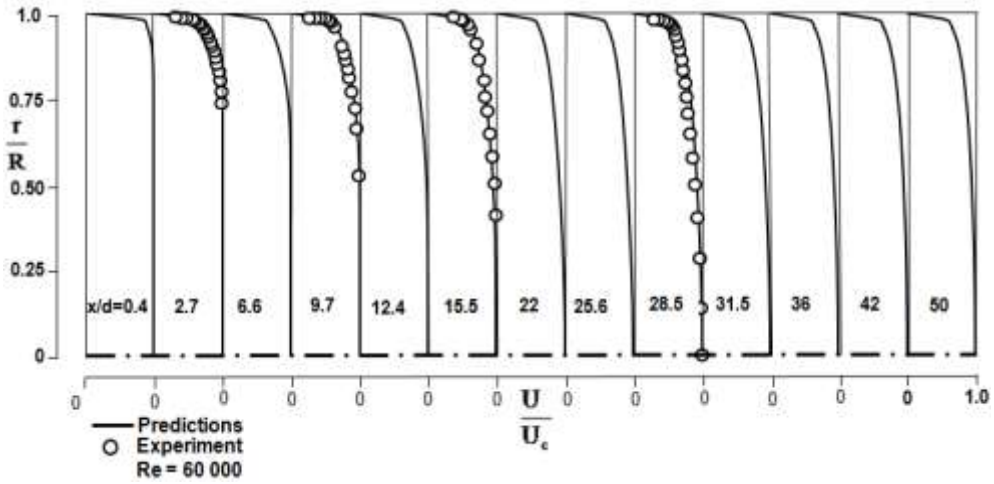

Figure 3. Comparison of predicted radial profiles of axial velocity along the pipe with experimental data of Kikuyama et al. (1983).

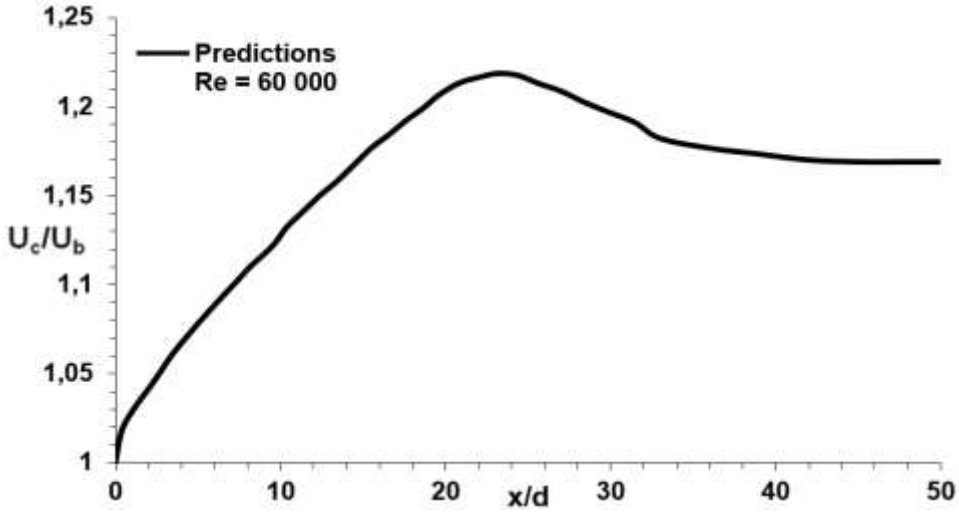

Figure 4. Predicted axial variation of dimensionless centre-line velocity along the pipe axis of Kikuyama et al. (1983).

In Figure 5, the predicted axial distribution of dimensionless turbulence kinetic energy $k^{0.5} / u_b$ along the symmetry axis of the pipe is revealed. As seen from the figure, the turbulence kinetic energy decreases until it attains its minimum value at about x/d=17.6, and thereafter increases sharply along the pipe axis until it reaches its maximum value at about x/d=39, and then after showing a little bit decrease it attains its fully-developed value, after which it remains constant along the pipe axis. Figures 6, 7 and 8 show the predicted radial profiles of turbulence kinetic energy, dissipation rate of turbulence kinetic energy and effective viscosity, respectively, along the pipe of Kikuyama et al. (1983) at the same downstream locations as in Figure 3. Here, the predicted profiles are normalised, respectively, with respect to square of bulk velocity u_b^2, maximum values of turbulence kinetic energy dissipation rate ε_{max} and effective viscosity $\mu_{e\ max}$ in the flow field. These figures indicate how the predicted turbulence kinetic energy, dissipation rate of turbulence kinetic energy and effective viscosity profiles develop along the pipe flow configuration of Kikuyama et al. (1983). Figure 9 displays the computed variation of the wall-shear stress along the pipe wall, in terms of the ratio τ_w / τ_{wd}, plotted against nondimensional distance x/d from the inlet plane of the pipe. The wall-shear stress has been made dimensionless with respect to its fully-developed value, τ_{wd}. For this flow situation, as can be seen from the figure, the fully-developed value of the wall-shear stress is reached at

x/d=45. Beyond this location, it remains practically constant. Finally, the computed distribution of the friction coefficient ($C_f = 2\ \tau_w / \rho\ u_b^2$) along the pipe wall, as a function of downstream distance x/d, is plotted in Figure 10. As seen from the figure, the friction coefficient exhibits the same trend as the wall-shear stress shown in Figure 9.

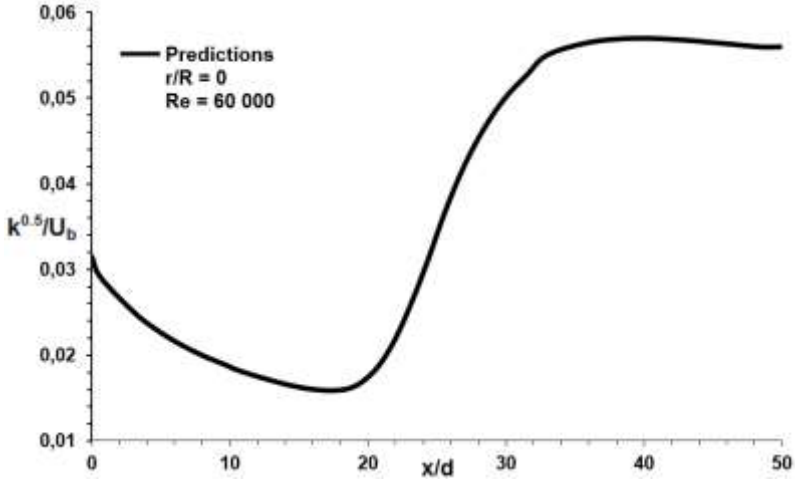

Figure 5. Predicted axial distribution of dimensionless turbulence kinetic energy along the pipe axis of Kikuyama et al. (1983).

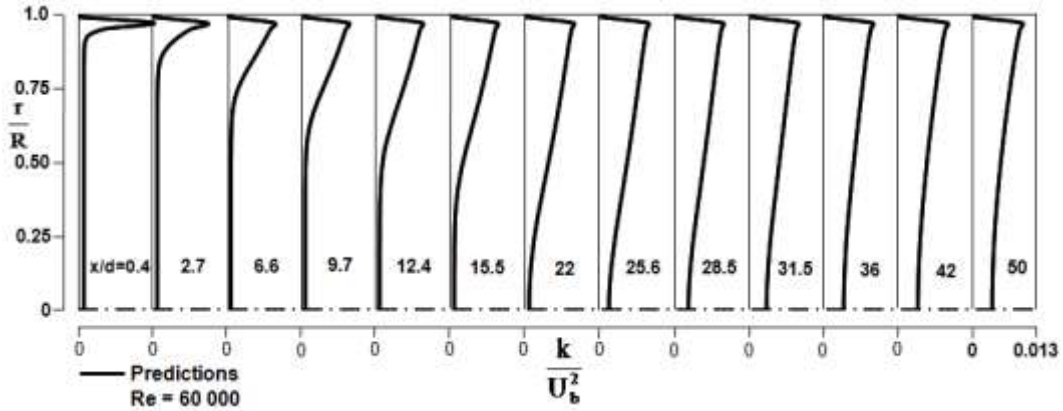

Figure 6. Predicted radial profiles of normalised turbulence kinetic energy along the pipe flow of Kikuyama et al. (1983).

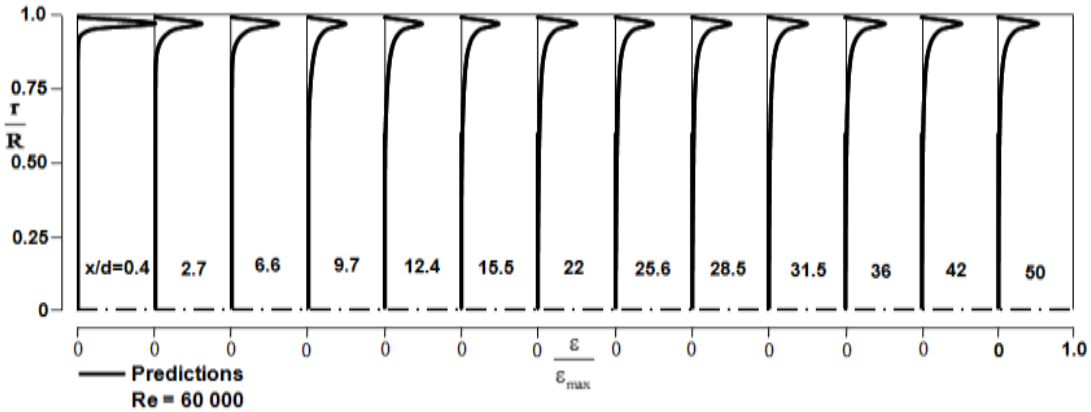

Figure 7. Predicted radial profiles of normalised turbulence kinetic energy dissipation rate along the pipe flow of Kikuyama et al. (1983).

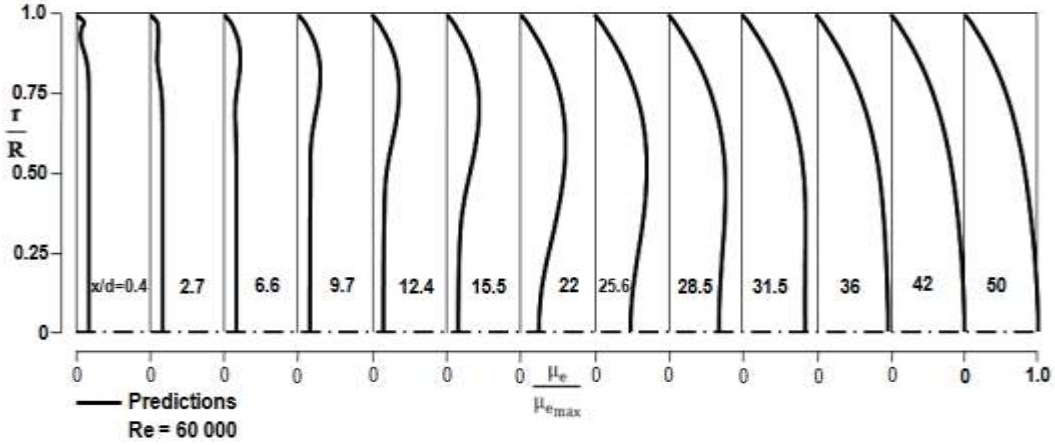

Figure 8. Predicted radial profiles of normalised effective viscosity along the pipe flow of Kikuyama et al. (1983).

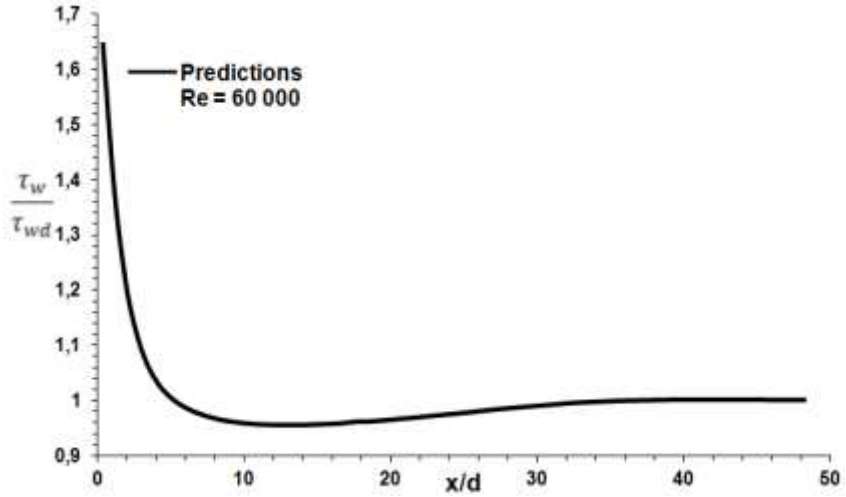

Figure 9. Computed variation of dimensionless wall-shear stress along the pipe wall of Kikuyama et al. (1983).

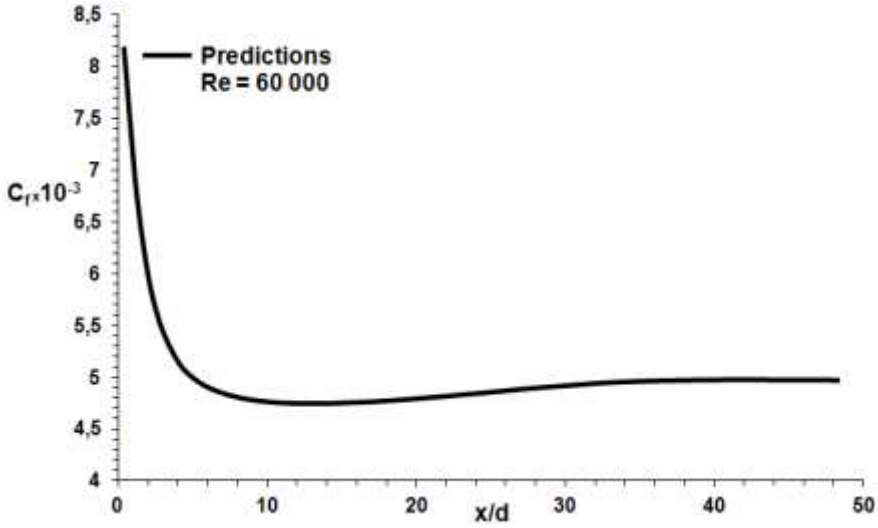

Figure 10. Computed distribution of friction coefficient along the pipe wall of Kikuyama et al. (1983).

With air used as the working fluid in the pipe, the experimental measurements of Pompeo and Matievic (1986/87) are secondly selected as the comparison basis for this numerical study. The Reynolds number based on the pipe diameter and bulk velocity is Re = 1.8 x 10^5 (Re = u_b d/ν, where u_b is the bulk velocity). For this flow situation, the calculation domain is extended to an axial distance of 100 diameters downstream from the inlet plane of the pipe. The computational grid distribution for the axisymmetric pipe flow of Pompeo and Matievic (1986/87) is indicated in Figure 11. The computed radial profiles of axial velocity along the pipe in dimensionless form u/u_b, and radial distance r/R, at axial positions ranging from x/d=2 to 100 are depicted in Figure 12, and compared with the experimental measurements of Pompeo and Matievic (1986/87). As seen from the figure, the computed axial velocity profile develops along the pipe, and at cross-sections x/d=4.5, 16.45, 27.5, and 55.3, the agreement obtained between the predictions and experimental measurements is very good. Figure 13, on the other hand, displays the predicted axial variation of dimensionless centre-line velocity (u_c) along the pipe axis, normalised to bulk velocity (u_b) and plotted as a function of downstream distance normalised to pipe diameter (d). As can be seen from the figure, the predicted axial variation of centre-line velocity increases until it reaches its maximum value and then decreases slightly to its fully-developed value downstream after which it remains constant. In Figure 14, the predicted axial distribution of dimensionless turbulence kinetic energy $k^{0.5} / u_b$ along the symmetry axis of the pipe is shown. As seen from the figure, the turbulence kinetic energy decreases until it attains its minimum value at about x/d=18.4, and thereafter increases sharply along the pipe axis until it reaches its maximum value at about x/d=46.8, and then after showing a little bit decrease it attains its fully-developed value, after which it remains constant along the pipe axis. Figures 15, 16 and 17 give the predicted radial profiles of turbulence kinetic energy, dissipation rate of turbulence kinetic energy and effective viscosity, respectively, along the pipe of Pompeo and Matievic (1986/87) at the same downstream positions as in Figure 12. Here, the predicted profiles are normalised, respectively, with respect to square of bulk velocity u_b^2, maximum values of turbulence kinetic energy dissipation rate ε_{max} and effective viscosity $\mu_{e\ max}$ in the flow field. These figures show how the predicted turbulence kinetic energy, dissipation rate of turbulence kinetic energy and effective viscosity profiles develop along the pipe flow configuration of Pompeo and Matievic (1986/87). In Figure 18, the predicted variation of the wall-shear stress in dimensionless form of τ_w / τ_{wd} along the pipe wall is given as a function of downstream distance normalised to pipe diameter. For this flow case, as can be seen from the figure, the fully-developed value of the wall-shear stress (τ_{wd}) is attained at about x/d=64. Beyond this location, it remains practically constant. Finally, the computed distribution of the friction coefficient ($C_f = 2\ \tau_w / \rho\ u_b^2$) along the pipe wall, as a function of downstream distance x/d, is displayed in Figure 19. As seen from the figure, the friction coefficient reveals the same trend as the wall-shear stress shown in Figure 18.

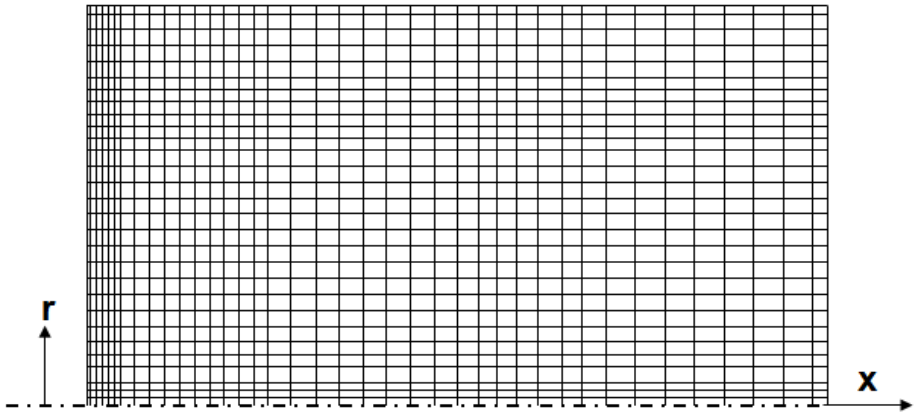

Figure 11. Computational grid distribution for pipe flow geometry of Pompeo and Matievic (1986/87).

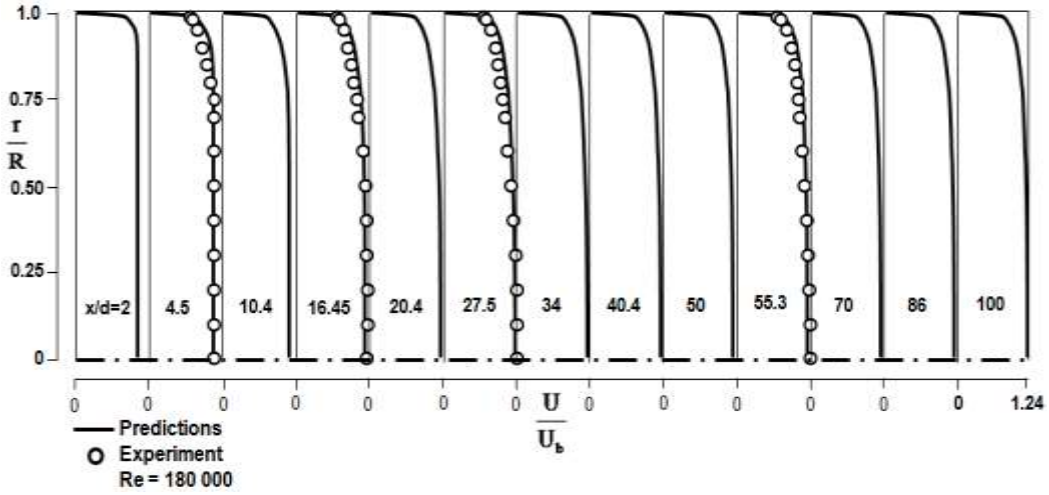

Figure 12. Comparison of predicted radial profiles of axial velocity along the pipe with experimental data of Pompeo and Matievic (1986/87).

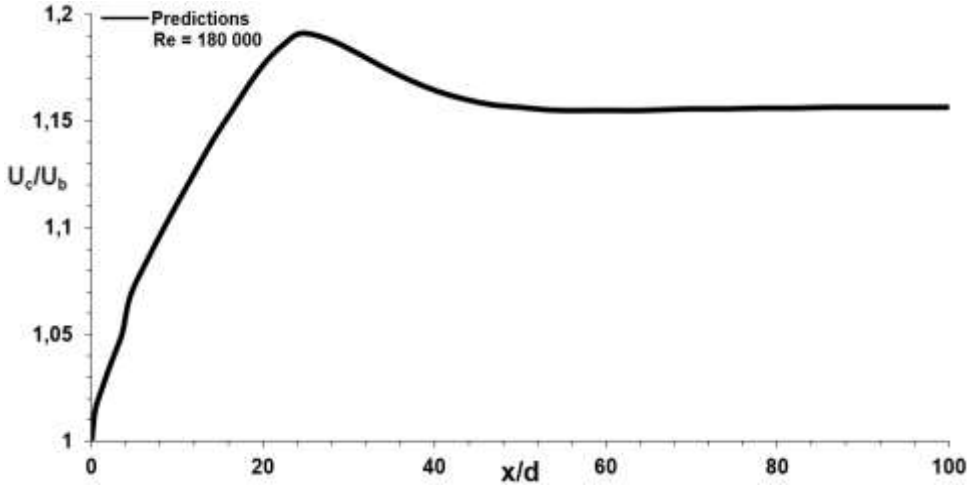

Figure 13. Predicted axial variation of dimensionless centre-line velocity along the pipe axis of Pompeo and Matievic (1986/87).

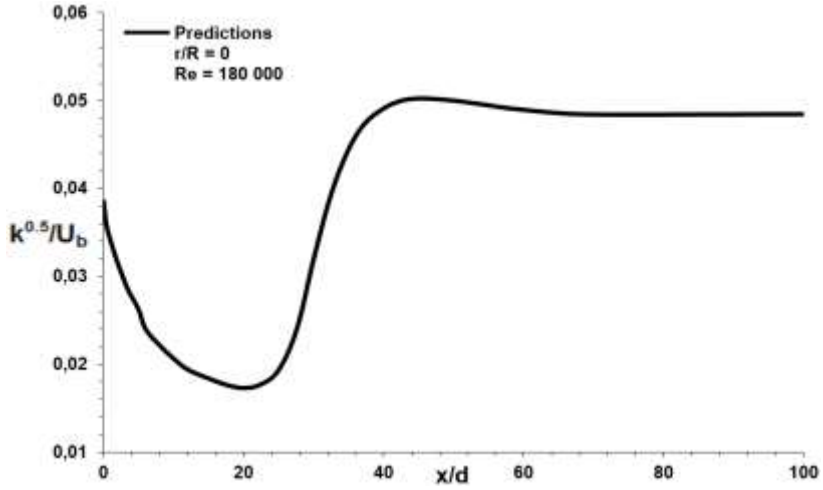

Figure 14. Predicted axial distribution of dimensionless turbulence kinetic energy along the pipe axis of Pompeo and Matievic (1986/87).

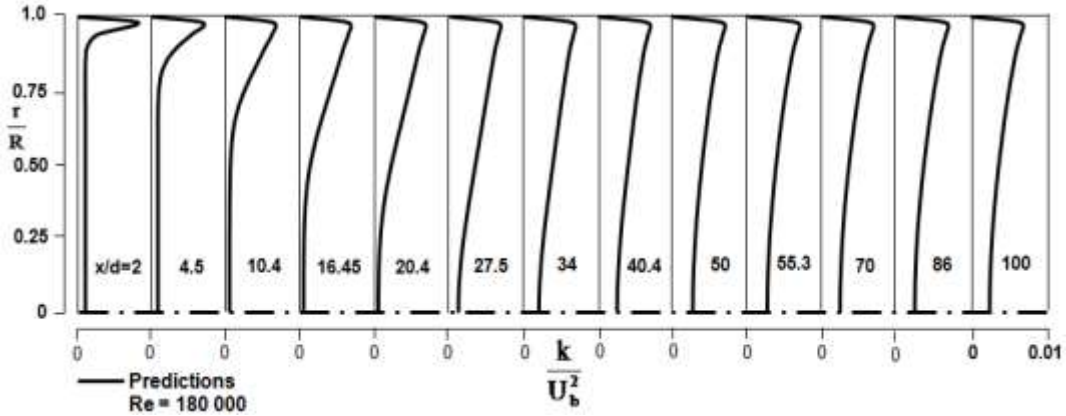

Figure 15. Predicted radial profiles of normalised turbulence kinetic energy along the pipe flow of Pompeo and Matievic (1986/87).

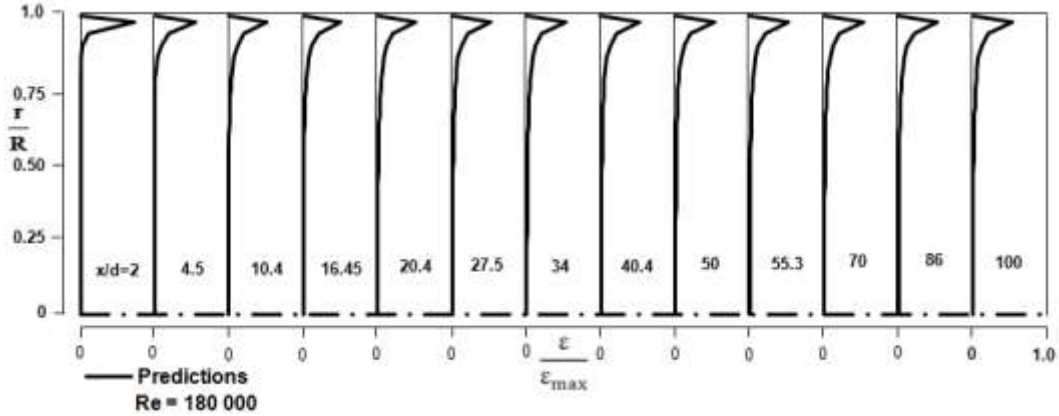

Figure 16. Predicted radial profiles of normalised turbulence kinetic energy dissipation rate along the pipe flow of Pompeo and Matievic (1986/87).

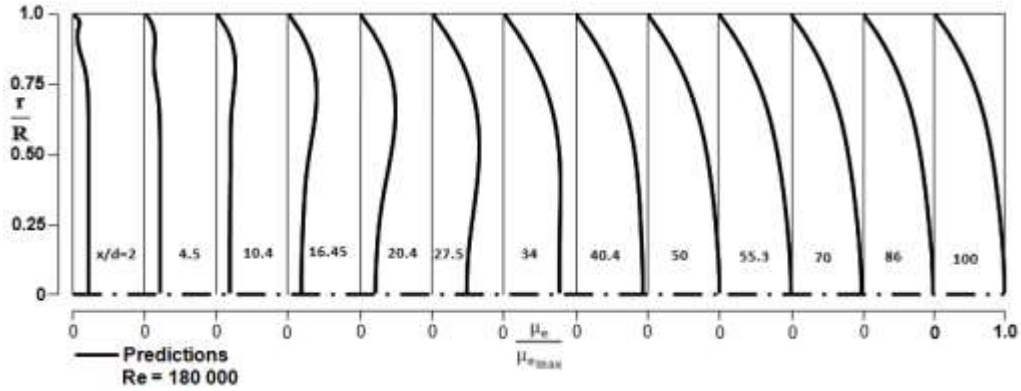

Figure 17. Predicted radial profiles of normalised effective viscosity along the pipe flow of Pompeo and Matievic (1986/87).

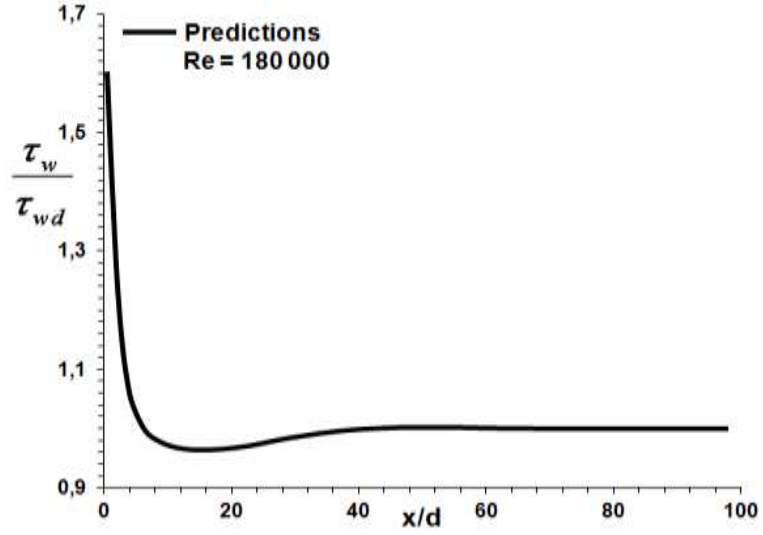

Figure 18. Predicted variation of dimensionless wall-shear stress along the pipe wall of Pompeo and Matievic (1986/87).

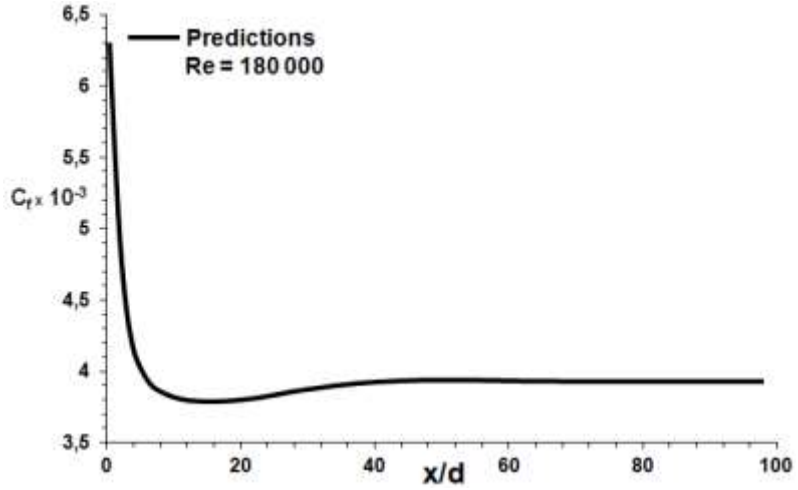

Figure 19. Computed distribution of friction coefficient along the pipe wall of Pompeo and Matievic (1986/87).

CONCLUDING REMARKS

The main concluding remarks from the numerical study of the present original research investigation can be summarised as follows. Developing turbulent flow in pipes of circular cross-section at two different Reynolds numbers has been computed numerically employing the standard k-ε turbulence model. Using the finite-volume method, a computer program based on the SIMPLE algorithm of Patankar (1980) has been developed. The performance of the standard k-ε turbulence model has been investigated for developing turbulent pipe flow. The computed radial profiles of axial velocity, turbulence kinetic energy, turbulence kinetic energy dissipation rate, effective viscosity, axial variation of centre-line velocity, wall-shear stress and friction coefficient distributions along the pipe are presented and, wherever availlable, compared with experimental measurements reported in the literature. The results of numerical study are generally in very good agreement with the experimental measurements.

REFERENCES

Barbin, A. J., and Jones, J. B., 1963, Turbulent flow in the inlet region of a smooth pipe, *J. Basic Engrg, Trans. ASME*, 29, p. 29-34.

Den Toonder, J. M. J, and Nieuwstadt, F. T. M., 1997, Reynolds number effects in turbulent pipe flow for low to moderate Re, *Phys. Fluids*, 9, 3398-3409.

Eggels, J. G. M., Unger, F., Weiss, M. H., Westerweel, J., Adrian, R. J., Friedrich, R., and Nieuwstadt, F. T. M., 1994, Fully developed turbulent pipe flow: a comparison between direct numerical simulation and experiment, *J. Fluid Mech.*, 268, 175-209.

Kikuyama, K., Murakami, M., and Nishibori, K., 1983, Development of three-dimensional turbulent boundary layer in an axially rotating pipe, *J. of Fluids Eng.*, 105, 154-160.

Karasu, T., 1980, *Numerical prediction of incompressible turbulent swirling flows in circular-sectioned ducts and annuli*, Ph.D. Thesis, University of London, London, U.K.

Karasu, T., Choudhury, P. R., and Gerstein, M., 1988, Prediction of some turbulent flows using upwind and hybrid discretisation schemes and the two-equation turbulence model, *Proc. 4th Miami international symposium on multi-phase transport and particulate phenomena*, Miami Beach, Florida, U.S.A., 5, 105-124.

Karasu, T., 1993, Numerical computation of turbulent flow in pipes, *Doğa-Tr. J. of Engineering and Environmental Sciences*, 17, 29-38.

Karasu, T., 1995, Numerical prediction of turbulent flow in circular pipes, *9th International Conference on Numerical Methods in Laminar and Turbulent Flow*, Atlanta, Georgia, U.S.A., Proceedings Book, Vol. 9, Part 2, pp. 1329-1339.

Karasu, T., 2016, Computational investigation of turbulent flow in pipes, *3rd International Conference on Advanced Technology and Sciences (ICAT'16)*, 01-03 September 2016, Selçuk University, Konya, Turkey, Proceedings Book, pp. 939-948.

Karasu, T., 2016, Computer simulation of turbulent flow in pipes, *9th International Conference on Sustainable Energy and Environmental Protection (SEEP'16)*, 22-25 September 2016, Erciyes University, Kayseri, Turkey, Proceedings Book, pp. 359-365.

Karasu, T., 2016, Computer simulation of developing turbulent flow in circular-sectioned pipes, *10th International Clean Energy Symposium (ICES'16)*, 24-26 October 2016, Istanbul Technical University, Istanbul, Turkey, Proceedings Book, pp. 742-753.

Launder, B. E., and Spalding, D. B., 1974, The numerical computation of turbulent flows, *Comp. Meth. Appl. Mech. Engng*, 3, 269-289.

Patankar, S. V., 1980, *Numerical heat transfer and fluid flow*, Hemisphere, McGraw-Hill, Washington, D.C., Chapters 5 and 6, 79-138.

Pompeo, L., and Matievic, T., (1986/87), Turbulenzbeeinflussung, Semesterarbeit in Fluiddynamik. ETH Zurich, Institut für Aerodynamik Report WS.

Richman, J. W., and Azad, R. S., 1973, Developing turbulent flow in smooth pipes, *Appl. Sci. Res.*, 28, 419-441.

Schildknecht, M., Miller, J. A., and Meier, G. E. A., 1979, The influence of suction on the structure of turbulence in fully developed pipe flow, *J. Fluid Mech.*, 90, 67-107.

Spalding, D. B., 1981, A general-purpose computer program for multi-dimensional one-and-two phase flow, *Math. Comput. Simulation*, XXIII, 267-276.

Wenger, C. W., and Devenport, W. J., 1999, Seven-hole pressure probe calibration method utilizing look-up error tables, *AIAA Journal*, 37(6), 675-679.

Wittmer, K. S., Devenport, W. J., and Zsoldos, J. S., 1998, A four-sensor hot-wire probe system for three-component velocity measurement, *Experiments in Fluids*, 24, 416-423.

DETECTING OF THE IONOSPHERIC DISTURBANCES WITH A FAST ALGORITHM

Ali Çınar[1], Seçil Karatay[1], Feza Arıkan[2]
[1] *Electrical&Electronics Engineering, Kastamonu University, Kastamonu, Turkey*
{acinar,skaratay}@kastamonu.edu.tr
[2] *Electrical&Electronics Engineering, Hacettepe University, Ankara, Turkey*
arikan@hacettepe.edu.tr

Abstract
Electron density is the basis parameter in the ionosphere. Anormally decreasing or increasing of electron density cause disturbances/anomalies in ionosphere. Electron density distribution varies depending on geographic location, seasons, altitude, solar, geomagnetic and seismic activities. Detecting of these disturbances are important for propagation of the radio signals which are used by space based communication, positioning and navigation systems. Travelling ionospheric disturbances (TIDs) are wave-like perturbations of the ionospheric plasma. They can be classified according to their frequency, duration and amplitude as Medium Scale Travelling Ionospheric Disturbances (MSTIDs) and Large Scale Travelling Ionospheric Disturbances(LSTIDs). These disturbances are easily detected analyzing Total Electron Content (TEC) data. TEC is proportional to the total number of electrons on a path crossing the atmosphere. TEC measurements are obtained by Global Positioning System (GPS). In this study, a new method is developed, namely is Differential Rate of TEC (DRoT), for investigating the disturbances in ionosphere. DRoT is the normalized metric norm between the RoT and its baseband trend structure. The effects of geomagnetic and seismic activities to the ionosphere in the midlattitude and equatorial region are analyzed. If DRoT value is lower than 50%, there are no significant disturbances. If DRoT value is between 50% and 70%, MSTIDs are observed. If DRoT value is higher than 70%, LSTIDs are observed.

Keywords: *Ionosphere, Travelling Ionospheric Disturbance, Total Electron Content, Differential Rate of TEC*

INTRODUCTION
The ionosphere is a region on the Earth's upper atmosphere which extends between 50 km to 1000 km from the ground. It is a layer that consists gases which are ionized by solar radiation. Ionization changes according to the altitude, geographic location, solar radiation and activity, geomagnetic activity and seismic activity. Electrons separate from their molecules and become free with solar radiation. Total Electron Content (TEC) is the total number of electrons integrated between two points, along a tube of 1 m2 cross section. TEC is in units of TECU which is 10^{16} electrons [Kouris, 2005; Kumluca et al., 1999]. TEC is one of the important parameter that changes according to solar, geomagnetic and seismic activitiy. Solar, geomagnetic, seismic activities and 11-year Solar Cycles cause disturbances in the ionospheric region for space based communication, navigation and positioning systems [Karatay et al., 2010; Karatay et al., 2017; Lastovicka, 2009]. Travelling ionospheric disturbances (TIDs) are wave-like perturbations of the ionospheric plasma [Hocke and Schlegel, 1996; Katamzi et al., 2012]. These disturbances are classified in two categories as Medium Scale Travelling Ionospheric Disturbances (MSTIDs) and Large Scale Travelling Ionospheric Disturbances (LSTIDs). MSTIDs have horizontal wavelengths of several hundred kilometers, horizontal velocities of 100–250 m/s, and periods of 15–60 minutes [Fedorenko et al., 2011; Husin et al., 2011]. LSTIDs have durations between 30 minutes and 3 hours and a horizontal wavelength of 1000–4000 km and velocities faster than 300 m/s [Nicolls et al., 2004; Ding et al., 2007]. It is necessary to understand the ionosphere's structure and follow variations in it to understand

how and how much it affects to space based communication, navigation and positioning systems. In theory, ionospheric disturbances are detected using Rate of TEC (RoT) algorithm. In this study, to determine TIDs in the midlatitude region and equatorial region, the Differential Rate of TEC (DRoT) algorithm is developed. DRoT is the normalized metric norm between the RoT and its baseband trend structure. TEC measurements are obtained from Global Positioning System (GPS). for anrk in the Turkish National Permanent GPS Network (TNPGN-Active) and solo and lae1 in International GPS Service (IGS). IONOLAB-TEC method is used for estimating TEC values for those stations [Arikan et al., 2008; Nayir et al., 2007]. Investigating periods are chosen between 01.11.2016-31.12.2016, 09.10.2011-26.10.2011, 16.10.2010 and 03.01.2010-06.01.2010. Between these periods how much disturbances related to geomagnetic and seismic activities on electron density distribution are investigated using DRoT algorithm. The DRoT values are obtained when these activities and no activity are observed.

DATA AND METHODS

In this study, DRoT method is developed for the detection of the ionospheric disturbances. Let $\boldsymbol{v}_{u;d}$ represents the set of TEC data of length M estimated for day of the d of any u receiver:

$$\boldsymbol{v}_{u;d} = \left[v_{u;d}(1) \dots \dots \dots \; v_{u;d}(m) \dots \dots \dots \; v_{u;d}(M)\right]^T \quad (1)$$

Bufffer is added to the start and end of the TEC data. For the day d, last fifty values of (d-1) day are added to start of the day d and first fifty values of the (d+1) day are added to the end of the day d. Buffer added data are shown as $\boldsymbol{x}_{u;d}$ vector. Let $\boldsymbol{x}_{u;d}$ represents the set of buffered TEC data of length M estimated for day of the d of any u receiver:

$$\boldsymbol{x}_{u;d} = \left[x_{u;d}(1) \dots \dots \dots \; x_{u;d}(n) \dots \dots \dots \; x_{u;d}(N)\right]^T \quad (2)$$

where T is the transpose operator. RoT is the time rate of the change of TEC with a time interval. In this study, first, RoT is computed over TEC data as:

$$R_{u;d} = \frac{\left[x_{u;d}(n+1) - x_{u;d}(n)\right]}{150} \quad (3)$$

where 150 is the sampling period for between TEC values in seconds. Then we can obtain a new vector related to Equation 4:

$$\boldsymbol{R}_{u;d} = \left[R_{u;d}(1) \dots \dots \dots \; R_{u;d}(n) \dots \dots \dots \; R_{u;d}(N)\right]^T \quad (4)$$

Here, ROT, $\boldsymbol{R}_{u;d}$, is units of $\mathrm{TECU/s}$. To remove the sudden amplitude changes due to the structure of ionosphere, the moving median filter for 5 is applied to $\boldsymbol{R}_{u;d}$ for obtaining $\boldsymbol{Y}$.

$$\boldsymbol{Y}_{u;d} = medfilt(\boldsymbol{R}_{u;d}, 5) \quad (5)$$

To estimate the linear trend structure $\widehat{\boldsymbol{Y}}$, the moving median filter for 101 is applied to $\boldsymbol{Y}$.

$$\widehat{\boldsymbol{Y}}_{u;d} = medfilt(\boldsymbol{Y}_{u;d}, 101) \quad (6)$$

Using Equations (5) and (6), difference vector $\boldsymbol{D}_{u;d}$ is obtained as follow:

$$\boldsymbol{D}_{u;d} = \boldsymbol{Y}_{u;d} - \widehat{\boldsymbol{Y}}_{u;d} \quad (7)$$

Finally, DRoT can be defined as the normalized metric norm between the RoT and its difference vector $\boldsymbol{D}_{u;d}$:

$$DRoT_{u;d} = \frac{\sqrt{\sum_{n=51}^{N-50}(D_{u;d}(n))^2}}{\sqrt{\sum_{n=51}^{N-50}(Y_{u;d}(n))^2}} \; x\,100 \qquad (8)$$

APPLICATION AND RESULTS

In this study, the effect of geomagnetic and seismic activities to the ionosphere are investigated for detecting disturbances. Firstly, TEC is obtained for the station lae1 using IONOLAB-TEC algorithm between 09.10.2011-26.10.2011 [www.ionolab.org]. DRoT values for lae1 station between 09.10.2011-26.10.2011 is given in Figure 1. As seen in Figure 1, between 15.10.2011-18.10.2011 and 23.10.2011-26.10.2011, MSTIDs are observed and no disturbances are observed in other days. Minor storm is observed in the ionosphere on 25.10.2011. On that day, max Kp index value is 6 and Ap index value is 26 [ftp://ftp.swpc.noaa.gov/pub/indices/old_indices/]. DRoT value is 61.47% so MSTIDs are observed on that day.

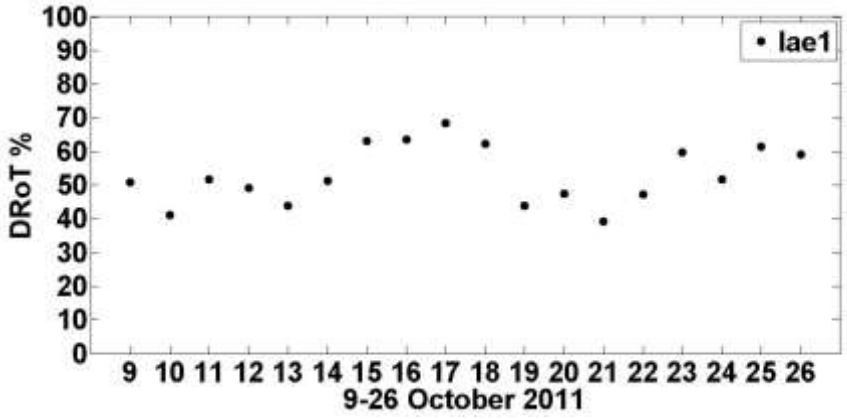

Figure 1. DRoT values for lae1 station between the dates 9-26 October 2011

TEC distribution of 25 October 2011 is given in Figure 2. Disturbances can be seen in Figure 2.

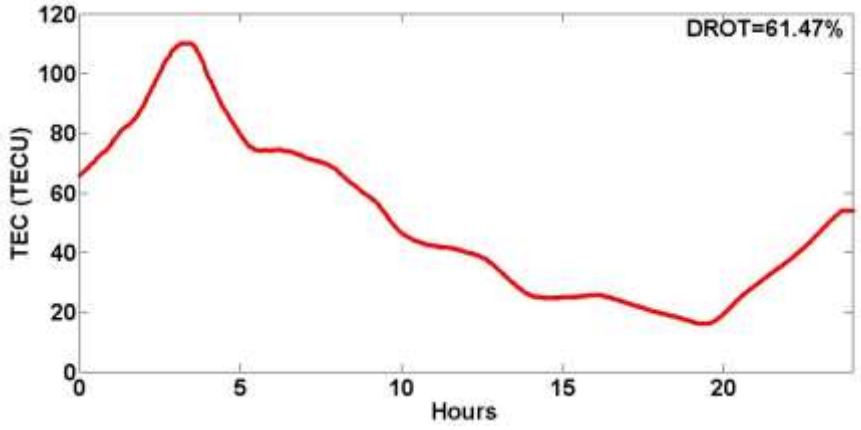

Figure 2. TEC Distribution of 25 October 2011

21 October 2011 is one of the days without disturbance. DRoT value is 39.25% on that day. TEC distribution of 21 October 2011 is given in Figure 3.

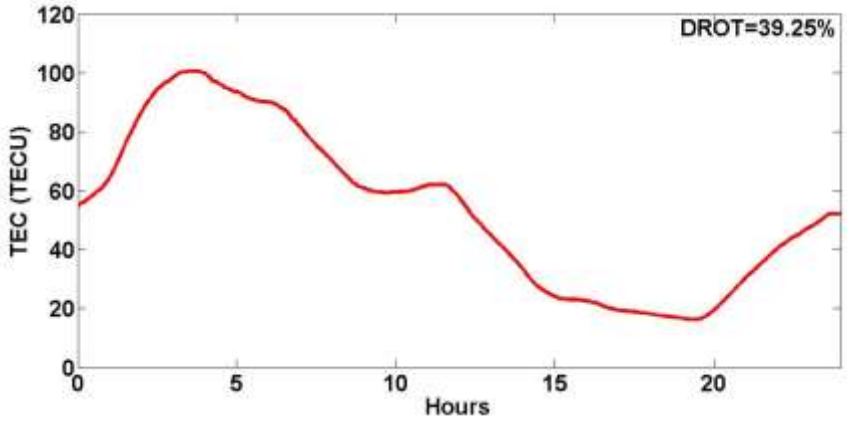

Figure 3. TEC Distribution of 21 October 2011

Secondly, solo station which is located in equatorial region is analyzed between the days 1 November-31 December 2016. DRoT values for solo station between the dates 01.11.2016-31.01.2016 is given in Figure 4. In Figure 4, blue line shows mean value of DRoT values, red line shows standard deviation which is higher than mean and green line shows standard deviation which is lower than mean. Mean value of DRoT's is 51% so it can be said that disturbances are observed all days which are upper than blue line. On 30 November and 8 December, LSTIDs are observed. DRoT values is 73.69% on 8 December. The other disturbances except LSTIDs are MSTIDs. Purple arrow shows earthquake day(9 December) which has magnitude of 8.0, occurred in Solomon Islands. Three days before the eartquake and 2 days after the eartquake, MSTIDs and LSTIDs are observed in the Ionosphere. This situation can be expresssed the effect of seismic activity to the ionosphere.

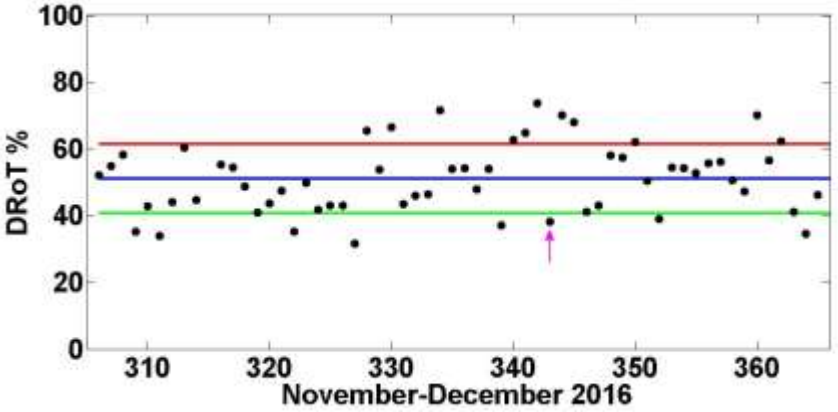

Figure 4. DRoT values for solo station between the dates 1 November-31 December 2016

Finally, anrk station which is located in midlatitude region is analyzed on 16.10.2010 and between the dates 03.01.2010-06.01.2010. TEC distributions and DRoT values for these days are given in Figure 5, Figure 6, Figure 7, Figure 8 and Figure 9. Between the dates 3-6 January 2010, LSTIDs are observed in the ionosphere. DRoT values between the dates 3-6 January are 99.85%, 92.65%, 94.03%, 86.08% respectively. High disturbances is seen in every distribution from 3 January to 6 January. These disturbances are expressed as bite-out effect. Bite-out effect are seen in midlattitude region. 16 October is an example of a day which has no disturbance. The day has a DRoT value which is 34.17%.

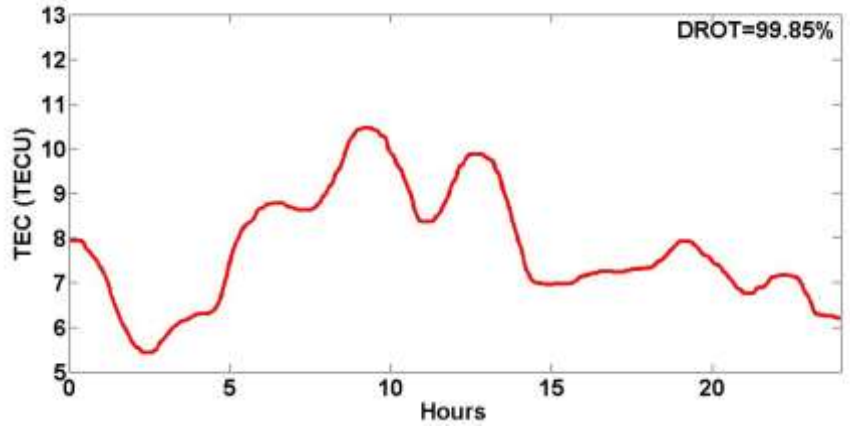

Figure 5. TEC Distribution of 3 January 2010

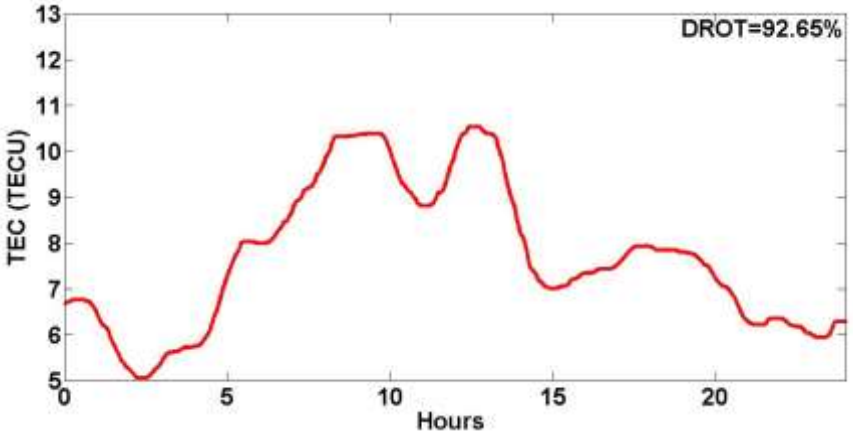

Figure 6. TEC Distribution of 4 January 2010

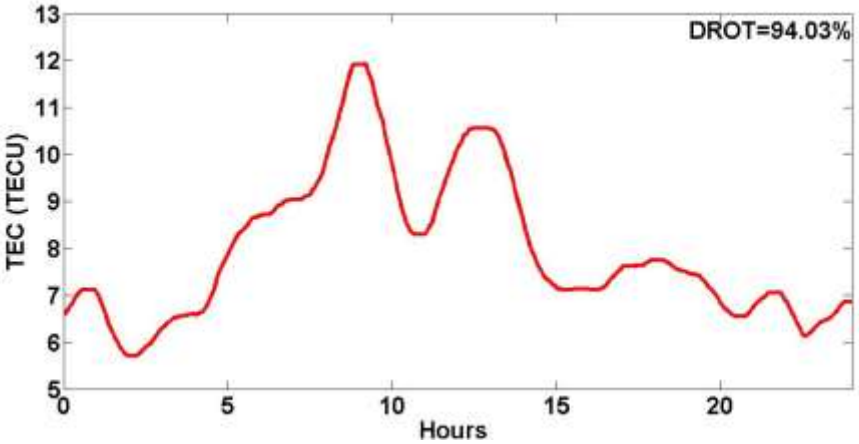

Figure 7. TEC Distribution of 5 January 2010

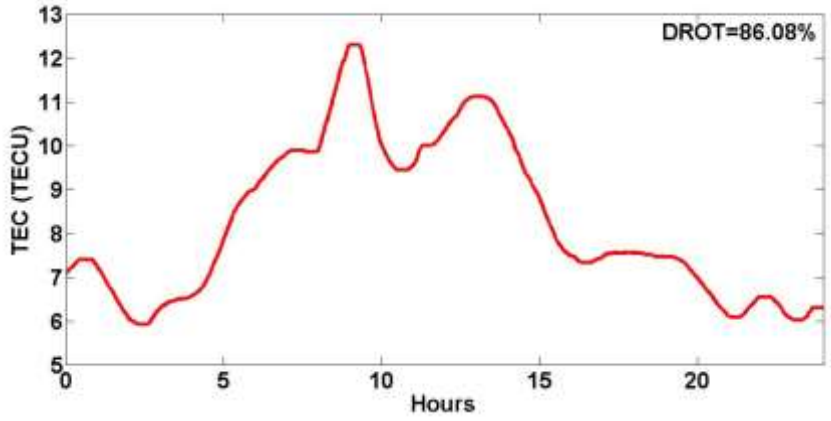

Figure 8. TEC Distribution of 6 January 2010

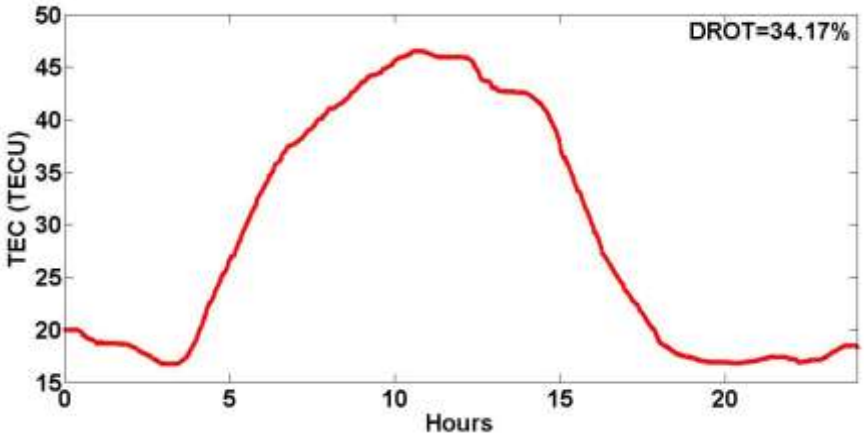

Figure 9. TEC Distribution of 16 October 2010

CONCLUSIONS AND RECOMMENDATIONS

It is seen that DRoT algorithm is a good indicator to detect disturbances or nondisturbances in the ionosphere. DRoT is the normalized metric norm between the RoT and its baseband trend structure. If geomagnetic activity is detected in a day, MSTIDs or LSTIDs are observed. Minor storm as MSTID is successfully detected in lae1 station. When ionosphere is quiet, no disturbances are observed. If seismic activitiy occured in a day, MSTIDs or LSTIDs are observed before and after that day. Disturbances which occurs by seismic activity are successfully detected in solo station. Bite-out effects are also successfully detected. Big depletions are seen in that days, so LSTID's are observed. Finally, if DRoT value is lower than 50%, there are no significant disturbances, if DRoT value is between 50% and 70%, MSTIDs are observed and if DRoT value is higher than 70%, LSTIDs are observed.

REFERENCES

Arikan, F., H. Nayir, U. Sezen and O. Arikan, (2008), Estimation of Single Station Interfrequency Receiver Bias Using GPS-TEC, Radio Science, 43(4), 1-13, doi:10.1029/2007RS003785.

Ding, F., W. Wan, B. Ning and M. Wang, (2007), Large scale traveling ionospheric disturbances observed by GPS total electron content during the magnetic storm of 29–30 October 2003, Journal of Geophysical Research Space Physics, 112(A6), 1-15, doi: 10.1029/2006JA012013.

Fedorenko, Y.P., V.N. Fedorenko and V.N. Lysenko, (2011), Parameters of the medium-scale traveling ionospheric disturbances model deduced from measurements, Geomagnetism and . Aeronomy, 51(1), 88-104, doi:10.1134/S0016793210061015.

Hocke, K. and K. Schlegel, (1996), A review of atmospheric gravity waves and travelling ionospheric disturbances: 1982–1995, Annales Geophysicae, 14(9), 917-940, doi:10.1007/s00585-996-0917-6.

Husin, A., M. Abdullah and M.A. Momani, (2011), Observation of mediumscale traveling ionospheric disturbances over Peninsular Malaysia based on IPP trajectories, Radio Science, 46(2), 1-10, doi:10.1029/2010RS004408.
IONOLAB, www.ionolab.org
Karatay, S., F. Arikan and O. Arikan, (2010), Investigation of TEC variability due to seismic and geomagnetic disturbances in the ionosphere, Radio Science. 45(5), 1-12, doi:10.1029/2009RS004313.
Karatay, S., A. Cinar and F. Arikan, (2017), Ionospheric responses during equinox and solstice periods over Turkey, Advances in Space Research, 60(9), 1958-1967, doi: 10.1016/j.asr.2017.07.038.
Katamzi, Z.T., N.D. Smith, C.N. Mitchell, P. Spalla and M. Materassi, (2012), Statistical analysis of travelling ionospheric disturbances using TEC observations from geostationary satellites, Journal of Atmospheric and Solar-Terrestrial Physics, 74, 64–80, doi:10.1016/j.jastp.2011.10.006.
Kouris S.S., K.V. Polimeris and L.R. Cander, (2005), Specifications of TEC variability, Advances in Space Research, 37(5), 983-1004, doi:10.1016/j.asr.2005.01.102.
Kumluca,A., E. Tulunay and I. Topalli, (1999), November-December 1999 temporal and spatial forecasting of ionospheric critical frequency using neural networks, Radio Science, 34(6), 1497-1506, doi:10.1029/1999RS900070.
Lastovicka, J., (2009), Lower ionosphere response to external forcing: A brief review, Advances in Space Research, 43(2009), 1–14, doi:10.1016/j.asr.2008.10.001.
Nayir, H., F. Arikan, O. Arikan and C.B. Erol, (2007), Total Electron Content estimation with Reg-Est, Journal of Geophysical Research, 112(A11), 1-11, doi:10.1029/2007JA012459.
Nicolls, M.J., M.C. Kelley, A.J. Coster, S.A. Gonzlez and J.J. Makela, (2004), Imaging the structure of a large-scale TID using ISR and TEC data. Geophysical Research Letters, 31(9), 1-4, doi:10.1029/2004GL019797.
NOAA, ftp://ftp.swpc.noaa.gov/pub/indices/old_indices/

ASSESSING THE PERFORMANCE OF ECMWF REANALYSIS DATA IN THE HYDROLOGY OF EAST BLACK SEA REGION

Sead Ahmed Swalih, Ercan Kahya
Istanbul Technical University, Civil Engineering Department, Istanbul, Turkey,
swalih@itu.edu.tr, kahyae@itu.edu.tr

Abstract
In this study, we tested the applicability of one climate reanalysis product to supplement the surface precipitation measurements for basins of small gauge density. We selected a basin in the Black Sea region with below-normal gauge density for the case study. The reanalysis data obtained from the European Centre for Medium-Range Weather Forecasts (ECMWF) was used for our case study and the observed precipitation data was used for control simulation. The accuracy of the data source was tested before its use in our hydrological model (Soil Water Assessment Tool - SWAT). In addition, daily average flow data from three flow gauging stations inside the basin were used to compare the model simulation accuracy. Daily grid satellite based precipitation estimates of ECMWF product were compared to first annual average observed ground rainfall, and second monthly average precipitation in the major river. The SWAT model was setup and simulated with the reanalysis precipitation data of ECMWF. The annual average comparison results show that ECMWF satellite provide an estimate of good quality for precipitation of the basin. Similarly, the seasonal comparison indicated a better performance for ECMWF data in capturing the amount and pattern of precipitation. The model simulation with SWAT using the ECMWF data revealed a good approximation of flow. We can say for poorly gauged basins with good quality reanalysis precipitation data, model simulation outputs could be improved significantly.

***Keywords**: Reanalysis data, ECMWF, Precipitation, SWAT, Hydrologic Modeling*

Introduction
The poor coverage of rain gage hinders drought forecasting for food safety studies and reduces the accuracy of prediction of discharge (both low flows and floods), sediment discharge and nutrient fluxes. Lack of good rainfall estimates could also be the reason, which as noted by Baveye (2013), that hydrologists seem reluctant to deal with pressing and unprecedented societal questions such as food deficits related to water resources. The growing availability of high-resolution satellite rainfall products can help hydrologists to obtain more accurate precipitation data particularly in developing countries and remote locations where weather radars are absent and conventional rain gauges are sparse (Worqlul, et al., 2014). Reanalysis precipitation data products have become powerful tools to supplement the surface based rainfall data. Some of the freely available spatially distributed Reanalysis precipitation data include, the European Centre for Medium-Range Weather Forecasts (ECMWF) (Balsamo, et al., 2015), Climate Forecast System Reanalysis (CFSR) (NCEP, 2015), Multi-Sensor Precipitation Estimate-Geostationary (MPEG), Tropical Rainfall Measuring Mission (TRMM), the NOAA/Climate Prediction Centre morphing technique (CMORPH), the Naval Research Laboratory's blended product (NRLB), Asian Precipitation - Highly-Resolved Observational Data Integration Towards Evaluation of Water Resources (APHRODITE) (Yatagai, et al., 2012) and many more. Recently, the use of these Reanalysis precipitation data for climate and hydrological modelling analysis has been increasing by researchers and experts. After analyzing three reanalysis weather data (including ECMWF) by forcing hydrological models over 460 Canadian and 370 USA basins, it was found that reanalysis data can successfully compensate for deficiencies in the surface observation record and provide significantly better hydrological modelling performance (Essou, 2016). Richard, in 2012

compared the two global Reanalysis data (ECMWF-ERA40 and NCEP-NDRa2) and found significant disagreements between these products in regions of large-scale higher topography (Richard, 2008). In addition, Manzato, 2015, studied the comparison of ECMWF reanalysis data with 104 gauging stations data in Italy; and found out that ECMWF always underestimates the precipitation significantly. The BIAS and RMSE outputs were worse even for the most homogeneous areas of Italy (Manzato, 2015). All of them focus on the comparison of gridded satellite rainfall estimation to a surface rainfall observation data. This study of ours validates the European Centre for Medium-Range Weather Forecast (ECMWF – Interim/Land) data using surface rainfall stations and flow data in the Rize province. As first step, the annual as well as seasonal performance of the data will be visually be compared. Then by making use of a calibrated SWAT model, the performance of the forecasted precipitation data on the hydrology of the basin will be assessed. Rize province is selected since the basin has been frequently affected by flood during the high flow season and the availability of long year daily rainfall data for few stations in the basin. The ECMWF- ERA Interim/Land reanalysis product was selected for its state of the art algorithm, wide use and free availability. In addition, the product has a relatively high spatial/temporal resolution and global coverage.

Study Area and Data

Study Area

The Rize province is located in the North-Eastern part of the Anatolian mainland called "Doğu Karadeniz Bölgesi" in Turkish or "the Eastern- Black sea region", Turkey, with an area coverage of 3920 sq.km, average yearly precipitation of 2250.5 mm and yearly total runoff of 2745 million m^3 (Kahya, et al., 2015). The Black Sea boarders the province on the Northern side. It is a mountainous region with heights reaching more than 3000amsl. The study area, Ikizdere basin, is located in the North-Eastern side of the Rize province (Fig.1).

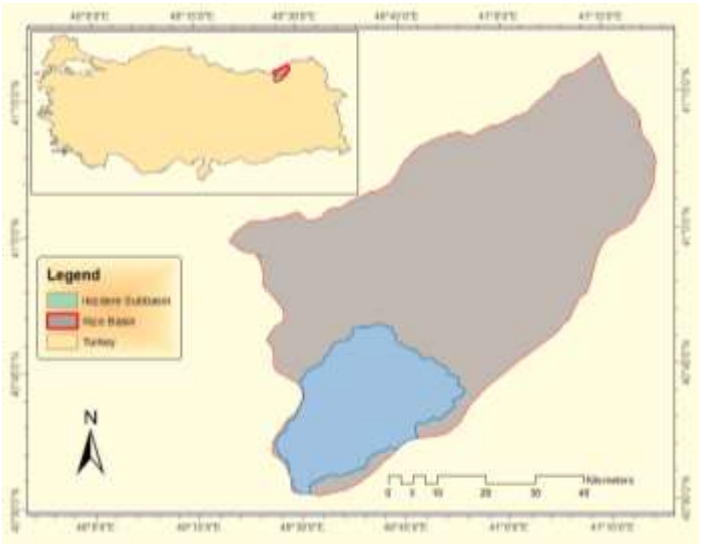

Figure 38. The Rize Province and the study area - Ikizdere sbasin, Turkey.

Stations Location

The predicted satellite rainfall estimate and observed gauged rainfall data have different spatial and temporal scales. The ground observation consists of a 14 daily observations of point rainfall amounts irregularly distributed across the Rize Province (Figure 2). The measured flow data at the outlet of the basin (Camlıkdere) was employed as the check for the simulation accuracy using the Reanalysis data. The location of observed MGM precipitation stations and ECMWF-ERA estimation grids is presented in figure 2.

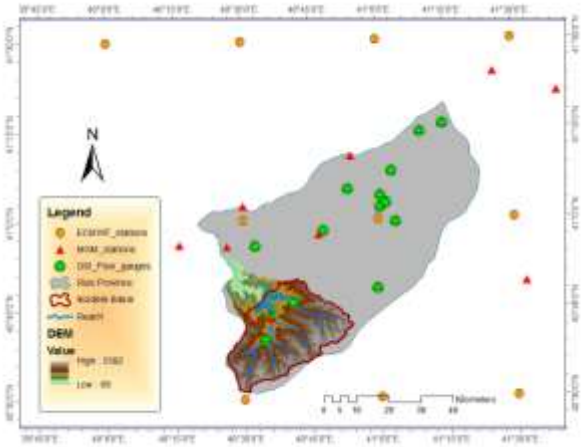

Figure 39. Ground rainfall and River flow observation stations for the Rize basin.

Data

Two precipitation data series were used for this study the impact of reanalysis data on the hydrology. The observed precipitation data was obtained from the Turkish Meteorological Directorate (MGM) (TÜMAS, 2015). Whereas the reanalysis precipitation product was downloaded from the European Centre for Medium-Range Weather Forecasts (ECMWF – ERA Interim/Land) (Balsamo, et al., 2012). In addition, daily flow data for the Camlıkdere gauging station of DSI (Ikizdere) was received from the Turkish General Directorate of State Hydraulic Works (DSI) for model simulation calibration and comparisons.

Methodology

The flow chart below depicts the general procedures flowed in this study. All the input data of SWAT was prepared before the model setup using the ArcGIS-10.1 geographical analysis tool. The SWAT model was also setup using the ArcGIS version of SWAT. The model was run with the MGM precipitation data and calibrated with the flow data obtained from DSI. Then the reanalysis precipitation data were used to force our hydrological model in place of the observed data. Then the reanalysis data forced simulation flows were analyzed to assess the degree of similarity with the observed flow at the basin outlet.

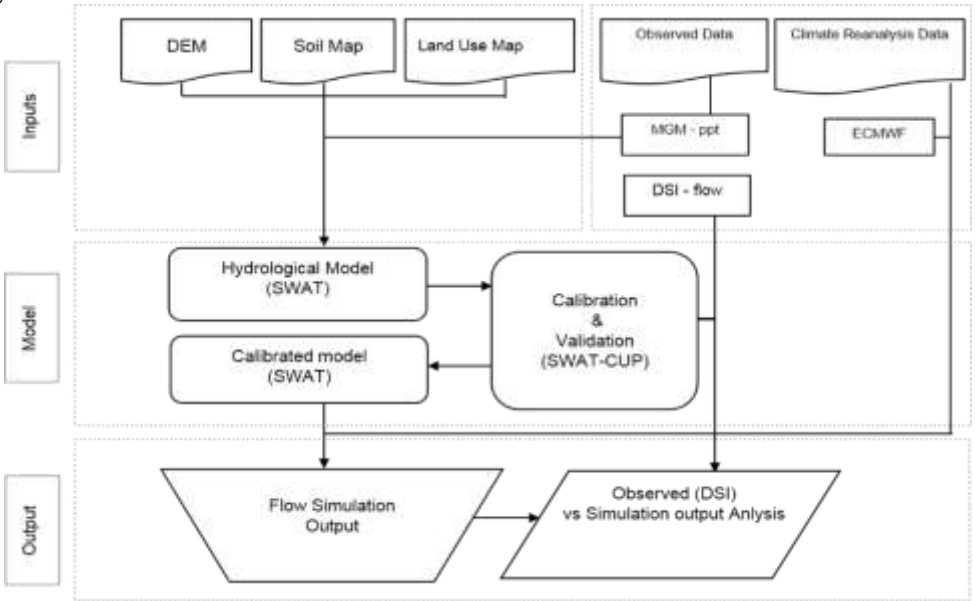

Figure 40. Flow Chart of the input–output setup and integration of the reanalysis data with SWAT.

Statistical Methods

Four statistical measures were used to compare the satellite rainfall estimates with the ground rainfall observations consisting of i. Nasch Sutcliff Efficiency (NS), ii. the Coefficient of Determination (R^2) iii. RMSE-observations standard deviation ratio (RSR) and iv. Percentage Bias (PBİAS). Nasch Sutcliff Efficiency (NS): is used to assess the degree of fitness exhibited by the satellite data with that of the observational data. Nasch Sutcliff Efficiency (NS) is the expression of the closeness of a value with the observed value. The Coefficient of Determination (*R*-Squared): is used to evaluate the goodness of fit of the relation. *R*-Square address the question on how well the satellite rainfall estimates correspond to the ground rainfall observations, it is the degree of linear association between the two terms. Root Mean Square Error (RMSE) measures the difference between the distributions of the ground observed rainfall and the distribution of satellite rainfall estimation and calculates a weighted average error, weighted according to the square of the error. RMSE is useful when large errors are undesirable. The lower the RMSE score, the closer the satellite rainfall estimation represents the observed ground rainfall measurement. RSR standardizes RMSE using the observations standard deviation, and it combines both an error index and the additional information (Moriasi, et al., 2007). RSR is calculated as the ratio of the RMSE and standard deviation of measured data. Percent bias (PBIAS) measures the average tendency of the simulated data to be larger or smaller than their observed counterparts (Moriasi, et al., 2007). The optimal value of PBIAS is 0.0, with low-magnitude values indicating accurate model simulation. In 2007, Moriasi recommended three quantitative statistics, Nash-Sutcliffe efficiency (NSE), percent bias (PBIAS), and ratio of the root mean square error to the standard deviation of measured data (RSR), and in addition, the graphical techniques were recommended be used in the model evaluation. In addition, he established the following model evaluation performance criteria for each of recommended statistics. He stated model simulations to be judged as satisfactory if NSE > 0.50 and RSR < 0.70, and if PBIAS < 25% for streamflow analysis and PBIAS < 55% for sediment transport modelling.

Results and Discussion

Model Performance

The SWAT model developed for the Ikizdere baisn was used extensively in this report. It is mainly due to the fact that the previous work on the Rize basin (Kahya, et al., 2015) had recommended to check the other basins for better modelling performance due to the difficulty faced in modelling the Kaptanpaşa basin with good model performance. Ikizdere basin has been successfully modelled with good model performance and proved to be used for scenario analysis. Before employing the model for our analysis, the model performance was tested for uncertainty and accuracy. Four statistical parameters NS, R2, RSR and PBIAS were calculated and presented on the table below. According to Moriasi, 2007, model simulation can be judged as satisfactory if NS > 0.50 and RSR < 0.70, and if PBIAS < ± 25% for streamflow analysis. Since our model performance parameters are in the recommended ranges, the model can be accepted and used for our analysis (see table below).

Table 13. Statistical Model Performance Indicators for the SWAT Model.

Statistic parameter	**Calibration**	**Validation**
NS	**0.72**	**0.69**
R2	0.74	0.75
RSR	**0.53**	**0.56**
PBIAS	**10.7**	**22.7**

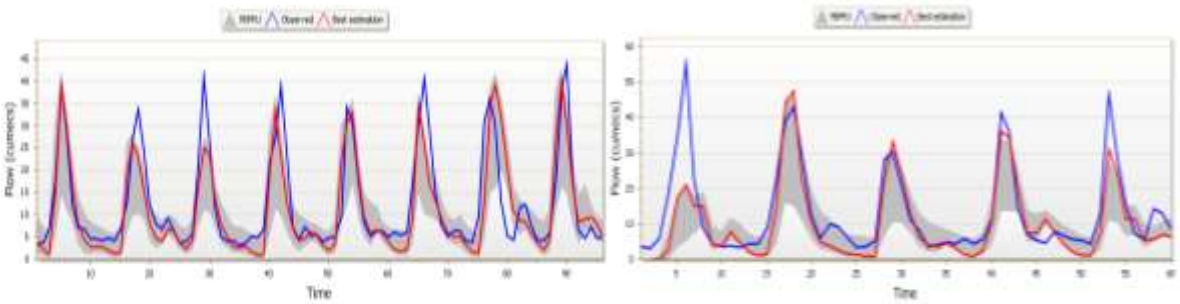

Figure 41. SWAT model best simulation represented by red line after calibration (left) and validation (right) compared with the observed flow represented by blue line at Camlıkderesi, Ikizdere subbasin.

The MGM Observed Precipitation Data

The seasonal precipitation distribution for selected gauging stations in Rize province depicted in figure 5 & 6. The results are in agreement with what was reported by Sensoy, 2008. He discussed the mountain influence on the precipitation distribution of the country. Due to the Taurus Mountains along the coastal areas, the rain clouds cannot penetrated into the interior parts of Turkey. That means, the majority of precipitation falls on the coastal regions making Rize province the most humid coastal regions of the country. These values are also in agreement with the reports of Şen, 2013, where the annual precipitation was reported to be above 1500mm for the majority of Rize province (fig. 5&6).

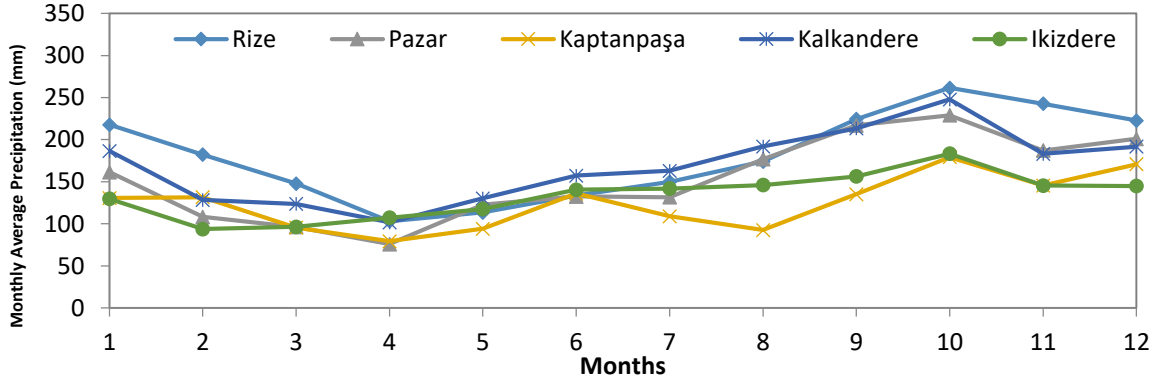

Figure 42. Average monthly precipitation values of selected MGM stations.

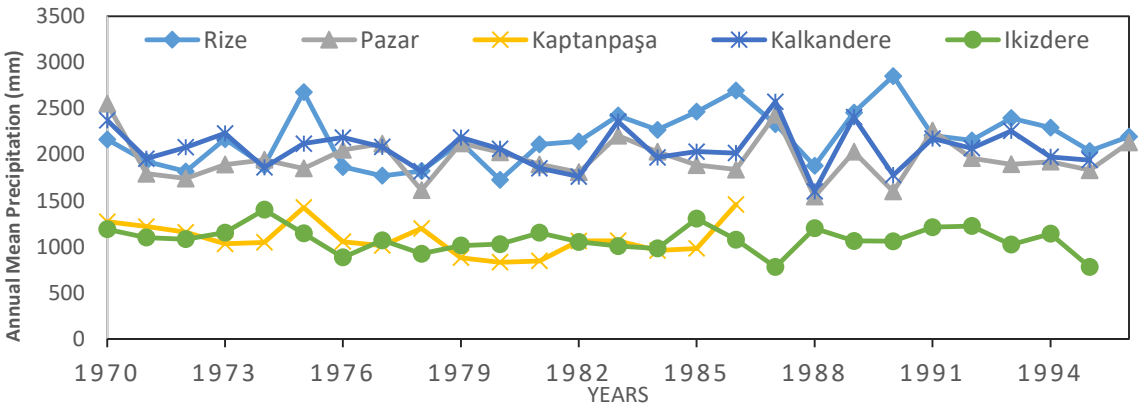

Figure 43. Yearly total precipitation values of selected MGM stations.

The figures above present the seasonal as well as yearly total precipitation of some selected gauging stations in the Rize basin. The seasonal distribution is more or less similar for the various stations. The precipitation peaks in October for all the stations but the values are higher

for the coastal regions (Rize and Pazar) than for those in the mountainous regions (Kaptanpaşa and Ikizdere). The same is true for the winter snow fall. The yearly average values are visibly higher for the coastal stations (Rize & Pazar) compared with the stations found in the mountainous regions (Ikizdere).

European Centre for Medium-Range Weather Forecasts (ECMWF) data

European Centre for Medium-Range Weather Forecasts (ECMWF) periodically uses its forecast models and data assimilation systems to 'reanalyse' archived observations, creating global data sets describing the recent history of the atmosphere, land surface, and oceans (Balsamo, et al., 2015). ERA-Interim/Land is a global reanalysis of land-surface parameters from 1979-2010 at 80 km spatial resolution. It was produced with a recent version of the HTESSEL land-surface model using atmospheric forcing from ERA-Interim, with precipitation adjustments based on GPCP v2.1 (Balsamo, et al., 2015)**.** The seasonal average as well as yearly total precipitation analysis of the grids in the Rize province (see figures below) exhibit a similarity with the MGM measurements except with underestimation for the peak flows in the autumn season and seasonal variability (figure 14).

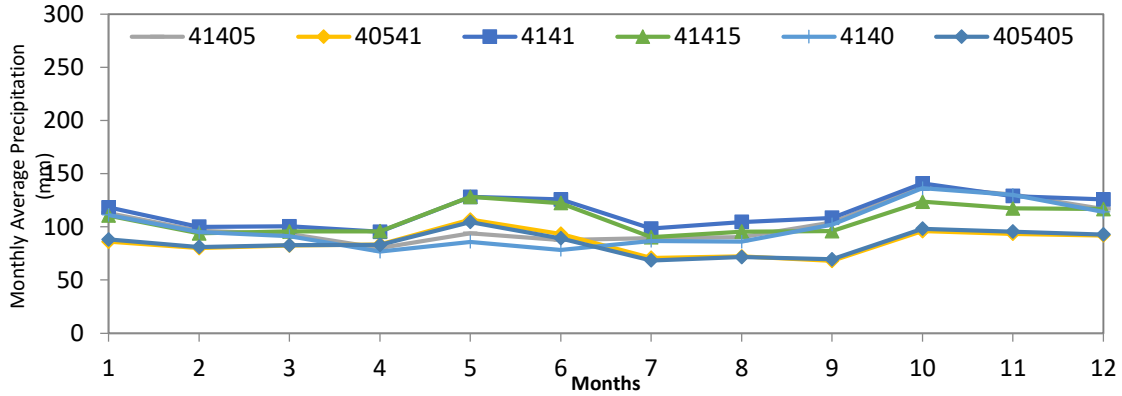

Figure 44. Plot of monthly average precipitation data (ECMWF).

There is no visible significant yearly precipitation trend change along the years for all the selected grid stations in contrary to the observed (MGM) (see the figure below).

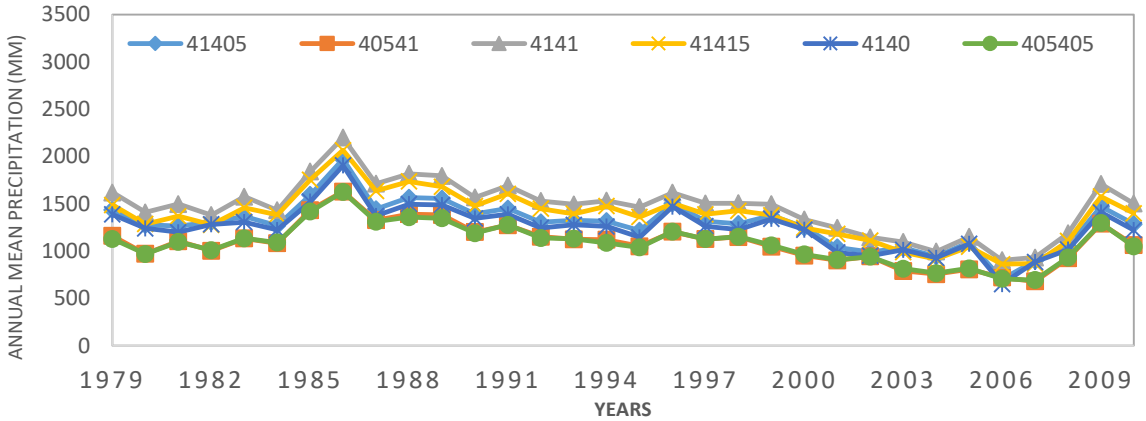

Figure 45. Total yearly precipitation for selected ECMWF grid locations.

The plot below illustrates the comparison of monthly average precipitation forecasts of ECMWF compared with the measured MGM values. Generally the ECMWF slightly overestimates the rainfall for summer and winter seasons. Especially, the overestimation for the summer season is significantly visible.

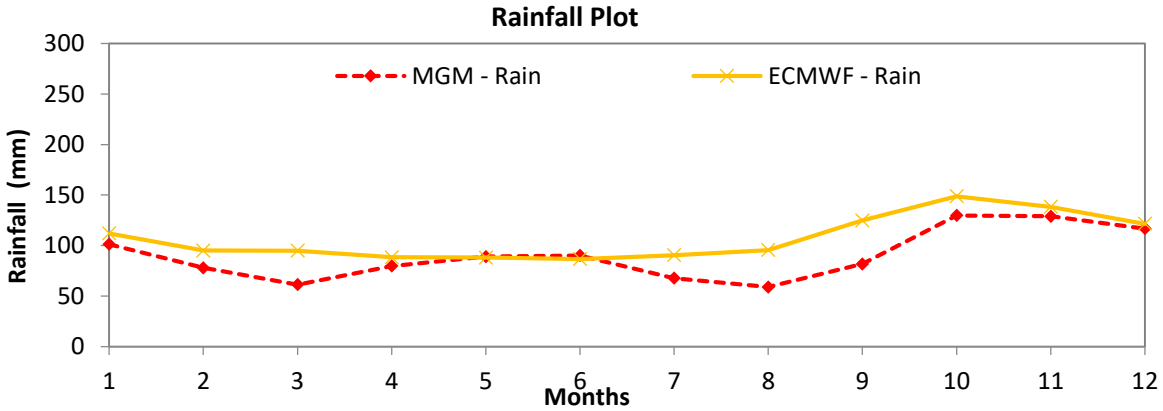

Figure 46. Comparison of ECMWF precipitation with the observed values.

Seasonal Analysis

The figure below is the normalized depiction of the total water yield (observed as well as simulated) for the Ikizdere Basin. The simulated flows resulted after employing the precipitation input data of MGM, and ECMWF reanalysis data to the validated SWAT model. The figure below summarizes the seasonal water yield as simulated by SWAT model using different precipitation inputs. The average monthly water yield plots in the figure below were analyzed from the flow series at the Camlıkdere gauging station, the SWAT simulations with the MGM, as well as ECMWF precipitation data. From the plots, we can observe that the seasonal flow values are quite similar except for the flows after May. The simulations with the observed precipitation data slightly under estimates the flows thought the summer season. ECMWF estimated the flow in the same period far better than MGM except for the autumn season where the flows were slightly overestimated.

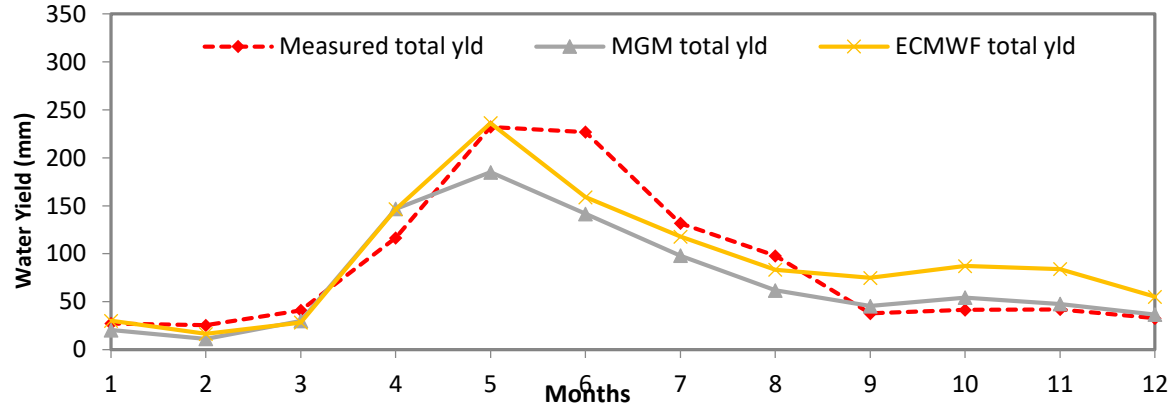

Figure 47. The monthly water yield for the actual measured flow vs simulated MGM & ECMWF simulations.

Components of hydrology as simulated by MGM data

For this simulation the precipitation data of MGM was used. Precipitation is dominated by snowfall in the first three months which can witnessed by low water yield for the same period. Then the water yield drastically increases up until May due to snow melt. Then the water yield starts to decrease with a constant rate until the end of summer. The precipitation reaches its peak in the moths of Oct-Nov but the majority falls as snow fall. The snow cover reaches its peak on January and then continuously melts increasing the river flow from February onwards up until its peak in May. Then the flow decreases slowly until the end of the year. The average CN was 69.3.

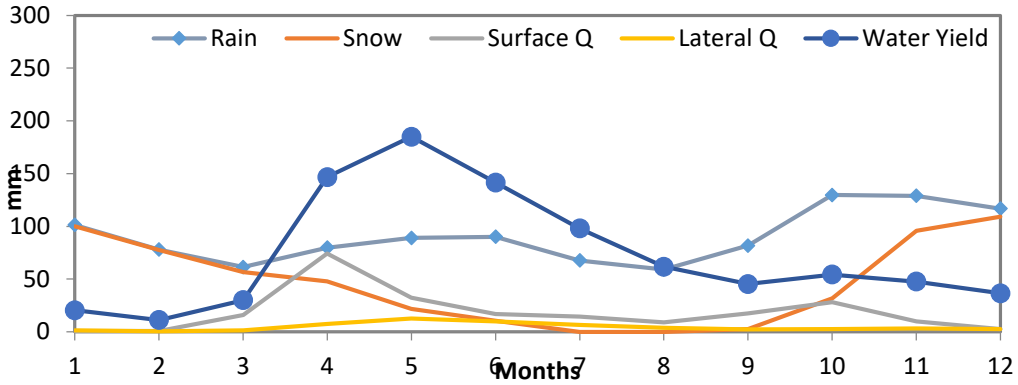

Figure 48. Average Monthly flow of the SWAT simulation with MGM precipitation data.

Components of hydrology as simulated by ECMWF data

In this case, ECMWF forecast precipitation data has been used in the SWAT model. It is obvious that the model has responded similar with the MGM simulation. The precipitation peaks in the October. The snow fall and snow melt trends are similar with the MGM case for the obvious reason that the precipitation distribution and temperature data are quite similar for both cases. The surface flow peaks in April and October as in the MGM case. The only exception is the peak water yield on the month of May where it is a little overestimated by the ECMWF simulation. So it can be deduced from the results that ECMWF has captured the hydrology of the basin satisfactorily.

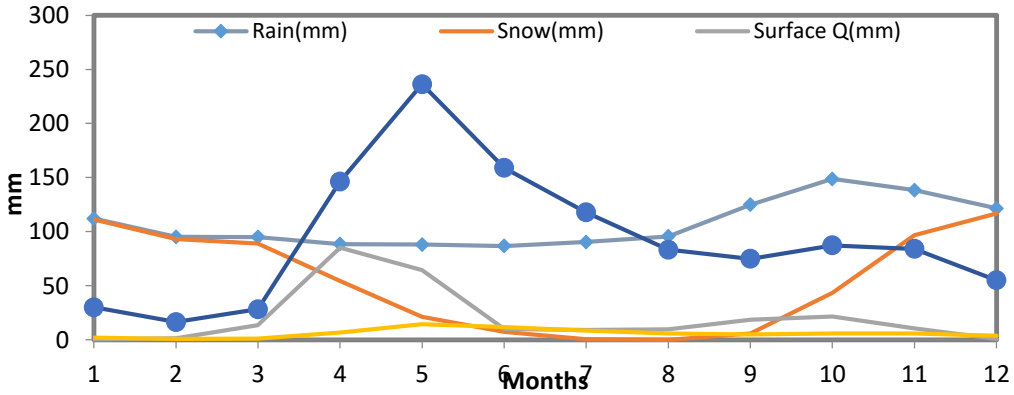

Figure 49. Average Monthly Basin Values for the SWAT simulation with the ECMWF data.

The table below demonstrated the overall similarity amongst the simulation of SWAT using the observed and ECMWF precipitation data with that of the measured flow at the out let of the basin (i.e. Camlıkderesi).

Table 14. Statistics of comparison amongst the various flow simulations with the observed flow.

	Camlıkderesi (measured)	MGM (simulation)	ECMWF (simulation)
Mean	13.32	11.65	14.90
St.Dev	12.09	9.34	11.03
Min	3.27	1.09	1.30
Max	56.92	45.23	53.74

The table below gives the evaluation of the model simulations (see section 3.2. for recommended values of each statistical indices). Both the simulations with MGM as well as ECMWF were compared with the observed flow data to get the values below. We can see a satisfactory model performance with the ECMWF data.

Table 15. Model performance evaluation for the study area

	MGM	ECMWF
NS	**0.6**	**0.5**
R^2	0.76	0.69
RSR	0.64	0.64
PBIAS	6.2	19.9

Temporal Model Performance

After conducting the global water balance and seasonal analysis for the simulations, the performance of the simulations at the temporal scale were analyzed (see the figures below). The overall simulation with the ECMWF data showed good performance. The simulation with the MGM data gives good estimation of the temporal flow except for the peak flows. SWAT model has generally been proven to have low performance in estimating the peak flows.

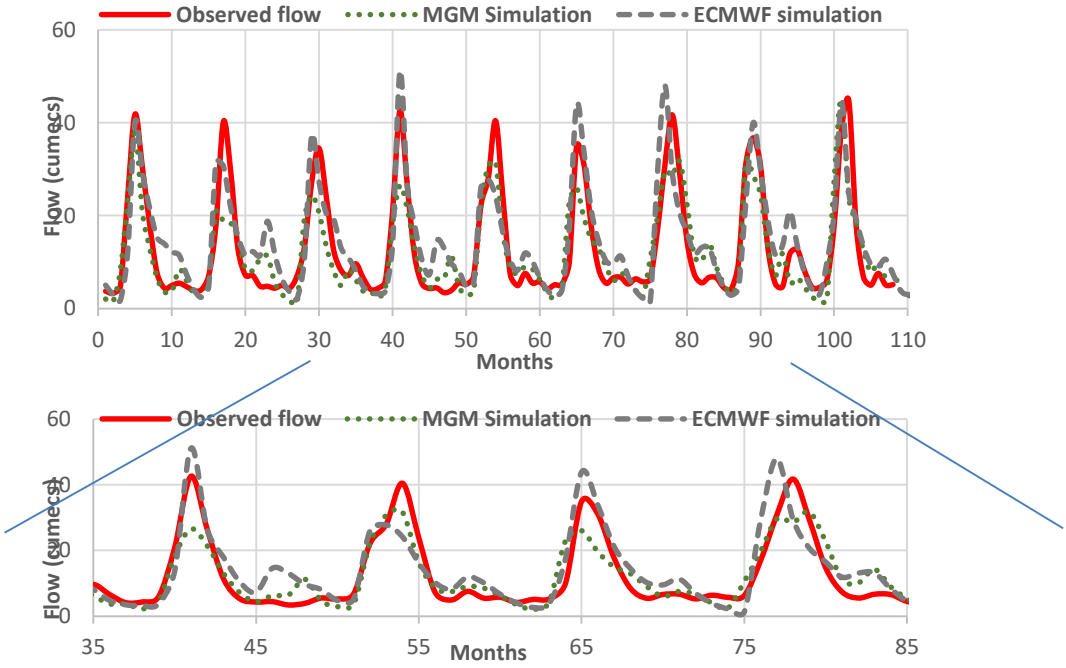

Figure 50. Comparision of the SWAT simulations with the observed flow data at Camlıkdere station.

On the other hand, the MGM and ECMWF precipitation data can be observed to have a satisfactory simulation outcome that are comparable with the observed flow data. It obvious that both MGM and ECMWF have a satisfactory performance. The figures below are plots of some components of the water regime as simulated by the model using the various precipitation data.

Conclusion

Reliable and accurate weather data is essential for the proper water resources management and its application in the various fields like agriculture, disaster management (flood and drought)

and sediment (as well as nutrient) transport studies. Regions with limited weather gauging stations are difficult to study arising the need for alternate data sources to augment the data scarcity. Satellite weather reanalysis data are good alternative data sources that could solve this particular problem. In this study, the European Centre for Medium-Range Weather Forecasts (ECMWF) climate reanalysis data was used. In addition, the historical weather data was accessed from the Turkish Meteorological Directorate (MGM) for control simulation observed flow data from the Turkish General Directorate of State Hydraulic Works (DSI). The Rize province, was selected as it is one of regions in the Black Sea most frequently affected by floods. The SWAT model was setup for Ikizdere basin of Rize province with a total area of 731.4 sq.km. The physically based hydrological model (SWAT) of the study area was set-up, calibrated and validated before employing to assess the quality of the climate reanalysis data. After model calibration, it was run with all the ECMWF precipitation data and compared with the simulation of MGM precipitation data. They were then assessed with the observed flow record at the outlet of the Camlıkderesi River. The simulation flow outputs of both MGM and ECMWF were first assessed for the global water balance. Then the simulations seasonal performance was compared. Finally the temporal model performance was assessed. All model simulation runs gave a good estimate of the global water balance. The ECMWF flow simulations has shown good agreement with the observed flows as well as MGM simulation flow. Models for other basins in the Rize province and the region need to be checked before generalizing that ECMWF reanalysis data is appropriate to be used for the Black Sea region.

Acknowledgements
We would like to acknowledge TUBİTAK (the Turkish Scientific and Technological Research Council) for providing the fund to accomplish this study. We are also indebted to the Turkish State Meteorological Service (MGM) and General Directorate of Hydraulic Works (DSI) for the observed weather and flow data access.

References

Balsamo, G., Albergel, C., Beljaars, A., Boussetta, S., Brun, E., Cloke, A., . . .Vitart, F. (2012). Shinfield Park, Reading, Berkshire RG2 9AX, England: ERA - Interim/Land : Global Land Surfae Reanalysis based on ERA - Interim meteorological forcing: ERA Report Series; European Centre for Medium Range Weather Forecasts.

Baveye, P. C. (2013). Hydrology and the looming water crisis: it is time to think, and act, outside the box. Journal of Hydrology and Hydromechanics, 89–96.

Essou, G. B.-P. (2016). Impacts of combining reanalyses and weather station data on the accuracy of discharge modelling. Journal of Hydrology, 120–131.

Kahya, E., Özger, M., Şeker, D. Z., Karaca, M., Can, İ., KÖMÜŞCÜ, A. Ü., . . . BAGHERI, F. (2015). Rize İl Sınırlarında Bulunan Su Havzalarının Taşkın Risk Tayini: İklim ve Hidrolojik Modellere Göre Mevcut ve Gelecekteki Durum. Istanbul: TÜBİTAK.

Richard, G. (2008). A comparison of selected fields in NCEP/DOE AMIP-II and ECMWF ERA-40 reanalyses . Journal of Dynamics of Atmospheres and Oceans, 108–142.

Manzato, A. A. (2015). 6-hour maximum rain in Friuli Venezia Giulia: Climatology and ECMWF-based forecasts. Journal of Atmospheric Research, 465–484.

Moriasi, D. N., Arnold, J. G., Liew, M. W., Bingner, R. L., Harmel, R. D., & Veith, T. L. (2007). MODEL EVALUATION GUIDELINES FOR SYSTEMATIC QUANTIFICATION OF ACCURACY IN WATERSHED SIMULATIONS. American Society of Agricultural and Biological Engineers, 50(3): 885−900.

Şen, Ö. L. (2013). A HOLISTIC VIEW OF CLIMATE CHANGE AND ITS IMPACTS IN TURKEY. Istanbul: Istanbul Policy Center (IPC), Sabancı University.

Sensoy, S. D. (2008). Climate of Turkey. Ankara, Turkey: Turkish State Meteorological Service,.

Worqlul, W., Maathuis, B., Adem, A., Demissie, S., Langan, S., & Steenhuis, a. S. (2014). Comparison of TRMM, MPEG and CFSR rainfall estimation with the ground observed data for the Lake Tana Basin. Hydrological Earth Syst. Sci., 11, 8013–8038.

Yatagai, A., Kamiguchi, K., Arakawa, O., Hamada, A., Yasutomi, N., & Kitoh, A. (2012). Constructing a Long-Term Daily Gridded Precipitation Dataset for Asia Based on a Dense Network of Rain Gauges. American Meteorological Society, 1401-1415.

HYDROCHEMICAL ASSESSMENT OF GROUNDWATER QUALITY FOR IRRIGATION: A CASE STUDY OF THE ZILAN AND BENDIMAHI RIVER BASINS IN VAN, TURKEY

Hacer DÜZEN

Istanbul University, Engineering Faculty, Department of Geological Engineering, 34320, Avcılar, İstanbul – Turkey, hcrduzen@gmail.com

Abstract

In order to characterize, classify and evaluate the suitability of groundwaters for irrigation in Zilan and Bendimahi basins hydrochemical assessment was conducted. In this paper, hydrographical methods were used to characterize water quality of groundwaters in Zilan and Bendimahi basins. Water chemical composition was studied by collecting 36 groundwater samples (6 samples in Zilan basin and 30 samples in Bendimahi basin). In content of this paper, % Na, sodium adsorbsion ratio (SAR), residual sodium carbonate (RSC), permeable index (PI), Kelly ratio, magnesium hazard (MH) and boron concentration were investigated. The quality assessment of Zilan basin for irrigation purposes showed that ''Very well – Well'' usable waters in terms of sodium percentage (% Na), they are in ''low sodium hazard and low salinity hazard'' region in terms of sodium adsorbsion ratio (SAR) and in C1S1 water class. Waters in Zilan basin have under the 2.5 meq/l in terms of carbonate and bicarbonate hazard RSC (residual sodium carbonate) and it shows that they are suitable for irrigation. 66 percent of waters in Zilan basin is in Class I and it is suitable for irrigation according to permeable index (PI), usable for irrigation according to Kelly ratio and it is suitable in terms of magnesium hazard (MH) because of MH values are lower than 50 for a lot of samples. The quality assessment of Bendimahi basin for irrigation purposes showed that waters are ''Very well – Well'' and ''Well-Usable'' water class in terms of sodium percentage (% Na), they are in ''low sodium hazard and low salinity hazard'' region in terms of sodium adsorbsion ratio (SAR) and in C1S1 water class. Much water in Bendimahi basin have under the 2.5 meq/l in terms of carbonate and bicarbonate hazard RSC (residual sodium carbonate) and it shows that they are suitable for irrigation. 90 percent of waters in Bendimahi basin is in Class I and it is suitable for irrigation according to permeable index (PI), usable for irrigation according to Kelly ratio and it is suitable in terms of magnesium hazard (MH) because of MH values are lower than 50 for a lot of samples (percent of 70). Various irrigation indices show good to permissible use of groundwater in agricultural activities.

Keywords: *Irrigation, water quality, hydrochemical assessment, Zilan and Bendimahi.*

Introduction

Each passing day, people need more water resorces especially for drinking and irrigation. To meet the growing demand of water for domestic, industrial and agriculture sector, exploration of alternative source of water especially for use in agriculture is important. So, irrigation water quality must be examined carefully. Moreover, the crop productivity is associated with the quality of soil and the quality of the water available for irrigation. Normally, investigation of irrigation water quality should focus on salt content, sodium concentration, the occurence of nutrients and trace elements, alkalinity, acidity, and hardness of the water. Water quality for agricultural purposes is determined on the basis of the effect of water on the quality and yield of the crops, as well as the effect on soil characteristics (Ayers and Westcot 1985). Quality of irrigation water is determined by its chemical composition and the conditions of use.

The main objective of this paper is to characterize water quality of groundwaters in Zilan and Bendimahi basins. In this study, % Na, sodium adsorbsion ratio (SAR), residual sodium carbonate (RSC), permeable index (PI), Kelly ratio, magnesium hazard (MH) and boron concentration were investigated in Zilan and Bendimahi basins. Also, electrical conductivity (EC), SAR and RSC were evaluated together for determining the salinity. Moreover, total dissolved solids (TDS), SAR, RSC and boron concentrations were evaluated together for purpose of determine water classes.

Study area

The study area has been located in eastern part of the Turkey, in Zilan basin and Muradiye – Çaldıran basin bounded by latitudes 38º 49'- 39º 24'N and longitudes 42º 59'- 43º 05'E (Fig. 1). Zilan and Bendimahi river basins' drainage areas are 1227 and 1887 km^2, respectively. In Zilan basin, mean precipitation for 53 years (between 1960 and 2012) is 659.51 x 10^6 m^3 and in Bendimahi basin mean precipitation for 53 years is 849.15 x 10^6 m^3. The summer temperature touches 20 – 25 ºC and winter temperatures ranges around -8 – +5 ºC.

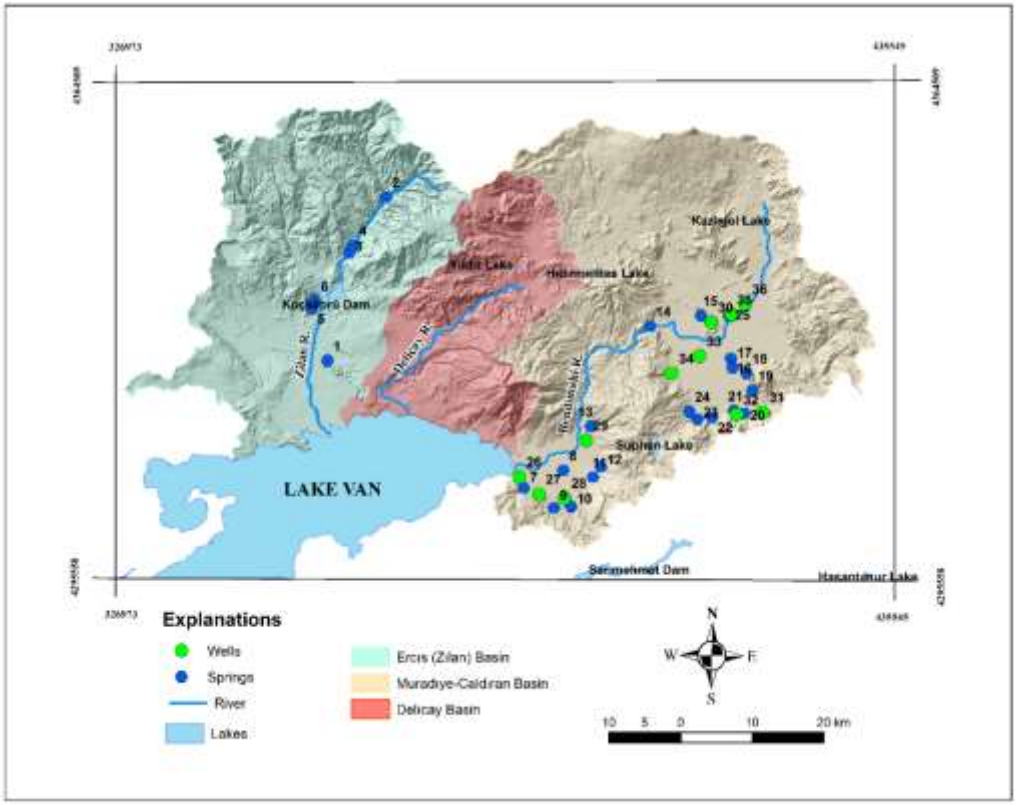

Figure 1. Location and sampling points map of study area.

Material and Methods

To understand the water quality of the study area, field works, laboratory analysis and data treatment carried out. Water chemical composition was studied by collecting 36 groundwater samples (6 samples in Zilan basin and 30 samples in Bendimahi basin) (Fig. 1). General parameters such as pH, EC and TDS were measured immediately at the time of sampling using a multi parameter ion meter. The physicochemical parameters were determined using the standard analytical methods (APHA 2005).

Also, the analytical precision for the accurate measurements of ions was determined by calculating electrical neutrality (EN %) which is acceptable at ±5 % (Appelo and Postma 1999). All the samples have EN % values within ±5 %.

Electrical Neutrality = ((Σ Cation + Σ Anion) / (Σ Cation - Σ Anion)) x 100

Study area, geological map and spatial distribution maps of parameters were prepared with the help of GIS based computer programmes.

Results and Discussion

Cation and Anion Chemistry

Among major analysed cationic concentrations (mg/l) in Zilan basin there are calcium (in 5 samples) and magnesium (in 1 sample) ions dominantly. Calcium is the dominating ion ranges 21.59–104.11 (mean 61.17) and magnesium ranges 1.40–30.23 (mean 15.10). Groundwaters in Bendimahi basin have calcium (in 20 samples), magnesium (in 6 samples) and sodium (in 4 samples) concentrations dominantly. Calcium ion concentrations range 10.20-170.63 (mean 65.92) and followed by magnesium ion concentrations range 0.41-148.27 (mean 35.52) and sodium ion concentrations range 4.24-1008 (mean 119.55). Bicarbonate is the only major anion in Zilan basin. Bicarbonate concentrations range 90-430 (mean 220.58). Among major analysed anionic concentrations (mg/l) in Bendimahi basin there are bicarbonate (in 24 samples), sulfate (in 5 samples) and chloride (in 1 sample) ions dominantly. Bicarbonate is the dominating ion ranges 2.30-1644 (mean 405.13) and followed by sulfate ranges 3–476 (mean 78.23) and chloride ranges 0.50-1440 (mean 110.77). Order of ionic abundance and water types of samples are in Table 1.

General Parameters

Physical parameters were analyzed for groundwater samples have been summarized in Table 2. pH is a measurement of activity of the free, un-complexed hydrogen ion which may lead to precipitation, co-precipitation and sorption processes that alter the chemical composition and reaction rates. pH ranges between 6.8 and 9.0 (mean 8.1) which depicts slightly alkaline nature of groundwater. Total hardness (mg/l as CaCO3) of groundwater is ranging from 41.6 to 1494.4 (mean 422.1). Total hardness has high levels in the study area. High Ca, Mg and HCO3 in groundwater are the probable reason for the hardness in basins. Conductance measurement provides an indication of ion concentration. EC (µS/cm) ranges between 55 and 1979 (mean 522.3). TDS (total dissolved solids) (mg/l) ranges between 218.5 and 1978.9 (mean 622).

Suitability for irrigation purposes

The values of hydrochemical parameters of groundwater used to determine irrigation suitability are %Na, SAR, RSC, EC, permeability index, Kelly's Index and magnesium hazard were evaluated with graphics and tables.

Sodium percent (% Na)

Sodium concentration is important in classifying irrigation water because it reacts with soils to reduce its permeability (Wilcox 1948). The high Na% might be due to long residence time of water, dissolution of minerals from lithological composition and chemical fertilizers (Latha and Rao 2012). Sodium content is usually expressed in terms of percent sodium (%Na). % Na is calculated that formula:

% Na = (Na+K) / (Ca + Mg + Na + K) x 100

The lowest percent of sodium in Zilan basin is numbered 6 (7.26 %) in the Kekliksırtı village and the highest value is numbered 1 (25.28 %) in the Yukarıışıklı village. The lowest percent of sodium in Bendimahi basin is numbered 31 (9.42 %) in the Yaykılıç village and the highest value is numbered 16 (85.99 %) in the Yağıbasan village. The quality assessment of Zilan basin for irrigation purposes showed that ''Very well – Well'' usable waters in terms of sodium percentage (% Na) and waters are ''Very well – Well'' and ''Well-Usable'' water class in terms of sodium percentage (% Na) in Bendimahi basin.

Table 1. Order of ionic abundance of groundwaters in Zilan and Bendimahi basins.

Sample Number	Location	Order of Ionıc Abundunce	Water Type
1	Zilan Basin- Yukarıışıklı Village	Mg > Ca > Na+K - HCO3 > SO4 > Cl	Mg-Ca-HCO3-SO4
2	Zilan Basin - Taşkapı V.	Ca > Mg > Na+K - HCO3 > SO4 > Cl	Ca-Mg-HCO3
3	Zilan Basin - Hasanabdal V.	Ca > Mg > Na+K - HCO3 > SO4 > Cl	Ca-Mg-HCO3
4	Zilan Basin - Hasanabdal V.	Ca > Mg > Na+K - HCO3 > SO4 > Cl	Ca-Mg-HCO3-SO4
5	Zilan Basin - Kekliksırtı V.	Ca > Na+K > Mg - HCO3 > SO4 > Cl	Ca- HCO3- SO4
6	Zilan Basin - Ağaçören V.	Ca > Mg > Na+K - HCO3 > SO4 > Cl	Ca- HCO3- SO4
7	Bendimahi Basin - Muradiye-Ovapınar V.	Ca > Mg > Na+K - HCO3 > SO4 > Cl	Ca-HCO3
8	Bendimahi B. - Muradiye-Köşkköy V.	Ca > Mg > Na+K - HCO3 > SO4 > Cl	Ca-Mg-HCO3
9	Bendimahi B. - Muradiye- Topuzarpa V.	Ca > Mg > Na+K - HCO3 > SO4 > Cl	Ca-Mg-HCO3
10	Bendimahi B. -Muradiye-Uluşar V.	Ca > Mg > Na+K - HCO3 > Cl > SO4	Ca-Mg-HCO3
11	Bendimahi B. -Muradiye- Beydağı V.	Ca > Mg > Na+K - HCO3 > SO4 > Cl	Ca-Mg-HCO3
12	Bendimahi B. -Muradiye- Yumaklı V.	Ca > Mg > Na+K - SO4 > HCO3 > Cl	Ca-Mg-SO4
13	Bendimahi B. -Muradiye- Town Center	Ca > Na+K > Mg - HCO3 > SO4 > Cl	Ca-Mg-HCO3-SO4
14	Bendimahi B. -Çaldıran-Ayrancılar V.	Ca > Na+K > Mg - SO4 > HCO3 > Cl	Ca- Na- SO4 - HCO3
15	Bendimahi B. - Çaldıran - Kalkandelen V.	Ca > Mg > Na+K - HCO3 > SO4 > Cl	Ca-Mg-HCO3-SO4
16	Bendimahi B. - Çaldıran - Yağıbasan V.	Na+K > Mg > Ca - HCO3 > SO4 > Cl	Na-HCO3
17	Bendimahi B. - Çaldıran - Altıyol V.	Na+K > Mg > Ca - HCO3 > SO4 > Cl	Na-HCO3
18	Bendimahi B. - Çaldıran - Yeniyaka V.	Ca > Mg > Na+K - HCO3 > SO4 > Cl	Ca-Mg-HCO3
19	Bendimahi B. - Çaldıran - Alikelle V.	Ca > Na+K > Mg - SO4 > HCO3 > Cl	Ca- Na- SO4
20	Bendimahi B. - Çaldıran - Kilimli V.	Ca > Mg > Na+K - HCO3 > SO4 > Cl	Ca-Mg-HCO3-SO4
21	Bendimahi B. - Çaldıran - Kilimli V.	Ca > Na+K > Mg - SO4 > HCO3 > Cl	Ca- Na- SO4
22	Bendimahi B. - Çaldıran - Salhane V.	Ca > Mg > Na+K - HCO3 > SO4 > Cl	Ca-Mg-HCO3
23	Bendimahi B. - Çaldıran - Evciler V.	Ca >Mg > Na+K - HCO3 > SO4 > Cl	Ca-Mg- Na- HCO3

24	Bendimahi B. - Çaldıran - Evciler V.	Mg > Ca > Na+K - Cl > HCO3 > SO4	Mg - Ca- Cl- HCO3
25	Bendimahi B. - Çaldıran - Hanköy V.	Na+K > Mg > Ca - HCO3 > Cl > SO4	Na-HCO3
26	Bendimahi B. - Muradiye - Ovapınar V.	Ca >Mg > Na+K - HCO3 > Cl > SO4	Ca-Mg-HCO3-Cl
27	Bendimahi B. - Muradiye - Kocasaban V.	Mg > Ca > Na+K - HCO3 > SO4 > Cl	Mg - Ca- Na- HCO3
28	Bendimahi B. - Muradiye - Uluşar V.	Ca >Mg > Na+K - HCO3 > SO4 > Cl	Ca-Mg-HCO3
29	Bendimahi B. - Muradiye - Fevzı Cakmak.	Ca > Na+K > Mg - HCO3 > SO4 > Cl	Ca - Na- Mg - HCO3
30	Bendimahi B. - Çaldıran - Yassıtepe V.	Ca > Na+K > Mg - HCO3 > SO4 > Cl	Ca-Mg-HCO3-SO4
31	Bendimahi B. - Çaldıran - Yaykılıç V.	Mg > Ca > Na+K - HCO3 > Cl > SO4	Mg - Ca- HCO3
32	Bendimahi B. - Çaldıran - Kilimli V.	Na+K > Ca > Mg - SO4 > HCO3 > Cl	Na-Ca- SO4
33	Bendimahi B. - Çaldıran - Koçovası V.	Mg > Ca > Na+K - HCO3 > Cl > SO4	Mg - Ca- Na - HCO3
34	Bendimahi B. - Çaldıran - Doyumalan V.	Ca > Na+K > Mg - HCO3 > Cl > SO4	Ca- Mg- HCO3- Cl-SO4
35	Bendimahi B. - Çaldıran - Hanköy V.	Mg > Na+K > Ca - HCO3 > Cl > SO4	Mg - Na- HCO3
36	Bendimahi B. - Çaldıran - Aşağıkuyucak V.	Mg > Na+K > Ca - HCO3 > Cl > SO4	Mg - Na - Ca - HCO3

*V. Village, B. Basin.

Table 2. Statistical summary of physical parameters and water indices in Zilan and Bendimahi basins.

Parameters	Zilan Basin		Bendimahi Basin	
	Range	Mean	Range	Mean
pH	7.76 - 9.00	8.54	6.80 - 8.81	8.05
Electrical Conductivity- EC (µS/cm)	55.00 - 624.00	272.03	88.90 - 1979.00	572.31
EC 25(µS/cm)	59.06 - 707.82	312.49	92.43 -2523.69	661.79
TDS (mg/l)	218.53 - 1088.90	603.99	224.11 -1978.90	625.61
Total Hardness (mg/l)	570.31 - 6659.10	2922.64	906.65 - 22513.44	6170.50
% Na	7.26 - 25.28	15.01	9.42 - 85.99	35.52
SAR	0.12 - 0.61	0.30	0.24 - 6.29	1.40
Kelly Ratio	0.04 - 0.18	0.11	0.06 - 3.69	0.63
RSC	- 1.12 - 0.14	-0.68	_4.04 - 5.38	-0.08
Magnesium Hazard	2.50 - 53.64	29.35	5.36 - 73.84	39.22
Permeability Index	42.75 - 59.56	49.84	33.04 - 116.28	59.71

Sodium and salinity hazard

Sodium and salinity hazard is usually expressed as (SAR). SAR is calculated that formula:

$$SAR = Na/ \sqrt{[(Ca + Mg) / 2]}$$

Groundwaters were evaluated in salinity-sodium hazard graphic in Figure 2. The lowest SAR value in Zilan basin is numbered 6 (0.12) in the Kekliksırtı village and the highest value is numbered 2 (0.61) in the Taşkapı village. In Zilan basin, groundwaters are in ‘’low sodium

hazard and low salinity hazard'' region in terms of sodium adsorbsion ratio (SAR) and in C1S1 water class. In Bendimahi basin, groundwaters are in ''low sodium hazard and low salinity hazard'' region in terms of sodium adsorbsion ratio (SAR) and in C1S1 water class. Much of the waters in Bendimahi are in ''low sodium hazard and low salinity hazard'' region and in in C1S1 water class. 7 water samples has been in ''low sodium hazard and medium salinity hazard'' region and in C2S1 water class. Well in Ovapınar village numbered 26 and well in Aşağıkuyucak village numbered 36 are in ''low sodium hazard and high salinity hazard'' region and in C3S1 water class. Also, well in Koçovası village numbered 33 is in ''low sodium hazard and very high salinity hazard'' region and in C4S1 water class. Moreover, well in Hanköy village numbered 35 is in ''medium sodium hazard and very high salinity hazard'' region and in C4S2 water class.

Kelly Ratio

Sodium measured against Ca and Mg was considered by Kelly (1940) and Paliwal (1967) to calculate this parameter. Kelly's ratio >1 indicates an excess level of sodium in water which is unsuitable and < 1 is suitable for irrigation uses (Patel et al.2016). Kelly ratio is calculated that formula:

$$KR = Na / (Ca + Mg)$$

Kelly ratio in Zilan basin changes between 0.04 meq/l and 0.18 meq/l. According to Kelly ratio criteria, all groundwaters in Zilan basin is suitable for irrigation. In Bendimahi basin, Kelly ratio changes between 0.06 meq/l and 3.69 meq/l. In Bendimahi basin, Kelly ratio is greater than 1 for samples numbered (16, 17, 25, 32) and that waters are not suitable for irrigation in terms of Kelly ratio.

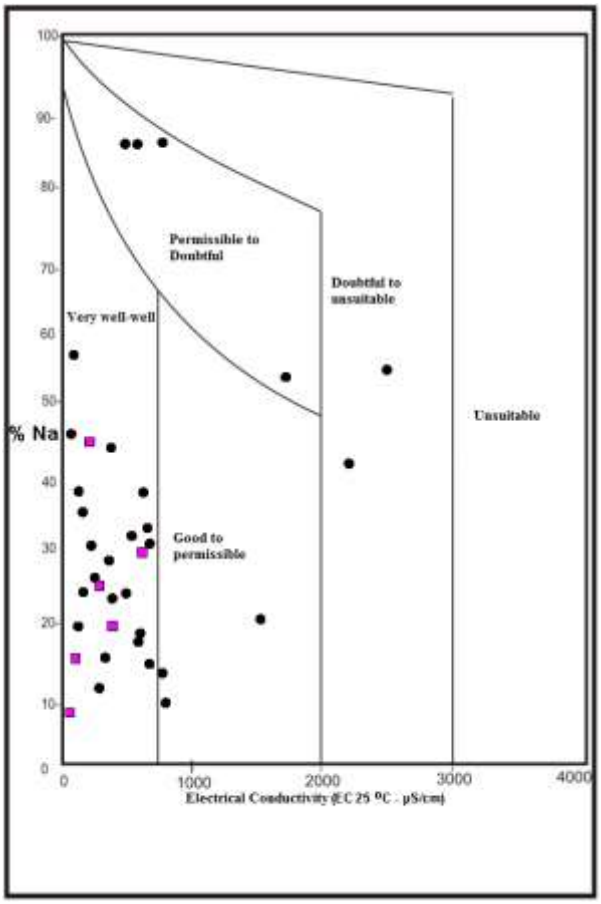

Figure 2. Rating of groundwater on the basis of EC and %Na (after Wilcox 1948).

Residual Sodium Carbonate (RSC)

The residual sodium carbonate (RSC) was calculated to determine the hazardous effects of carbonate and bicarbonate on the quality of groundwater for irrigation purposes (Patel et al.2016). A high value of RSC in water leads to an increase in the adsorption of sodium in soil (Eaton 1950). According to Eaton (1950), high values of RSC (> 2.5 meq/l) shows that waters can not be used for irrigation. Residual sodium carbonate is calculated that formula:

$$RSC = (CO3 + HCO3) - (Ca + Mg)$$

Waters in Zilan basin have under the 2.5 meq/l in terms of carbonate and bicarbonate hazard RSC (residual sodium carbonate) and it shows that they are suitable for irrigation. Much water in Bendimahi basin have under the 2.5 meq/l in terms of carbonate and bicarbonate hazard RSC (residual sodium carbonate) and it shows that they are suitable for irrigation.

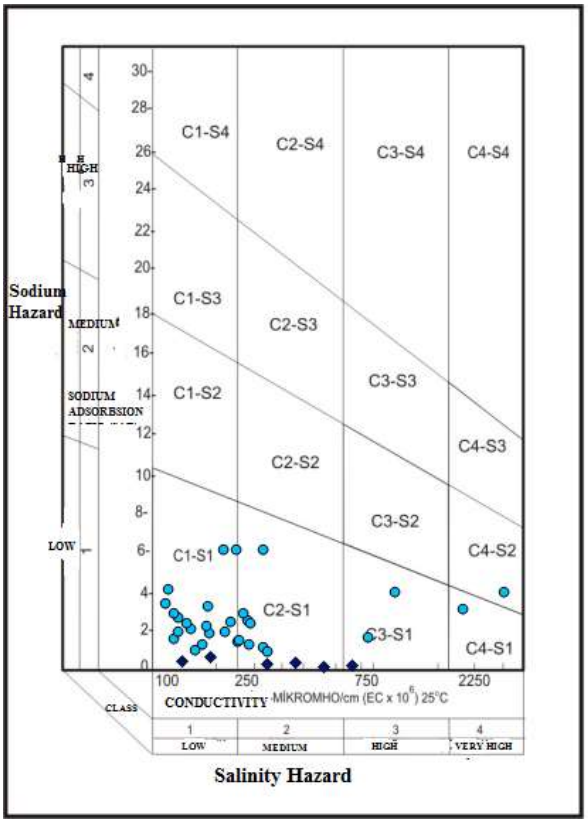

Figure 3. Rating of groundwater in relation to salinity and sodium hazard (after USSL 1954).

Magnesium Hazard (MH)

Szabolcs and Darab (1964) had proposed a magnesium hazard for assessing the suitability of water quality for irrigation. An increased proportion of Mg relative to Ca increases sodication in soils which causes the dispersion of clay particles thus damages soil structure and decreases the relative hydraulic conductivity of soils as Mg behaves like Na (Rasouli et al. 2012). If MH exceeds the value of 50, the water associated with such a value is considered to be harmful and hence is unsuitable for irrigation, because it adversely affects the crop yield (Patel et al. 2016). Magnesium Hazard (MH) is calculated that formula:

$$MH = (Mg / Ca + Mg) \times 100$$

Waters in Zilan basin are suitable in terms of magnesium hazard (MH) because of MH values are lower than 50 for a lot of samples. Waters in Bendimahi basin are suitable in terms of magnesium hazard (MH) because of MH values are lower than 50 for a lot of samples (percent of 70).

Permeability Index (PI)

WHO uses a criterion for assessing the suitability of water for irrigation based on the permeability index (Patel et al.,2016). Doneen (1964) has developed the diagram based on the PI to classify irrigation waters for soils of medium permeability. Based on the Doneen's chart classification, waters with maximum permeability represents Class I and with 75 % of permeability represents Class II and % 25 of permeability represents Class III waters. Most suitable waters are Class I for irrigation. Permeability Index (PI) is calculated that formula:

$$PI = [Na + \sqrt{(HCO3)} / Ca + Mg + Na] \times 100$$

66 percent of waters in Zilan basin is in Class I and it is suitable for irrigation according to permeable index (PI). 90 percent of waters in Bendimahi basin is in Class I and it is suitable for irrigation according to permeable index (PI).

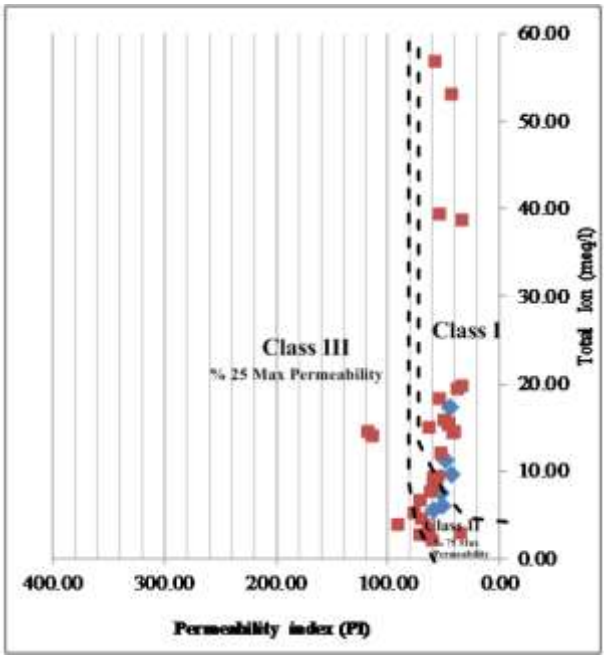

Figure 4. Doneen permeability index plot (Doneen 1964).

Conclusions

In order to characterize, classify and evaluate the suitability of groundwaters for irrigation in Zilan and Bendimahi basins hydrochemical assessment was conducted. Hydrographical methods were used to characterize water quality of groundwaters in Zilan and Bendimahi basins. Various irrigation indices show good to permissible use of groundwater in agricultural activities.

Acknowledgements

The author acknowledge the support of İstanbul University Research Fund (Project Number: 36796) and thanks to İstanbul University Research Fund.

REFERENCES

APHA, 2005, Standard methods for the examination of water and wastewater, 21st edn. American Public Health Association, Washington, DC.

Appelo CAJ, Postma D., 1999, Geochemistry, groundwater and pollution, 4th edn. Balkema, Rotterdam 536.

Ayers RS, Westcot DW., 1985, Water quality for agriculture. FAO Irrigation and Drainage Paper No. (29), Rev. (1), U.N. Food and Agriculture Organization, Rome.

Doneen L.D., 1964, *Notes on water quality in agriculture*, Published as a water science and engineering paper 4001, Department of Water Sciences and Engineering, University of California.

Eaton F.M., 1950, Significance of carbonate in irrigation waters, *Soil Sci*, 69 (2), 123–133.

Kelly, W.P., 1940, Permissible composition and concentration of irrigated waters, *Proceeding of the ASCF*, 66, 607.

Latha PS, Rao KN, 2012, An integrated approach to assess the quality of groundwater in a coastal aquifer of Andhra Pradesh, India. Environ Earth Sci 66:2143–2169.

Paliwal K.V., 1967, Effect of gypsum application on the quality of irrigation waters, *Madras Agric J*, 59, 646–647.

Patel, P., Raju, N.J., Reddy, B.C.S.R., Suresh, U., Gossel, W., Wycisk, P., 2016, *Environmental Earth Science*, 75 (611).

Rasouli, F., Pouya, A.K., Cheraghi, S.A.M., 2012, Hydrogeochemistry and water quality assessment of the Kor-Sivand Basin, Fars province, Iran, *Environ Monit Assess*, 184, 4861–4877.

Szabolcs, I., Darab, C., 1964, The influence of irrigation water of high sodium carbonate content of soils, *Proceedings of 8th international congress of ISSS, Trans II*, 803–812.

US Salinity Laboratory, 1954, Diagnosis and improvement of saline and alkali soils, Agricultural Handbook No. 60. USDA, p 160.

Wilcox, L.V., 1948, The quality of water for irrigation use, *US Department of Agriculture Technology Bulletin*, 40, 962.

EFFECTS OF MAGNETIC FIELD ON HUMAN LIFE

Fatih Şensoy and Orhan Şen
İstanbul Technical University, Faculty of Aeronautics and Astronautics, Deparartment of Meteorological Engineering, Maslak, Istanbul, Turkey. seno@itu.edu.tr.

Abstract
All materials have feeble and solid magnetic fields. Since person is a matter, he has his own particular magnetic field. Consequently, individuals are affected by both their own particular magnetic field and magnetic field of the earth in which they live. Other than the advantages to the general population, these magnetic fields have same harm, for example, the weakening of the normal adjust. Individuals are making their lives less demanding and utilize the time better quality and quicker by cell phones, PCs, and electrical home machines and high-voltage lines which they delivered. Then again, the utilization of this innovation brings down the nature of individuals' lives by the decrease in the age of a heart assault, the fall of the insusceptible framework, cerebral drain, usually found on growth, push, tinnitus, tired feeling etc. We must distinguish these gadgets' conceivable pollution of attractive field at source and take measures all together not to influence our lives unfavorably after quite a while. For his reason; the reviews on the attractive field and its potential consequences for human wellbeing and personal satisfaction are underlined on this review. Other than many advantages with the utilization of power, it has brought about some negative consequences for every single living thing.

Keywords: *Magnetic field, The electrical devices, Human health*

INTRODUCTION
The electrical device that are utilized spread undetectable electromagnetic field around them. The impact of these electromagnetic field on living creature ought to be known and it is important to beconscious users. The attractive field is a space which affected by moving and electrically charged particles and it happens subsequently of electrons inside the molecules revolution around the core and their own tomahawks. Attractive field can not be seen specifically and felt effectively but rather the consequences of them can be seen and felt. Today, with the advancement of innovation and with the assistance of measuring gadgets the estimation has turned out to be conceivable. Other than the inside and outside attractive field in the nature individuals are affected by attractive field of contamination they deliver their own particular electric gadgets. Attractive field of contamination is disregarded by the general population since it doesn't seen and its impact does not saw specifically and seen after quite a while. The wellspring of the attractive field contamination ought to be resolved and the important safeguards ought to be assumed in position to counteract. The personal satisfaction can be expanded by raising people's mindfulness for attractive field contamination other than contaminations, for example, environment and climate that influence human wellbeing. The electromagnetic (EM) fields have two parts as electric field and attractive field. The force of the electric field's voltage per meter is measured with voltmeter, the unit of estimation of the attractive field is Tesla or another unit is Gauss. The particulars of electronic and attractive fields are distinctive. Thusly, impacts on the organic structures of living of these regions is distinctive.

DATA AND METHODS
The tesla (symbol T) is a unit of measurement of the strength of a magnetic field. It is a derived unit of the International System of Units, the modern form of the metric system. A particle, carrying a charge of one coulomb, and passing through a magnetic field of one tesla, at a speed

of one metre per second, perpendicular to said field, experiences a force with magnitude one newton, according to the Lorentz force law. As an SI derived unit, the tesla can also be expressed as;

$$T = \frac{V \cdot s}{m^2} = \frac{N}{A \cdot m} = \frac{J}{A \cdot m^2} = \frac{H \cdot A}{m^2} = \frac{Wb}{m^2} = \frac{kg}{C \cdot s} = \frac{N \cdot s}{C \cdot m} = \frac{kg}{A \cdot s^2}$$

Units used:

A = ampere	m = metre	H = henry	Wb = weber
C = coulomb	kg = kilogram	V = volt	
N = newton	s = second	J = joule	

How these zones influences the general population is not yet completely caught on. Be that as it may, as indicated by studies; the attractive fields are more viable than electric field. Then again, attractive fields does not know obstruction, with the exception of some extraordinarily produced substances. The electric field makes a powerless current on the surface of the human body. Attractive fields prompt to the development of such frail stream in the interior organs by going into the body. Indeed, factor attractive fields container current in all conductives around them (human body can be considered as a conductor). As a measure of connection with living tissue and electromagnetic radiation made by radio, TV and radio frameworks, radar frameworks, satellite correspondence frameworks, microwave broilers, RF recurrence in prescription and industry representatives and frameworks, for example, GSM correspondence frameworks (working at 10kHz - 300 GHz recurrence range) is characterized "particular retention rate (SAR) ". SAR is about the power that ingested in the tissue and transformed into warmth. It is a question mark that there is no notice figures on the gadgets that show SAR esteem which is critical for human life . In the Electromagnetic Fields Organization led by World Health Organization for cell phone SAR qualities is suggested greatest 0.1 W/kg. The warm and non-warm impacts can happen in the living animals subsequently of the impact of non-ionizing electromagnetic waves in the earth. Warm impacts is characterized as electromagnetic vitality consumed by the human body is changed over to warm and an ascent in body temperature.

This temperature increases endures until warmth adjusted by evacuating with flow. The temperature increment brought on by radio recurrence (RF, for example, cell phone is very low and presumably can be debilitated effectively with the typical system of the human body. Contingent upon the non-warm impacts of RF wave it is asserted to be viable clutters and illnesses incorporate changes in mind action, rest issue, a lack of ability to concentrate

consistently scatter, a cerebral pain. Be that as it may, these dangers are shown to be successful in test high dosages and span. It is by and large said two impacts of electromagnetic fields. The first is the impact of warmth. Since the transmitted vitality is consumed as it goes through the human body, kept and a warmth gathering happens inside. This warmth can bring about undesirable outcomes. This outcomes the impacts are felt when we can state manifestations like cerebral pains, eye disturbance, weariness, shortcoming and unsteadiness. Additionally during the evening a sleeping disorder, daytime languor flow, not support in the public arena because of disdain and steady distress has likewise been accounted for in the writting. The second one's impact is that it influences and upsets and particles connected together in living creatures. The living being can repair, fixit self. In any case, it can be crazy for a minute. When it is crazy, it is suspected that it can bring about the demise of a straightforward two cells or a dangerous illness like malignancy. This second one's impact comes about just develop after quite a while. Since wherever on the planet advantage from power there are no individuals that are not presented to electromagnetic fields. Common level was fundamentally lower values in the climate of the electromagnetic field fifty years prior. Far reaching utilization of electromagnetic vitality alongside industrialization has made an expansion that influence human, creature and electronic framework in each recurrence of electromagnetic fields. In the event that we consider the utilization of the electromagnetic field will increment later on, the significance of this issue is expanded. Microwave, radio and cell phones, alert gadgets, programmed entryways, TV and radio transmitters and power transmission lines are cases of electromagnetic field vitality producing gadgets. Likewise lower recurrence RF warmers utilized for warming in modern procedures can be checked. The general population who’s work is identified with this application and upkeep personal are at essential hazard for remaining nearby to the nonstop light emanating gadget.

MATERIALS AND METHODS

As a result of experiments conducted on animals it has been seen that the electromagnetic field increase the cancer risk. The absence of these effects depends on electromagnetic field frequency, severity, the body size, the electrical properties of the body, the distance of electromagnetic field and its impact time. According to this the people who works high voltage lines and facilities, in radio and TV transmitters are exposed to danger. When the field level of the electrical equipment in the growing number, TV and radio stations and the mobile phones that everyone has, come up national and international standards it causes electromagnetic pollution like air pollution and it shows harmful effects on humans and equipment.

Therefore, TV, radio and mobile phone services in terms of the level of power the field level in the environment increases pollution. Also when the field levels exceed the limit values the devices which works with electromagnetic energy becomes incapable. Two points must be considered in the use of electromagnetic energy: First, the cautions related to devices that are used in homes and offices and second the initiatives that community will make common and the cautions against the electromagnetic pollution of environment. Most of the electric or magnetic field generated by humankind varies quickly and regular. These are alternative areas which characterized by their forces (intensity in varying levels) and frequency (variations in different speed). High-frequency and radio frequency fields are between 10 MHz and 300 GHz. In the highest part of the electromagnetic spectrum, the wide frequency range is used for telecommunication applications: radio waves, television, telecommunications, satellite, vb. Mobile phones and base stations create a level of 900 MHz or 1.8 GHz high frequency fields. Electromagnetic fields are detected only in very strong direct exposure situation by the human body; this situation arises only in a professional environment or carried out on 21 volunteers during experimental studies. The instantaneous effects are well-known in the international

scientific community that they are precise and repeatable. Unlike electric fields, the human body is not "sensitive" to magnetic fields. However, because of the body is conductive, when it exposes to magnetic field, it causes flows. But these flows are very low intensity and generally they are not felt in encountered exposure levels. Only exposure to intense magnetic field "snapshot" can bring a sense. However, as in the electric field perception threshold varies considerably from person to person.

The thresholds adopted by World Health Organization (WHO) are as follows (Leeuwey , 1999). In vivo experiments conducted on experimental animals investigate the influence on the mechanism of the animal health. However, the results of the interpretation in terms of the human body (extrapolation) requires the taken of certain cautions. The carcinogenic mechanisms are quite complex, in some aspects they are not yet clear, and it is known that they follow the two main phases: The initial stages of cell DNA altered and the proliferate phase of growth of cancerous cells. The experimental studies of the effects of electromagnetic fields are being conducted on these two phases .Unlike ionizing radiation, 50 to 60 Hz fields can not transfer energy sufficient to impact mutagens (causing genetic mutations) to cells. It was not observed any change or metamorphosis of DNA associated repair mechanisms in vitro studies. This also applies to areas with unusually high values. Thus, the experimental studies performed on cells mainly focused on the increase stage of tumor and emphasised on the effects of immune system and cell growth of electromagnetic fields (EMF). The other studies that based on "electromagnetic" hypothesis investigated the possible effects on cells that contain molecules sensitive to magnetic fields such as magnetite crystals or electrically charged elements (ions, free radicals). These studies show that there is no relationship between tumor formation and development by exposure to electromagnetic fields. It is not possible to repeat the results of few studies that show some effects emerging with the values of exceptionally high electromagnetic field (EMF). The small motors and converters of household appliances constitute much more important sources of magnetic fields than cables of these devices. The reason why the astronauts sent into space has fatigue, muscle pain, headache and dizziness could not be understood in the first years. As a result of extensive research carried out in later years it was determined that the lack of Earth's magnetic field caused these symptoms. The magnetic field in human body occurs from the movement of bioelectrical load. According to Biot-Savar theory, the moving electrical charges creates magnetic field.

The magnetic field is unquestionably in any field that comprises bio-electric. In this manner, organs like heart, muscles, nerves and cerebrum has a specific attractive field. The signs of attractive field which is utilized for speak with each different substances that make up the

human are in amicability with each other. These signs are in agreement with the world's attractive field. The agreement between the general population's inward attractive field and earth's attractive field can be separated in light of different reasons. One purpose behind this is the greatness of the attractive field where individuals live. There is a characteristic magnetic of the Earth's outside. The entire territory contains three factors; recurrence, spinner's bearing, size or power. At the point when these three factors suit human body the body underpins its own vitality. This attractive collaboration makes specialists trade in film conceivable. Along these lines, the cell as a production line representative make conceivable to keep up a fitting course of capacity and suitability by taking water, supplements, oxygen and fundamental minerals and by expelling waste and poisons from the body. In an investigation directed on epileptic patients, if there should arise an occurrence of progress of the attractive field of the subjects, the bioelectric movement of the cerebrum, in this manner guaranteeing reproduce the impacts of contamination in the event of sickness of neural connections. Around evening time the world increments cell oxygen attractive field, underpins rest, lessens irritation bolsters natural recuperating, diminish torment. Be that as it may, when the sun rises, the positive attractive field lessens cell oxygen, bolsters sharpness keeps the organic recuperating and increment torment. The pineal organ that oversees hormones in the focuses of the head, chemicals and resistant capacity is an attractive body containing attractive precious stones. It is exceptionally delicate to attractive vitality and the melatonin hormone shows up around evening time when the world's attractive field is viable. Themelatonin level ought to be high for a decent rest. Development hormone is connected with melatonin level. At the point when the general population get more established, they start to create these hormones less. The development hormone monitors hair, skin and muscle. Specialists' electromagnetic fields known as electromagnetic contamination or exhaust cloud made by individuals that are aggregate and it can make general discomfort, solidness in the neck, trunk torment, memory misfortune, migraines, change in heart rate and blood science, stomach related and circulatory issues. The innovation that is called electro exhaust cloud is one of the genuine dangers to human wellbeing components with the going with electromagnetic contamination. The electromagnetic spouses which is spread from the high-voltage lines to cell phone waves, from the radio and TV waves to PC and other electric apparatuses in homes and organizations the presentation electromagnetic contamination makes an undesirable climate in the social life environment. Electromagnetic brown haze harms the body's safe framework by blocking signals sent from the cerebrum to the phones. It has been still talked about whether the powerless attractive field is destructive to human wellbeing. These powerless fields has no harm evidently. In any case, in tests on creature cells, it has been judged to bring about natural operators, for example, changing the level of hormones and compounds of frail attractive fields and hindering the activity of chemicals in the tissue.

CONCLUSION

We are always presented to electric and attractive fields in our day by day lives. When we get up in the morning, we begin the day with the impacts of electric and attractive fields by turning on our lights. We live in reliance of the electrical and electronic frameworks that time and speed sparing by wrinkling our personal satisfaction at each point in our lives without monitoring in the day. Thus of the advancement of innovation we are attempting to live in an attractive field environment that brimming with these frameworks. There is no place that is not presented to this zones. These are influenced our wellbeing and our personal satisfaction in the short and long term. Temporary listening to issues, eye redness, tearing, smoldering, heart musicality aggravations, exceptional anxiety and consistent tiredness, the crumple of focus and consideration are the impacts which can be found in a brief timeframe. Cerebrum tumor, skin growth, hypertension, changeless listening to misfortune, miss hapening of platelets, coronary

illness, issues of the invulnerable framework are the impacts which can be found in quite a while. Therefore; any innovative advancements that enhance our personal satisfaction by rearranging our lives, likely go with losing something from our wellbeing.

REFERENCES:

Toros, H., & ve Şen, O. (2003). Manyetik alanın insan sağlığı üzerindeki etkisi, III. Atmosfer Bilimleri Sempozyumu, 19-21 Mart, İTÜ, İstanbul. ISBN.975-561-236-X.

Van Leeuwev, G.M., Lagendijk J.J., Van Leersum B.J., Zwamborn A.P., Hornsleth S.N., & Kotte, A.N., (1999). Calculation of chance in braintemperatures due to exposure to a mobile phone, Phys. Med. Biol., 44, 2367-2379.

Karaoğlu, B., 1996. Griftiths elektromagnetik Teori, Arte reklamcılık ve Tanıtım, 404 s.

Paper Collections of China XUAR, 1999. Overseas Scholars on Science and Technology.

Lindner G.M., 2002. www.todaysr.com/health19.htm, Ph.D.

ANALYSIS OF TROPOSPHERIC TEMPERATURE TRENDS OVER İSTANBUL, İZMIR AND ADANA

D.Demirhan Barı, Y. Ünal, H.S. Topçu, K. Turgut

Abstract

Global warming has been one of the greatest threat to our climate since the late 19th century. Due to the changing climate the lower and middle troposphere is continuously projected to increasing temperature trends but on the other hand upper troposphere is subject to consistently decreasing temperatures. Hence it is well-known that the fingerprints of the temperature change is not the same at every atmospheric level and also at every latitude. In this study we analyzed the temperature trends of three stations representing different climatic characteristics since they all belong to different regions of Turkey. The middle and upper tropospheric temperature for 850, 700, 500, 400, 300, 100 hPa pressure levels is analyzed by using the radiosonde data of İstanbul (Black Sea region), İzmir (Aegean region) and Adana (Mediterranean region) from 1986 to 2015 received from University of Wyoming website. It is observed that the temperature trends over Mediterranean and Aegean regions becomes steeper than İstanbul mainly after the year 1998. The fingerprints of the extremely warm year 2010 easily observed also at the middle troposphere especially over Mediterranean and Aegean regions. It is found that at 100hPa the temperature trends is mainly negative while this level is very much affected by the stratospheric cooling. In summer maximum trend at standard levels below 100hPa, is observed in Adana. On the other hand stratospheric cooling is least effective in Adana region.

Keywords: *Temperature trend, climate, İstanbul, İzmir, Adana*

Introduction

Temperature is the chief element to measure the climate change. It responses to both the natural and the anthropogenic forcings of the climate change. According to RCP 6.0 EPA simulations the temperature is expected to increase by 0.018°C per year until 2100 (EPA, 2016). Önol and Ünal (2012), also analyzed 114 stations between 2071-2100 around Turkey and obtained a temperature increase by 2-5 °C. Önol and Ünal (2012) explained that the temperature increase during summer will be 3°C higher than the winter season over the western Turkey. Çanlı (2015), studied the temperature change between 1961-2013 over the 2 cities in the Eastern Black Sea region, Trabzon and Rize and stated a temperature increase during the study period. Demir (2008) analyzed an increase in temperature in summer and spring seasons but a decrease in winter and autumn seasons over Turkey.

Global temperatures do not indicate a uniform geographic distribution, indeed there is a strong local differences. Hence climate change also indicates pronounced local differences. From the beginning of 1990s, climatologists have been using radiosonde and the satellite data to analyze the upper atmosphere (Bengtsson and Hodges, 2011; Yoo et al., 2011; Trenbert et al., 2002). Nowadays, especially the local changes in the tropospheric and stratospheric temperatures interest the climate scientists. They investigate the long term vertical temperature profiles and use their outcomes as an input to the climate models. For this reason in many of the recent climate studies vertical profiles of specific regions are analyzed. Thorne et al. (2010), analyzed the vertical temperature profiles from surface to upper troposphere and found that the temperature increase in the troposphere is much higher that the surface. Basha et al. (2015) examined the climatology of middle and upper tropospheric mean temperatures between the years 1985 and 2012 over Middle East including the Turkish cities of İzmir and Isparta and identified the vertical temperature profiles. They found a warming trend at the mid-troposphere

but a cooling trend at the upper troposphere. Additionally Philandras et al. (2015) analyzed the radiosonde data of Eastern Mediterranean region from 1965 to 2011 and showed that the atmospheric temperature is increasing especially after 1980. In the study of Philandras et al. (2015) maximum increasing trend which is 0.047°C/year is observed over Cagliari (Italy) at 700hPa. In this study in order to explain the latitudinal differences in the upper air temperature trends, 3 radiosonde stations, İstanbul, İzmir and Adana are choosen. Annual, seasonal temperature changes and their trends are investigated for the pressure levels 850, 700, 500 , 400, 300 and 100 hPa from 1986 to 2015.

Data

Latitudinal differences in the upper air temperature is investigated for İstanbul (41.0^{o}N 29.0 ^{o}E) , İzmir (38.4°N; 27.2°E) and Adana (37.0°N; 38.3°E) radiosonde stations which correspond to Marmara, Aegean and Mediterranean regions of Turkey, respectively. The temperature data at 00GMT for the pressure levels 850, 700, 500, 400, 300 and 100 hPa from 1986 to 2015 is analyzed. The hourly temperature data is received from the website of University of Wyoming, department of atmospheric science. Daily values were averaged to obtain seasonal and annual means. The latitude, longitude and the elevation of the stations is given below in Table 1.

Table 1. The geographical information about the study stations.

Stations	Latitude (N)	Longitude (E)	Elevation (m)
İstanbul	40.9°N	29.0°E	18m
İzmir	38.4°N	27.2°E	29m
Adana	37.0°N	38.3°E	27m

Annual change in temperature at standard pressure levels

Temperatures at standard pressure levels for specific latitudinal regions are examined. Obviously there is a difference in the amplitudes of the temperatures due to the latitudinal variation of the stations. It is evident that there is an increasing trend at all stations within the lower tropospheric levels (Figure 1). As being in the Mediterranean region, Adana, receives the highest solar radiation compared to the other stations. At 850hPa, highest temperature in Adana is observed to be 12.5°C (2010), maximum temperatures in İzmir and İstanbul are 10.9°C (2010) and 9.06°C (2012), respectively (Figure 1). The magnitude of increasing trend in temperature between 1986 and 2015 is similar at both 850hPa and 700hPa (Figure 1). At 700hPa, maximum temperatures in Adana, İzmir and İstanbul are given as 2.8°C (1989), 1.3°C (2010), -0.01°C (2012) respectively.

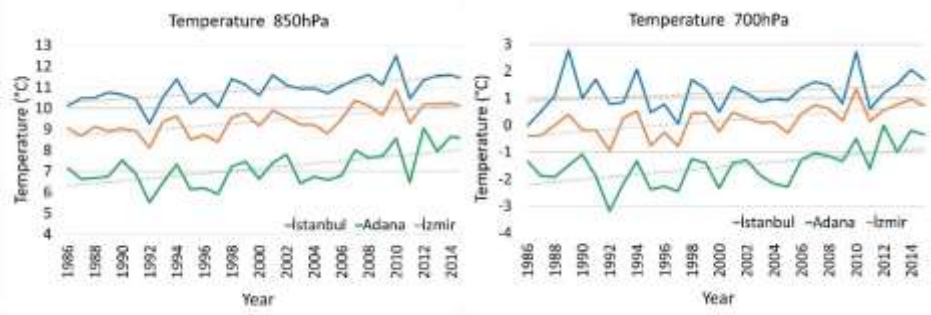

Figure 1. Annual change of temperature at 850hPa and 700hPa for İstanbul, Adana and İzmir between 1986 and 2015

In the middle troposphere, when three of the stations are compared, there has been seen a very slight difference in temperature trends of the stations until the year 1998. But mainly after 1998, a pronounced trend is observed in Adana and İzmir. At 500hPa, 400hPa and 300hPa, maximum temperatures in Adana are -14.1°C (1991), -26.3°C (2010) and -40.9°C (2010), respectively. The increasing temperature trend over İzmir is as pronounced as over Adana (Figure 2). Highest temperatures are somewhat lower than the ones in Adana. In İzmir, the maximum temperatures at 500hPa, 400hPa and 300hPa can be given as -15.5°C, -27.5 °C and -42.4°C in year 2010, respectively. Turkish climatological records also show that the year 2010 was exceptionaly warm. Maximum temperatures over İstanbul at 500hPa (-16.7°C) and 400hPa(-28.6°C) also observed in 2010, while at 300hPa maximum temperature of -43.4°C is observed in 2015. Observations at Adana and İzmir indicate that the response of these stations to climate change would be expected as similar to the ones below 400hPa (Figures 1,2). Especially in Adana at 400hPa and 300hPa (Figure 2) levels the rate of increase of temperature is much pronounced than the other stations.

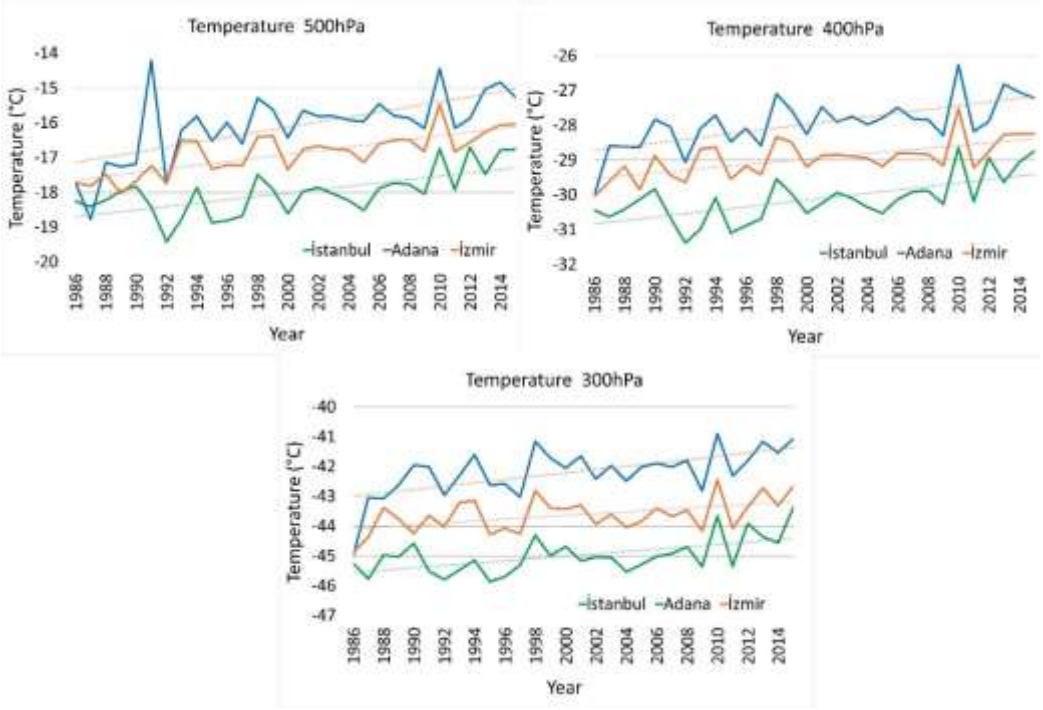

Figure 2. Annual change of temperature at 500hPa, 400hPa and 300hPa for İstanbul, Adana and İzmir between 1986 and 2015.

Upper troposphere has different characteristics from the lower troposphere. Upper troposphere is interacting with the lower stratosphere because chemistry and the dynamics of the lower stratosphere is strongly affected by the upper troposphere. In the atmosphere everything below the effective radiating level (≈6km) will warm up and everything above this level will cool down with the increasing greenhouse radiative forcing. Upper troposphere is located above the effective radiating level so it is cooling due to climate change (Graham, 2007). In this study 100hPa is chosen to represent the upper troposphere. The decrease in the temperatures of the upper troposphere is shown in Figure 3. The data of Adana for 100hPa are lacking for the years between 1986 and 1995. Adana station indicates the least decreasing trend compared to İstanbul and İzmir stations (Figure 3).

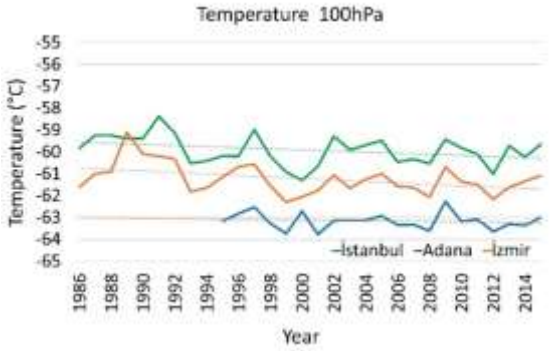

Figure 3. Annual change of temperature at 100hPa İstanbul, Adana and İzmir between 1986 and 2015.

Annual and seasonal temperature trends

Annual temperature trend is examined for standard pressure levels. In the lower troposphere, at 850 and 700 hPa, highest trends 0.067°C/year and 0.054°C/year is observed in İstanbul and İzmir respectively (Figure 4).

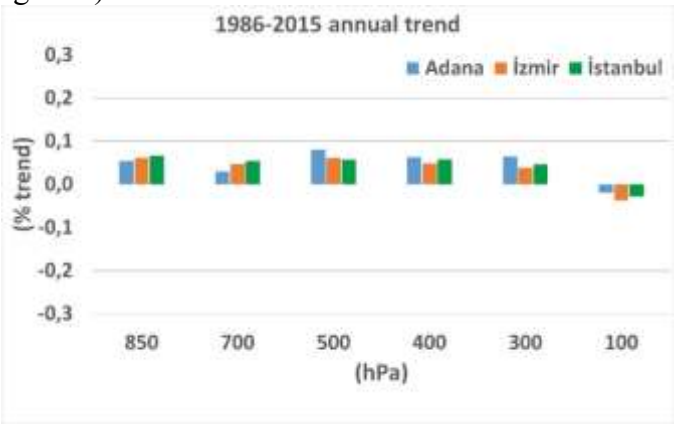

Figure 4. Annual temperature trends for standard pressure levels of 850, 700, 500, 400, 300 and 100hPa for Adana, İzmir and İstanbul.

At 850hPa, trends in Adana and İzmir are 0.054°C/year and 0.060 °C/year respectively in which İzmir shows a slightly higher trend than Adana. An increasing trend is observed at 850hPa, in autumn (0.06°C/year) and spring (0.054°C/year) over İzmir. Hence the lower tropospheric temperatures of all 3 stations shows a maximum at different seasons. At 700hPa the temperature trend of İstanbul is 70% higher than Adana. At 500, 400 and 300 hPa, Adana is distinctly higher than the other two stations. The temperature trend over Adana, at 500hpa is 0.08°C/year, at 400hPa, the trend is 0.063°C/year and at 300hPa, it is 0.064°C/year (Figure 4). The annual trend smooth out the seasonal variations. But the atmospheric heating has a seasonal cycle. The heating at the lower latitudes differs markedly from higher latitudes. Hence the temperature trends is also examined to be able to explain their behavior in different seasons. The involvement of the latitudinal distribution into the temperature trends is discussed. In summer Adana has the highest temperature trend at the lower and middle troposphere compared to the other stations (Figure 5). There is a clear increasing trend of 0.057°C/year in the lower troposphere over İstanbul in the winter season. However 100hPa level is highly effected by the lower stratosphere so there is a decreasing trend at this level. Adana (-0.006°C/year) and İstanbul (-0.02°C/year) stations show the minimum decreasing trend at the upper troposphere. During winter, autumn and spring the increasing temperature in Adana stations slows down at the lower troposphere. In spring at the middle troposphere, trends at all of the three stations is found to be decreasing.

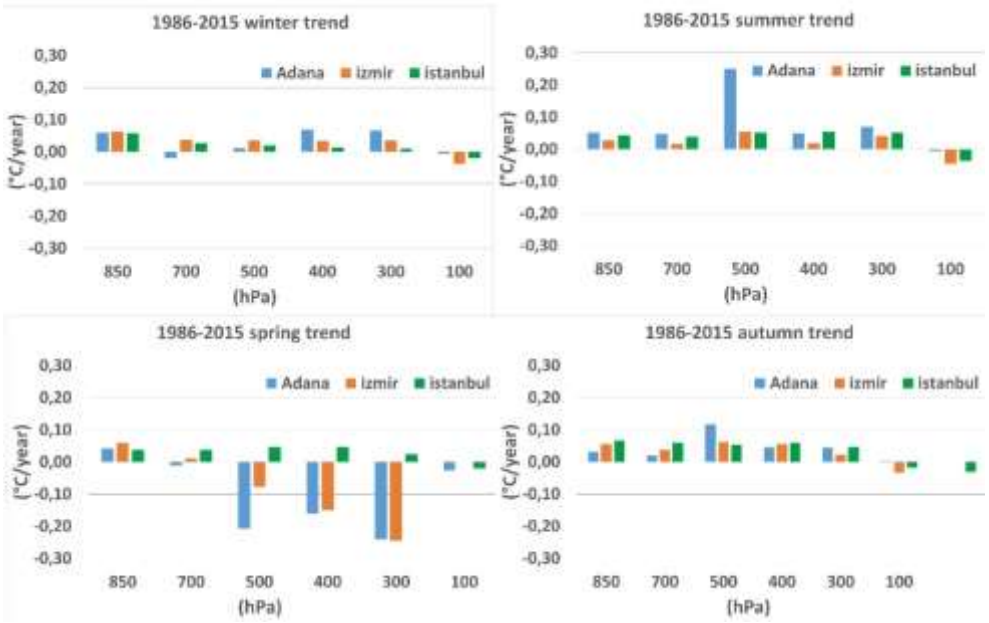

Figure 5. Temperature trends for standard pressure levels for Adana, İzmir and İstanbul in summer, winter, autumn and spring seasons.

Summary and results

In this study the temperature trends in Adana, İstanbul and İzmir radiosonde stations is investigated. The daily temperature data between 1986 and 2015 from the university of Wyoming is used. Seasonal and annual trend analysis is applied to the temperature data. It is found that the temperature over Adana is increasing with the greatest trend in the lower and the middle troposphere. In the upper troposphere, the temperature trends are mainly negative. The least decrease at 100hPa is observed in Adana. The seasonal variability of the temperature trends is examined. In the summer season at the lower and the middle troposphere, increase in the temperature trends is the highest in the Mediterranean region (Adana). In autumn and spring at 500hPa, there is a pronounced increasing trend over Adana. Winter temperatures of İstanbul at the lower troposphere tends to increase with 0.057°C/year.

REFERENCES

Çanlı, Ö., (2015). "Küresel İklim Değişiminin Doğu Karadeniz İllerinde Hissedilmesi Örneği", İTÜ Atmospheric Science symposium, Abstracts II: 771-780 (in Turkish).

Demir I., Kılıç G., Coşkun M., (2008) Precis bölgesel iklim modeli ile Türkiye için iklim öngörüleri: HaDAMP3 SRES A2 senaryosu, 4th ATMOS Semposium 25-28 March, İstanbul, p: 365-374.

EPA's report on the environment (2016) https://cfpub.epa.gov/roe/technical-documentation.cfm?i=89&pvw=

Graham, L.P., Andréasson, J. & Carlsson, B. Climatic Change (2007). 81(Suppl 1): 293. doi:10.1007/s10584-006-9215-2

İçel,G., Ataol, M.,(2014).Türkiye'de yıllık ortalama sıcaklıklar ile yağışlarda eğilimler ve NAO arasında ilişkileri(1975-2009)[The Trends in Annual Average Temperatures and Precipitations in Turkey and Relationship with NAO (1975-2009)].*Coğrafya Dergisi*. Retrieved from http://www.journals.istanbul.edu.tr/iucografya/article/view/5000079345/5000073777

Thorne,P.W., Lazenta,,J.R., Peterson, T.C.,Seidel, D.J.,Shine,K.P. (2010).Tropospheric temperature trends:history of an ongoing controversy. doi: 10.1002/wcc.80

Önol, B. & Unal, Y.S. Assessment of climate change simulations over climate zones of Turkey(2014). doi:10.1007/s10113-012-0335-0

SCENARIO SIMULATION PRODUCED USING ENVI-MET MODEL FOR THERMAL COMFORT THE EXAMPLE OF AZIZIYE PARK

Sevgi Yılmaz*[1], Başak Ertem Mutlu[2], Emral Mutlu[1]
[1] Ataturk Univ., Architecture and Design Fac., Dept. of Landscape Architecture, 25240, Erzurum/ Turkey
sevgiy@atauni.edu.tr; syilmaz_68@hotmail.com

Abstract
For the people living in of Erzurum, who spend long winter days in indoor areas, outdoor parks are especially important in the summer months. For this reason, it is important for the city people to design the parks considering the thermal comfort. Due to the high altitude, the city of Erzurum, which receives direct sunlight, is quite hot in summer. For this purpose, the Aziziye Park in the city center was chosen to be the sampling area. Hourly meteorological values were measured in the study area during the summer of 2017 and analyzed according to the data at 14:00. To determine which place is more comfortable; ENVI-met 4.2 model was used according to the existing situation of the park and the scenario alternatives were prepared. In this scenario, plants *Pinus sylvestris* L. (pine), *Betula verrucosa* L. (birch), *Acer negundo* L. (maple), ground coverings (grass, granite) and water surface are included. In this study the aim is to; produce alternative scenarios using different plants, water and ground covering materials and to present comfortable places for people in terms of climate. According to the ENVI-met 4.2 analysis, in the summer months, the most grass surfaces have been cooled and the water surface has followed this. In parks, comments were made according to scenarios where people feel more comfortable and relax in terms of climate, suggestions for park design.

Keywords: *ENVI-Met, Thermal Comfort, Park, Erzurum*

INTRODUCTION
ENVI-met model has been widely used in many fields of climatic research, including thermal comfort and urban heat island effect, and microclimate (Qaid et al., 2016; Bruse, 2017). Using the ENVI-met model, looking at the thermal comfort situation with different scenarios is very useful in determining which is more appropriate for energy-intensive urbanization.
In studies using ENVI-met model of the park located within the urban space (Spronken and Oke, 1998; Feyisa et al., 2014; Lin and Lin, 2016), different species of trees (Dimoudi and Nikolopoulou, 2003; Tan et al., 2016), the number of trees different (Chang et al., 2007; Lee et al., 2016) scenarios were studied thermal comfort and different floors (Du et al., 2016; Salata et al., 2016; Taleghani and Berardi, 2017). In the landscape design of the space, attention should be paid to the elements of the landscaping, their material and their positioning in consideration of the climate. Plants and flooring that affect the thermal comfort of the environment in each period should be carefully selected and placed according to design criteria.

MATERIAL AND METHOD
Meteorological Data Obtained
Meteorological data were collected from the Aziziye Park in July 2017, at an interval of 1 hour from a height of 1.5 m. 24-hour data were used for these measurements, while the remaining hourly data were kept waiting for the device's median optimization. In this study time interval of 1 hour is used WS300 sensitive meteorology recorder was used in the collection of data. The latitude of this Aziziye Park is 39° 54′ 16.5816"N and the longitude is 41° 15′ 36.4896"E. This is a park between the city center and Ataturk University that is visited by the public (Figure 1).

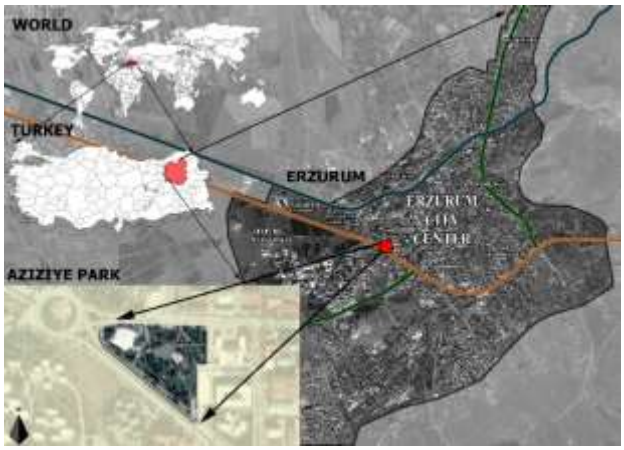

Figure 1. Aziziye Park location map

The Aziziye park covers an area of approximately 36,000 square meters. Park is located at the western entrance of the city and is a busy area between the city center and the university. The park has a large number of large trees. These are mostly *Betula verrucosa* L., *Acer negundo* L., *Ulmus glabra* L., *Fraxinus exelcior* L., *Pinus sylvestris* L. (Figure 2).


Figure 2. Aziziye park overwiev

While measuring the temperature values with the precision thermometer (WS300), the humidity values were taken with the YCOM-KMN 305 model temperature and humidity meter. TROTEC BA16 model anemometer is used for wind speed measurement (Figure 3).


a)WS300 model


b) YCOM-KMN 305 model


c) TROTEC BA16 model

Figure 3. Aziziye Park measuring devices

ENVI-met analysis different scenarios

A three-dimensional micro-climatic 3D modelling tool ENVI-met V4.2 Summer was used to evaluate meteorological data (Bruse, 2017). At the time of modeling, the most used time of the area was taken at 14:00. Although different versions of this software is available, the underlying logic is always the same. It has a horizontal resolution of 0.5 -10 meters (Yang et al., 2013; Lobaccaro and Acero, 2015). With this software, the air temperature (Ta; °C), vapor pressure, relative humidity (RH; %) , wind velocity (v; m/s), cloudiness (N octas) and the mean radian temperature (W/m) of the receptors can be calculated (Ketterer and Matzarakis 2014; Huttner, 2012; Qaid et al.,

RESULTS

Analysis for deciduous trees with ENVI-met model

Trees that are broad-leaved and previously adept in the city center have been selected for modeling. The deciduous plants used in this scenario are *Betula verrucosa* L. (birch) and *Acer negundo* L. (maple) (Figure 4).

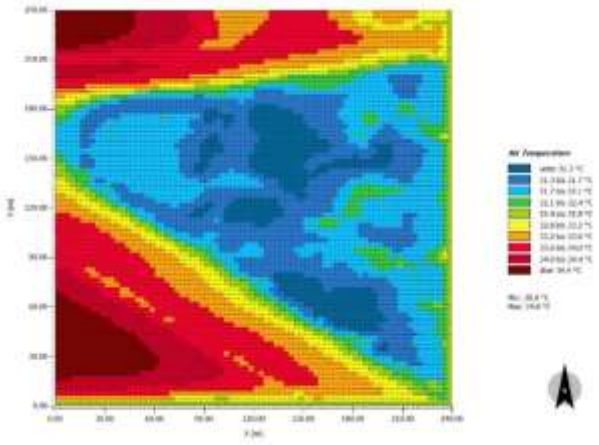

Figure 4. Analysis for deciduous trees

Analysis of pine trees with ENVI-met model

For the other suggestion scenarios, the thermal comfort effect was analyzed using only the manipulated species in the field. It is striking that these areas that remain visually green in winter are durable both in terms of aesthetic appearance and difficult conditions in winter. Scots pines (*Pinus sylvestris* L.*)*, also widely found in urban areas, have been selected (Figure 5). These coppice forests are very important for Erzurum which has a problem of very heavy air pollution caused by long winter period (Yilmaz et al. 2017).

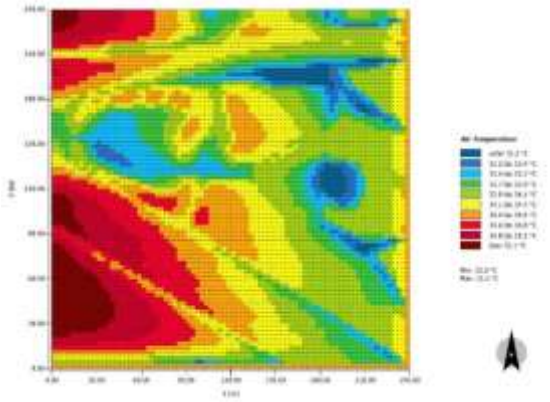

Figure 5. Analysis of pine trees

ENVI-met analaysis with mix trees

The area has been subjected to the thermal comfort analysis in the area using both the coniferous and deciduous species (Figure 6).

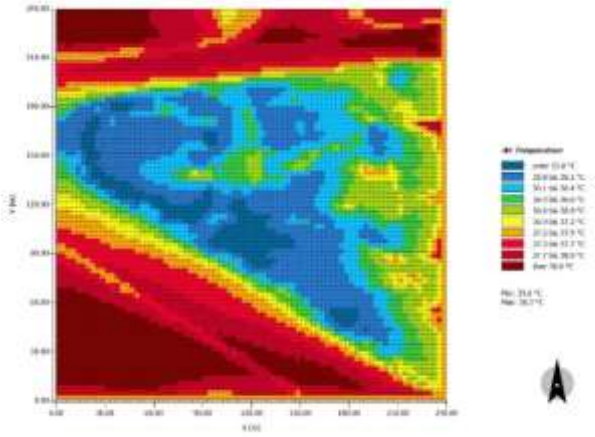

Figure 6. Analysis of mix trees

Analysis of granite surface ENVI-met Model

Instead of the basalt flooring available in the field, the proposed granite flooring proposal was introduced and the thermal comfort effect in the area analyzed (Figure 7).

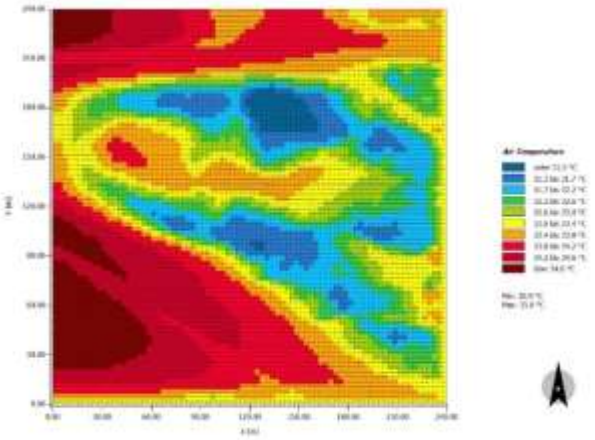

Figure 7. Analysis of granite surface

Analysis of water surface ENVI-met Model

An ornamental pond was added to the area to analyze the effect of the water surface on the thermal comfort and analyzed (Figure 8).

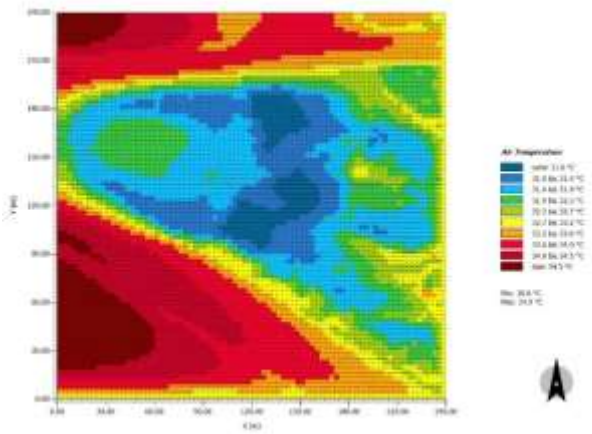

Figure 8. Analysis of water surface

Analysis of grass surface ENVI-met Model

The study area was entirely lawned so that the trees in the area were removed and the effect of this scenario on thermal comfort was measured (Figure 9).

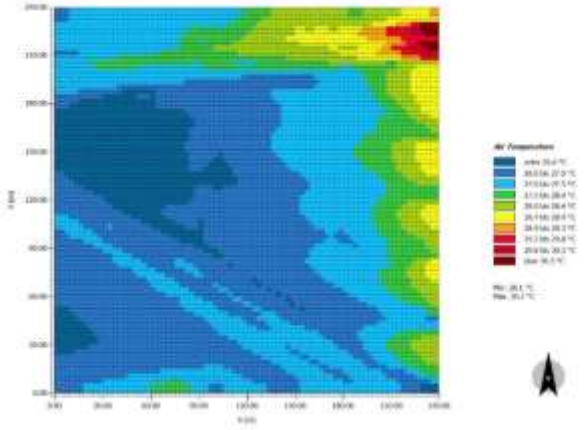

Figure 9. Analysis of grass surface

Comparison of Existing Situation and Recommendations

The thermal comfort effect of the current situation is measured and given in Figure 10. According to the other scenarios analyzed, it has been determined that grass surfaces cool the environment more (Figure 11).

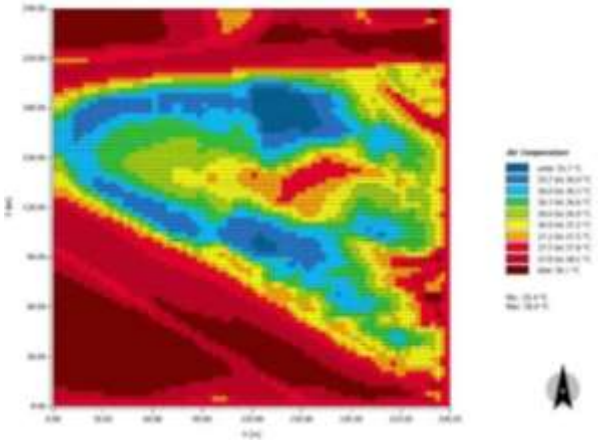

Figure 10. The model available for the 80x80x30 grid system in the city center where Aziziye Park is located

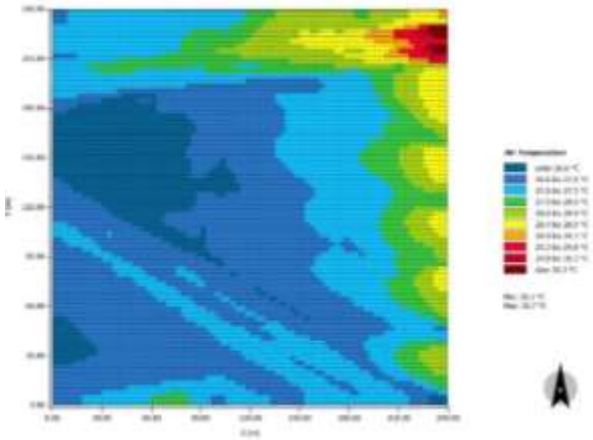

Figure 11. Effect of grass surfaces on thermal comfort

DISCUSSION AND CONCLUSIONS

It has been determined that using only the grass surface in the field gives better results in thermal comfort analysis for Aziziye Park. In the scenario, it is seen that the temperature is 7.7 ^{0}C cooler than the current situation. As a matter of fact, the similar work done in this issue has also determined the cooling effect of the green areas (Ng et al., 2012; Janicke et al., 2015). It has been determined that plants in Erzurum, which has especially extreme climatic conditions in urban areas, always give positive results in terms of thermal comfort. It has been determined that hard surface coatings heat the place especially in summer and disturb people from thermal point of view in places where there are no trees. Especially in recent years, it has been emphasized that climate-based studies have to be carried out with the condition of being multi-disciplinary for livable urbanization and energy-focused designs.

ACKNOWLEDGMENTS

This study was carried out by using the devices obtained with the 215O627 numbered project of TUBITAK (Scientific and Technological Research Council of Turkey). The authors express their gratitude to Michael Bruse for providing the ENVI-met software.

REFERENCES

Bruse, M. (2000), "Anwendung von mikroskaligen Simulationsmodellen in der Stadtplanung", In: Bernhard, L., Küger, T. (Eds.), Simulation Raumbezogener Prozesse: Methoden Und Anwendung. University of Münster

Bruse, M., 2017. ENVI-met 4: A Microscale Urban Climate Model. http://www.envi-met.info. [Accessed on February 2017].

Chang, C. R., Li, M. H., & Chang, S. D. 2007. A preliminary study on the local cool-island intensity of Taipei city parks. Landscape and Urban Planning, 80(4), 386-395.

Dimoudi, A., and Nikolopoulou, M. 2003. Vegetation in the urban environment: microclimatic analysis and benefits. Energy and buildings, 35(1), 69-76.

Du, S., Xiong, Z., Wang, Y. C., & Guo, L. 2016. Quantifying the multilevel effects of landscape composition and configuration on land surface temperature. Remote Sensing of Environment, 178, 84-92.

Feyisa, G. L., Dons, K., & Meilby, H. 2014. Efficiency of parks in mitigating urban heat island effect: An example from Addis Ababa. Landscape and Urban Planning, 123, 87-95.

Huttner S., 2012. Further development and application of the 3D microclimate simulation ENVI-met PhD Thesis Johannes Gutenberg-University Mainz , p. 135

Janicke, B., Meier, F., Hoelscher, M.-T., Scherer, D., 2015. Evaluating the effects offacade greening on human bioclimate in a complex urban environment. Adv.Meteorol. 15, http://dx.doi.org/10.1155/2015

Ketterer, C.; Matzarakis, A., 2014. Human-biometeorological assessment of heat stress reduction by replanning measures in Stuttgart, Germany. Lands. Urban Planning,122, 78–88

Lee, H., Mayer, H., Chen, L., 2016. Contribution of trees and grasslands to themitigation of human heat stress in a residential district of Freiburg, SouthwestGermany. Landscape Urban Planning, 148, 37–50,

Lin, B. S., and Lin, C. T. 2016. Preliminary study of the influence of the spatial arrangement of urban parks on local temperature reduction. Urban Forestry & Urban Greening, 20, 348-357.
Lobaccaro, G., Acero, J.A., 2015. Comparative analysis of green actions to improve outdoor thermal comfort inside typical urban street canyons. Urban Climate 14, 251–267.
Ng, E., Chen, L., Wang, Y., & Yuan, C. 2012. A study on the cooling effects of greening in a high-density city: an experience from Hong Kong. Building and Environment, 47, 256-271.
Salata, F., Golasi, I., de Lieto Vollaro, R., and de Lieto Vollaro, A. 2016. Urban microclimate and outdoor thermal comfort. A proper procedure to fit ENVI-met simulation outputs to experimental data. Sustainable Cities and Society, 26, 318-343.
Spronken-Smith, R. A., and Oke, T. R. 1998. The thermal regime of urban parks in two cities with different summer climates. International journal of remote sensing, 19(11), 2085-2104.a high-density city: an experience from Hong Kong. Build. Environ. 47, 256–271.
Qaid A., Lamit H.B., Ossen D.R., Shahminan R.N.R., 2016. Urban heat island and thermal comfort conditions at micro-climate scale in a tropical planned city. Energy and Buildings, 133,577-595
Taleghani, M., and Berardi, U. 2017. The effect of pavement characteristics on pedestrians' thermal comfort in Toronto. Urban Climate.
Tan, Z., Lau, K.K., Ng, E.1, 2016. Urban tree design approaches for mitigatingdaytime urban heat island effects in a high-density urban environment. Energy Building, 114, 265–274.
Yang, X., Zhao, L., Bruse, M., Meng, Q., 2013. Evaluation of a microclimate model forpredicting the thermal behavior of different ground surfaces. Build. Environment, 60, 93–104.
Yilmaz S., Yilmaz H., Irmak M.A., Kuzulugil A.C .and Koç A., 2017. Effects of Urban *Pinus sylvestris* (L.) Plantation Sites on Thermal Comfort. GREEN CITIES 2017 International Symposium on greener cities for more efficient ecosystem services in a climate changing world – Abst. 30,Oral presentation, 12/15 September Bologna, Italy

EFFECTS OF PLANT USAGE ON URBAN THERMAL COMFORT FOR SUSTAINABLE CITIES

Sevgi Yılmaz [1], Emral Mutlu[1]*, Hasan Yılmaz[1]
[1] *Ataturk Univ., Architecture and Design Fac., Dept. of Landscape Architecture, 25240, Erzurum/ Turkey*

Abstract
As a result of intensive urbanization and increasing urban population, heat islands are formed in many cities today. It is important to plant in the spaces to ensure proper thermal comfort in the spaces and to reduce the effects of heat islands. Although the use of plants in urban areas is mainly due to aesthetic concerns, in fact the plants realize many ecological functions. Thermal measurements of natural plants and exotic seasonal plants were made in Erzurum city center. It has been noted that exotic and natural species have the same colors in the study, that they are placed close to each other, and that the thermal image is taken from the same view. Measurements were taken at 13:00, the hottest hour of the day. In the work done, the surface temperatures of the flower colors of the plants were differentiated, and the surface temperature differences between the flowering fields and the empty plantless areas were examined. In the results of this study; the use of natural plants in cities produces 3.2 ºC cooler areas in the city in terms of surface temperatures than exotic vegetation. According to this result; the use of natural plants to reduce the effects of urban heat island has been proposed. Moreover, the use of natural plant; it is even more advantageous because it does not have energy expenditure, adaptability to the environment and economic maintenance costs.

Keywords: *Thermal Camera, Thermal Comfort, Plant Usage, Sustainable Cities.*

INTRODUCTION
Especially in the last years studies, urban spaces reveals that it is warmer than its surrounding and rural area (Unger, 1999; Bulgan et al. 2014; Zhang et al. 2010). There are many reasons for this increase in temperature in urban spaces. This increase in temperature not only increases energy consumption in urban spaces, but also reduces the comfort of people's thermal comfort. A large number of studies are being conducted to determine the factors that increase the thermal comfort values of the urban space. For this aim to; in parks, streets, open spaces, neighbourhood scale, continues to increase research etc. with trees. The use of thermal cameras also accelerates in thermal comfort determination studies (Smigaj et al., 2015; Yilmaz et al., 2015; Ginner et al. 2015; Aubrecht et al. 2016; Yilmaz et al., 2016, Yilmaz et al. 2017). Leuzinger and Körner (2007) in their study measured the from 35 m in height with a high-resolution thermal imaging camera from in the tree a surface temperature of the air temperature and the plant surface temperature has determined that the close values. Again, in the same study, it was determined that the coniferous plant surface temperature with the lowered surface temperature had lower surface temperature than the broader plant. Takebayashi and Moriyama (2009) found that on hard surfaces in parking lots increase urban heat when they have worked with thermal camera images. For this reason, it is necessary to consider the climate factor in new settlements for energy-focused, thermal comfort urbanization. The climate data of the study area should be analyzed and transferred to plan decisions. The aim to this study is to reduce the temperature stress experienced, in the summer months, especially in Erzurum, and to offer suggestions for people to design thermal comfortable spaces for people. For energy-focused, sustainable and thermal well-being urbanization, it has been suggested that such work be transferred to the local government's plan decisions.

MATERIAL AND METHOD

The study was carried out in Erzurum city center (Figure 1). In recent years, the areas of use of thermal camera images have be varied, from food to agriculture, clothing to health, from industry to military areas. These cameras, which can be recorded with the unmanned aerial vehicle, can measure the surface temperatures. This work was mostly used to improve the urban living spaces of thermal cameras.

In the summer of 2017 measurements were made at different times using a thermal camera. For this aim to; Optris® PI-450 (Optris, Berlin, Germany) longwave infrared camera with manual focus used for this study (Figure 2). The spectral range is 7.5 – 13 µm and a resolution of 382 x 288 pixels, with a temperature range of -20 / 900 °C (accuracy: ±2 °C, resolution of 0.1 °C, thermal sensitivity: 40 mK). The camera recordings are recorded and stored in the computer environment. In addition, data were collected with a WS 300 precision temperature gauge to compare with the surface temperatures of the air temperature. Optris software was used to evaluate the data. While the study, were evaluated the healthy and unhealthy grass surfaces and flowers of yellow, white, red, purple colors.

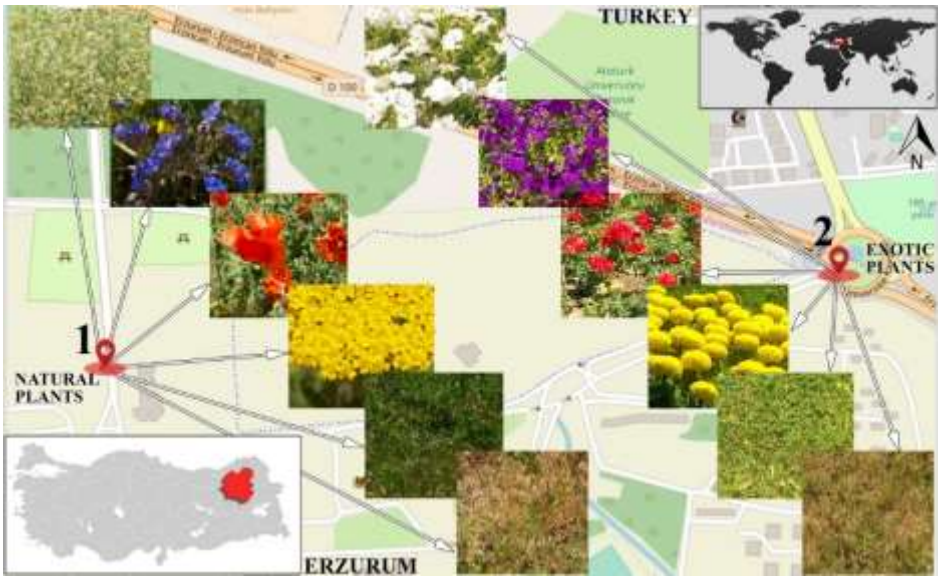

Figure 1. Study areas and images:
; natural plant (1), Exzotik plant (2), White flowers (3), Yellow flowers (4), Red flowers (5), Purple flowers (6) , Grass surface (7), Dry grass surface (8)

Figure 2. Optris® PI-450 thermal camera

RESULT AND DISCUSSION

Thermal photos taken from natural herbaceous plants have been detected the highest surface temperature 29.4 ºC with red flowering plant and lowest surface temperature 25.4 ºC with white flowering plant. In the measurements taken in the natural plant composition, from the warmest surface temperature to the lowest surface temperature; 29.4 ºC for red flowering, 27.8 ºC for purple flowering, 27.2 ºC for yellow flowering and 25.4 ºC for white flowering. On the lawn areas were compared to unhealthy and healthy lawns; healthy grass surfaces averaged 29.7 ºC; while unhealthy grass surfaces were identified as 35.6 ºC (Figure 2).

When you look at exotic plants; the hottest surface temperature was 36.7 ºC in purple flowering plants and the lowest surface were identified temperature was 28.6 ºC in white flowering plants. While starting from the plant that gives the highest surface temperature, if the plants that give the coolest surface temperature will be sorted; purple flowering plant 36.7 ºC, yellow flowering plant 30.8 ºC, red flowering plant 30.7 ºC and white flowering plant were detected as 28.6 ºC. If we look at the grass surfaces in these thermal images, the average temperature of healthy grass areas is 27.6 ºC and the temperature value of unhealthy grass surfaces were identified as 35.2 ºC. (Figure 3).

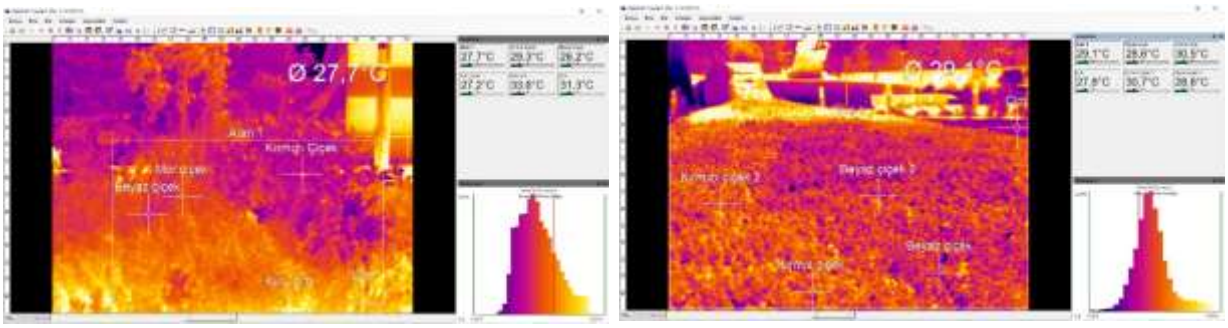

Figure 2. The analysis conducted for natural and exotic plants

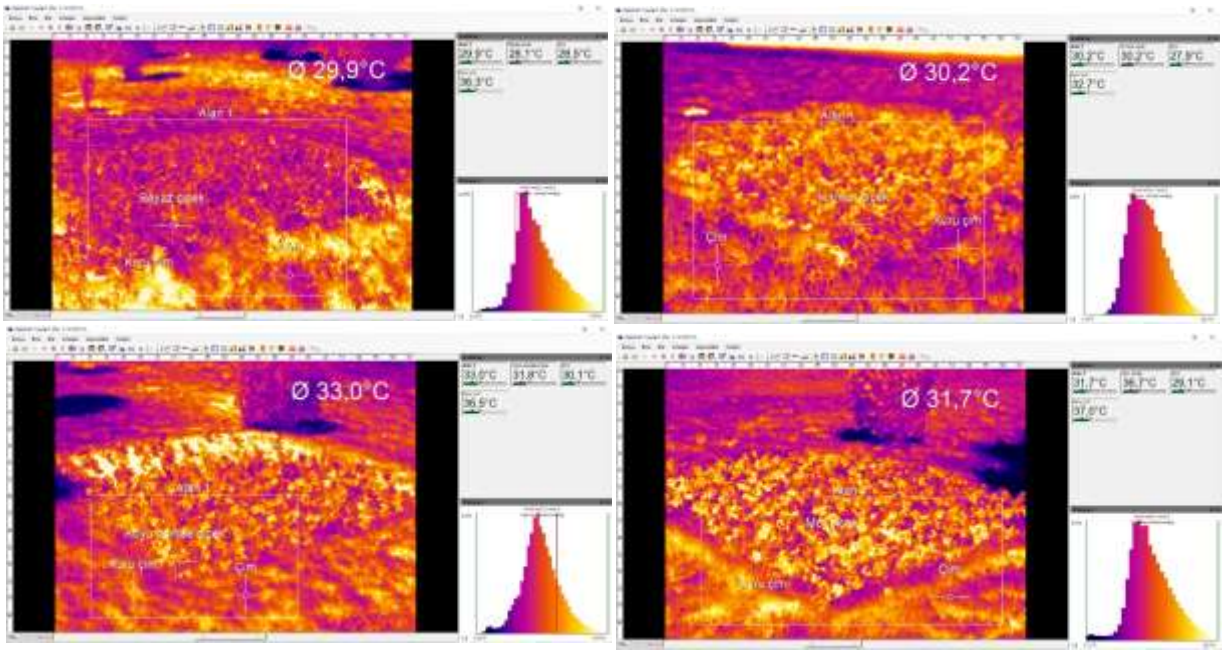

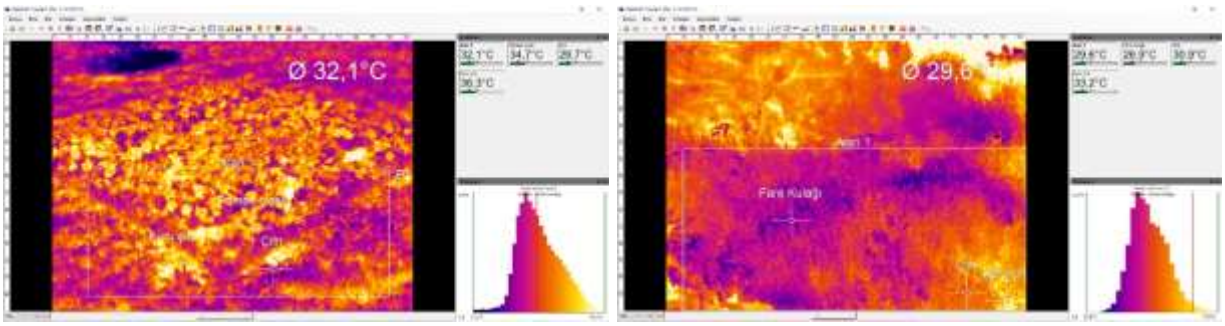

Figure 3. Thermal image analysis of plants

It has been observed that in two different plant compositions, natural plants constitute cooler environments than exotic plants. Prominently, no temperature difference was observed in the red flowering plants, although there was a temperature difference in the same colored plants. For other colors, it has been found that the temperature difference in the natural plant composition is at least 3.2 ^{o}C and the area where the exotic plants are present becomes more warmer (Tablo 1)

Table 1. Analysis of thermal camera nature and Exotic plants

Measurement	**Exotic Plants$_{(1)}$ Mean (C^{0})**	**Nature Plant$_{(2)}$ Mean (C^{0})**
White flowers$_{(3)}$	28.1	26.2
Yellow Flowers $_{(4)}$	30.8	27.2
Red flowers$_{(5)}$	30.6	29.3
Purple flowers$_{(6)}$	36.7	27.5
Grass surface$_{(7)}$	29.1	31.3
Dry grass surface$_{(8)}$	35.4	35.6
Mean Value	**31.8**	**29.5**

Parallel to the results obtained; Aguiar et al. (2014), natural trees provide 2 ^{o}C more cooler spaces than exotic trees.

CONCLUSION

Today, the urban heat island (UHI) is struggling with problems of urban areas to be planted with native plants is important. Especially Consideration of elements such as color, covering area and natural vegetation cover in seasonal plants is very important in terms of sustainable, thermal comfort and urban climate management. If you look at the results obtained in the study, plants with white flowers or lighter colors are creating a cooler environment. Also, the use of natural herbaceous plants will further reduce the impact of UHI. This will also provide an economic gain for local governments.

ACKNOWLEDGMENTS

The devices used for the measurements were purchased in the scope of a TUBITAK (Scientific and Technological Research Council of Turkey) supported scientific project no **215O627**.

REFERENCES

Aguiar A. C., French, K., Chisholm, L. A. 2014. A comparison of the ameliorating effects of native and exotic street trees on surface heat retention at dusk. Urban Climate 10 (2014) 56–62

Aubrecht D. M., Helliker B. R., Goulden M. L., Roberts D. A., Still C. J., Richardson A. D. 2016. Continuous, long-term, high-frequency thermal imaging of vegetation: Uncertainties and recommended best practices. Agricultural and Forest Meteorology, 228, 315-326

Bulgan E., Yilmaz **S**, Matzarakis A and Irmak MA, 2014. Quantification of summer thermal bioclimate of different land uses in an urban city centre. IC2UHI3, October 13-15, 2014, pp. 523-534, Venezia, Italy

Ginner S., Vogt J., Tharang A., Dettmann S., Roloff A., 2015. Role of street trees in mitigating effects of heat and drought at highly sealed urban sites. Landscape and Urban Planning, 143, 33-42. doi:10.1016/j.landurbplan.2015.06.005

Leuzinger S., Korner C., 2007. Tree species diversity affects canopy leaf temperatures in a mature temperate forest. Agricultural and Forest Meteorology, 146(1-2), 29-37

Smigaj, M.,; R. Gaulton, S. L. Barr ; J. C. Suárez , 2015. Uav-Borne Thermal Imaging for Forest Health Monitoring: Detection of Disease-Induced Canopy Temperature Increase. The International Archives of Photogrammetry, Remote Sensing and Spatial Information Sciences 40(3): 349.

Takebayashi, H., Moriyama, M., 2009. Study on the urban heat island mitigation effect achieved by converting to grass-covered parking. Solar Energy, 83-8,1211–1223

Unger J., 1999. Comparisons of urban and rural bioclimatological conditions in the case of a Central-European city. International Journalof Biometeorology, 43(3), 139-144.

Yilmaz H., Yildiz ND., Avdan U., Koc A., Matzarakis A., 2015. Analysis of human thermal conditions in winter for different urban structures in Erzurum. . ICUC9- 9th International Conference on Urban Climate jointly with 12th ymposium on the Urban Environment , 20-24 July, Oral presentation, Toulouse, France

Yilmaz H., Yilmaz S., Yavaş M., Mutlu E., Koç A., 2016. Climate-sensitive Pavement Modelling for Pedestrian Ways. 4th International Conference on Countermeasures to Urban Heat Island (UHI) 2016. Procedia Engineering, 169: 408-415

Yilmaz S., Mutlu M., Yilmaz H., Mutlu B.E., 2017. Impact of Microscale Vegetation on Urban Thermal Comfort With Thermal Infrared Imaging: Erzurum City Center. II. International Iğdır Symposium (IGDIRSEMP2017), oral presentation, 9-11 October, Iğdır/Turkey

METEOROLOGICAL STATIONS AND METEOROLOGICAL SERVICES ESTABLISHED DURING THE FIRST WORLD WAR IN THE OTTOMAN EMPIRE

Hasan TATLI [a*] **and Mithat ATABAY**[b]

[a*]*Department of Geography, Faculty of Sciences and Arts, Çanakkale Onsekiz Mart University 17020 Çanakkale, Turkey, tatli@comu.edu.tr*

[b]*Department of History, Faculty of Sciences and Arts, Çanakkale Onsekiz Mart University 17020 Çanakkale, Turkey.*

ABSTRACT

As the Ottoman Empire entered war with Germany during World War I, the Germans did not ignore the importance of meteorological conditions and stated that a meteorological observation network should be established in the Ottoman state. Within this framework, a meteorological organization was established in Istanbul under the name of "Kuvva-i *Havaiye Müfettişliği Rasadat-ı Cevviye Müdürlüğü*". Professor Ludwig Weickmann, head of the organization, had brought with himself sixty German experts to be able to operate meteorological stations in a short period of time. Those experts were the first members of the established meteorological organization. Turks who served as reserve officers in the Ottoman Army were assigned to these experts. In some of the installed meteorological stations, pilot balloon observations for aeronautical and artillery purposes were made, while hydrological observations have been made at the stations in river and water basins. The meteorological measurements made in Germany, Austria-Hungary, Bulgaria and Ottoman territories were first sent to Istanbul, then to Sofia, Vienna and Berlin as encrypted priority with the help of radio and telegraph. In Berlin, the experts were working on these maps to prepare weather-forecasts, and the estimates were still coded in Vienna, then in Sofia and Istanbul. Two main centers were established in the Ottoman Empire. One of them was Istanbul, and the other was Jerusalem Meteorology Center. These centers were institutions where both military and climate climatological observations were collected and evaluated. With the capture of Jerusalem by the British in 1917, Istanbul continued to operate as the only meteorological center until the end of the war. The meteorological observations made in the Ottoman Empire during the First World War were also compared with the observations made in the surrounding countries, and the determination of the climate of the Ottoman lands has been tried. The records have been kept in Ottoman and German languages and have undergone very little evaluation so far. One of the most important negative reasons for this is that researchers do not know the Ottoman language and not access to a significant part of German records.

Key Words: *Ottoman, Germany, First War, Meteorology, Istanbul, Jerusalem*

THE FIRST METEOROLOGY SERVICE IN THE OTTOMAN EMPIRE

Weather conditions have played many roles both in favour of and against the armies in world history. The European Hun Emperor Atilla was construed as "God does not want Rome to be captured" because of a thunderstorm that suddenly occurrence of a storm and deafened ears while he was capturing the Rome, however due to those meteorological conditions Atilla abandoned from this encirclement. By the ending of the Second World War, there was a stormy, extremely rainy weather in Normandy. This weather condition was against the Germans, however favouring the running ally. Accordingly, the German-Italian bloc was defeated on all fronts in Europe, and on 7 May 1945 it was announced that the war in Europe was over. As the Ottoman Empire entered war with Germany during World War I, the Germans have not ignored the importance of meteorological conditions and established a meteorological observation network in the Ottoman state.

The meteorological service in Istanbul started its activity in August 1915, under the name of "Kuvva-i Havaiye Müfettişliği Rasadat-ı Cevviye Müdürlüğü" at Caferağa Mansion in Kuruçeşme. Professor Ludwig Weickmann (Figure 1) who was the first manager of the meteorology service has brought sixty German meteorology experts for establishing the organization of meteorology service in the Ottoman state. The related experts were the first members of this meteorology organization. In addition to these German experts, many Turkish officers in the Ottoman Army were selected to work in the meteorology service. Throughout the war, Professor Ludwig Weickmann and his assistant Dr. Erich Obst were the managers of this centre (Niyazi and Obst, 1932).

Figure 1. The first Military Observation System in the Ottoman Empire was founded by Professor Ludwig Weickmann.

These reserve officers were trained in meteorology at the Ottoman-German General Headquarters in Istanbul.General, Fatin (Gökmen) have given courses at Headquarters. Fatih Gökmen was the founder who changed the Kandilli Observatory to serve as an earthquake research institute. The reserve officers who completed their training started to work at meteorological stations established by the German state. These stations are Edirne, Gallipoli, Izmir, Seydiköy, Zonguldak, Sinop, Ankara, Eskisehir, Konya, Sivas, Diyarbakir, Adana, Brumana, Beirut, Jerusalem and Mosul (Atabay and Aytaç, 2002).

METEOROLOGY SERVICE DURING THE FIRST WORLD WAR

The first meteorological forecasts were made by processing the maps those constructed by the observations gathered from these meteorological stations, and in addition the cryptographic observations from Bulgaria (October 5, 1915), Austria-Hungary and Germany, which were allied by the Ottoman Empire (Atabay and Aytaç, 2002).

Erich Obst was born in Berlin on June 13, 1886, studied geography and geology at the University of Yena and Breslau, and became associate professor in 1910 in Hamburg. He studied in East Africa in 1910-1912 and worked as a professor of geography at Marburg University between 1912-1915. When World War I started, Istanbul Darülfünun was assigned to the Department of Geography and remained in Istanbul until 1918 and later resumed his studies at Breslau University and later at Hannover University in Germany. Professor Obst analyzed the meteorological data obtained from the military meteorological

stations established in the Ottoman Empire during the war by analyzing the weather maps and wrote a book called "Turkey and European Climate"(Niyazi and Obst,1932).

Professor Ludwig Weickmann focused on the location, information exchange and working conditions of the military meteorological stations to be established during the war in the Ottoman Empire. The military meteorological stations established by Professor Ludwig Weickmann included barometer, barograph, psychrometer, hygrograph, maximum and minimum thermometers, rain gauge (pluviometer) and anemometer. The observations were made with these instruments three times a day at 07.00, 14.00 and 21.00. Moreover, in İstanbul Vaniköy, Edirne, Gelibolu, Seydiköy, Adana and Jerusalem, high-level wind measurements were taken from ground level to 6,000 meters. For these measurements, the balloon filled with hydrogen gas and a theodolite seen in Figure 2 were used to follow the balloon (Atabay and Aytaç, 2002).

Figure 2. Theodolite used for pilot-balloon observations during the war.

During the First World War, German experts Aladar Guerle had made valuable work on the Red River and its vicinity, and Erich Leward in Edirne and the Balkans on the weather events. In addition, some German meteorologists lost their lives during the war. For example, Kurt Niehoff, who is responsible for the inspection of meteorological stations and Karl Klingebiel, the manager of Zonguldak Meteorological Station, died because of the febrile diseases seen in Turkey (Atabay and Aytaç).

The observations made in Germany, Austria-Hungary, Bulgaria and Ottoman territories were first transmitted to Istanbul, then to Sofia, Vienna and Berlin as first priority and scrambled by radio transmission. Experts in Berlin were preparing maps of the weather and their forecasts were again encrypted and then delivered to Vienna, then to Sofia and Istanbul. These estimates were sent from Istanbul to the Army Commands in the Ottoman territory and necessary measures were taken.

Undoubtedly, one of the most effective weapons during the war of Çanakkale was the artilleries. It was necessary to know the meteorological conditions on the route followed by the artillery to increase the performance of the hit rate to the target during the artilleries' shoots and to adjust the ball side / ascend angles considering these parameters. The effect of meteorological factors in the effective range of various calibres is so small that it cannot be ignored. In a survey conducted, the effects of factors affecting artillery shooting are seen in Table 1.

Table 1. Factors affecting of the artilleries (Atabay, 1997)

Factors	15 Km (%)	25 Km (%)	35 Km (%)	45 Km (%)
Initial velocity	**36**	**38**	**44**	**40**
Meteorological factors	**52**	**47**	**35**	**32**
Ammunition specifications	**6**	**13**	**20**	**28**
Other	**6**	**2**	**1**	**< 1**
Total	**100**	**100**	**100**	**100**

The use of general meteorological information during artillery has encountered the following problems:

1. Meteorological information cannot be obtained at sufficient frequency for artillery shooting
2. The absence of meteorological data in the operation area,
3. The fact that meteorological information reaches fire control systems,
4. The centres where the meteorological information is received are far away from the operation area (Atabay, 1997).

Figure 3. In 1915, a Turkish soldier and a German military pilot were conducting meteorological balloon observations in Gallipoli.

In Gallipoli, balloons were thrown every morning and noon every day, and high winds were detected, and this information was the most important information for both the launching of artilleries and the up and down of planes (Figure 3). Undoubtedly, the most important date in terms of weather conditions during the Gallipoli Wars was 25-28 November 1915. This date was also the most important factor in their decision to evict the enemy of the Gallipoli peninsula.

What happened on this date, which was the turning point in the process that led the enemy out of Gallipoli? A low pressure and rainy weather over the Mediterranean will affect the environment around Çanakkale and Istanbul, winds will be in the form of a southwest, and a day later they will return to the open sky and then the stars and pavilions and then the air would cool down quickly. When this information was reached from Istanbul to the 5th Army, the weather was very beautiful in Gelibolu and Çanakkale. It was like a day of summer. Nobody paid much attention to this information. After lunch on November 26, 1915, the weather began to cloud, and the wind gradually began to increase in speed and turned into a storm around 4 pm. The torrential rain that started towards the evening began to worsen after the dark pillow.

Thunder and lightning struck all over. The floods come with the rain, suddenly filled the trenches and shelters. The arrival and departure times were covered with water. Soldiers, animals floated. The goods drifted and disappeared with floods. Small Anafarta Plain, all the trenches on both sides of Azmak were flooded. All the shelters were destroyed. Many drowned in the seller. Most of the men had to leave the trenches to go up to the high places and fell into despair.

The two enemy sides have struggled to rescue themselves in the face of this common catastrophe, and they have stopped fighting. The guns and tools were left under water and sand. There were summer dresses on Turkish troops who did not expect such an event and felt the heat of the southwest wind during daytime. Soldiers get soaked in their underwear (Genelkurmay, 2012). Mustafa Kemal wrote in his notebook of -The Chief of Staff Major Izzettin Bey- "It was a great rain at night." (Çalışlar, 1993). The water on the front and the trenches invaded the water and the soldiers had a great deal of trouble. The precipitation continued November 26, 1915 and the weather was getting colder. Especially the 18th and 59th Regiments in Azmak and the 36th Regiment in Anafarta Plain gave great losses. Because of the storm in the sea, no ship came to shore. No food and aid material could be brought to land. The animals opened. Pertev Pasha had gone to the 7th, but he was so wet that the 11th Bottom had to take shelter (Çalışlar, 1993).

Figure 4. The snow stack on November 27, 1915 at Conkbayir on the Çanakkale Front

On November 27, the morning air opened but there was such a cold weather that no one could stand outside (Figure 4). The clothes of all of them were wet. At the same time, the Austrian Artillery Battalion threw a few shoots to the enemy. Easterly wind has become increasingly violent. The Turkish soldiers in the plain were replaced with unit reserves. The disease has started. 27/28 November 1915, the night began to snow with a violent storm. The snow storm continued until the evening of November 28th. The temperature fell to -10 degrees in the night. Thousands of Turkish soldiers were sick with rain, followed by violent cold, followed by a snow storm, and frozen to death.

Between 25 and 28 November 1915, 11 soldiers were drowned in the 11th Army of the troops of the Anafartalar Group Command due to bad weather conditions and 17 soldiers were frozen. In the 12th division, the total number of died soldiers was 37, the number of martyrs who were frozen was 165, and the number of those who were stranded and lost was 147. The situations in the 9th division were very pain: 9 soldiers drowned, 37 soldiers frozen, and 86 soldiers have been lost. In the 6th division, 5 soldiers were drowned, 29 soldiers froze, and 22 soldiers lost

their lives. A total of 556 soldiers were cold and martyred (Genelkurmay, 2012). This corresponded to about 1% of the Turkish martyrs during the Gallipoli Wars (Moorehead, 2002). Because of the snow storm, the airplanes in Gallipoli were under the snow (Oglander, 2005). The snow was piling up with the wind and it was over 1.5 meters above the ground (Genelkurmay, 2012).

When the intensity of the wind decreased on November 30, the British had made a census. Entente Army lost 1/10 of your power. More than 5,000 soldiers from enemy troops were frozen and 2000 people were drowned. According to Hamilton's report: 12,000 soldiers from the Anafartalar Front and 2,700 soldiers from the Arıburnu Front, a total of 14,700 soldiers got sick.

During the Çanakkale War, the date of 25-28 November 1915 was a turning point, since the enemy made his final decision after this disaster: "Winter will not be passed in the Gallipoli Peninsula. The salvage will begin in ten days ". After the 26th of November, all the pontoon and alcoves in Anzac were sent to İmroz to get rid of the approaching storm. But from the ships that saw the breakwater, the ship in the middle was destroyed by the impact of the storm. The violent sea overflowed into the koya and began to hit the piers and docks. and all the water droplets and a torbidobot were either completely sunk or landed. At Anafartalar Port, which is sheltered against the north winds, the pontoon and scaffolds survived with little damage compared to the others.

On the other hand, Anzac and Seddülbahir were filled with water. There were so many casualties from the small transport facilities that even if the weather continuing good, there was no way to evacuate the three shores at the same time. Because of this three-day storm, a cycle of suffering for soldiers in the trenches began. The heavy thunderstorms that started after the November 26th lunch lasted 24 hours and even affected the soldiers' bones. The rain has suddenly turned into a snowfall. Two nights after this snow storm came the violent frost (Oglander, 2005).

Through the sheltered places that were completed during the summer months in Anzac, the military troops could find shelter from this storm. The hills surrounding the Anzac first line fenders protected part of the soldiers from the storm. The number of illnesses increased, especially among the Indian troops. Even in Seddülbahir, the soldiers were less affected by the storm when the trenches were located on the sloping terrain. The 9th British Corps in Anafartalar was the most affected troops. The troops on the Kireçtepe were completely exposed to the violent storm. The low-ranking soldiers were totally influenced. The dry and thirsty Anafartalar Plain flooded. Especially in the trenches near Azmakdere in the south, floods and muddy waters flowed in the trenches located at a few feet high, and the Turks who were saddled with floods, came to the English trenches. The trenches became unstoppable. In the trenches, the soldiers of the 29th division had to step backwards to the top of the trenches. The war has stopped for both sides.

The nights of 27-28 were two fearsome and troublesome nights in the entire Anafartalar. Many soldiers drowned on the front line. The extreme cold following the storm broke the health of the soldiers. Outside the Anafartalar Plain, those who went to the beaches lost their lives by freezing cold. All the warehouses, hospital tents, ammunition tents, briefly all the covered places became shelter for the people. The 86th division was completely out of the war. The doctors were desperate in disaster. Oglander has written those days as "it was not even possible to give soldiers hot food or even drinks." (Oglander, 2005). Meanwhile, all the excess material

was sent to Mondros, which included winter clothes. After 5000 soldiers had frozen and 2000 drowned, the sun came out on November 30, 1915 (Genelkurmay, 2012). The weather was clear, and the sea was stagnant. Important meteorological observations and services were also provided during the war in military meteorological stations established on other fronts than the Çanakkale Front.

In particular, the most noteworthy issue between 1915 and 1917 was the fact that a study on sudden pressure drop in barometers was made. The meteorological information obtained at Military Meteorological Stations in Edirne, Istanbul, Gallipoli, Zonguldak, Sinop, Giresun, Trabzon, İzmir, Antalya, Adana, Beirut, Jerusalem, Eskişehir, Ankara, Konya, Sivas, Diyarbakir, Mardin, Diagrams and maps were worked on regularly to establish a link between the effects of weather events on the stations (Figure 4).

The information obtained was published in monthly bulletins both in Ottoman (Turkish alphabet of Arabic origin) and German regularly. The names of the bulletins are "Memalik-i Osmaniye Military Rasadat-ı Miye Majması = Military Meteorology Magazine in Ottoman Territories". Between 1915 and 1918, these bulletins gave us valuable information about the meteorological conditions of the Ottoman country. Again, the forecast maps provide us to learn the meteorological conditions of the Mediterranean terrains, the Balkans, the North African coasts, the Anatolian and Basra Gulfs and the Gulf of Aden, starting with Spain in terms of navigation of air masses.

Figure 5. A Turkish soldier under snow on the Galician (Galiçya) Front

In 1918, the meteorological data obtained from Jerusalem and Baghdad was not seen in the bulletins because those places had been captured by Britishes. The most important issue that was observed in the military meteorological stations established in the Ottoman lands during the First World War and published in the bulletins was the thunderstorms. Actually, the records of all stations were given in the form of a table of daily thunderstorm days every month from 1915 to 1918. Another important issue was the presence of dust storms in meteorological bulletins observed in the south-eastern provinces of Anatolia, Syria and Iraq. For example; in the first week of January 1918, after a lunch in Mardin a powerful dust storm has suddenly started, and in the shortest time the dust even has entered the smallest holes, and Mardin's horizon has turned into a hell-like image. The vehicles have become unusable due to dust storms.

CONCLUSIONS

In Turkey, the observations measuring with modern meteorological instruments has begun in the 1930s. However, the historical weather events are made much more understandable with combining them with present-day observations by uncovering those old observations which are mostly in Ottoman and given in the meteorological bulletins. On the other hand, when it is desired to run the climate models backwards, these old records might be used for calibration and validation of the related models. If the old historical meteorological records belonging to the Ottoman state are taken out, we will have knowledge of the past weather events covering not only in Turkey day but in the geography of Europe, Middle East and North Africa.

REFERENCES

Antonio Sagona, Mithat Atabay, Richard Reid, Ian McGibbon, Chris Mackie, Muhammet Erat, Jessie Birkett-Rees, (2011) "The ANZAC (Arıburnu) Battlefield: New Perspectives and Methodologies in History and Archaeology," *Avustralian Historical Studies,* Nr:42, Issue:3, p.313-336.

Atabay, Mithat, Aytaç, (2002), Halil, *I.Dünya Savaşı Sırasında Osmanlı Topraklarında Almanların Kurduğu Askeri Meteoroloji Teşkilatı ve Buna Ait Bir Rapor,* DMİ Yayınları, Ankara (in Turkish).

Çalışlar, İzzeddin (1993), *Atatürk'le İki Buçuk Yıl, Orgeneral Çalışlar'ın Anıları,* yay. haz. İsmet Görgülü, Yapı Kredi Yayınları, İstanbul .1993 (in Turkish).

Genelkurmay Başkanlığı (2012), *Birinci Dünya Harbinde Türk Harbi, Çanakkale Cephesi Harekâtı, (Özetlenmiş Tarih),* c.V, Ankara (in Turkish).

Hamilton, Ian (2005), *Gelibolu Hatıraları 1915,* ed. Ö. Andaç Uğurlu, Örgün Yayınevi, İstanbul (in Turkish).

M. Niyazı ve Dr. Erich Obst (1932), *Boğazlar İstanbul-Çanakkale Mıntıkası İklimi,* Tefeyyüz Kitaphanesi, İstanbul (in Turkish).

Oglander, C. F. Aspinall (205), *Gelibolu Askeri Harekâtı,* 2.C., Yayına Hazıralayan: Metin Martı, Arma Yayınları, İstanbul (in Turkish).

COMPARISON OF RAINFALL USING DIFFERENT RADARS

Burak Bozkurt[1], Aysel Yılmaz[2]
1 Turkish State Meteorological Service Remote Sensing Department, bbozkurt@mgm.gov.tr
2 Gaziantep Airport Meteorological Service ayselyilmaz@mgm.gov.tr

Abstract
In this study, the rainfall estimations of three weather radars, X band mobile radar located in Ataturk Airport, C band radar located in Bursa and C band radar located at Istanbul-Çatalca are compared with ground rainfall observations. Three AWOS sites in Istanbul, Yalova and Tekirdağ are used in this study and there are three collocated gauges installed at each sites. The aim of study is to compare rainfall estimates of three radars with these ground observations for different rain cases. The results show that R-K_{DP} works better during convective type of rain like this case used in this study. Due to higher reflectivity, Marshall-Palmer Quantitative Precipitation Estimation (QPE) gives greater values for convective rains. On the other hand, using R-K_{DP} QPE is more useful for stratiform rains rather than using Marshall-Palmer (Z-R) QPE. Finally, radar altitude and beam blockage are main reasons lower radar measurement comparing with ground observation.

Keywords: *Weather radars, reflectivity, rain gauges*

Introduction
Meteorological radars do not estimate rainfall directly. Instead of this, they measure some parameters for instance reflectivity (Z), differential reflectivity (Z_H[3]/Z_V[4]), differential phase (PhiDP) and specific differential phase (K_{DP}). Quantitative Precipitation Estimation (QPE) can be estimated by means of one of these parameters or combination of these parameters. In this study Marshall-Palmer (MP) Z-R relationship (both X band and C band) and Pruppacher and Beard specific differential phase-rainfall (R-K_{DP}, for C band) and Ryzhkov-Zrnic specific differential phase-rainfall (R-$K_{DP,}$ for X band) relationship is used to estimate rainfall.

Data and Methods
Quantitative Precipitation Estimation is computed according to following formulas:

$Z=a*R^b$
$R(K_{DP})=a*(K_{DP})^b$
[5]

Table 1.Coefficient and Algorithm

coefficient	Marshall and Palmer (Z-R both X Band and C Band)	Pruppacher and Beard (R-KDP for C Band)	Ryzhkov and Zrnic (R-KDP for X Band)
a	200	18,87	17,38
b	1,6	0,835	0,79

Findings and Argument
Table 2 depicts that the comparison of three collocated gauge with 24 hours radar rainfall totals. G1, G2, G3 are collocated gauges located at a site. R-K_{DP} estimations are not available for Istanbul radar since the radar is single polarization.

[3] Horizontal Reflectivity
[4] Vertical Reflectivity
[5] While a and b are coefficient, R represents rainfall

Table 2.Rain gauge-Radar Rainfall

Date	23.10.2015					
Station	G1	G2	G3	Radar	RN24-RZ	RN24-RK_{DP}
Şişli	58,20	48,84	48,40	Mobile	2,78	28,64
				Bursa	18,44	25,36
				Istanbul	9,44	NA
Arnavutköy	60,60	65,82	64,80	Mobile	1,50	24,74
				Bursa	17,98	30,15
				Istanbul	6,84	NA
Anadolu Feneri	41,00	38,00	47,20	Mobile	1,445	13,95
				Bursa	10,91	14,16
				Istanbul	6,728	NA
Beykoz	61,20	61,24	56,20	Mobile	1,500	19,66
				Bursa	15,37	16,95
				Istanbul	8,66	NA
Sancaktepe	42,80	42,80	41,60	Mobile	7,13	19,52
				Bursa	11,18	21,41
				Istanbul	7,983	NA
Silivri	16,00	15,94	17,00	Mobile	0	0
				Bursa	12,05	38,38
				Istanbul	6,02	NA
Umraniye	0,00	35,84	35,60	Mobile	2,12	13,10
				Bursa	11,59	21,46
				Istanbul	6,51	NA
Uskudar	61,40	60,28	62,8	Mobile	1,44	21,66
				Bursa	15,37	24,07
				Istanbul	9,26	NA
Termal	54,50	59,43	55,20	Mobile	10,59	27,35
				Bursa	14,04	34,77
				Istanbul	10,75	NA
Saray	18,00	17,08	0,6	Mobile	0	0
				Bursa	8,87	28,34
				Istanbul	4,55	NA

In addition, Constant Altitude Plan Position Indicator (CAPPI) products of Mobile and Bursa Radar are given Figure 1 and Figure 2 on 05.02.2016. It is important that CAPPI heights are the equal. Due to altitude and condition of mobile radar, it could not be detected echoes around to Trakya region. (beam blockage effect)

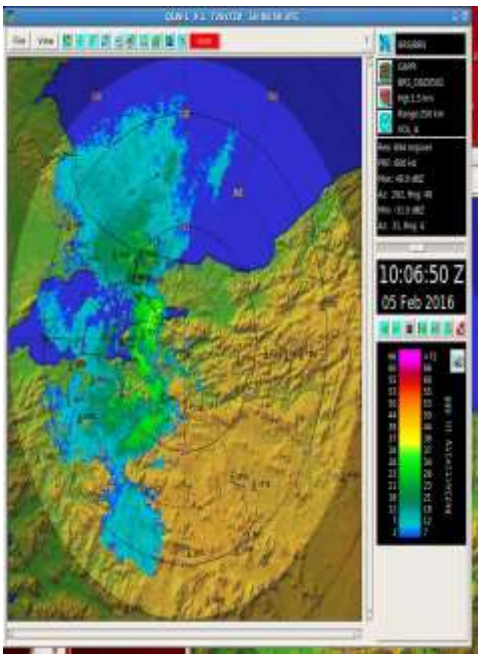

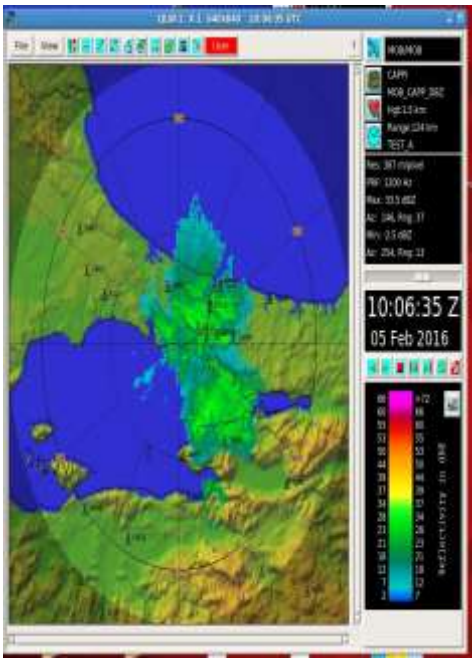

Figure 1.Bursa Radar CAPPI Product Figure 2.Mobile Radar CAPPI Product

During convective precipitation there is a large vertical mobility in atmosphere. It is observed high reflectivity as hail and thunderstorm. However, depending on shape of hydro meteor specific differential phase (K_{DP}) is near to zero degree/km. So Marshall-Palmer reflectivity-rain distribution provide over estimate values than surface estimation. When it is looked cross section products in weather radars, there are high reflectivity values in several heights.

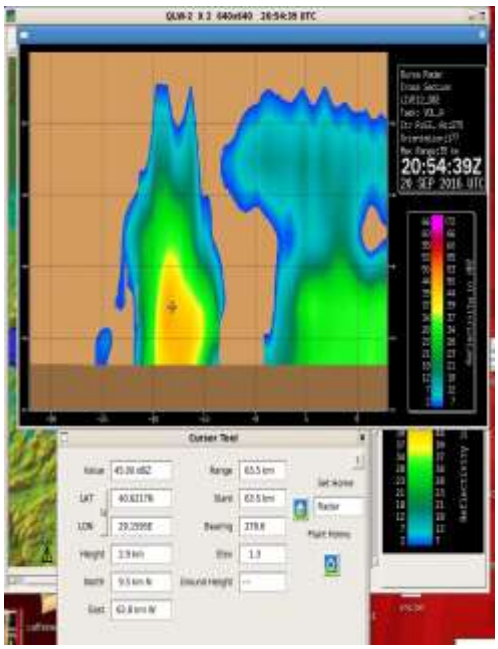

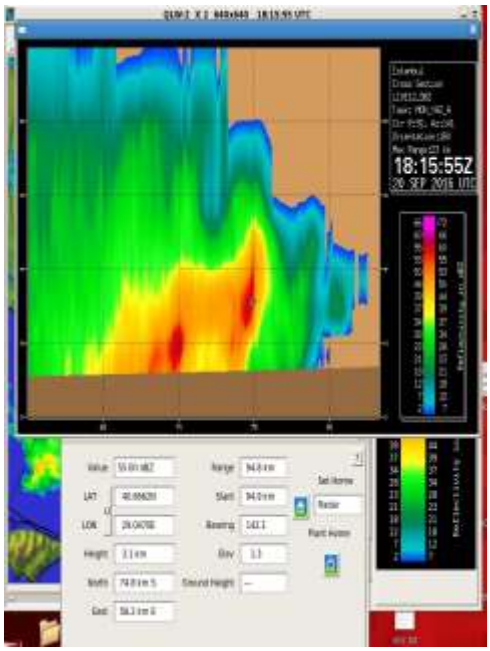

Figure 3.Bursa Radar Cross-Section Figure 4.İstanbul Radar Cross-Section

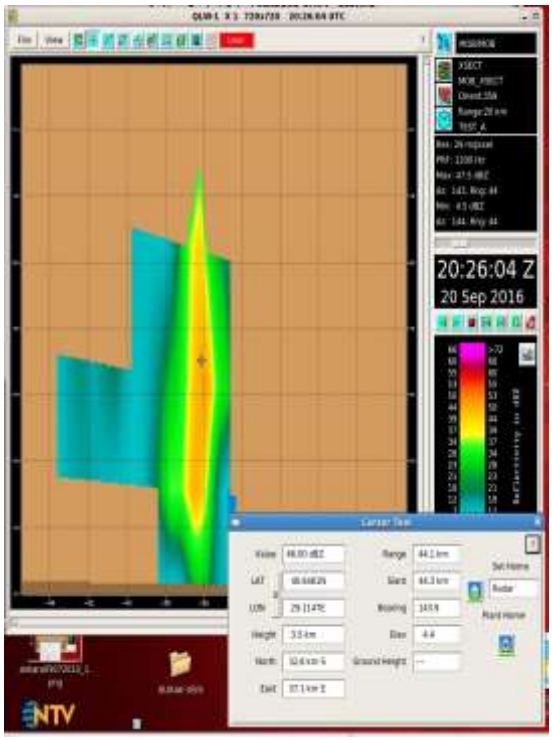

Figure 5.Mobile Radar Cross-Section

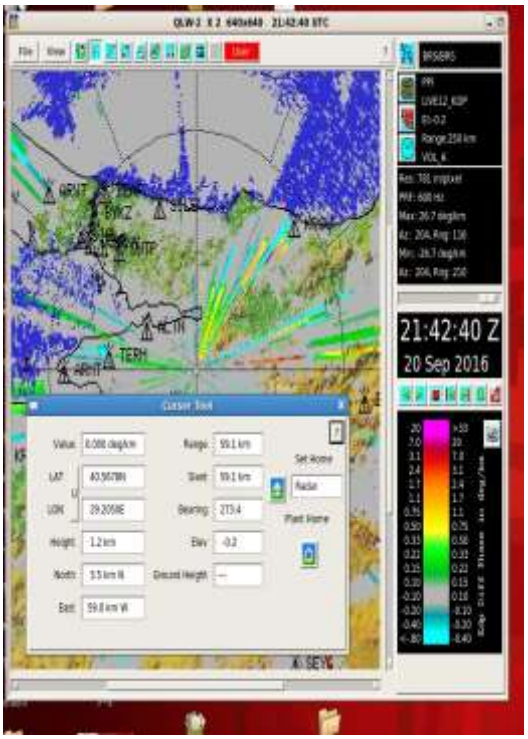

Figure 6.Bursa Radar K_{DP} Product

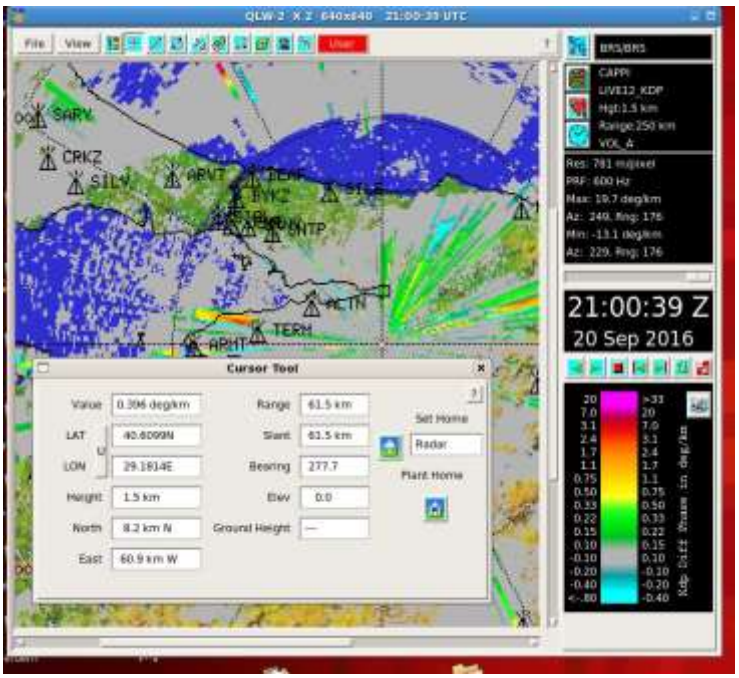

Figure 7. Bursa Radar CAPPI K_{DP}

Conclusion and Recommendation

According to this result, it is stated that the reason of the difference between two CAPPI products is beam blockage by terrain especially around Silivri, Tekirdağ regions and vicinities. Table 2 shows that there are significant differences between rain gauges and radar MP estimates (Istanbul and Mobile). Mobile radar is located at 40 m above MSL while Bursa radar is at 1239 m. Mobile radar is affected by beam blockage and attenuation. Even though R-K_{DP} estimator is also underestimates rain, the bias is less than MP estimator. The results show that

$R\text{-}K_{DP}$ works better during convective type of rain like this case used in this study. At some stations like Silivri and Saray, Bursa $R\text{-}K_{DP}$ overestimates. Because of range (the distance from Bursa Radar is approximately 190 km), change of PhiDP is greater than close stations to Bursa radar. Far away regions from radar, the quality of K_{DP} is getting decrease. In convective cases like hail and thunder storm, depending on mixed structure and melting ice crystal in hail, reflectivity is much higher. Therefore Marshall-Palmer reflectivity-rain QPE provide over estimate values especially in C band radars. Change of propagation speed of radar beams is also less than convective rain like hail. So K_{DP} values are near to zero deg/km. On the other hand, especially for X band radars, $R\text{-}K_{DP}$ estimates provide better results because of immune to attenuation and partial beam blockage.

References

H. Paulitsch, F. Teschl, and W.L. Randeu: Dual polarization C-band weather radar algorithms for rain rate estimation and hydrometeor classification in an alpine region

Marios N. Anagnostou, John Kalogiros, Emmanouil N. Anagnostou, Michele Tarolli, Anastasious Papadopoulos, Marco Borga: Performance evaluation of high resolution rainfall estimation by X band dual polarization radar for flash flood applications in mountainous basins

COMPARISON OF MONTHLY TRMM AND GROUND-BASED PRECIPITATION DATA IN AKARCAY BASIN, TURKEY

Emin Tas
Afyon Kocatepe University, emintas@aku.edu.tr

Abstract
The accurate representation of spatial precipitation is crucial for hydrological studies. The spatial precipitation is also a fundamental input data for distributed hydrological models. The accuracy and precision of the spatial precipitation affect performance of hydrological model. In many parts of the world, ground observation networks are insufficient to represent the spatial precipitation because gauge stations can not be established in everywhere it is necessary due to economic, geographical and so on reasons. Interpolation techniques which enable to obtain the spatial distribution from point measurements have also some limitations caused by scarcity and bad quality of data. Satellite-derived precipitation products are recently used in many estimation studies of the spatial precipitation. In this study, TRMM (Tropical Rainfall Measuring Mission) multi-satellite rainfall product 3B43, launched by NASA (National Aeronautics and Space Administration) and JAXA (Japan Aerospace Exploration Agency) is compared with ground-based observations for Akarcay Basin, Turkey on monthly and seasonal time scales. Performance criteria such as coefficient of correlation (R), RMSE (Root Mean Square Error), MAE (Mean Absolute Error) and BIAS are performed in validation of TRMM. The objective of this study is to evaluate the suitability of using high spatial resolution TRMM remote-sensed data to complement and/or be alternative to gauge-based data in the Akarcay Basin. Estimation of precipitation in sparse-gauged/ungauged areas is one of main motivations of this paper.

Keywords: *TRMM 3B43, multisatellite-derived precipitation, ground-based evaluation, spatio-temporal analysis, GIS.*

INTRODUCTION
Due to precipitation is a basic input for many hydro-meteorological studies, accurate and consistent representation of spatial precipitation by using satellite derived products besides of interpolation techniques is very important because of limited and insufficient rainfall stations. For spatiotemporal and multidimensional analysis of precipitation, satellite based products are frequently considered in recent years. Within the scope of this study, TRMM satellite based product is considered at monthly and seasonal time scales in ground based evaluation in Akarcay basin, Turkey.

In worldwide, many studies have been carried out on comparison of TRMM and ground observations (Fisher and Huffman, 2001; Nicholsan et al., 2003; Islam and Uyeda, 2007; Nair et al., 2009; Karaseva et al., 2012; Xue et al., 2013; Nastos et al., 2016). Barros and et al. (2000) studied 1999 monsoon rainfall in a mountainous region of Nepal using TRMM and rain gauge observations. It was stated that TRMM has more consistency at low altitude stations in comparison of at high altitude ones. Shin et al. (2001) compared monthly precipitation derived from different TRMM components. In addition, comparison studies with other data types such as radar, PERSIANN, CMORPH, IMERG and ECMWF besides of rainfall stations have been practiced. (Rahman et al., 2012; Ioannidou et al., 2016; Katiraie-Boroujerdy et al., 2017; Kim et al., 2017; Wehbe et al., 2017; Alijanian et al., 2017). Furthermore, validation of TRMM as main input data has been tested in hydrological modeling applications in some works (Collischonn et al., 2008; Meng et al., 2014). Kumar et al. (2017) assessed suitability of TRMM by driving a distributed hydrological model and improved TRMM performance by

combination with rainfall station data. It was pointed out that bias correction is essential for TRMM with higher degree of accuracy. There are also so many studies on increasing of TRMM performance by using some techniques such as calibration, combining, correction and downscaling (Yin et al, 2008; Immerzeel et al., 2009; Almazroui, 2011; Fang et al., 2013; Liu et al., 2017).

Although there are a few studies done on TRMM in Turkey (Soytekin, 2010; Ozcan et al., 2013; Yilmaz, 2017; Donmez and Tekeli, 2017; Yilmaz et al., 2017), in Akarcay basin which has high agricultural potential and drought risk, this is first study according to the author's knowledge. In this respect, this study is considerable. The objective of this study is to evaluate the suitability of using high spatial resolution TRMM remote-sensed data to complement and/or be alternative to gauge-based data in the Akarcay basin. Estimation of precipitation in sparse-gauged/ungauged areas is one of main motivations of this paper.

MATERIALS AND METHODS

This study is applied in semi-arid Akarcay closed basin (Fig. 1) which includes river basins of Eber and Aksehir Lakes, ecologically wetlands of international importance in the western of Turkey. These lakes are protected under the Ramsar Convention. A large part of the basin is located within borders of Afyonkarahisar province. The basin has an area of 7993 km^2 and ranges in altitude from 905 to 2561 m with a mean elevation 1207 m and a mean slope % 10. Approximately 40% of the basin area is the plain area. Sultan mountains in southeast of the basin are important mountainous areas. The main land cover types are agricultural (% 42) and pasture (% 28). Mean annual runoff volume of the basin is 0,49 km^3. Main river of the study basin is Akarcay whose average discharge is 6 m^3/s (at outlet to Eber Lake) with a max observed stream flow 165 m^3/s that is obtained from General Directorate of State Hydraulic Works of Turkey. The slope of main stream channel is % 2. Annual mean total precipitation and annual mean temperature are respectively about between 400-450 mm and 11 ^oC that are derived from meteorological stations of Turkish State Meteorological Service (Tas, 2017).

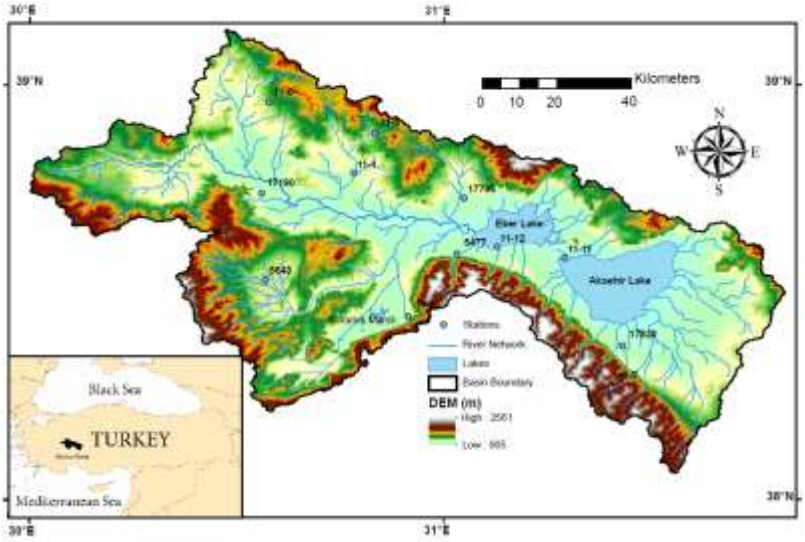

Figure 1. Geographical location of study area and position of rainfall stations

Observed monthly precipitation data of 12 meteorological stations (Table 1) located in study area is used for comparison. The stations have a range of elevation changing from 975 m to 1525 m. All of the stations except 11007 (highland station) are in lowlands. Mean monthly precipitation values of the stations are about between 30-60 mm. Observed maximum monthly

precipitation amounts change approximately from 130 mm to 440 mm. 11007 station located in Sultan mountains has more rainfall than the others.

Table 1. Used precipitation data of stations

Station		Altitude (m)	Period	Monthly precipitation (mm)				
No	Name			Min	Mean	Median	Max	Std. dev.
17190	Afyon	1034	1998-2014	0,2	37,7	32,1	151,7	28,8
17830	Aksehir	1010	1998-2010	0	43,9	37,0	298,3	39,8
17796	Bolvadin	1018	1998-2011	0,1	34,2	29,6	136,6	25,8
5477	Cay	1020	1998-2012	0	41,1	36,9	209,8	35,1
5643	Suhut	1130	1998-2005	0	37,0	31,0	132,1	30,1
11006	Bozhoyuk	1155	1998-2002	0	35,4	32,6	135,7	27,3
11007	Cankurtaran	1525	1998-2005	0	58,9	45,4	437,2	58,5
11012	Eber	975	1998-2010	0	30,8	24,2	136,6	26,2
11002	Kocbeyli	1065	1998-2010	0	46,7	37,9	216,8	40,3
11005	Seydiler	1150	1998-2003	0	34,5	32,6	135,7	27,0
11001	Seyitler	1060	1998-2009	0	26,5	23,9	104,0	22,3
11011	Taskopru	960	1998-2010	0	22,5	20,2	137,8	23,0

In this paper, TRMM (Period: 1998-2017-Spatial resolution: 0,25º), multi-satellite rainfall product 3B43, developed by NASA and JAXA is utilized for ground-based comparison. TRMM is the first space mission dedicated to measuring tropical and subtropical rainfall (50 º N-50 º S) through microwave and visible-infrared sensors, including the first space borne rain radar. TRMM provides information of 3D rainfall distribution (horizontal and vertical profile) over land as well as ocean. TRMM 3B43 product additively uses rain gauges for monthly rainfall estimation. 3B43 provides a best precipitation estimate in the TRMM region from all TRMM global data sources at each 1ºx1º grid (NASDA, 2001). As an example of TRMM raster data, gridded precipitation for 2017 April is given in Figure 2 that grid cell is about 25 km. Seasonal precipitation data is derived from TRMM with monthly temporal resolution.

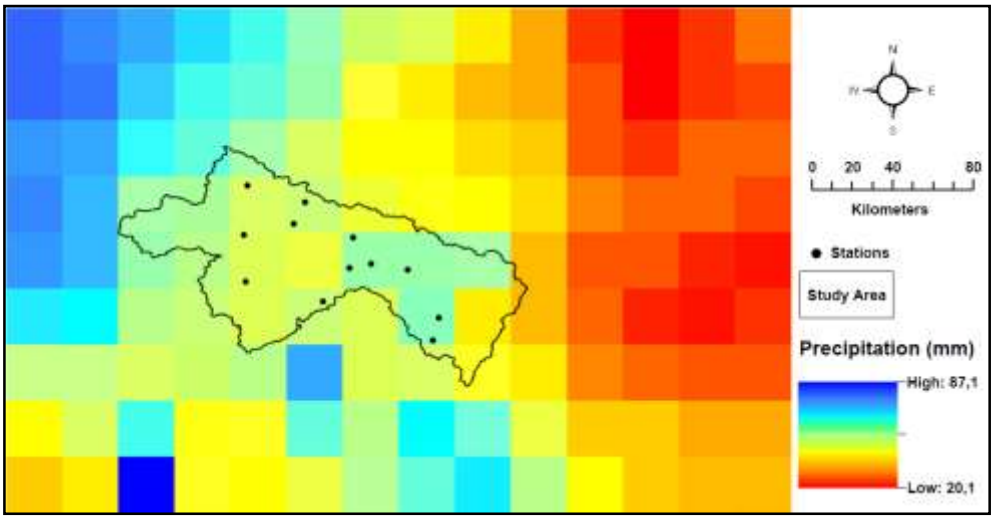

Figure 2. TRMM grids of 2017 April precipitation

In TRMM data processing, ArcGIS, a software of ESRI (Environmental Systems Research Institute, California) is used in this study. By building an iteration in GIS environment; downloaded TRMM data is transformed to convenient type of file for ArcGIS, clipped with Akarcay basin boundary, projected to appropriate coordinate system and extracted at station points for pixel based comparison.

TRMM is evaluated based on pixels-stations validation by comparison criteria R, R^2 (coefficient of determination), RMSE, MAE and BIAS. Performance criteria measure strength of statistical relationship between observed and predicted values. Pearson correlation coefficient is calculated as R that ranges from -1 to 1. Negative R values are in the meaning of inverse relationship in contrast with positive values. 0 value of R means that there is no relationship between variables. R^2 is proportion of observed data total variance explained by predicted data and calculates as square of R. RMSE, standard deviation of prediction residuals is used to analyze the errors. MAE is mean of the absolute errors while BIAS is mean of the errors. In evaluation process of sensitivity and suitability of TRMM, less RMSE, MAE and BIAS values mean better quality of estimation. Formulas of statistical performance benchmarks for validation are presented below:

$$R = \frac{\sum_{i=1}^{N}(O_i-\bar{O})(P_i-\bar{P})}{NS_O S_P} \quad (1)$$

$$RMSE = \sqrt{\frac{1}{N}\sum_{i=1}^{N}(P_i - O_i)^2} \quad (2)$$

$$MAE = \frac{1}{N}\sum_{i=1}^{N}|P_i - O_i| \quad (3)$$

$$BIAS = \frac{1}{N}\sum_{i=1}^{N}(O_i - P_i) \quad (4)$$

where P_i is the ith predicted value, O_i is the ith observation value, N is the total number of observations, $\bar{O}$ and $\bar{P}$ are respectively mean values of observed and predicted data. S_O and S_P respectively signify standard deviations of observed and predicted time series.

RESULTS

In Figure 3, observed data of 17190 rainfall station (longest observation period) versus TRMM data of related pixel are given. TRMM overestimated precipitation at this station as at other ones except a highland station in study area. At this station, TRMM caught the rainfall peaks better in recent years. Scatter diagrams of observed and TRMM data at monthly and seasonal scales are respectively showed in Figure 4 and 5. When looking at the scatter diagrams, high linear relationship between observed and TRMM is seen. Comparison results in terms of performance criteria are given in Table 2. Averages of R, R^2, RMSE, MAE and BIAS values based on stations are respectively 0,88; 0,77; 22,7; 17,0 and -11,6 at monthly scale; 0,91; 0,83; 51,5; 42,1 and -34,0 for seasonal data.

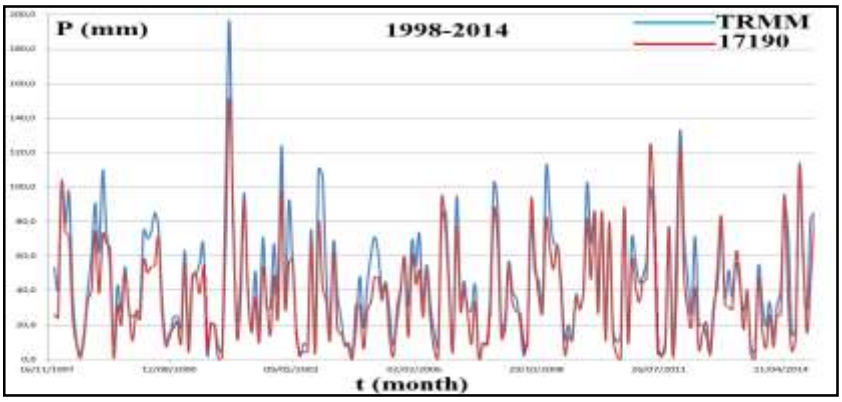

Figure 3. Monthly rainfall time series of 17190 station and TRMM during the period of 1998-2014

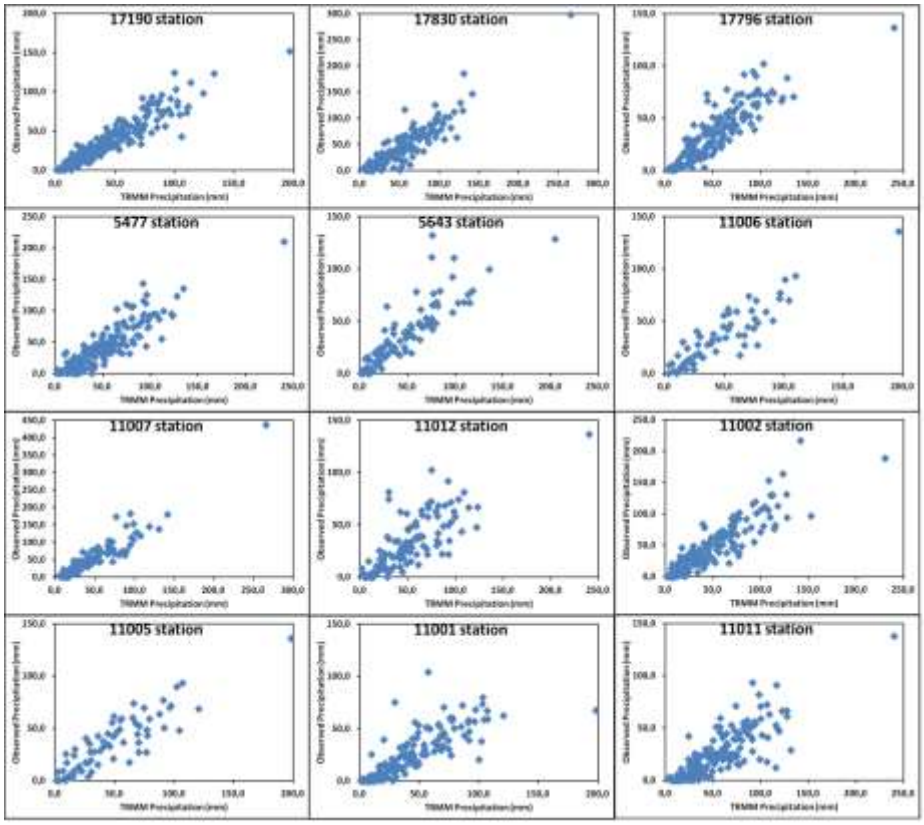

Figure 4. Scatter plots of observed versus TRMM data of monthly precipitation

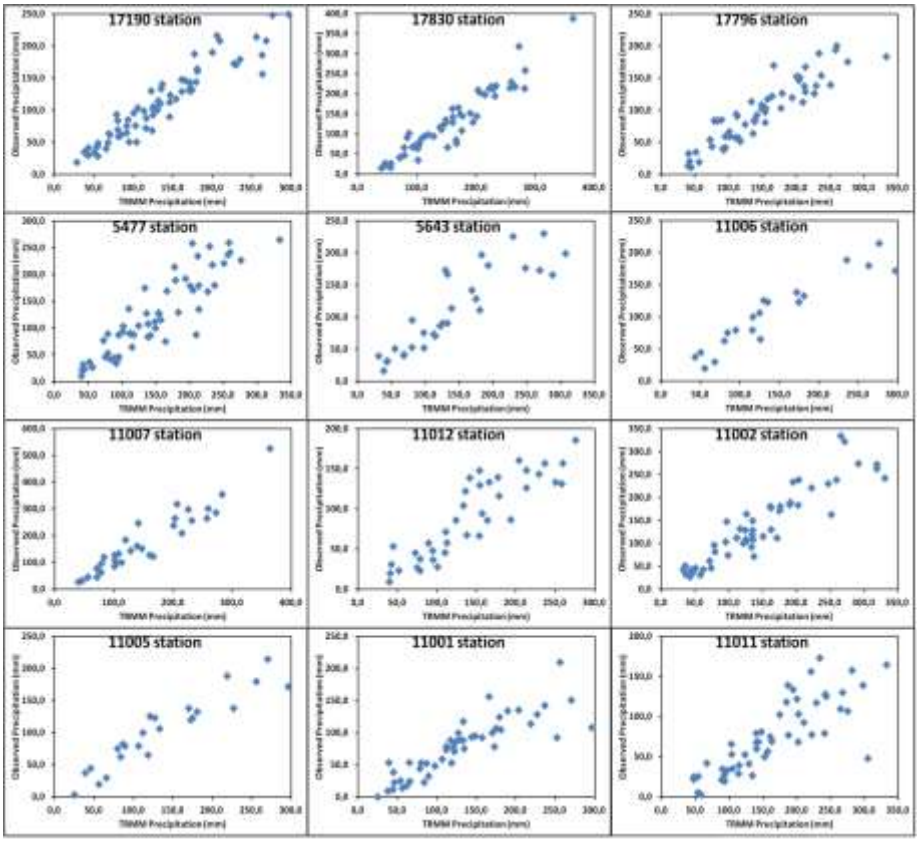

Figure 5. Scatter plots of observed versus TRMM data of seasonal precipitation

Table 2. Performance evaluation results in terms of statistical criteria

Station No	Monthly					Seasonal				
	Performance Criteria									
	R	R^2	RMSE	MAE	BIAS	R	R^2	RMSE	MAE	BIAS
17190	0,93	0,87	13,9	10,2	-8,2	0,95	0,90	32,6	25,7	-24,1
17830	0,91	0,83	18,8	14,1	-9,0	0,95	0,90	37,3	31,0	-27,1
17796	0,88	0,77	23,5	18,4	-17,0	0,92	0,84	58,2	50,1	-49,6
5477	0,90	0,80	17,7	13,8	-8,5	0,90	0,82	40,1	33,1	-25,1
5643	0,87	0,75	20,6	15,1	-10,2	0,89	0,79	47,6	37,8	-30,1
11006	0,90	0,82	20,1	15,4	-12,8	0,94	0,89	46,8	36,3	-36,3
11007	0,94	0,88	27,6	16,2	7,7	0,95	0,89	50,3	35,2	23,1
11012	0,79	0,62	28,6	22,1	-18,9	0,89	0,79	62,1	53,6	-53,2
11002	0,89	0,80	18,2	13,3	-2,8	0,92	0,85	32,7	24,5	-8,8
11005	0,89	0,78	20,8	15,5	-12,1	0,93	0,87	45,7	34,4	-34,0
11001	0,80	0,64	26,3	19,8	-17,9	0,86	0,75	64,3	53,7	-53,1
11011	0,82	0,67	36,3	30,2	-29,9	0,83	0,68	99,8	89,4	-89,4
Average	**0,88**	**0,77**	**22,7**	**17,0**	**-11,6**	**0,91**	**0,83**	**51,5**	**42,1**	**-34,0**

Spatial distribution of monthly and seasonal BIAS based on stations (Figure 6) are important in understanding of error characteristics.

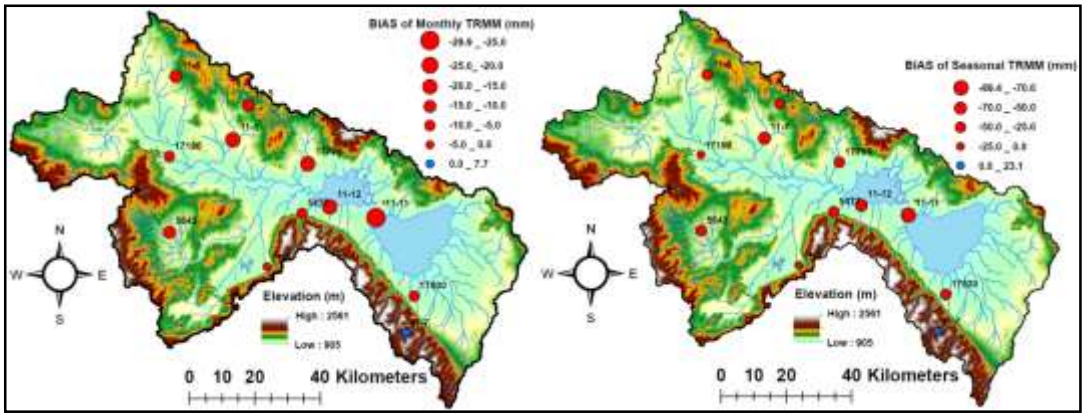

Figure 6. Map of BIAS based on stations

CONCLUSIONS AND RECOMMENDATIONS

In according to the results, it can be stated that although seasonal performance of TRMM is better than monthly performance, use of open access TRMM data is applicable for spatial precipitation at both monthly and seasonal scale in Akarcay basin. When looking at BIAS values, it is seen that TRMM is overestimated except 11007 station which has highest altitude. It can be a sign that TRMM generally underestimates in mountainous areas. R values are very close to 1 due to rainfall trend consistency of TRMM. Due to significance of using satellite based products besides of ground based data at specially ungauged areas in planning and management studies of water resources, evaluation of TRMM data is valuable in Akarcay basin which hasn't high density rainfall station network.

TRMM can be compared to other remote-sensed data such radar and IMERG, gauge-based data such APHRODITE and optimum interpolation method. Furthermore, it can be merged with different data types for better fit. TRMM can be also validated by inputting into a hydrological model in deference to model skills. Performance of TRMM can be increased by downscaling using geographical characteristics such as elevation and correction factor.

REFERENCES

Alijanian, M., Rakhshandehroo, G. R., Mishra, A. K. and Dehghani, M., 2017. Evaluation of satellite rainfall climatology using CMORPH, PERSIANN-CDR, PERSIANN, TRMM, MSWEP over Iran. Int. J. of Climatology, DOI: 10.1002/joc.5131.

Almazroui, M., 2011. Calibration of TRMM rainfall climatology over Saudi Arabia during 1998-2009. Atm. Res., 99, 400-414.

Barros, A. P., Joshi, M., Putkonen, J. and Burbak, D. W., 2000. A study of the 1999 monsoon rainfall in a mountainous region in central Nepal using TRMM products and rain gauge observations. Geophysical Research Letters, 27(22), 3683-3686.

Collischonn, B., Collischonn, W. and Tucci, C. E. M., 2008. Daily hydrological modeling in the Amazon basin using TRMM rainfall estimates. J. of Hydrology, 360, 207-216.

Donmez, S. and Tekeli, A. E., 2017. Comparison of TRMM-based flood indices for Gaziantep, Turkey. Nat. Hazards, 88(2), 821-834.

Fang, J., Du, J., Xu, W., Shi, P., Li, M. and Ming, X., 2013. Spatial downscaling of TRMM precipitation data based on the orographical effect and meteorological conditions in a mountainous area. Advances in Water Resources, 61, 42-50.

Fisher, B. L., and Huffman, G. J., 2001. Validation of TRMM satellite rainfall products over Oklahoma for a three year period (1998-2000). American Geophysical Union, Fall Meeting 2001.

Immerzeel, W. W., Rutten, M. M. and Droogers, P., 2009. Spatial downscaling of TRMM precipitation using vegetative response on the Iberian Peninsula. Remote Sensing of Environment, 113, 362-370.

Ioannidou, M. P., Kalogiros, J. A. and Stavrakis, A. K., 2016. Comparison of the TRMM precipitation radar rainfall estimation with ground-based disdrometer and radar measurements in south Greece. Atm. Res., 181, 172-185.

Islam, N. and Uyeda, H., 2007. Use of TRMM in determining the climatic characteristics of rainfall over Bangladesh. Remote Sensing of Environment, 108, 264-276.

Karaseva, M. O., Prakash, S. and Gairola, R. M., 2012. Validation of high-resolution TRMM-3B43 precipitation product using rain gauge measurements over Kyrgyzstan. Theor. Appl. Climatol., 108(1–2), 147-157.

Katiraie-Boroujerdy, P., Asanjan, A. A., Hsu, K. and Sorosshian, S., 2017. Intercomparison of PERSIANN-CDR and TRMM-3B42V7 precipitation estimates at monthly and daily time scales. Atm. Res., 193, 36-49.

Kim, K., Park, J., Baik, J. and Choi, M., 2017. Evaluation of topographical and seasonal feature using GPM IMERG and TRMM 3B42 over far-east Asia. Atm. Res., 187, 95-105.

Kumar, D., Pandey, A., Sharma, N. and Flügel, W., 2017. Evaluation of TRMM-precipitation with rain-gauge observation using hydrological model J2000. J. Hydrol. Eng., 2017, 22(5): E5015007.

Liu, X., Liu, F. M., Wang, X. X., Li, X. D., Fan, Y. Y., Cai, S. X. and Ao, T. Q., 2017. Combining rainfall data from rain gauges and TRMM in hydrological modelling of Laotian data-sparse basins. Appl. Water Sci., 7, 1487-1496.

Meng, J., Li, L., Hao, Z., Wang, J. and Shao, Q., 2014. Suitability of TRMM satellite rainfall in driving a distributed hydrological model in the source region of Yellow river. J. of Hydrology, 509, 320-332.

Nair, S., Srinivasan, G. and Nemani, R., 2009. Evaluation of multisatellite TRMM derived rainfall estimates over a western state of India. J. Meteorol. Soc. Japan, 87(6), 927-939.

NASDA, 2001. TRMM data users handbook. Japan.

Nastos, P. T., Kapsomenakis, J. and Philandras, K. M., 2016. Evaluation of the TRMM 3B43 gridded precipitation estimates over Greece. Atm. Res., 169, 497-514.

Nicholson, S. E., Some, B., McCollum, J., Nelkin, E., Klotter, D., Berte, Y., Diallo, B. M., Gaye, I., Kpabeba, G., Ndiaye, O., Noukpozounkou, J. N., Tanu, M. M., Thiam, A., Toure, A. A. and Traore, A. K., 2003. Validation of TRMM and other rainfall estimates with a high-density gauge dataset for West Africa. Part II: Validation of TRMM rainfall products. J. Appl. Meteorol. Climatol., 42(10), 1355-1368.

Ozcan, O., Musaoglu, N., Bookhagen, B. and Ormeci, C., 2013. Uydu ve yersel yağış verilerinin noktasal frekans analizi ile mekansal değerlendirmesi. TMMOB Coğrafi Bilgi Sistemleri Kongresi, 11-13 Kasım, Ankara.

Rahman, M., Arya, D. S., Goel, N. K. and Mitra, A. k., 2012. Rainfall statistics evaluation of ECMWF model and TRMM data over Bangladesh for flood related studies. Meteorological Applications, 19, 501-512.

Shin, D., Chiu, L. S. and Kafatos, M., 2001. Comparison of the monthly precipitation derived from the TRMM satellite. Geophysical Research Letters, 28(5), 795-798.

Soytekin, A., 2010. Evaluating the use of satellite-based precipitation estimates for discharge estimation in ungauged basins. M. Sc. Thesis of METU, Ankara.

Tas, E., 2017. Comparison of areal precipitation estimation methods in Akarcay basin, Turkey. International Symposium on GIS Applications in Geography&Geosciences, 18-21 Oct, Canakkale.

Wehbe, Y., Ghebreyesus, D., Temimi, M., Milewski, A. and Mandous A. A., 2017. Assessment of the consistency among global precipitation products over the United Arab Emirates. J. of Hydrology: Regional Studies, 12, 122-135.

Xue, X., Hong, Y., Limaye, A. S., Gourley, J. J., Huffman, G. J., Khan, S. I., Dorji, C. and Chen, S., 2013. Statistical and hydrological evaluation of TRMM based multi-satellite precipitation analysis over the Wangchu basin of Bhutan: Are the latest satellite precipitation products 3B42V7 ready for use in ungauged basins? J. Hydrol., 499, 91-99.
Yilmaz, M., 2017. Konya kapalı havzası'nın TMPA uydu kaynaklı yağış verileri ile kuraklık analizi. J. of the Faculty of Engineering and Architecture of Gazi University, 32: 2, 541-549.
Yilmaz, M., Amjad, M., Bulut, B. and Yilmaz, M. T., 2017. Uydu kaynaklı yağmur verilerinin hata oranlarının deniz kıyılarına olan uzaklığa bağlı analizi. İMO Teknik Dergi, 7993-8005.
Yin, Z., Zhang, X., Liu, X., Colella, M. and Chen, X., 2008. An assessment of the biases of satellite rainfall estimates over the Tibetan Plateau and correction methods based on topographic analysis. J. of Hydrometeorology, 9, 301-326.

REGIONAL EFFECTS OF CARBONDIOXIDE EMISSION IN THERMAL POWER PLANTS

Evren Özgür[1], Orhan Şen[1], and Fırat Oğuz Edis[2]
[1]*Istanbul Technical University, Faculty of Aeronautics and Astronautics, Department of Meteorological Engineering, Maslak, Istanbul, Turkey*
[2]*Istanbul Technical University, Faculty of Aeronautics and Astronautics, Department of Astronautical Engineering, Maslak, Istanbul, Turkey*
ozgurev@itu.edu.tr

Abstract
There is a continuous transformation between main carbon sources. Carbon dioxide is transmitted to the atmosphere through respiration and decay of plants and settled there. Then, it returns back to the soil within plants body. The exchange between the atmosphere and the oceans are based on sea surface temperature and oceanal transformation. Slow changes in the oceanic transformation, such as southern oscillations, may result in long term changes in the atmospheric concentration. Human interventions such as agricultural activities and industrial production unbalance the system and increase the rate of carbondioxide in the atmosphere. All amount of the CO_2 will not accumulate in the atmosphere. Some part will accumulate in forests by photosynthesis, while a part of CO_2 will kept by tree bodies. In addition, some part of carbondioxide will accumulate by the oceans. The rate of carbon dioxide continues to increase due to human resources in the atmosphere and it is predicted that it will cause an increase in temperature. Temperature observation records verified this situation. Apart from the effects of the pollutants in the stack gas, the thermal power plants have an effect as waste heat. When it is thought as a global effect, it is necessary to investigate the CO_2 concentration which is the most important greenhouse gas. The relative effect of waste heat from thermal power plants is calculated by increasing soil and water temperatures. A portion of 168 W/m^2 of 342 W/m^2 of solar energy coming from the sun is absorbed by the Earth. A 128 W/m^2 part is dispersing in the atmosphere as heat. The warming effect of greenhouse gases is calculated as 2.9 W/m^2. This value is about 2% of the energy that the Earth diffuses. World energy consumption in 2010 was 2.482 x 10^{20} J. This value includes renewable and fossil fueled thermal power plants. At the end of this, the portion in global warming is 0.0064 °C. In the study, a regioanl effect of a thermal power plant located in Çanakkale was investigated. Calculated fluids dynamics analysis has been applied in order to present the effect of hot gases emitted from the stack. Dominant wind directions were considered in calculations. The specified wind speeds were accepted as average wind speeds of 10 m height. The increase of wind speed with elevation in atmospheric boundary layer was modeled. If it is considered to operate 7500 hours a year, the amount of CO_2 released to the the atmosphere per year of the year will be 10.37 x 10^6 Tons/year for the thermal power plant.

Keywords: *CO_2, Air pollution, fluid dynamics, thermal power plants.*

INTRODUCTION
The amount of carbondioxide in the atmosphere has been increased in last years and it will continue to increase in near future. The temperature observation records were verified this situation (Sen, 2015). Figure 1 shows the time series of monthly averages of carbondioxide in Mauna Loa station. The amount of carbondioxide in May 2017 was 409,65 ppm while it was 407,70 ppm in one year ago.

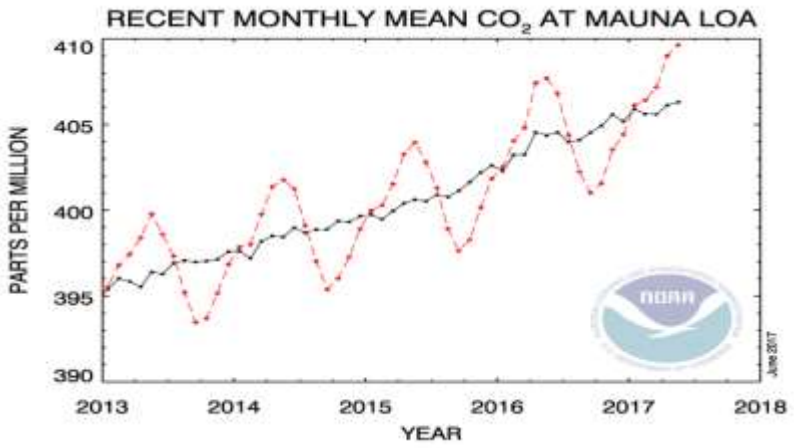

Figure 1. Monthly average CO_2 values for Mauna Loa station in 2013-2017 (http://www.esrl.noaa.gov/).

DATA AND METHODOLOGY

In the study, daily maximum wind data of Çanakkale station were used with the year of 2014 (MGM, 2015). After making analysis, it was revealed that 2014 was reference year for wind speed calculations. By using daily data, yearly wind rose was obtained in order to use in modeling applications. Figure 2 shows the yearly wind rose of Çanakkale meteorology station.

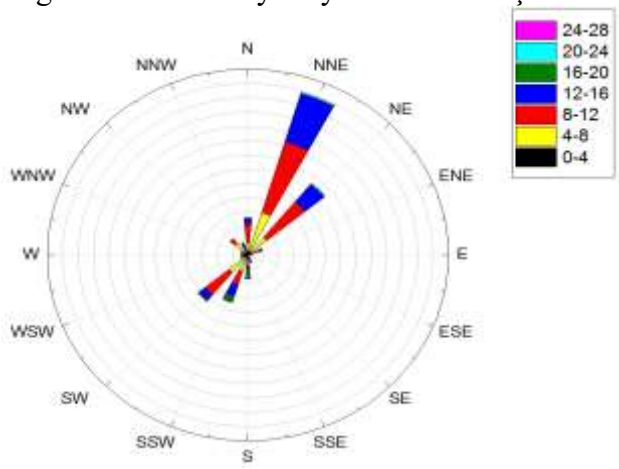

Figure 2. Yearly wind rose of Çanakkale for 2014

The first dominant wind direction was NNE with 10,37 m/s average value and 119 times. The second and third dominant wind directions were NE and SW with 10,28 m/s and 9,25 m/s averages, respectively. The maximum daily wind speed was 25,3 m/s in 2014.

In order to define the regional effects of CO_2 released from power plant stack, it was assumed that the gas discharged from the stack spread to a centrally located half sphere area as shown in Figure 3 (Zevenhoven and Beyene, 2011). The fresh air enters the half spherical space continuously and mixes with the gases released from the stack. If the average path taken by the wind to exit half a cube is considered to be the half-radius height shown in Figure 3, the time required to take that distance can be calculated by the equation (1).

$$\tau = \frac{R \cdot \sqrt{2}}{v_{wind}} \quad [s] \qquad (1)$$

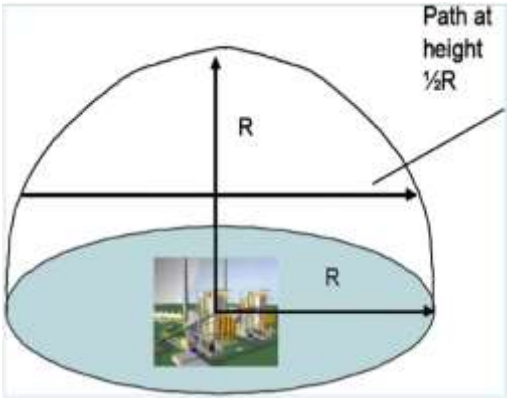

Figure 3. A half spherical area with power plant centered (Zevenhoven and Beyene, 2011).

The average mass concentration of CO_2 in the half-sphere region of the mixture of fresh air from the outside with the wind and the gases extracted from the blast can be found with the help of the equation (2).

$$c_{mass}(R) = c^{o}_{mass} + \frac{\dot{m}_{CO_2} \cdot \tau}{volume\ of\ half\ sphere}$$
$$= c^{o}_{mass} + \frac{\dot{m}_{CO_2} \cdot R \cdot \sqrt{2}}{v_{rüzgar} \cdot (2/3) \cdot \pi \cdot R^3} \quad [kg/m^3] \qquad (2)$$

where, $c_{mass}(R)$ is average mass CO_2 concentration, c^{o}_{mass} is fresh air mass CO_2 concentration, $\dot{m}_{CO_2}$ is mass flow of CO_2 gas release from the stack and τ is the average exit time of the wind from half sphere (Myre et. Al, 1998).

RESULTS

In order to obtain the effects of hot gases release from the stack, calculated fluid dynamics analysis were applied. Dominant wind directions for 10 m height were used to make calculations. Increments of wind speeds with increasing height were modeled in atmospheric boundary layer. The calculated values of CO_2 emissions in Karaburun Power Plants for different wind speeds and different radius are shown in Table 1. The third column is the amount of increments in carbondioxide concentrations from reference value as ppm. The other columns express the radiative forcing and near region radiative forcing, respectively. CO_2 flow was used as 293,2 kg/s in calculations. The normal value of CO_2 concentrations was accepted as 403 ppm-vol.

Table 1. Calculated values of CO_2 emissions in Karaburun Power Plants for different wind speeds and different radius.

Wind Speed (m/s)	Radii of power plant centered half sphere (R), km	Amount of increase in CO_2 concentration from reference value (ppm-vol)	Radiative forcing (W/m^2)	Near region radiative forcing (MW)
3.7	5	1.08261009	0.0429	3.37277813
	10	0.27065252	0.0108	3.38294398
	20	0.06766313	0.0027	3.38549822
10.37	5	0.38627361	0.0154	1.20651091
	10	0.09656840	0.0038	1.20781066
	20	0.02414210	0.0010	1.20813618
25.3	5	0.15832638	0.0063	0.49494545
	10	0.03958159	0.0016	0.49516412
	20	0.00989540	0.0004	0.49521883

The stacks of power plants are seperate, however; they are located in a bigger stack that covers both of them. In the analysis carried out in this study, the values of stack wastes and pollutant emission values were considered as the sum of two stacks.

REFERENCES

http://www.esrl.noaa.gov/gmd/webdata/ccgg/trends/co2_

MGM, (2015): Turkish State Meteorological Service, Ankara.

Myhre, G., Highwood, E.J., Shine, K. P., and Stordal, F. (1998): New estimates of radiative forcing due to well mixed greenhouse gases. Geophysical Research Letters, 25(14):2715-8.

Sen, O. (2015): Air Pollution Meteorology Lecture Notes, Istanbul Technical University, Department of Meteorological Engineering, Maslak, İstanbul.

Zevenhoven, R. and Beyene, A. (2011): The relative contribution of waste heat from power plants to global warming. Energy 36 (2011) 3754-3762.

ACTIVITIES ON EASTERN MEDITERRANEAN CLIMATE CENTER

Başak Yazıcı[1], Serhat Sensoy[1], Mesut Demircan[1], Hüdaverdi Gürkan[1], Ali Ümran Kömüşcü[1]

[1]Turkish State Meteorological Service, Ankara, Turkey

byazici@mgm.gov.tr, ssensoy@mgm.gov.tr, mdemircan@mgm.gov.tr, hgurkan@mgm.gov.tr, aukomuscu@mgm.gov.tr

Abstract

Improved climate monitoring and prediction services are very important for priority sectors including water, agriculture, health, energy and disaster risk reduction. In order to strengthen climate studies in the international level, Turkish State Meteorological Service (TSMS) took the initiative and established Eastern Mediterranean Climate Centre (EMCC) running under the Network of Regional Climate Centers (RCC) in RA VI which was built by WMO. The EMCC started to service in June, 2009 in an English website at: http://www.emcc.mgm.gov.tr. Targeted countries were determined in coordination with WMO as Greece, Turkey, Cyprus, Syria, Israel, Palestine, Lebanon, Jordan and Egypt where they are located in between 21.00°-43.00° north latitude and 19.00°-45.00° east longitude geographic coordinates. The products offered on the website are: Monthly and seasonal temperature and precipitation forecast, Climate monitoring for 2m temperatures (TT) and precipitation rates (RR), The Eastern Mediterranean Dataset and Climate watch advisories. EMCC web site contents will be enhanced step by step in order to help the sectors for making decisions or taking measures beforehand for reducing possible risks.

Keywords: *EMCC, RCC, Climate services, seasonal forecast*

INTRODUCTION

Climate monitoring and prediction is critical especially for sectors of water, agriculture, health, energy and disaster risk reduction. The World Meteorological Organization (WMO) framework has grown to include improving the National Meteorological and Hydrological Services (NMHSs) capabilities for producing up-to-date climate products for climate services, most importantly for climate adaptation and risk management (URL 1). Following the El Nino event of 1997/98 Regional Climate Center (RCC) idea was arised and an Intercommission Task Team on Regional Climate Centers elaborated a first framework for WMO *(RA VI RCC Network Implementation Plan)* (URL 2). The RA VI RCC Network in its initial phase consists of 3 nodes. RA VI RCC node on climate data; RA VI RCC node on climate monitoring, RA VI RCC node on Long-range Forecasting. Under Network of Regional Climate Centers (RCC) in RA VI Turkish State Meteorological Service established Eastern Mediterranean Climate Centre (EMCC) in order to improve the climate studies internationally (Sensoy et al, 2014). EMCC provides climate monitoring and prediction services by using data from TSMS, ECMWF and JMA, and producing monthly and seasonal maps of temperature and precipitation.

DATA AND METHODS

The data for producing monitoring maps are obtained both from National Oceanic and Atmospheric Administration (NOAA), (URL 3) and also Japan Meteorological Agency (JMA), (URL 4). Data for producing seasonal prediction of temperature and precipitation is obtained from ECMWF MARS Catalogue.

APPLICATION AND RESULTS

Monitoring maps are produced with the data taken from NOAA or JMA by using ArcGIS. These maps include 2m temperature and precipitation rates, and they are published on EMCC website, available for public use.

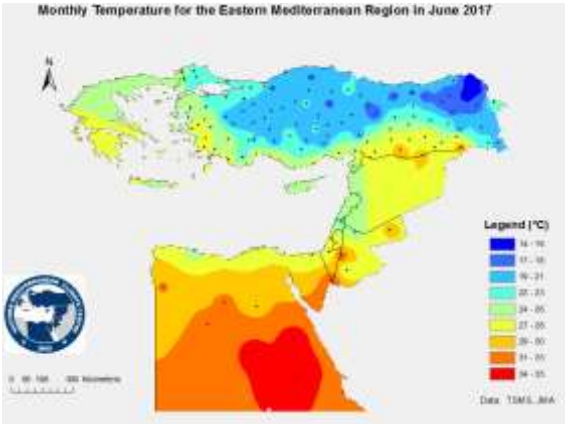

Figure 1. Monthly temperature for the Eastern Mediterranean Region in June 2017

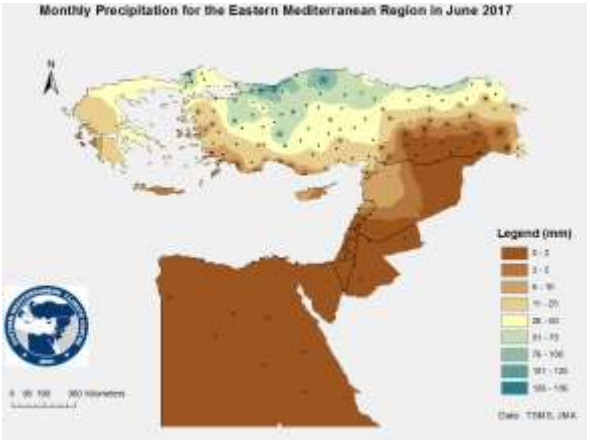

Figure 2. Monthly precipitation for the Eastern Mediterranean Region in June 2017

Figure 1 and 2 show monthly temperature and precipitation maps for June 2017.2m temperature and precipitation rate anomaly forecast data is being downloaded from ECMWF by selecting coordinates of N43, W19 S21 and E45 in 0.125°*0.125° resolution.

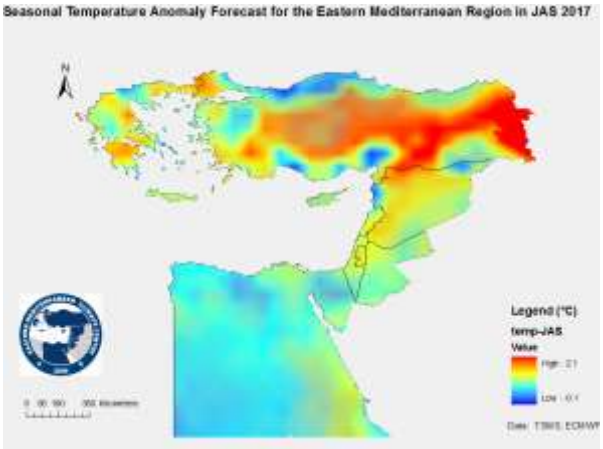

Figure 3. Seasonal temperature anomaly forecast for the Eastern Mediterranean Region in July- August-September 2017

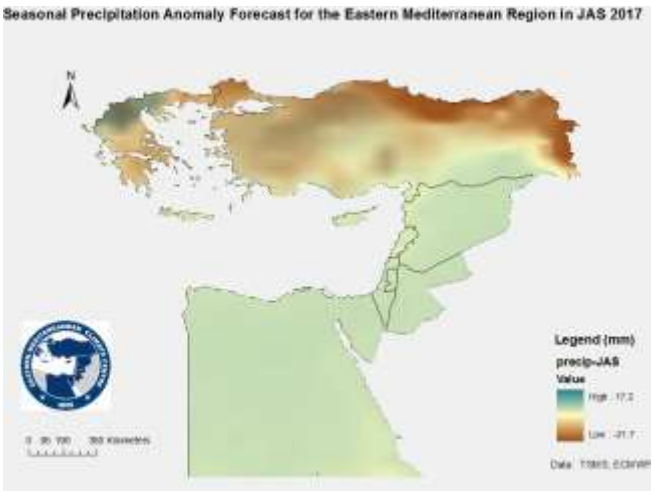

Figure 4. Seasonal precipitation anomaly forecast for the Eastern Mediterranean Region in July- August-September 2017

Figure 3 and 4 show three-month-anomaly forecasts for 2m temperature and precipitation anomalies.

CONCLUSIONS AND RECOMMENDATIONS

Adaptation to climate changes is very important for governments and sectors. Certain measures must be taken in order avoid socio-economical losses. The EMCC website also provide climate watch advisories for expected heat waves, floods and droughts in ordered to take proactive precaution. Therefore it is necessary to improve our skills and capabilities on climate studies. EMCC also aims to provide improved long range forecast products with further studies on this subject.

REFERENCES

Sensoy, S., Demircan, M., Ekici, M., Yazıcı, B. 2014, Activities on Eastern Mediterranean Climate Center As a Node of WMO RA VI RCC Network, www.wmo.int/pages/prog/wcp/ccl/ccl16/teco/documents/ppt/TECO-Presentations-PDF/30-6-2014/Session1/1150-1210/2-Sensoy-Poster-quick-fire.pdf .

URL 1.http://www.wmo.int/pages/prog/wcp/wcasp/rcc/rcc.php, Access Date: 30.07.2017

URL 2. rcccm.dwd.de/DWD-RCCCM/EN/overview/documents/1_WMO-RAVI-RCC-Implementation-Plan-official-final-Version.pdf;jsessionid=FBBE936DD49361BA0C43859D3079CA3B.live11053?__blob=publicationFile&v=4 , Access Date: 30.07.2017

URL 3. http://www.esrl.noaa.gov/psd/cgi-bin/db_search/DBSearch.pl?Dataset=CDC+Derived+NCEP+Reanalysis+Products+Surface+Level&Variable=Air+Temperature&Statistic=Mean&group=0&submit=Search, Access Date: 25.07.2017

URL 4. http://ds.data.jma.go.jp/gmd/tcc/tcc/products/climate/climatview/frame.php , Access Date: 26.07.2017

INVESTIGATION OF POSSIBLE RADIOACTIVITY IN AEROSOL SAMPLES IN ISTANBUL

S. Levent Kuzu[1], Özgür Akçalıakçali[1], Arslan Saral[1]
[1]*Yildiz Technical University*
skuzu@yildiz.edu.tr, akcali@yildiz.edu.tr, saral@yildiz.edu.tr

Abstract
In this study, aerosol samples taken in 2011 spring season at Davutpasa were analyzed for potential excess radioactivity content. Fukushima Nuclear Power Plant explosion was occurred in March 2011. After a series of equipment failures, nuclear meltdowns, radioactive materials released to the environment. Although Istanbul is too far to be affected from the accident, aeroplanes were suspected to be possible carriers of radioactive materials. Aerosol samples were analyzed according to Neutron Activation Analysis (NAA). This method is one of the most commonly used techniques to detect components in trace amounts. By means of this technique, stable isotopes are rendered radioactive as a result of the neutron capture reaction or are already radioactive, but are rendered measurable by transforming nuclei with low activity due to high half life into nuclei with shorter half-life. Blank filter samples and soil samples were analyzed prior to aerosol analyzes. No significant difference was detected between the aerosol and background samples. Sampling point is not regarded to be affected from radioactivity of aerosol origin.

Keywords: *Aerosol, Neutron activation analysis, radiation*

INTRODUCTION
Radiation in living spaces is due to natural causes, as well as industrial or medical productions. In the absence of physical contact, the effects of gamma coalescence dominate, while alpha and beta emitters are effective when there is physical contact. Basically we are living in a basic radiation that is caused by potassium, thorium and uranium compounds, which are found in our life through cosmic occurrence or through the Earth's structure. The dose amount originating from these factors varies from region to region and the global average is 2.4 msV / y. Regional values can reach very high values, such as 131 mSv / y, as in Iran's Ramsar region. For this reason, making regional measurements, instead of using the average value, is of great importance in understanding the effects on the environment and the human (Mortazavi and Karamb, 2005; Hendry et al., 2009).

Various detectors use many naturally occurring or artificially produced radioisotopes in the manufacture of phosphorus paints in mining, medical imaging and treatment, thickness measurements, pipelines to control leakage, and lifetime of lighting materials (Martin, 2006). Although all of these resources are produced under controlled conditions, it is not possible to obtain complete waste treatment under controlled conditions. Lighting equipment, phosphorescence paints or products using such dyes, especially prepared for domestic use, are sent to urban waste centers.

MATERIALS AND METHODS
Direct gamma-spectroscopy measurements do not allow for the detection of very low activities due to the long half-lives of both natural and industrial radionuclides, although the amount of mass in the sample is low. In addition, the sample was insufficient to obtain information because of the identity of the region being sampled and the region being measured. For this reason, it was decided to utilize nuclear transmutation in order to determine the materials in the sample.

Neutron Activation Analysis (NAA) is one of the most commonly used techniques for detecting trace amounts of matter. By means of this technique, stable isotopes are rendered radioactive as a result of the neutron capture reaction or are converted into nuclei with lower activity due to the high half life as well as being already radioactive, with shorter half-lives. The basic requirement for using this technique is high flux neutron sources. These studies mostly done using nuclear reactors. A TRIGA MARK II Reactor was used in this study.

RESULTS AND DISCUSSION

Measurements of radioactivity inside or around the city centers should be made taking into account the above-mentioned conditions. Measurements are mostly intended to determine contamination in soil and water samples, and no significant investigation has been done in air samples. This is mainly due to the inadequacy of the amount of material collected. While the background radiation measurement provides information on the general situation in the region (Figure 1), it did not provide a spectrum characterizing the collection of airborne particles. The difference between the sample-containing (yellow) and background sample (blue) measurements only contains the white noise of the system and did not provide computable information. In Figure 2 the situation is shown in more detail.

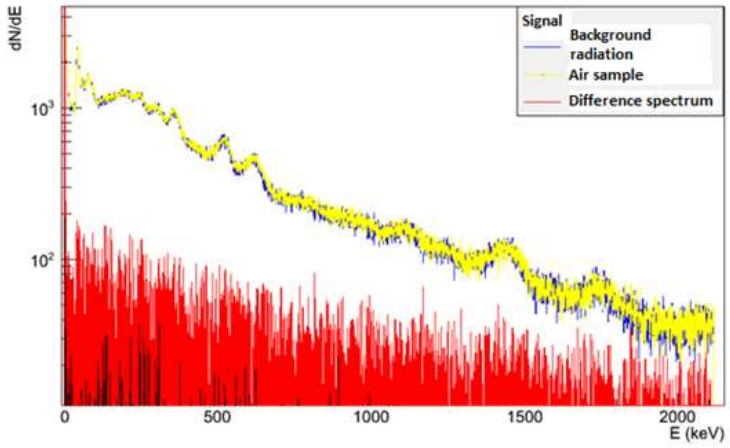

Figure 1. Background and sample measurements between 0 and 2150 keV

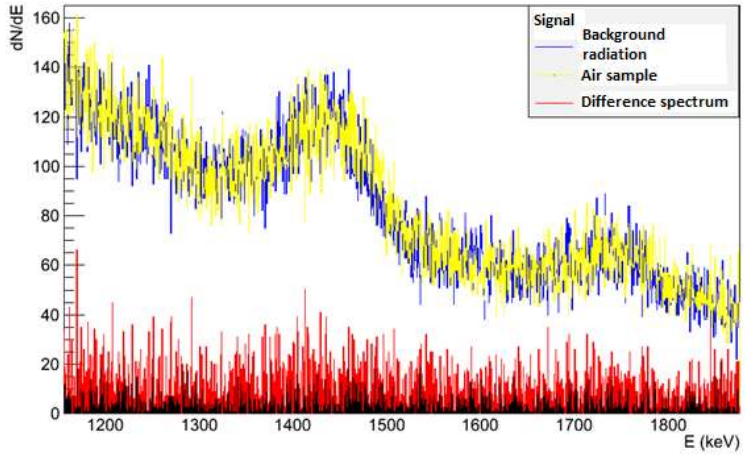

Figure 2. K40 entire energy peak

In the analysis using the NAA technique, the counting strategy and the statistical effect of the filters used were investigated in Figure 3 and Figure 4. It was observed that the filters were completely dependent on the storage and sample preparation process even if they are made

from the same materials. It was determined that the filters were open to contamination due to contact on account of contact. The signal from the 511 keV, 616 keV and 845 keV signals shown in Figure 4 (614 keV and 845 keV), which may be due to chlorine and potassium sources at 616 keV, is consistent with each other within the limits of error in both measurements.

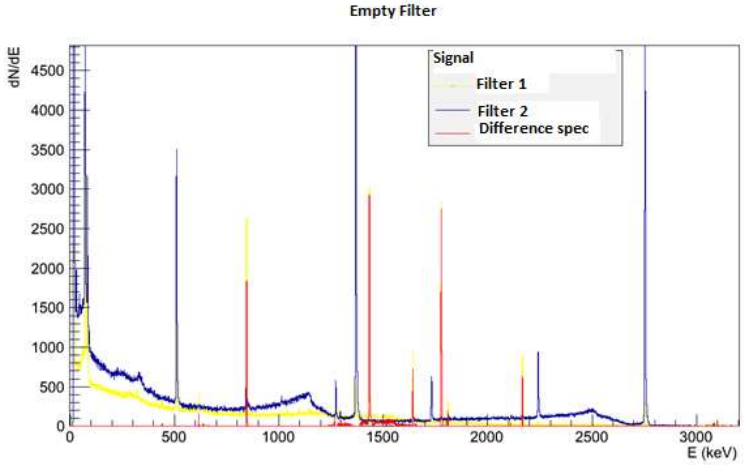

Figure 3. Empty air filters

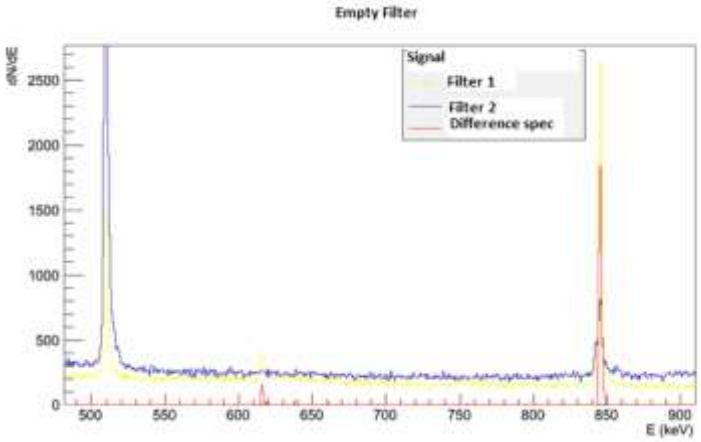

Figure 3. Empty air filter details

CONCLUSIONS AND RECOMMENDATIONS

In this study, NAA technique was applied in order to detect any radioactivity in air samples. Background spectrum of the sampling area was gathered from soil samples. Firstly, empty filters were subject to analyses. Then, filters, containing ambient particles, were subject to NAA. It was determined that there was no significant difference between ambient samples and background spectrum. Any radioactivity was not detected in the particles.

ACKNOWLEDGEMENTS

This research has been supported by the Yildiz Technical University Scientific Research Projects Coordination Department (Project no. 2010-05-02-ODAP02).

REFERENCES

Hendry JH, Simon SL, Wojcik A, Sohrabi M, Burkart W, Cardis E, Laurier D, Tirmarche M, Hayata I (2009) Human exposure to high natural background radiation: what can it teach us about radiation risks?, Journal of Radiological Protection 29 (2A): A29–A42.

James M (2006) Physics for Radiation Protection: A Handbook. p. 130, 2006.

Mortazavi SMJ, Karamb PA (2005) Apparent lack of radiation susceptibility among residents of the high background radiation area in Ramsar, Iran: can we relax our standards?, Radioactivity in the Environment 7, 1141–1147.

NATURAL CAUSES AND EFFECTS OF CLIMATE CHANGE

A. Nihal Yücekutlu[1]
[1]*Hacettepe University, Faculty of Science, Department of Chemistry, Beytepe, Ankara, Turkey*
nihal.yuce@gmail.com

Abstract
Human affects the environment and ecosystem in several ways. These effects include increased pollution and greenhouse gas emissions, depletion of natural resources (for example, decreased water quality) and contribution to global climate change. Climate change has affected human societies and the natural environment. The clearest today's impacts of climate change is seen in the natural environment. These impacts include changes in the growth and distribution of plants, animals and insects. The clearest today's impacts of climate change is seen in the natural environment. North African deserts are the world's largest sources of atmospheric mineral dust produced by aeolian and thus natural mineral dust interacts with climate and ecosystems. The dust storms in Africa is important to characterize the contribution of aerosol emissions to climate change. In the next decades, such as climate change, researches are underway to estimate how effect of Saharan dust and dust emissions will change. In this study, the investigation of the possible effects of Saharan dust on the receiving environment and ecosystem will be presented.

Key Words: *Saharan dust (mineral dust) event, Climate change, Nutrient cycle, Ecosystems.*

INTRODUCTION
This reviews investigate on the role of Saharan dust inputs in aerosols (Fig.1) as a contribution of natural fertilizer, mineralogical composition to the vegetation (Yücekutlu, 2012, 2013).

Figure 1. Eastern Mediterranean 2017.03.18 by anttilipponen Tags: Eastern Mediterranean Sahara Dust Cyprus Turkey Egypt İsrael Aqua Modis Satellite

A significant fraction of the atmospheric particulate burden consists of mineral dust; its injection rate into the atmosphere can vary temporally and spatially, e.g., as a result of dust storms, volcanic eruptions, and anthropogenic activities. The mineral-dust burden tends to be especially high near source regions (Li et al., 1996). (Fig.2). Moreover, changes in climate as well as land use can profoundly affect the amount of mineral dust that enters the troposphere.

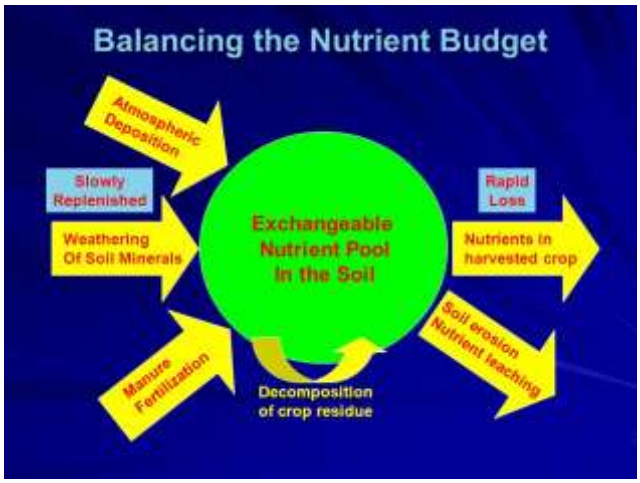

Figure 2. Balancing the nutrient budget

Aerosol effects on global climate

Aerosol particles also have a major influence on global climate and climate change; they can locally either intensify or moderate the effects of the greenhouse gases through the scattering or absorption of both incoming solar radiation and thermal radiation emitted from Earth's surface. Aerosols also act as cloud condensation nuclei (CCN) and thereby modify the radiative properties of clouds. Cloud droplets form on aerosol particles as nuclei. The number, sizes, and compositions of such CCN have major inf luences on cloud formation. Hygroscopic materials such as sulfates and sea salts are especially efficient as nuclei; mineral dust and combustion products can also be effective (Kaufman and Fraser, 1997).

In addition to the aerosol effects from nitrogen, there are both direct and indirect effects on climate from other aerosol sources. Components of the sulfur cycle exert a cooling effect through the formation of sulfate aerosols created from the oxidation of sulfur dioxide (SO_2) emissions. Further reductions in sulfur dioxide emissions have reduced the cooling effect of sulfate aerosols by half or more. Sulfate aerosol is an efficient scatterer of solar radiation; aerosol-climate models suggest that anthropojenic $SO_4^{=}$ aerosols could have a substantial cooling effect on climate (Charlson et al., 1992).

Causes of climate change

The causes of climate change can often be examined under several tittles; human-sourced (anthropogenic) factors, natural factors (e.g. Saharan dust storm), change of atmosphere's greenhouse effect factors, effects of atmospheric release particles factors. Human activities cause climate change by affecting the rate of greenhouse gases, aerosols and cloudiness in the atmosphere. The buildup of carbon dioxide and other gases in the atmosphere is known as the "greenhouse effect.

The importance of Saharan dust on climate change

Through long-range transport of dust, the Saharan desert supplies the most significant source of essential mineral aerosol to the receiving environment. The effect on the vegetative growth of plants of Saharan dust have been investigated and physical, chemical and mineralogical composition for its role in crop production have been analyzed (Yücekutlu, 2012). The mineral dust cycle responds to climate variations and plays an important role in the climate system. Dust affects climate by changing the radiative balance of the atmosphere through the absorption and scattering of incoming solar and outgoing terrestrial radiation (Balkanski et al., 2007). Additionally, mineral dust may impact climate by modifying cloud properties, acting as

cloud condensation nuclei (Karydis et al., 2011) or ice nuclei (Kuebbeler et al., 2014). The main mechanisms controlling dust emissions are vegetation cover, aridity, land surface/soil characteristics, wind speed, precipitation and topographical features. Therefore mineral dust is very sensitive to climate change, which has been evidenced by many observational studies (e.g. Kohfeld and Harrison, 2001).

What causes the greenhouse effect?

- Surface absorbs high-energy light from Sun
- Surface releases lower-energy light (infared)
- Infared light absorbed, re-emitted by gases
- Increases gas energy; results in temperature increase

There is widespread concern over the enhanced global warming that might result from the buildup of "greenhouse gases" in the atmosphere. Greenhouse gases (H_2O, CO_2, CH_4, N_2O, etc.) absorb IR radiation and radiate it back to Earth's surface. Anthropogenic emissions of greenhouse gases cause increases in surface temperature (the "greenhouse effect") (see Table 1) and can have profound effects on climate and thus on societal welfare (Farquhar, 1997).

Table 1. Comparison of natural and man-made source greenhouse gases

Greenhouse Gas	**Natural sources**	**Man-made sources**
Carbon Dioxide	Organic decay, Forest fires, Volcanoes	Burning fossil fuels-car and factory emissions, electricity generation
Methane	Wetlands, Organic decay, Termites	Natural gas and oil, extraction, biomass burning, Rice cultivation, Cattle, Refuse landfills
Nitrous Oxide	Forest, Grasslands, Oceans, Soils, Soil cultivation; Fertilizers	Biomass burning; Burning of fossil fuels
Chlorofluorocarbons (CFCs)	None	Refrigerators; Aerosol spray propellants; Cleaning solvents

Since the beginning of the industrial age the amount of carbon dioxide and other greenhouse gasses in the atmosphere has steadily increased along with a rise in global temperatures. It is believed by most scientists that this trend will continue at an accelerating rate and cause sea level rise from increased expansion of the oceans and hasten the melting of the ice sheets. Graphic illustration of causes for sea level change (Fig. 3).
(http://www.dnrec.delaware.gov/coastal/Documents/SLR%20Advisory%20Committee/AdaptEngage/3WhatCausesSeastoRise.pdf, Date of access: 2017.10.10)

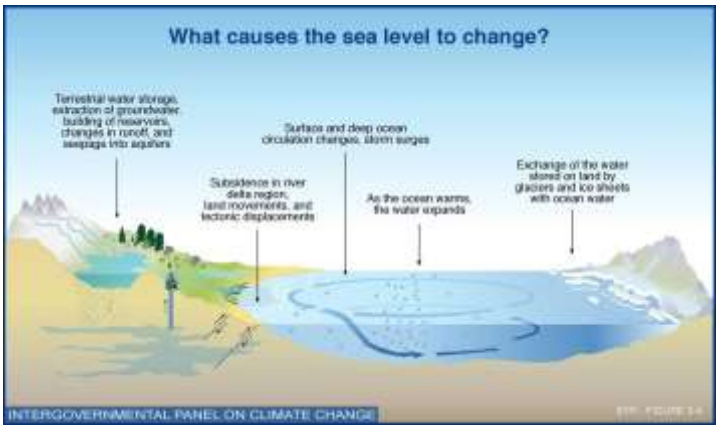

Figure 3. What causes the sea level to change? (Image Source: IPCC, Climate Change 2001: Global Sea Level Rise Scenarios for the United States National Climate Assessment)

Nutrient cycling

Nutrient cycling and soil or water fertility play key roles in terrestrial and aquatic systems, and these roles benefit many segments of society. Substantial human benefits are derived directly and indirectly from nutrient cycling and fertility services. Deposition from the atmosphere of nutrients, originating from industry, agriculture, biomass fires, and wind erosion, is spreading unprecedented quantities of N, P, and possibly Fe and Si to downwind ecosystems over large regions (Brasseur et al. 2003). Human-caused reactive nitrogen inputs are now at least five times greater than those from natural sources. At least some of the added nitrogen is converted to nitrous oxide (N_2O), which adds to the greenhouse effect in Earth's atmosphere (Suddick, 2013). Once created, a molecule of reactive nitrogen has a cascading impact on people and ecosystems as it contributes to a number of environmental issues (Fig. 4). It is predicted that the human population will reach 8 billion in 2025. To avoid or minimize food shortage, saline soils have to be rehabilitated and managed to meet the food demand of an ever growing human population (Ladeiro, 2012). Therefore, agriculture should be done in accordance with climate change.

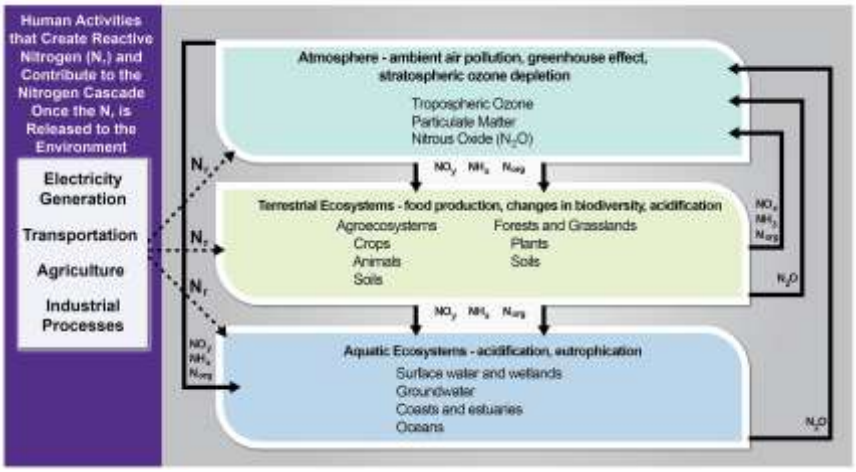

Figure 4. Human Activities that Form Reactive Nitrogen and Resulting Consequences in Environmental. (Figure source: adapted from EPA 2011;13 Galloway et al. 2003;17 with input from USDA. USDA contributors were Adam Chambers and Margaret Walsh).

DATA AND METHODS

The composition of Earth's atmosphere has changed in the past and is changing today. However, there are still a lot of unknowns about the impact of climate change.

Various methods are used to monitor climate change. One of them; original method for climate change detection, called temporal optimal detection method. The method consists in searching for a smooth temporal pattern in the observations. The method also allows to detect a climate change signal in precipitation. The ability of the method to provide an estimate of the spatial distribution of the change following the prescribed temporal patterns is also illustrated. This method will be referred to as the Temporal Optimal Detection (TOD). This assessment is based on the temporal optimal detection (TOD) method (Ribes et al., 2010).

APPLICATION AND RESULTS

Effect of dust aerosol on glacier climate change

Around 11,000 years ago, the Earth had just emerged from the last ice age and was beginning a new, interglacial epoch known as the Holocene. Geologists and archaeologists have found evidence that during this period the Sahara was much greener, wetter, and more livable than it is today. The Sahara is the largest source of windblown dust to the Earth's atmosphere. But

researchers from Massachusetts Institute of Technology, Yale University, and elsewhere now report that the African plume was far less dusty between 5,000 and 11,000 years ago, containing only half the amount of dust that is transported today. Ina Tegen, a professor at the Leibniz Institute for Tropospheric Research in Germany. says the group's results suggest that "dust effects today may be considerable as well." "Dust loads vary with changing climate, and due to the effects of dust on [solar] radiation, ice formation in clouds, and the carbon cycle, this may cause important climate feedbacks," says Tegen., who was not involved in the research. "The changing climate since the last ice age can be considered a 'natural laboratory' to study such effects. Understanding the past is the basis for predicting future changes with any confidence." (Chu J., Massachusetts Institute of Technology, News Office , 2016) (http://sustainability.mit.edu/article/saharan-dust-wind). Climate and topography are the primary drivers of glacial systems, and glaciers record the trends for all to observe. The climate is constantly changing, and glaciers have responded through time, with evidence of advance and retreat cycles recorded in the geologic record. The growing evidence of unprecedented warming rates and wide ranging effects is well documented, recently in the comprehensive and international Arctic Climate Impact Assessment (2005). The warming climate's effect on glaciers is well documented through the recreation of historic photos, field measurements, and interpretation of remotely sensed imagery (Adema et al., 2005).

CONCLUSIONS AND RECOMMENDATIONS

Carbon dioxide from fossil fuels will probably cause a "greenhouse effect" the gradual warming of the atmosphere. The rising temperatures may resulting temperatures may result in the melting of polar ice caps causing many coastal cities to be covered with water.

The key impacts of a 4°C warmer world by the end of this century; "A 4°C warmer world can, and must be avoided – we need to hold warming below 2°C," said World Bank Group President Jim Yong Kim. "Lack of action on climate change threatens to make the world our children inherit a completely different world than we are living in today. Climate change under a 4°C global warming scenario, resulting in adverse consequences for development: diminishing crop yields which threaten food production and human health, loss of biodiversity, spread of water scarcity and vector-borne diseases. Vector-borne diseases are human illnesses caused by parasites, viruses and bacteria that are transmitted by mosquitoes, sandflies, triatomine bugs, blackflies, ticks, tsetse flies, mites, snails and lice. The major vector-borne diseases, together, account for aeround 17% of all infectious diseases. The burden of these diseases is highest in tropical and subtropical areas and they disproportionately affect the poorest populations (WHO). Insect vectors have several physical traits that help them take advantage of climate impacts like flooding, increased precipitation, and warmer weather (Fig. 5).

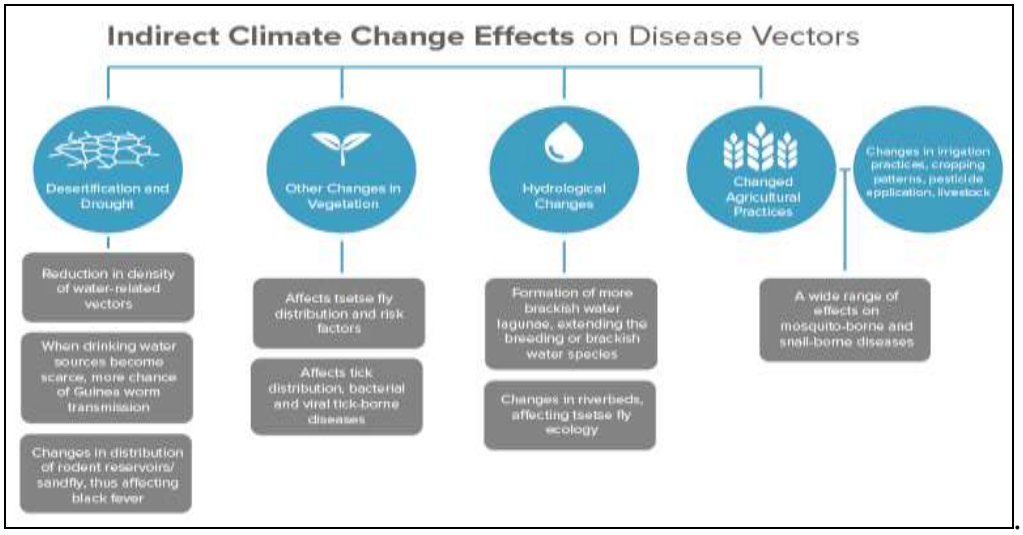

Figure 5. Vector-Borne diseases in a warming world (http://climatenexus.org/climate-issues/health/climate-change-and-vector-borne-diseases/ Date of access: 2017.10.10)

Defining a road-map for adaptation to physical risks of climate change. Finally, there is mounting evidence that mineral dust can also play an important role in global climate forcing. The global biogeochemical processes and the impact on the climate of dust transport of these interactions should be further investigated.

REFERENCES

Adema, Ronald D. Karpilo, Jr., and Bruce F. Molnia, Melting Denali: Effects of Climate Change on Glaciers. Denali National Park & Preserve. Last updated: January 12, 2015.

Balkanski, Y., Schulz, M., Claquin, T., and Guibert, S.: Reevaluation of Mineral aerosol radiative forcings suggests a better agreement with satellite and AERONET data, 7, 81–95, 2007.

Brasseur, G.P., P. Artaxo, L.A. Barrie, R.J. Delmas, I. Galbally, et al.,: An integrated view of the causes and impacts of atmospheric changes. In: Brasseur, G.P., R.G. Prinn, A.A.P. Pszenny (eds.) Atmospheric Chemistry in a changing world. IGBP Series, Springer: Berlin pp. 207–230, 2003.

Charlson, R. J., Schwartz, S. E., Hales, J. M., Cess, R. D., Coakley, J. A., Hansen, J. E. & Hofmann, D. J. Climate forcing by anthropogenic aerosols. Science, Wash . 255 , 423-430, 1992.

Farquhar G D. Science; 278:1411,1997.

Kaufman Y J, Fraser R S. Science; 277:1636–1639,1997.

Karydis, V. A., Kumar, P., Barahona, D., Sokolik, I. N., and Nenes, A.: On the effect of dust particles on global cloud condensation nuclei and cloud droplet number, J. Geophys. Res.,116, 2011.

Kohfeld, K. E. and Harrison, S. P.: DIRTMAP: the geological record of dust, Earth-Sci. Rev., 54,81–114, 2001.

Kuebbeler, M., Lohmann, U., Hendricks, J., and Kärcher, B.: Dust ice nuclei effects on cirrus clouds, Atmos. Chem. Phys., 14, 3027–3046, 2014.

Ladeiro, B., 2012. Saline Agriculture in the 21st Century: Using Salt Contaminated Resources to Cope Food Requirements. Journal of Botany, 7, 2012.

Li X, Maring H, Savoie D, Voss K, Prospero J M. Nature (London),380:416–419, 1996.

Suddick, E. C., P. Whitney, A. R. Townsend, and E. A. Davidson, The role of nitrogen in climate change and the impacts of nitrogen–climate interactions in the United States: Foreword to thematic issue. Biogeochemistry, 114, 1-10, 2013.

Ribes, A., Azais, J. M., and Planton, S.: A method for regional climate change detection using smooth temporal patterns, Clim. Dynam., 35, 391–406, 2010.

Yücekutlu A.N., 8th International Soil Science Congress on "Land Degradation and Challenges in Sustainable Soil Management, Volume 5, Investigation of the impact on vegetative growth of Saharan desert dust, 487-497, 2012.

Yücekutlu, A.N., ATMOS'2013, 6th Atmospheric Science Symposium, Istanbul Technical University (ITU), Investigation of the dynamic transport of Saharan Desert Dust-II, April 24–26, 2013.

A CASE STUDY ON ELECTRICITY GENERATION AT PRESSURE REDUCING STATION (PRS)

Mehmet Alparslan Neseli[a] , Huseyin Gokbakar[b], Onder Ozgener[c,] , Leyla Ozgener[d,]
[a]Graduate School of Natural and Applied Sciences, Solar Energy Science Branch, Ege University, TR-35100, Bornova, Izmir, Turkey, alpneseli03@gmail.com
[b] Graduate School of Natural and Applied Sciences, Solar Energy Science Branch, Ege University, TR-35100, Bornova, Izmir, Turkey
[c] Solar Energy Institute, Ege University, Bornova, Izmir 35100, Turkey
[dc] Department of Mechanical Engineering, Faculty of Engineering, Celal Bayar University, Muradiye, Manisa, Turkey

Abstract
Natural gas is transmitted from one point to another by high pressure. It can be used by lowering the pressure when it reaches the use area. Plants that require measurement and reduction of natural gas pressure are called Pressure Reducing Station (PRS). The pressure is reduced by regulator/retarding valve. Energy generation is aimed at turbo expanders at the pressure drop station. The 1.3 MW Tekirdağ Marmara Ereğli, located in Turkey, was operated in the pressure reduction station. Marmara Ereğli is Turkey's first PRS established in 1999. Actual thermal data collected. Using the actual system data, the system performance, energy, exergy efficiencies of the pressure reduction station, and the exergy destruction evaluation of the system were evaluated. According to the official BOTAŞ estimate, in 2030 Turkey's natural gas demand is estimated as 76.4 billion m^3. This shows that there is a potential for energy generation as a result of a process normally carried out at such stations.

Keywords: *Exergy, energy, naturalgas, Pressure Reducing Station*

Introduction
The main aims of this study are to calculate the energy and exergy values of flows entering and leaving the PRS control volume and its components and to evaluate the performance of this system by investigating the exergetic parameters of TE, HEs and the whole PRS system by using the actual operational system data. Turkey's importance in world energy markets is growing, not only as a regional energy transit hub but also as a growing consumer, and energy demand has increased quickly over the past few years and likely will continue to grow in the future (EIA, 2014). Whereas Turkey's natural gas use was 20.9 billion m^3 in 2003, it reached to the level of 45.6 billion m3 in 2013 (BP, 2014) [2]. Turkey's natural gas demand in the year 2030 is estimated as 76.4 billion m^3 according to the official BOTAS forecast (Erdogdu, 2010, Melikoglu, 2013,). By the end of year 2013, according to electric power generation sources, natural gas proportion was 43.8 % in Turkey (TETC, 2013). Natural gas is used not only in generating electricity, but also in heating and chemical industries, so as to consume and to use natural gas, its pressure needs to be reduced. The plants where the pressure of natural gas is metered and reduced are called Pressure Reduction Station (PRS). Marmara Eregli is the first PRS of Turkey that was built in 1999.

Case study
Electricity generation through PRS for general use was first realized in Marmara, Eregli Turkey with a 1.3 MW nominal PRS energy capacity. However, there are many combined heat and power (CHP) systems which are installed by private sector or government in Turkey and used NG as a fuel, due to increasing demand for electricity. In this study, actual operating data of an active combined cycle power plant named Marmara Eregli CHP, located in Tekirdag, is

used. Marmara Eregli CHP began to generate electricity in 1999. Produced power of CHP is 478 MW. CHP consists of two gas turbines (GT) and a steam turbine (ST). Installed capacities of one of the GT and ST are 150 MW and 178 MW, respectively. Electricity generation of CHP is approximately 3.6 billion kWh as an average annual value. Volumetric flow rate was approximately 77.880 Sm^3/h. Consumption of NG using natural gas in the electricity-generating facility was 0.54 billion Sm^3 for 2012. Consumption of NG was 45.2 billion Sm^3 in Turkey during 2012 (EMRA, 2012). Ratio of usage of NG in this CHP was 1.19%. While the electricity consumption of Turkey was 239.5 billion kWh in 2012 (TIS, 2014), ratio of its electricity was equal to 1.5% of Turkey's. As illustrated in Figure 1, CHP system uses NG as fuel from storage tanks of NG. Building CHP, PRS with turbo expander (TE) was installed for not only reducing pressure of NG but also producing electricity. A schematic of the PRS with TE system investigated is given in **Error! Reference source not found.**. This system consists of two heat exchangers and a TE on turbo line, a boiler (B), a HE and regulator (R) on regulator line. When inlet NG has a high pressure between 6 and 7 MPa from BOTAS's storage tank of NG, it should be dropped 1.9 MPa for using GT in CHP (Kelesoglu, 2006, Neseli, Ozgener, Ozgener, 2015, Neseli, Ozgener, Ozgener, 2016, Neseli, Ozgener, Ozgener, 2017).

Figure 1 Various views of the Marmara PRS

Analysis

Assumptions

Some assumptions were made during the calculations. These assumptions can be given as follows:

1.Whole process was assumed as steady state.
2.Potential and kinetic energy as well as exergy exchange were neglected.
3.Kinetic exergy and potential exergy were neglected.
4.Ambient temperature was taken in real environmental conditions from Ref. (TSMS, 2013) and atmospheric pressure was taken as 101.325 kPa.

Mass, energy and exergy balance equations

Thermodynamical performance analysis of the PRS is evaluated on TE section. Mass and energy balances are used to find flows and the values of enthalpy in all system points and its components (Figure 2).

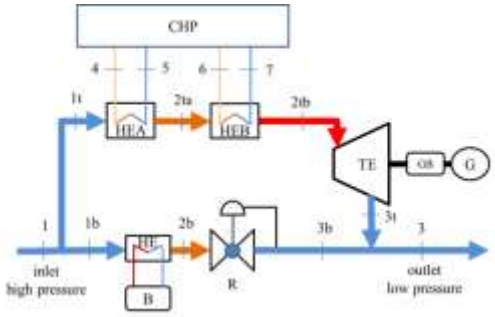

Figure 2 Simplified schematic view of Marmara PRS

Results and Discussion

In the present study, the exergetic efficiencies of HEA, HEB, TE and overall system were calculated as 17.79, 40.27, 26.08 and 78.25%, respectively. Energy and exergy efficiencies of Marmara Eregli PRS vary between 43.73% and 90.87% and between 73.90% and 84.83%, respectively (Figure 3).

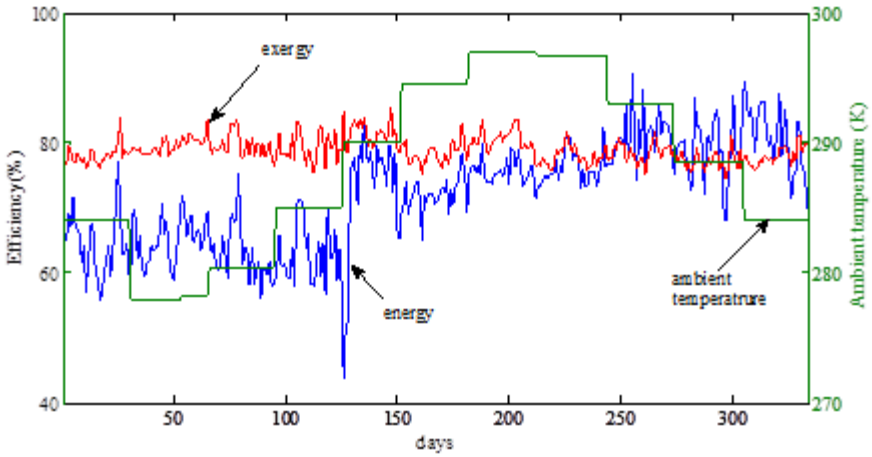

Figure 3 Daily variations of overall energetic and exergetic PRS system efficiencies

The total exergy input values were obtained for a range from 6860.55 to 21389.29 kW for different days during 2012. The corresponding reference state (dead state) temperatures were taken to be 277.95-296.95 K; respectively, as the environment temperatures.

Conclusion

In this study, we present thermo-mechanical exergy analysis of Marmara Eregli PRS system in Tekirdag, Turkey as a case study. It utilizes actual PRS data taken from the Marmara Eregli PRS to perform a system performance evaluation through energy and exergy efficiencies, exergetic improvement potential, as well as some other thermodynamic parameters. Additional observations and conclusions drawn from the present study may be summarized as follows:

- The average work of the PRS was determined to be 1000.2 kW, with 3.381 as pressure ratio (Pinlet/Poutlet) value and 80.42% as ratio of mass flow rate (Ratio),
- Average exergetic and energy efficiency of PRS was found to be 78.25 and 71.96%,
- Average exergetic and isentropic efficiencies of TE was found to be 26.08 and 66.55%, respectively, The highest exergy consumption between the components of the PRS system was occurred within the TE with an average value of 3204.98 kW,
- The energy recovery should be implemented on any CHP system and should be taken Marmara Eregli PRS as an example.
- The results of the paper, particularly this implementation on CHP, will help the researchers, government administration, and engineers in the area of PRS systems develop and adapt appropriate measures and policies.

References

BP, Petroleum British. "*Energy*," 2014. [Online]. Available: http://www.bp.com/statisticalreview.

EMRA, Energy Market Regulatory Authority. "Energy Market Regulatory Authority Sector Report," 2012. [Online]. Available: http://www.emra.org.tr. [Accessed 13 March 2014].

Erdogdu E. Natural gas demand in Turkey. *Applied Energy* 2010;87:211–19.

Kelesoglu S. Technical and economical research of energy recycling at natural gas pressure reducing stations. *Master's thesis*, Yildiz Technical University, Turkey, 2006.

Melikoglu M. Vision 2023:Forecasting Turkey's natural gas demand between 2013 and 2030. *Renewable and Sustainable Energy Reviews* 2013; 22:393–400.
Neseli MA, Ozgener O, Ozgener L. Analysis of the recoverable energy from natural gas pressure reduction stations (PRS), 2016, 8th International Ege Energy Symposium and Exhibition (IEESE8) May 11-13, Afyonkarahisar, Turkey.
Neseli MA, Ozgener O, Ozgener L. Energy and exergy analysis of electricity generation from natural gas pressure reducing stations. Energy Conversion and Management. 2015: 93;109-20.
Neseli MA, Ozgener O, Ozgener L. Thermo-mechanical exergy analysis of natural gas pressure reduction stations (PRS): Marmara Eregli case study. Renewable and Sustainable Energy Reviews, 2017, 77:80-88.
SEIA, U.S. Energy Information Administration. "countries," 17 April 2014. [Online]. Available: http://www.eia.gov.
TETC, Turkish Electricity Transmission Company. "Electricity generation & transmission statistics of Turkey," 2013. [Online]. Available: http://www.teias.gov.tr.
TIS, Turkish Statistical Institute. " Electricity generation - transmission statistics of Turkey (1975-2012)," 2014. [Online]. Available: http://www.turkstat.gov.tr. [Accessed 13 March 2014].
TSMS, Turkish State Meteorological Service. "Official Statistics (statistical data relating to cities)," 2013. [Online]. Available: http://www.mgm.gov.tr/veridegerlendirme/il-ve-ilceler-istatistik.aspx#sfU. [Accessed 5 August 2013].

THE ENSEMBLE MEAN OF MULTI-MODEL SCENARIO SIMULATIONS FOR TEMPERATURE AND PRECIPITATION OVER TURKEY

Semih Kahraman [1], Barış Önol[1]
[1]*Istanbul Technical University, Department of Meteorological Engineering*
kahramansem@itu.edu.tr, onolba@itu.edu.tr

Abstract
The aim of this study is to define future change of the mean temperature and precipitation over Turkey for period of 2025-2099 by using the ensemble mean of the various regional climate model outputs. The regional climate models (RCM) implemented over five different domains, which are all covers Turkey, have been assembled for the project called the Coordinated Regional Climate Downscaling Experiment (CORDEX). We have used simulations produced by 7 different RCM driven by 13 GCM over 5 different domains. In the study, RCP8.5 scenario selected for projected simulations. 1981-2005 period has been applied for reference period and for future period, 2025-2049, 2050-2074 and 2075-2099 has been selected. The gradual temperature increase among the future periods was calculated from the ensemble mean of the simulations. The highest temperature increase defined over the Eastern Turkey and the least increase over the Marmara region. At the end of the 21st century, temperature change over Eastern part of Turkey reaches 6 °C. In terms of precipitation change, water scarcity will escalate for the period of 2075-2099. Precipitation decrease over the Aegean and the Mediterranean region varies in the range of 20% to 30%. This may cause an inevitable circumstances in social, economic and environmental dimensions for Turkey.

***Keywords*:** *Climate change, regional climate simulations, ensemble mean.*

ELECTRICITY GENERATION IN WASTE EXHAUST GASES FROM INTERNAL COMBUSTION ENGINES

Huseyin Gokbakar[a], Onder Ozgener[b], , Leyla Ozgener[c],

[a] *Graduate School of Natural and Applied Sciences, Solar Energy Science Branch, Ege University, TR-35100, Bornova, Izmir, Turkey*

[b] *Solar Energy Institute, Ege University, Bornova, Izmir 35100, Turkey*

[c] *Department of Mechanical Engineering, Faculty of Engineering, Celal Bayar University, Muradiye, Manisa, Turkey*

Abstract

It is aimed to produce energy from waste exhaust gas which is thrown into the atmosphere from internal combustion engines.From internal combustion engines (ICE), energy is obtained in 3 different ways. Exhaust gases are also among the power generation methods for internal combustion engines. Due to the advantages of diesel engines today, energy, electricity and transportation sector has a wide use. However, a large part of the fuel energy is thrown into the atmosphere by the exhaust gas. Waste heat from automotive vehicles is also important. In the work done, 12-25% of fuel energy is converted to work for a typical ICE vehicle. 30-40% of fuel energy is discharged as exhaust gas, which causes fuel waste and environmental pollution. The best way to utilize this waste heat is to increase energy efficiency while at the same time saving fuel. Approximately all of the exhaust gas energy equals effective work. In the same way, it is also possible to produce energy during the airplane operation of aircraft engines which are internal combustion engines.

Keywords: *Internal combustion engine, exhaust gas, waste heat, energy*

Introduction

In the same way, aircraft engines with internal combustion engines are intended to generate energy from waste exhaust gas and determine its method during the aircraft test cell.

The automobile exhaust gas is discharged from the engine cylinder at a pressure of 300-500 kPa and a temperature of 500-700°C (Lu, et al, 2013). In general, the maximum exhaust gas temperature of gasoline engines is higher than that of compression ignition engines such as Diesel engines. The exhaust systems of light passenger cars operate at gas temperatures between 500 and 900°C and the heavy-duty engine produces exhaust gases between 400 and 650°C(Aghaali & Ångström, 2015). The energy content of an engine's exhaust gases (enthalpy) depends on the static pressure and the temperature at the exhaust outlet of the exhaust (Singh & Pedersen, 2016). Waste heat from automotive vehicles is also important.

In the work done, 12-25% of the fuel energy is converted to work for an internal combustion engine vehicle running on a typical gasoline fuel. 30-40% of the fuel energy is discharged as exhaust gas. This causes fuel waste and environmental pollution (Taylor, 1998), (Rowe, 1999), (Riffat & Ma, 2003), (El Chammas & Clodic, 2005), (Endo, at all, 2007), (Patterson, et al, 2009), (Miller, et al, 2009), (Conklin & Szybist, 2010), (Mavridou, et al, 2010), (Wanga, et al, 2011), (Zhang & Chau, 2011), (Katsanos, et al, 2013), (Chien-Chou & Mei-Jiau, 2013), (M. Hatami, 2014), (Zhao, et al, 2014), (Ghazikhan, et al, 2014), (Zhang, et al, 2014), (Tian, et al, 2015), (Rahman, et al, 2015), (Briggs), (Dolz, et al, 2012).

ICE Waste Heat Recycling Technologies

The advantage of waste heat recovery is listed as negligible cost of thermal energy input, energy saving and reducing emission value. For this reason, efforts are being made to evaluate the ICE waste heat and, consequently, to reduce the emission values and increase the

efficiency. Different technologies are used to provide waste heat recovery from the ICE during the studies (M.K.P.Taylor, 2008), (Saidur, et al, 2012), (M. Hatami, 2014), (Zhao, et al, 2014), (Aghaali & Ångström, 2015), (Zhao, et al, 2015), (Zhao, et al, 2016).

Thermoelectric Generators (TEG)

Thermoelectric generator is a unique heat motor. Thermoelectric devices are solid state devices. With the Seebeck effect, direct conversion of the temperature difference to electrical energy takes place. The TEG system, which works according to the Seebeck effect, is a reliable energy converter since it is not mechanically moving parts. It works quietly, does not contain vibration and is very reliable. Dimensions are small and light.

Because of these advantages, thermoelectric devices have a wide range of applications. However, due to its low efficiency (typically around 5%), it is limited to medical, military, aerospace and space applications, which are not costly (Rowe, 1999), (Riffat & Ma, 2003), (Tian, et al, 2015), (Akçay, 2015). TEG was first applied on the automobile in 1988 (Rowe, 1999), (Hsiao, et al, 2010).

Organic Rankine Cycle

Generally geothermal sources at temperatures of 150°C or lower are usually converted by dual type energy conversion systems. The ORC is an extraordinary but very promising technology for transforming low and medium temperature thermal energy into small diameter electrical and/or mechanical energy. The ORC system can be applied to waste heat recovery of unstable heat sources such as exhaust gas of automobile engines [44], [45], [24], [46]. ORC improves fuel consumption by 10% (DiPippo, 2004), (Vélez, et al, 2012), (Dolz, et al, 2012), (Shi, et al, 2016).

Six-Stroke Engines

In the present invention, overheating of the cylinder walls during the engine operation is prevented, as well as the useful work of recovering the heat of the flammable gases. Basically, the present invention is achieved by modifying the diesel engine. A patent for engine design based on the principle that the work is obtained from combustible fuel and that a liquid coolant is periodically injected into the combustion chamber (Patent No. US2671311 A, 1954).

Turbo Charger

The efficiency of the turbocharger is defined as the ratio of the adiabatic temperature drop at the inlet/outlet of the turbocharger compressor to the outlet/inlet of the turbocompressor türbine (Shiraishi & Ono, 2007). Turbocharged, fuel economy of up to 30-50% in diesel powered passenger cars (Saidur, et al, 2012), (Shu, et alerleri, 2013).

The turbine is a component that transfers enthalpy kinetic energy. If kinetic energy is used on a compressor, it is called a turbocharger. If it is used with a generator or coupled with a power device, it is called a power türbine (Jiangin, et al, 2014), (Jiangin, et al , 2014), (Değirmenci, 2015), (Rajeevana, et al, 2016).

Turbo Compounds

If both the turbocharger and the power turbine are used at the same time, this is called turbo compounding. The results show that overall system efficiency can be improved by 10.9% compared to a similar turbocharged engine (Thompson, 2012). The total cost of the turbo compound systems applied to the heavy duty vehicle engine was estimated at 1700 USD. The

power turbine costs $ 600, the liquid coupling costs $ 450, and the gearbox, It's $ 650 (Zhao, et al, 2015).

Exhaust Gas Recirculation (EGR)

In gasoline engines, EGR is used to reduce fuel consumption and NO_X emission levels (M. Hatami, 2014). At the same time, EGR is applied to block the stroke caused by the fuel enrichment of the petrol engine. The EGR effect on the performance and emissions of the petrol engine was examined and the EGR applications on the GDI and PFI engines were compared (We, et al, 2012). The result showed that the engine improved the engine's BSFC by 3% and significantly increased emissions because the engine reduced HC formation in the combustion chamber (Rahman, et al, 2015).

Exhaust Heat Exchangers

In order to take advantage of the exhaust gas heat, the ICE has been experimentally worked on a tank with an integrated winged pipe heat exchanger and energy storage. The performance of the heat exchanger is compared to that of the heat exchanger. Approximately 10-15% of the fuel energy is stored as heat in the combined storage system (Ghazikhan, et al, 2014), (Pandiyarajan, et al, 2011).

Analysis

Specific exergy of exhaust gases at location i in a given instant is defined by eq (Agudelo, et al, 2016).

$$e_g = (h - h_0)_g - T_0(s - s_0)_g + e_g^{ch} + \frac{1}{2}V_g^2 + gZ_g$$

Instantaneous exergy rate of exhaust gases at each location is defined in Eq., by using the measured mass flow:

$$\dot{E}_{g,ı} = \dot{m}_{g,i}\dot{e}_{g,i} \quad [W]$$

Mean energy and exergy of exhaust gases at each location are calculated by means of Eqs., respectively.

$$\dot{H}_{m,g,i} = \int_{t0}^{tf} \dot{m}_g \, \Delta h_{g,i} dt \quad [J]$$

$$\dot{E}_{m,g,i} = \int_{t0}^{tf} \dot{E}_{g,i} \, dt \quad [J]$$

Energy to energy ratio is defined using mean values of energy and exergy at each location in the exhaust system, according to Eq.

$$\delta_{m,g,i} = \frac{\dot{E}_{m,g,i}}{\dot{H}_{m,g,i}} x100 \ [\%]$$

Conclusions And Recommendations

As a result of this work, the hierarchical structure of the methods of energy recovery by recovering waste exhaust gas energy is shown.

In order to test the compliance of the jet engines, which are disassembled by airplane and maintenance adjustment processes, to the values stated in the tecnical orders, they are operated in place and checked and adjusted. This process takes an average of more than 6 hours. It is possible to generate electricity with one or more of the methods described in table 1.

Table 1 ICE Waste Heat Recycling Technologies

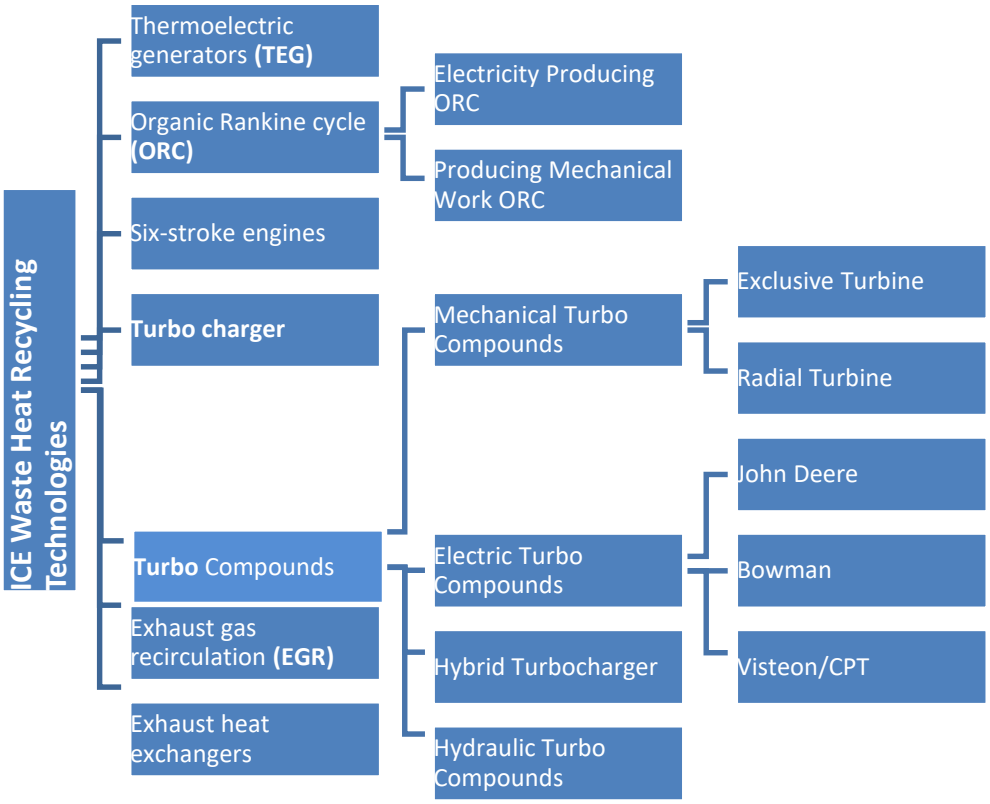

References

A. BBin Mamat, R. F. Martinez-Botas, S. Rajoo, A. Romagnoli ve S. Petrovic, «Waste heat recovery using a novel high performance low pressure turbine for electric turbocompounding in downsized gasoline engines: Experimental and computational analysis,» *Energy,* cilt 90, pp. 218-234, 2015

A. Rahman, F. Razzak , R. Afroz, M. AKM ve M. Hawlader, «Power Generation From Waste of IC Engines,» *Renewable and Sustainable Energy Reviews,* no. 51, pp. 382-395, 2015

A. S. Fayez, S. Laghrouche, A. Mehmood ve M. El Bagdouri, «Estimation of exhaust gas aerodynamic force on the variable geometry turbocharger actuator: 1D flow model approach,» *Energy Conversion and Management,* no. 84, pp. 436-447, 2014

A. T. Patterson, R. J. Tett ve J. McGuire, «Exhaust Heat Recovery using Electro-Turbogenerators,» SAE Paper, 2009.

B. d. In , H. i. Kim , J. w. Son ve K. h. Lee, «The study of a thermoelectric generator with various thermal conditions of exhaust gas from a diesel engine,» *International Journal of Heat and Mass Transfer,* no. 86, pp. 667-680, 2015

C. D. Rakopoulos ve E. G. Giakoumis, «Second-law analyses applied to internal combustion engines operation,» *Progress in Energy and Combustion Science,* no. 32, pp. 2-47, 2006.

C. O. Katsanos, D. T. Hountalas ve T. C. Zannis, «Simulation of a heavy-duty diesel engine with electrical turbocompounding system using operating charts for turbocharger components and power turbine,» *Energy Conversion and Management,* cilt 76, pp. 712-724, 2013.
C. Taylor, «Automobile engine tribology—design considerations for efficiency and durability,» *Wear,* cilt 221, pp. 1-8, 1998.
D. G. M. G.-B. M. Hatami, «A review of different heat exchangers designs for increasing the diesel exhaust waste heat recovery,» *Renewable and Sustainable Energy Reviews,* no. 37, pp. 168-181, 2014.
D. Rowe, «Thermoelectrics, An Environmentally-Friendly Source Of,» *Renewable Energy,* no. 16, pp. 1251-1256, 1999.
D. V. Singh ve E. Pedersen, «A review of waste heat recovery technologies for maritime applications,» *Energy Conversion and Management,* cilt 111, pp. 315-328, 2016.
E. W. Miller, T. J. Hendricks ve R. B. Peterson, «Modeling energy recovery using thermoelectric conversion Integrated with an organic rankine bottoming cycle,» *Journal of ELECTRONIC MATERIALS,* cilt 38, no. 7, 2009.
F. Vélez, J. J. Segovia, M. C. Martín, G. Antolína, F. Chejnec ve A. Quijanoa, «A technical, economical and market review of organic Rankine cycles for the conversion of low-grade heat for power generation,» *Renewable and Sustainable Energy Reviews,* cilt 16, pp. 4175-4179, 2012.
F. Vélez, J. J. Segovia, M. C. Martín, G. Antolína, F. Chejnec ve A. Quijanoa, «A technical, economical and market review of organic Rankine cycles for the conversion of low-grade heat for power generation,» *Renewable and Sustainable Energy Reviews,* cilt 16, pp. 4175-4179, 2012.
H. Aghaali ve H. E. Ångström, «A review of turbocompounding as a waste heat recovery system for internal combustion engines,» *Renewable and Sustainable Energy Reviews,* no. 49, pp. 813-824, 2015.
H. Akçay, Lpg ile çalışan buji ateşlemeli bir motorda, egzoz ve soğutma sisteminde kaybedilen ısının tej modülü ile kullanılabilir enerjiye dönüştürülmesi, Isparta: Süleyman Demirel Üniversitesi Fen Bilimleri Enstitüsü, 2015.
H. Caliskan, M. Ertunc Tat ve A. Hepbaşlı, «Performance assessment of an internal combustion engine at varying dead (reference) state temperatures,» *Applied Thermal Engineering,* pp. 3431-3436, 2009.
H. Chena, Q. Guob, L. Yangb, S. Liua, X. Xieb, Z. Chena ve Z. Liu, «A new six stroke single cylinder diesel engine referring Rankine cycle,» *Energy,* no. 87, pp. 336-342, 2015.
H. Chena, Q. Guob, L. Yangb, S. Liua, X. Xieb, Z. Chena ve Z. Liu, «A new six stroke single cylinder diesel engine referring Rankine cycle,» *Energy,* no. 87, pp. 336-342, 2015.
H. Lu, W. Ting, B. Shengqiang, X. Kangcong, H. Yingjie, G. Weimin, Y. Xianglin ve C. Lidong, «Experiment on thermal uniformity and pressure drop of exhaust heat exchanger for automotive thermoelectric generator,» *Energy,* no. 54, pp. 372-377, 2013.
H. Tian, X. Sun, Q. Jia, X. Liang, G. Shu ve X. Wang, «Comparison and parameter optimization of a segmented thermoelectric generator by using the high temperature exhaust of a diesel engine,» *Energy,* no. 84, pp. 121-130, 2015.
H. We, T. Zhu, G. Shu ve L. Tan, «Gasoline engine exhaust gas recirculation – A review,» *Applied Energy,* no. 99, pp. 534-544, 2012.
I. Briggs, «Modelling a turbogenerator for waste heat recovery on a diesel-electric hybrid bus».
I. G. M. Thompson, «Investigations into the effects of turbocompounding,» *Thesis (Ph.D.),* 2012.
J. C. Conklin ve J. P. Szybist, «A highly efficient six-stroke internal combustion engine cycle with water injection for in-cylinder exhaust heat recovery,» *Energy,* pp. 1658-1664, 2010.
J. Dellachà, L. Damiani, M. Repetto ve A. P. Prato, «Dynamic model for the energetic optimization of turbocompound hybrid powertrains,» *Energy Procedia,* cilt 45, pp. 1047-1056, 2014.
M. Ghazikhan, M. Hatami, D. D. Ganji, M. G. Bandpy, A. Behravan ve G. Shahi, «Exergy recovery from the exhaust cooling in a DI diesel engine for BSFC reduction purposes,» *Energy,* no. 65, pp. 44-51, 2014.

INFLUENCE OF LAND USE CHARACTERISTICS ON MICRO-CLIMATE DURING A HEAT WAVE EPISODE ON ITU CAMPUS

Yurdanur Ünal, Sema Topçu, Sibel Menteş, Cemre Yürük, Aslı İlhan, H. Perim Temizöz, Erkan Yılmaz, Onur Hakan Doğan, Gizem Buğday, Ceyhun Özcan, Tarık Kaytancı, Alperen Karataş, Umur Dinç, Ece Umut Kayaalp, Pelin Erdemir, Şevket Çağatay Ünal, Hümeyra Betül Akgül, Ayşe Ceren Saymaz, Fatma Başak Saka, Uğur Can Şimşek, Zeynep Feriha Ünal, Elif İnan, Nur Kapan, Deniz Hazel Diren and Gülsüm Somuncu

İstanbul Technical University, Department of Meteorological Engineering

ABSTRACT

Investigation of the effects of urban fabric on microclimate has been getting great interest since achievement of energy conservation and sustainability inside the cities become more crucial issues under the changing climate. The aim of this study is to investigate dependence of microclimatic conditions on the different surface characteristics. Therefore, a measurement campaign was carried out on the Campus of Istanbul Technical University on July 23-24, 2017. The 23 undergraduate and graduate students in ITU Meteorological Engineering Department took part in the measurement campaign. Field campaign conducted at 4 different locations of the campus, which have distinct land use characteristics. These locations are artificial lake, small pool nearby the Library building, forestry area and ARI2 techno city building. The campaign was executed on the 24th of July at 9 am till the next day. On that day, the city of Istanbul was under the influence of heat wave. Air temperature, humidity, wind speed at 1.5 m were measured hourly at each selected point and two more points which are 50 m and 100 m away from the central point on July 23-24, 2017. In addition, the surface brightness temperatures have been recorded using infrared thermometer on different urban materials such as lake surface, grass, asphalt, concrete surface and wall, pebble, pavement, which is specific to the measurement points and solar radiation was measured only at two locations: near lake and tall building.

Keywords: *Microclimate, land surface temperatures, urban heat island.*

INTRODUCTION

Urban population is growing faster than the world population so that the number of megacities is tripled in the past three decades. However, urbanization is one of the critical drivers of environmental problems in various scales. Rapid, poor planned expansion of the cities even further expose urban population to the effects of climate change which are elevated by the modifications on the surface radiation and energy balances. Therefore, microclimatic conditions of the cities are altered due to rapid urbanization. In urban areas, heat absorption in artificial surfaces modify the local climate characteristics and causes higher air temperatures compared to their surroundings, and affect the micro-circulation within the cities. So that temperature in the city centers become warmer than rural areas because of the urban constructions with high heat conductivities by creating urban heat island (Oke, 1982; 1987; Voogt and Oke, 2003). Usually, increased built-up areas and reduced vegetation cover in the city environment lead to heat storage, anthropogenic heat releases and eventually strengthening of the urban heat island intensity.

In the studies of Oke (1987) and Rajagopalan *et al*., (2014), it was shown that temperature difference between urban and rural areas peaks generally a few hours after sunset because the

city atmosphere is influenced by human induced heat transfer from the buildings and paved roads. Urban heat island intensity is best measured during calm, dry and clear sky days.
The urban heat island effects over the cities can be reduced by landscape design in urban planning. Susca et al., (2011) evaluated the positive effects of vegetation with a multi–scale approach in New York City. Sun and Chen (2012) suggested to increase water bodies in Beijing to mitigate the UHI effects. Furthermore, Santamouris (2014) has made a similar suggestion to reduce UHI effects such as urban cooling islands created by wetlands.

The heat waves are very likely to increase in both frequency and intensity due to the climate change (IPCC, 2013). Increase in urban population results in expansion of the built up areas, alters micro climate around cities and elevates urban heat island intensity. In urban regions, impacts of heat waves will escalate with the addition of the urban heat island because urban heat island raises nocturnal temperatures (Tan et al., 2010; Kunkel et al., 1996). Also, it is found that the added impact of heat waves is attributed to the lack of moistures in the city environment and the low wind speeds associated with the heat waves (Lin and Bou-Zeid, 2013) In this study, we explore the effect of the surface types on atmospheric conditions trough measured quantities on ITU Campus. Next section presents the measurement campaign and details. Then results and conclusions are followed.

MEASUREMENT CAMPAIGN

The investigation of the effects of urban fabric on microclimate is one of the purposes of the European Union ERAfrica project LOCLIM3. Therefore, in order to investigate dependence of microclimatic conditions on the surface characteristics, the measurement campaign was carried out in the Campus of Istanbul Technical University, which is a relatively green campus close to one of the business districts of Istanbul, Turkey. The 23 undergraduate and graduate students in ITU Meteorological Engineering Department took part in the measurement campaign.

Field campaign conducted at 4 different locations of the campus, which have distinct land use characteristics. Figure 1 illustrates the measurement location over ITU Campus map. These locations are artificial lake (south most point), small pond nearby the Library building (western part of the domain), forestry area (central part of the domain) and ARI2 techno city building (eastern part of the domain). At each location, the air measurements are taken 50 m and 100 m away from the central location to investigate difference in meteorological variables with increasing distance from a target location. For example, we wanted to measure the change of the lake effect on meteorological variables with distance.

Air temperature, humidity and wind speed were measured hourly at 1.5 m above the ground on each point. In addition, the surface brightness temperatures have been recorded using infrared thermometer on different urban materials such as lake surface, grass, asphalt, concrete surface and wall, pebble, shrub and pavement, which is specific to the measurement points, and solar radiation was measured only at two locations: near lake and tall building ARI2.

Figure 1. Location of the measurements on ITU Campus. Surface temperatures are measured along with the air measurements at the locations shown as magenta color.

The campaign was executed on the 24-25th of July and measurements are taken at each hour at least three times. On that day, the city of Istanbul was under the influence of heat wave.

RESULTS

The field measurements taken on July 23-24, 2017 on ITU campus are analyzed for air temperatures, surface temperatures, winds, humidity and solar radiation. Figure 2 demonstrate diurnal temperature, humidity and wind speed changes at six locations on the campus which are under the influence of different land use types. Even in a few km radii, the temperature difference can reach up to 7^{o}C because of the atmospheric circulation changes in micro scale. The hottest point of the campus among these location is the parking lot that is 100 m south of Techno-city ARI2 building. The coolest location is the lake region. The measurements in the forest area is slightly colder than the other locations. Relative humidity is quite high on the campus at 6 am, vary in the range of 85.63-99.98 and gradually decreases with increasing temperatures. Wind measurement shows that the weather is calm during the measurement day except that slightly windy measurements are obtained near ARI2 building because the measurements are subjected to the channeled winds between the two building and near the lake.

(a)

(b)

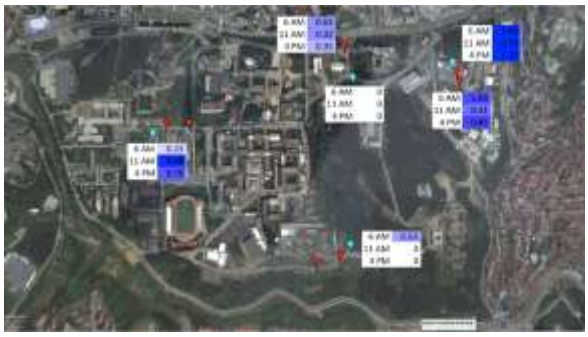

(c)

Figure 2. a) Air temperature, b) Relative humidity and c) Wind speed for 6 am, 11 am and 4 pm.

Solar radiation is measured by using KIMO solarimeter SL200 at 1.5 m above the ground. Diurnal variation of the measurement taken near the lake is illustrated in Figure 3. Maximum radiation amount, 892 W/m^2 is observed at 13:00.

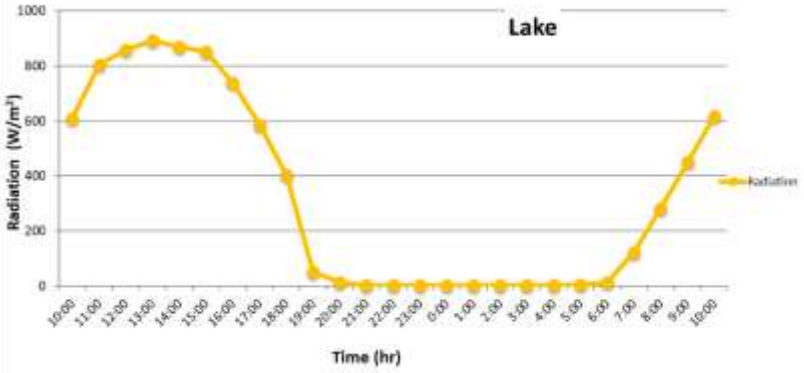

Figure 3. Diurnal variation of solar radiation on 24-25th of July at Lake point.

Diurnal variation of temperature, humidity and wind speed changes over the lake region are shown in Figure 4. The peak temperature near the lake is recorded around 15:00 while it is observed at 14:00 and 13:00, on the locations 50 m and 100 m away from the lake, respectively. Micro circulation between the lake and its surrounding delay the timing of the maximum air temperature. The temperatures at 50 m and 100 m start to be higher than the temperatures near the lake after midnight till noon. The difference at 100 m gets more than 3^{o}C before the sunrise. Similarly, the relative humidity is at least 10 percent higher near the lake than the other measurement points between midnight and sunrise. When radiation is absorbed by land, most of the net radiation is used for sensible heat transfer, only small amounts are used for latent heat transfer. As sensible heat transfer into the air is the dominant heat transfer, air temperatures increase over the land. Over water, much of the net radiation is used for evaporation and increase relative humidity near its vicinity. With little energy used for sensible heat transfer, air over water remains cooler than that over land, and this physical setting supports solenoidal circulation between lake and land. The wind speed therefore, gets stronger near the lake when the temperature difference between lake and land surfaces increases. Wind measurement around the lake depicts the similar picture. There is a significant difference on the winds near the lake during daytime which is as a result of the temperature difference over lake and the land areas in the vicinity. The relative humidity increase sharply from midnight to sunrise and 100% relative humidity value is recorded at 6:00 in the morning.

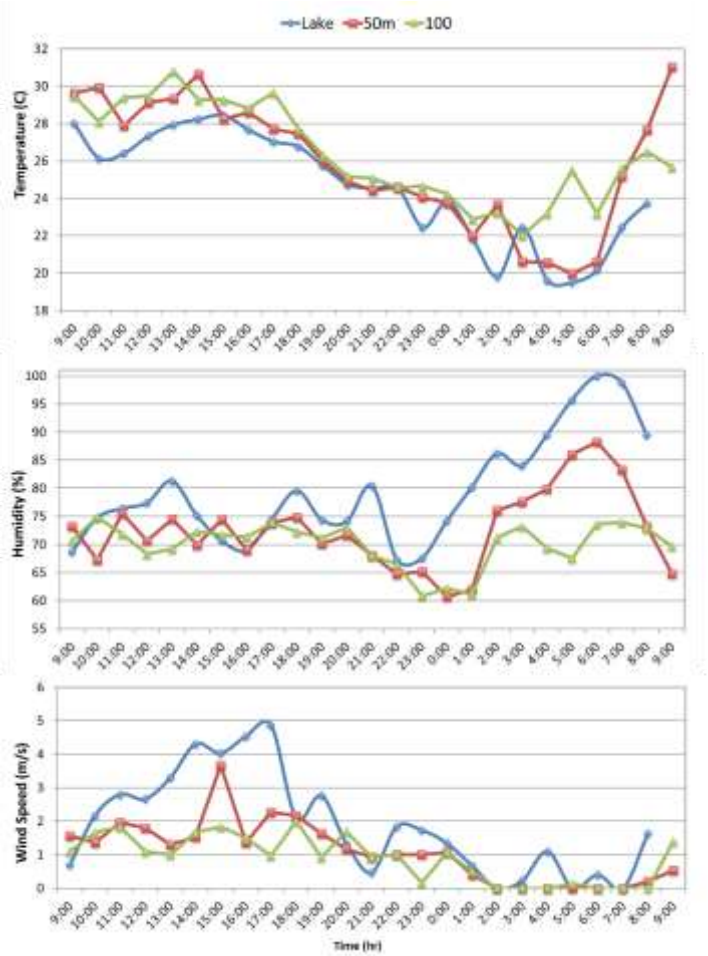

Figure 4. Diurnal change of temperature, humidity and wind speed on 24-25th of July at Lake point, 50 m south west and 100 m west of the central point.

Figure 5 shows the diurnal variations of the surface temperatures over different land covers. The upper panel corresponds to the measurements taken near the lake over water, pebble, soil and shrub. The temperature over soil, pebble and shrub are higher than the temperatures over water and the difference between the water and soil reaches up to 20ºC during the day time. On the other hand, the water surface temperatures become warmer between 8:00 pm and 6:00 am. The difference is recorded as 6ºC at 23:00. It is clear that the soil cools down at a slower rate than the pebble.

If the temperature and humidity observations (not shown) are compared among the locations such as technocity, library and forest, it is seen that the temperatures in the forest is a few degrees colder than the other locations and the maximum difference occurs around 10:00 in the morning. The relative humidity variations also illustrate different behavior in the forest. Over 10% difference is observed in the hours between 10:00 and 15:00.

The highest surface temperatures are recorded over asphalt next to the Technocity building, ARI2. For example, the surface temperature over asphalt is 53.8ºC at 2 pm while the air temperature at 1.5 m above the ground is 31ºC. The temperature change over the concrete is very similar to the asphalt except it is 4.5ºC lower than the asphalt around 2 pm. The temperatures are also taken on the south facing wall of the ARI2 building and over grass at 2 m south of the wall. During the measurement night, the sprinklers start to work after 9 pm and

the measurements over the grass corresponds to the wet grass temperatures afterwards. Hence, the grass temperatures remain approximately 19°C all night.

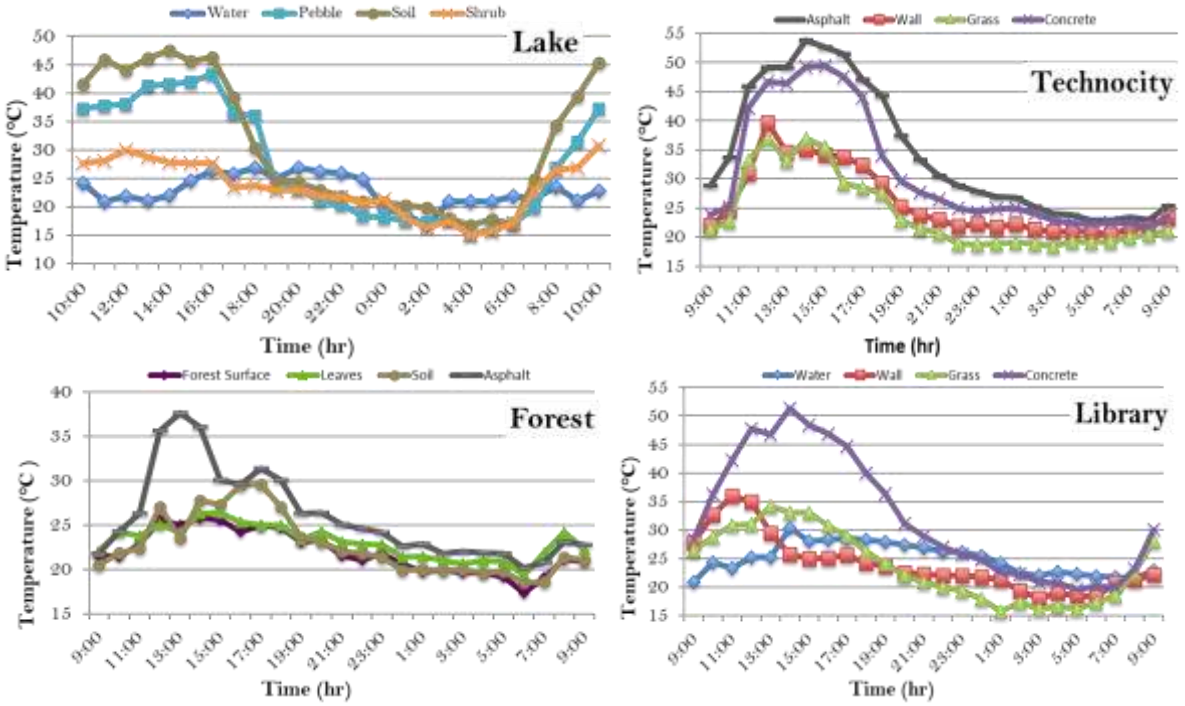

Figure 5. Diurnal change of surface temperatures over different surface types.

CONCLUSIONS

We investigate dependence of microclimatic conditions on the different surface characteristics during a heat wave episode day in Istanbul. The measurement campaign was carried out on the Campus of Istanbul Technical University on July 23-24, 2017 at 4 different locations, which have distinct land use characteristics. These locations are artificial lake, small pond nearby the Library building, forestry area and ARI2 techno city building. The results indicate that even in a few km radii, the temperature difference can reach up to 7°C. The hottest point of the campus among these location is the parking lot that is 100 m south of Techno-city ARI2 building. The comparison of the temperature and humidity observations reveals that the coolest location is the lake region and the forest area follows the lake region next. The temperatures in the forest is a few degrees colder than the other locations and the maximum difference occurs around 10:00 in the morning and the relative humidity difference is over 10% in the hours between 10:00 and 15:00. Relative humidity is quite high on the campus at 6 am, varies in the range of 85.63-99.98 over lake region and gradually decreases with increasing temperatures. Wind measurement shows that the weather is calm during day except slightly windy measurements are obtained near ARI2 building because the measurements are subjected to the channeled winds between the two building, and also near the lake during day time as a result of the different temperatures over the lake and the land surfaces. The timing of the maximum temperature is affected by the surface types which is attributable to the micro circulation between the different surface types, e.g. the lake and its vicinity. The maximum temperature is recorded around 15:00 at the observation point adjacent to the lake while it is at 14:00 and 13:00, on the locations 50 m and 100 m away from the lake, respectively. The temperatures become higher away from the lake after midnight till noon. The difference at 100 m change to more than 3°C before the sunrise. Similarly, the relative humidity is at least 10 percent higher near the lake than the other measurement points between midnight and sunrise. The highest surface temperatures (53.8°C at 2 pm) are recorded over asphalt next to the Technocity

building, ARI2. The temperature change over the concrete is very similar to the asphalt except it is 4.5^{o}C lower. On the other hand, temperatures over water and grass are always obtained lower than the other artificial surfaces, and controls the air temperatures in the vicinity. Our one-day measurement campaign results indicate that even in a few kilometer distance surface materials might have an influence on the radiation balance and change the micro circulation. Hence, in order to control the urban heat island and related problems associated with it, the most important mitigation strategy is not to disrupt the natural water cycle, and increase water bodies and green areas over the city.

ACKNOWLEDGMENT

This work is supported by The Scientific and Technological Research Council of Turkey (TUBITAK) with a project number 114Y047 and ERAfrica LOCLIM3. We would like to thank measurement team.

REFERENCES

IPCC. (2013). *Fifth Assessment Report* . Intergovernmental Panel on Climate Change,The Physical Science Basis.

Kunkel, K. E., Changnon, S.A., Reinke, B.C., and Arritt, R.W. (1996). The July 1995 heat wave in the Midwest: A climatic perspective and the critical factors, Bulletin of the American Meteorological Society, 77, 7, 1507-1518.

Li and Bou-Zeid. (2013). Synergistic Interactions between Urban Heat Islands and Heat Waves: The Impact in Cities Is Larger than the Sum of Its Parts, Journal of Applied Meteorology and Climatology, 52, 9, 2051-2064.

Oke, T. R. (1987). *Boundary Layer Climate* (2nd edition ed.). Routledge.

Oke, T. R. (1982). The energetic basis of the urban heat island. *Q. J. R. Meteorol. Soc. , 108*, 1-24.

Rajagopalan , P., Lim, K. C., and Jamei, E. (2014). Urban heat island and wind flow characteristics of a tropical city. *Solar Energy , 107*, 159-170.

Santamouris, M. (2014). Cooling the cities – A review of reflective and green roof mitigation technologies to fight heat island and improve comfort in urban environments. *Solar Energy , 103*, 682-703.

Sun, R., and Chen, L. (2012). How can urban water bodies be designed for climate adaptation? *Landscape and Urban Planning , 105*, 27-33.

Susca, T., Graffin, S. R., and Dell'Osso, G. R. (2011). Positive effects of vegetation: urban heat island and green roofs. *Environ. Pollut. , 159*, 2119-2126.

Voogt, J. A., and Oke, T. R. (2003). Thermal remote sensing of urban climates. *Remote Sensing of Environment , 86*, 370-384.

Tan, J.G., Zheng, Y.F., Tang, X, Guo, C.Y., Li, L.P., Song, G.X., Zhen, X.R., Yuan, D., Kalkstein, A.J., Li, F.R., … more. (2010) The urban heat island and its impact on heat waves and human health in Shanghai, Int. Journal of Biometeorology, 54, 1, 75-84

EFFECTS OF HIGH ALTITUDE IN MOUNTAINEERING

Buse Yakın[1] and Orhan Şen[1]

[1]Istanbul Technical University, Faculty of Aeronautics and Astronautics, Department of Meteorological Engineering, Maslak, Istanbul, Turkey, yakinbuse@gmail.com

Abstract

*L*ack of oxygen has several negative effects on health and it is called Hypoxia. High altitudes is the important factor for especially climbers due to Hypoxia. It's considered to be between 5,000 and 11,500 feet (1,524 and 3,505.2 m) above sea level. Very high altitude is any altitude between 11,500 and 18,000 feet (5,486.4 m), and extreme altitude is anything above 18,000 feet. At higher altitudes, atmospheric pressure decreases and it leads to having less oxygen. If climbers ascend to high altitudes, they will be in danger due to the change in altitude. Altitude sickness have many early and later symptoms such as headache, fatigue, insomnia, shortness of breath, nausea, loss of coordination, having blue or gray lips or fingernails, etc. There are three main types of high-altitude sickness; acute mountain sickness (AMS), high altitude pulmonary edema (HAPE), and high-altitude cerebral edema (HACE). AMS is the common sickness and causes headache, nausea, dizziness, difficulty sleeping, loss of appetite, weakness. HAPE is difficult to breathe because of fluid filling in lungs. A persistent cough, blue tinge to skin, chest tightness are effects of HAPE. HACE is the swelling of the brain caused by the lack of oxygen. It causes lack of coordination, feeling confused, hallucinations. Acclimatization is a progress that the body try to live with less oxygen because of high altitude. Effects of assimilation are increased heart rate, number of mitochondria in cell, oxidative enzymes. Prevention of altitude illness, climbers should ascend slowly, drink plenty water, eat digest food, don't consume alcohol, and drugs.

Keywords: *High Altitude, Mountaineering , Illness*

EFFECTS OF AIR POLLUTION AND METEOROLOGICAL CONDITIONS ON ASTHMA

Uğur Ömer Uçar[1] and Orhan Şen[1]

[1]Istanbul Technical University, Faculty of Aeronautics and Astronautics, Department of Meteorological Engineering, Maslak, Istanbul, Turkey, uguruomer@gmail.com

Abstract

Asthma is a chronic respiratory disease that recurrent attacks of breathlessness by the thickened airway walls and narrowed airways. World Health Organization estimates that there are 350 million asthma patients worldwide. Asthma's development has been correlated with many environmental circumstances and meteorological conditions such as air pollution, humidity and weather. Poor air conditions from pollutants such as traffic fumes or high ozone levels have been associated with both asthma development and increased asthma severity.

The Environment Protection Agency of United States have determined standards to minimize air pollution. Majority of cases in children in the United States occur in areas which do not fulfill EPA air quality standards. Air pollution is more frequent in low-welfare and low-income communities. Apart from air pollution, weather condition is also another factor causing asthma. It has been determined that cold, hot, and stormy weathers increase the attacks of asthmatic patients, although the reason and the functioning isn't completely explained. Main symptoms of asthma are wheezing, breathlessness and coughs. During asthma attack wheezing and couching become constant, heartbeats increases, patient could faint.

Keywords: *Asthma, Air Pollution, Weather*

ISBN 978-975561490-8